# NIST Special Publication 1276v2

# NIST Conference Papers
# Fiscal Year 2019
## Volume 2:
## Communications Technology Laboratory

Compiled and edited by:
Information Services Office

This publication is available free of charge from:
https://doi.org/10.6028/NIST.SP.1276v2

National Institute of
Standards and Technology
U.S. Department of Commerce

# NIST Special Publication 1276v2

# NIST Conference Papers Fiscal Year 2019

## Volume 2: Communications Technology Laboratory

Compiled and edited by:
Resources, Access, and Data Team
*Information Services Office*

This publication is available free of charge from:
https://doi.org/10.6028/NIST.SP.1276v2

April 2022


U.S. Department of Commerce
*Gina M. Raimondo, Secretary*

National Institute of Standards and Technology
*James K. Olthoff, Performing the Non-Exclusive Functions and Duties of the Under Secretary of Commerce for Standards and Technology & Director, National Institute of Standards and Technology*

**National Institute of Standards and Technology Special Publication 1276v2**
**Natl. Inst. Stand. Technol. Spec. Publ. 1276v2, 488 pages (April 2022)**
**CODEN: NSPUE2**

**This publication is available free of charge from:**
**https://doi.org/10.6028/NIST.SP.1276v2**

## Foreword

NIST is committed to the idea that results of federally funded research are a valuable national resource and a strategic asset. To the extent feasible and consistent with law, agency mission, resource constraints, and U.S. national, homeland, and economic security, NIST will promote the deposit of scientific data arising from unclassified research and programs, funded wholly or in part by NIST, except for Standard Reference Data, free of charge in publicly accessible databases. Subject to the same conditions and constraints listed above, NIST also intends to make freely available to the public, in publicly accessible repositories, all peer-reviewed scholarly publications arising from unclassified research and programs funded wholly or in part by NIST.

This Special Publication represents the work of researchers at professional conferences, as reported in Fiscal Year 2019.

More information on public access to NIST research is available at https://www.nist.gov/open.


## Key words

NIST conference papers; NIST research; public access to NIST research.

# Table of Contents

Guerrieri, Jeffrey. "RF Characterization of Latex-Coated Pyramidal Absorber." Paper presented at 34th Annual Symposium of the Antenna Measurements Techniques Association (AMTA), Bellevue, WA, United States. October 21, 2012 - October 26, 2012. . . . . SP-1

Coder, Jason; Novotny, David; Guerrieri, Jeffrey; Francis, Michael; Stillwell, Brian. " An Improved Antenna Gain Extrapolation Measurement." Paper presented at 34th Annual Symposium of the Antenna Measurements Techniques Association (AMTA), Bellevue, WA, United States. October 21, 2012 - October 26, 2012.. . . . . SP-6

Novotny, David; Gordon, Joshua; Coder, Jason; Guerrieri, Jeffrey; Francis, Michael. "Use of a Laser Tracker to Actively Coordinate the Motion of a 3-Meter Industrial Robot to Within 50 Microns." Paper presented at 2013 Coordinate Metrology Systems Conference, San Diego, CA, United States. July 22, 2013 - July 26, 2013. . . . . SP-11

Guerrieri, Jeffrey. "International Comparison of Ku-band Standard Gain Horn Characterization." Paper presented at 8th European Conference on Antennas and Propagation (EuCAP 2014), The Hague, Netherlands. April 6, 2014 - April 11, 2014. . . . . SP-18

Gordon, Joshua; Novotny, David. "A Non-contact Machine Vision System for the Precision Alignment of mm-Wave Antennas in all Six Degrees of Freedom." Paper presented at 91st ARFTG Microwave Measurement Symposium, Tucson, AZ, United States. October 12, 2014 - October 17, 2014. . . . . SP-20

Novotny, David; Guerrieri, Jeffrey; Gordon, Joshua. "Antenna Alignment and Positional Validation of a mmWave Antenna System Using 6D Coordinate Metrology." Paper presented at 91st ARFTG Microwave Measurement Symposium, Tucson, AZ, United States. October 12, 2014 - October 17, 2014.. . . . . SP-26

Gordon, Joshua; Novotny, David; Curtin, Alexandra. "A Single-Pixel Touchless Laser Tracker Probe." Paper presented at 2015 Coordinate Metrology Systems Conference (CMSC), Hollywood , FL, United States. July 20, 2015 - July 24, 2015.. . . . . SP-32

Francis, Michael; Wittmann, Ronald; Gordon, Joshua; Novotny, David. " Generalized Probe-Position Compensation Methods for Near-Field Antenna Measurements." Paper presented at 37th Annual Meeting and Symposium of the Antenna Measurement Techniques Association (AMTA 2015), Long Beach, CA, United States. October 11, 2015 - October 16, 2015. . . . . SP-42

Guerrieri, Jeffrey; Francis, Michael; Wittmann, Ronald. "Consensus Value Methods to Compile On-Axis Gain Measurement Results." Paper presented at 37th Annual Meeting and Symposium of the Antenna Measurement Techniques Association (AMTA 2015), Long Beach, CA, United States. October 11, 2015 - October 16, 2015. . . . . SP-45

Novotny, David; Gordon, Joshua; Francis, Michael; Wittmann, Ronald; Curtin, Alexandra; Guerrieri, Jeffrey. "Antenna Measurement Implementations and Dynamic Positional Validation Using a Six Axis Robot." Paper presented at 37th Annual Meeting and Symposium of the Antenna Measurement Techniques Association (AMTA 2015), Long Beach, CA, United States. October 11, 2015 - October 16, 2015. . . . . SP-50

Coder, Jason; Jacobs, Ryan; Musser, Vivian. "Spectrum Sensing with WLAN Access Points." Paper presented at 2016 33rd National Radio Science Conference (NRSC), Boulder, CO, United States. January 6, 2016 - January 9, 2016. . . . . SP-56

Williams, Dylan; Chamberlin, Richard; Zhao, Wei; Cheron, Jerome; Miguel, Urteaga. "Verification of a Foundry-Developed Transistor Model Including Measurement Uncertainty." Paper presented at 2016 International Microwave Symposium IMS, San Francisco, CA, United States. May 22, 2016 - May 27, 2016.. . . . . SP-58

Guerrieri, Jeffrey. "Comparison of Consensus Value Methods Used to Compile On-Axis Gain Measurement Results." Paper presented at 10th European Conference on Antennas and Propagation (EuCAP 2016), Davos, Switzerland. April 10, 2016 - April 15, 2016.. . . . . SP-62

Novotny, David; Francis, Michael; Wittmann, Ronald; Gordon, Joshua; Guerrieri, Jeffrey; Curtin, Alexandra. "Multi-purpose Configurable Range for Antenna Testing Up To 220 GHz*." Paper presented at 11th European Conference on Antennas and Propagation (EuCAP 2016), Davos, Switzerland. April 10, 2016 - April 15, 2016. . . . . SP-66

Cui, Xiaohai; Meng, Yu; Judaschke, Rolf; Ruehaak, Juergen; Crowley, Thomas;

Ginley, Ronald. "International Comparison of WR 15 (50 to 75 GHz) Power Measurements among NIST, NIM, PTB and NMC, A*STAR." Paper presented at 2016 Conference on Precision Electromagnetic Measurements (CPEM 2016), Ottawa, ON, Canada. July 10, 2016 - July 15, 2016.. . . . . SP-69

Papazian, Peter; Choi, Jae-Kark; Senic, Jelena; Jeavons, Peter; Gentile, Camillo; Golmie, Nada; Sun, Roy; Novotny, David; Remley, Catherine. "Calibration of Millimeter-wave Channel Sounders for Super-resolution Multipath Component Extraction." Paper presented at 10th European Conference on Antennas and Propagation (EuCAP 2016), Davos, Switzerland. April 10, 2016 - April 15, 2016. . . . . SP-71

Ribeiro, Diogo; Remley, Catherine; Hale, Paul; Wang, Chih-Ming; Williams, Dylan. "Comparison of Timebase Interpolation Methods for Traceable, Wideband mm-Wave Communication Signals." Paper presented at 87th ARFTG Microwave Measurement Conference, 2016, San Francisco, CA, United States. May 27, 2016 - May 27, 2016. . . . . SP-76

Wilson, Perry. "Acoustic and Electromagnetic Reverberation Chambers: Similarities and Differences." Paper presented at 7th Asia-Pacific International Symposium on Electromagnetic Compatibility & Signal Integrity and Technical Exhibition (APEMC 2016) , Shenzhen, China. May 18, 2016 - May 21, 2016.. . . . . SP-80

Wilson, Perry; Gordon, Joshua; Novotny, David; Guerrieri, Jeffrey. "Antenna Metrology for 100-500 GHz: A New Approach." Paper presented at 7th Asia-Pacific International Symposium on Electromagnetic Compatibility & Signal Integrity and Technical Exhibition (APEMC 2016) , Shenzhen, China. May 18, 2016 - May 21, 2016. . . . . SP-83

Dennis, Tasshi. "Saturation in Solar Cells from Ultra-Fast Pulsed-Laser Illumination." Paper presented at 43rd IEEE Photovoltaic Specialists Conference, Portland, OR, United States. June 5, 2016 - June 10, 2016.. . . . . SP-86

Dennis, Tasshi; Yasanayake, Chanud; Gerke, Tim; Payne, Alex; Eng, Lars; Fisher, Brent; Meitl, Matt. "A Programmable Solar Simulator for Realistic Seasonal, Diurnal, and Air-Mass Testing of Multi- Junction Concentrator Photovoltaics." Paper presented at 43rd IEEE Photovoltaic Specialists Conference, Portland, OR, United States. June 5, 2016 - June 10, 2016.. . . . . SP-90

Gentile, Camillo; Senic, Jelena; Papazian, Peter; Choi, Jae-Kark; Remley,

Catherine. "Pathloss Models for Indoor Hotspot Deployment at 83.5 GHz." Paper presented at , Washington, DC, United States. December 4, 2016 - December 8, 2016. . . . . SP-96

Williams, Dylan; Chamberlin, Richard; Zhao, Wei; Cheron, Jerome; Miguel, Urteaga. "The Role of Measurement Uncertainty in Achieving First-Pass Design Success." Paper presented at 2016 IEEE Compound Semiconductor Integrated Circuit Symposium (CSICS), Austin, TX, United States. October 23, 2016 - October 26, 2016. . . . . SP-102

Francis, Michael; Novotny, David; Gordon, Joshua; Curtin, Alexandra; Wittmann, Ronald. "Gain Comparison of a 3D-Printed Horn and an Electroformed Horn." Paper presented at 38th Annual Meeting and Symposium of the Antenna Measurement Techniques Association (AMTA), Austin, TX, United States. October 30, 2016 - November 4, 2016. . . . . SP-106

Gordon, Joshua; Holloway, Christopher; Simons, Matthew. "An Overview of Atom-Based SI-Traceable Electric-Field Metrology." Paper presented at 2016 Antenna Measurement Techniques Association, Austin, TX, United States. October 30, 2016 - November 4, 2016. . . . . SP-110

Ballato, A; Williams, Dylan; Lukaszek, T; Cho, F. "Power Flow Angle and Pressure Dependence of SAW Propagation Characteristics in Quartz." Paper presented at IEEE Ultrasonics Symposium, 1981, Chicago, IL, United States. October 14, 1981 - October 16, 1981. . . . . SP-116

Williams, Dylan; Cho, F. "Numerical Analysis of Doubly Rotated Cut SAW Devices." Paper presented at 34th Annual Symposium on Frequency Control, Philadelphia, PA, United States. May 28, 1980 - May 30, 1980. . . . . SP-120

Ginley, Ronald; Williams, Dylan; Ridler, N; Hesler, J; Kerr, Anthony; Pollard, R. " Towards Standardized Waveguide Sizes and Interfaces for Submillimeter Wavelengths." Paper presented at 21st International Symposium on Space Terahertz Technology 2010 (ISSTT 2010), Oxford, United Kingdom. March 23, 2010 - March 25, 2010.. . . . . SP-125

Mateu, Jordi; Collado, C; Hueltes, A; Garcia-Pastor, D; Perera, R; Joshi, Nikhil; Lu, Xifeng; Orloff, Nathan; Booth, James. "Comprehensive circuit model of autolimiting superconductor devices." Paper presented at Applied

Superconductivity Conference (ASC 2016), Denver, CO, United States. September 4, 2016 - September 9, 2016.. . . . . SP-130

Sun, Ruoyu; Papazian, Peter; Senic, Jelena; Lo, Yeh; Choi, Jae-Kark; Remley, Catherine; Gentile, Camillo. "Design and Calibration of a Double-directional 60 GHz Channel Sounder for Multipath Component Tracking*." Paper presented at 11th European Conference on Antennas and Propagation (2017 EUCAP), Paris, France. March 19, 2017 - March 24, 2017.. . . . . SP-134

Senic, Damir; Remley, Catherine; Williams, Dylan; Ribeiro, Diogo; Wang, Chih-Ming; Holloway, Christopher. "Radiated Power Based on Wave Parameters at Millimeter-wave Frequencies for Integrated Wireless Devices." Paper presented at 88th ARFTG Microwave Measurements Conference, Austin, TX, United States. December 8, 2016 - December 9, 2016.. . . . . SP-139

Ginley, Ronald. "Kicking the Tires of the NIST Microwave Uncertainty Framework, Part 1." Paper presented at 88th ARFTG Microwave Measurement Conference, Austin, TX, United States. December 8, 2016 - December 9, 2016. . . . . SP-143

Senic, Damir; Cavaliere, Diego; North, Matt; Becker, Maria; Remley, Catherine; Wang, Chih-Ming; Holloway, Christopher. "Isotropy Study for Over-the-Air Measurements in a Loaded Reverberation Chamber." Paper presented at 2017 IEEE International Symposium on Electromagnetic Compatibility and Signal/ Power Integrity, Washington D.C., DC, United States. August 7, 2017 - August 11, 2017. . . . . SP-147

Guerrieri, Jeffrey. "Validation of Robotics for Antenna Measurements." Paper presented at 11th European Conference on Antennas and Propagation (EUCAP 2017), Paris, France. March 19, 2017 - March 24, 2017. . . . . SP-153

Ginley, Ronald; Ridler, Nick. "A Review of the IEEE 1785 Standards for Rectangular Waveguides above 110 GHz." Paper presented at 89th ARFTG Microwave Measurement Conference, Honolulu, HI, United States. June 9, 2017 - June 9, 2017.. . . . . SP-156

Avolio, Gustavo; Williams, Dylan; Frey, Michael; Streett, Sarah; Schreurs, Dominique; Ferrero, Andrea; Dieudonne, Michael. "Software Tools for Uncertainty Evaluation in VNA Measurements: A Comparative Study." Paper presented at 89th ARFTG Microwave Measurement Conference, Honolulu, HI,

United States. June 9, 2017 - June 9, 2017.. . . . . SP-160

Jacobs, Ryan; Coder, Jason; LaSorte, Nickolas. "Verification of Coexistence Measurement Methods: Radiated Anechoic and Open Environment." Paper presented at 2017 IEEE International Symposium on Electromagnetic Compatibility and Signal/Power Integrity, Washington, DC, United States. August 7, 2017 - August 11, 2017.. . . . . SP-167

Wilson, Perry. "Multiple Sources in a Reverberant Environment: The Cocktail Party EffectÂ”." Paper presented at 2017 International Symposium on Electromagnetic Compatibility (EMC Europe 2017), Angers, France. September 4, 2017 - September 7, 2017.. . . . . SP-173

Remley, Catherine; Gentile, Camillo; Zajic, Alenka; Quimby, Jeanne. "Methods for Channel Sounder Measurement Verification." Paper presented at IEEE Vehicular Technology Conference, Toronto, Canada. September 24, 2017 - September 27, 2017.. . . . . SP-176

Gordon, Joshua; Novotny, David; Wittmann, Ronald; Francis, Michael; Guerrieri, Jeffrey; Lavanya, Periasamy; Gasiewski, Albin. "Assessment of a 3D-Printed Aluminum Corrugated Feed Horn at 118.7503 GHz." Paper presented at , Atlanta, GA, United States. October 15, 2017 - October 20, 2017.. . . . . SP-180

Allman, Michael; Novotny, David; Gordon, Joshua; Curtin, Alexandra; Sandwith, Scott. "Serial Robotic Arm Joint Characterization Measurements for Antenna Metrology." Paper presented at 39th Annual Meeting and Symposium of the Antenna Measurement Techniques Association (AMTA), Atlanta, GA, United States. October 15, 2017 - October 20, 2017.. . . . . SP-186

Horansky, Robert; Mujumdar, Mohit; Williams, Dylan; Remley, Catherine; Novotny, David; Francis, Michael. "Filtering Antenna-to-Antenna Reflections in Antenna Extrapolation Measurements." Paper presented at 39th Annual Meeting and Symposium of the Antenna Measurement Techniques Association (AMTA), Atlanta, GA, United States. October 15, 2017 - October 20, 2017.. . . . . SP-193

Novotny, David; Gordon, Joshua; Allman, Michael; Guerrieri, Jeffrey; Curtin, Alexandra; Hassett, Kim; McAdams, George; Ton, Quang. "A Multi-Robot Large Antenna Positioning System for Over-The-Air Testing at the National Institute of Standards and Technology." Paper presented at 39th Annual Meeting and

Symposium of the Antenna Measurement Techniques Association (AMTA), Atlanta, GA, United States. October 15, 2017 - October 20, 2017.. . . . . SP-198

Novotny, David; Gordon, Joshua; Allman, Michael; Guerrieri, Jeffrey; Curtin, Alexandra. "Three Antenna Ranges Based on Articulated Robotic Arms at the National Institute of Standards and Technology: Usability for Over-the-Air and Standard Near-Field Measurements." Paper presented at 2017 IEEE Conference on Antenna Measurements and Applications (CAMA), Tsukuba, Japan. December 4, 2017 - December 6, 2017. . . . . SP-204

Gordon, Joshua; Holloway, Christopher; Simons, Matthew. "Rydberg Atom Electric-Field Metrology." Paper presented at 90th ARFTAG Conference, Boulder, CO, United States. November 28, 2017 - December 1, 2017. . . . . SP-208

Becker, Maria; Horansky, Robert; Senic, Damir; Neylon, Vincent; Remley, Catherine. "Spatial Channels for Wireless Over-the-Air Measurements in Reverberation Chambers." Paper presented at 12th European Conference on Antennas and Propagation (EuCAP 2018), London, United Kingdom. April 9, 2018 - April 13, 2018.. . . . . SP-212

Sun, Roy; Papazian, Peter; Senic, Jelena; Gentile, Camillo; Remley, Catherine. " Angle- and Delay-Dispersion Characteristics in a Hallway and Lobby at 60 GHz." Paper presented at 12th European Conference on Antennas and Propagation (EuCAP 2018), London, United Kingdom. April 9, 2018 - April 13, 2018. . . . . SP-217

Ginley, Ronald. "Kicking the Tires of the NIST Microwave Uncertainty Framework, Part 2." Paper presented at 90th ARFTG Microwave Measurement Conference, Boulder, CO, United States. November 28, 2017 - December 1, 2017.. . . . . SP-222

Ginley, Ronald. "Establishing Traceability for SOLT Calibration Kits." Paper presented at 90th ARFTG Microwave Measurement Conference, Boulder, CO, United States. November 28, 2017 - December 1, 2017. . . . . SP-226

Coder, Jason; Ma, Yao. "On the Susceptibility of Coded OFDM to Interference: A Simulation Study." Paper presented at USNC-URSI National Radio Science Meeting 2018, Boulder, CO, United States. January 4, 2018 - January 7, 2018. . . . . SP-230

Kord, Azizollah. "On the Impacts of In-Band LTE Emissions." Paper presented at USNC-URSI National Radio Science Meeting 2019, Boulder, CO, United States.

January 4, 2018 - January 7, 2018. . . . . SP-232

Sanders, Aric; Ginley, Ronald; Long, Christian; Drisko, Jasper; Orloff, Nathan; Chamberlin, Richard. "Qualitative Multidimensional Calibration Comparison." Paper presented at 90th ARFTG Microwave Measurement Conference, Boulder, CO, United States. November 28, 2017 - December 1, 2017. . . . . SP-234

Orloff, Nathan; Drisko, Jasper; Stelson, Angela; Little, Charles; Booth, James; Mateu, Jordi; Long, Christian. "How to extract distributed circuit parameters from the scattering parameters of a transmission line." Paper presented at 90th ARFTG Microwave Measurement Conference, Boulder, CO, United States. November 28, 2017 - December 1, 2017. . . . . SP-238

Hagerstrom, Aaron; Long, Christian; Orloff, Nathan; Booth, James; Marksz, Eric. " Characterization of Transmission Lines with Nonlinear Dielectric Materials." Paper presented at 90th ARFTG Microwave Measurement Conference, Boulder, CO, United States. November 28, 2017 - December 1, 2017. . . . . SP-243

Diener, Joseph; Quimby, Jeanne; Remley, Catherine; Elsherbeni, Atef. " Millimeter-wave Frequency FDTD Simulation for Error Vector Magnitude of Modulated Signals." Paper presented at 2018 International Applied Computational Electromagnetics Society (ACES) Symposium, Denver, CO, United States. March 24, 2018 - March 29, 2018. . . . . SP-249

Basta, Nina; Drisko, Jasper; Hagerstrom, Aaron; Orlicki, Joshua; Sietins, Jennifer; Knorr, Jr., Daniel; Garboczi, Edward; Long, Christian; Orloff, Nathan. " Determining Carbon Fiber Composite Loading with Flip-Chip Measurements to 110 GHz." Paper presented at 48th European Microwave Conference, Madrid, Spain. September 23, 2018 - September 27, 2018.. . . . . SP-251

Senic, Damir; Remley, Catherine; Becker, Maria; Holloway, Christopher. "Spatial Uniformity Study in a Loaded Reverberation Chamber at Millimeter-Wave Frequencies." Paper presented at 2018 IEEE Symposium on Electromagnetic Compatibility, Signal Integrity and Power Integrity (EMC, SI & PI), Long Beach, CA, United States. July 30, 2018 - August 3, 2018.. . . . . SP-255

Guerrieri, Jeffrey; Novotny, David; Gordon, Joshua; Curtin, Alexandra; Allman, Michael; Hassett, Kim; Ton, Quang. "The New Large Antenna Positioning System for Over-The-Air Testing at the National Institute of Standards and Technology."

Paper presented at 12th European Conference on Antennas and Propagation (EuCAP 2018), London, United Kingdom. April 9, 2018 - April 13, 2018. . . . . SP-261

Ladbury, John. "Problems with Stirred Immunity Measurements in a Reverberation Chamber: Corrections to DO- 160G Section 20.6." Paper presented at 2018 IEEE International Symposium on Electromagnetic Compatibility & 2018 IEEE Asia-Pacific Symposium on Electromagnetic Compatibility (EMC/ APEMC) : 2018 Joint IEEE EMC & APEMC, Suntec City, Singapore. May 14, 2018 - May 17, 2018. . . . . SP-266

Horansky, Robert; Meurs, Thomas; Wang, Chih-Ming; Becker, Maria; Remley, Catherine. "Statistical Considerations for Total Isotropic Sensitivity of Wireless Devices Measured in Reverberation Chambers." Paper presented at 2018 International Symposium on Electromagnetic Compatibility (EMC), Amsterdam, Netherlands. August 27, 2018 - August 30, 2018. . . . . SP-270

Jargon, Jeffrey; Williams, Dylan. "A New Calibration Method for Achieving High Insertion-Loss Measurements with a Vector Network Analyzer." Paper presented at 91st ARFTG Microwave Measurement Symposium, Philadelphia, PA, United States. June 15, 2018 - June 15, 2018. . . . . SP-276

Stelson, Angela; Little, Charles; Orloff, Nathan; Long, Christian; Booth, James. " Measuring Ion-Pairing in Buffer Solutions with Microwave Microfluidics." Paper presented at 2018 IEEE/MTT-S International Microwave Biomedical Conference, Philadelphia, PA, United States. June 14, 2018 - June 15, 2018. . . . . SP-280

Jamroz, Benjamin; Williams, Dylan; Remley, Catherine; Horansky, Robert. " Importance of Preserving Correlations in Error-Vector-Magnitude Uncertainty." Paper presented at 91st ARFTG Microwave Measurement Symposium, Philadelphia, PA, United States. June 15, 2018 - June 15, 2018. . . . . SP-283

Ribeiro, Diogo; Williams, Dylan; Chamberlin, Richard; Carvalho, Nuno. "Impact of Phase Calibration on EVM Measurement Quality." Paper presented at 91st ARFTG Microwave Measurement Symposium, Philadelphia, PA, United States. June 15, 2018 - June 15, 2018. . . . . SP-287

Soares Boaventura, Alirio De Jesus; Williams, Dylan; Avolio, Gustavo; Hale, Paul. "Traceable Characterization of Broadband Pulse Waveforms Suitable for Cryogenic Josephson Voltage Applications." Paper presented at 2018 International

Microwave Symposium, Philidelphia, PA, United States. June 10, 2018 - June 15, 2018. . . . . SP-291

Holloway, Christopher; Simons, Matthew; Gordon, Joshua. "Development and Applications of a Fiber-Coupled Atom-Based Electric Field Probe." Paper presented at 2018 International Symposium on Electromagnetic Compatibility (EMC), Amsterdam, Netherlands. August 27, 2018 - August 30, 2018. . . . . SP-295

Sahoo, Anirudha; Hall, Timothy; Hagwood, Robert. "Optimal Dynamic Spectrum Access Scheme for Utilizing White Space in LTE Systems." Paper presented at IEEE Wireless Communications and Networking Conference (WCNC), Marrakech, Morocco. April 15, 2019 - April 19, 2019. . . . . SP-300

Williams, Dylan; Cheron, Jerome; Jamroz, Benjamin; Chamberlin, Richard. "On-Wafer Transistor Characterization to 750 GHz: the approach, results, and pitfalls." Paper presented at BiCMOS and Compound Semiconductor Integrated Circuits and Technology Symposium (BCICTS), San Diego, CA, United States. October 15, 2018 - October 17, 2018. . . . . SP-308

Ma, Yao; Young, William; Anderson, Eric; Coder, Jason. "Probability of Coexistence of LTE-LAA and WLAN Systems Based on Delay Constraints." Paper presented at The 27th International Conference on Computer Communications and Networks (ICCCN 2018), Hangzhou, China. July 30, 2018 - August 2, 2018. . . . . SP-312

Ma, Yao. "Analysis of Channel Access Priority Classes in LTE-LAA Spectrum Sharing System." Paper presented at The 27th International Conference on Computer Communications and Networks (ICCCN 2018), Hangzhou, China. July 30, 2018 - August 2, 2018.. . . . . SP-321

Simons, Matthew; Kautz, Marcus; Gordon, Joshua; Holloway, Christopher. " Uncertainties in Rydberg Atom-based RF E-field Measurements." Paper presented at 2018 International Symposium on Electromagnetic Compatibility (EMC), Amsterdam, Netherlands. August 27, 2018 - August 30, 2018.. . . . . SP-328

Holloway, Christopher; Anderson, Dave; Raithel, Georg. "High-resolution antenna near-field imaging and sub-THz measurements with a small atomic vapor-cell sensing element." Paper presented at 2018 11th Global Symposium on Millimeter Waves (GSMM), Boulder, CO, United States. May 22, 2018 - May 24, 2018. . . . . SP-333

Marksz, Eric; Long, Christian; Booth, James; Takeicjo, Ichiro; Orloff, Nathan. " Frequency- and electric field-dependent physical model of ferroelectric materials in the tens of GHz." Paper presented at IEEE MTT-S International Microwave Workshop Series on Advanced Materials and Processes for RF and THz Applications, Ann Arbor, MI, United States. July 16, 2018 - July 18, 2018. . . . . SP-336

Cheron, Jerome; Williams, Dylan; Lukasik, Konstanty; Chamberlin, Richard; Jamroz, Benjamin; Grossman, Erich; Wiatr, Wojciech; Schreurs, Dominique. " Propagation of Compact-Modeling Measurement Uncertainty to 220 GHz Power-Amplifier Designs." Paper presented at 2018 Asia-Pacific Microwave Conference (APMC), Kyoto, Japan. November 6, 2018 - November 9, 2018.. . . . . SP-339

Souryal, Michael; Nguyen, Thao; LaSorte, Nickolas. "3.5 GHz Federal Incumbent Protection Algorithms." Paper presented at IEEE International Symposium on Dynamic Spectrum Access Networks (DySPAN), Seoul, Republic of Korea. October 22, 2018 - October 25, 2018. . . . . SP-342

Novotny, David; Gordon, Joshua. "Practical Considerations When Using Commercial Robotic Arms for Antenna Metrology." Paper presented at 2018 International Symposium on Antennas and Propagation (ISAP), Busan, Republic of Korea. October 23, 2018 - October 26, 2018. . . . . SP-347

Caromi, Raied; Souryal, Michael; Yang, Wen-Bin. "Detection of Incumbent Radar In the 3.5 GHZ CBRS Band." Paper presented at 6th IEEE Global Conference on Signal and Information Processing (GlobalSIP 2018), Anaheim, CA, United States. November 26, 2018 - November 28, 2018.. . . . . SP-349

Holloway, Christopher; Simons, Matthew; Anderson, Dave; Raithel, Georg. " High-resolution near-field imaging and far-field antenna measurements with atomic sensors." Paper presented at 2018 International Symposium on Electromagnetic Compatibility (EMC), Amsterdam, Netherlands. August 27, 2018 - August 30, 2018.. . . . . SP-354

Puls, Audrey. "Antenna Radiation Pattern Measurements Using a Reverberation Chamber." Paper presented at 40th Annual Meeting and Symposium of the Antenna Measurement Techniques Association (AMTA 2018), Williamsburg, VA, United States. November 4, 2018 - November 9, 2018. . . . . SP-357

Vouras, Peter. "Gradient-Based Solution of Maximum Likelihood Angle

Estimation for Virtual Array Measurements." Paper presented at 6th IEEE Global Conference on Signal and Information Processing (GlobalSIP 2018), Anaheim, CA, United States. November 26, 2018 - November 28, 2018.. . . . . SP-363

Yuffa, Alexey; Jamroz, Benjamin; Rezac, Jake; Williams, Dylan. "A Systematic Study: Channel Sounding via Modal Expansion." Paper presented at 2018 Antenna Measurement Techniques Association Symposium (AMTA), Williamsburg, VA, United States. November 4, 2018 - November 9, 2018. . . . . SP-368

Simons, Matthew; Kautz, Marcus; Haddab, Abdulaziz; Gordon, Joshua; Holloway, Christopher; Crowley, Thomas. "Rydberg Atom-based RF Power Measurements." Paper presented at 40th Annual Meeting and Symposium of the Antenna Measurement Techniques Association (AMTA 2018), Williamsburg, VA, United States. November 4, 2018 - November 9, 2018.. . . . . SP-373

Gordon, Joshua; Novotny, David; Allman, Michael. "Precision Optical Antenna Alignment System for Tracking Antennas in 6-DOF." Paper presented at 40th Annual Meeting and Symposium of the Antenna Measurement Techniques Association (AMTA 2018), Williamsburg, VA, United States. November 4, 2018 - November 9, 2018. . . . . SP-377

Sahoo, Anirudha; Nguyen, Thao; Hall, Timothy. "A Practical Approach to Place Coastal Sensors for Spectrum Sharing in the 3.5 GHz Band." Paper presented at IEEE Wireless Communications and Networking Conference (WCNC), Marrakech, Morocco. April 15, 2019 - April 19, 2019. . . . . SP-382

Yuffa, Alexey; Wittmann, Ronald; Francis, Michael; Gordon, Joshua; Novotny, David. "Some Advantages of Using Bi-directional S-Parameters in Near-Field Measurements." Paper presented at 40th Annual Meeting and Symposium of the Antenna Measurement Techniques Association (AMTA 2018), Williamsburg, VA, United States. November 4, 2018 - November 9, 2018. . . . . SP-389

Rosete, Andre; Baker, Kenneth; Ma, Yao. "Using LZMA Compression for Spectrum Sensing with SDR Samples." Paper presented at 2018 9th IEEE Annual Ubiquitous Computing, Electronics & Mobile Communication Conference (UEMCON), New York City, NY, United States. November 8, 2018 - November 10, 2018. . . . . SP-395

Caromi, Raied; Mink, John; Wedderburn, Cosburn; Souryal, Michael; El Ouni,

Naceur. "3.5 GHz ESC Sensor Test Apparatus Using Field-Measured Waveforms." Paper presented at WInnComm 2018, Melbourne, FL, United States. November 14, 2018 - November 15, 2018.. . . . . SP-401

Caromi, Raied; Souryal, Michael. "Detection of Incumbent Radar in the 3.5 GHz CBRS Band Using Support Vector Machines." Paper presented at Sensor Signal Processing for Defence (SSPD), Brighton, United Kingdom. May 9, 2019 - May 10, 2019. . . . . SP-411

Jargon, Jeffrey; Williams, Dylan; Sanders, Aric. "Three-Port Vector-Network-Analyzer Calibrations using the NIST Microwave Uncertainty Framework." Paper presented at 92nd ARFTG Microwave Measurement Conference, Orlando, FL, United States. January 19, 2019 - January 22, 2019.. . . . . SP-416

Hagwood, Robert; Sahoo, Anirudha; Hall, Timothy. "Analytical Modeling of White Space Utilization for a Dynamic Spectrum Access System." Paper presented at IEEE Wireless Communications and Networking Conference, Marrakech, Morocco. April 15, 2019 - April 19, 2019. . . . . SP-420

Quimby, Jeanne; Michelson, David; Bennai, Mustapha; Remley, Catherine; Kast, Joshua; Weiss, Alec. "Interlaboratory Millimeter-Wave Channel Sounder Verification." Paper presented at 13th European Conference on Antennas and Propagation (EuCAP), Krakow, Poland. March 31, 2019 - April 5, 2019. . . . . SP-428

Weiss, Alec; Williams, Dylan; Quimby, Jeanne; Leonhardt, Rodney; Choi, Thomas; Chen, Zihang; Remley, Catherine; Molisch, Andreas; Jamroz, Benjamin; Rezac, Jake; Vouras, Peter. "Large-Signal Network Analysis for Over-the-Air Test of Up-Converting and Down-Converting Phased Arrays." Paper presented at 2019 International Microwave Symposium, Boston, MA, United States. June 2, 2019 - June 7, 2019.. . . . . SP-433

Sanders, Aric; Williams, Dylan; Kast, Joshua; Remley, Catherine; Horansky, Robert. "Large-Signal-Network-Analyzer Phase Calibration on an Arbitrary Grid." Paper presented at 2019 International Microwave Symposium, Boston, MA, United States. June 2, 2019 - June 7, 2019.. . . . . SP-437

Jargon, Jeffrey; Koepke, Amanda; Hale, Paul. "Investigating the Effects of IF Bandwidth and Averaging on Calibrated Scattering-Parameter Measurements." Paper presented at 93rd ARFTG Microwave Measurement Conference, Boston,

MA, United States. June 7, 2019 - June 7, 2019. . . . . SP-441

Soares Boaventura, Alirio De Jesus; Williams, Dylan; Hale, Paul; Gustavo, Avolio. "An Approach for Characterizing the Frequency Response of Sampling-Oscilloscopes Using a Large- Signal Network Analyzer." Paper presented at International Microwave Symposium Digest, 2019, Boston, MA, United States. June 2, 2019 - June 7, 2019.. . . . . SP-445

Jamroz, Benjamin; Williams, Dylan; Rezac, Jake; Frey, Michael; Koepke, Amanda. "Accurate Monte Carlo Uncertainty Analysis for Multiple Measurements of Microwave Systems." Paper presented at 2019 International Microwave Symposium, Boston, MA, United States. June 2, 2019 - June 7, 2019. . . . . SP-449

Sanders, Aric; Bass, John; Bhutani, Arpita; Ho, Mary; Booth, James. "Machine Learning in a Quality-Managed RF Measurement Workflow." Paper presented at 93rd ARFTG Microwave Measurement Conference, Boston, MA, United States. June 7, 2019 - June 7, 2019.. . . . . SP-453

Ma, Yao; Coder, Jason. "Analysis of Generalized CCA Errors and Mitigation in LTE-LAA Spectrum Sharing System." Paper presented at IEEE Global Communications Conference (GLOBECOM 2019)Â , Waikoloa, HI, United States. December 9, 2019 - December 13, 2019. . . . . SP-457

Mosleh, Somayeh; Ma, Yao; Coder, Jason; Perrins, Erik; Liu, Lingjia. "Enhancing LAA Co-existence Using MIMO Under Imperfect Sensing." Paper presented at 2019 IEEE Global Communications Conference: Workshop on Advancements in Spectrum Sharing, Waikoloa, HI, United States. December 13, 2019 - December 13, 2019. . . . . SP-464

# RF CHARACTERIZATION OF LATEX-COATED PYRAMIDAL ABSORBER

Jeff Guerrieri, Josh Gordon, David Novotny, Jason Coder, Brian Stillwell
National Institute of Standards and Technology
325 Broadway
Boulder, CO 80305

**ABSTRACT**

**We present a test procedure and results that compare RF performance of traditional pyramidal absorber to that with latex coating. Measurements were performed from 5 to 15 GHz, but the same measurement methodology can be applied to other frequency bands. Absorber with protective coating is being used in place of traditional absorber for outdoor antenna measurement facilities to reduce degradation of the absorber performance in harsh environments. Knowledge of the RF performance characteristics of coated absorber is especially necessary when it is used to replace uncoated absorber in an operational antenna measurement facility. Measurements are performed with a simple measurement setup based on a vector network analyzer and broadband horn antennas. Results from bi-static and mono-static measurements are presented.**

**Keywords**: bi-static, latex-coated absorber, mono-static, pyramidal absorber

## 1. Introduction

This paper describes the measurement techniques and setup for RF characterization of latex-coated pyramidal absorber.[1] The RF performance of the latex-coated absorber is compared to that of the same, non-coated absorber. Measurements were performed with bi-static and mono-static setups using dual ridge horns from 5 to 15 GHz.

## 2. Measurement Set Up

A reference signal, $S_{21ref}$, was established for the measurements by use of two dual ridge horns separated by 2 m, illustrated in Figure 1(a). This reference signal level is needed to align the horns in the bi-static and mono-static measurement setups. An accurate boresight alignment of the horns was performed with the overlay imaging aligner technique describe at AMTA 2011[2], shown in Figure 2 .



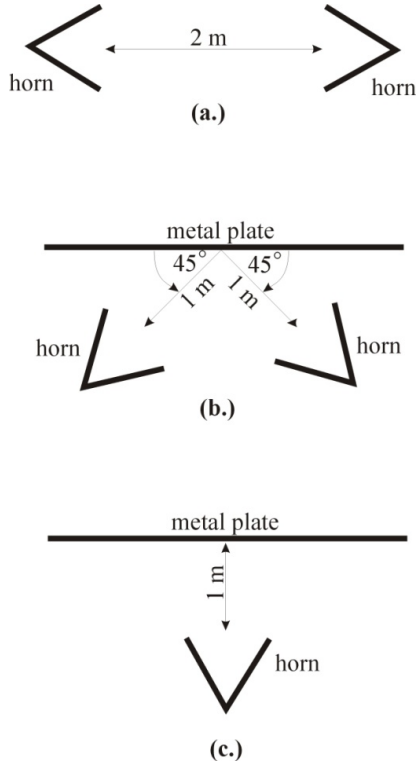


**Figure 1. Setup for reference signal (a), setup for bi-static measurements (b), and setup for mono-static measurements (c).**

A non-reflective measurement test fixture was constructed from non-metallic foam, shown in Figure 3. For the bi-static measurements the horns were placed at 45 degree angles 1 m from the fixture, illustrated in Figure 1(b). An alignment fixture with guides, shown on the test fixture in Figure 3 was used to the align horns. For the mono-static measurements, a single horn was placed at normal incidence at 1 m from the fixture, illustrated in Figure 1(c). The alignment fixture was used to the aligned the horn.



Guerrieri, Jeffrey.
"RF Characterization of Latex-Coated Pyramidal Absorber."
Paper presented at 34th Annual Symposium of the Antenna Measurements Techniques Association (AMTA), Bellevue, WA, United States.
October 21, 2012 - October 26, 2012.

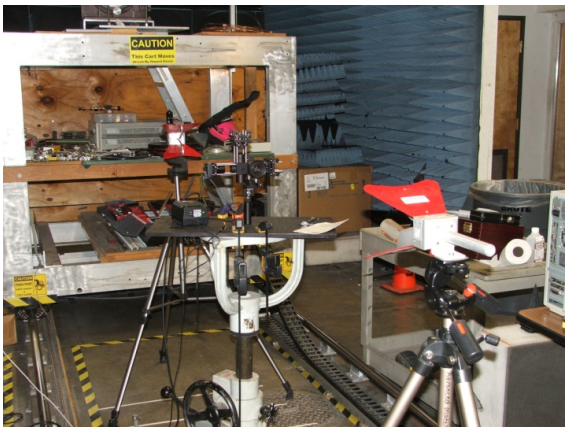


**Figure 2. Optical setup for overlay image aligner.**

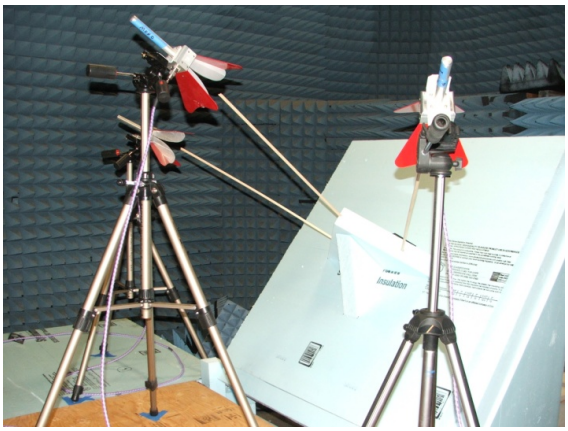

**Figure 3. Test fixture with alignment guides for both bi-static and mono-static measurements.**

A 1.2 m x 1.2 m (4 ft x 4 ft) metal plate placed in the test fixture, shown in Figure 4, was used as a scattering reference to verify the alignment of the setups for both bi-static and mono-static measurements. The correct distances for the bi-static and mono-static setups can be determined by comparing the time-domain transform of the transmitted signal with that of the direct horn-to-horn signal.

A simple application of the Friis transmission formula and time gating can correct for small differences in distances between setups and assure signal alignment. Starting with the Friis equation:

$$\frac{P_{recv}}{P_{trans}} = \left|S_{21}\right|^2 \propto \frac{G_{trans}G_{recv}}{d^2}L_{excess}, \qquad (1)$$

where $S_{21}$ is the transmission coefficient; $G_x$ are the gains for the transmit and receive antennas; d is the separation distance; and $L_{excess}$ is the loss due to the absorber ($L_{excess}$ = 1 for the maximum transmission cases).

Rewriting (1), we can see that if the distance-transmission coefficient product is a constant, so offsets from the reference distance can be corrected by altering the power level by the distance offset:

$$\left|S_{21}\right|^2 d^2 \propto G_{trans}G_{recv}L_{excess},$$

$$\frac{\left|S_{21test}\right|^2 d_{test}^2}{L_{test}} = \frac{\left|S_{21ref}\right|^2 d_{ref}^2}{1} \propto G_{trans}G_{recv},$$

$$L_{test} = \frac{\left|S_{21test}\right|^2 d_{test}^2}{\left|S_{21ref}\right|^2 d_{ref}^2}.$$

The data are time gated to remove any secondary reflections leaving:

$$L_{test_{Bi-static}} = \frac{\text{TimeGated}\left[\left|S_{21test}\right|^2 d_{test}^2\right]}{\text{TimeGated}\left[\left|S_{21ref}\right|^2 d_{ref}^2\right]}. \qquad (2)$$

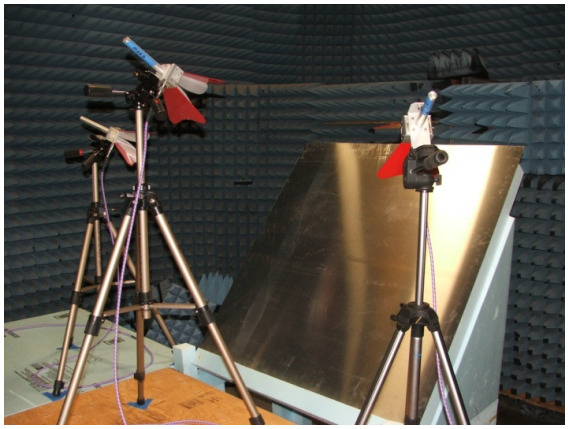

**Figure 4 Reference metal plate showing both bi-static and mono-static setups.**

Figure 5(a) shows that the time-domain transform of the bi-static signal, $S_{21\ bi\text{-}static\ metal}$, is earlier in time than the horn-to-horn signal, $S_{21\ ref}$, by 0.017 ns. This equates to a distance of 5.05 mm, therefore, the bi-static test distance should be 1.995 m. This is corrected with a 0.017 ns time delay, shown in Figure 5(b). The match in magnitude for the two signals also indicates polarization alignment.



Guerrieri, Jeffrey.
"RF Characterization of Latex-Coated Pyramidal Absorber."
Paper presented at 34th Annual Symposium of the Antenna Measurements Techniques Association (AMTA), Bellevue, WA, United States.
October 21, 2012 - October 26, 2012.

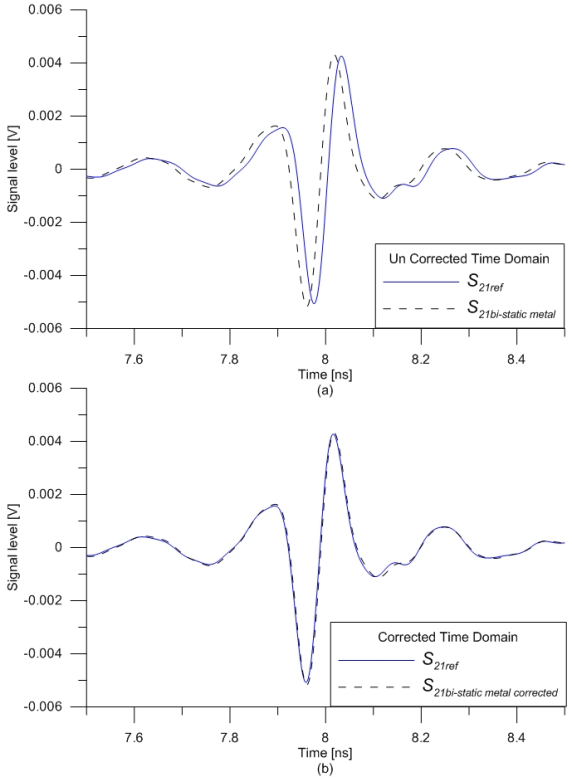


**Figure 5. Uncorrected bi-static time-domain signal (a) and corrected bi-static time domain signal (b).**

The mono-static measurement is also compared to $S_{21ref}$ to insure the alignment is correct and that propagation is normal to the plate. A slightly different method is required for the mono-static case. The $S_{11}$ signal contains the reflection from the cable-to-horn interface as well as the reflections from the plate. A background subtraction, where there is no target or support structure in front of the antenna is used to subtract out the systematic reflections from the antenna:

$$L_{mono-static} = \frac{\text{TimeGate}\left[\left|S_{11test} - S_{11background}\right|^2 d_{test}^2\right]}{\text{TimeGate}\left[\left|S_{21ref}\right|^2 d_{ref}^2\right]} \quad (3)$$

Figure 6(a) shows is the time-domain transform of the mono-static measurement showing all the systematic reflections from the antenna. These are removed by subtracting a measurement into empty space (without the plate or test stand). Figure 6(b) shows the area of interest from (a), similar to the bi-static case. The subtracted reflections show a 0.065 ns delay with respect to the reference. This equates to a 19.5 mm increase in the propagation path with respect to $S_{21ref}$. A distance correction, $d_{test}$ , of 2.015 m, is used to correct the mono-static measurements, shown in Figure 6(c).

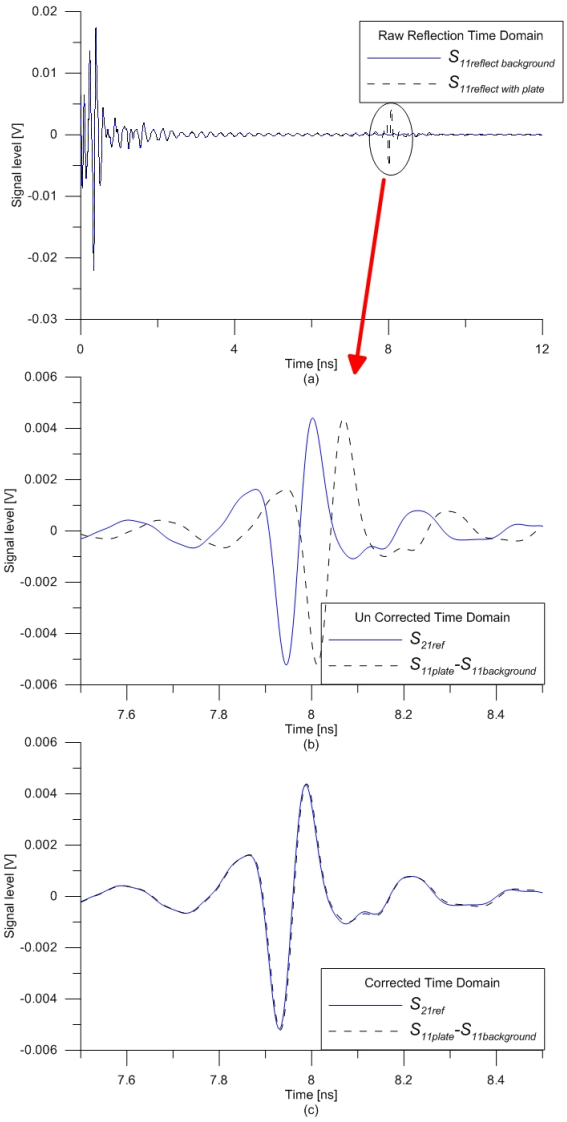


**Figure 6. Raw mono-static time-domain signal (a), uncorrected mono-static time domain signal (b) and corrected mono-static time domain signal (c).**



Guerrieri, Jeffrey.
"RF Characterization of Latex-Coated Pyramidal Absorber."
Paper presented at 34th Annual Symposium of the Antenna Measurements Techniques Association (AMTA), Bellevue, WA, United States.
October 21, 2012 - October 26, 2012.

### 3. Measurements

Bi-static and mono-static measurements were performed without the test fixture to establish the measurement background noise floor. Then the measurements were also performed on just the test fixture.

A 1.2 m x 1.2 m (4 ft x 4 ft) test sample of non-coated 8 inch absorber was constructed and placed in the sample fixture, shown in Figure 7. The bi-static and mono-static measurements were performed.

A 1.2 m x 1.2 m (4 ft x 4 ft) test sample of the latex coated 8 inch absorber was constructed and placed in the test fixture, shown in Figure 8. The bi-static and mono-static measurements were performed on the coated absorber.

**Figure 7. Non-coated absorber in the test fixture.**

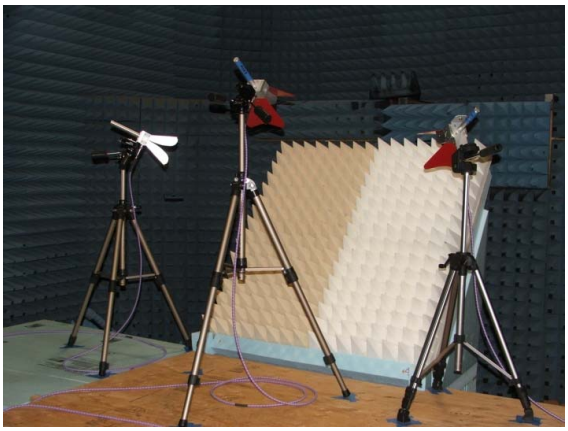

**Figure 8. Latex-coated absorber in the test fixture.**

### 4. Measurement Results

The graph in Figure 9 displays the frequency-domain results for the bi-static measurements. The measurement results were normalized to that of the metal plate. These measurements have an uncertainty of ±1 dB. The measurements results with just the test fixture are only -30 dB.

With the non-coated absorber sample on the test fixture the measured results are -34 dB from 5 to 8 GHz and better than -39 dB from 8 to 15 GHz. The measured results for the coated absorber in the fixture are similar to that of the traditional absorber. From 5 to 9 GHz the measured results are -33 dB. From 9 to 15 GHz the reflection levels are lower than -40 dB.

The graph in Figure 10 displays the frequency-domain measurement results from the mono-static measurements. These measurements results were also normalized to that of the metal plate. The measurement results for the test fixture are -35 dB.

The measurement results for the non-coated absorber in the test fixture are lower than -40 dB from 5 to 15 GHz. The results for the coated absorber are lower than -37 dB from 5 to 7 GHz and lower than -40 dB from 7 to 15 GHz.

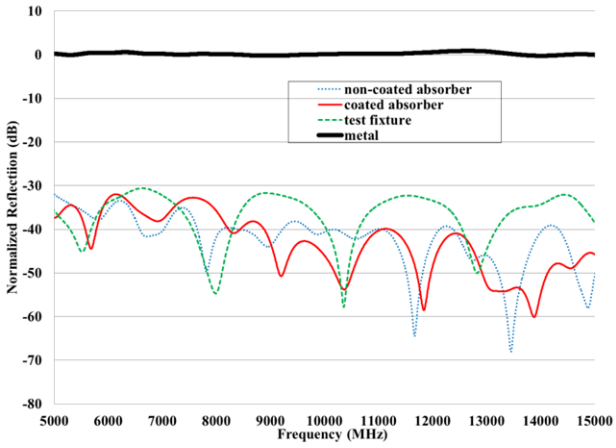


**Figure 9. Bi-static measurement results.**



Guerrieri, Jeffrey.
"RF Characterization of Latex-Coated Pyramidal Absorber."
Paper presented at 34th Annual Symposium of the Antenna Measurements Techniques Association (AMTA), Bellevue, WA, United States.
October 21, 2012 - October 26, 2012.

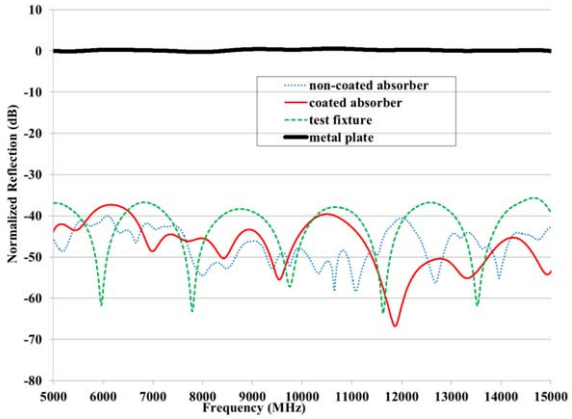


**Figure 10. Mono-static measurement results.**

## 5. Uncertainty

The major contributors to the uncertainty are horn alignment, polarization mismatch and edge diffraction due to the limited size of the metal plate. This is seen in the difference between bi-static and mono-static measurements of the metal plate, shown in Figure 11, which show an uncertainty of 1 dB.

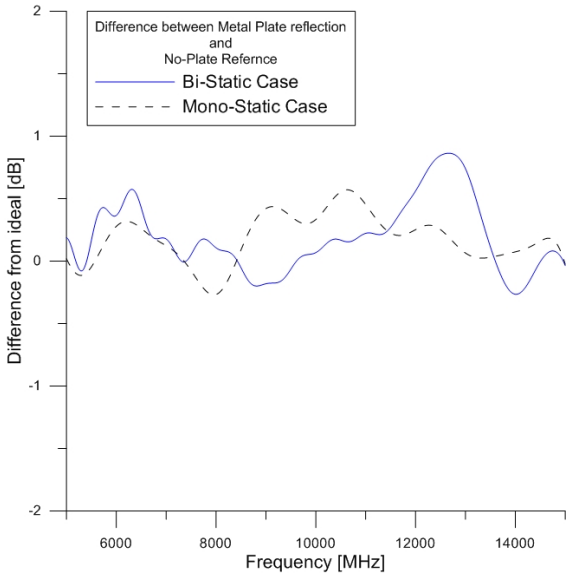


**Figure 11. The difference between the metal plate and the reference measurements.**

## 6. Summary

This paper discusses results for RF performance characterization of 8 inch pyramidal absorber with and without latex coating. A proven technique was used to perform measurements from 5 to 15 GHz. The results of these measurements do not indicate degradation of RF performance for the given latex-coated absorber.

## 7. References

[1] Novotny, D. R., Johnk, R. T., Ondrejka, A., "Low Cost Broadband Absorber Measurements", AMTA Proceedings 2000, pp. 357-362, Philadelphia, PA.

[2] Gordon, J. A., Novotny, D. R., "Alignment of Two mmWave Antennas Using an Improved Optical Alignment Tool", AMTA Proceedings 2011, pp. 245-250, Englewood, CO.

## 8. Acknowledgements

The authors wish to thank the U. S. Department of the Army's Electronic Proving Grounds in Ft. Huachuca, Arizona for sponsorship of this research project.



Guerrieri, Jeffrey.
"RF Characterization of Latex-Coated Pyramidal Absorber."
Paper presented at 34th Annual Symposium of the Antenna Measurements Techniques Association (AMTA), Bellevue, WA, United States.
October 21, 2012 - October 26, 2012.

# AN IMPROVED ANTENNA GAIN EXTRAPOLATION MEASUREMENT

Jason B. Coder, David R. Novotny, Jeffrey R. Guerrieri, Michael H. Francis, Brian C. Stillwell
National Institute of Standards and Technology, Mail Stop 818.02, 325 Broadway
Boulder, CO 80305 USA

## ABSTRACT

**An improved system for antenna gain extrapolation measurements is proposed. The improved method consists of a vector network analyzer, a pair of RF optical links, and a pair of waveguide mixers. This change in hardware equates to a system with better dynamic range and a simplified reference measurement. We present a detailed description of the new extrapolation measurement setup, discuss the advantages and disadvantages, and validate the new setup by measuring the gain of an antenna previously measured with a traditional extrapolation setup. After presenting the comparison, we will discuss applications of this measurement system that extend beyond extrapolation gain measurements (e.g., spherical near- and far-field pattern measurements).**

**Keywords**: Antenna Gain, Extrapolation Measurement, Spherical Near-Field, Vector Network Analyzer

## 1.0 Introduction

There are several methods of measuring the gain of an antenna. The main difference between these methods is where the measurements take place: anechoic chamber, outdoor area test site (OATS), or extrapolation range. Regardless of the environment used, the concept is the same.

First introduced in [1], the three antenna measurement method enables the determination of absolute antenna gain and polarization given three antennas. To use the three antenna method, one need not know the gain of any of the antennas. This feature is what made the method more appealing than the older "substitution" method, where an antenna was compared to a known standard. The original three antenna method has been modified and expanded to be applicable to any of the measurement environments listed above.

The first application of the three antenna method to extrapolation gain measurements was in [2], where it was shown that if a sufficient number of measurements were taken in the near-field of the antenna, the gain data could be extrapolated to the far-field of the antenna. This "conversion" from the near-field to the far-field was accomplished using a polynomial curve fitting process. Later, in [3], this procedure was summarized and updated. Since then, the NIST extrapolation gain measurement has essentially remained essentially unchanged.

This traditional method was still used by NIST through 2010, when the system was retired. In its place, a new measurement system was developed using modern hardware. Extrapolation gain measurements made using the original hardware configuration can still provide accurate data, as the technique and mathematics behind the measurement have not changed.

The result of modernizing the measurement system is a reduced number of components, a simplified reference/calibration procedure, improved dynamic range, and improved system stability over time and distance. The key components of this measurement system are a vector network analyzer (VNA), a pair of RF optical links, and a pair of waveguide mixers.

In this paper, a detailed description of the new extrapolation measurement setup is presented after a brief overview of the original system. A WR-42 standard-gain horn that was measured on the original system is then measured on the new system. The results of this measurement are compared as a means for validating the modern measurement setup. Finally, the advantages and disadvantages of the modern setup are discussed along with potential applications to other measurements.

## 2.0 Original NIST Measurement Setup

The goal of any extrapolation gain measurement is to measure the received power as a function of separation distance, given a constant transmitting power. To accomplish this, the ratio of transmitting and receiving power, and the separation distance must be measured.

In the original NIST measurement setup, outlined in Figure 1, measurement of the transmitted and received power was accomplished through a dual channel receiver (denoted as RCV) that measured the difference between the two signals. Harmonic mixers were used as needed to adapt the receiver to the desired frequency range. These mixers could be either coaxial or waveguide.

A rotary vane attenuator (RVA) was placed after the coupler to keep the received signal (on the load side) in the linear range of the receiver. This RVA was adjusted for each pair of horns/frequency range. It was critical that the RVA be precisely calibrated and tuned for each



Coder, Jason; Novotny, David; Guerrieri, Jeffrey; Francis, Michael; Stillwell, Brian.
"An Improved Antenna Gain Extrapolation Measurement."
Paper presented at 34th Annual Symposium of the Antenna Measurements Techniques Association (AMTA), Bellevue, WA, United States.
October 21, 2012 - October 26, 2012.

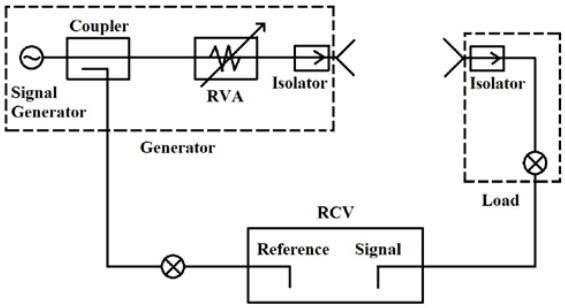


**Figure 1 – Original NIST extrapolation gain measurement setup.**

measurement. The uncertainty associated with the calibration of the RVA was accounted for in the final gain uncertainty, and typically added 0.05 dB to the unexpanded uncertainty.

To ensure the signal generator and receiver were working at the same frequency, they were phase-locked together. The phase locked signal was strictly a reference signal and contained no a priori information regarding the list of frequencies to be measured. This forced the measurement system to be locked to a single frequency because any sudden change in the signal generator's frequency would force the receiver to lose phase lock and measure the signal at an incorrect frequency.

To establish a reference for the received signal, the horns were removed and the generator and load sides were directly connected. This is commonly referred to as a "generator-load measurement." This measurement characterized the losses in the generator, load components, and cables, allowing them to be separated from the losses associated with the antennas being measured.

As with the extrapolation measurement, the receiver had to be kept in its linear range during this reference measurement. This meant the RVA must be adjusted again to have a higher attenuation during the generator-load measurement.

Data acquisition was accomplished by a computer connected to the receiver. Software was written to query the receiver, query the laser being used to measure the distance between the two antennas, and control the motor that physically moves the antennas apart. As the extrapolation measurement took place, the motor was set to a constant speed and the software constantly queried the laser until a specified interval was reached (e.g., every 2 mm). At this time software queried the receiver for the current value of received power.

Once the extrapolation measurement was complete, the data were saved. This process was repeated for each of the three antenna pairs. Once data had been collected for each pair, it was processed through software that calculates the far-field data based on a polynomial curve fit. From this, individual antenna gains can be found. This numerical process is detailed in [3].

### 3.0 An Improved Hardware Configuration

RF equipment has improved significantly over the last three decades. These improvements have translated into equipment with increased accuracy, dynamic range, and faster acquisition times.

Despite the change in measurement hardware, the goal of the extrapolation measurement remains the same: transmit a signal through one antenna, measure the amplitude and phase (if desired) of the received signal through another. This measurement requires a source and receiver phase locked through a reference. These components are available individually, but also as a single unit, vector network analyzer (VNA).

Though the network analyzer consolidates some of the hardware into a single unit, gain extrapolation measurements are commonly conducted over a span of meters. Coaxial cables may be used to cross the distance between the VNA and antennas, but their inherent attenuation negatively impacts the dynamic range and phase stability. In their place, a set of optical links can be used.

As with coaxial cables, optical links are subject to drift as a function of temperature and physical movement. Care must be exercised when selecting a pair of optical links for this measurement to ensure that the laser/oscillator are temperature controlled. Any systematic losses of the optical links (or coaxial cables) will be accounted for with a generator-load measurement. Any losses or phase changes that occur between the antenna and reference measurements (e.g., change in ambient temperature) will appear in the measurement data as an error. This error is accounted for in the measurement uncertainty.

The configuration of the network analyzer will depend on the exact hardware used. For simple setups, an $S_{21}$ (transmission) measurement may be sufficient. More complicated setups may require directly measuring the receiver monitoring the transmitter ($RX_A$) and the measurement receiver ($RX_B$).

Figure 2 shows the new extrapolation measurement setup that utilizes a VNA and optical links. The optical links are denoted as E/O or O/E, indicating electrical-to-optical or optical-to-electrical. In this measurement we also utilized a frequency mixer. The VNA was placed behind the generator with one port directly connected to it. The

Coder, Jason; Novotny, David; Guerrieri, Jeffrey; Francis, Michael; Stillwell, Brian.
"An Improved Antenna Gain Extrapolation Measurement."
Paper presented at 34th Annual Symposium of the Antenna Measurements Techniques Association (AMTA), Bellevue, WA, United States.
October 21, 2012 - October 26, 2012.

receiving antenna (the "load") is located 0.5-4 m from the generator. The optical links used to span this distance do not operate at a high enough frequency to directly couple the RF in this antenna measurement. To accommodate this, a frequency mixer was used to down-convert the received signal and feed it into the optical link. After the down-converted signal is passed through the optical link the network analyzer measures the IF signal.

The use of a frequency mixer is optional. It is shown here because the frequencies of interest exceed the capabilities of the optical links. To use mixers in this setup, the VNA analyzer must be capable of sourcing and receiving from the mixers. Modern network analyzers are available with options that make this possible (e.g., frequency offset mode and a configurable test set). Alternative hardware setups for VNAs that aren't capable of working with mixers are possible, but the number of components increases significantly. These configurations are beyond the scope of this paper.

A comparison of Figure 1 and Figure 2 reveals that the use of a RVA is no longer required. The receivers on the VNA have a linear range large enough to accommodate the wide variation in power between the generator-load measurement and the extrapolation measurement. The lack of a RVA will also have a positive impact on the uncertainty budget. This is reflected in the sample budget shown in Section 5.

The comparison also shows that the isolators have been replaced with fixed-value attenuators. This change is optional. The goal of both devices is to improve the impedance match between the measurement system and the antennas.

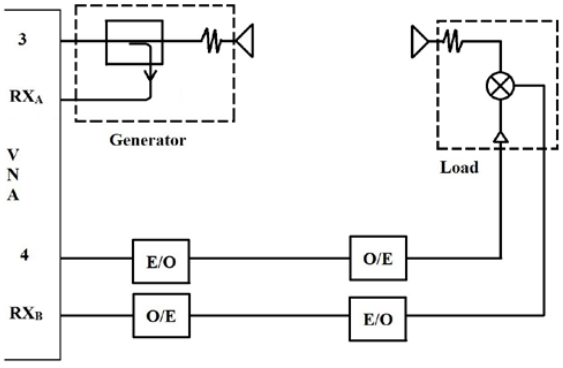


**Figure 2 – New extrapolation measurement setup.**

As with the original measurement system, there is a laser that measures the distance between the two antennas, a motion control system that automatically moves the load antenna, and a computer that interfaces with these systems.

The technique for completing the extrapolation measurement remains largely unchanged from the original system. Software is used to control the motor that separates the two antennas, and query the laser that measures the separation distance. The software also controls the VNA.

As the two antennas are separated at a constant speed, the software constantly queries the laser until a predefined distance interval is reached. At this point, the VNA is triggered; and both the generator and load receivers ($RX_A$ and $RX_B$, respectively) are measured at all frequencies of interest. All of these values are saved for processing.

Even though both receivers are measured, a reference generator-load measurement is still required. This measurement will characterize the losses in the generator and load so they can be separated from the antennas being measured.

Once all three antenna pairs have been measured, the data are fed into the same processing software used in the original measurement setup to calculate the far-field polynomial fit and individual antenna gain, as shown in [3].

## 4.0 Validation

Before the system can be used to calibrate unknown antennas, it must first be validated using antennas that have been calibrated on another system. We chose to validate the system in the WR-42 band (18.0-26.5 GHz). In this band, NIST has several well characterized horns. In particular, the measurement history on the horn used in this validation dates back to 1982.

The validation process consisted of measuring the gain of three antennas, in order to complete a standard three antenna gain calculation. The three horns used in this validation were all WR-42 standard gain waveguide horns. Two of the horns were nearly identical in size, but with no previous information on their individual gain.

After the data have been processed and the individual gains have been calculated, the gain of the NIST horn can be compared to historical data. This is done in Figure 3.

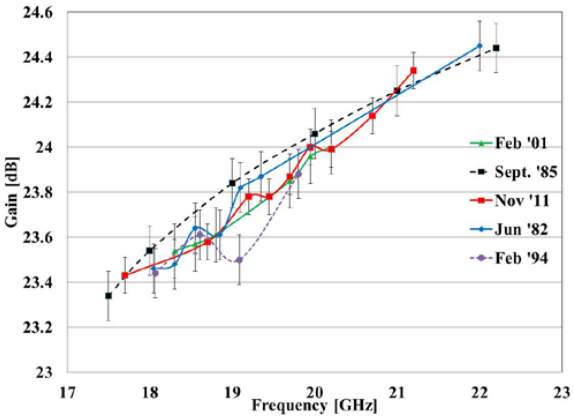


**Figure 3 – Historical antenna gain data compared with data from the new hardware configuration.**

Included in the plot of historical data are the data taken with the new extrapolation hardware setup described here. These data are labeled as "Nov '11." Though not all of the historical data sets are at exactly the same frequencies, there are enough in close proximity that a fair comparison can be made. Uncertainty bars for each data point are shown, and range from 0.08 dB to 0.12 dB, depending on the set. The uncertainty bars for the 1982, 1985, and 1994 data sets have a coverage factor of k=3. This is because the international standard governing uncertainties was not adopted until 1995. Data sets after 1995 use a k=2 coverage factor.

It should be noted that while the data points for each respective set shown in Figure 3 are connected with a line, this line is for illustrative purposes only. This line should not be read as an approximation of the actual gain between measured frequency points.

From the plot, it can be seen that the data taken with the new hardware configuration fall in line with the historical data. The only exception to this lies in the data from February 1994. At 19.085 GHz, there appears to be a statistically significant difference between the other four data sets and the 1994 set. This difference is most likely caused by an artifact of the coax-waveguide adapter used for that particular measurement.

## 5.0 Discussion

The biggest advantage of the new hardware setup is that the measurement time has been significantly reduced. Because the signal generator and receiver were physically separate pieces of equipment, the measurement system was limited to capturing a single frequency. If the antenna gain needed to be calculated at multiple frequencies, one measurement run was required for each frequency point.

With the new hardware configuration, the signal generator and receiver are within the same piece of equipment the VNA. The VNA has the ability to lock its signal generator and receiver together, thus allowing the frequency of both to be changed quickly and accurately.

For the particular system described in Section 3, we were able to acquire up to 10 evenly spaced frequency points across a single waveguide band. This number may change based on several factors including: antenna separation speed, VNA capabilities, and the spacing of frequency points.

The new hardware configuration also has the advantage of being able to capture both magnitude and phase of the transmitted and received signals. This advantage is only available in situations where harmonic mixers are not used. The phase of the signals is not required for a gain extrapolation measurement, but it does have other applications. See Section 6 for details.

The use of a VNA also allows for calibrating the power into the antenna (or into the mixer, if used) to help ensure that power is constant with frequency. These power calibrations are done with a power meter connected to the VNA and their data stored locally on the VNA. This power calibration helps to improve the overall system stability across the frequency band of interest.

By performing the proper one-port calibration on the VNA, one could also measure the reflections of the generator and load systems in place, before or after the gain extrapolation measurements. This eliminates the need to disassemble and reassemble the system elsewhere to perform these measurements.

An interesting point of the new hardware configuration is that it does not do much to decrease the measurement uncertainties. This is a result of the RVA not being a large contributor to the overall uncertainty. Table I shows the uncertainty budget calculated for the WR-42 validation measurement presented in the previous section.

These uncertainties are estimates generated for each known source of uncertainty. All components are Type B unless otherwise noted, and are assumed independent of other uncertainties. The expanded uncertainties use a coverage factor of k=2. The Ui (Kx) values are calculated by dividing the uncertainty by the positive square root of the variance of the distribution [4].

An examination of the uncertainty budget reveals that the only significant hardware dependent term is the non-linearity of the receiver. For gain extrapolation measurements, we are not necessarily concerned about the absolute accuracy of the receiver. Rather, we are concerned about the receiver's relative accuracy as it

**Table I – Uncertainty Budget**

| Source | Value (+/- dB) | Probability Distribution | Ui (kx) +/- dB |
|---|---|---|---|
| RX non-linearity | 0.02 | Rectangular (1.73) | 0.0116 |
| Impedance Mismatch | 0.05 | Rectangular (1.73) | 0.0289 |
| Antenna Alignment | 0.02 | Normal (3) | 0.0067 |
| Data Curve Fit | 0.02 | Rectangular (1.73) | 0.0116 |
| Connector Repeatability | 0.03 | Normal Type A (3) | 0.0100 |
| Residual Multipath | 0.03 | Rectangular (1.73) | 0.0173 |
| Random Uncertainties | 0.03 | Normal (3) | 0.0100 |
| Combined Uncertainty | | Normal | 0.0406 |
| **Expanded Uncertainty** | | **Normal (k=2)** | **0.08** |

measures a signal of decreasing amplitude (as distance between the antennas increases).

In the measurements with the original hardware configuration, the receiver non-linearity was 0.05 dB, and there was an additional term for the uncertainty of the RVA. The unexpanded uncertainty of the RVA was 0.04 dB. Both of these terms together raised the total expanded uncertainty to 0.12 dB, with a k=3 coverage factor. If a k=2 coverage factor is used, the uncertainty becomes 0.08 dB. This uncertainty is approximately the same for the new hardware configuration.

## 6. Additional Applications

This new hardware configuration need not be limited to extrapolation gain measurements. Depending on how one's antenna range is setup, it may be possible to mount this hardware in such a way that a spherical near-field antenna measurement can be accomplished with this hardware configuration. When mounted on a spherical range, this hardware setup will still provide the same benefits and suffer from the same drawbacks discussed in the previous section.

As mentioned in Section 5, it is possible to measure the phase of the transmitted and received signals using the proposed hardware configuration. This is only possible if harmonic mixers are omitted from the system. Measuring the phase of the signals as the distance between the antennas increases provides a good check of the system. Processing the phase information can provide information on how well the system is performing since the phase change vs. distance is well known for a standard gain horn antenna.

Measurement of the phase information allows one to easily calculate the group delay of the antenna under test. The group delay can be calculated using a method similar to the three antenna method. Except in this case, instead of received power vs. distance, phase vs. frequency is the desired quantity.

## 7. Conclusions

The traditional NIST gain extrapolation measurement system has been updated to include a revised hardware configuration is presented. The new measurement method consists of updated hardware (including a VNA, and optical links). This change in hardware has been shown to significantly reduce the measurement/acquisition time, but does not have a significant impact on the overall measurement uncertainty. The new method was validated by comparing antenna gain measurements taken over the past 30 years. The data acquired with the new hardware configuration matches the historical data within the measurement uncertainties.

## 8. REFERENCES

[1] R. W. Beatty, "Discussion of errors in gain measurements of standard electromagnetic horns," NIST Technical Note 351, March 1967.

[2] A. C. Newell, R. C. Baird, P. F. Wacker, "Accurate Measurement of Antenna Gain and Polarization at Reduced Distances by an Extrapolation Technique," IEEE Trans. on Antennas and Propagation, Vol. 21, No. 4, July 1973.

[3] A. G. Repjar, A. C. Newell, D. T. Tamura, "Extrapolation Range Measurements for Determining Antenna Gain and Polarization," NIST Technical Note, 1311, August 1987.

[4] B. N. Taylor, C. E. Kuyatt, "Guidelines for Evaluating and Expressing the Uncertainty of NIST Measurement Results," NIST Technical Note 1297, September 1994.

Coder, Jason; Novotny, David; Guerrieri, Jeffrey; Francis, Michael; Stillwell, Brian.
"An Improved Antenna Gain Extrapolation Measurement."
Paper presented at 34th Annual Symposium of the Antenna Measurements Techniques Association (AMTA), Bellevue, WA, United States.
October 21, 2012 - October 26, 2012.

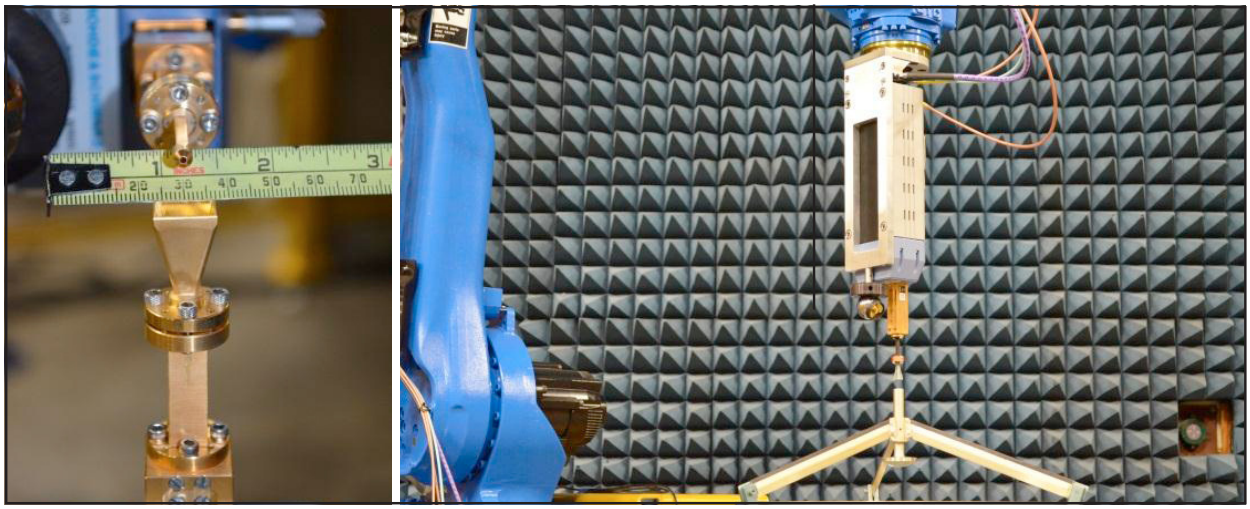

# Use of a Laser Tracker to Actively Coordinate the Motion of a 3-Meter Industrial Robot to Within 50 Microns

*by David Novotny, Joshua Gordon, Jason Coder, Jeff Guerrieri, and Michael Francis; National Institute of Standards and Technology*

The Antenna Metrology Lab at the National Institute of Standards and Technology in Boulder, Colorado, is developing a robotically controlled antenna facility that uses industrial-grade robotics guided by a metrology-grade laser tracker to perform antenna calibrations over the frequency range 50 GHz to 500 GHz. These measurements are performed by scanning a millimeter wave (mm wave) probe antenna about a test antenna over an arc using an articulated six degree of freedom (6DoF) robotic arm that has a reach of 3 meters. Such near-field measurements yield important antenna parameters such as gain, polarization, and radiation pattern. Operation at 500 GHz requires knowledge of the probe antenna position to within 15–20 $\mu$m as well as orientation normal to the scan surface (typically within ~ 0.05°) to minimize pointing errors. Ultimately, our ability to accurately position and orient the probe antenna relative to the test antenna, as well as our knowledge of actual position and orientation, determine the upper frequency limit of our measurement capability, and directly affect the uncertainty of our measurements.

## INTRODUCTION

We are designing a 50–500 GHz, multipurpose, antenna pattern and gain calibration range based on an industrial 6DoF articulated robot with a 3-meter reach, a precision (0.0001° resolution) azimuth rotator, and an alignment hexapod, as seen in figure 1. Antenna testing requirements are increasing in frequency above 110 GHz as high-speed satellite-to-satellite communications, short-range terrestrial point-to-point links, and absolute calibration techniques for remote sensing and climate monitoring research come to the forefront.[1] Our need to accurately position and align antenna under test (AUT) to fractions of a wavelength, and even more accurately know actual position during measurement, are driving forces in accurate coordinate measurement. Furthermore, the delicacy of equipment in these frequency ranges creates problems for physical contact by conventional (at least to the antenna measurement community) probing. Our eventual reliance on a combination and coordination of machine vision, movement methods, and positional measurement is forcing a new method of performing high-frequency antenna alignments and calibrations.

Current mm wave (above 100 GHz) antenna characterization facilities tend to focus on planar scanning techniques.[2] Planar scanning can give accurate pattern information over an approximate ± 30–35° angle range, is generally easier to align, requires less information about the radiation characteristics of the probe, and generally requires less complicated facilities. However, if accurate information is required beyond the central beam area, antenna efficiency is necessary (as in radiometer characterization), wide-angle polarimetric information is required, or full-pattern characterization of low gain antennas is needed, then other scan geometries, such as spherical or cylindrical, become more attractive.[3]

The use of a 6DoF robot for probe positioning and a laser tracker (with optional 6DoF measurement capability) for true positional measurements can provide the ability to perform multiple scan geometries, correct for positional and pointing errors in the AUT and probe, and determine actual *in situ* measurement positions to further improve overall result accuracy.[4] This coordinated 6DoF movement with independent 6DoF positional measurements might provide considerable reduction in uncertainty over conventional antenna characterization facilities that use stacked positional stages for each type of movement.



Novotny, David; Gordon, Joshua; Coder, Jason; Guerrieri, Jeffrey; Francis, Michael.
"Use of a Laser Tracker to Actively Coordinate the Motion of a 3-Meter Industrial Robot to Within 50 Microns."
Paper presented at 2013 Coordinate Metrology Systems Conference, San Diego, CA, United States. July 22, 2013 - July 26, 2013.

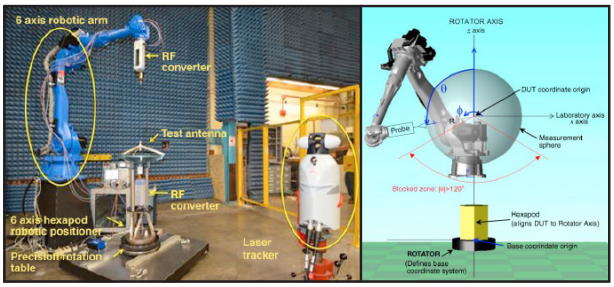


*Figure 1. Physical (left) and conceptual (right) layout of the antenna characterization facility setup in spherical measurement mode, as the central axis of the rotator sets the location and orientation of the AUT's z axis and origin of the probe scanning; major tasks include aligning hexapod movement to rotator axis for AUT alignment, clocking AUT rotation to probe scan plane (AUT polarization), aligning probe rotation to probe scan plane and center (probe polarization), and correcting probe location for kinematic offsets in robot movement (mechanical position correction)*

## SYSTEM OVERVIEW

The task of accurately and repeatably moving a probe antenna over a desired path at these frequency ranges is complicated because physical contact with the antennas is problematic, the limited size of the antennas makes accurate angular alignment difficult, and the aperture origin is often virtual, so it must be inferred from measurements, as seen in the graphic at the top of this article. The extrapolations of the probe coordinate systems and alignment of the multiple coordinate systems (e.g., rotator, hexapod, AUT, robot, probe, and scan geometry) complicates the desired coordinate positioning and measurement between the probe and the AUT.

To accomplish the desired scanning process of the probe around the AUT, the antenna range is built on two major robotics platforms. The first section consists of AUT positioning and clocking mechanisms. In figure 1, the rotation stage sits upon an *xy* stage that nominally places the rotation center and AUT in an optimal position to get maximum angular coverage from the robot. By fixing the position of the *xy* stage, the rotation stage is fixed, as is the central *z* axis of the entire measurement. The 6DoF hexapod then aligns the AUT to the *z* axis, both in lateral translation and rotational pointing alignment. Once aligned to the rotator, the *z* origin for the AUT is established. The robot and probe must now be aligned to the AUT reference frame. The resultant series of stacked alignments produces systematic pointing and position errors that need to be addressed.[5]

## ALIGNMENT

To accurately scan the probe around the AUT and to measure the radiating characteristics of the AUT, alignment of the multiple subsystem components must be performed.

### Main *z* axis definition from rotator measurements

The rotator is scanned with a corner cube reflector (CCR) affixed to the rotator table (below the hexapod), as seen in figure 3. Propagation obstructions due to the hexapod and cabling limit single-mounting point CCR scans to approximately 200° scans of the $\theta$ rotation. We can validate that the out-of-plane table movement is acceptable (< 20 $\mu$m), and multiple scans show acceptable variations in the pointing of the *z* axis (< 0.008°). It is imperative that the rotator measurement be as accurate as possible. It is the virtual baseline by which all the other alignments are based. Taking large numbers of points over as large a physical distance as possible is required to minimize the fitting errors of the central axis.

### Hexapod coordinate system definition

The absolute origin of the hexapod coordinate system was determined by measuring three arcs trajectories of a mounted CCR on the hexapod plane while the hexapod was commanded through its angular range of motion about the three angles, *Rx*, *Ry*, and *Rz*. These angles each correspond to movement about the *x*, *y*, and *z* Cartesian axes, respectively. Full circles were then fitted to these arcs and the normal of these circles determined. From the intersection of the three circle normals, the origin and orientation of the hexapod frame could be determined. In addition, movement of the hexapod along its three Cartesian coordinates relative to the $x = 0$, $y = 0$, and $z = 0$ home position verified the proper orientation and direction of the three axes. With this, the full hexapod frame seen in figure 4 was established, which allowed for information about the movement of the hexapod relative to the laser tracker and other frames in the system.

### AUT aperture coordinate definition and alignment to the *z* axis

The AUT aperture edges are measured and the centroid of the rectangular aperture is found, as seen in figure 5. A working frame is made at the centroid of the measured AUT aperture. The *z* axis of the AUT must be translated and rotated to be co-linear with the central *z* axis of the rotator. An ideal AUT frame is then erected as a goal frame, and the hexapod is used to guide the AUT. Based on a transformation between the measured AUT frame and the goal frame, a 6DoF set of offsets can be calculated by which to translate and rotate the hexapod, thereby aligning the AUT to the goal frame.

First, three widely spaced points on the hexapod plane are measured (relative to the AUT aperture to hexapod distance) from which an identical set of these three points is generated, but which are moved according to the AUT-to-goal transform. Two new frames are created from the first set of three points and a second translated set, respectively. The transform between these two new frames is then calculated to give the final *x*, *y*, *z*, *Rx*, *Ry*, and *Rz* coordinates to which the hexapod must be translated to align the AUT to the *z* axis of the rotator. The result of applying the AUT-to-goal transform can be seen in figure 6.

The three reference points are translated until the calculated AUT centroid is aligned with the central *z* axis. Errors can accumulate here, as the AUT-to-reference-point distance is large compared to the basis for the hexapod coordinate frame. To minimize these translation errors, the aperture needs to be measured again to verify the alignment of the aperture after the move.

### Robot coordinate system definition

Once the AUT is aligned to the rotation stage and the central *z* axis, robot alignment can be performed. The robot movement needs to be coordinated with the laser tracker. There are two



Novotny, David; Gordon, Joshua; Coder, Jason; Guerrieri, Jeffrey; Francis, Michael.
"Use of a Laser Tracker to Actively Coordinate the Motion of a 3-Meter Industrial Robot to Within 50 Microns."
Paper presented at 2013 Coordinate Metrology Systems Conference, San Diego, CA, United States. July 22, 2013 - July 26, 2013.

| Component | Task(s) | Nominal figures of merit |
|---|---|---|
| Rotation stage | • Sets central z axis of the entire measurement system<br>• Provides $\phi$ rotation of the AUT<br>• Sets polarization reference of the AUT | • Better than 20 $\mu$m flatness<br>• 3,600,000 steps/rotation (0.0001°)<br>• Repeatability better than 0.0005° |
| Hexapod | • Provides 6DoF alignment between AUT and central z axis | • Allows virtual pivot point alignment relative to AUT center<br>• <1 $\mu$m resolution<br>• 50 mm/±15° travel<br>• 30 kg AUT capacity |
| 6DoF robot | • Provides scan geometry ($\theta$ scan about AUT for spherical, 2D scan plane for planar) for the probe<br>• Aligns scan geometry to z axis<br>• Provides probe polarization<br>• Full 6DoF movement allows software correction of actual measurement position | • 30 kg load capacity (includes probe, mm wave hardware, supports, and cabling<br>• ±70 $\mu$m rated repeatability (not accuracy)<br>• 3-m reach can provide up to 1.25-m measurement radius at the probe aperture<br>• Up to 1.5 x 2 m planar scan size |
| Laser tracker | • Measures 3D position data<br>• With three nonlinear CCRs, accurate stationary 6DoF can be measured<br>• 6DoF sensors can measure in real time at moderates speeds (<1 m/s) | • Within the 2–3 m working range, repeatability and accuracy < 20 $\mu$m for direct CCR measurement<br>• 6Dof sensor ± 0.01° (18 $\mu$m/ 100 mm) pointing error and 50 $\mu$m positioning error relative to central reflector |

*Figure 2. Table showing subsystem specifications of the NIST mm wave antenna measurement range*

obvious methods of performing the frame translations between the robot and the laser tracker. We can create a frame similar to the hexapod movement of the AUT. We can also move the robot in its base *x*, *y*, and *z* motions to calculate a virtual laser tracker frame for the base robot movement that can be translated relative to the AUT frame. This will allow the altering of the robot geometry to match the scanning needs of the AUT in base robot coordinates. This allows for less error-prone movements when shifting a large robot around small, sensitive, and fragile objects.

Additionally, timing between the robot and the laser tracker must be coordinated. The robot movement to a given position must be coordinated with the laser tracker capture of the position data and a measurement of the radiated energy between the AUT and probe antennas.[6] The robot motion needs to be continuous; if the robot is stopped at each measurement point, the cables that phase-lock the mm wave measurements continue to vibrate and cause errors. In this scenario, a pause must be inserted at each point (1–2 seconds) to allow for the system to stabilize prior to measurement. This can cause a 250,000-point scan to have an additional 80 hours of measurement time (the number of points tends to scale as the square of frequency). We have found that as long as the movement of the probe is less than 1/50th of the measurement, wavelength during the mm wave measurement the error due to movement is generally acceptable. This limits probe movement to approximately 30 millimeters/second for measurements at 100 GHz.

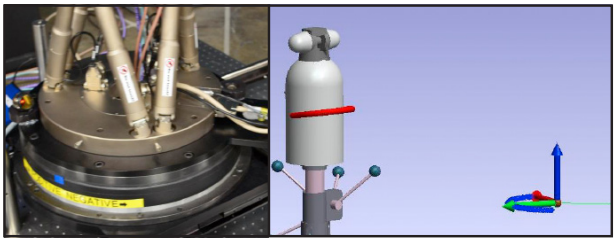

*Figure 3. Determining the central z axis of the system: a CCR is placed on the rotation stage and moved through the maximum rotation without blockage to the laser tracker from the hexapod and cabling; the accurate determination of the vertical z axis (right) is critical to the accuracy of the entire measurement, and every component is aligned to the rotation stage*

The robot has the ability to send a pre-trigger prior to arriving at a given point. A pulse can be sent out prior to arriving at the target point, to within the process timing cycle accuracy of the robot (~ 3 mS). This allows the positional placement, mm wave signal capture, and measurement of position to occur with minimal timing differences. The timing is initially estimated by robot speed. For a spherical scan of an AUT, the robot is scanned about the AUT, the AUT is rotated, and then the robot reverses its path. As seen in figure 7, we adjust the pre-triggering of the robot and delay of the instrumentation to ensure the data points are taken at the same point on the forward and reverse paths.

Once the basic timing of the robot is established, the robot is measured in its native *x*, *y*, and *z* movement, and a reference robot frame is established. This allows the errors in robot position to be translated directly into correction vectors in robot-coordinate space. As seen in figure 7, the robot repeatability at this speed is approximately 30 $\mu$m with a few outliers around 100 $\mu$m.

## Probe coordinate system definition

One of the most difficult alignment tasks is the determination of the probe location and pointing relative to the robot and relative to the AUT. As seen in the figure at the top of the article, the probe can be delicate, and the force of a CCR being pressed against it can cause damage. We are developing a combination of machine vision techniques with a 6DoF offset sensor

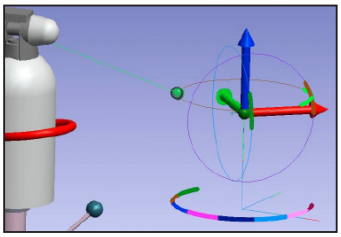

*Figure 4. By moving the hexapod in its base coordinate x, y, z, Rx, Ry, and Rz motions, a coordinate frame relative to the hexapod can be established; this allows for direct calculation of the AUT translation needed to align it to the central z axis in hexapod coordinates*



Novotny, David; Gordon, Joshua; Coder, Jason; Guerrieri, Jeffrey; Francis, Michael.
"Use of a Laser Tracker to Actively Coordinate the Motion of a 3-Meter Industrial Robot to Within 50 Microns."
Paper presented at 2013 Coordinate Metrology Systems Conference, San Diego, CA, United States. July 22, 2013 - July 26, 2013.

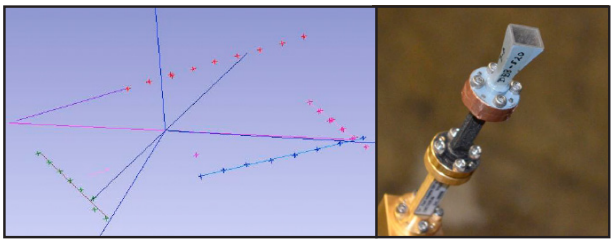

*Figure 5. Measurement of the initial position of the aperture: the AUT aperture is approximately 8 mm × 12 mm, and the initial position is measured relative to the rotator and hexapod frame; the lone point in the left graph is where the central z axis of the rotator intersects the plane of the aperture, while the frame of the aperture plane is seen as an offset from this ideal aperture location*

to determine probe location and orientation.[7] For verification of the positioning capability of the probe, a CCR is placed at the probe location, and a 6DoF sensor is offset approximately 250 millimeters away from the CCR. The CCR is driven to a given location to within robot step capability (~ 17 $\mu$m) from several different directions. The laser tracker measures the CCR in addition to the 6DoF sensor location and orientation. The robot joint set is also measured. The alignment of the probe tip relative to the 6DoF sensor and the robot tool interface are simultaneously measured. The knowledge of both of these offsets allows for first-order positioning and attitude control of the mm wave probe by the robot, and accurate measurement of the probe location and attitude by the 6DoF sensor.

To validate the alignment and accuracy of the 6DoF sensor relative to the laser tracker, the probe is scanned in the same arc used for the timing analysis. At each point in the forward and reverse arc, the 6DoF sensor is measured, and then the arc is repeated while measuring the CCR. Figure 8 demonstrates the differences between the probe position as measured by the CCR and 6DoF sensor. The measured differences are consistent with the manufacturer specifications seen in

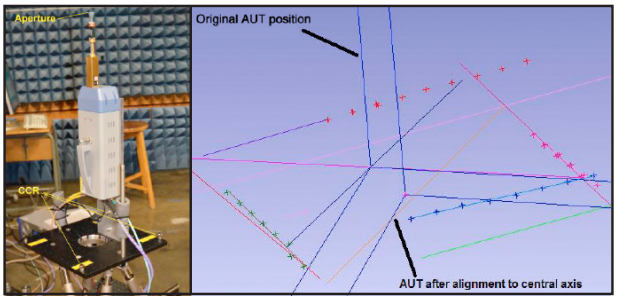


*Figure 6. Aperture translation and rotation via the hexapod: the calculation of the frame-to-frame translations between initial and desired position in the hexapod movement frame allows for direct hexapod movement relative to its base coordinates; the translation between the aperture and the base plate is done by measuring three nonlinear points on the base plate relative to the initial aperture position, and an iterative translation was done; post-alignment verification of the AUT aperture shows that alignment of the AUT to the central z axis is within ± 30 µm and ± 0.04°*

the table in figure 3, and the offset between the sensor and probe. The robot process timing accuracy of 3 mS may account for the outliers around 100 $\mu$m. Occasionally (< 0.5%) the robot may take an additional timing interval to process information; this additional 3 mS at a 30 mm/s velocity translates to a 90 $\mu$m offset. The robot may to be going to the programmed point much closer than figure 8 suggests for the 100 $\mu$m to 130 $\mu$m; there is just a slight variation in the pre-trigger delay from the robot, causing the tracker and RF equipment to trigger at a slightly different delay.

## Scan geometry alignment to the z axis and AUT aperture

The last alignment step prior to the actual measurement is to align the scan geometry to the $z$ axis of the rotator and AUT aperture. The measurement arc is roughly located over the $z$-aligned AUT by measuring the initial, uncorrected arc path and calculating the centroid of the path. The arc is moved, in robot coordinates, to be centered on the AUT aperture, as seen in figure 9. No corrections are initially made for scan tilt relative to the AUT. Once a rough alignment is done (within ~ 300 mm), a scan is performed in both directions while capturing the probe position and probe-pointing orientation. The AUT is then rotated to achieve alignment with the scan frame using the central rotator, and the $\phi = 0°$ coordinate for the measurement is set.

This is where the 6DoF coordinated movement of the robot has markedly attractive advantages over current systems. The robot can correct 6DoF position and pointing errors simultaneously. The initial errors are relatively large (on the order of 10–20 millimeters), mainly due to the installation tilt of the robot relative to the rotator. The errors in the positions and attitudes of each

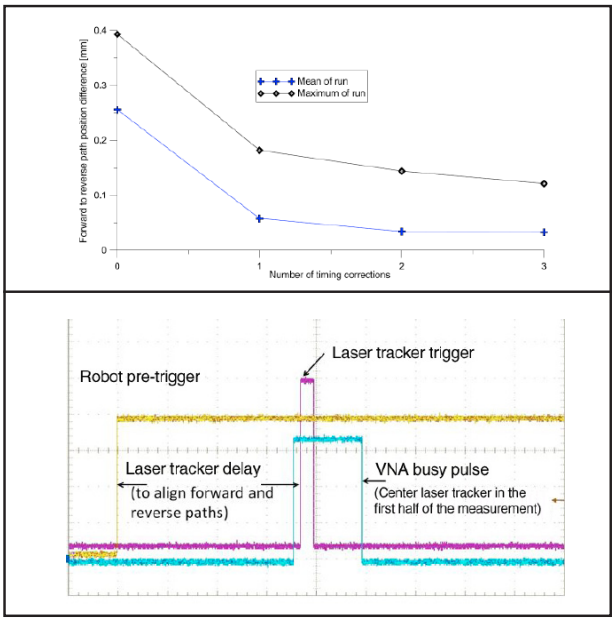


*Figure 7. Timing between the robot and the laser tracker: by adjusting the pre-trigger delay of robot and the tracker data acquisition delay (left), the relative position error between the forward and reverse scans can be minimized; once the tracker delay is set (right) the mm wave measurement is delayed to align to the laser tracker position capture*



Novotny, David; Gordon, Joshua; Coder, Jason; Guerrieri, Jeffrey; Francis, Michael.
"Use of a Laser Tracker to Actively Coordinate the Motion of a 3-Meter Industrial Robot to Within 50 Microns."
Paper presented at 2013 Coordinate Metrology Systems Conference, San Diego, CA, United States. July 22, 2013 - July 26, 2013.

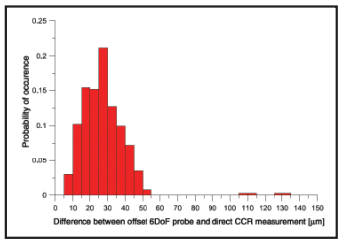


*Figure 8. Measured differences between the same scan performed with an offset 6DoF sensor measuring probe position and a CCR directly measuring probe position: the start and stop points of the scan cluster is mainly between 40 µm and 50 µm; the few points above 100 µm may be related to timing uncertainty in the robot, as they do not repeat in location over repeated runs; it should be noted that the differences seen here are due to both the 6DoF sensor pointing errors and the robot repeatability seen in figure 7; currently, this is one of the larger sources of positional uncertainty and is limiting the operation of the system to ~ 250 GHz*

individual measurement point is calculated, and the corrections (in the robot frame of movement) required to bring them to ideal are determined and sent back to the robot-positioning software. The first iteration of the corrections, as seen in figure 10, demonstrate that the measured error in the AUT frame is reduced to approximately 85 $\mu$m. Subsequent corrections can bring the mean positioning error to ~ 25 $\mu$m. We see little improvement after three rounds of positional iterations.

The resulting errors can be corrected, to first order, using position correction techniques.[8] The time it takes to align the scan geometry is trivial compared to that for the AUT to rotator. In less than 30 minutes, four iterations of 6DoF position corrections were completed for the 802-point scan. Once the probe-to-6DoF-sensor offset is established, the corrections can be done for any scan geometry. Aligning within the 0.01° uncertainty of the 6DoF sensor provides the ability to have acceptable probe pointing errors for the low and moderate gain horns we use for probes. This is particularly important because pointing errors cannot be addressed by current processing methods.

Figure 11 demonstrates the corrected arc aligned to the AUT. The average positioning errors, including 6DoF sensor errors, are approximately 40 $\mu$m. The $\phi$ (rotator) axis is clocked to the scan plane, and the 0° point of the robot scan ($\phi$ axis) is aligned with the $z$ axis of the rotator.

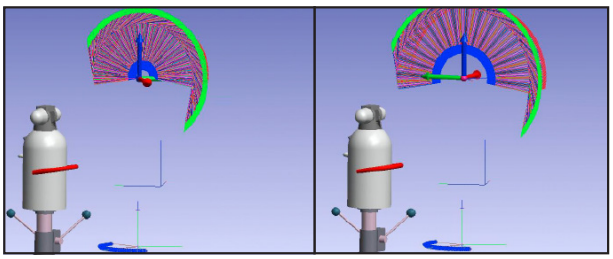

*Figure 9. The first step of aligning the scan geometry of the probe to the AUT: the measured center of the uncorrected scan (left) is offset to approximately match the AUT location by moving the entire ensemble by a constant 6DoF offset; this results in an arc (right) with a positional variation of ~ 200 µm from ideal*

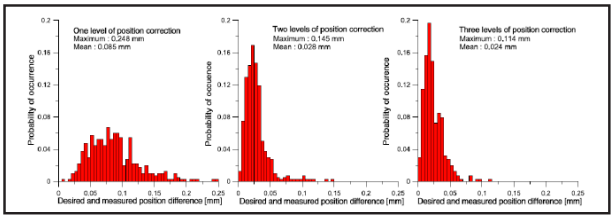


*Figure 10. The effects of successive levels of position correction: we can see the 90 µm positioning error due to robot timing clearly once the mean error drops below 30 µm, and we can implement position correction techniques to minimize the error of these outliers if they constitute a small portion of the total scan area or received power from the AUT; this error is independent of the 6DoF offsets in figure 8*

## POSITIONAL UNCERTAINTY ANALYSIS

Figure 12 demonstrates the basic background "noise" we see in positioning. The robot is stopped and there is no power to the motors, with the breaks on each axis. The resultant variation may be due to the floor moving, instability in the robot or laser track mounts, or the positional noise of the laser tracker itself. This represents a basic measurement limitation of the current setup. The raw position error/uncertainty/repeatability of the robot, as seen in figure 13, can be corrected to first order because the laser tracker is recording the actual position of the individual mm wave measurement. Currently the position uncertainty between the probe and the AUT can be estimated by the error in the probe as seen in figures 8 and 10. The root-sum-square (RSS) of the position displacements and the 6DoF sensor uncertainty is ~ 40 $\mu$m. However, better estimation of the actual probe and AUT aperture planes is needed. Measuring over a small surface and then extending the results to 100 times the length of measurement will lead to errors. The base error of the rotation stage as well as how it affects the alignment of the AUT frame and robot scan geometry needs to be assessed.

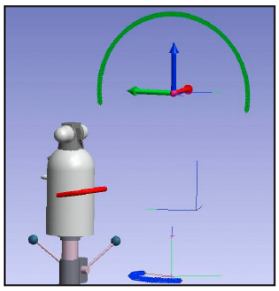

*Figure 11. Resultant measurement points for spherical scanning of an AUT: the scan points are fitted to a planar-circular arc, and the nominal mean AUT to probe position errors of ~ ± 40 µm; this does not include the systematic offset of the measured probe and AUT frames from the actual position and points of the antennas; timing between the robot, positional tracking systems, and the measurement have been minimized to limit errors due to the robot movement during scanning, and many of the measured errors and offset from desired positions can be mitigated with position correction*

## FUTURE WORK

The most difficult tasks are defining the AUT aperture plane and the probe aperture plane. Work is underway to accurately determine the actual position and orientation of the aperture



Novotny, David; Gordon, Joshua; Coder, Jason; Guerrieri, Jeffrey; Francis, Michael.
"Use of a Laser Tracker to Actively Coordinate the Motion of a 3-Meter Industrial Robot to Within 50 Microns."
Paper presented at 2013 Coordinate Metrology Systems Conference, San Diego, CA, United States. July 22, 2013 - July 26, 2013.

of the AUT and the probe; this should generate more accurate methods of determining the antenna center for location and antenna edges for determining orientation.[7] We will be assessing the possibility of stepping the robot and scanning the rotator. However, that puts more stress and strain on the RF cabling beneath the AUT. In this configuration, however, we can use three CCRs to align the probe tip, similar to the hexapod-to-AUT alignment. It may result in better probe aperture determination (down to the level of the base laser tracker error).

## CONCLUSION

We presented a method for controlling the probe position of a scanning antenna system to within 50 $\mu$m relative to a centrally defined antenna coordinate system. It is the first stage in a complex alignment consisting of multiple stages. Once a basic scanning surface is defined, positional scanning errors can be corrected to half a wavelength. We can mathematically correct, to first order, the positioning error of the 6DoF robot (~ 40 $\mu$m). The ~ 50 $\mu$m error in the 6Dof sensor can be reduced by placing the sensor closer to the actual probe tip location. This possibly results in a reduction of sensor errors to 30 or 40 $\mu$m. These uncertainties in position may allow us to achieve the 1/25th of a wavelength acceptable error to approximately 300 GHz. The tasks of performing more robust 6DoF sensor-to-probe-tip alignment and AUT determination are the major hurdles still to overcome.

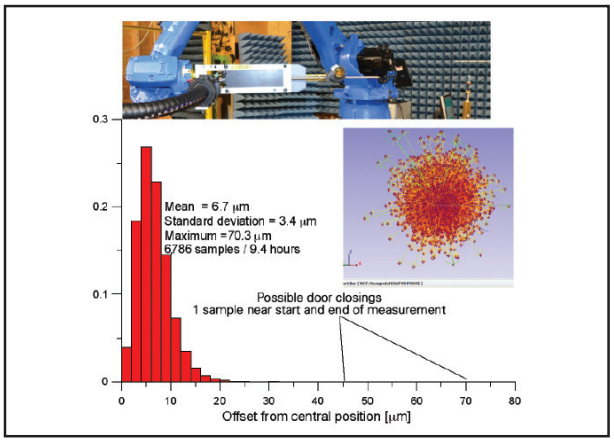


*Figure 12. Nominal movement of the robot with respect to the tracker when the robot is not moving and has brakes engaged; motion in the room can be seen as outliers in these data; the point cloud on the left shows uniformity of the movement with time*

## REFERENCES

[1] "Achieving Satellite Instrument Calibration for Climate Change (ASIC3);" Ohring, G. (ed.); National Oceanic and Atmospheric Administration; 2007.





Novotny, David; Gordon, Joshua; Coder, Jason; Guerrieri, Jeffrey; Francis, Michael.
"Use of a Laser Tracker to Actively Coordinate the Motion of a 3-Meter Industrial Robot to Within 50 Microns."
Paper presented at 2013 Coordinate Metrology Systems Conference, San Diego, CA, United States. July 22, 2013 - July 26, 2013.

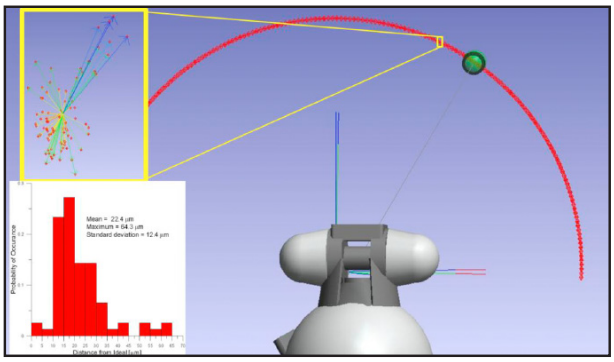

*Figure 13. Nominal position spread for a single commanded position on the measurement arc for 71 sweeps of that point; mean deviation from ideal is ~ 22 µm with a maximum deviation of ~ 64 µm*


[2] Slater, D., Hardy, J., Stek, P., Cofield, R., Dengler, R., Jarnot, R., and Swindlehurst, R.; "A Large Aperture 650 GHz Near-Field Measurement System for the Earth Observing System Microwave Limb Sounder;" *2001 Proceedings of the Antenna Measurement Techniques Association*; pp. 468–473; 2001.

[3] Hindman, G., Newell, A., Dicecca, L., and Angevain, J.C.; "Alignment Sensitivity and Correction Methods for Millimeter-Wave Spherical Near-Field Measurements"; *2010 Proceedings of the Antenna Measurement Techniques Association*; pp. 316–321; 2010.

[4] Rousseau, P., Wysock, W.C., and Turano, C.M.; "Using a Tracking Laser Interferometer to Characterize the Planarity of a Planar Near-Field Scanner"; *2002 Proceedings of the Antenna Measurement Techniques Association*; pp. 501–506; 2002.

[5] Francis, M. and Wittmann, R.; "Uncertainty Analysis for Spherical Near-Field Measurements"; *2003 Proceedings of the Antenna Measurement Techniques Association*; pp. 43–51, 2003.

[6] Novotny, D., Gordon, J., Coder, J., Francis, M., and Guerrieri, J.; "Performance Evaluation of a Robotically Controlled Millimeter-Wave Near-Field Pattern Range at NIST"; *Seventh European Conference on Antennas and Propagation*; pp. 4086–4089; 2013.

[7] Gordon, J., Novotny, D., Coder, J., Guerrieri, J., and Francis, M.; "Performance of a Robotically Controlled Near-Field Pattern Range in a Spherical Scan Geometry"; 2013 *Antenna Measurement Techniques Association;* 2013.

[8] Wittman, R., Alpert, B., and Francis, M.; "Planar Near-Field Antenna Measurements Using Non-Ideal Measurement Locations"; *1996 Proceedings of the Antenna Measurement Techniques Association;* pp. 74–79; 1996.








Novotny, David; Gordon, Joshua; Coder, Jason; Guerrieri, Jeffrey; Francis, Michael.
"Use of a Laser Tracker to Actively Coordinate the Motion of a 3-Meter Industrial Robot to Within 50 Microns."
Paper presented at 2013 Coordinate Metrology Systems Conference, San Diego, CA, United States. July 22, 2013 - July 26, 2013.

# International Comparison of Ku-band Standard Gain Horn Characterization

Jeff R. Guerrieri[1], Jason B. Coder[1], Michael H. Francis[1], Josh Gordon[1], David R. Novotny[1], Ronald C. Wittmann[1]
[1] National Institute of Standards and Technology, 325 Broadway, Boulder, CO 80305 USA, jguerrieri@nist.gov

***Abstract*— International comparison of antenna measurement results between national measurement laboratories supports interoperability of communication equipment in today's world market. The National Institute of Standards and Technology (NIST) is the pilot National Measurement Institute (NMI) for an international comparison measurement of two Ku-band standard gain horn antennas that involved eleven other NMIs. A variety of measurement techniques such as extrapolation, far field, gain transfer and reciprocity, were used in this international comparison. The individual measurement techniques used by each NMI are indicated and the gain measurement results and associated uncertainties from each NMI are presented in this paper.**

***Index Terms*— antenna gain, fixed frequency gain, international comparison, Ku-band, National Measurement Institute.**

## I. INTRODUCTION

NIST is the pilot lab for an international comparison of standard antennas for the Consultative Committee for Electricity and Magnetism (CCEM) under the Bureau International des Poids et Measures (BIPM). The CCEM.RF-K23.F is a key comparison measurement of two Ku-band standard gain horns, serial numbers 3935 and 3936 [1]. It involves 12 NMIs; Australia – National Measurement Institute of Australia (NMIA), China – National Institute of Metrology (NIM), Czech Republic – Czech Metrology Institute (CMI), France – Laboratoire national de metrologie et d'essais (LNE), Japan – National Metrology Institute of Japan (NMIJ), Russia – Russian Scientific Research Institute of Physico-Technical Measurements (VNIIFTRI), South Korea – Korea Research Institute of Standards and Science (KRISS), Sweden – Technical Research Institute of Sweden (SP), Switzerland – Federal Institute of Metrology (METAS), Turkey – The Scientific and Technological Research Council of Turkey (TUBITAK-UME), United Kingdom – National Physical Laboratory (NPL), and United States – National Institute of Standards and Technology (NIST). All of the NMIs performed on-axis gain measurements and uncertainty analyses at 12.4, 15 and 18 GHz on the two traveling standards. The comparison was conducted from 2008 to 2013.

## II. MEASUREMENT TECHNIQUES

Several different measurements techniques were used by the NMI's. Table 1 lists the measurement techniques used by each NMI.



TABLE I. NMI MEASUREMENT METHODS

| Country | NMI | Measurement Method |
|---|---|---|
| Australia | NMIA | 3 antenna, extrapolation |
| China | NIM | 3 antenna, 7.07 m |
| Czech Republic | CMI | 3 antenna, 2.4, 3.2, 4 m |
| France | LNE | reciprocity |
| Japan | NMIJ | 3 antenna, extrapolation |
| Russia | VNIIFTRI | 3 antenna, extrapolation |
| South Korea | KRISS | 3 antenna, extrapolation |
| Sweden | SP | gain transfer |
| Switzerland | METAS | 3 ant., ANSI C63.5-1998 |
| Turkey | TUBITAK-UME | 3 antenna, 9m |
| United Kingdom | NPL | 3 antenna, extrapolation |
| United States | NIST | 3 antenna, extrapolation |

## III. MEASUREMENT RESULTS

Each NMI performed fixed frequency, on-axis gain measurements at 12.4, 15.0 and 18.0 GHz on the two traveling standards. The measurements were made at the waveguide port of the antennas. Each NMI generated a report of their determined gain values and uncertainties that were sent to NIST to be compiled. The reported uncertainties are based on a standard uncertainty coverage factor of k=2. As the pilot lab, NIST performed the measurements at the beginning and end of the measurement campaign and has two reported measurement results, NIST 1st and NIST 2nd.

Averages for the gain and uncertainties reported by the NMIs were calculated as weighted averages of the (linear) gain measured by the participants. The weights were chosen as the inverses of the fractional error in gain as reported by the various laboratories [2]. Theoretical gain values for the traveling standards were also computed using the Naval Research Laboratory model [3].

Graphs of the NMIs reported gain results, weighted-average gains, and calculated gains for s/n 3935 and s/n 3936 are shown in Figure 1 and Figure 2, respectively. For ease in viewing, data reported in all of the graphs in this paper have been plotted nominally with respect to the measurement frequency.



Guerrieri, Jeffrey.
"International Comparison of Ku-band Standard Gain Horn Characterization."
Paper presented at 8th European Conference on Antennas and Propagation (EuCAP 2014), The Hague, Netherlands. April 6, 2014 - April 11, 2014.

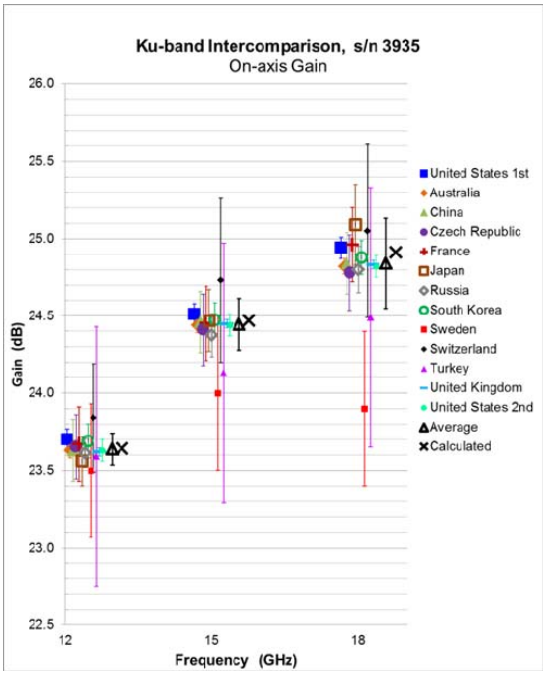


Fig. 1. On-axis gain results for s/n 3935.

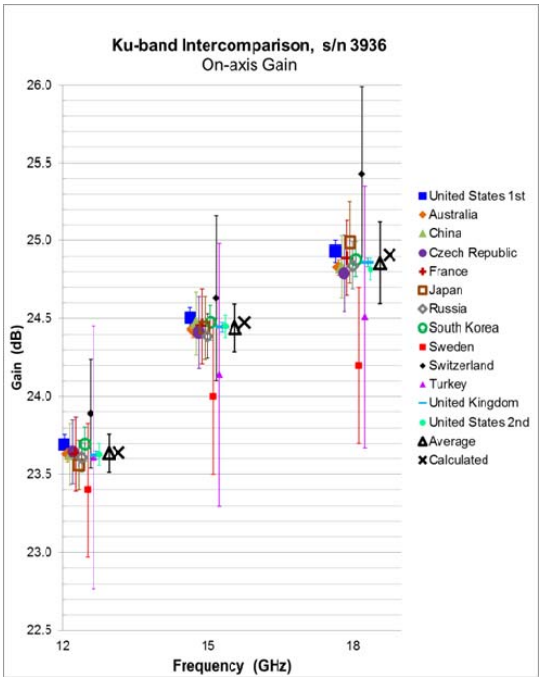


Fig. 2. On-axis gain results for s/n 3936.

Comparison of the compiled results of the NMI's gain values reveals favorable agreement. All of the NMI's reported gain values agree within their reported uncertainty values except gains measured by SP at 18 GHz for both of the traveling standards.

The NMI's reported gain values were also compared to the weighted average gains. It is interesting to note that the weighted-average gain values for the two antennas are nearly identical as a function of frequency. Here all of the NMI's gain values and uncertainties agree with the weighted gain values and uncertainties except gain measured by SP at 18 GHz for one of the traveling standards.

The calculated gain values were also included in the comparison. Theoretical on-axis gain calculation techniques typically do not account for the throat-to-aperture interaction of standard gain horns that can result in a ~ 0.6 dB peak-to-peak oscillation in the gain curve with respect to frequency. The calculated gains for the traveling standards agree within < 0.06 dB of the weighted average gains. An explanation for this remarkable agreement could be that the measurement frequencies are not at the peak of the oscillations on the gain curve.

## IV. CONCLUSION

An international comparison of on-axis gain measurements was conducted for BIPM involving 12 NMIs. As the pilot lab, NIST compiled the results. Most of the reported results from the NMIs agree within their reported uncertainties, the weighted-average gain, and calculated gain, including the two separate measurements performed at NIST. Only one gain measurement at 18 GHz, for both traveling standards, by one NMI, did not agree within the report uncertainty.

## ACKNOWLEDGMENT

The authors want to thank the NMIs for participating in this international comparison and the individuals who prepared the NMI reports; Dr Yu Ji, Dr L. M. Besley & F. M. Warner of NMIA, Wang Wei-long of NIM, Karel Dražil of CMI, Yannick Le Sage & Picou of LNE, Masanobu Hirose, Satoru Kurokawa & Koji Komiyama of NMIJ, Kolotygin Sergey of VNIIFTRI, Jin-Seob Kang & No-Weon Kang of KRISS, Lars Fast, Kristian Karlsson & Jan Carlsson of SP, Frédéric Pythoud of METAS, Mustafa Cetintas of TURBITAK-UME, and D. G. Gentle & A. Beardmore of NPL.

## REFERENCES

[1] http://kcdb.bipm.org/appendixB/KCDB_ApB_info.asp?cmp_idy=973&cmd_cod=CCEM.RF-K23.F&prov=exalead. Accessed June 27th, 2013.

[2] Guerrieri J. R., Coder J. B., Francis, M. H., Gordon J., Novotny D. R., Wittmann R.C., "International Comparison of Ku-Band Standard Gain Horn Characterization", 2013 Antenna Measurement Techniques Association Conference Proceedings.

[3] Slayton W. T., "Design and Calibration of Microwave Antenna Gain Standards", Naval Research Laboratory Report 4433, November 9, 1954.



Guerrieri, Jeffrey.
"International Comparison of Ku-band Standard Gain Horn Characterization."
Paper presented at 8th European Conference on Antennas and Propagation (EuCAP 2014), The Hague, Netherlands. April 6, 2014 - April 11, 2014.

# A Non-contact Machine Vision System for the Precision Alignment of mm-Wave Antennas in all Six Degrees of Freedom

*Joshua A. Gordon, David R. Novotny
Electromagnetics Division, National Institute of Standards and Technology
Boulder, CO 80305
*josh.gordon@nist.gov

***Abstract*— Although highly accurate relative position data can be achieved using laser tracking systems which are suitable for millimeter wave antenna characterization, a considerable gap exists in the ability to absolutely align antennas to laser tracker target coordinate systems. In particular this scenario arises in millimeter wave near-field measurements where probe antenna aperture dimensions are on the order of a millimeter, and the position of its origin must be known to better than 1/20th of a wavelength, and orientation known to fractions of a degree. The fragile nature and dimensions of such antenna negate the use of coordinated metrology measurement systems and larger touch probes typically used for accurate spatial characterization. The Antenna Metrology Laboratory at NIST in Boulder, Colorado is developing a new machine vision based technique for measuring the absolute position of small (~1 mm) millimeter wave antenna apertures relative to a laser tracker target coordinate system. A synergy with existing laser tracking systems, this approach will provide a non-contact method for determining the absolute position and orientation coordinate frame of the probe antenna aperture in all six degrees of freedom to within 30-60 microns. This alignment system technique is demonstrated using the CROMMA Facility at NIST in Boulder, CO.**

## I. INTRODUCTION

Laser trackers (LT) are effective for the spatial characterization of solid objects and are widely used for spatial metrology tasks such as 3D part characterization, tolerancing, and reverse engineering. They have also been indispensible in advanced surveying applications where high degrees of accuracy and precision are required, such as in aircraft assembly and telescope observatories[1]. LTs have also been useful in the construction and alignment of antenna ranges and antennas [2][3][4]. The type of object that can be spatially characterized with these systems is dependent on the type of LT target used. Perhaps the most common target is the spherical mirror reflector (SMR) made from three perpendicular mirror surfaces forming the corner of a cube. The SMR can be used on its own as a stencil that can be moved along a surface to in a spatial measurement. As typical SMRs are limited to 1" and 0.5" diameter spherical form factor, more complicated targets such as touch probes have been developed to provide increased versatility for manual scanning of objects allowing for rapid point cloud generation over larger surface areas and volumes.

In the context of precision antenna alignments, LTs are very useful. They allow one to obtain hi-fidelity spatial information at the tens of micron level, which is sufficient for antenna alignments necessary at frequencies in the millimeter-wave (mm-wave) range (100 GHz-300 GHz) [5]. Currently available LT targets are excellent performers for many applications when the object of interest is significantly larger than the target. However, when the object is much smaller than the LT target and too delicate to touch, current LT targets are not adequate. This scenario presents itself regularly when dealing with mm-wave components. As an example, a $\mu = \pm 1$ probe antenna in the WR-05 waveguide band that would be used in near-field scanning [5] has an aperture of 1.5 mm that is machined to a delicate knife edge. Due to the small size and fragile nature, using an SMR target would not be possible to spatially characterize this probe antenna.

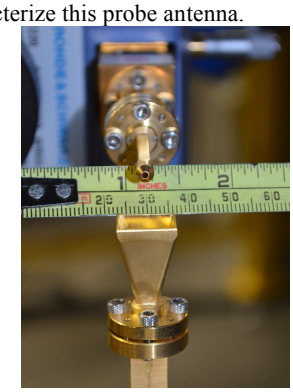

Figure 1. The probe antenna and standard gain horn. Sizes are shown by the ruler.

To address such LT target limitations, the Antenna Metrology Lab at NIST, Boulder, CO has developed a machine vision system. This system uses a set of three cameras in conjunction with LT SMR targets to provide a non-contact method for the spatial characterization and alignment of small mm-wave antennas. It embodies a synergy of machine vision with current LT SMR targets allowing for both the advantages of



Gordon, Joshua; Novotny, David.
"A Non-contact Machine Vision System for the Precision Alignment of mm-Wave Antennas in all Six Degrees of Freedom."
Paper presented at 91st ARFTG Microwave Measurement Symposium, Tucson, AZ, United States. October 12, 2014 - October 17, 2014.

spatial mapping and the stand-off nature of optical imaging with laser tracker point-cloud based spatial metrology. With this system, we can measure small and delicate antennas without physical contact to accuracies ~30 $\mu m$. In addition, this spatial information is linked to the LT coordinate system, and thus can be incorporated into a broader coordinated metrology framework. In the following sections we will cover the concept, design, function, and example data of this system for precision antenna alignments at 183 GHz at the NIST **C**onfigurable **Ro**botic **M**illi**M**eter-wave **A**ntenna (CROMMA) facility in Boulder, CO.

## II. CONCEPT

### *A. Non-Contact Machine Vision Linked to a Laser Tracker*

The basic concept of this approach is to create a point in space that is coincident with both an SMR target and a vision system. This point can then be used as a virtual touch probe and can also be used to reference other spatial information obtained from the vision system to LT coordinate frames. The use of a vision system opens up many possibilities for non-contact spatial characterization of antennas such as: aperture centroiding, aperture detection, fiducial marker locating, and inspection. Previously, we have presented on the use of machine vision for the relative alignment of antennas[6]; however, here we extend the use of machine vision for the absolute alignment of antennas by linking machine vision information to a LT. With this we can precisely locate mm-wave antennas for aligning and positioning, such as in a near-field scanner. Two mm-wave antennas in the WR-05 band are used to demonstrate this approach; a $\mu = \pm 1$ probe antenna used in spherical near-field scanning and a 24 dBi standard gain horn (SGH). These are shown in Figure 1 against a ruler for size reference.

With the proliferation of CCD and CMOS cameras, it is not hard to find high-end focal plane arrays (FPA) with pixel sizes on the order of a few microns with several megapixel densities. Furthermore, optical lenses with modulation transfer functions (MTF) above a hundred line pairs per mm are also easy to obtain to match these high resolution FPAs. It is therefore rather easy to achieve imaging resolution on the order of tens of microns. However, although this spatial resolution is readily obtained in the image plane transvers to the optical axis (OA), if we look at the spatial resolution along the OA this is dictated by the depth of focus (DOF) of the lens and not pixel resolution. The DOF is the distance over which an object can be shifted along the OA while still remaining in focus. In a ray optics picture this distance can be considered to be zero; however, for a real optical system due to the wave nature of light the DOF is a non-zero value that depends on the ratio of the focal length to lens aperture, i.e., the f-number F/#. The DOF for a rotationally symmetric lens can be closely modeled with a Gaussian beam. Consider the expression for a Gaussian beam generated by a lens, the DOF [7] is,

$$DOF = \frac{8\lambda}{\pi}\left(F/\#\right)^2 \quad . \tag{1}$$

If we want to measure the displacement of an object along the OA then we would want a relatively small DOF, such that we could determined the plane of our object to within the error provided by the DOF. From (1) we see that for small DOF we need small F/#. However this typically comes at the expense of a needing to bring the object we are imaging close the lens and so also a decrease in image field of view . For instance, a 50X, F/0.9 microscope objective has very good DOF resolution of $\approx 1\,\mu m$, but with an object-to-lens distance of only $\approx 1\,cm$, the field of view is $\approx 50\,\mu m$. For measuring antennas in practice, we wish to have a respectable working distance (>100 mm), such that the camera lens does not interfere with the antenna and accompanying mounting hardware, etc. We also wish to have a field of view large enough to image entire antenna components. In contrast to a microscope objective, a typical machine vision lens provides transvers resolution of tens of microns, with a field of view of tens of mm and object-to-lens distance of hundreds of mm, but with a comparatively *long* DOF of several mm. For the system we present here, the camera lens and FPA used allow for roughly a 30 $\mu m$ pixel resolution across a total FOV of roughly 3 cm x 3 cm at a working distance of 100 mm.

Therefore, in order to obtain the same spatial resolution along the OA that can be achieved in the image plane, we need a way to break the ambiguity that results from the relatively long DOF.

### *B. Three Camera Concept*

To address the DOF ambiguity, a three-camera approach is used. Three cameras are oriented such that the optical axis of one camera is projected along the image plane of the others. The orientation of the cameras used is shown in Figure 2. This way a movement along the axis of one camera is seen as a translation in the other two and thus the DOF ambiguity is broken. As such, the FPA of the other two cameras now provide the needed spatial resolution along the OA of the third camera. In this way we achieve spatial resolution in three directions, along the two dimensions of the image plane and along the OA, comparable to that of just the image plane alone. Below we describe the operation and function of this system and present examples of absolute antenna alignments at 183 GHz using the probe antenna and SGH in Figure 1. We have purposely left out specific details of optical system calibration and design as this is out of the scope of this paper, but will be presented in a future paper.



Gordon, Joshua; Novotny, David.
"A Non-contact Machine Vision System for the Precision Alignment of mm-Wave Antennas in all Six Degrees of Freedom."
Paper presented at 91st ARFTG Microwave Measurement Symposium, Tucson, AZ, United States. October 12, 2014 - October 17, 2014.

### C. Linking to Laser Tracker

It is desirable to link the spatial information obtained with the vision system to the coordinate system of the LT. To do this, a centroiding algorithm is implemented whereby all three cameras image a 0.5 inch SMR reflector, denoted as SMR0 in Figure 2, and determine it's centroid. Each camera then stores the pixel location of this centroid in memory. Five additional SMRs (SMR1 through SMR5) which have a fixed relationship to SMR0, are attached at the base of the cameras. The magnetic nest locations of these are also shown in Figure 2. SMR0 through SMR5 are then captured by the LT forming a constellation of LT points. This is shown in Figure 3.

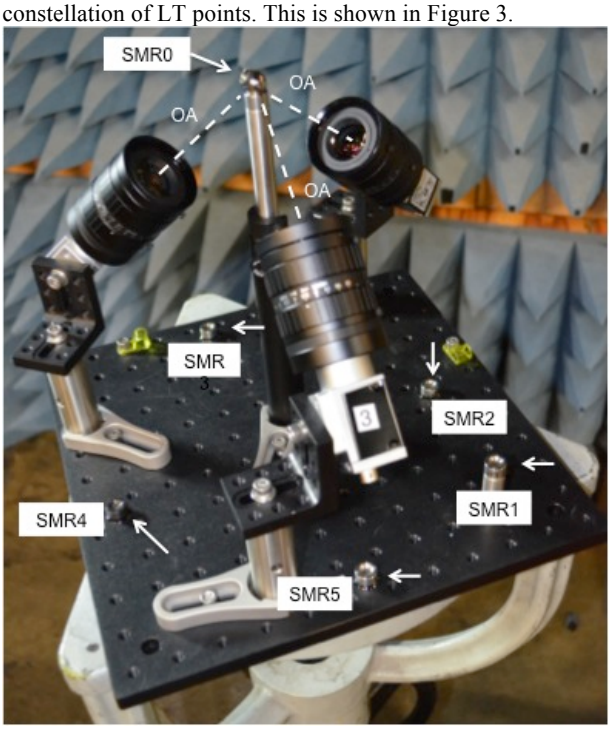


Figure 2. Three-camera vision system showing orientation of camera optical axis (dashed lines), and SMR locations .

Because there is a fixed relationship between SMR0 and SMR1:5, SMR0 is removed and only SMR1:5 need be measured by the LT to deduce the location of SMR0. After removal of SMR0 the pixels for the centroid location of SMR0 that are stored in memory are high-lighted in all the images captured by each camera. When an object appears to lie at the same location as the highlighted centroid pixels *in all three cameras simultaneously*, then that object occupies the same location as centroid of SMR0. This is by virtue of the fact that all three camera's centroid pixels correspond to the same point in space, the centroid of SMR0. Therefore, we need only to co-locate a feature on an object we wish to measure with these highlighted pixels in the image of all three cameras and measure the positions of SMR1 through 5 to determine the location of that feature in the LT coordinate system. The key here is that we have linked the location of SMR0 to the LT and the cameras without needing SMR0 to remain physically in place. As such we need only to co-locate the object we want to measure with the highlighted pixels in the camera images and capture the remaining SMRs 1 though 5. In this way we no longer need a physical target to touch the object we are trying to measure with the LT. In essence we have created a virtual LT target that is the size of the field of view of one camera pixel or about 30 microns.

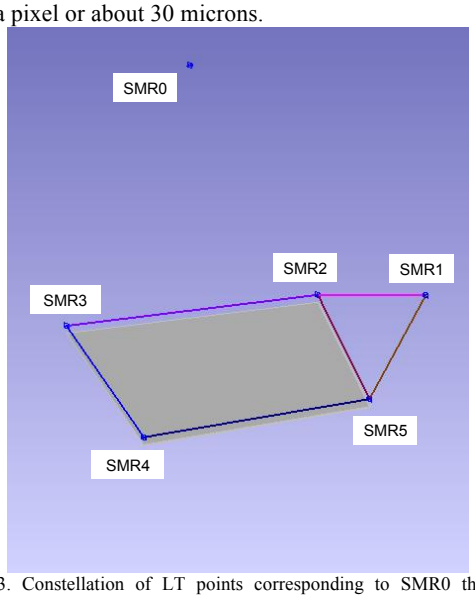


Figure 3. Constellation of LT points corresponding to SMR0 through 5 locations. Lines and plane joining points are shown to help show the reader spatial relationships.

This virtual target is used to "touch" off on points of an object we are trying to measure without ever actually touching it. Combined with machine vision algorithms this allows us to characterize very small antenna components (~1mm) to within tens of microns, yet within a FOV of tens of mm, at working distances of hundreds of mm and over volumes as large as the LT range-typically tens of cubic meters.

The spatial metrology enabled by this system enables us to determine coordinate frames in all six degrees of freedom for these antennas so that precision alignments can be achieved and linked to a LT coordinate system.

## III. FUNCTION

### A. Edge Detection and Centrioding

Using cameras allow us to take advantage of machine vision algorithms for finding antenna features useful for alignments and positioning at the pixel level. Furthermore the scribe marks used for mechanical references that are typically seen in much larger antennas are usually non-existent on mm-wave



Gordon, Joshua; Novotny, David.
"A Non-contact Machine Vision System for the Precision Alignment of mm-Wave Antennas in all Six Degrees of Freedom."
Paper presented at 91st ARFTG Microwave Measurement Symposium, Tucson, AZ, United States. October 12, 2014 - October 17, 2014.

antennas. As such using machine vision algorithms allows us to define mechanical references based on the entire antenna aperture itself. Here we demonstrate the use of such algorithms in conjunction with our LT linked camera system to locate and register antenna features from which an antenna coordinate system can be constructed. In this machine vision mode, two algorithms are used: 1) edge detection and 2) centroiding, which have proven useful for mm-wave antenna alignments in the NIST CROMMA facility. Many image processing software packages exist today that allow for various edge detection process. All three camera images are scanned to determine the pixel coordinates of antenna aperture edges. From the ensemble of edge pixel coordinates, the centroid of the antenna aperture is determined from a center of mass calculation. The centroid of the aperture is a cardinal point for the center of the antenna aperture and can be used to define the antenna coordinate system.

The edge detection and centroiding process for determining the center of the $\mu = \pm 1$ probe *in the LT coordinate system* is described next. In Figure 4, the aperture centroid determined from the edge detection process is represented as the center of the yellow circle. The green boundary defines the region of interest for edge detection. The center of the blue circle is the location of the center of SMR0 stored in pixel memory and know by the LT via the constellation of SMR1:5 (as described above in II.C). To determine the centroid of the aperture *in the LT coordinate system*, the aperture centroid (yellow circle) is co-located with the center of SMR0 (blue circle) in all cameras at the same time, see Figure 5. At this moment the LT captures SMR1:5. Because the center of the aperture occupies the same point in space as the center of SMR0, we immediately deduce the location of the aperture center relative to the constellation of LT points measured from SMR1:5. The absolute location of the centroid is then known in the LT coordinate system to within ~30 microns.

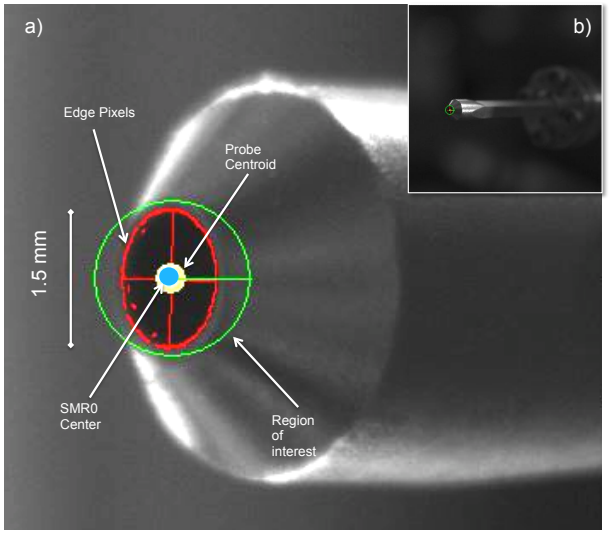


Figure 4. Zoomed in (a) and full FOV (b) images of WR-05 probe. Edge detect pixels (Red), probe centroid (Yellow), SMR0 center (Blue), and region of interest (Green) are shown.

The error in the alignment between the yellow and blue circles can also be determined in real-time from calculating the pixel offset from the center of each circle. This can be done at the sub-pixel resolution using pixel interpolation. Beyond knowing the centroid in the LT frame, we have the added utility that we can now register this centroid to any other LT target in our system. For example, if we wish to track the probe antenna while it is moving, we need only then measure a target that is fixed in position relative to this centroid. This technique is used to precisely locate and track the probe antenna while it is attached to the end of the moving robotic arm in the CROMMA facility. This system is also used for teaching the robot arm the centroid location. This allows the probe antenna to be used as the end effector in the robot kinematic model and aids in antenna probe positioning during near-field scans. The robot teach process is shown in Figure 6, where the robot arm brings the probe centroid into alignment with the location of the center of SMR0 (depicted by arrow) at several different orientations or poses (a)-(d).

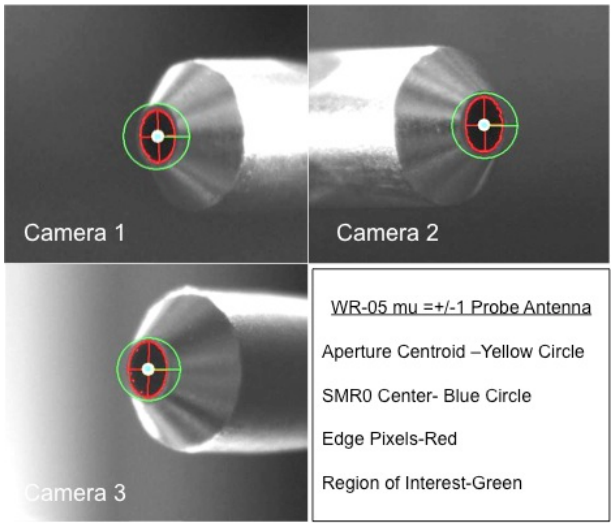


Figure 5. Simultaneous alignment of probe antenna centroid shown in all three cameras. Edge detect pixels (Red), probe centroid (Yellow), Center of SMR0 (Blue), and region of interest (Green) are shown.

### *B. Virtual Touch Probe Mode*

The method described above for locating the centroid of the aperture in the LT coordinate system does not also allow for the edge of the aperture to be located in the LT coordinate system. This is because the edge points used in determining the centroid are not measured directly in the LT frame of reference. This is in contrast to the aperture centroid, which was co-located with SMR0. Being able to measure the aperture edge is desirable for establishing a plane of reference for the antenna that can be used to define its orientation. We therefore extend this technique so that we can accurately



Gordon, Joshua; Novotny, David.
"A Non-contact Machine Vision System for the Precision Alignment of mm-Wave Antennas in all Six Degrees of Freedom."
Paper presented at 91st ARFTG Microwave Measurement Symposium, Tucson, AZ, United States. October 12, 2014 - October 17, 2014.

measure and determine the orientation of the aperture planes of small (~1mm) and larger (>10mm) antennas. We refer to this mode of operation as virtual touch probe mode. In this mode the virtual point defined by the center of SMR0 is used as one would use a physical touch probe, to touch off on a series of locations on an object so that the topology of that object can be determined in the LT coordinate system.

This mode of operation provides flexibility for determining absolute antenna dimensions, tracing out complex shapes, and registering alignment markers to within the 30 micron system resolution. An example of this is shown in Figure 7, where we have traced out the aperture of a the $\mu = \pm 1$ probe antenna. These data were obtained by using the robot arm to bring the probe aperture to the virtual touch probe point at several locations around its perimeter, and capture these locations with the LT. From these points, a circle fit was performed to determine the aperture diameter and plane orientation relative to the LT tracker target on the robot arm. Through this method, the diameter was determined to be 1.486 mm with an RMS fit error to an ideal circle of 22 microns. Furthermore, from the ideal circle fit, the planarity of probe aperture was determined to be within $\pm 30\ \mu m$ . This is consistent with design specification of a 1.5 mm diameter and demonstrates the level of precision and accuracy of this technique for measuring small antennas. It also demonstrates an ability to inspect and quantify the mechanical tolerances of such small antennas.

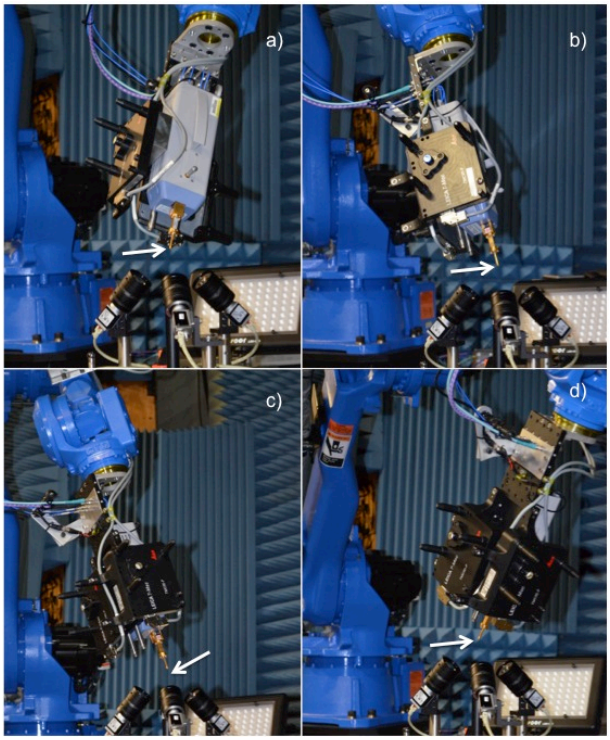

Figure 6. Teaching the location of the probe antenna centroid to the robotic arm in the CROMMA facility through poses (a)-(d) .

Similarly we also demonstrate measuring the aperture of the SHG shown in Figure 1 using virtual touch probe mode. An image of this antenna captured with the vision system is shown in Figure 8. Zoomed-in images of each corner are also shown. The arrows in these images show the location of virtual point used to "touch" off at the corners of the SGH. Line segment fits were then made to these corner points from which, the center, plane, and orientation of the was determined. It should be pointed out that a centroiding algorithm, similar to that used for the circular aperture, could have been used, but for a rectangular aperture it is simpler to use virtual touch probe mode.

Upon inspecting the SGH in the cameras, it was apparent that the wall thickness was not consistent and that the internal corners were rounded off and did not define the intersection of the wall edges. As such the blue dots in Figure 8 lie slightly inside the corners at the *effective* location where the walls intersect. This brings up the issue of the stringent mechanical tolerances needed on mm-wave components. In addition, having micro-machined scribe marks, such as can be achieve with laser etching, on such antennas would be beneficial and aid in alignment.

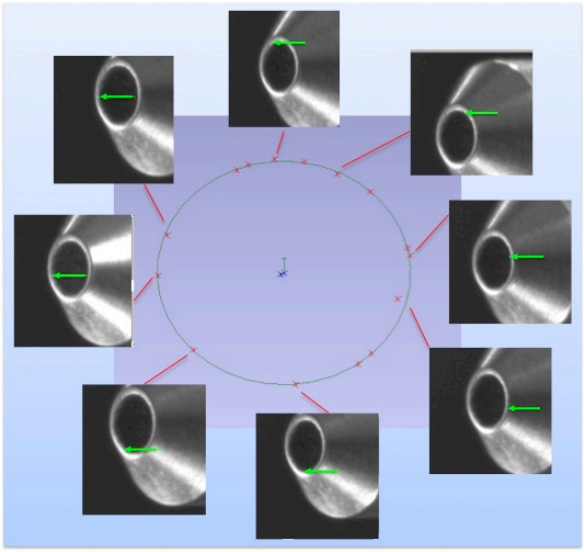
Figure 7. Measured points around the perimeter of the probe aperture using virtual touch probe mode. Arrows show location on probe. The measured diameter measured was 1.486 mm with an RMS error of 22 microns.

If for example a set of micro-machined marks existed on this SHG they would provide a repeatable set of locations to touch off to. This would help repeatability between alignments as well as intercomparison measurements because there would be clear agreement on alignment locations. With this camera system one can easily detect mechanical imperfections on the tens of micron level. Such imperfections become significant for mm-wave antennas because they approach the size of the operating wavelength. Without well defined mechanical reference locations, the mechanical uncertainty due to these imperfections does not allow one to use the geometry of the



Gordon, Joshua; Novotny, David.
"A Non-contact Machine Vision System for the Precision Alignment of mm-Wave Antennas in all Six Degrees of Freedom."
Paper presented at 91st ARFTG Microwave Measurement Symposium, Tucson, AZ, United States. October 12, 2014 - October 17, 2014.

component alone for alignment. This allows room for inconsistency between alignment measurements and could possibly affect agreement in antenna performance during intercomparisons. Using the touch probe mode, the length of each side of the SGH was determined to be 12.65 mm X 9.68 mm X 12.63 mm X 9.68 mm. These values are nominally consistent with the manufacturer specifications of 12.55 mm x 9.58 mm.

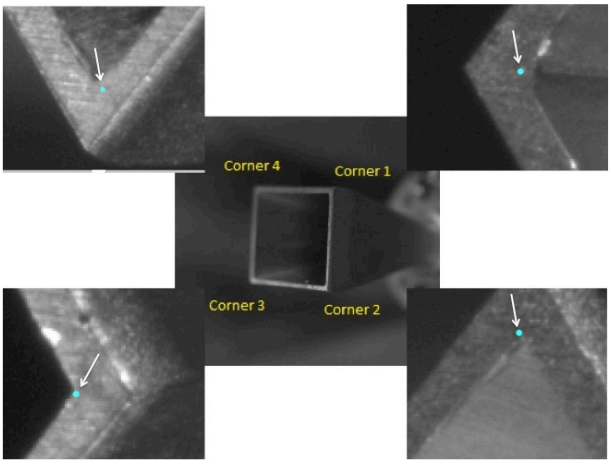

Figure 8. SGH corner measurements using the touch probe mode. Touch probe locations are shown in zoomed-in images by arrows (blue dots) .

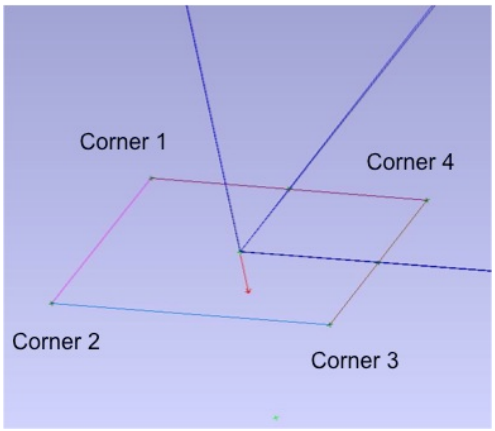

Figure 9. SGH plane and frame constructed from aperture corner locations that were measured with virtual touch probe mode.

## IV. 6 DOF Alignment of Antennas

Combining the aperture centroiding and aperture plane measurement capability of this system, we can readily construct a coordinate system (frame) for each antenna. This frame defines the pose of the antenna in all 6 degrees of freedom (orientation and location) in the LT coordinate system. The frame origins can be constructed from centroid locations, and frame orientation defined by the plane of the aperture. By virtue of these frames being linked to the LT, we can now track the frame of the 1.5 mm aperture probe antenna relative to the SHG, thereby perform alignments between them to within 30 microns in real time.

## V. Conclusion

In this paper we present a machine vision method for the absolute alignment of mm-wave antennas within a laser tracker coordinate system. The fragile nature and dimensions of these small (~1mm) antennas negate the use of coordinated metrology measurement systems and larger touch probes for accurate spatial characterization. Developed at The Antenna Metrology Laboratory at NIST in Boulder, Colorado this machine vision based technique uses a synergy of three cameras linked to a laser tracker to provide a non-contact method for determining the absolute position and orientation coordinate frame of the probe antenna aperture in all six degrees of freedom to within 30-60 microns. This alignment technique is demonstrated using the CROMMA facility at NIST in Boulder, CO. The concept, design, and function of this system are discussed. Example data for precision antenna alignments are presented, where we show how this system can be used for defining the coordinate systems and aligning a WR-05, $\mu = \pm 1$ probe antenna and 24 dBi gain standard gain horn operating at 183 GHz in all 6 degrees of freedom.

## References

[1] A. Rakich, "Alignment of LBT optics using a laser tracker", *Proc. SPIE* 7733, Ground-based and Airborne Telescopes III, 77335K, August 2010

[2] A. Leon-Huerta, et. al., " Alignment of a large outdoor antenna surface using a laser tracker ", Proc. SPIE 8788, Optical Measurement Systems for Industrial Inspection VIII, 878839 May 2013

[3] G. Hindman, A. Newell, L. Dicecca, and J.C. Angevain, "Alignment Sensitivity and Correction Methods for Millimeter- Wave Spherical Near-Field Measurements"; *2010 Proceedings of the Antenna Measurement Techniques Association*; pp. 316–321; 2010.

[4] P. Rousseau, W.C. Wysock, and C.M. Turano, J.R. Proctor, "Using a Tracking Laser Interferometer to Characterize the Planarity of a Planar Near-Field Scanner"; *2002 Proceedings of the Antenna Measurement Techniques Association*; pp. 501–506; 2002.

[5] M. H. Francis, R. C. Wittmann, in "Modern Antenna Hand Book", C. A. Balanis, Chp. 19, 929, 2008

[6] J. A. Gordon, D. R. Novotny, "Simultaneous Imaging and Precision Alignment of Two mm Wave Antennas Based on Polarization-Selective Machine Vision", IEEE Trans. Inst. Meas. vol. 61, pp. 3065-3071, November 2012

[7] J. E. Greivenkamp "Field Guide To Geometrical Optics", SPIE, Bellingham, WA 2004, pp. 3



Gordon, Joshua; Novotny, David.
"A Non-contact Machine Vision System for the Precision Alignment of mm-Wave Antennas in all Six Degrees of Freedom."
Paper presented at 91st ARFTG Microwave Measurement Symposium, Tucson, AZ, United States. October 12, 2014 - October 17, 2014.

# Antenna Alignment and Positional Validation of a mmWave Antenna System Using 6D Coordinate Metrology

David R. Novotny†, Joshua A. Gordon, Jeffrey R. Guerrieri
Physical Measurements Laboratory
National Institute of Standards and Technology
Boulder, Colorado, United States of America
†david.novotny@nist.gov

***Abstract*— We present the positional and alignment techniques and mmWave validation for the CROMMA, an antenna measurement system that uses an industrial robot to perform probe scanning of an AUT. We improved the positional accuracy of the commercial robot by using a laser tracker to measure and correct the scanned geometry. We are measuring and positioning the probe and AUT in six degrees-of-freedom (6DoF). We combine the 6DoF position and orientation measurements (x, y, z, yaw, pitch, roll) using coordinated spatial metrology to assess the quality of each motion stage in the system, and then tie the measurements of each individual alignment together to assess scan geometry errors. Finally, we take *in-situ* 6DoF position measurements to assess the positional accuracy throughout the measurement process, which can then be used for positional error correction in the final pattern analysis.**

**We performed dual polarization pattern measurements at 183 GHz. Our results show positioning errors, mmWave stability and pattern differences on two spherical scan surfaces at 100 and 1000 mm radii.**

## I. INTRODUCTION

The demand for millimeter Wave (mmWave) antenna measurements (> 100 GHz) has recently increased due to the practical realizations of many mmWave systems and applications. Point-to-point communication links from 92-95 GHz and 120 GHz are now commercially available and 220-650 GHz systems are being researched for medical and security applications. New developments in climate monitoring require traceability in radiometric and remote sensing equipment from 100-850 GHz, including calibrated power, emissivity and antenna gain [1].

In response to this demand, NIST has developed the Configurable Robotic Millimeter-wave Antenna Facility (CROMMA). We present here the validation testing and positional and measurement error assessment in the mmWave frequency range [2]. The CROMMA is an antenna measurement system (see fig. 1) built upon a 6 degree-of-freedom DoF robot arm used to scan a RF probe over a specified scan geometry. A 6 DoF hexapod is used to align the AUT to a $\phi$-rotation stage, and a 6 DoF laser tracker (LT) used to track the 3DoF position ($x,y,z$) and 3DoF orientation ($R_x,R_y,R_z$ or alternatively roll, pitch and yaw) of the probe and AUT.



The coordinated kinematic motion of the robot, along with its non-orthogonal motion axes, allows scanning in multiple geometries (planar, cylindrical, spherical, and linear extrapolation). Many present-day antenna ranges, including the NIST planar and spherical ranges, use dedicated stacked, orthogonal stages to generate the movement needed for a particular scan geometry. However, the orthogonality misalignments of these stages may introduce positional and/or pointing errors, which may not be fully correctable within the confines of the fixed movement stages. The use of 6DoF coordinated positioning system has been used for imaging purposes [3] and laser trackers have been used to characterize antenna ranges [4]. We are using coordinate metrology to generate 6DoF scanning geometries, and then to align multiple 6DoF movement stages and correct for the mechanical inaccuracies during the measurement. This dynamic, *in-situ* technique allows us to use less accurate but highly repeatable and configurable, positioning hardware for mmWave scanning with an eventual goal of extending the frequency range to at least 500 GHz.

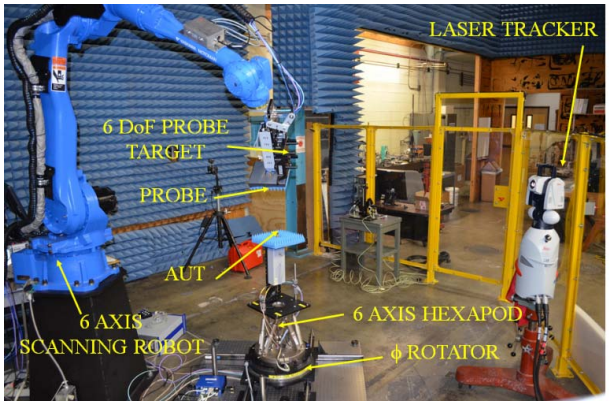


Figure 1. The CROMMA Facility. Major components include the 6-axis robot for probe scanning, the ϕ-azimuth rotator for AUT scanning, the hexapod to align the AUT to the rotator, and the laser tracker and probe targets for AUT and probe alignment and tracking.

Novotny, David; Guerrieri, Jeffrey; Gordon, Joshua.
"Antenna Alignment and Positional Validation of a mmWave Antenna System Using 6D Coordinate Metrology."
Paper presented at 91st ARFTG Microwave Measurement Symposium, Tucson, AZ, United States. October 12, 2014 - October 17, 2014.

Antenna alignment for near-field scanning was typically done at NIST with a multitude of instruments (theodolites, electronic levels, motor encoders) to align multiple stacked motion stages (linear, rotation). Many labs and systems now make use of laser trackers to measure ranges and perform periodic compensation across the scan geometry [5]. The current alignment system uses LTs with 6DoF coordinate metrology, not only for geometry creation, alignment and range qualification, but also *in-situ* positional analysis and data correction of routine measurements. This continuous position monitoring, allows for the correction of gravity, motion hysteresis, and different loading due to geometry or antenna changes. Eventually, we hope to correct for motion changes due to temperature and drive heating.

Alignment of the AUT and measurement probes to the scan geometry is often the most demanding and time consuming aspect of near-field measurements. As frequency increases, the typically acceptable positioning errors of λ/50 [6] tend to become more difficult to address. We will highlight the mechanical motion control available and the accuracies at which we can measure position of the probe and AUT.

We present pattern measurement results at 183 GHz using the CROMMA configured in an elevation over azimuth measurement coordinate system. The robot provides a $\theta$ elevation scan over the range of -105º to 105º, while the $\phi$-rotator provides 0-360º azimuth rotation.

## II. Overview of the CROMMA

The CROMMA was designed around a multi-axis coordinated-motion robot. Our base requirement was to perform spherical measurements at variable distances from 50 mm to 1m in diameter, provide probe rotation for arbitrary polarizations, have the payload capacity to hold both an antenna and typical waveguide vector network analzyer (VNA) waveguide extensions, and maintain the λ/50 position accuracy up to 500 GHz. These demanding requirements dictated the need to have 6 DoF position control throughout the scanning range.

Our method to fully correct position and pointing throughout the scan does not require the alignment of multiple stages but rather the individual alignment of every scan point in the geometry. The $\phi$-rotator, fig. 1, is characterized and its axis of rotation defines the system's $z$-axis. The scan geometry is arbitrary because of the full 6DoF capability of the robot. But every geometry needs to be verified by the LT. However, to get the positional accuracies similar to the axes intersection errors of other conventional dedicated geometry scanners [5], we need to use the tracker to correct for each scan geometry and probe loading of the robot.

The CROMMA has several fixed and movable coordinate systems: $\phi$-rotator, hexapod, AUT, probe (ideal and measured), robot movement, alignment fixtures. These all need to be active at once and data and positional offset easily translated between multiple reference points of view. We use a commercial coordinate analysis software package that controls and coordinates the LT measurement, and keeps track of the relative position of all the components of the system.

### A. Coordinate Notations

We will use the position and orientation notation of [7]. The Fixed (or extrinsic) XYZ convention for transforming between frames (compound position and rotational translations) differs from the traditional Elemental (or intrinsic) Euler Angle ZYZ convention typical of many spherical near-field antenna measurement treatises [6,8,9]. This mechanically based coordinate system is intrinsic to the robot, hexapod, and coordinate analysis software, so it is used, at least during the measurements and alignments of the system.

A frame (location and orientation) $\boldsymbol{B}$, in a Fixed XYZ coordinate system is defined by six coordinates relative to an initial frame $\boldsymbol{A}$. The Cartesian offset $\boldsymbol{x,y,z}$ from $\boldsymbol{A}$ generates the $\boldsymbol{B}$ location, and rotations $\boldsymbol{R_x,R_y,R_z}$ generate orientation relative to $\boldsymbol{A}$. Unlike traditional Euler Angle rotations, the Fixed XYZ rotations are relative to the initial fixed frame $\boldsymbol{A}$, fig, 2. There is a one-to-one mapping between the Euler ZYZ and Fixed XYZ that is used to translate the data for the final pattern analysis step.

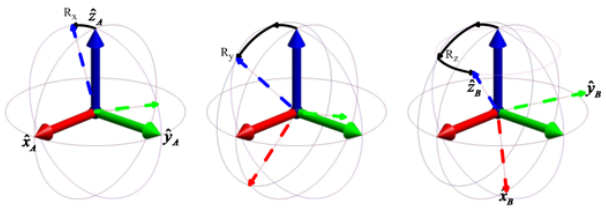


Figure 2. Rotation from Fixed XYZ frame $\boldsymbol{A}$ (solid) to frame $\boldsymbol{B}$ (dashed). The $\mathbf{R_x}$ rotation (left) about the $\boldsymbol{x}$ axis of $\boldsymbol{A}$, $\hat{x}_A$, followed by the $\mathbf{R_y}$ rotation about $\hat{y}_A$, followed by the $\mathbf{R_z}$ rotation about $\hat{z}_A$. The rotations together with the base $\boldsymbol{x,y,z}$ offset relative to $\boldsymbol{A}$, give a full 6DoF frame definition.

## III. Alignment

The traditional NIST method for a spherical scan alignment for larger ranges usually requires various translation stages (roll/azimuth or elevation/azimuth) to be aligned so the axes intersect to sub-wavelength precision (typically < λ/50 or λ/25). A theodolite is placed between the AUT and probe to align the AUT and probe axes. During typical spherical alignments (2 - 40 GHz) at NIST, the imperfections in the individual axes are averaged over a rotation to minimize overall error. The AUT/probe alignments are done at one azimuth point and two opposite roll angles. The errors in probe and AUT pointing, position and drift were then limited to the movement imperfections and differential loading of the combined system. At lower frequencies these errors were considered negligible; however at mmWave frequencies, this minimization of errors could lead to larger systematic position and pointing errors at individual points in the scan

Allowable mechanical errors decrease with increasing frequency. A 300 GHz the wavelength is approximately 1 mm so typical position and pointing errors need to be less than λ/50 or ~20 µm to be able to resolve a -60 dB sidelobe [6]. At these tolerances, issues such as axes imperfections and misalignment, differential gravity loading through the scan, and repeatability of the axes become larger components of measurement uncertainty.

Novotny, David; Guerrieri, Jeffrey; Gordon, Joshua.
"Antenna Alignment and Positional Validation of a mmWave Antenna System Using 6D Coordinate Metrology."
Paper presented at 91st ARFTG Microwave Measurement Symposium, Tucson, AZ, United States. October 12, 2014 - October 17, 2014.

Rather than build a fixed circular axis for the probe scanning and accept the errors in the axis, we are using an arbitrary 6DoF robot to scan the probe. The robot was not chosen for its absolute position uncertainty (measured at ~0.4 mm) but, rather for its path repeatability (manufacturer stated rms repeatability of ~0.07 mm). If individual points can be repeated, then position errors throughout the scan can be corrected on a point-by-point basis.

The alignment and measurement processes for this system presents new challenges [10]. We will measure each movement stage to determine its base orientation, and go through repeated measure, align, re-measure to verify each sub-alignment.

### A. Base $\phi$-Rotator Characterization

The $\phi$-rotator in fig. 1 is the only fixed stage of the CROMMA. We use the LT to measure the rotator movement and establish the center of the rotator and the axis of rotation, fig. 4. The AUT, probe scanning geometry, and all subsequent alignments will be referenced to the system $z$-axis.

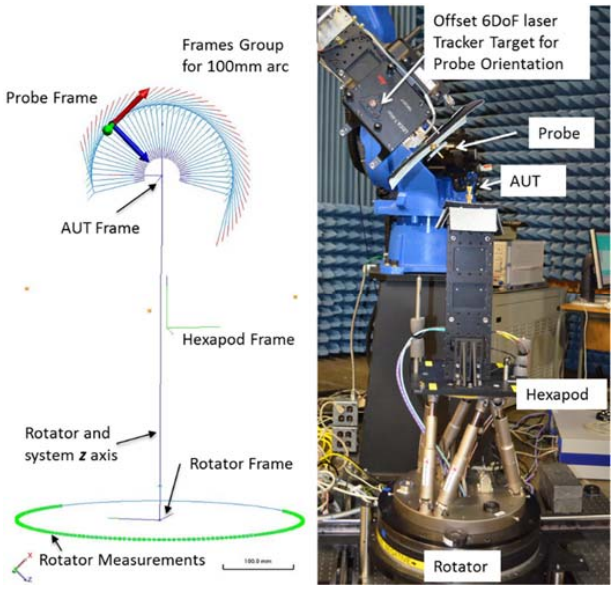


Figure 3. Alignments used in the CROMMA. The visualization of the position and orientation using the coordinate metrology software (left) is compared to the aligned hardware (right).

### B. Hexapod and AUT Alignment.

A particular challenge at these mmWave frequencies is that the AUTs tend to be small and delicate. The size of feed horns, and the coatings on broadband reflectors do not allow for contact with LT targets or attachment of reference mirrors. NIST has developed a non-contact method of measuring the AUT and probe position and orientation, and transferring those frames to an offset 6DoF LT target [11]. The Hexapod movement frame is then measured with the LT [10]. The initial AUT position is measured and the coordinate metrology software is used to calculate the required hexapod translation to align the AUT with the system $z$-axis.

### C. Probe Location

Similar to the AUT alignment, the probe frame is determined and transferred to a 6DoF target, fig 4 [11]. With the ability to measure the probe position and orientation directly, the scan geometry needs to be created. The robot is not accurately aligned to the $\phi$-rotator, so an initial guess of the $\theta$ elevation scan will lead to position and pointing errors that need to be addressed, figs. 4 - 5.

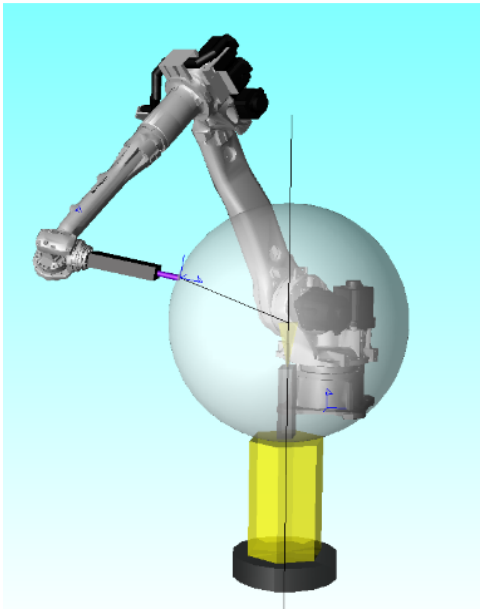

Figure 4. Conceptual image of pointing errors in the CROMMA. The sphere represents the ideal scan geometry and the line between the probe and the scan center highlights a correct probe position and incorrect probe pointing. Both types of errors are correctable in the CROMMA.

The initial scan will show the base robot error and misalignment. This is due mainly to robot alignment uncertainty and the gravity loading of the robot as the probe is scanned through the scan geometry. The resultant difference between the ideal and the measured probe frame, fig. 5, is determined by the coordinate metrology software and it calculates the correction in the robot movement frame for every scan point. This updated robot scan geometry is uploaded for re-verification by the LT.

The six-axis structure of the robot requires multiple axes to move between any two arbitrary probe locations, so single axis corrections are not sufficient for accurate probe positioning and orientation. The robot's overall accuracy was measured at ~400 µm; its measured repeatability, ~20 - 50 µm, is considerably better. Because local robot movement frames vary slightly due to gravity, loading, and robot imperfections, to get overall accuracies on the order of the base robot repeatability, multiple corrections to the path need to be performed using multiple axes to overcome the local irregularities in the robot movement.

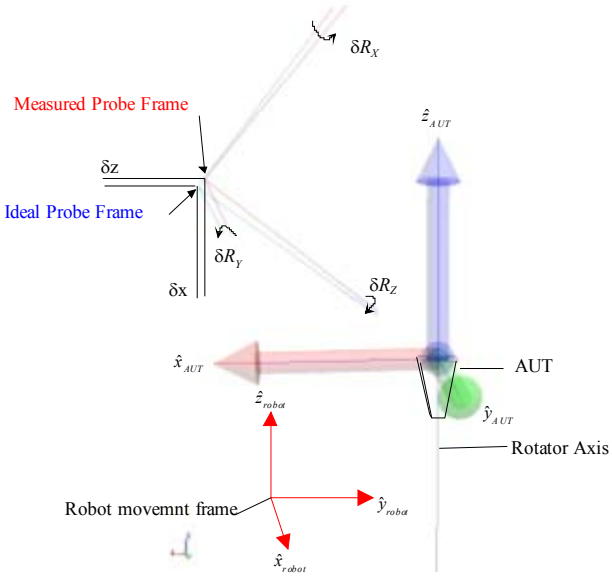


Figure 5. Position correction using multiple frames. The ideal and measured probe frames are defined relative to the AUT frame. The corrections (δx, δy, δz, δRX, δRY, δRZ) are calculated in the robot's absolute movement frame and sent as corrections to the robot trajectory. Note that for this case, the ideal probe location ($x,y,z,R_x,R_y,R_z$) or (79.86 mm, 0 mm, 60.12 mm, 180º,53º,180º) corresponds to an Euler ($r, \theta, \phi, \chi$) of (100 mm,53º,0º,0º) and pointing at the AUT origin.

We setup an elevation-over-azimuth spherical measurement at a radius $r$ =100 mm with a $\theta$ elevation scan from −105º to 105º. We set the scan center at the AUT aperture and set $\phi$=0º and the polarization $\chi$ =0º. The $\theta$ scan was run in both the forward and reverse directions to correct for differential path inaccuracies due to direction. The results, figs. 6-7, show that mean position errors are correctable to 25 µm and the pointing errors are reduced to less than 0.02º with three iterations.

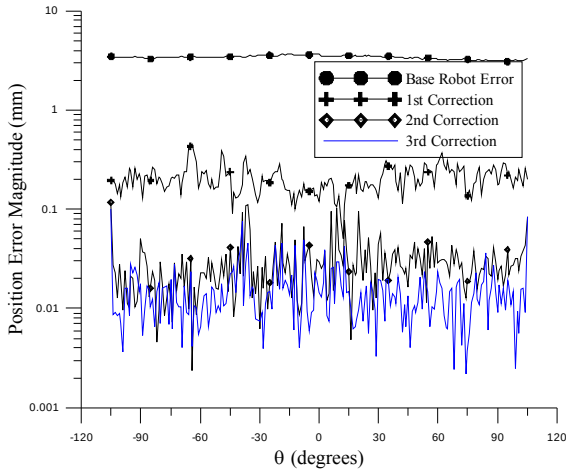


Figure 6. Scan geometry correction as a function of scan position and correction iteration. Some residual errors are seen around -32º and +5º which can be correctable with a nonlinear correction algorithm.

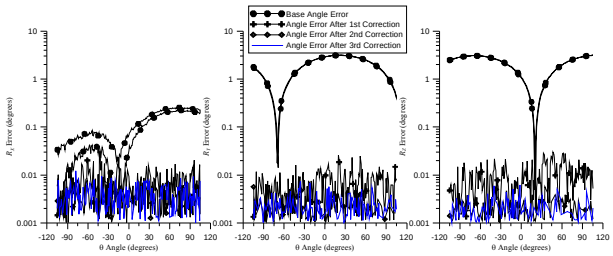


Figure 7. Pointing angle correction as a function of scan position and correction iteration. 6DoF target uncertainty is specified at ~0.01º. The base path has a forward to reverse difference seen in the $R_X$ pointing angle (left), this is addressed by the point-wise geometry correction.

## IV. Repeatability

The long-term repeatability of the CROMAA was assessed by comparing the probe frame variations during a series of twenty $\theta$ scans (25 minutes) to a full 360º $\phi$ scan (14 hours). 6DoF position as well as mmWave insertion at 183 GHz were recorded. Fig. 8 shows the range of robot movment required to perfrom a 100 mm radius spherical scan. The movement of the micrwave cabling needs to be miminized to prevent signal drift.

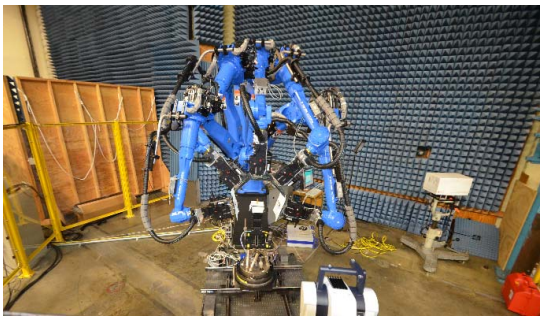

Figure 8. Robot and mmWave hardware movement during a −105º to +105º $\theta$ scan.

### A. Position Repeatability

The short-time twenty scan data, fig. 9, shows a measured radius of 99.998 ± 0.016 mm. The full scan, fig. 10, shows a radius of 99.976 ± 0.022 mm. The average radius seems to shrink by approximately 20 µm as the measurement proceeds, fig 11. This is primarily due to the thermal changes in the robot as the robot comes to a different quiescent operating point than during the alignment process. After the measurement is over and the robot has an opportunity to thermally stabilize again, the robot returns to the base profile measured in fig 9. While this raises concerns at higher frequencies (>300 GHz), the amount of change, approximately 20 µm, still results in an overall uncertainty of less than λ/50 or 32 µm at 183 GHz. The ability to capture full 6DoF scan data throughout the scan will, in the future, allow for either *in-situ* measurement correction of path or post-measurement, full-6DoF correction of the mmWave data to the actual measured positions.

Novotny, David; Guerrieri, Jeffrey; Gordon, Joshua.
"Antenna Alignment and Positional Validation of a mmWave Antenna System Using 6D Coordinate Metrology."
Paper presented at 91st ARFTG Microwave Measurement Symposium, Tucson, AZ, United States. October 12, 2014 - October 17, 2014.

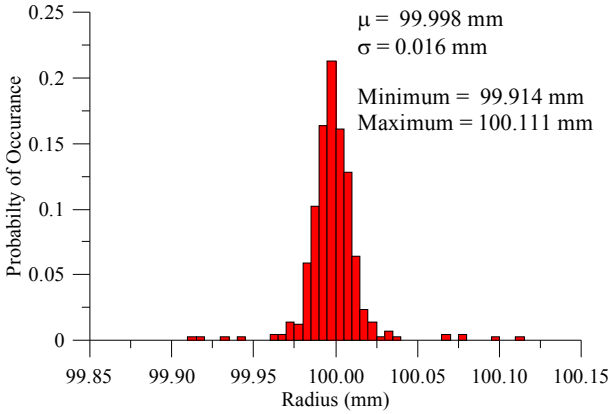


Figure 9. Radius histogram of twenty scans. The average radius is within the laser tracker uncertainty (10 μm) of the target 100 mm. The position uncertainty of 16 μm is less the λ/50 error, 32 μm, for discrimination of a -60 dB sidelobe at 183 GHz.

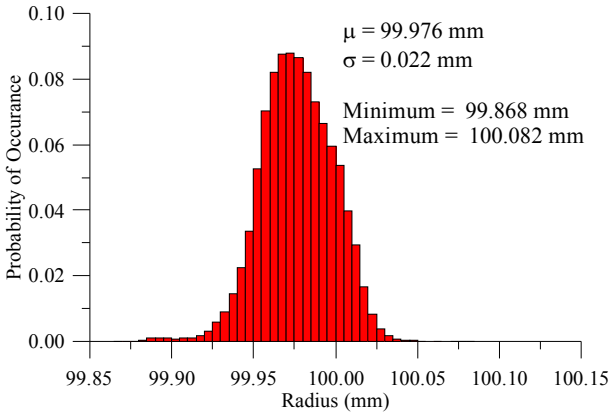


Figure 10. Radial uncertainty for the full 14 hour measurement. The uncertainty has grown to 22 μm.

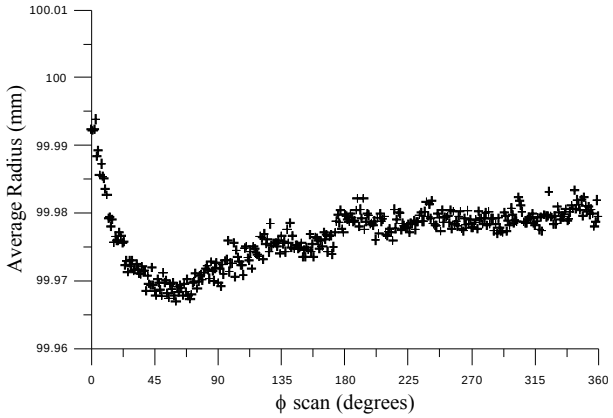


Figure 11. Mean radius as a function of $\phi$ position, or time. As the robot warms during long operations, the positional calibration changes slightly and introduces an ~20 μm position shift. This can be accounted for in future efforts at higher frequencies by pre-compensating the path for this effect, *in-situ* path correction, or post-processing the mmWave data to account for the positioning error.

### *B. mmWave Repeatability*

The stability of the position data allows us to measure the mmWave data with minimal concern that the variations in data are due to robot positioning errors. Amplitude and phase drift due to cable movement and thermal drift has to be analyzed to determine if it introduces significant effects on the measured pattern. Other research has raised concerns that use of externally driven sources and mixers [12] over moderate (1 m) distances may introduce unwanted errors. An advantage of the use of an industrial motion stage designed for tens of millions of operations is that cable routing is specifically designed for minimal cable stress. This is very useful for avoiding stress on microwave cabling. Fig. 12, shows the twenty scan mmWave data at zenith ($\theta$=0º, $\phi$=0º). The amplitude (< ±0.03 dB) and phase repeatability (< ±7º) are within established norms for near-field scanning measurements [6].

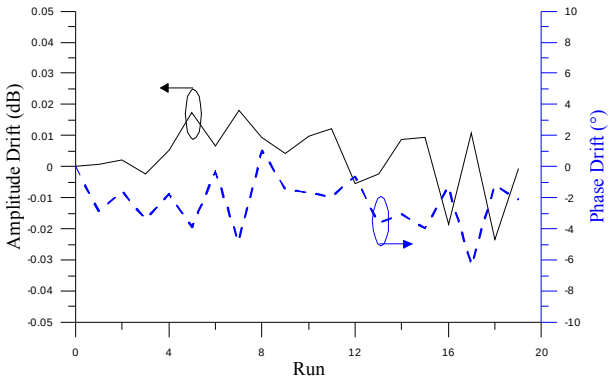


Figure 12. Zenith mmWave repeatability data for twenty $\theta$ = +105° to -105° scans. The microwave cables feeding the mmWave hardware undergo a displacement >100 cm while maintaining ±0.03 dB and ±7° stability at 183 GHz.

Novotny, David; Guerrieri, Jeffrey; Gordon, Joshua.
"Antenna Alignment and Positional Validation of a mmWave Antenna System Using 6D Coordinate Metrology."
Paper presented at 91st ARFTG Microwave Measurement Symposium, Tucson, AZ, United States. October 12, 2014 - October 17, 2014.

## V. Pattern Data

The elevation over azimuth data were performed at two polarizations and at two radial distances of 100 mm and 1000 mm. This required four path calibrations: $\chi = 0^{\circ}$ and $90^{\circ}$ at both 100 and 1000 mm. The far-field patterns, fig. 13, derived from the 100 and 1000 mm scans for both the E- and H-planes agreed to within ±0.5 dB above the -20 dB pattern level [13].

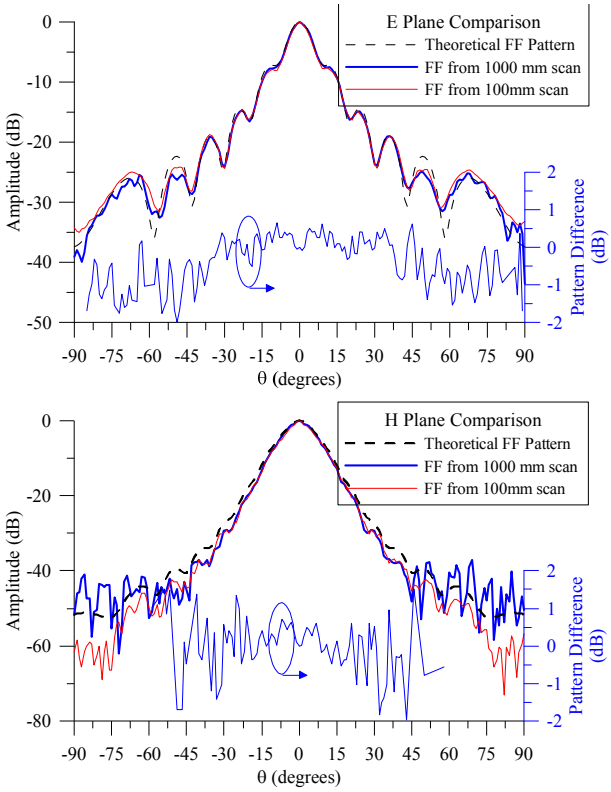


Figure 13. Theoretical, measured E-Plane (top) and H-Plane (bottom) patterns from two radial distances. The difference between the 100 and 1000 mm scan data is within ±0.5 dB for the central peak.

We can see, especially in the 1000 mm scan data that the noise floor is reached at large $\theta$ angles. This may be a future issue when measuring large antennas at high frequencies when very low-level side-lobe (<-50 dB) information are needed. This might be addressed by reducing the scan speed and increasing dwell time at each measurement point (at the cost of increased measurement time) or additional system gain (increased cost).

## VI. Conclusions

We have shown that using a 6DoF probe scanning and positional measurement hardware can provide adequate positioning for measuring patterns at 183 GHz. We are using a commercial material handling robot guided by metrology grade LTs and coordinate measurement software to perform near-field scanning with the precision required up to 300 GHz. The full 6DoF positioning, measurement and corrections performed allow for variable scanning, such as spherical, cylindrical, planar and extrapolation geometries. The 6DoF information also allows for mechanical position correction and post-measurement software correction of the collected data. We can use minimally accurate, but highly repeatable, lower-cost motion stages to deliver performance that may be cost prohibitive in custom single-axis motion systems.

We hope to be able to extend the frequency range in the future by bringing online algorithms that use the actual, non-ideal measurement locations measured by the LT [6]. We are currently correcting the scan geometry for the gross robot alignment, kinematic model and gravity loading effects to within ±25 µm. We will be addressing the robot dynamic and thermal changes that happen during long operational periods.

## References


[1] D.A Houtz, D. Gu, D.Walker, J. Randa, "An Investigation of Antenna Characterization Techniques in Microwave Remote Sensing Calibrations," IEEE International Geoscience and Remote Sensing Symposium, Munich, July 2012.

[2] J.A. Gordon, D.R. Novotny, M.F. Francis, R.C. Wittmann, "The CROMMA Facility at NIST Boulder: A Unified Coordinated Metrology Space for Millimeter-Wave Antenna Characterization," 2014 Proceedings of the Antenna Measurement Techniques Association.

[3] N. Petrovic, T. Gunnarsson, N. Joachimowicz, M. Otterskog, "Robot controlled data acquisition system for microwave imaging," 3rd European Conference on Antennas and Propagation (EuCAP), pp. 3356 – 3360, 2009.

[4] G. Hindman, A. Newell, L. Dicecca, J.C. Angevain, "Alignment Sensitivity and Correction Methods for Millimeter-Wave Spherical Near-Field Measurements," 2010 Proceedings of the Antenna Measurement Techniques Association, pp. 316–321, 2010.

[5] J. Fordham, T. Schwartz, G. Cawthon, Y. Netzov, S. McBride, M. Awadalla, D. Wayne, "A Highly Accurate Spheriecal Near-Field Arch Positioning System," AMTA 2011, pp. , Oct. 2011.

[6] R.C. Wittmann, B.K. Alpert, M.H. Francis, "Spherical near field antenna measurements using non-ideal measurement locations," 2002 Proceedings of the Antenna Measurement Techniques Association, pp 43-48, October 2002.

[7] J. J. Craig, Introduction to Robotics: Mechanics and Control, 3rd ed. New Jersey, Prentice Hall, 2004, pp. 38-74.

[8] A.C. Ludwig, "Near-Field Far-Field Transformations Using Sphereical Wave Expansions", IEEE Trans. A&P, March 1971, pp 214-220.

[9] J.E. Hansen, Sphereical Near-Field Antenna Measurements, Exeter, Peter Peregrinus, 1988.

[10] D.R. Novotny, J. Gordon, J. Coder, J. Guerrieri, M. Francis, " Use of a Laser Tracker to Actively Coordinate the Motion of a 3-meter Industrial Robot to Within 50 Microns," Journal of the CMSC, Autumn 2013, Vol 8, No 2, pp 26-32.

[11] J.A. Gordon, D.R. Novotny, "A Non-Contact Machine Vision System for the Precision Alignment of mm-Wave Antennas in all Six Degrees of Freedom," 2014 Proceedings of the Antenna Measurement Techniques Association.

[12] M. Htizler, S. Bader, C. Waldschmidt, "Key aspects of robot based antenna measurements at millimeter wave frequencies," 8th European Conference on Antennas and Propagation (EuCAP), pp. 474-478, 2014.

[13] M.H. Francis, R.C. Wittmann, D.R. Novotny, J.A. Gordon, "Spherical Near-Field Measurement Results at Millimeter-Wave Frequencies Using Robotic Positioning," 2014 Proceedings of the Antenna Measurement Techniques Association.



Novotny, David; Guerrieri, Jeffrey; Gordon, Joshua.
"Antenna Alignment and Positional Validation of a mmWave Antenna System Using 6D Coordinate Metrology."
Paper presented at 91st ARFTG Microwave Measurement Symposium, Tucson, AZ, United States. October 12, 2014 - October 17, 2014.

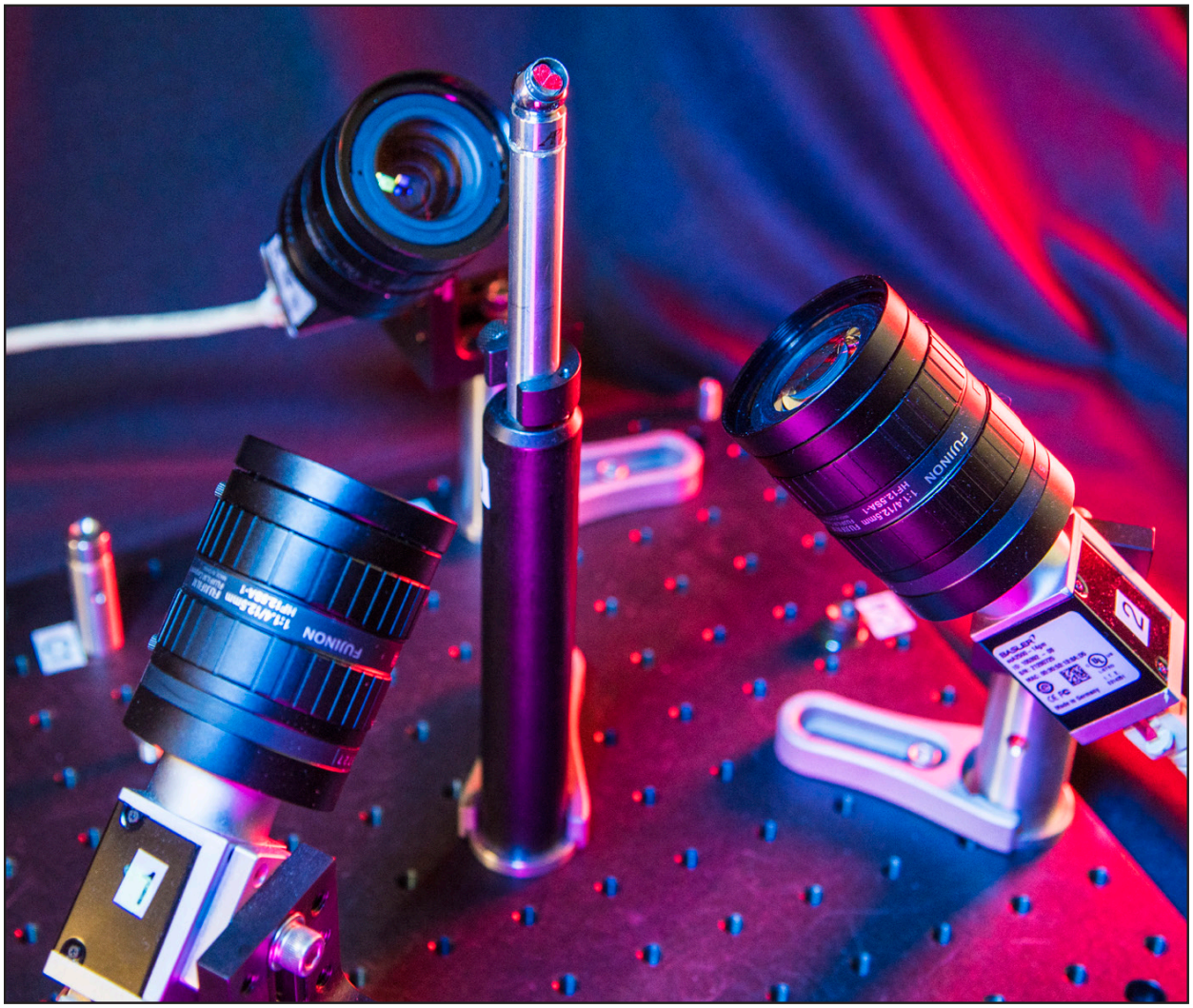


# A Single-Pixel Touchless Laser Tracker Probe

*by Joshua A. Gordon, David R. Novotny, and Alexandra E. Curtin, Radio Frequency Technology Division, National Institute of Standards and Technology*

In this article we will describe our development of a laser tracker probe, the Pixel Probe, that does not require physically contacting the object one is measuring and which has 3D spatial resolution of about 25 $\mu$m (in $X,Y,Z$) in the current configuration. This touchless laser tracker probe uses three machine vision cameras to discretize a scene down to the spatial resolution of a pixel. A single pixel from each camera field of view is linked to a laser tracker through a calibration process. The three pixels define a point in space that is used as a virtual touch probe, where one places these pixels on an object by means of viewing the camera images. This allows one to measure with a laser tracker the location of small features (tens of microns) on an object without needing physical contact. Given that the design of this system is easily scalable to higher resolution cameras and lenses, it is envisioned that this system could provide better than the current 25-$\mu$m resolution. The Pixel Probe excels at measuring objects that may prove difficult for existing laser tracker probes, such as those with sharp edges and corners, and those with amorphous, soft, and intangible features. In addition, one can register to



Gordon, Joshua; Novotny, David; Curtin, Alexandra.
"A Single-Pixel Touchless Laser Tracker Probe."
Paper presented at 2015 Coordinate Metrology Systems Conference (CMSC), Hollywood , FL, United States. July 20, 2015 - July 24, 2015.

the laser tracker features that appear in the images, and/or geometries that are derived using machine vision edge- and feature-recognition algorithms. With the Pixel Probe it is also envisioned that other physical quantities based on optical imaging, such as thermal infrared data, and spectral and polarimetric data, can be linked to a laser tracker. Following, we will present the concept, design, function, calibration, and operation of this system, as well as measurements using this system.

## INTRODUCTION

Laser trackers are effective for the spatial characterization of solid objects, and have many uses in industrial applications for spatial metrology tasks such as robot calibration, 3D part characterization, tolerancing, and reverse-engineering. They have also been indispensible in advanced surveying applications where high degrees of accuracy and precision are required, such as in aircraft assembly and telescope observatories.[1] Laser trackers have also been useful in the construction and alignment of antenna ranges and antennas.[2,3,4] The type of object that can be spatially characterized with these systems is dependent on the type of laser tracker probe used. Perhaps the most common probe is the spherically mounted retroreflector (SMR) made from three perpendicular mirror surfaces forming the corner of a cube. The SMR can be used on its own as a stencil that can be moved along a surface in a spatial measurement. As typical SMRs are limited to 1-in. and 0.5-in.-diameter spherical form factor, more complicated probes such as touch probes and laser line scanners have been developed to provide increased versatility for manual scanning of objects.

Laser trackers are very useful in the context of precision antenna alignments. They allow one to obtain high-fidelity spatial information, routinely measuring less than 100 $\mu$m, which is sufficient for antenna alignments necessary at frequencies in the millimeter-wave (mm-wave) range (100 GHz to 300 GHz).[5] Currently available laser tracker probes are excellent performers for many applications when the object of interest is significantly larger than the probe, made of solid material, can be physically contacted without deformation, has well-characterized albedo, and is lacking in sharp edges or corners.[6] However, when the object does not meet such requirements, current laser tracker targets may not be adequate. This scenario presents itself regularly when dealing with mm-wave components which have dimensions of interest that are on the order of 1 mm, have sharp corners and edges, are constructed of polished metal, and are too delicate to touch. The need for a new type of laser tracker probe that could provide useful spatial metrology of these mm-wave components is the motivating circumstance for this work.

This new laser tracker probe, called the Pixel Probe, is unlike other probes in that it is based on optical imaging. The Pixel Probe prototype presented here uses three cameras nominally arranged in a tetrahedral shape, which are constructed from three 2,592 × 1,944 complimentary metal oxide semiconductor (CMOS) pixel arrays, also known as focal plane arrays (FPA), and three 12.5-mm focal length low-distortion machine vision lenses. From each camera a single pixel is linked to a laser tracker through a calibration process which we will describe below. These three pixels are then used to unambiguously define a single point in space, P*, that is known in the native coordinate frame of the laser tracker. Because P* is defined through the camera images, it is in actuality a virtual object that is conjugate to the physical pixels in each FPA. As such, there is nothing physically there at the location of P*. In use, P* is defined as a set of pixel coordinates from each camera and can be virtually placed on the object we wish to measure by using the camera images. This is similar to the action performed when using a touch probe, or coordinate measuring machine (CMM). However, in this case nothing needs to physically touch the object under measure. The use of FPAs allows for spatial resolution on the order of tens of microns, and also makes the spatial resolution of this approach scalable by judicious choices of FPA pixel size and lens focal length. The Pixel Probe prototype we present here has approximately 25 $\mu$m spatial resolution.

The noncontact imaging nature of the Pixel Probe allows novel measurement modalities not obtainable with other laser tracker probes and targets, such as measuring sharp corners and sharp edges, objects that are soft or optically transparent, objects of high and low reflectance, and virtual objects (such as an image of a real object). In addition, other optical information, such as geometries determined from machine vision algorithms, thermal infrared data, and spectral and polarization information that represents other physical quantities, could also be simultaneously linked to the spatial measurement of the laser tracker. This provides a new type of measurement framework and opens up the ability to perform direct multi-physics measurements with a laser tracker. Such measurements could be used to compare multi-physics simulations with real data, in a similar fashion to when CAD models are compared to point-cloud data generated using a laser tracker or CMM. The Pixel Probe can also be used for robot tool center point (TCP) calibration and teaching with spatial resolution and accuracy on the order of tens of microns. The imaging properties of the Pixel Probe allow for robot tool end-effectors to be measured that may be difficult to otherwise characterize, such as water jets or laser welding spots.

Below, we will demonstrate the capability of the Pixel Probe by presenting data for several objects:

- A validation measurement using a glass plate camera target grid made of 250-$\mu$m-diameter electron beam-etched chrome dots; the plane of this plate is measured using the Pixel Probe and compared to a measurement of the plane of the glass plate using a 1.5-in. SMR
- The 1.5-mm-diameter aperture of a gold-plated circular antenna
- The 12.55 mm × 9.58 mm rectangular aperture of a gold-plated pyramidal horn antenna
- The shrinkage ratio of transparent Heat Shrink
- A man-made spider web fabricated from strands of clear epoxy

These objects are all quite challenging to measure with traditional laser tracker probes. They are either too delicate, too small, their optical properties make them difficult to measure, or they have a combination of such problematic attributes.



Gordon, Joshua; Novotny, David; Curtin, Alexandra.
"A Single-Pixel Touchless Laser Tracker Probe."
Paper presented at 2015 Coordinate Metrology Systems Conference (CMSC), Hollywood , FL, United States. July 20, 2015 - July 24, 2015.

## CONCEPT OF OPERATION

### Point projection to a pixel

With the proliferation of charge-coupled device (CCD) and CMOS cameras, it is not hard to find FPAs with pixel sizes on the order of a few microns, with several megapixel densities. Furthermore, optical lenses with modulation transfer functions (MTF) above a hundred line pairs per mm are also easy to obtain to match these high-resolution FPAs. It is therefore rather easy to achieve imaging resolution on the order of tens of microns. However, although this spatial resolution is readily obtained in the image plane transverse to the optical axis (OA), the spatial resolution along the OA is instead dictated by the depth of focus (DOF) of the lens, and not pixel resolution. The DOF is the distance over which an object can be shifted along the OA while still remaining in focus. In a ray optics picture this distance can be considered to be zero. However, due to the wave nature of light in a real optical system, the DOF is a non-zero value that depends on the ratio of the focal length to lens aperture, i.e., the f-number denoted as F/#. The DOF for a rotationally symmetric lens can be closely modeled with a Gaussian beam. Consider the expression for a Gaussian beam generated by a lens. The DOF for such a beam is:[7]

$$DOF = \frac{8\lambda}{\pi}\left(F/\#\right)^2 \qquad \text{(Equation 1)}$$

If we want to measure the displacement of an object along the OA, then we would want a relatively small DOF, such that we could determined the plane of our object to within the error provided by the DOF. From equation 1, we see that for small DOF we need small F/#. However, this typically comes at the expense of needing to bring the object we are imaging close the lens, and also in a decrease in image field of view. For instance, a 50×, F/0.9 microscope objective has very good DOF resolution of ≈ 1 $\mu$m, but with an object-to-lens distance (working distance) of only ≈ 1 cm, the field of view is ≈ 50 $\mu$m. In practice, we wish to have a respectable working distance (> 100 mm), such that the camera lens does not interfere with the object we are trying to measure. At the same time it would be nice to have a field of view much greater than that of the microscope.

In contrast to a microscope objective, a typical machine vision lens has a comparatively long DOF of several millimeters, yet does provide transverse resolution of tens of microns, with a respectable field of view of tens of millimeters and a working distance of hundreds of millimeters. For the system we present here, the camera lens and FPA used allow for roughly a 25-$\mu$m pixel resolution across a total FOV of roughly 3 cm × 3 cm at a working distance of 100 mm.

Using only a single lens to locate an object in three dimensions would result in good spatial discrimination of position of the object transverse to the OA in the image plane. However, this lens would produce a comparatively ambiguous measure of object location along the lens OA. Therefore, to obtain the same spatial discrimination along the OA that can be achieved in the image plane, we need a way to break the ambiguity that results from the relatively long DOF of the lens.

We employ the concept of point projection onto multiple image planes to address the DOF ambiguity of a single lens. To accomplish this, a three-camera approach is used. Three cameras are nominally oriented in a tetrahedral shape, such that the OA of one camera is projected along the image plane of the others. This way a movement of a point along the OA of one camera is seen as a translation in the other two, and thus the DOF ambiguity is broken. As such, the FPA of the other two cameras now provides the needed spatial resolution, and spatial discrimination along the OA of the third camera. In this way we achieve spatial resolution comparable to the FPA in three directions: along the two dimensions of the image plane and along the OA, as seen in figure 1.

In camera 1, $P_1$' remains in the center of image plane 1 with little detectable change, whereas $P_2$' is seen to have shifted by a measurable number of pixels denoted by ΔX. The extent of the shift on image plane 2 depends on the physical shift of $P_2$ and by the image magnification dictated by the lens focal length of camera 2 and the object image conjugate distances of $P_2$ and $P_2$'.[7] As such, $P_1$ has three conjugate images, one on each camera. Although strictly speaking a point in space is infinitely small, given that one pixel represents the smallest discernable element in the image planes, $P_1$' and $P_2$' can at best be represented as a set of pixel coordinates. Therefore a given $P_1$ will have a unique set of two-dimensional pixel coordinates ($x_p$, $y_p$) in each camera image. Thus, using three cameras $P_1$ is specified with a set of three pixel coordinates, (x1p, y1p), (x2p,y2p), and (x3p,y3p). If now we could link $P_1$ to a laser tracker, such that these pixel coordinates define a point that is also known to the laser tracker, $P_1$ becomes a laser tracker probe with the spatial resolution of a single pixel.

Next, we discuss the process of defining the coordinates of $P_1$ in each of the three cameras while simultaneously linking $P_1$ to a laser tracker coordinate system.

### Linking a pixel to a laser tracker

Using the principle of projection to the three image planes as was done for the single point $P_1$, a sphere that is imaged by

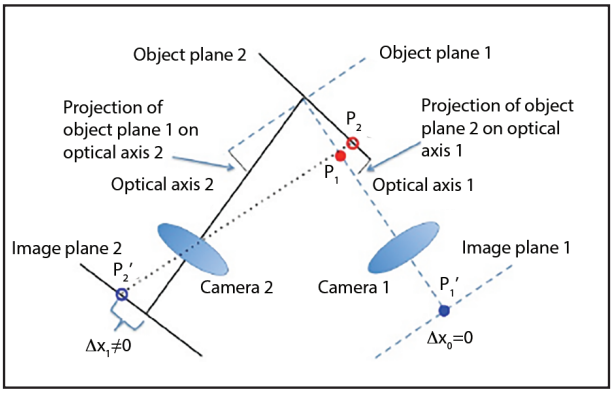


*Figure 1. Point projection onto multiple image planes; $P_1$ (solid red dot) is positioned on the OA of camera 1, but located by some amount inside the plane of best focus denoted as the object plane 1; point $P_1$ (solid red dot) coincident with the OA of camera 1 is projected along the object plane of camera 2, creating point $P_2$ (red circle). The image of this point in camera 1 is seen as $P_1'$ (blue dot) and in camera 2 as $P_2'$ (blue circle)*



Gordon, Joshua; Novotny, David; Curtin, Alexandra.
"A Single-Pixel Touchless Laser Tracker Probe."
Paper presented at 2015 Coordinate Metrology Systems Conference (CMSC), Hollywood , FL, United States. July 20, 2015 - July 24, 2015.

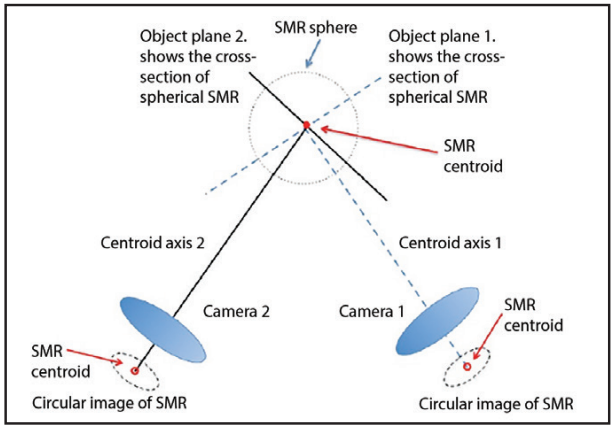


*Figure 2. Projection of an SMR that is used to link the cameras to a laser tracker; the circular images in camera 1 and camera 2 that are produced by the projection of the SMR are shown, and the centroid of these SMR images coincides with the centroid of the spherical form of the SMR*

the three cameras will result in three circular images at each of the image planes. Furthermore, the centroid of these three circular images, when projected back to the object plane, are all coincident with the 3D center of the sphere. Therefore, just as we were able to assign a unique set of three pixel coordinates to the single point, $P_1$, we can assign a similar set of three pixel coordinates to the centroid of the sphere. As is commonly known, the geometrical center of an SMR is also coincident with the location that is measured by the laser tracker to within a nominal alignment of 5–10 $\mu$m. Herein lays the trick: Because the cameras can identify the sphere center, by projection to the pixel arrays, as well as the laser tracker, we have a direct way to link the set of pixel coordinates of the sphere center to the laser tracker, as seen in figure 2.

The final Pixel Probe system prototype seen in figure 3 is generated by establishing a fixed constellation of SMRs relative to the three cameras, one of which (called SMR0) is placed in the center of the FOV of the three cameras and plays the role of the sphere described previously. Five other SMRs are mounted to the base of cameras, SMR1 through SMR5. To link the laser tracker to a single pixel from each of the cameras, a brightfield image of SMR0 is first captured by each camera, as seen in figure 4. A panel of light-emitting diodes is used as to generate a Lambertian brightfield background. A matte black shroud is placed around SMR0 and the cameras to stop unwanted reflections off the reflective SMR sphere. An edge-detection algorithm is then used to determine the set of pixel coordinates that define the centroid of SMR0. Figure 4 shows the brightfield image of SMR0. The red crosshairs locate the centroid, and the green border is the region of interest (ROI) used in the edge-detection process. Red dots on the perimeter of the SMR and inside the ROI are the location of the edge pixels determined from the edge-detection algorithm. These three pixel coordinates are stored in memory and highlighted in the images of the three cameras. Although the entire sphere is not visible due to the SMR nest, the validation measurement (details to follow) suggests that the uncertainty does not significantly affect the accuracy of this prototype. A future version of this prototype will address this.

Although SMR0 remains in the same position relative to the cameras and the rest of the constellation (SMR1 though SMR5), the laser tracker measures the entire constellation of SMRs. At this moment, SMR0 can be removed from the constellation because the centroid of SMR0 has been stored in memory as pixel coordinates, and these coordinates uniquely

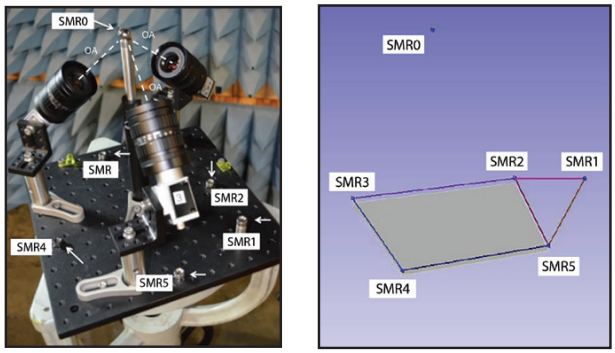


*Figure 3. (a) Pixel probe prototype developed at NIST (Boulder, CO); three cameras are nominally arranged in a tetrahedral with a constellation of five SMRs fixed in relation to the cameras, with the intersection of the optical axis (OA) for each camera to the location of SMR0 shown; (b) the points captured by the laser tracker representing the constellation of SMRs that is used to locate the pixel probe in the laser tracker coordinate frame*

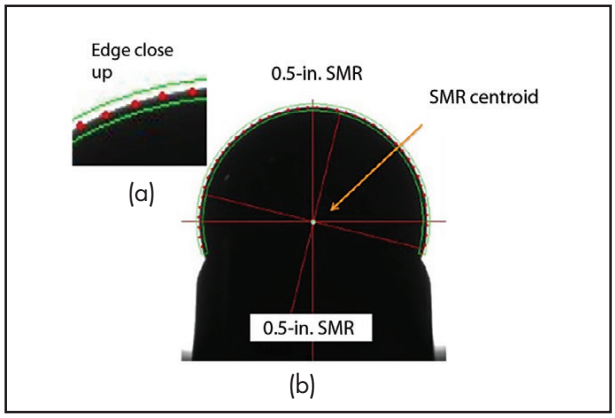


*Figure 4. The brightfield image of a 0.5-in. SMR as seen through the cameras of the Pixel Probe; this brightfield image is the implementation of the SMR projection depicted in figure 2; (a) a close-up of the SMR edge is shown; green boundary is the ROI used for the edge-detection process, and red dots show the location of the pixels at the SMR edge in the bright field; (b) the centroid of the SMR determined from fitting a circle to the edge pixels is also shown*



Gordon, Joshua; Novotny, David; Curtin, Alexandra.
"A Single-Pixel Touchless Laser Tracker Probe."
Paper presented at 2015 Coordinate Metrology Systems Conference (CMSC), Hollywood , FL, United States. July 20, 2015 - July 24, 2015.

define the point in space of the centroid of SMR0 relative to the rest of the constellation. As such, when a point on an object appears to be at the same location as the stored centroid pixels in all three cameras simultaneously, then that object occupies the same location as the centroid of SMR0. In the current incarnation of the Pixel Probe, the stored pixels are highlighted in each of the three images. The user then moves the cameras such that these highlighted pixels appear at the same location on the object one is trying to measure. That is, the user is in essence virtually placing the centroid of SMR0 at a known location on the object to be measured. At this moment the laser tracker then captures the rest of the SMRs in the constellation. Because the constellation has a fixed relationship to the centroid of SMR0, the location on the object under measure is also known by the laser tracker. In this way we no longer need a physical laser tracker target to touch the object we are trying to measure. In essence, we have created a virtual laser tracker probe that is the size of a single pixel, or about 25 $\mu$m in the prototype presented here.

In the rest of this article, we will refer to the point in space corresponding to the centroid of SMR0 just as SMR0. It is worth mentioning that, although for this prototype a constellation of SMRs is used in conjunction with SMR0, it would be equally effective to establish a coordinate frame using a six-degree-of freedom laser tracker target that had a fixed relationship to SMR0. This would have several advantages, such as easier tracking ability and quicker measurement time, as the processing of the SMR constellation relationship to SMR0 would not be needed.

In the following section, we describe the validation and measurements made with the Pixel Probe.

## MEASUREMENTS

### Validation measurement

A validation measurement was performed to compare the performance of the Pixel Probe to a standard 1-in. SMR. A glass 2 in. × 2 in. plate camera test target grid made of 250-$\mu$m-diameter electron-beam-etched chrome dots spaced by 500 $\mu$m was used. Because the grid dots are only a few hundred nanometers out of the plane of the glass, the dots are not distinguishable from the plane of the glass using a laser tracker. This allows for a comparison measurement of the plane of the test target to be made between the SMR and the Pixel Probe. As the Pixel Probe excels at measuring small features and the SMR excels at measuring surfaces, this test target combines both such aspects into a single geometry. The dots provide repeatable fiducials for the Pixel Probe to measure in the plane of the grid, and the optically flat glass substrate provides a repeatable surface for the SMR to measure. A spatial scan was performed as the SMR was moved along the surface of the glass grid. The Pixel Probe was used to measure several dots in the grid. Planes were then fitted to the individual data sets and the displacement and angular deviation of the normal were compared. Two SMR planes were measured and compared to the plane as determined by the Pixel Probe, as seen in figure 5. The RMS fit statistics for the Pixel Probe plane were 0.0021 mm, and the two SMR measured planes were 0.0038 mm and 0.0039 mm, respectively. This yielded a mean plane offset between the Pixel Probe

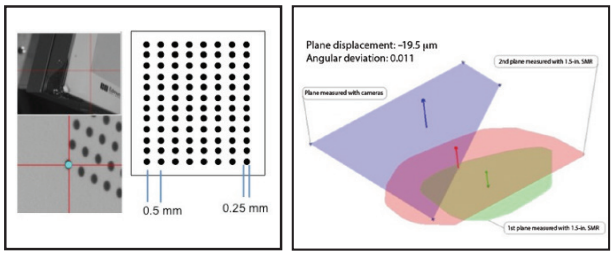


(a) (b)

*Figure 5. (a) Grid test target; square grid of 0.25-mm-diameter chrome dots spaced by 0.5 mm, with full field and zoomed-in images of the test target as seen in the Pixel Probe images also shown. In the lower left SMR0 is located at the blue dot at the intersection of the red cross hairs; (b) a visual comparison of planes determined from fits to data from the Pixel Probe (blue plane) and the 1-in. SMR (red and green planes) measurements. A mean plane displacement of 19.5 µm and mean angular deviation of 0.11° was determined.*

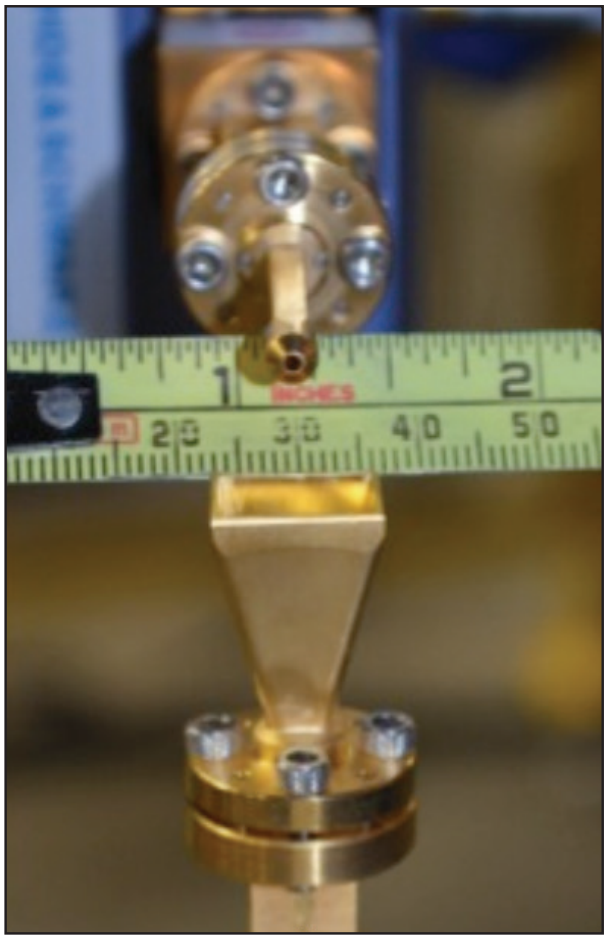


*Figure 6. Circular probe antenna with nominal aperture radius of 1.5 mm and pyramidal horn antenna with rectangular aperture of nominal dimensions 12.55 mm × 9.58 mm*



Gordon, Joshua; Novotny, David; Curtin, Alexandra.
"A Single-Pixel Touchless Laser Tracker Probe."
Paper presented at 2015 Coordinate Metrology Systems Conference (CMSC), Hollywood , FL, United States. July 20, 2015 - July 24, 2015.

measured plane and SMR measured planes of 19.5 $\mu$m, with an angular deviation of 0.11°. Both of these values are within the uncertainty of the laser tracker.

## Measuring mm–wave antenna apertures

Next, we will show the measurements of two mm-wave antenna apertures. A circular probe antenna and a pyramidal horn antenna with a rectangular opening are measured, as seen in figure 6. The manufacturer-specified dimensions for the circular aperture are 1.5-mm diameter and 12.55 mm × 9.58 mm for the rectangular aperture. Both of these antennas are gold plated, defined by sharp edges, and quite delicate. For the purposes of antenna metrology[8] it is important to define a coordinate frame for these antennas based on the plane, center, and orientation of the aperture using a laser tracker. These antennas are typically fixed to a mechanical positioner that is tracked with a laser tracker. Therefore, it is also important to know the antenna frame relative to the other laser tracker targets that are used to track the positioner. Recent advances in antenna scanning systems use these antennas as the end-effector tool of a robot arm.[8] Having a way to teach the robot the location of the antenna frame (i.e., tool-tip frame) was one of the motivating factors in developing the Pixel Probe. As these antennas are much smaller than an SMR, too delicate to touch, and require alignment accuracy of better than 50 $\mu$m, currently available methods for tool-tip calibration were not suitable. The Pixel Probe not only allows for tool-tip calibration through the robot controller routines, but allows for directly measuring the offset between the antenna aperture frame (i.e., tool tip) and a six-degree-of-freedom target, or set of SMRs fixed on the robot.

The Pixel Probe was used to trace out the edges of these antenna apertures. Geometries were then fitted to determine the center, plane, and orientation of each antenna aperture. Figure 7 and figure 8 show the Pixel Probe measurements and the fitted geometry for the circular probe and pyramidal horn, respectively. The circular aperture of the probe antenna was measured at 15 locations around the perimeter. These data were then fitted to a circle to determine the plane and diameter of the aperture. The circle fitting resulted in a diameter of 1.486 mm with an RMS fit error of 22 $\mu$m. This is consistent with the manufacturer specifications of a 1.5-mm-diameter aperture. The center and plane of this circle were used to define the coordinate frame of the probe antenna. The orientation of this frame in the plane of the circle was left arbitrary until an electrical alignment referenced to the plane of electric-field polarization to the test antenna was later performed.

The four corners of the pyramidal horn aperture were measured to determine the aperture dimensions. A rectangle was then fitted to these corners. A coordinate frame for the aperture was then defined in the plane of the rectangle and clocked to the short end of the rectangle. Figure 8 shows the measurement of the four corners and the resulting coordinate frame. The dimensions of the rectangular aperture determined from these measurements





Gordon, Joshua; Novotny, David; Curtin, Alexandra.
"A Single-Pixel Touchless Laser Tracker Probe."
Paper presented at 2015 Coordinate Metrology Systems Conference (CMSC), Hollywood , FL, United States. July 20, 2015 - July 24, 2015.

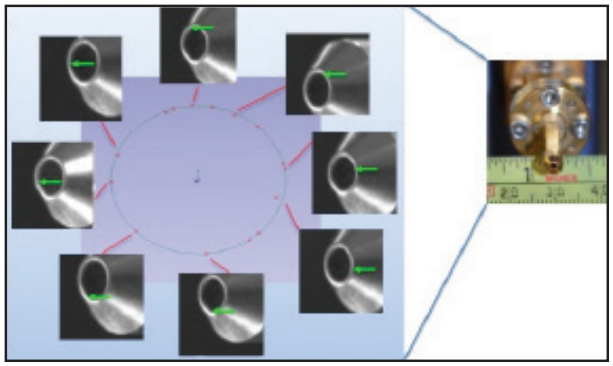

*Figure 7. Circle that was fitted to measurements made with the Pixel Probe around the perimeter of the antenna aperture; red data points lie along this fitted circle, and at each measurement location an inset photo of the aperture as seen with the Pixel Probe is shown. In each inset photo a green arrow points to locations on the aperture where the Pixel Probe obtained measurements; at right, photo of the circular probe antenna, with a ruler shown for scale; the diameter of this antenna aperture determined from the Pixel Probe measurements was 1.486 mm with an RMS fit error of 22 μm*

was 12.65 mm × 9.68 mm × 12.63 mm × 9.68 mm, with a fit error of ≈ 20 $\mu$m, which is in good agreement with the manufacturer specifications of 12.55 mm × 9.58 mm.

## Measuring transparent and soft objects with a laser tracker

The imaging and noncontact measuring capability of the Pixel Probe allows for soft material to be measured with a laser tracker without deforming the object. Furthermore, the imaging capability allows for objects constructed of weak albedo (low optically reflecting) material to be measured. We demonstrate this by measuring two objects with these attributes. First, measurements to determine the shrink ratio of clear Heat Shrink (mention of this product is not an endorsement but is used to clarify what was done in this work) before and after shrinkage were made.

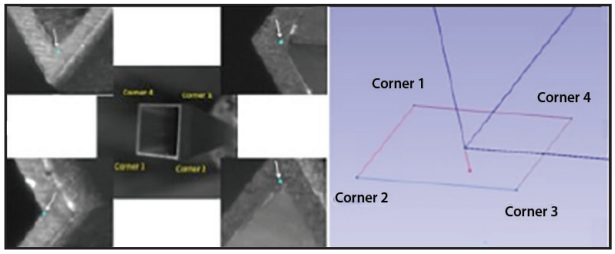


(a) (b)

*Figure 8. (a) The corners of the pyramidal horn antenna measured with the Pixel Probe; white arrows point to blue dots which define the locations at which the corners 1,2,3,4 were measured; (b) coordinate frame generated using these corners; the dimensions of aperture were determined to be 12.65 mm × 9.68 mm × 12.63 mm × 9.68 mm with a fit error of ≈ 20 μm*

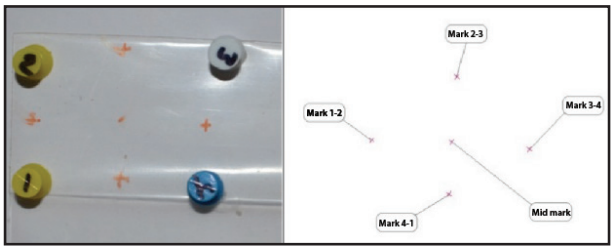


(a) (b)

*Figure 9. (a) Clear Heat Shrink fixed to foam board with thumb tacks; orange marks used to determine shrink ratio as well as numbered thumbtacks are visible; (b) Pixel Probe spatial data for the Heat Shrink*

Second, the geometry of a man-made spider web constructed from strands of clear epoxy was measured. This is an extreme case of an object with these attributes that is not easily measured with a laser tracker, but that can be routinely measured with the Pixel Probe.

The shrink ratio of the material we used was 2:1, such that it should shrink twice vs. its original size. However, Heat Shrink is anisotropic in its shrinking behavior, such that it is designed to shrink only in one direction according to the specified shrink ratio, and not shrink in the orthogonal direction. A tube of Heat Shrink was cut lengthwise to form a rectangle and fixed to a foam board with thumbtacks. Prior to shrinking, a permanent marker was used to mark the Heat Shrink along the direction of least shrinkage and most shrinkage. Figure 9a shows the Heat Shrink fixed to the foam board with thumbtacks prior to shrinking. The thumbtacks were numbered 1 through 4 so as to avoid accidental confusion with the orientation Heat Shrink during measurement. Figure 9b shows the measured marks with the Pixel Probe prior to shrinking. They are labeled mark 1–2, mark 2–3, mark 3–4, mark 4–1, and mid-mark for the thumbtacks that lie between. Because the Heat Shrink was meant for use as wire sheathing, the non-shrinking direction was taken as along the direction of the tube prior to cutting. Using the Pixel Probe, the separation between mark 2–3 and the mid-mark, and mark 3-4 and the mid-mark was measured to be 18.74 mm and 21.77 mm, respectively. After shrinking, the separation of these marks measured 6.89 mm and 22.67 mm. This gave a shrink ratio in the two directions of 2.77 and 0.96. This shows anisotropic shrinkage a bit larger than a 2:1 ratio. As a heat gun was used to shrink the material, the temperature applied was not as controlled as may be required by the manufacturer. This may be the biggest reason for the discrepancy between the measured shrink ratio and the specified one.

The spider web was supported by metal posts screwed to a small optical bread board that had ¼-20 tapped holes on 1-in. centers. The web was measured at several locations along strands and at the points of strand intersection. The dotted box in figure 10a shows the region of the web measured using the Pixel Probe. Figure 10b shows the close-up view through the Pixel Probe. The intersection of the red crosshairs identify the location of the SMR0 pixel. A singlet and doublet set of strands were identified to be measured. From these data the geometry of



Gordon, Joshua; Novotny, David; Curtin, Alexandra.
"A Single-Pixel Touchless Laser Tracker Probe."
Paper presented at 2015 Coordinate Metrology Systems Conference (CMSC), Hollywood , FL, United States. July 20, 2015 - July 24, 2015.

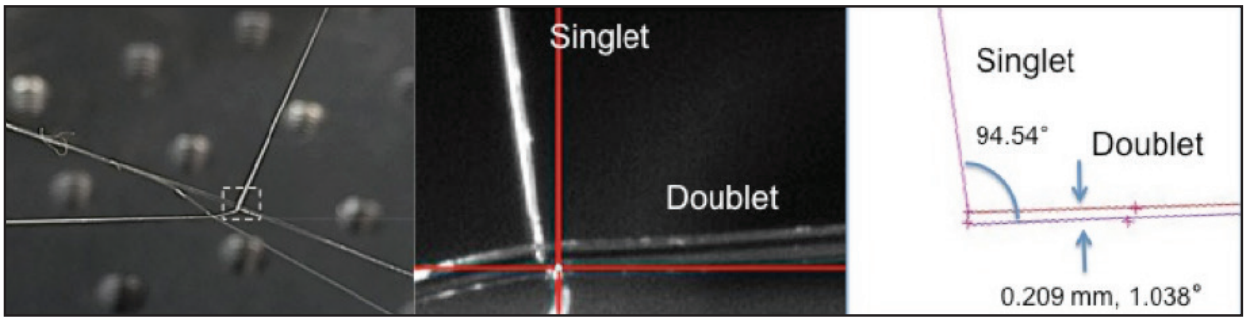


(a) (b) (c)

*Figure 10. (a) Photograph of the spider web made from stands of clear epoxy; ¼-20 holes on 1-in. centers in the optics bread board supporting the web are also visible in the background. Within the dotted box lies the junction of web strands that were measured with the Pixel Probe; (b) close-up image through the pixel probe of the web strands; red crosshairs mark the location of the SMR0 pixel, and a singlet and doublet strand were identified to be measured; (c) spatial data plot for the geometry of the singlet and doublet strands; angle between doublet members was determined to be 1.038° with a mean separation distance of 0.209 mm, and the angle between the singlet and doublet was determined to be 94.54°*

the spider web was determined, and the separation of the members of the doublet was determined as well as the angle made between the singlet and doublet. The angle between individual doublet members was determined to be 1.038°, with a mean separation distance of 0.209 mm. The mean angle between the singlet and doublet was determined to be 94.54° as seen in figure 10c.

## Linking machine vision-derived geometries to a laser tracker

Another aspect of the Pixel Probe is that geometries that are derived from machine vision algorithms can be directly linked to the laser tracker. An example of this is given for the circular antenna probe aperture seen in figure 11, where an ROI is defined in the images of the Pixel Probe around the circular





Gordon, Joshua; Novotny, David; Curtin, Alexandra.
"A Single-Pixel Touchless Laser Tracker Probe."
Paper presented at 2015 Coordinate Metrology Systems Conference (CMSC), Hollywood , FL, United States. July 20, 2015 - July 24, 2015.

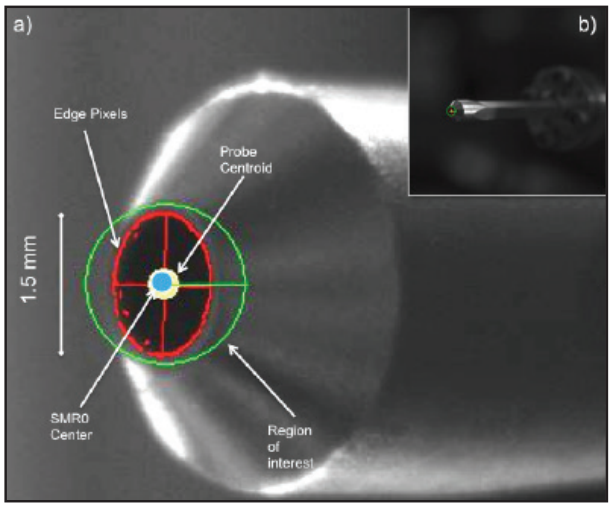


*Figure 11. (a) Close-up image of circular probe antenna and full field view; (b) edge-detected pixels (red), circular probe centroid (yellow), SMR0 center (blue), and region of interest (green) are shown*

aperture. An edge-detection algorithm is then applied within the ROI to find the edge of the aperture. An ellipse-fitting algorithm is then used to find the center of the aperture. Once the ellipse center is determined, the SMR0 point in the Pixel Probe image is then placed at the same location as the ellipse-centroid. At this moment, the centroid of the ellipse is now linked to the laser tracker. Figure 11 shows one image from the Pixel Probe depicting this process. The ROI is shown as the green border. The red border is made of highlighted pixels that were determined from the edge-detection algorithm. These pixels define the edge of the aperture and are used to fit the ellipse. The red crosshairs are the major and minor axis of the ellipse. The yellow circle is the fitted ellipse centroid. The blue circle is the location of SMR0 from the Pixel Probe. When the blue circle and yellow circle overlap in the Pixel Probe images, then the location of SMR0 and the centroid of the ellipse are in the same location in space. At this moment the ellipse centroid becomes linked to the laser tracker. Furthermore, the error in the alignment between the yellow and blue circles can be determined in real time from calculating the pixel offset from the center of each circle. Although we have not deliberately calibrated how this pixel offset error translates into *X, Y, Z* errors in the laser tracker frame, we envision that a volumetric calibration could be preformed to provide *X, Y, Z* tacking of alignment errors. This is the topic of future work, and it would allow direct tracking of errors between the Pixel Probe SMR0 point and machine vision-derived geometries. An application of this technique is available for noncontact robot TCP calibration. This technique is used at the NIST Configurable Robotic Millimeter-Wave Antenna (CROMMA) Facility[7] to teach the robot arm the location of the center of the circular probe antenna aperture end-effector. The robot arm is driven to five different poses, such that for all poses the TCP remains at the same point in space. This point in space is defined using the SMR0 point of the Pixel Probe. For each pose of the robot arm, the center of the circular probe aperture is determined using the edge-detection and ellipse-fitting algorithms just described. The robot is driven such that the center (yellow circle) of the fitted ellipse is aligned to the SMR0 point (blue circle) in the Pixel Probe, as seen in figure 11. Figure 12 shows the robot arm of the CROMMA in four of the five robot poses used to teach the robot controller the TCP location.

## CONCLUSION

We have demonstrated a new laser tracker probe, the Pixel Probe, based on the projection of a point in space to an individual pixel in three separate image arrays. This point is inked to a laser tracker such that it forms a laser tracker probe with an effective size of a single pixel about 25 $\mu$m. Given that the design of this system is easily scalable to higher-resolution cameras and lenses, it is envisioned that this system could provide better than the current 25-$\mu$m resolution. We have provided a conceptual description of this new laser tracker probe, including how spatial projections are used to link the pixel to the laser tracker. We then present several types of spatial data obtained with the Pixel Probe, of objects that would be difficult or extremely challenging to measure using existing laser tracker probes. These include measuring the sharp edge and corners of small, (1.5 mm) gold-plated antennas, the shrink ratio of clear Heat Shrink, and the linear and angular

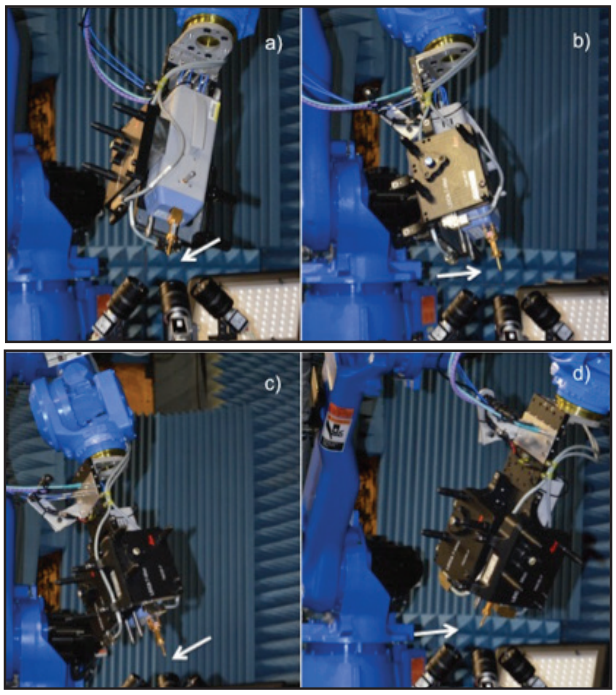


*Figure 12. The robotic arm in the CROMMA facility; the Pixel Probe is mounted to a tripod while the robot arm is driven to the five poses, (a) through (d), required of the TCP teach process (only four poses are shown here for brevity). The circular probe antenna is the robot end effector; white arrows point to the end of the antenna that is co-located with the SMR0 point of the Pixel Probe during the TCP calibration process*



Gordon, Joshua; Novotny, David; Curtin, Alexandra.
"A Single-Pixel Touchless Laser Tracker Probe."
Paper presented at 2015 Coordinate Metrology Systems Conference (CMSC), Hollywood , FL, United States. July 20, 2015 - July 24, 2015.

separation of strands in a man-made spider web constructed of clear epoxy. We also demonstrated how this probe can be used for robot tool-center point calibration as well as registering geometries derived from machine-vision algorithms to a laser tracker. Further applications that exploit the imaging nature of this probe are also discussed. These include directly registering laser tracker spatial data with other physical quantities that can be derived from spectral, polarization, and/or infrared thermal imagining, and is a topic of our future work on this probe. This could provide a new type of measurement framework where physical quantities are directly measured in conjunction with highly accurate mechanical boundary conditions. This would allow the ability to perform direct multi-physics measurements with a laser tracker. Such measurements could be used to compare multi-physics simulations with real-world data much like is done when mechanical CAD models are compared to real-world surface measurements obtained from a laser tracker or CMM.

## REFERENCES


[1] Rakich, A., "Alignment of LBT Optics Using a Laser Tracker," *Proceedings of the SPIE 7733, Ground-Based and Airborne Telescopes III*, 77335K, August, 2010.

[2] Leon-Huerta, A., et. al., "Alignment of a Large Outdoor Antenna Surface Using a Laser Tracker," *Proceedings of the SPIE 8788, Optical Measurement Systems for Industrial Inspection VIII,* 878839, May, 2013.

[3] Hindman, G., Newell, A., et. al.,"Alignment Sensitivity and Correction Methods for Millimeter-Wave Spherical NearField Measurements," *2010 Proceedings of the Antenna Measurement Techniques Association,* 2010.

[4] Wysock, Rousseau, et. al., "Using a Tracking Laser Interferometer to Characterize the Planarity of a Planar NearField Scanner," *2002 Proceedings of the Antenna Measurement Techniques Association,* 2002.

[5] Francis, M.H, and Wittmann, R.C., *Modern Antenna Handbook,* edited by Balanis, C.A., Chapter 19, pp. 929, Wiley, 2008.

[6] Boehler, W., Bordas Vicent, M., and Marbs, A.,"Investigating Laser Scanner Accuracy," CIPA (Scientific Committee for Documentation of Cultural Heritage) Symposium, Antalya Turkey, 2003.

[7] Greivenkamp, J. E., "Field Guide To Geometrical Optics", SPIE, Bellingham, WA, pp. 3, 2004.

[8] Gordon, J., Novotny, D., et. al., "The CROMMA Facility at NIST Boulder: A Unified Coordinated Metrology Space for Millimeter-Wave Antenna Characterization," *Proceedings of the Antenna Measurement Techniques Association,* 2014.







Gordon, Joshua; Novotny, David; Curtin, Alexandra.
"A Single-Pixel Touchless Laser Tracker Probe."
Paper presented at 2015 Coordinate Metrology Systems Conference (CMSC), Hollywood , FL, United States. July 20, 2015 - July 24, 2015.

# Generalized Probe-Position Compensation Methods for Near-Field Antenna Measurements[1]

Ronald C. Wittmann, Michael H. Francis, Joshua A. Gordon, and David Novotny
National Institute of Standards and Technology,
Boulder, CO 80305
Michael.francis@nist.gov

*Abstract*— **The National Institute of Standards and Technology (NIST) has developed computationally efficient near-to far-field transformation algorithms that allow for probe location and polarization compensation when measurements are not made on canonical grids. A major application of such methods is at higher frequencies, where it is difficult or impractical to locate a probe to required tolerances for the standard transforms. Our algorithms require knowledge of the actual position of the probe at the measurement points. This information can be furnished by state-of-the-art optical tracking devices. Probe position information is routinely obtained by the NIST CROMMA (Configurable Robotic MilliMeter-wave Antenna facility). Even at lower frequencies, probe-location compensation techniques allow in principle, the use of less precise and therefore less expensive scanning hardware. Our approach also provides the flexibility to process data intentionally collected on nonstandard grids (plane-polar, spiral, etc.) or with mixed geometries (such as a cylinder with a hemispherical or planar end cap). We present actual probe position compensation results at 183 GHz.**
**Keywords: near-field scanning; probe position compensation; spherical near-field scanning.**

## I. INTRODUCTION

Standard fast near- to far-field transforms require that complex (real and imaginary) data measured on a regular grid. Typically, probe-location accuracies of 0.01–0.02 wavelengths are needed to achieve acceptable sidelobe uncertainties [1]. Probe position compensation methods have been developed that do not require measurement points located on a regular grid but the actual probe positions still must be known to the stated accuracies [2, 3]. Implementation of these techniques for spherical near-field (SNF) measurements has been impractical until very recently. The new NIST CROMMA (Configurable Robotic MilliMeter-wave Antenna facility), however, can accurately track six degrees of freedom (three of location such as $r$, $\theta$, $\varphi$ and three of orientation such as roll, tilt and yaw) [4, 5, 6]. Therefore, CROMMA is able to record deviations from ideal probe location and polarization. Prior NIST work does not include correction for nonideal polarization. Here we present more general results for probe location and polarization compensation.



For spherical near-field measurements the position parameters are $r$, $\theta$, $\varphi$ (the usual spherical angles) and $\chi$ (the polarization angle of the probe). The original work [3] assumed no polarization deviations and that both polarizations were measured at the same point. Our new software allows for polarization discrepancies and does not require that both polarizations are measured at the same point.

We present some actual measurement results at 183 GHz from the NIST CROMMA Facility.

## II. MEASUREMENTS

Spherical near-field measurements were performed on a WR-5 standard gain horn with nominal gain of 24 dB. A standard near-field-to-far-field transform was used to calculate the far field pattern from the measured near-field data. These results were compared to both measured and theoretical patterns in Francis et al [7]. Location compensation was not employed in [7], even though the information was available. This is because the polarization compensation had not been implemented. Since then we have been able to implement the compensation for non-ideal polarization. Preliminary results are shown in Figure 1, which compares the pattern in the azimuth plane with and without position correction.

The information obtained by our laser tracker includes six degrees of freedom information including both location and orientation information [5]. Location information was evaluated and presented in [7]. However from this information, we are also able to evaluate the orientation of the probe during the measurements. A histogram of the pointing errors is presented in Figure 2 for the $\theta$ component and in Figure 3 for the $\varphi$ component. Note that the spread in the pointing error for the $\theta$ component is significantly greater than that for the $\varphi$ component. However, even though the spread in the pointing error is less for the $\varphi$ component, its average error is larger. That is, the offset in the $\varphi$ component is larger. The difference is due to the probe being rotated 90° between the two components resulting in a different mass distribution.

## III. CONCLUSIONS AND FUTURE WORK

We have successfully used the six degrees of freedom information obtained by the CROMMA to perform position correction for measurements of a WR-5 standard gain horn. The major effect is due to errors in the polarization axis $\chi$.

Francis, Michael; Wittmann, Ronald; Gordon, Joshua; Novotny, David.
"Generalized Probe-Position Compensation Methods for Near-Field Antenna Measurements."
Paper presented at 37th Annual Meeting and Symposium of the Antenna Measurement Techniques Association (AMTA 2015), Long Beach, CA, United States. October 11, 2015 - October 16, 2015.

Since the CROMMA facility provides information on six degrees of freedom, the possibility exists for including compensation for orientation errors (tilt and yaw) as well as the correction for errors in $r$, $\theta$, $\varphi$, and $\chi$. We intend to explore this possibility in future work.

The alignment of CROMMA is excellent at this frequency, so position compensation effects are small. More rigorous tests of position compensation ability are being planned. The possibility of compensating for known variations in probe pointing will be considered.

## REFERENCES


[1] Francis, M. H. and Wittmann, R. C., "Near-Field Scanning Measurements: Theory and Practice," Chp. 19 in *Modern Antenna Handbook,* ed. C.A. Balanis, Wiley & Sons, Inc., 2008.

[2] Wittmann, R. C., Alpert, B. K. and Francis, M. H., "Near-field antenna measurements using nonideal measurement locations," IEEE Trans. Antennas Propagat., vol. 46, pp. 716 – 722, May 1998.

[3] Wittmann, R. C., Alpert, B. K. and Francis, M. H., "Near-field, spherical-scanning antenna measurements with nonideal probe locations," IEEE Trans. Antennas Propagat., vol. 52, pp. 2184 – 2186, August 2004.

[4] Novotny, D. R., Gordon, J. A., Guerrieri, J. R., "Antenna alignment and positional validation of a mmwave antenna system using 6D coordinate metrology," *Proc. AMTA*, pp. 247 – 252, October 2014.

[5] Gordon, J. A., Novotny, D. R., Francis, M. H., Wittmann, R. C., Butler, M., Guerrieri, J. R., "The CROMMA facility at NIST Boulder: A unified coordinated metrology space for millimeter-wave antenna characterization," *Proc. AMTA*, pp. 351 – 356, October 2014.

[6] Gordon, J. A. and Novotny, D. R., "A non-contact machine vision system for the precision alignment of mm-wave antennas in all six degrees of freedom," *Proc. AMTA*, pp. 413 – 418, October 2014.

[7] Francis, M. H., Wittmann, R. C., Novotny, D. R., and Gordon, J. A., "Spherical Near-Field Measurement Results at Millimeter-Wave Frequencies Using Robotic Positioning," *Proc. AMTA*, pp. 231 – 234, October 2014.


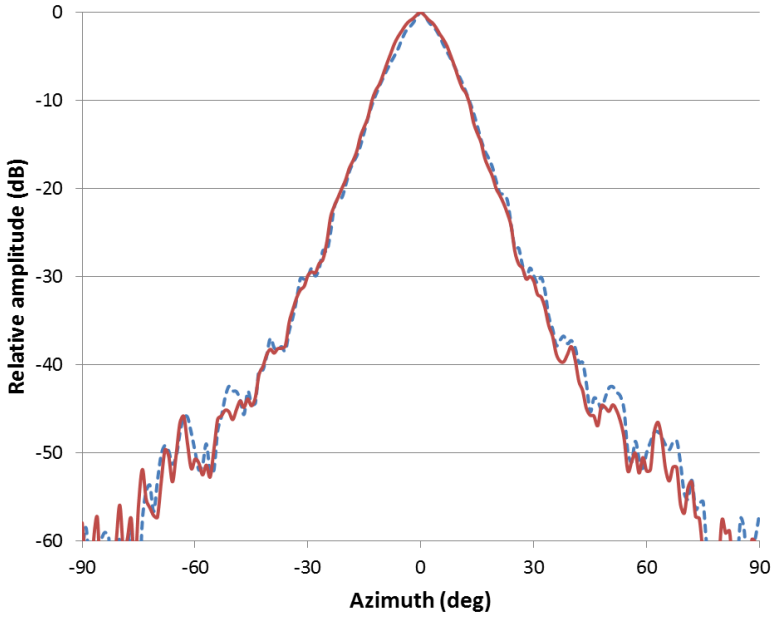


Figure 1. Azimuth pattern of a WR-5 standard gain horn with position correction (red, solid) and without position correction (blue, dashed).


Francis, Michael; Wittmann, Ronald; Gordon, Joshua; Novotny, David.
"Generalized Probe-Position Compensation Methods for Near-Field Antenna Measurements."
Paper presented at 37th Annual Meeting and Symposium of the Antenna Measurement Techniques Association (AMTA 2015), Long Beach, CA, United States. October 11, 2015 - October 16, 2015.

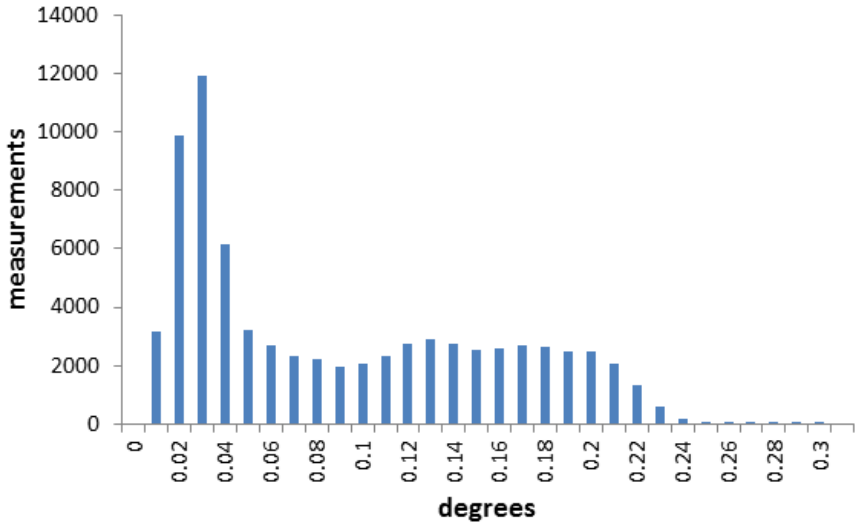


Figure 2. Histogram of the pointing error for the $\theta$ component.

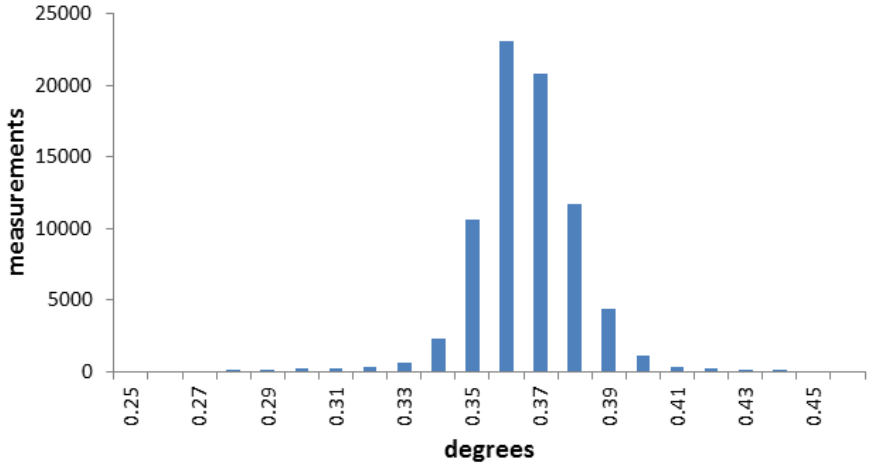


Figure 3. Histogram of the pointing error for the $\varphi$ component.

Francis, Michael; Wittmann, Ronald; Gordon, Joshua; Novotny, David.
"Generalized Probe-Position Compensation Methods for Near-Field Antenna Measurements."
Paper presented at 37th Annual Meeting and Symposium of the Antenna Measurement Techniques Association (AMTA 2015), Long Beach, CA, United States. October 11, 2015 - October 16, 2015.

# Consensus Value Methods to Compile On-Axis Gain Measurement Results

Jeff Guerrieri[1], Michael Francis and Ronald Wittmann
National Institute of Standards and Technology
325 Broadway
Boulder, CO 80305
[1]jeffrey.guerrieri@nist.gov

**Abstract – This paper compares methods for computing consensus values of on-axis gain measurements that have a large range of values and uncertainties. A variety of methods are used to analyze multiple data sets such as unweighted averages, weighted averages and other statistical means. The appropriate method is dependent on characteristics of the data sets such as, the number of data sets, the spread of the data set values and spread of the uncertainty values for each data set. One method computes a weighted mean where the weights are chosen as the inverses of the fractional error in the data values. A second method removes data sets that are determined to be outliers, then computes an unweighted mean. A third computes a simple unweighted mean. The results of this comparison show that the method chosen to compute a consensus value is fairly independent of the data sets.**

**Keywords:** consensus value, weighted mean, outlier removal, unweighted mean.

## I. INTRODUCTION

There are a variety of compilation methods that can be used for calculating consensus values, mean or dispersion of data [1] [2]. Often those compiling the data are not certain which method to use. This paper compares three potential methods for computing consensus values. One method uses weighted averages of the data, where the weights are chosen as the inverses of the fractional error in the data values [3]. This weighted mean method applies a larger weight to data values that have smaller uncertainty. It assumes that the measurement uncertainty is determined consistently. A second method for compiling data is an outlier removal method [4]. This method uses an algorithm that calculates a median value and removes data that vary by more than a specified amount from the median. An unweighted averaging technique can then be applied to the remaining data values. The third method computes an unweighted mean value. The data sets used for the comparison are twelve on-axis antenna gain values and accompanying measurement uncertainties.



## II. COMPILATION METHODS

Weighted Mean

The weighted mean value compilation method applies weighted averages. The weights are chosen as the inverses of the uncertainty in the data values. Beginning with on-axis gain values, $G_i'$ (dB) and uncertainties, $\Delta G_i'$ (dB), where, i refers to the i[th] data set.

$$G_i = 10^{G_i'/10},$$

and fractional uncertainty,

$$\Delta G_i/G_i = 1 - 10^{-\Delta G_i'/10}.$$

Next, we use a particular choice and associate the weight $w_i$ with the i[th] data set,

$$w_i = \frac{G_i}{\alpha \Delta G_i},$$

where,

$$\alpha = max\left(\frac{G_i}{\Delta G_i}\right), \quad w_i > 0, \quad \max(w_i) = 1$$

and the effective number of measurements is

$$w = \sum_i w_i$$

Then calculate the overall gain,

$$G_{weighted\ mean} = \frac{1}{w}\sum_i w_i G_i,$$

and the uncertainty,

$$u(G_{weighted\ mean}) = \frac{1}{w}\sqrt{\sum_i w_i (G_i - G_{weighted\ mean})^2}.$$



Guerrieri, Jeffrey; Francis, Michael; Wittmann, Ronald.
"Consensus Value Methods to Compile On-Axis Gain Measurement Results."
Paper presented at 37th Annual Meeting and Symposium of the Antenna Measurement Techniques Association (AMTA 2015), Long Beach, CA, United States. October 11, 2015 - October 16, 2015.

Finally, compute the value of weighted mean of the on-axis gain values in dB,

$$G'_{weighted\ mean} = 10 \log G_{weighted\ mean},$$

and the uncertainty for the compiled weighted mean,

$$u'(G_{weighted\ mean}) = -10log\left(1 - \left(\frac{u(G_{weighted\ mean})}{G_{weighted\ mean}}\right)\right).$$

Outlier Removal

The outlier removal compilation method tests for the presence of outliers. First, estimate the standard deviation σ of the underlying distribution. The most common such estimate is just the standard deviation of the sample, or data set in this paper. However, the sample standard deviation is itself quite sensitive to outliers, a more robust estimate can be obtained by using the Median of Absolute Deviations (MAD) [4].

Beginning with,

$$\sigma \approx S(MAD) \equiv 1.596 median_j\{|G_i - G_{med}|\}.$$

Where, $G_{med}$ is the median of the sample $\{G_i\}$, and the factor of 1.596 is a normalization factor that produces the correct estimate of σ for Gaussian error distributions (i.e., in the absence of outliers). A value of $G_i$ which differs from the median by more than 2.5 times S(MAD) is commonly considered an outlier, and the criterion to test each point.

If

$$|G_i - G_{med}| > 2.5 \times S(MAD),$$

the sample $G_i$ is identified as an outlier and is removed from the averaging process.

For this exercise the remaining on-axis gain values are compiled as an unweighted mean, $G_{outlier\ removal}$, defined as,

$$G_{outlier\ removal} = \frac{1}{N'} \sum_{i=1}^{N'} G_i ,$$

where $G_i$ are the remaining on-axis gain values and $N'$ is the number of remaining gain values after outlier removal.

The uncertainty after outlier removal, $u(G_{outlier\ removal})$, defined as,

$$u(G_{outlier\ removal}) = \frac{1}{N'} \sqrt{\sum_{i=1}^{N'} (G_i - G_{outlier\ removal})^2} ,$$

where $G_i$ are the values of the remaining on-axis gain values and N is the number of remaining gain values after outlier removal.

It is important to note that the gain values and uncertainties are converted to linear values before calculations and then converted back to dB values.

Unweighted Mean

The unweighted mean method is a simple average of all of the on-axis gain values, $G_{unweighted\ mean}$, defined as,

$$G_{unweighted\ mean} = \frac{1}{N} \sum_{i=1}^{N} G_i ,$$

where $G_i$ are the on-axis gain values and N is the number of gain values.

Similarly, the uncertainty for the unweighted mean of the on-axis gain values, $u(G_{unweighted\ mean})$, is defined as,

$$u(G_{unweighted\ mean}) = \frac{1}{N} \sqrt{\sum_{i=1}^{N} (G_i - G_{unweighted\ mean})^2},$$

where N is the number of gain values.

Again gain values and uncertainties are converted to linear values before the calculations then converted back to dB values.

## III. MEASUREMENT DATA SETS

The data sets are twelve, independently different, measured on-axis antenna gain values and accompanying measurement uncertainties. The measurements were performed at three different frequencies listed as f1, f2 and f3. These gain values and uncertainties are listed in Table I and are shown graphically in Figure 1. For ease in viewing, the values are plotted nominally with respect to the measurement frequency.



Guerrieri, Jeffrey; Francis, Michael; Wittmann, Ronald.
"Consensus Value Methods to Compile On-Axis Gain Measurement Results."
Paper presented at 37th Annual Meeting and Symposium of the Antenna Measurement Techniques Association (AMTA 2015), Long Beach, CA, United States. October 11, 2015 - October 16, 2015.

TABLE I. ON-AXIS GAIN VALUES AND UNCERTAINTIES*

| Data Set | Gain Value (dB) | | |
|---|---|---|---|
| | f1 | f2 | f3 |
| 1 | 23.63 ±0.05 | 24.43 ±0.05 | 24.83 ±0.05 |
| 2 | 23.63 ±0.20 | 24.47 ±0.20 | 24.83 ±0.20 |
| 3 | 23.65 ±0.21 | 24.41 ±0.23 | 24.79 ±0.25 |
| 4 | 23.63 ±0.24 | 24.45 ±0.24 | 24.89 ±0.24 |
| 5 | 23.56 ±0.16 | 24.44 ±0.20 | 24.99 ±0.26 |
| 6 | 23.61 ±0.09 | 24.39 ±0.14 | 24.84 ±0.15 |
| 7 | 23.70 ±0.11 | 24.47 ±0.11 | 24.88 ±0.11 |
| 8 | 23.40 ±0.43 | 24.00 ±0.50 | 24.20 ±0.50 |
| 9 | 23.89 ±0.35 | 24.63 ±0.53 | 25.43 ±0.56 |
| 10 | 23.61 ±0.84 | 24.14 ±0.84 | 24.51 ±0.84 |
| 11 | 23.62 ±0.03 | 24.44 ±0.03 | 24.86 ±0.03 |
| 12 | 23.66 ±0.07 | 24.48 ±0.07 | 24.88 ±0.07 |

* Uncertainties listed in Table I have a coverage factor of 2.

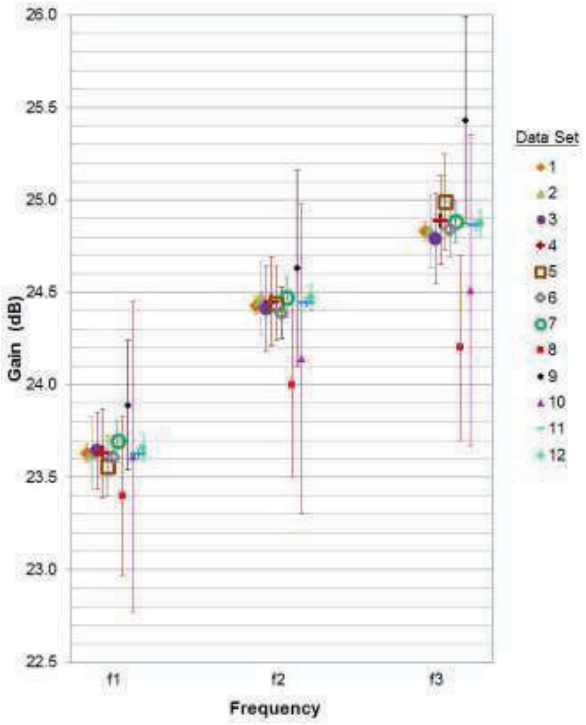


Figure 1. On-axis gain values.

## IV. APPLICATION OF COMPILATION METHODS

### Weighted Mean

First, the weighted mean compilation method is applied to the on-axis gain values for the three measurement frequencies. The results are listed in Table II.

TABLE II. COMPILED WEIGHTED MEANS AND STANDARD UNCERTAINTIES

| f1 | f2 | f3 |
|---|---|---|
| 23.63 ±0.03 | 24.44 ±0.04 | 24.85 ±0.07 |

### Outlier Removal

Next, the outlier removal compilation method is applied to the on-axis gain values for each measurement frequency. The outlier on-axis gain values are defined and listed in bold red italics in Table III. After the removal of outliers the unweighted mean is determined for the remaining on-axis gain values for each measurement frequency. These unweighted mean values are listed in bold blue italics at the bottom of Table III.

TABLE III. ON-AXIS GAIN VALUES WITH OUTLIERS DEFINED AND CALCULATED UNWEIGHTED MEAN AFTER OUTLIER REMOVAL

| Data Set | Gain Value (dB) | | |
|---|---|---|---|
| | f1 | f2 | f3 |
| 1 | 23.63 ±0.05 | 24.43 ±0.05 | 24.83 ±0.05 |
| 2 | 23.63 ±0.20 | 24.47 ±0.20 | 24.83 ±0.20 |
| 3 | 23.65 ±0.21 | 24.41 ±0.23 | 24.79 ±0.25 |
| 4 | 23.63 ±0.24 | 24.45 ±0.24 | 24.89 ±0.24 |
| 5 | 23.56 ±0.16 | 24.44 ±0.20 | ***24.99 ±0.26*** |
| 6 | 23.61 ±0.09 | 24.39 ±0.14 | 24.84 ±0.15 |
| 7 | 23.70 ±0.11 | 24.47 ±0.11 | 24.88 ±0.11 |
| 8 | ***23.40 ±0.43*** | ***24.00 ±0.50*** | ***24.20 ±0.50*** |
| 9 | ***23.89 ±0.35*** | ***24.63 ±0.53*** | ***25.43 ±0.56*** |
| 10 | 23.61 ±0.84 | ***24.14 ±0.84*** | ***24.51 ±0.84*** |
| 11 | 23.62 ±0.03 | 24.44 ±0.03 | 24.86 ±0.03 |
| 12 | 23.66 ±0.07 | 24.48 ±0.07 | 24.88 ±0.07 |
| **Unweighted Mean & Standard Uncertainty (After Outlier Removal)** | **23.63 ±0.10** | **24.44 ±0.05** | **24.85 ±0.06** |



Guerrieri, Jeffrey; Francis, Michael; Wittmann, Ronald.
"Consensus Value Methods to Compile On-Axis Gain Measurement Results."
Paper presented at 37th Annual Meeting and Symposium of the Antenna Measurement Techniques Association (AMTA 2015), Long Beach, CA, United States. October 11, 2015 - October 16, 2015.

Unweighted Mean

Finally, the unweighted mean compilation method is applied to the on-axis gain values for the three measurement frequencies. The results are listed in Table IV.

TABLE IV. COMPILED UNWEIGHTED MEANS AND STANDARD UNCERTAINTIES

| f1 | f2 | f3 |
|---|---|---|
| 23.63 ±0.03 | 24.40 ±0.05 | 24.84 ±0.08 |

## V. RESULTS

The results after applying each compilation method to the twelve data sets at the three measurement frequencies are listed in Table V. These results are also shown graphically along with the on-axis gain values in Figure 2. For ease in viewing, the values are plotted nominally with respect to the measurement frequency.

The results are comparable for the compilation. The compiled results are the same for f1 except for the uncertainties. This is expected due to the close grouping of the on-axis gain values except for the two outlier data sets 8 and 9. The outliers offset each other for the unweighted mean method, are not included in the outlier removal method and due to their large measurement uncertainty have little effect in the weighted mean method. The difference between compiled results is greatest at f2. There are three outlier on-axis gain values for the measurements at f2, data sets 8, 9 and 10. Data sets 5, 8, 9 and 10 are defined as outliers for f3. The compiled on-axis gain and uncertainty results are similar at f3.

TABLE V. RESULTING GAIN CONSENSUS VALUES AND STANDARD UNCERTAINTIES OF COMPILATION METHODS

| Compilation Method | f1 | f2 | f3 |
|---|---|---|---|
| Weighted Mean | 23.63 ±0.03 | 24.44 ±0.04 | 24.85 ±0.07 |
| Outlier Removal | 23.63 ±0.10 | 24.44 ±0.05 | 24.85 ±0.06 |
| Unweighted Mean | 23.63 ±0.03 | 24.40 ±0.05 | 24.84 ±0.08 |

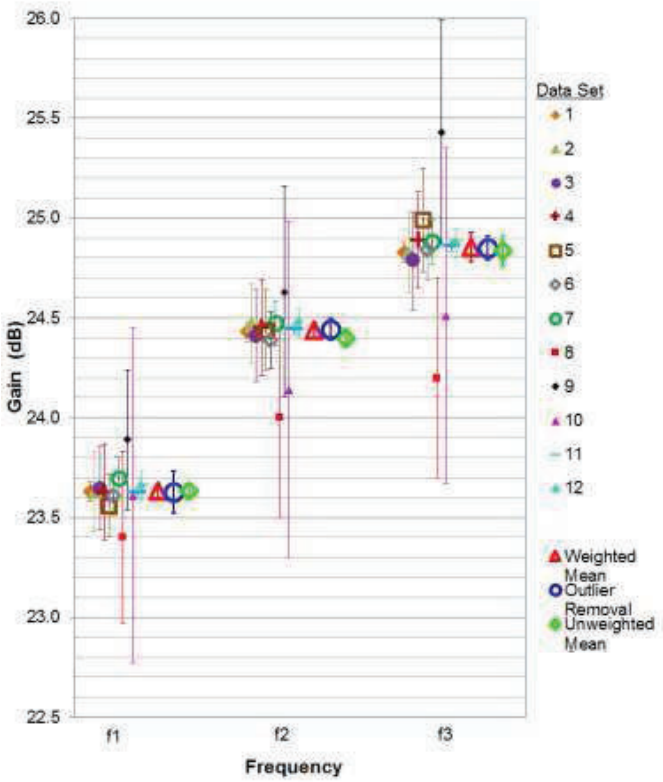


Figure 2. On-axis gain values and the results of the three compilation methods.

## VI. CONCLUSION

Three potential compilation methods for computing consensus values were compared using on-axis antenna gain values and associate uncertainties. The compiled gain values compared favorably. The unweighted mean method at f2 differs by the largest amount, but is still within the uncertainty. The uncertainty determined by outlier removal method is larger at f1. The outlier removal method is probably better suited for data sets where the calculated uncertainties are suspect and the comparison can afford to remove data sets. The weighted mean method allows for all data sets to be used in the compilation, which is important for small samples sizes. However, it assumes that the uncertainties are reasonable.

There are a variety of methods used to compile data. One method is not necessarily better, or more correct than another. However, it is important to inform associated parties of the method used and to provide the relevant data for result verification and additional calculation.



Guerrieri, Jeffrey; Francis, Michael; Wittmann, Ronald.
"Consensus Value Methods to Compile On-Axis Gain Measurement Results."
Paper presented at 37th Annual Meeting and Symposium of the Antenna Measurement Techniques Association (AMTA 2015), Long Beach, CA, United States. October 11, 2015 - October 16, 2015.

REFERENCES


[1] Duewer D. L., “A Robust Approach for the Determination of CCQM Key Comparison Reference Values and Uncertainties”, National Institute of Standards and Technology Report.

[2] Paule, R.C. and Mandel, J., “Consensus Value and Weighting Factors,” J. Res. Natl. Bur. Stand., vol. 87, pp. 377 – 385, Sept.-Oct., 1982.

[3] Guerrieri J. R., Coder J. B., Francis, M. H., Gordon J., Novotny D. R., Wittmann R.C., “International Comparison of Ku-Band Standard Gain Horn Characterization”, 2013 Antenna Measurement Techniques Association Conference Proceedings.

[4] Randa J., “Update to Proposal for KCRV & Degree of Equivalence for GTRF Key Intercomparisons”, GT-RF/2005-04.





Guerrieri, Jeffrey; Francis, Michael; Wittmann, Ronald.
”Consensus Value Methods to Compile On-Axis Gain Measurement Results.”
Paper presented at 37th Annual Meeting and Symposium of the Antenna Measurement Techniques Association (AMTA 2015), Long Beach, CA, United States. October 11, 2015 - October 16, 2015.

# Antenna Measurement Implementations and Dynamic Positional Validation Using a Six Axis Robot[1]

David R. Novotny†, Joshua A. Gordon, Michael Francis, Ronald Wittmann, Alexandra Curtin, Jeffrey Guerrieri
Communications Technology Laboratory
National Institute of Standards and Technology
Boulder, CO, United States of America
†david.novotny@nist.gov

***Abstract*—We have performed spherical and extrapolation scans of two antennas at 118 GHz using a commercial 6-axis robot. Unlike spherical scanning, linear extrapolations do not precisely conform to the natural circular movement about individual robot axes. To characterize the quality of the data, we performed dynamic position and orientation characterization of the robotic systems. A laser tracker is used to measure the probe antenna movement relative to the antenna under test, this information is used to continually update the position and posture of the probe during scanning. We correlated the laser tracker data with the mmWave insertion phase to validate dynamic measurement position results at speeds up to 11 mm/s. We previously demonstrated spherical measurements with this system. The extrapolation measurements presented here require more stringent accuracies for pointing that general pattern analysis.**

## I. INTRODUCTION

Higher frequencies, multiple geometries, many antennas, multiple frequencies, rapid beam state changes, shorter testing requirements…. We are attempting to address many of these antenna testing issues simultaneously.

There are requirements to test at higher frequencies for climate, security, and communications applications that need tighter tolerances on positioning, orientation and timing between system components than at lower frequencies. The ability to test multiple geometries such as planar scans at various orientations, or a spherical and extrapolation measurement with one setup, may allow for more rigorous testing with minimal increases in test time. We now see cell phones and spacecraft with many operational antennas that may need to be tested independently and having a test facility that can accommodate multiple testing requirements (NFC, Bluetooth, GPS, Cellular & Wi-Fi), might prove valuable. Finally, the ability to rapidly move probe antennas around test objects while maintaining orientation relative to the object under test may have applications in dynamic antenna testing and conformal testing such as medical and shielding applications.

The use of coordinated robotics with multiple degrees of freedom and using laser-based positioning metrology equipment to guide and correct the scan geometries may offer solutions to these antenna testing issues.

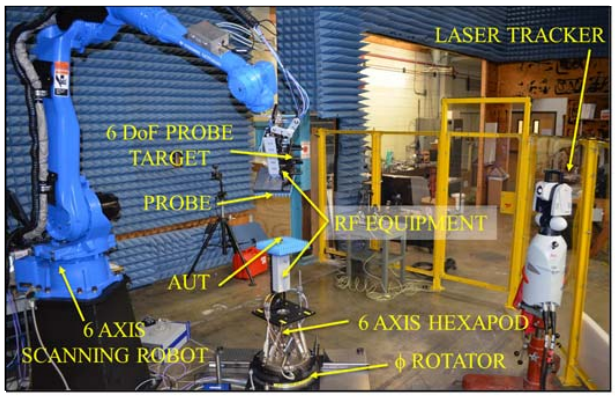


Figure 1. Major components of the Configurable MilliMeter Robotic Antenna Facility (CROMMA).

## II. OVERVIEW

Previously, the Antenna Metrology project at NIST and others have presented results of mmWave spherical scanning using a six Degree-or Freedom (6DoF) robotic system [1,2]. The Configurable Robotic MilliMeter Antenna facility (CROMMA), fig. 1, has produced pattern and imaging measurement results from 60 to 225 GHz [1,3].

The major goal of this endeavor is to develop a configurable platform that can use different measurement geometries with minimal setup and alignment. The 6DoF positioning capabilities of the antenna under test (AUT) and probe stages, guided by the laser tracker, allow for correcting both pointing and positioning throughout the scan geometry with minimal alignment effort between the antenna and positioner.

We continue to explore the ability of commercial-off-the-shelf (COTS) hardware to perform high accuracy testing. There is a lively debate on the practical ability to perform large volumetric scans using conventional mmWave measurement equipment [4,5]. Both positioning of the antennae and mmWave stability need to be determined to assess the quality of the entire measurement. If there is a considerable amount of variation in mmWave phase or amplitude (e.g. due to cable flexing or temperature shifts) then significant errors may be seen in the calculated antenna parameters. Similarly, if the quality of



Novotny, David; Gordon, Joshua; Francis, Michael; Wittmann, Ronald; Curtin, Alexandra; Guerrieri, Jeffrey.
"Antenna Measurement Implementations and Dynamic Positional Validation Using a Six Axis Robot."
Paper presented at 37th Annual Meeting and Symposium of the Antenna Measurement Techniques Association (AMTA 2015), Long Beach, CA, United States. October 11, 2015 - October 16, 2015.

position data from the laser tracker degrades when the target changes speed, resulting position errors translate directly into pattern and gain errors.

We are currently focusing on the quantification of errors in the CROMMA facility for multiple measurements types. In this paper, we concentrate on how one setup, which involves locating the probe and AUT relative to their robotic stages and laser tracker targets, can be used for multiple geometry testing. High frequency testing requires positioning accuracies on the order of λ/25 to λ/50. So at 118 GHz, with a wavelength, λ, of approximately 2.5 mm, we may desire positional accuracies on the order of 50 to 100 µm. Pointing accuracies are generally more antenna than frequency dependent: knowledge of the pointing angle to 1/50$^{th}$ of the expected beam-width is a starting point. With such tight mechanical tolerances, coordinating the mmWave measurement, the robotic path, and measurement of the antenna position is critical. Finally, many laser trackers are not quantified for measurements while the target is moving, so the dynamic accuracy of the laser tracker itself needs to be determined.

To support an upcoming test for a climate radiometer, we performed antenna tests at approximately 118 GHz, using a 15 dBi standard gain horn as the probe antenna and a 9 dBi, µ=±1 antenna as the AUT. We performed a spherical scan followed by an extrapolation measurement using only one antenna alignment. We calibrated the robotic path for each geometry and updated the path during the measurement to account for robot warmup and mechanical drift. During the extrapolation measurement, we compared the mmWave phase measurement, translated to distance, to the laser tracker measured distance.

## III. CROMMA

The use of coordinated-motion robotics for antenna and imaging techniques is being explored by several groups and manufacturers. Full 6DoF positioning has great possibilities for reducing errors that independent stacked stages of earlier generations of antenna positioning systems employ. However, while many of the modern day 6- and 7-axis robots are very repeatable, they are not always very accurate. CROMMA, fig. 1, uses laser trackers to locate the antennas relative to the robotic stages, relative to other antenna locations and most importantly, relative to the positional measurement targets used to infer antenna position[6].

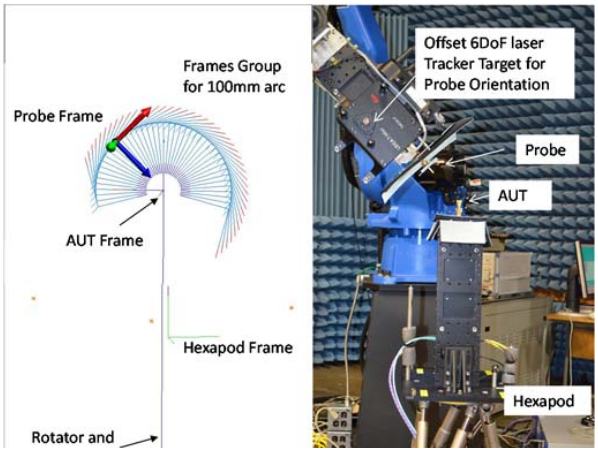


Figure 2. The modeled (left) and actual (right) layout of the CROMMA. The actual locations of each part of the system have been measured by the laser tracker to facilitate alignment and measurements.

We locate all the components within CROMMA using the laser tracker: the base φ rotator axis, the hexapod's coordinate frame and the robot's base movement frame, fig. 2. We measured the location of the antennas with an absolute-position, single-pixel camera target [6] and simultaneously aligned the antennas to the robot and rotator using the robot's tool tip calibration procedure and direct hexapod movement.

We start with an ideal scan geometry using the native robotic coordinate system. The laser tracker sends position and pointing error data back to the coordinate metrology software and it is used to continuously improve robotic positioning performance throughout the measurement, fig. 2.

Continuous correction is needed to achieve the best possible positioning accuracies of the system. If accuracies on the order of base robot repeatability are acceptable, in our case, approximately 70 µm [7], then continuous laser-tracker feedback is not required. Large volume, periodic, 6DoF robotic calibration that can maintain validity for many months has been used to correct robot accuracy to approximately the robotic repeatability specification [8]. For lower frequency applications or those not requiring such stringent positioning specifications, laser tracker data throughout the measurements may not be needed. Though, it can be shown that position data from an imperfect scan can be used to improve the final pattern data [9].

## IV. The Dynamic Problem

Most antenna measurements are taken "on-the-fly", or while either the probe or AUT are moving. This is done to reduce measurement time. However we are trying to accurately locate

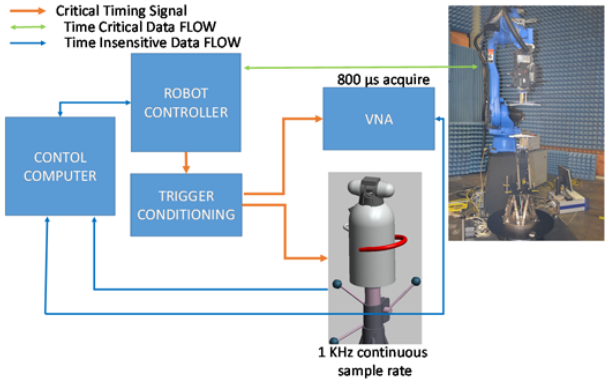


Figure 3. System timing diagram for the CROMMA. The robot controller generates the timing pulse prior to reaching a programmed position. The pusle is delayed and amplitude adjusted for the VNA and the laser tracker. Position and mmWave data is queued and retrived by the computer in a non-time critical serivce loop.

Novotny, David; Gordon, Joshua; Francis, Michael; Wittmann, Ronald; Curtin, Alexandra; Guerrieri, Jeffrey.
"Antenna Measurement Implementations and Dynamic Positional Validation Using a Six Axis Robot."
Paper presented at 37th Annual Meeting and Symposium of the Antenna Measurement Techniques Association (AMTA 2015), Long Beach, CA, United States. October 11, 2015 - October 16, 2015.

the antennas to roughly the accuracy of the laser tracker, ~±20 µm, while the antenna is moving and coordinate it with the mmWave transmission measurement. Compounding the problem: the instrument we rely on for scan correction, the laser tracker, does not have a test for or specifications on dynamic accuracy. So we will attempt to break the problem into two sections: the mmWave measurement errors and then the comparison between the mmWave and optical measurement of position.

*A. Sysetem Timing Setup.*

Timing between robot positioner, the laser tracker and the Vector Network Analyzer (VNA) is critical to maintaining the desired accuracy. To maintain minimal operating system delays, the robot is used to generate the main timing signal, fig 3. It generates a pulse prior to arriving at a programmed point and that signal is delayed and distributed to the laser tracker and VNA so the position data is taken at the midpoint of the mmWave measurement. Data is transferred to the robot and from the laser tracker and VNA via non-time-critical queues.

Characterization of the laser tracker timing is critical. The VNA timing is well characterized, timing uncertainties are specified as less than 12.5 ns [10]. Trigger conditioning adds less than 3 ns jitter. So the measurement of the mmWave data is well coordinated in time. The laser tracker polls the elevation and azimuth encoders (1 KHz), distance interferometer (1 KHz), and orientation sensors (250 Hz) continuously at different rates and interpolating between samples depending on the trigger arrival.

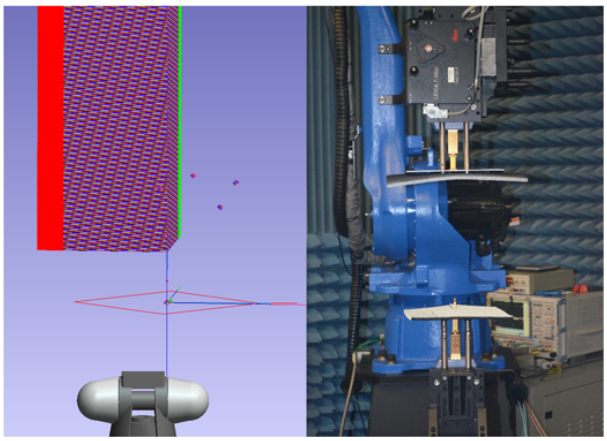

Figure 4. Extrapolation path used in this measurement. The robot taking data in 0.84 mm (λ/3) steps. The path is corrected to maintain proper pointing throughout the measurement.

*B. mmWave tracking errors.*

We performed an extrapolation measurement to compare the timing and dynamic position accuracy of the laser tracker versus the VNA, fig. 4. We performed a linear scan from 50 mm ($\sim 2D^2/\lambda$) to 600 mm ($\sim 24D^2/\lambda$). We corrected the path until we attained optimal pointing and positioning errors, fig. 5.

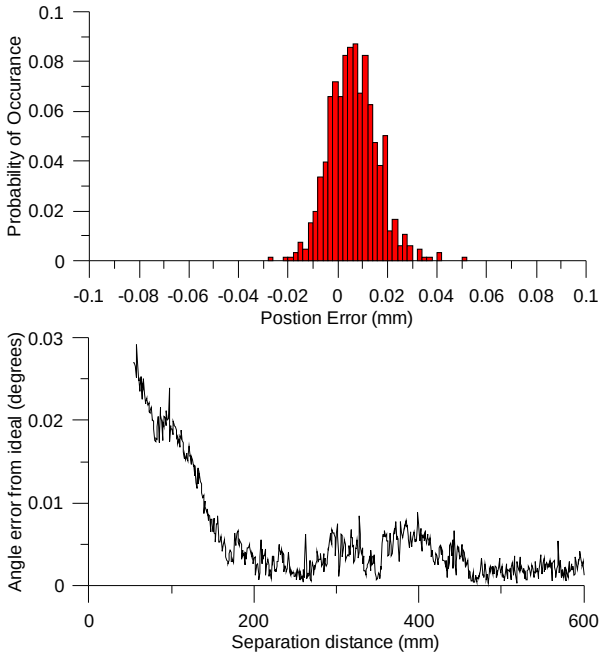


Figure 5. Histogram of position errors (upper) and angular errors along the path (lower) for the extrapolation measurement after path correction. The rise at small distances is due to polarization rotation because of the angle to the 6DoF sensor.

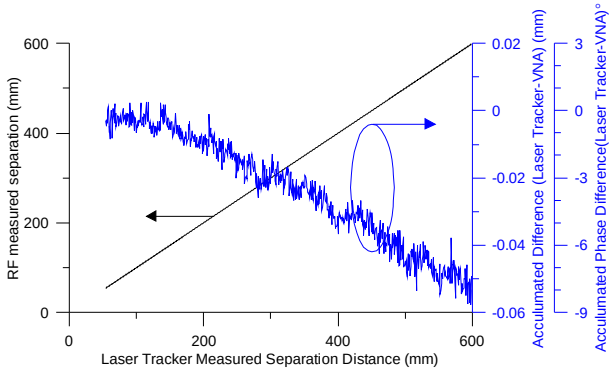


Figure 6. Distance between antennas as measured by the laser tracker and the VNA at a robot speed of 1 mm/s. A difference of ~8° over a 600mm linear separation is mainly attributed to cable flexure. The inherent positional noise is approximately 10 µm which is a combination of the VNA and laser tracker.

In order to use the mmWave analyzer as a basis for comparing with the laser tracker, we need to perform a basic assessment on the stability of the mmWave system. The two most prominent sources of mmWave stability errors are cable movement and temperature. The temperature in the laboratory is regulated to ±2 C, so we expect minimal thermal drift in the VNA. By running the cables along the robot's control cable path, we previously showed single point position repeatability of 25 µm, with mmWave repeatability of 7° and 0.02 dB [4]. For this measurement we looked at unwrapped phase and used it to

Novotny, David; Gordon, Joshua; Francis, Michael; Wittmann, Ronald; Curtin, Alexandra; Guerrieri, Jeffrey.
"Antenna Measurement Implementations and Dynamic Positional Validation Using a Six Axis Robot."
Paper presented at 37th Annual Meeting and Symposium of the Antenna Measurement Techniques Association (AMTA 2015), Long Beach, CA, United States. October 11, 2015 - October 16, 2015.

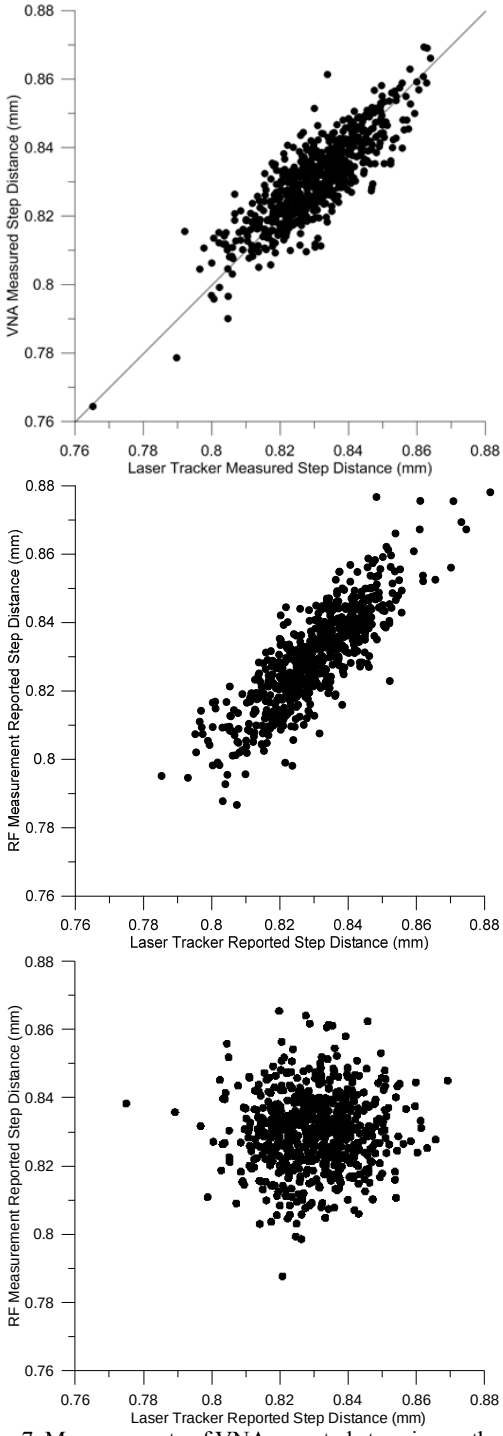


Figure 7. Measurements of VNA reported step size vs the laser tracker reported step at three speeds (ideal step 0.842 mm). At 1.1 mm/s (top) we see very good correlation. At 3.5 mm/s (middle) correlation is reduced. At 11.0 mm/s (bottom) we lose 1-1 correlation but we have tighter control over position variation.

infer distance. We compared the results with the reported laser tracker position and compared the differences, fig. 6. We see a systematic phase progression as the cable moves which imparts an offset, linear with distance, of about 8° or 50 µm over the 550 mm scan. This error level of $10^{-4}$ or -40 dB and the phase correlation between the tracker and the VNA show that the system is nominally stable enough with movement to perform varying velocity scans.

### *C. Dymanic Accuracy at varying veloicities.*

Since the slow movement showed high correlation between mmWave and tracker measurements, we increased speed of separation between the probe and the AUT. Fig. 7 shows the reported step size by the VNA compared to the laser tracker at speeds of 1.1, 3.5 and 11 mm/s. The laser tracker is sampling data constantly and outputs an interpolated position between samples based on the arrival of the trigger [11]. The VNA was setup with a 1 KHz IFBW, which averages mmWave data for approximately 800 µs. We see very good distance correlation between the VNA and Laser Tracker when not moving or at slow speeds (1.1 mm/s). The correlation in positon gets slightly worse at 3.5 mm/s but agreement is generally still within ±10 µm RMS. At 11 mm/s the fine correlation in position is lost but the tracker and VNA are still reading within ±20 µm. at 11 mm/s The antennas move approximately 9.9 µm during the course of the VNA measurement, Table 1. The averaging of phase over this travel could cause a large portion of the loss in correlation. The speeds examined here are relatively slow for production line measurements, however, they do show that at these speeds, the laser tracker is producing results consistent with an independent instrument. Further work will decrease the VNA averaging time and increase the speed of the scan.

## V. MMWAVE ANTENNA RESULTS

The overarching goal for CROMMA is to measure antenna parameters such as gain and pattern. We performed an

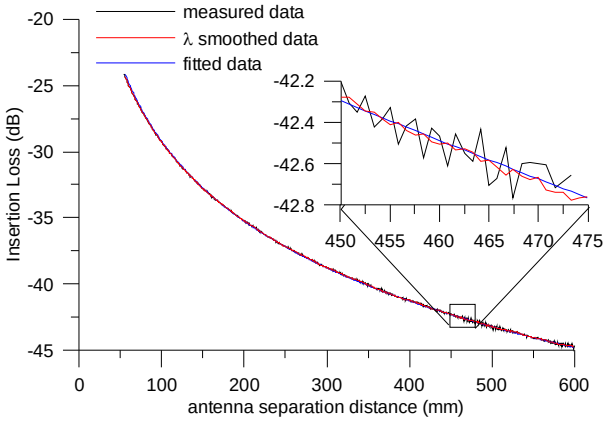


Figure 8. Plot of extrapolation data at 118 GHz for the µ±1 probe vs a 15 dBi standard gain horn. The data spans a $2D^2/\lambda$ to $24D^2/\lambda$ range, there is little evidence of exterior reflections until a spacing of 450 mm which is removed by the wavelength level smoothing.

Novotny, David; Gordon, Joshua; Francis, Michael; Wittmann, Ronald; Curtin, Alexandra; Guerrieri, Jeffrey.
"Antenna Measurement Implementations and Dynamic Positional Validation Using a Six Axis Robot."
Paper presented at 37th Annual Meeting and Symposium of the Antenna Measurement Techniques Association (AMTA 2015), Long Beach, CA, United States. October 11, 2015 - October 16, 2015.

extrapolation scan at approximately 118 GHz, followed by three far-field spherical scans at approximately 112, 118 and 125 GHz, all using the same antenna alignment. The patterns were measured at a radius of 100 mm, or at approximately twice the nominal far-field criterion of $2D^2/\lambda$.

The extrapolation was performed for only one pair of antennas, fig. 8, so we can only calculate combined pair gain, $G_P G_{AUT}$ , for the Probe, $G_P$, and AUT, $G_{AUT}$. A simple fit with distance, $R$, to the far-field Friis transmission formula:

$$\frac{P_r}{P_t} = S_{21} = G_P G_{AUT} \left(\frac{\lambda}{4\pi R}\right)^2 |\alpha_P \cdot \alpha_{AUT}{}^*|^2 [M]$$

where $\alpha_P \cdot \alpha_{AUT}$ is the polarization mismatch and, $[M]$, is generated from the mismatch the antenna ports, yields the pair gain, fig. 8. The reflection mismatch is accounted for by the full two port-calibration, and the polarization mismatch is minimal with the small angular errors. The confinement of phase also shows that we are in a valid range of fitting to far-field paramenters [12]. Table 1, summarizes the gain caclualted for each velocity sweep.

TABLE I. EXTRAPOLATION RESULTS.

| **Probe Speed** | **1.1 mm/s** | **3.5 mm/s** | **11.0 mm/s** |
|---|---|---|---|
| Movement during VNA measurement | 1 µm | 3.1 µm | 9.9 µm |
| Movement during LT measurement | .4 µm | 1.2 µm | 3.6 µm |
| $G_P G_{AUT}$ Pair Gain (dB) | 24.69 | 24.70 | 24.62 |
| uncertianity | ±0.1 dB | ±0.1 dB | ±0.1 dB |

The far-field pattern measurements of the µ=±1 antenna, fig. 9, show minimal change across the frequency band of interest (<0.4 dB change in relative peak level). And less than 1° change in the -6 dB beam width.

The cross polarization pattern measurements show that cross polarization can't be accurately determined in the far-field. We only have approximately 80 dB of dynamic range at 118 GHz. The nominal insertion loss on boresight from the extrapolation measurements, fig. 8, is approximately -39.4 dB at 100 mm. This leaves only 40 dB of measurement sensitivity. Decreasing the measurement radius and performing a full spherical near-field analysis is needed to fully determine the antenna pattern.

## VI. CONCLUSIONS

We have demonstrated that the CROMMA is capable of accuratly scanning multiple geometries. The 6DoF robotic arm naturally operates in circular motion which is optimal for spherical and cylindrical scanning. However, we have shown that fine control allows for effective linear motion on the order of at least 20 µm accuracy. Using the λ/50 rule, this allows for

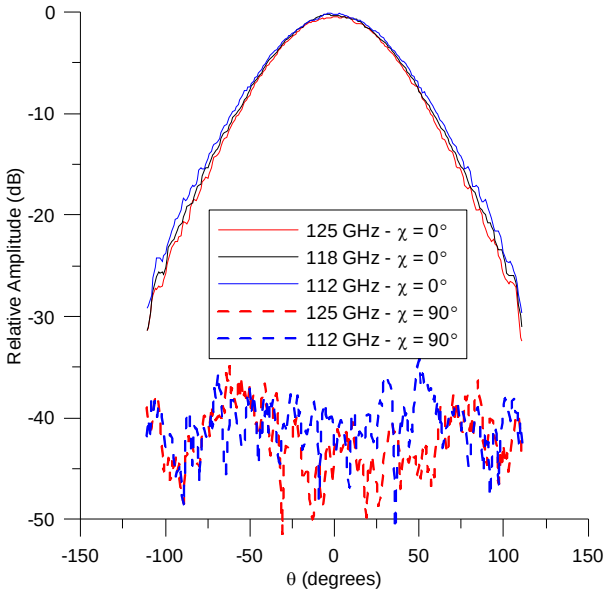


Figure 9. Far-field spherical data at three frequencies. At 100 mm, ~ $4D^2/\lambda$, the χ = 0° peaks are within 0.5 dB. The cross-polarized data for the probe is below the -40 dB limit of the measurement system to detect.

linear motion needed for planar and extrapolation scanning to at least 300 GHz.

Additionally, we have demonstrated the dynamic accuracy of the laser tracker used to guide the robot during the scan. Previously, the accuracy of the tracker was only specified for static measurements. These three pieces, the demonstrated 6DoF scan capability, the mmWave stability and the validated, dynamic tracking "close the loop" and allow the confident use of these 6DoF systems for arbitrary antenna scan geometers at high frequencies. Use of these systems, once characterized [8], at lower frequencies, without the use of a laser tracker, can generate precise patterns with λ/50 accuracy.

Future work will concentrate on increasing the scanning speed of the system and testing high performance antennas. We would like to extend the capabilities to the *dynamic* testing of beamforming antennas. Tests such as measurement of side lobes and spurious emissions as main beams scan or track targets, or *in-situ* testing of multi-beam systems using user-equipment emulation systems as probes.

## REFERENCES


[1] J. A. Gordon, D. R. Novotny, J. B. Coder, J. R. Guerrieri, B. Stillwell, "Robotically controlled mm-wave near-field pattern range," Proceedings of the 2012 Antenna Measurement Techniques Association., Nov 2012.

[2] L. Boehm, F. Boegelsack, M. Hitzler, C. Waldschmidt, "An automated millimeter-wave antenna measurement setup using a robotic arm," 2015 IEEE International Symposium on Antennas and Propagation and North American Radio Science Meeting, TUP-A1.5A.7, 19-24 July 2015.



Novotny, David; Gordon, Joshua; Francis, Michael; Wittmann, Ronald; Curtin, Alexandra; Guerrieri, Jeffrey.
"Antenna Measurement Implementations and Dynamic Positional Validation Using a Six Axis Robot."
Paper presented at 37th Annual Meeting and Symposium of the Antenna Measurement Techniques Association (AMTA 2015), Long Beach, CA, United States. October 11, 2015 - October 16, 2015.

[3] M. H. Francis, R. C. Wittmann, D. R. Novotny, J. A. Gordon, ”Spherical near-field measurement results at millimeter-wave frequencies using robotic positioning,” Proceedings of the 2014 Antenna Measurement Techniques Association, Oct 2014.

[4] D. R. Novotny, J. A. Gordon, J. R. Guerrieri, “Antenna alignment and positional validation of a mmWave antenna system using 6D coordinate metrology,” Proceedings of the 2014 Antenna Measurement Techniques Association, Oct 2014.

[5] M. Hitzler, S. Bader, C. Waldschmidt, "Key aspects of robot based antenna measurements at millimeter wave frequencies," Antennas and Propagation (EuCAP), 2014 8th European Conference on , vol., no., pp.392,396, 6-11 April 2014.

[6] J.A. Gordon, D.R. Novotny, “A Non-Contact Machine Vision System for the Precision Alignment of mm-Wave Antennas in all Six Degrees of Freedom,” Proceedings of the 2014 Antenna Measurement Techniques Association, Oct 2014.

[7] Motoman/Yaskawa MH50 / MH50-35 Datasheet, avialble at http://www.motoman.com.

[8] T. Nielsen, S. Sandwidth,”Production line robot calibration verification test results,” Proceedings of the Coordinate Metrology Society Conference, July 2015.

[9] R. C. Wittmann, M. H. Francis, J. A. Gordon, D. Novotny, “Generalized probe-position compensation methods for near-field antenna measurements,” Proceedings of the 2015 Antenna Measurement Techniques Association, Oct 2015, unpublished.

[10] “R&S® ZVA Vector Network Analyzer: Specifications”. Version 13.02 May 2015. Avialabe at http://www.rohde-schwarz.us.

[11] “Leica Tracker Programming Interface: Programmers Manual: Tracker Trigger Interface,” Version 3.6, August 21,2009.

[12] J. B. Coder, D. R. Novotny, M. H. Francis, J. R. Guerrieri, “On the use of phase data when conducting an extrapolation measurement,” Proceedings of the 2013 Antenna Measurement Techniques Association, Nov 2013.

Novotny, David; Gordon, Joshua; Francis, Michael; Wittmann, Ronald; Curtin, Alexandra; Guerrieri, Jeffrey.
”Antenna Measurement Implementations and Dynamic Positional Validation Using a Six Axis Robot.”
Paper presented at 37th Annual Meeting and Symposium of the Antenna Measurement Techniques Association (AMTA 2015), Long Beach, CA, United States. October 11, 2015 - October 16, 2015.

# Spectrum Sensing with WLAN Access Points

Ryan T. Jacobs, Jason B. Coder
Communications Technology Laboratory
National Institute of Standards and Technology
325 Broadway St., Boulder, CO 80305
Ryan.Jacobs@nist.gov

Vivian M. Musser
Department of Electrical and Computer Engineering
University of Maryland
2410 A.V. Williams Bldg., College Park, MD 20742

***Abstract*—With wireless communication becoming increasingly common in simple everyday devices, the available spectrum is quickly filling up and the risk of interference is increasing. This interference could be a slight nuisance or a disruption to critical services. To better understand the quantity and type of traffic in congested environments, a potential spectrum sensing solution in the ISM bands is discussed. By using a commercially available wireless access point we may be able to monitor the spectrum within range of the access point. If the electromagnetic environment is better understood, device manufacturers should be better able to test their products before deployment, ensuring they can still perform in a crowded electromagnetic environment.**

## I. Introduction

The use of spectrum sharing technologies and methods is growing at a rapid rate. As new methods and technologies are developed and deployed, device manufacturers need to be able to characterize new and existing devices to ensure they will perform in a congested RF environment. One component of this characterization involves understanding what activity is taking place in the electromagnetic environment of interest. A better understanding of the environment leads to a characterization test that is more appropriate and realistic.

One example of a popular, uncoordinated spectrum sharing scenario is the 2.4 GHz ISM band. As this band (2.4 GHz -2.5 GHz) is loosely regulated in the U.S., there are many different protocols and devices that make use of this band. Two of the largest occupants are IEEE 802.11 and IEEE 802.15 wireless devices. As new 802.11 and 802.15 standards are developed, understanding how they perform (i.e., send/receive data) in this crowded environment is crucial.

But without an understanding of the actual electromagnetic activity in the ISM band, the characterization test these devices undergo represent estimates, at best. For example, in-field measurements of the ISM band may show that at 2450 MHz, there is consistently a high level of traffic. This information can be fed back into the device development and measurement standards efforts which would recommend an appropriate amount of testing that corresponds to the actual usage seen in the field.

Accomplishing the task of understanding what's happening in the ISM band may sound simple, but considering the amount of traffic and its widespread geographic use this is a daunting task. One option would be to deploy high-end instrumentation that is capable of taking very detailed measurements, but this is not practical for measurements outside of a laboratory setting. However, most buildings have several wireless access points (WAPs) that make up their 802.11 network. These networks facilitate the 802.11 traffic, perform Clear Channel Assessments (CCA), can detect other wireless networks, and measure the noise level in the environment. These data are collected by WAPs for use in selecting the best channel to use with connected clients. With some modification and automation, we show that we can acquire the spectrum data from the WAP and process it for spectrum occupancy information. We also discuss some of the challenges associated with using a WAP network as a spectrum sensor.

## II. Information Available From the Access Point

Here, our goal was to examine how much spectrum information we could acquire from the WAP. For the WAP tested, there are two modes that are of interest: access point mode and scanner mode [1, pg. 4-10].

When in access point mode, the WAP allows wireless devices to connect to it for access to the network. While in this mode, the 802.11 channel can be set manually or automatically via a CCA. By manually selecting the 802.11 channel, the WAP is still able to perform CCAs, but does not take any action based on their results. When preforming CCAs, the WAP is able to detect wireless devices utilizing 802.11 a/b/g/n/ac. We can also retrieve the RF power level in the channel, as measured by the WAP. Here, we refer to this as noise power because this is a simple power measurement, without regard for what device is generating the power, or what protocol is being used.

The other WAP mode of interest is the scanner mode. This mode will allow the WAP to be dedicated to scanning for traffic in its frequency band and RF spectrum. To use Scanner mode, there must be more than one WAP on the network. For this study only one WAP was used so it was not possible to put the WAP into scanner mode.

## III. Measurement Setup

Figure 1 shows the measurement setup. For the WAP to be used, a Layer 2 managed switch and WAP controller are required. The managed switch provides the main interface into the network, a Layer 2 switch does switching only (based on the MAC address). This is where the WAP, WAP controller and computer are connected to the wired network. The WAP controller is used to provide the command line interface to the



Coder, Jason; Jacobs, Ryan; Musser, Vivian.
"Spectrum Sensing with WLAN Access Points."
Paper presented at 2016 33rd National Radio Science Conference (NRSC), Boulder, CO, United States. January 6, 2016 - January 9, 2016.

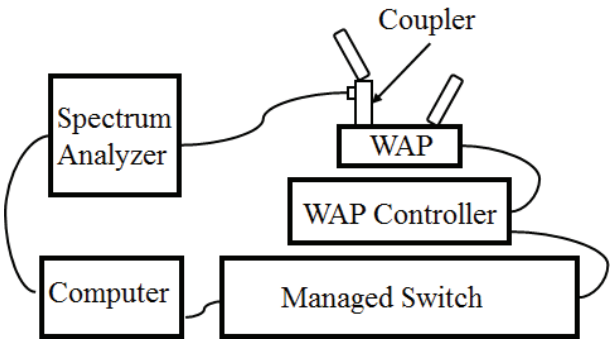


*Figure 1: Block diagram for WAP measurement setup.*

WAP. The controller enables us to control the WAP's radios, transmit power levels, and set the IP address of the WAP. It is also used to setup and configure how the WAP can be accessed by network administrators (e.g., TELNET, SSH, Serial, SNMP, etc.). For our experiments, we communicated with the controller and WAP via TELNET. We chose TELNET because we could easily write scripts to access the controller and WAP, and acquire data. In addition to collecting RF data with the WAP, a spectrum analyzer was also connected to one of the WAP's antennas via a directional coupler. By collecting data from the spectrum analyzer and WAP at the same time, we can compare the data sets collected by each to see how similar they are.

## IV. Measured Data

After verifying the measurement setup with known signals, we acquired data over a 48 hour period. Figure 2 shows a cumulative plot of the measured noise power over the 48 hour period for each of the 11 standard 802.11 channels. These data were recorded in an office environment over a weekend. Thus, we would not expect to see a significant amount of activity.

Figure 3 shows a comparison between the recorded WAP data and a spectrum analyzer. Since the spectrum analyzer takes data once every second and the WAP only updates once every 60 seconds, the data collected from the spectrum analyzer are condensed into smaller "blocks" to make it match the update

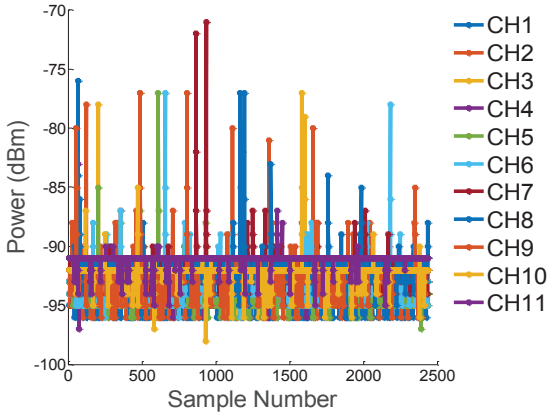


*Figure 2: Recorded spectrum noise from the WAP*

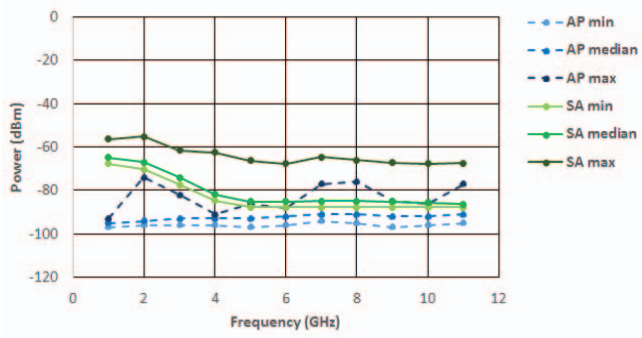


*Figure 3: Spectrum analyzer vs. Wireless access point*

frequency of the WAP. This is done by taking every 60 samples of spectrum analyzer data and finding the peak value for each frequency. By doing this, we are able to directly compare the data from the WAP to the recorded data from the spectrum analyzer. As seen from Figure 3, there is not much correlation between the spectrum analyzer and the WAP. There are two likely reasons why the signals do not have better correlation. The first reason could be that because the signals appear so infrequently, the WAP either does not see them because it is scanning across the channel, or because the RF detector on the WAP, based on an average (or average-like) detection and does not register a signal of shorter duration. The offset between the WAP and spectrum analyzer data may be the result of different amounts of loss in the RF cabling and RF circuitry present inside the WAP.

## V. Future Work and Conclusions

The data shown in Section IV indicate that we can get general spectrum occupancy data from a WAP, though the accuracy of the data may be an issue. Also, the granularity of the data acquired from the WAP (in terms of frequency) may not be enough to draw conclusions about what traffic is traversing the environment. The WAP likely has the hardware to provide data with increased granularity, the current firmware does not provide access to it. Additional capabilities may be possible with the use of the "scanner mode" discussed earlier. Future work may involve setting up a larger test network to examine a WAP with scanner mode enabled.

In addition to the characterization performed here, additional work needs to be done to show how well the WAP (in any mode) responds to signals other than the 802.11 standard. For example, how well does the WAP respond to 802.15 signals, or other non-standard "pulse-type" signals frequently seen in the ISM bands. Here, we have shown some preliminary measurements investigating how feasible it is to use a WAP as a spectrum sensor for the purpose to better understanding the traffic in the crowded ISM bands. The data indicate that more work needs to be done to ensure that the WAP is capable of making RF measurements with an accuracy appropriate for spectrum sensing.

## References

[1] Cisco Systems, Inc., "Cisco Aironet Access Points Configuration Guide for Cisco IOS Software," Cisco IOS Release 15.2(4)JB3a, 6-1. Accessed September 21, 2015.

Coder, Jason; Jacobs, Ryan; Musser, Vivian.
"Spectrum Sensing with WLAN Access Points."
Paper presented at 2016 33rd National Radio Science Conference (NRSC), Boulder, CO, United States. January 6, 2016 - January 9, 2016.

# Verification of a Foundry-Developed Transistor Model Including Measurement Uncertainty

Dylan Williams,[1] Wei Zhao, [1] Richard A. Chamberlin, [1] Jerome Cheron, [1] and Miguel Urteaga[2]

[1]National Institute of Standards and Technology

[2]Teledyne Scientific

**Abstract — We verify a foundry model for state-of-the-art 250 nm heterojunction bipolar transistors with large-signal measurements. We demonstrate the propagation of correlated measurement uncertainties through the verification process, and use them to quantify the differences we observe in the measurements and models.**

**Index Terms — Model, transistor, measurement.**

## I. Introduction

We propagate the uncertainty in large-signal measurements through a transistor-model verification process, and use those uncertainties to better quantify the differences in our measurements and simulations. This gives us far greater insight into the model and how well it performs under large-signal operating conditions.

Practical limitations always restrict the data sets used in even the most comprehensive transistor-model extraction procedures. Compact models such as the foundry model studied here are designed to capture the essential physics governing the transistor's behavior and to be used well outside the space of measurements used in the extraction process. Nevertheless, we neeed to verify the model in regions of operation not used in the extraction process.

Measurement uncertainties are not usually considered in the verification process. This leaves open the possibility that observed differences between the actual and predicted behavior of the transistor in the verification process are due to measurement error, and not to process variations or the inability of the model to predict the transistor behavior in regions of operation not used in the extraction process.

A number of authors have studied two-tier approaches [1-5] and parasitic extraction techniques [5-8] to improve transistor characterization. Lenk and Rudolph performed a very interesting sensitivity analysis of an heterojunction bipolar transistor (HBT) extraction process in [9]. They used it as a tool for evaluating the sensitivity of the extraction process to measurement error and identifying poorly conditioned models. Miranda *et al*. studied the impact of on-wafer calibration kits on the extraction of HEMT models at microwave frequencies in [10]. Williams *et al*. argue that on-wafer thru-reflect-line calibrations improve the accuracy of HBT and CMOS transistor measurements in [11;12].

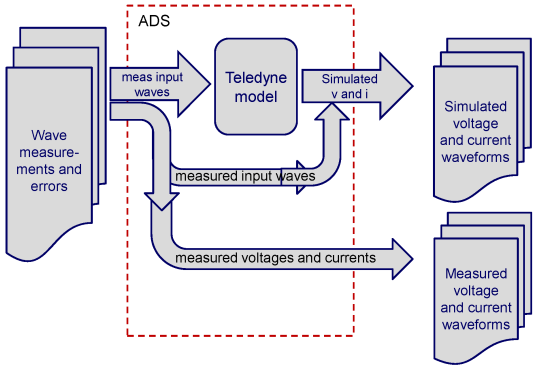


Fig. 1. The verification approach. We programmed ADS to read in the measured wave parameters, simulate the response of the Teledyne HBT model to the input waves, and convert the input and output waves to voltage and current waveforms.

Here, we propagate measurement uncertainties through the process of verifying the large-signal performance of a compact Keysight[1] HBT model [13] derived from DC and small-signal measurements. We use the uncertainty information to better quantify the results of the comparisons between measurements and models.

## II. Model Verification

The transistors we studied were fabricated at Teledyne Scientific with a state-of-the-art 250 nm HBT process. Teledyne Scientific provided a model for the transistors based on version 2.0 of the Keysight HBT model (see [13]) implemented in their Advanced Design System (ADS) software, and included that model in their design kit. The

[1] We identify commercial products only to accurately describe the experiments and analysis we performed. The National Institute of Standards and Technology does not endorse commercial products. Other products may work as well or better.

Williams, Dylan; Chamberlin, Richard; Zhao, Wei; Cheron, Jerome; Miguel, Urteaga.
"Verification of a Foundry-Developed Transistor Model Including Measurement Uncertainty."
Paper presented at 2016 International Microwave Symposium IMS, San Francisco, CA, United States. May 22, 2016 - May 27, 2016.

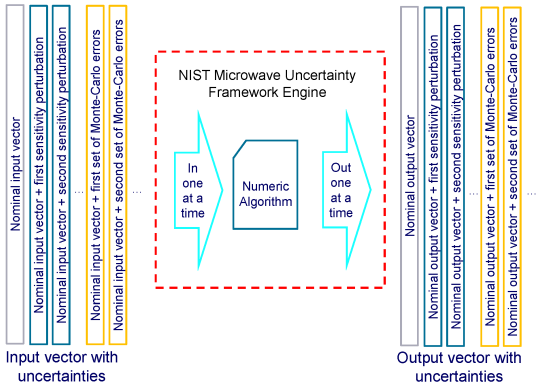


Fig. 2. Approach used for uncertainty propagation by the NIST Microwave Uncertainty Framework.

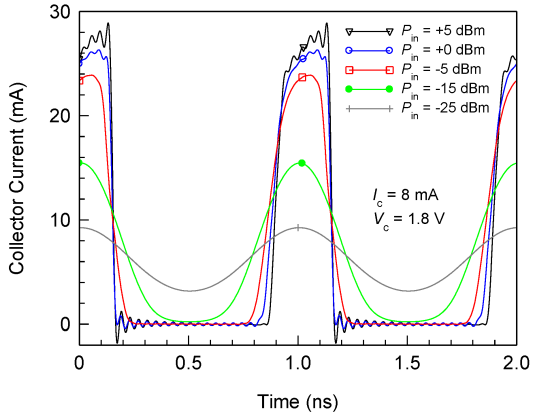


Fig. 3. Representative plots of collector current as a function of 1 GHz drive level.

parameters used in the model were extracted at Teledyne Scientific from DC and small-signal measurements with a proprietary approach.

Here we verify the ability of the Teledyne model to predict the behavior of an HBT with a 6 µm by 250 nm emitter under large-signal excitation, and evaluate the impact of measurement errors on the verification process. By propagating our measurement uncertainties through the verification process, we are able to show when the differences in the transistor behavior predicted by the Teledyne model and the transistor behavior we observed in the verification process were significant and when they were not.

Figure 1 illustrates the approach we took to verify the large-signal performance of the transistor model obtained from Teledyne Scientific. We used a Keysight PNA-X Vector Network Analyzer to excite the transistor in a common-emitter configuration with a 1 GHz sine wave and drive it into a large-signal operating state. We also used the analyzer to measure the incoming and outgoing waves from 1 GHz to 25 GHz at an on-wafer reference plane next to the transistor as a function of the transistor's DC bias state and the drive level of the 1 GHz fundamental. Finally, we used the Keysight ADS software package to emulate our measurement setup, and drive the transistor model with the same incoming waves we measured. We then calculated the voltage and current waveforms at the transistor terminals from our measurements and simulations. Finally, we compared our measured and simulated voltage and current waveforms to each other.

We used the thru-reflect-line calibrations described in [11;14] throughout to ensure the highest accuracy possible and to simplify the uncertainty analysis.

## III. Uncertainty Propagation

We used the NIST Microwave Uncertainty Framework [15] to propagate our measurement uncertainties through the model verification process. This allowed us to track and account for correlations in the measured and simulated voltage and current waveforms we compared.

Figure 2 illustrates how the Microwave Uncertainty Framework accomplishes this with a single input and a single output.[2] At each stage of the calculation, each result and its uncertainty is represented by a single vector containing a nominal measurement or simulation result, a series of vectors containing measured or simulated results from a sensitivity analysis, and a series of vectors containing measured or simulated results from a Monte-Carlo simulation. Depending on the stage of the analysis, these vectors contained lists of complex wave parameters measured by the vector network analyzer at the 25 harmonics of the 1 GHz drive frequency, temporal voltage or current waveforms at the transistor terminals, or various metrics determined from these waveforms. This structure maintains correlations between the measurements we performed at different frequencies throughout the analysis.

Over 400 sources of uncertainty were required in the uncertainty analysis to separately capture all of the individual error mechanisms in the measurements.[3] Each of these

[2] The NIST Microwave Uncertainty Framework allows for multiple inputs as well, and includes algorithms for ensuring that elements in the sensitivity analysis are not double counted.

[3] Independent sources of uncertainties cannot in general be combined if all of the correlations are not captured, as it is difficult to predict how correlated uncertainties will add after various transformations are applied to the measurements.

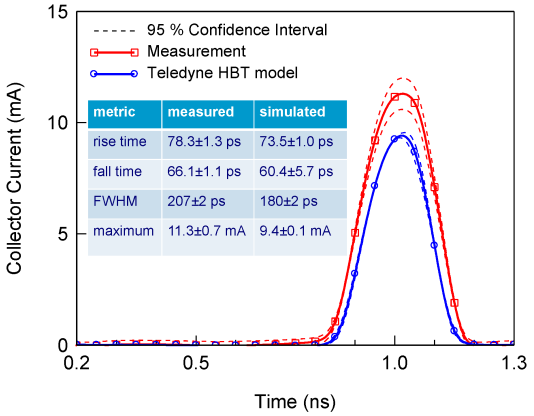


Fig. 4. Transistor collector current, pulse parameters and uncertainties in deep class A/B at a -5 dBm drive level with bias $V_c = 1$ V and $I_c = 2$ mA. Except for an overall scaling factor, the simulates and measured collector-current waveforms are qualitatively quite similar.

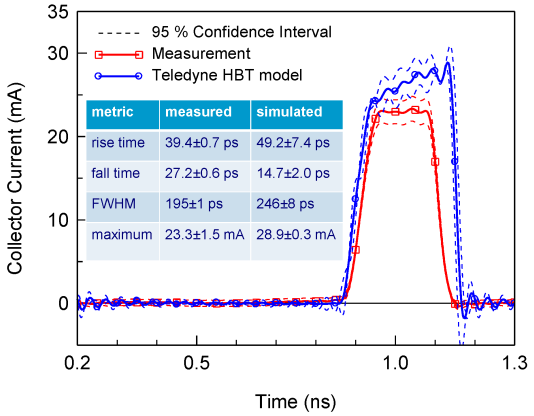


Fig. 5. Transistor collector current, pulse parameters and uncertainties in deep compression at a +5 dBm drive level with bias $V_c = 1.8$ V and $I_c = 8$ mA. The differences in the shapes of the measured and simulated collector-current waveforms are much greater in deep compression.

uncertainty sources was assigned a unique name. These names were used by the Microwave Uncertainty Framework to "turn on" each error mechanism once and only once at each stage of the sensitivity analysis.

The Uncertainty Framework also generates unique seeds for use in the Monte-Carlo analyses. This allows the uncertainties for each error mechanism to be generated separately in different parts of the analysis and still be properly correlated when combined later into a single result.

This attention to correlations is important in this application. The errors in measuring the amplitudes and phases of the incoming waves during the model verification must be propagated through the simulation process before the simulated voltages and currents can be calculated and compared with the measured voltage and current waveforms at the transistor terminals. In addition, the correlations with frequency must be maintained as well if they are to be propagated through the Fourier transform to generate temporal results and to the various metrics we will compare later.

## IV. Verification Results

We varied the 1 GHz drive level from -25 dBm to + 5 dBm and performed large-signal measurements at a number of bias states to explore the behavior of the model provided by Teledyne Scientific. Figure 3 plots the collector currents we measured as a function of the drive level.

We found excellent agreement between the measured and predicted base and collector voltage and current waveforms up to a transistor drive level of about -5 dBm. Figure 4 compares the collector current we measured at a drive level of -5 dBm with the predictions from the Teledyne model, and illustrates good agreement in deep class AB. The transistor drive level is high enough that the collector current pulses on and off rapidly as the transistor turns on. Yet the Teledyne model predicted very similar performance within what appears to be a fairly modest scaling factor that might be attributable to differences in process variations.

Nevertheless, the table in the inset reveals some statistically significant differences in the collector-current rise time and full-width-half-max not immediately obvious from the nominal values and uncertainties plotted in the graph. This illustrates how propagating measurement uncertainties can aid in the analysis of the verification results.

Figure 5 compares a measured collector-current waveform in deep compression at a drive level of +5 dBm with the current predicted by the Teledyne model. Here, we see much larger discrepancies.[4] Not only have the differences between the collector-current rise times and the full-width-half-max grown significantly, as we might have expected from the statistics in the inset in Fig. 5, but there is a large reduction in the simulated collector-current fall time that was not evident in Fig. 5.

## V. Conclusion

We verified the ability of the HBT models provided with the Teledyne Scientific design kits for their 250 nm HBT process to accurately predict HBT performance under large-signal operating conditions. We also eliminated our measurement

[4] The ringing with an approximately 0.05 ns period in the Teledyne model is due to the 25 harmonics we used in the measurements and simulations. While we were capable of including more harmonics in the harmonic-balance simulations performed by ADS, we found convergence difficult when we increased the number of harmonics beyond 25. We ignored this ringing in our analysis.

Williams, Dylan; Chamberlin, Richard; Zhao, Wei; Cheron, Jerome; Miguel, Urteaga.
"Verification of a Foundry-Developed Transistor Model Including Measurement Uncertainty."
Paper presented at 2016 International Microwave Symposium IMS, San Francisco, CA, United States. May 22, 2016 - May 27, 2016.

uncertainty as a significant contributor to the differences we observed at very high drive levels.

## ACKNOWLEDGEMENT

The authors thank David Root, Masaya Iwamoto and Else Schmidt of Keysight Technologies for their insight and assistance in understanding and using the Keysight HBT models and software.

This work was supported by the Defense Advanced Research Projects Agency's Terahertz Electronics Program. The views, opinions, and/or findings contained in this article are those of the author and should not be interpreted as representing the official views or policies, either expressed or implied, of either the Defense Advanced Research Projects Agency or the Department of Defense.

Work supported by US government, not subject to US copyright.

## REFERENCES

[1] Q. Liang, J. D. Cressler, G. Niu, Y. Lu, G. Freeman, D. C. Ahlgren, R. M. Malladi, K. Newton, and D. L. Harame, "A simple four-port parasitic deembedding methodology for high-frequency scattering parameter and noise characterization of SiGe HBTs," *IEEE Trans. Microwave Theory Tech.*, vol. 51, no. 11, pp. 2165-2174, Nov.2003.

[2] Q. Liang, W. Kuo, J. D. Cressler, and A. J. Joseph, "Accurate AC transistor characterization to 110 GHz using a new four-port selfcalibrated extraction technique," *IEEE Topical Meeting on Silicon Monolithic Integrated Circuits in RF Systems*, pp. 282-285, Sept.2004.

[3] X. Wei, K. Xia, G. Niu, Y. LI, S. L. Sweeney, Q. Liang, X. Wang, and S. S. Taylor, "An Improved On-chip 4-Port Parasitics De-embedding Method with Application to RFCMOS," *Topical Meeting on Silicon Monolithic Integrated Circuits in RF Systems*, pp. 24-27, Dec.2007.

[4] L. F. Tiemeijer, R. J. Havens, A. B. M. Jansman, and Y. Bouttement, "Comparison of the 'pad-open-short' and 'open-short-load' deembedding techniques for accurate on-wafer RF characterization of high-quality passives," *IEEE Trans. Microwave Theory Tech.*, vol. 53, no. 2, pp. 723-729, Feb.2005.

[5] K. H. Yau, E. Dacquay, I. Sarkas, and S. P. Voinigescu, "Device and IC Characterization Above 100 GHz," *IEEE Microwave Magazine*, pp. 30-54, Feb.2012.

[6] A. Rumiantsev, P. Sakalas, N. Derrier, D. Celi, and M. Schroter, "Influence of probe tip calibration on measurement accuracy of small-signal parameters of advanced BiCMOS HBTs," *IEEE Bipolar/BiCMOS Circuits and Technology Meeting*, pp. 203-206, Sept.2011.

[7] A. Rumiantsev, S. L. Sweeney, and P. L. Corson, "Comparison of on-wafer multiline TRL and LRM+ calibrations for RF CMOS applications," *Automatic RF Techniques Group Conference Digest*, vol. 72, pp. 132-136, Oct.2008.

[8] A. Rumiantsev, P. L. Corson, S. L. Sweeney, and U. Arz, "Applying the calibration comparison technique for verification of transmission line standards on silicon up to 110 GHz," *Automatic RF Techniques Group Conference Digest*, vol. 73, pp. 1-6, Dec.2009.

[9] F. Lenk and M. Rudolph, "Extraction of GaAs-HBT equivalaent circuit considering the impact of measurement errors," *Innovations with Microwaves and Light: Research reports from the Ferdinand-Braun-Institut fur Hochstrfrequenztechnik*, vol. 3, pp. 95-103, 2015.

[10] J. M. Miranda, C. Fager, H. Zirath, P. Sakalas, S. oz, and J. L. Sebastian, "Influence of the calibration kit on the estimation of parasitic effects in HEMT devices at microwave frequencies," *Instrumentation and Measurement, IEEE Transactions on*, vol. 51, no. 4, pp. 650-655, Aug.2002.

[11] D. F. Williams, A. C. Young, and M. Urteaga, "A Prescription for Sub-Millimeter-Wave Transistor Characterization," *IEEE Trans. THz Sci. Technol.*, pp. 433-439, Mar.2013.

[12] D. F. Williams, P. L. Corson, J. Sharma, H. Krishnaswamy, W. Tai, Z. George, D. Ricketts, P. Watson, E. Dacquay, and S. Voinigescu, "Calibration-Kit Design for Millimeter-Wave Silicon Integrated Circuits," *IEEE Trans. Microwave Theory Tech.*, vol. 61, no. 7, pp. 2685-2694, June2013.

[13] M. Iwamoto, D. E. Root, J. B. Scott, A. Cognata, P. M. Asbeck, B. Hughes, and D. C. D'Avanzo, "Large-signal HBT model with improved collector transit time formulation for GaAs and InP technologies,", 2 ed 2003, pp. 635-638.

[14] D. F. Williams, W. Zhao, R. Chamberlin, J. Cheron, and M. Urteaga, "Verification of a foundry-developed transistor model with measurement uncertainty," *2016 IEEE MTT-S Int. Microwave Symposium*, May2015.

[15] D. F. Williams and A. Lewandowski, "NIST Microwave Uncertainty Framework," National Institute of Standards and Technology, http://www.nist.gov/ctl/rf-technology/related-software.cfm, 2011.

# Comparison of Consensus Value Methods Used to Compile On-Axis Gain Measurement Results

Jeff R. Guerrieri, Mike Francis and Ronald Wittmann
National Institute of Standards and Technology, 325 Broadway, Boulder, CO 80305 USA, jguerrieri@nist.gov

***Abstract*** **This paper compares methods for computing consensus values of data sets. Three methods are used to analyze multiple data sets. The data sets are, on-axis gain measurements that have a large range of values and uncertainties. The appropriate method is dependent on characteristics of the data sets such as, the number of data sets, the spread of the data set values and spread of the uncertainty values for each data set. One method computes a weighted mean where the weights are chosen as the inverses of the fractional error in the data values. A second method removes data sets that are determined to be outliers, then computes an unweighted mean. A third computes a simple unweighted mean. The results of this comparison show that the method chosen to compute a consensus value is fairly independent of the data sets.**

***Index Terms*** **— consensus value, weighted mean, outlier removal, unweighted mean.**

## I. INTRODUCTION

There are a variety of compilation methods that can be used for calculating consensus values, mean or dispersion of data [1] [2]. Often those compiling the data are not certain which method to use. This paper compares three potential methods for computing consensus values. One method uses weighted averages of the data, where the weights are chosen as the inverses of the fractional error in the data values [3]. This weighted mean method applies a larger weight to data values that have smaller uncertainty. It assumes that the measurement uncertainty is determined consistently. A second method for compiling data is an outlier removal method [4]. This method uses an algorithm that calculates a median value and removes data that vary by more than a specified amount from the median. An unweighted averaging technique can then be applied to the remaining data values. The third method computes an unweighted mean value. The data sets used for the comparison are twelve on-axis antenna gain values and accompanying measurement uncertainties.

## II. COMPILATION METHODS

Weighted Mean

The weighted mean value compilation method applies weighted averages. The weights are chosen as the inverses of the uncertainty in the data values. Beginning with on-axis gain values, $G_i'$ (dB) and uncertainties, $\Delta G_i'$ (dB), where, *i* refers to the $i^{th}$ data set.

$$G_i = 10^{G_i'/10},$$

and fractional uncertainty,

$$\Delta G_i/G_i = 1 - 10^{-\Delta G_i'/10}.$$

Next, we use a particular choice and associate the weight $w_i$ with the $i^{th}$ data set,

$$w_i = \frac{G_i}{\alpha \Delta G_i},$$

where,

$$\alpha = max\left(\frac{G_i}{\Delta G_i}\right), \qquad w_i > 0, \qquad \max(w_i) = 1$$

and the effective number of measurements is

$$w = \sum_i w_i.$$

Then calculate the overall gain,

$$G_{weighted\ mean} = \frac{1}{w}\sum_i w_i G_i,$$

and the uncertainty,

$$u(G_{weighted\ mean}) = \sqrt{\left(\frac{1}{w(N-1)}\right)\sum_i w_i (G_i - G_{weighted\ mean})^2},$$

where *N* is the number of data sets and the variability between data sets is assumed to be 0.

Finally, compute the value of weighted mean of the on-axis gain values in dB,

$$G'_{weighted\ mean} = 10 \log G_{weighted\ mean},$$

and the uncertainty for the compiled weighted mean,

$$u'(G_{weighted\ mean}) = -10log\left(1 - \left(\frac{u(G_{weighted\ mean})}{G_{weighted\ mean}}\right)\right).$$



Guerrieri, Jeffrey.
"Comparison of Consensus Value Methods Used to Compile On-Axis Gain Measurement Results."
Paper presented at 10th European Conference on Antennas and Propagation (EuCAP 2016), Davos, Switzerland. April 10, 2016 - April 15, 2016.

Outlier Removal

The outlier removal compilation method tests for the presence of outliers. First, estimate the standard deviation σ of the underlying distribution. The most common such estimate is just the standard deviation of the sample, or data set in this paper.

However, the sample standard deviation is itself quite sensitive to outliers, a more robust estimate can be obtained by using the Median of Absolute Deviations (MAD) [4].

Beginning with,

$$\sigma \approx S(MAD) \equiv 1.4826\, median_j\{|G_i - G_{med}|\}.$$

Where, $G_{med}$ is the median of the sample $\{G_i\}$, and the factor of 1.596 is a normalization factor that produces the correct estimate of σ for Gaussian error distributions (i.e., in the absence of outliers). A value of $G_i$ which differs from the median by more than 2.5 times S(MAD) is commonly considered an outlier, and the criterion to test each point.

If

$$|G_i - G_{med}| > 2.5 \times S(MAD),$$

the sample $G_i$ is identified as an outlier and is removed from the averaging process.

For this exercise the remaining on-axis gain values are compiled as an unweighted mean, $G_{outlier\ removal}$, defined as,

$$G_{outlier\ removal} = \frac{1}{N'}\sum_{i=1}^{N'} G_i\ ,$$

where $G_i$ are the remaining on-axis gain values and $N'$ is the number of remaining gain values after outlier removal.

The uncertainty after outlier removal, $u(G_{\text{outlier removal}})$, defined as,

$$u(G_{outlier\ removal}) = \sqrt{\left(\frac{1}{N'(N'-1)}\right)\sum_{i=1}^{N'}(G_i - G_{outlier\ removal})^2}\ ,$$

where $G_i$ are the values of the remaining on-axis gain values and $N'$ is the number of remaining gain values after outlier removal.

It is important to note that the gain values and uncertainties are converted to linear values before calculations, as in the weighted case, and then converted back to dB values.

Unweighted Mean

The unweighted mean method is a simple average of all of the on-axis gain values, $G_{unweighted\ mean}$, defined as,

$$G_{unweighted\ mean} = \frac{1}{N}\sum_{i=1}^{N} G_i\ ,$$

where $G_i$ are the on-axis gain values and $N$ is the number of gain values.

Similarly, the uncertainty for the unweighted mean of the on-axis gain values, $u(G_{\text{unweighted mean}})$, is defined as,

$$u(G_{unweighted\ mean}) = \sqrt{\left(\frac{1}{N(N-1)}\right)\sum_{i=1}^{N}(G_i - G_{unweighted\ mean})^2},$$

where $N$ is the number of gain values.

Again gain values and uncertainties are converted to linear values before the calculations then converted back to dB values.

## III. Measurement Data Sets

The data sets are twelve, independent measurement of on-axis antenna gain values and accompanying measurement uncertainties. The measurements were performed at three different frequencies listed as f1, f2 and f3. These gain values and uncertainties are listed in Table I and are shown graphically in Fig. 1. For ease in viewing, the values are plotted nominally with respect to the measurement frequency.

TABLE I. ON-AXIS GAIN VALUES AND UNCERTAINTIES*

| Data Set | Gain Value *(dB)* | | |
|---|---|---|---|
| | f1 | f2 | f3 |
| 1 | 23.63 ±0.05 | 24.43 ±0.05 | 24.83 ±0.05 |
| 2 | 23.63 ±0.21 | 24.47 ±0.21 | 24.83 ±0.21 |
| 3 | 23.65 ±0.23 | 24.41 ±0.23 | 24.79 ±0.23 |
| 4 | 23.63 ±0.24 | 24.45 ±0.24 | 24.89 ±0.24 |
| 5 | 23.56 ±0.23 | 24.44 ±0.23 | 24.99 ±0.23 |
| 6 | 23.61 ±0.14 | 24.39 ±0.14 | 24.84 ±0.14 |
| 7 | 23.70 ±0.11 | 24.47 ±0.11 | 24.88 ±0.11 |
| 8 | 23.41 ±0.50 | 23.99 ±0.50 | 24.20 ±0.50 |
| 9 | 23.89 ±0.51 | 24.64 ±0.51 | 25.44 ±0.51 |
| 10 | 23.61 ±0.85 | 24.13 ±0.85 | 24.52 ±0.85 |
| 11 | 23.62 ±0.03 | 24.44 ±0.03 | 24.86 ±0.03 |
| 12 | 23.66 ±0.07 | 24.48 ±0.07 | 24.88 ±0.07 |

* *Uncertainties listed in Table I have a coverage factor of 2.*

Guerrieri, Jeffrey.
"Comparison of Consensus Value Methods Used to Compile On-Axis Gain Measurement Results."
Paper presented at 10th European Conference on Antennas and Propagation (EuCAP 2016), Davos, Switzerland. April 10, 2016 - April 15, 2016.

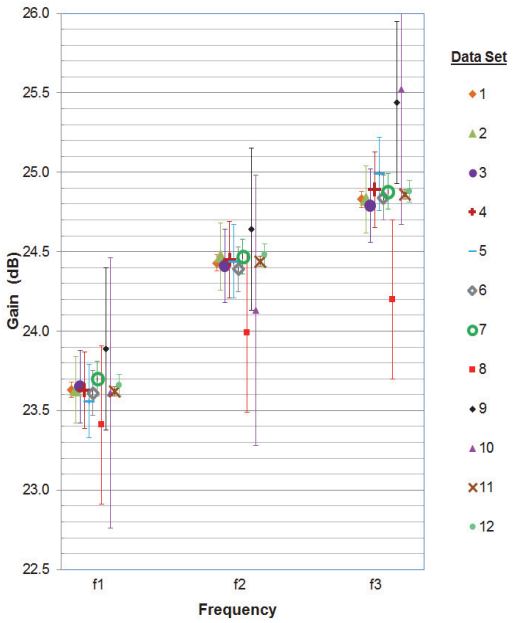


Fig. 1. On-axis gain value.

## IV. Application of Compilation Methods

### Weighted Mean

First, the weighted mean compilation method is applied to the on-axis gain values for the three measurement frequencies. The results are listed in Table II.

TABLE II. COMPILED WEIGHTED MEANS AND STANDARD UNCERTAINTIES

| f1 | f2 | f3 |
|---|---|---|
| 23.63 ±0.01 | 24.44 ±0.01 | 24.87 ±0.01 |

### Outlier Removal

Next, the outlier removal compilation method is applied to the on-axis gain values for each measurement frequency. The outlier on-axis gain values are defined and listed in ***bold red italics*** in Table III. After the removal of outliers the unweighted mean is determined for the remaining on-axis gain values for each measurement frequency. These unweighted mean values are listed in ***bold blue italics*** at the bottom of Table III.

TABLE III. ON-AXIS GAIN VALUES WITH OUTLIERS DEFINED AND CALCULATED UNWEIGHTED MEAN AFTER OUTLIER REMOVAL

| Data Set | Gain Value *(dB)* | | |
|---|---|---|---|
| | f1 | f2 | f3 |
| 1 | 23.63 ±0.05 | 24.43 ±0.05 | 24.83 ±0.05 |
| 2 | 23.63 ±0.21 | 24.47 ±0.21 | 24.83 ±0.21 |
| 3 | 23.65 ±0.23 | 24.41 ±0.23 | 24.79 ±0.23 |
| 4 | 23.63 ±0.24 | 24.45 ±0.24 | 24.89 ±0.24 |
| 5 | 23.56 ±0.23 | 24.44 ±0.23 | 24.99 ±0.23 |
| 6 | 23.61 ±0.14 | 24.39 ±0.14 | 24.84 ±0.14 |
| 7 | 23.70 ±0.11 | 24.47 ±0.11 | 24.88 ±0.11 |
| 8 | ***23.41 ±0.50*** | ***23.99 ±0.50*** | ***24.20 ±0.50*** |
| 9 | ***23.89 ±0.51*** | ***24.64 ±0.51*** | ***25.44 ±0.51*** |
| 10 | 23.61 ±0.85 | ***24.13 ±0.85*** | ***24.52 ±0.85*** |
| 11 | 23.62 ±0.03 | 24.44 ±0.03 | 24.86 ±0.03 |
| 12 | 23.66 ±0.07 | 24.48 ±0.07 | 24.88 ±0.07 |
| ***Unweighted Mean & Standard Uncertainty (After Outlier Removal)*** | ***23.63 ±0.11*** | ***24.44 ±0.06*** | ***24.87 ±0.06*** |

### Unweighted Mean

Finally, the unweighted mean compilation method is applied to the on-axis gain values for the three measurement frequencies. The results are listed in Table IV.

TABLE IV. COMPILED UNWEIGHTED MEANS AND STANDARD UNCERTAINTIES

| f1 | f2 | f3 |
|---|---|---|
| 23.63 ±0.03 | 24.40 ±0.05 | 24.92 ±0.10 |

## V. Results

The results after applying each compilation method to the twelve data sets at the three measurement frequencies are listed in Table V. These results are also shown graphically along with the on-axis gain values in Fig. 2. For ease in viewing, the values are plotted nominally with respect to the measurement frequency.

Guerrieri, Jeffrey.
"Comparison of Consensus Value Methods Used to Compile On-Axis Gain Measurement Results."
Paper presented at 10th European Conference on Antennas and Propagation (EuCAP 2016), Davos, Switzerland. April 10, 2016 - April 15, 2016.

The results are comparable for the compilation. The compiled results are the same for f1 except for the uncertainties. This is expected due to the close grouping of the on-axis gain values except for the two outlier data sets 8 and 9. The outliers offset each other for the unweighted mean method, are not included in the outlier removal method and due to their large measurement uncertainty have little effect in the weighted mean method. There are three outlier on-axis gain values for the measurements at f2 and f3, data sets 8, 9 and 10. The difference between compiled results is greatest at f3. The compiled uncertainties are smallest for the weighted mean results.

TABLE V. RESULTING GAIN CONSENSUS VALUES AND STANDARD UNCERTAINTIES OF COMPILATION METHODS

| Compilation Method | f1 | f2 | f3 |
|---|---|---|---|
| Weighted Mean | 23.63 ±0.01 | 24.44 ±0.01 | 24.87 ±0.01 |
| Outlier Removal | 23.63 ±0.11 | 24.44 ±0.06 | 24.87 ±0.06 |
| Unweighted Mean | 23.63 ±0.03 | 24.40 ±0.05 | 24.92 ±0.10 |

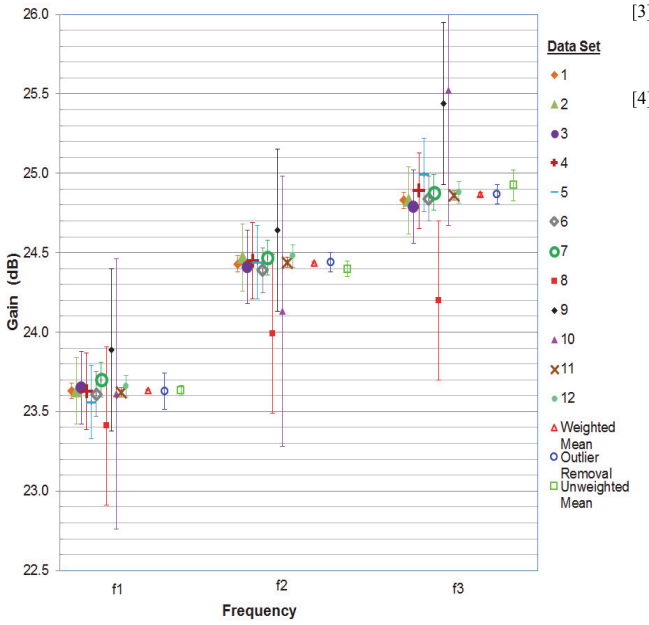


Fig. 2 .On-axis gain values and the results of the three compilation methods.

## VI. CONCLUSION

Three potential compilation methods for computing consensus values were compared using on-axis antenna gain values and associate uncertainties. The compiled gain values compared favorably. The unweighted mean method at f3 differs by the largest amount, but is still within the uncertainty. The uncertainty determined by outlier removal method is larger at f1. The outlier removal method is probably better suited for data sets where the calculated uncertainties are suspect and the comparison can afford to remove data sets. The weighted mean method allows for all data sets to be used in the compilation, which is important for small samples sizes. However, it assumes that the uncertainties are reasonable.

There are a variety of methods used to compile data. One method is not necessarily better, or more correct than another. However, it is important to inform associated parties of the method used and to provide the relevant data for result verification and additional calculation.

## REFERENCES


[1] Duewer D. L., "A Robust Approach for the Determination of CCQM Key Comparison Reference Values and Uncertainties", National Institute of Standards and Technology Report.

[2] Paule, R.C. and Mandel, J., "Consensus Value and Weighting Factors," J. Res. Natl. Bur. Stand., vol. 87, pp. 377 – 385, Sept.-Oct., 1982.

[3] Guerrieri J. R., Coder J. B., Francis, M. H., Gordon J., Novotny D. R., Wittmann R.C., "International Comparison of Ku-Band Standard Gain Horn Characterization", 2013 Antenna Measurement Techniques Association Conference Proceedings.

[4] Randa J., "Update to Proposal for KCRV & Degree of Equivalence for GTRF Key Intercomparisons", GT-RF/2005-04.



Guerrieri, Jeffrey.
"Comparison of Consensus Value Methods Used to Compile On-Axis Gain Measurement Results."
Paper presented at 10th European Conference on Antennas and Propagation (EuCAP 2016), Davos, Switzerland. April 10, 2016 - April 15, 2016.

# Multi-purpose Configurable Range for Antenna Testing Up To 220 GHz*

David Novotny[1], Michael Francis[1], Ronald Wittmann[1], Joshua Gordon[1], Jeffrey Guerrieri[1], Alexandra Curtin[1]
[1] (Affiliation): Communications Technology Laboratory, National Institute of Standards and Technology, Boulder, CO, USA,
david.novotny@nist.gov


***Abstract*—NIST has developed a multi-purpose test range for performing several types of antenna testing including spherical, cylindrical, and planar near-field scanning, as well as extrapolation measurements. This range uses a commercial, off-the-shelf, six-axis robot and a laser tracker to accomplish highly accurate positioning that allows scanning up to 220 GHz. Near-field measurements require positioning accuracies on the order of 0.01 to 0.02 wavelengths. We have evaluated the positioning capability of the robot and performed spherical near-field measurements at 183 GHz. We have performed spherical far-field and extrapolation measurements from 112 – 125 GHz. In addition, position data are acquired continuously using the laser tracker, which allows us to compensate for position errors in software. We report on the results of these measurements.**

***Index Terms*—extrapolation measurements, millimeter-wave antenna measurements, multi-frequency measurements, near-field measurements.**

## I. Introduction

Higher frequencies, multiple geometries, many antennas, multiple frequencies, rapid beam-state changes, shorter duration testing requirements… there is an increasing metrology need for all of these. There are requirements to test at higher frequencies for climate monitoring, security, and communications applications that require tighter tolerances for positioning, orientation, and timing between system components than are required at lower frequencies. The ability to test multiple geometries, such as planar scans at various orientations, or a spherical and extrapolation measurement with one setup, would allow for more rigorous testing with minimal increases in test time. Cell phones and spacecraft with many operational antennas need a test facility that can accommodate multiple testing requirements. Finally, the ability to rapidly move probe antennas around test objects while maintaining orientation relative to the object under test may have applications in medical and shielding tests.

The use of coordinated robotics with multiple degrees of freedom (DoF) and the use of laser-based positioning metrology equipment to guide and correct scan geometries may offer solutions to these antenna testing issues. Recently, the National Institute of Standards and Technology (NIST) has reported the capabilities of its new configurable robotic millimeter-wave antenna facility (CROMMA) and some preliminary antenna measurement results [1-6]. The CROMMA uses a commercial-off-the-shelf robotic system with six degrees of freedom (6DoF).

The major goal of this work is to develop a configurable platform that can use different measurement geometries with minimal setup. The 6DoF positioning capabilities of the antenna under test (AUT) and probe, guided by the laser tracker, allow for correcting both location and orientation throughout the scan geometry between the antenna and positioner with minimal effort. Near-field measurements typically require positioning accuracies on the order of 0.01λ to 0.02λ [7].

In a step toward the above goals, we report here on CROMMA antenna pattern measurements at 112 – 125 GHz and 183 GHz at the NIST laboratories. We also report on the results of extrapolation measurements performed at 112, 118, and 125 GHz, as well as the positional accuracies achieved in both the antenna pattern and gain measurements.

## II. The Measurement System

The measurement system, shown in Fig. 1, consists of a six-axis robot (with the probe antenna mounted on one end), a six-axis hexapod, which serves to align the test antenna relative to the azimuthal axis and an azimuthal rotator (for positioning the antenna under test), a laser tracker, and a RF

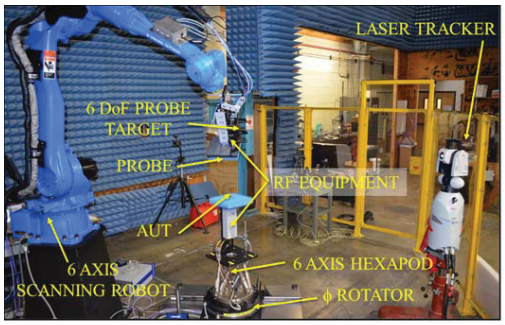


Fig 1. Major components of the Configurable MilliMeter-wave Robotic Antenna Facility (CROMMA).

Novotny, David; Francis, Michael; Wittmann, Ronald; Gordon, Joshua; Guerrieri, Jeffrey; Curtin, Alexandra.
"Multi-purpose Configurable Range for Antenna Testing Up To 220 GHz*."
Paper presented at 11th European Conference on Antennas and Propagation (EuCAP 2016), Davos, Switzerland. April 10, 2016 - April 15, 2016.

network analyzer. The robot, in combination with the azimuthal rotator, allows scanning for several geometries including spherical, cylindrical, and planar geometries and, in principle, a combination thereof. Extrapolation measurements, where the probe antenna and test antenna point directly at each other while the separation distance increases, are also possible.

Out of the box the robot is capable of positioning to an uncertainty of 2 – 3 mm. However, feedback from the laser tracker can be used to improve its positioning to 20 – 25 µm [2]. The laser tracker itself can record positions to approximately 15 – 20 µm (due to uncertainties in the transverse encoders). This position information can be used in software to compensate for the probe position discrepancies.

## III. MEASUREMENT RESULTS

At 183 GHz, we performed spherical near-field antenna measurements, from which we determined the antenna far-field pattern. In the 112–125 GHz band we determined the antenna far field at 112, 118 and 125 GHz by a direct measurement of the far field, using spherical scanning. At 118 GHz, we determined the on-axis pair gain of a standard gain horn and $\mu = \pm 1$ probe.

### *A. 183 GHz Measurements*

We performed spherical near-field measurements at 183 GHz on a standard gain horn with an aperture size of 9.67 mm x 12.62 mm, using a $\mu=\pm 1$ circular aperture probe with a diameter of 1.5 mm. (This $\mu=\pm 1$ probe is described in [7].) Near-field measurements were done at a radius of 10 cm, then transformed to the far field, and a probe correction was performed. Fig. 2 shows a comparison of the theoretical far-field pattern and the transformed far-field pattern for the E-plane. As indicated earlier, the actual positions where the near-field data were taken were recorded using the laser tracker. There were small differences between these points and the ideal measurement locations. This information was used to do position compensation as described in [8,9].

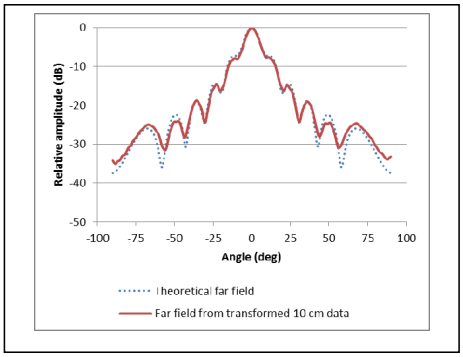


Fig. 2. Comparison of theoretical far field to that obtained from transforming 10 cm near-field data for the E-plane at 183 GHz.

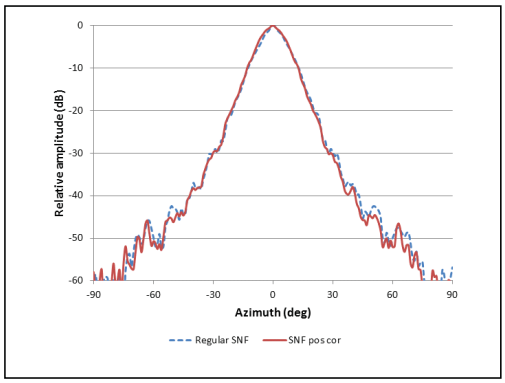


Fig. 3. Far-field H-plane pattern, derived from spherical near-field (SNF) measurements, of a WR-5 standard gain horn with position correction (red, solid) and without position correction (blue, dashed).

A comparison of the position-compensated pattern and the traditionally derived pattern is shown in Fig. 3 for the H-plane.

### *B. 112 – 125 GHz Measurements*

We performed spherical far-field measurements at three frequencies in the 112–125 GHz band for a $\mu=\pm 1$ probe. Measurements were made at 100 mm, which corresponds to $4D^2/\lambda$. Sample co- and cross-polarization results are shown in Fig. 4. In this case, $\chi=0°$ corresponds to the co-polarization and $\chi=-90°$ corresponds to the cross polarization. The co-polarization peaks at 112, 118, and 125 GHz agree within ±0.5 dB. The cross polarization data are generally below the -40 dB level, which is the detectable limit for the measurement system.

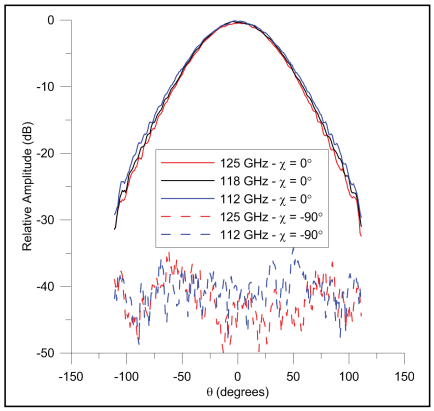


Fig. 4. E-plane pattern at a separation distance of 100 mm for three frequencies. The solid lines correspond to the co-pol patterns and the dashed lines to the cross-pol pattern.

Novotny, David; Francis, Michael; Wittmann, Ronald; Gordon, Joshua; Guerrieri, Jeffrey; Curtin, Alexandra.
"Multi-purpose Configurable Range for Antenna Testing Up To 220 GHz*."
Paper presented at 11th European Conference on Antennas and Propagation (EuCAP 2016), Davos, Switzerland. April 10, 2016 - April 15, 2016.

The three-antenna extrapolation method is used to determine the gain of three antennas without having a priori knowledge of any of the antenna gains [10]. So far, we performed extrapolation measurements of only one pair of

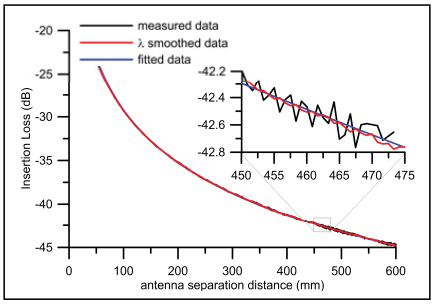


Fig. 5. Plot of extrapolation data at 118 GHz for the $\mu$=±1 probe versus a 15 dBi standard gain horn.

antennas at 118 GHz. Because we have measured only one pair, we are only able to determine a combined pair gain at this time. This pair gain is derived from the leading term of a power series fit to the data in $1/r^n$ [10]. Here $r$ is the separation distance between the two antennas. Sample extrapolation results are shown in Fig. 5. The smoothed data in Fig. 5 come from averaging data over a wavelength to account for multiple reflections between the two antennas. A pair gain of 24.69 dB was determined from these measurements. The data span a range of $2D^2/\lambda$ to $24D^2/\lambda$ (where $D$ is the diameter of the largest antenna).

## IV. CONCLUSIONS AND FUTURE WORK

We have demonstrated that a robotic arm is capable of scanning in more than one geometry (spherical, and extrapolation geometries, to date). We have demonstrated fine controls that allow CROMMA to control location with an uncertainty of 20 μm or better. Using the λ/50 rule, we can provide sufficient accuracy for extrapolation (and planar) measurements up to at least 300 GHz. Finally, we have demonstrated that we can compensate (in software) when location and polarization are not standard.

Future work will concentrate on increasing the scanning speed of the system, testing high-performance antennas and undertaking a thorough uncertainty analysis for the above measurements (including, for example, antenna-antenna multiple reflections and truncation). We would like to extend the capabilities to the *dynamic* testing of beamforming antennas. We want to begin measurements of side lobes and spurious emissions as the main beams scan or track targets, or *in-situ* testing of multi-beam systems using user-equipment emulation systems as probes. We will be improving processing software to use a standard interface and provide increased flexibility to handle frequency-multiplexed data, hybrid geometries, and pointing compensation.

## REFERENCES


[1] D. Novotny, J. Gordon, M. Francis, R. Wittmann, A. Curtin, J. Guerrieri, "Antenna measurement implementations and dynamic positional validation using a six axis robot," Proc. of the 2015 Antenna Meas. Tech. Assoc., pp. 15 – 20, October 2015

[2] J. A. Gordon, D. R. Novotny, J. B. Coder, J. R. Guerrieri, B. Stillwell,"Robotically controlled mm-wave near-field pattern range," Proc. of the 2012 Antenna Meas. Tech. Assoc., pp. 384 – 389, November 2012.

[3] L. Boehm, F. Boegelsack, M. Hitzler, C. Waldschmidt, "An automated millimeter-wave antenna measurement setup using a robotic arm," 2015 International Symposium on Antennas and Propagation and North American Radio Science Meeting, TUP-A1.5A.7, 19-24 July 2015.

[4] M. H. Francis, R. C. Wittmann, D. R. Novotny, J. A. Gordon, "Spherical near-field measurement results at millimeter-wave frequencies using robotic positioning," Proc. of the 2014 Antenna Meas.Tech. Assoc., pp. 231 – 234, October 2014.

[5] D. R. Novotny, J. A. Gordon, J. R. Guerrieri, "Antenna alignment and positional validation of a mmWave antenna system using 6D coordinate metrology," Proc. of the 2014 Antenna Meas. Tech. Assoc., pp. 247 – 252, October 2014.

[6] J. A. Gordon, D. R. Novotny, M. H. Francis, R. C. Wittmann, M. L. Butler, A. E. Curtin, J. R. Guerrieri, "Millimeter-Wave Near-Field Measurements Using Coordinated Robotics," IEEE Trans. Antennas Propagat., Submitted May 2015.

[7] M.H. Francis and R.C. Wittmann, "Near-field scanning measurements: Theory and practice." In *Modern Antenna Handbook*, edited by C.A. Balanis, Chp. 19, New York, NY: John Wiley & Sons, 2008.

[8] R.C. Wittmann, B.K. Alpert, M.H. Francis, "Near-field antenna measurements using nonideal measurement locations," IEEE. Trans. Antennas Propagat., vol. AP-46, pp. 716 – 722, May 1998.

[9] R.C. Wittmann, B.K. Alpert, M.H. Francis, "Near-field, spherical-scanning antenna measurements with nonideal probe locations," IEEE Trans. Antennas Propagat., vol. AP-52, pp. 2184 – 2186, August 2004.

[10] A.C. Newell, R.C. Baird, and P.F. Wacker, "Accurate measurement of antenna gain and polarization at reduced distances by an extrapolation technique," IEEE Trans. Antennas Propagat., vol. AP-21, pp. 418 – 431, July 1973.



Novotny, David; Francis, Michael; Wittmann, Ronald; Gordon, Joshua; Guerrieri, Jeffrey; Curtin, Alexandra.
"Multi-purpose Configurable Range for Antenna Testing Up To 220 GHz*."
Paper presented at 11th European Conference on Antennas and Propagation (EuCAP 2016), Davos, Switzerland. April 10, 2016 - April 15, 2016.

# International Comparison of WR15 (50 to 75 GHz) Power Measurements among NIST, NIM, PTB and NMC, A*STAR

Xiaohai Cui[1], Yu Song Meng[2], Rolf Judaschke[3], Jürgen Rühaak[3], T. P. Crowley[4, 5], and R. A. Ginley[4]

[1]National Institute of Metrology, Beijing, China
E-mail: cuixh@nim.ac.cn

[2]National Metrology Centre, Agency for Science, Technology and Research (A*STAR), Singapore

[3]Physikalisch-Technische Bundesanstalt, Braunschweig, Germany

[4]National Institute of Standards and Technology, Boulder, CO, USA[A]

[5]present affiliation: Xantho Technologies, Madison, WI, USA

***Abstract* — This paper reports preliminary measurement results of an informal international power comparison in WR15 (50 GHz to 75 GHz) waveguide among NIST, NIM, PTB and NMC, A*STAR. The goal of the comparison was to demonstrate the precision measurement capabilities and validate the equivalence of power measurements in WR15 waveguide at participating laboratories.**

***Index Terms* — Comparison, power measurements, standards, uncertainty, WR15, thermistor sensor**

## I. INTRODUCTION

We have conducted an informal international comparison of WR15 (50 GHz to 75 GHz) waveguide power measurements among the National Institute of Standards and Technology (NIST) of the USA, the National Institute of Metrology (NIM) of China, the Physikalisch-Technische Bundesanstalt (PTB) of Germany, and the National Metrology Centre (NMC) of the Agency for Science, Technology and Research (A*STAR) of Singapore.

The main motivation of this comparison is a desire to demonstrate the precision measurement capabilities and validate the equivalence of WR15 waveguide power measurements at participating National Metrology Institutes (NMIs) which have made recent changes [1-3]. In addition, to our knowledge, the only previous international comparison with same waveguide size was conducted only at 62 GHz [4].

This comparison was piloted by NIM, China, and performed between May 2014 and December 2015. In this paper, preliminary results of the comparison will be reported and briefly discussed.

## II. TRAVELING STANDARDS

[B]Three traveling standards (all are Hughes 45774H-1100 thermistor power sensors[C]) were provided by the NIM, China. The third one was included only for the last round. They are identified as,

1. NIM-1 with S/N 097,
2. NIM-2 with S/N 461, and
3. NIM-3 with S/N 149 (Measured by NIM and PTB only).

It is also noted that after arrival of NIM-1 and NIM-2 at NIST, their flanges were inspected and some rough spots were sanded using very fine sandpaper.

Table 1. Comparison schedule and measured quantities.

| NMIs | Period | $\eta_e$ | $K_c$ |
|---|---|---|---|
| NIM | May 2014, July 2015 | NIM-1, 2, 3 | NIM-1, 2 |
| NMC | September 2014 | | NIM-1, 2 |
| NIST | February 2015 | NIM-1, 2 | NIM-1, 2 |
| PTB | December 2015 | NIM-1, 2, 3 | NIM-1, 2, 3 |

In this comparison, the two measurands, effective efficiency $\eta_e$ and calibration factor $K_c$ were measured from 50 GHz to 75 GHz in 1 GHz steps. The relationship between the effective efficiency and the calibration factor is given by,

$$K_c = \eta_e(1 - |\Gamma|^2)\,. \qquad (1)$$

Here, $|\Gamma|$ is the magnitude of input reflection coefficient of the traveling standards. Table 1 summarizes the comparison schedule and the measured quantities of each NMI.

## III. MEASUREMENT SYSTEMS AND METHODOLOGIES

NIST, NIM and PTB performed the measurements using their own microcalorimeters, with $\eta_e$ measured directly and then converted to the calibration factor $K_c$ using $|\Gamma|$.

NMC, A*STAR applied a *direct comparison transfer* technique [3] for measuring the calibration factor $K_c$ only in this comparison. Their waveguide reference standards are Agilent V8486A power sensors which are calibrated and traceable to the microcalorimeter at the National Physical Laboratory of the UK.



[B] This is supported by the National Science and Technology Supporting Program "Wireless Communication Power Measurement Standard and Traceability Technology Research" of China, Grant No. 2014BAK02B02.

[C] Identification of commercial equipment does not imply endorsement by the authors or their institutions.

Cui, Xiaohai; Meng, Yu; Judaschke, Rolf; Ruehaak, Juergen; Crowley, Thomas; Ginley, Ronald.
"International Comparison of WR 15 (50 to 75 GHz) Power Measurements among NIST, NIM, PTB and NMC, A*STAR."
Paper presented at 2016 Conference on Precision Electromagnetic Measurements (CPEM 2016), Ottawa, ON, Canada. July 10, 2016 - July 15, 2016.

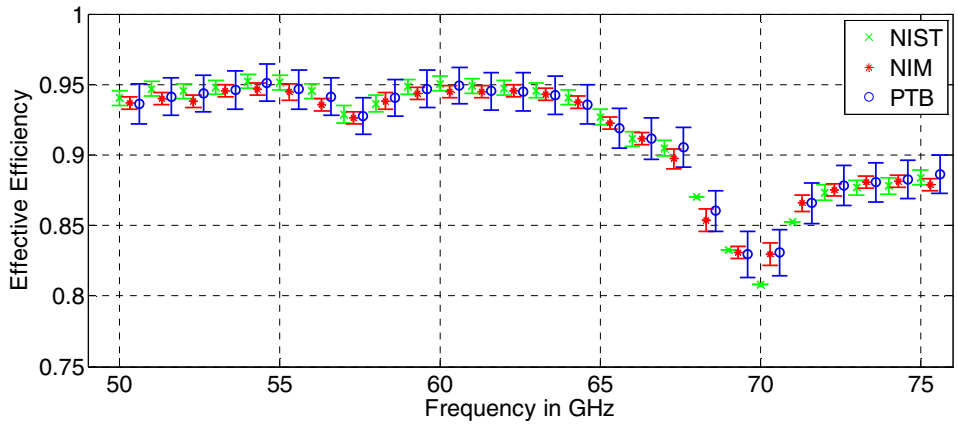


Fig. 1. Preliminary results of $\eta_e$ for NIM-1. Uncertainty bars are shown for $k$ = 2. Frequency values are shifted for better readability. No uncertainty value provided by NIST for 68, 69, 70 and 71 GHz.

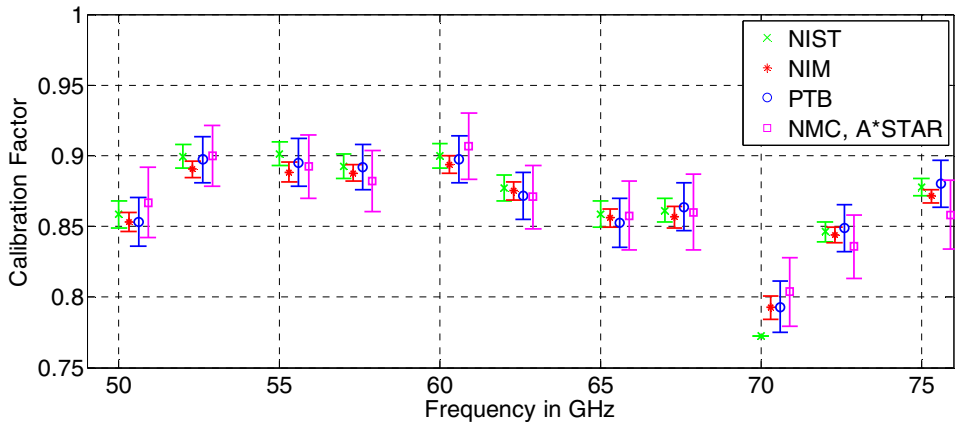


Fig. 2. Preliminary results of $K_c$ for NIM-1. Uncertainty bars are shown for $k$ = 2. Frequency values are shifted for better readability. No uncertainty value provided by NIST for 70 GHz.

In addition to the effective efficiency and calibration factor, the corresponding uncertainties were also given.

## IV. Preliminary Results and Analysis

Preliminary results for the traveling standard (NIM-1) at each NMI, together with their expanded uncertainties are shown in Fig.1 and Fig.2. From Fig.1 and Fig.2, it can be observed that generally there are good agreements among the measurement results from each NMI for NIM-1. It is noted that the relative large uncertainty for the calibration factor measured by the NMC, A*STAR is dominated by their reference standards.

However, agreement was not as good for NIM-2 measurements. For NIM-3, there was very good agreement except at two frequencies with large differences. The discrepancies that exist are currently under investigation. More detailed results and analysis for all the traveling standards (NIM-1, NIM-2, and NIM-3) are in process and will be reported later.

## References

[1] R. Judaschke and J. Rühaak, "Determination of the correction factor of waveguide microcalorimeters in the millimeter-wave range," *IEEE Trans. Instrum. Meas.*, vol. 58, no. 4, pp. 1104–1108, Apr. 2009.

[2] X. Cui and T. P. Crowley, "Comparison of experimental techniques for evaluating the correction factor of a rectangular waveguide microcalorimeter," *IEEE Trans. Instrum. Meas.*, vol. 60, no. 7, pp. 2690–2695, Jul. 2011.

[3] Y. Shan, Y. S. Meng, and Z. Lin, "Generic model and case studies of microwave power sensor calibration using direct comparison transfer," *IEEE Trans. Instrum. Meas.*, vol. 62, no. 6, pp. 1834–1839, Jun. 2013.

[4] J. Achkar, B. Mellouet, L. Velasco, *et al*. "The GT-RF/95-1 key comparison of power measurements at 62 GHz," *IEEE Trans. Instrum. Meas*., vol. 50, no. 2, pp. 406–408, Apr. 2001.

Cui, Xiaohai; Meng, Yu; Judaschke, Rolf; Ruehaak, Juergen; Crowley, Thomas; Ginley, Ronald.
"International Comparison of WR 15 (50 to 75 GHz) Power Measurements among NIST, NIM, PTB and NMC, A*STAR."
Paper presented at 2016 Conference on Precision Electromagnetic Measurements (CPEM 2016), Ottawa, ON, Canada. July 10, 2016 - July 15, 2016.

# Calibration of Millimeter-wave Channel Sounders for Super-resolution Multipath Component Extraction

Peter B. Papazian[1], Jae-Kark Choi[2], Jelena Senic[1], Peter Jeavons[1], Camillo Gentile[2], Nada Golmie[2], Ruoyu Sun[1], David Novotny[1], Kate A. Remley [1]

National Institute of Standards and Technology (NIST), Communications Technology Laboratory

[1]Boulder, Colorado, USA [2]Gaithersburg, Maryland, USA

***Abstract*—Millimeter-wave communication systems will rely on highly directional antennas to compensate for the greater pathloss expected in their frequency bands of operation. Hence, electronic beamforming will form a cornerstone for the technology. For the effective design of these systems, accurate estimation of the multipath component characteristics of the environment is essential, in particular their three-dimensional angle-of-arrival. Super-resolution techniques enable extracting these components with high fidelity, even in the presence of diffuse scattering. Applying these techniques, however, requires precision calibration of our 28, 60, and 83 GHz channel sounders. This paper outlines calibration procedures implemented to deliver such precision. Specifically, we account for impulse-response distortion stemming from internal system reflections and linear distortion by RF components. We also characterize the phase centers and complex antenna patterns of the receiver array elements, and gauge the drift of our synchronization clocks.**

***Keywords—Cellular communication; channel sounder; millimeter-wave communication; propagation channel; radio channel; wireless system***



## I. INTRODUCTION

Millimeter-wave communication systems will employ directional antennas with beamwidths on the order of degrees, rather than tens of degrees [1]. Because of their high gain, typically 25-40 dBi, these *pencilbeams* can compensate in part for the greater pathloss expected in the associated frequency bands of operation. To provide for ubiquitous coverage, electronic steering and/or spatial multiplexing will be required at the mobile station. For effective design of these technologies, accurate estimation of the multipath component characteristics of the environment is essential, in particular their three-dimensional (azimuth and elevation) angle-of-arrival (AoA). Super-resolution techniques provide for extracting these components with high fidelity, even in the presence of diffuse scattering. Applying these techniques, however, requires precise calibration, especially when operating in the frequency regime of the 28, 60, and 83 GHz systems.

The scope of this paper is to outline calibration procedures implemented to deliver such precision. In the next section, we provide an overview of the channel sounder architecture common to all three systems. Section III is the main section, in it, we explain how to compensate for impulse-response distortion due to internal system reflections and linear distortion caused by the RF components. In order to extract AoA accurately, the positions and phase centers of the receiver array elements must be measured to within fractions of a wavelength. This is difficult when the wavelength at 83 GHz is only 3.6 mm. Thus, we describe a procedure using a NIST laser-tracking system. Finally, we outline our antenna calibration and characterize the clock drift. In Section IV, we describe how the SAGE algorithm, used to extract the multipath components, incorporates the calibration measurements and present some results.

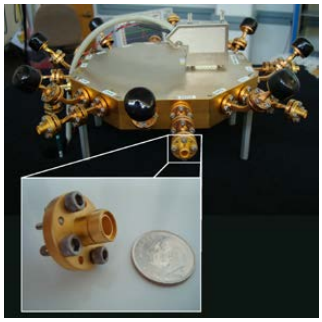

Figure 1. 83 GHz antenna array with inset of scalar feed horn. Eight straight elements (no covers) and eight slanted elements.

## II. CHANNEL SOUNDER ARCHITECTURE

The three NIST mm-wave channel sounders share common hardware sections such as the arbitrary waveform generator, digitizer, timing circuitry, and automated mobile positioning robot. They also use multiplexed scalar feed horn antenna to create antenna arrays. They differ chiefly in the transmitter, where the 83 and 28 GHz channel sounders, effectively have a Single-Input Multiple-Output (SIMO) architecture while the 60 GHz sounder also has Multiple Input (MIMO) and a higher chip rate.

### *A. Transmitter*

The 83 and 28 GHz systems transmit a periodic 2047-bit pseudorandom noise (PN) code occupying a 2 GHz null-to-null bandwidth. The chip rate is 1 GB/s, translating to a code period of 2.047 $\mu$s. The code period determines the maximum range of 600 m and the number of chips per code determines the correlation gain of 66 dB. A 12-bit, 12 GS/s arbitrary

Papazian, Peter; Choi, Jae-Kark; Senic, Jelena; Jeavons, Peter; Gentile, Camillo; Golmie, Nada; Sun, Roy; Novotny, David; Remley, Catherine. "Calibration of Millimeter-wave Channel Sounders for Super-resolution Multipath Component Extraction." Paper presented at 10th European Conference on Antennas and Propagation (EuCAP 2016), Davos, Switzerland. April 10, 2016 - April 15, 2016.

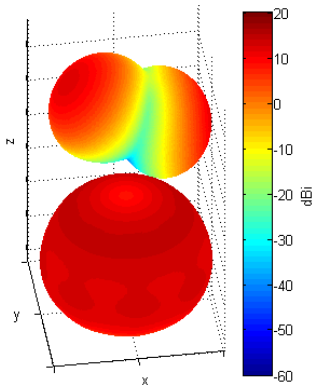


Figure 2. Synthesized antenna patterns for two receiver array elements (top, shifted upwards to avoid overlap) and all 16 elements together (bottom).

waveform generator (AWG) produces a BPSK-modulated IF signal. The AWG allows modification of the transmit waveform: its bit rate and bandwidth can be changed, and pre-distortion filters applied. The IF signal is then upconverted to the appropriate center frequency and the high-side signal is band-pass filtered to remove local-oscillator leakage from the single balanced millimeter-wave mixer. This signal is then amplified and a directional coupler monitors the transmit power at the antenna terminals. An omnidirectional or widebeam transmit antenna is used so all angles-of-arrival can be estimated by the receive antenna array in one fast recording. The 60 GHz system has similar IF components but instead employs an eight-element array at the transmitter so that the angle-of-departure can also be estimated. Other noteworthy differences are the 2 GB/s chip rate and 4 GHz RF bandwidth. For more details concerning the antenna and RF systems, see [2].

### *B. Receiver Antenna Array*

The key features of the receiver are the antenna array, the fast electronically switched multiplexer (MUX), synchronized timing circuitry, and 40 GS/s IF digitization. Figure 1 shows the 83 GHz array and the MUX. The inset shows one of the 16 scalar feed horn (SFH) antennas. The array is octagonal in shape with one face every 45°. This allows two antennas to be placed side-by-side per face: one pointing straight and the other slanted upwards at 45°. The feed horns have symmetrical Gaussian beam shapes with 45° beamwidth covering most of the upper hemisphere. Synthesized beam patterns are shown in Figure 2: the top for two elements (one straight and one slanted) on opposite sides of the array, each with a boresight gain of 12.2 dB, the bottom is for all 16 elements together. The latter reveals an omnidirectional pattern in azimuth while in elevation the boresight gain is 14.1 dB at 47° and the beamwidth is 87°. The received IF signal is digitized directly and correlation of the transmitted PN pulse is performed in post-processing [3]. While requiring a faster digitizer, this method is three-to-four orders of magnitude faster than analog


Figure 3. Room floor plan made by navigation system with 1 m grid lines. The red circle indicates the robot position.

sliding-correlation processing because it reduces the measurement period to that of the transmitted code alone. The speed of the antenna MUX allows mobile measurement of angle-of-arrival within the coherence time of the channel.

### *C. Robotic Positioning System*

The TX-RX system can collect channel impulse response data in a mobile, untethered mode. Indoors, a mobile robot is used to navigate and provide position information. Before a measurement campaign begins, the robot maps an environment such as a room, a series of hallways, or even the entire floor of a building. One such mapping is displayed in Figure 3. Here, the robot is designated with a red oval, the walls and solid surfaces as black lines, and the colored lines indicate what the navigation system can see from its current position. Once the mapping is complete and the measurement campaign begins, the robot is fed a set of two-dimensional waypoints. As it proceeds between waypoints, it collects data at uniformly spaced time intervals while reporting its state, position, heading, and velocity at each. The data collected at each site corresponds to 32 MUX rotations (one rotation encompasses IF digitization of the 16 receive antennas) over a distance of about 10 wavelengths. The routes can be repeated within an accuracy of several centimeters to provide statistics on data repeatability. This accuracy was determined with surveying equipment. The robot can also sense obstacles such as people and avoid them by changing its route or waiting for moving obstacles to pass. Outdoors, GPS localization can be utilized instead.

### *D. Timing and Syncronization*

Timing and synchronization are maintained with two rubidium clocks, one at the transmitter and the other at the receiver. At the transmitter, the clock's 10 MHz reference is applied to the AWG and the RF section of the upconverter. Before indoor measurements commence each day, the clocks are synchronized through a direct connection of the PPS output of the receiver clock connected to the PPS input of the transmitter clock. Outdoors the PPS synchronization of the clocks can be maintained via GPS if a signal is present. After the clocks are synchronized, a start trigger is sent to the

Papazian, Peter; Choi, Jae-Kark; Senic, Jelena; Jeavons, Peter; Gentile, Camillo; Golmie, Nada; Sun, Roy; Novotny, David; Remley, Catherine. "Calibration of Millimeter-wave Channel Sounders for Super-resolution Multipath Component Extraction." Paper presented at 10th European Conference on Antennas and Propagation (EuCAP 2016), Davos, Switzerland. April 10, 2016 - April 15, 2016.

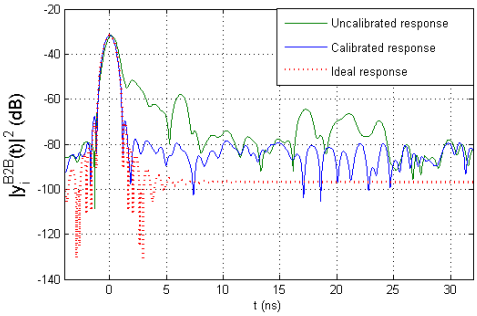


Figure 4. Impulse-response calibration.

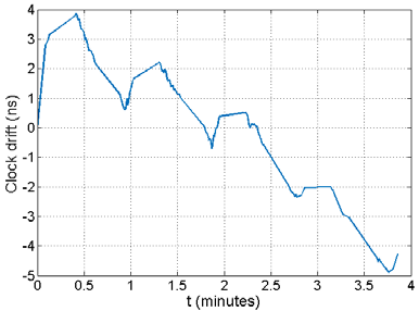


Figure 5. Clock drift when the robot is moving as measured with time-lag properties from the PN correlation function.

receiver from the AWG. This start trigger will synchronize the digitizer trigger and the 4-bit output signal used to switch the MUX between array elements. In this way, the digitizer trigger and antenna switching are synchronized with the transmission of PN codewords. Once the timing circuit is triggered at the receiver, the start trigger cable is disconnected and the receiver can become mobile.

The receiver is able to measure the absolute time-of-arrival plus the clock drift. The receiver timing circuit runs at the bit rate of the transmitter and has an initial divider ratio to create triggers with a granularity of two code periods. This rate is used to switch the antenna elements while a second divider provides triggers to the digitizer at integer multiples of 32 codewords, the equivalent of a single MUX rotation through all 16 antenna elements. By dwelling at each antenna position for two codewords, a complete word is digitized between the finite rise and fall times of the MUX switching. Hence, a total channel measurement (or single rotation) takes 32 × 2.047 $\mu$s = 65.5 $\mu$s. This is the minimum time between successive impulse recordings and so dictates the maximum Doppler frequency measurable by the system, 7.6 kHz, limiting Doppler measurement to speeds of 60 mph.

## III. Channel Sounder Calibration

The ensuing subsections treat the power and frequency calibrations of the channel impulse responses, how clock drift is gauged, and the characterization of the phase centers and complex antenna patterns of the receiver array elements.

### *A. Channel Impulse Response*

Through the post-processing described in Section II.B, the IF-digitized data at the receiver are converted into the *uncalibrated* impulse response of the array elements, $\hat{y}_i(t), i = 1 \dots 16$. Each response, in block sequence, is composed from: the transmitted pulse (which is the autocorrelation of the null-to-null PN sequence) $p(t)$, the system response and the antenna pattern of the transmitter $h^{TX}(t)$ and $g^{TX}$ respectively, the channel response between the transmitter and the element $h_i(t)$, the antenna pattern and the system response of the element, $g_i^{RX}$ and $h_i^{RX}(t)$, respectively, plus noise:

$$\hat{y}_i(t) = p(t) * h^{TX}(t) * g^{TX} * h_i(t) * g_i^{RX} * h_i^{RX}(t) + n(t). \quad (1)$$

The purpose of the impulse-response calibration is to de-embed the linear $h^{TX}(t)$ and $h_i^{RX}(t)$ from (1). To this end, a back-to-back method [3] was used. In this configuration, the antenna port of each transmitter and each receiver element are sequentially connected through a waveguide and a set of variable vane attenuators such that $g^{TX} = g_i^{RX} = 1$ and $h_i(t) = \delta(t)$. A directional coupler monitors the transmitter power at the antenna port by use of a wideband power sensor. The AWG is then configured to transmit the modulated IF signal while operating at full power. The variable attenuators are set to maximum attenuation so that the received signal lies in the noise. The attenuation is then decreased in steps to the point of receiver compression. This enables us to determine the linear range of system operation and to bias the system around the midpoint. At the bias point, a set of $N$ impulse responses are collected and the input power level $P_i$ recorded; the input power at the receiver antenna terminal is known from the power meter reading, the attenuator setting, and waveguide loss. In this way, a back-to-back calibration signal is calculated for all elements:

$$\begin{aligned}\hat{y}_i^{B2B}(t) &= \frac{1}{N}\sum_{j=1}^{N} \hat{y}_{ij}(t; g^{TX} = g_i^{RX} = 1, h_i(t) = \delta(t)) \\ &\approx p(t) * h^{TX}(t) * h_i^{RX}(t).\end{aligned} \quad (2)$$

Averaging is carried out to virtually eliminate noise such that the approximation above holds; we found that $N$ = 256 samples was sufficient.

The *calibrated* response is then obtained by deconvolving $\hat{y}_i^{B2B}(t)$ from $\hat{y}_i(t)$:

$$\begin{aligned}y_i(t) &= \sqrt{\frac{P_i}{\frac{1}{T}\int_{t=0}^{T}|p(t)|^2 dt}} \cdot p(t) * \mathcal{F}^{-1}\left[\frac{\mathcal{F}[\hat{y}_i(t)]}{\mathcal{F}[\hat{y}_i^{B2B}(t)]}\right] \\ &= p(t) * g^{TX} * h_i(t) * g_i^{RX} + n(t),\end{aligned} \quad (3)$$

Papazian, Peter; Choi, Jae-Kark; Senic, Jelena; Jeavons, Peter; Gentile, Camillo; Golmie, Nada; Sun, Roy; Novotny, David; Remley, Catherine. "Calibration of Millimeter-wave Channel Sounders for Super-resolution Multipath Component Extraction." Paper presented at 10th European Conference on Antennas and Propagation (EuCAP 2016), Davos, Switzerland. April 10, 2016 - April 15, 2016.

with $\mathcal{F}$ symbolizing the Fourier transform. Because the deconvolution effectively removes the pulse shape from the signal, $p(t)$ must again be included, as given in (3). As well, the square-root scaling factor is required such that the power of $y_i(t)$ corresponds to the power recorded when in calibration mode.

Referring to Figure 4, the ideal response of each element is the 2 GHz bandlimited pulse $p(t)$. The uncalibrated back-to-back response, however, contains the linear system effects, including pulse distortion and extraneous internal reflections. By applying the calibration in (3), the desired pulse is corrected and the linear distortion removed. Other experiments at NIST have revealed only small residual amounts of nonlinear distortion and noise remain. The calibration also accounts for the relative delay between the receive array elements. The worst case observed was 180 ps. On average, the slanted elements have 77 ps greater delay than the straight elements because they have longer waveguide connections. These relative channel delays were verified by means of VNA group delay measurements of the MUX subsystem.

*B. Clock Drift*

The stability of a frequency source in the time domain is based on the statistics of its phase or frequency fluctuations over time. When using free-running clocks, we can predict the timing error of the clocks from the initial offset of the clocks, $T_o$ (zero in our case because the clocks are initially synchronized with the PPS signal), the fractional frequency offset $\Delta f/f$, the aging rate (or frequency drift) $D$, and the noise deviation $\sigma_x(t)$ over the calculation period. This relationship is expressed as [4]

$$\Delta T = T_o + (\Delta f/f) \cdot t + \tfrac{1}{2} D \cdot t^2 + \sigma_x(t). \quad (4)$$

In practice, the most significant source of timing error for our short measurment times is the fractional frequency offset, and so, to a first-order approximation, we use

$$\Delta T = (\Delta f/f) \cdot t. \quad (5)$$

From our clock specifications, often referred to as Stratum-1 or time stability holdover $\Delta f/f = 10^{-11}$. This means that at $t$ = 60 s, $\Delta T$ = 600 ps. Since we are using two clocks, they can be drifting in opposite directions, translating to a maximum drift of 1.2 ns/min. This calculation, however, does not take into account environmental fluctuations. In addition, the specifications supplied by the manufacturer are not measured over the time scale relevant to our application (on the order of minutes, not hours) and so just serve as a guideline.

Using the time-lag properties of the correlation and the position information provided by the robot, we can gauge our time drift when the robot is stationary or mobile. Through this analysis, we can see the actual time drift of our clocks and some of the environmental effects which can decrease clock stability (Figure 5). These data were collected during a measurement campaign over 4.1 minutes. Observe the slope change and level areas with small slopes where the robot reaches a waypoint and subsequently pauses to download data. The total time drift was 9 ns or 2.20 ns/min.

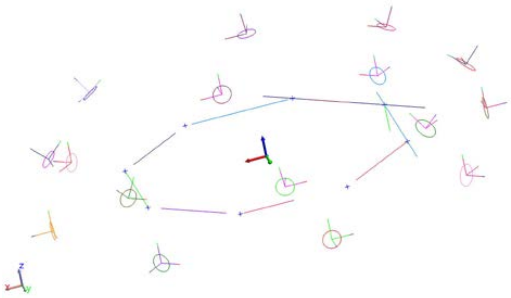

Figure 6. 28 GHz antenna aperture diagram. Data provide ($r_i$, $\theta_i, \phi_i$) for each element antenna aperture relative to the center of array body.

Clock drift can affect the relative time-of-arrival estimates between antenna elements used to calculate angle-of-arrival. Specifically, it takes 65.5 $\mu$s for a single channel measurement. Over that segment, the clock drift is only 0.0024 ps. If we use 2.20 ns/min , this equates to a phase error of 0.075 degrees at 83 GHz in 65.5 µs. Hence, as described in the next section, this timing error is more than an order of magnitude less than the phase errors in our system calibration.

To gauge the actual properties of our clocks, we measured the frequency (or phase) drift of the clock versus a more stable reference available at NIST. The preliminary analysis results are complex and vary in time. A more complete analysis of the clocks will be undertaken in the future.

*C. Receiver Array Phase Centers and Antenna Patterns*

Critical to the accurate estimation of AOA are the phase center locations of the array antennas. In order to precisely measure the constellation of the array elements with respect to its reference center, NIST has developed a near-field scanner which uses a laser interferometer capable of measuring the position of antenna apertures with an accuracy of 50 nm [6]. This translates to a phase accuracy of about 5 degrees at 83 GHz.

Figure 6 shows the array geometry as measured in the NIST antenna lab. With element $i$ located at ($r_i$, $\theta_i, \phi_i$), a multipath component approaching from angle $(\theta, \phi)$ will hit the element with a relative delay of

$$\Delta\tau_i(\theta, \phi) = \frac{r_i}{c} \boldsymbol{x}(\theta_i, \phi_i) \cdot \boldsymbol{x}^T(\theta, \phi), \quad (6)$$

with respect to the array center, where $\boldsymbol{x}(\theta, \phi) = [\cos\theta \cos\phi, \sin\theta \cos\phi, \sin\phi]$ and $c$ is the speed of light.

Equally important to accurate AoA estimation is the angular response of the feed horn array. These horns have Gaussian beam patterns with equiphase planes at radial offsets from the antenna's phase center. Once the positions of the antenna

Papazian, Peter; Choi, Jae-Kark; Senic, Jelena; Jeavons, Peter; Gentile, Camillo; Golmie, Nada; Sun, Roy; Novotny, David; Remley, Catherine.
"Calibration of Millimeter-wave Channel Sounders for Super-resolution Multipath Component Extraction."
Paper presented at 10th European Conference on Antennas and Propagation (EuCAP 2016), Davos, Switzerland. April 10, 2016 - April 15, 2016.

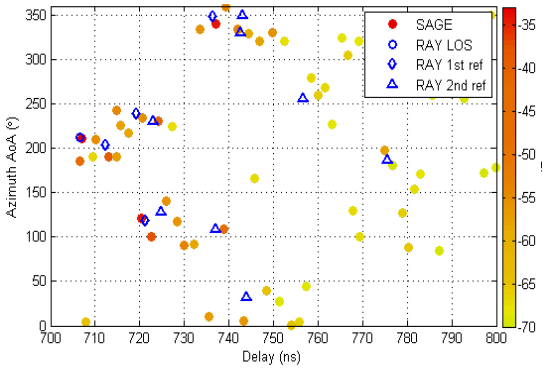


Figure 7. Multipath components extracted through the SAGE algorithm appear as color-coded solid circles vs. the dominant components predicted through raytracing shown in blue.

apertures, relative to the array center, are known, a near-field scan will be made for each of the 16 antenna elements. This scan will be made at three frequencies covering the 2 GHz bandwidth of the channel sounder at 1 degree angular spacing. We can transformed the near-field data into the far field using methods developed by NIST and others [7,8] . These data will then provide the antenna phase centers relative to the antenna apertures and array center. They will also provide the measured amplitude and phase response of the antenna pattern. Because the transmit antenna has an omnidirectional pattern, its complex gain can be combined with the complex directional gain of the receive antenna as

$$g_i(\theta,\phi) = g^{TX} g_i^{RX}(\theta,\phi). \qquad (7)$$

## IV. Multipath Component Extraction

The channel impulse response for array element $i$ can be expressed as the superposition of $L$ multipath arrivals:

$$h_i(t;\boldsymbol{\zeta}) = \sum_{l=1}^{L} \alpha_l \cdot \delta(t - \tau_l - \Delta\tau_i(\theta_l,\phi_l)). \qquad (8)$$

In this notation, the channel is explicitly conditioned on the set $\boldsymbol{\zeta} = \{\zeta_1, \zeta_2, \ldots, \zeta_L\}$. The set contains the parameters $\zeta_l = \{\alpha_l, \tau_l, \theta_l, \phi_l\}$ characterizing arrival $l$ where $\alpha_l$ is the complex amplitude, $\tau_l$ the delay, and $(\theta_l, \phi_l)$ the azimuth and elevation angles-of-arrival. By substituting (8) into (3), (3) can be rewritten compactly as

$$y_i(t) = \sum_{l=1}^{L} s_i(t;\zeta_l) + n(t), \qquad (9)$$

where $s_i(\tau;\zeta_l) = \alpha_l \cdot p(t - \tau_l) * c_i(\theta_l,\phi_l)$ is the $l^{th}$ multipath pulse impinging on the $i^{th}$receive element and

$$c_i(\theta,\phi) = g_i(\theta,\phi) \cdot \delta\big(t - \Delta\tau_i(\theta,\phi)\big), \qquad (10)$$

is the array "beamformer" given from (6) and (7).

We have implemented SAGE, an Expectation-Maximization (EM)-based algorithm, for the super-resolution[1] extraction of the multipath component parameters. In line with the notation in [5], $y_i(t)$ in (9) represents the *observable* data. The objective of the algorithm is essentially to reconstruct $y_i(t)$ as a composition of multipath pulses $s_i(t;\zeta_l')$. It proceeds by iterating on the parameter set $\boldsymbol{\zeta}'$ through maximum- likelihood estimation such that the residual, the noise $n(t;\boldsymbol{\zeta}')$, obeys a Gaussian distribution.

Figure 7 displays the processed results for a single channel measured in a lab environment. Each solid circle represents a multipath component extracted with SAGE, shown only in azimuth vs. delay; the power is indexed according to the colorbar. Superimposed in blue are the LOS, 1st, and 2nd reflections predicted through simplistic raytracing modeling of the room as a paralellepiped. Considering the imprecisions of the model, good agreement is seen.The unmatched arrivals correspond to diffuse scattering clustered around the reflected paths as well as higher-order (> 2) reflections.

## V. Conclusions

Multiple channels sounders are being tested and deployed at NIST to support 5G channel model development. The probes span a frequency range from 28 to 83 GHz with bandwidths ranging between 2 GHz and 4 GHz. They are undergoing an extensive set of calibrations for the RF sections, timing sections, and antennas.

## References


[1] T.S. Rappaport, S. Shu, R. Mayzus, H. Zhao, Y. Azar, K. Wang, G.N. Wong, J.K. Schulz, M. Samimi, and F. Gutierrez, "Millimeter wave mobile communications for 5G cellular: It will work!" *IEEE Access*, vol. 1, May 2013, pp. 335-349.

[2] Papazian, P., Remley, K.A., Gentile, C., Golmie, N., "Radio Channel Sounders for Mobile Millimeter-Wave Communications: Angular Delay Spread and Doppler," *Submitted for review*

[3] J.A. Wepman, J.R. Hoffman, L.H. Loew, and V.S. Lawrence, "Comparison of wideband propagation in the 902-928 and 1850-1990 MHz bands in various microcellular environments," *NTIA Report 93-299,* Sep. 1993.

[4] Riley, W.J., "Handbook of Frequency Stability Analysis," *NIST Special Publication 1065*, pp. 19, July 2008.

[5] Hausmair, K., Witrisal, K., Meissner, P, Steiner, C., Kail, G., "SAGE Algorithm for UWB Channel Parameter Estimation," *Proceedings of COST 2100 Management Committee Meeting*, Athens, Feb. 2010.

[6] Josh Gordon, David Novotny, "High-Tech Measurments for High Frequency Antennas", http://www.nist.gov/ctl/rf-technology/rf_fields/robot-arm-aids-antenna-calibration.cfm

[7] *IEEE Special Issue on Near-Field Scanning Tehniques, vol36, Issue 6, June 1988.*

[8] Near-Field Scanning Measurments: Theory and Practice, Michael Francis and Ronald Wittmann, pp. 929-976, 2008 Wiley and Sons


[1] Super-resolution because it yields a delay resolution above the 1 GHz bandwidth equivalent of 1 ns.


Papazian, Peter; Choi, Jae-Kark; Senic, Jelena; Jeavons, Peter; Gentile, Camillo; Golmie, Nada; Sun, Roy; Novotny, David; Remley, Catherine. "Calibration of Millimeter-wave Channel Sounders for Super-resolution Multipath Component Extraction." Paper presented at 10th European Conference on Antennas and Propagation (EuCAP 2016), Davos, Switzerland. April 10, 2016 - April 15, 2016.

# Comparison of Timebase Interpolation Methods for Traceable, Wideband mm-Wave Communication Signals

Robert D. Horansky[a], Diogo C. Ribeiro[a,b], Kate A. Remley[a], Paul D. Hale[a], Chih-Ming Wang[a], Dylan F. Williams[a], and Nuno B. Carvalho[b]

[a]NIST Communications Technology Laboratory, Boulder, CO 80305, [b]Universidade de Aveiro – DETI, Instituto de Telecomunicações, Aveiro, Portugal

***Abstract* — An integral part of processing a signal from a calibrated, equivalent-time sampling oscilloscope is accurately determining sampling times and then interpolating the resulting irregularly-spaced time grid to create a uniform time spacing. In this paper, we present simulations and measurements to determine the effect of the interpolation choice on the fidelity of a modulated signal. We judge the effect by calculating the error-vector-magnitude of the resultant signal from each interpolation.**

***Index Terms* — Digitally modulated signal, error vector magnitude, interpolation, microwave measurement, millimeter-wave wireless communication, oscilloscope, wireless system.**

## I. Introduction

Calibration of a high-speed oscilloscope, traceable to primary standards, provides a traceability path for receivers and transmitters across the spectrum. The key to the traceability path is the correction of an equivalent-time sampling oscilloscope by a photodiode that has been characterized by an electro-optic sampling system (EOS) traceable to the primary volt, meter, ohm and second standards. A recorded signal is first processed to remove drift, systematic timebase distortion (TBD), and timing jitter [1]. The resulting trace no longer has a regular grid of time points. Therefore, in order to convert back to regular timebase-points for voltage correction and conversion to frequency space for mismatch correction, the corrected signal must be regularized in time by use of an appropriate interpolation method. In this paper, we examine optimization of this interpolation step with both simulated and measured precision, wideband, millimeter-wave (mm-Wave) signals using the error-vector-magnitude (EVM) as the figure-of-merit.

There are two reasons we chose to use mm-Wave signals for this study. First, there is intense interest in expanding the available wireless spectrum to these high frequencies [2]. Second, we have developed at NIST a method using predistortion for generating a precise, calibrated communication signal at these frequencies that allows a rigorous estimate of uncertainties [3].

The EVM is a useful metric for characterizing the quality of the modulated signal produced since it provides information on both the amplitude and phase of a signal [4]. Prior work [5]-[8], including our own [3] has allowed accurate uncertainty estimates for this metric. Thus, the EVM provides an ideal measurement with which to compare the choice of an interpolation method in reconstructing a modulated signal.

In the remainder of this paper, we will first describe the signal generation process using predistortion to motivate the role of the interpolation. We then compare the effect of three different interpolation methods on the final signal EVM in both simulation and measurement.

## II. Predistortion

While the method for creating a broadband, modulated signal with minimized EVM has been discussed previously [3], a brief summary will be presented here. This method will work for a modulated signal in any protocol. The signal we use in the present study for both measurement and simulation is a pseudo-random bit-sequence encoded with a 64-quadrature-amplitude-modulation (64-QAM) scheme. The signal is generated to produce 1 GSymbol/s and is 320 ns long (320 symbols in length). The signal is modulated at an intermediate frequency (IF) of 4 GHz and a root-raised-cosine filter is applied. We then create a periodic multisine [9], based on the Fourier components of this signal, to upload to an arbitrary waveform generator (AWG). The output of the AWG is fed to a frequency converter. We use a 10 GHz signal, multiplied by 4, to create a 40 GHz local oscillator to upconvert our IF to 44 GHz. This same 10 GHz signal is also used as the internal clock for the AWG. The AWG also creates a trigger for the equivalent-time sampling oscilloscope to measure the 44 GHz signal. Repeat measurements of the signal are carried out to improve the signal-to-noise and reduce measurement uncertainty.

At this point, the set of modulated signals measured are corrected for drift, timebase errors, and jitter, yielding signals with irregular time grids. Before the voltage can be corrected by the EOS calibrated photodiode, the timebase must be interpolated back to a regular grid. In the study presented here, we look at three interpolation methods typically used in our group. The first we call the least-squares method with midpoint knots. All acquired data sets are combined with simultaneous triggers. Then, the time points that lie between the midpoints of the desired time grid are collected and approximated by a linear least-squares fit. The desired time grid point is then calculated from this line. Each linear fit between the midpoints



Ribeiro, Diogo; Remley, Catherine; Hale, Paul; Wang, Chih-Ming; Williams, Dylan.
"Comparison of Timebase Interpolation Methods for Traceable, Wideband mm-Wave Communication Signals."
Paper presented at 87th ARFTG Microwave Measurement Conference, 2016, San Francisco, CA, United States. May 27, 2016 - May 27, 2016.

(the knots) is independent from the next. The second method linearly interpolates the regular time grid from the nearest-neighbor measured time points. The linear interpolation is performed on each measured signal, then all of the evenly-time-spaced-signals are averaged. Finally, we use a shape-preserving interpolation based on piecewise cubic Hermite polynomials, termed PCHIP. Similar to the linear interpolation, the PCHIP interpolation is performed on each measured waveform before they are all averaged.

Once the measured signals are on an even time grid, averaged if necessary, and calibrated in voltage, the next step is to create a modulated signal that corrects for hardware non-idealities through predistortion. The resultant measured waveform is used to predistort the ideal desired signal. The predistorted signal is calculated element-wise according to

$$X_{predist} = X_{ideal}\left(\frac{X_{ideal}}{X_{meas}}\right), \qquad (1)$$

where $X_{predist}$ is the newly calculated predistorted signal, $X_{ideal}$ is the ideal signal, and $X_{meas}$ is the calibrated result of the interpolation step. The predistorted waveform is uploaded to the AWG, which now transmits a waveform closer to the ideal signal. A single predistortion step will account for linear distortions in the generation and upconversion, but this process can be repeated as many times as necessary to account for non-linear distortions. Once an adequate signal is produced, one additional interpolation step is necessary to process the final signal.

## III. Simulation

We examined the effect of interpolation choice using a simulated noisy signal. We used the random binary sequence that we then modulated with a 64-QAM protocol, as described above. The waveform was oversampled to be used with an AWG with an output of 20 GSamples/s. This waveform serves as an "ideal" reference for the calculation of EVM at the end of the simulation. The IF signal is filtered by a root-raised-cosine function, then digitally upconverted to 44 GHz.

At this point, sampling of the signal by the oscilloscope was emulated using time intervals randomly shifted from a nominal oscilloscope time step. We simulated oscilloscope time steps of 0.5 to 5 ps, replicating values used in our mmWave signal measurements. Representative results are shown in Fig. 1 for a simulation with a 2.5 ps oscilloscope time step. To model the results of the time base correction, the time points were shifted with a normally-distributed set of random offset values where the distribution width ranged from 0.5 to 2.5 ps. These values are shown as the $\hat{y}$-axis in Fig. 1. The resulting waveform provides the correct voltage at the estimated, but irregular sampling points. However, we know from measurements that the time base correction has a residual uncorrected jitter of 200 fs [1]. This uncorrected jitter is then added to the irregular time base by a normally distributed random value, with no change to the voltage value. Finally, we add voltage noise to the waveform with a normally distributed random number, where the distribution widths are between 0 and 1.25 mV, shown as the $\hat{x}$-axis in Fig. 1.

We simulated 25 noisy signals which were then interpolated with one of the three methods described. The root-raised-cosine filter was applied, the signal was demodulated, and the root-mean-square (RMS) EVM was calculated by comparing the resultant symbols with those originally encoded [10].

The EVM for each interpolation method, as a function of timebase offsets and voltage noise, is shown in Fig. 1. Since a nominal oscilloscope time increment of 2.5 ps is most routinely used in our lab, that is the one chosen. Table 1 shows the computation time to produce the values in each subplot of Fig. 1. We see that the least-squares method is the most computationally expensive. The other two methods are much faster and similar to each other.

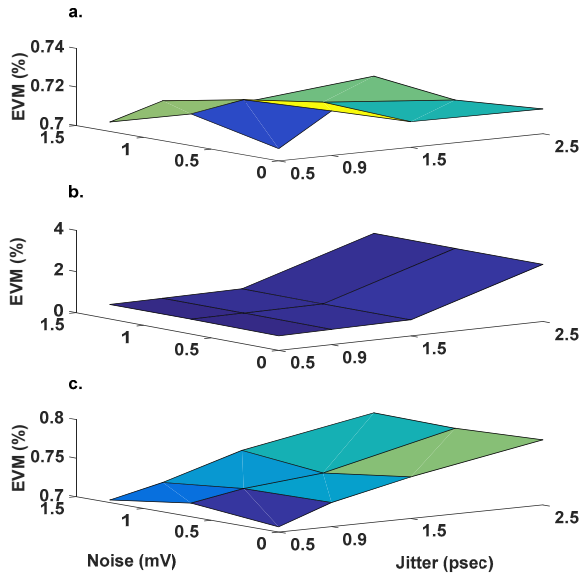


Fig. 1. (a) Surface plot showing the calculated EVM for an oscilloscope time base of 2.5 ps as a function of voltage noise and time base offsets for the least-squares interpolation. (b) Same plot for the linear, nearest-neighbor method. (c) For the PCHIP method.

**Computation time at 2.5 ps time base**

| | Least-Squares | PCHIP | Linear |
|---|---|---|---|
| CPU Time (s) | 30.12 | 0.17 | 0.13 |

Table 1. Computation time for each interpolation on the 2.5 ps timebase data.

Although not plotted here, our simulations showed that for 0.5 ps oscilloscope time steps, the choice of interpolation method is immaterial since the fine grid produces equivalent EVM results for all values of offset and noise. As the time step increases, as seen in the 2.5 ps results of Fig. 1, both the PCHIP and the linear interpolation methods become sensitive to the increased time-step offsets introduced by the time-base correction. The least-squares method can handle the larger timing jitter and still provide a low EVM result. All interpolation methods are weakly sensitive to voltage noise. We conclude from this simulation study that, for smaller time

Ribeiro, Diogo; Remley, Catherine; Hale, Paul; Wang, Chih-Ming; Williams, Dylan.
"Comparison of Timebase Interpolation Methods for Traceable, Wideband mm-Wave Communication Signals."
Paper presented at 87th ARFTG Microwave Measurement Conference, 2016, San Francisco, CA, United States. May 27, 2016 - May 27, 2016.

steps, we can use a computationally-cheaper interpolation method, such as PCHIP or linear interpolation. Yet, for longer time steps, or with an oscilloscope that requires large timing corrections, we can better use the more expensive least-squares method.

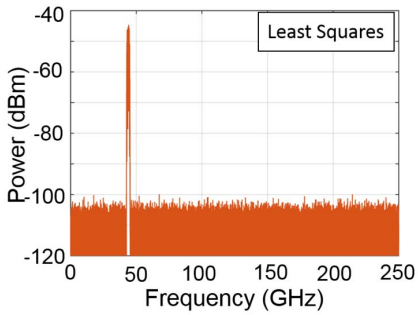


Fig. 2. Simulation of a 44 GHz, 64-QAM signal after combining 25 oscilloscope time records and fitting points between midpoint knots with a linear least-squares fit. The signal before interpolation was simulated with a 2 ps time increment, 1.5 ps noise added to the time points and 1.25 mV noise added to the voltage samples.

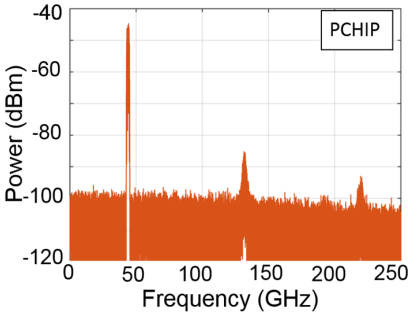


Fig. 3. Simulation of a 44 GHz, 64-QAM signal after averaging 25 time records that were individually interpolated onto a 2 ps time grid with a cubic interpolation. The signal before interpolation was simulated with a 2 ps timebase, 1.5 ps noise added to the time points and 1.25 mV noise added to the voltage samples.

A salient feature of each interpolation method is the effect on the frequency spectrum noise floor. The resultant 44 GHz signal, after the least-squares linear fit with midpoint knots, is shown in Fig. 2. The noise floor is shown to be spectrally flat. The 44 GHz simulated signal with PCHIP interpolation is shown in Fig 3, where there is now a higher noise floor near 44 GHz and a downward ramp toward higher frequencies. Also, the cubic interpolation imparts harmonic distortion to the signal. The same ramp without the distortion products was seen with the linear interpolation.

## IV. MEASUREMENT

We also examined the effect of the interpolation choice on measurement. A difference in the effect of interpolation on measurement versus simulation is that the measurements require a minimum of two interpolation steps, rather than one, assuming only linear corrections. In the simulations, an ideal signal with voltage and timing imperfections induced by the oscilloscope was created in software. Experimentally, in order to obtain this ideal signal from an AWG, we must first predistort the ideal signal. Therefore, we must measure the distorted signal from the AWG, correct the measurement, then interpolate it to obtain the predistortion. This predistorted signal is then measured, corrected and interpolated to see the effect on EVM. The 40 GSample/s interleaved AWG we used at 20 GSamples/s single channel was linear in its distortion and did not require correction for the interleave imbalance. Therefore, we achieved low EVM values with only one predistortion step.

| 0.5 ps time step | 2nd Interpolation for Calculation | | |
|---|---|---|---|
| 1st Interp for Predistortion | Least Squares 2nd EVM(%) | PCHIP 2nd EVM(%) | Linear 2nd EVM(%) |
| Least Squares w/ sm | **0.602** | 0.603 | 0.603 |
| PCHIP w/ sm | 0.600 | **0.605** | 0.602 |
| Linear w/sm | 0.615 | 0.615 | **0.616** |
| 2.5 ps time step | | | |
| 1st Interp for Predistortion | Least Squares 2nd EVM(%) | PCHIP 2nd EVM(%) | Linear 2nd EVM(%) |
| Least Squares w/ sm | **0.598** | 0.689 | 0.772 |
| PCHIP w/ sm | 0.731 | **0.814** | 0.883 |
| Linear w/sm | 0.583 | 0.682 | **0.763** |
| 5 ps time step | | | |
| 1st Interp for Predistortion | Least Squares 2nd EVM(%) | PCHIP 2nd EVM(%) | Linear 2nd EVM(%) |
| Least Squares w/ sm | **3.04** | 3.580 | 3.872 |
| PCHIP w/ sm | 2.785 | **3.563** | 3.862 |
| Linear w/sm | 2.8 | 3.705 | **3.978** |

Table 2. Resultant EVMs for measurements of the same 64-QAM signal as was used for simulation. The signal was predistorted as described earlier for the interpolation method shown on the left, but with the addition of a smoothing function. The final interpolations for EVM calculation are shown across the top of each table. Results are shown for oscilloscope time steps of 0.5, 2.5, and 5 ps.

Using two interpolations, we could not separate the effects of each individual interpolation. Therefore, we predistorted the waveform using each interpolation method described and measured 25 traces of the final 44 GHz signal from each. All three sets of data were calibrated, and then the three interpolation methods were again used on each set to interpolate the measured waveform and determine the EVM. Therefore, 9 combinations of interpolations were possible. The EVM results for oscilloscope time bases of 0.5, 2.5, and 5 ps time steps are shown in Table 2. The interpolation used for the predistortion is listed on the left. For the predistortion, a smoothing function was also applied to the correction so as to alleviate large noise induced offsets. The second interpolation leading to the final EVM calculation is listed across the top of the table. For simplicity, and to observe the trends in the results, we can look at only the diagonals of Table 2, shown in bolder font. The diagonals show the measurements where the same interpolation method was used for both the predistortion

Ribeiro, Diogo; Remley, Catherine; Hale, Paul; Wang, Chih-Ming; Williams, Dylan.
"Comparison of Timebase Interpolation Methods for Traceable, Wideband mm-Wave Communication Signals."
Paper presented at 87th ARFTG Microwave Measurement Conference, 2016, San Francisco, CA, United States. May 27, 2016 - May 27, 2016.

determination and the final processing. The measured EVM values were higher than those simulated, but this is not surprising given nonlinear distortion introduced by the upconversion and other real-world effects, as compared to the simulated signal. The trends for each time step matched the simulation. The measurements had no dependence on the final interpolation used for 0.5 ps time steps due to the fine grid this provides. The relative dependence increased with increasing time steps. The least-square fit of combined data was the most robust method, followed by PCHIP and linear interpolations before averaging. This corroborated with what was observed in the simulations.

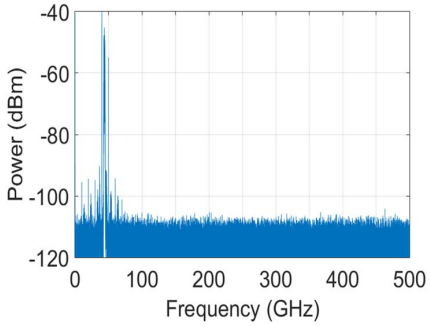


Fig. 5. 44 GHz measured signal after predistortion and interpolating with linear least squares of combined data.

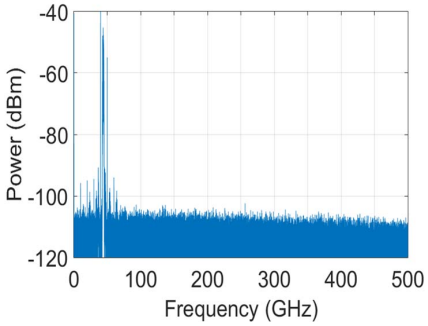


Fig. 6. 44 GHz measured signal after precorrection and interpolating with PCHIP method and averaging.

Trying to elucidate the trend in the measurements, we look at the effect of interpolation on the noise floor. In Fig. 4, the least-squares interpolation results in a flat noise power level. In Fig. 5, the noise floor treated with the PCHIP method is higher near the signal, but again has a downward ramp toward higher frequencies. The harmonic distortions seen in the simulation are not present.

## V. Conclusion

We have simulated and measured a 44 GHz, 2 GHz wide 64-QAM modulated signal to assess the effect of interpolation on our precision modulated-signal source. The simulations and measurements provided identical trends for the choice of interpolation.

At fine time grids for the recorded signal, the choice of interpolation is not critical so that the computationally-least expensive method can be chosen. For larger time steps, or more jitter, simulations show that the least squares linear fit of the combined data is the preferred method.

The simulations were corroborated by measurements. However, the time base corrections seen experimentally for our system, show that the interpolation choice has a relatively small effect on EVM for our typical 2.5 ps time step. Although the EVM values, as shown in Table 1, are small, the uncertainty analysis in [3] yielded an average EVM of approximately 1.5%. Thus, although we can minimize EVM of our precision source, the effect is not significant. Other quality metrics such as signal-to-noise-ratio, intermodulation distortion, or harmonic distortion may possibly be more sensitive to the choice of interpolation.

## Acknowledgement

D. Ribeiro was supported by the Fundação para a Ciência e a Tecnologia under grant SFRH/BD/92746/2013. The authors thank Tabb Warsinske and Bill Byrom of Tektronix for loan of the 40 GS/s AWG. The National Institute of Standards and Technology does not endorse commercial products. Other products may work as well or better.

## References

[1] J. A. Jargon, P. D. Hale, and C. M. Wang, "Correcting sampling oscilloscope timebase errors with a passively mode-locked laser phase-locked to a microwave oscillator," *IEEE Trans. Instrum. Meas.*, vol. 59, no. 4, 916-922, Apr. 2010.

[2] T.S. Rappaport *et al.*, "Millimeter wave mobile communications for 5G cellular: It will work!," *IEEE Access*, vol. 1, pp. 335-349, May 2013.

[3] K. A. Remley, D. F. Williams, P. D. Hale, C.M. Wang, J. Jargon, and Y. Park, "Millimeter-Wave Modulated-Signal and Error-Vector-Magnitude Measurement With Uncertainty," *IEEE Trans. Microwave Theory & Tech.*, vol. 63, no. 5, pp. 1710-1720, May 2015.

[4] *IEEE Standard for Minimum Performance Characteristics of IEEE 802.20*, IEEE Computer Society, Apr. 22, 2010.

[5] M. Hudlicka, "Laboratory system for a traceable measurement of error vector magnitude," in *Proc. 39th Eur. Microw. Conf.*, Rome, Italy, 2009, pp. 1-4.

[6] D. A. Humphreys and R. T. Dickerson, "Traceable measurement of error vector magnitude (EVM) in WCDMA signals," in *Proc. IEEE Int. Waveform Design Diversity Conf.*, Jun. 4-8, 2007, pp. 270-274.

[7] D. A. Humphreys and J. Miall, "Traceable measurement of source and receiver EVM using a real-time oscilloscope," *IEEE Trans. Instrum. Meas.*, vol. 62, no. 6, pp. 1413-1416, Jun. 2013.

[8] C. Cho, J.-G. Lee, J.-H. Kim, and D.-C. Kim, "Uncertainty analysis in EVM measurement using a Monte-Carlo simulation," in *Precision Electromagn, Meas. Conf.*, Aug. 24-29, 2014, pp. 700-701.

[9] N. Borges Carvalho, K. A. Remley, D. Schreurs, and K. G. Gard, "Multisine signals for wireless system test and design," *IEEE Microw. Mag.,* vol. 9, no. 3, pp. 122-138, Jun. 2008.

[10] M. D. McKinley, K. A. Remley, M. Myslinski, J. S. Kenney, D. Schreurs, and B. Nauwelaers, "EVM Calculation for Broadband Modulated Signals," *64th ARFTG Conf. Dig.*, Orlando, FL, pp. 45-52, Dec. 2004.

Ribeiro, Diogo; Remley, Catherine; Hale, Paul; Wang, Chih-Ming; Williams, Dylan.
"Comparison of Timebase Interpolation Methods for Traceable, Wideband mm-Wave Communication Signals."
Paper presented at 87th ARFTG Microwave Measurement Conference, 2016, San Francisco, CA, United States. May 27, 2016 - May 27, 2016.

# Acoustic and Electromagnetic Reverberation Chambers: Similarities and Differences

Perry F. Wilson
RF Technology Division
National Institute of Standards and Technology
Boulder, Colorado, USA

***Abstract*—Acoustic reverberation chambers predate electromagnetic (EM) reverberation chambers. EM reverberation chamber researchers occasionally make reference to acoustic equivalents when describing test methods and results. However, most EM reverberation chamber users are not familiar with acoustics and may not be aware of similarities and differences. This paper presents a sampling of results for acoustic and EM reverberation chambers, how they relate, and explore whether insights from acoustics can help inform EM reverberation chamber use.**

**Keywords—acoustics; reverberation chambers**

## I. INTRODUCTION

Acoustic reverberation chambers were in use well before electromagnetic reverberation chambers were first proposed in the late 1960s [1] and early electromagnetic reverberation chamber researchers make reference to acoustic and thermodynamic equivalents when describing their work [e.g., 2]. However, many current EM reverberation chamber users may not be familiar with reverberation acoustics, and thus not aware of similarities and differences. This paper presents a brief sampling of results for acoustic and electromagnetic reverberation chambers, how they relate, and explores whether results from acoustics can help inform reverberation chamber use.

## II. BACKGROUND

A basic understanding of sound as a propagating wave dates back to the Romans (200 BC), if not earlier, and empirical application to room acoustics goes back centuries in the design of concert halls, churches, and other large acoustic spaces. However, room acoustics as a science really began in 1895 with the work of Wallace Sabine, a young Harvard University physics professor [3]. At the time, Harvard had recently completed construction of the new Fogg Lecture Hall which was to be a centerpiece facility; however, the reverberation in the room was so long that a person speaking could not be well understood as word sounds lingered and mixed with the next spoken word, much like interference due to multipath. Correcting the acoustics was considered impossible by senior staff in the physics department and so the assignment was passed down to Sabine, although he had no particular background in acoustics. Sabine used an organ pipe (512 Hz), a stop watch, and his ear to establish that reverberation time ($T_{60}$, from full sound to not audible, roughly 60 dB in his case) for rooms large compared to the wavelength (overmoded) was directly proportional to the volume ($V$) and inversely proportional to the absorptive surface area ($A$):

$$T_{60} = \frac{0.161V}{A} \quad . \tag{1}$$

The Fogg Lecture Hall when empty had a $T_{60}$ of about 5.5 s whereas other good lecture halls Sabine measured had values just below 1 s (about 0.8 s is considered optimal). Sabine introduced absorbing materials (seat cushions, drapes, carpet) to reduce the reverberation time to an acceptable level, in essence modifying the chamber quality factor (Q) similar to introducing absorber in an electromagnetic reverberation chamber to accelerate reverberant decay. While (1) holds only in an averaged sense and is restrictive, it established an important starting point that later researchers built upon to formulate modern room acoustics.

## III. BASIC EQUATIONS

The basic wave equations for the acoustic (AC) and electromagnetic (EM) cases in a homogenous space are familiar. We write them here as:

$$\begin{aligned} (\nabla^2 + k^2)p = 0,\ p = P_0 e^{-ikz},\ \text{AC} \\ (\nabla^2 + k^2)\bar{E} = 0,\ \bar{E} = \bar{E}_0 e^{-ikz},\ \text{EM} \end{aligned} \tag{2}$$

where $p$ represents wave pressure, $\bar{E}$ the electric field (a similar expression exists for the magnetic field), an $i\omega t$ time convention is assumed, $\omega = 2\pi f$, $f$ is the frequency, $k = \omega/c$, $z$ denotes position, and $c$ is the AC or EM wave propagation speed in the medium, here assumed to be homogenous. The solutions of (2) represent plane waves with magnitudes $P_0$ and $E_0$ respectively, with the primary difference being that $\bar{E}_0$ is transverse (two polarizations, in the plane of propagation and perpendicular), while $P_0$ is longitudinal.

The field in an AC or EM reverberation chamber can be well modeled as a superposition of plane waves with arbitrary direction and magnitudes, see [3, 6.1] for the AC case and [4, 7.1] for the EM case. A field that is direction- and position-independent in its averages is termed diffuse and is an ideal that both types of reverberation chambers seek to produce over a large test volume. Both AC and EM reverberation chambers can use moving diffusers, such as rotating paddles and curtains, as well as fixed diffusers, such as suspended spheres and periodic structures [5], to improve performance.





Wilson, Perry.
"Acoustic and Electromagnetic Reverberation Chambers: Similarities and Differences."
Paper presented at 7th Asia-Pacific International Symposium on Electromagnetic Compatibility & Signal Integrity and Technical Exhibition (APEMC 2016) , Shenzhen, China. May 18, 2016 - May 21, 2016.

## IV. ABSORPTION AND REVERBERATION

The absorptive area $A$ in (1) can be generalized to account for different materials, apertures, and levels of absorption:

$$A = \sum_i \alpha_i S_i \quad , \tag{3}$$

where $\alpha_i$ is the absorption coefficient associated with the surface element $S_i$, and $\alpha = 1 - r^2$ for any given surface element, where $r$ is the reflection coefficient (amplitude of the reflected wave over amplitude of the incident wave). Thus, $\alpha$ can be related to aperture loss and wall losses in an EM reverberation chamber. An open window (no reflection) has a value of $\alpha = 1$. Values for $\alpha$ at 1 kHz range from 0.04 for brick, to 0.12 for glass, 0.37 for heavy carpet on concrete, 0.69 for 5 cm-tall grass, and 0.99 for 2 cm-thick suspended acoustical tile.

In acoustics, absorptive area is given the units sabins ($m^2$) and is related to EM absorbing cross section. Values have been measured carefully for persons and seats, as these are two of the primary absorbers in concert halls and lecture rooms, where acoustic design is critical. A seated musician with instrument is about 1.08 sabins at 1 kHz, a cloth covered seat about 0.67 sabins at 1 kHz, and a man standing with a heavy coat about 1.30 sabins at 1 kHz. While ideally the absorptive area is intrinsic to the object in a diffuse field, in a practical chamber location issues, such as when two objects are positioned close to each other or an object is on the floor versus suspended into the diffuse volume, are important variables. This is similar to the case of RF absorber suspended or near a floor, wall, etc. in an EM reverberation chamber [6].

A more general form of (1) for the decay function in an AC reverberation chamber [3, eq. 6-1.4] along with the EM equivalent [4, eq. 1.51] are given by:

$$W_{AC} = e^{-\left(\frac{Ac}{4V}\right)t} ,$$
$$W_{EM} = e^{-\left(\frac{\omega}{Q_{EM}}\right)t} , \tag{4}$$

where $c$ is the speed of sound in the AC chamber medium, $\omega$ is the angular frequency, and $Q_{EM}$ is the quality factor in the EM case. In the EM case, if we assume a plane wave normally incident on a highly conducting wall, then it is straight forward to find the reflection coefficient and the equivalent absorption coefficient which is $\alpha_{EM} = 4\pi\frac{\delta}{\lambda}$ . Using (4), we can equate exponents and then substitute in this equivalent absorptive coefficient yielding

$$Q_{AC} = \omega\frac{4V}{Ac} = 8\pi\frac{V}{\lambda\alpha S} = \frac{2V}{\delta S} = Q_{EM} , \tag{5}$$

where $Q_{EM}$ is the same as [4, eq. 1.43] for the EM case. $Q_{EM}$ is a rough approximation which doesn't fully account for the polarization (direction) of the EM field near the boundary, but is actually quite close to the better estimate found, once direction is considered [4., eq. 1.44].

Spatial autocorrelation functions look very similar for both chamber types. For the acoustic pressure [3,6-8.2] and total electric field [4,7.47], we have:

$$\langle p(x,t), p(x+\Delta x)\rangle = \langle \bar{p}^2\rangle \frac{\sin(k|\Delta x|)}{k|\Delta x|} ,$$
$$\langle \bar{E}(0)\cdot\bar{E}(\hat{z}r)\rangle = E_0^2\frac{\sin(kr)}{kr} \quad , \tag{6}$$

where $x$ and $z$ represent spatial offsets.

Averaging to achieve a good diffuse field can take multiple forms, as indicated above, including modal stirring, frequency stirring, and position stirring. In acoustics an equivalence between frequency stirring and position stirring for acoustic pressure is given by [3, 6-8.14]

$$k\Delta L \approx \tau\Delta\omega \quad , \tag{7}$$

where $\Delta\omega$ is the bandwidth change, $\tau$ is the decay constant defined by (4), and $\Delta L$ is the position change. Substituting for $\tau$ using (4) yields

$$\frac{A\Delta L}{4V} = \frac{\Delta\omega}{\omega} . \tag{8}$$

This result suggests that averaging over a larger bandwidth (including more modes) is equivalent to averaging over positions roughly in proportion to the wall loss to volume ratio. This is consistent with measured results for a NIST chamber [4, Figs. 9.2 – 9.3].

Differences arise from the differences between the AC scaler wave equation [3, eq. 6-61] and the EM vector wave equation [3, eq. 1.31]. An example is mode numbers and density:

$$N_{AC}(\omega) \approx \frac{1}{6}\frac{V}{\pi^2}\frac{\omega^3}{c^3}, \quad \frac{dN_{AC}}{d\omega} = \frac{1}{2}\frac{V}{\pi^2}\frac{\omega^2}{c^3} ,$$
$$N_{EM}(\omega) \approx \frac{1}{3}\frac{V}{\pi^2}\frac{\omega^3}{c^3}, \quad \frac{dN_{EM}}{d\omega} = \frac{V}{\pi^2}\frac{\omega^2}{c^3} . \tag{9}$$

Note the difference by a factor of 2, representing the lack of vector polarization (TE,TM) in the acoustic case. Other differences exist due to the presence of a propagating medium and wave pressure. The full paper will explore the above similarities and differences in more detail.

An interesting acoustics insight with potential for application in coexistence testing is the "cocktail party effect". This is the situation where multiple persons are speaking in a reverberant room which raises the sound level causing persons to cluster in groups. These clusters tend to be separated by a distance large enough so that each cluster is dominated by the direct path sound and the other clusters contribute not directly but through reverberant sound. This is a similar situation to the unstirred versus stirred energy case discussed in [4, Section 9.2] For a person to understand the conversation in a cluster, the signal to noise ratio (direct conversation to other diffuse talkers) has to be greater than 1. Given K clusters (groups of people or source locations) and assuming isotropic sound radiation from each person (spherical spreading), we can show that



Wilson, Perry.
"Acoustic and Electromagnetic Reverberation Chambers: Similarities and Differences."
Paper presented at 7th Asia-Pacific International Symposium on Electromagnetic Compatibility & Signal Integrity and Technical Exhibition (APEMC 2016) , Shenzhen, China. May 18, 2016 - May 21, 2016.

$$\frac{S}{N} = \frac{(\frac{r_0}{r})^2+1}{K-1}\ , \qquad (10)$$

where $r_0$ is the radius of reverberation similar to $r_e$ as defined in [4, eq. 9.23] for the EM case where the direct (unstirred) energy becomes equal to the indirect (stirred) reverberant energy. Expression (10) could be used as a starting point to describe a coexistence test in a reverberation chamber where K devices with similar radiated powers are causing potential interference. Adding sources (increasing K) reduces the S/N but also will increase loss; however, the increased loss will be dominated by increased noise power for reasonable values of K. As we increase the use of unlicensed spectrum with multiple emitters confined to reverberant volume, an EM version of the "cocktail party effect" may help guide how devices can be tested in advance for their ability to understand a conversation; that is, to maintain a reliable wireless link.

## V. CONCLUSION

This paper has touched on some of the similarities and differences between acoustic and electromagnetic reverberation chambers. Acoustics reverberation chamber research has long focused on loss mechanisms and multiple sources. The insights gained may prove useful to the EM reverberation chamber community as we continue to look at questions related to multi-path, communications systems, coexistence testing, and other problems different from an unloaded, very high Q chamber.

## REFERENCES

[1] H. A. Mendez, "A new approach to electromagenetic field-strength measurements in shielded enclosures," Wescon Tech. Papers, laos Angeles, CA, Aug. 1968.
[2] P. Corona, G. Latmiral, E. Paolini, "Performance and analysis of a reverberating enclosure with variable geometry," IEEE Trans. On Electromagn. Compat., vol. 22, no. 1, pp. 2-5, Feb. 1980.
[3] A. Pierce, Acoustics: An Introduction to its Physical Principles and Applications, Acoustical Society of America, Ch. 6, 1989.
[4] D. Hill, Electromagnetics in Cavities: Deterministic and Statistical Theories, IEEE Press, Wiley & Sons., 2009.
[5] A. Marvin, E. Karadimou, "The use of wave diffusers to reduce the contribution of specular wall reflections to the unstirred energy in a reverberation chamber," in Proc. 2013 IEEE Intl. Symp. on Electromagn. Compat. (Denver, CO), pp. 227-231, Aug. 2013.
[6] J. Coder, J. Ladbury, C. Holloway, K. Remley, "Examining the true effectiveness of loading a reverberation chmaber: How to get your chamber consistently loaded," in Proc. 2012 IEEE Intl. Symp. on Electromagn. Compat. (Pittsburgh, PA), pp. 210-215, Aug. 2012.



Wilson, Perry.
"Acoustic and Electromagnetic Reverberation Chambers: Similarities and Differences."
Paper presented at 7th Asia-Pacific International Symposium on Electromagnetic Compatibility & Signal Integrity and Technical Exhibition (APEMC 2016) , Shenzhen, China. May 18, 2016 - May 21, 2016.

# Antenna Metrology for 100-500 GHz: A New Approach

Perry F. Wilson, Joshua A. Gordon, David R. Novotny, Jeffrey R. Guerrieri
RF Technology Division
National Institute of Standards and Technology
Boulder, Colorado, USA

***Abstract* — A typical near-field scanning range for antenna measurements is based on simple translation stages (planar) or stacked rotators (spherical), or both (cylindrical). Above 100 GHz, problems arise in both specialized waveguide components, such as precision rotators, and in positioning and alignment accuracy. NIST is pioneering a new approach based on an off-the-shelf, industrial six-degrees-of-freedom, articulated-arm robot. Pattern measurements at 118 GHz and 183 GHz, and positioning accuracies within 25 µm confirm the effectiveness of the approach.**

**Keywords — antenna measurements, millimeter-wave, near-field scanning, robotics, spatial metrology**

## I. INTRODUCTION

Near-field scanning at mm-wave frequencies by use of traditional stacked motion stages (linear, rotary) becomes difficult as waveguide components decrease in size, precision rotators become unavailable, and λ/50 positioning accuracies prove challenging. The National Institute of Standards and Technology (NIST) is pioneering a new near-field scanning range based on an off-the-shelf industrial six-degrees-of-freedom (6DoF) robot. The robot allows for arbitrary scan geometries, takes advantage of stable cable routing to avoid the need for precision rotators, and in combination with a dynamic laser tracker system, allows for precision positioning and alignment in both location (x,y,z) and direction (pitch, roll, yaw). A coordinated spatial-metrology approach allows for the position of the scan probe and test antenna to be tracked in real time with known relation to an overall reference frame. This creates coordinated motion of the robotics in concert with the antenna apertures.

## II. ROBOTICS BASED ANTENNA RANGE

Fig. 1 shows the current robotics-based antenna range at NIST, designated as the configurable robotic millimeter-wave antenna facility, or CROMMA. The 6DoF articulated-arm robot (shown with mounted probe antenna) is coupled to a 6DoF hexapod positioner (shown with the test antenna) and both are linked to a dynamic laser tracker system [1]. The robotic arm can support a 35 kg payload and scan arbitrary paths over a volume of radius greater than 1 m with an uncorrected (out of the box) repeatability of better than 100 µm. The hexapod supports a payload of 30 kg, has positioning accuracy and repeatability of around 1 µm, a motion range of about 50 mm, and a pointing range of about 30°. The hexapod itself is located on a rotator and planar positioner to allow rough alignment first. Together with the optical and spatial metrology coordination, the CROMMA specifications are summarized in Table I.

## III. OPTICAL METROLOGY

Spherical mirror reflectors (SMRs) and an optical frame system mounted on the robot arm allow frames of reference to be established between the robot arm and the hexapod for alignment, and for scans to be accurately traced and mechanically corrected. A new optical pixel probe has been developed to solve the problem of translating from the SMRs and optical frame location to the tip of the probe antenna [2]. Specifically, the pixel probe establishes a virtual point in space with known spatial coordinates linked to the laser tracker. This virtual point can then be used to map the aperture of the probe or test antenna to locate their rotational centers and aperture normals, all with accuracy on the order of 25 µm. Using these tools together we can achieve very accurate alignment, critical to good near-field scans, for most any geometry of interest. Fig. 2 shows the pixel probe mapping a standard gain horn, while Fig. 3 shows the relative sizes of two SMRs and WR-05 circular probe antenna.

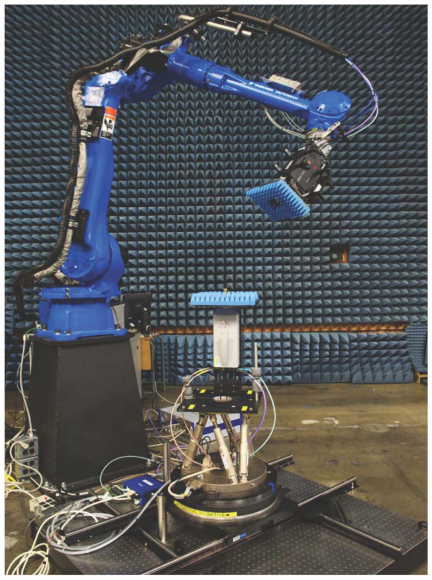

Fig. 1. 6DoF robotic arm with mounted probe antenna and the 6DoF hexapod positioner with mounted test antenna.





Wilson, Perry; Gordon, Joshua; Novotny, David; Guerrieri, Jeffrey.
"Antenna Metrology for 100-500 GHz: A New Approach."
Paper presented at 7th Asia-Pacific International Symposium on Electromagnetic Compatibility & Signal Integrity and Technical Exhibition (APEMC 2016) , Shenzhen, China. May 18, 2016 - May 21, 2016.

Table I.
NIST CROMMA Facility Specifications

| | |
|---|---|
| Probe Payload | 35 kg |
| AUT Payload | 30 kg |
| Accuracy (X,Y,Z) | $< 25$ $\mu$m (rms) |
| Repeatability (X,Y,Z) | $< 25$ $\mu$m (rms) |
| Accuracy (Roll, Pitch, Yaw) | $< 0.01°$ (rms) |
| Repeatability (Roll, Pitch, Yaw) | $< 0.01°$ (rms) |
| Working Volume | 1 m Radius |
| $\theta$ Range | $\pm 120°$ |
| $\phi$ Range | $\pm 360°$ |
| Frequency Range | 75 GHz - 500 GHz |

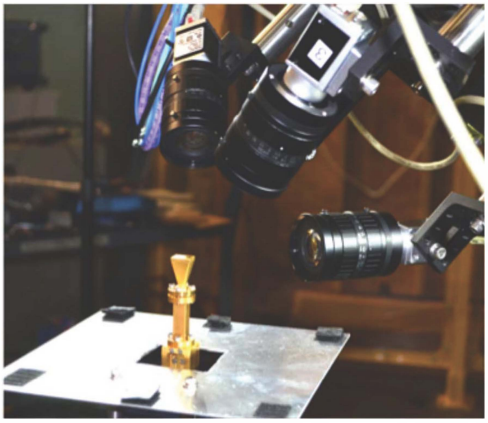

Fig. 2. Pixel probe mapping of a standard gain horn.

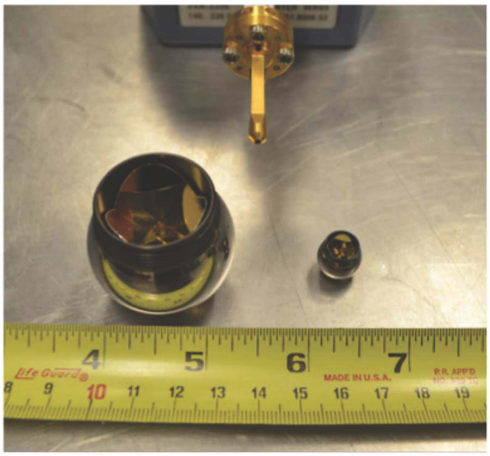

Fig. 3. 38 mm (1.5") and 13 mm (0.5") SMRs, and a 1.5 mm-diameter aperture probe antenna.

## IV. Spatial Metrology

A knowledge of the local coordinate systems and alignment of the probe and test antennas, both linked to an overall coordinate system and the dynamic laser tracker allows the accurate control of the robot kinematics. During a scan, position and motion are captured and can be compared to the target scan geometry and RF data acquisition grid. Corrections to scan geometries can then be calculated and converted to robot commands. Together, the system allows alignment, positional uncertainty, and motion during a scan to be recorded and analyzed. An example of a scan visualization is given in Fig. 4.

Further, knowledge of the exact locations of data acquisition across the scan, even if not on the ideal target grid (position errors), allow for analytical corrections on post processing [3]. Together, these mechanical, spatial, and analytical tools should allow the system to make accurate antenna measurements at frequencies up to and likely above 500 GHz ($\lambda$= 0.6 mm, $\lambda/50$ = 12 µm).

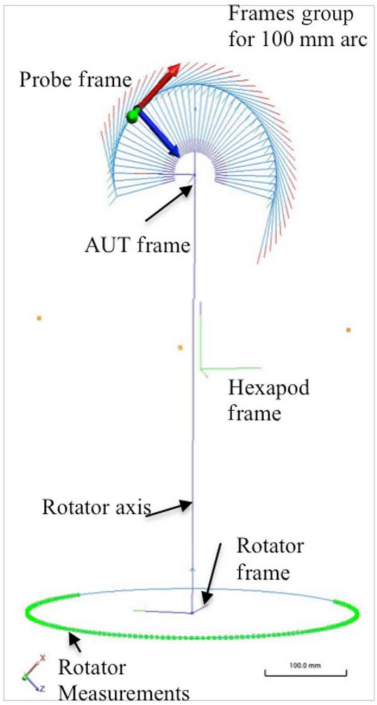


Fig. 4. Visualization of the local (probe, test antenna, hexapod and rotator) and global coordinate systems for a 100 mm radius spherical scan.

## V. Sample Measurement Results

183 GHz represents an important water vapor line frequency in microwave radiometry. A standard gain horn was measured at a 100 mm radius (in the near-field), at a 1000 mm-radius (nominally in the far-field), and calculated theoretically (based on its physical dimensions). Agreement is good between all three patterns down to -20 dB below the peak, as shown in Fig. 5. Note the 1000 mm scan shows noise at low amplitude levels due to limitations on transmit power (-12 dBm).



Wilson, Perry; Gordon, Joshua; Novotny, David; Guerrieri, Jeffrey.
"Antenna Metrology for 100-500 GHz: A New Approach."
Paper presented at 7th Asia-Pacific International Symposium on Electromagnetic Compatibility & Signal Integrity and Technical Exhibition (APEMC 2016) , Shenzhen, China. May 18, 2016 - May 21, 2016.

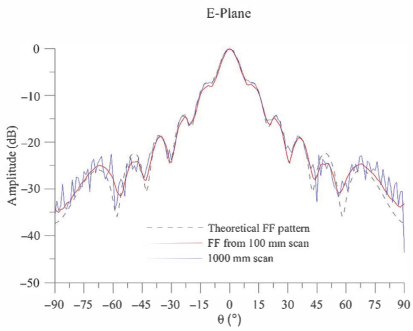


Fig. 5. E-plane data measured at 183 GHz: a) transformed far-field (FF) data from a 100 mm radius spherical near-field scan, b) direct FF data from a 1000 mm radius scan, and c) a theoretical FF pattern.

A second example shows spherical scan data over 118 – 125 GHz for a $\mu = \pm 1$ probe (see Fig. 6). Measurements were made at a radius of 100 mm ($\approx 4D^2/\lambda$, where $D$ is the probe diameter). Both co- and cross-polarization E-plane data are shown for several frequencies with the cross-polarization data generally below -40 dB, which represents the detectable limit for the system in this configuration.

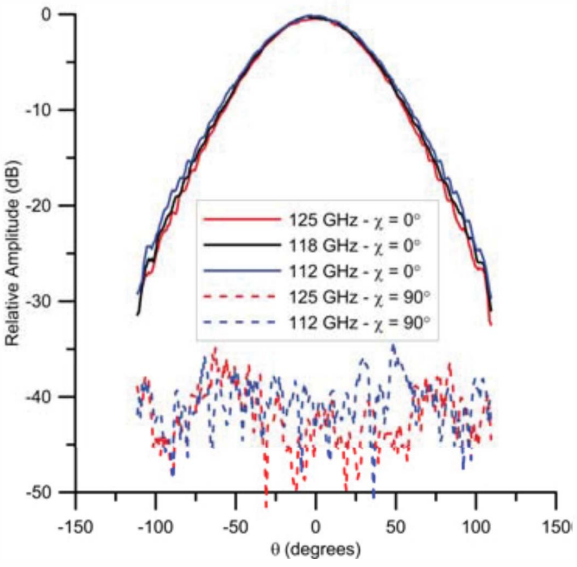


Fig. 6. E-plane patterns at three frequencies (112 GHz, 118 GHz, and 125 GHz) for a $\mu = \pm 1$ probe processed from a 100 mm spherical near-field scan.

CROMMA can also be used in an extrapolation mode, i.e., a linear scan along the aperture normal over multiple wavelengths to estimate the antenna gain. Figure 7 shows extrapolation data for the above $\mu = \pm 1$ probe at 118 GHz. The data represent a scan range of approximately $2D^2/\lambda$ to $24D^2/\lambda$. For this measurement, only a pair of antennas were measured; three are needed to extract absolute gain via the three antenna method. However, a pair gain of 24.7 dB can be estimated form these data and agrees well with theoretical predictions.

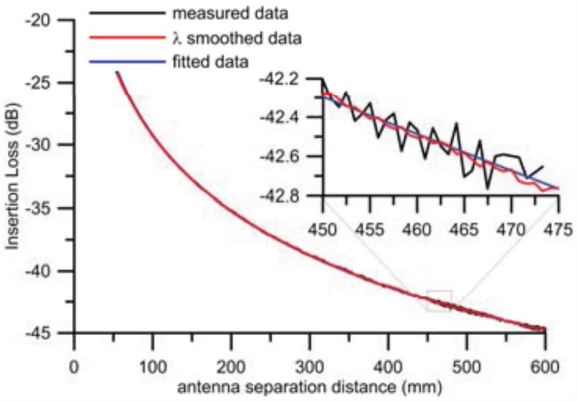


Fig. 7. Extrapolation scan data for the $\mu = \pm 1$ probe paired with a 15 dB standard gain horn at 118 GHz.

## VI. Summary

A robotics based near-field antenna range applicable to frequencies from 100 – 500 GHz and beyond has been described and sample measurement data at 183 GHz and near 118 GHz shown. The combination of optical and spatial metrology with coordinated robotics allows for quick and accurate alignment, yielding precision scans over a very flexible range of geometries. Future work will explore higher frequencies, more complicated test objects such as small satellites and printed antennas, as well as the continuing to refine the overall coordinated spatial and kinematic software capability.

## VII. References

[1] J. Gordon, D. Novotny, M. Francis, R. Wittmann, M. Butler, A. Cutin, J. Guerrieri, "Millimter-wave near-field measurements using coordinated robotics," IEEE Trans. Antennas Propagat., vol. 63, no. 12, pp. 5351-5362, Dec. 2015.

[2] J. Gordon, D. Novotny, A. Cutin, "A single pixel touchless laser tracker probe," J. CMSC, vol. 10, no. 2, pp. 12-21, Autumn 2015.

[3] R. Wittmann, B. Alpert, M. Francis, "Near-field antenna measurements using nonideal measurement locations," IEEE Trans. Antennas Propagat., vol. 28, no. 2, pp. 216-230, May 1998.



Wilson, Perry; Gordon, Joshua; Novotny, David; Guerrieri, Jeffrey.
"Antenna Metrology for 100-500 GHz: A New Approach."
Paper presented at 7th Asia-Pacific International Symposium on Electromagnetic Compatibility & Signal Integrity and Technical Exhibition (APEMC 2016) , Shenzhen, China. May 18, 2016 - May 21, 2016.

# Saturation in Solar Cells from Ultra-Fast Pulsed-Laser Illumination

Tasshi Dennis

National Institute of Standards and Technology, Boulder, CO 80305, USA

***Abstract* — We investigate the potential saturation of a silicon solar cell in response to excitation from continuous-wave and ultra-fast pulsed lasers of equivalent average optical power. Because ultra-fast pulsed sources, such as the super-continuum laser, have very high peak powers, they may be expected to cause solar cells to exhibit nonlinear and saturation effects at much lower irradiance levels compared to continuous-wave lasers and solar simulator lamps. Our experimental results strongly suggest that this is not the case, and that ultra-fast lasers do not intrinsically give rise to enhanced nonlinearities caused by their pulsed nature.**

***Index Terms* — concentrator photovoltaic, efficiency, super-continuum laser, solar simulator, nonlinearity**



## I. Introduction

Traditional laboratory light sources used for solar-cell testing include broadband lamps [1], lasers [2], and LEDs [3]. These sources are typically operated continuous-wave, or CW, with a constant temporal amplitude characteristic like the sun. Xenon arc lamps may be run in a pulsed mode with a low duty-cycle for the testing of concentrator solar cells. Recently, a new type of solar simulator based on a super-continuum laser has been demonstrated [4]. The super-continuum laser is a high-power, broadband light source with the potential to provide vastly improved optical excitation for photovoltaic materials and devices. This novel laser is rapidly pulsed at repetition rates up to 80 MHz, resulting in a quasi-continuous beam of light. This novel source offers coverage from the short-wavelength blue out to the infrared, with tens of watts of optical beam power in a single spatial mode.

Previously, NIST has shown that this source can be spectrally-shaped efficiently, and appears sun-like to a variety of photovoltaic materials [4]. That work was performed at irradiances of 1 sun, at which nonlinearity and saturation effects in solar cells would not typically be expected. Other researchers have made use of a wavelength tunable lasers to study two-photon absorption in silicon solar cells using ultra-short pulses [5]. In that work a comprehensive theoretical treatment for the nonlinearities was developed; however, the laser source was not nearly as broadband as a super-continuum.

The single spatial mode of a super-continuum laser allows the output beam to be highly concentrated for the testing of multi-junction, concentrator photovoltaic cells of small area [6]. In these instances, saturation and non-linear effects may be occurring. The high average power combined with a pulse duration of picoseconds results in extremely high peak powers of tens of kilowatts. This situation raises the question of whether solar cell materials are "blind" to this stimulus, or whether they are able to respond by generating photoelectrons and a measurable current. At some high level of irradiance, all solar cell materials will reach a state of saturation. In this work, we present results which strongly suggest that this doesn't occur any sooner for pulsed lasers as it does for CW lasers of the same average optical power.

## II. Experimental Challenges

Significant technical challenges are presented when trying to conduct experiments which compare ultra-fast pulsed to CW excitation of a solar cell. In order for the results to be conclusive, the ideal measurement scenario must be able to isolate the potential measurement effects as originating solely from the temporal characteristics of the light. Some of these challenges originate from the light sources themselves. CW lasers by nature have very narrow spectral bandwidths, often described in terms of frequency rather than wavelength. The common helium-neon (He-Ne) laser operates with a gain medium having a bandwidth of 1.5 GHz, or 2 picometers at a wavelength of 632.8 nm. By contrast, ultra-fast pulsed lasers can have bandwidths ranging from 10 nm to more than 100 nm. The wide bandwidth is a consequence of the ultra-fast, pulsed characteristic in the time domain. By design, the broadest super-continuum lasers used for solar simulators [4] have bandwidths of 2000 nm. The primary impact of

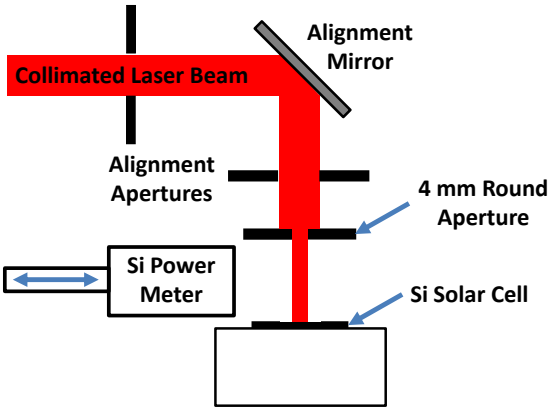


Fig. 1. The experimental apparatus for comparing a pulsed and CW laser on a silicon solar cell with collimated light and low irradiance.



Dennis, Tasshi.
"Saturation in Solar Cells from Ultra-Fast Pulsed-Laser Illumination."
Paper presented at 43rd IEEE Photovoltaic Specialists Conference, Portland, OR, United States. June 5, 2016 - June 10, 2016.

illuminating solar cells with dramatically different optical bandwidths results in efficiency variations caused by a non-uniform spectral responsivity.

Another technical challenge presented by the light sources themselves is optical beam quality. CW sources such as lamps and LEDs radiate into large solid angles, making it difficult to collimate them into a beam capable of propagation over practical working distances without losing excessive optical power through divergence. Divergence makes illuminating a solar cell over a well-controlled, finite area difficult.

The spectral mismatch between pulsed and CW sources dictates that only single junction solar cells should be considered for comparison. Multi-junction solar cells are often designed to operate under high-concentration, high-irradiance conditions in which saturation effects are more likely to be observed, but would be subject to junction current-limiting which is spectrally dependent.

Other practical considerations include having to illuminate only a small, sub-area of a solar cell to maintain high optical concentration. Also, precisely the same sub-area of a solar cell should be illuminated by each light source so that grid lines and surface non-uniformity of the cell do not impact the measured efficiency.

## III. Collimated Light Measurement

Even without concentration, past measurements of efficiency with pulsed, super-continuum laser light have contained measurement uncertainties sufficient to mask possible pulse effects [4]. Without a need for concentration, collimated beams can be used to conduct a CW-to-pulsed comparison, greatly easing experimental complexity. For CW illumination, we used a 632.8 nm He-Ne laser, with its output expanded into a collimated beam of 6 mm diameter. For the pulsed source, a super-continuum laser with a repetition rate of 80 MHz and sub-nanosecond pulses was spectrally filtered to a bandwidth of 16 nm centered on a wavelength of 633 nm. The filtered output of the super-continuum laser was expanded into a beam of 8 mm diameter.

Fig. 1 illustrates the experimental apparatus we constructed to compare pulsed and CW illumination of a solar cell at low irradiance. Alignment apertures and alignment mirrors were used to direct each of the laser beams down the same optical path to the solar cell sample. A round ~4 mm aperture restricted the beam illumination area on the solar cell sample. By overfilling the aperture with the collimated beams from the lasers, the irradiance incident on the solar cell had an approximately uniform, square-top profile. With collimated light, the aperture could be positioned a sufficient distance away from the solar cell surface to allow an optical power meter head to be brought into position to sample the exact beam power incident on the solar cell. The short circuit current of the solar cell was measured with a 4-wire current-voltage meter. The solar cell was a crystalline silicon device, with a phosphorus-diffused emitter, full area Al-BSF, p-type Czochralski (100) structure and a total area of about 1 $cm^2$.

| | Irradiance | $I_{sc}$ |
|---|---|---|
| He-Ne Laser | 20.5 $mW/cm^2$ | 1.171 mA |
| Super-Continuum Laser | 20.5 $mW/cm^2$ | 1.174 mA |

Table. 1. Results for the comparison of a silicon solar cell illuminated with a He-Ne laser and a filtered super-continuum laser in terms of incident optical power and measured short-circuit current.

Table 1 shows the precise setting of the optical irradiance on the silicon solar cell from each of the laser sources. The currents measured from each of the laser sources differ by just 0.3 %, demonstrating no appreciable difference between the two sources of illumination. The AM 1.5 solar reference spectrum [7] contains 2.3 mW of integrated power between the wavelengths of 624 nm and 640 nm over which the super-continuum laser was filtered. Over a 4 mm aperture this power corresponds to an irradiance of 18.3 $mW/cm^2$. Therefore, on a per-wavelength basis the irradiance considered in this

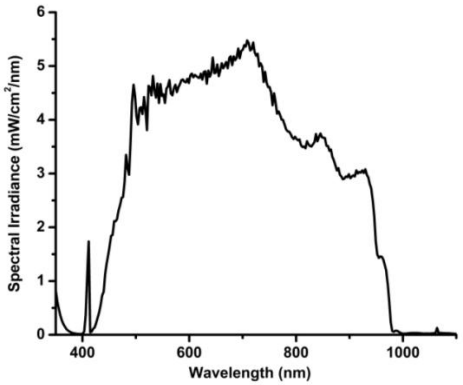


Fig. 2. The measured spectrum of the pulsed super-continuum laser narrowed to the spectral responsivity range of silicon solar cells and optical power sensors.

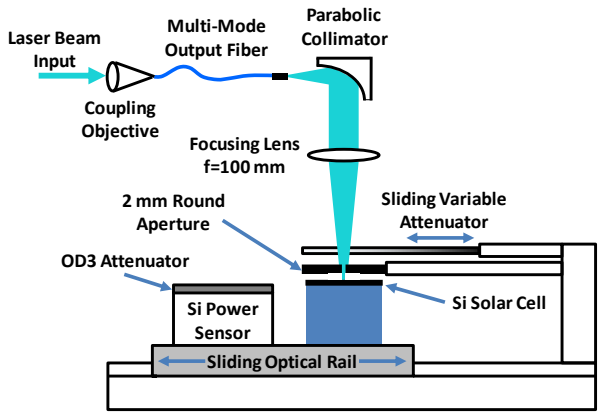


Fig. 3. The experimental apparatus for comparing a pulsed and CW laser on a silicon solar cell with concentrated light and high irradiance.



Dennis, Tasshi.
"Saturation in Solar Cells from Ultra-Fast Pulsed-Laser Illumination."
Paper presented at 43rd IEEE Photovoltaic Specialists Conference, Portland, OR, United States. June 5, 2016 - June 10, 2016.

experiment is on par with a 1-sun illumination of the solar cell. At this relatively low level of irradiance, saturation effects would not normally be expected.

Unfortunately, this experiment was inconclusive because it amounted to a comparison between two silicon solar cells, not two different light sources. The optical power meter sensor was a large-area, silicon photodiode operating without bias, in photovoltaic mode. By use of a silicon photovoltaic device to set the incident optical power, any effect of the pulsed nature of the super-continuum light may have been compensated for and masked.

As an alternative, thermopile-based power meters can be used to measure the average power of both pulsed and CW laser sources, although they typically lack sensitivity sufficient for measurements of a few milliwatts or less. Pyroelectric energy meters are too slow to respond directly to the 80 MHz repetition rate of a super-continuum laser. Optically chopping the beam to create a slow modulation of a few tens of hertz would allow a pyroelectric meter to measure both the super-continuum as well as the He-Ne laser. Radiometers and calorimeters may also be used to measure the average optical power of either light source, but their bulk may require a significant redesign of the experimental apparatus.

## IV. Concentrated Light Measurement

In order to achieve precise concentration through beam focusing, our experiment at high-irradiance made use of laser sources for both CW and pulsed illumination. A super-continuum laser with a repetition rate of 80 MHz and sub-nanosecond pulses was spectrally narrowed to span between 400 nm and 1000 nm thereby coinciding with the spectral responsivity bandwidth of silicon solar cells. The filtered super-continuum laser spectrum is shown in Fig. 2, and was able to provide up to 400 mW of optical power. A frequency-doubled diode laser operating at 532 nm was used as the CW laser source, and was capable of generating more than 5 watts of optical power.

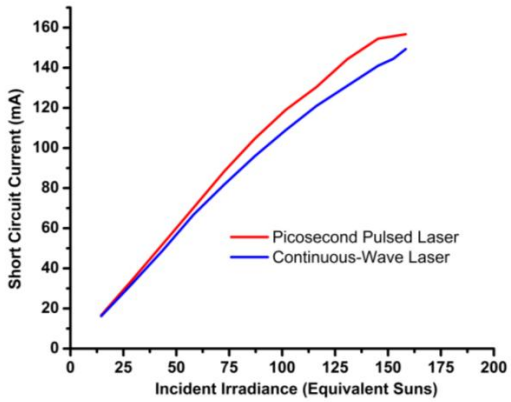


Fig. 4. The high-irradiance comparison of a CW laser and a picosecond pulsed laser. The incident irradiance is report as "equivalent suns" to indicate the magnitude of the excitation.

Figure 3 illustrates the experimental apparatus we constructed for concentrated light measurements performed on the same crystalline solar cell used in our collimated light measurements. In order to remove alignment issues with focused light, the lasers were each coupled into optical fibers that could be connected precisely to the experimental setup. The collimated light from the lasers was focused with a lens having a focal length of 100 mm, creating a soft focus on the solar cell surface. The focused beam passed through a sliding variable attenuator plate and a circular aperture of 2 mm in diameter. The focused light over-filled the aperture so the area of the transmitted light was well defined. By placing the solar cell at the beam waist of the focused light and the aperture as close to the solar cell as possible, diffraction effects were kept to a minimum.

During measurement operation, the optical power of the light incident on the solar cell was adjusted with the sliding variable attenuator. Adjusting the control settings of the super-continuum laser would have also influenced its relative spectral shape. The solar cell was mounted together with a silicon diode power sensor on the sliding stage of an optical rail. The optical rail allowed the solar cell and the power sensor to each be positioned precisely under the focused illumination for each measured data point. An optical attenuator of density equal to three was place in front of the power sensor to ensure that it was operated in a low-power, linear regime. Unlike the experiment with collimated light, the use of a silicon photodiode power meter did not inherently compromise the measurement integrity because the experiment was a relative comparison. The experiment attempted to resolve whether pulsed illumination would cause a nonlinear response at substantially lower optical power than CW illumination.

Figure 4 presents the measurement of short circuit current from the silicon solar cell as a function of incident irradiance. The horizontal axis has been converted to equivalent suns based on the integrated irradiance of the AM 1.5 reference spectrum between 400 nm and 1000 nm. While this may not be a precise definition, the unit helps convey the magnitude of the irradiance being considered by the experiment. The maximum measurement value was 158 equivalent suns.

We see from the sub-linear curves of Fig. 4 that the two laser sources each cause the solar cell to exhibit some nonlinear behavior that might be associated with saturation. Localized heating could also have been at play at high irradiance. To minimize transient thermal effects, the cell current was measured after more than 10 seconds of illumination. Regardless, the illumination by both laser sources causes similar measured effects, and indicates, at the very least, that the pulsed laser source is not intrinsically more likely to cause nonlinear cell performance at these irradiance levels. We note that the two curves have slightly different slopes, and there could still be some influence from spectral mismatch. Because the optical bandwidth of the pulsed laser



Dennis, Tasshi.
"Saturation in Solar Cells from Ultra-Fast Pulsed-Laser Illumination."
Paper presented at 43rd IEEE Photovoltaic Specialists Conference, Portland, OR, United States. June 5, 2016 - June 10, 2016.

source is substantially greater than the CW laser, it is possible that the optical powers are not as equivalent as presented. A silicon power sensor was used with the silicon solar cell to minimize this impact. Various thermal and pyroelectric power sensors would have avoided the errors associated with wavelength dependence, but would have been more difficult to incorporate into the experimental apparatus because of their bulk.

## V. Conclusion

Our efforts to make a precise comparison of cell efficiency measurements with collimated illumination would suggest that ultra-fast pulsed lasers do not intrinsically cause saturation effects in silicon solar cells at low irradiance. Unfortunately, our results are far from conclusive because a second silicon solar cell was essentially used to quantify the incident irradiance. This difficulty further illustrates the challenge of making valid comparisons between pulsed and CW illumination.

Our concentrated light measurements support the notion that even at high-irradiance, ultra-fast pulsed lasers do not cause saturation or nonlinear effects substantially more than CW lasers of nominally equivalent optical power. These results have been obtained with a crystalline silicon material which is known to have minority carrier lifetimes of a few tens of microseconds. Other materials such as the III-V semiconductor material GaAs have lifetimes of a few nanoseconds, and therefore represent interesting subjects for future comparisons.

## Acknowledgement

The author gratefully acknowledges former colleague J. Schlager for the concept of using super-continuum lasers as solar simulators, and for initially motivating the comparison of pulsed and CW illumination of solar cells. The author also gratefully acknowledges M. Spidel of NIST for use of the frequency doubled diode laser at 532 nm.

## References

[1] K. Emery, D. Myers, and S. Rummel, "Solar simulation – problems and solutions", in *Twentieth PVSC*, Las Vegas, NV, pp. 1087-1091, 1988.

[2] C. H. Seager, "The determination of grain-boundary recombination rates by scanned spot excitation methods," *J. Appl. Phys.*, vol. 53, no. 8, pp. 5968-5871, 1982.

[3] B. H. Hamadani, J. Roller, B. Dougherty, and H. Yoon, "Fast and reliable spectral response measurements of PV cells using light emitting diodes," in *Thirty-ninth PVSC*, Tampa, FL, 2013.

[4] T. Dennis, J. B. Schlager, and K. A. Bertness, "A Novel Solar Simulator Based on a Super-Continuum Laser for Solar Cell Device and Materials Characterization," *IEEE J. Photovoltaics*, vol. 4, no. 4, pp. 1119-1127, 2014.

[5] M. Mundus, J. A. Giesecke, P. Fisher, J. Hohl-Ebinger, and W. Warta, "Interaction of ultrashort laser pulses and silicon solar cells under short circuit conditions," *J. Appl. Phys.*, vol. 117, 085702, 2015.

[6] T. Dennis, B. Fisher, M. Meitl, and J. Wilson, "A High-Concentration Programmable Solar Simulator for Testing Multi-Junction Concentrator Photovoltaics," in *Forty-second PVSC*, New Orleans, LA, 2015.

[7] Standard Tables for Reference Solar Spectral Irradiances: Direct Normal and Hemispherical on 37° Tilted Surfaces, G173003, 2008. Available: http://astm.org

# A Programmable Solar Simulator for Realistic Seasonal, Diurnal, and Air-Mass Testing of Multi-Junction Concentrator Photovoltaics

Tasshi Dennis[1], Chanud Yasanayake[1], Tim Gerke[2], Alex Payne[3], Lars Eng[3], Brent Fisher[4], and Matt Meitl[4]

[1]National Institute of Standards and Technology, Boulder, CO 80305, USA; [2]Fianium, Inc., Eugene, OR 97401, USA; [3]Silicon Light Machines, Sunnyvale, CA 94086, USA; [4]Semprius, Inc., Durham, NC 27713, USA

***Abstract* — We built a spectrally programmable super-continuum solar simulator and applied it to the realistic laboratory testing of a multi-junction concentrator solar cell. The novel solar simulator generated a broad range of illumination conditions representing changes in time of day, time of year, and air mass. The simulator is based on a spatially coherent, super-continuum laser as the light source and a hybrid pair of prism-based spectrometers with spatial light modulators to precisely control the spectrum. The enhanced spectral coverage of this simulator significantly reduced the spectral mismatch over previous implementations. Geometries for both focused as well as divergent sample illumination were considered, achieving irradiances of approximately 100 suns and 190 suns, respectively. The measured performance of the cell was compared favorably to predictions based on both measured and theoretical spectra and representative quantum efficiency curves.**

***Index Terms* — concentrator photovoltaic, multi-junction solar cell, quantum efficiency, solar simulation, spatial light modulator, spectral mismatch, super-continuum laser**

Work partially supported by the US government; not subject to US copyright.

## I. Introduction

Characterizing the optical and electrical performance of a photovoltaic device or material constitutes a fundamental description which is crucial to allowing the solar cell designer to systematically increase efficiency, improve reliability, and reduce overall device cost. The measurements required must be made with high accuracy under controlled conditions using an illumination source, or solar simulator, which must be carefully controlled spectrally, spatially, and temporally. Traditionally, the laboratory light sources used for solar-cell testing have included broadband lamps [1], lasers [2], and LEDs [3]. Significant drawbacks exist for each of these sources when used in various measurement scenarios. Arc lamps, for example, can provide a powerful and broad spectrum, but are difficult to spectrally alter for the light biasing of multi-junction solar cells [4] and the realistic modeling of air-mass variations [5]. Lasers are powerful and easy to concentrate, but have unrealistically narrow spectra [2]. LEDs are broader spectrally than lasers, but must be interleaved spatial in arrays to provide better coverage of the solar spectrum [3]. Lamps and LEDs both radiate into large solid angles, making them difficult to concentrate or alter spectrally with beam optics.

The super-continuum laser is a high-power, broadband light source with the potential to provide vastly improved optical excitation for photovoltaic materials and devices. Unlike a flashed xenon arc lamp, the super-continuum laser is rapidly pulsed at maximum repetition rates of up to 60 to 80 MHz, resulting in a quasi-continuous emission. This novel source offers spectral coverage from the short-wavelength blue out to the infrared, with tens of watts of optical power in a single spatial mode. Previously, NIST has shown that this source can be spectrally shaped, and appears sun-like to a variety of photovoltaic materials [6]. This novel source has been tightly focused to create spatially selective, full-spectrum, optical beam-induced current maps [6], and concentrated to an irradiance of many hundreds of suns [7]. Cell saturation effects from pulsed, super-continuum illumination have been shown to be similar to continuous illumination, even at concentrations of more than 150 suns [8].

In this work, we report on the full-area illumination of a multi-junction, concentrator photovoltaic (MJ-CPV) cell with programmable, simulator light which realistically mimics seasonal, diurnal or hour-of-day, and air-mass variations. Experimental setups for both divergent and collimated illumination of the cell are considered. Measurements of cell efficiency are compared to calculations based on measured quantum efficiency and measured and ideal simulator spectra.

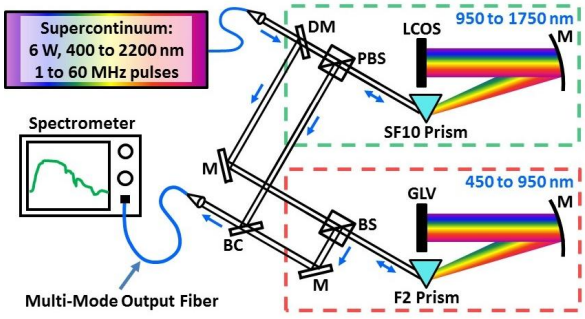


Fig. 1. The programmable solar simulator with concentrator is shown. M: collimation and steering mirrors; DM: dichroic mirror; BS: beam splitter; PBS: polarization beam splitter; BC: beam combiner; GLV: grating light valve; LCOS: liquid crystal on silicon; MJ-CPV: multi-junction concentrator photovoltaic.



Dennis, Tasshi; Yasanayake, Chanud; Gerke, Tim; Payne, Alex; Eng, Lars; Fisher, Brent; Meitl, Matt.
"A Programmable Solar Simulator for Realistic Seasonal, Diurnal, and Air-Mass Testing of Multi- Junction Concentrator Photovoltaics."
Paper presented at 43rd IEEE Photovoltaic Specialists Conference, Portland, OR, United States. June 5, 2016 - June 10, 2016.

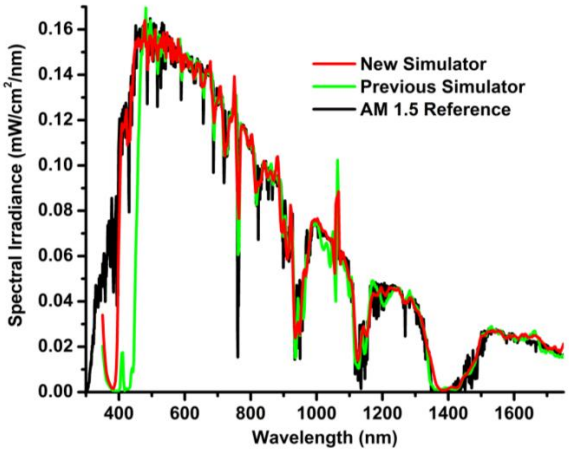


Fig. 2. The simulator output matched to the AM 1.5 reference spectrum is shown. The addition of 50 nm of coverage toward the ultraviolet over a previous simulator implementation is a significant improvement.

## II. Simulator Design and Operation

The topology of the NIST programmable solar simulator illustrated in Fig. 1 has been described previously [7]. In this instance, a recently-available, 6 watt super-continuum laser with a spectrum spanning from below 400 nm to beyond 2200 nm was used. The lower limit below 400 nm represents a significant bandwidth increase of more than 50 nm beyond previous demonstrations, thereby reducing the spectral mismatch in the more energetic region of the solar spectrum.

The spectrum below 950 nm was controlled by a grating light valve spatial light modulator (GLV-SLM), which is a linear array device with 1088 pixels that operates as a steerable diffraction grating [9]. Spectral components incident on the GLV from a prism made of Schott F2 glass [10] were attenuated by steering them out of the dispersed beam. The desired spectrum was then reflected back through the prism and exited the short wavelength spectral shaper. The spectrum above 950 nm was controlled by a liquid crystal on silicon spatial light modulator (LCOS-SLM) comprised of a $512 \times 512$ array of pixels, which was operated as a polarization diversity switch. As shown, the incident light passed through a polarization beam splitter (PBS) before being dispersed by a prism made of Schott SF10 glass [10]. The LCOS-SLM selectively rotates the polarization state of the reflected spectrum, such that it reflects off the PBS and out of the long-wavelength spectral shaper.

Light from the two prism spectrometers was then recombined in a multimode fiber with a 200 µm core. Accurate spectral shaping was achieved with an iterative loop between the voltage patterns driving the SLMs and a scanning spectrometer measuring the simulator output from the optical fiber.

Figure 2 presents spectral shaping of our simulator to match the AM 1.5 (ASTM G-173-03) solar reference spectrum [11], resulting in a concentrated irradiance of 100 suns. The 50 nm increase in spectral coverage reduces the mismatch remaining

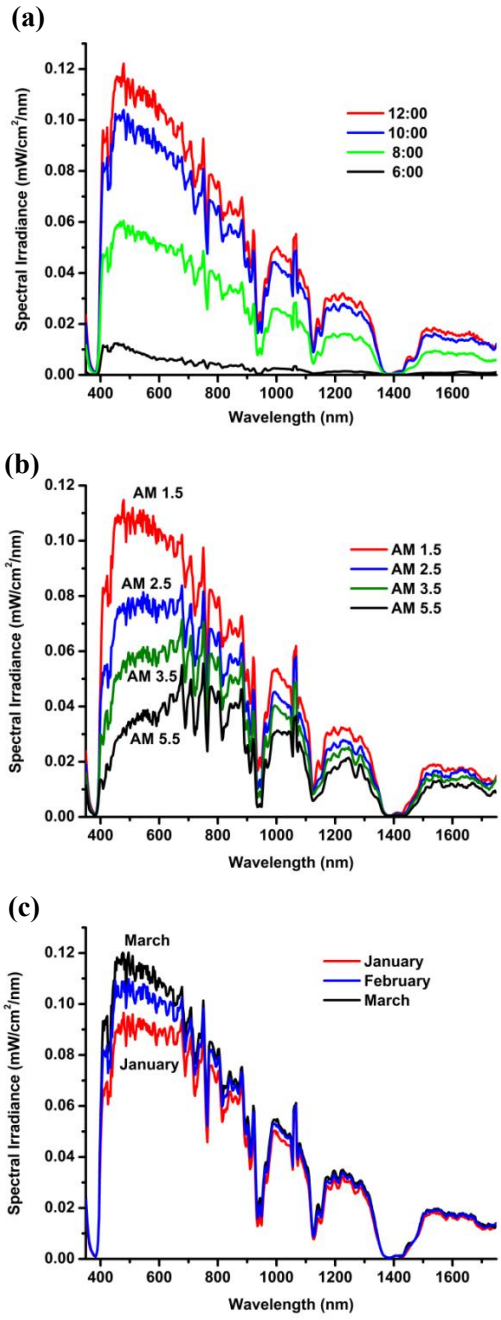


Fig. 3. Selected measurements of the simulator output are shown for the spectral variation with (a) time of day, (b) air-mass, and (c) time of year. The variations are based on SMARTS.



Dennis, Tasshi; Yasanayake, Chanud; Gerke, Tim; Payne, Alex; Eng, Lars; Fisher, Brent; Meitl, Matt.
"A Programmable Solar Simulator for Realistic Seasonal, Diurnal, and Air-Mass Testing of Multi- Junction Concentrator Photovoltaics."
Paper presented at 43rd IEEE Photovoltaic Specialists Conference, Portland, OR, United States. June 5, 2016 - June 10, 2016.

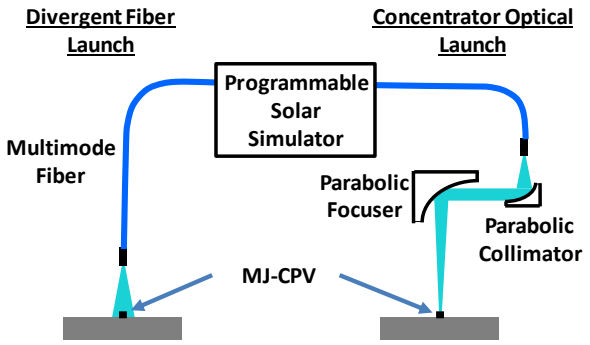


Fig. 4. The two experimental setups used to illuminate an MJ-CPV cell, consisting of a divergent beam with no additional optics and a focused beam created by parabolic mirrors.

between 300 nm and 400 nm to less than 5 % of the total integrated irradiance. The spectral resolution of the shaping was sufficient to replicate all but the sharpest spectral features, with the highest resolution of ~1 nm achieved at short wavelengths. Finite amplitude extinction limited the ability to attenuate the sharp feature at 1064 nm caused by laser pump light. Figure 3 shows selected output spectra as the simulator mimicked the sun during time of day, air mass, and time of year variations based on the Simple Model of the Atmospheric Radiative Transfer of Sunshine (SMARTS) [5].

Figure 4 illustrates two setups for illuminating a small-area MJ-CPV concentrator cell. In the direct divergent setup, no additional optics are required and the tip of the simulator output fiber was brought to within 2 to 3 mm of the solar cell being measured. This approach takes advantage of the inherent spatial confinement of the optical fiber, which in this setup had an inner core diameter of 200 µm with a numerical aperture of 0.22. The spectrum incident on the cell can be estimated from the scanning spectrometer measurement of the output optical fiber. This estimate assumes that the beam diverges uniformly with wavelength, when in fact long wavelengths will diverge more than short wavelengths. The irradiance on the cell is difficult to estimate because of the beam divergence and the uncertainty in the distance between the fiber tip and the cell. In the concentrated setup, the simulator light was collimated and focused with broadband parabolic mirrors. The relatively long focal length of the focusing mirror (f = 152 mm) resulted in a soft focus with a large beam waist of 1 mm. By definition, the light is collimated at the waist, where the incident optical power could be measured through an aperture of known size. However, in order for the spectrum incident on the cell to be known, spectral losses associated with the concentrator optics had to be accounted for in advance. Clearly, each of these setups has advantages and disadvantages for the quantitative testing of solar cells.

## III. Measurements with Focused Illumination

We used the simulator to generate time-of-day spectra representing every hour from 5:00 and 19:00, similar to the example curves in Fig. 3(a). Figure 5 shows the measured short-circuit current of an MJ-CPV solar-cell chip that was fully illuminated by the concentrated beam shown on the right side of Fig. 4. The square solar cell had an active area of approximately 600 µm × 600 µm. The concentrated irradiance on the cell was approximately 100 suns. As expected, the current peaked in the middle of the day at 12:00. Using characteristic quantum efficiency curves for the solar cell, currents were calculated based on measured spectra (labeled "Model") as well as ideal spectra (labeled "SMARTS"). The model curve lies above the SMARTS curve because the limited resolution of the spectral shaping tended to generate

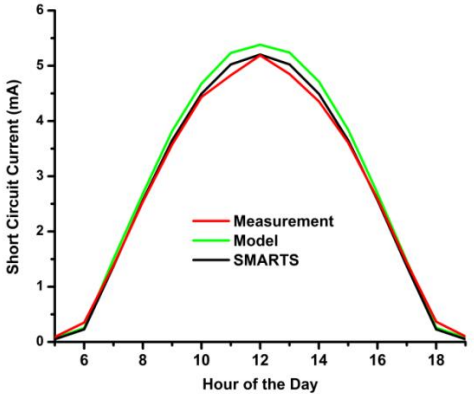


Fig. 5. The measured output of a MJ-CPV cell in response to simulated hour-of-the-day variations is shown for concentrated illumination. Predictions based on measured spectra (Model) and ideal spectra (SMARTS) are included.

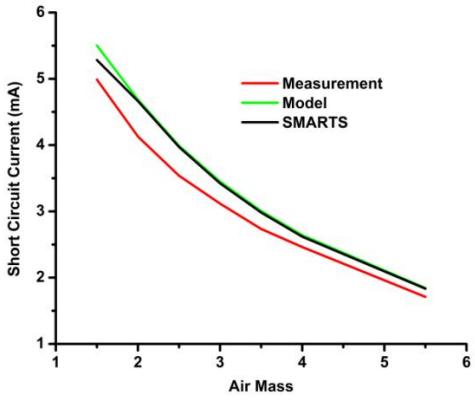


Fig. 6. The measured output of a MJ-CPV cell in response to simulated air mass variations is shown for concentrated illumination. Predictions based on measured spectra (Model) and ideal spectra (SMARTS) are also shown.



Dennis, Tasshi; Yasanayake, Chanud; Gerke, Tim; Payne, Alex; Eng, Lars; Fisher, Brent; Meitl, Matt.
"A Programmable Solar Simulator for Realistic Seasonal, Diurnal, and Air-Mass Testing of Multi- Junction Concentrator Photovoltaics."
Paper presented at 43rd IEEE Photovoltaic Specialists Conference, Portland, OR, United States. June 5, 2016 - June 10, 2016.

higher average irradiance in regions with substantial fine structure. The agreement between model and measurement depends on the accuracy of the quantum efficiency curves, calibration of the spectrometer relative to the concentrated beam power, equipment dynamic range, and compensation for spectral losses. Because the simulated spectra were measured at the multimode fiber output, spectral compensation for the collimator and focusing mirror, and correction for the finite area of the solar cell was required. The agreement would likely improve significantly if the incident spectrum could be measured directly. Overall, the agreement in Fig. 5 is quite good at better than 10 %, and indicates that the simulator can realistically mimic the sun based on SMARTS spectra

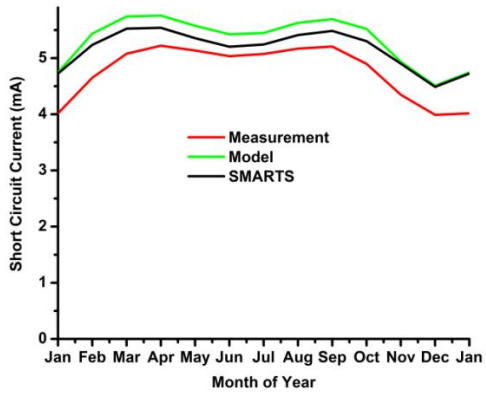


Fig. 7. The measured output of a MJ-CPV cell in response to simulated seasonal variations is shown for concentrated illumination. Predictions based on measured spectra (Model) and ideal spectra (SMARTS) are included for comparison.

Figure 6 shows the decrease in measured short circuit current from the MJ-CPV in response to simulated light for increasing air-mass. Similar to the time-of-day curves, the measurement and model agree to 10 % or better. At an air-mass of 1.5, the difference between model and SMARTS is on par with Fig. 5, but becomes negligible at higher values. This is caused by a transition from the total current being limited by one junction of the cell to another junction of the cell, combined with a reduction in spectral shaping error.

In Fig. 7 the measured seasonal performance of the MJ-CPV is presented for illumination by the concentrated beam. A characteristic double peak in the current production is apparent, with maxima occurring during the spring and fall seasons. During the winter months, the model and SMARTS curves agree almost exactly. However, the model curve is consistently higher during the spring, summer, and fall seasons as the junction limiting the total cell current is influenced by more spectral shaping error from finite resolution. Both of the predicted curves are consistently above the measured curve, which is attributed to uncertainty between the measured spectra and the actual irradiance delivered to the cell surface. If we assume that 10 % less total optical power was delivered to the cell, then both the model and SMARTS curves shift down to better overlap with the measured curve.

## IV. Measurements with Divergent Illumination

Using the direct divergent illumination setup shown on the left side of Fig. 4, we measured the response of the same MJ-CPV cell as above. Figure 8 shows the measured short-circuit current of the cell in response to hour-of-the-day variations, where the effective irradiance on the cell was approximately 190 suns. The measurements agree very well

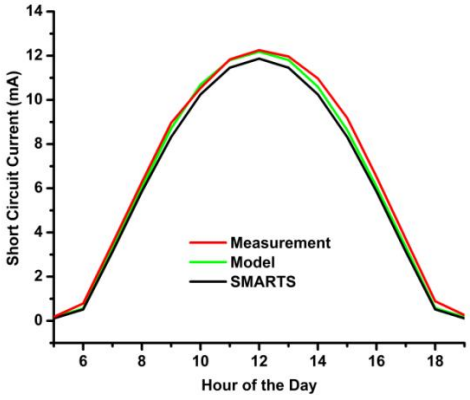


Fig. 8. The measured output of a MJ-CPV cell in response to simulated hour-of-the-day variations is shown for direct divergent illumination. Predictions based on measured spectra (Model) and ideal spectra (SMARTS) are included.

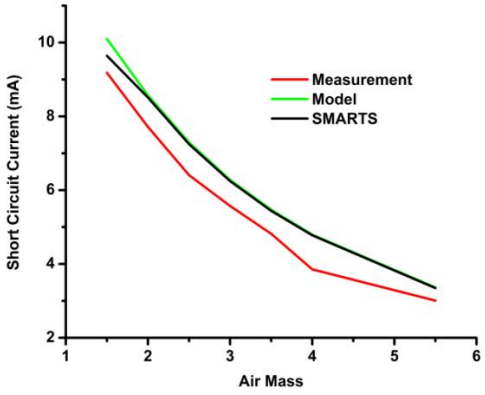


Fig. 9. The measured output of a MJ-CPV cell in response to simulated air mass variations is shown for direct divergent illumination. Predictions based on measured spectra (Model) and ideal spectra (SMARTS) are also shown.



Dennis, Tasshi; Yasanayake, Chanud; Gerke, Tim; Payne, Alex; Eng, Lars; Fisher, Brent; Meitl, Matt.
"A Programmable Solar Simulator for Realistic Seasonal, Diurnal, and Air-Mass Testing of Multi- Junction Concentrator Photovoltaics."
Paper presented at 43rd IEEE Photovoltaic Specialists Conference, Portland, OR, United States. June 5, 2016 - June 10, 2016.

with calculated results based on a model of the multi-junction cell for both measured spectra (labeled "Model") as well as ideal spectra (labeled "SMARTS"). As mentioned previously, it is difficult to accurately determine the total optical power incident on the solar cell surface with divergent light. Therefore, a scaling factor for the measured spectra used in the model calculations was selected which gave good visual agreement for the curves of short circuit current. Once determined, this same scaling factor was used in all subsequent measurements with divergent light. However, irrespective of this scaling factor, the functional agreement or shape of the curves matches very well, indicating again that the simulator can realistically mimic the sun based on SMARTS spectra.

Figure 9 shows the decrease in measured short circuit current from the MJ-CPV for increasing air-mass with direct divergent illumination. As compared to the concentrated illumination results above, the difference between the measurement and model curves is generally somewhat larger, and may indicate that the spectral scaling factor had drifted slightly. Note also that the average short circuit current is about twice as large as the concentrated illumination measurement.

The dependence of the MJ-CPV short circuit current on the month of the year is shown in Fig. 10 for direct divergent illumination. While the average agreement between the measured and model curves is very good and a consequence of the spectral scaling factor, the shapes differ some. The measured dependence has less of a pronounced dip in current in the middle of the summer. While the exact cause has not been determined, it may be the result of current limiting or luminescent coupling between the junctions that is not captured by our simplistic model. This same behavior was also observed in the concentrated illumination measurements of Fig. 7.

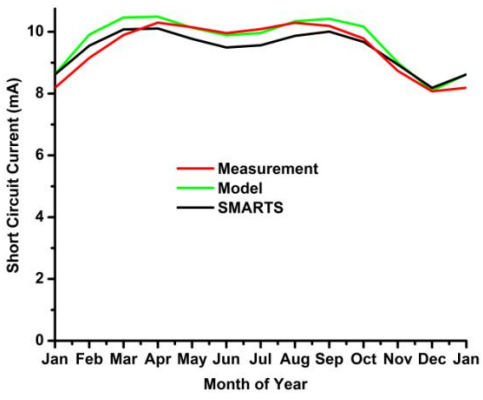


Fig. 10. The measured output of a MJ-CPV cell in response to simulated seasonal variations is shown for direct divergent illumination. Predictions based on measured spectra (Model) and ideal spectra (SMARTS) are included for comparison.

## V. Discussion and Conclusion

By use of a super-continuum laser with an additional 50 nm of spectral coverage down to 400 nm, we were able to reduce the theoretical limit for spectral mismatch from 11 % down to less than 5 %. This limit assumes that the spectral shaping process has sufficiently high resolution so as not to introduce spectral mismatch of its own. In a multi-junction cell, the impact of the remaining mismatch of 5 % depends on which junction is responsible for limiting the total cell current. In this work, the remaining lack of light between 300 and 400 nm had less impact on measurements than not knowing exactly what light was being delivered to the cell surface. Super-continuum lasers are now available which extend down to 350 nm and below; however, they tend to produce low optical power.

We expect that the observed differences between our measurements and predictions of short circuit current could be significantly reduced with a more sophisticated method of measuring the spectrum and total optical power delivered to the cell surface. Our demonstration of two different cell illumination geometries illustrated some of the challenges. For the focused illumination, we could determine fairly accurately the power delivered to the cell surface, yet could not know the exact shape of the spectrum. The required spectral correction factors can potentially vary slightly with time as well as beam alignment. In the case of the direct divergent illumination, we could determine the spectrum incident on the cell fairly well, but could not accurately estimate the total irradiance over the active area of the cell. For this geometry, better measurement agreement may also be obtained by quantifying the beam divergence as a function of wavelength. One solution for measuring the spectrum and optical power delivered to the cell may be to use an area-matched aperture in place of the solar cell followed by an integrating sphere for spatial uniformity.

It may seem counterintuitive that the divergent illumination resulted in a higher concentration of irradiance than the focused one; however, this is simply a consequence of the optics, losses, and working distances selected. The direct divergent illumination makes use of the spatial confinement of the 200 µm optical fiber core. With a numerical aperture of 0.22, the emitted light expands to a 1 mm diameter at a distance of 2.2 mm. For focused illumination, a measured spot size of 1 mm was achieved with a parabolic objective having a focal length of 152 mm. The loss and broadband compensation for the spectral dependence of the parabolic mirrors limits the total amount of light that can be delivered to the focused spot. A smaller spot would increase the concentration but result in less uniform illumination.

The novel super-continuum solar simulator has been shown to be a sophisticated tool for the characterization of the complex operation of solar cells such as multi-junctions at high concentration. With commercial laser systems on the horizon that offer substantial increases in optical power, we anticipate that an even wider range of measurement conditions will become available to the solar cell researcher.

978-1-5090-2724-8/16/$31.00 ©2016 IEEE


Dennis, Tasshi; Yasanayake, Chanud; Gerke, Tim; Payne, Alex; Eng, Lars; Fisher, Brent; Meitl, Matt.
"A Programmable Solar Simulator for Realistic Seasonal, Diurnal, and Air-Mass Testing of Multi- Junction Concentrator Photovoltaics."
Paper presented at 43rd IEEE Photovoltaic Specialists Conference, Portland, OR, United States. June 5, 2016 - June 10, 2016.

## REFERENCES


[1] K. Emery, D. Myers, and S. Rummel, "Solar simulation – problems and solutions", in *Twentieth PVSC*, Las Vegas, NV, pp. 1087-1091, 1988.

[2] C. H. Seager, "The determination of grain-boundary recombination rates by scanned spot excitation methods," *J. Appl. Phys.*, vol. 53, no. 8, pp. 5968-5871, 1982.

[3] B. H. Hamadani, J. Roller, B. Dougherty, and H. Yoon, "Fast and reliable spectral response measurements of PV cells using light emitting diodes," in *Thirty-ninth PVSC*, Tampa, FL, 2013.

[4] S. R. Kurtz, K. Emery, and J. M. Olson, "Methods for analysis of two-junction, two-terminal photovoltaic devices," in *Proc. World Conf. Photovoltaic Energy Convers.*, Waikoloa, HI, USA, pp. 1733-1737, 1994

[5] C. Gueymard, "Parameterized Transmittance Model for Direct Beam and Circumsolar Spectral Irradiance," *Solar Energy*, 71:5, pp. 325-346, 2001.

[6] T. Dennis, J. B. Schlager, and K. A. Bertness, "A Novel Solar Simulator Based on a Super-Continuum Laser for Solar Cell Device and Materials Characterization," *IEEE J. Photovoltaics*, vol. 4, no. 4, pp. 1119-1127, 2014.

[7] T. Dennis, B. Fisher, M. Meitl, and J. Wilson, "A High-Concentration Programmable Solar Simulator for Testing Multi-Junction Concentrator Photovoltaics," in *Forty-second PVSC*, New Orleans, LA, 2015.

[8] T. Dennis, "Saturation in Solar Cells from Ultra-Fast Pulsed-Laser Illumination," in *Forty-third PVSC*, Portland, OR, 2016.

[9] D. T. Amm and R. W. Corrigan, "Optical Performance of the Grating Light Valve Technology," in *Proc. SPIE 3634, Projection Displays V*, pp. 71-78, 1999.

[10] Product names are only used in the paper for clarity and do not represent an endorsement by NIST.

[11] Standard Tables for Reference Solar Spectral Irradiances: Direct Normal and Hemispherical on 37° Tilted Surfaces, G173003, 2008. Available: http://astm.org





Dennis, Tasshi; Yasanayake, Chanud; Gerke, Tim; Payne, Alex; Eng, Lars; Fisher, Brent; Meitl, Matt.
"A Programmable Solar Simulator for Realistic Seasonal, Diurnal, and Air-Mass Testing of Multi- Junction Concentrator Photovoltaics."
Paper presented at 43rd IEEE Photovoltaic Specialists Conference, Portland, OR, United States. June 5, 2016 - June 10, 2016.

# Pathloss Models for Indoor Hotspot Deployment at 83.5 GHz

Camillo Gentile[†], Jelena Senic[‡], Peter B. Papazian[‡], Jae-Kark Choi[†], and Kate A. Remley[‡]
National Institute of Standards and Technology
Communications Technology Laboratory
Wireless Networks Division[†] Radio-Frequency Technology Division[‡]
Gaithersburg, Maryland, USA Boulder, Colorado, USA

***Abstract* — Conventional pathloss models are based on the received power from an omnidirectional antenna. Millimeter-wave receivers, conversely, will feature highly directional antennas that can be steered towards the angle with maximum power, exploiting their high gain in order to compensate for the greater pathloss witnessed in the upper spectrum. Hence models for the maximum power are also valuable. In this paper, we present both model types for indoor hotspot deployment at 83.5 GHz. The environments considered – a basement, lobby, and hallway in line- and non-line-of-sight conditions up to 24 m range – are typical of such deployments. To fit the models, a measurement campaign with over 1500 different transmitter-receiver configurations was conducted using a correlation-based channel sounder. Computation of the maximum-power model is enabled by the sounder's custom-designed antenna array which can resolve the receiver power into three-dimensional angles-of-arrival.**

***Keywords* — *E band; mmWave; millimeter-wave; channel propagation modeling; wireless system***

Figure 1: Custom-designed 16-port octagonal receiver antenna array.

## I. INTRODUCTION

Over less than a decade, radio-frequency transmission from data-intensive mobile devices has created a "spectrum crunch" below 6 GHz, prompting the wireless community to investigate the millimeter-wave band (30 – 300 GHz) as an alternative [1]. Although propagation is less favorable in this regime, channels with much wider bandwidths will be available. To effectively design communication systems here, fundamental understanding of the propagation characteristics expressed through channel models is required. The most basic and useful of models for link-layer analysis is pathloss. To our knowledge, indoor pathloss models for next-generation Wireless Local Area Networks (WLAN) and Local Multipoint Distribution System (LMDS) deployments are still lacking to date.

The choice spectrum allocated by the Federal Communications Commission (FCC) for fixed-mobile, up to 850 MHz wide, lies on the band edge around 30 GHz [2]. Hence a reasonable number of publications for indoor pathloss models there have already appeared in the literature. Some of the most recent, which consider obstructed- and/or non-line-of-sight in the range up to tens of meters, are [3][4][5]. Similar set-ups can be found at 60 GHz in [6][7][8]: although less favorable due to oxygen absorption loss, it is still attractive given the broad unlicensed band from 57-63 GHz (recently extended as 57-71 GHz). As such, these two bands have been studied the most.

The E band (71-76 GHz, 81-86 GHz, and 92-95 GHz) has received significantly less attention than 60 GHz due to licensing requirements and greater freespace propagation loss. Nevertheless, the fact that it is not subject to oxygen absorption loss more than compensates for the latter; hence the lack of propagation measurements, both indoors and outdoors, for this band is surprising: in [9], spatio-temporal models are provided at 72 GHz (and 63 GHz) for an office environment from 24 measurements, however only in line-of-sight (LOS) conditions up to a range of 10 m. In [10], wideband measurements were taken at 70, 88, and 108 GHz in LOS up to 6 m. Less recently, slightly longer-range measurements were taken at 94 GHz in LOS and obstructed-LOS conditions [11][12]. And in [13], pathloss models and dispersion statistics in LOS and non-LOS (NLOS) at 73 GHz (and 28 GHz) are provided for an indoor office environment; the models were collected for 48 different TX-RX configurations in the range 4 - 46 m.



Gentile, Camillo; Senic, Jelena; Papazian, Peter; Choi, Jae-Kark; Remley, Catherine.
"Pathloss Models for Indoor Hotspot Deployment at 83.5 GHz."
Paper presented at , Washington, DC, United States. December 4, 2016 - December 8, 2016.

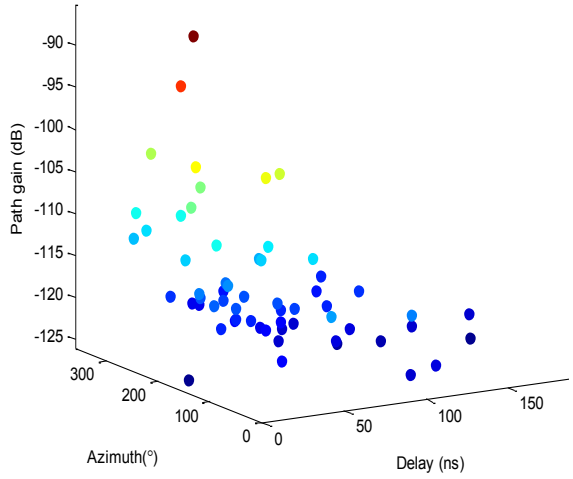


Figure 2: Directional channel impulse response of an example TX-RX configuration. Each circle indicates an extracted multipath-channel component color-coded according to path gain.

In this paper, we present pathloss models at 83.5 GHz for two indoor environments: a basement and a lobby / hallway area. The models were generated from measurements over 1500 different transmitter-receiver configurations using a correlation-based channel sounder. Conventional pathloss models are based on received power from an omnidirectional antenna. Millimeter-wave receivers, however, are envisioned to have highly directional antennas which can be steered towards the angle with maximum power. Hence models for the maximum power are also valuable. Given the custom-designed antenna array at the receiver, our channel sounder is capable of resolving the received power into three-dimensional angles-of-arrival. Accordingly, we provide two pathloss models: one for the maximum-power path and one for the paths combined from all directions.

The paper is organized as follows: Section II describes the channel sounder used to collect measurements and how the measurements were processed into pathloss data points. Section III presents the general breakpoint model we adopted and how its parameters were fit to the model in the environments; discussion on the parameters is provided in this section as well. The paper is concluded with a summary.

## II. MEASUREMENT SYSTEM

This section describes the channel sounder we designed and how it measures channel impulse responses (CIRs). Also described is how the responses were processed for the purpose of fitting pathloss models to the data collected.

### A. *Channel Sounder*

The channel sounder consists of a transmitter (TX) section and a receiver (RX) section. At the TX, an arbitrary waveform generator synthesizes a 2047-bit length pseudorandom-noise (PN) code which is BPSK modulated by a 3 GHz intermediate-frequency (IF) carrier. The bit rate of the code is 1 Gbit/s and it occupies a 2 GHz null-to-null bandwidth. The code is repeated continuously. The signal is upconverted to a center frequency of 83.5 GHz and into the transmitter port with 12 dBm power. The antenna is omndirectional in azimuth with a 45° beamwidth in elevation; its gain is 4 dBi.

The front end of the receiver is a custom-designed octagonal waveguide antenna multiplexer (see Figure 1). Connected to the 16 input ports of the array are scalar-feed-horn antennas. The antennas have a 45° beamwidth with an associated gain of 12.2 dBi. Eight of the antennas are oriented toward the horizon while the other eight are oriented 45° upward. This arrangement was chosen to enable coverage of the upper hemisphere. Switching between the output ports is accomplished through sequential on/off biasing of the low-noise amplifiers (LNAs). The LNAs have a 25 dB gain and a noise figure of 6 dB. Together with the other elements of the link budget, the maximum-measureable dynamic range of the system [14] is 140.2 dB. The 16 LNAs are multiplexed into a single waveguide output port. The 83.5 GHz wideband modulated signal from the RX antenna array is then downconverted to a 5 GHz IF and digitized at a rate of 40 Gsymbols/s. Because there are 16 ports and each port is sampled for the duration of two codewords, a complete array sweep lasts 32 codewords or 65.5 µs.

To analyze the measured data, position, velocity, and heading of the receiver array are needed. This information is provided through a robotic mobile positioning system (red box-like apparatus in the foreground of Figure 3(a)). The survey area is first mapped through the robot's laser range-finder. Once the map is created, the onboard computer can direct the robot to waypoints while simultaneously recording position information from the navigation system and controlling the digitizer. In this way, the information can be queried and stored with the digitizer data at millisecond intervals while the robot is moving. Internal studies at NIST have shown position errors of 20 cm at 100 m range and angular errors of ~1°. Further details of the channel sounder and mobile positioning system are provided in [15].

### B. *Measured Data Points*

The system collected measurements at a number of TX-RX configurations throughout each environment. Let $i$ denote the configuration index and $d_i$ the associated distance recorded. At the receiver, the digitized IF signal at the array port was converted to baseband and subsequently correlated with the PN code. This resulted in the impulse response of the channel between the TX and the RX port. A post-distortion filter was applied to remove the system effects through a back-to-back calibration step [16]. That way the output of the filter represented the response of the channel plus the antennas only.



Gentile, Camillo; Senic, Jelena; Papazian, Peter; Choi, Jae-Kark; Remley, Catherine.
"Pathloss Models for Indoor Hotspot Deployment at 83.5 GHz."
Paper presented at , Washington, DC, United States. December 4, 2016 - December 8, 2016.

(a) Photograph

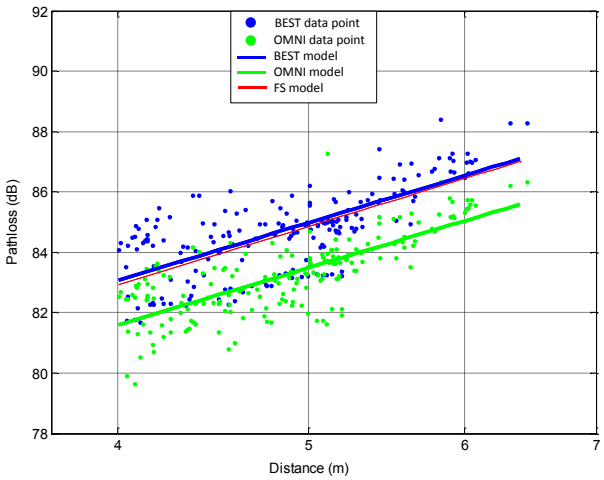


(b) Pathloss model

Figure 3: Basement environment

The 16 CIRs from one measurement were synthesized through the Space-Alternating Generalized Expectation-maximization (SAGE) algorithm [17] to yield the directional impulse response of the channel. The scope of the algorithm is twofold: 1. to deconvolve the receiver array antenna patterns from the impulse responses; 2. to extract the $j^{th}$ multipath component of the directional channel, namely its complex amplitude $(a_{ij})$, delay, and angle-of-arrival (azimuth and elevation). Figure 2 displays a three-dimensional plot of the multipath components (elevation dimension is omitted) for an example directional impulse response.

From the extracted multipath components, two pathloss metrics were computed: one for the maximum-power path, $PL^{BEST}$, and one for the paths combined from all directions, $PL^{OMNI}$:

$$PL^{BEST}(d_i) = -10\,log_{10}\,\max_j |a_{ij}|^2 \quad (1a)$$

$$PL^{OMNI}(d_i) = -10\,log_{10}\sum_j |a_{ij}|^2 . \quad (1b)$$

For each configuration, 32 measurements were collected over a period of 67 ms while the robot was in motion. Depending on its speed, the robot traveled 20 – 40 mm, roughly seven to ten wavelengths. To factor out small-scale fading, the metrics were averaged over the 32 points. Once collected, the robot downloaded the data and then began measuring for the next configuration. The average distance between configurations was about 30 cm.

## III. Pathloss Models

In this section, we present pathloss models for the two environments investigated. The generalized breakpoint model we adopt in decibels is

$$PL(d) = \begin{cases} 10\,\alpha_0\,log_{10}\left(\frac{d}{d_0}\right) + \beta_0 + \mathcal{N}(0,\sigma_0),\ d \le d_1 & (2a) \\ \overline{PL}(d_1) + 10\,\alpha_1\,log_{10}\left(\frac{d}{d_1}\right) + \beta_1 + \mathcal{N}(0,\sigma_1), d > d_1 & (2b) \end{cases}.$$

The parameter $\beta_0$ denotes the reference pathloss at $d_0$ = 1 m while $\alpha_0$ and $\sigma_0$ respectively denote the pathloss exponent and standard deviation of the normally distributed shadowing component before the breakpoint distance, $d_1$. The parameters have analogous values $(\alpha_1, \beta_1, \sigma_1)$ in the second piecewise segment, except for $\beta_1$which is the additional loss above the breakpoint average. The average breakpoint loss is defined as

$$\overline{PL}(d_1) = 10\,\alpha_0\,log_{10}\left(\frac{d_1}{d_0}\right) + \beta_0. \quad (3)$$



Gentile, Camillo; Senic, Jelena; Papazian, Peter; Choi, Jae-Kark; Remley, Catherine.
"Pathloss Models for Indoor Hotspot Deployment at 83.5 GHz."
Paper presented at , Washington, DC, United States. December 4, 2016 - December 8, 2016.

(a) Photograph

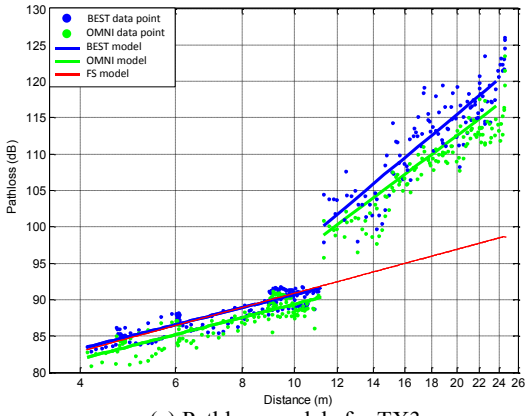


(c) Pathloss models for TX3

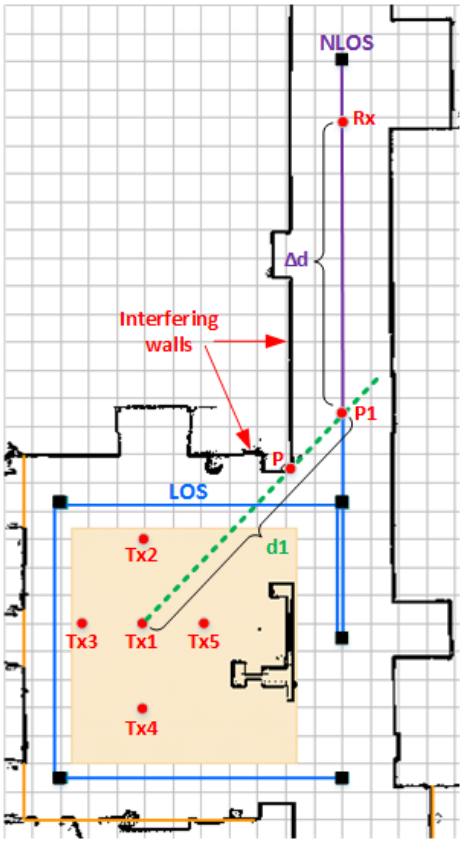


(b) Floorplan

Figure 4. The Lobby / Hallway environment

### A. *Basement Environment*

The first indoor environment we considered is the basement[1] area shown in Figure 3(a). The floor of this area is a metal ground plane and the walls of the room are cinderblock. The room ceiling is 4.9 m high. The photograph shows a hotspot set-up, which applies to all environments described in this paper, with the transmitter antenna fixed at 2.5 m height (background left, mounted on the tripod) and the receiver antenna at 1.6 m (foreground middle, mounted on the robot).

Figure 3(b) illustrates the BEST pathloss model for the Basement as a blue line. It was obtained by fitting (2a) to the $PL^{BEST}(d_i)$ data (blue dots) in (1a) through least-squares regression. Because all measurements were in LOS and the range was so small (less than 7 m), no breakpoint was necessary. Also shown in the plot is the free-space (FS) model [18] in red. The fit to the FS is good, both in terms of $\alpha_0^{BEST}$ = 1.97 ($\alpha^{FS}$ = 2.0) and $\beta_0^{BEST}$ = 71.17 dB ($\beta^{FS}$ = 70.85 dB). The nominal transmitter / receiver antenna patterns from the manufacturer were used in the SAGE algorithm (Section II.B) since the antennas have not yet been properly calibrated in an anechoic chamber. The maximum variation from spec is listed as 2 dB to which we attribute deviations of the data points from the FS line.

The OMNI pathloss model (green line) was similarly obtained from the $PL^{OMNI}(d_i)$ data (green dots) in (1b) instead. Notice that the difference between BEST and OMNI is about 1.4 dB; this means that the maximum path accounts for 72% of the total power and conversely that the secondary paths account

[1] The area is actually a laboratory, but since the walls are cinderblock and there are no windows, it is representative of a basement.



Gentile, Camillo; Senic, Jelena; Papazian, Peter; Choi, Jae-Kark; Remley, Catherine.
"Pathloss Models for Indoor Hotspot Deployment at 83.5 GHz."
Paper presented at , Washington, DC, United States. December 4, 2016 - December 8, 2016.

| environment | # data points | range (m) | wall materials | $\alpha_0$ | $\beta_0$ (dB) | $\sigma_0$ (dB) | $d_1$ (m) | $\alpha_1$ | $\beta_1$ (dB) | $\sigma_1$ (dB) |
|---|---|---|---|---|---|---|---|---|---|---|
| Basement | 351 | 4.0 – 6.5 | cinderblock | 1.97 | 71.18 | 1.09 | | | | |
| | | | | 1.96 | 69.80 | 0.86 | | | | |
| Lobby / Hallway TX1 | 234 | 4.0 – 21.4 | stone / wood / metal | 2.37 | 67.87 | 2.34 | 10.1 | 7.45 | 2.66 | 3.87 |
| | | | | 2.39 | 66.85 | 1.73 | | 5.30 | 3.94 | 2.28 |
| Lobby / Hallway TX2 | 210 | 4.0 – 18.5 | | 1.75 | 73.26 | 1.13 | 7.8 | 4.21 | 14.92 | 3.74 |
| | | | | 1.46 | 74.66 | 1.22 | | 3.00 | 12.96 | 1.92 |
| Lobby / Hallway TX3 | 296 | 4.1 – 22.0 | | 1.87 | 72.00 | 1.25 | 11.3 | 6.16 | 8.44 | 3.04 |
| | | | | 1.90 | 70.41 | 1.41 | | 5.52 | 7.09 | 2.03 |
| Lobby / Hallway TX4 | 241 | 4.0 – 24.0 | | 2.05 | 70.16 | 1.27 | 13.3 | 4.38 | 4.40 | 5.35 |
| | | | | 2.05 | 69.34 | 1.10 | | 4.11 | 3.48 | 3.83 |
| Lobby / Hallway TX5 | 217 | 5.0 – 20.6 | | 1.57 | 74.49 | 1.19 | 9.6 | 3.35 | 6.10 | 5.08 |
| | | | | 1.68 | 72.70 | 1.19 | | 3.00 | 5.38 | 3.73 |

Table 1: Environment settings and pathloss model parameters. The light- and dark-shaded entries pertain respectively to the BEST and OMNI models only.

for only 28% of it. Furthermore, because each data point in OMNI also incorporates many other secondary arrivals, the fluctuation in the max arrival will be dampened by the fluctuations in the other arrivals. For this reason, OMNI exhibits a smaller standard deviation ($\sigma_0^{OMNI}$ = 0.86 dB) compared to BEST ($\sigma_0^{BEST}$ = 1.09 dB) in this environment and, as we shall see, in the other environment for the most part. Table I shows the settings and pathloss model parameters for the environments.

### *B. Lobby / Hallway Environment*

In the second environment that we investigated, the transmitter was placed at five different locations in a lobby area connected to a hallway. The ceiling heights of the lobby and hallway are 3 m and 7 m respectively. A photograph of the environment is pictured in Figure 4(a) and the locations (TX1 – TX5) are shown on the floorplan in Figure 4(b). For each location, the robot traversed the same trajectory delineated by the black waypoints: the LOS segment appears in blue and the NLOS in purple. Non-line-of-sight was created by the interfering walls when the direct path was lost at breakpoint $P_1$ as the RX moved down the hallway. The breakpoint was computed analytically as the intersection of the line (green dotted) containing the TX position and the corner (P) and the line along the robot's trajectory in the hallway. The breakpoint distance, $d_1$, is given as the distance from the TX to this point. Note that each transmitter has a distinct breakpoint.

The breakpoint served to partition the collected pathloss data into LOS and NLOS points. First, for each TX, the $(\alpha_0, \beta_0, \sigma_0)$ parameters were extracted from the LOS points and used to compute $\overline{PL}(d_1)$ from (3). The latter was then subtracted from the measured pathloss of the NLOS points. Finally, rearranging (2b), the parameters $(\alpha_1, \beta_1, \sigma_1)$ were fit to the difference:

$$PL(d) - \overline{PL}(d_1) = 10\,\alpha_1\, log_{10}\left(\frac{d}{d_1}\right) + \beta_1 + \mathcal{N}(0, \sigma_1). \quad (4)$$

For $d > d_1$, the distance was computed as $d = d_1 + \Delta d$, where $\Delta d$ denotes the incremental distance along the hallway (see Figure 4(b)). This metric provided a better fit than the Euclidean distance and is supported by evidence in [19][20]. The better fit stems from the fact that at this center frequency there is no noticeable wall penetration by the signal; it is therefore more accurate to model the distance along the maximum propagation path.

Table I shows the parameter values for the five TX locations. For instance, consider the pathloss model for TX3 in Figure 4(c). In line-of-sight conditions, the extracted parameters match well to freespace, as before, and the difference between BEST and OMNI is about 1.6 dB (secondary power accounts for 31% of total power), comparable to Basement. In non-line-of-sight, the direct path is lost and so the propagation mechanisms of the dominant path (diffraction and reflection rather than direct transmission) are the same as the secondary paths. This is why the exponent and the standard deviation both increase precipitously from $\alpha_0^{BEST}$ = 1.87 to $\alpha_1^{BEST}$ = 6.16 and from $\sigma_0^{BEST}$ = 1.25 dB to $\sigma_1^{BEST}$ = 3.04 dB respectively. Although they experience the same propagation mechanisms, the exponent of OMNI is smaller than BEST, meaning that the dominant path dies down at a faster rate than the secondary paths. From the different exponents, it follows that the gap between BEST and OMNI begins to widen at the breakpoint and ultimately reaches 3.4 dB. At this end range, the secondary power accounts for more than half of the total power.



Gentile, Camillo; Senic, Jelena; Papazian, Peter; Choi, Jae-Kark; Remley, Catherine.
"Pathloss Models for Indoor Hotspot Deployment at 83.5 GHz."
Paper presented at , Washington, DC, United States. December 4, 2016 - December 8, 2016.

## IV. Summary and Conclusion

In this paper, we presented pathloss models for indoor hotspot deployment at 83.5 GHz. The indoor environments investigated are typical of such deployments, namely a basement, lobby, and hallway in line- and non-line-of-sight conditions up to a range of 24 m. To fit the models, a custom-designed channel sounder recorded measurements over 1500 different transmitter-receiver configurations. In LOS, a good match was observed between our pathloss models and freespace prediction, validating our calibration procedures. In NLOS, the pathloss exponents increased precipitously, varying between 3.00 and 7.45 depending on the model and the TX position. This is because the direct path goes undetected due to the high penetration loss of the interfering walls at this frequency.

## References


[1] "Cisco Visual Networking Index: Global Mobile Data Traffic Forecast Update, 2015–2020," white paper, Feb. 2016.

[2] Federal Communications Commission Office of Engineering and Technology Policy and Rules Divison, "FCC Online Table of Frequency Allocations," 47 C.F.R. § 2.106, March 2016.

[3] T.S. Rappaport, S. Shu, R. Mayzus, H. Zhao, Y. Azar, K. Wang, G.N. Wong, J.K. Schulz, M. Samimi, and F. Gutierrez, "Millimeter wave mobile communications for 5G cellular: It will work!" *IEEE Access*, vol. 1, pp. 335-349, May 2013.

[4] M. Lei, J. Zhang, T. Lei, D. Du, "28-GHz indoor channel measurements and analysis of propagation characteristics," *IEEE Personal, Indoor, and Mobile Radio Communication Conf.*, pp. 208-212, Sept. 2014.

[5] O.H. Koymen, A. Partyka, S. Subramanian, J. Li, "Indoor mm-Wave Channel Measurements: Comparative Study of 2.9 GHz and 29 GHz," *IEEE Global Communications Conf.*, pp. 1-6, Dec. 2015.

[6] N. Moraitis, P. Constantinou, "Indoor channel measurements and characterization at 60 GHz for wireless local area network applications," *IEEE Transactions on Antennas and Propagation*, vol. 52, no. 12, pp. 3180 -3189, Dec. 2004.

[7] S. Geng, J. Kivinen, X. Zhao, P. Vainikainen, "Millimeter-Wave Propagation Channel Characterization for Short-Range Wireless Communications," *IEEE Transactions on Vehicular Technology,* vol. 58, no. 1, pp. 3-13, Jan. 2009.

[8] M.-W. Jung, J. Kim, Y.-K. Yoon, "Measurements of path loss in MM-wave for indoor environments," *IEEE Asia Pacific Microwave Conf.*, pp. 1068-1071, Dec. 2009.

[9] K. Haneda, J. Järveläinen, A. Karttunen, M. Kyrö, and J. Putkonen, "A Statistical Spatio-Temporal Radio Channel Model for Large Indoor Environments at 60 and 70 GHz," IEEE Trans. on Antennas and Propagation, vol. 63, no. 6, pp. 2694-2704, June 2015.

[10] M. Jacob and T. Kurner, "Radio channel characteristics for broadband WLAN/WPAN applications between 67 and 110 GHz," *IEEE European Conf. on Antennas and Propagation*, pp. 2663 - 2667, March 2009.

[11] A. Kajiwara, "Indoor propagation measurements at 94 GHz," *Personal, Indoor, and Mobile Radio Communications Conf*., pp. 1026-1030, Sept. 1995.

[12] J. Helminger, J. Detlefsen, H. Groll, "Propagation properties of an indoor-channel at 94 GHz," *Intl. Conf. on Microwave and Millimeter Wave Technology*, pp 9-14, Aug. 1998.

[13] S. Deng, M.K. Samimi, T.S. Rappaport, "28 GHz and 73 GHz Millimeter-Wave Indoor Propagation Measurements and Path Loss Models," IEEE Intl. Conf. on Communications, pp. 1244-1250, June 2015.

[14] T.S. Rappaport, G.R. MacCartney, Jr., M.K. Samimi, and S. Sun, "Wideband Millimeter-Wave Propagation Measurements and Channel Models for Future Wireless Communication System Design," IEEE Trans. on Communication, vol. 63, no. 9, pp. 3029-3056, Sept. 2015.

[15] P.B. Papazian, C. Gentile, K.A. Remley, J. Senic, and N. Golmie, "A Radio Channel Sounder for Mobile Millimeter-Wave Communications: System Implementation and Measurement Assessment," *To appear in IEEE Transactions on Microwave Theory and Techniques*, Jan. 2017.

[16] P.B. Papazian, J.-K. Choi, J. Senic, P. Jeavons, C. Gentile, N. Golmie, R. Sun, D. Novotny, K.A. Remley, "Calibration of Millimeter-wave Channel Sounders for Super-resolution Multipath Component Extraction," *IEEE European Conf. on Antennas and Propagation*, pp. 1-5, April 2016.

[17] K. Hausmair, K. Witrisal, P. Meissner, C. Steiner, G. Kail, "SAGE Algorithm for UWB Channel Parameter Estimation," *COST 2100 Management Committee Meeting*, pp. 1-7. Feb. 2010.

[18] H. Friis, "A note on a simple transmission formula*," Proceedings of the IRE*, vol. 34, no. 5, pp. 254–256, May 1964.

[19] D.W. Matolak, K.A. Remley, C. Gentile, C.L. Holloway, Q. Wu, and Q. Zhang, "Peer-to-Peer Urban Channel Characteristics for Two Public-Safety Frequency Bands," *IEEE Antennas and Propagation Magazine*, vol. 56, no. 5, pp. 101-115. Oct. 2014.

[20] A.F. Molisch, A. Karttunen, S. Hur, J. Park, J. Zhang, "Spatially consistent pathloss modeling for millimeter-wave channels in urban environments," *IEEE European Conf. on Antennas and Propagation*, pp. 1-5, April 2016.




Gentile, Camillo; Senic, Jelena; Papazian, Peter; Choi, Jae-Kark; Remley, Catherine.
"Pathloss Models for Indoor Hotspot Deployment at 83.5 GHz."
Paper presented at , Washington, DC, United States. December 4, 2016 - December 8, 2016.

# The Role of Measurement Uncertainty in Achieving First-Pass Design Success

Dylan F. Williams,[1] Richard A. Chamberlin, [1] Wei Zhao, [2] Jerome Cheron, [1] Miguel E. Urteaga[3]

[1]National Institute of Standards and Technology (NIST), Boulder, CO, 80302, USA, [+1] (303) 497-3138, dylan.williams@nist.gov. [2]Xidian University, Xi'an, Shaanxi province, China. [3]Teledyne Scientific, Thousand Oaks, CA USA.

***Abstract*— We investigate the role of measurement uncertainty in achieving first-pass design success at microwave frequencies. We develop a model for state-of-the-art 250 nm heterojunction bipolar transistors, and demonstrate the propagation of correlated measurement uncertainties through the model-extraction and verification process. We then investigate the accuracy of the extracted model parameters and the role of measurement uncertainty in gauging the ability of the model to predict the behavior of the transistor in large-signal operating states.**

***Index Terms*—measurement uncertainty, microwave measurement, model verification, transistor model.**

## I. Introduction

Compact models are designed to capture the essential physics governing a transistor's behavior and to be used well outside the space of measurements used in the model-parameter extraction process. Nevertheless, practical limitations always restrict the data sets used in even the most comprehensive transistor-model extraction procedures, and models are often used well outside of the operating conditions under which they were developed. Here, we investigate the role of uncertainty in microwave measurements used to extract model parameters that are later used to predict transistor behavior outside of the measurement space.

A number of authors have studied two-tier approaches [1-5] and parasitic extraction techniques [5-8] to improve transistor characterization. Lin and Zhang studied error propagation in large-signal network analysis in [9]. Lenk and Rudolph performed a very interesting sensitivity analysis of a heterojunction bipolar transistor (HBT) extraction process in [10]. They used it as a tool for evaluating the sensitivity of the extraction process to measurement error and identifying poorly-conditioned models. Miranda *et al*. studied the impact of on-wafer calibration kits on the extraction of high-electron-mobility-transistor (HEMT) models at microwave frequencies in [11]. Williams *et al*. argue that on-wafer thru-reflect-line calibrations improve the accuracy of HBT and complementary-metal-oxide (CMOS) transistor measurements in [12;13].

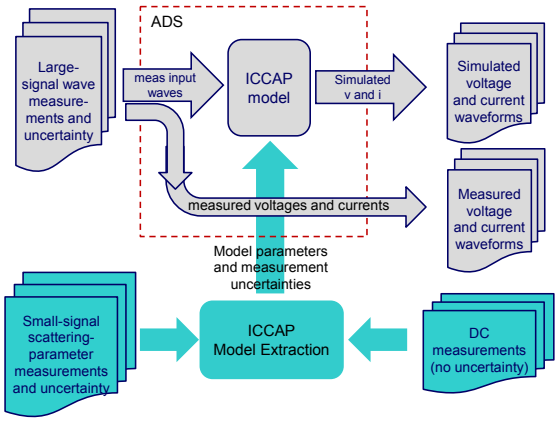


Fig. 1. Our extraction and verification approach. Measurement uncertainties were accounted for in both the model-extraction and verification procedures. From [16].

Avolio *et al*. examined the impact of measurement uncertainty on transistor capacitances and the temporal current and voltage waveforms and impedances at the transistor current-generator plane in [14], and used the measurements to develop a measurement-based transistor model.

In [15;16], we demonstrated the propagation of measurement uncertainty through the model-extraction process, and compared the measured behavior of the transistor under large-signal operating conditions to its simulated performance.

## II. Model Extraction

Figure 1 shows the model-verification procedure we used in our prior work [16]. The transistors we studied were

This work was supported in part by the Defense Advanced Research Projects Agency's Terahertz Electronics Program. The views, opinions, and/or findings contained in this article are those of the author and should not be interpreted as representing the official views or policies, either expressed or implied, of either the Defense Advanced Research Projects Agency or the Department of Defense.



Williams, Dylan; Chamberlin, Richard; Zhao, Wei; Cheron, Jerome; Miguel, Urteaga.
"The Role of Measurement Uncertainty in Achieving First-Pass Design Success."
Paper presented at 2016 IEEE Compound Semiconductor Integrated Circuit Symposium (CSICS), Austin, TX, United States. October 23, 2016 - October 26, 2016.

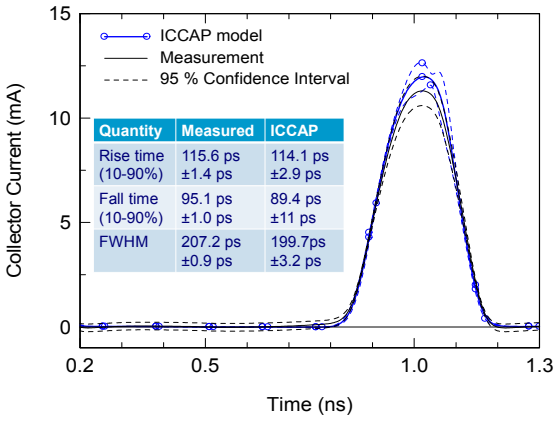


Fig. 2. Transistor collector current, pulse parameters and uncertainties in deep Class A/B at a -5 dBm drive level with bias $V_c$ = 1 V and $I_c$ = 2 mA. After [16].

fabricated at Teledyne Scientific with a state-of-the-art 250 nm HBT process. We extracted a model based on version 2.0 of the Keysight[1] HBT model using the Keysight Integrated-Circuit Characterization and Analysis Program (ICCAP) software. implemented in their Advanced Design System (ADS) software (see [17]). In [16], we were able to verify the ability of the Teledyne model to predict the behavior of an HBT with a 6 µm by 250 nm emitter under large-signal excitation, and to evaluate the impact of measurement errors on the verification procedure.

### A. Calibration

In prior work [18;19], we found that accurate calibrations improve the model extraction process. We used the custom thru-reflect-line (TRL) on-wafer calibration kit described in [20] to calibrate the scattering-parameters and wave parameters measured in this study. We had two reasons for this choice.

First, we have shown in prior work that on-wafer TRL calibration kits allow the measurement reference plane to be moved right next to the transistor under test. In this way, parasitics associated with the contact pads and access line can be removed from the scattering-parameter calibrations and the voltages and currents at the transistor terminals can be measured with greater fidelity than is possible with other methods.

Second, the TRL calibration is based on transmission-line propagation. It rigorously solves for forward and backward-wave amplitudes, and then constructs voltages and current waveforms from those amplitudes in a clearly defined way. As a result, the systematic errors of the TRL calibration are few and are easily characterized with simple, well-understood models. This made it much easier for us to identify and track correlations in measurement uncertainty throughout the analysis.

[1] We identify commercial products only to accurately describe the experiments and analysis we performed. The National Institute of Standards and Technology does not endorse commercial products. Other products may work as well or better.

We also used a conventional first-tier 2.4 mm short-open-load-thru (SOLT) calibration to perform the power and phase calibrations needed to fix the wave amplitudes and phases of the large-signal measurements we made. Both the 2.4 mm SOLT and the on-wafer TRL calibrations were implemented in the NIST Microwave Uncertainty Framework [21], which we used to model measurement errors and propagate them through the calibration and analysis.

### B. Uncertainty Propagation Through the ICCAP Model-Extraction Procedure

No measurements are perfect, including the small-signal measurements we used in the ICCAP procedure to extract the HBT model parameters. The errors in these measurements will add error to the HBT model parameters extracted by ICCAP.

We used the NIST Microwave Uncertainty Framework [21] not only to estimate our measurement errors, but also to propagate our measurement uncertainties through the ICCAP model-extraction procedure. That allowed us to estimate the uncertainties of the model parameters determined by ICCAP due to the errors in the measurements used in the model-parameter extraction procedure. Table I lists a few representative parameters and their uncertainties.

The table shows that ICCAP did a good job of extracting model parameters like the transistor's saturation current IS, collector capacitance CJC, and low-current transit time TFC0 despite the errors in the small-signal measurements that we used in the extraction procedure. These parameters are needed to simulate small-signal and high-frequency transistor behavior, as well as transit times when current flow through the transistor is low.

However, Table I also reveals that the ICCAP extraction procedure did not do nearly as good a job of determining the high-current transit time TCMIN from our measured data, and completely failed to determine the Kirk-effect critical current IKRK accurately. These model parameters are used to calculate transit times when current flow through the transistor is very high.

## III. Model Verification

The uncertainties listed in Table I indicate that we expect the ICCAP model to accurately predict small-signal performance, but not transistor behavior in large-signal operating states that drive currents in the Kirk-effect region. To test this, we measured the response of our HBTs to a 1 GHz drive signal under large-signal operating conditions at a number of bias states. We varied the drive level of that signal

TABLE I
Extracted ICCAP Model Parameters

| Parameter | Units | Nominal Value | Standard Uncertainty | Relative Uncertainty |
|---|---|---|---|---|
| IS | fA | 1.39 | ± 0.09 | 6 % |
| CJC | fF | 12.1 | ± 1.1 | 9 % |
| TFC0 | fs | 355 | ± 55 | 15 % |
| TCMIN | fs | 74 | ± 43 | 58 % |
| IKRK | mA | 46 | ± 161 | 350 % |

Williams, Dylan; Chamberlin, Richard; Zhao, Wei; Cheron, Jerome; Miguel, Urteaga.
"The Role of Measurement Uncertainty in Achieving First-Pass Design Success."
Paper presented at 2016 IEEE Compound Semiconductor Integrated Circuit Symposium (CSICS), Austin, TX, United States. October 23, 2016 - October 26, 2016.

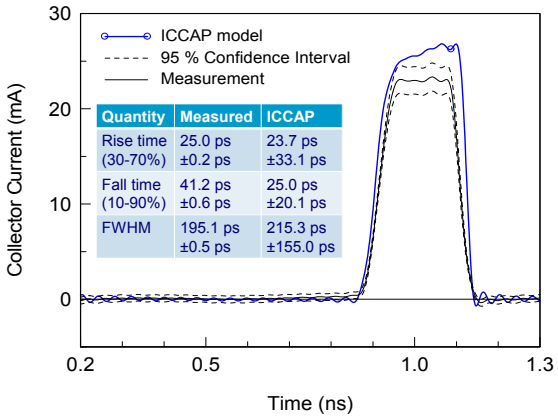


Fig. 3. Transistor collector current, pulse parameters and uncertainties in deep compression at a +5 dBm drive level with bias $V_c$ = 1.8 V and $I_c$ = 8 mA. The differences in the shapes of the measured and simulated collector-current waveforms are much greater in deep compression. The uncertainties in the collector current derived from simulations based on the ICCAP model are shown in Fig. 4 for clarity. After [16].

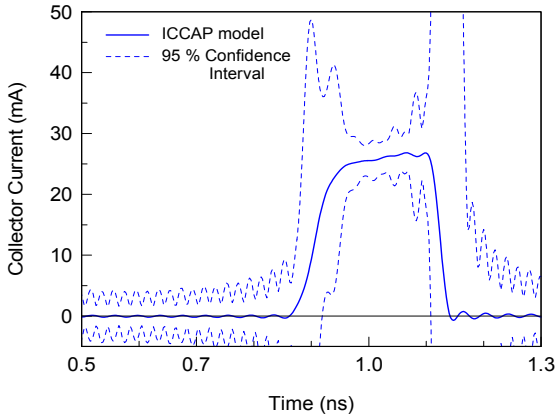


Fig. 4. Uncertainties of the transistor collector-current waveform derived from simulations based on the ICCAP model in deep compression at a +5 dBm drive level with bias $V_c$ = 1.8 V and $I_c$ = 8 mA. The large uncertainty levels are due in part to instability in the extraction procedure as the model becomes non-physical in the Kirk-effect region. From [16].

from -25 dBm to + 5 dBm, sweeping through regions of linear operation, deep class A/B operation, and finally, deep compression where we expect the Kirk effect to become important.

### A. *Deep Class A/B Operation*

We found excellent agreement between the measured and predicted base and collector voltage and current waveforms up to a transistor drive level of about -5 dBm. Figure 2 shows an example at a -5 dBm drive level, which exhibited the worst performance over this range and corresponds to deep Class AB operation. Furthermore, the differences between the ADS simulations and measurements are comparable to the uncertainties we estimated, and we see that the measurement uncertainty predicts well the performance of the model.

### B. *Deep Compression*

When the drive level exceeded 0 dBm, the discrepancies between simulations and our verification measurements became quite noticeable, as we might expect from the uncertainties in Table I. Figure 3 compares the measured collector currents and their uncertainties at a drive level of +5 dBm to ADS simulations based on the two models.

We also see that the simulations fall well outside of the uncertainties of the measured collector-current waveform. The uncertainties in the collector-current rise time, fall time, and full-width-half-max (FWHM) simulated with the ICCAP model as listed in the inset table of Fig. 3 are significantly larger than those shown in Fig. 2.

Figure 4 shows the uncertainty in the collector-current waveform calculated from the ICCAP model, and it is also considerably larger than the uncertainties in Fig. 2. These uncertainties in the simulations based on the ICCAP model seem unexpectedly high, at least when compared to the uncertainties in our measurements.

### C. *Interpretation of Uncertainty in Simulated Results*

The procedure we used in Fig. 1 was designed to propagate our estimates of our small-signal measurement uncertainties through the ICCAP model extraction procedure and our simulations. What we see in Figs. 2-4 is the usefulness of propagating our measurement uncertainty all the way through the simulation process. Here we see that the uncertainty in our simulations due to error in the small-signal measurements used in the model-extraction process is low where we expect the model to perform accurately, but becomes very large when the transistors are driven into operating states that cause the model to fail. This indicates a possible role for measurement uncertainty in predicting first-pass design success that goes well beyond simply increasing confidence in the measurements themselves.

## IV. Conclusion

We propagated measurement uncertainty through the ICCAP extraction procedure, and assigned uncertainties to the model parameters extracted by ICCAP. This, in turn, led to the identification of the parameters that were determined accurately in the extraction procedure, and which parameters were not.

In this particular case, we found that ICCAP determined most of the parameters of the model quite accurately. However, an examination of the uncertainties in the model parameters we extracted with ICCAP showed that we were not able to accurately determine some parameters in the model needed to characterize the transit time and Kirk effect in deep compression, where the fits used to model the transit time appeared to not be physical.

Later, during the verification stage of the work, we showed that propagating our measurement uncertainty through the simulations allowed us to identify which simulations were accurate and which were not. This points to a possible role for

Williams, Dylan; Chamberlin, Richard; Zhao, Wei; Cheron, Jerome; Miguel, Urteaga.
"The Role of Measurement Uncertainty in Achieving First-Pass Design Success."
Paper presented at 2016 IEEE Compound Semiconductor Integrated Circuit Symposium (CSICS), Austin, TX, United States. October 23, 2016 - October 26, 2016.

measurement uncertainty in predicting first-pass design success.

A full uncertainty analysis will require adding process variations to the model. This should not be difficult to do in the framework we have adopted for propagating uncertainty. However, additional work will also be required to better quantify errors due to non-physical fits employed in the models, perhaps relying on cross-validation approaches. Even so, we expect to be able to propagate measurement uncertainties all the way through the circuit-design process, and predict the accuracy of circuit simulations based on models extracted from measurement.

## ACKNOWLEDGMENT

The authors thank David Root, Masaya Iwamoto and Else Schmidt of Keysight Technologies for their insight and assistance in teaching us how to use the Keysight HBT models and software.

## REFERENCES

[1] Q. Liang, J. D. Cressler, G. Niu, Y. Lu, G. Freeman, D. C. Ahlgren, R. M. Malladi, K. Newton, and D. L. Harame, "A simple four-port parasitic deembedding methodology for high-frequency scattering parameter and noise characterization of SiGe HBTs," *IEEE Trans. Microwave Theory Tech.*, vol. 51, no. 11, pp. 2165-2174, Nov.2003.

[2] Q. Liang, W. Kuo, J. D. Cressler, and A. J. Joseph, "Accurate AC transistor characterization to 110 GHz using a new four-port selfcalibrated extraction technique," *IEEE Topical Meeting on Silicon Monolithic Integrated Circuits in RF Systems*, pp. 282-285, Sept.2004.

[3] X. Wei, K. Xia, G. Niu, Y. LI, S. L. Sweeney, Q. Liang, X. Wang, and S. S. Taylor, "An Improved On-chip 4-Port Parasitics De-embedding Method with Application to RFCMOS," *Topical Meeting on Silicon Monolithic Integrated Circuits in RF Systems*, pp. 24-27, Dec.2007.

[4] L. F. Tiemeijer, R. J. Havens, A. B. M. Jansman, and Y. Bouttement, "Comparison of the 'pad-open-short' and 'open-short-load' deembedding techniques for accurate on-wafer RF characterization of high-quality passives," *IEEE Trans. Microwave Theory Tech.*, vol. 53, no. 2, pp. 723-729, Feb.2005.

[5] K. H. Yau, E. Dacquay, I. Sarkas, and S. P. Voinigescu, "Device and IC Characterization Above 100 GHz," *IEEE Microwave Magazine*, pp. 30-54, Feb.2012.

[6] A. Rumiantsev, P. Sakalas, N. Derrier, D. Celi, and M. Schroter, "Influence of probe tip calibration on measurement accuracy of small-signal parameters of advanced BiCMOS HBTs," *IEEE Bipolar/BiCMOS Circuits and Technology Meeting*, pp. 203-206, Sept.2011.

[7] A. Rumiantsev, S. L. Sweeney, and P. L. Corson, "Comparison of on-wafer multiline TRL and LRM+ calibrations for RF CMOS applications," *Automatic RF Techniques Group Conference Digest*, vol. 72, pp. 132-136, Oct.2008.

[8] A. Rumiantsev, P. L. Corson, S. L. Sweeney, and U. Arz, "Applying the calibration comparison technique for verification of transmission line standards on silicon up to 110 GHz," *Automatic RF Techniques Group Conference Digest*, vol. 73, pp. 1-6, Dec.2009.

[9] M. Lin and Y. Zhang, "Covariance-Matrix-Based Uncertainty Analysis for NVNA Measurements," *Instrumentation and Measurement, IEEE Transactions on*, vol. 61, no. 1, pp. 93-102, Jan.2012.

[10] F. Lenk and M. Rudolph, "Extraction of GaAs-HBT equivalaent circuit considering the impact of measurement errors," *Innovations with Microwaves and Light: Research reports from the Ferdinand-Braun-Institut fur Hochstrfrequenztechnik*, vol. 3, pp. 95-103, 2015.

[11] J. M. Miranda, C. Fager, H. Zirath, P. Sakalas, S. oz, and J. L. Sebastian, "Influence of the calibration kit on the estimation of parasitic effects in HEMT devices at microwave frequencies," *Instrumentation and Measurement, IEEE Transactions on*, vol. 51, no. 4, pp. 650-655, Aug.2002.

[12] D. F. Williams, A. C. Young, and M. Urteaga, "A Prescription for Sub-Millimeter-Wave Transistor Characterization," *IEEE Trans. THz Sci. Technol.*, pp. 433-439, Mar.2013.

[13] D. F. Williams, P. L. Corson, J. Sharma, H. Krishnaswamy, W. Tai, Z. George, D. Ricketts, P. Watson, E. Dacquay, and S. Voinigescu, "Calibration-Kit Design for Millimeter-Wave Silicon Integrated Circuits," *IEEE Trans. Microwave Theory Tech.*, vol. 61, no. 7, pp. 2685-2694, June2013.

[14] G. Avolio, A. Raffo, J. Jargon, P. D. Hale, D. M. M. Schreurs, and D. F. Williams, "Evaluation of Uncertainty in Temporal Waveforms of Microwave Transistors," *Microwave Theory and Techniques, IEEE Transactions on*, vol. 63, no. 7, pp. 2353-2363, July2015.

[15] D. F. Williams, W. Zhao, R. Chamberlin, J. Cheron, and M. Urteaga, "Verification of a foundry-developed transistor model with measurement uncertainty," *ARFTG Microwave Measurement Conference Digest*, vol. 87 May2016.

[16] D. F. Williams, R. Chamberlin, W. Zhao, J. Cheron, and M. Urteaga, "Transistor Model Verification Including Measurement Uncertainty," *IEEE Trans. Microwave Theory Techn.*, vol. Accepted for publication Nov.2016.

[17] M. Iwamoto, D. E. Root, J. B. Scott, A. Cognata, P. M. Asbeck, B. Hughes, and D. C. D'Avanzo, "Large-signal HBT model with improved collector transit time formulation for GaAs and InP technologies,", 2 ed 2003, pp. 635-638.

[18] D. F. Williams, A. C. Young, and M. Urteaga, "A Prescription for Sub-Millimeter-Wave Transistor Characterization," *IEEE Trans. THz Sci. Technol.*, pp. 433-439, Mar.2013.

[19] D. F. Williams, P. L. Corson, J. Sharma, H. Krishnaswamy, W. Tai, Z. George, D. Ricketts, P. Watson, E. Dacquay, and S. Voinigescu, "Calibration-Kit Design for Millimeter-Wave Silicon Integrated Circuits," *IEEE Trans. Microwave Theory Tech.*, vol. 61, no. 7, pp. 2685-2694, June2013.

[20] D. F. Williams, A. C. Young, and M. Urteaga, "A Prescription for Sub-Millimeter-Wave Transistor Characterization," *IEEE Trans. THz Sci. Technol.*, pp. 433-439, Mar.2013.

[21] D. F. Williams and A. Lewandowski, "NIST Microwave Uncertainty Framework," National Institute of Standards and Technology, http://www.nist.gov/ctl/rf-technology/related-software.cfm, 2011.

# Gain Comparison of a 3D-Printed Horn and an Electroformed Horn*

Michael Francis, David Novotny, Joshua Gordon, Alexandra Curtin, and Ronald Wittmann
Communications Technology Laboratory
National Institute of Standards and Technology Boulder, Colorado USA
Michael.francis@nist.gov


***Abstract*— The National Institute of Standards and Technology (NIST) has used the three-antenna extrapolation method to determine the on-axis gain of three horn antennas in the WR8 frequency band. One antenna is an electroformed μ=±1 probe with gain of about 9 dB. The second antenna is an electroformed pyramidal horn with a nominal gain of 15 dB. The third antenna is a 3D-printed corrugated horn with nominal gain of 24 dB. The gains of these horns are measured and compared to the predicted value. Our preliminary measurement results show that the 3D-printed horn has a gain that is substantially less than that expected based on its geometry. The two electroformed antennas are closer to their predicted gain values.**

## I. INTRODUCTION

This There is interest in climate monitoring in the 118 GHz molecular oxygen absorption band. The desire is to place instruments for this purpose on nanosatellites as described in [1]. To reduce costs and increase availability of parts, 3D-printed horns are being considered. The University of Colorado at Boulder (UCB) recently designed and manufactured a prototype corrugated 3D-printed circular-aperture horn and requested that NIST measure its gain and pattern.

A visual inspection of the 3D-printed corrugated horn reveals that the surface of this horn is significantly rougher than that of a similarly electroformed horn. We desire to know if this surface roughness leads to larger ohmic losses than in an electroformed horn or if there are other effects.

To determine if the gain is affected, we determined the on-axis gain of this prototype 3D-printed corrugated horn, plus an electroformed pyramidal standard gain horn and an electroformed μ=±1 probe using the three-antenna extrapolation method [2]. These gains were compared to values predicted by simulations from a finite element method solver for the μ=±1 probe and pyramidal horn and to a directivity value supplied by UCB for the 3D-printed horn [3]. UCB's directivity value is based on the design dimensions of the 3D-printed horn. [Note: the difference between gain and directivity is the ohmic loss.] The predicted gains/directivity of the antennas at 118.75 GHz are shown in Table I. The standard horn and the μ=±1 probe are gold plated to reduce ohmic loss. The 3D-printed conical horn is made of sintered aluminum.

NIST used the three-antenna extrapolation method [2] to determine the gains of the three antennas at 118.75 GHz. The NIST CROMMA (Configurable RObotic MilliMeter-wave Antenna) facility [4] was used to perform the extrapolation measurements. The extrapolation method fits the power received as a function of separation distance to a power series in 1/(separation distance)$^n$. The leading term in the power series is proportional to the pair gain $\sqrt{G_i G_j}$. By making measurements of three antennas in three unique pairs (1 vs 2, 1 vs 3, and 2 vs 3), we can determine the gain of all three antennas without knowing any of them *a priori*. For more details on this method, see [2].

TABLE I. THEORETICAL GAINS (DB) AT 118.75 GHZ.

| Antenna type | Gain (dB) | [Directivity (dB)] |
|---|---|---|
| μ=±1 probe (electroformed) | 8.94 | |
| Pyramidal horn (electroformed) | 15.40 | |
| 3D-printed corrugated circular horn | | 24.75 |

## II. THREE-ANTENNA MEASUREMENTS

AMTA The gains of the electroformed μ=±1 probe (with nominal gain of 9 dB), the electroformed standard gain horn (with nominal gain of 15 dB) and the 3D-printed horn with nominal directivity of 24 dB were measured at 118.75 GHz with the three-antenna extrapolation method. The three antennas are shown in Figures 1-3. The results are found in Table II.

Table 3 contains a summary of the sources of uncertainty and the estimated uncertainty due to each source. Table III shows that the main source of uncertainty is due to signal drift. While the NIST antenna ranges are undergoing renovation, the NIST CROMMA facility is housed in a temporary location with much poorer temperature control than the permanent facility. This poorer temperature control leads to significantly larger signal drift. Typical measurement uncertainty for this type of measurement would be less than ±0.2 dB.

Francis, Michael; Novotny, David; Gordon, Joshua; Curtin, Alexandra; Wittmann, Ronald.
"Gain Comparison of a 3D-Printed Horn and an Electroformed Horn."
Paper presented at 38th Annual Meeting and Symposium of the Antenna Measurement Techniques Association (AMTA), Austin, TX, United States. October 30, 2016 - November 4, 2016.

## III. DISCUSSION

As we can see, the gain of the 3D-printed corrugated horn is more than 4 dB below the directivity predicted by calculation. This implies ohmic losses of about 4 dB. In contrast, the pyramidal horn and the μ=±1 probe have measured and predicted gains that are within the measurement uncertainty. This is consistent with predicted ohmic losses of less than 0.1 dB. We believe that this difference is due to the surface roughness of this prototype 3D-printed corrugated horn and the lower density and conductivity of the material used in fabricating the horn. We expect these to significantly increase the ohmic losses and hence to reduce the gains, particularly as the frequency of operation increases.

TABLE II. GAINS (DB) AT 118.75 GHZ FROM THREE-ANTENNA EXTRAPOLATION METHOD.

| Antenna | Gain (dB) |
|---|---|
| μ=±1 probe (electroformed) | 8.60 ± 0.5 |
| Electroformed horn, model 1 | 15.47 ± 0.5 |
| 3D-printed corrugated circular horn | 20.32 ± 0.5 |

TABLE III. GAINS UNCERTAINTIES AT 118.75 GHZ.

| Source of uncertainty | Gain uncertainty (dB) |
|---|---|
| Signal drift | 0.5 |
| Multiple reflections | 0.1 |
| Mismatch | 0.01 |
| Alignment | 0.05 |
| Polynomial fit | 0.1 |
| Noise | 0.05 |
| **RSS** | **± 0.5** |

## IV. FUTURE WORK

To further explore the effects of 3D printing, we plan to measure the on-axis gains of three 3D-printed pyramidal horns and an electroformed pyramidal horn at 112, 118 and 125 GHz. These horns have a nominal gain of 24 dB. To test our hypothesis that the ohmic losses are increased by the surface roughness, we plan on polishing one of the 3D printed horns and retesting it to see if the gain improves. We also plan on polishing another horn and plating it with gold to test the effects of different material used in the 3D printing process as compared to the electroforming process.


## ACKNOWLEDGEMENT

We want to thank L. Periasamy and A. Gasiewski of the University of Colorado Boulder for designing and supplying the 3-D printed horn.


## REFERENCES


[1] W. Blackwell, G. Allen, C. Galbraith, T. Hancock, R. Leslie, I. Osaretin, L. retherford, M. Scarito, C. Semisch, M. Shields, M. Silver, D. Toher, K. Wight, D. Miller, K. Cahoy, and N. Erickson, "Nanosatellites for earth environmental monitoring: The MicroMas Project," IGARSS 2012.6359010, pp. 206 – 209.

[2] A.C. Newell, R.C. Baird, and P.F. Wacker, "Accurate measurement of antenna gain and polarization at reduced distances by an extrapolation technique," IEEE Trans. Antennas Propagat., vol. AP-21, pp. 418 – 431, July 1973.

[3] L. Periasamy and A. Gasiewski, the University of Colorado at Boulder, Center for Environmental Technology, Department of Electrical, Computer, and Energy Engineering, private communication, June 2016..

[4] D. Novotny, M. Francis, R. Wittmann, J. Gordon, J. Guerrieri, A. Curtin, "Multi-purpose configurable range for antenna testing up to 220 GHz," Proc. Antenna Meas. Tech. Assoc., pp. 15 – 20, October 2015.



Francis, Michael; Novotny, David; Gordon, Joshua; Curtin, Alexandra; Wittmann, Ronald.
"Gain Comparison of a 3D-Printed Horn and an Electroformed Horn."
Paper presented at 38th Annual Meeting and Symposium of the Antenna Measurement Techniques Association (AMTA), Austin, TX, United States. October 30, 2016 - November 4, 2016.

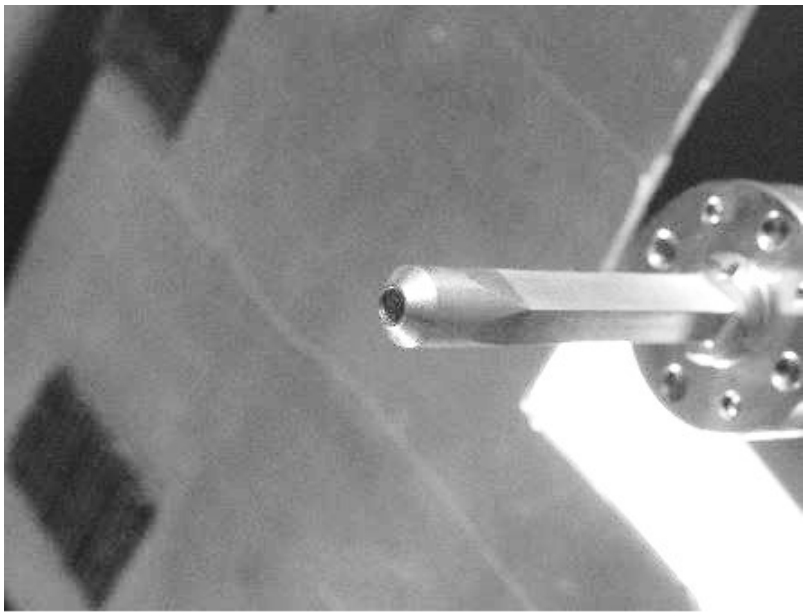

Figure 1. Photo of WR8 μ=±1 probe

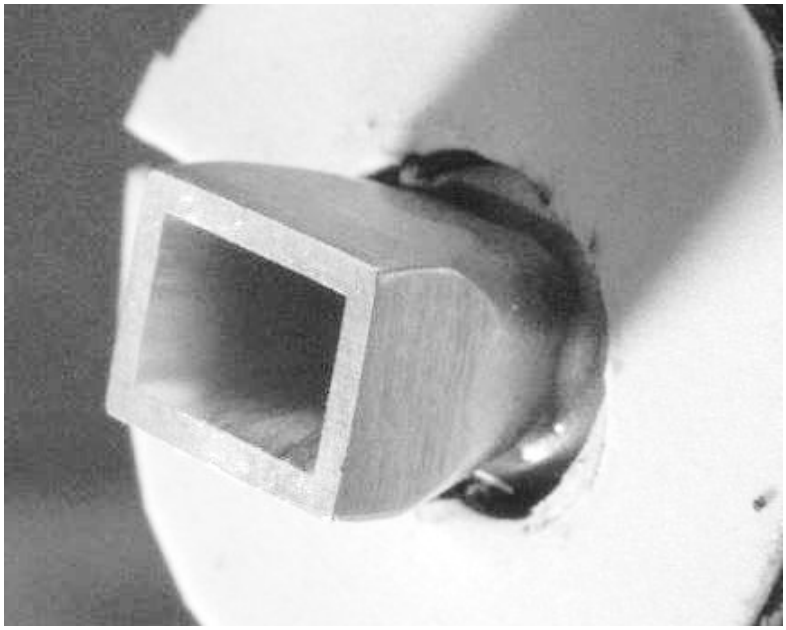

Figure 2. Photo of WR8 15 dB standard gain horn

Francis, Michael; Novotny, David; Gordon, Joshua; Curtin, Alexandra; Wittmann, Ronald.
"Gain Comparison of a 3D-Printed Horn and an Electroformed Horn."
Paper presented at 38th Annual Meeting and Symposium of the Antenna Measurement Techniques Association (AMTA), Austin, TX, United States. October 30, 2016 - November 4, 2016.

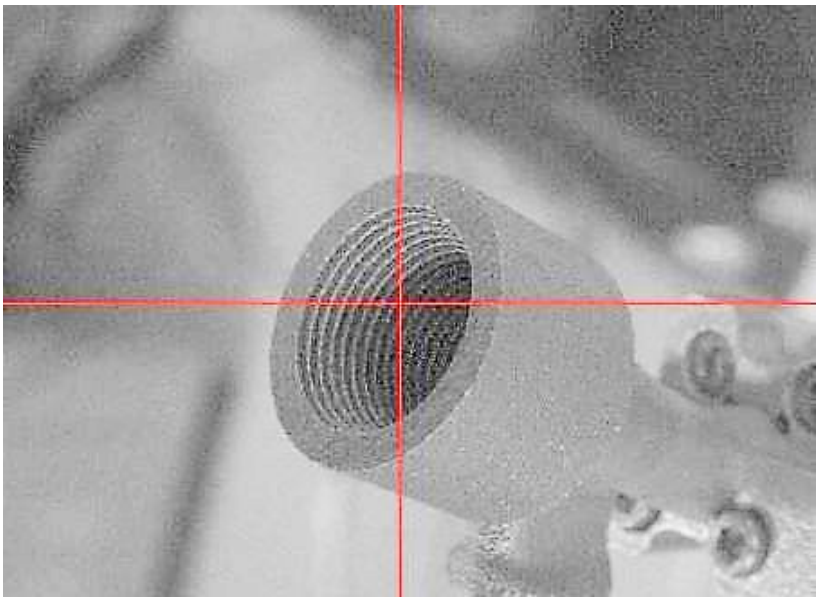

Figure 3. Photo of WR8 corrugated 3D-printed horn with alignment crosshairs.

Francis, Michael; Novotny, David; Gordon, Joshua; Curtin, Alexandra; Wittmann, Ronald.
"Gain Comparison of a 3D-Printed Horn and an Electroformed Horn."
Paper presented at 38th Annual Meeting and Symposium of the Antenna Measurement Techniques Association (AMTA), Austin, TX, United States. October 30, 2016 - November 4, 2016.

# An Overview of Atom-Based SI-traceable Electric-Field Metrology

*Joshua A. Gordon, Christopher L. Holloway, Matthew Simons
*Contact: Josh.gordon@nist.gov

National Institute of Standards and Technology
Communications Technology Laboratory, Boulder CO 80305


**Abstract:** We present an overview of radio frequency (RF) electric-field measurements using Rydberg atoms. This technique exploits the rich resonance response of these atoms which can occur across a large frequency range from about 500 MHz-500 GHz. This measurement utilizes alkali atoms such as rubidium and cesium atoms confined in a glass vapor cell that are excited optically by two different lasers to high energy Rydberg states. Once in the Rydberg state the atoms exhibit a significant response to RF fields. The presence of the RF field alters the optical spectrum of the atoms, which can be interrogated to determine the RF field strength. One of the main goals of this work is an atomic standard measurement of RF fields that is intrinsically calibrated, directly linked to the SI and atomic structural constants.

**Key Words:** Electric Field; Rydberg Atoms; Radio Frequency; Electromagnetically Induced Transparency (EIT)

## I. Introduction

Over the past several years many advances have been made in using atoms to directly measure radio-frequency (RF) electric-fields [1-5]. In particular, a new technique for converting an RF field amplitude into an optical frequency response in a gas of atoms has shown much promise. The goal is an atomic standard measurement of RF fields that is intrinsically calibrated and directly linked to the SI. In this approach a gas of room temperature alkali atoms such as Rubidium (Rb) and Cesium (Cs) contained in a glass vapor cell are optically excited to a high enough energy that the atoms become resonant to RF fields. Two laser are used to accomplish this. One laser is used to excite the lower energy levels of the atoms while the second increases the atom's energy to the point that the outer most electron orbit is larger enough that the atom behave much like a hydrogen atom. Such an atom is referred to as a Rydberg atom [6] and can act like a nano-sized antenna which as we show can respond to RF fields.

While in the Rydberg state, the atom exhibits a large response, i.e. a large dipole moment, to RF-fields over the frequency range of about 500 MHz-1 THz. To the lasers, the atomic gas acts like a non-linear optical medium that experiences changes in electrical susceptibility when interacting with an RF field. More specifically, where the atomic gas would preferentially transmit a single optical frequency, in the presence of the RF-field two optical frequencies are preferentially transmitted. It can be shown that the difference in the two optical frequencies is linearly proportional to the applied RF-field amplitude. We will discuss the theory behind this technique and show how this technique provides an atomic linked SI traceable RF-field measurement. Experimental data are presented for electric fields radiated by antenna sources which are compared to electromagnetic theory and finite element simulations.

## II. Atom Based Electric Field Measurement

### a) Rydberg Atom Preparation

For the remainder of this paper we will focus on measurements made using Rb atoms. Rydberg atoms are prepared using two different wavelength lasers. The probe laser is tuned to excite the $D_2$ transition ($5S_{1/2} - 5P_{3/2}$) around $\lambda_p \cong 780\ nm$ (red) and the coupling laser is tuned to $\lambda_c \cong 480\ nm$ (blue) in order

Gordon, Joshua; Holloway, Christopher; Simons, Matthew.
"An Overview of Atom-Based SI-Traceable Electric-Field Metrology."
Paper presented at 2016 Antenna Measurement Techniques Association, Austin, TX, United States. October 30, 2016 - November 4, 2016.

to excite the final Rydberg states. Tuning the coupling laser to different wavelengths allows for different Rydberg states to be accessed. Figure 1 shows the scenario for the specific excitation of the $5P_{3/2} - nD_{5/2}$ transition, where $n$ is the principle quantum number and depends on the exact $\lambda_c$ chosen. The Rydberg state leads to a strong RF response of the atoms which manifests as the $nD_{5/2} - (n+1)P_{3/2}$ transition. These two lasers are aligned to counter propagate collinearly and are focused at the center of the vapor cell to a nominal $1/e$ beam diameter of around $100\ \mu m$. Beam powers for the probe and coupling laser are nominally 100 nW and 30 mW respectively. A dichroic filter which reflects $\lambda_c$ and transmits $\lambda_p$ is used to overlap the two beams. The probe transmission through the vapor cell is measured with a silicon photodiode detector. To reject unwanted signal from room lights, etc., a $10\ nm$ wide band pass filter centered at $780\ nm$ is placed in front the detector. Heterodyne detection of the *probe* beam signal using a nominal amplitude modulation of 20 kHz-30 kHz on the *coupling* laser beam aids in improving signal to noise and was used in the data we present here. Figure 2 shows the optical layout for generating Rb Rydberg atoms while simultaneously measuring the transmission of the probe beam.

### b) E-Field Determined from Atom Vapor Optical Susceptibility

In this approach we wish to relate the optical response of the atoms to an incident RF field. This can be achieved by deriving the optical susceptibility, $\chi$ for a volume filled with a gas of alkali atoms excited through four energy levels. As a full derivation of the susceptibility is outside the scope of this paper, we refer the reader to [7] and [8] for an in depth theoretical treatment of this atomic system. Here we present the final results important for RF electric-field metrology. The imaginary part of the refractive index can be determined using the fact that $\sqrt{(1+\chi)} = n + jk$, where $n$ is the real part and $k$ the imaginary part of the refractive index which governs the degree of absorption experienced by the probe beam as it traverses the vapor cell.

In the case where only the probe laser is present and tuned to the $D_2$ transition, much of the light will be absorbed by the atoms. However, it can be shown that when both the probe (tuned $D_2$ transition) and the coupling (tuned to excite a Rydberg transition) lasers are present, a transparency window occurs where absorption of the probe laser is significantly reduced. This phenomenon is call Electromagnetically Induced Transparency (EIT) [9] and is observed as a *peak* in the *absorption* spectrum of the probe laser. Furthermore, when the RF field is also present and on resonance with the Rydberg transition, the EIT peak splits into two peaks. These two peaks occur above and below the center frequency of the $D_2$ transition, $f_{D2} = 384.23\ldots THz$. It can be shown that the frequency separation of these two peaks, $\Delta f_{probe}$ measured in the probe absorption spectrum is proportional to the RF field strength by [10],[11],

$$\Delta f_{Probe} = \frac{\lambda_c}{\lambda_p}\frac{\wp_{RF}|E_{RF}|}{2\pi\hbar} \qquad (1)$$

where $\wp_{RF}$ is the atoms dipole moment for the RF transition (much like the dipole moment of an antenna), $\hbar$ is Plank's constant, and $|E_{RF}|$ is the magnitude of the RF field and $\lambda_c$ and $\lambda_p$ are the wavelengths of the coupling and probe lasers respectively. With this a measurement of the RF electric field magnitude has been reduced to an optical frequency measurement. The probe laser spectrum with and without an RF field is shown in Figure 3. The splitting is clearly observed when an RF field at a frequency of 104.77 GHz is incident on the vapor cell. For reference this splitting corresponds to a strength of 2.8 V/m.

### c) Broad RF Tunability

For each Rydberg state there is a corresponding RF transition and associated dipole moment. Therefore by changing the coupling laser wavelength, $\lambda_c$ one can tune which RF frequency the atom responds to. This is shown in Figure 4 for two cases where the coupling laser is set to $\lambda_c = 479.32\ nm$ and $\lambda_c = 483.60\ nm$ in order to tune the atom's RF resonance from 2.03 GHz to 150.40 GHz. The RF transition frequency for a given coupling $\lambda_c$ can be calculated using the total ionization energy of the atom and corresponding quantum

defects [11]. Results of such a calculation for all $nD_{5/2} - (n+1)P_{3/2}$ RF transitions from $20 \leq n \leq 130$ are shown in Figure 5. From this we see that the coupling laser need only change a few nanometers in order to tune the atom from about 500 GHz up to about 500 GHz. This shows the broad tunability of this technique throughout the radio, microwave, millimeter-wave, and sub-terahertz regimes.

### d) Self-Calibration and SI-Traceability

From Equation (1) we see that $\Delta f_{probe}$ is proportional to $|E_{RF}|$ and the atom's dipole moment, $\wp_{RF}$. The dipole moment is an intrinsic parameter of the atom and is also a constant for any given RF transition. It can be accurately determined using atomic spectra measurements and quantum theory [6]. All other variables, $\lambda_c$, $\lambda_p$ , and $\hbar$ can be determined independent of the RF field and the dipole moment. This suggests this approach can lead to a self-calibrated electric field measurement because all free parameters can be known a priori to measuring the RF field.

Furthermore, through Equation (1) we see that $|E_{RF}|$ is proportional to Plank's constant. Therefore, the calculation of the RF-field strength based on the optical frequency measurement is linked to an SI constant. This also suggests a directly SI-traceable measurement. Progress is currently being made toward establishing a full traceability path where the uncertainties associated with each part of the measurement are well understood.

## III. Measurements

We present measurement results for several RF frequencies. A block diagram of the setup that was used for these measurements is shown in Figure 6 which includes the vapor cell, source antenna, lock-in amplifier for heterodyne detection, photo diode detector, probe laser, and coupling laser. Measurements performed at 15.59 GHz, 17.04 GHz, and 104.77 GHz are shown in Figure 7 where the spitting is plotted versus the square root of the power input to the source antenna by the signal generator, $\sqrt{P_{SG}}$. The linear slope for the frequency splitting as predicted by Equation (1) is clearly observed as it should be since $\sqrt{P_{SG}} \propto |E_{RF}|$. These data were also compare to both analytical far-field calculations and full 3D finite element numerical simulations. These comparisons are shown in Figure 8. We see good agreement between the theoretically predicted values for the E-field strength and the values based on this Rydberg atom measurement. These data also demonstrate the large tunability of this measurement. We would like to point out that only one optical setup (Figure 6.) was needed to make these measurements across the ≈ 90 GHz frequency range, whereas three separate RF sources were required to generate the signals.

## IV. Conclusion

In conclusion, we have given a short overview of a recently developed atom based technique for measuring RF fields over the frequency range of ≅ 500 MHz-500 GHz. This technique uses alkali atoms confined in a glass vapor cell that are excited to Rydberg states by two different lasers. An RF measurement is made by observing a frequency splitting in the optical spectrum of the atomic gas when an RF field is present. This frequency splitting is proportional to the magnitude of the applied RF field. We present a brief theoretical description of how the applied RF field can be interpreted from an all-optical measurement and provide reference for further in depth reading. We present data of E-field measurements at 15.59 GHz, 17.04 GHz, and 104.77 GHz using this technique which are compared to both analytical far-field and 3D finite element simulations. These data show the broadly tunable capability of this technique and the theoretical predicted linearity of the optical spectral to applied RF fields. This technique shows much promise for realizing a self-calibrating, SI-traceable, and broadly tunable E-field measurement that is linked to atomic constants.

## V. References


[1] J. A. Gordon, C. L. Holloway, A. Schwarzkopf, D. A. Anderson, S. A. Miller, N. Thaicharoen, and G. Raithel,Appl. Phys. Lett. 105, 024104 (2014)

[2] C. L. Holloway, J. A. Gordon, S. Jefferts, A. Schwarzkopf, D. A. Anderson, S. A. Miller, N. Thaicharoen, and G. Raithel, IEEE Trans. Antennas Propag. Soc. (2014).

[3] C. L. Holloway, J. A. Gordon, A. Schwarzkopf, D. A. Anderson, S. A. Miller, N. Thaicharoen, and G. Raithel, Appl. Phys. Lett. 104, 244102 (2014).

[4] J. A. Sedlacek, A. Schwettmann, H. Kubler, R. Low, T. Pfau, and J. P. Shaffer, Nature Phys. 8, 819 (2012).

[5]J. A. Sedlacek, A. Schwettmann, H. Kubler, and J. P. Shaffer, Phys. Rev. Lett. 111, 063001 (2013).

[6] T. F. Gallagher, Rydberg Atoms (Cambridge University Press, 1994).

[7] S. N. Sandhya and K. K. Sharma, Phys. Rev. A 55, 2155 (1997).

[8] P. Meystre and M. Sargent III, Elements of Quantum Optics, 4th Ed. Springer, chapter 9, 2007.

[9] K. J. Boller, A. Imamoglu, and S. E. Harris, Phys. Rev. Lett. 66, 2593 (1991).

[10] S. H. Autler and C. H. Townes, Phys. Rev. 100, 703 (1955).

[11] T. Y. Abi-Salloum, Phys. Rev. A 81, 053836 (2010).


## VI. Acknowledgments


This work was funded in part by the DARPA QuASAR program.


## VII. Figures

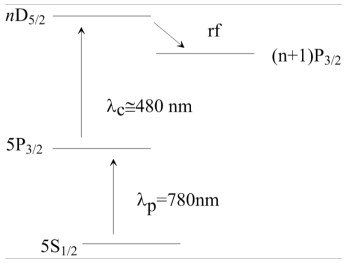


Figure 1. Rb energy levels for generating Rydberg states for $n \gtrsim 20$. Atomic transitions for the different photon energies of the probe, coupling and RF fields are shown.

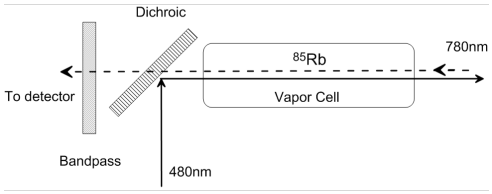


Figure 2. Optical layout for generating Rydberg atoms in a vapor cell full of $^{85}$Rb atoms and detecting probe laser transmission. (Dotted) The probe and (Solid) coupling laser are in actuality overlapping for these measurements, but are shown here displaced for clarity.

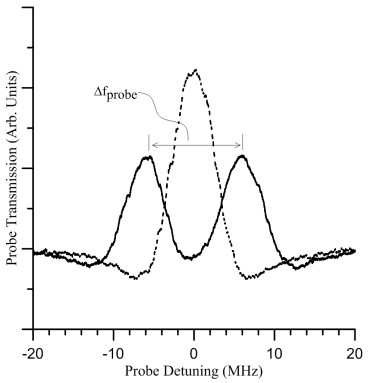


Figure 3. Optical spectrum for the probe laser with (solid) an RF field of 2.8 V/m at 104.77 GHz is incident on the vapor cell and without (dotted) the RF field present. The splitting of the EIT peak resulting from the RF field is clearly visible.

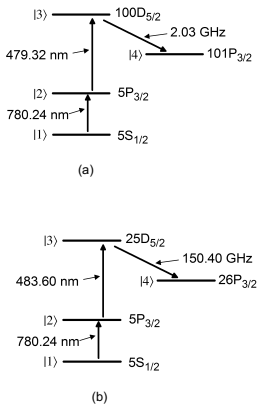


Figure 4. Tuning of the RF transition by changing the coupling laser wavelength, $\lambda_c$. (a) For $\lambda_c = 479.32\ nm$, the atoms will respond to an RF frequency 2.03 GHz. (b) For $\lambda_c = 483.60\ nm$, the atoms will respond to an RF frequency 150.40 GHz.

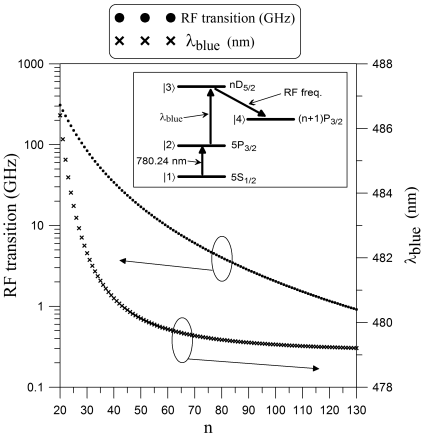


Figure 5. RF tuning range of the atoms for changing coupling (blue) laser wavelength for the $nD_{5/2} - (n+1)P_{3/2}$ transitions.

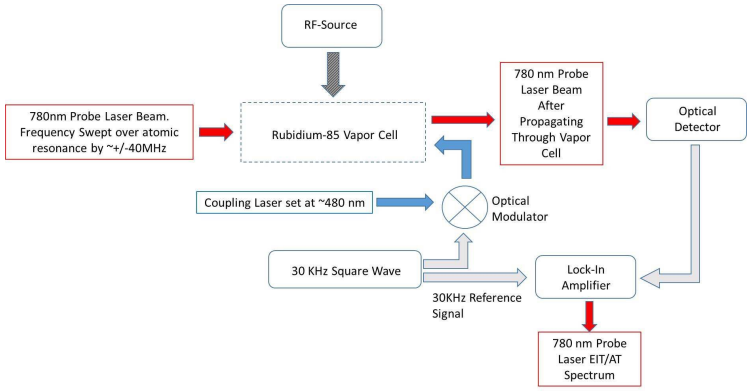


Figure 6. Experimental layout block diagram.

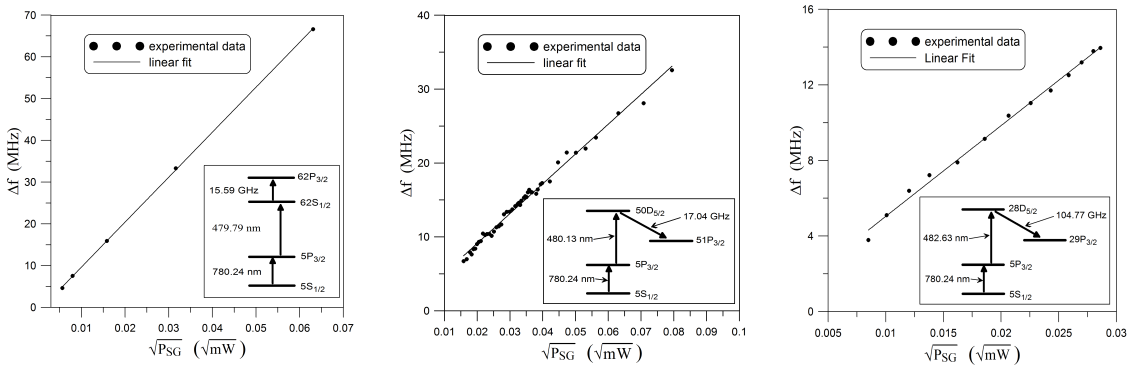


Figure 7. Linearity of the frequency splitting on the probe laser spectrum versus $\sqrt{P_{SG}}$ (the square root of the input power to the source antenna from the signal generator). Measurements for RF frequencies of 15.59 GHz, 17.04 GHz, and 104.77 GHz respectively are shown. Linear least squares fits are also shown.

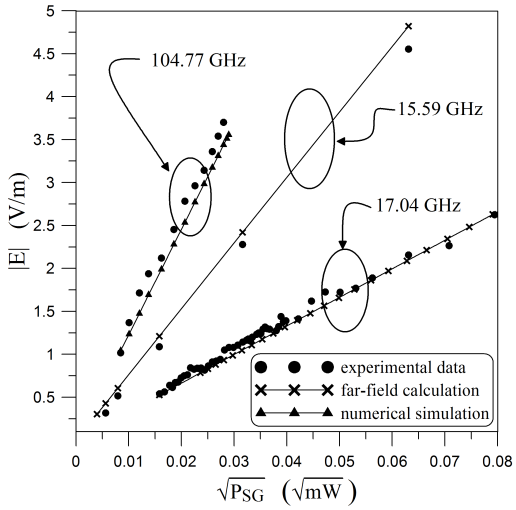


Figure 8. E-field as determined from the frequency splitting of Figure 7. Data are compared to analytical far-field calculations and 3D finite element simulations.

# POWER FLOW ANGLE AND PRESSURE DEPENDENCE OF SAW PROPAGATION CHARACTERISTICS IN QUARTZ

A. Ballato* and T. Lukaszek*; D. F. Williams+ and F. Y. Cho+

*US Army ERADCOM, Fort Monmouth, New Jersey, 07703
+Motorola, GED, Scottsdale, Arizona 85252

## ABSTRACT

Surface acoustic wave propagation on doubly rotated cuts of quartz is considered. Sample static frequency-temperature results are given corresponding to regions where the second order temperature coefficient is small, and these are compared to singly rotated cuts. The force-frequency effect is measured, as is power flow angle, for sample cuts, and it is shown how the static frequency-temperature curve may be compensated using the power flow variation with temperature. The anisotropy ratio is tabulated for a number of doubly rotated cuts.

## INTRODUCTION

The evolution of bulk acoustic wave (BAW) resonators from single rotated types to doubly rotated cuts[1] led to a number of improvements, despite the greater difficulty of manufacture. Almost certainly the most significant advance has been the development of the SC cut.[2] It is in the spirit of these BAW developments that doubly rotated SAW cuts have been investigated.[3] We report here on a number of aspects of this investigation.

## FREQUENCY-TEMPERATURE

The static frequency-temperature (f-T) behavior of a resonator is represented by the cubic relation $\Delta f/f = a\Delta T + b\Delta T^2 + c\Delta T^3$, with $\Delta T = T - To$. T is the temperature variable, and $To = 25^oC$ is the reference temperature. Table 1 lists the nominal values for the coefficients b and c (in units of $10^{-9}/K^2$ and $10^{-12}/K^3$, respectively) for the single rotated AT and BT BAW cuts, the SC doubly rotated BAW cut, and the ST and SST[4] singly rotated SAW cuts. The "a" coefficient is zero; the reference temperature is $25^oC$.

Table 2 gives a number of doubly rotated orientations with parabola constants (b values) for SAW propagation that are representative of the best determined in this study. An experimental f-T curve is shown in Fig. 1.

Shown in Fig. 2 is a comparison of the singly rotated ST and SST cuts with one of the best doubly rotated cuts. It is seen that the doubly rotated (dr) cut is slightly better than the SST cut, particularly at higher temperatures. In Fig. 3 is seen the effect of small changes in the

Table 1. Temperature Coefficients

| CUT | b | c |
|---|---|---|
| AT | - 0.5 | +109. |
| BT | -40. | -128. |
| SC | -12. | + 58. |
| ST | -34. | - 18. |
| SST | -20. | + 96. |

Table 2. Superior TCF of Doubly Rotated SAW Cuts.

| (yxw-φ/Θ/Ψ (DEGREES) | TCF (1) ($10^{-6}$/K) | TCF (2) ($10^{-9}$/K$^2$) | TCF (3) ($10^{-12}$/K$^3$) | VELOCITY (M/S) | K$^2$ (%) | PFA (DEGREES) |
|---|---|---|---|---|---|---|
| 12.01/31.21/39.8 | 0.06 | -11.9 | 45 | 3243 | 0.101 | -1.1 |
| 15.13/31.13/37.33 | 0.11 | -11.8 | 25.3 | 3245 | 0.098 | -4.6 |
| 14.31/41.07/40.56 | 0.37 | -13 | 51 | 3315 | 0.094 | -8.6 |
| -1.05/28.07/136.5 | --- | -11 | 73 | 3259 | 0.11 | +1.5 |

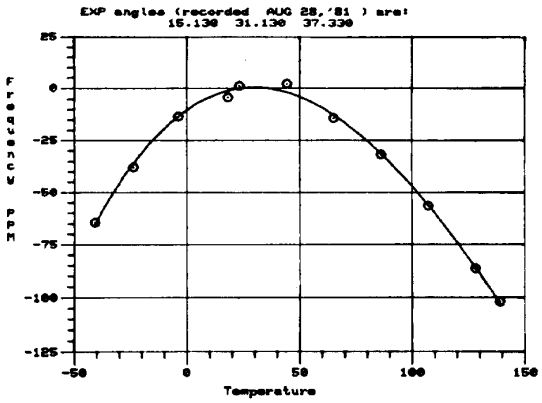


Fig. 1. Frequency-Temperature Plot of SAW on Doubly Rotated Quartz Plate.

Ballato, A; Williams, Dylan; Lukaszek, T; Cho, F.
"Power Flow Angle and Pressure Dependence of SAW Propagation Characteristics in Quartz."
Paper presented at IEEE Ultrasonics Symposium, 1981, Chicago, IL, United States. October 14, 1981 - October 16, 1981.

angle $\psi$ (see the diagram inset in Fig. 2). For this cut $\partial a/\partial\psi$ is approximately $+2.7 \times 10^{-6}/K, {}^{o}\psi$.

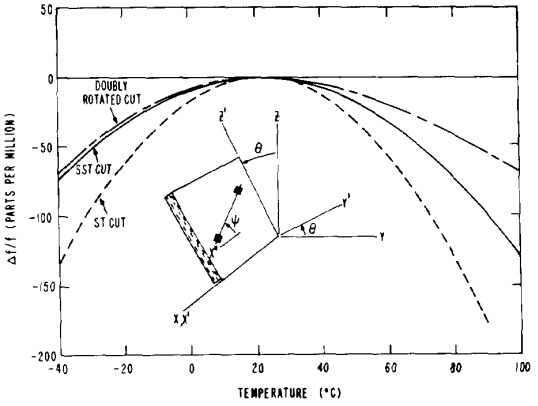


Fig. 2. Frequency-Temperature Behavior Comparison of Select Orientations.

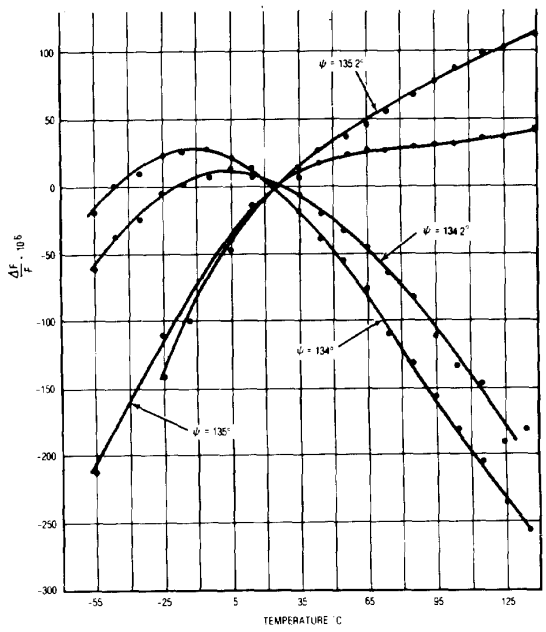


Fig. 3. Frequency-Temperature Dependence on $\psi$.

## FORCE-FREQUENCY

The force-frequency effect was measured with the apparatus shown in Fig. 4. The SAW plates were rounded and subjected to in-plane, diametric force pairs. The phase change upon force application was translated into a normalized frequency shift $\Delta f/f$. This shift, divided by the magnitude of the force applied and multiplied by the disc cross-sectional area, $\phi_a \cdot t_a$, defines the coefficient $\overline{K}_f$ chosen to characterize the effect. Figure 5 is a plot of phase and impedance of a dr SAW device measured as a two-port delay line. The device dimensions are $\phi_a$ = 11 mm, $t_a$ = 0.9 mm, a = 166$\lambda$, b = 140$\lambda$, and c = 1 mm. (Cf. Fig. 7 for definitions).

In Fig. 6 is shown $\overline{K}_f$ measured for an ST cut disc as function of force azimuth $\Psi$. The symmetry of the ST about the X ($\Psi$ = 0°) and Z' ($\Psi$ = 90°) axes is apparent. Figure 7 shows the corresponding curve of $\overline{K}_f$ for a representative dr cut. The curve is unsymmetric and larger in magnitude.

Fig. 4. Force-Frequency Apparatus and Measurement Instrumentation.

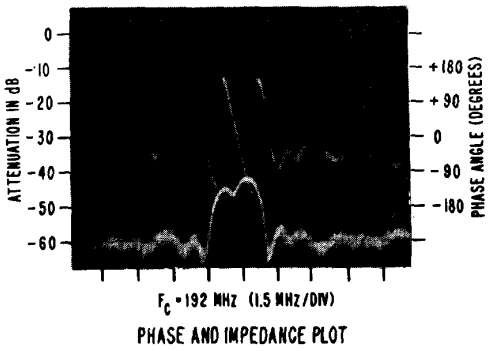


Fig. 5. Phase and Impedance Response of Doubly Rotated Crystal (Unmatched).

## POWER FLOW ANGLE

Power flow angle (pfa) is the angle between phase and group velocity vectors, as depicted in Fig. 8. This angle is a function of temperature as seen in Fig. 9 for a dr cut. Table 3 provides measured values of pfa for a variety of cuts at three temperatures. The sensitivity to temperature of the pfa may be applied to compensate for



Ballato, A; Williams, Dylan; Lukaszek, T; Cho, F.
"Power Flow Angle and Pressure Dependence of SAW Propagation Characteristics in Quartz."
Paper presented at IEEE Ultrasonics Symposium, 1981, Chicago, IL, United States. October 14, 1981 - October 16, 1981.

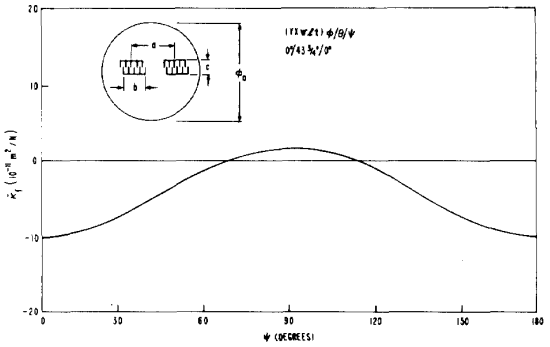

Fig. 6. Force-Frequency Azimuth Curve for ST Cut.

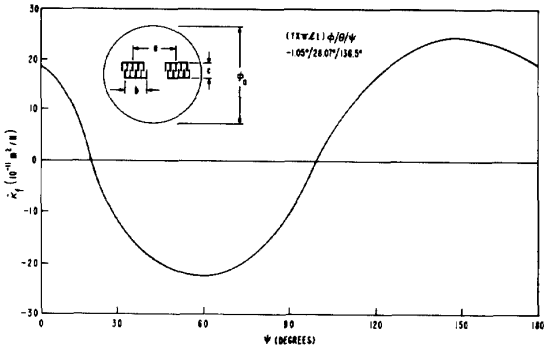

Fig. 7. Force-Frequency Azimuth Curve for Doubly Rotated Quartz Cut.

the static f-T behavior of the SAW device. This is accomplished[5] by employing small-aperture auxiliary IDT transducers to sense the changing pfa with temperature. Combining the outputs of these auxiliary transducers with that of the main transducer produces a phase correction with temperature to correct frequency. Figure 10 shows an example of the technique.

The power flow angle is related to the incremental slope of the inverse velocity surface. It is characterized by the anisotropy ratio $\gamma$.[5,6] The temperature dependence of $\gamma$ is given for a number of SAW singly and doubly rotated orientations in Table 4.

## CONCLUSION

Doubly rotated SAW cuts exist that are superior to singly rotated cuts in f-T behavior. Because of the asymmetry of these cuts and of the phase propagation angle necessary to produce small "a" values, the pfa values are not zero, and the curves for such effects as force-frequency are unsymmetrical. Notwithstanding these complications, dr SAW plates have certain attractive features,

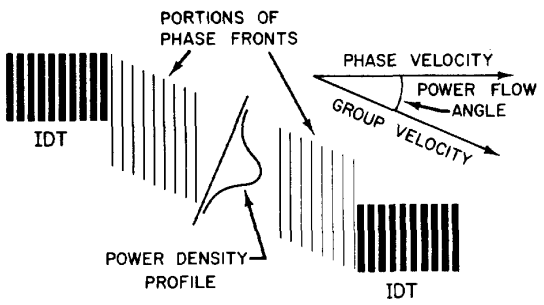


Fig. 8. Schematic of Power Flow Angle

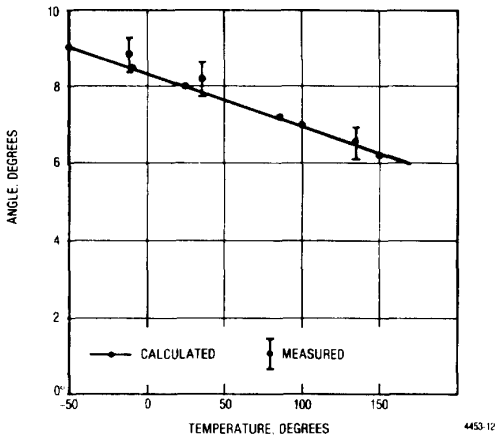


Fig. 9. Power Flow Angle vs. Temperature for (YXwℓt) 14.283/39.117/40.6 Plate.

such as the ability to be temperature compensated over wide ranges, and, for some orientations, a high force sensitivity. In addition, cuts that are compensated for various nonlinearities (as is the SC BAW cut) remains an intriguing possibility.

## REFERENCES

1. A. Ballato, "Doubly Rotated Thickness Mode Plate Vibrators," in Physical Acoustics (W. P. Mason and R. N. Thurston, eds.), Academic, New York, 1977, Chapter 5, pp. 115-282.

2. J. A. Kusters, "The SC Cut Crystal - An Overview," these proceedings.



Ballato, A; Williams, Dylan; Lukaszek, T; Cho, F.
"Power Flow Angle and Pressure Dependence of SAW Propagation Characteristics in Quartz."
Paper presented at IEEE Ultrasonics Symposium, 1981, Chicago, IL, United States. October 14, 1981 - October 16, 1981.

Table 3. TEMPERATURE DEPENDENCE OF THE POWER FLOW ANGLE ON DOUBLY ROTATED CUTS AT ORIENTATIONS (YX WLT) PHI/THETA/PSI

| Orientation | | | Power Flow Angle | | |
|---|---|---|---|---|---|
| PHI | THETA | PSI | T = 25°C | T = 150°C | T = −50°C |
| −1.330 | 28.100 | 137.692 | +1.2 | −0.1 | +1.8 |
| −1.050 | 28.067 | 136.534 | +2.5 | +1.0 | +3.2 |
| −0.967 | 26.233 | 138.449 | +1.1 | −0.2 | +1.8 |
| −0.33 | 26.700 | 138.859 | +0.5 | −0.7 | +1.1 |
| 0.633 | 26.150 | 137.016 | +1.4 | +0.1 | +2.1 |
| 5.583 | 27.833 | 135.194 | +0.3 | −0.9 | +1.0 |
| 5.583 | 27.833 | 134.940 | +0.5 | +0.1 | +1.1 |
| 5.583 | 27.833 | 134.994 | +0.4 | −0.8 | +1.1 |
| 6.000 | 26.967 | 135.812 | −0.1 | −1.2 | +0.5 |
| 6.067 | 25.933 | 133.099 | +1.7 | +0.3 | +2.4 |
| 6.567 | 26.883 | 134.925 | +0.1 | −1.0 | +0.7 |
| 7.410 | 27.380 | 134.2 | +0.1 | −1.0 | +0.8 |
| 8.033 | 26.967 | 134.618 | −0.3 | −1.4 | −0.3 |
| 8.05 | 25.900 | 135.71 | −0.7 | −1.6 | −0.1 |
| 14.283 | 39.117 | 40.627 | −8.1 | −6.2 | −9.0 |
| 15.300 | 40.683 | 40.031 | −8.6 | −6.8 | −9.6 |
| 16.117 | 41.267 | 37.309 | −7.2 | −5.5 | −8.1 |

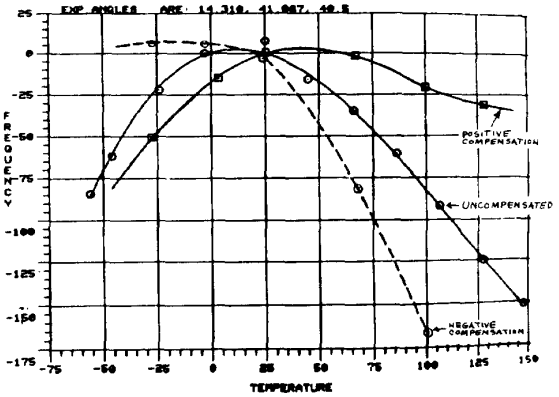


Fig. 10. Frequency-Temperature Compensation Employing PFA Correction.

3. D. F. Williams and F. Y. Cho, Reports DELET-TR-79-0275-1, 2, 3, and F on Contract DAAK20-79-0275, "Doubly Rotated Cut SAW Devices," 1979-1981. US Army ERADCOM, Fort Monmouth, NJ 07703.

4. T. Lukaszek and A. Ballato, "What SAW Can Learn from BAW: Implications for Future Frequency Control, Selection, & Signal Processing," Proc. 1980 IEEE Ultrasonics Symposium, November 1980, pp. 173-183.

Table 4. Temperature Dependence of $\gamma$.

| ORIENTATION | | | ANISOTROPY PARAMETER $\gamma$ | | |
|---|---|---|---|---|---|
| PHI | THETA | PSI | T = −50°C | T = 25°C | T = 150°C |
| 0 | 42.5 | 0 | 0.369 | 0.375 | 0.369 |
| 0 | 27.0 | 137.72 | 0.669 | 0.616 | 0.669 |
| 7 | 27.0 | 135.64 | 0.444 | 0.379 | 0.444 |
| 12.5 | 35.0 | 130.62 | 0.704 | 0.645 | 0.704 |
| 14.3 | 39.1 | 40.6 | 0.625 | 0.614 | 0.625 |
| 15.0 | 32.5 | 38.55 | 0.775 | 0.756 | 0.775 |
| 15.0 | 40.0 | 40.0 | 0.637 | 0.621 | 0.637 |

5. D. F. Williams, F. Y. Cho, A. Ballato, & T. Lukaszek, "The Propagation Characteristics of Surface Acoustic Waves on Singly and Doubly Rotated Cuts of Quartz," Proc. 35th Annual Frequency Control Symposium, US Army Electronics R&D Command, Fort Monmouth, NJ 07703, May 1981, in press.

6. H. Matthews, ed., Surface Wave Filters, Wiley, New York, 1977, pp. 48-51, 160,373.



Ballato, A; Williams, Dylan; Lukaszek, T; Cho, F.
"Power Flow Angle and Pressure Dependence of SAW Propagation Characteristics in Quartz."
Paper presented at IEEE Ultrasonics Symposium, 1981, Chicago, IL, United States. October 14, 1981 - October 16, 1981.

Proc. 34th Ann. Freq. Control Symposium, USAERADCOM, Ft. Monmouth, NJ 07703, May 1980

# NUMERICAL ANALYSIS OF DOUBLY ROTATED* CUT SAW DEVICES

**D.F. Williams and F.Y. Cho**
**Motorola Government Electronics Division**

## ABSTRACT

Results of a numerical study of the properties of surface acoustic waves (SAW) on doubly rotated cuts of alpha quartz are presented. First and second order TCF's have been calculated on a 10° x 10° x 10° grid spanning the range of angles (XY wlt) 0 to 30°/-90° to 90°/0 to 180°. The Finite Difference method was employed. SAW velocities were calculated at -50° C, 25° C, and 100° C. The corresponding frequencies were determined and curve fitted. Angular maps created from the data base by these calculations were used to identify zero first and second order TCF surfaces. Families of cuts with zero first order TCF and small second order TCF's have been identified and further explored on smaller angular grids (as small as 1.0° x 1.0° x 1.0°).

The results of Sinha and Tiersten's approach are correlated with the finite difference method and used to find cuts with zero first order TCF.

Families of cuts on alpha quartz with SAW temperature stability superior to that found on ST cut Quartz are identified. Coupling coefficients, power flow angles, phase-temperature plots and other parameters are given for selected cuts.

## INTRODUCTION

Quartz is one of the most commonly used substrates for fabricating surface acoustic wave (SAW) devices. In SAW narrowband filter, oscillator and resonator applications, the temperature stability of the device is an important design parameter. Currently, almost all temperature stable SAW devices fabricated on quartz use the ST cut[1]. This cut exhibits a parabolic frequency dependence in tem perature. For many applications, the temperature dependence of devices fabricated on ST quartz is too large. Thus it is desirable to find crystal cuts with superior temperature performance. Of course, many other design parameters must be considered when choosing a crystal cut. Some of the more important parameters are the piezoelectric coupling coefficient, acoustic losses, dependence of device performance on cut misorientation, excitation of bulk modes, and beam steering angle. These parameters are all determined for a given cut.

The objective of this paper is to locate crystal cuts which exhibit lower SAW temperature coefficients of delay than the ST cut. The method used to characterize and calculate the temperature dependence of a crystal orientation is discussed. Use is made of computer models to investigate the temperature dependence of different cuts of crystal for SAW devices. Calculated and measured results are presented and compared. Finally, plans for future experimental work are outlined.

## CALCULATION OF TEMPERATURE COEFFICIENTS

Defining $\tau$ as the delay time for an acoustic wave to propagate between two points on the surface of the crystal, we wish to find orientations for which $\tau$ is constant in temperature. It has been shown that determining the temperature dependence of $\tau$ (time delay) is equivalent to determining the temperature dependence of F frequency via the relation $F \propto 1/\tau$.[2]

The most straightforward method for calculating the frequency-temperature characteristics of a SAW device is the Finite Difference method[3,4]. The Rayleigh wave velocities are calculated for different temperatures, yielding the values $Vs(T_i)$,i=1,2,....., n. This is done by first calculating the fundamental constants at the temperature $T_i$ of interest. These constants[4] are then rotated into the coordinate system of interest. An iterative procedure[3] is used to calculate a velocity $V_s$ for which Christoffel's equation and the boundary conditions are satisfied simultaneously. Linear regression is used to calculate the temperature dependence of a Rayleigh wave and requires a complete solution of the problem to be performed at several temperatures.

Sinha and Tiersten[5] have provided a computer program to calculate the first order TCD using a perturbation approach. The constants used in this program were derived from the original experimental data of Bechmann, Ballato, and Lukaszek[6], and properly includes coordinate axis skewing. A comparison of results using the Finite Difference method and the first order temperature derivatives calculated by Sinha and Tiersten's program shows the later method to be more accurate[5], and angular orientations of the zero $TCF^{(1)}$ surfaces calculated by the two programs differ by as much as 3 degrees on off axis cuts. Although the program does not calculate the second and third order TCD's, it verifies and refines results for the first order TCD. Both computer programs were used extensively in this study.

## ANALYTICAL APPROACH

IRE standard angle definitions (YX wlt) PHI/THETA/PSI for quartz were used throughout the investigation.[7] Using the Finite Difference approach with the available crystal constants, the calculated results show that the zero $TCF^{(1)}$ surfaces do not intersect with the zero $TCF^{(2)}$ surfaces, based on the interpolated results of the 10° x 10° x 10° resolution. It is not likely that a finer resolution will provide contrary information because $TCF^{(1)}$ and $TCF^{(2)}$ are relatively slow varying functions. A list of the crystal elastic constants and their temperature derivatives on which these calculations are based are given in reference 6. Calculations were performed on a 10° x 10° x 10° grid over the angular ranges $0 \leq PHI \leq 30°$, $0 \leq PSI \leq 180°$, and $-90° \leq THETA \leq 90°$. These initial calculations defined the "angular volumes" of low TCF orientations. Calculations were then performed on a 2.5° x 2.5° x 2.5° grid near promising orientations. In this way, the entire angular range was explored and a large computer-based data file built. Maps of first and second order TCF's were generated.[8] Despite the number and density of points at which the first and second order TCF's were calculated, wherever $TCF^{(1)}$ was found to be less than or equal to zero, we found $TCF^{(2)}$ to be less than 0.

The investigative approach used has been to first locate the surfaces of zero $TCF^{(1)}$ (the most significant term) with the Finite Difference program. Near these surfaces of zero $TCF^{(1)}$, low values of $TCF^{(2)}$ are sought, using already calculated results of the Finite Difference programs. Where low values of $TCF^{(2)}$ have been found, the perturbation approach was used to more accurately locate the zero $TCF^{(1)}$ surface, this being the most significant term in the total temperature dependence. $TCF^{(3)}$'s are then calculated to assure that their effect on the total temperature dependence is small. To date, this has always been found to be the case.

*Work supported by U.S. Army Electronics Command, Fort Monmouth, N.J., under contract DAAK 20-79-C-0275

## RESULTS OF THE INVESTIGATIVE APPROACH

Table 1 consists of a summary of the results of using the investigative approach described above. Out of the many areas with low TCF cuts, some of which have been identified in this program and some previously identified.[1,2,4,8,9,10] There are three where especially low TCF cuts have been located. These areas are centered near (YX wlt) 0/27/138, (YX wlt) 7/27/135.5, and (YX wlt) 15/40/40. These orientations have zero $TCF^{(1)}$, calculated by Sinha and Tiersten approach, with $TCF^{(2)}$ and $TCF^{(3)}$ calculated using the Finite Difference approach. These areas are chosen because of zero $TCF^{(1)}$ and low $TCF^{(2)}$. $TCF^{(3)}$ can be mostly cancelled out by $TCF^{(1)}$ if the propagation direction is slightly rotated away from the zero $TCF^{(1)}$ direction, so that the $TCF^{(2)}$ term will dominate the performance characteristics. The angular resolution in these areas is 1° x 1° x 1°. The cuts potentially have one half to one third the temperature coefficients of ST-Cut quartz.

Table 1. Propagation Characteristics of Selected Orientations

| ANGLES OF $ZTCF^{(1)}$ DEGREES (S AND T'S PROGRAM) | | | $TCF^{(2)}/°C^2$ ($X10^{-8}$) FINITE DIFFERENCE PROGRAM | $TCF^{(3)}/°C^3$ ($X10^{-10}$) FINITE DIFFERENCE PROGRAM |
|---|---|---|---|---|
| PHI | THETA | PSI | | |
| 6 | 26 | 136.31 | -1.4 | |
| 6 | 27 | 135.93 | -1.3 | 0.67 |
| 6 | 28 | 135.59 | -1.3 | 0.57 |
| 7 | 26 | 135.99 | -1.5 | |
| 7 | 27 | 135.64 | -1.4 | |
| 7 | 28 | 135.27 | -1.3 | 0.65 |
| 8 | 26 | 135.74 | -1.4 | 0.65 |
| 8 | 27 | 135.36 | -1.4 | |
| 8 | 28 | 134.97 | -1.3 | |
| 1 | 26 | 137.78 | -1.2 | 0.68 |
| 1 | 27 | 137.48 | -1.2 | 0.65 |
| 1 | 28 | 137.17 | -1.1 | 0.67 |
| 0 | 26 | 138.07 | -1.2 | 0.67 |
| 0 | 27 | 137.78 | -1.1 | 0.68 |
| 0 | 28 | 137.49 | -1.1 | 0.62 |
| -1 | 26 | 138.37 | -1.2 | 0.60 |
| -1 | 27 | 138.09 | -1.2 | 0.62 |
| -1 | 28 | 137.80 | -1.1 | 0.73 |
| 14 | 39 | 40.195 | -1.0 | 0.64 |
| 14 | 40 | 40.415 | -1.0 | 0.66 |
| 14 | 41 | 40.64 | -1.0 | 0.75 |
| 15 | 39 | 39.79 | -1.0 | 0.63 |
| 15 | 40 | 40 | -1.0 | 0.74 |
| 15 | 41 | 40.23 | -1.0 | 0.73 |
| 16 | 39 | 39.4 | -1.0 | 0.68 |
| 16 | 40 | 39.605 | -1.0 | 0.66 |
| 16 | 41 | 39.825 | -1.1 | 0.60 |

To insure the suitability of the cuts described above for SAW applications, the coupling coefficients, SAW velocity, and powerflow angles have been calculated for these cuts and are summarized in Table 2. Inverse velocity plots have been made for orientations with promising SAW temperature characteristics to check for the possibility of leaky surface waves and minimum values of $f_b$ were calculated and compared with $f_{SAW}$. The polar plots of the inverse velocities for a (YX wlt) 0/27/137.8 and 7/27/135.59 are shown in Figure 1 and Figure 2, respectively. The inverse surface wave velocity for 0/27/137.8 is $3.06 \times 10^{-4}$, that for 7/27/137.8 is $3.03 \times 10^{-4}$. These values are larger than the maximum $(1/v_{bulk}) \cos \theta$ ($< 2.9 \times 10^{-4}$), therefore, the analysis indicates that a leaky mode does not exist (see Table 2 for the SAW velocities).

Table 2. Propagation Characteristics of Selected Orientations

| ANGLES OF $ZTCF^{(1)}$, DEGREES (S AND T'S PROGRAM) | | | VELOCITY (MSEC) | $K^2$ ($X10^{-3}$) | POWER FLOW ANGLE (DEGREES) |
|---|---|---|---|---|---|
| PHI | THETA | PSI | | | |
| 6 | 26 | 136.31 | 3296.84 | 1.12 | -0.3 |
| 6 | 27 | 135.93 | 3293.60 | 1.12 | -0.2 |
| 6 | 28 | 135.59 | 3290.63 | 1.12 | -0.1 |
| 7 | 26 | 135.99 | 3303.33 | 1.12 | -0.5 |
| 7 | 27 | 135.64 | 3299.70 | 1.12 | -0.4 |
| 7 | 28 | 135.27 | 3296.33 | 1.12 | -0.3 |
| 8 | 26 | 135.74 | 3310.15 | 1.12 | -0.7 |
| 8 | 27 | 135.36 | 3306.11 | 1.12 | -0.6 |
| 8 | 28 | 134.97 | 3302.32 | 1.10 | -0.5 |
| 1 | 26 | 137.78 | 3268.80 | 1.10 | +0.7 |
| 1 | 27 | 137.48 | 3267.44 | 1.10 | +0.9 |
| 1 | 28 | 137.17 | 3266.36 | 1.10 | +1.0 |
| 0 | 26 | 138.07 | 3264.09 | 1.12 | +0.9 |
| 0 | 27 | 137.78 | 3263.09 | 1.10 | +1.1 |
| 0 | 28 | 137.49 | 3262.35 | 1.10 | +1.2 |
| -1 | 26 | 138.37 | 3259.65 | 1.10 | +1.1 |
| -1 | 27 | 138.09 | 3259.01 | 1.10 | -1.3 |
| -1 | 28 | 137.80 | 3258.64 | 1.08 | +1.5 |
| 14 | 39 | 40.195 | 3298.60 | 0.96 | -7.7 |
| 14 | 40 | 40.415 | 3306.67 | 0.96 | -8.1 |
| 14 | 41 | 40.64 | 3315.19 | 0.94 | -8.6 |
| 15 | 39 | 39.79 | 3301.82 | 0.96 | -7.8 |
| 15 | 40 | 40.00 | 3310.14 | 0.94 | -8.3 |
| 15 | 41 | 40.23 | 3319.09 | 0.98 | -8.6 |
| 16 | 39 | 39.4 | 3305.38 | 0.96 | -8.0 |
| 16 | 40 | 39.605 | 3314.03 | 0.98 | -8.4 |

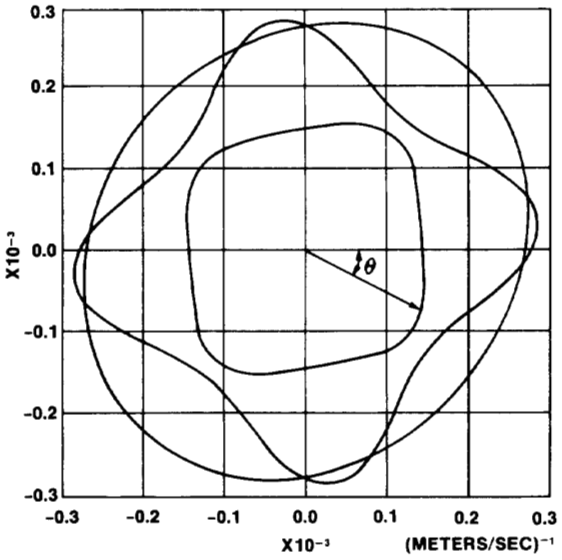


Figure 1. Polar Plots of Inverse Velocities for a (YXwlt) 0/27/137.8



Williams, Dylan; Cho, F.
"Numerical Analysis of Doubly Rotated Cut SAW Devices."
Paper presented at 34th Annual Symposium on Frequency Control, Philadelphia, PA, United States. May 28, 1980 - May 30, 1980.

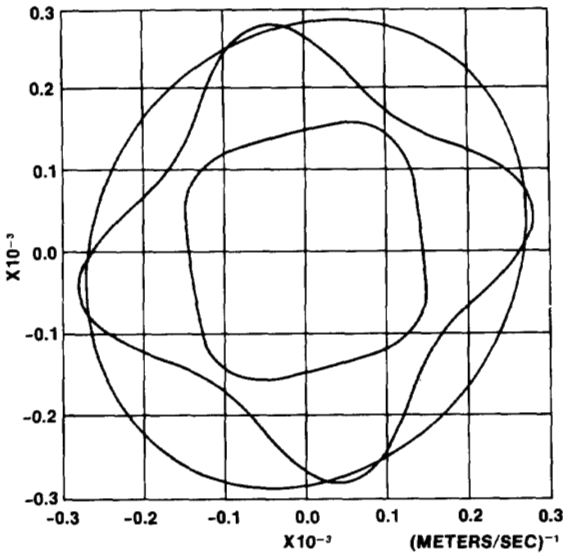


Figure 2. Polar Plots of Inverse Velocities for a (YXwlt) 7/27/135.59

In cutting quartz and aligning masks on it, there is always some maximum achievable accuracy. Thus it is useful to know how all of the acoustic quantities considered vary with angle. Quantities such as TCD, phase velocity, power flow angle, $\Delta$ V/V, and bulk wave velocity surfaces, are of interest to this program. These quantities can be accurately determined by directly calculating the quantities at $\phi = (\phi_0 + \Delta\phi)$, $\theta = (\theta_0 + \Delta\theta)$, and $\psi = (\psi_0 + \Delta\psi)$ with the same computer program discussed earlier.

Calculation of the angular dependence on the first, second, and third order TCD's is, of course, our primary task. Of these three quantities, the first order TCF is most sensitive to angular variation. Quantities such as velocity (Table 2), power flow angles (Table 2), BAW velocities (Figures 1 and 2), coupling coefficients (Table 3), and second and third order TCF's (Table 1) do not vary quickly with angle. This is not the case for $TCF^{(1)}$. Table 3 contains a summary of $\partial\, TCF^{(1)}/\partial\psi$. The large values of $\partial\, TCF^{(1)}/\partial\psi$ impose strict fabrication tolerances on the SAW cuts and mask alignment. Fabrication accuracy to within 6 minutes is required to keep the total temperature variation due to $TCF^{(1)}$ within 45 ppm for $\partial\, TCF^{(1)}/\partial\psi$ = 3(PPM/°C)/degree over the temperature range -50°C to 100°C. Table 4 contains summaries of $\partial\, TCF^{(1)}/\partial\phi$ and $\partial\, TCF^{(1)}/\partial\theta$. These values impose fabrication tolerances on the rotated quartz plate angles $\phi$ and $\theta$ of 12 minutes to keep the total temperature variation due to $\partial\, TCF^{(1)}(15/40/40)/\partial\phi$ within 45 ppm over the temperature range -50°C to 100°C. This linear temperature variation may be compensated for by varying $\psi$ on any particular cut if all other cut parameters vary slowly with angle.

Table 3. $\partial\, TCF^{(1)}/\partial\psi$ for Selected Cuts

| ANGLES OF $ZTCF^{(1)}$, DEGREES (S AND T'S PROGRAM) | | | $\partial TCF^{(1)}/\partial\psi$ |
|---|---|---|---|
| PHI | THETA | PSI | |
| 6 | 26 | 136.31 | +2.7 (PPM/C°)/DEGREE |
| 6 | 27 | 135.93 | +2.7 |
| 6 | 28 | 135.59 | +2.7 |
| 7 | 26 | 135.99 | +2.7 |
| 7 | 27 | 135.64 | +2.7 |
| 7 | 28 | 135.27 | +2.7 |
| 8 | 26 | 135.74 | +2.7 |
| 8 | 27 | 135.36 | +2.7 |
| 8 | 28 | 134.97 | +2.7 |
| 1 | 26 | 137.78 | +2.8 |
| 1 | 27 | 137.48 | +2.8 |
| 1 | 28 | 137.17 | +2.8 |
| 0 | 26 | 138.07 | +3.0 |
| 0 | 27 | 137.78 | +3.0 |
| 0 | 28 | 137.49 | +3.0 |
| -1 | 26 | 138.37 | +3.0 |
| -1 | 27 | 138.09 | +3.0 |
| -1 | 28 | 137.80 | +3.0 |
| 14 | 39 | 40.195 | -3.5 |
| 14 | 40 | 40.415 | -3.5 |
| 14 | 41 | 40.64 | -3.5 |
| 15 | 39 | 39.79 | -3.5 |
| 15 | 40 | 40 | -3.5 |
| 15 | 41 | 40.23 | -3.5 |
| 16 | 39 | 39.4 | -3.7 |
| 16 | 40 | 39.605 | -3.7 |
| 16 | 41 | 39.825 | -3.7 |

Table 4. $\partial\, TCF^{(1)}/\partial\phi$ and $\partial\, TCF^{(1)}/\partial\theta$ for Selected Cuts

| ANGLES OF $ZTCF^{(1)}$ (S AND T'S PROGRAM), DEGREE | | | $\partial TCF^{(1)}/\partial\phi$ | $\partial TCF^{(1)}/\partial\theta$ |
|---|---|---|---|---|
| PHI | THETA | PSI | | |
| 7 | 27 | 135.64 | -0.7(PPM/C°)/DEGREE | -0.5(PPM/C°)/DEGREE |
| 0 | 27 | 137.78 | -0.8 | -0.8 |
| 15 | 40 | 40.00 | +1.5 | -0.7 |

## EXPERIMENTAL VERIFICATION

Wafers with the orientation listed in Table 1 are being fabricated. Considerable care has been taken to reduce fabrication tolerances of the devices fabricated for this study. For these cuts, $\phi$ and $\theta$ are known to be within ±4 minutes. $\psi$ is known to be within ±15 minutes. Two wafers with orientation (YX wlt) 8.05°/25.9°/135.7° and (YX wlt) 6.57°/26.88°/134.9° as well as a commercially supplied ST-cut wafer have been tested. A delay line oscillator was used to measure the temperature dependence of the SAW delay time. The experimental apparatus is shown in Figure 3. No coils were used to match the devices in order to eliminate inductance changes in the matching circuit over the temperature range tested. The complete experimental error is estimated to be within ±10 ppm.



Williams, Dylan; Cho, F.
"Numerical Analysis of Doubly Rotated Cut SAW Devices."
Paper presented at 34th Annual Symposium on Frequency Control, Philadelphia, PA, United States. May 28, 1980 - May 30, 1980.

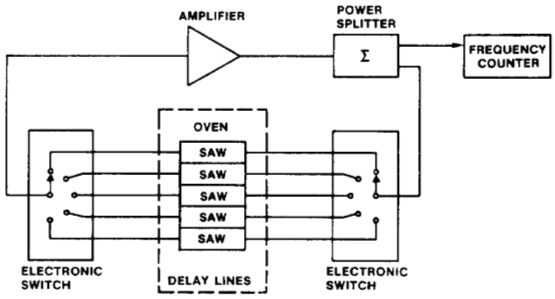


Figure 3. Measurement System

The frequency-temperature behavior of the device fabricated on the commercially supplied ST-cut wafer (YX wlt) 0/42.75/0 (angular tolerance is not known) is shown in Figure 4. Both the calculated and experimental results are plotted. Plots of the measured frequency-temperature behavior of the two devices fabricated at Motorola are shown in figure 5 and 6.

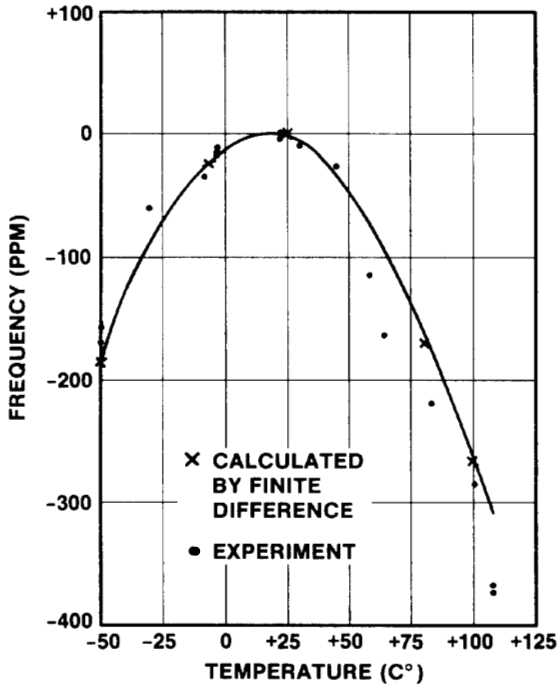


Figure 4. (YXwlt) 0/42.75/0 ST-CUT

The linear term in temperature is virtually absent in the device fabricated at (YX wlt) 6.57/26.88/134.9 (figure 5). The linear frequency term in the device fabricated at (YX wlt) 8.05/25.9/135.7 (figure 6) could be compensated for by a rotation of the mask by about 0.5 degrees. This small rotation would not, according to our calculations, appreciably affect $TCF^{(2)}$. Both devices have a calculated second order $TCF^{(2)}$ of about $-0.15 \times 10^{-7}$, about half as large as that of ST-Cut Quartz. This result is born out by the experimental measurements, a linear regression analysis which shows a $TCF^{(2)}$ of $-0.16 \times 10^{-7}$. These results are summarized in Table 5.

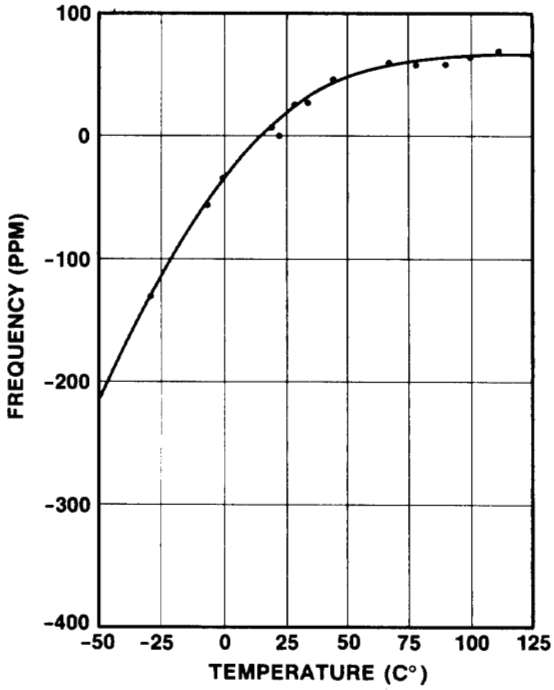


Figure 5. (YXwlt) 8.05/25.9/135.7)

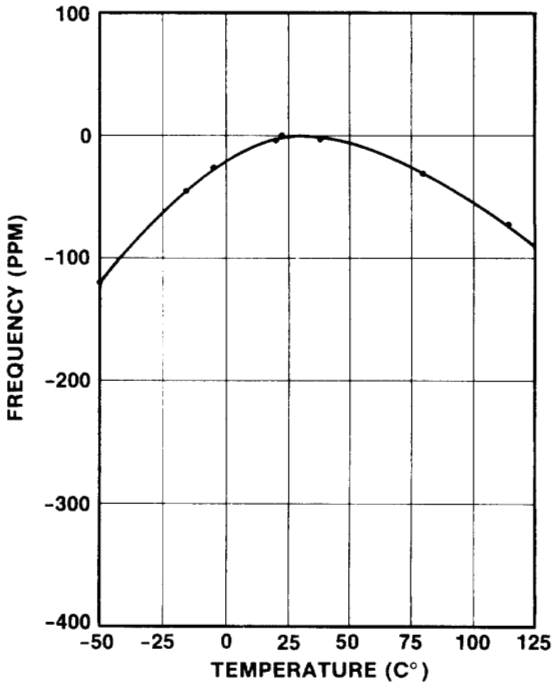


Figure 6. (YZwlt) 6.57/26.88/134.9



Williams, Dylan; Cho, F.
"Numerical Analysis of Doubly Rotated Cut SAW Devices."
Paper presented at 34th Annual Symposium on Frequency Control, Philadelphia, PA, United States. May 28, 1980 - May 30, 1980.

Table 5. Comparison of Experimental and Calculated Results

| Angles | | | Calculated | | | | Measured | | |
|---|---|---|---|---|---|---|---|---|---|
| Phi | Thet | Psi | TCF [1] †† | TCF [1] ††† | TCF [2] ††† | TCF [3] ††† | TCF [1] | TCF [2] | TCF [3] |
| 0 | 42.75 | 0† | $-0.07 \times 10^{-5}$ | $0.06 \times 10^{-5}$ | $-0.40 \times 10^{-7}$ | $0.11 \times 10^{-10}$ | $-0.1 \times 10^{-5}$ | $-0.37 \times 10^{-7}$ | $-0.17 \times 10^{-10}$ |
| 8.05 | 25.9 | 135.7 | -0.01 | 0.74 | -0.15 | 0.42 | 0.16 | -0.16 | 0.58 |
| 6.57 | 26.88 | 134.9 | -0.24 | 0.55 | -0.15 | 0.48 | 0.025 | -0.16 | 0.47 |

†Wafer obtained commercially. Angular tolerance is unknown.

††Calculated using Sinha and Tiersten's program.

†††Calculated using Finite Difference Approach.

The agreement between the experimental and calculated results has been excellent to date. Calculations using the Finite Difference method indicate that the doubly rotated wafers in fabrication should possess a slightly improved frequency response with $TCF^{(2)} = -0.1 \times 10^{-7}$ (see Table 1) but does not include the effects of coordinate axis skewing[5] taken into account by the Sinha and Tiersten computer program, which may become significant for these cuts which are farther off of the crystaline axes.

## SUMMARY

The results of a study of the temperature coefficients of frequency on doubly rotated cuts of quartz were presented. Both a Finite Difference technique[3] and a Perturbation technique developed by Sinha and Tiersten[5] were used to select orientations with temperature stability superior to ST-Cut quartz. Experimental results are found to be in agreement with the calculations and show a two fold improvement in frequency stability over the ST-Cut.

## ACKNOWLEDGEMENTS

The authors wish to thank Dr. A. Ballato for stimulating technical discussions; we wish to thank Mr. D. Green, Mr. R. Welles, Mr. J. Balacio, Mr. R. Caputo, Ms. C. Peterson and Ms. L. Fredericks in the material and fabrication areas.

## REFERENCES

1"Surface Acoustic Wave Delay Lines with Small Temperature Coefficient", Schulz, Manfred B., Proc. IEEE, Sept. 1970, pp. 1361-1632.

2"Higher Order Temperature Coefficients of Quartz SAW Oscillators", D. Handen, M. Michael, J.J. Gagnepain, Frequency Control Symposium, 1978, pp. 77-86.

3"Numerical Computation of Acoustic Surface Waves in Layered Piezoelectric Media-Computer Program Descriptions", William Jones, William Smith, Donald Perry, Final Report F19628-70-C-0027, prepared for Air Force Cambridge Research Laboratories by Hughes Aircraft Company.

4"The Temperature Coefficients of Acoustic Surface Wave Velocity and Delay on Lithium Niobate, Lithium Tatalate, Quartz, and Tellerium Dioxide", Andrew Slobodnik, Report #AFCRL-72-0082, Air Force Cambridge Research Laboratories.

5"The Temperature Dependence of the Velocity of Surface Waves in Quartz", B.K. Sinha and H.F. Tiersten, IEEE, 1978, Ultrasonics Symposium, pp. 662-665.

6"Higher Order Temperature Coefficients of the Elastic Stiffnesses and Compliances of Alpha-Quartz", R. Bechmann, A. Ballato, T. Lukaszek, IRE, Aug. 1962, pp. 1812-1822.

7"Standards on Piezoelectric Crystals 1949", Pro. IRE 14, Dec. 1949, pp. 1378-1395.

8"Numerical Analysis of Doubly Rotated Cut SAW Devices", Williams and Cho, 1979 USP, IEEE Cat. No. 79CH 1482-9SU.

9"Surface and Shallow Bulk Acoustic Waves Propagating on Doubly Rotated Quartz Substrates," A. Ballato, T. Lukasek, K. Yen, R. Kagiwada, Technical Report DELET-TR-79-23, U.S. Army Electronics Technology and Devices Laboratory, Fort Monmouth, N.J.

10"A New Cut of Quartz Giving Improved Temperature Stability to SAW Oscillators", Ian Browning and Meirion Lewis, Proc. 32nd Annual Symposium on Frequency Control, 1978, pp. 87-92.



Williams, Dylan; Cho, F.
"Numerical Analysis of Doubly Rotated Cut SAW Devices."
Paper presented at 34th Annual Symposium on Frequency Control, Philadelphia, PA, United States. May 28, 1980 - May 30, 1980.

# Towards Standardized Waveguide Sizes and Interfaces for Submillimeter Wavelengths

N. M. Ridler[1*], R. A. Ginley[2], J. L. Hesler[3], A. R. Kerr[4], R. D. Pollard[5], D. F. Williams[2]
[1]*National Physical Laboratory (NPL), Teddington, UK*
[2]*National Institute of Standards and Technology (NIST), Boulder, CO, USA*
[3]*Virginia Diodes, Inc, Charlottesville, VA, USA*
[4]*National Radio Astronomy Observatory (NRAO), Charlottesville, VA, USA*
[5]*University of Leeds, Leeds, UK*

*Contact: nick.ridler@ieee.org, phone +44-208-943-7116

***Abstract*—This paper describes an activity that has begun recently to develop an international standard for rectangular metallic waveguides and their interfaces for frequencies of 110 GHz and above. The IEEE's Microwave Theory and Techniques Society (MTT-S) is sponsoring the development of this standard. The MTT-S Standards Committee has set up the P1785 Working Group tasked with undertaking the work that is necessary to write this standard. This paper describes the work to date of this Working Group and the future activities that will be necessary to complete the standard.**

***Index terms*—Waveguides, rectangular waveguides, millimetre-wave, submillimeter-wave, waveguide flanges, waveguide interfaces**

## I. Introduction

At the present time, no international document standards exist for defining sizes and interfaces for rectangular metallic waveguides used at submillimeter wavelengths (i.e. at frequencies above 325 GHz). Some proposals for sizes and interfaces have been published in recent years (e.g. [1-7]) but these have not yet been adopted by any of the international standards-making bodies (e.g. ISO, IEC, IEEE). This situation was recognized recently by the IEEE Standards Association, and this has led to a project being initiated to put in place an IEEE standard for both waveguide sizes (i.e. the aperture dimensions) and their associated interfaces (e.g. flanges) suitable for use at all frequencies above 110 GHz. Although standards already exist for waveguides in the 110 GHz to 325 GHz range (see, for example, [8, 9]), these waveguides will also be included in the new IEEE standard to allow their tolerances to be re-evaluated in the context of contemporary manufacturing capabilities.

The development of the new standard is being sponsored by the Standards Committee of the IEEE's Microwave Theory and Techniques Society (MTT-S). A working group has been set up (and assigned the project number P1785) that will write the standard and ensure that it is published in a timely manner. This working group held its first meeting during the International Microwave Symposium (IMS) in Atlanta, GA, USA, in June 2008. The working group has since met a further three times (i.e. approximately every six months), with the next meeting scheduled to take place during IMS in Anaheim, CA, USA, in May 2010 (www.ims2010.org). Membership of the P1785 Working Group is open to all persons with an interest in this area, and membership to the P1785 Working Group can be achieved by attending at least one, or more, of the working group meetings. The working group currently has 22 members.

It is envisaged that the standard will be published in two parts: one part dealing with waveguide dimensions and recommended frequency bands; the other part dealing with waveguide interfaces (including flanges). The working group is already making good progress with Part 1 of the standard and it is likely that a first draft will be available for public comment during 2011.

This paper gives a review of all the activities of the P1785 Working Group. The paper describes the progress of the working group to date – specifically, the work on defining frequency bands and waveguide aperture dimensions. This includes a review of the waveguide size scheme that has been provisionally chosen for inclusion in the IEEE standard. The paper also describes the planned working group activities for the future, including: the other remaining steps needed to complete Part 1 of the standard; and, information about waveguide interfaces to be included in the standard. More information about the standard, and the activities of the P1785 Working Group, can be found at: **http://grouper.ieee.org/groups/1785**.

## II. Progress to Date

Much of the first two meetings of the P1785 Working Group, in June and December 2008, were concerned with defining the general scope of the standard and the level of detail for the information to be included in the standard. It was also agreed during these early discussions that metric units[1] (i.e. millimeter and micron) will be used in the standard, rather than the Imperial units (i.e. inch and mil) that had been used in the existing MIL standard [8]. Similarly, although no official standard for frequency bands and waveguide dimensions currently exists for frequencies above 325 GHz, it was recognised that a significant amount of scientific work is already taking place at these higher frequencies. Much of this work has used the proposed

[1] Following the International System of units (i.e. **S**ystème **I**nternational d'unités, abbreviated to **SI**).

Ginley, Ronald; Williams, Dylan; Ridler, N; Hesler, J; Kerr, Anthony; Pollard, R.
"Towards Standardized Waveguide Sizes and Interfaces for Submillimeter Wavelengths."
Paper presented at 21st International Symposium on Space Terahertz Technology 2010 (ISSTT 2010), Oxford, United Kingdom. March 23, 2010 - March 25, 2010.

frequency bands given in [3] – see, for example, [10] and [11]. These waveguide bands use an extension of the WR naming convention given in the MIL standard [8], leading to waveguide names such as WR-2.8, WR-2.2, etc. However, the dimensions of these waveguide bands are defined in terms of Imperial units[2] and so do not meet the agreed requirement that the IEEE standard will use dimensions defined in terms of metric units.

At the third P1785 Working Group meeting (in Boston, MA, USA, in June 2009), a great deal of attention was given to the subject of defining the waveguide frequency bands and aperture sizes. This led to the setting up of a dedicated sub-group, within the P1785 Working Group, tasked with recommending to the main P1785 Working Group potential schemes for defining waveguide frequency bands and aperture sizes. This sub-group[3], with membership from the USA and Europe, communicated regularly using email and teleconferencing. Over a period of six months or so, the sub-group developed a series of potential waveguide schemes that fitted, to a greater or lesser degree, some generally agreed design criteria. However, it also became clear that no unique waveguide scheme existed that perfectly met all the design criteria. The ten design criteria that were established during this process are described below.

*A. Frequency bands*

The frequency bands (i.e. the suggested lower and upper frequencies of each waveguide band) should:

1. Be memorable (i.e. use whole numbers);
2. Form two contiguous interleaved series (i.e. should not contain gaps or overlaps in the frequencies covered by each series);
3. Be easily extendable from lower frequencies to higher frequencies (i.e. mapping from one decade to the next);
4. Agree with the existing values for WR-10 to WR-03, as given in the MIL standard [8].

*B. Waveguide dimensions*

It was soon agreed that a ratio of 2:1 would be used to describe the relationship between the waveguide aperture width and height (i.e. the ratio of the broad- to narrow-wall dimensions). Therefore, it was only necessary to define the waveguide broad-wall dimension (called the 'width', by convention). The waveguide widths should:

5. Where appropriate, be effectively identical (within stated tolerances) to sizes WR-10 to WR-03, as given in the MIL standard [8]);
6. Where appropriate, be very similar to sizes WR-2.8 to WR-1.0, as given in [3];
7. Avoid fractional micron values (i.e. *x.y* microns).

*C. Related quantities*

In addition to the above, the waveguide scheme should provide, for all bands:

8. Relatively uniform fractional bandwidths;
9. Approximately constant *k*-factors[4] (where $k_1 \approx 1.25$ and $k_2 \approx 1.90$);
10. Similar ratios of cut-off frequencies (or, equivalently, waveguide widths) for adjacent bands.

The subgroup developed a spreadsheet to assist in the development and evaluation of candidate waveguide schemes. The spreadsheet included plots of size deviations from current standards, worst-case reflection coefficients due to these size deviations, cutoff-frequency ratios, fractional bandwidths, and *k*-factors. This spreadsheet will soon be made available at: **http://grouper.ieee.org/groups/1785**. The spreadsheet and design criteria discussed above were used to establish a short-list of three candidate waveguide schemes[5] that were presented subsequently to the P1785 Working Group for discussion, followed by a vote.

The first scheme was derived from [3]. It retained the familiar WR names and recommended operating bands currently being used, but used metric sizing. This scheme resulted in excellent compatibility with existing practice and retained familiar nomenclature and operating bands while providing a metric framework for dimensions. The disadvantages were seen to be an irregularity in the progression of the scheme, fractional numbers in the nomenclature and significant variations in the mismatch and *k*-factor spread.

The second scheme was developed within the subgroup itself [12], and used the names WM *n*, where *n* was an integer or half integer denoting the waveguide size. This resulted in names of the form WM 0, WM 0.5, WM 1, WM 1.5, etc, keeping names short and making it easy to identify neighbouring bands. Sizes for WM 0 to WM 2.5 were chosen from a table to correspond closely to existing standards, but above WM 2.5, the waveguide width, *a*, is determined by rounding $10^{(-2n/11)} \times 2540$ µm to three significant digits. This formula-based approach ensured a uniform and unlimited geometric progression of center frequencies with exceptionally uniform operating bandwidths to simplify the development of certain instrumentation and even allowed for the natural definition of quarter-band sizes when necessary, while keeping deviations from established bands below the measureable limits of today's instrumentation and standards. However, the scheme did break from the convention of using the waveguide sizes themselves as names, changing the current nomenclature style by having numbers increasing with decreasing waveguide size, and adjusted recommended operating frequency bands somewhat from existing practice.

[2] The number 2.8 in the name WR-2.8 refers to the defined broad-wall dimension of the waveguide, i.e. (2.8 ×10) mil = 28 mil.

[3] The members of the subgroup were Jeffrey Hesler, Anthony Kerr, Roger Pollard, Nick Ridler and Dylan Williams.

[4] These *k*-factors are the multipliers used to establish the suggested minimum frequency, $f_{min}$, and maximum frequency, $f_{max}$, from the cutoff-frequency, $f_c$, for each waveguide band: $f_{min} = k_1 \times f_0$; $f_{max} = k_2 \times f_0$.

[5] Two of these schemes were derived from [3] and [6], along with a third scheme proposed in [12].

Ginley, Ronald; Williams, Dylan; Ridler, N; Hesler, J; Kerr, Anthony; Pollard, R.
"Towards Standardized Waveguide Sizes and Interfaces for Submillimeter Wavelengths."
Paper presented at 21st International Symposium on Space Terahertz Technology 2010 (ISSTT 2010), Oxford, United Kingdom. March 23, 2010 - March 25, 2010.

The provisional scheme eventually selected, following a discussion and vote by the P1785 Working Group, is shown in Table 1, where *a* and *b* refer to the width and height dimensions of the waveguides, respectively.

TABLE I
PROPOSED FREQUENCY BANDS AND WAVEGUIDE DIMENSIONS FOR THE IEEE STANDARD

| Name | *a* (μm) | *b* (μm) | $f_c$ (GHz) | $f_{min}$ (GHz) | $f_{max}$ (GHz) |
|---|---|---|---|---|---|
| WM-2540 | 2540 | 1270 | 59.014 | 75 | 110 |
| WM-2032 | 2032 | 1016 | 73.767 | 90 | 140 |
| WM-1651 | 1651 | 825.5 | 90.790 | 110 | 170 |
| WM-1295 | 1295 | 647.5 | 115.75 | 140 | 220 |
| WM-1092 | 1092 | 546 | 137.27 | 170 | 260 |
| WM-864 | 864 | 432 | 173.49 | 220 | 330 |
| WM-710 | 710 | 355 | 211.12 | 260 | 400 |
| WM-570 | 570 | 285 | 262.97 | 330 | 500 |
| WM-470 | 470 | 235 | 318.93 | 400 | 600 |
| WM-380 | 380 | 190 | 394.46 | 500 | 750 |
| WM-310 | 310 | 155 | 483.53 | 600 | 900 |
| WM-250 | 250 | 125 | 599.58 | 750 | 1100 |
| WM-200 | 200 | 100 | 749.48 | 900 | 1400 |
| WM-164 | 164 | 82 | 913.99 | 1100 | 1700 |
| WM-130 | 130 | 65 | 1153.0 | 1400 | 2200 |
| WM-106 | 106 | 53 | 1414.1 | 1700 | 2600 |
| WM-86 | 86 | 43 | 1743.0 | 2200 | 3300 |

This scheme, which is based on [6], was produced as follows:

(i) use the existing MIL series [8] as the basis;
(ii) scale widths by dividing by 10;
(iii) express the resulting widths using rounded metric units, i.e. microns.

Minor adjustments have been made to the widths in three bands (but keeping the frequency bands the same) to make the ratios of cut-off frequency values between bands closer to the ideal value of $10^{(1/11)} \approx 1.233$ without appreciably increasing the mismatch when connected to the corresponding waveguides given in [3]. The scheme also uses a suggested upper frequency for the WM-864 band of 330 GHz (rather than 325 GHz), and an associated suggested lower frequency of 330 GHz for the WM-570 band.

In terms of meeting the above design criteria, the frequency bands:

1. Are memorable, i.e. the suggested minimum and maximum frequencies are ten times the values for the MIL frequency bands [8] used for the decade below (with the exception that 325 GHz has been changed to 330 GHz), thus giving full backward compatibility with existing waveguide bands;
2. Link together as two contiguous, interleaved, series: (i) WM-710, WM-470, WM-310, etc; and, (ii) WM-570, WM-380, WM-250, etc;
3. Are extendable to higher frequencies (i.e. smaller waveguide sizes) as follows:
   a. use the waveguide sizes that are unshaded in Table 1;
   b. divide mechanical dimensions by 10;
   c. multiple frequencies by 10;
   d. rename the waveguide accordingly.

   For example, the next two sizes in this series (derived from WM-710 and WM-570) are shown in Table 2;

TABLE II
EXTENDED FREQUENCY BANDS AND WAVEGUIDE DIMENSIONS FOR THE IEEE STANDARD

| Name | *a* (μm) | *b* (μm) | $f_c$ (GHz) | $f_{min}$ (GHz) | $f_{max}$ (GHz) |
|---|---|---|---|---|---|
| WM-71 | 71 | 35.5 | 2111.2 | 2600 | 4000 |
| WM-57 | 57 | 28.5 | 2629.7 | 3300 | 5000 |

4. Are identical with the MIL standard bands [8] in the overlap region, shaded in Table 1, with the exception that 325 GHz has been changed to 330 GHz.

Similarly, the waveguide dimensions (i.e. the widths):

5. Are within 0.05% of MIL standard widths [8] in the overlap region, shaded in Table 1. This produces a worst-case mismatch (i.e. return loss) when connecting to the corresponding MIL standard bands [8] of -70 dB (not including mismatch due to waveguide tolerances);
6. Are within 3% of the widths given in [3]. This produces a worst-case mismatch (i.e. return loss) when connecting to the corresponding bands in [3] of -35 dB (not including mismatch due to waveguide tolerances);
7. Do not use fractional micron values (until the series has been extended to include WM-16.4, i.e. for the frequency range 11 THz to 17 THz!)

Similarly, for the related quantities for all bands:

8. Ratios of minimum to maximum frequency vary between 1.47 and 1.57, indicating that all bands have relatively uniform bandwidths;
9. *k*-factor values are relatively constant, ranging from $1.20 \le k_1 \le 1.27$ and $1.83 \le k_2 \le 1.91$;
10. Ratios of cut-off frequencies for adjacent bands vary between 1.19 and 1.27 and so are considered similar.

Finally, a new naming convention has been developed for these waveguide bands. Since the sizes are defined in terms of metric units, the letters WM are used to indicate that the size refers to **W**aveguide using **M**etric dimensions. These letters are followed by a number that indicates the size (in microns) of the waveguide broad wall dimension. Table 3 gives a comparison between these new names and the names of related waveguides in the existing MIL standard [8]. Table 4 gives a comparison between the new names and the nearest waveguides given in [3] (i.e. the 'extended MIL' bands).

Ginley, Ronald; Williams, Dylan; Ridler, N; Hesler, J; Kerr, Anthony; Pollard, R.
"Towards Standardized Waveguide Sizes and Interfaces for Submillimeter Wavelengths."
Paper presented at 21st International Symposium on Space Terahertz Technology 2010 (ISSTT 2010), Oxford, United Kingdom. March 23, 2010 - March 25, 2010.

TABLE III
COMPARISON BETWEEN NEW IEEE AND EXISTING MIL WAVEGUIDE NAMES

| MIL name | New IEEE Name | $f_{min}$ (GHz) | $f_{max}$ (GHz) |
|---|---|---|---|
| WR-10 | WM-2540 | 75 | 110 |
| WR-08 | WM-2032 | 90 | 140 |
| WR-06 | WM-1651 | 110 | 170 |
| WR-05 | WM-1295 | 140 | 220 |
| WR-04 | WM-1092 | 170 | 260 |
| WR-03 | WM-864 | 220 | 330 |

TABLE IV
COMPARISON BETWEEN NEW IEEE AND 'EXTENDED MIL' WAVEGUIDE NAMES

| 'Extended MIL' name | New IEEE Name | $f_{min}$ (GHz) | $f_{max}$ (GHz) |
|---|---|---|---|
| WR-2.8 | WM-710 | 260 | 400 |
| WR-2.2 | WM-570 | 330 | 500 |
| WR-1.9 | WM-470 | 400 | 600 |
| WR-1.5 | WM-380 | 500 | 750 |
| WR-1.2 | WM-310 | 600 | 900 |
| WR-1.0 | WM-250 | 750 | 1100 |

This naming convention can easily accommodate 'specialized' (i.e. custom made) waveguide bands, should they be needed, simply by giving the WM letters followed by the broad wall dimension of the custom made waveguide, expressed in microns.

## III. FUTURE ACTIVITIES

### A. Other waveguide size information

Having chosen a scheme for defining the frequency bands and the waveguide dimensions, this information will be contained in a table in Part 1 of the IEEE standard. It is envisaged that this table will also contain some additional information about each waveguide size. For example, it will be useful to specify tolerances on the critical mechanical dimensions of the waveguide. It has already been discussed within the P1785 Working Group that perhaps two 'grades' of waveguide quality may be given, based on the specified tolerances of the critical dimensions – a 'precision' grade, based on the best achievable tolerances using state-of-the-art manufacturing techniques, and a 'general' grade, that will be realisable using more routine manufacturing techniques.

Other specification parameters for the waveguides are also likely to be given – for example, typical attenuation per unit length, typical mismatch due to waveguide tolerances, etc.

### B. Waveguide interfaces

The other main topic that will be covered by this IEEE standard is the definition of suitable interfaces for waveguides used above 110 GHz. It is widely recognised that the popular waveguide interfaces used at millimetre-wave frequencies up to 110 GHz (for example, MIL-DTL-3922/67D [13], also known as UG-387) will not be suitable for use at these higher frequencies. This is because waveguide misalignment, due to tolerances on the critical dimensions of the interfaces, will cause unacceptably large reflections in these smaller waveguide sizes when fitted with such interfaces.

Instead, the suitability of alternative interface designs will be investigated for use with the waveguide sizes specified in the IEEE standard. There are already several interface designs that could be included in the standard. These include:

1. A precision version of UG-387, with tighter tolerances and anti-cocking mechanisms [3]. This could also include additional alignment pins directly above and below the waveguide aperture [1];
2. A miniature flange (the so-called Grammer miniature flange) [3] that has been developed by NRAO for use with the ALMA project[6];
3. A 'plug-and-socket' style of interface [4];
4. A ring-centered flange (see [5] and [7]), of similar dimensions to the UG-387 flange (i.e. with an outer diameter of approximately 19 mm);
5. A miniature ring-centered flange [5], of similar dimensions to the Grammer miniature flange (i.e. with an outer diameter of approximately 12.7 mm).

It is likely that several different types of waveguide interface will be included in the standard so that users can select a suitable design for their particular application (including frequency range).

## IV. CONCLUSIONS

This paper has described an on-going activity to develop an international standard for waveguides and their interfaces for use at frequencies of 110 GHz and above. The work to date on defining the frequency bands and waveguide dimensions has been described in detail. It is hoped that potential users of these waveguides will study these proposed frequency bands and waveguide sizes and comment on their suitability for their applications.

The plans for the future development of the standard have also been described. This has included a description of some waveguide interfaces that may be included in the standard. As before, it is hoped that potential users of these interfaces will study these proposed designs and comment on their suitability. Any such comments, either on frequency bands, waveguide sizes or waveguide interfaces, should be sent to: nick.ridler@ieee.org. Comments concerning the proposed frequency bands and waveguide sizes should be sent before May 2010, since this is when the P1785 Working Group will make a decision on whether to accept these proposed frequency bands and waveguide sizes.

## ACKNOWLEDGMENTS

The funding for Mr Ridler's involvement with this activity is provided by the National Measurement Office of the UK government's Department of Business, Innovation and Skills. The National Radio Astronomy Observatory is a facility of

[6] ALMA is the Atacama Large Millimeter / submillimeter Array, www.alma.nrao.edu.

the National Science Foundation operated under cooperative agreement by Associated Universities, Inc.

## REFERENCES


[1] C. Oleson and A. Denning, "Millimeter Wave Vector Analysis Calibration and Measurement Problems Caused by Common Waveguide Irregularities", *Proc. 56th ARFTG Microwave Measurement Conf.*, Boulder, CO, USA, December 2000.

[2] J. S. Ward, "New Standards for Submillimeter Waveguides", *Proc. 17th Int. Symp. on Space THz Tech.*, Paris, France, May 2006.

[3] J. L. Hesler, A. R. Kerr, W. Grammer and E. Wollack, "Recommendations for Waveguide Interfaces to 1 THz", *Proc. 18th Int. Symp. on Space THz Tech.*, Pasadena, CA, USA, March 2007.

[4] Y. S. Lau and A. Denning, "An Innovative Waveguide Interface for Millimeter Wave and Sub-millimeter Wave Applications", *Proc. 69th ARFTG Microwave Measurement Conf.,* Honolulu, HI, USA, June 2007.

[5] A. R. Kerr and S. Srikanth, "The Ring-centered Waveguide Flange for Submillimeter Wavelengths", *Proc. 20th Int. Symp. on Space THz Tech.*, Charlottesville, VA, USA, April 2009.

[6] N. M. Ridler, "Recommendations for Waveguide Sizes at Submillimeter Wavelengths", *Proc. 73rd ARFTG Microwave Measurement Conf.*, Boston, MA, USA, June 2009.

[7] H. Li, A. R. Kerr, J. L. Hesler, H. Xu, R. M. Weikle II, "A Ring-centered Waveguide Flange for Millimeter- and Submillimeter-wave Applications", accepted for publication, *IEEE MTT-S International Microwave Symposium*, Anaheim, CA, USA, May 2010.

[8] MIL-DTL-85/3C, "Waveguides, rigid, rectangular (millimetre wavelength)", October 2005.

[9] IEC 60153-2, "Hollow metallic waveguides. Part 2: relevant specifications for ordinary rectangular waveguides", 2nd edition, 1974.

[10] C. Oleson, A. Denning and Y. Lau, "325 to 500 GHz Vector Network Analysis System", *Proc. 66th ARFTG Microwave Measurement Conf.*, Washington, DC, USA, December 2005.

[11] L. Samoska et al, "A Submillimeter-wave HEMT Amplifier Module with Integrated Waveguide Transitions Operating Above 300 GHz", *IEEE Trans. Microwave Theory Tech.*, vol. 56, pp. 1380-1388, June 2008.

[12] D. F. Williams, "A Split-Geometric Scheme", private email communication, 11 February 2010.

[13] MIL-DTL-3922/67D, "Flanges, waveguide (contact), round, 4 hole (millimeter)", December 2009.


Ginley, Ronald; Williams, Dylan; Ridler, N; Hesler, J; Kerr, Anthony; Pollard, R.
"Towards Standardized Waveguide Sizes and Interfaces for Submillimeter Wavelengths."
Paper presented at 21st International Symposium on Space Terahertz Technology 2010 (ISSTT 2010), Oxford, United Kingdom. March 23, 2010 - March 25, 2010.

# Comprehensive Circuit Model of Autolimiting Superconductor Devices

J. Mateu, *Senior Member, IEEE*, C. Collado, *Senior Member, IEEE*, A. Hueltes, J. M. O'Callaghan, *Senior Member, IEEE*, D. Garcia-Pastor, R. Perea-Robles, N. Joshi, X. Lu, N. Orloff, and J. C. Booth

***Abstract*—This paper presents a phenomenological equivalent circuit to model the phenomenon occurring when a section of superconducting transmission line transits from a superconducting state to a normal state. This phenomenon allows the use of superconductors for the design of autolimiting structures based on superconducting transmission line sections. Although this autolimiting effect happens when the current density achieved in the superconductor exceeds the critical current inherent to the superconducting material, heating effects also play a significant role in this behavior. The equivalent circuit presented in this work accounts for both electric and thermal effects, and the interaction between them. The circuit model is then used for the evaluation of a practical microwave and frequency selective IMUX configuration.**

***Index Terms*—Nonlinearity, heating effects, autolimiting, microwave devices, filters.**

## I. Introduction

THE use of superconducting (HTS) auto-limiting structures has been proven over the past few years through the realization of power-limiting superconductor transmission lines [1]–[2], which exploit the transition phenomenon from superconductor to normal state. This achievement suggests the use of superconductors on the design of complex, frequency-selective, and functional auto-limiting architectures [3]. Application of those devices are several, including radar protection from jamming signals and the coexistence between very different RF/microwave systems, such as cellular communication and high-power radars. When these systems coexist, they need to operate without mutual interference or hardware damage. This challenge motivates continued research on novel multifunctional devices.

In response to this challenge, our work presents a phenomenological circuit model that accounts for the transition of the HTS section from the superconducting state to the normal state. This transition is responsible for the auto-limiting function.

Manuscript received August 31, 2016; accepted December 6, 2016. Date of publication December 12, 2016; date of current version January 6, 2017. This work was supported in part by the Generalitat de Catalunya under Grant 2014 SGR 1551 and in part by the U.S. Government.

J. Mateu, C. Collado, A. Hueltes, J. M. O'Callaghan, D. Garcia-Pastor, and R. Perea-Robles are with the Department of Signal Theory and Communication, Universitat Politecnica de Catalunya, Barcelona 08034, Spain (e-mail: jmateu@tsc.upc.edu).

N. Joshi, X. Lu, N. Orloff, and J. C. Booth are with the CTL, National Institute of Standards and Technology, Boulder, CO 80305 USA.

Color versions of one or more of the figures in this paper are available online at http://ieeexplore.ieee.org.

Digital Object Identifier 10.1109/TASC.2016.2638419

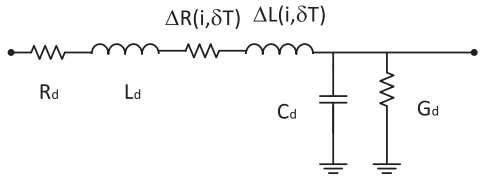


Fig. 1. Elemental section *dz* of a superconducting transmission line that includes non-linear intrinsic and heating effects [4].

The circuit model may be used to evaluate the auto-limiting performance of a complex structure such as a frequency selective multiplexer. In this work, a conventional circulator-coupled multiplexer is assessed under several realistic scenarios. These scenarios address the limiting effects in both the channel where the jamming signal occurs and in adjacent channels. This analysis may be used to verify the suitability of the multiplexer configuration.

Note that this work goes one step beyond previous work [3] and [4]. In [3], we evaluated the limiting effect of a single channelizing filter without considering thermal effects, whereas in [4], we proposed a local electro-thermal model that was only used to evaluate the limiting effects of superconducting transmission lines. This work complements both by developing a new phenomenological electro-thermal model, and by evaluating the limiting effects in a practical multiplexing configuration.

## II. Electro-Thermal Model in a Superconducting Transmission Line Section

Superconductors have the ability to switch from a high-loss normal state to a low-loss superconducting state, when cooled down to the critical temperature $T_c$. This transition also occurs for high-power signals when the current density in the superconductor exceeds the critical current $j_c$, due to the non-linear surface impedance [5]. For a quasi-TEM propagation mode, as occurs in a section of transmission line, an equivalent circuit model as the one shown in Fig. 1 can be outlined [5]. This circuit model corresponds to an elemental section *dz* where $L_d$, $R_d$, $C_d$ and $G_d$, correspond to the inductance, resistance, capacitance and conductance, per unit length, at the operating temperature. The additional terms $\Delta L(i, \delta T)$ and $\Delta R(i, \delta T)$ represent the distributed nonlinear inductance and resistance, respectively. These account for the superconducting transition, and depend on the current, *i*, flowing through the line and the temperature rise in the superconductor $\delta T$.

Mateu, Jordi; Collado, C; Hueltes, A; Garcia-Pastor, D; Perera, R; Joshi, Nikhil; Lu, Xifeng; Orloff, Nathan; Booth, James.
"Comprehensive circuit model of autolimiting superconductor devices."
Paper presented at Applied Superconductivity Conference (ASC 2016), Denver, CO, United States. September 4, 2016 - September 9, 2016.

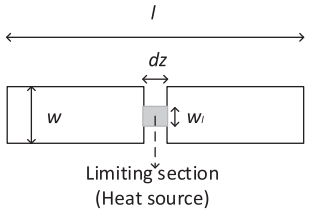


Fig. 2. Superconducting transmission line with an inserted SLS, *dz*.

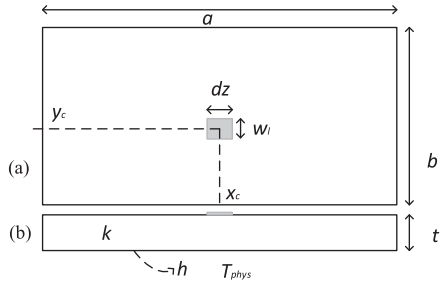


Fig. 3. Heating source on top of the substrate. (a) Top view, (b) side view.

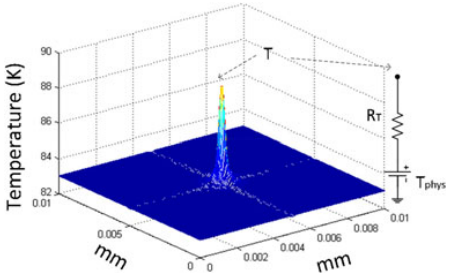


Fig. 4. Temperature distribution along the top surface of the substrate. Right side inset: Thermal modeling of the temperature rise.

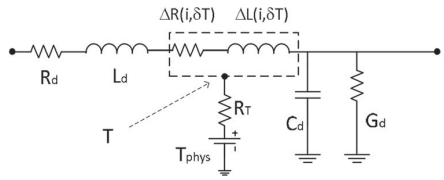


Fig. 5. Elemental section *dz*, of a SLS, considering the non-linear intrinsic effects and heating effect. Additionally, the heating flow through the substrate is included.

Determination of these linear and non-linear terms is crucial for creating an accurate circuit model of superconducting devices. The distributed inductance and resistance are obtained by means of the method described in [5]–[7]. These methods calculate the current density distribution along the cross-section of the limiting transmission line. Application of the current distribution through the non-linear conductivity is then used to obtain the distributed terms $L_d$ and $R_d$, and its corresponding non-linear terms $\Delta L(i,0)$ and $\Delta R(i,0)$.

At low powers, the temperature rise due to self-heating is negligible ($\delta T = 0$) because the losses are very small. But at higher powers, the losses start to increase and the dissipation increases. This then produces a temperature rise ($\delta T > 0$), which contributes to the transition to normal state, and therefore to the limiting effect [4].

In order to account for the temperature rise effect, we apply the methodology developed in our previous work [4], where a local thermal model was used along with the non-linear current dependence, to obtain $\Delta L(i, \delta T)$ and $\Delta R(i, \delta T)$.

Complete modeling of the electro-thermal phenomena that occurs in the limiting effect requires consideration of not only the electromagnetic terms of the dielectric $C_d$ and $G_d$, which can be obtained from several EM simulators, but also requires consideration of the heat conduction through the dielectric. A thermal model of the dielectric and its coupling into the electromagnetic and self-heating effects in the circuit of Fig. 1 are detailed in the following section.

## III. Thermal Effect of the Substrate

This section outlines the procedure to model the heating flow through the dielectric supporting the superconducting limiting section (SLS). As in [3] the SLS consists of a small segment of superconducting transmission line $d_z$ with much narrower strip section $w_l$, as outlined in Fig. 2.

When the SLS is in its normal-metal state, it dissipates power and acts as a heating source. In turn, this heat is spread throughout the dielectric. The distribution of heat through the dielectric can be modeled as a thermal resistance, which connects the heating source (SLS) through the convection boundary conditions [8].

The total thermal resistance is defined by $R_T = (\overline{T_s} - T_{\mathrm{phys}})/Q$, where $\overline{T_s}$ is the average temperature in the heating source, $T_{\mathrm{phys}}$ is the temperature of the cold plate set at the operating temperature and $Q$ is the heat flow rate, which can be calculated from circuit analysis.

Under this assumption, an analytical solution can be used to solve for an eccentric heat source on a finite rectangular flux channel in an isotropic substrate [8]. Details of the heating scenario are given in Fig. 3. Fig. 3a shows the top view of the aforementioned heating source on the dielectric. Dimensions ($d_z$ and $w_l$) and position ($x_c$ and $y_c$) of the heating source correspond to the area of the SLS and its location on the substrate. Fig. 3b shows the side view of the heating source, where *t* is the substrate thickness, *k* is the thermal conductivity of the substrate and *h* is the heat transfer coefficient.

To illustrate this, Fig. 4 shows the temperature on top of the dielectric when a heating source is placed in the middle of the dielectric. The heating source consists of a SLS placed on top of a sapphire substrate, where $w_l = 10\,\mu$m, $d_z = 0.2\,$mm ($\approx \lambda/15$), $a = b = 10\,$mm, $t = 0.5\,$mm, $k = 42\,\mathrm{W/(K \cdot m)}$, and a heat flow rate of $Q = 0.1\,$W is assumed. The substrate is thermally connected to the chuck operating at $T_{\mathrm{phys}} = 83\,$K. The temperature rise observed in Fig. 4 can be model by the thermal resistance, as indicated in the right side of Fig. 4, where $R_T = 63\,\Omega$. Identical simulation for a quartz substrate with $k = 2\,\mathrm{W/(K \cdot m)}$, results in a higher thermal resistance $R_T = 1300\,\Omega$. These two values will be used in Section IV.

The thermal model outlined in the inset of Fig. 4 can be coupled to the electromagnetic domain, as indicated in Fig. 5.

Mateu, Jordi; Collado, C; Hueltes, A; Garcia-Pastor, D; Perera, R; Joshi, Nikhil; Lu, Xifeng; Orloff, Nathan; Booth, James.
"Comprehensive circuit model of autolimiting superconductor devices."
Paper presented at Applied Superconductivity Conference (ASC 2016), Denver, CO, United States. September 4, 2016 - September 9, 2016.

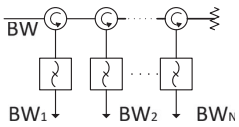


Fig. 6. Multiplexing architecture based on a Circulator-Coupled approach.

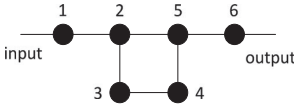


Fig. 7. Single limiting channel of the hybrid-coupled approach, under the limiting concept of [10].

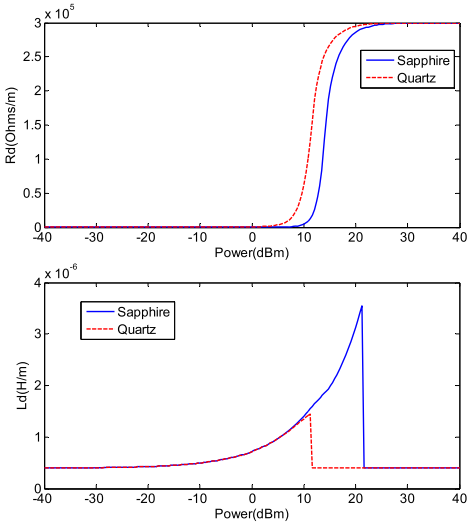


Fig. 8. Distributed resistance and inductance as a function of power.

As indicated above. $T_{\mathrm{phys}}$ is the reference temperature set by the boundary conditions at the bottom of the substrate, where the sample is usually in very good thermal contact with a copper chuck to keep the sample thermally stable at the desired operating temperature. The dissipated power (heat) is used as the input for the thermal domain model and the temperature rise is obtained at the SLS, defining the value of the distributed inductance and resistance at a given power.

## IV. Autolimiting Superconducting Multiplexer

The circuit model described above is used to evaluate the performance of a frequency-selective, auto-limiting superconducting multiplexing candidate. The configuration of the multiplexing approach is based on a conventional architecture, see Fig. 6 [9]. This approach uses circulators to route the full bandwidth (BW) signal to each channelizing filter, $\mathrm{BW_i}$. Only two channels are considered in this work, where the channelizing filters $\mathrm{BW_1}$ and $\mathrm{BW_2}$ have an identical bandwidth of 80 MHz, being centered at 3.5 GHz and 3.7 GHz, respectively. All filters consist of a sixth order Chebyshev response with a single pair of transmission zeros, symmetrically placed at the normalized frequency of $+/-j\cdot 1.75$. Evaluation of the filters assume a topology based on halfwave 50 Ω superconducting-transmission-line coupled

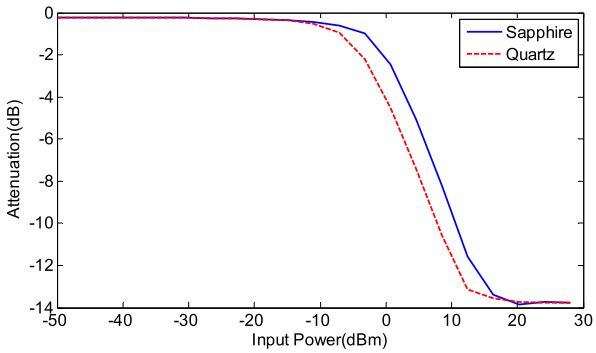


Fig. 9. In-band attenuation as a function of the input power.

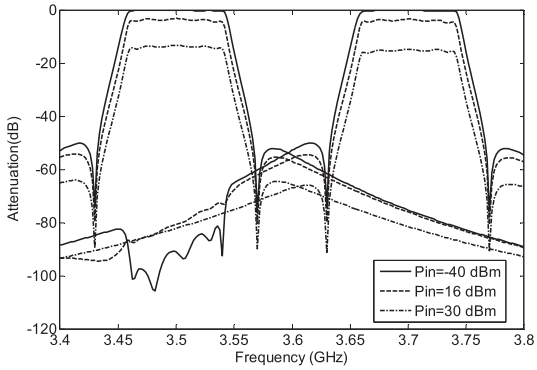


Fig. 10. Attenuation frequency dependence. Note that this corresponds to the transmission $S_{21}$ term for each input power, Pin.

resonators [9]. The filter topology is outlined in Fig. 7, where each resonator is indicated by a black circle and the lines indicate the coupling between resonators. Creation of transmission zeros has been performed by cross coupling between resonators 2 and 5 [9].

### A. Limiting Section

To evaluate the limiting performance, a SLS such as the one shown in Fig. 2 will be inserted in the middle of one of the six resonators that form the filter. Note that in a λ/2 resonant transmission line, the maximum current occurs in the middle of the resonator.

The dimensions of the SLS, properties of the substrates and operating temperature are the same at those listed in Section III. The additional properties of the SLS that are used in this section are 150 $\mu$m of thickness, $T_c = 90\,\mathrm{K}$ and $j_c = 5\times 10^{10}\ \mathrm{A/m^2}$. Analysis for both substrates (sapphire and quartz) is also considered in the analysis. Values of the distributed resistance and inductance of the phenomenological model of Fig. 4, as a function of power, are shown in Fig. 8. These dependencies are consistent with the ones reported in [4], for the local approach.

### B. Simulation Scenarios

In order to assess the suitability of this multiplexing configuration, several scenarios have been considered: The first scenario evaluates the effects in a single channelizing filter. This would assume an isolated filter with a high-power jamming

Mateu, Jordi; Collado, C; Hueltes, A; Garcia-Pastor, D; Perera, R; Joshi, Nikhil; Lu, Xifeng; Orloff, Nathan; Booth, James.
"Comprehensive circuit model of autolimiting superconductor devices."
Paper presented at Applied Superconductivity Conference (ASC 2016), Denver, CO, United States. September 4, 2016 - September 9, 2016.

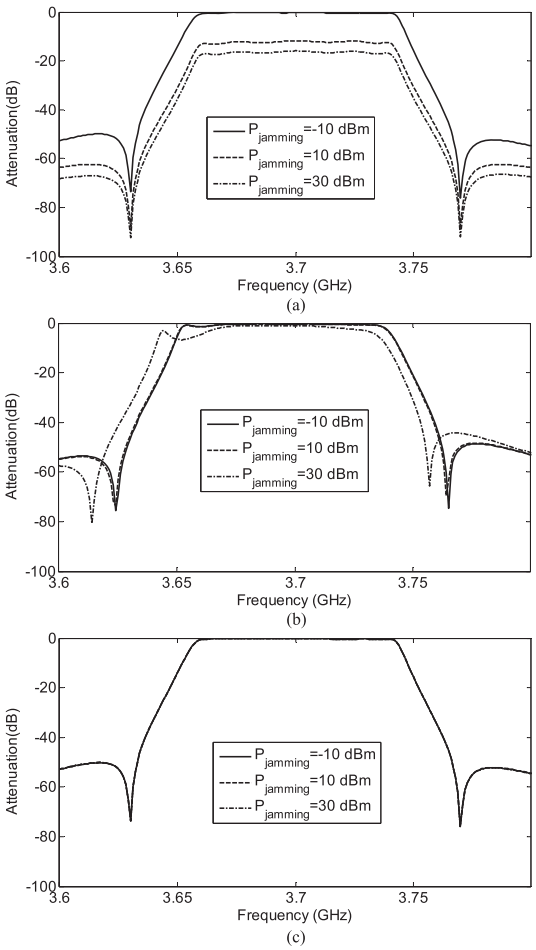


Fig. 11. Filter attenuation response ($S_{21}$ parameter) when a jamming signal of $-10$ dBm, 10 dBm and 30 dBm is set at the adjacent channel. (a) SLS at the first resonator, (b) SLS at the 3rd resonator and (c) SLS at the last resonator.

signal at the central frequency of the filter (3.5 GHz for filter $BW_1$). The SLS is placed in the middle of resonator 1. Fig. 9 shows the attenuated signal as a function of the input power. The solid line corresponds to dielectric sapphire, whereas the dashed line corresponds to quartz. As expected, there is less attenuation for sapphire, until complete saturation is achieved. The second scenario outlines the frequency dependence of the attenuation when a high-power signal is swept over the multiplexer bandwidth. This case only considers the sapphire substrate and, as in previous case, the SLS is placed in resonator 1. Results are shown in Fig. 10, for input powers of $-40$, 16 and 30 dBm. Note that the filter performance is barely affected and only an increase of insertion losses is observed over the whole bandwidth. This is because the current in the first resonator is barely modified along the band, so the limiting effect is almost equal. The third scenario looks at the effect of a jamming signal in an adjacent channel. In particular, a jamming signal is set at the central frequency of the first filter at 3.5 GHz and the performance of the second filter from 3.6 to 3.8 GHz is observed. Under this scenario, we consider three different cases: the SLS is set in resonator 1 (Fig. 11a), resonator 3 (Fig. 11b) and the last resonator (Fig. 11c).

From scenario 2 alone, we could conclude that a conventional multiplexing configuration (such as the one in Fig. 6, where the channelizing filters include a SLS in the first resonator) is a suitable topology for obtaining a frequency-selective limiter. However, this conclusion is not supported by the results of scenario 3.

In scenario 3, we see that by locating a SLS in resonator 1, an undesired attenuation effect occurs in the adjacent channel. Placing the SLS in resonator 3 also results in an undesired effect, namely a change on the position of the transmission zeros. This occurs because the cancellation effect produced by the quadruplet section is modified [9]. Finally, from scenario 3, we see that when the multiplexing channels are quite far apart ($f_2 = f_1 + 2.5\mathrm{BW}_1$), a suitable solution is obtained by placing the SLS in the last resonator. In this case a jamming signal in the adjacent channel does not affect the performance at the band of interest. This is because the maximum current in the last resonator follows the same frequency selectivity than the filter transmission response [9].

## V. Conclusion

Although the analysis above corresponds to very specific scenarios, the frequency dependence of the limiting effect in these scenarios enables identification of the optimal location of a SLS in the studied filter topology, and evaluation of the performance of the resulting filter. Further, we can readily extend this study to other types of jamming signals, other filter designs and other multiplexing topologies using the presented approach. We may conclude, therefore, that the equivalent circuit proposed in this work is very useful to design and evaluate limiting systems based on SLS circuit elements.

## References


[1] J. C. Booth, K. Leong, and S. A. Schima, "A superconducting microwave power limiter for high performance receiver protection," in *Proc. IEEE MTT-S Int. Microw. Symp. Dig.*, 2004, vol. 1, pp. 139–142.

[2] J. C. Booth, D. A. Rudman, and R. H. Ono, "A self-attenuating superconducting transmission line for use as a microwave power limiter," *IEEE Trans. Appl. Supercond.*, vol. 13, no. 2, pp. 305–310, Jun. 2003.

[3] E. Rocas *et al.*, "Superconducting multiplexer filter bank for a frequency-selective power limiter," *IEEE Trans. Appl. Supercond.*, vol. 21, no. 3, pp. 542–546, Jun. 2011.

[4] E. Rocas, J. C. Collado, N. Orloff Mateu, and J. C. Booth, "Modeling of self-heating mechanism in the design of superconducting limiters," *IEEE Trans. Appl. Supercond.*, vol. 21, no. 3, pp. 547–550, Jun. 2011.

[5] T. Dahm and D. J. Scalapino, "Theory of intermodulation in superconducting microstrip resonator," *J. Appl. Phys.* vol. 81, no. 4, pp. 2002–2012, Feb. 1997.

[6] W. T. Weeks *et al.*, "Resistive and inductive skin effect in rectangular conductors," *IBM J. Res. Develop.*, vol. 23, pp. 652–660, Nov. 1979.

[7] D. M. Sheen, S. M. Ali, D. E. Oates, R. S. Withers, and J. A. Kong, "Current distribution, resistance, and inductance for superconducting transmission lines," *IEEE Trans. Appl. Supercond.*, vol. 1, no. 3, pp. 108–115, Jun. 1991.

[8] Y.S. Muzychka, J. R. Culham, and M. M. Yovanovich, "Thermal spreading resistance of eccentric heat source on rectangular flux channels," *J. Electron. Packag.*, vol. 125, pp. 178–185, Jun. 2003.

[9] R. J. Cameron, C. M. Kudsia, and R. R. Mansour, *Microwave Filters for Communication Systems. Fundamentals, Design, and Applications*. New York, NY, USA: Wiley, 2007.

[10] C. Collado, A. Hueltes, E. Rocas, J. Mateu, J. C. Booth, and J. M. O'Callaghan, "Absorptive limiter for frequency-selective circuits," *IEEE Microw. Wireless Comp. Lett.*, vol. 24, no. 6, pp. 415–417, Jun. 2014.



Mateu, Jordi; Collado, C; Hueltes, A; Garcia-Pastor, D; Perera, R; Joshi, Nikhil; Lu, Xifeng; Orloff, Nathan; Booth, James.
"Comprehensive circuit model of autolimiting superconductor devices."
Paper presented at Applied Superconductivity Conference (ASC 2016), Denver, CO, United States. September 4, 2016 - September 9, 2016.

# Design and Calibration of a Double-directional 60 GHz Channel Sounder for Multipath Component Tracking*

Ruoyu Sun[1], Peter B. Papazian[1], Jelena Senic[1], Yeh Lo[1], Jae-Kark Choi[2], Kate A. Remley[1], Camillo Gentile[2]

[1]RF Technology Division, National Institute of Standards and Technology, Boulder, CO, USA, ruoyu.sun@nist.gov
[2]Wireless Networks Division, National Institute of Standards and Technology, Gaithersburg, MD, USA


***Abstract*—The 60 GHz band is being considered for many high-bandwidth wireless applications. To support standards development for these applications, NIST has developed an untethered 60 GHz, 8×16 MIMO channel sounder. It employs a pseudorandom bit sequence with a bandwidth of 4 GHz. The sounder can precisely measure radio propagation channel characteristics such as path loss, small-scale fading, delay dispersion, absolute delay, angle-of-arrival (AoA), angle-of-departure (AoD), and Doppler power spectrum. Its ability to measure the time dynamics of the millimeter-wave radio channel, when untethered and in motion, is unique. It employs electronically-switched MIMO antenna arrays, a robot for moving measurements and an automated one-dimensional positioner for precision measurements at fixed locations. Sounder performance is improved by use of pre-distortion filters and precision calibration of the RF and timing systems. Data showing initial AoD and AoA estimation error are presented along with initial test results for ground-plane reflection.**

***Index Terms*—mmWave, MIMO, channel; measurement.**

## I. Introduction

In July 2016, the Federal Communications Commission (FCC) granted approval of licensed operation in new 28, 37, and 39 GHz bands and extended the unlicensed 60 GHz band from 57 – 71 GHz, releasing in total about 11 GHz of millimeter-wave (mmWave) spectrum [1]. The band at 95 GHz is also currently under review. The order was prompted by the saturation of the sub-6 GHz allocations over the past decade, in particular by data-intensive smartphones. Although less favorable in terms of propagation, the new bands will admit channel bandwidths three orders of magnitude wider; indeed, the IEEE 802.11ay standardization efforts in process have already provisioned for 4.4 GHz channels to support use cases including outdoor backhaul, wireless server backup, augmented reality headsets, and mass video distribution [1].

More than a simple shift in center frequency, mmWave communication systems embody a significant departure in technology from their predecessors. The tiny wavelengths relax the conditions for implementing phased-array antennas with tens to hundreds of elements on a mobile handset (as well as at the base station). The massive arrays can synthesize extremely narrow beams on the order of degrees. The purpose is, through their associated gain in excess of 30 dBi, to compensate for the greater path loss witnessed in the upper spectrum. In order for beamforming to take full advantage of the propagation environment, channel sounding will allow a base station and user device to jointly determine which angles-of-departure (AoDs) and angles-of-arrival (AoAs) correspond to viable transmission paths. The beams will then be steered in those multipath directions. Frequent updating of the channel state through multipath component tracking will be necessary in mobile environments to avoid the beams falling out of alignment with the multipaths. Hence multipath tracking represents a novel but critical aspect of mmWave channel propagation modeling.

To help meet the demands of these next-generation models, NIST has designed the 60 GHz channel sounder described in this paper. The three-dimensional antenna arrays at the transmitter (TX) and receiver (RX) permit extraction of double-directional multipath components in both azimuth and elevation. By virtue of the electronically-switched arrays, a complete channel measurement can be realized in just 262 µs. Combined with the untethered design enabled by synchronization through rubidium clocks, mobile environments up to a closing speed of 35 km/h can be characterized. Finally, the 4 GHz null-to-null bandwidth of the system can accommodate the use cases anticipated for mmWave systems.

## II. System Design

### A. Overview

The 60 GHz sounder system has design features which are similar to the 83 GHz sounder described in [2]-[4]. As with the E-band system, it utilizes a pseudorandom bit sequence (PRBS) to measure the complex channel impulse response (CIR), a 16-element antenna array with fast switching multiplexer (MUX) at the receiver, and a mobile positioner to provide position information and mapping. In contrast to the single transmit antenna, this 60 GHz system has an 8-element switched array. Thus, the MIMO capability allows measurement of AoD as well as AoA. Both antenna arrays use scalar feed horns (SFHs) which have symmetrical patterns, maximum gain of 18.1 dBi and side-lobe levels below -10 dBi. This is important when combining patterns in an array processing program and making use of the space-alternating generalized expectation-maximization (SAGE) algorithm [5] to calculate the equivalent omni-directional CIRs. In addition to its mobile measurement capabilities, a one-dimensional (1-D) positioner has been added for stationary measurements at sub-wavelength increments. The system parameters as well as additional calibration methods are discussed in the following sections.

### B. Transmitter and Receiver

The TX utilizes an arbitrary waveform generator (AWG) with a sampling rate of 12 Gsamples/s. The AWG generates a

Sun, Ruoyu; Papazian, Peter; Senic, Jelena; Lo, Yeh; Choi, Jae-Kark; Remley, Catherine; Gentile, Camillo.
"Design and Calibration of a Double-directional 60 GHz Channel Sounder for Multipath Component Tracking*."
Paper presented at 11th European Conference on Antennas and Propagation (2017 EUCAP), Paris, France. March 19, 2017 - March 24, 2017.

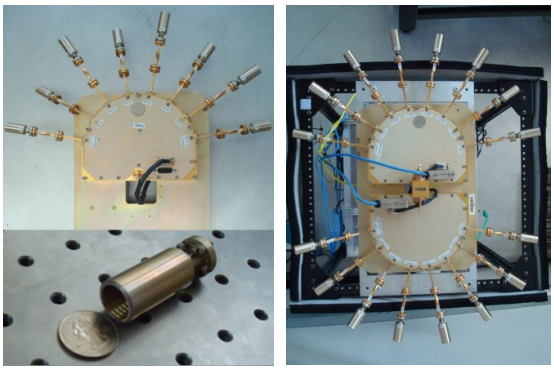

Fig. 1. Photos of TX MUX (upper left), RX MUX (right) on top of Robot and horn antenna (lower left).

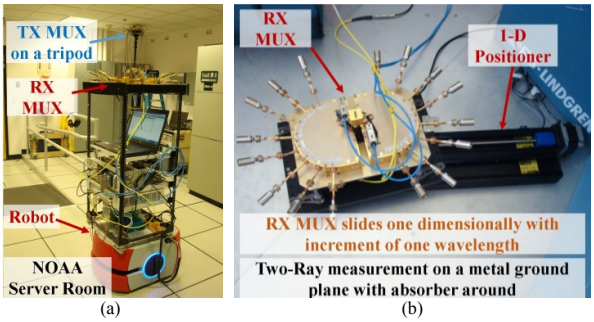


(a) (b)

Fig. 2. Positioning system (a) TX MUX on a tripod and RX MUX on the robotic positioner (for moving cases); (b) RX MUX on a 1-D positioner (for static cases).

3-GHz intermediate frequency (IF) signal with BPSK modulation with a 2047-bit pseudorandom (PN) code word. The bit (or chip) rate is 2 Gbits/s, yielding a delay resolution of 0.5 ns and a maximum delay span of 1023.5 ns. The RF section then up-converts the IF signal to 60.5 GHz. The maximum transmit power for the TX MUX amplifiers is 20 dBm.

The RX MUX has 16 low-noise amplifiers (LNAs) with noise figures < 5 dB. The MUX output is down-converted to 3 GHz, amplified, and then digitized at 40 Gsamples/s. The analog-to-digital converter (ADC) is 8 bit with a programmable IF amplifier. The raw IF data for all 128 channels are then stored on a solid-state drive along with location information from the positioners. The dynamic range of the system for path-loss measurements is 162.2 dB[1]. We synthesized the omni-directional CIR by combining 128 directional CIRs using the SAGE algorithm. The maximum CIR or power delay profile (PDP) updated rate is 488,519 CIRs per second, or 3816 CIRs per second for omni-directional CIRs. The maximum CIR update rate is only available for a short duration until the memory in the digitizer is full.

The MIMO antenna arrays are shown in Fig. 1. The half power beamwidth of the SFHs is 22.5°. The TX multiplexer has 8 antennas which covers 180° in the azimuthal plane (adjacent antennas are 22.5° apart). The RX MUX includes 16 antennas that provide 360° azimuth coverage. Odd antennas have zero elevation angles, while even indices are tilted up (or tilted down depending on test cases) by 22.5° to provide elevation plane coverage. The RX MUX has a second configuration which allows both hemispheres of the antenna arrays to be stacked vertically. In this configuration, the angle between antennas is reduced to 11.25°, and the antennas are replaced with 11.25° beamwidth, 25 dBi gain SFHs. This increases the dynamic range to 169 dB while allowing greater angular resolution.

The MUXs are electronically-switched and controlled by the synchronization and timing circuits. The switching time is less than 25 ns for both TX and RX MUXs. To avoid switch rise-and-fill times, two CIRs (2047 ns) are collected but only one CIR (1023.5 ns) is extracted for channel modeling.

### C. *Positioning Systems*

A mobile positioner is used for mobile measurements, and a 1-D positioner is developed for static test cases. Figure 2(a) shows the TX MUX mounted on a tripod at ceiling height to simulate a Wi-Fi deployment in a server room. The RX MUX is mounted on the mobile positioner and is ready to make an automated measurement.

Figure 2(b) is the RX MUX and precision 1-D positioner on a metal ground plane. The TX MUX was also positioned on the ground plane at a fixed point. This configuration was used to measure the two-ray channel. The precision 1-D positioner was used to move the receiver in one-wavelength steps, relative to the transmitter. This allowed local moving averaging to remove small-scale fading, as well as characterization of the reflected signals from the metal ground plane. Results of a two-ray ground bounce response is given in Section IV.B. The 1-D positioner has a minimum step size of 6.35 μm and a range of 30 cm.

## III. SYSTEM CALIBRATION

### A. *Pre-distortion Filters*

In order to compensate for the non-ideal hardware transfer functions of the transmitter and receiver chains, system calibration is necessary. In previous work related to our 83 GHz system, a post-distortion filter was implemented [3]. Pre-distortion filtering, however, is preferable because it can be applied to high signal-to-noise ratio data at the transmitter. This avoids increasing the noise level at the receiver. The pre-distorted signal is generated by the AWG as well.

Since the amplifiers and waveguides of the TX and RX MUX chains are slightly different, the 128 channels must be equalized individually. Let the measured baseband frequency response of the $i^{th}$ transmitter and $j^{th}$ receiver chain be:

$$Y_{ij}(f) = W_{ij}(f) \cdot P(f) \cdot H_i^{TX}(f) \cdot G_i^{TX}(f) \cdot H_{ij}(f) \cdot G_j^{RX}(f) \cdot H_j^{RX}(f) + N(f), \quad (1)$$

[1] This is determined for the 0.1 dB saturate TX power for the power amplifiers (+20 dBm) + antenna gains (36.2 dB) – RX Noise floor (-78 dBm *ktB* + LNA noise figure 5 dB) + processing gain (33 dB).

Sun, Ruoyu; Papazian, Peter; Senic, Jelena; Lo, Yeh; Choi, Jae-Kark; Remley, Catherine; Gentile, Camillo.
"Design and Calibration of a Double-directional 60 GHz Channel Sounder for Multipath Component Tracking*."
Paper presented at 11th European Conference on Antennas and Propagation (2017 EUCAP), Paris, France. March 19, 2017 - March 24, 2017.

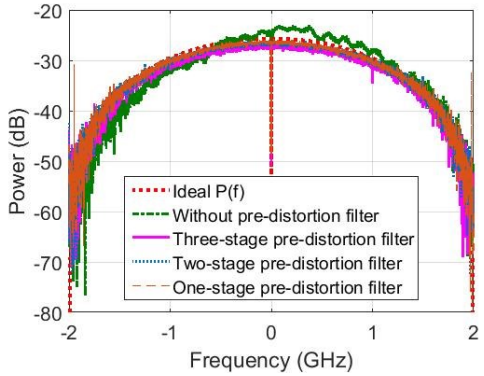


Fig. 3. Power spectrum with and without pre-distortion filter for the 2nd TX antenna and 2nd RX antennas using B2B calibration.

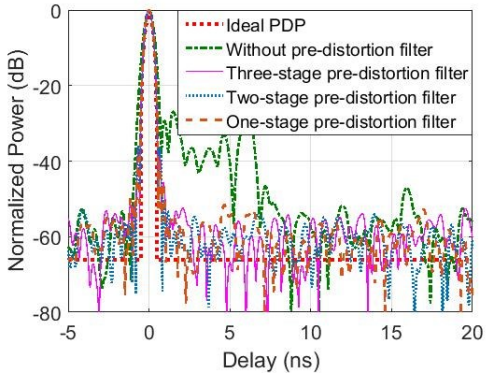


Fig. 4. Example individual normalized power-delay profiles with and without the pre-distortion filter for the 2nd TX antenna and 2nd RX antenna using B2B calibration.

where $W_{ij}(f)$ denotes the pre-distortion filter, $P(f) = p(f) \cdot p^*(f)$ the matched-filter response of the ideal PN sequence $p(f)$, $H_i^{TX}(f)$ and $G_i^{TX}(f)$ the respective transfer function and antenna pattern of the transmitter and $H_j^{RX}(f)$ and $G_j^{RX}(f)$ the same for the receiver, $H_{ij}(f)$ the channel transfer function, and $N(f)$ the system noise. The calibration is based on a back-to-back (B2B) method [6]. In this method, the antennas are removed ($G_i^{TX} = G_j^{RX} = 1$) and the TX and RX connected directly through waveguides and attenuators such that $H_{ij} = A$. The B2B measurement then follows from (1) as:

$$Y_{ij}^{B2B}(f) = \frac{1}{M}\sum_{m=1}^{M} Y_{ij}^{m}(f; G_i^{TX} = G_j^{RX} = 1; H_{ij} = A) \quad (2a)$$

$$\approx W_{ij}(f) \cdot P(f) \cdot H_i^{TX}(f) \cdot A \cdot H_j^{RX}(f). \quad (2b)$$

Averaging in (2a) over $M$ samples indexed through $m$ is carried out to virtually eliminate noise such that the approximation in (2b) holds; we found that $M$ = 128 was sufficient.

The design criteria for the pre-distortion filter is that the output of the B2B measurement be the ideal matched-filter response (plus the attenuators), or

$$Y_{ij}^{B2B}(f) = A \cdot P(f). \quad (3)$$

Now for convenience, (2b) can be rewritten as

$$Y_{ij}^{B2B}(f) \approx W_{ij}(f) \cdot Y_{ij}^{B2B}(f; W_{ij} = 1). \quad (4)$$

By equating (3) and (4), the solution for the pre-distortion filter is given as

$$W_{ij}(f) = \frac{A \cdot P(f)}{Y_{ij}^{B2B}(f; W_{ij} = 1)}. \quad (5)$$

What remains is to take a B2B measurement with no filter $Y_{ij}^{B2B}(f; W_{ij} = 1)$; i.e., with the ideal PN sequence applied at the input.

Fig. 3 displays the power spectrum, $\left|Y_{ij}^{B2B}(f)\right|^2$ both with and without filtering for $i = j = 2$. Notice that the spectrum becomes much smoother with the filter. Also displayed in Fig. 4 is the equivalent power-delay profile $\left|\mathcal{F}^{-1}\left[Y_{ij}^{B2B}(f)\right]\right|^2$ normalized to a peak value of 0 dB. The filter reduces the non-ideal lobes by more than 50 dB from the peak.

Under the assumption of a non-linear system, multiple filter stages can be realized. In each stage, the output of the previous stage is fed to the AWG and the filter is computed recursively as

$$W''_{ij}(f) = \frac{A \cdot P(f)}{Y_{ij}^{B2B}\left(f; W_{ij} = W'_{ij}\right)} \quad (6)$$

.

Also displayed in Figs. 3 and 4 are results up to stage three. Although mild improvement in performance is observed, the system indeed is close to linear and so, to simplify the process, one-stage pre-distortion filters are employed in our system.

To simplify this process further, a calibration matrix approach is used [7]. Through this method, we can reduce the number of measurements from 128 to just 23 by measuring $Y_{ii}^{B2B}(f; W_{ii} = 1), i = 1 \ldots 8$ and $Y_{1j}^{B2B}(f; W_{1j} = 1), j = 2 \ldots 16$. The measurements are applied to compute the filters as

$$W_{ij}(f) = \frac{A \cdot P(f) \cdot Y_{1i}^{B2B}(f; W_{1i} = 1)}{Y_{ii}^{B2B}(f; W_{ii} = 1) \cdot Y_{1j}^{B2B}(f; W_{1j} = 1)}. \quad (7)$$

The calibration matrix method may be particularly useful for Massive-MIMO transfer functions when the number of channels is in the hundreds or thousands. The results were spot-checked by measuring several additional transfer functions. Both measured and calculated transfer functions yielded similar results.

Note that the AWG must generate 128 different waveforms (due to 128 filters) and that the duration of each code word lasts 2047 ns. This requires precision synchronization between the TX and RX to ensure the RX antenna switching is synchronized with the start of a frame of code words. This synchronization is discussed in Section III.C. We also found that the TX MUX needs to warm up to a constant temperature of approximately 35 °C before measurements, because temperature affects the TX power and the pre-distortion filter performance.

Sun, Ruoyu; Papazian, Peter; Senic, Jelena; Lo, Yeh; Choi, Jae-Kark; Remley, Catherine; Gentile, Camillo.
"Design and Calibration of a Double-directional 60 GHz Channel Sounder for Multipath Component Tracking*."
Paper presented at 11th European Conference on Antennas and Propagation (2017 EUCAP), Paris, France. March 19, 2017 - March 24, 2017.

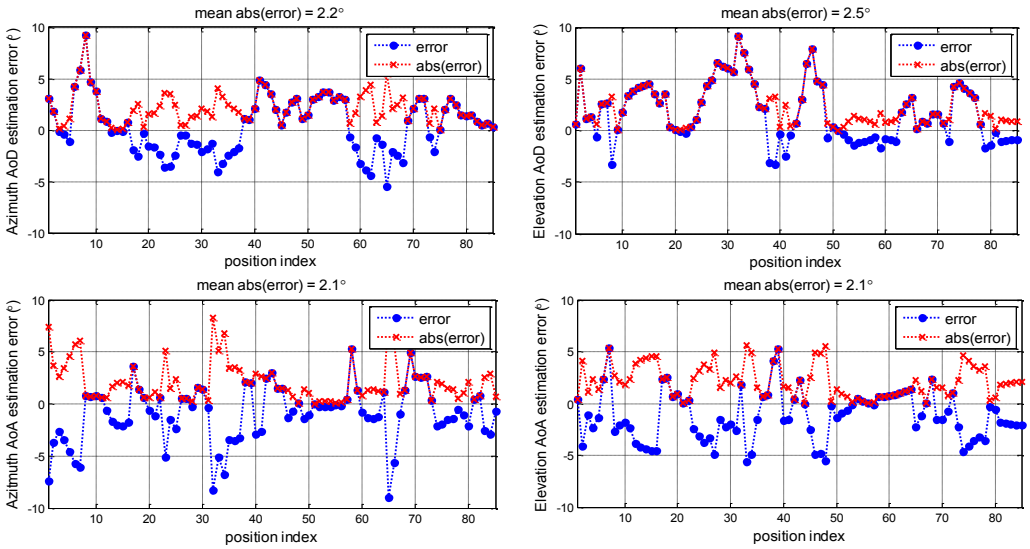


Fig. 5. Error in estimated vs. ground-truth angle. Estimated denotes extracted from measurements while ground-truth denotes reported from navigation system.

The geometries of the TX and RX arrays play an essential role in the precise estimation of AoA and AoD. To accurately measure the array aperture constellation relative to its reference center, a laser interferometer was used as described in [8]. This system has a precision of 50 µm.

### B. *Multiplexer Timing Synchronization*

We measured multipath delay using the time lag properties of the PN sequence correlation function. This is a random value without any synchronization between the AWG, RX MUX, TX MUX and digitizer trigger. RX MUX antennas switch once per two code words (2047 ns). This avoids processing code word data during the MUX switching period. The TX multiplexer switches at increments of 32 code words to provide a two code-word window for each of the 16 RX MUX channels. Since the pre-distortion filters make each of the 128 transmitted signals unique, the start times must be aligned between the transmitter code word $i$=1 and the RX receiver acquisition $j$=1.

We achieved alignment using a two-stage synchronization approach termed coarse sync and fine sync. The AWG provides start triggers for both TX MUX timing circuitry which uses a 3-bit word to access each of the 8 channels as well as the RX MUX digital switching signal which is a 4-bit word to access each of the 16 channels. This is termed coarse sync, and reduces the random delay to within 2047 ns. However, the AWG itself and the divider/counter module in the RX introduce a random delay between zero and 2047 ns. Hence, we use the pulses from the divider/counter module in the RX to trigger the AWG, and termed fine sync. This removes the random delay between zero and 2047 ns. The coarse sync aligns the indices of code words (but not boundaries) of the TX and RX antenna switching time slots and the fine sync aligns the boundaries (but not indices). Combination of the coarse and fine synchronization provides the required switching synchronization. The synchronization cables can now be removed and timing stability is maintained with rubidium clocks.

The same circuitry, using internal counters, provides a digitizer trigger which is aligned with code word $i$=$j$=1, but is repeated at integer numbers of 256 code words. This allows impulses for all channels to be recorded at programmable repetition rates with a granularity of 262 µs and preserve both channel alignment and fine synchronization. The cable length difference and some non-ideal electronic device delays introduce some delay biases. We compensate for these biases by adjusting the start triggers generated by the AWG. Merging Global Positioning System (GPS) into our synchronization circuitries for outdoor measurements is under development. The coarse synchronization is expected to be replaced by the GPS.

## IV. System Performance Verification and Initial Results

Initial data from the channel sounder includes AoA and AoD measurements, and a laboratory measurement of a two-ray channel (a direct signal with a ground reflected signal). We also discuss short-term time stability measurements.

### A. *AoA and AoD*

The AoA and AoD of the direct multipath component were measured in line-of-sight conditions. The experiments were conducted on a 7 m by 7 m ground plane in a 10 m by 15 m room with cinder block walls [4]. The transmitter was set on a tripod at a height of 2.5 m and the receiver was set on the robotic positioner at a height of 1.5 m. Using the robot's navigation system, we could accurately determine the relative angle (heading) between the TX MUX antenna array and the RX MUX antenna array as well as the velocity of the RX with respect to the TX. The set of experiments consisted of moving the robot in a grid pattern on the ground plane from the fixed transmitter. At each position, the robot collected multiple bursts of data consisting of all 128 antenna channels. We used

Sun, Ruoyu; Papazian, Peter; Senic, Jelena; Lo, Yeh; Choi, Jae-Kark; Remley, Catherine; Gentile, Camillo.
"Design and Calibration of a Double-directional 60 GHz Channel Sounder for Multipath Component Tracking*."
Paper presented at 11th European Conference on Antennas and Propagation (2017 EUCAP), Paris, France. March 19, 2017 - March 24, 2017.

the SAGE algorithm to estimate the AoA and AoD on an angular grid with better resolution than our antenna angular separation. The comparison between measured values and the known transmitter/receiver angle for the direct path is given in Fig. 5. We see the SAGE estimations of AoA and AoD have an average error in azimuth less than 2.2° and in elevation less than 2.5°.

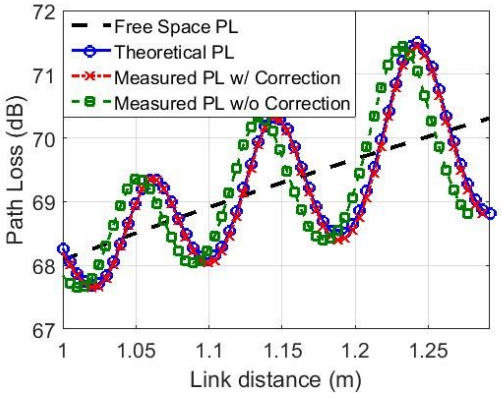


Fig. 6 Two-Ray channel path loss measurement showing good agreement with the theoretical model after applying the phase center correction.

### B. Two-Ray Measurements

We collected two-ray data using the precision 1-D positioner with the transmitter and receiver positioned over a conducting ground plane, see Fig. 2(b). The positioner was configured for measurements at one-wavelength spacing for 60 wavelengths. The antennas were vertically oriented and 19.84 cm above the ground plane. By precisely aligning the TX and RX antennas at boresight and adjusting the separation to 1 m, we were able to measure the two-ray lobing pattern of the path loss (PL) caused by the change in the direct and reflected signal path length. This change in path length causes the signals to add constructively or destructively over several phase rotations or cycles, as shown in Fig. 6. Using the geometry of the paths as the 1-D positioner moved and accounting for the antenna patterns, we compared the measured and calculated results. As we can see in Fig. 6, there is an excellent fit. We see the period of the lobing pattern is approximately 0.1 m and its magnitude is 3 dB near 1.25 meters. This increase in lobing magnitude occurred as the reflected path antenna gain increases over link distance due to a decreasing angle relative to the antenna boresight.

We first calculated the antenna separation by measuring the distance between antenna aperture faces, see the green dashed line in Fig. 6. However, the true phase center is inside the horn antenna, which increased the link distance. We obtained the best fit by increasing the measured separation by 1 cm, indicating the location of the phase center of the antennas. By dividing the distance in half, we estimated that the phase center of each antenna is 5 mm behind the antenna aperture. This is useful because it will help in the AoA and AoD estimation with the SAGE algorithm. We have not applied this correction to the AoA and AoD results presented in this paper.

### C. Time Stability

The short-term time stability of the CIR is a key characteristic of a channel-sounder measurement which is important for calculation of AoA and AoD. We estimated this by recording 500 CIRs in the B2B configuration. The CIRs were spaced at 2 μs intervals, the period was 1 ms. The data were analyzed by tabulating the phase at the peak of the CIRs. After converting these phase values back to time, we found that the times at the peak were Gaussian distributed with a standard deviation of 8 ps.

## V. Conclusion

An untethered 60 GHz MIMO channel sounder has been developed at NIST. The 8×16 MIMO antennas are electronically-switched. The null-to-null bandwidth is 4 GHz, yielding a delay resolution of 0.5 ns. The timing and synchronization enable the employment of a custom pre-distortion for each of the 128 MIMO channels, as well as absolute delay. The sounder has undergone extensive calibration and synchronization. Preliminary measurement results indicate AoA and AoD can be measured with an average error of less than 2.5°. The sounder has been used to measure rack-top-to-rack-top CIRs and inter-rack CIRs with full AoA and AoD capability. These data will be presented in a sequel and could also be used to develop IEEE 802.11ay standards. Future work includes noise analysis and thresholding, developing a positioning system with a new robot and GPS for outdoor environments, detailed analysis of phase stability, and practical characterization of antennas.

## References

[1] Federal Communication Commission, Report and Order FCC-16-89, July 14, 2016.

[2] P. B. Papazian, K. A. Remley, C. Gentile and N. Golmie, "Radio channel sounders for modeling mobile communications at 28 GHz, 60 GHz and 83 GHz," *2015 Global Symposium On Millimeter Waves (GSMM),* pp. 1-3, Montreal, QC, 2015.

[3] P. B. Papazian, J. Choi, J. Senic, P. Jeavons, C. Gentile, N. Golmie, R. Sun, D. Novotny, K. A. Remley, "Calibration of millimeter-wave channel sounders for super-resolution multipath component extraction," *2016 10th European Conference on Antennas and Propagation (EuCAP)* , pp. 1-5, Davos, Switzerland, 2016.

[4] P. B. Papazian, C. Gentile, K. A. Remley, J. Senic, N. Golmie, "A Radio Channel Sounder for Mobile Millimeter-Wave Communications: System Implementation and Measurement Assessment," *IEEE Transactions on Microwave Theory and Techniques*, Early View, vol.PP, no.99, pp.1-9, Aug. 2016.

[5] J. A. Fessler and A. O. Hero, "Space-alternating generalized expectation-maximization algorithm," *IEEE Transactions on Signal Processing*, vol. 42, no. 10, pp. 2664-2677, Oct. 1994.

[6] J. A. Wepman, J. R. Hoffman, L. H. Loew, V. S. Lawrence, "Comparison of wideband propagation in the 902-928 and 1850-1990 MHz bands in various microcellular environments," *NTIA Report 93-299*, Sep. 1993.

[7] P. B. Papazian, Y. Lo, J. J. Lemmon, M. J. Gans, "Measurements of Channel Transfer Functions and Capacity Calculations for a 16x16 BLAST Array over a Ground Plane," *NTIA Report TR-03-403*, June 2003.

[8] J. A. Gordon, D. R. Novotny, M. H. Francis, R. C. Wittmann, M. L. Butler, A. E. Curtin, J. R. Guerrieri, "Millimeter-Wave Near-Field Measurements Using Coordinated Robotics," *IEEE Transactions on Antennas and Propagation*, vol. 63, no. 12, pp. 5351-5362, Dec.2015.

Sun, Ruoyu; Papazian, Peter; Senic, Jelena; Lo, Yeh; Choi, Jae-Kark; Remley, Catherine; Gentile, Camillo.
"Design and Calibration of a Double-directional 60 GHz Channel Sounder for Multipath Component Tracking*."
Paper presented at 11th European Conference on Antennas and Propagation (2017 EUCAP), Paris, France. March 19, 2017 - March 24, 2017.

# Radiated Power Based on Wave Parameters at Millimeter-wave Frequencies for Integrated Wireless Devices

Damir Senic[1], Kate A. Remley[1], Dylan F. Williams[1], Diogo C. Ribeiro[2], Chih-Ming Wang[1], Christopher L. Holloway[1]

[1]National Institute of Standards and Technology, Boulder, Colorado, USA,
[2]University of Aveiro, Aveiro, Portugal

***Abstract* — We provide total radiated power measurements at millimeter-wave frequencies using a reverberation chamber and a power-calibrated vector network analyzer capable of measuring wave parameters. We compare total radiated power results obtained from two different approaches. In the first approach, applicable when the terminals of the antenna under test are accessible, the total radiated power is calculated directly from forward and reflected waves. In the second approach, when we cannot access the terminals of the antenna under test, the total radiated power is calculated from measured forward and reflected waves at the receive antenna taking into account chamber loss. The results from the two different approaches have excellent agreement, and are within the measurement uncertainty. The uncertainty in our total radiated power measurements is below 2%.**

***Index Terms* — Antenna measurement, communication systems, internet of things, millimeter-wave wireless, reverberation chamber, radiated power measurement, wave parameters, wireless systems.**

## I. Introduction

Modern communications systems rely on the modulation of radio-frequency (RF) signals to exchange information. Different equipment can be used to analyze RF signals, including power meters, spectrum analyzers, oscilloscopes, vector signal analyzers, and vector network analyzers (VNAs). Here, we will focus on use of a VNA for analyzing RF signals in terms of total radiated power (TRP).

Power-calibrated VNAs have been traditionally used for conducted power measurements. While this was feasible for devices with accessible output terminals, modern communication devices have integrated antennas and direct measurement at the antenna terminals is not possible. Consequently, the only available solution is a transition from on-wafer to over-the-air (OTA) measurements. Reverberation-chamber-based test methods are efficient, and standardized approaches are recently available for OTA test [1].

Traditionally, reverberation chambers (RCs) were used for various measurements in electromagnetic compatibility (EMC) [2] and, more recently, wireless communications [1]. An RC is an electrically-large resonator with a high-$Q$ value [3], [4]. Due to that fact, the instantaneous spatial distribution of the electromagnetic fields inside such an environment is not uniform. In order to estimate a quantity of interest from measurements in a reverberation chamber, we need to average over measured randomized field samples. Field randomization, or "mode-stirring" techniques include mechanical paddle stirring, where electrically-large paddle(s) move and change the boundary conditions inside a chamber, and position stirring, where the device under test (DUT) antenna is moved.

In this paper, we study total radiated power based on wave-parameter measurements at millimeter-wave frequencies inside an RC. In the past, radiated-emission tests from different RF sources were performed in anechoic chambers or open area test sites, where the limits referred to the maximum electric field strength at certain distance, defined by *e.g.*, [5]. On the other hand, emissions tests performed inside an RC provide us with compliance in terms of TRP. The advantages of using RCs compared to anechoic chambers or open area test sites are mainly in their low cost, simplicity, and shorter measurement times. Much of the prior work on total power radiated by intentional and unintentional sources can be found in [6]-[11].

Wave parameters have the advantage that a power-calibrated VNA can report the forward and reverse waves' power levels directly. By adding a phase reference [12], we can obtain both magnitude and phase information of each frequency component. Even though this paper focuses on TRP from a CW signal, we plan to use the same setup for periodic modulated signals, where a phase reference is of the utmost importance.

Since millimeter-wave frequencies will most likely be used in the next-generation wireless networks [13], we decided to do our research at this frequency range.

## II. Radiated Power

According to [2], the amount of RF power radiated ($P_{\text{rad}}$) by a device under test can be determined by measuring the amount of power received by the receive antenna ($P_{\text{rec}}$). Taking into account chamber loss ($G_{\text{ref}}$), $P_{\text{rad}}$ can be expressed as:

$$P_{\text{rad}} = \frac{P_{\text{rec}}}{G_{\text{ref}}}. \tag{1}$$

To determine $G_{\text{ref}}$ from measurements, we must remove the effects of efficiency and mismatch at the antennas ports. In this case, $G_{\text{ref}}$ can be expressed as:

$$G_{\text{ref}} = \frac{\left\langle |S_{21}|^2 \right\rangle}{\eta_{\text{TX}}\eta_{\text{RX}}\left(1-\left|\langle S_{11}\rangle\right|^2\right)\left(1-\left|\langle S_{22}\rangle\right|^2\right)}, \tag{2}$$

Senic, Damir; Remley, Catherine; Williams, Dylan; Ribeiro, Diogo; Wang, Chih-Ming; Holloway, Christopher.
"Radiated Power Based on Wave Parameters at Millimeter-wave Frequencies for Integrated Wireless Devices."
Paper presented at 88th ARFTG Microwave Measurements Conference, Austin, TX, United States. December 8, 2016 - December 9, 2016.

where the brackets denote the ensemble average over the mode-stirring sequence, $S_{21}$ is the forward transmission scattering parameter, and the terms in the denominator represent the free-space radiation efficiency ($\eta_{TX}$ and $\eta_{RX}$) and mismatch for the two antennas. These may be measured in either an anechoic chamber or in an unloaded chamber, such as we have here.

The power at the receive antenna is traditionally measured by a spectrum analyzer, power meter, or base station emulator. In this paper, we will show that power at the receive antenna can be more easily measured by a power-calibrated VNA because all mismatch corrections are performed automatically even while the chamber characteristics are changing. The power will be defined in terms of wave parameters $a$ and $b$, where $a$ is proportional to the voltage of the incident wave and $b$ is proportional to the voltage of the reflected wave at the measurement reference plane, normalized to the square of the system characteristic impedance [14]. In this study, we can access the DUT's antenna terminals. Thus, we can measure the radiated power at the transmit antenna directly in terms of incident ($a_1$) and reflected ($b_1$) waves as:

$$P_{\text{rad,direct}} = \left\langle |a_1|^2 - |b_1|^2 \right\rangle \eta_{\text{TX}} . \tag{3}$$

On the other hand, to simulate a DUT whose antenna terminals cannot be accessed, we can also assess total radiated power from (1) by measuring chamber loss (2) and the power at the receive antenna:

$$P_{\text{rad,integrated}} = \frac{P_{\text{rec}}}{G_{\text{ref}}} = \frac{\left\langle |b_2|^2 - |a_2|^2 \right\rangle}{G_{\text{ref}}} , \tag{4}$$

where $a_2$ and $b_2$ are wave parameters measured by the VNA at the receive antenna port.

We next describe the measurement setup that we used. In Section IV, we will give the results from (3) and (4) and compare them in order to verify the VNA's applicability for power measurements of wireless devices with integrated antennas.

## III. Measurement Setup and Procedures

We performed total radiated power measurements over a frequency range from 43 GHz to 47 GHz using an RC with a power- and phase-calibrated 50 GHz VNA, as shown in Fig. 1. Power was calibrated by a wideband, diode-based power sensor connected to the power meter. Phase calibration was achieved by use of two comb generators, one connected to port 2 of the VNA during the measurements and the other connected to the transmit calibration plane during the calibration of the VNA. Even though a phase calibration is not necessary for total radiated power measurements, we plan to use this setup as a base for more complex, modulated signals measurements where precise phase information of each frequency component is required.

The chamber was equipped with two mechanical stirrers. The larger one rotated about a horizontal ($H$) axis within a cylindrical volume of 0.6 m height and 0.2 m diameter, while the smaller one rotated about a vertical ($V$) axis within a cylindrical volume of 0.5 m height and 0.2 m diameter. The RC's size was 1 m ($l$) × 0.65 m ($w$) × 0.55 m ($h$), which corresponds to an electrical size of approximately 150 λ × 100 λ × 80 λ at the center frequency of 45 GHz.

We used three different transmit antennas that have different radiation patterns (from highly directional to omnidirectional in half-space) to simulate a wide range of real integrated antennas. Measured antennas included a waveguide horn antenna, an open-ended waveguide (OEW), and a microstrip patch antenna. The transmit and receive antennas were oriented away from each other in order to lower the unstirred energy ($K$ factor) between them [15]. The RC's bulkhead was equipped with two feedthroughs, one waveguide that was connected to the VNA's port 3 and the other a 2.4 mm coaxial connected to the VNA's port 1. The waveguide horn receive antenna at port 3 was oriented toward the vertical stirrer (see Fig. 1). The signal from the 2.4 mm feedthrough was brought to the transmit antenna via a coaxial cable for the microstrip patch antenna and a coaxial-to-waveguide transition for OEW and waveguide horn antenna.

The transmit antennas were oriented toward the horizontal stirrer and positioned in the middle of the RC's working volume (see Figs. 1 and 2). Key measurement parameters are summarized in Table I.

Wave parameters were measured for 2500 paddle orientations (50 vertical and 50 horizontal). Calibration standards and DUT measurements were collected as raw data, and calibration was performed afterwards within the NIST Microwave Uncertainty Framework [16], [17].

TABLE I: Measurement Parameters

| Parameter | | Value |
|---|---|---|
| Frequency range | | 43 GHz – 47 GHz |
| Number of frequency points | | 1601 |
| IF bandwidth | Calibration | 100 Hz |
| | Measurements | 2 kHz |
| VNA output power level | | -10 dBm |
| VNA dwell time | | 10 μs |
| Paddle step size ($V \times H$) | | 7.2° × 7.2° |
| Number of paddle orientations ($V \times H$) | | 50 × 50 |

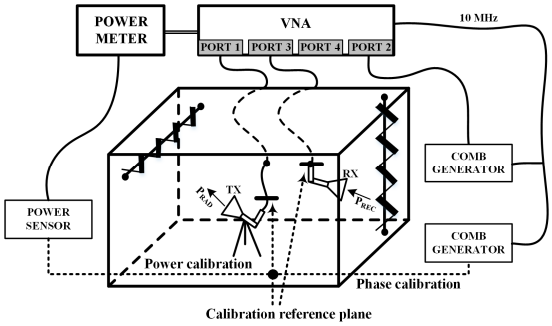


Fig. 1. Schematic layout of measurement setup for total radiated power measurements based on a power- and phase-calibrated VNA.

Senic, Damir; Remley, Catherine; Williams, Dylan; Ribeiro, Diogo; Wang, Chih-Ming; Holloway, Christopher.
"Radiated Power Based on Wave Parameters at Millimeter-wave Frequencies for Integrated Wireless Devices."
Paper presented at 88th ARFTG Microwave Measurements Conference, Austin, TX, United States. December 8, 2016 - December 9, 2016.

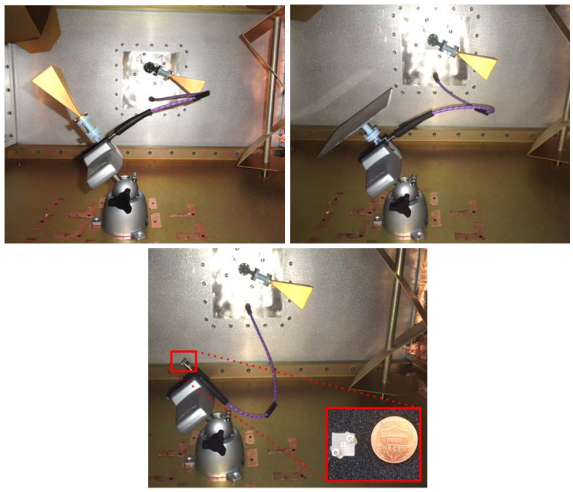

Fig. 2. Three different transmit antennas used for total radiated power measurements; a waveguide horn antenna (top left), an open-ended waveguide (top right), and a microstrip patch antenna (bottom) (compared to a U.S. penny for size).

## IV. Results

In this section, we compare total radiated power results measured directly from the wave parameters using (3) to those obtained from scattering-parameters measurements of $G_{ref}$ using (4). We measured $G_{ref}$ with the same pair of antennas we used for our DUT measurements which could artificially lower the uncertainty. Even though these would typically be different pairs of antennas, our focus is on the difference in the approaches from (3) and (4). Note that to calculate the total radiated power by applying (3), we need to have access to the transmit antenna terminals. Common DUTs generally do not have accessible antenna terminals. In that case, we need to use (4). Taking (3) as true value for total radiated power, we will show how good our estimate of total radiated power (4) is based on the received power and chamber loss measurements.

In order to simulate different DUTs, the VNA was connected to various transmit antennas, each with its own radiation pattern and efficiency. The VNA was set to -10 dBm output power. In Fig. 3, we present TRP results for the three different transmit antennas obtained from (3) as solid lines and (4) as dotted lines. The differences in calculated TRP from (3) and (4), given as $\Delta_{Prad}$, are shown in Fig. 4 with error bars as uncertainty values. The mean (over a 4 GHz bandwidth) differences between the two different approaches for the waveguide horn antenna, OEW, and microstrip patch antenna were 0.053 dB, 0.051 dB, and 0.055 dB. Excellent agreement is seen, with differences at or within our measurement uncertainty given in Section V.

Our research indicates that the waveguide horn antenna had the highest average (over 4 GHz bandwidth) TRP of -16.24 dBm. This is due to its high efficiency (low losses and good impedance match). At the same time OEW radiated -16.55 dBm on average, and microstrip patch antenna -17.48 dBm. Note also that the patch TRP drops very fast above 45 GHz. The reason for the drop is poor matching above that frequency. A similar effect was observed in the antenna efficiency study given in [18].

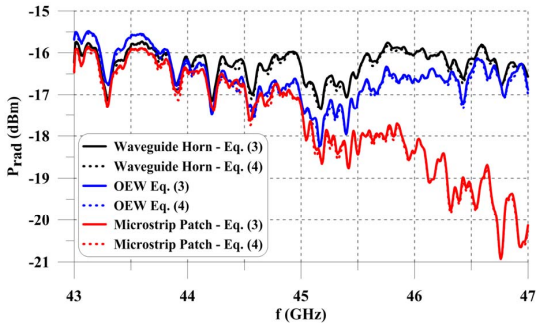


Fig. 3. Total radiated power results calculated from (3) and (4) for three different transmit antennas.

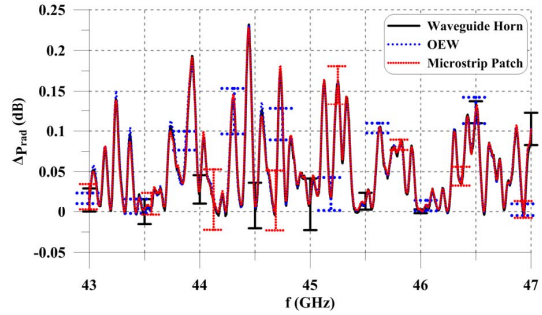


Fig. 4. Differences in TRP results obtained from two different approaches and their associated uncertainties.

## V. Measurement Uncertainty

In this section, we provide measurement uncertainty results from the NIST Microwave Uncertainty Framework [16],[17] calculated using both sensitivity and Monte Carlo approaches. The Framework is a NIST-developed software package that allows assignment of uncertainties and probability distributions to error mechanisms in the calibration, and propagates the associated uncertainties to the end result. From repeat measurements, it can also determine random components of measurement uncertainty.

The Framework represents the resulting errors as perturbed measurement vectors that are propagated from one calculation step to the next. This enables uncertainties to be correctly correlated throughout the calculations even when the same uncertainty mechanism is present at different steps of the calculation. The Framework captures and propagates the uncertainties of wave-parameter measurements and finds the correlation between them. By identifying the error mechanisms in the calibration standards, we can determine the correlations between the wave parameters across frequencies, which can then be propagated into the measurement uncertainties.

Senic, Damir; Remley, Catherine; Williams, Dylan; Ribeiro, Diogo; Wang, Chih-Ming; Holloway, Christopher.
"Radiated Power Based on Wave Parameters at Millimeter-wave Frequencies for Integrated Wireless Devices."
Paper presented at 88th ARFTG Microwave Measurements Conference, Austin, TX, United States. December 8, 2016 - December 9, 2016.

In [15], [18], we showed that the uncertainty due to the lack of spatial uniformity is not significant for our unloaded chamber. Therefore, we will study only the uncertainty due to the finite number of mode-stirring measurement samples. Regarding future measurements of modulated signals, for which we need to load the chamber to broaden the coherence bandwidth, the uncertainty due to the lack of spatial uniformity should be taken into account.

The uncertainty in the differences between two approaches for the three different simulated DUTs is given in Fig. 4. While the uncertainties for the waveguide horn antenna and the OEW are similar, the higher uncertainty values can be seen for the microstrip patch antenna. The reason for that is caused by the added uncertainty from the de-embedding of a coaxial-to-waveguide adapter. Note that the calibration was performed at the waveguide plane. Maximum uncertainty values from the NIST Microwave Uncertainty Framework for the waveguide horn, OEW, and microstrip patch antennas were 1.75% (0.075 dB), 1.66% (0.071 dB), and 2.41% (0.103 dB).

## VI. Conclusion

In this paper, we presented TRP measurement results inside an RC obtained with a power-calibrated VNA at millimeter-wave frequencies. We derived TRP expressions in terms of wave parameters for the two different cases: 1) for accessible DUT antenna terminals, and 2) for integrated DUT antennas. In the first case, the TRP can be easily calculated by measuring power levels of forward and reflected waves. In the second case, besides measuring power levels of forward and reflected waves at the receive antenna, we also need to measure the chamber loss. Results obtained from the two different approaches were compared and showed excellent agreement within our calculated measurement uncertainties.

We performed measurement uncertainty analysis using the Microwave Uncertainty Framework, which assigns uncertainties and probability distributions to error mechanisms in the calibration, and propagates the associated uncertainties to the end result. The uncertainties we obtained agree well with uncertainty calculations in our previous research employing an unloaded RC.

Here, we showed that a power-calibrated VNA extended existing methods for radiated power measurements. Our future work will include TRP measurements of modulated signals at millimeter-wave frequencies based on an RC and power- and phase-calibrated VNA.

## Acknowledgement

The authors would like to thank to Michael D. Janezic of the NIST National Advanced Spectrum and Communications Test Network (NASCTN) who provided us with a precision WR22 calibration kit needed for our measurements.

## References

[1] CTIA Certification, “Test Plan for Wireless Large-Form-Factor Device Over-the-Air Performance” Sep. 2016.

[2] “IEC 61000-4-21: EMC, Part 4: Testing and Measurement Techniques; Section 21: Reverberation Chamber Test Methods,” Int. Electrotech. Comm., Geneva, 2011.

[3] D. A. Hill, “Electromagnetic theory of reverberation chambers,” U.S. National Institute of Standards and Technology Technical Note 1506, 1998.

[4] D. Kajfez, *Q factor*, Oxford: MS: Vector Fields, 1994.

[5] “IEC 61000-4-22: EMC, Part 4: Testing and Measurement Techniques; Section 22: Radiated emissions and immunity measurements in fully anechoic rooms (FARs),” *Int. Electrotech. Comm.*, Geneva, 2010.

[6] P. Corona, G. Latmiral, E. Paolini, and L. Piccioli, “Use of reverberating enclosure for measurements of radiated power in the microwave range,” *IEEE Trans. Electromagn. Compat.*, vol. 18, no. 2, pp. 54–59, May 1976.

[7] D. A. Hill, D. G. Camell, K. H. Cavcey, and G. H. Koepke, “Radiated emissions and immunity of microstrip transmission lines: theory and reverberation chamber measurements,” *IEEE Trans. Electromagn. Compat.*, vol. 38, no. 2, pp. 165–172, May 1996.

[8] M. B. Slocum and M. O. Hatfield, “Evaluation of proposed IEC reverberation chamber methodology for radiated emissions measurements using a reference radiator,” in *IEEE Int. Symp. Electromagn. Compat.*, pp. 734–739, Aug. 13–17, 2001.

[9] H. G. Krauthäuser, “On the measurement of total radiated power in uncalibrated reverberation chambers,” *IEEE Trans. Electromagn. Compat.*, vol. 49, no. 2, pp. 270–279, May 2007.

[10] C. Orlenius, P. Lioliou, M. Franzén, and P-.S. Kildal, “Measurements of total radiated power of UMTS phones in reverberation chamber,” in *European Conference on Antennas Propag., EuCAP*, Nov. 11–16, 2007.

[11] V. Monebhurrun, T. Letertre, “Total radiated power measurements of WiFi devices using a compact reverberation chamber,” in *IEEE Int. Symp. Electromagn. Compat.*, Jan. 12–16, 2009.

[12] P. Roblin, *Nonlinear RF circuits and nonlinear vector network analyzers*, New York: Cambridge University Press, 2011.

[13] T. S. Rappaport, S. Sun, R. Mayzus, H. Zhao, Y. Azar, K. Wang, G. N. Wong, J. K. Schulz, M. Samimi, and F. Gutierrez, “Millimeter wave mobile communications for 5G cellular: It will work!,” *IEEE Access*, vol. 1, pp. 335–349, 2013.

[14] Keysight Technologies Application Note 5988-9215EN, “Fundamentals of RF and microwave power measurements (Part 3),” USA, August 1, 2014.

[15] D. Senic, K. A. Remley, C.-M. Wang, D. F. Williams, C. L. Holloway, D. C. Ribeiro, and A. T. Kirk, “Estimating and reducing uncertainty in reverberation-chamber characterization at millimeter-wave frequencies,” *IEEE Trans. Antennas and Propag.*, vol. 64, no. 7, pp. 3130–3140, Jul. 2016.

[16] D. F. Williams, NIST Microwave Uncertainty Framework, Beta Version. NIST, Boulder, CO, USA, Jun. 2014. Available online: https://www.nist.gov/services-resources/software/wafer-calibration-software

[17] J. A. Jargon, D. F. Williams, T. M. Wallis, D. X. LeGolvan, and P. D. Hale, “Establishing traceability of an electronic calibration unit using the NIST Microwave Uncertainty Framework,” in *79th ARFTG Conf. Dig*, Montreal, QC, Canada, Jun. 2012, pp. 32–36.

[18] D. Senic, D. F. Williams, K. A. Remley, C.-M. Wang, C. L. Holloway, Z. Yang, and K. F. Warnick, “Improved antenna efficiency measurement uncertainty in a reverberation chamber at millimeter-wave frequencies,” *IEEE Trans. Antennas Propag.*, IN PROCESS

Senic, Damir; Remley, Catherine; Williams, Dylan; Ribeiro, Diogo; Wang, Chih-Ming; Holloway, Christopher.
”Radiated Power Based on Wave Parameters at Millimeter-wave Frequencies for Integrated Wireless Devices.”
Paper presented at 88th ARFTG Microwave Measurements Conference, Austin, TX, United States. December 8, 2016 - December 9, 2016.

# Kicking the Tires of the NIST Microwave Uncertainty Framework, Part 1

Ronald A. Ginley
National Institute of Standards and Technology (NIST) RF Technology Division
325 Broadway, mc 672.01, Boulder, CO 80305, USA, rginley@boulder.nist.gov

***Abstract* — As with anything new, especially metrology tools, you want to know how good the new tool is. This is generally done through comparisons with existing systems. In this paper, such a comparison is described. The new NIST method of processing measurements and uncertainties, the Microwave Uncertainty Framework will be compared to the established NIST method for measuring one and two-port scattering-parameters. The setup of the comparison, results, and a discussion of the results will be covered. This paper, Part 1, will cover the comparison of the responses generated by the different methods. Part 2 will discuss the comparison of the uncertainties calculated with the different approaches.**

***Index Terms* — Microwave measurements, coaxial connectors, s-parameters, uncertainties**

## I. Introduction

As with anything new you want to see how good it is. The colloquial expression for this is "kicking the tires" which has been defined as "checking the viability of an unknown system by a quick test" (derived from literally kicking the tires of an automobile). In the world of microwave metrology we have more formal approaches to testing the viability of a new analysis or measurement approach. The comparison of results and uncertainties from different techniques is one of the standard methods used to evaluate new approaches.

The NIST Microwave Uncertainty Framework (or Framework or MUF for short) is a recently developed tool for producing measurement results and uncertainties [1-5]. The ability of the MUF to produce accurate results must be verified and this will be done by comparing the MUF results against the existing technique used at NIST. The established technique used at NIST for s-parameter measurements is the multiline method for network analyzer calibration [6]. The multiline method is applied in a NIST software package titled "Multical." Data is taken from the Vector Network Analyzer (VNA) and analyzed using other NIST software packages.

## II. Kicking the Tires – How do you kick a tire?

There are several steps involved in this comparison process. The VNA needed to be calibrated both with the multiline method and the method employed in the MUF (a version of the multiline calibration). Next, data was taken for a series of devices under test (DUTs). A set of six DUTs were measured, three one-ports (two matched terminations and an offset short) and three two-ports (a low-loss device, 20 dB and 50 dB attenuators). All of the devices, calibration standards and DUTs, had 3.5 mm connectors and the frequencies measured were from 0.2 to 33.0 GHz by 0.1 GHz steps. Finally, the corrected DUT results were compared.

The MUF process can be described as: take raw measurements of the calibration standards and the DUTs, the MUF will then generate the error correction coefficients based on the raw calibration standards' data, finally the correction coefficients are applied to the DUT raw data to get the final results. The established NIST technique is a bit different: take raw measurements of the calibration standards, use Multical to generate the correction coefficients, download these to the VNA, then take corrected measurements of the DUT.

The specifics of the actual process steps are as follows:

1) Uncertainty models were established in the MUF for the devices used in the VNA calibration
2) Raw measurements (no VNA correction applied) were taken of the devices used for the VNA calibration
3) The identical data was used in both Multical and the MUF to form the error correction matrices for the VNA
4) Starting with the VNA correction turned off, raw measurements were taken of one of the DUTs.
5) Without touching the DUT, the VNA correction from Multical was applied and corrected data of the DUT was taken using the NIST measurement software (a program called MeaslpX was used to take the corrected data from the VNA and another program called Calrep was used to analyze the data taken by MeaslpX)
6) All DUTs were measured by use of the process of 4) and 5)
7) The raw calibration standards data and the raw DUT data were processed through the MUF to arrive at the corrected response for each DUT
8) The corrected MUF responses were compared to the results from the Multical and NIST measurement software process

Throughout this comparison, we tried to keep the two measurement paths as similar as possible. Because of the



Ginley, Ronald.
"Kicking the Tires of the NIST Microwave Uncertainty Framework, Part 1."
Paper presented at 88th ARFTG Microwave Measurement Conference, Austin, TX, United States. December 8, 2016 - December 9, 2016.

differences in the two measurement paths, it was necessary to take both the uncorrected and corrected measurements of the DUTs. The uncertainty models used for the calibration standards will be detailed in Part II of this paper which will be published later. That being said, it is still necessary to have a basic understanding of the uncertainty models used for the Monte-Carlo analysis in the MUF. Figure 1 shows the basic model that was used for the airline standards in the MUF.

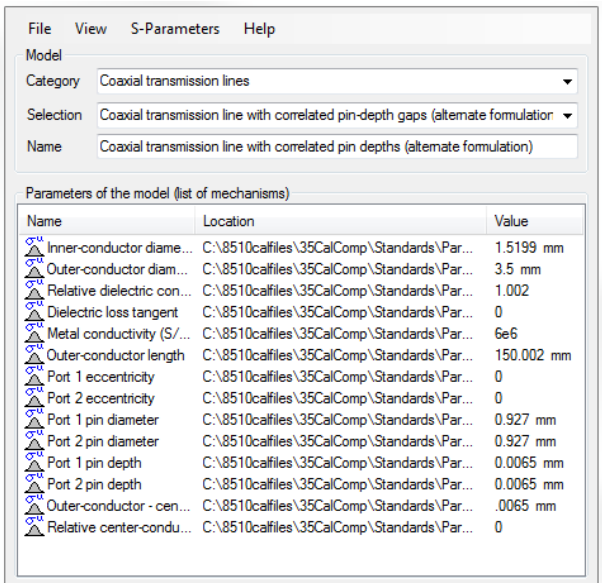


Figure 1. Airline uncertainty model used in the MUF

## III. I'VE KICKED THE TIRES - HERE'S HOW THEY FELT

In all, three sets of data are being compared. One from our established technique (notated as Calrep) and two sets from the MUF. One of these sets is the Nominal Value result which is produced when only the base data is used and is not perturbed by any uncertainty components (notated as MUF SA (for Sensitivity Analysis)). The other MUF result is the result from the Monte-Carlo process (MUF MC) that includes a statistical bias introduced in the results (in other words, this is the average value calculated from the results of all of the Monte-Carlo passes) [7].

Figure 2 shows the $S_{11}$ response results from one of the DUTs, a matched termination. There are several items that are noteworthy on the chart. Except at frequencies below approximately 2.5 GHz, there is good agreement between the results from the established technique (Calrep) and the two MUF results (MUF SA and MUF MC). The two MUF responses agree with each other as one would expect. The MUF Monte-Carlo response shows more "raggedness" which is also expected because of the statistical nature on which it is based (100 Monte-Carlo simulations were used). The differences between the various results can be seen in figure 7.

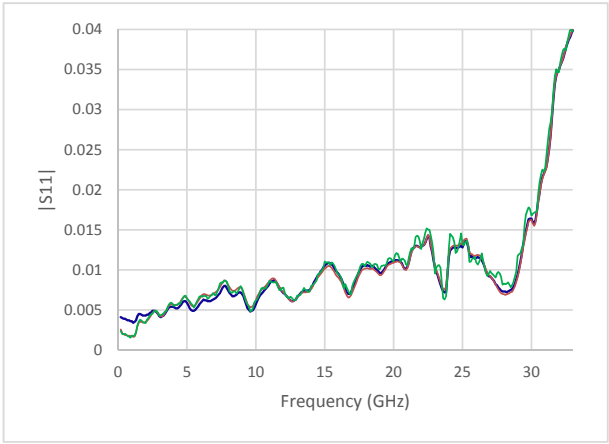


(a)

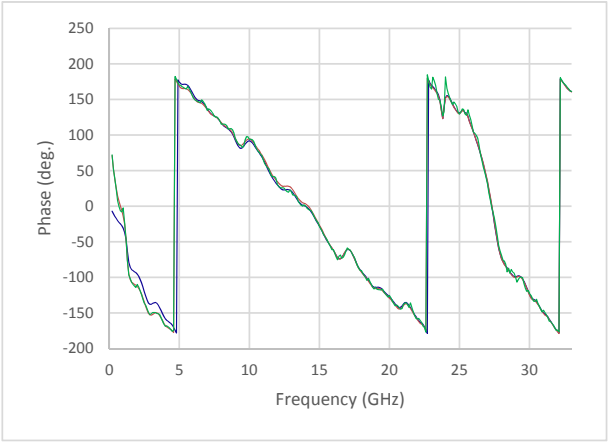


(b)

Figure 2. $S_{11}$ magnitude (a) and phase (b) results for a matched termination. Blue line is the Calrep response, Red is the MUF SA response and Green is the MUF Monte-Carlo response (note the orange and green plots lie virtually on top of each other).

Figure 3 shows the S21 magnitude results for a 50 dB attenuator. Here there is good agreement between all three responses. The statistical variations in the Monte-Carlo result are about the same magnitude as the dynamic range variations.

Figure 4 shows the results from the offset short DUT. Here, 100 Monte-Carlo simulations were used and there is reasonable agreement between the two MUF results. Figure 5 shows the absolute value of the differences between the Calrep and the MUF results with the Calrep uncertainty also shown for the offset short. At the higher frequencies there is good agreement between the Calrep and the MUF results; however, at the

bottom end, about 5 GHz and below, there are discrepancies in the results. Note that there was very good phase agreement between all three approaches (less than 0.3 degrees).

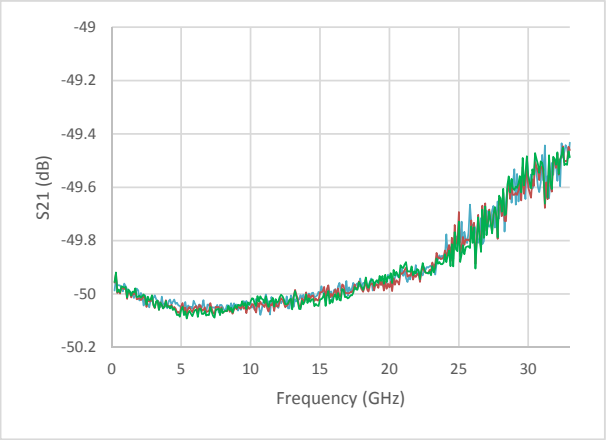


Figure 3. $S_{21}$ magnitude results for a 50 dB attenuator. Blue line is the Calrep response, Red is the MUF SA response and Green is the MUF MC response.

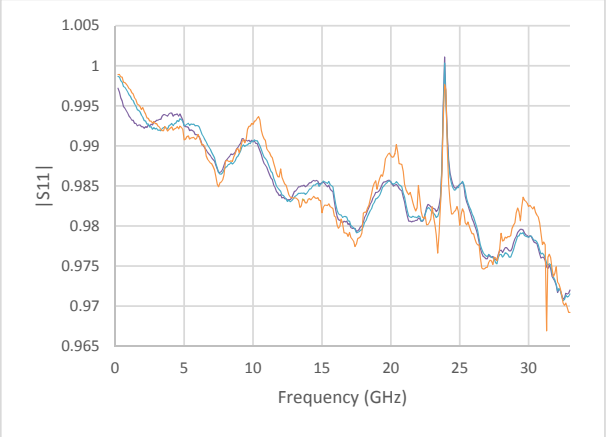


Figure 4. $S_{11}$ magnitude results for an offset short. Blue line is the Calrep response, Orange is the MUF SA response and Green is the MUF MC response.

There are several common treads found from the results. In general, there is good agreement between the different methods used for obtaining the results. Discrepancies are seen at the low frequencies (5 GHz and below), although these differences are fairly small (on the order of 0.002 for $S_{11}$ and on the order of 0.04 dB for $S_{21}$). This low frequency problem is seen in both reflection and transmission responses, but not seen in all of the DUT responses. The Monte-Carlo response shows more variation than the other responses due mostly to the statistical nature of its derivation.

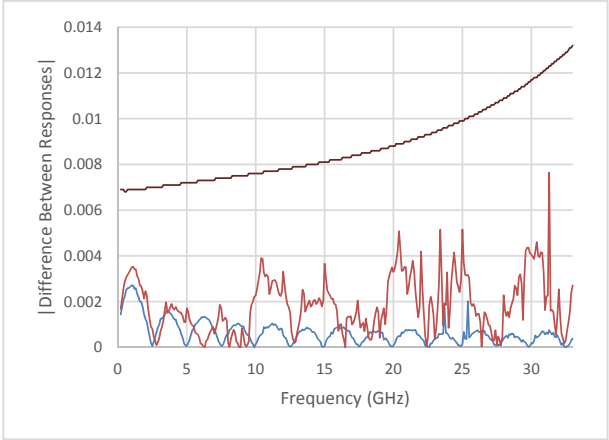


Figure 5. Absolute value of differences in responses for the offset short. Blue is |Calrep – MUF SA| and red is |Calrep – MUF MC|. The brown line represents the typical uncertainty associated with the Calrep measurement.

## IV. What have I really learned from kicking the tires

There are several points of discussion coming from the results of the "kick". First, there is generally good agreement between the results from our established technique and the results from the MUF.

Increasing the number of Monte-Carlo iterations from 100 to 1000 does not greatly influence the difference between the Monte-Carlo responses and the unperturbed Nominal Solution from the sensitivity analysis. This can be seen in figure 6 which shows the difference between the nominal unperturbed solution and the Monte-Carlo 100 iteration and 1000 iteration solutions. There is a periodicity to the difference that needs to be investigated further (maybe a Part III?)

As pointed out earlier, there is a difference in the responses at frequencies less than approximately 5 GHz. The difference is between the established technique and both of the MUF results (SA and MC). This is best seen in figure 2a. To investigate this issue, we have taken several steps. The first was to process the exact same DUT raw file through the Multical software and through the MUF (this differs with how we took the Calrep data which was obtained as corrected data through the use of another NIST software package). The results of this can be seen in figure 7. There is essentially no difference between the Calrep results and the results obtained by processing the files through the Multical software. There is the

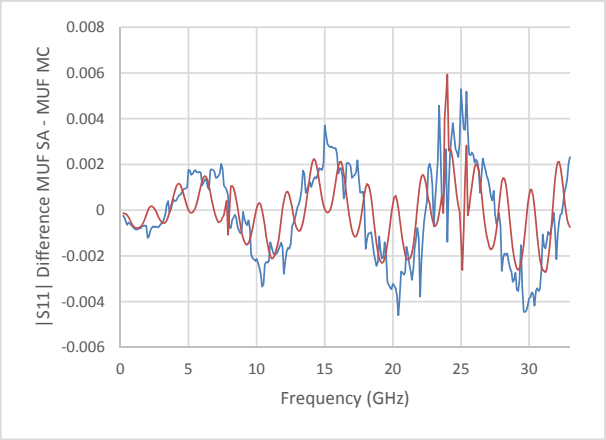


Figure 6. Differences in the Monte-Carlo $|S_{11}|$ responses for the offset short. Blue is (MUF Nominal Solution – MUF Monte-Carlo 100 iterations) and red is (MUF Nominal Solution – MUF MC 1000 iterations).

difference, as seen before, with the MUF results. This indicates that there is a difference in how Multical and the MUF are applying the multi-line calibration technique. The best guess as to a cause for this is the different way that Multical handles moving from an 8 to 12-term solution versus how the MUF uses the 8 and 12-term solutions. Investigation into this is ongoing.

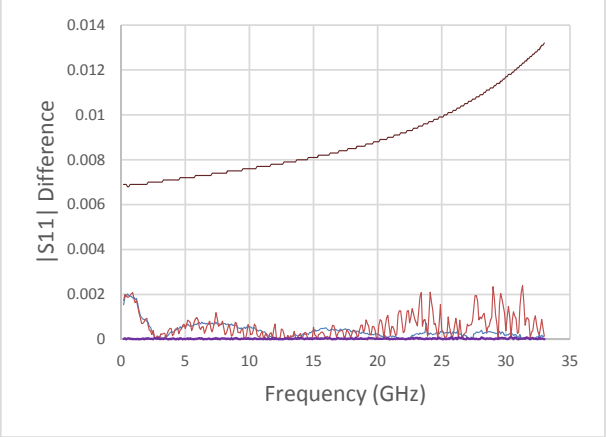


Figure 7. $|S_{11}|$ Differences for the matched termination. Blue is |Calrep - MUF SA|, red is |Calrep – MUF MC|, brown is the Calrep uncertainty (k=2), and purple is |Calrep – Multical| (which is essentially zero).

## V. My toe is sore from kicking – what else have I learned

The response results from the NIST Microwave Uncertainty Framework show good agreement with our established method with a few caveats. We are still investigating differences in responses at low frequencies and periodicity issues related to the Monte-Carlo responses.

Stay tuned for Part II or "My Tires Have Air, How Certain am I that they Will Roll?"

## References

[1] D. F. Williams, NIST Microwave Uncertainty Framework, Beta Version, http://www.nist.gov/ctl/rf-technology/relatedsoftware.cfm, 2015.

[2] J. A. Jargon, D. F. Williams, T. M. Wallis, D. X. LeGolvan, and P. D. Hale, "Establishing traceability of an electronic calibration unit using the NIST Microwave Uncertainty Framework," *79th ARFTG Microwave Measurement Conference*, Montreal, CANADA, Jun. 2012.

[3] J. A. Jargon, U. Arz, and D. F. Williams, "Characterizing WR-8 waveguide-to-CPW probes using two methods implemented within the NIST Uncertainty Framework," *80th ARFTG Microwave Measurement Conference*, San Diego, CA, Nov. 2012.

[4] J. A. Jargon, D. F. Williams, P. D. Hale, and M. D. Janezic, "Characterizing a noninsertable directional device using the NIST Uncertainty Framework," *83rd ARFTG Microwave Measurement Conference*, Tampa Bay, FL, Jun. 2014.

[5] J. A. Jargon, C. H. Cho, D. F. Williams, and P. D. Hale, "Physical models for 2.4 mm and 3.5 mm coaxial VNA calibration kits developed within the NIST Microwave Uncertainty Framework," *85th ARFTG Microwave Measurement Conference*, Phoenix, AZ, May 2015.

[6] R. B. Marks, "A multiline method of network analyzer calibration," *IEEE Trans. Microwave Theory Tech.*, vol. 39, no. 7, pp. 1205–1215, July 1991.

[7] K.A. Remley, D.F. Williams, P.D. Hale, C.M. Wang, J. Jargon, and Y. Park, "Millimeter-Wave Modulated-Signal and Error-Vector-Magnitude Measurement With Uncertainty," *IEEE Trans. Microwave Theory Tech.*, vol.63, no. 5, pp. 1710-1720, May 2015

# Isotropy Study for Over-the-Air Measurements in a Loaded Reverberation Chamber*

Damir Senic, Diego Cavaliere, Matt V. North, Maria G. Becker, Kate A. Remley,
Chih-Ming Wang, Christopher L. Holloway
National Institute of Standards and Technology
Boulder, CO
damir.senic@nist.gov

***Abstract*—We performed a field isotropy study based on the reverberation chamber transfer function for three different reverberation chamber configurations. Guidance for reducing the anisotropy based on the polarization-balanced antenna is also provided. We show that chamber isotropy is strongly influenced by loading such that an unloaded chamber can be considered as an isotropic environment, while a loaded chamber is more-or-less anisotropic depending on the amount of loading present. The loading of the chamber is crucial for wireless tests involving modulated signals. Its purpose is to create a flat channel, which enables successful demodulation of the signal without distortion. Consequently, understanding this effect is important in quantifying measurement uncertainty in loaded conditions.**

***Keywords—dipole antenna; isotropy; loading; polarization balance; reverberation chamber; wireless tests***

## I. Introduction

Reverberation chambers can be considered to be electrically-large resonators where, ideally, fields impinge on the device under test (DUT) equally from all directions creating rich isotropic environments [1],[2]. Many metrics, including the chamber transfer function [2],[3], antenna efficiency [4]-[7], shielding effectiveness [8],[9], absorption cross section [10]-[14], spatial correlation [15],[16], *etc*. have been derived under an isotropy premise. However, direct evaluation and confirmation of chambers' isotropy have been lacking. To the authors' knowledge, studies that investigated isotropy inside reverberation chambers are limited to a select few [2],[17],[18].

Empirical study of real reverberation chamber isotropy is particularly interesting to the wireless community, which employs reverberation chambers for over-the-air (OTA) tests [2],[19]-[22]. Contrary to electromagnetic compatibility (EMC) tests, wireless tests of modulated signals generally require a loaded chamber. Loading broadens and flattens the channel inside the chamber, which is necessary for demodulating modulated signals without distortion [3],[23]. However, heavy loading also has negative impacts on the chamber's behavior, as it decreases field homogeneity and increases chamber anisotropy primarily due to the unstirred multipath components. Hence, real-world deviations from ideal chamber isotropy will affect basic metrics unless compensated for by the stirring sequence.

A real reverberation chamber setup will exhibit some anisotropy depending on the amount of loading. The level of anisotropy is an important figure of merit in standardized tests. A common way to characterize the chamber isotropy is based on polarization balance, where the electric field or received power is measured for each of three orthogonal orientations of a field probe or an antenna. This method for performing isotropy characterization of a reverberation chamber is described in the IEC 61000-4-21 standard [24]. The IEC test proposes electric-field measurements with an electric-field probe capable of measuring three orthogonal polarizations at eight different locations inside the chamber that form the edge of the chamber's working volume. Electric-field probes are suggested because they have small dimensions and should, therefore, not perturb the fields inside the chamber. The small size of the field probe also means that undesirable field averaging characteristic of larger antennas can be avoided. Tuned dipoles are sometimes used for this purpose, as well.

In this paper, the assumption of a statistically isotropic reverberation chamber environment is evaluated by measuring the transfer function for different dipole antenna orientations and loading cases at ten locations inside the chamber (see Fig. 1).

This paper is organized as follows: the measurement setup and procedures for measuring polarization balance are given in Section II. Section III follows with the isotropy measurement results and evaluation of a chamber in terms of measured anisotropy. In Section IV, guidance for reducing the chamber's anisotropy is given. Statistical analysis is given in Section V, and concluding remarks can be found in Section VI.

## II. Chamber Setup for Polarization Balance Measurements

Polarization balance measurements were performed in terms of the chamber transfer function ($G_{\text{ref}}$) of a 1.9 m ($l$) × 1.4 m ($w$) × 2 m ($h$) reverberation chamber shown in Fig. 1. The chamber's transfer function ($G_{\text{ref}}$) is defined as

$$G_{\text{ref}} = \frac{\left\langle |S_{21}|^2 \right\rangle}{\eta_{\text{TX}}\eta_{\text{RX}}\left(1-\left|\langle S_{11}\rangle\right|^2\right)\left(1-\left|\langle S_{22}\rangle\right|^2\right)}, \qquad (1)$$

where the brackets denote the ensemble average over the mode-stirring sequence, $S_{21}$ is the forward transmission scattering parameter measured by a VNA, and the terms in the

* Work supported by U.S. government, not protected by U.S. copyright



Senic, Damir; Cavaliere, Diego; North, Matt; Becker, Maria; Remley, Catherine; Wang, Chih-Ming; Holloway, Christopher.
"Isotropy Study for Over-the-Air Measurements in a Loaded Reverberation Chamber."
Paper presented at 2017 IEEE International Symposium on Electromagnetic Compatibility and Signal/Power Integrity, Washington D.C., DC, United States. August 7, 2017 - August 11, 2017.

denominator represent the free-space radiation efficiencies ($\eta_{TX}$ and $\eta_{RX}$) and mismatch corrections for the two antennas. The radiation efficiency can be measured in either an anechoic chamber or in an unloaded reverberation chamber [4]-[7]. The chamber was equipped with a pair of electrically large paddles and a turntable. One paddle moved a maximum vertical distance of 1.4 m spanning the length of the chamber's side wall. The other paddle moved a maximum horizontal distance of 1.3 m spanning the length of the chamber's ceiling. The longitudinal resolution of both paddles was 7.5 μm. The angular resolution of the turntable was 0.005°, according to manufacturer's specifications. All measurements are made in stepped mode under stationary conditions.

Measurements were performed over the Personal Communications Service (PCS) band (1850 MHz – 1990 MHz) [22] with a linearly-polarized, half-wavelength dipole receive (RX) antenna oriented in the three orthogonal orientations mounted on the turntable. Horizontal and vertical translation stages, combined with the turntable, were used to automate positioning of the receive antenna (see Fig. 2) at the ten different locations shown in Fig. 1. The first four locations were on the edge of the lower base of the cylinder indicated in Fig. 1, separated by 90° of the turntable rotation. The fifth position was at the center of the cylinder's lower base. The other five locations were the same as the first five but elevated an additional 20 cm. At each RX antenna location, all *S*-parameters were measured for each of the three orthogonal polarizations.

Two different transmit antennas were used in this study. The first, shown in Fig. 3 (left), was a stationary, vertically polarized, broadband (650 MHz – 3.5 GHz) discone monopole antenna. It was used to quantify field anisotropy in Section III. The second, Fig. 3 (right), was a polarization-balanced, double-sided, tapered, self-grounded monopole antenna [25]. This antenna was used to demonstrate a method for reducing the effects of field anisotropy in Section IV. Measurements were performed with a 50 GHz VNA. Key measurement parameters are summarized in Table I. The transmit and receive antennas were physically separated by a metallic shield intended to avoid direct energy coupling between them (see Figs. 1 and 2).

In order to study the effect of chamber loading on isotropy, measurements were repeated for three different chamber loading configurations: unloaded, partially loaded, and heavily loaded. Loading was achieved with RF absorbers magnetically mounted on the chamber's walls, as shown in Fig. 2. For the heavily loaded case, five large absorbers with dimensions of 15 cm ($l$) × 6 cm ($w$) × 60 cm ($h$), and four small absorbers with dimensions of 15 cm ($l$) × 6 cm ($w$) × 15 cm ($h$), were used. Absorber layout and orientation for the heavily loaded chamber is shown in Figs. 1 and 2. The partially loaded chamber had three large absorbers. Chamber loading is commonly used to broaden the chamber's coherence bandwidth (CBW) and to create a flat channel in order to measure modulated signals. The CBWs corresponding to the unloaded, partially loaded, and heavily loaded chambers were 2.86 MHz, 7.76 MHz, and 12.26 MHz, respectively, calculated with the method of [23].

TABLE I. MEASUREMENT PARAMETERS

| Parameter | Value |
|---|---|
| Frequency range | 1850 MHz – 1990 MHz |
| Number of frequency points | 1401 |
| IF bandwidth | 2 kHz |
| VNA output power level | -10 dBm |
| VNA dwell time | 10 μs |
| Turntable locations (static) | 10 |
| Number of paddle positions-stepped ($V \times H$) | 15 × 15 |

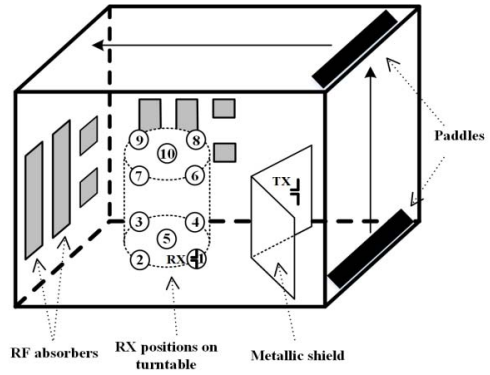


Fig. 1. Schematic of chamber setup for polarization balance measurements.

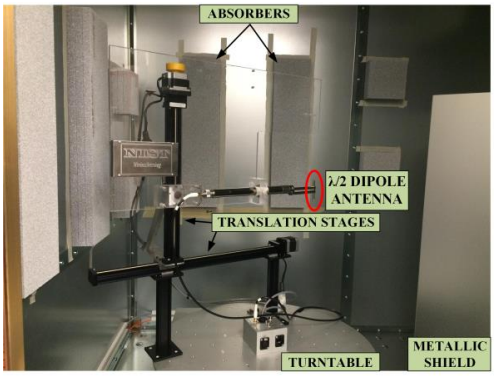


Fig. 2. Heavily loaded chamber and receive antenna fixture consisting of horizontal and vertical translation stages placed on the turntable.

Fig. 3. Two transmit antennas; left: vertically-polarized broadband discone monopole antenna; right: polarization-balanced, double-sided, tapered, self-grounded monopole antenna [25].



Senic, Damir; Cavaliere, Diego; North, Matt; Becker, Maria; Remley, Catherine; Wang, Chih-Ming; Holloway, Christopher.
"Isotropy Study for Over-the-Air Measurements in a Loaded Reverberation Chamber."
Paper presented at 2017 IEEE International Symposium on Electromagnetic Compatibility and Signal/Power Integrity, Washington D.C., DC, United States. August 7, 2017 - August 11, 2017.

## III. Evaluation of Reverberation Chamber Performance in Terms of Field Anisotropy

To study the effects of polarization imbalance as a function of loading, the method of [24] was used. The chamber transfer function ($G_{ref}$) from (1) was calculated for the three different chamber loading configurations and for ten RX antenna locations. The $G_{ref}$ results, averaged over the PCS band, are summarized in Table II for the linearly-polarized TX antenna, at each RX antenna location and for each chamber loading configuration.

The unloaded chamber provides a nearly isotropic environment where the *Z* component is only 0.5 dB higher than the *X* and *Y* components. Regarding the partially loaded and heavily loaded chambers, differences of 0.22 – 1.43 dB and 0.88 – 5.23 dB, respectively, between the *Z* component and the *X* and *Y* components are observed. This effect is seen at each RX antenna location, as well as on average over the ten RX antenna locations shown at the bottom of Table II. Note that the dominance of the *Z* component is due to the vertical (*Z*) polarization of the TX antenna.

TABLE II. $G_{REF}$ Results in Decibels for Vertically-Polarized Monopole TX Antenna Averaged over PCS Band

| RX | | RC | PARTLY | HEAVILY |
|---|---|---|---|---|
| Location | Orientation | UNLOADED | LOADED | LOADED |
| 1 | *X* | -18.07 | -22.09 | -27.14 |
| | *Y* | -18.12 | -22.32 | -28.45 |
| | *Z* | **-17.34** | **-21.08** | **-24.20** |
| 2 | *X* | -18.20 | -22.25 | -27.78 |
| | *Y* | -17.93 | -21.75 | -27.35 |
| | *Z* | **-17.87** | **-21.97** | **-25.67** |
| 3 | *X* | -18.03 | -22.20 | -27.65 |
| | *Y* | -18.10 | -22.34 | -27.25 |
| | *Z* | **-17.69** | **-20.99** | **-23.83** |
| 4 | *X* | -18.14 | -22.13 | -26.64 |
| | *Y* | -18.10 | -21.87 | -26.31 |
| | *Z* | **-17.77** | **-21.01** | **-23.39** |
| 5 | *X* | -17.97 | -21.82 | -28.36 |
| | *Y* | -17.97 | -22.00 | -27.06 |
| | *Z* | **-17.59** | **-20.82** | **-23.50** |
| 6 | *X* | -17.89 | -21.81 | -27.47 |
| | *Y* | -18.02 | -21.88 | -25.00 |
| | *Z* | **-17.30** | **-20.63** | **-22.24** |
| 7 | *X* | -18.25 | -22.84 | -25.54 |
| | *Y* | -18.29 | -22.39 | -27.58 |
| | *Z* | **-17.83** | **-21.55** | **-24.66** |
| 8 | *X* | -18.04 | -22.19 | -26.74 |
| | *Y* | -18.04 | -22.27 | -25.07 |
| | *Z* | **-17.25** | **-20.84** | **-24.02** |
| 9 | *X* | -18.07 | -22.01 | -24.13 |
| | *Y* | -18.12 | -21.78 | -26.06 |
| | *Z* | **-17.90** | **-21.30** | **-22.68** |
| 10 | *X* | -18.16 | -22.21 | -27.12 |
| | *Y* | -18.05 | -22.04 | -26.50 |
| | *Z* | **-17.48** | **-21.20** | **-24.22** |
| Average | *X* | -18.08 | -22.15 | -27.48 |
| | *Y* | -18.07 | -22.06 | -27.26 |
| | *Z* | **-17.60** | **-21.12** | **-24.53** |

In Fig. 4 we show the measured $G_{ref}$ averaged over the ten RX antenna locations (antenna stirring) for the vertically-polarized monopole TX antenna. Fig. 4 a) through c) illustrate the trend of increased anisotropy with increased loading. The unloaded chamber results, given in Fig. 4, indicate that all three field components have similar values, as expected. With the addition of loading, the *Z* component becomes increasingly larger than the *X* and *Y* components. Note that in Fig. 4 a) and b) a 0.5 dB per division scale is used and in c) the scale is 2 dB per division.

The data presented in the plots of Fig. 4 are the result of averaging $G_{ref}$ over ten turntable locations. Therefore, we see that antenna location stirring by itself does not improve field isotropy; only field homogeneity (spatial uniformity) can be improved, leading to the need for polarization stirring [2],[17] or other techniques, as described in the next section. In the next section, guidance for reducing the anisotropy in the case of a loaded reverberation chamber is provided.

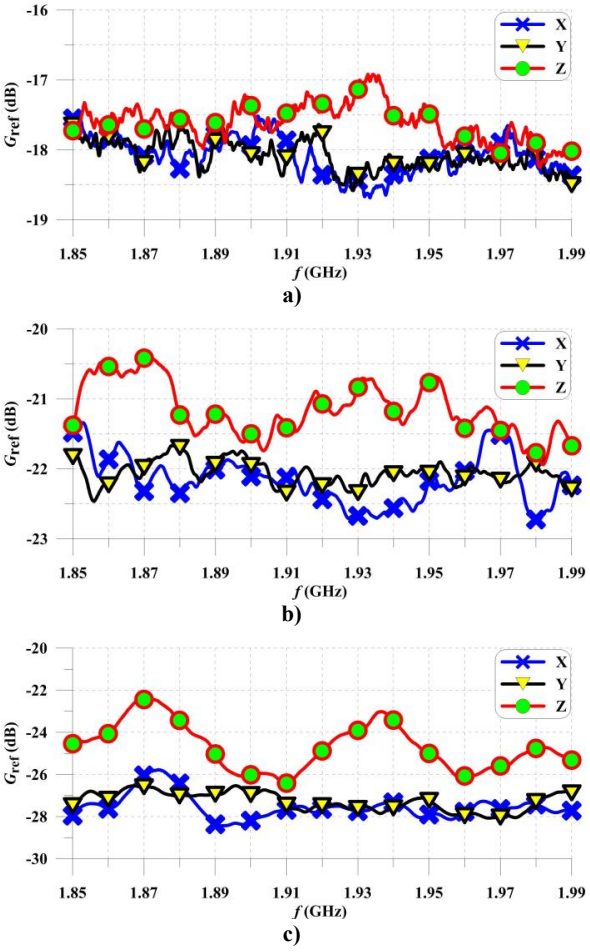


Fig. 4. $G_{ref}$ measured over the PCS band and averaged over 10 RX antenna locations for a vertically-polarized monopole TX antenna inside: a) unloaded chamber, b) partially loaded chamber, and c) heavily loaded chamber.



Senic, Damir; Cavaliere, Diego; North, Matt; Becker, Maria; Remley, Catherine; Wang, Chih-Ming; Holloway, Christopher.
"Isotropy Study for Over-the-Air Measurements in a Loaded Reverberation Chamber."
Paper presented at 2017 IEEE International Symposium on Electromagnetic Compatibility and Signal/Power Integrity, Washington D.C., DC, United States. August 7, 2017 - August 11, 2017.

## IV. Methods for Reducing Reverberation Chamber Anisotropy

Many reverberation-chamber-based tests rely on linearly-polarized TX antennas such as monopole, dipole, log-periodic, loop, standard horn, and double-ridged horn antennas. As shown in the previous section, such antennas are capable of measuring isotropic environments as long as the chamber is not loaded. Hence, we can use linearly-polarized antennas for the majority of tests in EMC. However, since wireless tests generally require a loaded chamber, we should be aware of the effects of possible anisotropic chamber environments if linearly polarized antennas are used. Polarization stirring is one solution to this issue [2],[17].

In this section, we will show that besides polarization stirring, we can compensate for loading-induced field anisotropy by using a polarization-balanced antenna. Here, a double-sided, tapered, self-grounded monopole antenna [25], shown in Fig. 3 (right) was used in place of the linearly-polarized TX antenna. However, any kind of polarization-balanced antenna (such as a helix antenna in axial or end-fire mode) could be used for the same purpose.

TABLE III. $G_{REF}$ Results in Decibels for Polarization-Balanced Monopole TX Antenna Averaged over PCS Band

| RX | | RC | PARTLY | HEAVILY |
|---|---|---|---|---|
| **Location** | **Orientation** | **UNLOADED** | **LOADED** | **LOADED** |
| **1** | ***X*** | -18.69 | -22.53 | -24.15 |
| | ***Y*** | -18.81 | -23.22 | -24.72 |
| | ***Z*** | **-18.58** | **-22.40** | **-23.53** |
| **2** | ***X*** | -18.97 | -23.43 | -25.46 |
| | ***Y*** | -18.78 | -22.50 | -25.58 |
| | ***Z*** | **-18.91** | **-23.08** | **-25.15** |
| **3** | ***X*** | -18.74 | -22.67 | -24.37 |
| | ***Y*** | -18.81 | -22.59 | -24.73 |
| | ***Z*** | **-18.70** | **-22.36** | **-23.83** |
| **4** | ***X*** | -18.81 | -22.34 | -23.91 |
| | ***Y*** | -18.45 | -21.16 | -22.84 |
| | ***Z*** | **-18.60** | **-21.78** | **-23.00** |
| **5** | ***X*** | -19.01 | -22.86 | -24.37 |
| | ***Y*** | -18.79 | -22.40 | -23.75 |
| | ***Z*** | **-18.72** | **-22.20** | **-23.57** |
| **6** | ***X*** | -18.58 | -21.76 | -23.92 |
| | ***Y*** | -18.20 | -22.17 | -23.35 |
| | ***Z*** | **-18.66** | **-22.44** | **-23.50** |
| **7** | ***X*** | -18.80 | -23.24 | -24.97 |
| | ***Y*** | -18.70 | -22.82 | -24.64 |
| | ***Z*** | **-18.66** | **-23.05** | **-24.77** |
| **8** | ***X*** | -18.76 | -22.71 | -23.67 |
| | ***Y*** | -18.64 | -22.26 | -24.26 |
| | ***Z*** | **-18.77** | **-22.47** | **-24.28** |
| **9** | ***X*** | -18.61 | -22.39 | -24.07 |
| | ***Y*** | -18.35 | -21.39 | -22.52 |
| | ***Z*** | **-18.56** | **-22.06** | **-23.14** |
| **10** | ***X*** | -18.89 | -22.90 | -24.93 |
| | ***Y*** | -18.91 | -22.48 | -24.38 |
| | ***Z*** | **-18.68** | **-22.30** | **-23.60** |
| **Average** | ***X*** | -18.79 | -22.66 | -24.35 |
| | ***Y*** | -18.64 | -22.26 | -23.98 |
| | ***Z*** | **-18.68** | **-22.40** | **-23.79** |

In Table III, the chamber transfer function results for the polarization-balanced transmit antenna are shown for the ten RX antenna locations and three chamber loading configurations. Very similar $G_{ref}$ values were measured for all three field components at all RX antenna locations and for all three chamber configurations. We conclude, therefore, that we can reduce the effects of field anisotropy due to the loading when a polarization-balanced antenna is used. This effect is shown in Fig. 5 a) through c), where the chamber transfer function is averaged over ten RX antenna locations. Similar $G_{ref}$ results were obtained for all three field components for a partially loaded chamber (0.13 – 0.82 dB) and for heavily loaded chamber (0.02 – 1.33 dB).

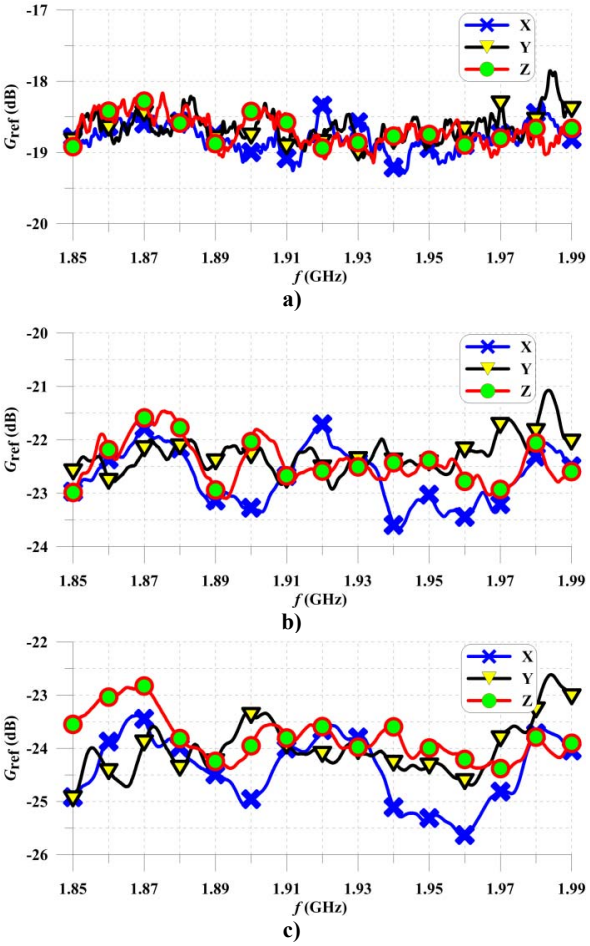


Fig. 5. $G_{ref}$ measred over the PCS band and averaged over 10 RX antenna locations for a polarization-balanced monopole TX antenna inside: a) unloaded chamber, b) partially loaded chamber, and c) heavily loaded chamber.



Senic, Damir; Cavaliere, Diego; North, Matt; Becker, Maria; Remley, Catherine; Wang, Chih-Ming; Holloway, Christopher.
"Isotropy Study for Over-the-Air Measurements in a Loaded Reverberation Chamber."
Paper presented at 2017 IEEE International Symposium on Electromagnetic Compatibility and Signal/Power Integrity, Washington D.C., DC, United States. August 7, 2017 - August 11, 2017.

## V. STATISTICS

In order to evaluate the observed improvement in the average field isotropy when using a polarization-balanced antenna, we calculated the standard deviation of the $G_{\text{ref}}$ values over the ten antenna locations for each chamber configuration and for each of the two different TX antennas. The results are given in Table IV where the standard deviations of the $G_{\text{ref}}$ values for the unloaded chamber are shown to be similar for both TX antennas. Table IV shows that, as chamber loading increases, the standard deviation for the vertically-polarized monopole antenna becomes larger than the standard deviation for the polarization-balanced antenna. This is particularly true for the heavily loaded chamber, which indicates that care must be taken in choosing both stirring sequence and antennas to minimize the effect of field anisotropy due to loading.

TABLE IV. STANDARD DEVIATION OF $G_{\text{REF}}$ IN DECIBELS FOR VERTICALLY-POLARIZED AND POLARIZATION-BALANCED MONOPOLE TX ANTENNAS

| TX ANTENNA | RC UNLOADED | PARTLY LOADED | HEAVILY LOADED |
|---|---|---|---|
| **Vertically-Polarized Monopole** | **0.28** | **0.56** | **1.76** |
| **Polarization-Balanced Monopole** | **0.17** | **0.51** | **0.76** |

We also characterized the chamber's performance in terms of field isotropy from the planar and total field anisotropy coefficients [24]

$$\left\langle A_{\alpha\beta} \right\rangle = \left\langle \frac{\left(\left|E_\alpha\right|^2 / P_{\text{i}}\right) - \left(\left|E_\beta\right|^2 / P_{\text{i}}\right)}{\left(\left|E_\alpha\right|^2 / P_{\text{i}}\right) + \left(\left|E_\beta\right|^2 / P_{\text{i}}\right)} \right\rangle = \left\langle \frac{\left|S_{21,\alpha}\right|^2 - \left|S_{21,\beta}\right|^2}{\left|S_{21,\alpha}\right|^2 + \left|S_{21,\beta}\right|^2} \right\rangle, \quad (2)$$

$$\left\langle A_{\text{total}} \right\rangle = \left\langle \sqrt{\left(A_{XY} + A_{XZ} + A_{YZ}\right)/3} \right\rangle, \quad (3)$$

where $|E_{\alpha,\beta}|$ and $S_{21,\alpha,\beta}$ represent the measured received field strength and forward transmission scattering parameter, respectively, of the arbitrary rectangular component $\alpha$ or $\beta = X$, $Y$, $Z$ and $P_{\text{i}}$ is the net input power injected into the chamber.

Anisotropy coefficients from [24] were calculated for the two different TX antennas and three chamber configurations given in Table V. According to the method of [24] (Annex J), we compared them with typical coefficient values for "medium" and "good" reverberation chamber quality, as shown in Table VI. Because we used 15 × 15 = 225 paddle positions, all calculated anisotropy coefficients fall either in the "good" or "medium" chamber quality category. Bearing in mind the observed polarization imbalance for the heavily loaded chamber excited by the vertically-polarized monopole antenna, we conclude that the current standard test method [24] is rather forgiving considering field anisotropy.

TABLE V. CALCULATED TOTAL FIELD ANISOTROPY COEFFICIENTS FOR THREE CHAMBER CONFIGURATIONS AND TWO TX ANTENNAS

| TX ANTENNA | RC UNLOADED | PARTLY LOADED | HEAVILY LOADED |
|---|---|---|---|
| **Vertically-Polarized Monopole** | **-14.03** | **-11.28** | **-10.79** |
| **Polarization-Balanced Monopole** | **-17.68** | **-14.55** | **-13.60** |

TABLE VI. TYPICAL VALUES FOR TOTAL FIELD ANISOTROPY COEFFICIENTS FOR "MEDIUM" AND "GOOD" REVERBERATION QUALITY [24]-TABLE J.1

| Number of paddle positions $N$ | $N = 100$ | $N = 300$ |
|---|---|---|
| **"Medium" stirring quality** | **-7.5** | **-10** |
| **"Good" stirring quality** | **-12.5** | **-15** |

## VI. CONCLUSION

In this paper, we presented a reverberation chamber field isotropy study for three different loading scenarios: unloaded, partially loaded, and heavily loaded chambers. In an ideal chamber, a rich isotropic environment is created no matter what type of excitation is used. Loaded-chamber isotropy deviates from the ideal case when a linearly-polarized TX antenna excites the chamber. Thus, we conclude that loading may deteriorate the field isotropy.

Loading also reduces the spatial uniformity, which then can be compensated for by applying antenna stirring. We showed that antenna stirring was not beneficial for improving the field isotropy. Other techniques need to be employed instead, such as polarization stirring or the use of polarization-balanced antennas. The approach for reducing the effects of field anisotropy demonstrated here was based on the use of the polarization-balanced antenna. It resulted in a significant reduction in the anisotropy effect.

Results obtained indicate a need for polarization stirring of the measurement antenna or for use of a polarization-balanced measurement antenna when measuring a large-form-factor DUT that cannot be rotated.

Future work on this topic is expected to involve the development of a robust test method for isotropy validation for loaded reverberation chambers. Such efforts are motivated by the fact that current test methods based on [24] do not result in the rejection of the isotropy hypothesis for a heavily loaded chamber with a vertically-polarized monopole antenna, even though obvious polarization imbalance is present.

## REFERENCES


[1] D. A. Hill, *Electromagnetic Fields in Cavities*, Piscataway: Wiley IEEE Press, 2009.

[2] P.-S. Kildal, X. Chen, C. Orlenius, M. Franzen, and C. S. L. Patane, "Characterization of reverberation chambers for OTA measurements of wireles devices: Physical formulation of channel matrix and new uncertainty formula," *IEEE Trans. Antennas and Propag.*, vol. 60, no. 8, pp. 3875–3891, Aug. 2012.

[3] K. A. Remley, J. Dortmans, C. Weldon, R. D. Horansky, T. B. Meurs, C.-M. Wang, D. F. Williams, C. L. Holloway, and P. F. Wilson, "Configuring and verifying reverberation chambers for testing cellular wirelss devices," *IEEE Trans. Electromagn. Compat.*, vol. 58, no. 3, pp. 661–672, June 2016.





Senic, Damir; Cavaliere, Diego; North, Matt; Becker, Maria; Remley, Catherine; Wang, Chih-Ming; Holloway, Christopher.
"Isotropy Study for Over-the-Air Measurements in a Loaded Reverberation Chamber."
Paper presented at 2017 IEEE International Symposium on Electromagnetic Compatibility and Signal/Power Integrity, Washington D.C., DC, United States. August 7, 2017 - August 11, 2017.

[4] M. Piette, “Antenna radiation efficiency measurements in a reverberation chamber,” in *Proc. Asia-Pacific Radio Science Conf.*, Aug. 24–27, 2004, pp. 19–22.

[5] H. G. Krauthauser and M. Herbrig, “Yet another antenna efficiency measurement method in reverberation chambers,” in *Proc. IEEE Int, Symp. on Electromagn. Compat.*, Jul. 25–30, 2010, pp. 536–540.

[6] C. L. Holloway, H. Shah, R. J. Pirkl, W. Young, J. Ladbury, and D. A. Hill, “Reverberation chamber techniques for determining the radiation and total efficiency of antennas,” *IEEE Trans. Antennas Propag.*, vol. 60, no. 4, pp. 1758–1770, Apr. 2012.

[7] D. Senic, D. F. Williams, K. A. Remley, C.-M. Wang, C. L. Holloway, Z. Yang, and K. F. Warnick, “Improved antenna efficiency measurement uncertainty in a reverberation chamber at millimeter-wave frequencies,” *IEEE Trans. Antennas Propag*., IN PROCESS

[8] C. L. Holloway, D. A. Hill, M. Sandroni, J. M. Ladbury, J. Coder, G. Koepke, A. C. Marwin, and Y. He, “Use of reverberation chambers to determine the shielding effectiveness of physically small, electrically large enclosures and cavities,” *IEEE Trans. Electromagn. Compat*., vol. 50, no. 4, pp. 770–782, November 2008.

[9] D. Senic, A. Sarolic, V. Roje, "GTEM cell setup and method for measuring shielding effectiveness of resonant enclosures", *International Symposium on Electromagnetic Compatibility (EMC Europe)* 2011, pp. 192 - 197.

[10] D. Senic, A. Sarolic, and Z. M. Joskiewicz, “Preliminary results of human body average absorption cross section measurements in reverberation chamber,” *International Symposium on Electromagnetic Compatibility (EMC Europe)* 2013, pp. 887-890.

[11] D. Senic, C. L. Holloway, J. M. Ladbury, G. H. Koepk, and A. Sarolic, “Absorption characteristics and SAR of a lossy sphere inside a reverberation chamber,“ *International Symposium on Electromagnetic Compatibility (EMC Europe)* 2014, pp. 962-967.

[12] I. D. Flintoft, M. P. Robinson, G. C. R. Melia, J. F. Dawson and A. C. Marvin, "Average absorption cross-section of the human body measured at 1-12 GHz in a reverberant environment: Results of a human volunteer study", *IOP Physics in Medicine and Biology*, vol. 59, no. 13, pp. 3297-3317, July 2014.

[13] I. D. Flintoft, G. C. R. Melia, M. P. Robinson, J. F. Dawson and A. C. Marvin, “Rapid and accurate broadband absorption cross-section measurement of human bodies in a reverberation chamber”, *IOP Measurement Science and Technology*, vol. 26, no. 6, pp. 065701, June 2015.

[14] D. Senic, A. Sarolic, J. M. Joskiewicz, and C. L. Holloway, "Absorption cross-section measurements of a human model in a reverberation chamber," *IEEE Trans. Electromagn. Compat*., vol. 58, no. 3, pp. 721-728, June 2016.

[15] R. J. Pirkl, K. A. Remley, and C. L. Patané, “Reverberation chamber measurement correlation,” *IEEE Trans. Electromagn. Compat.*, vol. 54, no. 3, pp. 533–545, Jun. 2012.

[16] D. Senic, K. A. Remley, C.-M. Wang, D. F. Williams, C. L. Holloway, D. C. Ribeiro, and A. T. Kirk, “Estimating and reducing uncertainty in reverberation-chamber characterization at millimeter-wave frequencies,” *IEEE Trans. Antennas and Propag.*, vol. 64, no. 7, pp. 3130–3140, Jul. 2016.

[17] P.-S. Kildal and C. Carlsson, “Detection of a polarization imbalance in reverberation chambers and how to remove it by polarization stirring when measuring antenna efficiencies,” *Microw. Opt. Technol. Lett*., vol. 34, no. 2, pp. 145–149, July 2002.

[18] R. J. Pirkl and K. A. Remley, “Experimental evaluation of the statistical isotropy of a reverberation chamber’s plane-wave spectrum,” *IEEE Trans. Electromagn. Compat.*, vol. 56, no. 3, pp. 498–509, Jun. 2014.

[19] C. Orlenius, P.-S. Kildal, and G. Poilasne, “Measurements of total isotropic sensitivity and average fading sensitivity of CDMA phones in reverberation chamber,” in *Proc. IEEE AP-S Int. Symp*., vol. 1, Washington, DC, USA, Jul. 3–8, 2005, pp. 409–412.

[20] S. J. Floris, K. A. Remley, and C. L. Holloway, “Bit error rate measurements in reverberation chambers using real-time vector receivers,” *IEEE Antennas Wireless Propag. Lett*., vol. 9, pp. 619–622, 2010.

[21] E. Genender, C. L. Holloway, K. A. Remley, J. Ladbury, and G. Koepke, “Simulating the multipath channel with a reverberation chamber: Application to bit error measurements,” *IEEE Trans. Electromagn. Compat*., vol. 52, no. 4, pp. 766–777, Nov. 2010.

[22] CTIA Certification, “Test Plan for Wireless Large-Form-Factor Device Over-the-Air Performance” Oct. 2016.

[23] J. N. H. Dortmans, K. A. Remley, D. Senic, C.-M. Wang, C. L. Holloway, “Use of absorption cross section to predict coherence bandwidth and other characteristics of a reverberation chamber setup for wireless-system tests,” *IEEE Trans. Electromagn. Compat.*, vol. 58, no. 5, pp. 1653–1661, Oct. 2016.

[24] “IEC 61000-4-21: EMC, Part 4: Testing and Measurement Techniques; Section 21: Reverberation Chamber Test Methods,” *Int. Electrotech. Comm*., Geneva, 2011.

[25] A. Al-Rawi, A. Hussain, J. Yang, M. Franzen, C. Orlenius, and A. A. Kishk, “A new compact wideband MIMO antena – The double-sided tapered self-grounded monopole array,” *IEEE Trans. Antennas and Propag.*, vol. 62, no. 6, pp. 3365–3369, Jun. 2014.



Senic, Damir; Cavaliere, Diego; North, Matt; Becker, Maria; Remley, Catherine; Wang, Chih-Ming; Holloway, Christopher.
”Isotropy Study for Over-the-Air Measurements in a Loaded Reverberation Chamber.”
Paper presented at 2017 IEEE International Symposium on Electromagnetic Compatibility and Signal/Power Integrity, Washington D.C., DC, United States. August 7, 2017 - August 11, 2017.

# Validation of Robotics for Antenna Measurements

Jeff R. Guerrieri, David Novotny, Josh Gordon, Mike Francis, Alexandra Curtin
National Institute of Standards and Technology, 325 Broadway, Boulder, CO 80305 USA, jguerrieri@nist.gov

***Abstract* — This paper presents recent measurements using the newly developed Configurable Robotic Millimeter-Wave Antenna (CROMMA) facility by the Antenna Metrology Lab at the National Institute of Standards and Technology (NIST). NIST set out to develop an antenna measurement facility that would be reconfigurable to different near-field antenna measurement geometries and perform antenna measurements from 100 to 500 GHz. The positioning capability of the robot has been evaluated and spherical near-field measurements performed at 183 GHz. Spherical far-field and extrapolation measurements have been performed at 112, 118 and 125 GHz. Spherical near-field measurements have been performed at 118 GHz on a CubeSat feed horn and compared to simulated results. Finally, the concept of multiple robot antenna measurement facility is discussed.**

***Index Terms* — robotic arm, millimeter wave, spherical near-field, extrapolation technique.**

## I. Introduction

The explosion of mobile communications demands more data and is pushing the industry into the millimeter wave (mmwave) spectrum. This also increases the demand for accurate mmwave antenna measurements. To address this demand, the National Institute of Standards and Technology (NIST) developed a new robotic arm scanning system to perform near-field antenna measurements at mmwave frequencies above 100 GHz. The goal of this work was to develop a configurable platform that can perform different measurement geometries with minimal setup and have dynamic probe position correction to 0.02λ at frequencies above 100 GHz [1].

## II. CROMMA Facility Components

The **C**onfigurable **RO**botic **M**illi**M**eter-wave **A**ntenna (CROMMA) facility shown in Fig. 1 uses two robotic positioners and one rotary positioner. [2,3]. The robotic arm uses a serial kinematic model that consists of six rotation joints connected in series by ridged linkages. This allows for six degrees of freedom (6DoF), x, y, z, roll, pitch and yaw, positioning of the probe. The robotic arm has a 2 m reach which spans a spherical volume of ~ 1 m radius. CROMMA is capable of extrapolation, planar, spherical, cylindrical, and mixed-geometry scanning. The position and orientation information provided by a laser tracker are used along with spatial metrology software to assess the quality of the alignment and provide information for the implementation of dynamic position and orientation correction, and post processing correction algorithms [4].



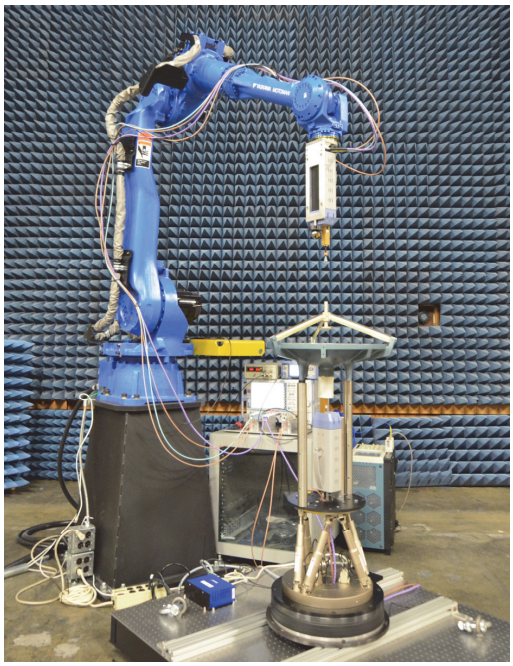

**Fig. 1.** CROMMA facility positioners. Serial 6DoF robotic arm, parallel 6DoF hexapod, precision rotary stage, probe and test antenna.

## III. Measurements and Results

Antenna measurements have been made in various geometries in mmwave bands at NIST to exercise the ability of CROMMA and verify its capability.

Spherical near-field measurements were performed on a WR-5 standard gain horn at 183 GHz at a radius of 10 cm and compared to a theoretical model and far-field measurements with favorable results [2]. Fig. 2 and Fig. 3 are the comparison of the E- and H-plane far fields, respectively, for: (1) measured at 100 cm, (2) transforming the 100 cm data to the 'true' far field, (3) theoretical, and (4) transforming the 10 cm near-field data to far field.

Guerrieri, Jeffrey.
"Validation of Robotics for Antenna Measurements."
Paper presented at 11th European Conference on Antennas and Propagation (EUCAP 2017), Paris, France. March 19, 2017 - March 24, 2017.

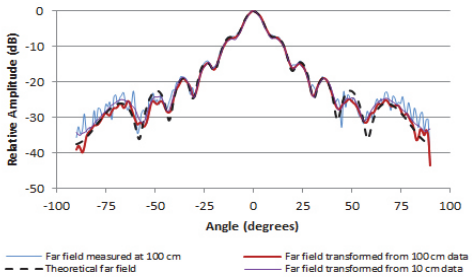


**Fig. 2.** E-plane far field comparison.

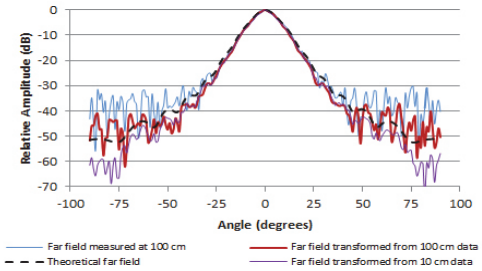


**Fig. 3.** H-plane far field comparison.

Spherical far-field measurements were performed at three frequencies, 112, 118, and 125 GHz, for a μ=±1 probe at 100 mm, which corresponds to $4D^2/\lambda$. Sample co- and cross-polarization results are shown in Fig. 4. In this case, $\chi = 0°$ corresponds to the co-polarization and $\chi = -90°$ corresponds to the cross polarization. The co-polarization peaks agree within ±0.5 dB. The cross polarization data are generally below the -40 dB level, which is the detectable limit for the measurement system [5].

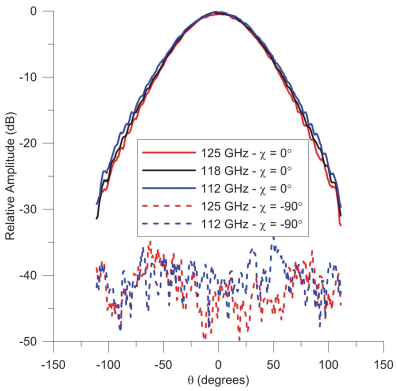


**Fig. 4.** E-plane pattern at a separation distance of 100 mm for three frequencies. The solid lines correspond to the co-pol patterns and the dashed lines to the cross-pol pattern.

The three-antenna extrapolation method is used to determine the gain of the μ=±1 probe along with two standard gain horns at 118 GHz without having a priori knowledge of any of the antenna gains [5]. This pair gain is derived from the leading term of a power series fit to the data in $1/r^n$ [6]. Here r is the separation distance between the two antennas. Sample extrapolation results are shown in Fig. 5. The smoothed data in Fig. 5 come from averaging data over a wavelength to account for multiple reflections between the two antennas. A pair gain of 24.69 dB was determined from these measurements. The data span a range of $2D^2/\lambda$ to $24D^2/\lambda$ (where D is the diameter of the largest antenna).

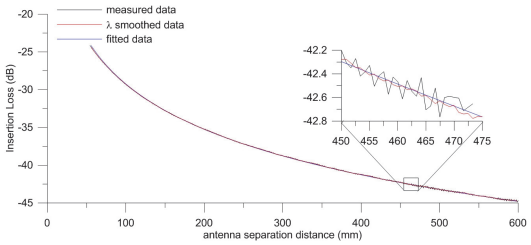


**Fig. 5.** Plot of extrapolation data at 118 GHz for the μ=±1 probe versus a 15 dBi standard gain horn.

Spherical near-field measurements were performed on a CubeSat feed horn with a 17 degree offset at 118 GHz. The transformed far field for the measurements and simulated far field are shown in Fig. 6.

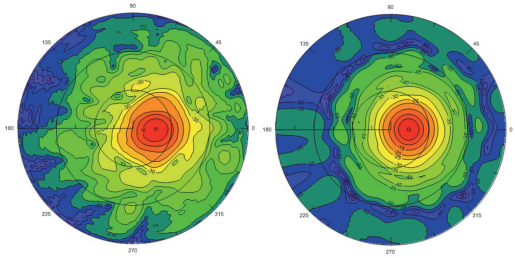

**Fig. 6.** Far field pattern of CubeSat feed horn at 118 GHz from near-field measurements, (left), and simulated (right).

## IV. Future Multiple Robot System

A multiple robot facility using the CROMMA technology is being developed at NIST. Fig. 7 is a conceptual drawing that shows one stationary robot and one attached to a cart on a rail system that will all be integrated to operate as one system. The rail system will offer 7 m of travel to expand the extrapolation technique past the articulated reach of a single robotic arm. It will still support the three traditional near-field measurement


Guerrieri, Jeffrey.
"Validation of Robotics for Antenna Measurements."
Paper presented at 11th European Conference on Antennas and Propagation (EUCAP 2017), Paris, France. March 19, 2017 - March 24, 2017.

geometries (planar, spherical and cylindrical). More importantly the multiple robot system provides the ability to actively track multiple beams and perform dynamic beamforming characterizing of electronically steerable array antenna systems.

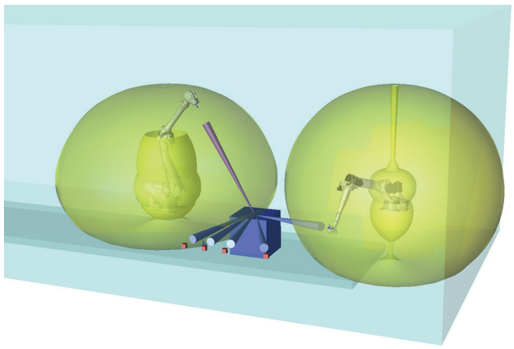

**Fig. 7.** NIST proposed multiple robot antenna measurement system.

## V. Conclusion

NIST has demonstrated the viability of using commercial available robotics, guided by laser trackers and other metrology equipment to perform quality antenna testing.

This paper shows measurement results that demonstrate the successful integration of an industrial robot and positioners with a laser tracker that monitors and corrects the relative position and orientation of the probe. Using position correction feedback and spatial analyzer software the system can provide adequate positioning for antenna measurements in different measurement geometries for frequencies above 100 GHz. Finally, the paper introduces the concept of a multiple robot antenna measurement facility that would support performance testing of communication antenna systems in real world environments.

## References


[1] M.H. Francis and R.C. Wittmann, "Near-field scanning measurements: Theory and practice." In Modern Antenna Handbook, edited by C.A. Balanis, Chp. 19, New York, NY: John Wiley & Sons, 2008.

[2] J.R. Guerrieri J.A., Gordon, D.R. Novotny, M.H. Francis, R.C. Wittmann and M Butler, " Configurable Robotic Millimeter-Wave Antenna Facility ", *Proc. European Conf. on Antennas and Propagation.*, Lisbon, Portugal, 2015.

[3] J. A. Gordon, D. R. Novotny, M. H. Francis, R. C. Wittmann, M. L. Butler, A. E. Curtin, J. R. Guerrieri, "Millimeter-Wave Near-Field Measurements Using Coordinated Robotics," IEEE Trans. Antennas Propagat., Submitted May 2015.

[4] D. R. Novotny, J. A. Gordon, J. R. Guerrieri, "Antenna alignment and positional validation of a mmWave antenna system using 6D coordinate metrology," Proc. of the 2014 Antenna Meas. Tech. Assoc., pp. 247 – 252, October 2014.

[5] D.R. Novotny, M.H. Francis, R.C. Wittmann J.A., Gordon, J.R. Guerrieri and A. Curtin, " Multi-purpose Configurable Range for Antenna Testing Up To 220 GHz ", *Proc. European Conf. on Antennas and Propagation.*, Davos, Switzerland, 2016.

[6] A.C. Newell, R.C. Baird, and P.F. Wacker, "Accurate measurement of antenna gain and polarization at reduced distances by an extrapolation technique," IEEE Trans. Antennas Propagat., vol. AP-21, pp. 418 – 431, July 1973.

# A Review of the IEEE 1785 Standards for Rectangular Waveguides above 110 GHz

N M Ridler* and R A Ginley†[1]

*NPL, Teddington, UK; †NIST, Boulder, CO, USA

**Abstract—A new series of standards has recently been published by IEEE defining waveguide for use at millimeter-wave and terahertz frequencies. The series comprises three standards covering different aspects of this technology: (i) frequency bands and waveguide dimensions; (ii) waveguide interfaces; and (iii) recommendations for performance and uncertainty specifications. This paper describes each of these standards.**

**Index terms — IEEE 1785, millimeter-wave, rectangular waveguides, submillimeter-wave, terahertz, waveguide apertures, waveguide interfaces, waveguide tolerances.**

## I. Introduction

Until recently, no international document standards existed for defining sizes and interfaces for rectangular metallic waveguides used at submillimeter-wave frequencies (i.e. at frequencies above 325 GHz). Some proposals for sizes and interfaces had been published (e.g. [1-5]) but these had not been adopted by any of the international standards-making bodies (e.g. ISO, IEC, IEEE). This situation was recognized in 2007 by the IEEE Standards Association, and this led to a project being initiated to put in place IEEE standards for both waveguide sizes (i.e. the aperture dimensions) and their associated interfaces (i.e. flanges) suitable for use at all frequencies above 110 GHz. Although some standards already existed for waveguides in the 110 GHz to 325 GHz range (see, for example, [6, 7]), it was decided that these waveguides should be included in the new IEEE standards to allow their tolerances to be re-evaluated in the context of contemporary manufacturing capabilities.

The development of the new standards was sponsored by the Standards Committee of the IEEE's Microwave Theory and Techniques Society (MTT-S). A working group was set up (and assigned the project number P1785) to write the standards. This working group held its first meeting during the IEEE MTT-S International Microwave Symposium in Atlanta, GA, USA, in June 2008. The working group then met regularly (approximately every six months) in order to develop the necessary standards.

It was decided to publish the standard in three parts: Part 1 – frequency bands and waveguide dimensions [8]; Part 2 – waveguide interfaces [9]; Part 3 – recommendations for performance and uncertainty specifications [10]. Part 1 was published in 2013, and Parts 2 and 3 were published in 2016. This paper gives an overview of all three parts.

## II. IEEE Std 1785.1-2012

Part 1 of the IEEE 1785 series of standards [8] gives specifications for the waveguide (including aperture dimensions, frequency range, cut-off frequency, etc). The standard considers the tolerances of the waveguide aperture dimensions and the impact these have on the electrical properties (in terms of return loss, transmission loss, etc) of the waveguide. The standard lists a series of waveguide sizes for use at frequencies up to 3.3 THz – see Table 1. The shaded region of Table 1 corresponds to sizes that have already been defined in previous standards [6, 7]. Table 1 also shows the naming convention that has been introduced by this standard. Since the waveguide sizes given in the standard are defined in terms of metric units, the letters WM are used to indicate that the size refers to **W**aveguide using **M**etric dimensions. The numbers that follow these letters correspond to the broad wall dimension of the waveguide specified in micrometers (μm). For example, WM-250 refers to waveguide with a broad wall dimension of 250 μm.

The standard gives a procedure for extending the series of waveguide sizes to produce waveguides for use at frequencies above 3.3 THz. The standard also defines different grades of waveguide based on the tolerance for the height and width of the waveguide aperture. Grades are established based on the tolerances being less that a certain percentage of the aperture broad wall dimension. For example, if the dimensional tolerances are less than ±0.2% of the broad wall dimension, then this waveguide is graded as 0.2. The worst-case reflection coefficient for several grades of waveguide are also given in the standard, along with a table showing the dimensional tolerances needed to achieve selected waveguide grades (and hence worst-case reflection coefficients).

[1] N M Ridler and R A Ginley are the Chair and Vice Chair, respectively, of the IEEE P1785 Working Group that developed the IEEE 1785 series of standards.

Ginley, Ronald; Ridler, Nick.
"A Review of the IEEE 1785 Standards for Rectangular Waveguides above 110 GHz."
Paper presented at 89th ARFTG Microwave Measurement Conference, Honolulu, HI, United States. June 9, 2017 - June 9, 2017.

Part 1 also contains two annexes. Annex A gives plots of reflection coefficient caused by tolerances in the waveguide aperture height, width and corner radii. Annex B gives calculated values of attenuation constant (in dB/cm) due to loss in the waveguide conductor, assuming the classical skin effect and the waveguide walls are perfectly smooth.

TABLE I
FREQUENCY BANDS AND WAVEGUIDE DIMENSIONS [8]

| Name | $a$ (µm) | $b$ (µm) | $f_c$ (GHz) | $f_{min}$ (GHz) | $f_{max}$ (GHz) |
|---|---|---|---|---|---|
| WM-2540 | 2540 | 1270 | 59.014 | 75 | 110 |
| WM-2032 | 2032 | 1016 | 73.767 | 90 | 140 |
| WM-1651 | 1651 | 825.5 | 90.790 | 110 | 170 |
| WM-1295 | 1295 | 647.5 | 115.75 | 140 | 220 |
| WM-1092 | 1092 | 546 | 137.27 | 170 | 260 |
| WM-864 | 864 | 432 | 173.49 | 220 | 330 |
| WM-710 | 710 | 355 | 211.12 | 260 | 400 |
| WM-570 | 570 | 285 | 262.97 | 330 | 500 |
| WM-470 | 470 | 235 | 318.93 | 400 | 600 |
| WM-380 | 380 | 190 | 394.46 | 500 | 750 |
| WM-310 | 310 | 155 | 483.53 | 600 | 900 |
| WM-250 | 250 | 125 | 599.58 | 750 | 1100 |
| WM-200 | 200 | 100 | 749.48 | 900 | 1400 |
| WM-164 | 164 | 82 | 913.99 | 1100 | 1700 |
| WM-130 | 130 | 65 | 1153.0 | 1400 | 2200 |
| WM-106 | 106 | 53 | 1414.1 | 1700 | 2600 |
| WM-86 | 86 | 43 | 1743.0 | 2200 | 3300 |

## III. IEEE STD 1785.2-2016

Part 2 of the IEEE 1785 series of standards [9] gives specifications for waveguide interfaces (also known as flanges). The standard considers the tolerances of the waveguide interface dimensions and the effect these have on the electrical properties (in terms of reflection coefficient) of the waveguide. The standard defines three waveguide interfaces that are suitable for use with waveguides used at 110 GHz and above. The three interfaces are called IEEE 1785-2a ("Precision Dowel"), IEEE 1785-2b ("Ring-Centered") and IEEE 1785-2c ("Plug and Jack"). A generic engineering drawing for all three interfaces is shown in Figure 1.

The primary alignment mechanism for the Precision Dowel interface is two dowels (of different diameters) that are inserted into the holes labelled "D" in Figure 1. The Precision Dowel interface is shown in Figure 2.

The primary alignment mechanism for the Ring Centered interface is a centering ring that fits over the central boss section of the interface – see Figure 3.

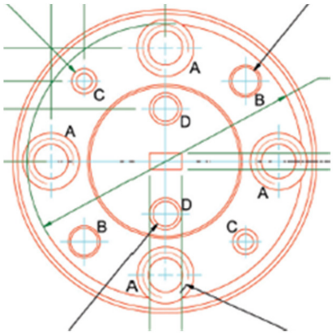


Fig. 1: Waveguide interface containing 4 screw holes (A), 4 alignment holes (B and D) and 2 fixed alignment pins (C)

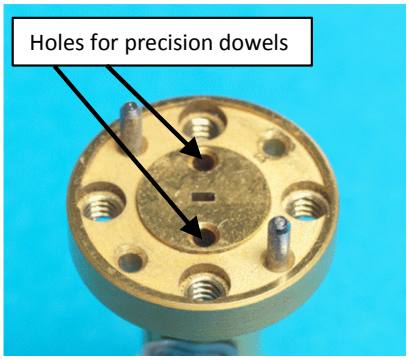


Fig. 2: IEEE 1785-2a "Precision Dowel" interface, showing holes for inserting the precision dowels

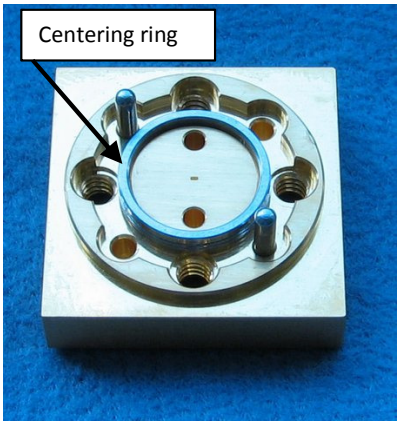


Fig. 3: IEEE 1785-2b "Ring Centered" interface, showing detachable centering ring

Ginley, Ronald; Ridler, Nick.
"A Review of the IEEE 1785 Standards for Rectangular Waveguides above 110 GHz."
Paper presented at 89th ARFTG Microwave Measurement Conference, Honolulu, HI, United States. June 9, 2017 - June 9, 2017.

The Plug and Jack interface is a male/female design and relies on this feature as the primary alignment mechanism – see Figure 4.

All three interfaces are mechanically compatible with each other, and with the interface commonly known as UG-387 [11] and most of its common variants (e.g. [3, 12, 13]). However, the resulting electrical performance when mated with these UG-387 type interfaces is not as good as when mating the interfaces in the standards with themselves.

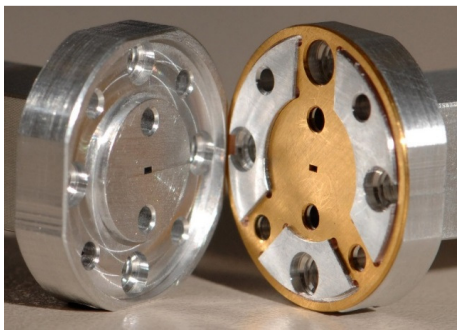

Fig. 4: IEEE 1785-2c "Plug and Jack" interface, showing both male and female halves of the interface

Part 2 also contains detailed engineering drawings for all three interfaces, as well as the accessories (alignment dowels and centering ring) used with the interfaces. It also gives values of worst-case reflection coefficient due to the interface dimensional tolerances given in the standard. This allows end-users to predict the performance from a mated pair of interfaces for each waveguide size given in Part 1 of the standard [8]. Part 2 also contains an annex giving plots of reflection coefficient caused by both linear ($x$, $y$) interface misalignment and angular interface misalignment.

## IV. IEEE Std 1785.3-2016

Part 3 of the IEEE 1785 series of standards [10] gives recommendations for summarizing the performance and the expected uncertainty of the reflection coefficient of the rectangular waveguide apertures and interfaces given in Parts 1 and 2 of the standard [8, 9]. The information provided also facilitates the development of a complete uncertainty analysis for the performance of rectangular waveguide interfaces. For example, it includes the dimensional information necessary for calculating the uncertainty in both reflection and transmission coefficients for interfaces provided by different manufacturers, if both manufacturers follow the guidance give in this standard [10].

The standard lists the dimensional data (with associated uncertainty) that is needed to undertake the uncertainty analysis. These include: the height, width and corner radius of the waveguide aperture; and, the lateral displacement of the aperture due to linear and angular interface misalignment. Guidance is given on the propagation of uncertainty from the dimensional data to electrical performance data (i.e. reflection coefficient). This guidance is in line with appropriate internationally agreed recommendations [14, 15].

Finally guidance is given on summarizing and reporting the information. This includes example plots (graphs) showing expected electrical performance, an example uncertainty budget, and details of analysis software that adheres to the recommendations given in the standard.

## V. Discussion

Part 1 of these standards [8] has, for the first time, provided standardized sizes for waveguides used to 1 THz and beyond. This is more than adequate for the current state of the art for test instrumentation operating in this frequency range (e.g. [16]). Information on aperture tolerances given in the standard indicates that a 5 μm tolerance for an aperture used at 1 THz will give rise to a worst-case reflection coefficient of the order of -20 dB.

Part 2 of these standards [9] has introduced three new types of waveguide interface that enable waveguide technology to be used, with acceptable electrical performance, across the whole of the submillimeter-wave band (to 3 THz). For example, worst-case reflection coefficient due to interface dimensional tolerances for these interfaces, when used at 1 THz, is of the order of -20 dB.

Part 3 of these standards [10] has, for the first time, given guidance necessary to estimate the uncertainty due to the combined effects of both waveguide aperture and waveguide interface. For example, for the above situations (a 5 μm aperture tolerance and nominal tolerances for the interfaces given in part 2 of the standard at 1 THz) an overall expanded uncertainty [14] in reflection coefficient is expected to be of the order of -15 dB.

## VI. Conclusion

This paper has reviewed three new IEEE standards [8-10] that have recently been published relating to rectangular metallic waveguides used at millimeter-wave and terahertz frequencies. These standards provide a reference for all organizations using rectangular waveguides at these frequencies. This will enable efficient trade between customers and suppliers, and common design criteria and practices for component, systems, and design engineers, and, all other end-users. It is therefore expected that these standards will have a major impact on science, engineering and technology employing the use of these frequencies, for many years to come.

## Acknowledgement

The authors would like to thank all members, past and present, of the IEEE P1785 Working Group ("Waveguides for Millimeter and Submillimeter Wavelengths") that developed

this new series of standards. N M Ridler acknowledges financial support from the UK government National Measurement System for his contribution to this work.

## REFERENCES

[1] J S Ward, "New Standards for Submillimeter Waveguides", *Proc. 17th Int. Symp. on Space THz Tech*., Paris, France, May 2006.

[2] N M Ridler, "Recommendations for Waveguide Sizes at Submillimeter Wavelengths", *Proc. 73rd ARFTG Microwave Measurement Conf*., Boston, MA, USA, June 2009.

[3] J L Hesler, A R Kerr, W Grammer and E Wollack, "Recommendations for Waveguide Interfaces to 1 THz", *Proc. 18th Int. Symp. on Space THz Tech.*, Pasadena, CA, USA, March 2007.

[4] Y S Lau and A Denning, "An Innovative Waveguide Interface for Millimeter Wave and Sub-millimeter Wave Applications", *Proc. 69th ARFTG Microwave Measurement Conf.,* Honolulu, HI, USA, June 2007.

[5] H Li, A R Kerr, J L Hesler, H Xu, R M Weikle II, "A Ring-centered Waveguide Flange for Millimeter- and Submillimeter-wave Applications", *IEEE MTT-S International Microwave Symposium*, Anaheim, CA, USA, May 2010.

[6] MIL-DTL-85/3C, "Waveguides, rigid, rectangular (millimetre wavelength)", October 2005.

[7] IEC 60153-2, "Hollow metallic waveguides. Part 2: relevant specifications for ordinary rectangular waveguides", 2nd edition, 1974.

[8] IEEE Std 1785.1-2012: "IEEE Standard for Rectangular Metallic Waveguides and Their Interfaces for Frequencies of 110 GHz and Above—Part 1: Frequency Bands and Waveguide Dimensions".

[9] IEEE Std 1785.2-2016: "IEEE Standard for Rectangular Metallic Waveguides and Their Interfaces for Frequencies of 110 GHz and Above—Part 2: Waveguide Interfaces".

[10] IEEE Std 1785.3-2016: "IEEE Recommended Practice for Rectangular Metallic Waveguides and Their Interfaces for Frequencies of 110 GHz and Above—Part 3: Recommendations for Performance and Uncertainty Specifications".

[11] MIL-DTL-3922/67E w/Amendment 1, "Flanges, waveguide (contact), (round, 4 hole) (millimeter)", 27 May 2014.

[12] A R Kerr, E Wollack and N Horner, "Waveguide flanges for ALMA instrumentation", ALMA Memorandum 278, November 1999.

[13] C Oleson and A Denning, "Millimeter-wave Vector Analysis Calibration and Measurement Problems Casued by Common Waveguide Irregularities", 56th ARFTG Microwave Measurement Conference, Boulder, CO, December 2000.

[14] JCGM 100:2008, "Evaluation of measurement data – Guide to the expression of uncertainty in measurement"

[15] JCGM 101:2008, "Evaluation of measurement data – Supplement 1 to the "Guide to the expression of uncertainty in measurement" – Propagation of distributions using a Monte Carlo method".

[16] T W Crowe, B Foley, S Durant, K Hui, Y Duan, J L Hesler, "VNA frequency extenders to 1.1 THz,", 36th International Conference on Infrared, Millimeter and Terahertz Waves (IRMMW-THz), 2011.

# Software Tools for Uncertainty Evaluation in VNA Measurements: A Comparative Study*

G. Avolio[1], D. F. Williams[2], S. Streett[2], M. Frey[2], D. Schreurs[1], A. Ferrero[3], M. Dieudonné[3]
[1]KU Leuven, Belgium, [2]NIST, Boulder (CO), USA, [3]Keysight Technologies Inc (CA), USA

***Abstract* — We compared three software tools designed for scattering-parameter measurement uncertainty evaluation. These tools propagate uncertainty to calibrated S-parameters by means of a sensitivity analysis. We also validated the sensitivity analysis with Monte-Carlo simulations performed with one of the software tools and the Keysight ADS circuit simulator.**

***Index Terms* — Microwave measurements, Monte-Carlo simulations, sensitivity analysis, S-parameters, uncertainty.**

## I. Introduction

There have been a number of recent efforts in both academia and industry to develop software tools to quantify uncertainty in scattering- (S-) parameter measurements and other quantities at microwave frequencies [1]-[6]. For example, a comparison of existing software tools was conducted by Teppati *et al.* in [7].

Along the lines of [7], we compare three software packages. The first two packages represent the Microwave Uncertainty Framework (MUF) [2]-[3], developed by the National Institute of Standards and Technology (NIST) in the United States, and VNA Tools II [4]-[5], developed by the Swiss Metrological Institute (METAS). The third package is an implementation† of the work in [6]. In what follows we will refer to the third package as 'SW3'. All of these software tools carry out uncertainty propagation by means of a sensitivity analysis, each using a slightly different approach. The NIST tool also simultaneously performs a Monte-Carlo analysis that maintains correlations throughout the process of determining and propagating uncertainties.

To evaluate the three software tools, we calibrated VNA measurements and propagated uncertainties in the calibration standards to the corrected S-parameters of an attenuator. Physical models of the calibration standards have been developed and verified by NIST [8]. These models include tolerances in their electrical characteristics and mechanical dimensions, thus allowing traceable uncertainty analysis.

## II. Software-Tool Overview

While the detailed description of how the three software tools perform uncertainty analysis is beyond the scope of this paper, a general overview helps to better understand our experimental results. Given a model for a measurement:

$$\underline{Y} = \boldsymbol{f}(\underline{X}), \tag{1}$$

with $X$ being a vector of input quantities with uncertainty, an estimate of the covariance matrix of the vector of output quantities $Y$ can be computed by

$$\sum_Y = \underline{J} \sum_X \underline{J}^T , \tag{2}$$

where $\sum_X$ is the estimated covariance matrix of the input quantities and $J$ is the Jacobian matrix of $f$ [9]. Equation (2) is the result of a first-order approximation of (1). In the context of VNA measurements, $\sum_X$ typically accounts for uncertainties in the calibration standards definition, repeatability, and instrument noise.

The NIST MUF approximates $J$ with a finite-difference approach [2]. In VNA Tools II, $J$ is calculated by a method based on automatic differentiation [1]. SW3 derives $J$ analytically [6].

### A. Calibration standards

To run the NIST MUF, the user inputs models of the calibration standards along with tolerances in the mechanical dimensions and electrical properties of those models. We built the covariance matrix $\sum_Y$ of each calibration standard, in a format compatible with METAS VNA Tools II (*.sdatcv* format) and SW3 (*.dsd* format), starting from models available in the NIST MUF. We generated $\sum_Y$ by using (2), with $\sum_X$ being a diagonal matrix with uncertainties associated with the mechanical tolerances and electrical properties, and $f$ the function describing the model of each of the calibration standards. If correlations across frequencies are also needed [10], [11], we could add them when generating $\sum_Y$. We did not populate $\sum_Y$ with those correlations since in this work we looked at S-parameters at each frequency separately. However, with the current version of these software packages, only the NIST MUF and METAS VNA Tools II can account for correlations across frequencies.

### B. Noise and repeatability

Both noise and cable and connector repeatability can be accounted for in the three software tools. The NIST MUF accounts for noise by averaging repeated measurements. In METAS VNA tools II the user can define the VNA noise floor and the trace noise [7]. In SW3, the covariance matrix for noise

* Work partially supported by US government, not protected by US copyright.
† The US National Institute of Standards and Technology does not endorse commercial products. Other products may work as well or better.

Avolio, Gustavo; Williams, Dylan; Frey, Michael; Streett, Sarah; Schreurs, Dominique; Ferrero, Andrea; Dieudonne, Michael.
"Software Tools for Uncertainty Evaluation in VNA Measurements: A Comparative Study."
Paper presented at 89th ARFTG Microwave Measurement Conference, Honolulu, HI, United States. June 9, 2017 - June 9, 2017.

is estimated by repeated measurements of a matched and reflective DUT [6].

As in our analysis, we were interested in comparing three uncertainty evaluation methods. We included for simplicity only systematic uncertainties in the calibration standards definition and neglected uncertainties due to noise and repeatability.

In Table I we summarize the main features of the three software packages.

TABLE I: MAIN FEATURES OF THE THREE SOFTWARE PACKAGES

| | NIST MUF | METAS VNA Tools II | SW3 |
|---|---|---|---|
| Sensitivity Analysis | ✓ | ✓ | ✓ |
| Monte-Carlo Analysis | ✓ | | |
| Speed | + | ++ | +++* |
| Frequency Correlations | ✓ | ✓ | |

*Notably for multiport calibrations

## III. EXPERIMENTAL RESULTS

### A. Nominal calibration

We used Keysight PNA-X software to perform coaxial measurements from 200 MHz to 44 GHz with 30 Hz resolution bandwidth. We fixed cables and minimized cable movement between each measurement as best as we could. We used a 2.4 mm commercial calibration kit with corresponding NIST models [8]. In total we included 68 uncertainty sources. We calibrated the S-parameters of a 20 dB attenuator with an unknown-thru algorithm (S-O-L-R) [12]. We used physical models for the open and short standards. For the load we used a measurement based model, traceable to a coaxial multiline thru-reflect-line (TRL) calibration [8].

In Fig. 1, we show the calibrated magnitude and phase of the $S_{11}$ and $S_{21}$ parameters of our DUT. In Fig. 2, we also report the difference between these values. While we were able to use the same raw input data to calibrate the data with the NIST MUF and METAS VNA Tools II, we did not have access to raw data used by SW3 during the calibration procedure. In Fig. 2 we observe that the difference between the magnitude and phase of $S_{11}$ and $S_{21}$ as calibrated by the NIST MUF and METAS VNA Tools II is negligible. Note that the difference in the raw input data affects not only the calibrated S-parameters (1), but may also change the results of the sensitivity analysis (2). The matrix $J$ (2) contains the partial derivatives of $Y$ versus $X$ calculated at the nominal value of all the quantities in $X$, and, therefore, $J$ is a function also of the raw input data.

### B. Sensitivity analysis

We show the results of the sensitivity analyses computed by the three software tools in Fig. 3 and the difference between the calculated uncertainties in Fig. 4. Any difference observed in the estimated uncertainty should be mainly ascribed to the method utilized to compute the $J$ matrix. In our study, this was the case for the uncertainty computed by the NIST MUF and the METAS VNA Tools II, as we inputted exactly the same raw data into both tools. (Recall that the NIST MUF computes partial derivatives by means of a finite-difference approximation and METAS VNA Tools II employs an automatic differentiation method [1]-[13].)

On the other hand, the slight disagreement between the uncertainty estimated by NIST MUF or METAS VNA Tools II and SW3 may be due to the difference between the raw input data used for calibration, especially at higher frequencies. Nevertheless, we see that at lower frequencies, where there is less discrepancy between raw input data (see Fig. 2), the METAS VNA Tools II and SW3 sensitivity analyses agree better with each other than they do with the NIST MUF. As expected, depending on the shape of the function $f$ in (1), the finite-difference approximation adopted by NIST MUF to calculate $J$ (2) might be somewhat less accurate than the analytic approach used in SW3 [6] or the automatic differentiation approach used in the METAS VNA Tools II [13].

## IV. MONTE-CARLO SIMULATIONS

A sensitivity analysis relies on a first-order approximation of (1). If $f$ is nonlinear, the covariance matrix estimated by (2) will incompletely describe the uncertainties and their probability distributions. The NIST MUF uses Monte-Carlo simulations to assess the more complex uncertainties and probability distribution functions that result when $f$ is nonlinear.

Here we use the built-in Monte-Carlo simulations in the NIST MUF to examine the results of the sensitivity analyses that are exclusively relied on by the other two software packages. This is not only a standard way of verifying the validity of sensitivity analyses [14], but lends insight into the differences between the approaches for estimating uncertainties.

### A. Comparison of Monte-Carlo and Sensitivity Analyses

We performed a Monte-Carlo analysis with the NIST MUF, which uses a built-in random-number generator and specially generated seeds to maintain correlations. By using Monte-Carlo simulations, the average and standard deviation of $Y$ can be estimated by evaluating (1) directly as a function of randomly generated realizations of vector $X$. When $f$ is strongly nonlinear, the distribution of $Y$ is no longer normal.

In Fig. 5 we compare the uncertainty estimated by sensitivity analysis to that from 1000 Monte-Carlo simulations. The two analyses agree reasonably well over many frequency ranges, but clearly do not agree at all frequency points. In particular, there is a clear discrepancy in the uncertainty of the magnitude of calibrated $S_{21}$. Moreover, the histogram shown in the inset of Fig. 5c, clearly indicates that the distribution of the magnitude of $S_{21}$ at 44 GHz is not normal, as expected by sensitivity analysis.

Avolio, Gustavo; Williams, Dylan; Frey, Michael; Streett, Sarah; Schreurs, Dominique; Ferrero, Andrea; Dieudonne, Michael.
"Software Tools for Uncertainty Evaluation in VNA Measurements: A Comparative Study."
Paper presented at 89th ARFTG Microwave Measurement Conference, Honolulu, HI, United States. June 9, 2017 - June 9, 2017.

### B. Verification of the Monte-Carlo Analyses

To verify the correctness of our Monte-Carlo analysis, we ran the same calibration and performed Monte-Carlo simulations both in the NIST MUF and in a commercial circuit simulator (Keysight ADS). For the sake of simplicity, we considered one source of uncertainty, instead of 68 uncertainty sources included in our original calibration. We then performed a more in-depth investigation and found that, by considering only the uncertainty in the electrical conductivity of the coaxial line used to model the open standard, we could reproduce a situation similar to that in Fig. 5 based on the same raw data from the original calibration. We set the electrical conductivity to the same nominal value and distribution that we used for the original calibration, namely 5 MS/m, and a uniform distribution with support between 1 MS/m and 9 MS/m. We ran 1000 Monte-Carlo simulations with both the NIST MUF and Keysight ADS, and compared the estimated uncertainties. We repeated Monte-Carlo simulations with Keysight ADS by increasing the number of iterations to 5000 and did not observe any significant change in the results.

As in the original calibration, we observed disagreement between the uncertainty estimated by Monte-Carlo simulations and sensitivity analysis, particularly for the magnitude of the calibrated $S_{21}$ (Fig. 6). For this quantity, we show the histogram obtained by Monte-Carlo simulations at 44 GHz in Fig. 7. First, we observe that the histograms obtained with the NIST MUF and Keysight ADS are very similar (see also Appendix). Most significantly, the shape of those histograms clearly shows that the underlying probability distribution is not normal.

### C. Origin of the discrepancy

We also investigated the origin of the disagreement in Fig. 6 and the histograms asymmetry in Fig. 7a. Since the electrical conductivity was the only input variable with uncertainty in the simplified calibration, we looked at the dependence on this variable of the magnitude of the calibrated $S_{21}$ at 44 GHz.

The dependence of $S_{21}$ is nonlinear, as shown in Fig. 7b. When running Monte-Carlo simulations, the electrical conductivity varies over a large range, based on the support of its probability distribution function. Looking at Fig. 7b, in the low-loss region, the magnitude values of $S_{21}$ saturate, as opposed to the high-loss region, where dependence on the electrical conductivity is greater, creating the asymmetric shape of the histograms in Fig. 7a. Thus, we see that a sensitivity analysis, which relies on a linearization around the nominal value (see Fig. 7b), poorly captures these large variations and inaccurately estimates uncertainty.

To further corroborate our analysis, we show in Fig. 7a an approximate probability density function (*pdf*), derived analytically (as explained in the Appendix).

## V. Conclusions

We compared three software tools which compute uncertainty in S-parameter measurements at microwave frequencies. These tools propagate uncertainty based on a sensitivity analysis and, despite the fact that they utilize different methods to perform their sensitivity analyses, the estimated uncertainties agree very well. However, sensitivity analysis relies on a first-order approximation, which is not always valid. When this occurs, Monte-Carlo simulations should be used in lieu of sensitivity analysis, since the sensitivity analysis results will be inaccurate.


## Acknowledgement

This work was partially supported by Keysight Technologies Belgium. G. Avolio is supported by FWO Vlaanderen (Belgium). Authors would like to thank J. A. Jargon, J. Wang, and A. Koepke for useful discussions.


## Appendix

In Fig. 7a we show an approximate *pdf* of the magnitude of $S_{21}$. The magnitude of $S_{21}$ is linked to the electrical conductivity by a quite complicated function. However, in order to qualitatively validate our Monte-Carlo results, we approximated that complicated expression with a simpler function allowing us to derive analytically the *pdf* associated with this function. The comparison between the original and fitted function is shown in Fig. 8a. In Fig. 8a, the fitted function is

$$Y = A + B * \operatorname{atan}[C * (X + D)], \quad \text{A.1}$$

where, in our case, $Y$ is the magnitude of $S_{21}$ and $X$ the electrical conductivity. Given the *pdf* of $X$, if $Y$ is a monotonic function of $X$, then the *pdf* of $Y$ is equal to

$$pdf(Y) = pdf(X)\frac{dX}{dY}, \quad \text{A.2}$$

where *pdf(X)* is the *pdf* of the electrical conductivity which is constant for a uniform distribution. By applying (A.2) to (A.1), we can straightforwardly derive the *pdf(Y)* as:

$$pdf(Y) = \frac{pdf(X)}{C * B}\left(1 + tan^2\left(\frac{Y - A}{B}\right)\right), \quad \text{A.3}$$

which is plotted in Fig. 7a.

In Fig. 8b we show a quantile-quantile plot (q-q plot) to graphically assess the similarity between the probability distributions underlying the two histograms in Fig. 7a. The samples from Monte-Carlo simulations performed with the NIST MUF and Keysight ADS align quite well with the unitary-slope ideal line which the samples would lie on if the two histograms were exactly the same.

## References


[1] B. D. Hall, "Calculating measurement uncertainty using automatic differentiation," *Meas. Sci. Technol.*, vol. 13, no. 4, pp. 421–427, 2002.

[2] A. Lewandowski, D. Williams, P. Hale, C. M. Wang, and A. Dienstfrey, "Covariance-matrix-based vector-network-analyzer uncertainty analysis for time-and frequency-domain measurements," *IEEE Trans. Microw. Theory Techn.*, vol. 58, no. 7, pp. 1877-1866, Jul. 2010.
[3] [Online]. Available: https://www.nist.gov/services-resources/software/wafer-calibration-software.
[4] M. Wollensack, J. Hoffmann, J. Ruefenacht, and M. Zeier, "VNA tools II: S-parameter uncertainty calculation," in *Proc. 79th ARFTG Conf.*, Montreal, QC, Canada, Jun. 2012, pp. 1–5.
[5] M. Wollensack and J. Hoffmann. (2012, Apr.). METAS VNA Tools II-Math Reference [Online]. Available: http://www.metas.ch/vnatools.
[6] M. Garelli and A. Ferrero, "A unified theory for S-parameter uncertainty evaluation," *IEEE Trans. Microw. Theory Techn.*, vol. 60, no. 12, pp. 3844-3855, Dec. 2012.
[7] V. Teppati and A. Ferrero, "A comparison of uncertainty evaluation methods for on-wafer S-parameter measurements," *IEEE Trans. Instrum. Meas.*, vol. 63, no. 4, pp. 935-942, Apr. 2014.
[8] J. A. Jargon, C. Cho, D. F. Williams, and P. D. Hale, "Physical models for 2.4 mm and 3.5 mm coaxial VNA calibration kits developed within the NIST microwave uncertainty framework," *85th Microwave Measurement Conference (ARFTG)*, pp. 1-7, 2015.
[9] N. M. Ridler and M. J. Salter, "Propagating S-parameter uncertainties to other measurement quantities," *58th Microwave Measurement Conference (ARFTG)*, vol. 40, pp. 1-9, 2001.
[10] D. F. Williams, "Covariance-based uncertainty analysis of the NIST electroptic sampling system," *IEEE Trans. Microw. Theory Techn.*, vol. 54, no. 1, pp. 481-491, Jan. 2006.
[11] G. Avolio, A. Raffo, J. A. Jargon, P. D. Hale, D. M. M. -P. Schreurs, and D. F. Williams, "Evaluation of Uncertainty in Temporal Waveforms of Microwave Transistors," *IEEE Trans. Microw. Theory Techn.*, vol. 63, no. 7, pp. 2353-2363, Jan. 2015.
[12] A. Ferrero and U. Pisani, "Two-port network analyzer calibration using an unknown 'thru'," *IEEE Microw. Guided Wave Lett.*, vol. 2, no. 12, pp. 505–507, Dec. 1992.
[13] R. Boudjemaa, M. G. Cox, A. B. Forbes, and P. M. Harris, "Automatic differentiation and its application in metrology," *Advanced Mathematical and Computational Tools in Metrology VI*, pp. 170 – 179, Italy, 2003.
[14] B. D. Hall, "Evaluating methods of calculating measurement uncertainty," *Metrologia*, vol. 45, n. 2, pp. 1-5, 2008.

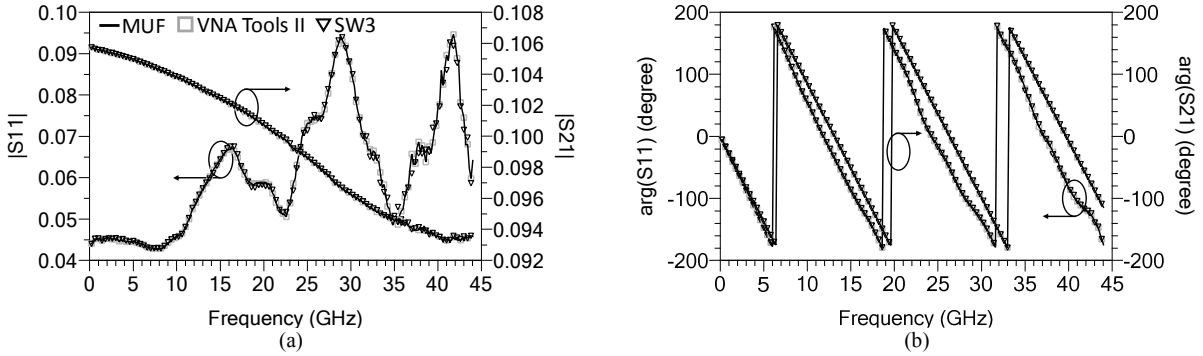


Fig. 1: S-O-L-R calibrated magnitude (a) and phase (b) of $S_{11}$ (left Y-axis) and $S_{21}$ (right Y-axis) of a 20 dB attenuator: NIST MUF (continuous line), METAS VNA Tools II (squares), and SW3 (triangles).

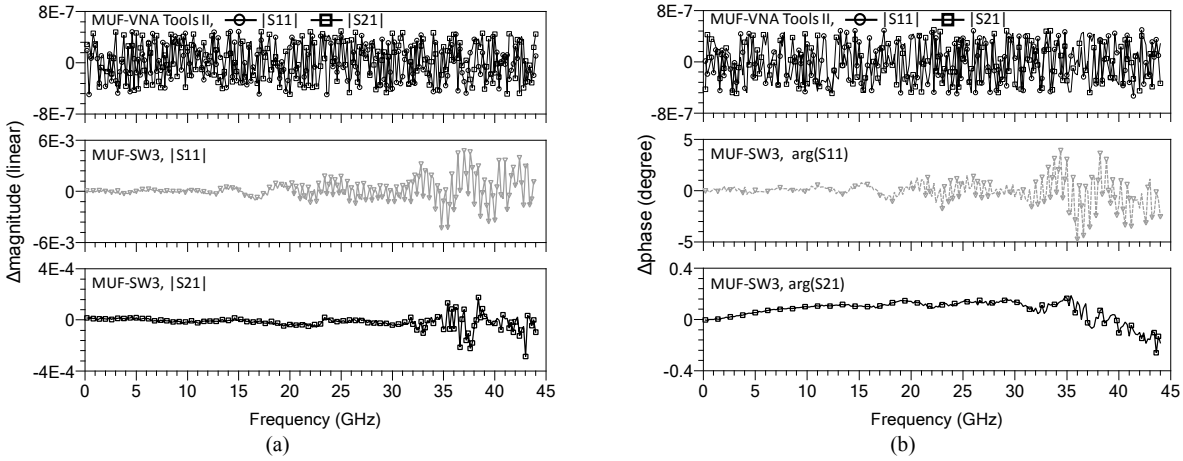


Fig. 2: Difference between magnitude (a) and phase (b) of $S_{11}$ and $S_{21}$ of a 20 dB attenuator calibrated with the three software tools. In both (a) and (b) the top plot shows the difference between the NIST MUF and METAS VNA Tools II, for which we inputted exactly the same raw data. The middle and bottom plots show the difference between the magnitude (a) and phase (b) of $S_{11}$ and $S_{21}$ computed by the NIST MUF and SW3.

Avolio, Gustavo; Williams, Dylan; Frey, Michael; Streett, Sarah; Schreurs, Dominique; Ferrero, Andrea; Dieudonne, Michael.
"Software Tools for Uncertainty Evaluation in VNA Measurements: A Comparative Study."
Paper presented at 89th ARFTG Microwave Measurement Conference, Honolulu, HI, United States. June 9, 2017 - June 9, 2017.

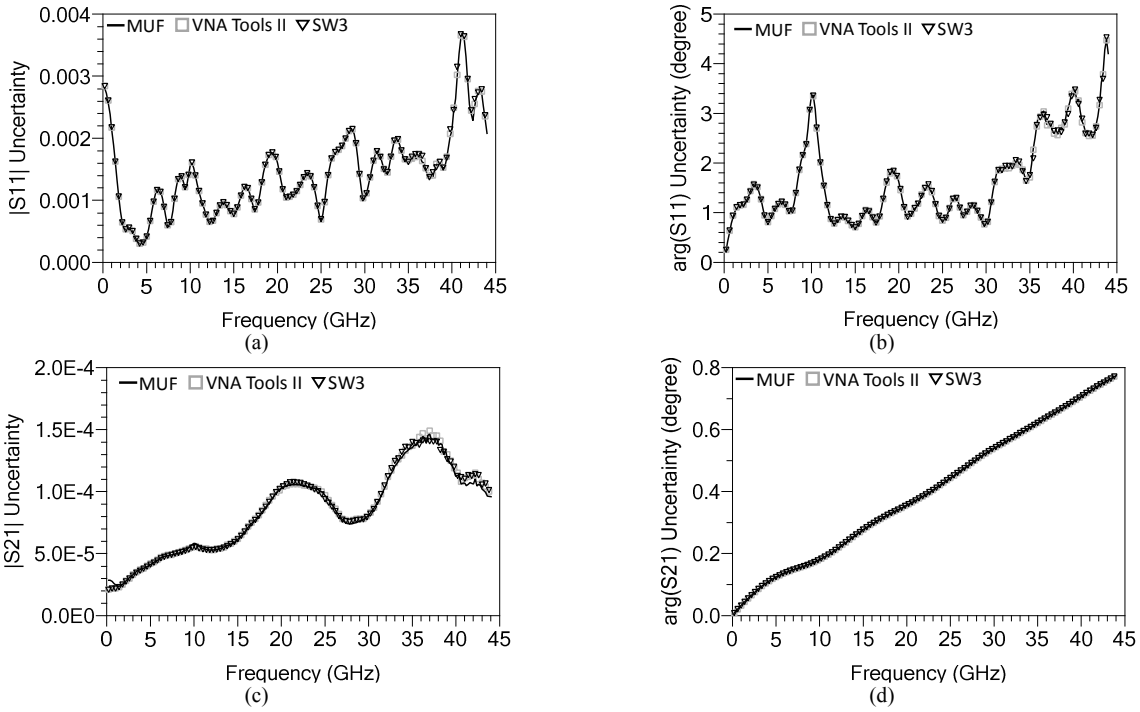


Fig. 3: Standard uncertainty estimated by the three software packages' sensitivity analyses. Magnitude and phase of $S_{11}$ (a)-(b) and of $S_{21}$ (c)-(d).

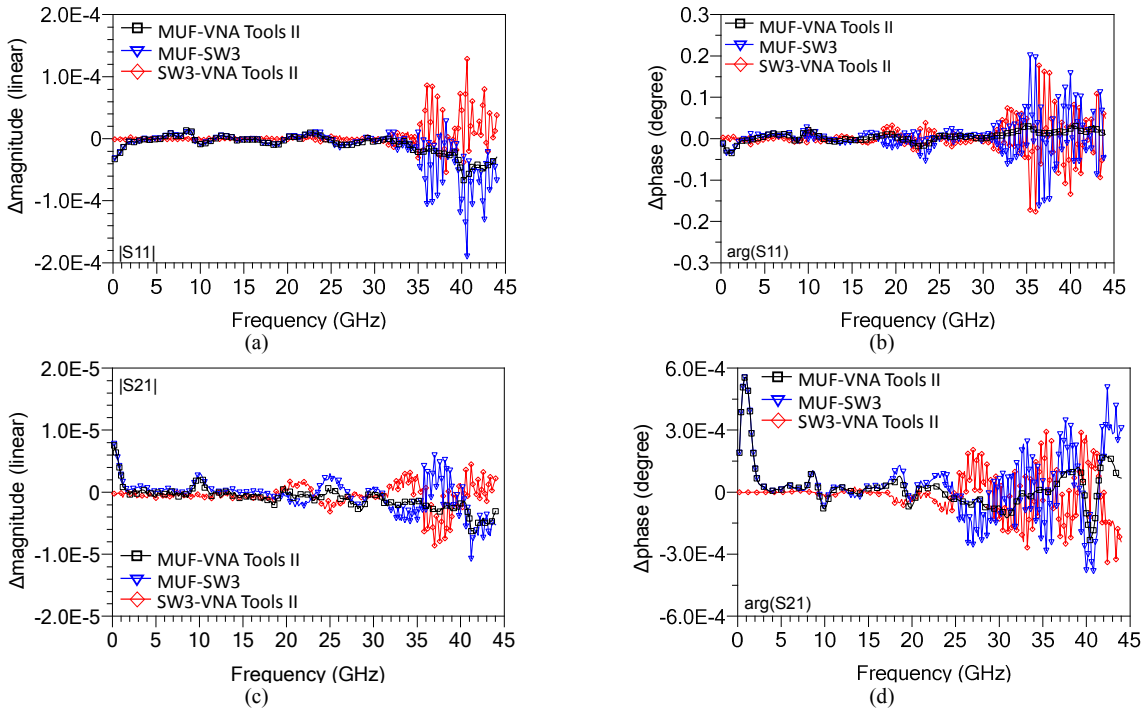


Fig. 4: Difference between the standard uncertainty in magnitude and phase of $S_{11}$ (a)-(b) and $S_{21}$ (c)-(d).

Avolio, Gustavo; Williams, Dylan; Frey, Michael; Streett, Sarah; Schreurs, Dominique; Ferrero, Andrea; Dieudonne, Michael.
"Software Tools for Uncertainty Evaluation in VNA Measurements: A Comparative Study."
Paper presented at 89th ARFTG Microwave Measurement Conference, Honolulu, HI, United States. June 9, 2017 - June 9, 2017.

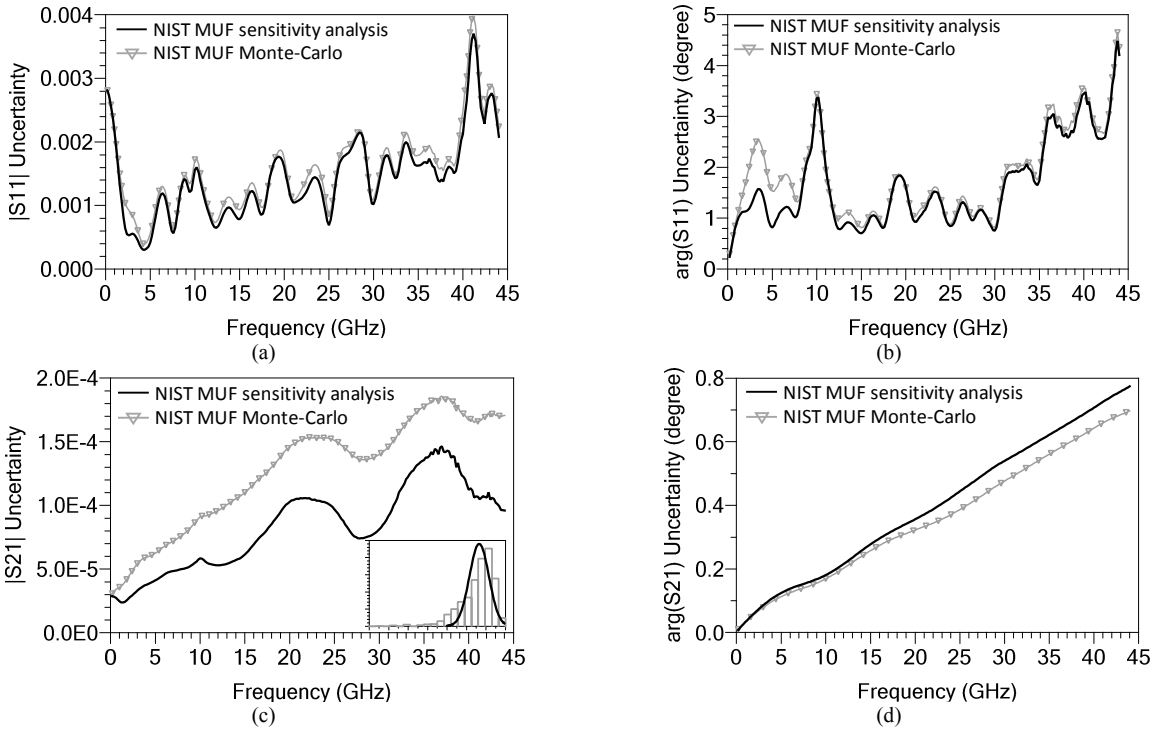


Fig. 5: Uncertainty in the calibrated magnitude and phase of $S_{11}$ (a)-(b) and $S_{21}$ (c)-(d) estimated by sensitivity (continuous line) and Monte-Carlo (symbols) analyses performed by the NIST MUF. The inset to Fig. 5c shows the distribution of the magnitude of $S_{21}$ at 44 GHz resulting from Monte-Carlo (grey) and sensitivity (black) analyses.

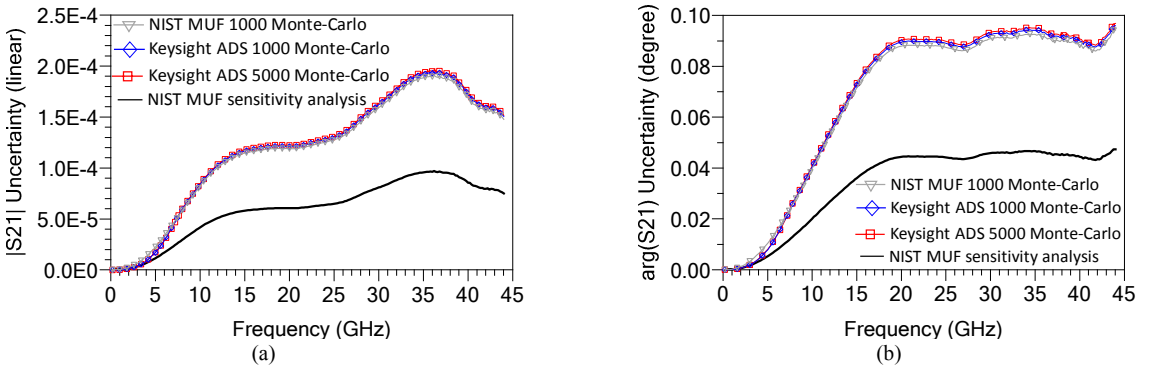


Fig. 6: Uncertainty estimated by Monte-Carlo simulations executed with the NIST MUF (triangles) and a commercial circuit simulator (diamonds and squares) and uncertainty estimated by the NIST MUF sensitivity analysis (continuous line). Raw data were S-O-L-R calibrated both in the NIST MUF and the commercial software and only one uncertainty contribution was propagated to the calibrated S-parameters.

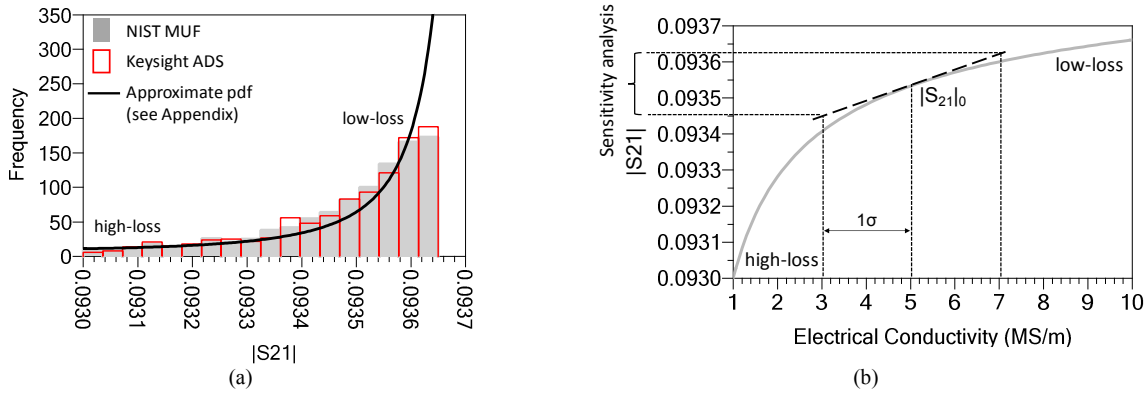


Fig. 7: Histogram of the magnitude of $S_{21}$ at 44 GHz resulting from 1000 Monte-Carlo simulations (a). In the same plot, we show an approximate *pdf* (continuous line), derived analytically as explained in the Appendix. The area of the approximate *pdf* is normalized to the histogram area. In (b) we show the magnitude of calibrated $S_{21}$ at 44 GHz, as a function of electrical conductivity of the coaxial line which models the open standard. The long-dashed line in (b) graphically indicates how the first-order approximation around the nominal value underlying the sensitivity analysis varies from the electrical conductivity beyond the region of the nominal value.

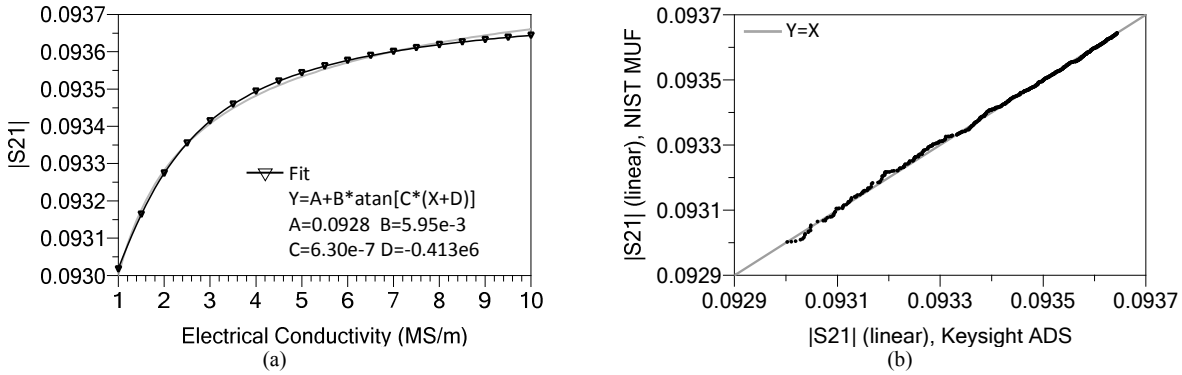


Fig. 8: Approximate fit (symbols) of the function in Fig. 7b (continuous grey line) (a) and q-q plot (dots) of the histograms of Fig. 7a (b). The grey continuous line in (b) depicts the line which the dots would lie on if the histograms in Fig. 7a were exactly the same.

# Verification of Coexistence Measurement Methods: Radiated Anechoic and Open Environment

Ryan T. Jacobs and Jason B. Coder
Communication Techology Laboratory
National Institute of Standards and Technology
Boulder, Colorado, U.S.A.

Nickolas J. LaSorte
National Telecommunications and Information Administration
Washington, DC

***Abstract*—With an abundance of wireless devices saturating daily life, the ability of devices to coexist among other devices is of increasing interest. While standards are starting to incorporate coexistence measurements, the robustness of coexistence measurement methods is still an area of active research. To demonstrate the robustness of the multiple test methods, a series of measurements needs to be conducted that compare a measurement methods. Ideally, if the same coexistence test is performed by use of each of the four methods, the end result should be the same. Here, we compare two popular radiated test methods: an anechoic chamber test and a radiated open-environment test. Both methods are part of the ANSI C63.27 standard. We examine the impact two of the possible environments may have on the outcome of a coexistence test. For this, we use Bluetooth low energy and Wi-Fi networks. Overviews of generalized coexistence testing and future work are also presented.**

## I. Introduction

With the number of wireless devices that operate in the industrial scientific and medical (ISM) band growing at a rapid rate, coexistence testing methods are necessary to ensure device functionality in a crowded RF environment. Depending on the device under test's (DUT's) intended use, the coexistence requirement could be a safety concern (e.g., for a medical device), or a general-use concern (e.g., to ensure the end user's experience is acceptable). Regardless of the DUT's intended use, the goal of coexistence testing is to examine how well the device can perform in a crowded RF environment.

While interference testing has been studied extensively in past works and standards [1] [2], coexistence is a slightly different problem. Coexistence is defined as the ability of two or more spectrum-dependent devices or networks to operate without harmful interference [3]. With coexistence testing, the performance of both the DUT and the unintended network are examined. This differs from interference testing, where typically only the DUT is considered. The inclusion of both networks are important as the RF spectrum is becoming increasingly crowded and thus a more sought-after resource. In an attempt to establish a consistent set of coexistence measurement methods, the upcoming ANSI C63.27 standard provides a procedure for quantifying a device's ability to coexist [4]. Four test methods have emerged in the draft standard: conducted test, radiated anechoic test, radiated open-environment (ROE) test, and a hybrid/two-chamber test. Though the robustness of each test method has been demonstrated individually, results comparing the test methods has yet to be published. For example, if one lab tests a DUT by use of an anechoic chamber test, and another tests the same DUT by use of the ROE test, how close will the results be? This is the question we examine here for two of the test methods.

The coexistence methods themselves and the detailed test planning steps are not described here. Instead, we focus on the test environment and layout of the DUT and unintended network. We expect that by changing the layout of networks, the environment in which the test is performed, and by repeating the measurements, the results will be similar. If true, this would indicate that the layout of the devices and the test environment does not play a critical factor in the outcome of measurements. However, if significant variations in the measurements are observed, then either the environment or the layout could be impacting the final results.

## II. General Coexistence Measurements

In true coexistence measurements not only is the DUT monitored for changes but the unintended network is also measured simultaneously. These coexistence measurements look at multiple parameters to quantify the performance of wireless communication links. Here, we look at test layouts in the environment and the robustness of the radiated anechoic and ROE methods. The anechoic environment is used as a baseline to measure the coexistence capabilities between the networks while the ROE can better approximate a real-world deployment environment. In the work presented here, the contributions of the DUT (and its network) are not quantified. Only the DUT's ability to perform in the presence of an unintended network is examined.

Interference and coexistence between wireless devices is affected by three parameters: time, frequency, and physical separation. By modifying any one of these parameters we can influence the level of interference/coexistence between devices. Since devices of interest are relatively close together geographically, the use of power, network throughput, and frequency separation between DUT and unintended network's channels are varied to measure the coexistence capability of a DUT. Here, the DUT uses a Bluetooth Low Energy (BLE) link between two devices, one of which is the DUT and the

 

Jacobs, Ryan; Coder, Jason; LaSorte, Nickolas.
"Verification of Coexistence Measurement Methods: Radiated Anechoic and Open Environment."
Paper presented at 2017 IEEE International Symposium on Electromagnetic Compatibility and Signal/Power Integrity, Washington, DC, United States. August 7, 2017 - August 11, 2017.

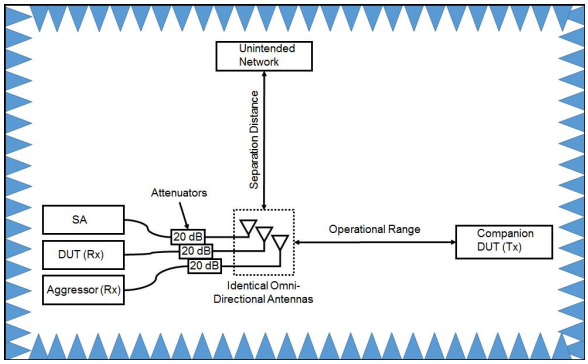


Fig. 1. Setup 1 - Block diagram used in both radiated anechoic and ROE.

unintended network uses a Wi-Fi link. For the coexistence test shown in Figure 1, there are several test parameters measured and recorded: packet error rate (PER), RF power in the environment, reported Wi-Fi received RF power, intended network throughput and frequency, and PER of the DUT network. Since the BLE link is what the DUT utilized, the PER is used as the primary metric for coexistence. On the unintended network, both throughput and transmitted power are recorded. A vector signal transceiver (VST) is used in spectrum analyzer mode to monitor the RF environment and the data recorded.

There are several different test parameters used to measure the coexistence between intended and unintended networks. Parameters include (but are not limited to): signal to interference ratio (SIR), throughput, and frequency. SIR is defined as the ratio of the averaged received carrier power and the averaged received interference power.

While this paper only discusses anechoic and ROE methods, it is important to note that there are a total of four possible test methods: conducted, radiated anechoic, ROE, and hybrid/two chamber (a mix between conducted and radiated involving two coupled anechoic chambers). The design of the DUT will play a significant role in determining which method is most appropriate and which case is appropriate for testing.

Conducted testing is the simplest setup and is designed for DUTs where the RF port(s) are accessible to those performing the test. Here, transmission lines, attenuators, power splitters, and combiners are used for all connections in the test setup. This test setup does not account for multipath, path loss, antenna efficiency and other radiated effects. The radiated test setup is done in an anechoic environment or an ROE with the devices spaced apart either line of sight (LoS) or non-line of sight (NLoS). The radiated test methods allow for some flexibility in recreating the deployment environment. Recreating the environment during the coexistence test can yield results that are more likely to predict in-field performance. Where strict control and isolation between the DUT and unintended network are desired, the two-chamber method can be of use.

## III. Measurement Setup

The experimental setup consisted of an IEEE 802.11 access point (Wi-Fi access point), an IEEE 802.11 client (Wi-Fi client), and an unidirectional IEEE 802.15 link (BLE link). The first test method was the radiated anechoic shown in Figure 1. The anechoic chamber helped to ensure that outside disturbances were not having an impact on the wireless links.

The second method tested is the ROE shown in Figure 3. Here, two network layouts are tested and compared to the anechoic test results. The experimental setup was automated so that repeated measurements of the same configuration could be done and the data stored.

Both the Wi-Fi and the BLE wireless networks are implemented with commercially available off-the-shelf development boards. Coexistence testing with the Wi-Fi development boards requires control over the transmission power, throughput, and Wi-Fi channel. BLE development boards must report back the PER to the computer. Further, the BLE development boards have their channel number fixed and manually selected during the SIR and throughput tests. The values for PER are reported back in percent. The percentage value is calculated from the number of packets decoded with errors compared to the total number sent. If there are no packets received then, we assume that all packets are lost due to the unintended network (Wi-Fi), thus giving a PER of 100%.

For each setup environment, there are three separate test runs: SIR, throughput, and frequency tests. In the SIR test the Wi-Fi power is increased from 1 dBm to 9 dBm in increments of 1 dBm, with BLE transmission power and frequency held constant. In the throughput test, IEEE 802.11n standard was used with Wi-Fi throughput increased from 1 Mbps to 100 Mbps adjusted non-linearly as follows: 1-25 Mbps incremented by 1 Mbps, 25-55 Mbps incremented by 5 Mbps, and the last increment sets the Wi-Fi throughput to 100 Mbps. The BLE transmission power and frequency are held constant for the throughput test. Finally, for the frequency tests, Wi-Fi transmission power, throughput, and BLE transmission power are held constant while the BLE channel is adjusted from 1-37.

### A. Anechoic Chamber Test Setup

A block diagram showing the anechoic chamber test setup is shown in Figure 1 and pictured in Figure 2. Three identical omni-directional antennas are placed 10 cm apart from each other. The received signals are recorded on a VST, the DUT receiver, and by the unintended network receiver. With this setup the susceptibility to interference is varied by the separation distance and the operational distance. The operational distance is determined by the received power level at the DUT receiver. This distance may be adjusted to achieve a -60 dBm power level at the DUT receiver, with the unintended network disabled. Separation distance of the Wi-Fi network is ideally set so the SIR curve has no interference until half the Wi-Fi channel throughput is utilized.



Jacobs, Ryan; Coder, Jason; LaSorte, Nickolas.
"Verification of Coexistence Measurement Methods: Radiated Anechoic and Open Environment."
Paper presented at 2017 IEEE International Symposium on Electromagnetic Compatibility and Signal/Power Integrity, Washington, DC, United States. August 7, 2017 - August 11, 2017.

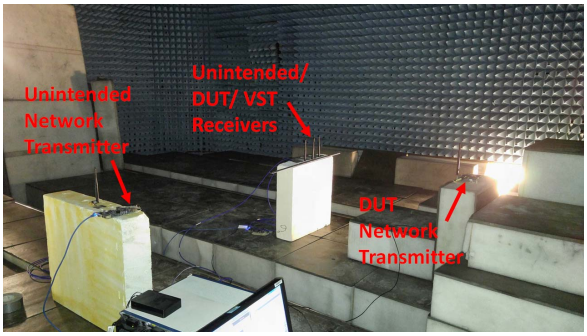


Fig. 2. Radiated anechoic Test Setup 1.

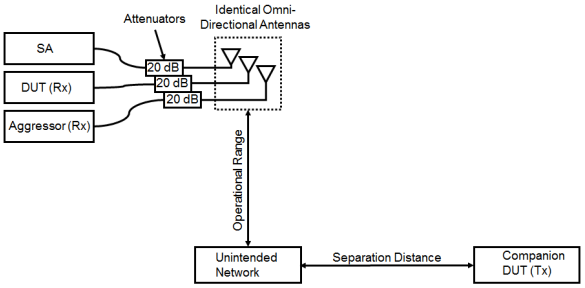


Fig. 3. Setup 2 - Block diagram used in ROE.

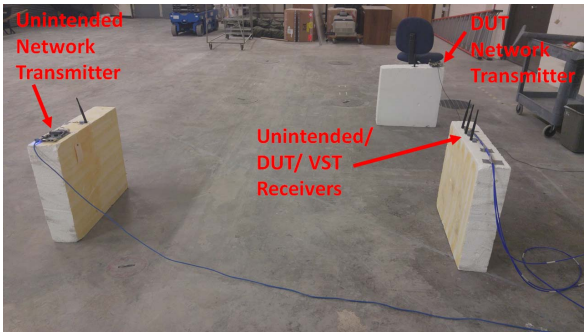


Fig. 4. Radiated Open-Environment Setup 1.

TABLE I
SUMMARY OF NETWORK LAYOUT AND ENVIRONMENTS

| | **Setup 1 - ROE** | **Setup 2 - ROE** | **Setup 1 - Anechoic** |
|---|---|---|---|
| **Network Layout #** | 1 | 2 | 1 |
| **Environment** | ROE | ROE | Radiated Anechoic |
| **BLE Parameters** | PER | PER | PER |
| **Wi-Fi Parameters** | Throughput, Rx RSSI | Throughput, Rx RSSI | Throughput, Rx RSSI |
| **Test Type** | SIR, Frequency, Throughput | SIR, Frequency | SIR, Frequency, Throughput |

### *B. Radiated Open-Environment Lab Test Setup*

For the ROE setup, two different measurement setups were used. The first, test layout is identical to the setup in the anechoic chamber test. (See Figure 1.) The second test setup is shown in Figure 3 and pictured in Figure 4. Three identical omni-directional antennas are placed 10 cm apart from each other. The received signals are recorded on a VST, the DUT receiver and by the unintended network receiver. With this setup, the level of interference is adjusted by changing the separation distance and the operational distance. The operational distance is determined through the power level received at the DUT receiver. This distance may be adjusted to achieve a -60 dBm power level at the DUT receiver. Separation distance of the Wi-Fi network is ideally set so the SIR curve has no interference until half of the Wi-Fi channel throughput is utilized.

A summary of the network layout and test environment used is shown in Table I. Network layout is shown in Figure 1 and Figure 3. The BLE and Wi-Fi parameters that are measured for each test environment are listed in Table I.

## IV. DATA

The recorded test data are averaged over the total number of repeat test runs performed for each test. Table II shows the minimum and maximum standard deviation for each test; in this case 10 test runs. The minimum deviation occurs when the PER is at 100% since the Wi-Fi signal dominates in power and throughput. The maximum deviation occurs roughly at 50% PER. This is likely due to variations in the Wi-Fi CCA. The computed average is plotted and the standard deviation is shown in Table II. Here, the averaged data are shown in three subsections: PER, Wi-Fi throughput and calculated difference between PER and Wi-Fi throughput.

Because PER is constrained to the bounded interval [0,1], confidence intervals based on a normal approximation can incorrectly fall outside of the valid range. To address this problem, confidence intervals were estimated with the aid of a logit transformation, following [7]. First, the logit function, which maps the interval [0,1] to the real line, was applied to the PER. Next, a 95% confidence interval for the mean logit-transformed PER was estimated with the usual approach based on a normal approximation. Lastly, the confidence interval in logit space was transformed back to PER with the inverse logit transformation (a.k.a. the logistic function). The resulting confidence interval for mean PER was consequently constrained to the interval [0,1], i.e., 0-100% when multiplied by 100.

### *A. Packet Error Rate Results*

Figures 5 - 7 show the averaged PER for radiated anechoic and ROE. Figure 5 shows how the PER is affected by increasing the Wi-Fi transmit power on the unintended network. All device layouts and environment tests have a fixed number of discrete test increments. These increments are referred to as a test run number.



Jacobs, Ryan; Coder, Jason; LaSorte, Nickolas.
"Verification of Coexistence Measurement Methods: Radiated Anechoic and Open Environment."
Paper presented at 2017 IEEE International Symposium on Electromagnetic Compatibility and Signal/Power Integrity, Washington, DC, United States. August 7, 2017 - August 11, 2017.

TABLE II
STANDARD DIVINATION OF PER

| | | Min(%) | Max(%) |
|---|---|---|---|
| Setup 1 - Anechoic | SIR | 0.1133 | 1.6461 |
| | Frequency | 0 | 0.7457 |
| | Throughput | 0.1286 | 0.86 |
| Setup 1 - ROE | SIR | 0.1336 | 4.4065 |
| | Frequency | 0 | 2.7409 |
| | Throughput | 0.2104 | 5.7067 |
| Setup 2 - ROE | SIR | 0.0801 | 1.8805 |
| | Frequency | 0 | 0.9182 |
| | Throughput | N/A | N/A |

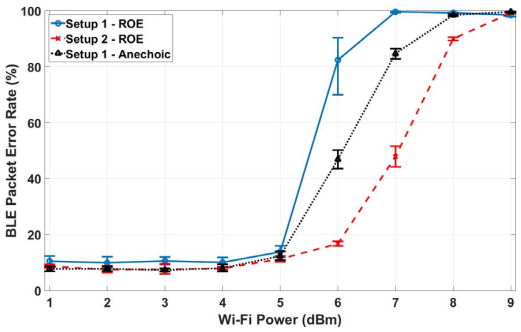


Fig. 5. SIR test - Average PER results.

Figure 6 shows the effects on PER when the BLE channel overlaps with a Wi-Fi channel. When the DUT transmits in the same band as the unintended network, the PER is high. When transmitting outside the unintended networks band there is little to no PER.

Figure 7 shows the effects of increasing the unintended network's throughput. The PER of the DUT increases as the Wi-Fi throughput increases, as expected.

### B. Wi-Fi Throughput Results

Figures 8 - 10 show the averaged Wi-Fi throughput for radiated anechoic and ROE. The development boards that were used implement a version of the IEEE 802.11n standard. Therefore, a clear channel assessment (CCA) is done before each throughput test begins. If too much RF power is detected the throughput will be lowered to maintain the quality of the communication link.

For the SIR and frequency test, Wi-Fi throughput is held constant. The recorded Wi-Fi throughput is shown in Figure 8 and 9. Figure 10 shows the configured throughput versus that throughput measured by the Wi-Fi boards.

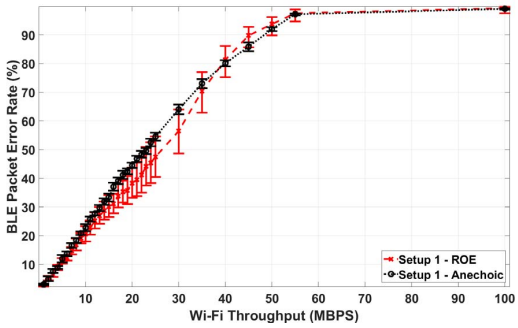


Fig. 7. Throughput test - Average PER results.

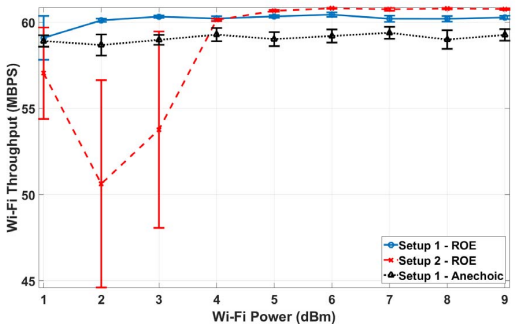


Fig. 8. SIR test - Average Wi-Fi throughput results.

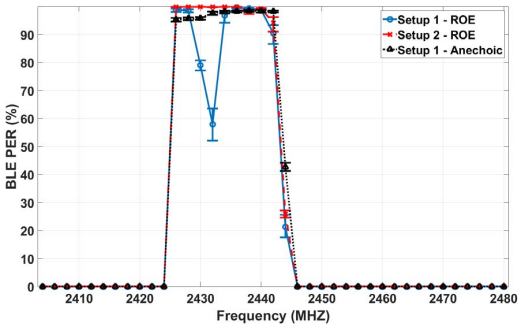


Fig. 6. Frequency test - Average PER results.

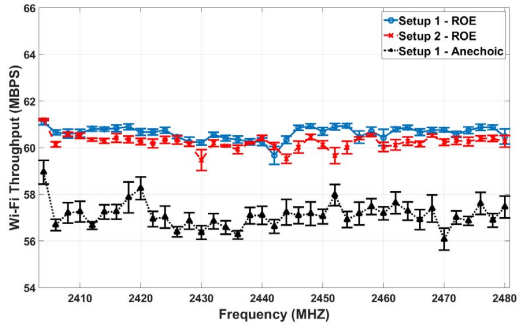


Fig. 9. Frequency test - Average Wi-Fi throughput results.



Jacobs, Ryan; Coder, Jason; LaSorte, Nickolas.
"Verification of Coexistence Measurement Methods: Radiated Anechoic and Open Environment."
Paper presented at 2017 IEEE International Symposium on Electromagnetic Compatibility and Signal/Power Integrity, Washington, DC, United States. August 7, 2017 - August 11, 2017.

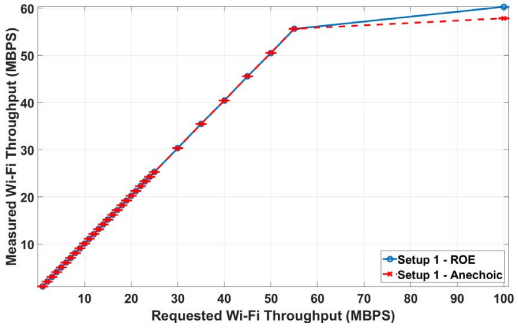


Fig. 10. Throughput test - Average Wi-Fi throughput results.

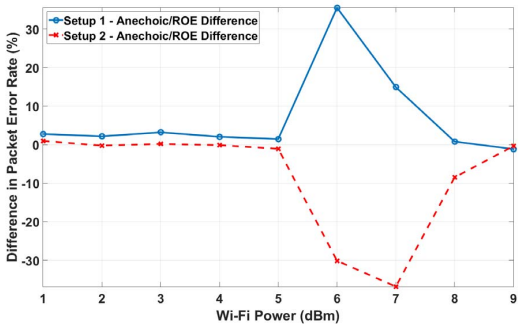


Fig. 11. SIR test - Difference in PER between radiated anechoic setup 1 and ROE setup 1 and between radiated anechoic setup 1 and ROE setup 2.

### C. Calculated Difference in Packet Error Rate and Throughput

Figures 11 - 13 shows the differences in PER between ROE and radiated anechoic measurements. By using the anechoic data as a baseline, we can examine the similarity between the different test setups and network layouts.

Figure 14 shows the difference in throughput for the radiated anechoic and ROE tests where we use the radiated anechoic test data as a baseline.

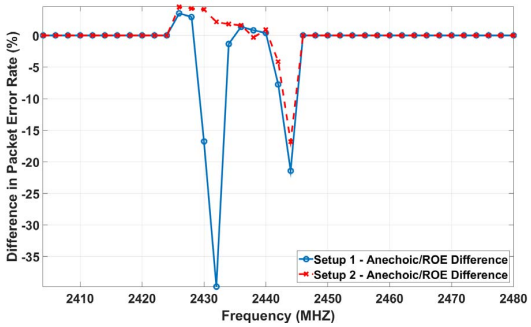


Fig. 12. Frequency test - Difference in PER between radiated anechoic setup 1 and ROE setup 1 and between radiated anechoic setup 1 and ROE setup 2.

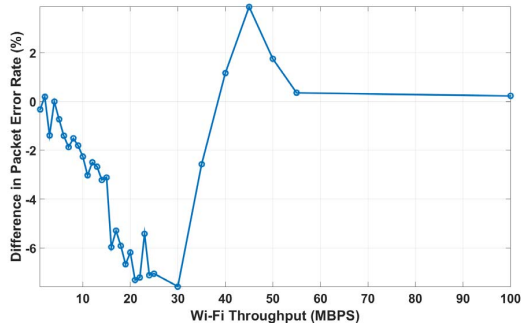


Fig. 13. Throughput test - Difference in PER between radiated anechoic setup 1 and ROE setup 1.

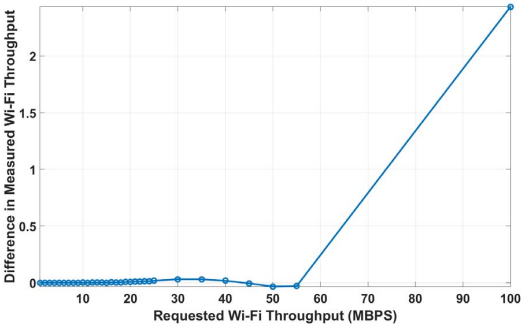


Fig. 14. Throughput test - Difference in measured throughput between radiated anechoic setup 1 and ROE setup 1.

## V. Analysis

The PER data from the radiated anechoic and ROE follows the same trend with slight variations between different physical layouts. The variations between the PER results for the SIR test is shown in Figure 11. Recall that the ROE test utilizes two different physical network layouts, thus there is a sign difference with respect to the anechoic measurement. We can calculate this difference by using the anechoic setup as a baseline. Differences in the ROE measurements are visible in Figure 5, as a result of the variation in power received by the DUT. The DUT received power ranged from -58 dBm to -65 dBm due to changes in the separation distance between the DUT transmitter and receiver. Since the DUT received power differs, the PER susceptibility caused by the effects of the unintended network will also vary.

For the frequency test, the PER data between the radiated anechoic and the ROE setup 2 are similar. Here, the DUT is changing its center frequency for each test step. As the DUT enters the same frequency space as the unintended network, the PER goes from 0% to 100%. For ROE setup 1, there is a drop of 40% in the PER. This drop in the PER is most likely due



Jacobs, Ryan; Coder, Jason; LaSorte, Nickolas.
"Verification of Coexistence Measurement Methods: Radiated Anechoic and Open Environment."
Paper presented at 2017 IEEE International Symposium on Electromagnetic Compatibility and Signal/Power Integrity, Washington, DC, United States. August 7, 2017 - August 11, 2017.

to environmental effects. In the ROE test, the environment is dynamic and may not be precisely the same between the two different network layouts. The difference between the ROE setups is shown in Figure 12.

The throughput test not only compares how close the PER rate is in Figure 13 but also the throughput of the actual test shown in Figure 14. There is a high degree of correlation between the radiated anechoic test and the ROE setup 2. The data indicate the difference between setups is nearly zero, with the exception of the 100 Mbpbs test. This indicates that the environment does not have a significant effect on the measured PER. With throughput between the two different environments being nearly identical the development boards did not lower throughput based on the measured RF environment.

All test runs are LoS between transmitter and receiver. Since all test layouts and test runs are similar, we conclude the layout of the devices does not affect the outcome of the coexistence measurements.

This paper did not examine non-line of sight effects (e.g., multipath). NLoS situations may be used when one desires to replicate the actual deployment environment of a device. In these situations, there may be additional variation between the anechoic and ROE environments. In NLoS conditions the ability to recreate the same multipath conditions will have a significant impact on the ability to reproduce results across environments.

## VI. Conclusion

The ANSI C63.27 standard discusses four popular coexistence measurement methods. Here, two methods are examined to investigate what impact the test environment has on the outcome of the test. The test data recorded in different layouts for the different test runs (SIR, throughput, and frequency tests) indicate that the layout of the devices in the network do not have a significant effect on the coexistence measurements when the separation distance between the devices is set as described in Section III (in this case, -60 dBm).

With the DUT transmitters and receivers being in LOS of each other, the coexistence measurements strongly agree between radiated anechoic and ROE. Any physical layout of the devices will yield similar results so long as they have a clear LoS and follow the test procedure. However, each environment is used to test different aspects. Anechoic environments attenuate external RF signals and allow an examination of the coexistence between the DUT and unintended networks. The ROE can be a closer approximation to a real deployment environment. The disadvantage of ROE tests is that they are susceptible to ambient signals not part of the coexistence test.

Future work will examine multiple test layouts in all test environments: conducted, radiated anechoic, ROE, and hybrid. This could also include measurements of the DUT's impact on other devices and testing in NLoS conditions.

## References


[1] Electromagnetic compatibility (EMC) - Part 4-3: Testing and measurement techniques - Radiated, radio-frequency, electromagnetic field immunity test," IEC 61000-4-3:2006

[2] Electromagnetic compatibility (EMC) - Part 4-21: Testing and measurement techniques - Reverberation chamber test methods," IEC 61000-4-21:2011

[3] IEEE Recommended Practice for the Analysis of In-Band and Adjacent Band Interference and Coexistence Between Radio Systems," in IEEE Std 1900.2-2008 , vol., no., pp.1-94, July 29 2008 doi: 10.1109/IEEESTD.2008.4584236

[4] American National Standards Institute (ANSI) ASC C63, C63.27 Standard for Evaluation of Wireless Coexistence. 2016, ANSI C63 Committee, C63.org

[5] Jangeun Jun, P. Peddabachagari and M. Sichitiu, "Theoretical maximum throughput of IEEE 802.11 and its applications," Second IEEE International Symposium on Network Computing and Applications, 2003. NCA 2003., Cambridge, MA, USA, 2003, pp. 249-256. doi: 10.1109/NCA.2003.1201163

[6] W. F. Young, J. B. Coder and L. A. Gonzalez, "A review of wireless coexistence test methodologies," 2015 IEEE Symposium on Electromagnetic Compatibility and Signal Integrity, Santa Clara, CA, 2015, pp. 69-74.

[7] L. Held and D. Sabanes Bove, "Applied Statistical Inerencce: Likelihood and Bayes," Heidelberg, Springer, 2014, p.115





Jacobs, Ryan; Coder, Jason; LaSorte, Nickolas.
"Verification of Coexistence Measurement Methods: Radiated Anechoic and Open Environment."
Paper presented at 2017 IEEE International Symposium on Electromagnetic Compatibility and Signal/Power Integrity, Washington, DC, United States. August 7, 2017 - August 11, 2017.

Proc. of the 2017 International Symposium on Electromagnetic Compatibility - EMC EUROPE 2017, Angers, France, September 4-8, 2017

# Multiple Sources in a Reverberant Environment: The "Cocktail Party Effect"

Perry F. Wilson
RF Technology Division
National Institute of Standards and Technology
Boulder, CO, USA
pfw@nist.gov

***Abstract* — Acoustics and electromagnetics have many parallels based on similar equations describing propagation, reflection, and reverberation. This paper considers one example, the "cocktail party effect", that describes speech comprehension in the presence of multiple background conversations. An electromagnetic equivalent is developed that may have application to describing the quality of a wireless communications link in the presence of multiple and similar background signals.**

***Keywords—acoustics; coexistence; reverberation chamber; wireless communications***

## I. INTRODUCTION

The "cocktail party effect", coined by an acoustics researcher in 1953 [1], is a well-known phenomenon describing what happens when many people have multiple conversations in a reverberant room [2-5]. As the number of conversations increases and the ambient noise in the room rises, people in individual conversations will tend to physically cluster and separate from other conversations to be better understood and to enable listening, as depicted in Fig. 1. More interesting is the processing that we naturally do to effectively increase the signal to noise ratio (*S/N*). These largely take three forms based on binaural (two ears) listening [3]: interaural time differences (time of arrival or phase), interaural level differences (amplitude), and interaural decorrelation (coherence). These are similar to the diversity gain and orthogonal coding techniques used in wireless links to improve performance. Listeners with in only one active ear, for example a person using a hearing aid in one ear only, are severely disadvantaged in a high ambient noise environment since these binaural effects are not possible. Acoustic shadowing also occurs where the head blocks sounds and one ear can be favorably positioned. It has also been shown [3] that listeners, without knowing it, can also follow secondary conversations (data streams) simultaneous to the primary conversation with sudden awareness triggered by hearing their name, or certain key or taboo words. We also have extensive ability to correct for missing or mispronounced phonemes (differentiating sounds) and words, much like error correcting codes can overcome missing and incorrect bits.

The acoustics community has also developed quantitative tools to describe speech information that help or hinder understanding in the presence of noise. A basic approach is to divide the speech frequency range into a set of bands, rank these bands in terms of importance to speech comprehension, and track *S/N* in these bands for various types of noise signals. This allows both target and interfering sounds to be modeled in a repeatable way and provides insights into experiments designed to test comprehension versus noise. One result is that as the interfering signal fills the bands to similar levels as the target conversation, comprehension decreases. Thus, listeners will often have more difficulty understanding conversations if noise speakers have the same gender as the primary speaker, as similar speakers tend to have similar spectrums. This has parallels in the spoofing of wireless signals, where signals with similar but slightly corrupted modulation and frequency may cause more problems than simple higher amplitude white noise. Speech comprehension is also affected by sound level fluctuations (modulation), frequency hopping, time domain effects and clipping, spatial location of the sound sources, and more [3]. Whether these acoustic and speech insights can benefit wireless communications, MIMO processing techniques, and data coding protocols is an open question, but awareness of these results may be of interest.

Fig. 1. People having separate conversations tend to cluster and group as the ambient noise level rises.



Wilson, Perry.
"Multiple Sources in a Reverberant Environment: The "Cocktail Party Effect"."
Paper presented at 2017 International Symposium on Electromagnetic Compatibility (EMC Europe 2017), Angers, France. September 4, 2017 - September 7, 2017.

This paper looks at only one small example of the above work on speech comprehension versus noise. A sound propagation model of the cocktail party effect can be developed as a simple approximate equation which gives a *S/N* value, namely, the acoustic energy density of the intended conversation over the reverberant energy density of the undesired background conversations. An electromagnetic equivalent to this acoustic *S/N* can be readily found using the same basic derivation. This *S/N* expression can form a starting point to think about the "coexistence" of wireless devices where a similar problem to the cocktail party exists, namely, how to maintain a desired link in the presence of multiple, allowable sources broadcasting in the same frequency band with similar spectral characteristics. We will first review the acoustic case in Section II followed by the electromagnetic equivalent in Section III. We then conclude with a brief discussion.

## II. Multiple, Simultaneous Conversations in a Reverberant Room

The derivation of the basic equation describing the cocktail party effect may be found in [2, Chapter 6] and will be summarized here. Suppose there are $K$ conversations occurring in a reverberant room. We assume one speaker per conversation at any given time with a speaking power $P_t$. Initially, we will let $P_t$ be the same for each conversation cluster, but this can be readily generalized. Each conversation will involve some number of people, with the total number of people in the room being $M$ ($M > 2K$). We will assume that each conversation cluster is separated from any other cluster by a distance greater than the radius of reverberation $r_0$; that is, the distance at which direct path energy density and reverberant paths energy density are equal. While speech is somewhat directional, we will assume for simplicity spherical spreading (i.e., isotropic radiation) for any given conversation. Then, the direct energy density $w_d$ within a conversation is given by [2, eq. (1-12-1)]:

$$w_d = \frac{P_t / c}{4\pi r^2}, \tag{1}$$

where $r$ is the distance between speaker and listener ($r < r_0$), and c is the sound speed. The reverberant energy density $w_r$ due to the K conversations [2, eq. (6-2.13)] is simply K times the power per conversation $P_t$ reduced by ¼ the room constant $R_c$ (proportional to the room absorbing power):

$$w_r = \frac{4KP_t / c}{R_c} \quad , \tag{2}$$

where $R_c$ is given by [2, eq. (6-2.13)]

$$R_c = \alpha S /(1-\alpha) \quad , \tag{3}$$

where $S$ is the room surface area and $\alpha$ is the absorption coefficient for the wall surfaces, assumed uniform here over the whole room.

Combining these we have the total energy density $w$ given by [2, eq. (6-3.9)]:

$$w = \frac{P_t}{c}\left(\frac{1}{4\pi r^2} + \frac{4K}{R_c}\right) \quad . \tag{4}$$

This expression can be used to give a criterion for a conversation to be understood by an isotropic listener, namely, that a conversation cluster "signal" energy density (the direct conversation plus the desired speaker's reverberant energy contribution) be greater than the "noisy" other $K$-1 cluster's reverberant energy density ($S/N > 1$):

$$S/N = \frac{\frac{1}{4\pi r^2} + \frac{4}{R_c}}{\frac{4(K-1)}{R_c}} \quad . \tag{5}$$

If we note that $r_0 = (R_c / 16\pi)^{1/2}$ [2, eq. (6-2.15)], then the above may be rewritten as [2, eq. (6.3-11)]:

$$S/N = \frac{(r_0 / r)^2 + 1}{K - 1} \quad . \tag{6}$$

As is intuitively expected, we see that as the number of conversation clusters $K$ increases, the *S/N* decreases. In addition, as $K$ increases, then r must decrease to maintain the same S/N, implying that people in a conversation cluster must move closer together. This clearly sets a limit on *K,* and or *M,* as r may not be made arbitrarily small. Ignored here is the effect of adding people on the room constant $R_c$. In an acoustic room, the *S/N* ratio will drop too low and the room become too crowded well before $R_c$ increases enough to make a difference. This may be different for RF reverberation chambers, however, which we consider next.

## III. Multiple, Simultaneous RF Sources in a Reverberation Chamber

The above acoustic model has a direct analogy in a RF reverberation chamber. If we consider the average power density $P_d$ (averaged over paddle stirring) in a reverberation chamber from $K$ sources as consisting of a dominant direct path contribution (we will again initially assume isotropic radiation and reception) plus reverberant power (with all sources assumed to have equal strength), then we can write [6, eqs. (1-2)]

$$\langle P_d \rangle = P_t\left(\frac{1}{4\pi r^2} + \frac{K\lambda Q}{2\pi V}\right), \tag{7}$$

where $\lambda$ is the wavelength, $Q$ is the chamber quality factor, and $V$ the chamber volume. We note that $Q$ is approximately equivalent to [4, eq. (5)], where

Wilson, Perry.
"Multiple Sources in a Reverberant Environment: The "Cocktail Party Effect"."
Paper presented at 2017 International Symposium on Electromagnetic Compatibility (EMC Europe 2017), Angers, France. September 4, 2017 - September 7, 2017.

$$Q = 8\pi \frac{V}{\lambda \alpha S_c} \tag{8}$$

in the acoustic case (this approximation is based on normal incidence to the walls only as discussed in [7, Section 1.3], where α is the absorption coefficient and $S_c$ is the surface area of the chamber. Inserting $Q$ into (7) and noting that

$$\alpha S_c = R_c \tag{9}$$

for small α, (that is for highly reflective walls), we arrive at

$$\langle P_d \rangle = P_t \left( \frac{1}{4\pi r^2} + \frac{4K}{R_c} \right) , \tag{10}$$

which is equivalent to (4) for the reverberation chamber power density. Alternately, if we note that [6, eq. (3)] that

$$Q = \frac{V}{2\lambda r_e^2} , \tag{11}$$

then we see that (7) can also be rewritten as

$$\langle P_d \rangle = P_t \left( \frac{1}{4\pi r^2} + \frac{K}{4\pi r_e^2} \right) . \tag{12}$$

We can readily generalize this for unequal source powers to

$$\langle P_d \rangle = \left( \frac{P_1}{4\pi r^2} + \frac{\sum_{i=1}^{K} P_i}{4\pi r_e^2} \right) , \tag{13}$$

where $P_1$ represents the desired source to be received. The equivalent signal to noise ratio (6), that is, the desired direct path signal plus its desired signal reverberation over undesired signal reverberation is given by

$$S/N = \frac{P_1 \left( (r_e / r)^2 + 1 \right)}{\sum_{i=1}^{K} P_i} . \tag{14}$$

Noting that for the undesired reverberant power only the sum of the powers matters and letting

$$P_{RT} = \sum_{i=1}^{K} P_i , \tag{15}$$

we arrive at

$$S/N = \frac{P_1 \left( (r_e / r)^2 + 1 \right)}{P_{RT}} . \tag{16}$$

Finally, we may generalize this to include a directive intended source with directivity $D_s$ and receiver $D_r$ (these can be inserted in the direct power path in (13)) giving

$$S/N = \frac{P_1 (D_s D_r (r_c / r)^2 + 1)}{P_{RT}} . \tag{17}$$

As in the acoustic case, we see that as the total background reverberant power $P_{RT}$ increases, then the distance from the desired source to the receiver will need to decrease to maintain an equivalent *S/N* or the directivity of the desired source D will need to increase. Alternately, the effective radius $r_e$, which is inversely proportional to Q, will need to increase.

The above discussion uses a simple ratio of powers to describe *S/N*. More interesting would be some communications metric, such as bit error rate (BER). We would not expect BER to follow a simple inverse relationship but there may be a S/N level as given by (17) that is representative of when BER reaches an unacceptable level for a given type of system or set of modulation characteristics. This would need to be explored with experimental data which is not considered here.

## IV. Conclusion

We have reviewed some basic concepts in acoustics on how humans comprehend speech in the presence of background noise, the "cocktail party effect", and how this relates to an electromagnetic equivalent. A simple power ratio is formed to represent signal to noise, or *S/N*. Future work could look at actual communication signal metrics such as BER, error vector magnitude (EVM), or other quantities to explore whether the *S/N* ratio given by (17) provides useful guidance on the performance of this metric. This may have application to coexistence standards where multiple sources and receivers are expected to operate in close proximity. More generally, the rich acoustics literature may provide additional insights into communications systems based on the ability of humans to process and filter signals in a variety of creative ways and how these can be translated to communications systems equivalents.

## References


[1] C. Cherry, "Some experiments on the recognition of speech, with one and two ears," Journal of the Acoustical Society of America, vol. 25, no. 5, pp. 975-979, 1953.

[2] A. Pierce, Acoustics: An Introduction to its Physical Principles and Applications, Acoustical Society of America, Ch. 6, 1989.

[3] A. Bronkhorst, "The cocktail-party problem revisited: early processing and selection of multi-talker speech," Journal of Attention Perception & Psychophysics, vol. 77, no 5, pp. 1465-1487, April 2015

[4] P. Wilson. "Acoustic and electromagnetic reverberation chambers: similarities and differences," in Proc. 2016 Asian-Pacific Intl. Symp. On Electromagn. Compat. (Shenzhen, China), May 2016.

[5] D. Wang, "Deep learning reinvents teh hearing aid," IEEE Spectrum, vol. 54, no. 3, pp. 32-37, March 2017.

[6] C. Holloway, D. Hill, J. Ladbury, and G. Koepke, "Requirements for an effective reverberation chamber: unloaded and loaded," IEEE Trans. Electromagn. Compat., vol. 48, no. 1, pp. 187-194, Feb. 2006.

[7] D. Hill, Electromagnetics Fields in Cavities: Deterministic and Statistical Theories, IEEE Press, Wiley & Sons., 2009.



Wilson, Perry.
"Multiple Sources in a Reverberant Environment: The "Cocktail Party Effect"."
Paper presented at 2017 International Symposium on Electromagnetic Compatibility (EMC Europe 2017), Angers, France. September 4, 2017 - September 7, 2017.

# Methods for Channel Sounder Measurement Verification


Kate A. Remley
*Communications Technology Laboratory*
*NIST*
Boulder, CO, USA
kate.remley@nist.gov

Camillo Gentile
*Communications Technology Laboratory*
*NIST*
Gaithersburg, MD, USA
camillo.gentile@nist.gov

Alenka Zajic
line 2: *Department of Electrical and Computer Engineering*
Georgia Technical University
Atlanta, GA, USA
alenka.zajic@ece.gatech.edu

Jeanne T. Quimby
*Communications Technology Laboratory*
*NIST*
Boulder, CO, USA
jeanne.quimby@nist.gov



***Abstract*—We describe an activity of the 5G mmWave Channel Sounder Alliance to verify the hardware performance of channel sounders operating at mmWave frequencies. Such verification procedures are critical when attempting to compare data from sounders having different architectures in various environments. Two different methods are described and illustrated with simple measurement examples.**



***Keywords—channel sounder, measurement verification millimeter-wave wireless system, propagation channel measurement.***




## I. Introduction

The 5G mmWave Channel Model Alliance[1] was formed to take a longer, research-oriented view of issues related to channel measurement and modeling than that required by many standards groups. The group's goal is to address issues that impede progress in standards development and hardware optimization.

One key Alliance strength is that participating groups utilize a wide range of channel sounders of various architectures. This allows the group to study representative propagation environments with several different channel-sounder technologies, ultimately resulting in more robust channel models. For example, VNA-based channel sounders provide a high dynamic range, allowing detailed insight into the fading characteristics of a specific environment, but primarily for slowly varying or static channels. On the other hand, sampler-based channel sounders are often fast, providing instantaneous channel information. As another example, some sounders have active antenna arrays capable of resolving the angle-of-arrival of multipath components in the plane of the antenna to within a few degrees, while others have antenna coverage over a hemisphere with nominally lower angular resolution, and yet others use lens antenna arrays for analog multi-beamforming that can provide spatial resolutions comparable to or finer than existing phased arrays.

In order for Alliance members to combine measured data from sounders having different architectures, it is essential to have confidence that each channel sounder is performing as expected. This includes verifying that the resulting measured data and the post-processing routines provide results in agreement with theory. Verified data can then be used to extract statistically representative metrics that feed into channel models, such as path loss and power delay profile.

[1] Here "5G" refers to the next generation of mobile wireless communication systems.

## II. Channel Sounder Verification Options

The participants in the Alliance have established a channel-sounder verification program [1]. The program allows labs to compare their measured, processed data to theory or to an artifact with known characteristics. Two types of verification are described here, "in-situ" verification, and "controlled-condition" verification.

### A. In-Situ Verification

In-situ verification may be conducted during field tests to provide confidence that the channel sounder is behaving as expected. Such verification is conducted in environments that are expected to provide known propagation conditions such as a relatively open area that exhibits free-space or two-ray propagation and path-loss behavior. A second example of in-situ verification includes the prediction of power-delay-(angle)-profile characteristics such as individual multipath component time delays or angles of arrival from map-based knowledge of a room.

As an example, NIST has performed in-situ verification measurements of their 83-GHz channel sounder [2] in the lobby area shown in Fig. 1. The measurements were performed over several separation distances between 4 m and 13 m and the path loss exponent was estimated from the Friis equation [3]

$$PL = \frac{(4\pi d)^2}{\lambda^2} . \quad (1)$$

Figure 1: NIST lobby area.




Remley, Catherine; Gentile, Camillo; Zajic, Alenka; Quimby, Jeanne.
"Methods for Channel Sounder Measurement Verification."
Paper presented at IEEE Vehicular Technology Conference, Toronto, Canada. September 24, 2017 - September 27, 2017.

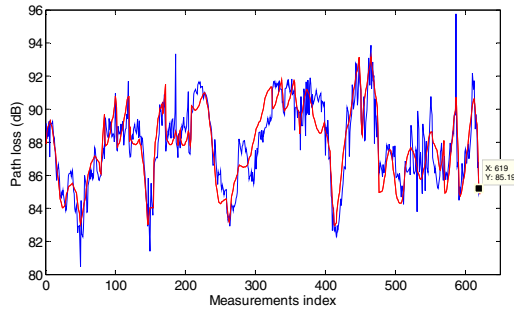


(a)

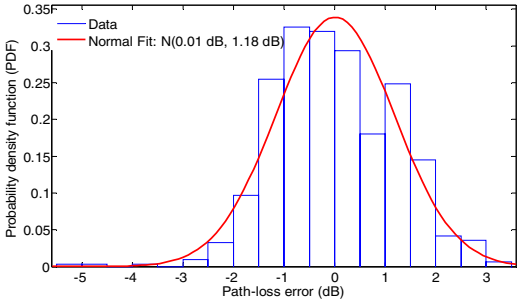


(b)

Figure 2 (a) Temporal variation of the path loss. (b) The measurement error (from [4]).

The Friis equation shows that the received power decreases as the square of the distance *d*. This power of two is an important parameter called the path-loss exponent. Often, the in-situ path loss verification method checks whether measured results produce a path-loss exponent equal to 2 (or very close to 2).

Data were collected while the channel-sounder receiver was in motion. The temporal variation of the path loss and the difference between the theoretical values in (1) and measurements are shown in Fig. 2. [4]. The path loss exponent, estimated from (1), was 1.93 (very close to 2). The nominal transmitter/receiver antenna patterns from the manufacturer were used in the SAGE algorithm [5] since the antennas have

Figure 3: (a) Conference room environment at the NIST Boulder Labs used for power-delay-profile verification.

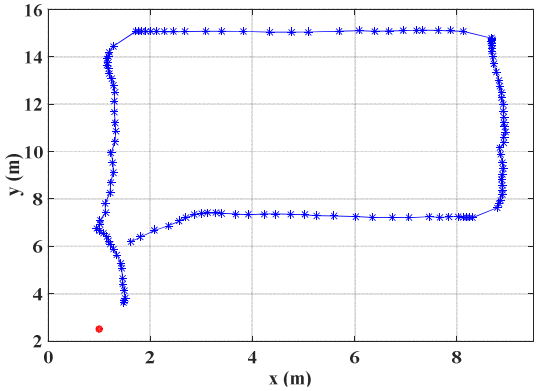


Fig. 4: RX antenna trajectory with measured data points (blue stars) and TX antenna location (red dot).

not yet been properly calibrated in an anechoic chamber. The maximum variation from the manufacturer's specifications is listed as 2 dB to which we attribute deviations of the data points from the free-space line.

NIST also performed in-situ power delay profile verification measurements of their 83-GHz channel sounder in the conference room area shown in Fig. 3. The RX antenna positioner was moving during the measurements along the path shown in Fig. 4, while the TX antenna was stationary in the corner of the room at a height of 2.5 m. Each blue star corresponds to a location where data were acquired. These points were used to calculate the signal delay.

The measured and computed delays are compared in Fig. 5(a) and the measurement error is plotted in Fig. 5(b). The results show excellent agreement between the measured and

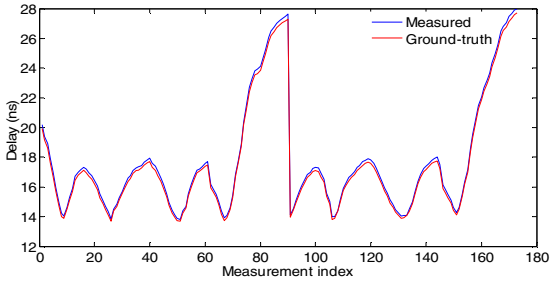


(a)

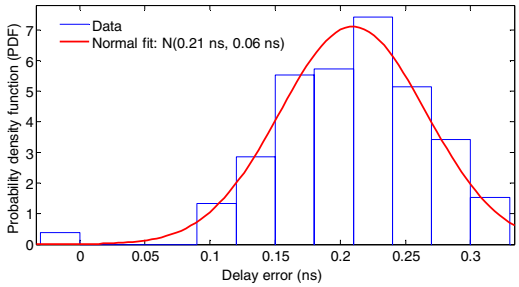


(b)

Figure 5: (a) Comparison of measured and computed time delays ("Ground-truth"). (b) The measurement error.

Remley, Catherine; Gentile, Camillo; Zajic, Alenka; Quimby, Jeanne.
"Methods for Channel Sounder Measurement Verification."
Paper presented at IEEE Vehicular Technology Conference, Toronto, Canada. September 24, 2017 - September 27, 2017.

calculated time delays.

### B. *Controlled-Condition Verification*

Controlled-condition verification involves channel-sounder measurements of an environment or artifact having known characteristics, where conditions are determined by design. Here, we report on two types of controlled-condition verification results. First, falling in the category of controlled environments, are measurements made in free-space conditions where reflectors are used to simulate controlled multipath and unintended multipath is suppressed with RF absorbers. Measurements conducted in anechoic chambers would also fall under the controlled-environment verification category. A second type of controlled-condition verification consists of an artifact that provides an artificial-multipath channel such as an electronic channel emulator or an artifact made from coaxial cables of different lengths.

As an example, Georgia Tech has performed path loss verification of their VNA-based channel sounders at 26-43 GHz (Ka-band) and 110-170 GHz (D-band) [6]–[7]. Received power was measured in an open laboratory shown in Fig. 6. Both TX and RX were covered with RF absorbers, as are the floor and surrounding elements. The goal was to eliminate all possible multipath components and create true line-of-sight environment. The TX-RX separation distances ranged from 20 to 180 cm for the Ka-band, with at least 10 measurement points. For the D-band channel sounder, the distances ranged from 30 cm to 85 cm. This range was limited by the transmitted power.

Figure 6: Ga Tech channel sounder. 110-170 GHz measurement setup.

Figure 7 shows that the path loss exponent was estimated as 2.001 for the Ka-band and 1.98 GHz for the D-band measurements. Additionally, a standard deviation of 0.2 dB was observed for both set of measurements [7].

## III. Best Practices for Verification

For all measurement verification methods, utilization of best-practice techniques can maximize the accuracy. Best-practice techniques include, but are not limited to, the following:

- sufficient directionality and correct orientation of the antennas (to avoid transmitting or receiving reflections or scattering, adjustment for movement)
- sufficient time resolution in the measured PDP to ensure that only the first arriving direct LOS over the air path is being recorded (for path loss and timing)
- sufficient distance separation to not overload the receiver (to ensure linear operating range)
- calibration to remove system hardware non-idealities (*e.g.*, back-to-back)
- use of absorbers (and reflectors) to provide controlled environment
- collection of sufficient number of samples to provide statistical significance (*e.g.*, repeat measurements or, if the antenna is mobile, measurements made along a track, and repeated if possible.)

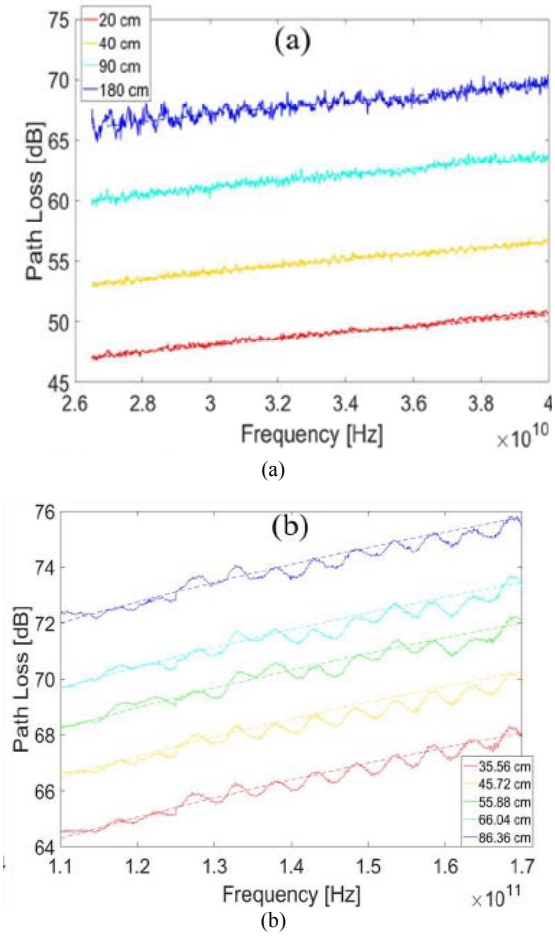


Figure 7: Path loss as a function of frequency for several separation distances for (a) Ka-band, and (b) D-band measurements.

Remley, Catherine; Gentile, Camillo; Zajic, Alenka; Quimby, Jeanne.
"Methods for Channel Sounder Measurement Verification."
Paper presented at IEEE Vehicular Technology Conference, Toronto, Canada. September 24, 2017 - September 27, 2017.

## IV. Summary

Channel-sounder verification provides a "sanity check" that hardware is operating within expected parameters. This becomes more critical at mmWave frequencies where hardware is pushing the state of the art. Verification allows different labs to confidently utilize data from different but nominally similar environments to develop channel models.

## Acknowledgment

The authors acknowledge the members of the 5G mmWave Channel Model Alliance for their participation, contributions and dedication to improving the science of channel-sounder measurements and modeling.

## References

[1] K.A. Remley, A. Zajic, *et al.*, "Verification Techniques for mmWave Channel Sounders, Activities of the 5G mmWave Channel Model Alliance," White Paper, *in process*.

[2] H. T. Friis, "A note on a simple transmission formula," *Proceedings of the IRE*, vol. 34, no. 5, pp. 254–256, May 1946.

[3] P. B. Papazian, C. Gentile, K. A. Remley, J. Senic, N. Golmie, "A Radio Channel Sounder for Mobile Millimeter-Wave Communications: System Implementation and Measurement Assessment," *IEEE Transactions on Microwave Theory and Techniques*, Early View, vol.PP, no.99, pp.1-9, Aug. 2016.

[4] C. Gentile, J. Senic, P. B. Papazian, J.-K. Choi, and K. A. Remley, "Pathloss models for indoor hotspot deployment at 83.5 GHz," *IEEE Global Communications Conference: The First International Workshop on 5G Millimeter-Wave Channel Models (GLOBECOM 2016)*, pp. 1-6, Dec. 2016.

[5] K. Hausmair, K. Witrisal, P. Meissner, C. Steiner, and G. Kail, "SAGE Algorithm for UWB Channel Parameter Estimation," *Proceedings of COST 2100 Management Committee Meeting*, Athens, Feb. 2010.

[6] S. Kim, W. T. Khan, A. Zajić, and J. Papapolymerou, "D-band channel measurements and characterization for indoor applications," *IEEE Transactions on Antennas and Propagation*, vol. 63, no. 7, pp. 3198-3207, July 2015.

[7] Chia-Lin Cheng, S. Kim and A. Zajić, "Comparison of path loss models for indoor 30 GHz, 140 GHz, and 300 GHz channels," *Proceedings of the 11th European Conference on Antennas and Propagation (EuCAP)*, pp. 1-5, 19-24 March 2017, Paris, France.

Remley, Catherine; Gentile, Camillo; Zajic, Alenka; Quimby, Jeanne.
"Methods for Channel Sounder Measurement Verification."
Paper presented at IEEE Vehicular Technology Conference, Toronto, Canada. September 24, 2017 - September 27, 2017.

# Assessment of a 3D-Printed Aluminum Corrugated Feed Horn at 118.7503 GHz

Joshua A. Gordon, David R. Novotny, Michael H. Francis,
Ronald C. Wittmann, Jeffery R. Guerrieri
Communications Technology Laboratory
National Institute of Standards and Technology
Boulder, CO, 80305, USA
josh.gordon@nist.gov

Lavanya Periasamy , and Albin Gasiewski
ECEE Department
University of Colorado
Boulder, CO, USA

***Abstract*—All-metal 3D printing is investigated as a viable option for millimeter wave applications. 3D printing is finding applications across many areas and may be a useful technology for antenna fabrication. The ability to rapidly fabricate custom antenna geometries may also help improve cub satellite prototyping and development time. However, the quality of an antenna produced using 3D printing must be considered if this technology can be relied upon. Here, we investigate a corrugated feed horn that is fabricated using the powder bead fusion process for use in the PolarCube cube satellite radiometer. AlSi10Mg alloy is laser fused to build up the feed horn, including the corrugated structure on the inner surface of the horn. The intricate corrugations, and tilted waveguide feed transition of this horn made 3D printing a compelling and interesting process to explore. Measurements were performed at the atmospheric oxygen line of 118.7503 GHz with the NIST configurable robotic millimeter-wave antenna facility (CROMMA). A comparison of these measurements to theoretical predictions provides an assessment of the performance of the feed horn. A description of the 3D printing process is also given.**

## I. Introduction

Cube Satellites (CubeSats) offer an accessible and effective platform for a wide variety of space-based applications. Many off-the-shelf components are allowing fast prototyping of CubeSats and subsystems. Space-based applications benefit from millimeter-waves (mm-waves) since shorter wavelengths allow for low diffraction, high bandwidth and small form factor. Radiometers rely on mm-waves due to the ubiquity of passive black body emissions and the existence of atmospheric spectral features. Emerging applications such as global internet [1] are projected to use constellations of over a thousand CubeSats operating above 100 GHz for satellite-to-satellite and satellite-to-ground communications. Often times instrumentation and scientific needs drive antenna designs that are not available off-the-shelf as opposed to many other CubeSat components. Therefore, antennas must be designed on a case by case basis in order to achieve desired performance characteristics such as gain, and sidelobe level.

The ability to quickly prototype, fabricate and test mm-wave antennas with the same ease as obtaining other off-the-shelf components would allow CubeSats to be used more readily. Recent advances in 3D printing could enable antennas to be quickly custom fabricated with complex structure to meet specific application needs. However, the quality and performance of printed antennas is not as well established as more traditional fabrication techniques such as machining and electroforming. Fabrication tolerances become more precise at high mm-wave frequencies. Edge fidelity of apertures, corrugated features, etc., can be challenging to reproduce since 3D printing creates inherently rough surfaces. This could impact antenna performance. Depending on the performance requirements, trade offs in antenna performance may be

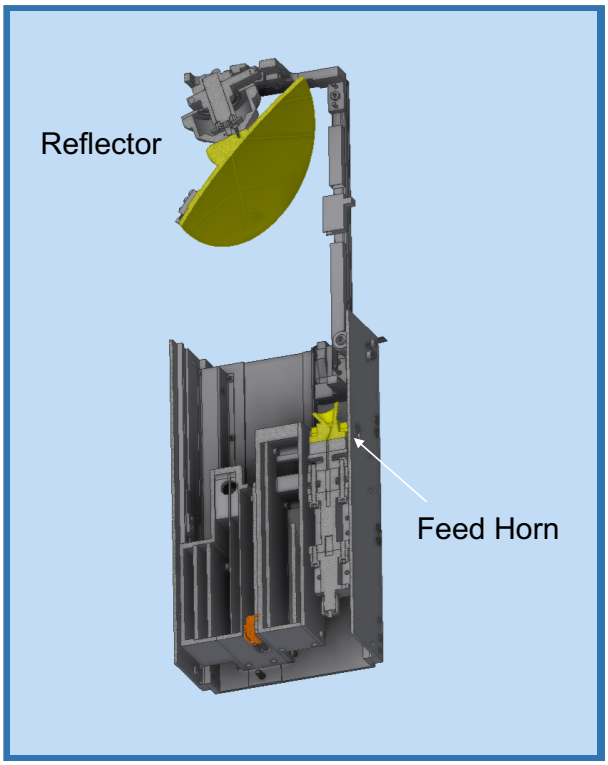


Fig. 1. Cross section view of the optical train front end of the PolarCube CubeSat radiometer. The parabolic reflector and 3D-printed metal feed horn are highlighted in yellow.

†Mention of this product is not an endorsement but only serves to clarify what was done in this work.



Gordon, Joshua; Novotny, David; Wittmann, Ronald; Francis, Michael; Guerrieri, Jeffrey; Lavanya, Periasamy; Gasiewski, Albin.
"Assessment of a 3D-Printed Aluminum Corrugated Feed Horn at 118.7503 GHz."
Paper presented at , Atlanta, GA, United States. October 15, 2017 - October 20, 2017.

offset by the conveniences of 3D printing. In this paper we present a comparison between the measured and theoretical gain and far-field pattern at 118.7503 GHz of an all metal 3D-printed conical corrugated feed horn antenna that will be used in the radiometer payload of the PolarCube cube satellite.

## II. PolarCube Satellite

PolarCube is a 3U CubeSat satellite with a payload comprised of an eight channel, double sideband 118.75 GHz scanning passive microwave temperature sounder, MiniRad [2], [3]. Radiometric observations near the 118.7503 GHz oxygen line are used to profile atmospheric temperature [4],[5]. The radiometer payload is comprised of a spinning offset paraboloidal main reflector and a stationary conical corrugated feed horn. The main reflector is an off-axis ellipse with a projected circular aperture of 8 cm. The feed horn+reflector combination is intended to have a gain is 38.03 dB. Figure 1 shows a cross-section view of the PolarCube optical front end with corrugated feed horn and deployable parabolic reflector shown in yellow. The feed horn couples radiation from the main reflector to the radiometer receiver electronics. The spinning reflector configuration allows for maximum aperture area resulting in a 3 dB footprint size of 16 km for nadir observation. The reflector is supported by a single strut that minimizes sidelobe scattering and antenna temperature uncertainty.

## III. Feed Horn

### A. 3D Printing

In recent years 3D printing in plastic has led to the investigation of dielectric microwave structures such as reflect arrays [6] and band gap materials [7]. Metal-coated 3D-printed plastic antennas [8] have also been demonstrated for use in mm-wave and THz applications. The structural integrity offered by solid metal construction is advantageous however, and 3D printing of pure metal alloys is also being investigated for constructing antennas. 3D printing using metal alloys has many of the same advantages as polymer printing with added structural integrity and possibly better longevity. It is not clear whether the fidelity obtainable with current metal printing technology is adequate for fabricating mm-wave antennas and what trade-offs may need to be considered.

The PolarCube feed horn, shown in Figure 2, was made from the aluminum alloy AlSi10Mg and fabricated using powder bead fusion (PBF) (colloquially refereed to as metal 3D-printing). AlSi10Mg is optimized for the PBF process and was chosen for its strength, hardness, and because its structural integrity is maintained even when formed into thin and complex shapes. Furthermore, this alloy can be machined and polished after the PBF process without loss of structural integrity. No supports were needed during the fabrication of the feed horn as the build direction was set such that the horn cone axis was aligned with gravity. After PBF the horn was finished with a glass bead blast to reduce surface roughness

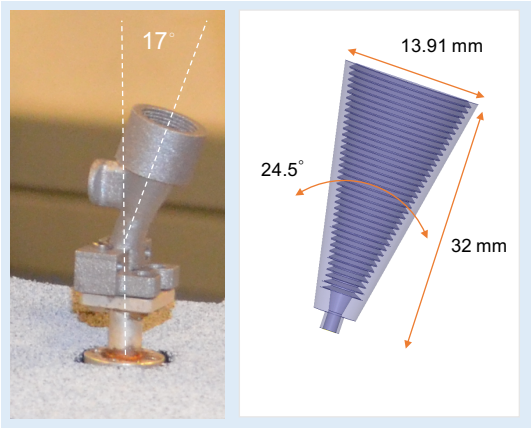


Fig. 2. (Left) Photograph of the 3D Printed metal AlSi10Mg feed horn. (Right) Schematic showing dimension of the feed horn conical section.

from an Ra of 300 $\mu in$ to 125 $\mu in$. The waveguide flange screw holes were made using a standard tap.

### B. Antenna Design

The horn was designed per [9] to support an $HE_{11}$ hybrid mode that is well matched to the main reflector. The horn is fed by a rectangular WR-08 waveguide which transitions to a circular cross section into the conical flare. This transition is further complicated in that it includes the necessary tilt angle of 17° used to angle the feed horn toward the main reflector. The feed horn was designed with a circular diameter aperture of $D = 13.91$ mm, cone angle $\theta_h = 24.5°$, and length (aperture-to-cone apex) $L = 32$ mm. The corrugations were optimized to a depth of $\approx 0.28\lambda$ with a spacing of $\approx \lambda/3$ and given a chamfer angle of $\approx 30°$ in order to provide proper mode conversion from the circular waveguide into the cone section. The horn therefore has many sub-mm and intricate mechanical features which make 3D printing worth investigating as a fabrication option.

## IV. Measurement Setup

### A. Robotic Antenna Range

Measurements were performed using the **C**onfigurable **Ro**botic **M**illi**m**eter-wave **A**ntenna facility (CROMMA) [10]-[13] at NIST Boulder, CO. The use of robotics allows multiple scan geometries to be executed autonomously using a single antenna alignment and electrical calibration. This capability allows for rapid antenna characterization since both near-field and in-situ extrapolation measurements could be made without the need to change setups, re-align antennas, or re-calibrate. With CROMMA, near-field measurements are achieved by using the robotic arm (see Figure 3) to scan a $\mu = \pm 1$ probe antenna [14] over a surface about the antenna under test (AUT). The AUT sits atop a 6-axis hexapod and rotator. To perform spherical scanning, the robot arm is moved along an arc ($\theta$ direction) while the AUT can be rotated ($\phi$ direction) creating a spherical geometry. Extrapolation scans

†Mention of this product is not an endorsement but only serves to clarify what was done in this work.



Gordon, Joshua; Novotny, David; Wittmann, Ronald; Francis, Michael; Guerrieri, Jeffrey; Lavanya, Periasamy; Gasiewski, Albin.
"Assessment of a 3D-Printed Aluminum Corrugated Feed Horn at 118.7503 GHz."
Paper presented at , Atlanta, GA, United States. October 15, 2017 - October 20, 2017.

are performed by scanning the probe along a linear path boresight between the AUT and probe antennas. A laser tracker and 6 degree of freedom (6Dof) optical targets are used to provide spatial metrology of the coordinate frames of the probe antenna, AUT, robot, hexapod, and rotator. Spatial metrology software was used to capture and manipulate laser tracker data for the alignment of the probe and AUT during measurements. The robotic arm can reconfigure itself based on this spatial metrology feedback with an accuracy of $< 25\ \mu m$ which enables autonomous changes between near-field and extrapolation scan geometries [10],[15]. This was used to perform in-situ extrapolation measurements in series with the near-field measurement. This sped up antenna characterization and allowed the extrapolation data to be used as diagnostics to optimize the near-field measurement (discuss below).

The $\mu = \pm 1$ probe antenna and feed horn apertures were directly measured with a laser tracker and PixelProbe [16] (a machine-vision-based touchless laser tracker probe). Images of the feed horn from the PixelProbe during the alignment process are shown in Figure 4. The corrugations and surface roughness resulting from the 3D printing process are clearly visible. In Figure 4 (top left) the white arrow points to a measurement location on the aperture where the active pixel (highlighted blue) of the PixelProbe was placed. The size of the blue pixel corresponds to the effective spatial resolution (i.e. pixel footprint). For this alignment the PixelProbe resolution used was $\approx$30 $\mu$m ($\lambda$/85 at 118 GHz). A series of measurements around the aperture perimeter were taken to construct the aperture geometry

and pose of the feed horn after the initial setup. Fitting a circle to these measurements produced an aperture radius of 13.98 mm. This is consistent with the intended aperture diameter of $D = 13.91$ mm and the known roughness of the aperture edge due to the 3D printing process. Translation and orientation offset errors in the initial setup alignment of the feed horn from the ideal measurement alignment were calculated using the spatial metrology software. These offsets were then input to the hexapod to align the center of the feed horn aperture to the origin of the spherical scan geometry while keeping the 17° tilt angle in $\theta$.

The scan arc and linear path for the spherical near-field and extrapolation measurements respectively are shown in Figure 5. Following these two paths are the stacks of coordinate frames which result from measuring the 6-Dof laser tracker target when tracking the probe antenna.

### *B. Millimeter-Waves*

A four-port 50 GHz vector network analyzer (VNA) and WR-08 frequency extenders were used to generate and detect mm-waves during measurements. The VNA was set up for two-port measurements. A short, offset-short, load, unknown through electrical calibration was performed over the full WR-08 band (90 GHz-140 GHz). The $\pm$ 180° phase ambiguity from the unknown through was able to be removed because of the full bandwidth calibration. The RF cables on the probe and AUT sides were stabilized with appropriate service loops

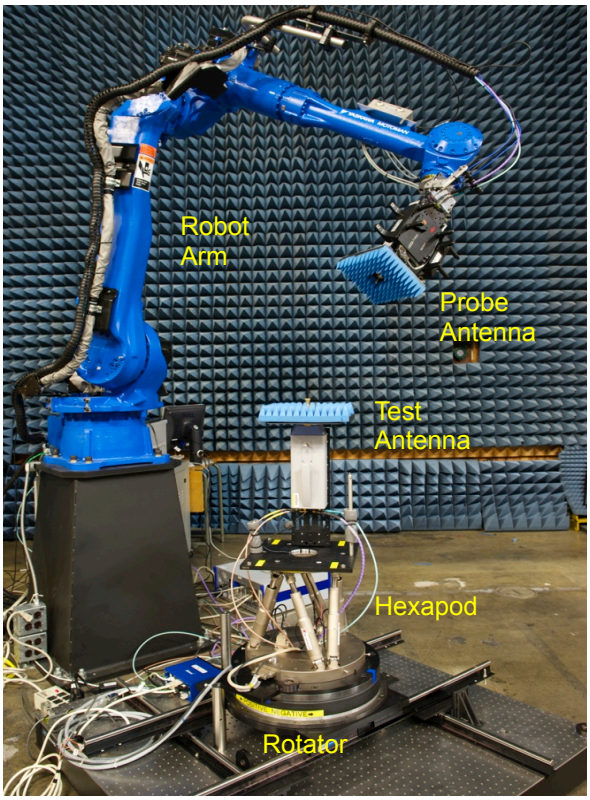


Fig. 3. The CROMMA facility. Main system components are shown: robotic arm, hexapod, rotator table, probe and test antenna locations.

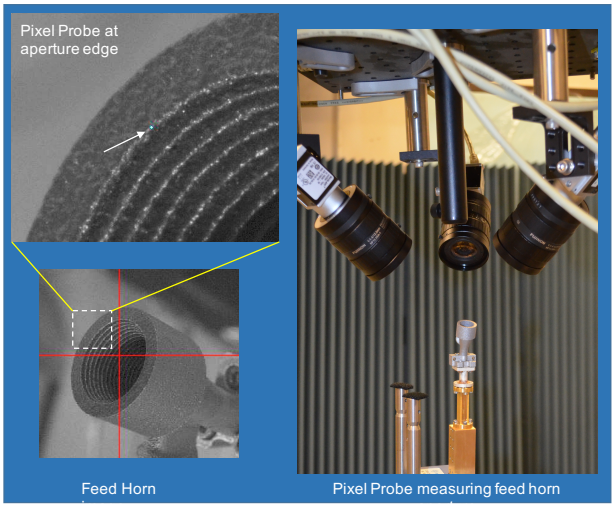


Fig. 4. (Right) Alignment measurement of feed horn using the PixelProbe. (Bottom Left) The feed horn as seen through one of the cameras of the PixelProbe where it is first centered in the red cross hairs. (Top Left) The pixel probe is positioned to measure the aperture edge. The white arrow points to the active pixel, highlighted in blue, that is used to measure a location on the edge of the aperture. Also visible is the surface roughness due to the 3D printing process.

†Mention of this product is not an endorsement but only serves to clarify what was done in this work.



Gordon, Joshua; Novotny, David; Wittmann, Ronald; Francis, Michael; Guerrieri, Jeffrey; Lavanya, Periasamy; Gasiewski, Albin.
"Assessment of a 3D-Printed Aluminum Corrugated Feed Horn at 118.7503 GHz."
Paper presented at , Atlanta, GA, United States. October 15, 2017 - October 20, 2017.

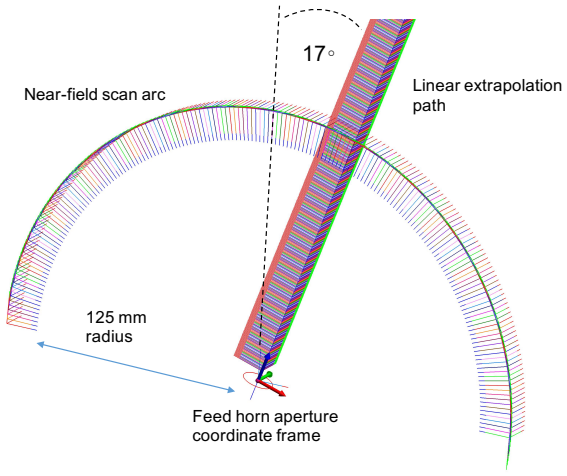


Fig. 5. Spatial metrology from the laser tracker showing the feed horn aperture and the dual scan geometries executed by the robotic arm. The stacks of coordinate frames for each probe antenna location along the extrapolation path and near-field arc are shown. The extrapolation path follows the 17° tilt angle of the feed horn aperture.

and mounting fixtures. The VNA was triggered externally by the robot controller I/O trigger output and preconditioned with a pulse generator to adjust timing of the VNA with the robot position. Amplitude and phase of S-parameters were captured at each probe measurement location along the spherical near-field scan arc.

## V. Antenna Measurements

### A. Extrapolation Measurements

Extrapolation measurements [17] were performed to determine the gain of the feed horn as well as to optimize the near-field scan radius for maximum dynamic range. During a near-field measurement dynamic range can be increased by reducing the probe-to-AUT distance. However, this comes at the cost of increased mutual coupling and reflections between the probe and AUT which reduces signal quality. The $HE_{11}$ mode of this feed horn has inherently very low sidelobes so it was important to increase the dynamic range (as measured from the main beam to noise floor) such that any sidelobe structure could be detected beyond $\pm 30^\circ$ of the main beam. Mutual coupling strength was determined from observing the oscillations in $|S_{11}|$ in the extrapolation measurement.

Data was taken every 400 $\mu$m ($\approx \lambda/6$ *at* 118.7503 GHz) as the probe was translated over a distance ranging from 15 mm to 400 mm to the the feed horn aperture. The separation distance at which these oscillations dropped to $\Delta|S_{11}| \leq 0.1$ dB (peak-to-peak) was taken as the closest radius usable for the near-field measurement. This turned out to be at a distance of 125 mm. The gain of the feed horn as determined from the extrapolation measurement was $G_{extrap} = 20.32$ dB $\pm$ 0.5 dB.

TABLE I
Measurement Parameters

| | |
|---|---|
| Scan Type | Spherical Scan |
| $\theta$ Range | $\pm 90^\circ$ |
| $\phi$ Range | $\pm 360^\circ$ |
| $\Delta\theta$ | $1^\circ$ |
| $\Delta\phi$ | $1^\circ$ |
| Operating Frequency | 118.7503 GHz |
| Wavelength | 2.54 mm |
| Measurement Radius | 125 mm |
| Positional Accuracy (rms) | $\lambda/100$ ($< 25$ $\mu$m) |
| Dynamic Range* | 70 dB |

**From main beam peak to noise floor*

### B. Spherical Near-field Measurements

The far-field pattern of the feed horn was also measured. Beam spill-over and sources of leakage into the optical train can affect radiometer calibration so it was important to characterize as much of the off-axis beam as posible. For PolarCube, the angle subtended by the main reflector as seen by the feed horn is $\approx 35^\circ$. Knowledge of the energy spillover outside this region is taken into account during radiometer calibration. Therefore, spherical near-field measurements were performed as opposed to planar [18] measurements in order to provide large solid angle coverage. With CROMMA the front hemisphere ($0 \leq \theta \leq +90^\circ, 0 \leq \phi \leq 360^\circ$) was able to be covered which allowed off-axis beam performance to be measured directly.

The far-field antenna pattern was obtained using the spherical near-field-to-far-field transform described in [14],[19]-[21]. The 125-mm scan radius determined via the extrapolation measurement was used for the spherical near-field scan. The effective radius, $r_0$ (as defined in Chapter 19 of [14]) of the volume enclosing the feed horn was taken to be 20 mm. This fully encompassed the feed horn and angled waveguide feed transition. Using this and the expression $\Delta\theta, \Delta\phi \leq 360/[2(kr_0 + 10) + 1]$ (given in Chapter 19 of [14]) an upper limit on the angular sampling step sizes over the scan arc was determined to be $\Delta\theta, \Delta\phi \leq 3.0^\circ$. An actual step size of $\Delta\theta = \Delta\phi = 1^\circ$ was used which is within the sampling criteria. The measured far-field pattern normalized to the peak for the front hemisphere ($0 \leq \theta \leq +90^\circ, 0 \leq \phi \leq 360^\circ$) for the total field $|E_{tot}|$ is shown in Figure 6($a$).

## VI. Feed Horn Simulation

Numerical simulations were performed to determine the theoretical gain and pattern of the feed horn. The ideal horn geometry was used. The finite element software package †Ansys HFSS (mention of this product is not an endorsement but only serves to clarify what was done) was used for this. The horn was modeled as being made from aluminum and perfectly matched layer radiation boundary conditions were used. Mesh optimization was also performed within regions containing critical structures such as inside the horn (including corrugations), and around the throat and aperture. The simulation was optimized until the change of $|S_{11}|$ at the input port of the

†Mention of this product is not an endorsement but only serves to clarify what was done in this work.



Gordon, Joshua; Novotny, David; Wittmann, Ronald; Francis, Michael; Guerrieri, Jeffrey; Lavanya, Periasamy; Gasiewski, Albin.
"Assessment of a 3D-Printed Aluminum Corrugated Feed Horn at 118.7503 GHz."
Paper presented at , Atlanta, GA, United States. October 15, 2017 - October 20, 2017.

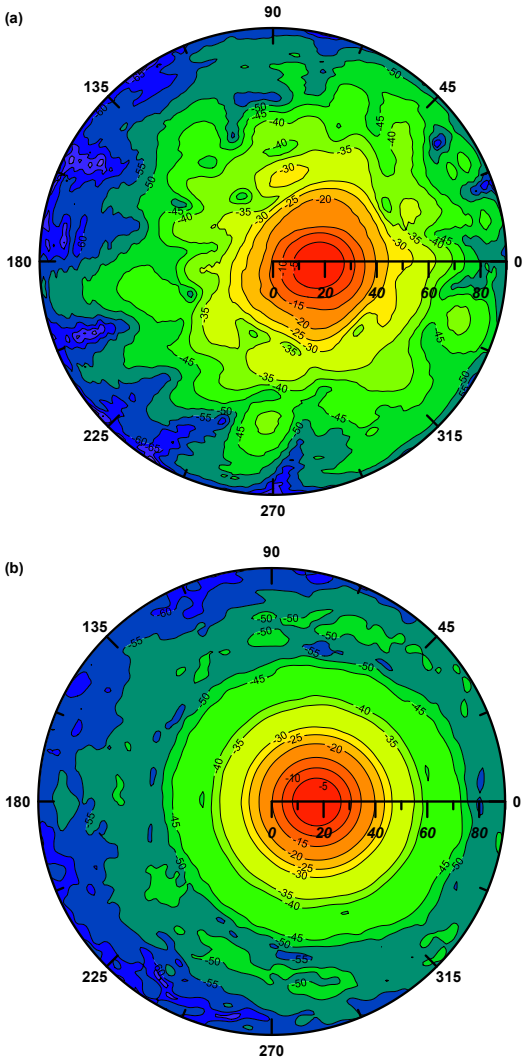


Fig. 6. Far-field patterns of the magnitude of the total electric-field over the front hemisphere of the feed horn. Patterns are normalized to the peak value. (a) Measured pattern. (b) Simulated pattern.

feed horn was reduced to $\Delta|S_{11}| < 0.003$ between iterations. The gain was determined to be $G_{sim} = 22.18$ dB from the simulation. The theoretical far-field pattern normalized to the peak for the front hemisphere $(0 \leq \theta \leq +90°, 0 \leq \phi \leq 360°)$ for the total field $|E_{tot}|$ is shown in Figure 6$(b)$.

## VII. Discussion

Comparing the simulated and measured gain and far-field patterns provides a measure of the antenna performance obtained using 3D printing. A comparison reveals a reduction in the gain between the simulated and actual feed horn. The gain determined from the simulation was 22.18 dB where as the measured gain was 20.32 dB.

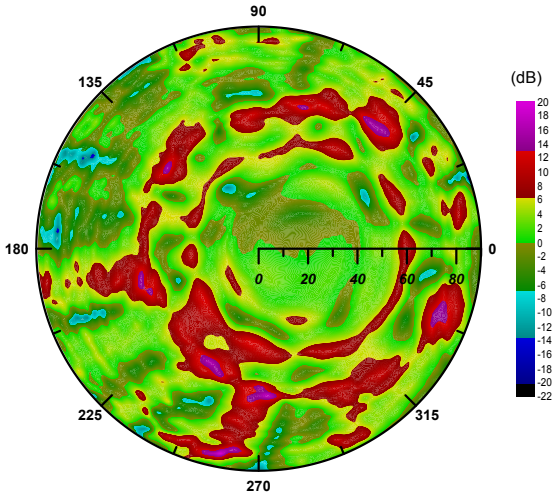


Fig. 7. dB difference between the measured and the simulated normalized far-field patterns.

Figure 7 shows the dB difference between the measured and simulated far-field patterns. The patterns themselves show good agreement within the first $\pm 20°$ centered on the main beam where the difference straddles the 0 dB level. The inflection in the difference appears at the $\theta = 17°$ near where the peaks overlap as they should. Past about $\pm 30°$ from the main beam larger differences between the two patterns appear due to more local structure and increased energy in the side lobes in the actual pattern versus the simulated pattern. This is indicative of roughness and imperfections in horn geometry imparting phase and amplitude errors across the aperture. A consequence of energy spreading into the side lobes is the reduction in the gain from the simulated performance. As the simulated pattern has circular symmetry about the main beam (as it should for an $HE_{11}$ mode) this local structure shows up as more drastic differences between the two patterns in excess of 10 dB in some places. Past about $\theta = 70°$ differences become dominated by simulation noise. However, averaging the difference within the $35°$ cone centered on the main beam (i.e. the angular subtense by the main reflector) shows a average agreement of $\approx 1.1$ dB. Having good agreement (i.e. close to 0 dB) between the measured and simulated performance within the -3 dB beam width from the main beam was most important for this application. These results show that this is indeed the case, and that 3D printing the feed horn out of aluminum is a viable option for this CubeSat application.

## VIII. Conclusion

We present a comparison of the measured and theoretical performance of a corrugated conical feed horn 3D-printed

†Mention of this product is not an endorsement but only serves to clarify what was done in this work.



Gordon, Joshua; Novotny, David; Wittmann, Ronald; Francis, Michael; Guerrieri, Jeffrey; Lavanya, Periasamy; Gasiewski, Albin.
"Assessment of a 3D-Printed Aluminum Corrugated Feed Horn at 118.7503 GHz."
Paper presented at , Atlanta, GA, United States. October 15, 2017 - October 20, 2017.

from the solid aluminum alloy AlSi10Mg using the powder bead fusion process. The feed horn was designed for the radiometer payload of the CubeSat PolarCube and operates at the atmospheric oxygen line of 118.7503 GHz. Spherical near-field and gain extrapolation measurements were performed at the CROMMA facility at NIST in Boulder CO. The far-field antenna pattern over the front hemisphere of the feed horn was obtained using the spherical near-field to far-field transform.

In-situ $S_{11}$ extrapolation data were used to determine the optimum near-field scan radius in order to maximize dynamic range. This allowed sidelobe structure in the feed horn pattern to be detected up to 70 dB below the main beam peak while keeping mutual coupling between the probe antenna and feed horn to $\Delta|S_{11}| \leq$0.1 dB (peak-to-peak). Numerical simulations of the feed horn were used to determine theoretical performance (pattern and gain). From these measurements it was determined that the gain of 3-D printed horn was 20.32 dB $\pm$0.5 dB, where as the simulated gain was 22.18 dB. The far-field patterns showed good agreement within $\pm 30^\circ$ of the main beam. The average difference within the $35^\circ$ cone centered on the main beam (i.e. the angular subtense by the main reflector) shows agreement of $\approx$ 1.1 dB. Within the -3 dB beam width from the main beam agreement hovered around 0 dB which was most important for this application. These results show that 3D printing the feed horn out of aluminum is a viable option for this CubeSat application.

## ACKNOWLEDGMENTS

Special thanks goes to Glenda Alvarenga, Brian Sanders and the Polar Cube team at the University of Colorado Space Grant Consortium for providing the feed horn, support on the systems and designs for Polar Cube and for many helpful discussions.

## REFERENCES

[1] F. Khan, "Mobile Internet from the Heavens", arXiv:1508.02383, Aug (2015).

[2] L. Periasamy, A.J. Gasiewski, et al., "Pre-launch Calibration and Performance Study of the PolarCube 3U Temperature Sounding Radiometer Mission". Radio Science Meeting (USNC-URSI NRSM), 2016 United States National Committee of URSI National. IEEE, 2016.

[3] L. Periasamy, A.J. Gasiewski, "Precision Design, Analysis And Manufacturing of Quasi-Optic Lens/Reflector Antenna Systems for CubeSat MMMW/SMMW Radiometers", IEEE APS Symp. Ant. and Prop, Vancouver, Canada, July 2015.

[4] A.J. Gasiewski and J.T. Johnson, "Statistical Temperature Profile Retrievals in Clear-Air Using Passive 118-GHz $O_2$ Observations," IEEE Trans. Geo. Sci. Rem. Sensing, vol. 31, 1993.

[5] Klein, Marian, and Albin J. Gasiewski. "Nadir sensitivity of passive millimeter and submillimeter wave chan- nels to clear air temperature and water vapor variations. Journ. of Geo. Re. : Atmo (1984- 2012) 105.D13 (2000): 17481-17511.

[6] P. Nayeri, M. Liang, R. A. Sabory-Garc, M. Tuo, F. Yang, M. Gehm, H. Xin, and A. Z. Elsherbeni, "3D Printed Dielectric Reflect Arrays: Low-Cost High-Gain Antennas at Sub-Millimeter Waves", IEEE Trans. Ant. Prop, vol. 62, no. 4, pp. 2000-2008, 2014.

[7] Z. Wu, J. Kinast, M. E. Gehm, and Hao Xin, "Rapid and inexpensive fabrication of terahertz electromagnetic bandgap structures", Opt. Expr. vol. 16, no. 21, pp. 16442-16451, 2008.

[8] A. Macor, E. de Rijk, S. Alberti, T. Goodman, and J-Ph., "Note: Three-dimensional stereolithography for millimeter wave and terahertz applications" , Rev. Sci. Inst. 83, pp. 046103, 2012.

[9] Clarricoats, P.J.B. and A.D. Olver, "Corrugated Horns for Microwave Antennas," IEE Electromagnetic wave series 18, 1984.

[10] J. A. Gordon, D. R. Novotny, M. H. Francis, R. C. Wittmann, M. L. Butler, A. E. Curtin, J. R. Guerrieri, "Millimeter-Wave Near-Field Measurements Using Coordinated Robotics", IEEE Trans. Ant. Prop, vol. 63, no. 12, pp. 5351- 5362, 2015.

[11] J. A. Gordon, D. R. Novotny, J. B. Coder, J. R. Guerrieri and B. Stillwell, "Robotically controlled mm-wave near-field pattern range", Proc. Antenna Meas. Tech. Assoc., vol. 34, pp. 384-389, 2012.

[12] J.A. Gordon, D. Novotny, M. Francis, R. Wittmann and J. Guerrieri, "The CROMMA Facility at NIST Boulder: A unified coordinated metrology space for millimeter-wave antenna characterization", Proc. Antenna Meas. Tech. Assoc., vol. 36, pp. 351-356, 2014.

[13] M.H. Francis, R.C. Wittmann, D.R. Novotny, J.A. Gordon, "Spherical Near-Field Measurement Results at Millimeter-Wave Frequencies Using Robotic Positioning", Proc. Antenna Meas. Tech. Assoc. vol. 36, pp. 231-234, 2014.

[14] C. A. Balanis, "Modern Antenna Handbook", John Wiley and Sons, 2008.

[15] D. R. Novotny, J. A. Gordon, M. Francis, R. Wittmann, A. E. Curtin, J. R. Guerrieri, "Antenna Measurement Implementations and Dynamic Positional Validation Using a Six Axis Robot", Proc. Antenna Meas. Tech. Assoc., vol. 37, pp. 15-20, 2015.

[16] J. A. Gordon, D. R. Novotny, A. E. Curtin, "A Single Pixel Touchless Laser Tracker Probe", The Journal of the CMSC, Vol. 10, No. 2, pp. 12-21. , Autumn 2015.

[17] A. C. Newell, R. C. Baird, AND P. F. Wacker, "Accurate Measurement of Antenna Gain and Polarization at Reduced Distances by an Extrapolation Technique", Trans. Ant. Prop., vol. AP-21, No.4, 1973.

[18] D. M. Kerns and E. S. Dayhoff, "Theory of diffraction in microwave interferometry", J. Res. Natl. Bur. Stand., Vol. 64B, pp. 1-13, 1960.

[19] P. F. Wacker, "Non-planar near-field measurements: spherical scanning", National Bureau of Standards (U.S.), NBSIR 75-809, June 1975.

[20] J.E. Hansen, "Spherical Near-Field Antenna Measurements", Peter Peregrinius Ltd., 1988.

[21] R. C. Wittmann and C. F. Stubenrauch, "Spherical near-field scanning: experimental and theoretical studies", National Institute of Standards and Technology Internal Report NISTIR 3955, 1990.

†Mention of this product is not an endorsement but only serves to clarify what was done in this work.



Gordon, Joshua; Novotny, David; Wittmann, Ronald; Francis, Michael; Guerrieri, Jeffrey; Lavanya, Periasamy; Gasiewski, Albin.
"Assessment of a 3D-Printed Aluminum Corrugated Feed Horn at 118.7503 GHz."
Paper presented at , Atlanta, GA, United States. October 15, 2017 - October 20, 2017.

# Serial Robotic Arm Joint Characterization Measurements for Antenna Metrology

Michael S. Allman, David Novotony,
Joshua Gordon, Alex Curtin
Communications Technology Laboratory
National Institute of Standards and Technology
Boulder, CO, USA
mallman@nist.gov

Scott Sandwith
New River Kinematics
Williamsburg, VA, USA
scott@kinematics.com

***Abstract*— We improved the accuracy of our six-axis serial robotic arm used for antenna characterization measurements by calibrating a kinematic robot model based on our robot's physical dimensions. The model was calibrated over a 0.4 $m^3$ working cell. We validated the calibration using a 1 $m^2$ plane embedded within the calibration cell. The positioning errors for the calibrated case showed a fourfold improvement in accuracy as compared to the uncalibrated case. For a maximum positioning error tolerance of λ/50, the calibrated model should allow for open-loop antenna characterization measurements up to 35 GHz.**

***Keywords*— Antennas, near-field measurements, positioning, gain, pattern.**

## I. Introduction

The accurate alignment of antennas and field probes is a critical aspect of modern antenna metrology systems, particularly in the millimeter-wave region of the spectrum, [1,2,3]. Commercial off-the-shelf robotic arms provide a sufficient level of positional accuracy for many industrial applications [4]. However, to be useful for millimeter-wave antenna metrology, robotic arms need to be operated in conjunction with spatial metrology equipment. The Antenna Metrology Project in the Communications Technology Laboratory at the National Institute of Standards and Technology has shown that path-corrected commercial robotic arms, both in hardware and software analysis, can be used to achieve sufficient positioning and alignment accuracies (positioning error ~ λ/50) for antenna characterization measurements such as gain extrapolation and near-field pattern up to 183 GHz [3].

The robot used in this work is a six-axis serial robotic arm. Each link is manipulated by a revolute joint. Starting at the base of the robot and working toward the end link, the joints are labeled (Fig 2.) J0: Base, J1: Sweep (S), J2: Lower (L), J3: Upper (U), J4: Roll (R), J5: Bend (B), J6: Twist (T). The orientation of each link is described by a conceptual coordinate system, called a "link frame", firmly affixed to each link [5]. Attached to the T joint is a flange that allows the attachment of the robot "end effector." The end effector can be any object that performs some function (e.g. drill, welder, mechanical gripper, laser, probe antenna etc.). At some location on the end effector, exists the tool control point (TCP) frame. This frame defines the robot's position and orientation. The robot controller uses a kinematic model to calculate the joint angles required to move the TCP to a commanded position and orientation in space. In this work, the accuracy of the robot refers to the relative error (both offset and orientation) between the robot's commanded TCP position and the actual TCP position. This error is directly related to the accuracy of the parameters that comprise the kinematic model used by the controller.

There are two methods to compensate the robot position accuracy performance. First, a spatial metrology system, in this case a laser tracker with a 6-degree-of-freedom (6DOF)

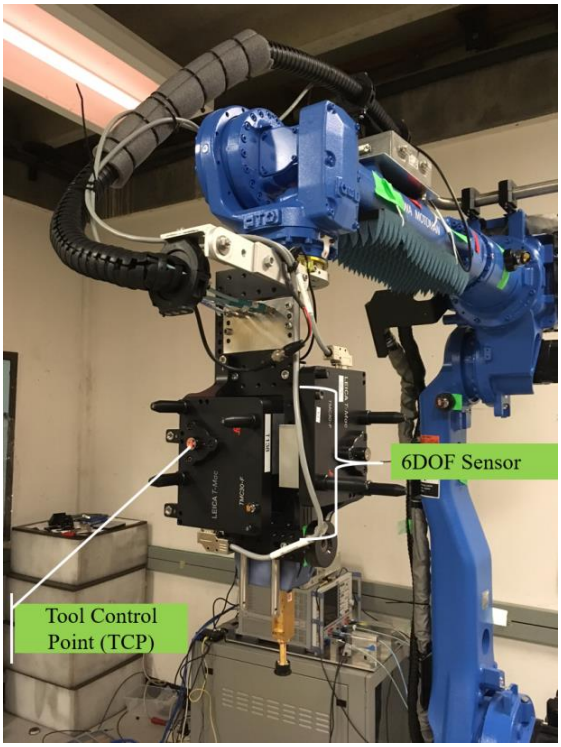


Figure 1. Robot showing end effector and TCP location.

Allman, Michael; Novotny, David; Gordon, Joshua; Curtin, Alexandra; Sandwith, Scott.
"Serial Robotic Arm Joint Characterization Measurements for Antenna Metrology."
Paper presented at 39th Annual Meeting and Symposium of the Antenna Measurement Techniques Association (AMTA), Atlanta, GA, United States. October 15, 2017 - October 20, 2017.

sensor acting as the robot's TCP (Fig. 1), can be used to iteratively correct the robot's TCP position until it is within tolerance of its goal position and orientation [3,6]. This technique is called Move-Measure-Correct (MMC). When using the MMC technique, the TCP's actual position is measured using the laser tracker and compared to its commanded goal position as the TCP moves through its intended path. A real-time path correction based on these comparisons is iteratively applied to the robot until the desired level of accuracy is achieved in the frequency range of interest. This "closed loop" method of robot motion control results in the most accurate TCP positioning and requires minimal a priori knowledge of the robot link frames, but requires that the positioning metrology system constantly monitor the TCP position during the measurement. In an actual antenna measurement, the TCP would reside centered on the aperture of a probe antenna, requiring knowledge of an additional frame transformation between the 6DOF sensor and the TCP. We already have an accurate means for measuring that transformation [7].

At lower frequency ranges (< 40 GHz), a second method to improve positioning accuracy can be employed where the metrology system is used to acquire a calibrated model of the robot [6, 8]. This technique has the advantage that after the calibration is performed and used to compute accurate robot poses, the metrology system is not needed in the cell to provide real-time path corrections while the robot is in motion. However, the success of this approach hinges on improved knowledge of the robot link frame transforms. This paper will focus on the calibration process and results using this second "open loop" technique to improve robot accuracy.

The complete calibrated robot model can be divided into two sets of parameters. The first set, referred to here as an extrinsic calibration, establishes the robot base frame and TCP transforms (Fig 2). The second, intrinsic, set of parameters establishes an improved kinematic model of the robot. In other words, the extrinsic calibration solves for where the robot is relative to the world frame and the intrinsic calibration optimizes the robot's kinematic model. The kinematic model is based on knowledge of the link frame transformations between adjacent links and can also model deviations due to gravitational loading on the joints and small mechanical offsets between the joints. Each link frame, *i*, is described by four physical quantities, known as Denavit-Hartenberg (DH) parameters [5]:

- $a_i$ is the length of the common normal line between the ith and (i+1)th joint rotation axes. These axes also define $Z_i$ and $Z_{i+1}$ respectively.
- $\alpha_i$ is the angle between $Z_i$ and $Z_{i+1}$ as a rotation about $X_i$.
- $d_i$ is the distance between $X_{i-1}$ and $X_i$ as measured along $Z_i$.
- $\theta_i$ is the angle from $X_{i-1}$ to $X_i$ as a rotation about $Z_i$.

The parameter, $a_i$, is commonly referred to as the "link length", parameter, $\alpha_i$, the "twist angle", parameter $d_i$, the "length offset", and parameter $\theta_i$, the "joint angle." The

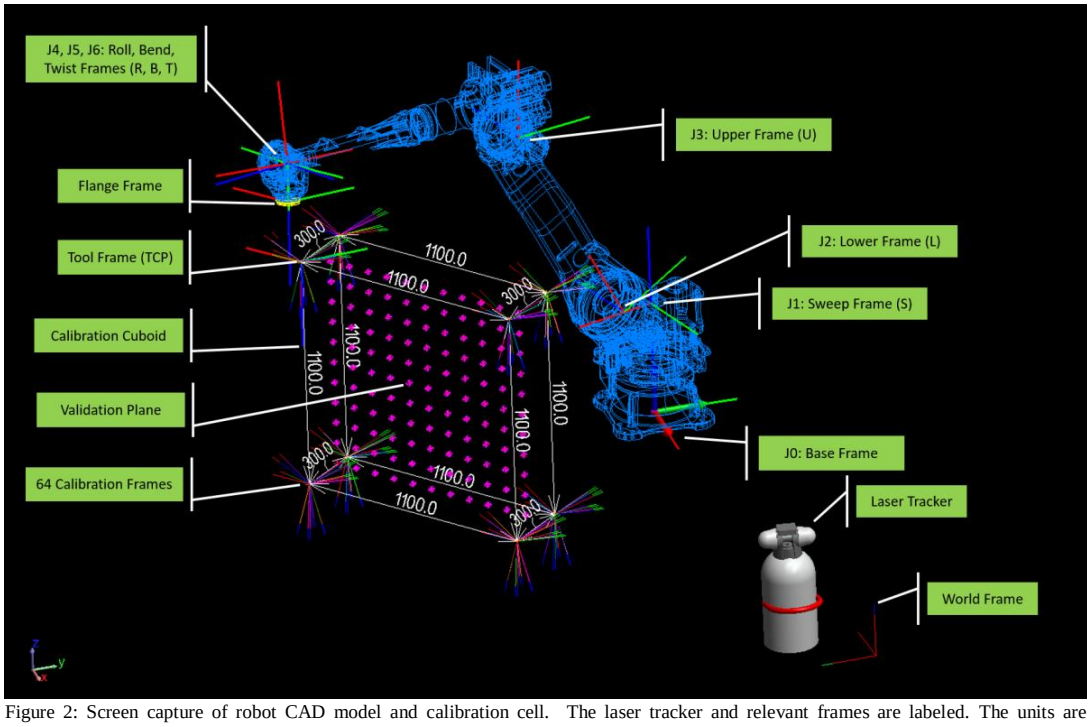


Figure 2: Screen capture of robot CAD model and calibration cell. The laser tracker and relevant frames are labeled. The units are millimeters.

transform between the (i-1)th and ith link frame in terms of the DH parameters is:

$$ {}^{i-1}_{i}T = \begin{bmatrix} \cos(\theta_i) & -\sin(\theta_i) & 0 & a_{i-1} \\ \sin(\theta_i)\cos(\alpha_{i-1}) & \cos(\theta_i)\cos(\alpha_{i-1}) & -\sin(\alpha_{i-1}) & -d_i \sin(\alpha_{i-1}) \\ \sin(\theta_i)\sin(\alpha_{i-1}) & \cos(\theta_i)\sin(\alpha_{i-1}) & \cos(\alpha_{i-1}) & d_i \cos(\alpha_{i-1}) \\ 0 & 0 & 0 & 1 \end{bmatrix} \quad (1) $$

Robot joint-link deflection is modeled as rotation about the link XYZ axes respectively as a linear torsional spring constant. The deflection is compensated by computing a joint angle to counter the deflection based on load and robot pose. Although our calibration software can model deflection, the focus of the work presented here was to investigate the accuracy limits of our robot with a simpler kinematic model that does not account for gravity.

## II. Calibration Procedure

### A. Software

For the calibration procedure, we wrote a custom software application called "NIST Robot Calibrator (NRC)" to interface with the robot controller and New River Kinematics Spatial Analyzer (SA) Machine Software†. NRC provides an easy-to-use automated software development kit (SDK) interfaced into SA's robot calibration functionality to configure and solve for the robot calibration in our test range. Additionally, the NRC application automates measurement configuration and acquisition for the laser tracker and interfaces to the robot controller to automate manipulating the physical robot.

A complete, nominal kinematic SA model of the robot was developed based on CAD models from the robot manufacturer. This robot model provided nominal joint-link frame parameters (DH parameters) as well as a method to visualize robot motion in SA. Fig. 2 shows the robot model and the link frames laid over the CAD model from the robot manufacturer.

### B. Calibration Cell

Using the NRC software, we defined the corners of a cuboid in SA. Centered on each of these 8 corners, 8 virtual frames were created at orientations of +/- 20 degrees about each axis of rotation. The orientations of the corner frames had to be chosen carefully so that the 6DOF sensor remained in view of the laser tracker for all the calibration poses. We then commanded the robot model to align its TCP frame with each of the 64 frames. Sets of robot joint angles for each frame where then computed using inverse kinematics based on the relative position of the robot base and the SA model of the robot. The physical robot was moved to each joint set where the actual position of the TCP was measured by the spatial metrology system and the actual joint encoder count was read from the robot controller. Encoder counts were converted to joint degrees. The resulting measured TCP frames and the achieved joint angles for each pose were fed into SA's kinematic optimization routine that outputs offsets to correct the intrinsic and extrinsic robot parameters such that the errors between the TCP's target poses and achieved poses were minimized.

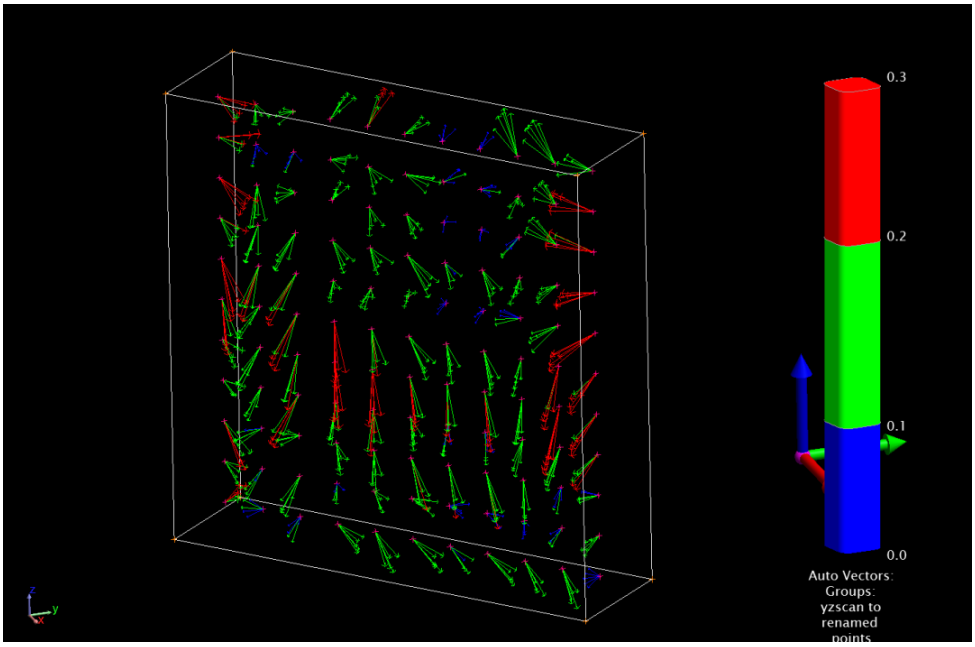


Figure 3. Calibration validation over 1 $m^2$ planar surface. Five separate validation results are shown. The error vectors are magnified 500 X. The green vectors are within 1 std of the mean. The red vectors are above the mean. The blue vectors are below the mean. The units are millimeters.

† Mention of this product is not an endorsement but only serves to clarify what was done in this work. U.S. Government work. Not protected by copyright.

Allman, Michael; Novotny, David; Gordon, Joshua; Curtin, Alexandra; Sandwith, Scott.
"Serial Robotic Arm Joint Characterization Measurements for Antenna Metrology."
Paper presented at 39th Annual Meeting and Symposium of the Antenna Measurement Techniques Association (AMTA), Atlanta, GA, United States. October 15, 2017 - October 20, 2017.

### C. Two-Step Calibration

The calibration was performed in two steps. The first step was an extrinsic calibration to position the robot model's base frame to within a few millimeters of its physical lab location with respect to the laser tracker. Initially, the robot model was aligned to the default world frame whose orientation with respect to the laser tracker is arbitrary. Additionally, the robot model's initial TCP frame transform with respect to the end link was set to zero. The initial calibration was performed using a cubic calibration cell of volume ~1/8 $m^3$; centered in front of the robot. Once the robot model's base and TCP transforms were roughly aligned to the laser tracker, we adjusted the calibration cell so that we could validate the calibration using a planar surface, nominally 1$m^2$ in area embedded inside the cuboid. We biased the cuboid to the (+X,-Y,+Z) quadrant of the robot's base frame (shown in Fig. 2) to keep the robot's center of gravity forward of the robot base while keeping the 6DOF target beyond the laser tracker's 1.5 m minimum range limit. Figure 2 shows the calibration cuboid with virtual pose frames at each corner.

### D. Choosing Fit Parameters

Depending on the range of motion of each robot joint pose used in the calibration, some fit parameters may be dependent on each other. In fact, some parameters will always be dependent. For example, an offset in the θ DH parameter for the S link frame (S(θ), Fig. 2) can always be perfectly negated by an offset Z-rotation of the robot base frame (Base($R_z$)). Thus S(θ) and Base($R_z$) should never be included together in the optimization. Additionally, any link frame whose Z rotation axis is nominally parallel to the previous link's Z rotation axis should not include the link offset parameter (d) in the fit, since there exists an infinite number of possible link offsets that can be chosen for that link configuration. Determining the best subset of DH parameters to optimize over in a given calibration cell is part of the "art" of acquiring a good kinematic model of the robot. The correlation matrix between the fit parameters (automatically generating by SA) provides good insight into which parameters are too strongly correlated to be fit simultaneously. Table 1 lists the link parameters that were fit.

TABLE 1. DH Parameters optimized in calibration.

| Joint | DH Parameter | | | |
|---|---|---|---|---|
| | ***α*** | ***A*** | ***d*** | ***θ*** |
| S | | | | |
| L | ✓ | ✓ | ✓ | ✓ |
| U | ✓ | ✓ | | ✓ |
| R | ✓ | ✓ | ✓ | ✓ |
| B | | ✓ | ✓ | ✓ |
| T | ✓ | ✓ | | |

### E. Optimization Results

The initial DH values used in the kinematic solver were a combination of nominal values reported by the robot manufacturer and values that we could directly measure in the lab. By moving the joints S, L, U, and R independently while tracking their positions with the spatial metrology system, we could directly measure their link lengths or link offset (depending on the axis). The link lengths/link offsets for B and T could not be measured because their link frames nominally coincide. Table 2 lists the DH parameter starting values and the corrections output by the optimization routine for this calibration.

Table 2. DH parameter initial values and corrections

| Joint | DH Parameter | | | |
|---|---|---|---|---|
| | α (deg) | a (mm) | d (mm) | θ (deg) |
| S (initial value) | 0 | 0 | 540 | 0 |
| S (correction) | n/a | n/a | n/a | n/a |
| L (initial value) | 90.0000 | 144.967[a] | 0 | 0 |
| L (correction) | -0.0064 | -2.4375 | 0.27615 | 0.11663 |
| U (initial value) | 0 | 1151.3155[a] | 0 | 0 |
| U (correction) | 0.0218 | 0.4283 | n/a | -0.0265 |
| R (initial value) | 90 | 210.5065[a] | 1224.7863[a] | 0 |
| R (correction) | 0.00133 | -0.8884 | 0.2665 | -0.0119 |
| B (initial value) | 90 | 0 | 0 | 0 |
| B (correction) | n/a | -0.1858 | -0.1618 | -0.0317 |
| T (initial value) | -90 | 0 | 0 | 90 |
| T (correction) | 0.0153 | -0.0903 | n/a | n/a |

[a] Directly measured

The correction offset for DH parameter, a, for joint L seems excessive. Physically, this parameter describes the normal distance between the S and L rotation axes. We do not believe this distance to deviate from the nominal value by such a large degree. We suspect this offset is an indication that the robot kinematics could be improved by adding deflection to the model. Future work will attempt to verify if our suspicions are correct.

## III. Calibration Validation

### A. Validation Using Calibrated Model

We validated this calibration using a 1 $m^2$ planar grid of points embedded in the cuboid. The spacing between points was 100 mm. A grid of this type represents a typical near-field planar scan geometry. Fig. 2 shows the validation plane inside the cuboid. The TCP offset error vectors (magnified 500×) for five separate validation scans, taken on different days, are shown. The mean offset error magnitude of all five scans was 170 µm. The maximum offset error was 339 µm. The minimum offset error was 20 µm. The overall standard deviation was 64 µm. Table 3 lists the results for the individual scans.

TABLE 3. Calibrated model validation scan results

| Scan | Offset Error Magnitude (µm) | | | |
|---|---|---|---|---|
| | **Mean** | **Std** | **Max** | **Min** |
| 1 | 189 | 68 | 339 | 26 |
| 2 | 169 | 61 | 294 | 22 |
| 3 | 175 | 65 | 316 | 20 |
| 4 | 155 | 58 | 280 | 34 |
| 5 | 160 | 59 | 291 | 30 |

Allman, Michael; Novotny, David; Gordon, Joshua; Curtin, Alexandra; Sandwith, Scott.
"Serial Robotic Arm Joint Characterization Measurements for Antenna Metrology."
Paper presented at 39th Annual Meeting and Symposium of the Antenna Measurement Techniques Association (AMTA), Atlanta, GA, United States. October 15, 2017 - October 20, 2017.

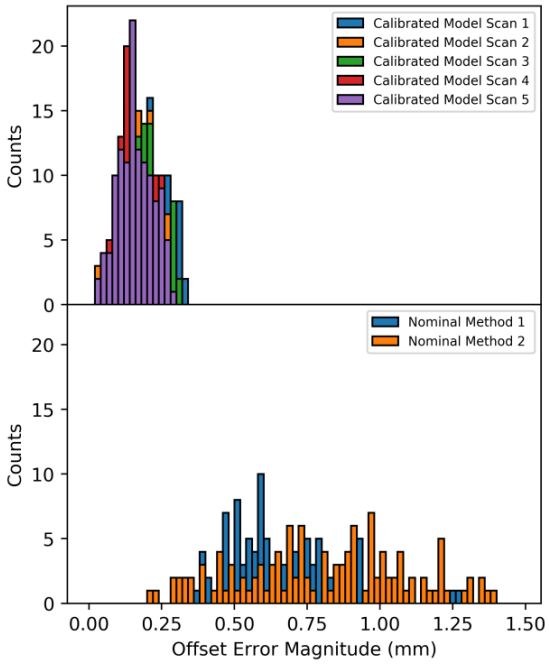


Figure 4. Offset error magnitudes of the validation scans for the calibrated model and the nominal robot model. The overall mean offset error magnitude was 170 µm with 64 µm standard deviation. The uncalibrated model mean offset error magnitude was 696 µm with a 225 µm standard deviation.

### *B. Validation Using Nominal Model (For Comparison)*

#### *1) Method 1 (Extrinsic Calibration)*

We also performed the same validation scan using the nominal kinematic model of the robot using two different methods. For the first method, we performed only an extrinsic calibration of the robot model, fitting only the robot model's base and tool transform offsets and orientations. The DH parameters used in the kinematic model we held fixed at their nominal or lab-measured values. The scan poses were calculated using this partially calibrated model. These poses were applied to the physical robot and measured using the same validation plane for the fully-calibrated case.

#### *2) Method 2 (Robot Controller Base Frame)*

For the second method, we used the physical robot's internal base frame as the reference frame. To do this, we had to locate the physical robot's internal base frame in SA. This procedure involved two primary steps. We first input the tool offset into the robot controller using a tool alignment calibration procedure programmed into the robot controller. Once the tool parameters were set, we then drove the robot to a set of (X,Y,Z) positions with respect to the physical robot's internal base frame and measured these positions with the laser tracker. In SA, the measured frames were back-transformed using the coordinate values reported by the robot controller. The resulting cluster of frames centered on the physical robot's base frame location in SA was then averaged. Once this frame was set in SA, the validation coordinates with respect to the physical robot's base frame were programmed into the robot controller and measured. The purpose of this lengthy second method of uncalibrated validation was to simulate how a user would typically perform a planar scan without the benefit of robot calibration software

#### *3) Results*

Table 4 lists the results of the method 1 and method 2 uncalibrated scans. Fig. 4 shows histograms of the validation scan plane offset error magnitudes for the calibrated and uncalibrated validation scans. In Fig. 5 histograms of the (X,Y,Z) projections of the offset errors in the robot base frame coordinate system are shown for calibrated model scan 1 and nominal model method 1. The X and Y components showed the largest improvement with the calibration. The Z components showed essentially no difference between the calibrated and nominal model. Fig.6 shows the orientation errors for the same scans shown in Fig. 5. These orientations are with respect to the target frame at each validation plane point. For each validation point, only a single frame was used. To calculate the orientation of the measured frame with respect to the nominal target frame, first an X rotation ($R_x$) is performed, then a Y rotation ($R_y$), then a Z rotation ($R_z$) about the nominal frame X,Y, and Z axes. Table 5 lists the mean orientation errors. The uncertainties are 1 std values.

TABLE 4. Uncalibrated validation scan results.

| Scan | Offset Error Magnitude (µm) | | | |
|---|---|---|---|---|
| | **Mean** | **Std** | **Max** | **Min** |
| Method 1 | 694 | 228 | 1311 | 320 |
| Method 2 | 803 | 288 | 1397 | 203 |

TABLE 5. Orientation errors.

| Rotation Axis | Orientation Error (degrees) | |
|---|---|---|
| | **Calibrated** | **Uncalibrated** |
| $R_x$ | $(5.3 \pm 9.8) \times 10^{-3}$ | $(10.0 \pm 15.4) \times 10^{-3}$ |
| $R_y$ | $(4.0 \pm 6.1) \times 10^{-3}$ | $(-0.7 \pm 17.0) \times 10^{-3}$ |
| $R_z$ | $(-2.7 \pm 13.8) \times 10^{-3}$ | $(0.0 \pm 14.1) \times 10^{-3}$ |

### C. *Mechanical Hysteresis*

Some level of mechanical hysteresis is always present when dealing with positional manipulators and our robot is no different. Intuitively, we expect the degree of hysteresis to be a limiting factor in achievable positioning accuracy. We measured the hysteresis for each joint by performing repeated movements of each link to a nominal position from opposing directions. The measured points from each direction were averaged and the distance between the averaged points was divided by the radial distance of the averaged point to the axis of rotation. Table 6 lists our backlash measurements. The combined cluster of measured points was averaged resulting in an RMS deviation of 91 µm. Thus, we expect this value to be close to the ultimate accuracy limit achievable with our robot for bi-directional joint movement.

Table 6. Joint mechanical hysteresis measurements.

| Joint | Hysteresis (deg) |
|---|---|
| S | $(8.6 \pm 0.4) \times 10^{-3}$ |
| L | $(1.4 \pm 0.4) \times 10^{-3}$ |
| U | $(1.6 \pm 0.2) \times 10^{-3}$ |
| R | $(8.0 \pm 0.6) \times 10^{-3}$ |
| B | $(14.8 \pm 1.0) \times 10^{-3}$ |
| T | $(46.4 \pm 2.2) \times 10^{-3}$ |

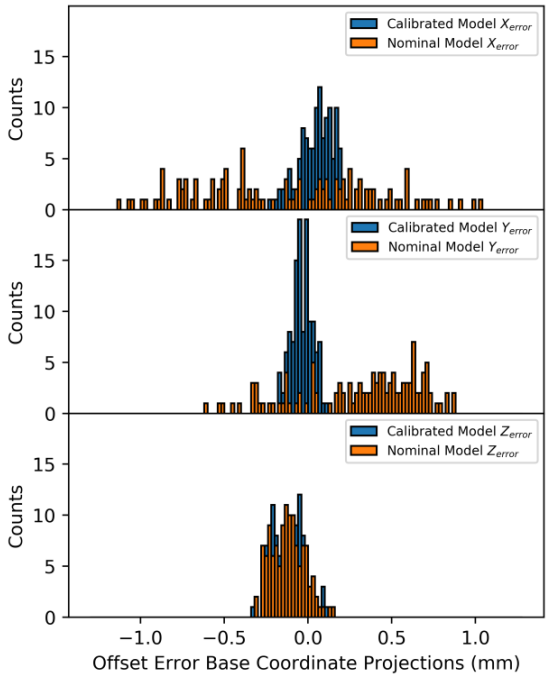


Figure 5: XYZ projections of the offset error in the robot base coordinate system. The X and Y components showed the largest improvement using the calibrated model. The Z component showed essentially no improvement.

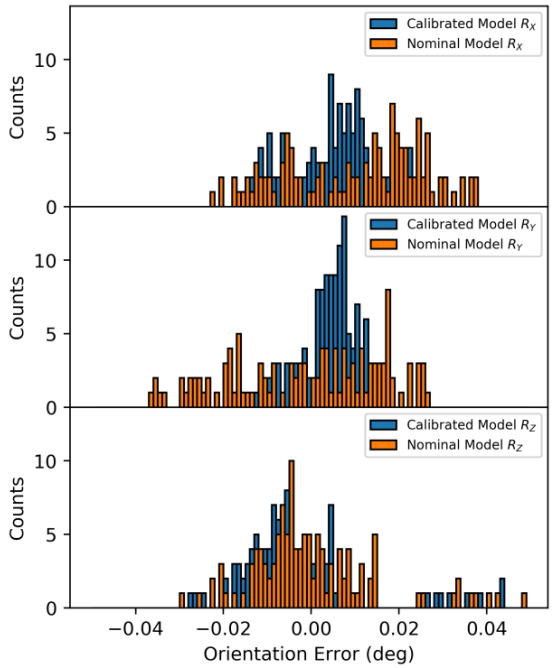


Figure 6. Orientation errors with respect to the nominal target frame for calibrated and uncalibrated validation scans.

## IV. Conclusion

In summary, we have developed a calibrated kinematic model of our six-axis robot using an optimization routine provided by SA. We developed custom software to interface with SA and the robot controller, that provides a simple user interface to create a custom calibration cell, automate robot motion, calculate robot pose joint angles and configure the spatial metrology system. Using our custom software interface, we performed an intrinsic and extrinsic calibration of our robot over a 0.4 $m^3$ cell. We validated the calibration using a 1 $m^2$ planar grid embedded within the calibration cell and compared the TCP offset and orientation errors with the same measurements using an uncalibrated model. We also measured the mechanical hysteresis of each joint to get an estimate of the ultimate achievable accuracy of the calibrated robot. Our calibrated model showed a fourfold improvement in accuracy compared to the uncalibrated model. Using a maximum positioning tolerance error of $\lambda/50$, the calibrated robot model should allow for open loop antenna characterization measurements up to approximately 35 GHz. Future work will investigate accuracy improvements by adding gravitational deflection to the kinematic model. Additionally, we will test the dynamic accuracy of the calibrated robot model.

## References

[1] J. Hatzis, P. Pelland, G. Hindman, "Implementation of a Combination Planar and Spherical Near-Field Antenna Measurement System using an

Industrial 6-Axis Robot" Proceedings of the Antenna Measurements Techniques Association, pp 416-422, 2016

[2] F. Ferrero, Y. Benoit, L. Brochier, J. Lanteri, J-Y Dauvignac, C. Migliaccio, S. F. Gregson, "Spherical Scanning Measurement Challenge for Future Millimeter Wave Applications" Proceedings of the Antenna Measurements Techniques Association, 2015

[3] D. R. Novotny, J.A. Gordon, J.R. Guerrieri, "Antenna Alignment and Positional Validation of a mm Wave Antenna System Using 6D Coordinate Metrology, " Proceedings of the Antenna Measurements Techniques Association, pp 247-252, 2014

[4] J. Sulzer, I. Kovac, "Enhancement of Positioning Accuracy of Industrial Robots with a Reconfigurable Fine-Positioning Module," Precision Engineering, vol. 34, pp 201-217, 2010

[5]. J.J. Craig, "Introduction to Robotics: Mechanics and Control, 3rd ed.," New Jersey, Prentice Hall, 2004, pp. 62-69

[6] R. Swanson, G. Balandran, S. Sandwith, "50-micron Hole Position Drilling Using Laser Tracker Controlled Robots, " Journal of the CMSC, Vol 9, No 1, Spring 2014

[7] J.A. Gordon, D.R. Novotny, M.H. Francis, R.C. Wittman, M.R. Butler, A.E. Curtin, J.R. Guerrieri, "Millimeter-Wave Near-Field Measurements Using Coordinated Robotics," IEEE Transactions on Antennas and Propagation, vol. 63, no. 12, pp 5351-5362, 2015

[8] A. Nubiola, I.A. Bonev, "Absolute calibration of an ABB IRB 1600 robot using a laser tracker," Robotics and Computer-Integrated Manufacturing, vol. 29, issue 1, pp 236-245, 201

Allman, Michael; Novotny, David; Gordon, Joshua; Curtin, Alexandra; Sandwith, Scott.
"Serial Robotic Arm Joint Characterization Measurements for Antenna Metrology."
Paper presented at 39th Annual Meeting and Symposium of the Antenna Measurement Techniques Association (AMTA), Atlanta, GA, United States. October 15, 2017 - October 20, 2017.

# Filtering Antenna-to-Antenna Reflections in Antenna Extrapolation Measurements[1]

Robert D. Horansky, Mohit S. Mujumdar, Dylan F. Williams, Kate A. Remley, Joshua A. Gordon, David R. Novotny, Michael H. Francis
Communications Technology Laboratory
NIST
Boulder, CO USA
horansky@nist.gov

***Abstract*—To provide modulated-signal traceability into the free-field, we are extending the three-antenna, extrapolation method used for on-axis antenna gain, from using only scalar data, to using the full magnitude and phase information between the antennas. We have examined several aspects of the extrapolation fitting, such as averaging of the data and the stability of fitting methods. Here, we will present our simulation result showing that, in our antenna range, filtering of reflections between antennas is an unnecessary step in the extrapolation method.**

## I. Introduction

Within the communications field, there is a large breadth of wireless devices that require characterization and testing. These tests may be for metrics such as antenna pattern, as well as full signal path metrics such as receiver sensitivity. With the shrinking size of mobile devices, as well as the use of multiple antennas, many wireless devices are foregoing test ports for separately characterizing the antennas, receivers and transmitters. The use of a test cable may change the behavior of a device antenna negating the meaningfulness of conducted-device testing. As such, the use of over-the-air (OTA) testing has become ubiquitous for mobile wireless devices with many of the relevant metrics requiring a communication link with the device under test.

Since OTA tests dominate the measurements of wireless devices, and given the variety of techniques to conduct these measurements, there is a paramount need for a meaningful way to compare measurements between setups. Many metrics, such as receiver sensitivity, require demodulation of a communication signal. Thus, both the phase and magnitude of a reference field are necessary. At NIST, we have developed a connectorized, wide-band, precision, modulated-signal source [1]. The waveforms generated by the source and the related uncertainties are traceable to primary standards. Accurately characterizing the magnitude and phase of the on-axis gain of the antennas is the next step to creating known modulated signals in a free-field environment, and motivates the present work.

The traceability path for a conducted signal at millimeter-wave frequencies is described in Ref. [1]. The traceability is provided using a calibrated sampling oscilloscope as the receiver to both verify the modulated signal and predistort it to correct for hardware errors. The sampling oscilloscope is traceable to primary standards where all uncertainties and any correlations between the uncertainties are tracked in every step of the measurement process through an in-house software suite called the NIST Microwave Uncertainty Framework [2].

To extend this traceability from the connectorized source into free-space, as shown in Fig. 1, we need to include in the traceability chain the scattering matrix of a radiating antenna, and the correlated uncertainties required for modulated-signal traceability. We have started doing this with on-axis measurements, with a planned extension to off-axis patterns. We will discuss the correlated uncertainties elsewhere.

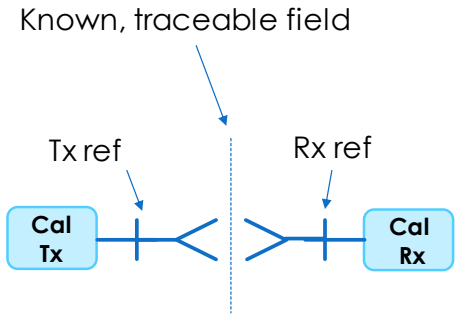


Figure 1: The goal of the work presented here is to provide a precision, free-field modulated signal source, traceable to primary standards. This will be accomplished by using a calibrated transmitter, shown on the left, and the known antenna scattering parameters, to provide the traceable signal shown at the dotted line located anywhere between the two antennas. We can verify this field with a calibrated receiver such as an equivalent-time sampling oscilloscope shown on the right. In both cases, we require fully calibrated antennas to transform the connectorized reference planes "Tx ref" and "Rx ref" to the free-field between the antennas.



Horansky, Robert; Mujumdar, Mohit; Williams, Dylan; Remley, Catherine; Novotny, David; Francis, Michael.
"Filtering Antenna-to-Antenna Reflections in Antenna Extrapolation Measurements."
Paper presented at 39th Annual Meeting and Symposium of the Antenna Measurement Techniques Association (AMTA), Atlanta, GA, United States. October 15, 2017 - October 20, 2017.

Currently, on-axis, far-field gain of an antenna is provided by using a three-antenna extrapolation measurement. This is achieved by measuring the pair gain of at least three permutations of the antenna pairs. We can then extract the individual gain of each antenna without having to rely on a known reference antenna [3].

Since it is difficult to measure pair gain in the far field, either due to space limitations or low signal levels, the pair gain is currently fit as a function of antenna distance in the near-to-mid-field regime at NIST. This has traditionally been done at NIST using scalar measurements of the transmission coefficients between the two antennas as a function of their separation distance. *However, for a free-field modulated signal source, we need the full complex scattering-parameter matrix of the antenna*. Thus, in this work, we are extending the extrapolation method to use the full complex transmission coefficient $S_{21}$ obtained from the pair measurement, as also proposed in Refs. [4,5].

In the process of fitting the complex transmission coefficients, we have examined some of the algorithm choices that have traditionally been used in the extrapolation method. To aid us in our analysis, we created a simulated data set to compare algorithm steps. Here we present an example of one such study looking at the use of filtering to remove the presence of multiple reflections between antenna pairs.

In this paper, we will first discuss how extrapolation measurements are currently done and the algorithm for fitting the data. Then we will show the simulations that we performed to analyze the effect of filtering on the extrapolation fits. Finally, we show results that suggest filtering at reflection magnitudes relevant to experimental values is not required in our range at the distances we use to perform the extrapolations, and may cause degradation in the accuracy of some measurements.

## II. NIST Extrapolation Measurements

### A. Pair Gain Using Power Fits

When NIST provides antenna gain to a customer, the result comes from the three-antenna, extrapolation measurement, which provides the on-axis antenna gain. The antenna gain can then be used to normalize pattern measurements.

The extrapolation measurement is performed with a vector network analyzer (VNA), which measures the scattering parameters of each pair of antennas, and is carried out as a function of distance between them. When the extrapolation method was first developed, phase measurements were either not possible, or the uncertainty was much higher than for measuring power. Therefore, the algorithms developed for fitting an expansion to the extrapolation measurements were based on total power transmitted between the two antennas (*i.e.* the square of the magnitude of the transmission coefficient $|S_{21}|^2$), as a function of distance between the antennas. At the time, this allowed lower uncertainties, but ignored phase information.

The distance in the extrapolation measurement is now provided by the NIST CROMMA system, which is an articulated robotic arm that provides very accurate position measurements, which is especially beneficial at millimeter-wave frequencies. Furthermore, with modern instrumentation, we can perform very precise measurements of the relative phase between the two antennas [6]. We bring those two together here to measure both the magnitude and phase of pair gain.

In the absence of reflections between the antennas, the dependence of the transmission coefficient $S_{21}$ with distance $\bar{r} = r - r_0$ is given by,

$$S_{21} = \frac{e^{ik\bar{r}}}{\bar{r}}\left(A_{00} + \frac{A_{01}}{\bar{r}} + \frac{A_{02}}{\bar{r}^2} + \frac{A_{03}}{\bar{r}^3} + \cdots\right), \quad (1)$$

where $r$ is the distance between the antennas and $r_0$ sets the origin of the expansion used in (1). This is typically determined geometrically and set to 0. The $A_{0n}$ terms are the coefficients of the expansion and $k = \frac{2\pi}{\lambda}$, with $\lambda$ being the wavelength of the measurement. The first-order series in (1), multiplied by $\frac{e^{ikr}}{\bar{r}}$, represents the unreflected transmission coefficient between the antennas being measured. The leading term $A_{00}$ is the dominant term in the far-field, and the other $A$ terms in the first-order series correct for the near- to mid-field behavior [7]. The magnitudes of a typical NIST extrapolation data set are shown in blue in Fig. 2. We are using a measurement done at 118.75 GHz between a $\mu = \pm 1$ probe antenna with a nominal gain of 8 dB, and a standard gain horn with nominal gain of 15 dB. The dominant antenna aperture, $D$, is from the horn antenna and is 0.0248 m. In eq. (1), the $A$ terms are complex providing two fit parameters each in the fitting procedure. The goal in the extrapolation measurement is to extract only the first order series to determine the $A_{00}$ term, which will then provide far-field behavior [3].

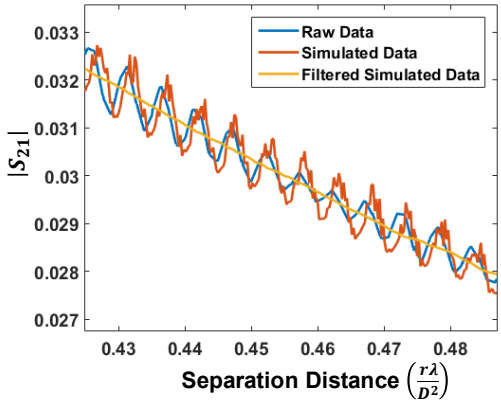


Figure 2: Example of an extrapolation measurement between a $\mu = \pm 1$ probe antenna and a standard gain horn at 118 GHz. The raw data are shown in blue versus the distance normalized by $D^2/\lambda$. The simulated data with the magnitude of ripples chosen to match the raw data and noise are shown in red. The sinc filtered model data are shown in yellow.

Horansky, Robert; Mujumdar, Mohit; Williams, Dylan; Remley, Catherine; Novotny, David; Francis, Michael.
"Filtering Antenna-to-Antenna Reflections in Antenna Extrapolation Measurements."
Paper presented at 39th Annual Meeting and Symposium of the Antenna Measurement Techniques Association (AMTA), Atlanta, GA, United States. October 15, 2017 - October 20, 2017.

Reflections between the antennas introduce higher-order terms in the series. While the reflections are complicated, and may originate at several different distances, to first order, they can be represented with additional terms of the form $\frac{e^{3ikr}}{\bar{r}^3}$ and $\frac{e^{5ikr}}{\bar{r}^5}$, representing reflections that traverse three times and five times the distance of the first order series. The resulting expression is

$$S_{21} = \frac{e^{ikr}}{\bar{r}}\left(A_{00} + \frac{A_{01}}{\bar{r}} + \frac{A_{02}}{\bar{r}^2} + \frac{A_{03}}{\bar{r}^3} + \cdots\right) \frac{e^{3ikr}}{\bar{r}^3}\left(A_{10} + \frac{A_{11}}{\bar{r}} + \frac{A_{12}}{\bar{r}^2} + \cdots\right) + \frac{e^{5ikr}}{\bar{r}^5}\left(A_{20} + \frac{A_{21}}{\bar{r}} + \cdots\right) + \cdots, \quad (2)$$

We use the higher-order terms $A_{10}$ and $A_{20}$in (2) to simulate multiple reflections in our range. The first order series in (2) is a function whose magnitude is monotonically decreasing, while the higher order series impart a ripple on top of this decreasing behavior, as can be seen in Fig. 2. A simulation using eq. (2) is shown in red in Fig. 2.

When power is used for the extrapolation measurement, we must then use the squared magnitude of eq. (1). There will be complex ripple terms from the higher order series, but the first order series will yield,

$$|S_{21}|^2 \approx \frac{1}{\bar{r}^2}\left(A'_{00} + \frac{A'_{01}}{\bar{r}} + \frac{A'_{02}}{\bar{r}^2} + \frac{A'_{03}}{\bar{r}^3} + \cdots\right), \quad (3)$$

where the $A'$ terms now represent scalar quantities. The far field term has a simple relation back to the vector quantity given by,

$$A'_{00} = |A_{00}|^2, \quad (4)$$

and is proportional to the far-field pair gain.

The previous NIST algorithm for fitting the extrapolation data and extracting the pair gain uses the work flow shown in Fig. 3. The raw $S_{21}$ data are converted to transmitted power-like quantity, which destroys the phase information. Next, a distance gate is applied to the power-like data to remove effects from near-field behavior, typically around $2D^2/\lambda$. This also removes data from too large a distance where external reflections and poor signal-to-noise are problematic. Then, a boxcar filter the width of the excitation wavelength is applied to the raw data to remove the multiple reflections. The fourth step is an averaging of the smoothed data to improve processing time. Next, the data are normalized by $\lambda r/D^2$, where $\lambda$ is the wavelength being measured, $r$ is the distance between the antennas, and $D$ is the larger antenna aperture. The square of the normalization factor is divided out of eq. (3). This removal of the normalization has the effect of giving greater weight in a least-squares fit to data at longer distances by a factor of $r^2$. Also, the normalization step allows the extrapolation to be fit by a polynomial, which is computationally faster.

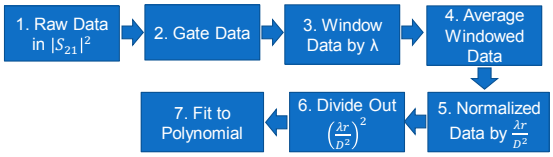


Figure 3. Algorithm used to extract far-field pair gain from an extrapolation measurement that fits the measured power transmitted between the antennas.

### B. *Pair Scattering Using Magnitude and Phase*

Since the primary goal of this work is to extend traceability from a conducted precision communication signal to a free-space signal, both magnitude and phase information are necessary to allow demodulation. In the process of adapting the work flow of Fig. 3, we studied the necessity of several of the steps. In fitting the complex data, we use the raw scattering-parameter measurements in step 1. The gating in step 2 is accomplished by using data where the relative phase between the antennas is linear. The windowing of step 3 will be shown in the next section in Fourier space. Step 4 reduces the amount of data with averaging, but is no longer necessary since modern computing power can easily handle the amount of extrapolation data that is taken. The normalization in step 5 is accomplished by weighting the least squares fit by $r$ for complex data, or if power-like data are used, $r^2$. Finally, we found that fitting to a polynomial was only marginally faster than fitting the series in eq. (1) explicitly. Also, when fitting the series explicitly, we can adjust the origin $r_0$ of the expansion if desired. This allows exploration of the effect of changing the origin of the expansion on the resultant pair gain or scattering matrix.

## III. Simulated Data

We are interested in exploring the necessity of the windowing step in the extrapolation method. Since we are using the full complex data, the windowing in r-space is equivalent to applying a sinc filter in k-space (inverse r-space). We decided to explore the usefulness of the filtering step by creating data with (2) where we know the $A_{00}$ term and could compare the fitted results to that value.

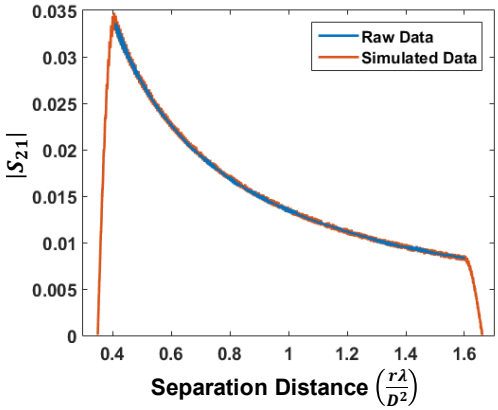


Figure 4. The raw extrapolation data (blue) used for creating the model data. The simulated data used for the filtering experiment are shown in red. The simulated data extends further in distance due to the buffers used at the end of the data to smooth the Fourier transform and reduce side lobes.

Horansky, Robert; Mujumdar, Mohit; Williams, Dylan; Remley, Catherine; Novotny, David; Francis, Michael.
"Filtering Antenna-to-Antenna Reflections in Antenna Extrapolation Measurements."
Paper presented at 39th Annual Meeting and Symposium of the Antenna Measurement Techniques Association (AMTA), Atlanta, GA, United States. October 15, 2017 - October 20, 2017.

By starting with the values for the $A$ terms extracted from a least-squares fit of eq. (2) to the raw data shown in Fig. 2, we created simulated data that included higher-order terms that approximated the ripples we observed in our measurements. The simulated data contain four terms in the first-order series, one term for the third order-series, $A_{10}$, and one term for the fifth-order, $A_{20}$.

The raw data shown in Fig. 2 came from six measurements moving the antennas apart then together, three times each. We used the minimum and maximum distances and evenly spaced the model data using the same number of points as the 6 raw data runs combined, then added additional buffer points on both sides of the data. The buffers were then smoothly decreased to zero with a sinusoidal multiplier to allow a smooth Fourier transform of the data and reduce side lobes. The simulated data used is shown in Fig. 4, and compared to the raw data that were used as the starting point. A magnified version of the data is shown in Fig. 2.

The windowing that was done for the power data is accomplished for the complex data by filtering the Fourier transform of the simulated data. Figure 5 shows the Fourier transform of 100 copies of the simulated data, each with a different normally distributed random noise added to the data. The Fourier transform yields $k$ as the x-axis, but this is converted to a frequency, $f$, by multiplying by the speed of light. Overlaid on the model data is the sinc filter, which is the Fourier transform of the boxcar window. Fig. 6 shows model data with the higher order reflections amplified to appear on a linear scale. The Butterworth filter, which we also simulated, is shown as well.

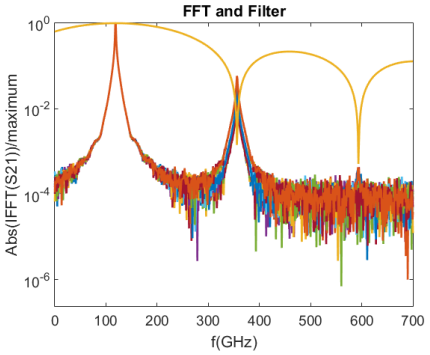


Figure 5: Plot of the simulated extrapolation data, with several levels of noise in Fourier space versus frequency, converted from inverse distance. Also shown, in yellow, is the sinc filter used to remove the higher-order reflections.

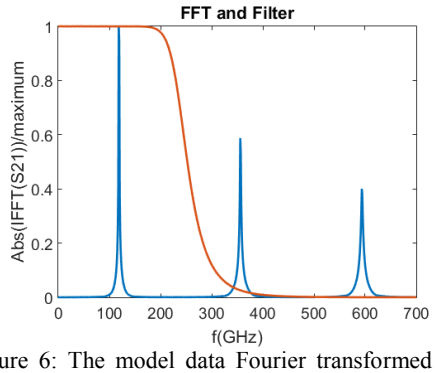


Figure 6: The model data Fourier transformed to k-space with the higher-order reflections made very large. In red is shown the Butterworth filter at a given cutoff.

## IV. Results

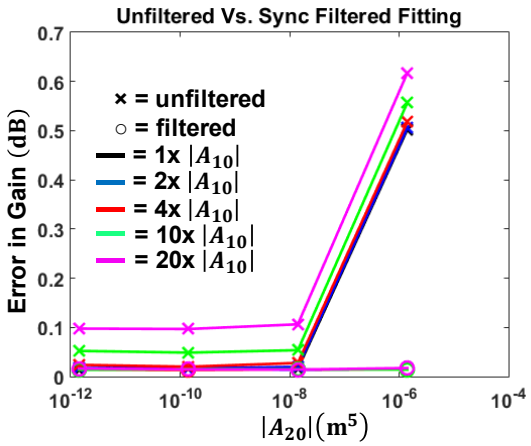


Figure 7: Plot of the relative error in the pair gain taken from the magnitude of the pair scattering compared to the value defined in model data. The error is plotted versus the magnitude of the fifth-order series term in the extrapolation expansion. The data represented with x's are the values taken from fits to unfiltered data. The open circles are filtered by a sinc function. The legend shows the multiplier of the third order term, where multiplying by one yields an oscillation magnitude equivalent to the measured data.

We compared the results of filtering the simulated data first against performing the least-squares fit without filtering. The magnitude of the third-order term, $A_{10}$, was increased from 0.5e-6 $m^3$, which yielded ripples of similar magnitude to experimental data, up to 1e-5 $m^3$. For each value of $A_{10}$, the magnitude of the fifth-order terms, $A_{20}$, was varied from 1e-12 $m^5$ to 1e-6 $m^5$. Finally, for each value of the third- and fifth-order magnitudes, 100 iterations of normally distributed noise were added to each point. The average of the resultant fits to the first-order series are shown as the data points in Figs. 7 and 8. Fig.7 shows the comparison between filtering with a sinc filter as shown in Fig. 5, while Fig. 8 shows the Butterworth filter comparison. The y-axis of the plot shows the relative error in the pair gain found from fitting the data over the 100 noise iterations, compared to the actual value defined in the model data. The x-axis shows the increasing magnitude of $A_{20}$. The plots with x's are the model data fitted with no filtering. The lines with circles show the relative error in the magnitude of the $A_{00}$ term when filtered data is fitted. The increase magnitude of $A_{10}$ is shown by the varying colors of the lines.

Horansky, Robert; Mujumdar, Mohit; Williams, Dylan; Remley, Catherine; Novotny, David; Francis, Michael.
"Filtering Antenna-to-Antenna Reflections in Antenna Extrapolation Measurements."
Paper presented at 39th Annual Meeting and Symposium of the Antenna Measurement Techniques Association (AMTA), Atlanta, GA, United States. October 15, 2017 - October 20, 2017.

If we look at a single-color pair, we can see the effect of the fifth-order term. Only at very high values, over 10,000 times larger than what is observed in experimental data, filtering helps to reduce the error in the far-field, pair scattering parameter. Next, one can look at the progression of the different color lines. This is an increase in the third-order term, where the black plots are those for oscillations seen in the raw data in Fig. 2. At lower values of the third-order term, the filtering does not help lower the relative error in $|A_{00}|$. However, if a situation arises where the magnitude of the third-order term is 10x larger than seen in these raw data, then filtering could play a helping role in the analysis.

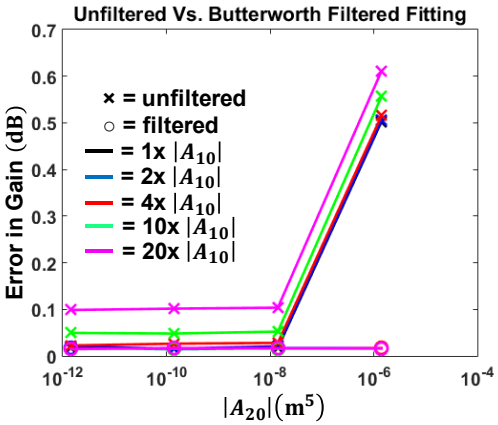


Figure 8: Plot of the relative error in the pair gain compared to the value defined in model data. The data was filtered using the Butterworth filter shown in Fig. 6.

## V. Conclusion

We are extending NIST's traditional on-axis gain measurements to use the full complex scattering parameters we measure to determine complex pair-gain. This is a necessary step needed to extend a traceable modulated signal to free-space locations and be able to establish a traceable communication link to wireless devices. A traceable, free-space, modulated signal would allow calibration and comparison of OTA test methods across a broad range of frequencies and bandwidths.

In performing the extrapolation data fits, to find the far-field pair scattering parameter, we determined that filtering the reflections between the antenna pairs was unnecessary with the antennas we used in our range and at the distances we used in the fits. There may be cases where it becomes useful, perhaps at closer distances where the reflections are orders of magnitude higher that seen in this experimental, 118 GHz data. However, in the range of useful fitting, the ripples are filtered adequately in our data by the least-squares fit itself, and usually with less error than when filtering is used.

Our next step in the traceability process will be to incorporate this complex fitting into our uncertainty analysis software suite. We have already accounted for fitting and pointing errors and are currently incorporating calibration uncertainties for the VNA measurements. The next step will be to present the results of the full uncertainty analysis accounting for correlations for the far field scattering matrix of our radiating antenna.

## References


[1] K. A. Remley, D. F. Williams, P. D. Hale, C.-M. Wang, J. Jargon, and Y. Park, "Millimeter-Wave Modulated-Signal and Error-Vector-Magnitude Measurement with Uncertainty," IEEE Trans. Microw. Theory and Tech., vol. 63, pp. 1710-1720, April 2015.

[2] D. F. Williams, "NIST Microwave Uncertainty Framework, Beta Version", NIST, Boulder, CO, USA, JJun. 2014 [Online]. Available: http://www.nist.gov/pml/electromagnetics/relate-software.cfm

[3] A. C. Newell, R. C. Baird, P. F. Wacker, IEEE Trans. Antenna Propagat., vol. 21, no. 4, July 1973.

[4] E. Van Lil, P. Govaerts, A. Van de Capelle, "Improved Extrapolation Methods for Antenna Gain Measurements," IEEE Microw Conf, 1990 20th Europe.

[5] P. F. Wacker, "Theory and numerical techniques for accurate extrapolation of near-zone antenna and scattering measurements", NBS Report 10 733, Apr. 1972.

[6] J. A. Gordon, D. R. Novotny, M. H. Francis, R. C . Wittmann, A.E. Curtin, M. L. Butler, and J. R. Guerrieri, "Millimeter-Wave Near-Field Measurements Using Coordinated Robotics," IEEE Trans. Antenna Propagat., vol. 63, pp. 5351-5362, October 2015.

[7] A. G. Repjar, A. C. Newell, and D. T. Tamura, "Extrapolation Range Measurements for Determining Antenna Gain and Poarization," NBS Tech Note 1311, August 1987.



Horansky, Robert; Mujumdar, Mohit; Williams, Dylan; Remley, Catherine; Novotny, David; Francis, Michael.
"Filtering Antenna-to-Antenna Reflections in Antenna Extrapolation Measurements."
Paper presented at 39th Annual Meeting and Symposium of the Antenna Measurement Techniques Association (AMTA), Atlanta, GA, United States. October 15, 2017 - October 20, 2017.

# A Multi-Robot Large Antenna Positioning System for Over-The-Air Testing at the National Institute of Standards and Technology[1]

David R. Novotny‡, Joshua A. Gordon, Michel S. Allman,
Alexandra E. Curtin, Jeff R. Guerrieri
*Communications Technology Laboratory*
*National Institute of Standards and Technology*
Boulder, CO
‡david.novotny@nist.gov

Kim Hassett, Quang Ton, George McAdams
*NSI-MI Technologies*
Torrance, CA

***Abstract*— To address dynamic testing requirements of new communications systems and RF processes that use non-static beam forming, NIST proposed the Large Antenna Positioning System (LAPS). The LAPS consists of two kinematically-linked six axis robotic arms, one of which is integrated with a 7 m linear rail system. This repositionable, multi-robot system can perform arbitrary scans around a device under test. The dynamic 13 degree-of-motion capability is designed to perform complex spatial interrogation of systems.**

**The coordinated-motion capabilities of the system are key to support not only traditional antenna measurement geometries (i.e. spherical, cylindrical, planar, gain-extrapolation), but are also intended to be used to dynamically interact with changing RF conditions. The robots can independently scan or interrogate multiple bearings toward a device under test, perform MIMO illumination, or trace out complex 6D paths during system testing.**

**Initial RF and mechanical testing results in the factory where it was built show deviations from an ideal linear scan at 0.032 ± 0.02 mm, much better than the λ/50 system design specification at 30 GHz. Further improvements to the basic kinematic models of each robot will allow this generation of robotic antenna range to operate open loop without laser tracker feedback.**

***Keywords— antennas; near-field measurements; robots; positioning; gain, pattern; extrapolation; MIMO.***

## I. INTRODUCTION

Industrial robotics offer a large range of motion, high speed automation, and well-developed kinematics for a wide variety of tasks. The large production volumes (i.e., economies of scale) reduce the cost, time, and infrastructure needed to develop applications (in our case, antenna and over-the-air (OTA) communications tests). To complement configurability advantages, the Robot Operating System (ROS) project is currently working on developing plug-and-play interfaces with the goal of allowing computer code and applications to become relatively robot independent, similar to the universal serial bus (USB) interface for consumer level equipment [1].

Historically, improvements in industrial robotics have been focused primarily on increasing tool speed and repeatability. New manufacturing processes are driving the need for better repeatability. Absolute accuracy is not as critical as long as processes can be repeated within manufacturing tolerances. However in recent years, there has been a concerted effort to improve the absolute accuracy of multi-axis articulated robotic arms [2-4]. The combination of lower cost, versatility, easy-to-use hardware and software integration tools, and improving accuracies lead the National Institute of Standards and Technology (NIST) to develop the configurable robotic millimeter-wave antenna (CROMMA) facility [5]. The CROMMA facility demonstrated 0.03 mm RMS accuracies ($\lambda/50 \approx 200$ GHz) over a 2 m diameter volume, but it required a laser tracker, very selective RF cable routing, and constant monitoring [5-7]. The intent for CROMMA was to push the upper frequency range of antenna scanning metrology [8,9]. It soon became apparent the arbitrary and configurable nature of the system showed possibilities for utility in lower frequency bands of operation [10,11]. Multiple input, multiple output (MIMO) testing at arbitrary angles, testing dynamic paths, investigating Doppler effects, and integrated testing of communications systems where test RF signals cannot be injected into the system antennas were prime applications for taking advantage of this technology.

The Large Antenna Positioning System (LAPS), Fig. 1, was proposed to address these needs. A large scan volume

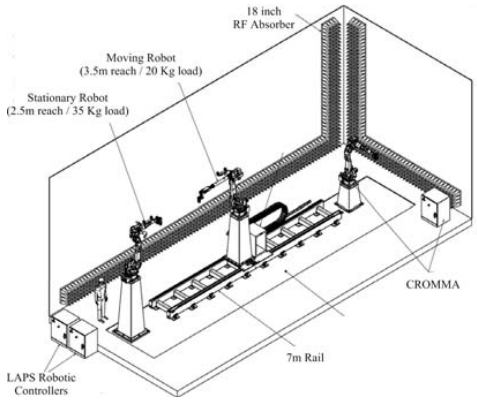


Figure 1. The Large Antenna Positioning System and CROMMA co-located in the NIST Advanced Communications Metrology Laboratory.

[1] US Government Work. Not subject to copyright.



Novotny, David; Gordon, Joshua; Allman, Michael; Guerrieri, Jeffrey; Curtin, Alexandra; Hassett, Kim; McAdams, George; Ton, Quang. "A Multi-Robot Large Antenna Positioning System for Over-The-Air Testing at the National Institute of Standards and Technology." Paper presented at 39th Annual Meeting and Symposium of the Antenna Measurement Techniques Association (AMTA), Atlanta, GA, United States. October 15, 2017 - October 20, 2017.

suitable for testing across common communications bands (500 MHz - 30 GHz) with modest absolute RMS accuracies of least 0.250 mm was desired. This combination of range (> 8 m separation) and accuracy allows for standard near–field testing and gain extrapolation, and physical separation required to ensure reasonable field uniformity when illuminating small devices with moderate gain antennas. The use of multiple robots allows for multiple bearings to a device, simultaneous emissions and immunity analysis, and interference testing. The push for an accurate open-loop robot calibration, one that does not require a laser tracker or other metrology during the measurement, allows for more dynamic movements by the positioning system, faster robot movements, and the ability of the system to rapidly respond to stimuli [12].

## II. The Large Antenna Positioning System

The LAPS was designed around two commercially available six-axis robots: a moving robot on a base rail (MR) and a stationary robot (SR) on a pedestal located at one end of the rail. The economy-of-scale advantages become apparent when the additive features are examined. Inherent to the robot controllers are a large number of required functionalities that aid in rapid integration. Some of these functions, listed below, require large investments in design and test and, are available mainly because of the size of the articulated robotic arm automation industry. In addition to the RF-dictated positional requirements, there are many functional tools common to the industrial robotic community that are being leveraged.

### *A. Multi-Robot Positional Integration*

The robot controller can be linked through kinematic models to an external "base" axis, Fig 2., so that the robot is aware of the tool relative to the "robot" frame of reference and the base axis orientation and location. This allows calculation of position and trajectory from multiple robot systems with a single interface that is routinely updated. The MR is linked to a 7 m base rail. Configuring the rail carriage as a "base" enables the controller to recognize/define the 5 m (H) x 6 m (W) x 10m (L) working envelope from a kinematic perspective. The terminology for "base" as the location of the external axis and "robot" as the nominal location of the robot come from definitions of the Yaskawa† robots used in the LAPS [12]. Alignment between the robot and the base rail is fine-tuned using a laser tracker and the final orientation of the rail to the manipulator in 6D can be inputted into the robot kinematic model to account for gross misalignments between the system components.

The multiple robotic controllers in the LAPS are linked together to share the same kinematic space. This allows the robots to position antennas, probes, and devices under test (DUT) either absolutely in space or relative to each other.

There are practical limitations to this model. The Denavit Hartenburg (DH) parameters implemented in many commercial systems are mainly idealized to minimize cycle time, so effects from inaccuracies such as encoder/servo non-uniformity, axis warping, and motor eccentricities are not addressed at the typical controller level but can be seen and are addressed in many near-field ranges. These present practical limitations to a linear model of the robot are being partially addressed using more complex models [12].

### *B. Alignment*

Alignment for antenna testing can often be more time consuming than measurements. The LAPS robot controllers have multi-point teaching algorithms that allow fiducials of the antennas to be manually positioned to a common point in space and then used to calculate the transform between the robot interface and antenna orientation, known as the tool control point (TCP) [13]. This allows the antenna (or tool) to be incorporated into the kinematic model of the robot, and desired antenna positions and orientations to be directly input without the need to calculate offsets. This multi-point teach method yields typically sub-mm TCP location knowledge. For applications where better antenna-robot position accuracies are required, or if physical contact with the antennas are problematic, we use a NIST designed, non-contact alignment method with less than 0.030 mm of uncertainty [14].

### *C. Performance Specifications*

The LAPS targets antenna and systems testing in the 500MHz to 30 GHz frequency range. The $\lambda/50$ rule of thumb, namely to get accurate measurements 50 dB below the peak signal level typically requires $1/50^{th}$ of a wavelength positioning knowledge, guided the basic design. It is assumed that the primary operational mode of the LAPS will not employ a laser tracker, so data are dependent on the coordinate reporting of the robot controller to determine location.

Table 1. Basic Physical Design Specifications of the LAPS

| Moving Robot (MR) and Rail | |
|---|---|
| Robot horizontal reach | 3.5 m |
| Robot vertical reach | 5 m |
| Robot path repeatability | 0.15 mm |
| Robot payload | 20 Kg |
| Minimum planar scan plane size | 2.5 m x 3 m |
| Minimum spherical radius (with a 356 mm probe) | 1 m |
| Rail travel | 7 m |
| TCP wobble at scan plane center (deviation from best fit line) | RMS: 0.25mm |
| TCP wobble at scan plane center (deviation from best fit line) | MAX: 0.5 mm |
| Stationary Robot (SR) | |
| Robot horizontal reach | 2.5 m |
| Robot vertical reach | 4 m |
| Robot path repeatability | 0.07 mm |
| Robot payload | 35 Kg |
| Minimum planar scan plane size | 2 m x 2.5 m |
| Minimum spherical radius (with a 356 mm probe) | 1 m |

### *D. Additional Calibration*

There are two major tasks in accurately characterizing a serial robotic system: extrinsic and intrinsic calibrations [12]. Extrinsic calibrations, Fig. 2, which typically remove the majority of the systematic accuracy uncertainties, measure the robot relative to external references, i.e., define where the robot

† The use of trade names does not constitute an endorsement by the U.S. Government. Mention is for informational purposes only.



Novotny, David; Gordon, Joshua; Allman, Michael; Guerrieri, Jeffrey; Curtin, Alexandra; Hassett, Kim; McAdams, George; Ton, Quang. "A Multi-Robot Large Antenna Positioning System for Over-The-Air Testing at the National Institute of Standards and Technology." Paper presented at 39th Annual Meeting and Symposium of the Antenna Measurement Techniques Association (AMTA), Atlanta, GA, United States. October 15, 2017 - October 20, 2017.

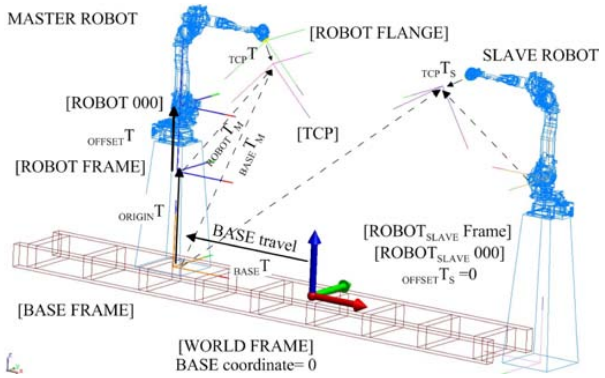


Figure 2. Extrinsic frames, e.g. [BASE], and the 6D solid-line transforms ($_{BASE}T$, $_{ORIGIN}T$, $_{OFFSET}T$, $_{TCP}T$) between them, determined during calibration of a robot's kinematic model. This allows more accurate knowledge of tool location (dashed lines: $_{ROBOT}T_M$, $_{BASE}T_M$) using only the robot controller. Similar measurements are made for the SLAVE/stationary robot (SR).

frame is physically located and determine the location and orientations of base axes and TCPs. This can typically reduce errors to the millimeter level or less in the LAPS class of robot.

Intrinsic calibrations characterize the error in the robot's DH composition, differences of robot link lengths, offsets, and orientations differences from nominal. For the class of robots such as the LAPS, this should bring the typical accuracy errors into the ±0.2 mm range [12].

### *E. Safety – Collision Avoidance*

The LAPS is integrated with a Functional Safety Unit† (FSU) that is aware of the unified coordinate space of the entire LAPS system. It is designed to prevent the collision of robots with themselves and each other and any attached antennas (or tooling), and limit collisions with the surrounding environment.

### *F. Safety – Personnel Avoidance*

The FSU has redundant systems to protect operators. The robots can have large kinetic potentials and control of these potentials are integral to safe operation. The controllers are equipped with laser safety radars that stop autonomous motion when the working volume of the LAPS is encroached upon. When personnel are in the working envelope, for example during manual operation, alignment or mounting, enabling devices to allow robot movement must be positively activated prior to servo activation.

## III. The LAPS Measurement Capabilities

The LAPS is tasked with performing a large suite of measurements. Traditional near-field scanning: planar, cylindrical and spherical geometries, gain extrapolation and polarization ratio, and hybrid geometries which involve moving both robots and interrogating systems from multiple dynamic bearings.

### *A. Robot Scan Capabilities*

The MR is configured as the LAPS master robot controller; it is responsible for all safety and robot positioning commands. The load capacity is rated at 20 Kg for a full speed stop at maximum kinetic loading. Sample scan geometries, Figs. 3-4, are not the maximum achievable by the MR (or SR in the case of Figs. 5-6) but are chosen to minimize the gravity deflections of larger loads, which tend to be most pronounced at extended arm reach [3].

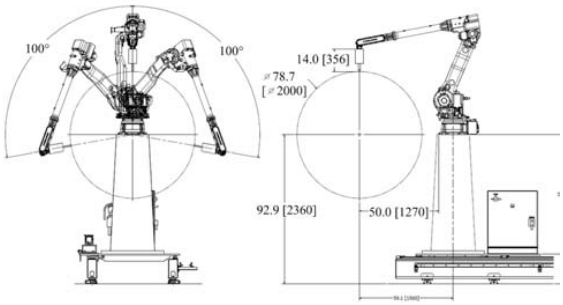


Figure 3. Moving Robot typical spherical scan plane geometry in inches [mm].

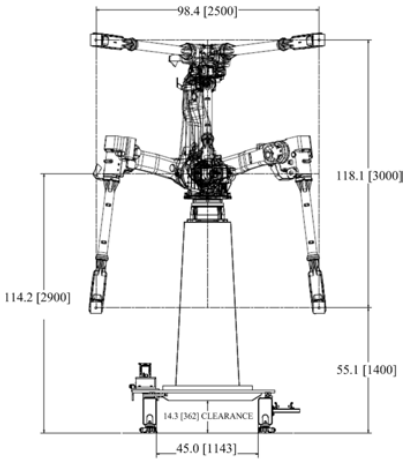


Figure 4. Moving Robot typical planar scan size in inches [mm].

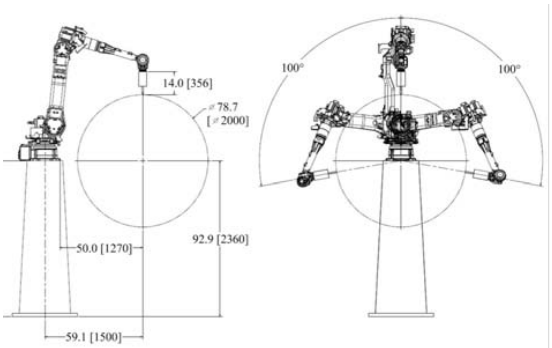


Figure 5. Stationary Robot typical spherical scan plane geometry in inches [mm].



Novotny, David; Gordon, Joshua; Allman, Michael; Guerrieri, Jeffrey; Curtin, Alexandra; Hassett, Kim; McAdams, George; Ton, Quang. "A Multi-Robot Large Antenna Positioning System for Over-The-Air Testing at the National Institute of Standards and Technology." Paper presented at 39th Annual Meeting and Symposium of the Antenna Measurement Techniques Association (AMTA), Atlanta, GA, United States. October 15, 2017 - October 20, 2017.

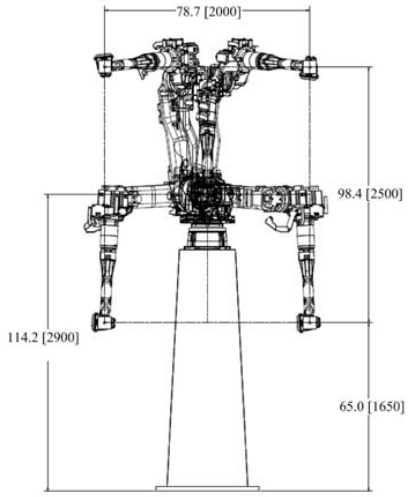


Figure 6. Stationary Robot planar scan size in inches [mm].

### B. *Maximum Scan Plane Using the Rail*

Using the rail in conjunction with the MR, a 5 m x 7.5 m scan plane can be realized, Fig 7. Since the MR and rail are kinematically linked, coordinated motion between the two motion systems is controlled with a single command and timing between the systems is accounted for to the level of the robot cycle time.

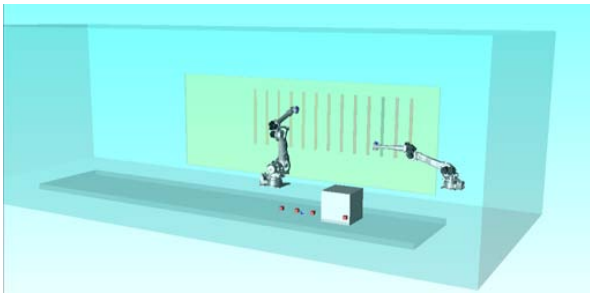

Figure 7. A robot reach simulation of the LAPS scanning a large planar structure, the MR on its base rail can perform a scan up to 5 m x 7.5 m.

### C. *OTA Testing*

In addition to the standard near field geometries, LAPS will be able to perform active OTA interrogation of communication systems. Figs. 8-9 show two possible multi-interrogation test scenarios. Fig. 8 describes a scenario of testing a beam-forming network by sampling the high signal-to-noise (SNR) region while simultaneously and coherently measuring off-axis performance.

By sampling the emissions coherently, in the near-field, pattern analysis can be made without the injection of a test RF signal into the system under test. We propose that a more realistic test of these systems could be developed using the system itself as the stimulus and response. The success of this type of test will depend on ensuring enough high SNR reference samples are taken to assure good pattern SNR over the frequency range of interest.

Fig 9 depicts multiple sources interrogating a single DUT, as in the case of a MIMO test. By utilizing the 2.5 to 5 m reach of the robots and the rail, a suitably uniform field may be generated to illuminate the DUT under conditions resembling the far-field. Arbitrary angles, to a limited degree (the system will limit robot collisions and upwards facing angles), might be used as a platform to develop OTA MIMO tests with rapidly varying spatial and Doppler conditions.

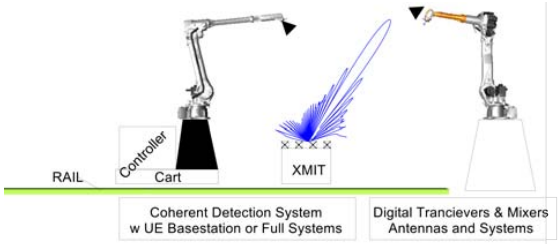


Figure 8. A depiction of simultaneous measurements of a beam-forming system with the LAPS; SR (right) is measuring the main beam while the MR is probing off angle performance.


Figure 9. A depiction of multiple interrogation of a beam-forming system with the LAPS; SR (right) and MR are illuminating the UE in a MIMO fashion from multiple orientations

## IV. Initial Validation

The achievable accuracy of the LAPS in open-loop operation, i.e., without in-situ external positional metrology, is going to be limited mainly by the tolerances of the robots and the rail system. Systematic offsets and inaccuracies can be corrected by calibration. However non-modeled errors in the LAPS, such as rail straightness and variable errors such as robot vibrations and backlash are harder to correct. NIST performed pre-validation testing of some parameters in the non-ideal manufacturing facility where the LAPS was assembled. The initial tests were done to show viability of the overall system.

### A. *Basic Deviation of the Rail*

The TCP wobble specification in Table 1 is a major component of positional uncertainty that is difficult to correct. It is affected by MR posture and loading, rail flatness, cart motion, the MR riser stiffness, and rail deflection under varying load conditions. The influence of the rail variations is magnified by the distance from the rail to the MR TCP. The variability of these errors makes them difficult to correct so minimizing them at the outset is the most straight-forward approach to dealing with these error sources.



Novotny, David; Gordon, Joshua; Allman, Michael; Guerrieri, Jeffrey; Curtin, Alexandra; Hassett, Kim; McAdams, George; Ton, Quang.
"A Multi-Robot Large Antenna Positioning System for Over-The-Air Testing at the National Institute of Standards and Technology."
Paper presented at 39th Annual Meeting and Symposium of the Antenna Measurement Techniques Association (AMTA), Atlanta, GA, United States. October 15, 2017 - October 20, 2017.

Laser tracker targets were mounted to the MR pedestal (~1.3 m above the rail) and the end of the MR in an extended pose with a 5 kg load (~4.1 m above the rail), Figs. 10,11. They were tracked the MR was moved through a 2-m span of the rail at a constant rate of 23 mm/sec. The pedestal-mounted target had a small deviation from the best fit line: 14 ± 7 μm, with a 61 μm maximum, Fig. 12. A satisfying TCP wobble result, compared to specification in Table 1, from the target mounted near the antenna was a 32 ± 20 μm deviation with a 182 μm maximum. The maximum deviations in both cases occurred at the beginning of the sweep when the robot starts motion.

These results demonstrate the basic mechanical capabilities of the system seem to be more than adequate for λ/50 (200 μm) operation at 30 GHz.

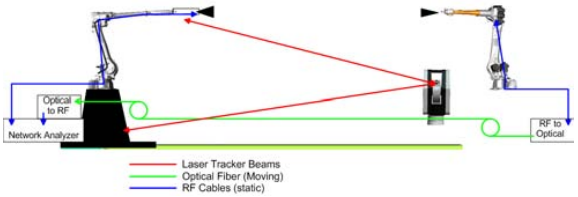


Figure 10. RF setup of the measurement system to compare commanded position by the robot controller, measured position by the laser tracker, and RF insertion distance by the network analyzer.


Figure 11. Positions of the laser tracker targets on the MR base and TCP to measure cross range movement while the MR is moving.

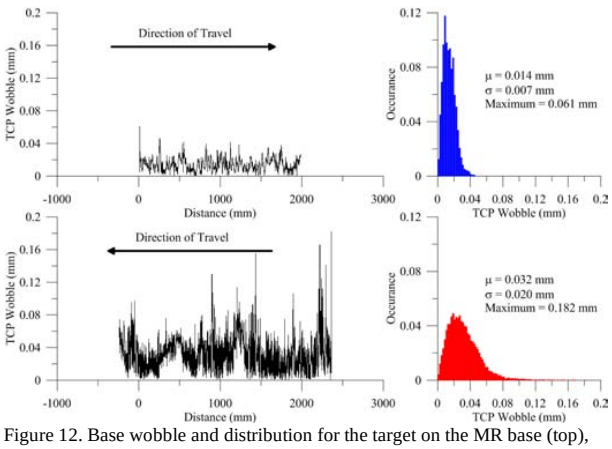


Figure 12. Base wobble and distribution for the target on the MR base (top), and the TCP wobble and distribution for the target on the robot arm (bottom).

*B. Dynamic Motion of the Rail*

The system is intended to be used for testing during dynamic motion. This will stress the need for coordination between the timing of an attached RF system with the motions of the LAPS. A measurement controller that synchronizes the robot and external equipment is an integral part of the delivered system. To help assess the basic dynamic wobble of a tool during MR stop-motion, travel in both directions was measured. The rail was commanded in 2.5-mm steps at a speed of 30 mm/sec. Motion was stopped at each position, then RF insertion data and laser tracker data were taken prior to motion commencing. The expectation was that the rapid-stop motion in different directions would highlight the vibrational modes of the system. The setup of the measurement is seen in fig. 10. Fig. 13 shows the insertion loss between the antennas and the difference between the antenna separation inferred from the laser tracker and the RF measurement at 9 GHz.

The laser tracker position data, fig. 13, is directly inferred by measuring the target near the TCP (TCP target), fig. 11. Previously, the horns we aligned parallel to the axis of movement determined from the best fit line for the measurements highlighted in fig. 12. Then the apertures were confirmed with the tracker and the nominal separation relative to the TCP target was determined. The antenna separation is then derived from the movement of the TCP target.

If more than 4 points per wavelength are taken, the RF separation, $d_{phase}$, is determined by taking the phase of the insertion measurement, $RF_i$, unwrapping the phase versus distance and then converting phase to distance [15]:

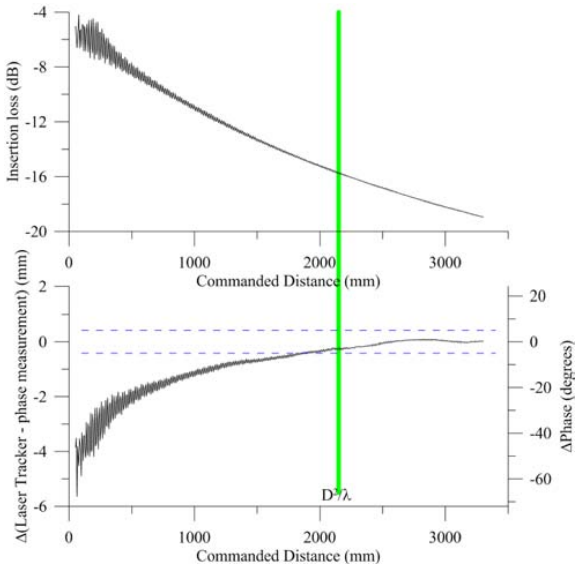


Figure 13. Results of an RF insertion measurement at 9 GHz using the LAPS, the amplitude (top) shows near-field horn-to-horn effects at closer distances than $D^2/\lambda$. The antenna separation (bottom) measured by the laser tracker and inferred from the RF data shows good correlation as the separation gets larger. At close distances, the deviations from linear phase are more apparent than *1/r* amplitude variations. The ±5° lines (dotted blue) show that the system is stable and predictable enough for accurate extrapolation measurements [15].



Novotny, David; Gordon, Joshua; Allman, Michael; Guerrieri, Jeffrey; Curtin, Alexandra; Hassett, Kim; McAdams, George; Ton, Quang. "A Multi-Robot Large Antenna Positioning System for Over-The-Air Testing at the National Institute of Standards and Technology." Paper presented at 39th Annual Meeting and Symposium of the Antenna Measurement Techniques Association (AMTA), Atlanta, GA, United States. October 15, 2017 - October 20, 2017.

$$d_{phase} = \text{atan}\left(\frac{\text{Re}(RF_i)}{\text{Im}(RF_i)}\right)\frac{\lambda}{2\pi}360 \quad (1)$$

The correlation of laser tracker and RF inferred distance show that the robot and cabling are not experiencing excessive movement during position and velocity changes.

## V. Conclusions

While the LAPS can perform standard near-field antenna pattern and gain testing, the goal is to perform dynamic multi-pronged OTA system tests. Initial validation of the LAPS at the factory, Fig. 14, show that basic mechanical operation of the system is within the specified design tolerances for static and dynamic testing to at least the designed 30 GHz operational specification. The measured antenna (or TCP) wobble of 32 ± 20 μm with a 181 μm maximum deviation over a limited range highlights the overall rigidity and stability of the MR portion of the LAPS.

Figure 14. The LAPS in the manufacturing facility during preliminary system testing.

## VI. Future Work

These were the first operational tests of the LAPS. Testing at extended reach, especially when the robots are extended across the rail are important to determining suitability for fast planar and rapid OTA test scenarios. System timing using the measurement controller, and verification of motion when the robots are loaded with RF absorber are also needed to ensure adequacy for the wide series of measurements planned for the system.

## References


[1] The ROS project: http://www.ros.org.

[2] A. Nubiola and I.A. Bonev, "Absolute calibration of an ABB IRB 1600 robot using a laser tracker," *Robotics and Computer-Integrated Manufacturing*, Vol. 29, No. 1, 2013, pp. 236–245.

[3] H.N. Nguyen, J. Zhou, H.J. Kang, "A New Full Pose Measurement Method for Robot Calibration," *Sensors*, vol 13, pp 9132-9147, 2013: doi:10.3390/s130709132.

[4] R. Swanson, G. Balandran, S. Sandwith, "50-micron Hole Position Drilling Using Laser Tracker Controlled Robots," in *Jour. of the Coordinate Systems Metrology Conf*, Vol 9, No 1, Spring 2014

[5] D. Novotny, J. Gordon, J. Coder, M. Francis and J. Guerrieri, "Performance evaluation of a robotically controlled millimeter-wave near-field pattern range at the NIST," *2013 7th European Conference on Antennas and Propagation (EuCAP)*, Gothenburg, 2013, pp. 4086-4089.

[6] J. A. Gordon *et al*., "Millimeter-Wave Near-Field Measurements Using Coordinated Robotics," in *IEEE Transactions on Antennas and Propagation*, vol. 63, no. 12, pp. 5351-5362, Dec. 2015. doi: 10.1109/TAP.2015.2496110

[7] J. A. Gordon *et al*., "An All-Metal, 3-D-Printed CubeSat Feed Horn: An assessment of performance conducted at 118.7503 GHz using a robotic antenna range," in *IEEE Antennas and Propagation Magazine*, vol. 59, no.2, pp. 96-102, April 2017. doi: 10.1109/MAP.2017.2655574

[8] F. Ferrero *et al*., "Spherical Scanning Measurement Challenge for Future Millimeter-Wave Applications," in *Proc. of the Antenna Measurement Techniques Assoc.*, Nov 2015.

[9] J. Snow, B. Slowey, "SCARA Scanner for Portable Near-Field Antenna Testing," *Proc. of the Antenna Measurement Techniques Assoc.,* Nov. 2005.

[10] J. Hatzis, P. Pelland, G. Hindman," Implementation of a Combination Planar and Spherical Near-Field Antenna Measurement System using an Industrial 6-Axis Robot," in *Proc. of the Antenna Measurement Techniques Assoc.*, Nov 2016.

[11] K. A. Remley *et al*., "Measurement Challenges for 5G and Beyond: An Update from the National Institute of Standards and Technology," in *IEEE Microwave Magazine*, vol. 18, no. 5, pp. 41-56, July-Aug. 2017. doi: 10.1109/MMM.2017.2690882

[12] M.S. Allman *et al*., "Serial Robotic Arm Joint Characterization Measurements for Antenna Metrology," in *Proc. of the Antenna Measurement Techniques Assoc*., Nov 2017 (in process).

[13] *DX100 Instructions: FOR NORTH AMERICAN (ANSI/RIA) STANDARD*, Part No. 155494-1CD, Rev. 2, Yaskawa Electric Corporation, pp 8-23,29.

[14] J.A Gordon, D.R. Novotny, A.E. Curtin, "A Single Pixel Touchless Laser Tracker Probe," in *Jour. of the Coordinate Systems Metrology Conf*, vol. 10, no. 2, Autumn 2015.

[15] J. Coder, D.R. Novotny, M Francis, J. Guerrieri, "On the Use of Phase Data When Conducting an Extrapolation Measurement," *Proc. of the Antenna Measurement Techniques Assoc.*, Nov. 2013.





Novotny, David; Gordon, Joshua; Allman, Michael; Guerrieri, Jeffrey; Curtin, Alexandra; Hassett, Kim; McAdams, George; Ton, Quang. "A Multi-Robot Large Antenna Positioning System for Over-The-Air Testing at the National Institute of Standards and Technology." Paper presented at 39th Annual Meeting and Symposium of the Antenna Measurement Techniques Association (AMTA), Atlanta, GA, United States. October 15, 2017 - October 20, 2017.

# Three Antenna Ranges Based on Articulated Robotic Arms at the National Institute of Standards and Technology†

## Usability for Over-the-Air and Standard Near-Field Measurements

David R. Novotny‡, Joshua A Gordon, Michael Shane Allman, Jeff R. Guerrieri, Alexandra E. Curtin
Communications Technology Laboratory
National Institute of Standards and Technology
Boulder, Colorado, United States of America
‡david.novotny@nist.gov

***Abstract*—NIST has developed an antenna range that uses coordinated industrial robotic systems for measuring milli-meter wave (mmWave) antenna patterns and gain. The Configurable Robotic millimeter Antenna (CROMMA) facility employs a multi-axis articulated serial robotic arm to place probes accurately around a test article. The positional and temporal capabilities, shown by CROMMA, has become a springboard to develop two new robotic ranges for use primarily from 0.5 - 30 GHz. Both of these systems are based upon commercial-coordinated-kinematic systems with multiple degrees of freedom. The first is the dual six-axis, robotic-arm Large Antenna Positioning System (LAPS). It is designed to perform large volume scanning with an emphasis on Multiple-Input Multiple-Output (MIMO) and Over-the-Air (OTA) testing. The second system employs a seven-axis robotic arm to perform communication testing of Single-Input Single-Output (SISO) systems and will be used to establish modulated and continuous-wave field references.**

**We will discuss the advantages, limitations and techniques employed to use these commercial robotic systems for accurate time-sensitive positioning and coordination with communications measurement equipment.**

***Keywords—antenna; measurement; OTA; near-field; gain***

## I. Introduction

There is an expectation that the proposed commercial communications systems in the proposed 5G bands will require much more comprehensive testing to ensure that reliable multi-user connections are established and maintained [1]. Current 2G, 3G, 4G, and LTE mobile systems work on broad sectored base stations patterns and near omnidirectional antennas on mobile user equipment (UE). In July 2016, the Federal Communications Commission (FCC) opened up limited spectrum for 5G mobile radios covering 27.5-71 GHz [2]. To overcome path loss, battery-limited transmit power availability, and antenna gain limitations on UE receiver sensitivity in these frequency ranges, we expect that these new systems will incorporate dynamic beamforming to reduce link loss [3].

Conventional near-field testing systems can measure static beams, far-field systems can test moving beams over limited angles, but offer little in dynamic beam quality. Techniques such as the two-stage substitution, reverberation chamber, and boundary array or multi-probe anechoic methods (MPAC), seek to generate or simulate illumination of the UE from many directions using many antennas [1,4]. There is a need for a dynamic OTA testing method that investigates system performance while providing real-world field interactions.

The aging antenna facilities at the National Institute of Standard and Technology (NIST) were being replaced and the new design philosophy was focused on long term relevance for general communication and radio frequency (RF) measurements. While a need for standard near-field testing was required to support probe calibrations, gain-extrapolation and polarization reference measurements, a large consideration for these new ranges was the ability to perform much more arbitrary testing than in previous systems. To address the potential need for testing dynamic beamforming systems and simulated MIMO style tests, the new ranges were based on full 6 degree of freedom (6DoF) articulated robots augmented by external axes. CROMMA showed that coordinated motion in 6DoF can greatly reduce control overhead and perform corrected dynamic positioning of antennas over a large volume, specifically ±0.03 mm accuracy over a 3 m diameter volume [5,6]. The experience gained with CROMMA was leveraged into the design of two additional ranges: the LAPS and the SISO/Reference range.

Fig. 1 shows the three robotic ranges NIST is installing. Two, CROMMA and LAPS, will be collocated in the same anechoic chamber of the Advanced Communications Metrology Laboratory (ACML) at NIST. The SISO/Reference field range is being deployed into an existing anechoic facility to create a low noise environment for generating standard fields and high isolation to limit interaction from potentially high electromagnetic field-levels with other external experiments.

The combination of large volume, velocity, and range of motion in LAPS, the high frequency capability of CROMMA, and the limited intrusion of the SISO/Reference facility will give NIST the ability measure dynamic communications systems while supporting basic metrology required for reference antenna measurements on a common measurement platform.



Novotny, David; Gordon, Joshua; Allman, Michael; Guerrieri, Jeffrey; Curtin, Alexandra.
"Three Antenna Ranges Based on Articulated Robotic Arms at the National Institute of Standards and Technology: Usability for Over-the-Air and Standard Near-Field Measurements."
Paper presented at 2017 IEEE Conference on Antenna Measurements and Applications (CAMA), Tsukuba, Japan. December 4, 2017 - December 6, 2017.

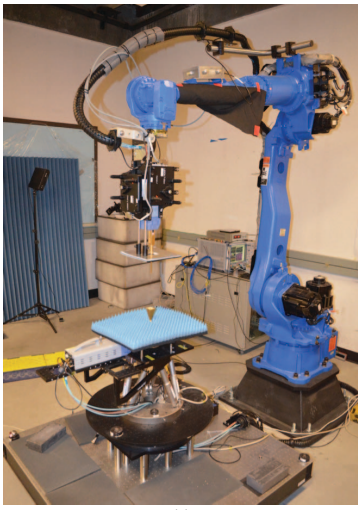

(a)

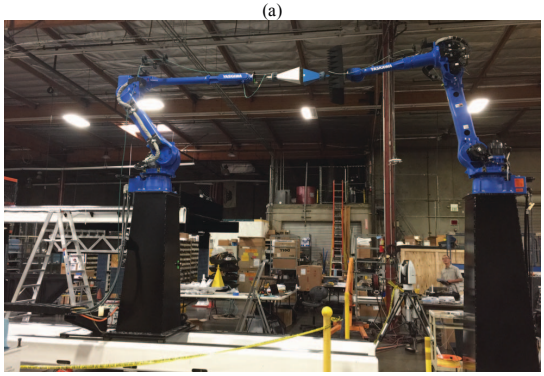

(b)

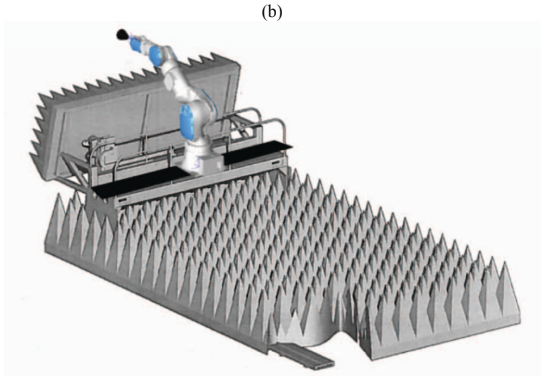

(c)

Figure 1. The three robotic ranges designed for NIST: CROMMA, (a), performing a 73 GHz gain measurement, the LAPS, (b), undergoing repeatability, accuracy and RF stability tests at the factory, and the new SISO/Reference Field facility, (c), that will be used to place and scan antennas with minimal field perturbation using a 7-axis robot mounted on a 4.5 m rail.

## II. The Use of Commercial Robotic Systems for Antenna Measurements

### A. Repeatability Versus Accuracy

Most commercial articulated robotic arm manufacturers are geared toward improving repeatability and speed. The ability to repeat a process with minimal deviations at high speed is a driving need of most articulated robotic arms. Path repeatability is more important than point accuracy, e.g. a command between a list of specified poses in a given order is repeated very well while a command for going to a point at a specific pose is less accurate. So, the use of industrial versus antenna specific positioning hardware requires a change in system control philosophy. Instead of moving individual axes, e.g. $\phi$ axis movement during a spherical measurement or a $y$ axis step during a planar scan, all six degrees of freedom are continually commanded to move to a specific path via a series of corrected 6DoF, $x,y,z,Rx,Ry,Rz$, poses [7].

Unlike the rigid structures that constitute many standard near-field scanning systems, the extended nature of an articulated robot leads to gravitation droop and the serial nature of articulated arms tend to magnify pose uncertainties from hysteresis in the joints. For accurate antenna measurements, these need to be addressed. Since many antenna scanning geometries are a series of similar paths (i.e. extrapolation, spherical, planar), iteration can be used to successively improve the accuracy of paths to the repeatability level of the robot. NIST uses a laser tracker slaved to the robot to measure the location of the probe at the same time as the RF measurement. The laser tracker measures the difference between the commanded and actual pose, and the results are used to iteratively correct the probe location. With this method, there are initial "sacrificial' scans until the robot is corrected to an acceptable level [6].

### B. Kinematic Model and Calibration

Most commercial articulated robotic systems can control the movement of a tool control point (TCP) in addition to individual joint rotations. The TCP is a kinematic offset from the end of the robot. For standard near-field scanning, we locate the TCP at the aperture of the probe, Fig. 2. There are several methods for determination of the TCP to robot flange [8,9]. Once determined, direct movement of the probe can be performed without the need for additional offset calculation.

In addition to direct joint control, the robots can move in direct pose control. Using the fixed X-Y-Z angle convention [7], we can calculate the ($\Delta x,\Delta y,\Delta z$, $R_x=\alpha$, $R_y=\beta$, $R_z=\gamma$) transform from a pose {start} to {end} given by:

$$ {}^{\{end\}}_{\{start\}}T_{\{ref\}} = \begin{bmatrix} \left[ {}^{\{end\}}_{\{start\}}R_{XYZ}(\alpha,\beta,\gamma) \right] & \begin{matrix} \Delta x \\ \Delta y \\ \Delta z \end{matrix} \\ \begin{matrix} 0 & 0 & 0 \end{matrix} & 1 \end{bmatrix} \quad (1) $$

where the 3x3 rotation matrix, $R_{XYZ}$, in (1) is given in [7] and the common reference frame for the current location and transform is denoted by {ref}. Fig 2. shows the frames used in the iterative

Novotny, David; Gordon, Joshua; Allman, Michael; Guerrieri, Jeffrey; Curtin, Alexandra.
"Three Antenna Ranges Based on Articulated Robotic Arms at the National Institute of Standards and Technology: Usability for Over-the-Air and Standard Near-Field Measurements."
Paper presented at 2017 IEEE Conference on Antenna Measurements and Applications (CAMA), Tsukuba, Japan. December 4, 2017 - December 6, 2017.

correction method. Since the distance offsets in (1) are relative, all that is needed is the rotation reference of the robot. From a common pose, the robot is moved and recorded with the laser tracker as translations are made in *x*, *y* and z. This results in the knowledge needed to construct a reference frame {ROBOT}.

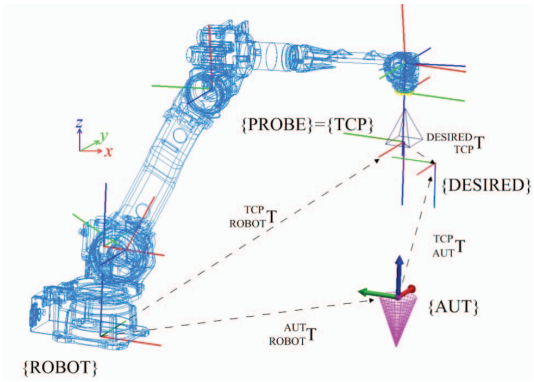


Figure 2. The relative frames for one point in a scan, {poses}, and transforms ${}_{x}^{y}T$ that are required for simple iterative correction of the robot

To perform the iterative correction, the antenna under test, (AUT), and the probe (TCP) must be spatially located [9,10]. Uncertainties and error in these poses are direct contributors to overall position uncertainties. The {DESIRED} scan geometry is constructed relative to the {AUT}. The robot is then sent to perform a rudimentary scan quite a distance from the AUT to avoid contact. This unaligned scan is measured with the laser tracker to determine the initial {PROBE} and {DESIRED}.

${}_{ROBOT}^{TCP}T$ is the current robot position and ${}_{TCP}^{DESIRED}T$ is the transform of the between where the probe actually is and its ideal location. As long as both of those transforms are known relative to the {ROBOT} frame, the new goal for the robot to get to the {DESIRED} location can be determined by:

$$ {}_{\{ROBOT\_CURRENT\}}^{\{ROBOT\_NEXT\}}T = {}_{\{ROBOT\}}^{\{DESIRED\}}T = {}_{\{TCP\}}^{\{DESERIED\}}T \; {}_{\{ROBOT\}}^{\{TCP\}}T \tag{2} $$

The major advantage of using this limited correction algorithm is that only a rudimentary knowledge of the relative orientation of the robot is needed. We can also correct the major gravity deflections and localized robot movement inaccuracies. Orientation errors in {ROBOT} may reduce convergence, however, even with an orientation error of 0.5°, on CROMMA, errors are typically within 100 microns after two iterations and 50 microns after four iterations. Monitoring during the entire measurement allows for corrections to account for thermal and environment changes in the robot [6].

### C. Kinematic Model and Calibration

Groups are working to better robot calibration techniques, by measuring each linkage in an articulated arm [10-11]. A better model of the arm with actual joint lengths, offsets, and gravity deflection models are used versus the nominal factory values. This can result in more accurate robot movement. This knowledge can shorten the alignment process, and as the operational frequency range of a system is inversely proportional to positioning errors, decreasing the physical errors allows the robot to operate open-loop at higher frequencies.

## III. The Three NIST Robotic RF Measurement Facilities

NIST is installing two new ranges based on the same design principal as CROMMA: a six or seven axis articulated arm that is augmented by other motion stages to allow for accurate large volume coverage. All three ranges will be running on the same 6DoF kinematic control platform so measurement processes can be used between systems.

### A. CROMMA

CROMMA (Fig. 1a) is comprised of two robotic systems, an articulated robotic 6DoF arm for probe positioning around the AUT [6]. A 6DoF hexapod mounted on a rotation stage allows for alignment of the AUT. The rotation stage defines the axis of rotation and the AUT direction. The hexapod aligns the AUT to the rotator. Gain-extrapolations and pattern measurements between 50 and 220 GHz have been successfully performed with CROMMA.

### B. The LAPS

The conceptual layout of the collocated LAPS and CROMMA facilities is shown in Fig. 3. The LAPS has a stationary 2.5m reach robot and a 3.5m moving robot mounted on a 7m travel rail that creates an effective 5 m x 6 m x 10 m volume to position antennas. The LAPS corrected open-loop accuracy is designed for operation from 500 MHz to 30 GHz [12]. The dual robot configuration can be used to perform standard scanning or easily reconfigured to perform larger OTA testing and arbitrary, multi-point interrogation of RF system (see Figs. 4,5).

### C. The SISO and Reference Field Facility

The SISO and Reference Field facility is designed to minimally perturb the fields generated within it. A seven-axis articulated arm was chosen for the probe positioner. The additional degree of freedom allows the majority of the robot could remain behind the absorber cowling when locating a probe in a field, see Fig. 1(c). The 4.5 m travel is used to separate the source and probe source and probe to limit field taper across the length of the probe.

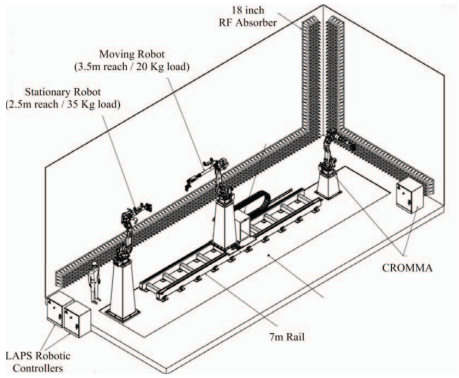


Figure 3. The Large Antenna Positioning System and CROMMA co-located in the NIST Advanced Communications Metrology Laboratory.

Novotny, David; Gordon, Joshua; Allman, Michael; Guerrieri, Jeffrey; Curtin, Alexandra.
"Three Antenna Ranges Based on Articulated Robotic Arms at the National Institute of Standards and Technology: Usability for Over-the-Air and Standard Near-Field Measurements."
Paper presented at 2017 IEEE Conference on Antenna Measurements and Applications (CAMA), Tsukuba, Japan. December 4, 2017 - December 6, 2017.

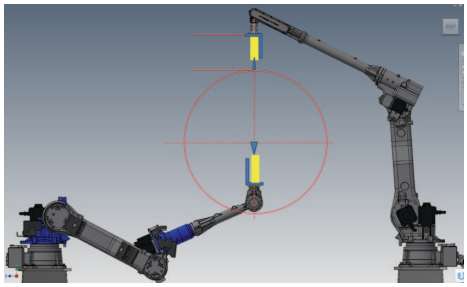

Figure 4. The LAPS setup for traditional scanning. The robot kinematics can account for mounting offsets and misalignments.

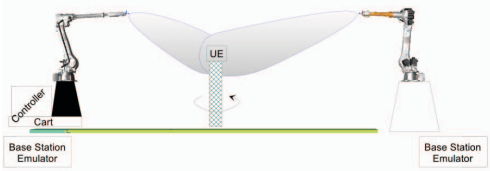


Figure 5. A depiction of multiple interrogation of a beam-forming system with the LAPS. Both robots are illuminating the UE in a MIMO fashion from multiple orientations.

## IV. System Validation and Measurement Results

### A. LAPS Deviation from Linear Movement

The LAPS was tested at the factory to determine its uncorrected straightness and effect on the TCP as it travelled along the rail, Fig. 6. Testing the lateral movement of the antenna with the arm extended (Fig. 1(b)) showed maximum deviations of less than 200 µm which corresponds to a λ/50 error over 30 GHz. This sets a practical frequency limit for open loop (uncorrected) operation for extrapolation measurements.

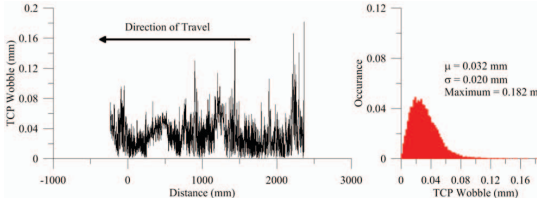


Figure 6. TCP/Antenna wobble at the end of the robot during a 2.6 m move at 23 mm/s

### B. CROMMA Stability

To validate stability, we require a canonical geometry that provides a known RF response relative to position. An extrapolation scan should have a linear unwrapped phase change with distance. We have experienced phase errors due to cable stresses. As our mmWave systems employ harmonic up conversion, any phase errors in feed cables are multiplied by this up-conversion factor. The robots have a cable path with minimal stress for the motor and tool control [6]. We run our phase-sensitive local oscillator (LO) cabling along this path. At 118 GHz, we have an LO up-conversion factor of six. The results, Fig. 7, show that over a 560 mm displacement (~225 λ), the 118 GHz phase errors are less than 8°. This means we are controlling LO phase errors to ~1.3°. The full-length movement of this scan is generally more aggressive than we see on a typical 1 m spherical or planar scan. We can use this to infer that typical phase errors are approximately 1° at base LO frequencies.

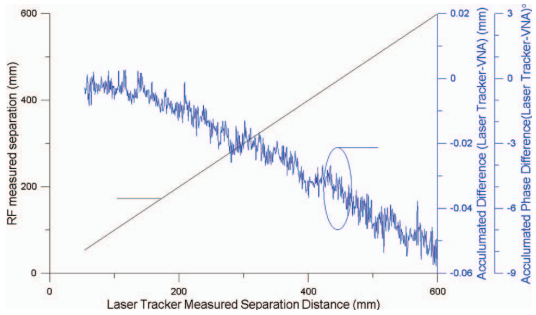


Figure 7. Distance inferred by phase change during a 118 GHz RF insertion measurement compared to the distance measured directly by a laser tracker.

## V. Conclusion

NIST's use of industrial coordinated motion robotics has shown usefulness in a metrology setting. To realize the full accuracy that these systems can deliver, a coordinate metrology analysis and path optimization for scans have been developed. We have performed highly accurate, feedback-based scans using an *in-situ* laser tracker and open-loop methods at lower frequencies where positional needs are less stringent.

## References

[1] M. Fogelle, "Advances in Over-the-Air Performance Testing Methods for mmWave Devices and 5G Communications," *Proc. of the Antenna Measurement Techniques Assoc.*, Nov 2016.

[2] *Use of Spectrum Bands Above 24 GHz For Mobile Radio Services*, FCC order 16-89A, July 2016.

[3] K. A. Remley *et al*., "Measurement Challenges for 5G and Beyond: An Update from the National Institute of Standards and Technology," *IEEE* Microwave Magazine, vol. 18, no. 5, pp. 41-56, July-Aug. 2017. doi: 10.1109/MMM.2017.2690882.

[4] M. Rumney *et al*., "Testing 5G: Evolution or Revolution?," *Radio Propagation and Technologies for 5G (2016)*, Durham, 2016, pp. 1-9. doi: 10.1049/ic.2016.0067.

[5] D. Novotny, J. Gordon, J. Coder, M. Francis and J. Guerrieri, "Performance evaluation of a robotically controlled millimeter-wave near-field pattern range at the NIST," *2013 7th European Conference on Antennas and Propagation (EuCAP)*, Gothenburg, 2013, pp. 4086-4089.

[6] D. R. Novotny, J. Gordon, M. Francis, R. Wittmann, A.E. Curtin, J. Guerrieri, "Antenna Measurement Implementations and Dynamic Positional Validation Using a Six Axis Robot," *Proc. of the Antenna Measurement Techniques Assoc.*, Nov 2015.

[7] J. J. Craig, *Introduction to Robotics: Mechanics and Control*, 3rd ed., New York, NY, Pearson Education, Inc, 2004, ISBN 9780201543612.

[8] J.A. Gordon, D.R. Novotny, A.E. Curtin, "A Single-Pixel Touchless Laser Tracker Probe," *J. of the Coordinate Measurement Soc. Conference*, vol. 10, no. 2, pp. 12-22, Autumn 2015.

[9] *DX100 Instructions: FOR NORTH AMERICAN (ANSI/RIA) STANDARD*, Part No. 155494-1CD, Rev. 2, Yaskawa Electric Corporation, pp 8-23,29.

[10] S. Droll, "Real-Time Path Correction of Industrial Robots with Direct End-Effector Feedback from a Laser Tracker," *J. of the Coordinate Measurement Soc. Conference*, vol. 10, no. 1, pp. 20-25, Spring 2015.

[11] M.S. Allman *et al*., "Serial Robotic Arm Joint Characterization Measurements for Antenna Metrology," in *Proc. of the Antenna Measurement Techniques Assoc.*, Nov 2017 (in process).

[12] D. Novotny *et al*., "A Multi-Robot Large Antenna Positioning System for Over-The-Air Testing at the National Institute of Standards and Technology," *Proc. of the Antenna Measurement Techniques Assoc*., Oct 2017 (in process).

Novotny, David; Gordon, Joshua; Allman, Michael; Guerrieri, Jeffrey; Curtin, Alexandra.
"Three Antenna Ranges Based on Articulated Robotic Arms at the National Institute of Standards and Technology: Usability for Over-the-Air and Standard Near-Field Measurements."
Paper presented at 2017 IEEE Conference on Antenna Measurements and Applications (CAMA), Tsukuba, Japan. December 4, 2017 - December 6, 2017.

*ARFTAG 2017 SUMMARY*

# Rydberg Atom Electric-Field Metrology

Joshua A. Gordon, Matthew T. Simons, Christopher L. Holloway

National Institute of Standards and Technology, Communication Technology Lab, Boulder, CO, 80305

***Abstract* — We present a technique which shows great promise for realizing an atomic standard measurement of RF fields that is intrinsically calibrated, directly linked to the SI and atomic structural constants. This technique relies on the response of Rydberg atoms to radio frequency (RF) electric-field measurements. The rich resonance response of these atoms occurs across a large frequency range from hundreds of MHz and approaching 1 THz. Alkali atoms such as rubidium (Rb) and cesium (Cs) confined in a glass vapor cell are optically excited by two different lasers to high energy Rydberg states. Once in the Rydberg state the atoms exhibit a significant response to RF fields which alters the optical spectrum of the atoms. The RF field strength is then directly obtained from the optical spectrum. We discuss the theory behind this technique. Measurements in the far-field of a standard gain horn antenna as well as a coplanar waveguide mode are made. We also show a recently developed quantum electric-field probe based on this Rydberg atom technique, which is constructed from a fiber optically coupled vapor cell is used for these measurements.**

***Index Terms* — Antenna; Coplanar waveguide; Electromagnetically Induced Transparency (EIT); Far-Field; Electric Field; Radio Frequency; Rydberg Atoms**

## I. Introduction

In the past several years much progress has been made in atom-based sensing of radio- frequency (RF) electric-fields [1-5]. In particular, a relatively new technique for converting an RF field amplitude into an optical frequency response in a gas of atoms has shown much promise. A primary goal is to realize an atomic standard measurement of RF fields that is intrinsically calibrated and directly linked to the SI. Such a measurement consists of a gas of room temperature alkali atoms such as Rubidium (Rb) and Cesium (Cs) contained in a glass vapor cell which are optically excited to a high enough energy such that the atoms become resonant to RF fields. Two lasers can be used to accomplish this. One for initial excitation and a second to increase the atom's energy to where the outer electron orbit is large enough such that the atom behaves much like a hydrogen atom. Such an atom is referred to as a Rydberg atom [6] and can act like a nano-sized antenna which will respond favorably to RF fields.

While in the Rydberg state, the atom exhibits a large response (i.e., a large dipole moment) to RF-fields over the frequency range of about 500 MHz-1 THz. To the lasers, the atomic gas acts like a non-linear optical medium that experiences changes in electrical susceptibility when interacting with an RF field. A consequence of this is that in the absence of the RF field the atomic gas would preferentially transmit a single optical frequency when an RF-field is present two optical frequencies are preferentially transmitted. It can be shown that the difference in the two optical frequencies is linearly proportional to the applied RF-field amplitude [1,4]. In this paper, we discuss the theory behind this phenomenon and how it can be used for performing atom-linked SI-traceable measurements of RF fields. Experimental results are obtained using a recently developed quantum electric field probe based on a fiber optic coupled Rydberg atom micro vapor cell. Results demonstrating the broad frequency range of operation, field strength in the far-field of a standard gain horn antenna, and the near-field mode structure of a coplanar waveguide are presented.

## II. Atom Based Electric Field Metrology

### *A. Measurement Scenario*

A typical measurement scenario is shown in Fig. 1. Rydberg atoms are generated using two different wavelength lasers. For example, in Rb vapor, the probe laser is tuned to excite the $D_2$ transition ($5S_{1/2} - 5P_{3/2}$) around $\lambda_p \cong 780\ nm$ (red) and the coupling laser is tuned to $\lambda_c \cong 480\ nm$ (blue) in order to excite the final Rydberg states. Fig. 1. shows the specific scenario of exciting the $5P_{3/2} - nD_{5/2}$ transition, where $n$ is the principle quantum number and depends on the exact $\lambda_c$ chosen. The Rydberg state leads to a strong RF response of the atoms which manifests as the $nD_{5/2} - (n+1)P_{3/2}$ transition. That is, the energy required to cause a Rydberg atom to transition states is matched with that carried by an RF photon. These two lasers are aligned to counter propagate collinearly and are focused at the center of the vapor cell to a nominal $1/e$ beam diameter of around $100\ \mu m$. Beam powers for the probe and coupling laser are nominally 100 nW and 30 mW respectively. A dichroic filter which reflects $\lambda_c$ and transmits $\lambda_p$ aids in overlapping the two beams and a band pass filter rejects stray light. The probe laser transmission through the vapor cell is measured with a silicon photodiode detector. It is the *spectrum of the transmitted probe laser* that is of primary interest in determining the strength of the incident RF field.



Gordon, Joshua; Holloway, Christopher; Simons, Matthew.
"Rydberg Atom Electric-Field Metrology."
Paper presented at 90th ARFTAG Conference, Boulder, CO, United States. November 28, 2017 - December 1, 2017.

This is discussed next. For a more detailed discussion of this type of laser system setup the reader is encouraged to see [1].

### *B. Electric Field Through Rydberg Atom Spectrum*

The action of the RF field on the atoms can be connected to the probe laser spectrum by considering the optical susceptibility $\chi$ of the Rydberg vapor. As a full derivation of the susceptibility is outside the scope of this paper, we refer the reader to [7] and [8] for an in depth theoretical treatment. Here, we present the thought process and final important results for RF electric-field metrology. The imaginary part of the refractive index can be obtained using the fact that $\sqrt{(1+\chi)} = n + jk$. With $n$ being the real part, thus affecting the phase of the probe beam, and $k$ the imaginary part, which governs the degree of absorption experienced by the probe beam as it traverses the vapor cell. When only the probe laser is present and resonant with the $D_2$ transition, much of the light will be absorbed by the atoms. However, it can be shown that when both the probe (resonant with $D_2$ transition) and the coupling (resonant with a Rydberg transition i.e. $5P_{3/2} - nD_{5/2}$) lasers are present, a transparency window occurs for the probe laser beam where absorption of the probe laser is significantly reduced. This phenomenon is well documented and known as Electromagnetically Induced Transparency (EIT) [9].

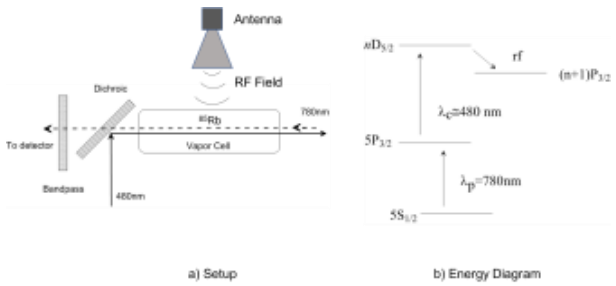


Fig. 1. a) Typical elements in a setup for sensing RF fields using Rydberg atoms in a vapor cell full of $^{85}$Rb atoms. (Dotted) The 780 nm probe and 480 nm (Solid) coupling laser would in actuality be overlapping, but are shown here displaced for clarity. b) Energy level diagram for $^{85}$Rb.

EIT is observed as a *transmission peak* in the *absorption* spectrum of the probe laser. Furthermore, when in addition to the probe and coupling lasers, an RF field is present and on resonance with a Rydberg transition, the EIT peak splits into two peaks. These two scenarios, one with RF and one without are shown in Fig. 2. The two peaks occur above and below the center frequency of the $D_2$ transition, $f_{D2} = 384.23 \ldots THz$. Through the susceptibility $\chi$ it is found that the frequency separation of these two peaks $\Delta f_{probe}$ as measured in the probe laser absorption spectrum is proportional to the RF field strength [10], [11], as,

$$\Delta f_{Probe} = \frac{\lambda_c}{\lambda_p} \frac{\wp_{RF}|E_{RF}|}{2\pi\hbar} , \qquad (1)$$

where $\wp_{RF}$ is the atom's dipole moment for the RF transition (analogous to the dipole moment of an antenna), $\hbar$ is Plank's constant, $|E_{RF}|$ is the magnitude of the RF field and $\lambda_c$ and $\lambda_p$ are the wavelengths of the coupling and probe lasers respectively. From this expression, a measurement of the RF electric field magnitude has been reduced to an optical frequency measurement. An example spectrum is shown in in Fig 2. The splitting is clearly observed when an RF field at a frequency of 182.15 GHz is incident on a Rb vapor cell. For reference this splitting corresponds to a strength of 0.735 V/m.

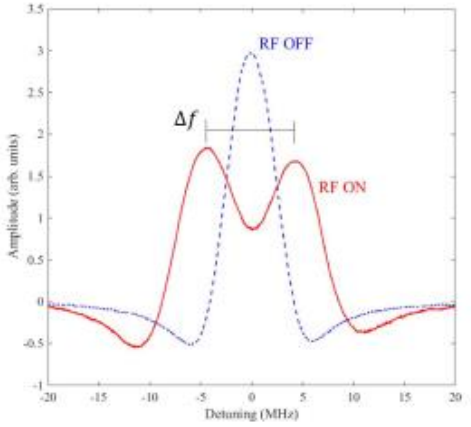


Fig. 2. The optical spectrum for the probe laser. (Dotted) RF field turned off. Only a single EIT peak is observed. (Solid) An applied RF field of 0.735 V/m at 182.15 GHz incident on the vapor cell splits the peak into two peaks separated by an amount $\Delta f$.

## III. Measurements

### *A. Field Strength Measurements*

For each Rydberg state, there is a corresponding RF transition and associated dipole moment. The RF transition frequency for a given coupling $\lambda_c$ can be calculated using the total ionization energy of the atom and corresponding quantum defects [11]. Therefore, the coupling laser need only change a few nanometers in order to tune the atom from about 500 MHz up to about 1 THz. As an example, with $^{85}$Rb consider cases (a) where the coupling laser is set to $\lambda_c = 479.32\, nm$, and case (b) where $\lambda_c = 483.60\, nm$. In case (a) the corresponding RF frequency occurs at 2.03 GHz whereas in case (b) it occurs at 150.40 GHz. This is depicted in the energy diagram shown in Fig. 3. where by tuning $\lambda_c$ by about 4 nm the RF resonance frequency is tuned by almost 150 GHz.



Gordon, Joshua; Holloway, Christopher; Simons, Matthew.
"Rydberg Atom Electric-Field Metrology."
Paper presented at 90th ARFTAG Conference, Boulder, CO, United States. November 28, 2017 - December 1, 2017.

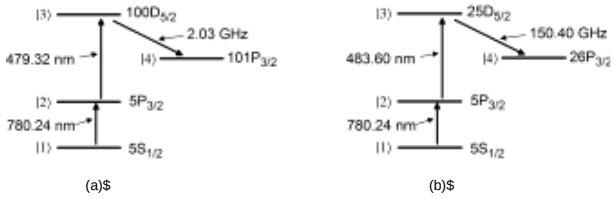


Fig. 3. Energy diagram for $^{85}$Rb showing RF frequency tuning via couple laser wavelength. Tuning the coupling laser by approximately 4 nm achieves almost 150 GHz of RF tuning.

Field measurements across the ULF, L, D, and G bands demonstrating this broadband tuning are shown in Fig. 4. RF frequencies at 723.78 MHz, 1.013 GHz, 132.65 GHz, 171.41 GHz, 182.16 GHz, and 203.32 GHz are shown over various field strengths. As there are no traceable sources above 110 GHz this Rydberg approach may provide a path to a solution. These measurements were obtained in the far field of a standard gain horn antenna operating in-band for the respective frequencies.

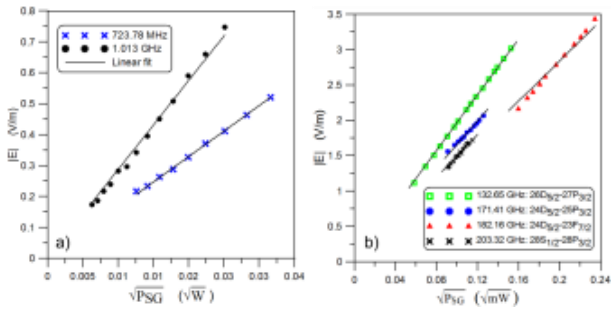


Fig. 4. Demonstration of the broad tuning property of the Rydberg atom approach. Plot a) is within the ULF to L band. Plots b) show measurements within the D and G band.

*B. Near-field Coplanar Waveguide Mode*

A newly developed quantum E-field probe head [12] was constructed by bonding single mode optical fiber to a cubic micro vapor cell 10 mm on a side. The micro cell was filled with $^{133}$Cs atoms. The quantum E-field probe head is shown in Fig. 5. Traditional use of free-space laser beams confines measurements to an optical table, however, fiber coupling the micro cell overcomes this limitation and allows for the quantum E-field probe to be removed from the optical table. This is a recent advancement which now enables measurements off the optical table. This is demonstrated by measuring the mode symmetry of an unbalanced coplanar waveguide mode [12] as shown in Fig. 6. The symmetrical mode for an ideal CPW was simulated using Ansys HFSS software (mention of this product is not an endorsement but only serves to clarify what was done). However, imperfections in the feed structure and lack of air bridges produce asymmetries in the mode not easily simulated. This is apparent in Fig. 6.

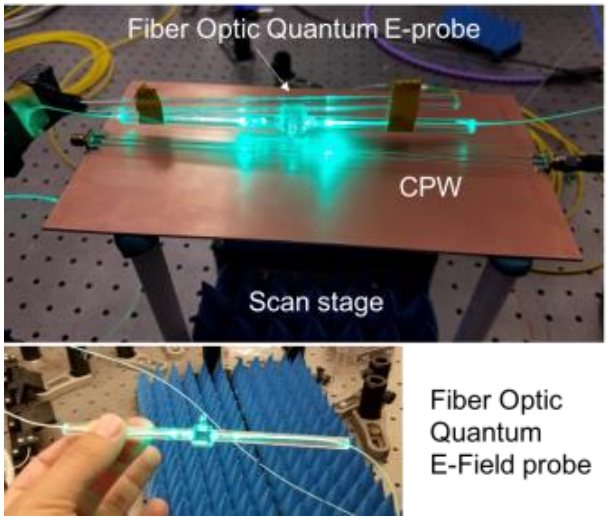


Fig. 5. (Top) CPW and fiber optic quantum electric-field probe. Scan stage moves CPW relative to quantum E-field. (Bottom) Development of this new type of quantum E-field probe allows laser beams, and vapor cell to be taken off of the optics table and held in hand.

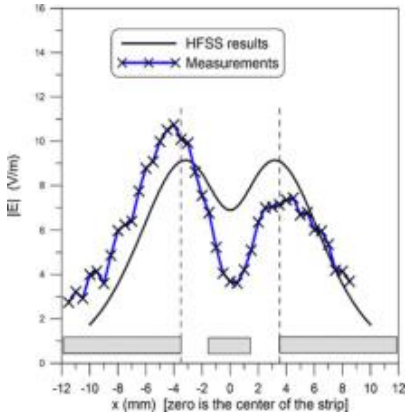


Fig. 6. Coplanar waveguide mode asymmetry determined near-field measurement using the fiber optic quantum E-field probe.



Gordon, Joshua; Holloway, Christopher; Simons, Matthew.
"Rydberg Atom Electric-Field Metrology."
Paper presented at 90th ARFTAG Conference, Boulder, CO, United States. November 28, 2017 - December 1, 2017.

## IV. Acknowledgments

This work was funded in part by the DARPA QuASAR program and NIST On A Chip program.

## References

[1] C. L. Holloway. J. A. Gordon, S. Jefferts, et al., "Broadband Rydberg atom-based electric-field probe for SI-traceable, self-calibrated measurements," *IEEE Trans. Antenna Propag., vol. 62, no. 12, pp. 6169–6182, Dec. 2014.*

[2] J. A. Gordon et al., "Millimeter-wave detection via Autler-Townes splitting in rubidium Rydberg atoms," *Appl. Phys. Lett., vol. 105, 2014, no. 024104.*

[3] C. L. Holloway, J. A. Gordon, A. Schwarzkopf, et al., "Sub-wavelength imaging and field mapping via electromagnetically induced transparency and Autler-Townes splitting in Rydberg atoms," Appl. Phys. Lett., vol. 104, 2014, Art. no. 244102.

[4] J. A. Sedlacek, A. Schwettmann, H. K¨ubler, R. Low, T. Pfau, and J. P. Shaffer, "Microwave electrometry with Rydberg atoms in a vapor cell using bright atomic resonances," *Nature Phys., vol. 8, pp. 819–824, 2012.*

[5] J. A. Sedlacek, A. Schwettmann, H. K¨ubler, and J. P. Shaffer, "Atom based vector microwave electrometry using rubidium Rydberg atoms in a vapor cell," *Phys. Rev. Lett., vol. 111, 2013, Art. no. 063001.*

[6] T. F. Gallagher, *"Rydberg Atoms"* (Cambridge University Press, 1994).

[7] S.N. Sandhya and K.K. Sharma, "Atomic coherence effects in four level systems: doppler-free absorption within an electromagnetically induced-transparency window", *Phys. Rev. A, vol. 55, no. 3, pp. 2155-2158, 1997.*

[8] P. Meystre and M. Sargent III, "Elements of Quantum Optics", 4th Ed. Springer, chapter 9, 2007.

[9] K.J. Boller, A. Imamolu, and S.E. Harris, "Observation of electromagnetically induced transparency," *Phys. Rev. Lett., vol. 66, no. 20, pp. 2593-2596, May, 1991.*

[10] S.H. Autler and C.H. Townes, "Stark Effect in Rapidly Varying Fields," *Physical Review, vol. 100, no. 2, pp. 703722, 1955.*

[11] T. Y. Abi-Salloum, "Electromagnetically induced transparency and Autler-Townes splitting: Two similar but distinct phenomena in two categories of three-level atomic systems", *Phys. Rev. A 81, 053836 (2010).*

[12] C. L. Holloway, M. T. Simons, J. A. Gordon, P. F. Wilson, et. .al., "Atom-Based RF Electric Field Metrology: From Self-Calibrated Measurements to Subwavelength and Near-Field Imaging", *IEEE TRANS. ELEC. COMP.*, vol. 59, no. 2, 2017



Gordon, Joshua; Holloway, Christopher; Simons, Matthew.
"Rydberg Atom Electric-Field Metrology."
Paper presented at 90th ARFTAG Conference, Boulder, CO, United States. November 28, 2017 - December 1, 2017.

# Spatial Channels for Wireless Over-the-Air Measurements in Reverberation Chambers*

Maria G. Becker[1], Robert D. Horansky[1], Damir Senic[1], Vincent Neylon[1], Kate A. Remley[1]
[1]RF Technology Division, National Institute of Standards and Technology, Boulder CO, USA, maria.becker@nist.gov


***Abstract*—NIST is developing a hybrid test chamber for over-the-air characterization of the next generation of wireless devices in spatial channel environments. By combining features of both reverberation and anechoic chambers, the hybrid chamber will produce anisotropic, multipath environments intended to test spatial diversity and beamforming capabilities of multiple-element antenna. Here, we present results that investigate our ability to control spatial channels. Synthetic-aperture measurements are used to determine the channel's power-angle profile and power-delay-angle profile, which characterize the angle-of-arrival and time-of-arrival of received power. Comparisons are made between an unloaded and loaded chamber. For the loaded configuration, strategically placed RF absorber is shown to create an anisotropic, spatial channel. The hybrid chamber is expected to provide a cost-effective solution for over-the-air measurements of next-generation wireless devices.**

***Index Terms*—Millimeter-wave metrology, power-angle profile, power-delay-angle profile, synthetic-aperture measurement, reverberation chamber, wireless system.**

## I. Introduction

The widespread use of data-intensive smartphones, tablets, and other wireless devices is placing growing demands on communication channels. As a solution to this so-called spectrum crunch, a new generation of communication technology (5G) is being developed to operate at millimeter-wave frequencies [1,2]. The use of beamforming and spatial diversity requires multiple-element antenna systems that transmit and receive along directional, spatially-independent channels. The metrology infrastructure for telecommunications in directional-channel environments and at millimeter-wave frequencies is, however, incomplete. In response to the need for over-the-air (OTA) characterization procedures for the next generation of integrated wireless devices, we are developing a hybrid chamber that will combine reverberation and anechoic properties to produce controllable, spatial-channel testing environments. Contrary to conventional applications of reverberation chambers in OTA measurements where performance metrics are based on statistically isotropic channels [3-8], this innovative measurement technique will use reverberation chambers to produce highly anisotropic spatial channels with known, repeatable test conditions.

The hybrid chamber concept involves heavily loading a reverberation chamber with the intended goal of producing a static, anisotropic, multipath environment. The spatial and temporal properties of the channel produced inside the chamber are evaluated by means of a synthetic-aperture measurement, as described in [9]. The calculated power-angle profile provides a measure of the received power as a function of angle-of-arrival, while the power-delay-angle profile provides the instantaneous distribution of received power as a function of arrival time and angle-of-arrival.

As a preliminary step in developing a hybrid chamber for use at millimeter-wave frequencies, we have conducted a proof-of-concept study at microwave frequencies in a comparison of two chamber configurations, unloaded and loaded. In the loaded configuration, RF absorber covered a significant portion of one wall of the chamber (Fig. 1), while the rest of the chamber was free of absorber. The azimuthal angle-of-arrival is evaluated in terms of a power-angle profile for each chamber configuration. The presence of absorber creates an anisotropic channel that is qualitatively predictable. This suggests that we will be capable of reproducing specific spatial channel models in the hybrid chamber. The arrival times of the reflected signals (multipath components) are also evaluated in power-delay-angle profiles.

We begin in Section II by describing the 2-D synthetic-aperture measurements used to sample the chamber's wireless channel as a function of frequency and position. In Section III, we present a power-angle-profile analysis for each chamber configuration. The corresponding power-delay-angle profile analysis follows in Section IV. Concluding remarks and a discussion of the future outlook for the hybrid chamber are presented in Section V.

## II. Synthetic-Aperture Measurements

Synthetic-aperture measurements have been used to study the spatial characteristics of static wireless channels [10,11], including those in reverberation chambers [9,12-15]. The latter work, which forms the basis of our analysis, involved measurement that scan an antenna through discrete locations on a two-dimensional spatial grid, creating a synthetic aperture in the azimuthal plane.

The measurement setup is illustrated in Fig. 1(a). The interior dimensions of the reverberation chamber are 1.875 m × 1.28 m × 1.76 m. Wall (0.88 m × 0.30 m) and ceiling (0.97 m × 0.40 m) paddles have travel distances of 1.4 m and 1.3 m, respectively. A vertically-polarized discone antenna functioned as the receive antenna, which was scanned across a horizontal synthetic-aperture grid; we used a 2-D positioning

* Work supported by U.S. government, not protected by U.S. copyright.

Becker, Maria; Horansky, Robert; Senic, Damir; Neylon, Vincent; Remley, Catherine.
"Spatial Channels for Wireless Over-the-Air Measurements in Reverberation Chambers."
Paper presented at 12th European Conference on Antennas and Propagation (EuCAP 2018), London, United Kingdom. April 9, 2018 - April 13, 2018.

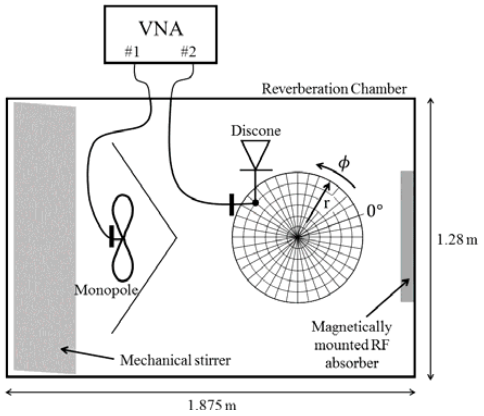


(a)

(b)

Fig. 1. Experimental setup for synthetic-aperture measurements: (a) top-down diagram and (b) photograph of chamber with loaded wall at left.

system, which consisted of an automated turntable and radial translation stage. The vertical position of the antenna within the chamber was 0.70 m above the floor and 0.42 m above the turntable platform. For each turntable position, the radial translation stage stepped through multiple positions, starting at the center of the turntable and ending at its outer diameter. In Fig. 1(b), the radial translation stage is positioned at its outermost position. The sample points of the synthetic aperture are the intersection points of concentric circles corresponding to different radii and radial lines corresponding to different turntable positions, as illustrated in Fig. 1(a). The angular resolution of the turntable is $84.5(\pm 0.1)$ $\mu$rad, and the linear resolution of the translation stage is $6.35(\pm 0.18)$ $\mu$m per manual specifications.

The transmit antenna was a polarization-balanced, double-sided, tapered, self-grounded monopole antenna [16]. It was positioned ~0.5 m above the floor and behind a metal shield to eliminate line-of-sight components of the channel [17]. Both unloaded and loaded chamber configurations were evaluated to investigate our ability to create directional channels. In the loaded configuration, a 60 cm × 90 cm section of a wall was covered with RF absorber, as shown in Fig. 1(b).

The transmit and receive antennas were connected to ports 1 and 2, respectively, of a calibrated vector network analyzer (VNA). The receive antenna was scanned across the 2-D grid at 36 angular steps of 10° and 7 radial steps of 4.5 cm, creating a circular synthetic-aperture with a diameter of 54 cm. Thus, the distance between adjacent grid points was less than $\lambda/2$ in accordance with the Nyquist criterion [10]. At each grid point and paddle orientation, complex $S_{21}$ measurements were recorded from 1.8 to 2.2 GHz at 4001 uniformly spaced frequencies. The VNA's intermediate frequency (IF) bandwidth was 1 kHz and the dwell time was 10 $\mu$s. We recorded measurements at nine independent paddle configurations using three vertical and three horizontal paddle positions. To a first order, the $S_{21}$ scattering parameter represents the wireless channel's transfer function $h^{(n)}(f, \boldsymbol{r})$, where $f$ is frequency, $\mathbf{r} = (r, \theta)$ is the receive antenna position on the 2-D grid, and $n = 1 \ldots 9$ indicates paddle configuration. Including mismatch correction and antenna efficiency in the formulation is the subject of future work.

## III. Power-Angle Profiles

To extract angle-of-arrival information from synthetic-aperture measurements of the channel's transfer function, we use Fourier analysis. The resulting power-angle profiles indicate the distribution of received power as a function of azimuthal arrival angle.

As described in [9], we obtain the 2-D power-wavevector profile $p^{(n)}(f, \mathbf{k})$ by taking the magnitude squared of the Fourier transform with respect to position of the channel transfer function for a particular frequency and paddle configuration:

$$p^{(n)}(f, \mathbf{k}) = \left| \int h^{(n)}(f, \mathbf{r}) e^{j\mathbf{k}\cdot\mathbf{r}} d\mathbf{r} \right|^2. \quad (1)$$

The 2-D wavevector is indicated by $\mathbf{k} = (k, \beta)$, where $\beta$ is an outgoing angle. Prior to taking the Fourier transform in (1), we apply a 2-D Hamming window to the transfer function to minimize aperture sidelobes. Also, to simplify the analysis, we convert the channel transfer function, recorded in polar coordinates, to Cartesian coordinates prior to the Fourier transform. To achieve this, we interpolate the polar coordinate data onto a Cartesian grid with a step size that matches the largest step size of the polar grid. We calculate power-angle profiles by converting back to polar coordinates $(k, \beta)$, again using an interpolation technique, and integrating over wavenumber, we get:

Becker, Maria; Horansky, Robert; Senic, Damir; Neylon, Vincent; Remley, Catherine.
"Spatial Channels for Wireless Over-the-Air Measurements in Reverberation Chambers."
Paper presented at 12th European Conference on Antennas and Propagation (EuCAP 2018), London, United Kingdom. April 9, 2018 - April 13, 2018.

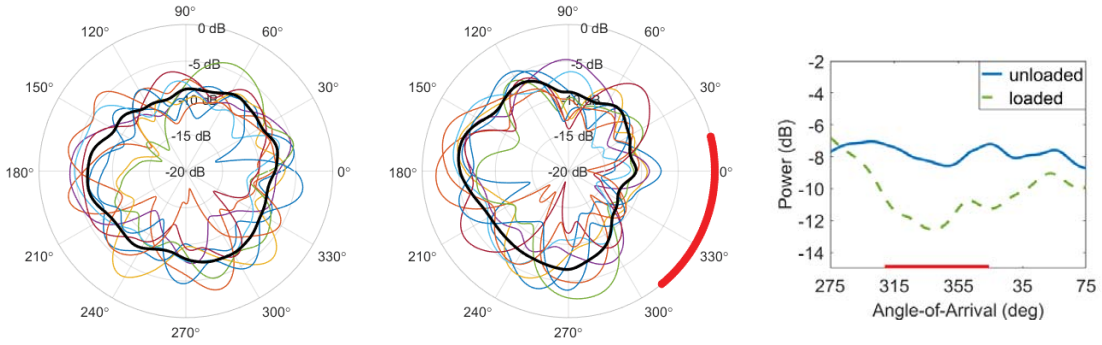


(a) (b) (c)

Fig. 2. Power-angle profiles at 2 GHz in the (a) unloaded and (b) loaded chamber. The nine, thin, colored profiles, each normalized to the total integrated received signal level, correspond to nine independent paddle positions; the thick, black trace corresponds to their average. The direction of the absorber is indicated in red on the angular axis at 0 dB for the loaded chamber. (c) The average power-angle profiles are plotted for angles spanning the placement of absorber; the difference is approximately 3-5 dB in the direction of the absorber, indicated in red.

$$p^{(n)}(f,\phi) = \int_0^{k_0} p^{(n)}(f,k,\beta+\pi)\,dk, \qquad (2)$$

where $k_0$ is the free-space wavenumber. This integration over wavenumber corresponds to an integration with respect to elevation angle, such that multipath components arriving from above and below the horizon are projected onto the azimuthal plane. The outgoing propagation angle $\beta$ has been mapped to the incoming arrival angle $\phi$ with the addition of $\pi$.

Power-angle profiles for the loaded and unloaded configurations are shown in Figs. 2(a) and (b), respectively, for nine independent paddle configurations (thin lines), as well as their average (thick line). For the loaded case, the position of the RF absorber is also indicated (thick line at edge of polar plot). Each profile has been normalized to the total integrated signal level, such that an integral of a single profile with respect to the polar angle would give 0 dB. The result is a relative power based on $|S_{21}|^2$. The uncertainty in the angle $\phi$ is given by the turntable repeatability of 4.25 $\mu$rad.

As expected, the stirred, unloaded chamber produces an isotropic environment relative to the hybrid chamber, indicated by little variation in the mean power-angle profile (Fig. 2(a)) as a function of azimuth angle. Additional paddle stirring is expected to further increase the isotropicity. When the chamber wall is loaded, however, there is less power received from the direction of the loaded wall relative to other directions. On average, the power is reduced by approximately 3-5 dB in the direction of absorber, as indicated by Fig. 2(c). Thus, a directional channel has been created in the reverberation chamber.

The angular resolution of the synthetic-aperture measurements is limited by the diameter of the aperture. It can be approximated with the Rayleigh criterion [18]:

$$\sin\theta_R = 1.22\frac{\lambda}{D}, \qquad (3)$$

where $\lambda$ is wavelength, $D$ is the diameter of the aperture, and $\theta_R$ is the minimum resolvable angular beamwidth. Based on this criterion, our experimental setup ($D = 54$ cm, $\lambda = 15$ cm) is capable of resolving beamwidths down to 20° at 2 GHz. This estimate is consistent with the lobes in the power-angle profiles of Figs. 2(a) and 2(b). The long-term goal of this project is to create and characterize directional channel environments for millimeter-wave frequencies, where much higher angular resolution is desired. At 28 GHz, the same array diameter will provide 1.4° resolution, which is expected to meet the future demands of the wireless industry.

We note that antenna-environment multiple scattering effects could include perturbation of the channel by the receive antenna and its positioning system [14]. The error due to such effects was not studied in this initial investigation, but will be part of future work.

## IV. Power-Delay-Angle Profiles

Fourier analysis can also be used to extract time-of-arrival information from synthetic-aperture measurements of the channel's transfer function. The resulting power-delay-angle profiles indicate the instantaneous distribution of received (relative) power as a function of arrival time $\tau$, as well as azimuthal arrival angle $\phi$. As described in [9], the 2-D power delay-wavevector profile $p^{(n)}(\tau,\mathbf{k})$ is obtained by taking the magnitude squared of the Fourier transform of the channel transfer function with respect to position and frequency for a particular paddle position:

$$p^{(n)}(\tau,\mathbf{k}) = \left|\iint h^{(n)}(f,\mathbf{r})e^{j2\pi\tau f}e^{j\mathbf{k}\cdot\mathbf{r}}df\,d\mathbf{r}\right|^2. \qquad (4)$$

To avoid sidelobes, a 1-D Hamming window is applied to the channel transfer function in the frequency dimension, in addition to the 2-D Hamming window in the spatial domain, prior to the Fourier transforms in (4). We arrive at the power-

Becker, Maria; Horansky, Robert; Senic, Damir; Neylon, Vincent; Remley, Catherine.
"Spatial Channels for Wireless Over-the-Air Measurements in Reverberation Chambers."
Paper presented at 12th European Conference on Antennas and Propagation (EuCAP 2018), London, United Kingdom. April 9, 2018 - April 13, 2018.

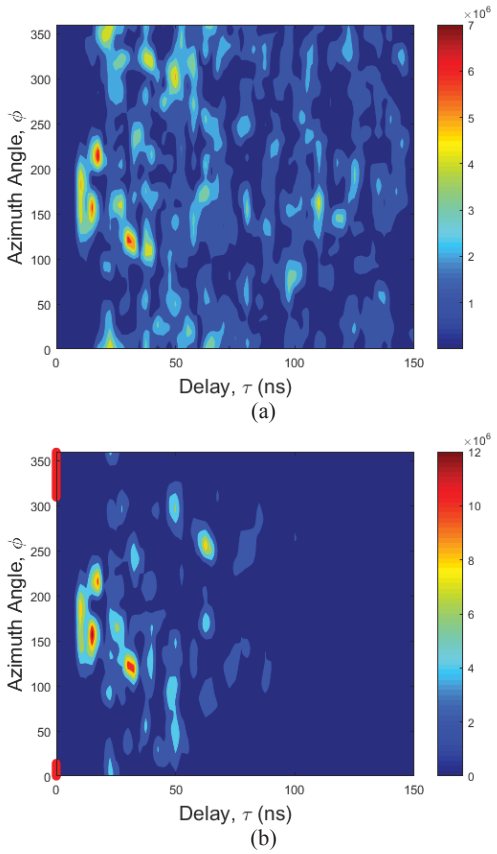


Fig. 3. Power-delay-angle profiles in the (a) unloaded and (b) loaded chamber for a single paddle position. Each profile is normalized to the total integrated signal.

delay-angle profile for a particular paddle position by integrating over wavenumber:

$$p^{(n)}(\tau, \phi) = \int p^{(n)}(\tau, k, \beta + \pi) dk. \qquad (5)$$

Power-delay angle profiles for the loaded and unloaded chamber configurations are shown in Fig. 3 for a single paddle orientation. For the loaded case, the angular position of the RF absorber is also indicated. Each profile has been normalized to the total integrated signal level such that integrating over delay and azimuth would result in unity. The time interval used in Figs. 3(a) and (b) is $\Delta t = 2.5$ ns and the angle interval is $\Delta\phi = \pi/360$. While the color scale for relative power values is given in linear units, the corresponding decibel values can be obtained by multiplying by the time and angle interval values given above, then taking the log and multiplying by ten.

As expected, less power is received at longer delay times for the loaded configuration, as compared to the unloaded configuration. The absence of power received from the direction of the loaded wall is also evident.

The temporal resolution of the power-delay-angle profile is determined from the bandwidth of frequencies used in the Fourier transform of (5) according to $\Delta t = 1/\Delta f$. The resulting temporal resolution from our 400 MHz bandwidth is 2.5 ns.

## V. Conclusion

A hybrid chamber designed to create spatial channels that replicate millimeter-wave channel models is being developed at NIST for OTA characterization of next generation wireless devices. In a proof-of-concept study at microwave frequencies, we have demonstrated our ability to create a sample spatial channel environment with strategic placement of RF absorber. We characterized the spatial and temporal properties of the spatial channel in 2-D power-angle and power-delay-angle profiles using synthetic-aperture measurements. Ongoing work towards the development of the hybrid chamber will include extending the analysis to three dimensions. In our preliminary study, we measured vertically-polarized plane-waves. Future work will include analyzing spatial-channel environments for all three plane-wave polarizations. Accounting for mismatch correction, antenna efficiency, multiple scattering effects, and uncertainty will also be subjects of future work.

The hybrid chamber is expected to increase the flexibility of the reverberation chamber setup for testing wireless devices by emulating anisotropic, directional-channel environments. This cost-effective approach has the potential for high impact applications in the wireless industry where multiple-element antenna systems are being integrated in an increasing number of wireless devices, with the performance of each new model needing to be tested under directional-channel conditions prior to certification. Development of the hybrid chamber supports advanced wireless communication technology by providing necessary metrology infrastructure and standardized, measurement methods, ultimately with known uncertainties. The development of such technology is essential for meeting the expected increase in demand for wireless channel capacity.

## References

[1] T. S. Rappaport, S. Sun, R. Mayzus, H. Zhao, Y. Azar, K., Wang, G. N. Wong, J. K. Schulz, M. Samimi, and F. Gutierrez, "Millimeter wave mobile communications for 5G cellular: It will work!" *IEEE Access*, vol. 1, pp. 335-349, May 2010.

[2] K. A. Remley, J. A. Gordon, D. Novotony, A. E. Curtin, C. L. Holloway, M. T. Simons, R. D. Horansky, M. S. Allman, D. Senic, M. Becker, J. A. Jargon, P. D. Hale, D. F. Williams, A. Feldman, J. Cheron, R. Chamberlin, C. Gentile, J. Senic, R. Sun, P. B. Papazian, J. Quimby, M. Mujumdar, and N. Golmie, "Measurement challenges for 5G and beyond," *IEEE Microwave Magazine*, pp. 41-56, July/Aug. 2017.

[3] P. D. Donker and R. Meys, "Statistical response of antennas under uncorrelated place wave spectrum illumination," *Electromagnetics*, vol. 24, no. 6, pp. 409-423, 2004.

[4] P.-S. Kildal and K. Rosengren, "Correlation and capacity of MIMO systems and mutual coupling, radiation efficiency, and diversity gain of their antennas: Simulations and measurements in a reverberation

Becker, Maria; Horansky, Robert; Senic, Damir; Neylon, Vincent; Remley, Catherine.
"Spatial Channels for Wireless Over-the-Air Measurements in Reverberation Chambers."
Paper presented at 12th European Conference on Antennas and Propagation (EuCAP 2018), London, United Kingdom. April 9, 2018 - April 13, 2018.

chamber," *IEEE Commun. Mag.*, vol. 42, no. 2, pp. 104-112, Dec. 2004.

[5] K. Rosengren and P.-S. Kildal, "Radiation efficiency, correlation, diversity gain and capacity of a six-monopole antenna array for a MIMO system: Theory, simulation and measurement in reverberation chamber*," IEEE Proc.-Microw. Antennas Propag.*, vol. 152, no. 1, pp. 7-16, Feb. 2005.

[6] U. Carlberg, J. Carlsson, A. Hussain, and P.-S. Kildal, "Ray based multipath simulation tool for studying convergence and estimating ergodic capacity and diversity gain for antennas with given far-field functions, in *Proc. ICECom*, Dubrovnik, Croatia, Sep. 20-23, 2010, pp. 1-4.

[7] T. B. Hansen, "Correlation and capacity calculations with reference antennas in an isotropic environment," *Int. J. Antennas Propag*., vol. 2012, pp. 1-4, 2012.

[8] R. J. Pirkl and K. A. Remley, "MIMO channel capacity in 2-D and 3-D isotropic environments," *Int. J. Antennas Propag.*, vol. 2012, pp. 1-11, 2012.

[9] R. J. Pirkl and K. A. Remley, "Experimental evaluation of the statisitical isotropy of a reverberation chamber's plane-wave spectrum," *IEEE Trans. Electromagn. Compat*., vol. 56, no. 3, pp. 498-509, June 2014.

[10] J. Fuhl, J.-P. Rossi, and E. Bonek, "High-resolution 3-D direction-of-arrival determination for urban mobile radio," *IEEE Trans. Antennas Propag.*, vol. 45, no. 4, pp. 672-682, Apr. 1997.

[11] J. Larila, K. Kalliola, M. Toeltsch, K. Hugl, P. Vainikainen, and E. Bonek, "Wide-band 3-D characterization of mobile radio channels in urban environment," *IEEE Trans. Antennas Propag.*, vol. 50, no. 2, pp. 233-343, Feb. 2002.

[12] R. J. Pirkl, "Spatial autocovariances os S-parameter measurements in a lossy reverberation chamber," *IEEE Trans. Electromagn. Compat.*, vol. 55, no. 4, pp. 671-682, Aug. 2013.

[13] R. J. Pirkl, J. M. Ladbury, and K. A. Remley, "The reverberation chamber's unstirred field: a validation of the image theory interpretation," in *Proc. Int. Symp. Electromagn. Compat.*, Long Beach, CA, USA, Aug. 14-19, 2011, pp. 670-675.

[14] R. J. Pirkl and K. A. Remley, "Antenna-environment multiple scattering in reverberation chambers," in *IEEE AP-S*, Spokane, WA, USA, Jul. 4-8, 2011, pp.1-4.

[15] A. A. Glazunov, S. Prasad, and P. Handel, "Experimental characterization of the propagation channel along a very long virtual array in a reverberation chamber," *Progress in Electromagnetics Research B*, vol. 59, pp.205-217, 2014.

[16] A. Al-Rawi, A. Hussain, J. Yank, M. Franzén, C. Orlenius, and A. Kishk, "A new compact wideband MIMO antenna- The double-sided tapered self-grounded monopole array," *IEEE Trans. Antennas Propag.*, vol. 62, no. 6, June 2014.

[17] P.-S. Kildal, X. Chen, C. Orlenius, M. Franzén, and C. S. Lötbäck Patané, "Characterization of reverberation chambers for OTA measurements of wireless devices: Physical formulations of channel matrix and new uncertainty formula," *IEEE Trans. Antennas Prpag.*, vol. 60, no. 8, Aug. 2012.

[18] E. Hecht and A. Zajac, Optics. Reading, MA, USA:Addison-Wesley Publishing, 1974, pp. 353-354.

Becker, Maria; Horansky, Robert; Senic, Damir; Neylon, Vincent; Remley, Catherine.
"Spatial Channels for Wireless Over-the-Air Measurements in Reverberation Chambers."
Paper presented at 12th European Conference on Antennas and Propagation (EuCAP 2018), London, United Kingdom. April 9, 2018 - April 13, 2018.

# Angle- and Delay-Dispersion Characteristics in a Hallway and Lobby at 60 GHz*

Ruoyu Sun[1], Peter B. Papazian[1], Jelena Senic[1], Camillo Gentile[2], Kate A. Remley[1]
[1] RF Technology Division, National Institute of Standards and Technology, Boulder, CO, USA, ruoyu.sun@nist.gov
[2] Wireless Networks Division, National Institute of Standards and Technology, Gaithersburg, MD, USA


***Abstract*—In this paper, we present results from measurement data collected in a hallway and lobby up to 33 meters in line-of-sight and non-line-of-sight conditions. The data were collected with a custom double-directional 60 GHz channel sounder. By tracking the angle-of-departure and angle-of-arrival of the strongest path, regions with a direct path as well as single-, double- and triple-bounce paths are identified. This was validated against the geometry of the hallway. In addition, power angle- and delay- profiles are presented as well as complementary root-mean-square angle and delay spreads. The root-mean-square delay spread was characterized with variable beamwidth using a synthetic antenna pattern applied in post processing.**

***Index Terms*—millimeter-wave wireless, multiple-input-multiple-output antenna array, phased-array antenna, propagation channel, measurement, wireless systems.**

## I. Introduction

Due to saturation of the sub-6 GHz bands over the past decade, the wireless industry is expanding to the millimeter-wave (mmWave) spectrum for 5G deployment (by definition 30 – 300 GHz). To compensate for the much higher path loss in this frequency regime, very high-gain phased-array antennas (in excess of 26 dBi) will likely be employed at both the transmitter (TX) and receiver (RX). The higher the gain, the narrower the beamwidth; pencilbeams arrays on the order of a few degrees beamwidth are currently under design [1]. Because their beamwidths are so small, the boresights of TX and RX antennas must be steered towards viable propagation paths between the respective TX and RX.

In line-of-sight (LOS) conditions, the beams will be steered towards the direct path, which is typically the strongest available. When obstructed – say by human bodies which severely attenuate the signal – the beams must be redirected towards other available paths to maintain connectivity. Even if the direct path is clear, other strong propagation paths are necessary to implement spatial multiplexing. Hence, knowing the angle spread, a key measure of the relative strength of the various paths, is important. In non-line-of-sight (NLOS) conditions, the direct path will likely go undetected altogether since materials have much higher penetration losses at mmWave frequencies [2]. Thus, in NLOS, understanding the spread of power in the various directions is even more critical.

The delay spread is also a very important quantity, the longer the spread, the more processing is required for equalization, thereby increasing the cost of hardware. Once a suitable path has been found for beamforming, the pencilbeam antennas can hone in on the path, reducing the delay spread significantly by admitting fewer paths into the beam.

In this paper, we report on the root-mean-square angle spread (RMS-AS) and delay spread (RMS-DS) derived from measurements conducted in a lobby and hallway environment in both LOS and NLOS conditions. The measurements were taken using our custom double-directional channel sounder at 60.5 GHz [3]. The measurement campaign and details of the equipment are described in Section II, followed by a description of the dominant propagation mechanisms in the environment in Section III. Section IV presents our results and finally our conclusions are documented in the last section.

## II. Measurements

### A. Measurement Equipment

Fig. 1(a) displays the TX and RX of our 60 GHz channel sounder. The TX features a semicircular array of eight horn antennas, each with 18.1 dBi gain and 22.5° beamwidth (identical in vertical and horizontal planes). To avoid any "blind spots," the angular spacing between the elements matches the beamwidth of the horns. Specifically, the elements are spaced at 22.5° horizontally, and vertically adjacent elements are pointed outwards at 0° and upwards at 22.5°. Consequently, the horizontal beamwidth of the array is 180° and its vertical beamwidth is 45°. The 3D spatial diversity allows for characterizing the antennas angle-of-departure (AoD) in both azimuth and elevation. The RX features two semicircular arrays to estimate angle-of-arrival (AoA) – each one is a replica of the TX array – extending the azimuthal beamwidth of the array to an omnidirectional view. The omnidirectional design at the RX is essential because the RX is mounted on a mobile robotic positioning system, whereas the TX is fixed – typical for hot-spot deployments – hence emission from the backside of the TX is less important.

The transmitting system generates a repeating 2047-bit pseudorandom (PN) codeword that has a chip rate of 2 GHz, equivalent to a delay resolution of 0.5 ns, transmitted at 20 dBm. With precision synchronization using Rubidium clocks, the signal is transmitted from a single TX element while the received signal is measured by sequentially switching through the RX elements every two codewords. Note that the extra codeword is used to buffer the electronic switching time. After a full RX cycle, the TX element is then also switched to the next TX element. Thus, a measurement consisting of a full sweep of the 128 (8 × 16) pairs requires 262 µs. The codeword

Sun, Roy; Papazian, Peter; Senic, Jelena; Gentile, Camillo; Remley, Catherine.
"Angle- and Delay-Dispersion Characteristics in a Hallway and Lobby at 60 GHz."
Paper presented at 12th European Conference on Antennas and Propagation (EuCAP 2018), London, United Kingdom. April 9, 2018 - April 13, 2018.

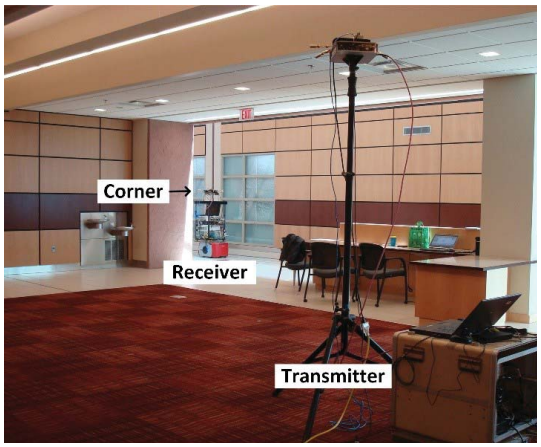


Fig. 1(a). Photo of the measurement system and the lobby site. The TX antenna array is mounted on a tripod and the RX antenna array is placed on the robotic mobile positioning system.

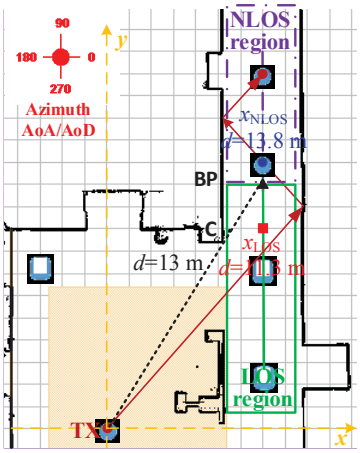


Fig. 1(b). Floorplan of the hallway/lobby. TX was placed in the lobby area and RX was moving along the hallway in LOS (solid green line) and NLOS (dash-dotted purple line) conditions. Raytracing prediction for the reflected path along the hallway is depicted with red solid arrows.

is generated at an intermediate frequency (IF) of 3 GHz and then upconverted to an RF center frequency of $f_c$ = 60.5 GHz. At the RX, the received signal is downconverted back to the IF and then digitized at 40 G samples/sec. For each TX/RX measurement pair, the received signal is correlated with the known PN codeword to generate a complex channel impulse response (CIR). Non-ideal effects from the electronics within the TX and RX are carefully corrected with back-to-back measurements [3]. The dynamic range of the sounder is 162.2 dB [3].

### *B. Measurement Campaign*

Measurements were performed in a hallway/lobby inside the Physical Measurement Laboratory (PML) building on the National Institute of Standards and Technology (NIST) campus in Boulder, CO USA. The height of the ceiling is 3 m in the lobby and 7 m in the hallway. The width of the hallway is approximately 4 m. The walls are made of finely ribbed wood, glass (with flat surface) or concrete with a rough, stone-like surface. The floor is covered with carpet in the lobby area and porcelain tiles in the hallway. The ceiling is made of acoustic tiles. Occasionally people were walking in the area.

To emulate a hot-spot deployment, the TX was fixed in the lobby area at 2.5 m height while the RX was mounted on the mobile-positioning robot 1.6 m above the floor. Fig. 1(a) shows a snapshot of the deployment with the TX positioned in the lobby area and the RX moving in the hallway close to a corner. The TX was oriented to cover the continuous azimuth-angle ranges from 320° to 140° (defined in Fig. 1(b)) so that most of the energy was transmitted towards the hallway direction.

A floorplan of the environment marked with the TX position and the RX trajectory along the hallway is shown in Fig. 1(b). The map, with a grid spacing of 1 m, was created with the robot's laser range-finder. The $x$ and $y$ axes and the orientation of the azimuth angle are also marked. The robot moved along a straight line in the middle of the hallway at a constant velocity of 0.08 m/s. The corresponding TX-RX distance $d$ ranged from 7.5 m to 33.5 m. Note that, due to inconstant data-writing speed from the buffer on the digitizer to the solid-state hard drive, data for distances 25.2 m < $d$ < 29.2 m were not recorded. The robot transitioned from LOS (green solid line) to NLOS (dash-dotted purple line) conditions after the breakpoint (BP) right after the corner (C). The NLOS conditions were created by the interfering walls. The robot's mobile positioning system reports its position, velocity and heading at each data collection point. We collected 365 omnidirectional power-angle-delay profiles (PADPs).

## III. Data Analysis

In post-processing, the 128 CIRs from a single measurement were combined through the space-alternating generalized expectation-maximization (SAGE) algorithm [4] in order to extract the channel multipath components (MPCs). Given the phase centers of the TX and RX horns gauged within an accuracy of 50 μm [3], the departure and arrival angles were estimated by comparing the arrival times of the MPCs between the various CIRs. The accuracy of the angle estimation for the direct path was estimated with an average error of 2.1° [3]. Upon extraction, the path gain ($PG_i$) of the $i^{\text{th}}$ MPC is indexed according to delay ($\tau_i$), departure angle at the TX ($\theta_i^{TX}, \phi_i^{TX}$), and arrival angle at the RX ($\theta_i^{RX}, \phi_i^{RX}$), where $\theta$ denotes azimuth and $\phi$ elevation. The SAGE algorithm also de-embeds the directional antenna patterns of the array elements, estimated from the manufacturer's specifications. In this section, we analyze the MPCs to describe the propagation mechanisms in play throughout the lobby/hallway environment.

Sun, Roy; Papazian, Peter; Senic, Jelena; Gentile, Camillo; Remley, Catherine.
"Angle- and Delay-Dispersion Characteristics in a Hallway and Lobby at 60 GHz."
Paper presented at 12th European Conference on Antennas and Propagation (EuCAP 2018), London, United Kingdom. April 9, 2018 - April 13, 2018.

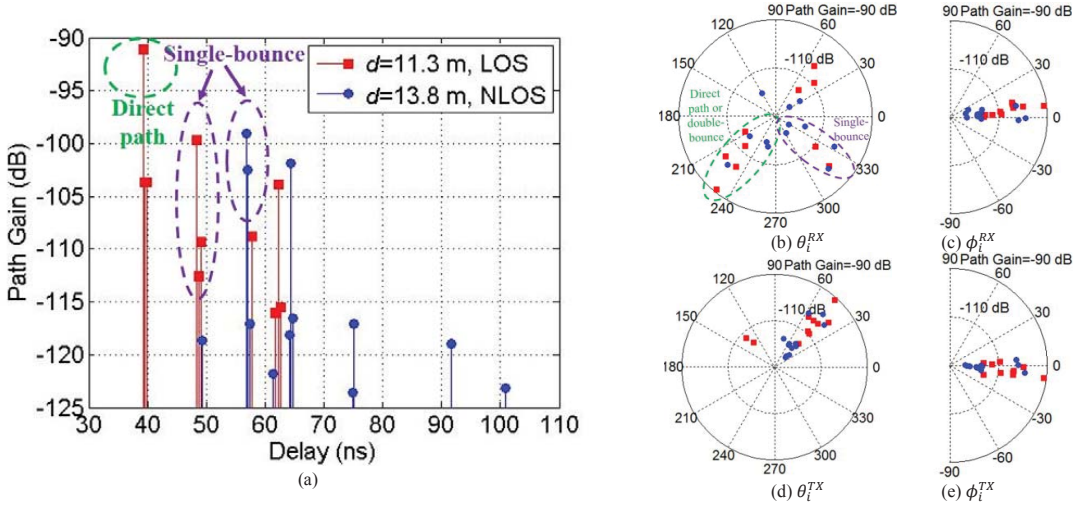


(a)

Fig. 2 Power-delay profiles (a) and power-angle profiles (b)-(e) for two example locations in LOS (red squares) and NLOS (blue circles). The azimuthal power-angle profile is shown in (b) and (d) over 360°, while the elevation is shown in (c) and (e) over 180° only.

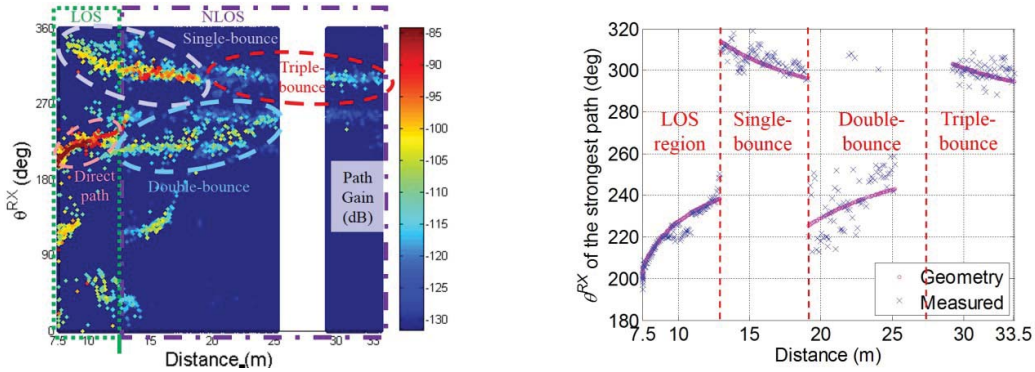


(a) (b)

Fig. 3. PAPs for all measurement locations, (a) Sequence of PAPs over distance for $\theta^{RX}$, (b) Azimuth arrival angle ($\theta^{RX}$) of strongest path over distance.

### *A. Illustrative Example with Two Locations*

We first consider an illustrative example at two specific measurement locations. One location was in LOS conditions right before the breakpoint ($\boldsymbol{x}_{\mathrm{LOS}}$ at $d$ = 11.3 m) and the other in NLOS right after the breakpoint ($\boldsymbol{x}_{\mathrm{NLOS}}$ at $d$ = 13.8 m). The locations are marked in Fig. 1(b).

The path gain of the MPCs versus delay, often referred to as the *power-delay profile* (PDP), for the two locations are superimposed in Fig. 2(a). For $\boldsymbol{x}_{\mathrm{LOS}}$, the three paths clustered at $\tau_i$ = 39.3, 39.4 and 39.9 ns represent the direct path – the strongest of the three – followed by the weaker reflections off of the wall near the corner. Note that when the robot moves up the hallway into an NLOS condition at $\boldsymbol{x}_{\mathrm{NLOS}}$, the direct path is no longer detected, as mmWave signals cannot penetrate these materials; rather, they are replaced by the much weaker single path at 49.2 ns representing diffraction from the corner [2]. The second cluster of paths for $\boldsymbol{x}_{\mathrm{LOS}}$ and $\boldsymbol{x}_{\mathrm{NLOS}}$ together represent the paths reflected from the right wall in the hallway. The path for $\boldsymbol{x}_{\mathrm{LOS}}$ at 48.4 ns represents the specular component followed by two weaker diffuse components at 48.7 and 49.1 ns. Analogously, the strongest path for $\boldsymbol{x}_{\mathrm{NLOS}}$ at 56.7 ns represents the specular component followed by two weaker diffuse components at 57.1 and 57.5 ns. The later paths in the PDPs represent reflections from other walls or obstacles in the environment or permutations thereof.

Analogously, Figs. 2(b)-(e) display the path gain of the MPCs versus each of the four angles, often referred to as the *power-angle profile* (PAP), for the two locations. Note the angles of the direct path for $\boldsymbol{x}_{\mathrm{LOS}}$ – the strongest path with $PG_i$ = −92 dB: its elevation departure and arrival angles are slightly negative (−5°) and positive (6°), as expected, given that the TX is higher than the receiver. In fact, most arrivals follow the same trend for $\boldsymbol{x}_{\mathrm{LOS}}$ – and $\boldsymbol{x}_{\mathrm{NLOS}}$ too – barring exceptions for the ground bounces. The azimuthal AoD for both points are bound by the angles formed between the TX and the entrance to the hallway on the left and right sides, as energy can only propagate in the hallway since the interfering

Sun, Roy; Papazian, Peter; Senic, Jelena; Gentile, Camillo; Remley, Catherine.
"Angle- and Delay-Dispersion Characteristics in a Hallway and Lobby at 60 GHz."
Paper presented at 12th European Conference on Antennas and Propagation (EuCAP 2018), London, United Kingdom. April 9, 2018 - April 13, 2018.

walls are impenetrable by the signal. For the azimuthal AoA, the two clusters from Fig. 2(a) distinctly appear and are so labeled. All of the extracted angles agree with the geometry in the hallway/lobby area shown in Fig. 1(b).

### B. All Locations Combined

The propagation mechanisms illustrated from the two example locations existed to some degree throughout all locations recorded in the lobby/hallway environment. Fig. 3(a) plots the power-angle profiles for the azimuthal arrival angle as a function of distance, where the clusters of MPCs of direct path, single-, double, triple-bounce and other scattering paths could be identified. Fig. 3(b) shows the azimuthal AoA of the strongest path as a function of distance. The theoretical results based on geometry is also provided in Fig. 3(b). Besides highlighting the direct path and single-bounce from the right wall of the hallway, as in the illustrative example in the last section, the plot shows the double-bounce from the right-then-left walls and the triple-bounce from the right-then-left-then-right walls. The $\theta^{RX}$ of the strongest path varies over 40° in the double-bounce region, while it only varies within 24° in the single- and triple-bounce regions. This is likely because the left wall is made of simulated rock, presenting a rough surface that scatters the signal over a larger range than the wooden wall with the finely ribbed surface on the right side of the hallway.

## IV. Angle and Delay Dispersion

The RMS-AS and RMS-DS are the most widely used measures for angle and delay dispersion, respectively. In this section, we compute their values for each of the measurements from the extracted MPCs. As the distance between the TX and RX increased, fewer and fewer MPCs were detected because they fell below the noise floor of the channel sounder, biasing the results towards smaller spreads. To avoid this, following common practice, we verified that the strongest MPC was at least 25 dB above the noise floor for each measurement in order for the measurement to be included in the results. The maximum distance observed that satisfied this condition was 18.9 m, which is the transition distance from the single-bounce region to double-bounce region. In addition, for each measurement we applied a 25 dB threshold from the strongest MPC so that spreads across all measurements were computed with the same dynamic range across. This resulted in a total of $N$ remaining MPCs per measurement.

### A. RMS Angle Spread

Since we extracted four different angles for each MPC, the angle spread was computed separately for $\varphi = \{\theta^{TX}, \phi^{TX}, \theta^{RX}, \phi^{RX}\}$. Specifically, the RMS-AS for each measurement was computed as

$$\sigma_{\varphi} = \sqrt{\frac{\sum_{i=1}^{N} PG_i \cdot (\varphi_i - \mu_{\varphi})^2}{\sum_{i=1}^{N} PG_i}}, \quad (1)$$

$$\mu_{\varphi} = \frac{\sum_{i=1}^{N} PG_i \cdot \varphi_i}{\sum_{i=1}^{N} PG_i}, \quad (2)$$

where $\varphi_i$ is the angle for the $i^{th}$ MPC. We saw little variation in the departure and arrival elevation angles, $\phi^{TX}$ and $\phi^{RX}$, in our measurements, primarily because the vertical distance between the TX and RX was much smaller than the horizontal distance. In fact, $\sigma_{\phi^{TX}}$ was observed only up to 11.2° with a median value of 2.8°; similarly, $\sigma_{\phi^{RX}}$ was only up to 9.8° with a median value of 2.7°. While more variation was observed in the departure azimuth angle, $\theta^{TX}$, since all of the detected energy in NLOS was channeled along the corridor, $\theta^{TX}$ only varied between the values corresponding to the left and right walls at the entrance to the hallway. Accordingly, $\sigma_{\theta^{TX}}$ was up to 43.7° with a median value of 3.7°.

By far the most variation was in the azimuthal arrival angle, $\theta^{RX}$, because the RX array is omnidirectional in azimuth; also because, since the RX was in the hallway, paths could arrive from any azimuthal direction. In fact, $\theta^{RX}$ was up to 84.2° with a median value of 24.6°. Fig. 4(a) also presents $\sigma_{\theta^{RX}}$ as a function of distance. In LOS conditions, the figure shows that most of the detected energy was in the direct path but gave way to paths from other arrival directions as it weakened with increasing distance. Due to the absence of the direct path in NLOS, the energy was spread in multiple arrival directions, increasing the RMS-AS. The $\theta^{RX}$ RMS-AS was typically smaller than 60° but occasionally jumped to over 80° due to intermittent MPCs from smaller ambient objects. For example, the spike near 15 m was due to the cluster of MPCs shown in Fig. 3(a) at that same distance and for $\theta^{RX}$ between 110° and 150°.

### B. RMS Delay Spread

Millimeter-wave systems will employ steerable pencilbeam antennas with beamwidths as low as 3° but unlikely greater than 30° [1]. As noted earlier, a larger angle spread means that more paths are available to steer energy from the directional TX to the directional RX. Smaller beamwidths will translate into narrower delay spreads as fewer paths will be admitted into the beam. Understanding this effect can help improve the design of pencilbeam antenna arrays.

In order to investigate this, we computed the RMS-DS by applying, after the MPCs have been extracted, an ideal, synthetic antenna pattern with variable beamwidth to the TX and RX. We assume a Gaussian beam pattern steered at $(\bar{\theta}, \bar{\phi})$ which can be expressed as

$$G^{\omega}(\theta, \phi; \bar{\theta}, \bar{\phi}) = e^{-\frac{(\theta-\bar{\theta})^2 + (\phi-\bar{\phi})^2}{\omega^2/log_e 16}}, \quad (3)$$

where $\omega$ is the synthetic beamwidth of the antenna in both azimuth and elevation. At the TX, the beam is steered towards $(\bar{\theta}^{TX}, \bar{\phi}^{TX})$ and at the RX towards $(\bar{\theta}^{RX}, \bar{\phi}^{RX})$, corresponding to the respective departure angle and arrival angle of the strongest MPC in the measurement.

Fig. 3(b) shows $\bar{\theta}^{RX}$ versus distance for all measurements. Again, the reason we chose to illustrate $\bar{\theta}^{RX}$ is because the azimuthal arrival angle exhibits the most variability of the four

Sun, Roy; Papazian, Peter; Senic, Jelena; Gentile, Camillo; Remley, Catherine.
"Angle- and Delay-Dispersion Characteristics in a Hallway and Lobby at 60 GHz."
Paper presented at 12th European Conference on Antennas and Propagation (EuCAP 2018), London, United Kingdom. April 9, 2018 - April 13, 2018.

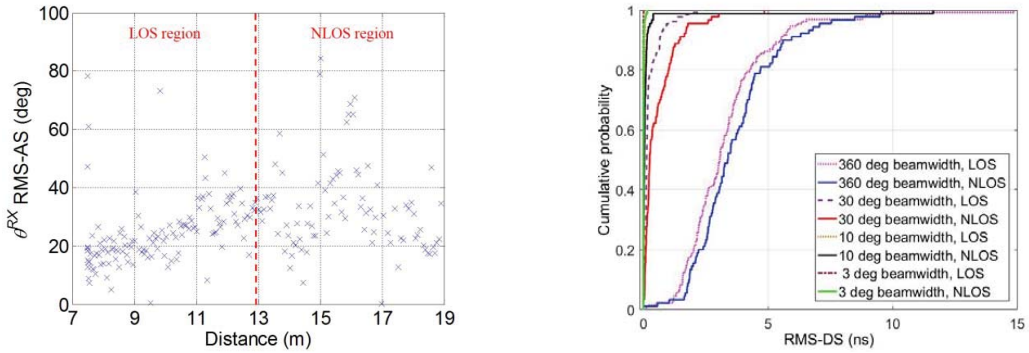


(a) (b)

Fig. 4. Delay and angle spreads for all measurements, (a) RMS-AS of $\theta^{RX}$ over distance for measurements made in the hallway, (b) CDF of RMS-DS for various beamwidths synthetically applied in post processing at both TX and RX antennas for all measured data in the lobby/hallway scenario.

and, hence, may have the most significant impact on array design. The figure shows that in LOS conditions the strongest path is the direct path, while in NLOS conditions the receive array should be steered towards the single, second, and/or third wall bounces as the receiver advances up the hall. Note that the azimuthal AoA agrees with the geometry of the TX and RX locations with respect to the left and right walls.

By using the synthetic TX and RX beams, the directional delay spread was computed as

$$\sigma_\tau^\omega = \sqrt{\frac{\sum_{i=1}^{N} \widehat{PG}_i^\omega \cdot (\tau_i - \mu_\tau^\omega)^2}{\sum_{i=1}^{N} \widehat{PG}_i^\omega}}, \quad (4)$$

$$\mu_\tau^\omega = \frac{\sum_{i=1}^{N} \widehat{PG}_i^\omega \cdot \tau_i}{\sum_{i=1}^{N} \widehat{PG}_i^\omega}, \quad (5)$$

where $\widehat{PG}_i^\omega = PG_i \cdot G^\omega(\theta_i^{TX}, \phi_i^{TX}; \bar{\theta}^{TX}, \bar{\phi}^{TX}) \cdot G^\omega(\theta_i^{RX}, \phi_i^{RX}; \bar{\theta}^{RX}, \bar{\phi}^{RX})$ is the weighted path gain of the $i^{th}$ MPC, all in linear scale.

In contrast to Fig. 4(a), no obvious trend was observed with distance for the RMS-DS. As such, Fig. 4(b) shows the cumulative distribution function (CDF) of the RMS-DS for the four beamwidths investigated in LOS and NLOS conditions. The RMS-DS in the NLOS region was slightly larger than in the LOS region, increasing with synthetic beamwidth. The maximum value of the RMS-DS for synthesized RX beamwidths of 3°, 10°, 30° and 360° are 0.2, 11.6, 4.9 and 14.9 ns, respectively. The median value was 3.1 ns for the 360° synthetic beamwidth and smaller than 0.2 ns for the other three synthetic beamwidths. These values agree well with those in [5], where the authors employed omnidirectional antennas at 60 GHz, and the RMS-DS in small offices, conference rooms, library and laboratory environments had a maximum value of 20 ns and a median value of approximately 3 to 6 ns, based on 20 or 30 dB multipath threshold, respectively [6].

## V. Conclusion

We analyzed 60 GHz channel measurement data in a hallway/lobby scenario under both LOS and NLOS conditions. We included examples of individual power-delay profiles and power-angle profiles. The channel evolution is illustrated by power-angle profiles over distance. The $\theta^{RX}$ of the strongest MPC clearly tracks LOS, single-, double- or triple-bounce regions, which agree with the geometry. We observed the rough wall surface strongly affects the TX RX antenna boresight direction in beamforming deployment. The $\theta^{RX}$ of the strongest MPC varied over a large range of over 40° when reflected from a rough wall surface, while the variation was less than 24° with reflection from a finely ribbed wooden wall. The RMS-AS is investigated that provides evidence for optimizing the beamwidth of antenna or antenna array in future 5G system design. The RMS-AS for $\theta^{RX}$ has a maximum value of 84.2° and the median value was 24.6°. The RMS-DS is studied with multiple synthetic beamwidths of 360°, 30°, 10° and 3°. The RMS-DS generally increases with synthesized beamwidth, but no strong trend with respect to distance is observed. Future work includes analysis for larger data sets, comparison of results over 28, 60 and 83 GHz.

## References


[1] S. Zahir, O.D. Gurbuz, et. al. "60-GHz 64- and 256-Elements Wafer-Scale Phased-Array Transmitters Using Full-Reticle and Subreticle Stitching Techniques," *IEEE Transactions on Microwave Theory and Techniques*, vol. 64, no. 12, pp. 4701– 4719, Nov. 2016.

[2] J. Senic; C. Gentile; P. B. Papazian; K. A. Remley; J. K. Choi, "Analysis of E-band Path Loss and Propagation Mechanisms in the Indoor Environment," in *IEEE Transactions on Antennas and Propagation* , Early View, July 2017.

[3] R. Sun, P. B. Papazian, J. Senic, Y. Lo, J. Choi, K. A. Remley, C. Gentile, "Design and Calibration of a Double-directional 60 GHz Channel Sounder for Multipath Component Tracking," *11th European Conference on Antennas and Propagation (EuCAP 2017)*, pp. 3336-3340, Paris, France, 19-24 Mar. 2017.

[4] J. A. Fessler and A. O. Hero, "Space-alternating generalized expectation-maximization algorithm," *IEEE Transactions on Signal Processing*, vol. 42, no. 10, pp. 2664-2677, Oct. 1994.

[5] T. Zwick, T. J. Beukema and Haewoon Nam, "Wideband channel sounder with measurements and model for the 60 GHz indoor radio channel," in *IEEE Transactions on Vehicular Technology*, vol. 54, no. 4, pp. 1266-1277, July 2005.

[6] G. R. Maccartney, T. S. Rappaport, S. Sun and S. Deng, "Indoor Office Wideband Millimeter-Wave Propagation Measurements and Channel Models at 28 and 73 GHz for Ultra-Dense 5G Wireless Networks," in *IEEE Access*, vol. 3, pp. 2388-2424, 2015.



Sun, Roy; Papazian, Peter; Senic, Jelena; Gentile, Camillo; Remley, Catherine.
"Angle- and Delay-Dispersion Characteristics in a Hallway and Lobby at 60 GHz."
Paper presented at 12th European Conference on Antennas and Propagation (EuCAP 2018), London, United Kingdom. April 9, 2018 - April 13, 2018.

# Kicking the Tires of the NIST Microwave Uncertainty Framework, Part 2

Ronald A. Ginley
National Institute of Standards and Technology (NIST) RF Technology Division
325 Broadway, mc 672.01, Boulder, CO 80305, USA, rginley@boulder.nist.gov

***Abstract* — Traceability of a measurement requires two parts: 1) an unbroken chain of measurements and 2) uncertainties for each link of the chain. The NIST Microwave Uncertainty Framework (MUF) can provide both the required parts for a single link in the chain or for multiple links. In Part 1 of this work [1] the scattering-parameter measurement results determined by the MUF were compared to the established technique used at NIST. In this Part 2, the comparison of the uncertainties calculated with the different approaches will be examined and discussed.**

***Index Terms* — Microwave measurements, coaxial connectors, s-parameters, uncertainties**

## I. Introduction

The NIST Microwave Uncertainty Framework (MUF) is a recently-developed tool for producing measurement results and uncertainties [2-6]. The ability of the MUF to produce accurate results and uncertainties must be verified and this will be done through a comparison of the MUF results against the existing technique used at NIST. This is "checking the viability of an unknown system by a quick test" or "kicking the tires".

The established technique used at NIST for s-parameter measurements is the multiline method for network analyzer calibration [7]. The multiline method is applied in a NIST software package titled "Multical." Data is taken from the Vector Network Analyzer (VNA) and analyzed using other NIST software packages.

## II. The Experimental setup

The measurement setup is the same as that used in Part 1[1]. As a quick refresher, all of the devices measured, calibration standards and DUTs, had 3.5 mm connectors and the frequencies measured were from 0.2 to 33.0 GHz by 0.1 GHz steps. The specifics of the actual measurement process steps are as follows:

1) Uncertainty models were established in the MUF for the devices used in the VNA calibration
2) Raw measurements (no VNA correction applied) were taken of the devices used for the VNA calibration
3) The identical data was used in both Multical and the MUF to form the error correction matrices for the VNA
4) Starting with the VNA correction turned off, raw measurements were taken of one of the DUTs.
5) Without touching the DUT, the VNA correction from Multical was applied and corrected data of the DUT was taken using the NIST measurement software (a program called MeaslpX was used to take the corrected data from the VNA and another program called Calrep was used to analyze the data taken by MeaslpX)
6) All DUTs were measured by use of the process of 4) and 5)
7) The raw calibration standards data and the raw DUT data were processed through the MUF to arrive at the corrected response for each DUT
8) The corrected MUF responses were compared to the results from the Multical and NIST measurement software process[1].

Throughout this comparison, we have tried to keep the two measurement paths as similar as possible. Because of the differences in the two measurement paths, we needed to take both the uncorrected and corrected measurements of the DUTs.

## III. Discussion of uncertainty components

To have a legitimate comparison of uncertainties we needed to make sure that we are comparing the same essential components. The established NIST technique has uncertainty components from three major sources, which are instrumentation, systematic effects and random effects [8]. Instrumentation uncertainties come from the hardware of the system including signal generation, signal processing, signal detection, and other general electronics errors. The random components of uncertainty include long-term variation in the error reduction parameters and short-term connector non-repeatability. Systematic components of uncertainty are generally associated with the connectors and calibration standards. The systematic components included in the analysis for the established NIST technique (also called the Calrep technique) are:

1. Test Port Connectors
   a. More than one mode present at the reference plane
   b. Eccentricity of center conductor relative to outer conductor
   c. Discontinuity capacitance due to misalignment of conductors
   d. Gap in center conductor when mated to airline
2. Standard Airlines
   a. Specifications
   b. Dimensions of lines; $Z_{00}$ of lossless line
   c. Conductivity of lines; skin depth correction
   d. Outer Diameter and Inner Diameter not equal to specified dimensions
   e. Non-uniformity of inner and outer conductor diameters
   f. Uncertainty in $Z_0$
   g. Step capacitance due to line diameters not equal to specified diameters
   h. Electrical length of line too close to $n\pi$ (n=0,1,…)
   i. Length of inner conductor not equal to length of outer conductor



Ginley, Ronald.
"Kicking the Tires of the NIST Microwave Uncertainty Framework, Part 2."
Paper presented at 90th ARFTG Microwave Measurement Conference, Boulder, CO, United States. November 28, 2017 - December 1, 2017.

3. Reflect Termination
   a. Reflect connectors are not some as line connectors causing $\Gamma_1 \neq \Gamma_2$
   b. Coupling between test port and terminations

For the MUF, the uncertainty model for an airline standard is shown in figure 1. Similar, but simpler models are also used for the reflects. An identity matrix is used for the isolation terms.

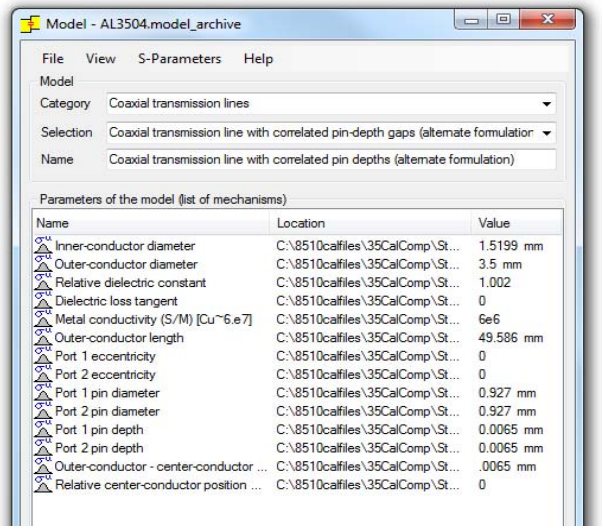


Figure 1. Airline uncertainty model used in the MUF

The most significant uncertainty sources are included in both the established technique and the MUF model. A rectangular probability distribution was used for all of the uncertainty components used in the MUF. Figure 2 shows the parameter definition for one of the uncertainty components.

A difficult part of the comparison process is to make sure that we are comparing as similar as possible combinations of uncertainty components. It should be noted that the MUF directly handles only the uncertainty due to systematic effects (other type of components can be added using post-processors). Because of this, for the comparison, the instrumentation and components of uncertainty due to random effects will be deconvoluted from the Calrep uncertainty.

There is not an exact one-to-one matching between all of the components of the two different models. The Calrep model has a few more minor terms than the MUF model. These should not have a significant effect on the comparison.

The MUF provides two different calculations of the uncertainty. One is through a sensitivity analysis (SA) where the uncertainty is calculated from a compilation of varying one uncertainty component at a time and a Monte-Carlo analysis (MC) where all uncertainty components are randomly varied at once [9]. Both results will be examined in the comparison.

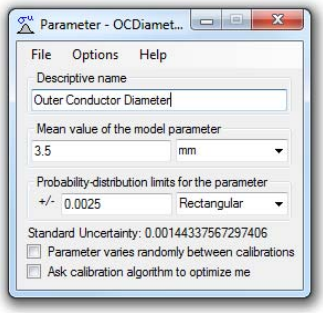


Figure 2. Uncertainty parameter dialog box from the MUF

## IV. Results of the Comparison

In figure 3 we show the results of the measurements of a matched termination. There is very little difference between the three curves. The same data is plotted in figure 4, but now the curves show the difference between the Calrep response and the MUF sensitivity analysis and the MUF Monte-Carlo results respectively. Also shown in figure 4 is the expanded Calrep uncertainty (k=2). The takeaway from figure 4 is that the differences between the responses of the established technique and the MUF are very small and well under the Calrep uncertainty.

Figure 5 again shows the difference curves, but this time only the systematic component of the Calrep uncertainty (k=1) and the MUF SA and MC uncertainty estimates (equivalent k=1). Uncertainty results similar to those shown in Figure 5 are shown for high reflect, low loss, and 20 dB devices in Figures 6, 7, and 8 respectively. It should be noted that the phase results of the devices in figures 7 and 8 are very similar to those shown in figure 6b and will not be shown.

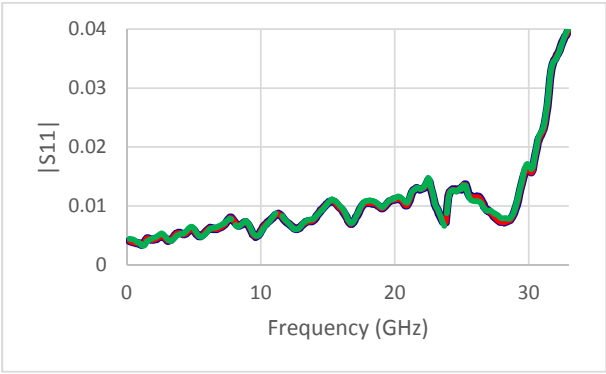


Figure 3. Measurement results for a matched termination showing the Calrep response (blue), the MUF SA response (red) and the MUF MC response (green).

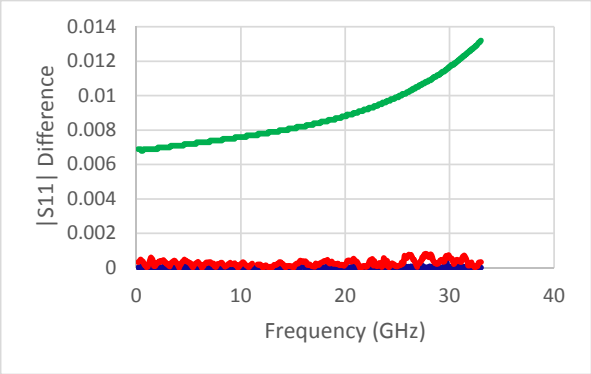


Figure 4. Difference plot for $|S_{11}|$ of a matched termination. Calrep – MUF SA (blue), Calrep – MUF MC (red), and the expanded Calrep uncertainty (k=2) (green).

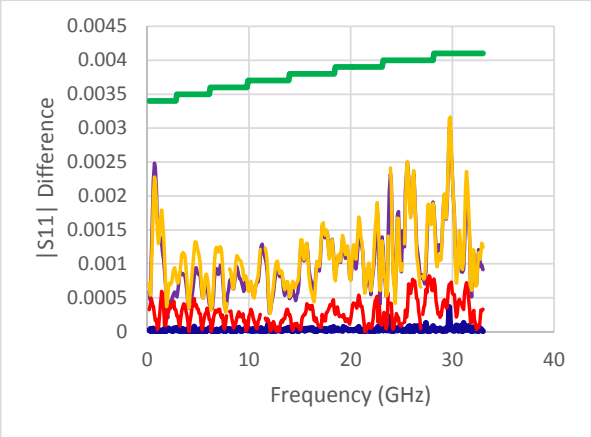


Figure 5. Difference plot for $|S_{11}|$ of a matched termination (blue, red) and Calrep systematic (k=1) (green), MUF SA (purple), and MUF MC (orange) uncertainty values.

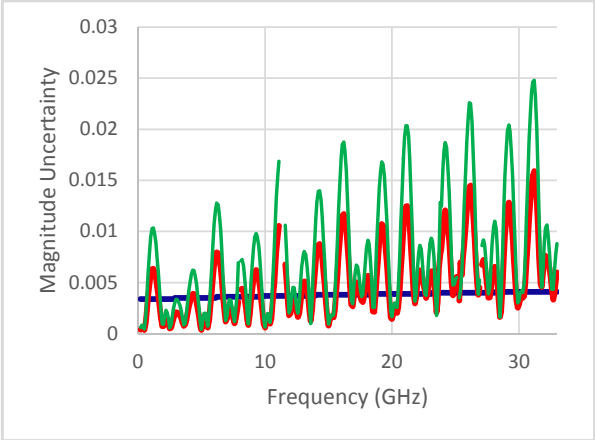


(6a)

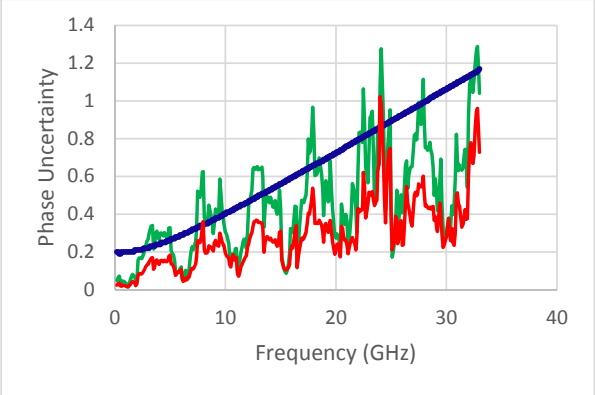


(6b)

Figure 6. Uncertainties for $S_{11}$ of a high-reflect device. Magnitude data (6a), phase (6b). Calrep systematic uncertainty (blue), MUF SA uncertainty(red), and MUF MC uncertainty (green).

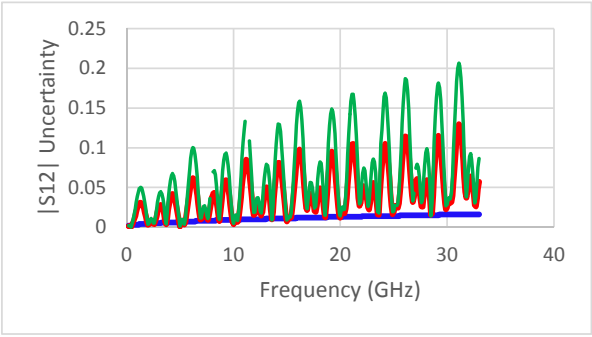


Figure 7. Uncertainties for the $|S_{21}|$ of a low loss device (~0.3 dB). Calrep systematic uncertainty (blue), MUF SA uncertainty(red), and MUF MC uncertainty (green).

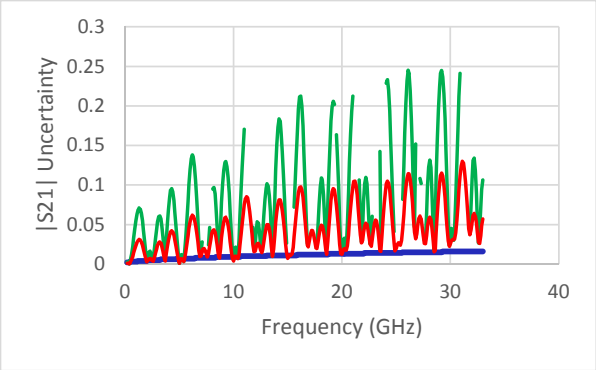


Figure 8. Uncertainties for the $|S_{21}|$ of a high loss device (~50 dB). Calrep systematic uncertainty (blue), MUF SA uncertainty(red), and MUF MC uncertainty (green).

## V. Discussion of Results

There are several general trends that can be seen in figures 5 through 8. The uncertainty from the established technique and the uncertainties generated from the MUF are of the same order of magnitude. The Calrep uncertainties have a very structured nature. The MUF uncertainties have a more random nature with some structure.

For a matched termination, figure 5 shows that the MUF uncertainty (SA or MC) is smaller than the Calrep uncertainty due to systematic effects. This was seen in the $S_{11}$ data for the two-ports as well. For a high reflect device the uncertainties are more comparable for both magnitude and phase (figure 6). For both of the two-port devices, for magnitude results, the MUF uncertainties are larger than the Calrep uncertainties (figure 7 and 8) and the MUF phase uncertainties (not shown) are slightly smaller than those from Calrep.

The Calrep uncertainties have well defined shapes which is not surprising due to the formulaic approach used to determine the uncertainties. The MUF uncertainties have a more random nature which is also expected due to their statistical determination. While the expectation is that the MUF uncertainties should be totally random in nature, the uncertainties are dependent on the value of the parameter that they correspond to and this causes the more structured form. This can be seen in all of the results. Changing the number of Monte-Carlo iterations from 100 to 1000 or 10000 does not change the structures that are seen in the Monte-Carlo uncertainties.

As was stated earlier, it is very difficult to make sure that we are comparing similar uncertainty quantities. There likely are still differences in how the uncertainty components from the different techniques are assigned values. As an experiment, all of the uncertainty component distribution limits for all of the calibration standards were halved and the same calibration standard data and DUT data were again processed through the MUF. The results are shown in figure 9. The resulting uncertainty still shows the same structure, but the overall magnitude has been reduced by over half. The take-away from this is that care must be taken in describing the uncertainty distributions. Further work may be needed to make sure the uncertainty components are fully understood and evaluated, and for future comparison, are truly comparable between the established technique and the MUF.

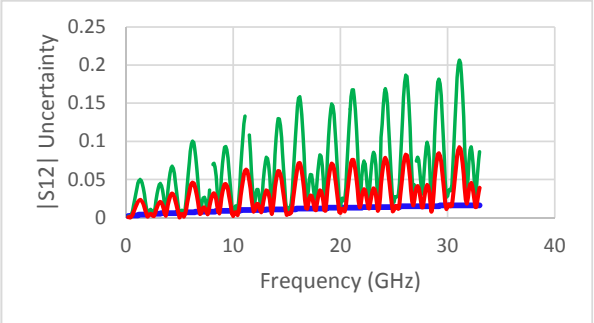


Figure 9. Comparison of uncertainties using different uncertainty distribution limits for the $S_{12}$ magnitude of a low loss device. Calrep systematic uncertainty (blue), MUF MC uncertainty(green), and MUF MC uncertainty half limits (red).

## VI. Conclusions

The uncertainty results from the NIST Microwave Uncertainty Framework agree to the same order of magnitude with our established method. The results depend on the type of s-parameter being measured. These conclusions apply to both magnitude and phase uncertainties, although the phase uncertainties from the established technique tend to be more conservative. It was also seen that care must be used in setting the distribution limits for the uncertainty components.

## References

[1] R.A. Ginley "Kicking the Tires of the NIST Microwave Uncertainty Framework, Part 1," 88th ARFTG Microwave Measurement Symposium, Austin, TX, Dec. 2016.
[2] D. F. Williams, NIST Microwave Uncertainty Framework, Beta Version, http://www.nist.gov/ctl/rf-technology/relatedsoftware.cfm, 2015.
[3] J. A. Jargon, D. F. Williams, T. M. Wallis, D. X. LeGolvan, and P. D. Hale, "Establishing traceability of an electronic calibration unit using the NIST Microwave Uncertainty Framework," *79th ARFTG Microwave Measurement Conference*, Montreal, CANADA, Jun. 2012.
[4] J. A. Jargon, U. Arz, and D. F. Williams, "Characterizing WR-8 waveguide-to-CPW probes using two methods implemented within the NIST Uncertainty Framework," *80th ARFTG Microwave Measurement Conference*, San Diego, CA, Nov. 2012.
[5] J. A. Jargon, D. F. Williams, P. D. Hale, and M. D. Janezic, "Characterizing a noninsertable directional device using the NIST Uncertainty Framework," *83rd ARFTG Microwave Measurement Conference*, Tampa Bay, FL, Jun. 2014.
[6] J. A. Jargon, C. H. Cho, D. F. Williams, and P. D. Hale, "Physical models for 2.4 mm and 3.5 mm coaxial VNA calibration kits developed within the NIST Microwave Uncertainty Framework," *85th ARFTG Microwave Measurement Conference*, Phoenix, AZ, May 2015.
[7] R. B. Marks, "A multiline method of network analyzer calibration," *IEEE Trans. Microwave Theory Tech.*, vol. 39, no. 7, pp. 1205–1215, July 1991.
[8] C.A. Hoer, R.M. Judish, J.R. Juroshek, G.F. Engen "Theory, Uncertainty Analysis, and Statistical Control for the NIST 2-18 GHz Dual 6-Port Automatic Network Analyzer," unpublished NIST Special Publications Note, 1986
[9] K.A. Remley, D.F. Williams, P.D. Hale, C.M. Wang, J. Jargon, and Y. Park, "Millimeter-Wave Modulated-Signal and Error-Vector-Magnitude Measurement With Uncertainty," *IEEE Trans. Microwave Theory Tech.*, vol.63, no. 5, pp. 1710-1720, May 2015

# Establishing Traceability for SOLT Calibration Kits

Ronald A. Ginley
National Institute of Standards and Technology (NIST) RF Technology Division
325 Broadway, mc 672.01, Boulder, CO 80305, USA, rginley@boulder.nist.gov

***Abstract* — Establishing traceability for a measurement is very important in that the results of the measurement can be used in a common framework for comparisons and understanding. The standard path of traceability for Short-Open-Load-Thru (SOLT) Vector Network Analyzer (VNA) calibrations has been through empirical models and is tenuous at best. Additionally, the uncertainties do not contain any information about cross-frequency correlations.**

**This work describes a technique for establishing traceability for SOLT calibration kits with fully correlated uncertainties. The calibrations performed using calibration kits evaluated with this new approach are traceable back to dimensional standards. This paper describes the new technique and shows the results of measurements based on this technique.**

***Index Terms* — Microwave measurements, coaxial connectors, s-parameters, uncertainties, calibration kits**

## I. Introduction

Traceability of a measurement requires two parts: 1) an unbroken chain of measurements and 2) uncertainties for each link of the chain [1]. In general, traceability means showing how, through an unbroken chain, measurements are linked back to fundamental principles or measurements. When a VNA is calibrated, several different error reduction methods (also referred to as calibrations) can be used. The two principle methods are Line-Reflect-Line (LRL) and the SOLT family (**S**hort-**O**pen-**L**oad, **S**hort-**O**pen-**L**oad-**T**hru, **S**hort-**O**pen-**L**oad-**R**eciprocal Thru). The LRL technique has high accuracy, but is difficult to implement; the SOLT technique has lower accuracy, but is much easier to use. The method most people use to calibrate their VNAs is the SOLT technique. The LRL method uses dimensional measurements of the airline standards to establish traceability. SOLT uses empirical models to define the standards [2].

The calibration methods for VNAs are well known [3]. Basically, a raw measurement of a calibration standard (one with no correction) is compared to a response of a model for that device. For LRL the model of the airline standards is developed through first principles and is based on the dimensional measurements of the airlines. For SOLT, empirical models are used that are based on data obtained through other measurement processes (like an LRL calibration).

Traceability is difficult to show for the empirical models used for SOLT. Additionally, the uncertainty analyses for measurements made based on SOLT calibrations do not contain any information on the frequency-to-frequency correlations. These correlations are necessary if transformations are to be made between different realms (for example from the frequency domain to the time domain and vice-versa). Being able to carry uncertainty information through the domain transformations is very important to support advanced measurements (for example, to support the advanced communications community). A new process has been developed that provides a direct-traceability path for the SOLT family of calibrations and determines fully correlated uncertainties and is described in detail in what follows.

## II. Defining the New Process

The new method will use higher-order calibrations to evaluate the lower-order calibration standards. Simply put, an LRL calibration is used on the VNA, based on airline standards, to measure the responses of the SOLT calibration standards. These responses are then used directly as the models for the SOLT standards, which, in turn are used to calibrate a VNA and make device under test (DUT) measurements. The process can be seen graphically in figure 1.

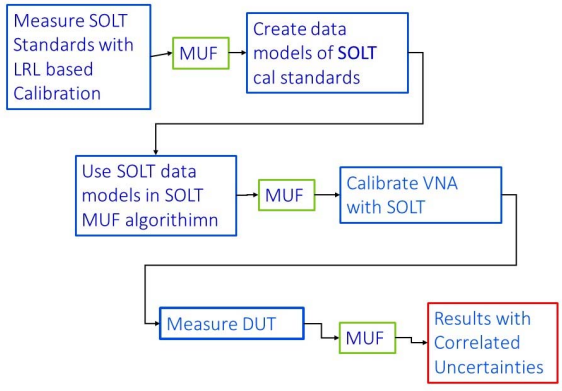


Figure 1. Graphical depiction of the process to create traceable SOLT measurements with correlated uncertainties.



Ginley, Ronald.
"Establishing Traceability for SOLT Calibration Kits."
Paper presented at 90th ARFTG Microwave Measurement Conference, Boulder, CO, United States. November 28, 2017 - December 1, 2017.

The NIST Microwave Uncertainty Framework (MUF) [4-8] is used to process all of the measurements. The MUF utilizes parallel sensitivity and Monte-Carlo analyses, and enables us to capture and propagate the significant scattering-parameter measurement uncertainties and statistical correlations between them. By identifying and modeling the physical error mechanisms in the calibration standards, we can determine the statistical correlations between both the scattering-parameters at a single frequency and uncertainties at different frequencies [9].

The existing SOLT calibration process uses two different types of loads if frequencies above 2 GHz are being used. A fixed load is used below 2 GHz and a sliding load is used above 2 GHz. For the new method, the sliding load is not necessary. The sliding load was used because the fixed loads do not have a flat response across a broad frequency band. By measuring the response of the fixed load, any deviations from a flat response are accounted for and corrected. For the new technique, the fixed load is used across the entire frequency band.

## III. Implementing the New Process

The airline standards used for this work have dimensional measurements of the inner diameter of the outer conductors, outer diameter of the inner conductors, and airline lengths These dimensional measurements are traceable to gauge blocks and ring gauges calibrated by the NIST Dimensional Laboratory. These measurements are the basis for the traceability of the LRL VNA calibration. Figure 2 shows the calibration setup menu in the MUF for the LRL calibration. Each standard has a definition file, an example of which is shown in figure 3. The definition file contains the various uncertainty components for that standard. One of those files, a parameter file, is shown in figure 4.

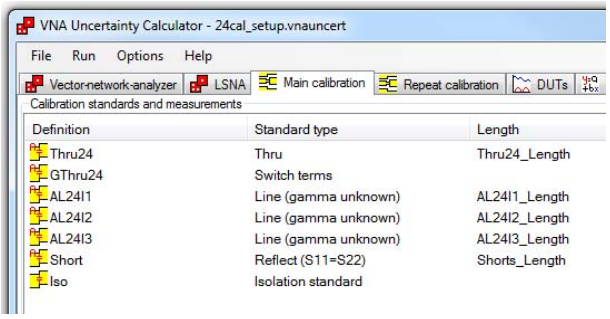


Figure 2. MUF LRL calibration setup showing devices and associated definition files.

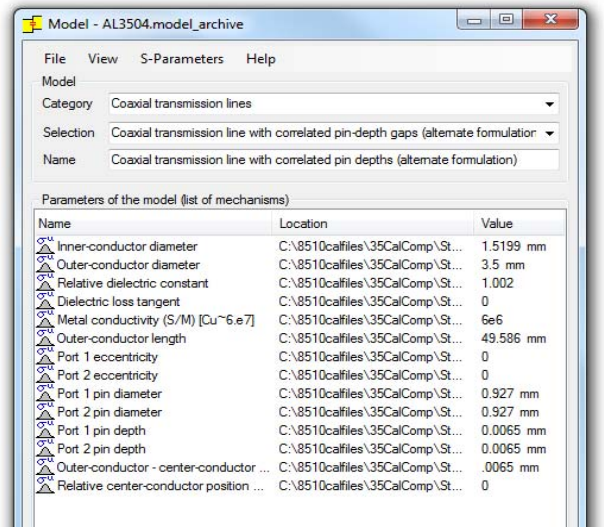


Figure 3. MUF calibration standard definition file.

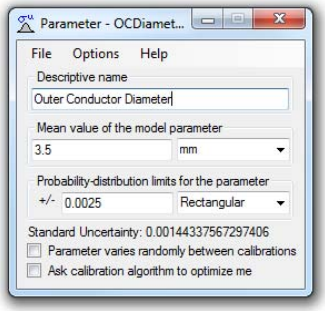


Figure 4. MUF standard parameter definition file

To test the process outlined in figure 1, we evaluated the standards from a 2.4 mm commercial calibration kit. Based on the measurements of the LRL calibration standards and the 2.4 mm shorts, opens, broadband loads (male and female for all of the standards), and a true thru (the two test ports connected together), the MUF created a measurement-results file (.meas file) for each set of like standards (i.e., male and female shorts in one file). This file essentially contains the corrected, complex results of the measurement and information to create the correlated uncertainty matrix from both a sensitivity analysis (SA) and a Monte-Carlo (MC) analysis [10].

These .meas files can then be used as the definition of the standards in the SOLT MUF algorithm. Figure 5 shows the MUF calibration setup menu for the SOLT calibration. In this setup, instead of the definition and parameter files, as seen in figures 3 and 4, we simply use the .meas file for each standard type which is shown in the left column of figure 5. All of the uncertainty information and the links for traceability are in the .meas files.

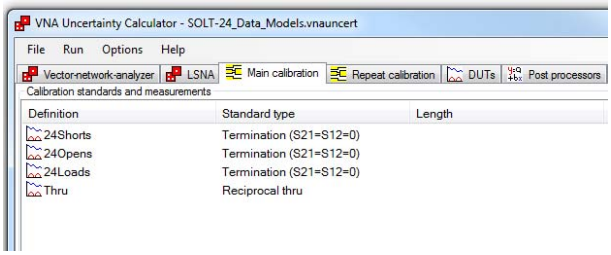


Figure 5. MUF SOLT calibration setup

To measure a DUT with the SOLT calibration setup as described, raw measurements (no correction applied to the VNA) of the calibration standards (short, open, loads, and thru) and the DUT are made on the VNA, then we can process all of the raw measurements through the MUF SOLT algorithm and DUT corrected results are obtained.

## IV. Results

To test the effectiveness of this process, we made measurements of a DUT based on new measurements of the calibration standards and the DUT over a span of approximately five months. This means that we performed a separate new, SOLT calibration for each DUT measurement. All of these different SOLT calibrations used the same calibration kit and the same .meas definition files for the calibration kit standards. These results are shown in figure 6.

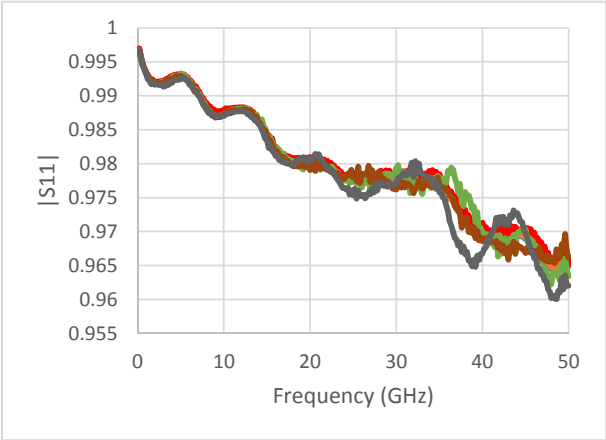


Figure 6. |S11| results from multiple SOLT/DUT measurements. Established NIST measurement process (light blue), MUF LRL calibration (orange), SOLT: 6/23/2017 (red), 6/27/2017(green), 8/3/2017 (brown), and 10/25/2017 (gray).

In figure 6, we show curves not only for the multiple SOLT calibration/measurements, but also for a measurement of the DUT using the established NIST measurement process (multical) [11] and a measurement based on the LRL calibration from the MUF. Figure 7 shows the differences for all of the plots using the multical data as the reference value. Also plotted in figure 7 are the uncertainty bars (k=2) for the established NIST measurement technique.

Figure 8 shows the phase results for the same DUT. With the scale shown, no difference can be seen. In figure 9 the differences between the multical phase measurements and the MUF LRL and several SOLT measurements are shown along with the uncertainty for the multical measurements (k=2). There is very good agreement for the phase measurements. The differences from the reference multical measurement are well within the multical uncertainty.

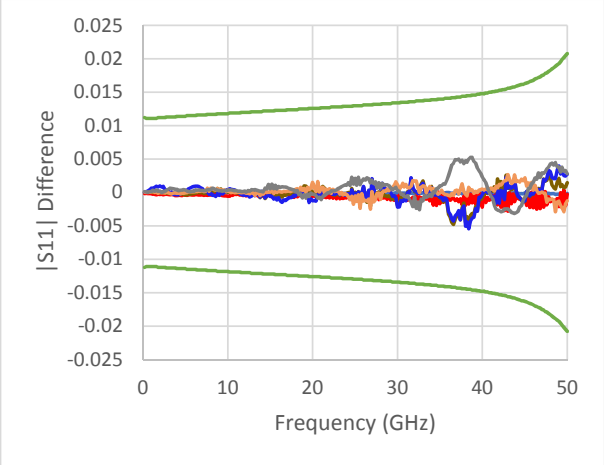


Figure 7. Multical - |S11| results from multiple SOLT/DUT measurements. Multical minus MUF LRL calibration (light blue), minus SOLT: 6/23/2017 (red), 6/27/2017(MUF SA-brown), 6/27/2017(MUF MC-dark blue), 8/3/2017 (orange), multical uncertainties (green), and 10/25/2017 (gray)

Other devices measured at the same time as the one DUT being shown showed similar results: good magnitude and phase agreement. The time span for these measurements was also five months.

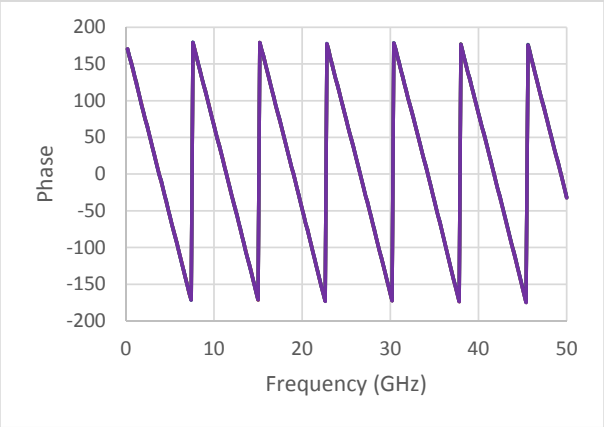


Figure 8. Phase results from multical (green), the MUF LRL calibration (orange), and from multiple SOLT/DUT measurements. 6/23/2017 (dark blue), 6/27/2017(light blue), 8/3/2017 (red), and 10/25/2017 (purple).

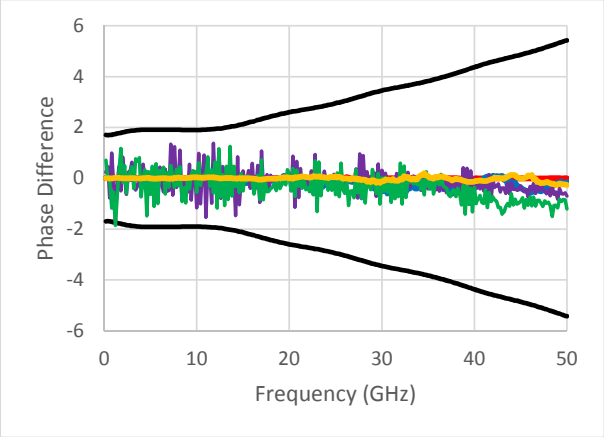


Figure 9. Phase difference plot showing the difference between the multical phase result and multiple SOLT results. The black lines are the multical uncertainty, multical-MUF LRL (red), multical-6/23/2017 (green), multical-6/27/2017 (blue), multical-8/3/2017 (purple), and multical-10/25/2017 (orange).

## V. Discussion of Results

The results shown in figures 6 and 7 show that measurements from multiple calibrations based on the same set of measured definitions for the calibration standards will produce repeatable results. While there are some differences between the different measurements, the differences are much less than the uncertainty from the LRL measurement of the device. The test was performed over a five-month time period; however, more experiments are needed to see if the data definitions of the calibration standards are stable over an even longer time period.

The .meas file for the DUT measurements contains all of the information necessary to establish a traceability path for the device. It also contains the correlation matrix that will allow the uncertainties to be carried through domain transformations.

There are several future plans for this calibration kit evaluation technique. The first will be to extend this to other coaxial connector sizes, then to waveguide connectors. Finally, this will be applied to automatic calibration units.

## VI. Conclusion

A new technique has been described that uses the NIST Microwave Uncertainty Framework to establish a well-defined traceability path for SOLT calibrations. In addition, measurements results are determined with correlated uncertainties. Repeated passes through the process yielded repeatable magnitude and phase device measurement results.

## References

[1] "International Vocabulary of Metrology – Basic and General Concepts and Associated Terms (VIM 3rd edition)," BIPM, 2012

[2] "Specifying Calibration Standads and Kits for Keysight Vector Network Analyzers," KeySight Application Note #5989-4840EN, 2016

[3] "Understanding VNA Calibration," Anritsu Application Note #111410-00673A, 2012

[4] D. F. Williams, NIST Microwave Uncertainty Framework, Beta Version, http://www.nist.gov/ctl/rf-technology/relatedsoftware.cfm, 2015.

[5] J. A. Jargon, D. F. Williams, T. M. Wallis, D. X. LeGolvan, and P. D. Hale, "Establishing traceability of an electronic calibration unit using the NIST Microwave Uncertainty Framework," *79th ARFTG Microwave Measurement Conference*, Montreal, CANADA, Jun. 2012.

[6] J. A. Jargon, U. Arz, and D. F. Williams, "Characterizing WR-8 waveguide-to-CPW probes using two methods implemented within the NIST Uncertainty Framework," *80th ARFTG Microwave Measurement Conference*, San Diego, CA, Nov. 2012.

[7] J. A. Jargon, D. F. Williams, P. D. Hale, and M. D. Janezic, "Characterizing a noninsertable directional device using the NIST Uncertainty Framework," *83rd ARFTG Microwave Measurement Conference*, Tampa Bay, FL, Jun. 2014.

[8] J. A. Jargon, C. H. Cho, D. F. Williams, and P. D. Hale, "Physical models for 2.4 mm and 3.5 mm coaxial VNA calibration kits developed within the NIST Microwave Uncertainty Framework," *85th ARFTG Microwave Measurement Conference*, Phoenix, AZ, May 2015.

[9] J. A. Jargon, D. F. Williams, and P. D. Hale, "Developing Models for Type-N Coaxial VNA Calibration Kits within the NIST Microwave Uncertainty Framework," *87th ARFTG Microwave Measurement Conference,* San Francisco, CA, May 2016

[10] K.A. Remley, D.F. Williams, P.D. Hale, C.M. Wang, J. Jargon, and Y. Park, "Millimeter-Wave Modulated-Signal and Error-Vector-Magnitude Measurement With Uncertainty," *IEEE Trans. Microwave Theory Tech.*, vol.63, no. 5, pp. 1710-1720, May 2015

[11] C.A. Hoer, R.M. Judish, J.R. Juroshek, G.F. Engen "Theory, Uncertainty Analysis, and Statistical Control for the NIST 2-18 GHz Dual 6-Port Automatic Network Analyzer," unpublished NIST Special Publications Note, 1986

# On the Susceptibility of Coded OFDM to Interference: A Simulation Study

Jason B. Coder and Yao Ma
Communications Technology Laboratory, National Institute of Standards and Technology
325 Broadway, Boulder, CO 80305 USA
jason.coder@nist.gov; yao.ma@nist.gov

***Abstract*—The susceptibility of broadband wireless communications signals (e.g., LTE, IEEE 802.11) to interference has been a topic of significant research. In this paper, we implement a simulation-based study on the impact that interference can have on the bit error rate (BER) performance of coded orthogonal frequency-division multiplexing (OFDM) transmissions. Our study covers two types of interference (a narrow-band tone signal and a pulse train signal), and two popular coding schemes (Turbo and LDPC). Simulation results show that Turbo and low-density parity check (LDPC) coding schemes provide large coding gains in the presence of white noise (without other interference), but are not effective against the narrow-band tone and pulse train interference. This observation calls for more robust coding and/or filtering design against interference for coded OFDM transmissions.**

## I. Introduction

We know that error correction codes (ECC) are effective in protecting signal transmissions in noisy channels. Turbo code and Low Density Parity Check (LDPC) codes are powerful schemes that have been adopted for $4^{th}$ generation (4G) Long Term Evolution (LTE) systems [1] and new 5G radio systems [2], respectively. Both of these technologies make use of orthogonal frequency-division multiplexing (OFDM) and its variations. OFDM is a very efficient modulation scheme that can provide high spectral efficiency, low side lobes (i.e., adjacent-band emissions), and simplified receiver processing.

The ability to recover corrupt bits is the primary reason for the use of ECC. In some cases, bits may be corrupted by the characteristics of the propagation channel, and in other cases they may be corrupted by an interfering signal (either intentional or unintentional). ECC aids in recovering the original packets while adding some small amount of redundancy/overhead. However, despite the use of ECC, some corrupted packets may not be recoverable.

In the context of LTE applications there appears to be little open literature focused on this important topic. Traditional susceptibility measurements and discussions typically focus on the overall impact of one system on another, such as adjacent band interference, or spectrum sharing systems which may use overlapped, broad spectrum bands.

In this paper, we consider two types of interference that are narrow in either frequency or time domains, namely, a narrow-band tone signal and a pulse train signal. An interferer is introduced into the same frequency channel as the intended coded OFDM signal and the impact is measured by examining changes in bit error rate (BER).

This examination begins to answer two questions: how does the type of interfering signal (e.g., tone vs. pulse train) impact the receiver's ability to decode the signal? Is one type of ECC more robust against interfering signals than another?

## II. Simulation Model and Method

We devise a model consisting of information that is coded using an ECC, and processed through quadrature phase shift keying (QPSK) modulation, and applied to OFDM subcarriers to form symbols. Then, the encoded signal is passed through an ideal channel and subjected to either white noise or an interfering signal.

We construct an OFDM signal to mimic a simplified downlink LTE signal, modeling only the modulation and coding parts of the data payload. We assume perfect synchronization and channel estimation at the receiver. The OFDM signal has a 10 MHz bandwidth with either Turbo [3] or LDPC [4] ECC. The parameters for OFDM modulation are given in Table I.

The interference signal types considered include a random single-tone continuous wave (CW) signal, and a random pulse train signal. The tone signal has a bandwidth that is equal to the OFDM subcarrier bandwidth, and its center frequency changes randomly either after an OFDM symbol duration (for the uncoded case) or after a code block length duration (for the coded cases). For simplicity, the pulse train signal uses a Gaussian pulse with frequency $0.1 f_s$ and fractional bandwidth 0.5, where $f_s$ is the sample rate of the OFDM signal. The pulse occurs once per OFDM symbol duration, but the pulse starting time varies for different OFDM symbols.

We simulate a rate-1/3 Turbo code and a rate-1/2 LDPC code. The Turbo-coded OFDM method encodes 396 infor-

TABLE I
OFDM Parameters Used for Simulation

| Parameter | Value |
|---|---|
| FFT Length | 1024 |
| Number of data subcarriers | 600 |
| Number of guard subcarriers | 424 |
| Subcarrier bandwidth | 15 kHz |
| CP Length | 73 (samples) |
| Symbol duration | 1/14 ms |
| Sample rate $f_s$ | 15.358 MSam/s |



Coder, Jason; Ma, Yao.
"On the Susceptibility of Coded OFDM to Interference: A Simulation Study."
Paper presented at USNC-URSI National Radio Science Meeting 2018, Boulder, CO, United States. January 4, 2018 - January 7, 2018.

mation bits to 1,200 coded bits, which are converted to 600 QPSK symbols, and put on the 600 data subcarriers in an OFDM symbol. The LDPC-coded method has a block length of 32,400 information bits, which are then coded by LDPC, modulated by QPSK and carried by OFDM symbols.

When interference is considered, the power of white noise is set to zero. The interference power is averaged over each OFDM symbol duration. Thus, for single-tone or pulse train signals, the interference powers have significant peak values in either the frequency or time domain.

## III. Simulation Results

We provide the BER results of uncoded, Turbo-coded, and LDPC-coded OFDM signals vs. signal-to-noise ratio (SNR) or signal-to-interference ratio (SIR), in Figs. 1-3. For uncoded transmission (Fig. 1), the SNR (SIR) is defined as bit SNR (SIR) per source bit. For coded transmission (Figs. 2 & 3), the SNR (SIR) is defined as the bit SNR (SIR) observed at each channel sample.

In the presence of white noise, Turbo code and LDPC code both provide good data protection in terms of BER, and when the $SNR = -1$ dB, have coding gains of more than 10 dB compared to the uncoded case. LDPC provides a BER result that drops more sharply than the Turbo code, and presents a lower error floor. However, the ECC schemes were not as effective when presented with interference. At a BER of $10^{-5}$, the pulse train interference caused a loss of about 7.5 dB in coding gain for both Turbo code and LDPC schemes compared to the case of white noise. The loss in coding gain caused by the single tone interference is even larger. Yet, the tone interference may be mitigated by filtering or spreading the interference energy to many subcarriers instead of one. This may be achieved by use of linear pre-coding and single-carrier frequency division multiple access (SC-FDMA). This result may be provided in future work.

## IV. Conclusion

We have implemented a simulation to examine the impact of interference on some example Turbo- and LDPC-coded OFDM transmissions. Simulation results show that Turbo and LDPC coding schemes are effective in reducing the BER for white noise type interference, and Turbo code may be more effective than LDPC for pulsed interference types. However, neither type is substantially effective in mitigating the detrimental effects of narrow tone or pulsed type interference. This observation requires more analysis of the signal's susceptibility, and calls for the design of more robust signals that are less susceptible to a variety of interference types. Future work will include a study of methods to suppress the effect of non-white-noise interference on coded-OFDM and LTE signal detection. Experiments with radiated signals can also be implemented to verify the computer simulation results shown here.

## References


[1] "Group Radio Access Network, Evolved Universal Terrestrial Radio Access, "Multiplexing and Channel Coding, 3GPP TS 36.212, June 2017.

[2] 3GPP TSG RAN & NR, "Multiplexing and Channel Coding," TS 38.212 V1.0.0, Sept, 2017.

[3] B. Sklar, *Digital Communications: Fundamentals and Applications*, Prentice Hall, second edition, 2001.

[4] J. G. Proakis and M. Salehi, *Digital Communications*, McGraw-Hill, fifth edition, 2008.


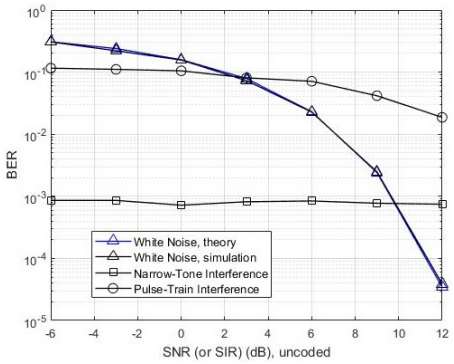


Fig. 1. BER of uncoded OFDM, affected by white noise or interference.

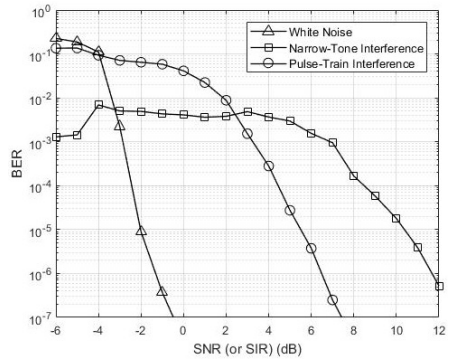


Fig. 2. BER of Turbo-coded OFDM, affected by white noise or interference.

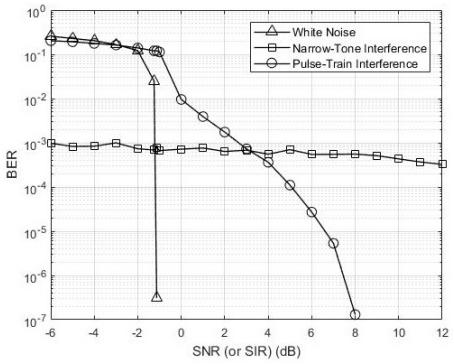


Fig. 3. BER of LDPC-coded OFDM, affected by white noise or interference.


Coder, Jason; Ma, Yao.
"On the Susceptibility of Coded OFDM to Interference: A Simulation Study."
Paper presented at USNC-URSI National Radio Science Meeting 2018, Boulder, CO, United States. January 4, 2018 - January 7, 2018.

# On the Impacts of In-Band LTE Emissions

Aziz Kord and Jason B. Coder
Communications Technology Laboratory
National Institute of Standards and Technology
325 Broadway Boulder, CO 80305
azizollah.kord@nist.gov; jason.coder@nist.gov

***Abstract*—With the introduction of low-power Internet of Things (IoT) and Device-to-Device (D2D) communications in the Long Term Evolution (LTE) system protocol, the in-band interference from other User Equipment (UE) with higher-power requires special attention. These higher power devices (e.g., smartphones) may cause in-band interference against the lower power devices. To examine this possibility, we examine the in-band spectra of an LTE UE with four different resource block configurations. The results show that as the number of allocated resource blocks decrease, the amount of ripple or "mirroring" increases within the channel. This mirrored signal may raise the noise floor as observed by lower power devices. In turn, these devices may have to radiate more power to overcome this additional noise. Future work includes a study on the effects of this type of interference on: power, latency of victim UE, as well as how the impact varies with network traffic (e.g., voice, real-time streaming, etc.).**

## I. Introduction and Background

Long Term Evolution (LTE) is the next generation of Universal Mobile Telecommunications System (UMTS) protocol for high-speed mobile broadband communication. This paper focuses on the impacts of the physical (PHY) layer LTE signal on other LTE devices operating in the same frequency channel.

LTE makes use of a PHY layer technology known as Orthogonal Frequency-Division Multiplexing (OFDM). In OFDM, the channel is divided into smaller 15 kHz sub-carriers. Each sub-carrier may carry information for control, broadcast, or payload data. The LTE protocol divides its channel into a larger group of 180 kHz frequency chunks, known as resource blocks (RBs). Based on Evolved Node B (eNB) scheduling decisions, one or more RBs may be allocated to each UE. The number of RB allocations and the starting location of these RBs may change during normal operation. This is done based on the UE's RF condition and its service demand. The eNB scheduler may allocate one or more RBs among UEs in that cell in a single transmit interval.

The OFDM technology, adopted by LTE for its physical layer communications, has been known to the research community for some time. In a communications channel, use of narrow band sub-carriers to reduce the chance of interfering with the whole channel is more efficient. With OFDM, the channel is divided into smaller channels. These smaller channels are orthogonal to each other for ease of detection and aid in reducing interference to each other. The disadvantage of these narrow band sub-carriers is that mirroring of the original signal can appear in neighboring sub-carriers. An example of this is shown in Figure 1. There are many reasons that may cause this effect in LTE systems: I/Q gain imbalance, quadrature impairments, etc. [1]



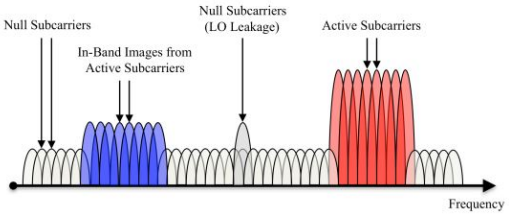


Fig. 1. Quadrature Impairments, as shown in [1]

If a UE is assigned RBs on the same sub-carriers that are impacted by mirroring, their noise floor will be higher. This may cause their radiated power to increase as a means of compensating for the decrease in signal to noise ratio (SNR). Additionally, their bit error rate (BER) may increase, and in the worst case scenario, they may be forced to re-transmit data. The magnitude of this impairment will depend on the distance between the victim UE relative to the transmitting UE.

This mirroring impairment is known to the LTE community and was accounted for in the 3GPP technical specifications, TS 36.521 Table 6.5.2.3F.3-1. The limits for in-band emissions are also shown in Table 1. This limit was selected to help protect other high-power UEs in the same channel.

Today, there are many new devices that utilize LTE, e.g. Narrow Band Internet of Things (NB-IoT), Device-to-Device (D2D), etc. These lower-power devices are designed to last for a long time without their batteries being replaced or

TABLE I
In-band Emissions Requirements from [1]

| Parameter Description | Unit | Limit | |
|---|---|---|---|
| General | dB | $Max\{-25 - 10 * \log_{10} \frac{N_{RB}}{L_{CRBs}}, 20 * log_{10} EVM - 3 - 5 * \frac{(\triangle_{RB}\|1)}{L_{CRBs} * -57dBm/180KHz - P_{RB}}\}$ | |
| IQ Image | dB | -25 | |
| Carrier Leakage | dBc | -25 | Output power >0 dBm |
| | | -20 | -30 dBm <Output power <0 dBm |
| | | -10 | -40 dBm <Output power <-30 dBm |

Kord, Azizollah.
"On the Impacts of In-Band LTE Emissions."
Paper presented at USNC-URSI National Radio Science Meeting 2019, Boulder, CO, United States. January 4, 2018 - January 7, 2018.

recharged. Their data are short and commonly in the form of bursts. Those features make this category of UE more susceptible to interference caused by the mirroring effect than higher powered UEs. As more of these types of devices are deployed in the field, the risk of in-band interference from higher powered devices grows.

## II. Setup and Equipment

To illustrate the in-band emissions of a UE allocated a given number of RBs, a high-dynamic range measurement was set up. This setup consists of an eNB emulator, UE, RF pre-selector (low-noise amplifier, filter, and a noise diode for calibration purposes), vector signal analyzer (VSA), and laptop. As the measured UE had no conducted ports available, an RF chamber, receiving antenna, and series of splitters and circulators were employed. The eNB emulator is used to force the UE to radiate its maximum transmission power and to select the location and number of RBs in the channel.

As the UE transmits its data, the uplink and downlink signals are split. The uplink signal is then fed into the RF pre-selector where it is eventually measured by the VSA. Additional details on the pre-selector can be found in [2].

The RF spectrum data was measured by the VSA with an RMS type detector at a resolution bandwidth of 1 MHz. Four different RB configurations (5, 12, 25, and 50) were selected and measured for comparison: .

Note that this measurement setup was also used to measure the out-of-band emissions described in [3]. These measurements took place in the AWS-3/Band 66 frequency band. However, the results discussed here are frequency agnostic and should be considered in any band.

## III. Measurement

The power spectra is shown in Figure 3. Data shown have been normalized to the peak signal. As seen in this figure, the ripple increases as the number of RBs decrease. That is, the mirroring effect is strongest in the 5 RB configuration.

The power of the mirrored signals met the 3GPP mask limit but the victim UE(s) operating in these frequencies needs to:

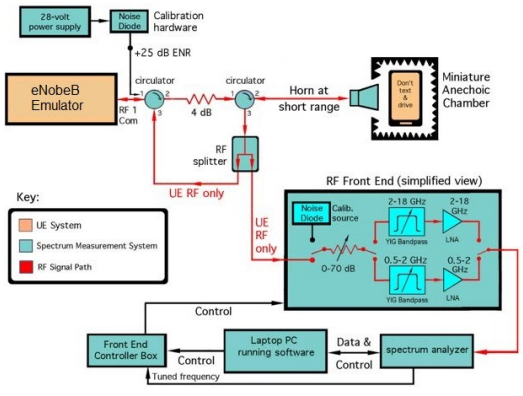


Fig. 2. Test Setup. Adapted from [2].

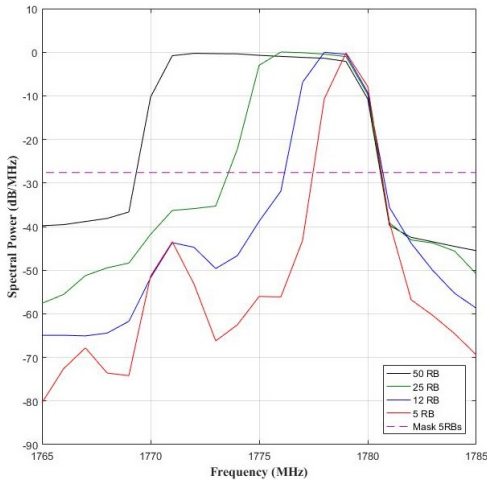


Fig. 3. The RMS power spectra collected for 5, 12, 25, and 50 RBs. The 3GPP mask is shown as a dashed line.

increase their power to compensate for the raise in their noise floor, request to move to a different RB allocation, or change their modulation and coding Scheme (MCS). While these in-band emissions are easily overcome by higher power UEs, new lower-power UEs will likely experience more of an impact.

## IV. Discussion and Conclusion

Although most LTE UEs meet the power mask level designated by 3GPP, the limit and shape of in-band interference may be of concern to new lower-power devices. In this paper we measured the spectra emitted by a higher-power LTE UE to illustrate its in-band emissions. As shown in Figure 3, the magnitude of the mirroring effect increases as the number of allocated RBs decreases. Depending on the exact cause of the mirroring, various solutions may be available. For example, if it is caused by I/Q gain imbalance, the path for I/Q needs to be closely balanced. If it is caused by quadrature impairments, then the up conversion modulators may need to be reexamined [1]. Another solution may be to address the impacts of mirroring within the 3GPP community by adjusting the in-band limits such that they are more "friendly" to lower-power UEs. Future study will reveal the impact of in-band emission of high power LTE UEs to the connectivity, performance, battery life, and different type of network traffic.

## References


[1] National Instruments, "Introduction. to LTE Device Testing: From Theory to Transmitter and Receiver Measurments", *National Instruments*.http://download.ni.com/evaluation/rf/Introduction_to_LTE_Device_Testing.pdf

[2] M. Fry, J. Splett, G. Sanders, J. Ladbury, F. Sanders, A. Kord, R. Jacobs, *Measured Emission Spectra of Selected AWS-3 LTE Transmitters*. NASCTN.

[3] 3GPP TS 36.521-1 V14.3.0 "Evolved Universal Terrestrial Radio Access (E-UTRA); User Equipment (UE) conformance specification; Radio transmission and reception" https://portal.3gpp.org/desktopmodules/Specifications/SpecificationDetails.aspx?specificationId=2469



Kord, Azizollah.
"On the Impacts of In-Band LTE Emissions."
Paper presented at USNC-URSI National Radio Science Meeting 2019, Boulder, CO, United States. January 4, 2018 - January 7, 2018.

# Qualitative Multidimensional Calibration Comparison

Aric W. Sanders, Ronald A. Ginley, Cristian J. Long, Jasper A. Drisko, Nathan D. Orloff, and Richard A. Chamberlin

National Institute of Standards and Technology, RF Technology Division, 325 Broadway, MS 672.01, Boulder, CO 80305, sandersa@nist.gov

***Abstract* — We present a technique for the visual comparison of any two vector network analyzer calibrations. This method visualizes the comparative action of the calibrations for multiple complex scattering parameters. This method is independent of the calibration model. This comparative visualization of the two calibrations facilitates quick assessment of different calibration and error models, guides the choice of verification standards for later comparison, creates an easy way to monitor instrument stability over time, and can help guide the development of new on wafer calibration schemes.**

***Index Terms* — calibration comparison, scattering parameters, impedance, synthetic DUTs, microwave measurements.**

## I. Introduction

Vector network analyzer (VNA) calibrations for scattering parameters vary in complexity and uncertainty. Each type of calibration is generated by the measurement of a set of well-understood artifacts, calculated, and then applied to subsequent measurements. Frequently, by comparing two of these calibrations, we gain insight into fundamental questions about the algorithm or measurement. While comparison techniques that create bounds for the worst-case difference of two calibrations [1]-[2] have been previously reported on, these techniques simplify the problem into a single frequency-dependent metric. These techniques have the advantage of being easy to interpret, but have the disadvantage that more nuanced questions are left unanswered. For example, when two methods of on-wafer calibration are compared, we are not presented with any information that identifies calibrations that are identical for certain devices, while widely different for others. Without this information, measurements on a limited set of devices, by use of a specialized calibration techniques, might be disregarded although they are of high quality. In addition, other methods do not give information pertaining to the device types most likely to show differences between calibrations, and hence give little to no direction as to the best choice of verification standards. In order to provide a more complete, easy-to-interpret, qualitative comparison of two calibrations, we have developed an easy-to-apply visual technique.

## II. Method

Given two calibrations C1 and C2 that we desire to compare, we construct a plot of the relative action of the two calibrations. We assume that the corrections apply to the same frequency points. This is not a strict requirement, but prevents complications from interpolated data sets.

To create the visual comparison, we:

1) Create a series of synthetic device under tests (DUTs) in the calibrated measurement plane. These standards are constant complex scattering parameters grouped around multiple amplitudes with different phases. For Figs. 1-8, we have chosen three reflection amplitudes of 0.98, 0.60 and 0.20 for ease of viewing. The standards are created such that they are reciprocal and conserve energy. This leads to the constraint that transmission is symmetric (S21 = S12) and their amplitudes are 0.20, 0.80 and 0.98 respectively [3]. In Fig. 1, we show the complex scattering parameters of 20 synthetic DUTs, four with the reflection amplitude of 0.20, eight each with the reflection amplitudes of 0.80 and 0.98.

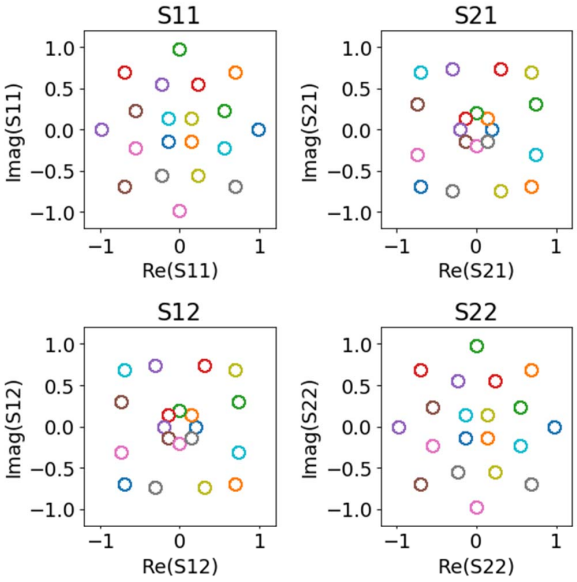


Fig. 1. The Synthetic DUTs' Scattering Parameters. The scattering parameters are plotted at the calibrated plane with all frequencies being simultaneously shown. The standards are constant in frequency, reciprocal and conserve energy, the phase is chosen to provide the most coverage of the plane. Here each symbol on the plot represents a single standard.



Sanders, Aric; Ginley, Ronald; Long, Christian; Drisko, Jasper; Orloff, Nathan; Chamberlin, Richard.
"Qualitative Multidimensional Calibration Comparison."
Paper presented at 90th ARFTG Microwave Measurement Conference, Boulder, CO, United States. November 28, 2017 - December 1, 2017.

2) Apply the inverse calibration ($C1^{-1}$) to the standards. This maps the synthetic DUTs to the uncorrected reference plane. In Fig. 2 the result of applying the inverse calibration $C1^{-1}$, is shown for a test thru-line-reflect (TRL) calibration. In the raw or uncorrected reference plane, our synthetic DUTs have scattering parameters that depend on the inverse of the specific correction.

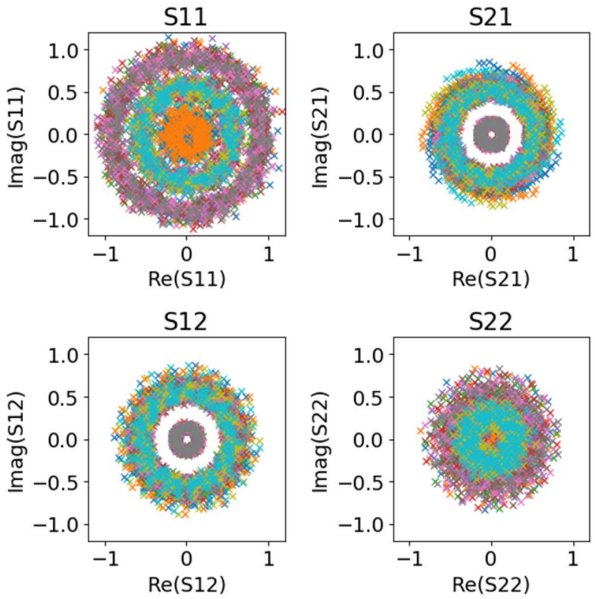


Fig. 2. The Synthetic DUTs' Uncalibrated Under C1 Scattering Parameters. After applying the inverse of the first calibration, the synthetic DUTs have a pattern that is controlled by the nature of the calibration. Since the calibration has a rich frequency dependence of amplitude and phase, the constants will now typically follow a different pattern in the uncorrected plane.

3) Calibrate the resulting uncorrected standards with the calibration (C2) that is to be compared. In Fig. 3 the result of applying another test calibration to the data in Fig. 2 is plotted. Once the comparison correction (C2) is applied the resulting pattern displays the comparative action of the two calibrations. In cases where the calibrations are similar, the plots will be nearly identical.

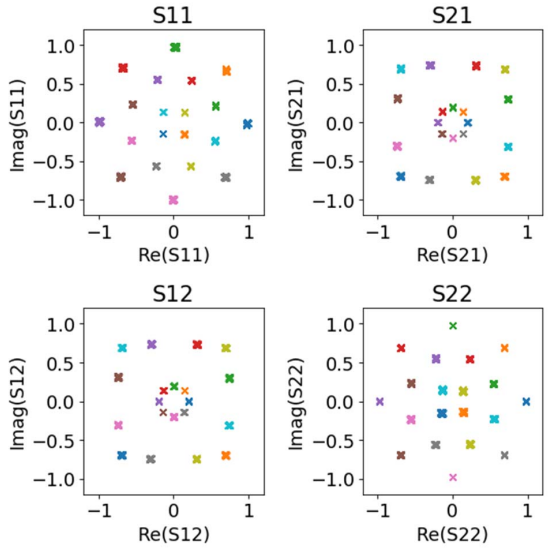


Fig. 3. The Standards' Scattering Parameters Under the Comparison Calibration. Once the synthetic DUTs have been mapped to the raw or uncalibrated plane, they are calibrated with the comparison calibration (C2). Each symbol represents the DUTs after calibrating with C2.

4) Overlay the original plot of the synthetic DUTs and the resulting calibrated standards on the complex plane (see Fig 4.). This resulting plot can be all frequencies or a sub set of frequencies of interest. If the calibrations are equivalent, the resulting plot will be identical to one another, otherwise the new location of the resulting calibrated standards will show the comparative action. The choice of complementing symbols emphasizes this relationship. In Figs. 4-8. the original location of the synthetic DUTs are indicated by circles, while the comparative action on the synthetic DUTs are indicated by the symbol x. If the calibrations are close but not exact, the comparative action will appear to blur and move slightly from center. If the calibrations deviate significantly, the resultant scattering parameters will be in different locations from the original synthetic DUTs. For calibrations that correct measurements to the same amplitude but vary in phase, a series of arcs will appear at the amplitudes chosen for the original synthetic DUTs.

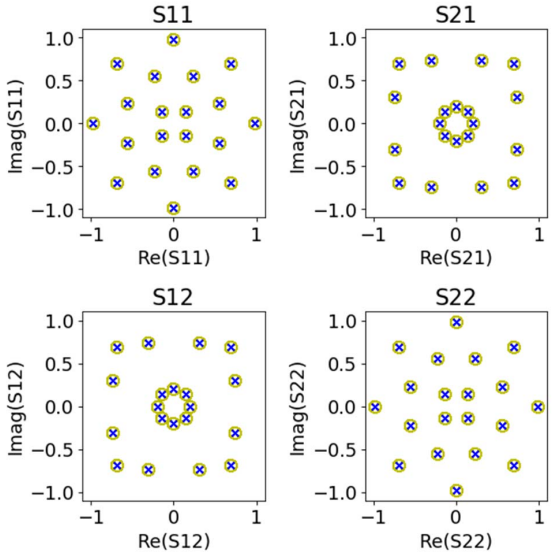


Fig. 4. Comparison of C1 = Synthetic DUTs with the C2 = Uncalibrated-Calibrated Synthetic DUTs. This is a plot of identical calibrations for clarity. The circles are chosen, original synthetic DUT locations to be the same size as the comparative action markers (x). Subsequent plots conserve space by following the convention that the vertical axis is always imaginary.

## III. TRL vs OSLT

Sanders, Aric; Ginley, Ronald; Long, Christian; Drisko, Jasper; Orloff, Nathan; Chamberlin, Richard.
"Qualitative Multidimensional Calibration Comparison."
Paper presented at 90th ARFTG Microwave Measurement Conference, Boulder, CO, United States. November 28, 2017 - December 1, 2017.

Once the method of visualization is understood, we can use it to compare different calibration techniques or how the same calibration changes over time. For instance, two calibration techniques of interest are the multiline thru-reflect-line (TRL) and the open-short-load-thru (OSLT). The TRL provides high accuracy, and the OSLT makes use of simple standard artifacts and is less time consuming. In Fig. 5 we compare an OSLT calibration with a TRL calibration within the same measurement session. In this specific instance, we have replaced the simple definitions describing the calibration standards in the OSLT by higher accuracy measurements of the standards. The typical way to compare different calibration error models like these is to use a correspondence of the error coefficients [4] which is unnecessary in this case. In addition to showing that the calibrations are close to the same, Fig. 5

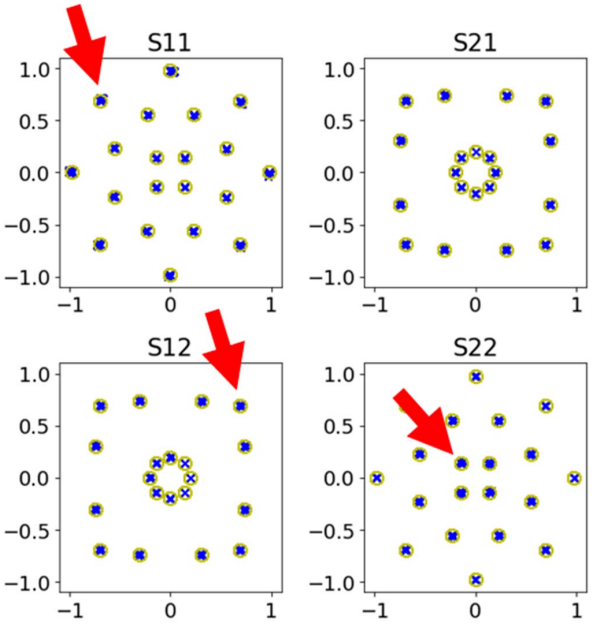


Fig. 5. Comparison of C1 = TRL and C2 = Data Defined OSLT. The arrows mark points were disparities are easily noticeable, potentially guiding the selection of future verification standards. Circles are of the unprocessed synthetic DUTs, while the symbol x represents those standards transformed first using

can give us insight into which verification standards to choose from. Specifically, by plotting the scattering parameters that have the largest difference between the two calibrations, it allows us to choose verification standards that have similar scattering parameters. This choice exploits places of highest variation in order to put the most stringent conformance criteria on subsequent calibrations, and hence achieve the highest degree of calibration algorithm agreement. By comparing calibrations in different measurement on different days, it also gives us a qualitative tool for investigating instrument stability. For example, close examination of the comparison plot in Fig. 5 reveals that the complex impedance points close to a reflectance of 1 (0.98) for S11, show the most disparity. If we desire a verification standard to compare measurements later, we should choose a high-reflect standard for the S11 verification process. In comparison, the points of highest transmission, or closest to the origin for the S21 and S12 plot show the highest discrepancy. Taken together with the fact that the S22 points close to the origin show a large discrepancy, this indicates a low-loss line should also be chosen to provide verification of subsequent calibrated measurements.

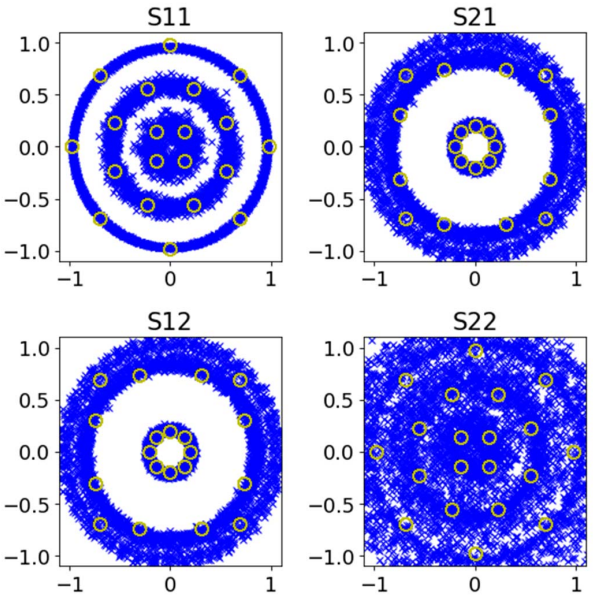


Fig. 6. Comparison of C1 = TRL and C2 = OSLT, 42 Days Later. The amplitude of S11 for DUTs at 0.98 remains relatively constant overtime. However, the phase does not. The test port with longer cables attached (port 2) is seen to be more variable.

Additionally, this type of visualization allows us to appraise the stability of calibrations over time. Consider Fig. 5 that shows the comparison of a TRL and OSLT. If we repeat the OSLT at some much later date, we can observe how the calibration changes over time. In Fig. 6, we see when the OSLT standards used in Fig. 5, are measured using the same experimental configuration 42 days later. In this case, Fig. 6 shows that the corrected amplitude of S11 remains close, but the phase has changed significantly. This type of similar correction that differs greatly in phase creates a particular pattern of arcs and can indicate an abrupt change in measurement conditions; we are still investigating the causes of the pattern in Fig. 6.

Sanders, Aric; Ginley, Ronald; Long, Christian; Drisko, Jasper; Orloff, Nathan; Chamberlin, Richard.
"Qualitative Multidimensional Calibration Comparison."
Paper presented at 90th ARFTG Microwave Measurement Conference, Boulder, CO, United States. November 28, 2017 - December 1, 2017.

## IV. On-Wafer TRL vs Series Resistor

In contrast to connectorized calibrations, those for use in an on-wafer environment are often more complex and can have multiple tiers. Each tier moves the reference plane, and if we

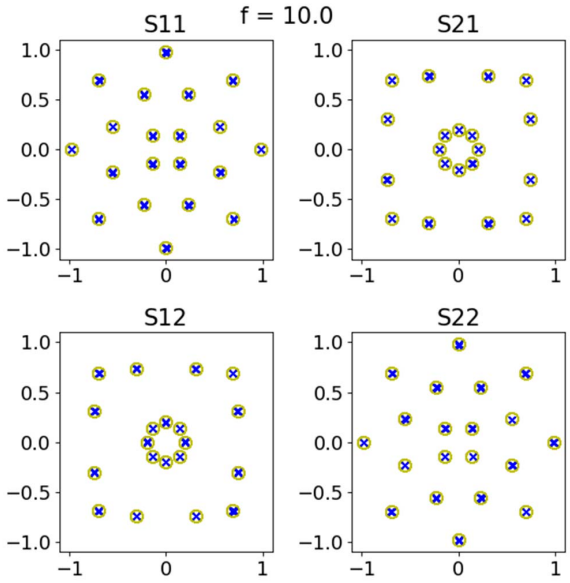


Fig. 7. Comparison of C1 = On-wafer TRL and C2 = Series Resistor, Over the Range of 1-10 GHz. The calibrations are close to identical over this range

are comparing calibrations at the same reference plane, we can also investigate by use of this visualization method. For example, consider an on-wafer TRL method, compared to an on-wafer series resistor method [5]-[6]. The TRL method provides a small uncertainty, but is incompatible with very-low frequencies (< 200 MHz) while the series resistor calibration makes use of more compact standards and provides a convenient way to calibrate to very low frequencies. In Figs. 7 and 8 comparing these calibrations at different frequencies gives insight into the range over which the calibrations perform essentially the same and where they differ significantly. Here, we compare broad-band calibrations calculated over the range 1-110 GHz via measurement of a large set of thin-film standards.

In Fig. 7, which covers the range of 1-10 GHz, we see that the calibrations are almost identical, with little distortion in phase or amplitude. In contrast, over the full range of the measurement 1-110 GHz, displayed in Fig. 8, we see that the calibrations have significant disagreement. In particular, for all scattering parameters not on the real axis there is notable amplitude distortion at the higher frequencies. This is indicative of the series resistor calibration not performing to the same accuracy as the TRL at the higher frequency range.

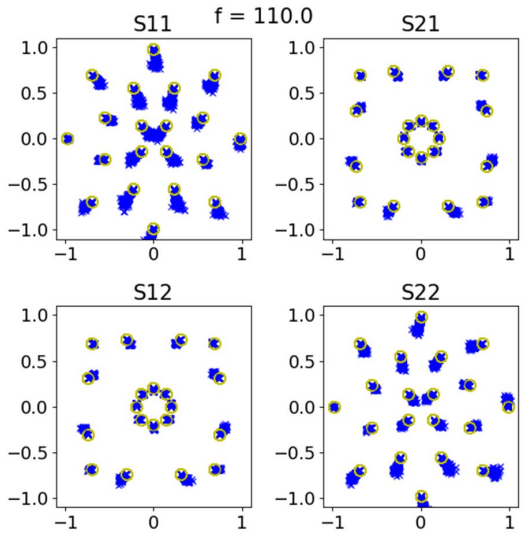


Fig. 8. Comparison of C1 = On-wafer TRL and C2 = Series Resistor, Over the Range of 1-110 GHz. As frequency increases differences in the calibrations become more evident. For synthetic standards along the negative real axis (short-like), we see agreement at even these frequencies.

## V. Conclusion

We presented a method for the visual comparison of two calibrations. This comparison technique yields qualitative information about the comparative action on synthetic DUTs with scattering parameters distributed in the complex plane. This qualitative information is used to identify potential verification standards, inspect the stability of calibrations over time, and determine the frequencies over which two calibration algorithms coincide.


## Acknowledgement

We thank Dylan Williams, Jeffrey Jargon and Jim Booth for insightful conversations relating to scattering parameters and calibrations.


## References


[1] R. B. Marks, J. A. Jargon and J. R. Juroshek, "Calibration Comparison Method for Vector Network Analyzers," *48th ARFTG Conference Digest, Clearwater, FL, USA, 1996, pp. 38-45.*

[2] D. F. Williams, R. B. Marks and A. Davidson, "Comparison of On-Wafer Calibrations," *38th ARFTG Conference Digest, San Diego, CA, USA, 1991, pp. 68-81.*

[3] D. M. Pozar, *Microwave Engineering,* Hobak NJ: Wiley, 2005.

[4] R. B. Marks, "Formulations of the basic vector network analyzer error model including switch terms," *50th ARFTG Conference Digest, Portland, OR, USA, 1997, pp. 115-126.*

[5] D. F. Williams and D. K. Walker,, "Series-resistor calibration," *50th ARFTG Conference Digest, Portland, OR, USA, 1997, pp. 131-137.*

[6] N. D. Orloff, J. Mateu, A. Lewandowski, E. Rocas, J. King, D. Gu, X. Li, C. Collado, I. Takeuchi, J. Booth, "A Compact Variable-Temperature Broadband Series-Resistor Calibration," *IEEE Transactions on Microwave Theory and Techniques, vol. 59, no. 1, pp. 188-195, Jan. 2011.*



Sanders, Aric; Ginley, Ronald; Long, Christian; Drisko, Jasper; Orloff, Nathan; Chamberlin, Richard.
"Qualitative Multidimensional Calibration Comparison."
Paper presented at 90th ARFTG Microwave Measurement Conference, Boulder, CO, United States. November 28, 2017 - December 1, 2017.

# How to extract distributed circuit parameters from the scattering parameters of a transmission line

Nathan D. Orloff[1], Nina Popovic[2], Jasper A. Drisko[1], Angela Stelson[1], Charles A. E. Little[1,2], James C. Booth[1], Jordi Mateu[3], and Christian J. Long[1]

[1]National Institute of Standards and Technology, Boulder, CO, [2]University of Colorado, Boulder, CO, [3]Universitat Politecnica de Catalunya, Catalunya, Spain

***Abstract* — Distributed circuit parameters parameterize the transmission and reflection off a given transmission line in terms of a distributed resistance, inductance, capacitance, and conductance, which are per-unit-length, frequency-dependent quantities. While there are analytical models for extracting the distributed circuit parameters, these models are discontinuous as a function of frequency when the argument approaches a branch cut. Here, we develop a nonlinear least-square regression algorithm that accurately extracts the distributed circuit parameters. Compared to existing approaches and finite element models, our algorithm successfully extracts the distributed circuit parameters as a function of frequency, all while being less sensitive to these phase conditions. Such an algorithm is useful for understanding how to deembed transmission lines, and how to extract electrical properties of the materials used in a circuit.**

***Index Terms* — transmission line, fitting, distributed circuit parameters, S-parameters.**

## I. Introduction

Understanding how voltages and currents propagate in a transmission line has been important to electrical engineers since the invention of the first working telegraph in 1816 by Francis Rolands [1]. Indeed, some of the greatest pioneers in electricity and magnetism got their start on this very topic. Chief among them is Oliver Heaviside, who was the first to write down what we commonly refer to as the telegrapher's equations [2]. The Telegrapher's equations describe how a voltage and current change as a function of time as they propagate down a transmission line. At their conception, these equations allowed electrical engineers to predict how far their signals could propagate and account for distortion.

Since then, Telegrapher's equations have become an essential part of every electrical engineer's toolbox. We use them to model the magnitude and phase of a voltage and current at a given position and time, whether that be in an integrated circuit or coaxial cable. In fact, there are very good analytical models of the distributed circuit parameters in the literature, with several outstanding examples for coplanar waveguide (CPW) transmission lines [3], [4]. More generally, we can measure the scattering (S-) parameters of a transmission line, correct them, and then use analytical models to extract the distributed circuit parameters [5]. This analytical approach is useful when the exact geometry of the transmission line is unknown, or when there is no analytical model that describes this specific type of transmission line. The problem with this approach lies in the phase of the reflection and the transmission as a function of frequency. At a high enough frequency, these phases produce a branch cut in the argument used to compute the propagation constant, which results in a large discontinuity in the extracted distributed circuit parameters.

Inspired by previous work, we have developed a nonlinear least-squares algorithm to mitigate this problem, and permit the extraction of the distributed circuit parameters over the full frequency regime. Our approach starts with corrected S-parameters of a transmission line. We then computed estimates for the distributed circuit parameters, and scale them such that they all varied with the same frequency dependence and had an order of magnitude close to one. We then passed the estimates to the nonlinear least-squares optimization algorithm, computed the difference between the model and the data, and minimized the difference. The key idea was to scale the distributed circuit parameters, which improved how we used trust-region-reflective [6] and Levenberg-Marquardt [7], [8] optimization. There are some potential trade-offs to our algorithm. If the distributed circuit parameters are negative as a function of frequency, then our algorithm may need to be modified to work.

In this paper, we demonstrate that the distributed circuit parameters can be fit with a nonlinear least-squares algorithm, which considers the relative scaling of the fit parameters to minimize the sensitivity of the fit to phase of the S-parameters. We describe our algorithm step-by-step and explain the reasoning behind each step. We validate our algorithm with coplanar waveguide transmission lines on fused silica substrate, which were corrected with an optimized multiline thru-reflect-line (TRL) calibration algorithm. After applying our algorithm, we compare the distributed circuit parameters extracted with analytical expressions and our algorithm, which we contrast to finite element simulations of the same transmission lines. Taken together, this paper provides a detailed description of an algorithm to extract the distributed circuit parameters of a transmission line as a function of frequency that is more robust against the phase uncertainties than analytical models.

## II. Theory

For a lossy transmission line, we parameterize the distributed circuit in terms of a resistance ($R$), inductance ($L$), capacitance ($C$), and conductance ($G$) per unit length.

Orloff, Nathan; Drisko, Jasper; Stelson, Angela; Little, Charles; Booth, James; Mateu, Jordi; Long, Christian.
"How to extract distributed circuit parameters from the scattering parameters of a transmission line."
Paper presented at 90th ARFTG Microwave Measurement Conference, Boulder, CO, United States. November 28, 2017 - December 1, 2017.

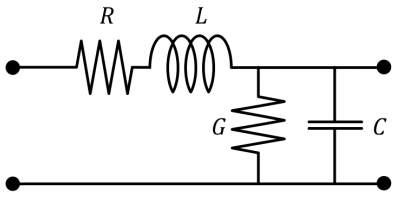


Fig. 1. The distributed circuit for a transmission line modeled by a resistance (***R***), inductance (***L***), capacitance (***C***) and conductance (***G***) per unit length.

In the most general sense, $R, L, C$ and $G$ depend on frequency (Fig. 1). Applying Kirchhoff's point and loop rules to Fig. 1, we obtain the Telegrapher's equations,

$$\frac{\partial}{\partial x}\tilde{V}(x) = -L\frac{\partial}{\partial t}\tilde{I}(x) - R\cdot\tilde{I}(x) \text{ and}$$
$$\frac{\partial}{\partial x}\tilde{I}(x) = -C\frac{\partial}{\partial t}\tilde{V}(x) - G\cdot\tilde{V}(x). \quad (1)$$

Next, we assume a sinusoidal time dependence,

$$I(x,t) = \tilde{I}(x) = I(x)e^{i\omega t} \text{ and}$$
$$V(x,t) = \tilde{V}(x) = V(x)e^{i\omega t}. \quad (2)$$

Then, we insert (2) into (1), and solve the wave equation to define the propagation constant,

$$\gamma = \sqrt{(R+i\omega L)}\sqrt{(G+i\omega C)}, \quad (3)$$

and the characteristic impedance,

$$Z = \frac{\sqrt{(R+i\omega L)}}{\sqrt{(G+i\omega C)}}. \quad (4)$$

*A. Eiensentadt's analytical model for transmission lines*

Now that we understand where the distributed circuit parameters come from, we can use them to develop analytical models of a transmission line. In [5], Eisenstadt and Eo developed their analytical expressions for $\gamma$ and $Z$ from ABCD matrices. In general, ABCD-parameters are convenient for modeling both lumped element and distributed circuits, as well as for cascading elements together [9]. A general ABCD matrix is given by,

$$\boldsymbol{M} = \begin{pmatrix} A & B \\ C & D \end{pmatrix}. \quad (5)$$

ABCD-parameters are also intuitive, because they relate physical currents and voltages in a two-port network. We can convert S-parameters to ABCD-parameters following the expressions in Refs. [5] and [9].

For a uniform two-port transmission line of length $\ell$ corrected to a characteristic impedance $Z_r$, the ABCD-parameters are given by,

$$\boldsymbol{M} = \begin{pmatrix} cosh(\gamma\ell) & Z_r\cdot sinh(\gamma\ell) \\ \frac{1}{Z_r}\cdot sinh(\gamma\ell) & cosh(\gamma\ell) \end{pmatrix} \quad (6)$$

We take (6), combining terms and geometrical identities, to derive an argument involving the propagation constant ($\gamma$) and length of the transmission line ($\ell$),

$$e^{-\gamma\ell} = cosh(\gamma\ell) + sinh(\gamma\ell) = \frac{A+D}{2} + \sqrt{B\cdot C} \quad (7)$$

Eisenstadt and Eo [5] took (7) one step further and solved for $\gamma$ and $Z$ in terms of the corrected S-parameters. We use this analytical model for comparison here. For completeness, we reproduce these expressions here,

$$\gamma = -\frac{1}{\ell}\ln\left[\left\{\frac{1-S_{11}^2+S_{21}^2}{2S_{21}} \pm K\right\}^{-1}\right]$$
$$K = \left\{\frac{(S_{11}^2-S_{21}^2+1)^2-(2S_{11})^2}{(2S_{21})^2}\right\}^{\frac{1}{2}} \quad (8)$$

and the characteristic impedance,

$$Z^2 = Z_r^2\frac{(1+S_{11})^2-S_{21}^2}{(1-S_{11})^2-S_{21}^2}. \quad (9)$$

The problem with (8) and (9) are the potential sign ambiguities that arise when the phase of the argument in (8) go through π or -π. As in Ref. [5], we compute $R, L, C$ and $G$,

$$R = \Re(\gamma\cdot Z) \quad (10)$$
$$L = \Im(\gamma\cdot Z)/\omega \quad (11)$$
$$C = \Im\left(\frac{\gamma}{Z}\right)/\omega, \text{ and} \quad (12)$$
$$G = \Re\left(\frac{\gamma}{Z}\right). \quad (13)$$

*B. Our analytical model for transmission lines*

Instead of the Eisenstadt and Eo [5] model, we used the T-matrix form of a transmission line, because the T-matrix formalism does not require a defined reference impedance. In this case, the model for the T-matrix of a transmission line in a 50 Ω reference impedance is,

$$\boldsymbol{T} = Q_Z^{50}\begin{pmatrix} e^{-\gamma\ell} & 0 \\ 0 & e^{\gamma\ell} \end{pmatrix}Q_{50}^Z, \quad (14)$$

where the impedance transformer is given by,

$$\boldsymbol{Q}_{\boldsymbol{Z_m}}^{\boldsymbol{Z_n}} = \frac{1}{2\sqrt{Z_n\cdot Z_m}}\begin{pmatrix} Z_m+Z_n & Z_m-Z_n \\ Z_m-Z_n & Z_m+Z_n \end{pmatrix}. \quad (15)$$

We have used this model with great success in the past; see, for example, Refs. [10]–[14].

## III. Fabrication

We fabricated the CPW devices on a 500 μm thick, 7.62 cm diameter fused silica (quartz) wafer. We chose quartz, because it has low electrical conductivity and isotropic permittivity [15].

Orloff, Nathan; Drisko, Jasper; Stelson, Angela; Little, Charles; Booth, James; Mateu, Jordi; Long, Christian.
"How to extract distributed circuit parameters from the scattering parameters of a transmission line."
Paper presented at 90th ARFTG Microwave Measurement Conference, Boulder, CO, United States. November 28, 2017 - December 1, 2017.

The electrode layer consisted of a 5 nm Ti adhesion layer followed by 500 nm of Au that we deposited by electron beam evaporation. The CPWs on the calibration chip had a nominal characteristic impedance of ~50 Ω with 20 μm-wide center conductors, 2 μm-wide gaps, and 200 μm-wide ground planes (Fig. 2). The devices on the calibration chip had contact pads for on-wafer probe measurements. The pads were reinforced with ~115 nm of palladium, which was used for the contact pads due to its low evaporation temperature, minimal oxidation, and hardness [14].

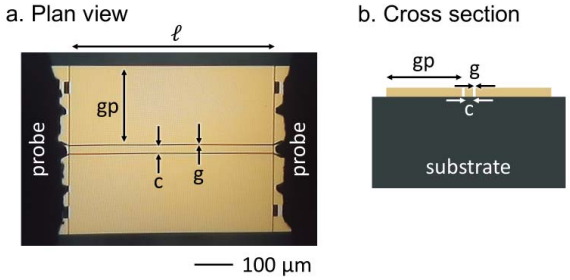


Fig. 2. (a) A plan view of a coplanar waveguide transmission line with measurement probes. (b) The cross section of the coplanar waveguide transmission line. In both (a) and (b), the center conductor is labeled c, the gap is labeled g, and the ground plane is labeled gp. The center conductor was nominally 20 μm wide, the gap was nominally 2 μm wide, and the ground plane was nominally 200 μm wide. The coplanar waveguide transmission line has a length $\boldsymbol{\ell}$.

## IV. Step-by-step Algorithm

1. Measure and then correct S-parameters of uncorrected transmission line.
2. Estimate initial guess of the distributed circuit parameters, with either finite-element simulations, or analytical models.
3. Scale the estimates for the initial guess of the distributed circuit parameters.
4. Impose physical bounds. Optional: Impose recursion.
5. Apply nonlinear least-squares routine:
    a. Rescale estimates for the distributed circuit parameters.
    b. Compute the T-matrix model for the transmission line.
    c. Compute and return the error function.
6. Return the optimized distributed circuit parameters.

## V. Scaling

The key idea in this paper and the real contribution to the literature is the realization that the distributed circuit parameters can be scaled to roughly the same order of magnitude. This scaling is a critical part of optimally leveraging the strengths of the trust-region-reflective [6] and Levenberg-Marquardt [7], [8] optimization.

On close examination of [16], Marks and Williams identified some important relationships; namely, $R, L, C$ and $G$ are directly related to Maxwell's equations through the material properties used to make the transmission line. For simplicity, the distributed circuit parameters are related to physical material properties and associated integrals through,

$$R \propto \omega(\mu_i) \text{ and/or } \sigma \cdot \sqrt{\omega}, \quad (16)$$

$$L \propto \mu_r, \quad (17)$$

$$C \propto \epsilon_r, \text{ and} \quad (18)$$

$$G \propto \omega\epsilon_i. \quad (19)$$

Here, the complex permittivity of the transmission line is given by $\epsilon = \epsilon_r - i\epsilon_i$, the complex permeability is $\mu = \mu_r - i\mu_i$, and the conductivity of the conductors is $\sigma$.

From these relationships, (14)-(15), we know that $G/\omega$ has the same units as $C$, and that (14)-(15) are proportional to the complex permittivity. Typically, our CPWs have a capacitance around 1 pF/cm. Furthermore, we know that changes in both the real and imaginary part necessarily have the same order of magnitude due to the Kramers-Kronig relations [17]. We can understand $R$ and $L$ by considering a nonmagnetic transmission line where $\mu_r = 1$ and $\mu_i = 0$. In this case, this assumption reduces (12) to a geometrical constant multiplied by the conductivity of the conductors and the square root of frequency. Thus, we can decrease the frequency dependence $R/(\sqrt{\omega})$ must have roughly the same order of magnitude as $L$. The last step in the scaling is to take $\log_{10}(R, L, C, \text{and } G)$, take the mean of this value, and then divide its order of magnitude to scale the distributed circuit parameters to values around one. This last step is essential for leveraging conventional optimization routines.

## VI. Measurement and Calibration

We measured the S-parameters with a vector network analyzer (VNA), contacting each structure with on-wafer probes. We moved the probes to measure each device. For these measurements, we measured 512 frequency points from 70 kHz to 110 GHz with -20 dBm signals that had an intermediate frequency bandwidth of 50 Hz. We performed all measurements on a temperature controlled probe station.

### *C. On-wafer calibration*

Our approach relies on an on-wafer calibration, where the calibration used S-parameters measurements of known artifacts on the calibration chip. We also measured the switch terms, and corrected for switch terms [18].

To perform the on-wafer calibration, we measured the S-parameters of seven different-length CPWs with $\ell$ = (0.420, 1.000, 1.735, 3.135, 4.595, 7.615, 9.970) mm, a series resistor, a series capacitor, and a short-circuit reflect. We performed both the multiline TRL calibration [19] and then used a series-resistor calibration to compute the capacitance per unit length of the CPWs ($C_o$) [20], which allowed us to transform the reference impedance to 50 Ω [21]. For frequencies from 100 MHz to 110 GHz, we used the multiline TRL calibration to correct the S-parameter data. Below, we used the series-resistor

Orloff, Nathan; Drisko, Jasper; Stelson, Angela; Little, Charles; Booth, James; Mateu, Jordi; Long, Christian.
"How to extract distributed circuit parameters from the scattering parameters of a transmission line."
Paper presented at 90th ARFTG Microwave Measurement Conference, Boulder, CO, United States. November 28, 2017 - December 1, 2017.

calibration to correct the S-parameter data. These on-wafer calibrations allowed us to correct all subsequent S-parameters to the center of the thru and to 50 Ω.

Fortuitously, the multiline TRL calibration yielded the propagation constant of the CPW, which is written as $\gamma = \sqrt{(R + i\omega L)(i\omega C_o)}$ where ω is the angular frequency and $R$, $L$, and $C_o$ are the distributed resistance, inductance, and capacitance per unit length of the CPW as a function of frequency. Recall that the conductance was assumed to be zero, following Ref. [21]. These results served as a check for the fitting algorithm, which we will discuss later.

## VII. Results

To test our algorithm, we corrected the six different CPW transmission lines lengths $\ell$ = (1.000, 1.735, 3.135, 4.595, 7.615, 9.970) mm to the center of the thru. We chose the same CPWs transmission line that were included in the calibration set. We then applied Eisenstadt and Eo [5] analytical model, (10)-(13), and our nonlinear least-squares algorithm, extracting $R, L, C$ and $G$ (orange lines, Fig. 3-6, respectively). Next, we applied our algorithm, allowing all four distributed circuit parameters vary (blue lines, Fig. 3-6, respectively). We repeated the same algorithm constraining the capacitance, $C$, and conductance, $G$, to match the result from multiline TRL (green lines, Fig. 3-6, respectively). This constraint demonstrates that one can further improve the nonlinear regression if some of the fit parameters are known. Finally, we compared these results to what we obtained from multiline TRL (black lines, Fig. 3-6, respectively). Although we computed $R, L, C$ and $G$ for each line, we only show the results for the longest line ($\ell$ = 9.970 mm) for clarity. All the figures have the same legend, hence it is only show in Fig. 3.

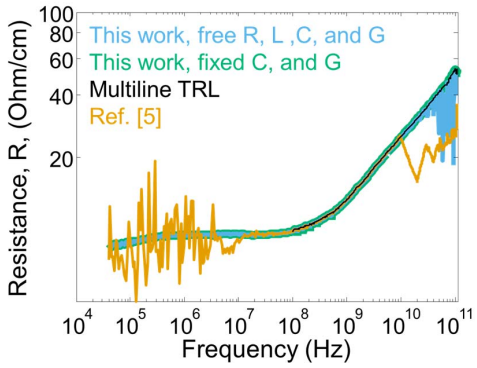


Fig. 3. Resistance per unit length comparison.

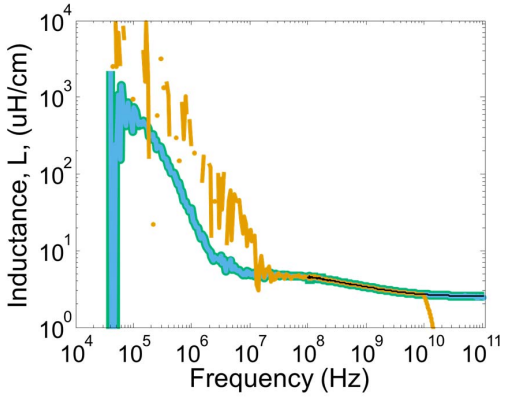


Fig. 4. Inductance per unit length comparison. The case where $\boldsymbol{R, L, C}$, **and** $\boldsymbol{G}$ are free is shown, however it overlaps with the blue line.

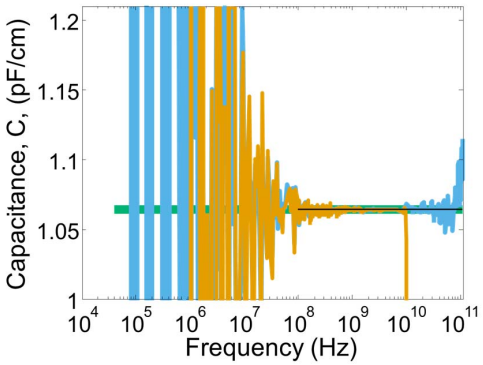


Fig. 5. Capacitance per unit length comparison.

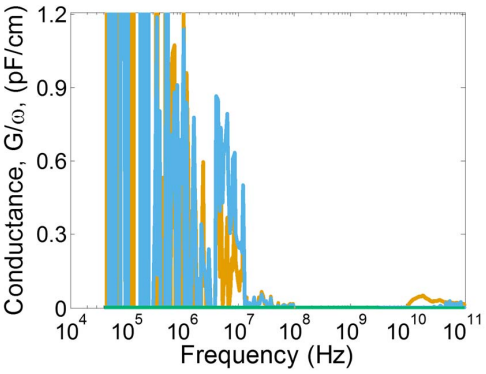


Fig. 6. Conductance per unit length comparison.

## VIII. Conclusion

In this paper, we demonstrated an algorithm to extract the distributed circuit parameters from a nonlinear least-squares regression. It has long been established that analytical model fails at high frequencies due to branch cuts in the complex plane. Here, we showed that by scaling the distributed circuit

Orloff, Nathan; Drisko, Jasper; Stelson, Angela; Little, Charles; Booth, James; Mateu, Jordi; Long, Christian.
"How to extract distributed circuit parameters from the scattering parameters of a transmission line."
Paper presented at 90th ARFTG Microwave Measurement Conference, Boulder, CO, United States. November 28, 2017 - December 1, 2017.

parameters we can accurately extract the distributed circuit parameters even at high frequencies where the analytical expression breaks down. This algorithm allowed us to increase the range of frequencies that we could extract the distributed circuit parameters to the bounds of our measurement.

We summarize by stating that the distributed circuit parameters of a corrected transmission line can be computed directly from a least-squares regression, so long as the circuit parameters are scaled according to the physics that controls their frequency dependence.

## ACKNOWLEDGEMENT

The authors thank the critical review of Dr. R. Horansky and Dr. A. Fox with the National Institute of Standards and Technology (NIST), for their critical feedback during this research, and their comments on this manuscript.



## REFERENCES

[1] B. F. Ronalds, "Francis Ronalds (1788 #x2013;1873): The First Electrical Engineer? [Scanning Our Past]," *Proc. IEEE*, vol. 104, no. 7, pp. 1489–1498, Jul. 2016.

[2] O. Heaviside, "XXXIX. On the electromagnetic effects due to the motion of electrification through a dielectric," *Philos. Mag.*, vol. 27, no. 167, pp. 324–339, Apr. 1889.

[3] H. Klingbeil and W. Heinrich, "Calculation of CPW AC resistance and inductance using a quasi-static mode-matching approach," *IEEE Trans. Microw. Theory Tech.*, vol. 42, no. 6, pp. 1004–1007, Jun. 1994.

[4] S. Gevorgian, L. J. P. Linner, and E. L. Kollberg, "CAD models for shielded multilayered CPW," *IEEE Trans. Microw. Theory Tech.*, vol. 43, no. 4, pp. 772–779, Apr. 1995.

[5] W. R. Eisenstadt and Y. Eo, "S-parameter-based IC interconnect transmission line characterization," *IEEE Trans. Compon. Hybrids Manuf. Technol.*, vol. 15, no. 4, pp. 483–490, Aug. 1992.

[6] T. Coleman and Y. Li, "An Interior Trust Region Approach for Nonlinear Minimization Subject to Bounds," *SIAM J. Optim.*, vol. 6, no. 2, pp. 418–445, May 1996.

[7] K. Levenberg, "A method for the solution of certain non-linear problems in least squares," *Q. Appl. Math.*, vol. 2, no. 2, pp. 164–168, 1944.

[8] D. Marquardt, "An Algorithm for Least-Squares Estimation of Nonlinear Parameters," *J. Soc. Ind. Appl. Math.*, vol. 11, no. 2, pp. 431–441, Jun. 1963.

[9] D. A. Frickey, "Conversions between S, Z, Y, H, ABCD, and T parameters which are valid for complex source and load impedances," *IEEE Trans. Microw. Theory Tech.*, vol. 42, no. 2, pp. 205–211, Feb. 1994.

[10] N. D. Orloff, "Broadband In-plane Relative Permittivity Characterization of Ruddlesden-Popper Sr(n+1)Ti(n)O(3n+1) Thin Films," 2010.

[11] J. C. Booth, "Quantitiative Permittivity Measurements of Nanoliter Liquid Volumes in Microfluidic Channels to 40 GHz," *IEEE Trans. Instrum. Meas.*, vol. 59, no. 12, p. 3279 to 3288, 2010.

[12] C.-H. Lee *et al.*, "Exploiting dimensionality and defect mitigation to create tunable microwave dielectrics," *Nature*, vol. 502, no. 7472, pp. 532–536, Oct. 2013.

[13] F. Mirri *et al.*, "Lightweight, Flexible, High-Performance Carbon Nanotube Cables Made by Scalable Flow Coating," *ACS Appl. Mater. Interfaces*, vol. 8, no. 7, pp. 4903–4910, Feb. 2016.

[14] C. A. E. Little, N. D. Orloff, I. E. Hanemann, C. J. Long, V. M. Bright, and J. C. Booth, "Modeling electrical double-layer effects for microfluidic impedance spectroscopy from 100 kHz to 110 GHz," *Lab. Chip*, vol. 17, no. 15, pp. 2674–2681, Jul. 2017.

[15] D. M. Pozar, "Considerations for millimeter wave printed antennas," *IEEE Trans. Antennas Propag.*, vol. 31, no. 5, pp. 740–747, 1983.

[16] R. Materese, "A General Waveguide Circuit Theory," *NIST*, 01-Oct-1992. [Online]. Available: https://www.nist.gov/node/639581. [Accessed: 26-Nov-2016].

[17] B. Y. Hu, "Kramers–Kronig in two lines," *Am. J. Phys.*, vol. 57, no. 9, pp. 821–821, Sep. 1989.

[18] R. B. Marks, "Formulations of the Basic Vector Network Analyzer Error Model including Switch-Terms," in *50th ARFTG Conference Digest*, 1997, vol. 32, pp. 115–126.

[19] R. B. Marks, "A multiline method of network analyzer calibration," *IEEE Trans. Microw. Theory Tech.*, vol. 39, no. 7, pp. 1205–1215, Jul. 1991.

[20] D. F. Williams and D. K. Walker, "Series-Resistor Calibration," in *50th ARFTG Conference Digest*, 1997, vol. 32, pp. 131–137.

[21] N. D. Orloff *et al.*, "A Compact Variable-Temperature Broadband Series-Resistor Calibration," *IEEE Trans. Microw. Theory Tech.*, vol. 59, no. 1, pp. 188–195, Jan. 2011.

# Characterization of Transmission Lines with Nonlinear Dielectric Materials

Aaron M. Hagerstrom*, Eric Marksz*†, Christian J. Long*, James C. Booth*, Nathan D. Orloff*
*National Institute of Standards and Technology †University of Maryland

***Abstract*—Nonlinear transmission lines are interesting for several device applications including harmonic generators, and phase shifters. They are also good candidates for characterizing nonlinear materials at $\mathrm{mm}$-wave frequencies. Regardless of the application, circuit modeling is challenging because nonlinear waveguides are described by a nonlinear wave equation. In this paper, we focus on characterizing the nonlinear mixing products generated by coplanar waveguides on a nonlinear ferroelectric $\mathrm{Ba_{0.5}Sr_{0.5}TiO_3}$ (BST) film. We developed a perturbative solution to the nonlinear wave equation, and validate our model by using a nonlinear vector network analyzer (NVNA) to measure the nonlinear mixing products. Our approach is useful for predicting spurious signals generated by nonlinear mixing in devices with nonlinear dielectrics, and predicting the performance of nonlinear devices such as harmonic generators.**

***Index Terms*—Materials characterization, nonlinear vector network analysis, On-wafer metrology, tunable dielectrics**

## I. Introduction

Some examples of devices employing nonlinear transmission lines include broadband phase shifters [1], 3rd harmonic generators [2], and non-reciprocal, non-magnetic receiver front-ends [3]. Generally speaking, there are two common ways of creating a nonlinear distributed capacitance: periodically loading a transmission line with tunable capacitors (either varactor diodes or nonlinear dielectric capacitors), and depositing the waveguide on a nonlinear dielectric material. In each case, the nonlinearity is described by a voltage-dependent capacitance and conductance. The same nonlinear wave equation will apply. We focus on nonlinear dielectrics, because dielectric nonlinearity is an important consideration for filters and phase shifters, and because the literature on nonlinear dielectric characterization at $\mathrm{mm}$-wave frequencies is scarce.

Tunable dielectric materials are an attractive solution for frequency-agile microwave components because their permittivity can be tuned by an applied electric field. This field-tunability can be used to build voltage-tunable filters and phase shifters [4]. In a nonlinear material, the field-tunability can be described by modeling the displacement field $D$ as a power series in the electric field $E$:

$$D \sim \varepsilon^{(1)}E + \varepsilon^{(2)}E^2 + \varepsilon^{(3)}E^3 + \cdots . \tag{1}$$

The linear permittivity $\varepsilon^{(1)}$ is well-known to be strongly frequency-dependent in the 10's of $\mathrm{GHz}$ for many materials of interest [5]. With a few notable exceptions [6], dielectric relaxation is a major limitation in many applications. For this reason, we need to understand the frequency dependence of any nonlinear dielectric in a particular circuit design in order to predict that circuit's performance. Dielectric characterization is often performed in an on-wafer environment because it is difficult to fabricate many materials of interest in bulk, and because the eventual application requires on-wafer devices.

The nonlinear permittivity $\varepsilon^{(n>1)}$ is also frequency-dependent. In the ferroelectric literature, measurements of the dispersion $\varepsilon^{(3)}$ at low frequencies ($<$1 $\mathrm{GHz}$) are common. For example, Glazouov and Tagansev used nonlinear measurements to distinguish between different thermodynamic models of a relaxor ferroelectric [7]. $\varepsilon^{(2)}$ and $\varepsilon^{(3)}$ are also routinely measured at optical frequencies, where $\varepsilon^{(2)}$ describes 3-wave mixing, 2nd-harmonic generation, optical rectification, the electro-optic effect, and many other phenomena, while $\varepsilon^{(3)}$ describes 3rd order phenomena including 4-wave mixing, self-phase modulation, and 3rd-harmonic generation.

In the 10's of $\mathrm{GHz}$, nonlinear permittivity characterization is difficult, especially in an on-wafer environment. At low frequencies, we can use capacitors, and measure current and voltage directly. At optical frequencies, nonlinear crystals are often large compared to the wavelength of light, and nonlinear mixing can be analyzed by the slowly-varying envelope approximation. At 10's of $\mathrm{GHz}$, the wavelength of light and the size of the device are both on the order of millimeters, so a fully-distributed description is necessary.

Although nonlinear permittivity characterization is difficult, it is also necessary for accurate circuit modeling. For filters and phase shifters, nonlinear mixing products are viewed as spurious signals that degrade performance. For soliton generators, harmonic generators, and non-reciprocal non-magnetic front-ends, nonlinear frequency mixing is the goal of the device. In either case, we needs to know the nonlinear permittivity to accurately predict nonlinear mixing products.

In this paper, we provide an analytic description of frequency mixing in a waveguide with nonlinear distributed admittance per unit length. Much of the previous work on nonlinear dielectric transmission lines focuses on 3rd-order nonlinear effects, which are dominant when the sample is not poled by an external electric field [8], [9]. In contrast, we apply a DC electric field, and observe 2nd-order effects. Since we are focusing on a 2nd-order nonlinearity, we had to develop a new analytical solution. From a mathematical perspective, the techniques we apply are well-known [10], [11], but we have yet to see our solution to this nonlinear problem elsewhere in the literature, and our solution appears to be easy to implement numerically and accurate. For these reasons, we feel that it is of interest to the measurement community.

Hagerstrom, Aaron; Long, Christian; Orloff, Nathan; Booth, James; Marksz, Eric.
"Characterization of Transmission Lines with Nonlinear Dielectric Materials."
Paper presented at 90th ARFTG Microwave Measurement Conference, Boulder, CO, United States. November 28, 2017 - December 1, 2017.

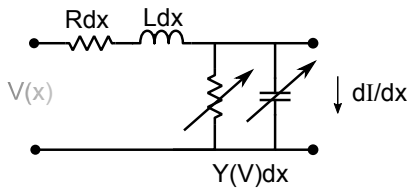


Fig. 1: Conceptual picture of an infinitesimal section of a nonlinear transmission line.

We compare these theoretical predictions to wave parameter measurements of transmission lines that are lithographically patterned on a BST sample. We also discuss the discuss the extraction of $Y^{(2)}$, the strength of the distributed circuit nonlinearity, and $\varepsilon^{(2)}$, the material nonlinearity, from measurements.

## II. Formulation

In this section, we derive a model for the nonlinear waves generated by the mixing of two incident sinusoidal signals in a nonlinear transmission line. Figure 1 shows a conceptual picture of an infinitesimal section of transmission line $dx$ with an nonlinear distributed capacitance $C(V)$ and conductance $G(V)$. We lump these two parameters into a distributed admittance $Y(V) = j\omega C(V) + G(V)$. We expect that the admittance will have a similar power series expansion to Equation (1):

$$\frac{dI}{dx} - \sim Y(V)V \sim -Y^{(1)}V - Y^{(2)}V^2 + ... \tag{2}$$

We will focus on 2nd-order nonlinearities, which means we will include $Y^{(1)}$ and $Y^{(2)}$ in our model, but not higher terms. These parameters are both frequency-dependent, because we expect that they are linearly related to $\varepsilon^{(1)}$ and $\varepsilon^{(2)}$.

We consider the case where the waveguide is excited by two waves with angular frequencies $\omega_1$ and $\omega_2$. These waves will generate nonlinear mixing products at $\omega_1 + \omega_2$, $\omega_1 - \omega_2$, $2\omega_1$ and $2\omega_2$. The voltage in the transmission line, as a function of position and time, can be decomposed into components that vary sinusoidally in time:

$$\begin{aligned} V(x,t) = &\hat{V}_1(x)\exp\left[j\omega_1 t\right] + \\ &\hat{V}_2(x)\exp\left[j\omega_2 t\right] + \\ &\hat{V}_{1+2}(x)\exp\left[j\left(\omega_1+\omega_2\right)t\right] + \\ &\hat{V}_{1-2}(x)\exp\left[j\left(\omega_1-\omega_2\right)t\right] + \\ &\hat{V}_{2\times1}(x)\exp\left[j\left(2\omega_1\right)t\right] + \\ &\hat{V}_{2\times2}(x)\exp\left[j\left(2\omega_1\right)t\right] + c.c. \end{aligned} \tag{3}$$

Here, $c.c.$ denotes complex conjugate of all of the terms that are written explicitly in Equation (3). A similar expansion can be written for the current. We will use subscripts to denote frequency. $\hat{V}_1(x)$ is the voltage wave with frequency $\omega_1$ , $\hat{V}_{1+2}$ has a frequency of $\omega_1 + \omega_2$, $\hat{V}_{2\times1}$ has a frequency of $2\omega_1$, and so on.

This model assumes small signal amplitudes. The meaning of "small" depends on context. The permittivity of our BST sample tuned by a factor of 2 with a bias voltage of 13.5 V, so we expect that signals with an amplitude on the order of 100 $\mathrm{mV}$ are still small. Small signals allow for two simplifying assumptions in our model: first, as we have already stated, we will ignore mixing products beyond the 2nd order. Second, we will assume that $\hat{V}_1, \hat{V}_2 >> \hat{V}_{1+2}, \hat{V}_{1-2}, \hat{V}_{2\times1}, \hat{V}_{2\times2}$, which will allow us to ignore the nonlinearity when solving for the voltage and current waves associated with the incident tones. This is called the undepleted pump approximation in nonlinear optics.

### A. Nonlinear wave equations

Under the assumption that the incident tones are much larger than the nonlinear mixing products, the voltage and current waves are given by:

$$\frac{d\hat{I}_i}{dx} \approx -Y^{(1)}(\omega_i)\hat{V}_i \tag{4}$$

$$\frac{d\hat{V}_i}{dx} \approx -\left[R(\omega_i) + j\omega_i L(\omega_i)\right]\hat{I}_i, \tag{5}$$

where $R(\omega_i)$ and $L(\omega_i)$ are the distributed resistance and inductance per unit length, respectively. The index $i \in \{1,2\}$ indicates that the waves at $\omega_1$ and $\omega_2$ are described by the same equations.

Equations (4) and (5) have a well-known solution in terms of the unknown coefficients $\hat{V}_i^+$ and $\hat{V}_i^-$ [12]:

$$\hat{V}_i(x) = \hat{V}_i^+\exp(\gamma x) + \hat{V}_i^-\exp(-\gamma x) \tag{6}$$

$$\hat{I}_i(x) = \frac{-\hat{V}_i^+}{Z}\exp(\gamma x) + \frac{\hat{V}_i^-}{Z}\exp(-\gamma x) \tag{7}$$

Here, $\gamma = \sqrt{(R + j\omega_i L)Y^{(1)}}$ is the propagation constant and $Z = \sqrt{(R + j\omega_i L)/Y^{(1)}}$ is the characteristic impedance. The coefficients are determined by boundary conditions, as described in Section (II-B).

For the waves generated by nonlinear mixing, equation (5) takes its usual form, but Equation (4) must be modified.

$$\begin{aligned} \frac{d\hat{I}_{1+2}}{dx} \approx &-Y^{(1)}(\omega_1+\omega_2)\hat{V}_{1+2} - \\ &2Y^{(2)}(\omega_1,\omega_2)\hat{V}_1\hat{V}_2 \end{aligned} \tag{8}$$

$$\begin{aligned} \frac{d\hat{I}_{1-2}}{dx} \approx &-Y^{(1)}(\omega_1-\omega_2)\hat{V}_{1-2} - \\ &2Y^{(2)}(\omega_1,-\omega_2)\hat{V}_1\hat{V}_2^* \end{aligned} \tag{9}$$

$$\frac{d\hat{I}_{2\times1}}{dx} \approx -Y^{(1)}(2\omega_1)\hat{V}_{2\times1} - Y^{(2)}(\omega_1,\omega_1)\hat{V}_1^2 \tag{10}$$

$$\frac{d\hat{I}_{2\times2}}{dx} \approx -Y^{(1)}(2\omega_2)\hat{V}_{2\times2} - Y^{(2)}(\omega_2,\omega_2)\hat{V}_2^2 \tag{11}$$

Here, the $*$ denotes the complex conjugate, and the factors of 2 in Equations (8) and (9) appear in a straightforward way when we calculate the square of Equation (3).

The key insight of Equations (8-11) is that, because we ignored the nonlinear term when calculating $\hat{V}_1(x)$ and $\hat{V}_2(x)$, we can treat the term proportional to $Y^{(2)}$ as a known function of $x$. These equations can be solved by a Green's function.

Hagerstrom, Aaron; Long, Christian; Orloff, Nathan; Booth, James; Marksz, Eric.
"Characterization of Transmission Lines with Nonlinear Dielectric Materials."
Paper presented at 90th ARFTG Microwave Measurement Conference, Boulder, CO, United States. November 28, 2017 - December 1, 2017.

### B. Boundary conditions

To determine the coefficients $\hat{V}_i^+$ and $\hat{V}_i^-$, we need to know some relationship between the current and voltage at each end of the transmission line. NVNA's can measure the $a$ and $b$ waves, which are defined in terms of a port impedance $Z_p = 50\ \Omega$ as

$$a \equiv \frac{V + Z_p I}{2} \quad (12)$$

$$b \equiv \frac{V - Z_p I}{2}. \quad (13)$$

We express the $a$ and $b$ waves explicitly in terms of the current and voltage at each end of the transmission line as follows:

$$a_{0,i} = \frac{\hat{V}_i(0) + Z_p \hat{I}_i(0)}{2} \quad (14)$$

$$a_{l,i} = \frac{\hat{V}_i(l) - Z_p \hat{I}_i(l)}{2} \quad (15)$$

$$b_{0,i} = \frac{\hat{V}_i(0) - Z_p \hat{I}_i(0)}{2} \quad (16)$$

$$b_{l,i} = \frac{\hat{V}_i(l) + Z_p \hat{I}_i(l)}{2}. \quad (17)$$

Here, the index $i$ refers to the frequency $\omega_i$, and the subscript 0 refers to the left end of the transmission line, $x = 0$, and the subscript $l$ refers to the right end of the transmission line, $x = l$. The negative sign in Equation (15) and the positive sign in Equation (17) reflect the convention that the $a$ and $b$ waves are defined in terms of the current leaving the test port, whereas $\hat{I}_i(x)$ is the current flowing in the $x$ direction.

As a boundary condition, we assume that the $a$ waves are known at each end of the transmission line at the frequencies $\omega_1$ and $\omega_2$. With some algebra, we can rearrange Equations (14-15), along with Equations (6-7), to solve for the unknown coefficients $\hat{V}_i^+$ and $\hat{V}_i^-$. With some algebra, we can rearrange Equations (14-15), along with Equations (6-7), to find a linear system of equations for $\hat{V}_i^+$ and $\hat{V}_i^-$:

$$\frac{1}{1+\Gamma}\begin{bmatrix} \Gamma & 1 \\ e^{\gamma l} & \Gamma e^{-\gamma l} \end{bmatrix}\begin{bmatrix} \hat{V}_i^+ \\ \hat{V}_i^- \end{bmatrix} = \begin{bmatrix} a_{0,i} \\ a_{l,i} \end{bmatrix}, \quad (18)$$

with the reflection coefficient $\Gamma$ defined as:

$$\Gamma \equiv \frac{Z - Z_p}{Z + Z_p}. \quad (19)$$

The matrix in Equation (18) can be inverted explicitly:

$$\begin{bmatrix} \hat{V}_i^+ \\ \hat{V}_i^- \end{bmatrix} = \frac{1+\Gamma}{D}\begin{bmatrix} \Gamma e^{-\gamma l} & -1 \\ -e^{\gamma l} & \Gamma \end{bmatrix}\begin{bmatrix} a_{0,i} \\ a_{l,i} \end{bmatrix}, \quad (20)$$

where we have defined the constant

$$D \equiv \Gamma^2 e^{-\gamma l} - e^{\gamma l}. \quad (21)$$

Once we know the coefficients $\hat{V}_i^+$ and $\hat{V}_i^-$, we can calculate $\hat{I}_i(x)$, $\hat{V}_i(x)$ from Equations (6-7). Finally, from the current and voltage, we calculate the outgoing $b$ waves at each port using Equations (16-17). This procedure will faithfully reproduce the linear scattering parameters. We verified this, but don't have space to show it here. Calculating the voltage and current waves at frequencies $\omega_1$ and $\omega_2$ is the first step toward calculating the nonlinear mixing products.

### C. Green's Function

The nonlinear wave Equations (8-11) are of the form

$$\frac{d\hat{V}}{dx} = -\left[R(\omega) + j\omega L(\omega)\right]\hat{I} \quad (22)$$

$$\frac{d\hat{I}}{dx} = -Y^{(1)}(\omega)\hat{V} - Y^{(2)}N(x), \quad (23)$$

where $Y^{(2)}N(x)$ is a known function of $x$ that represents the current generated by the nonlinear interaction of the incident waves. These equations can be solved by a Green's function approach [10].

The Green's function approach involves solving for $G_V(x, y)$ and $G_I(x, y)$, the voltage and current waves that are generated by a point current source at a position $y$ along the transmission line. These functions satisfy the differential equations

$$\frac{dG_I(x,y)}{dx} = -Y^{(1)}(\omega)G_V(x,y) + I_0\delta(x-y) \quad (24)$$

$$\frac{dG_V(x,y)}{dx} = -\left[R(\omega) + j\omega L(\omega)\right]G_I(x,y). \quad (25)$$

Here, $\delta(x-y)$ is the Dirac $\delta$ function, which models the point-like current source. We include the overall scaling constant $I_0$ with dimensions of current so that the current Green's function $G_I$ will also have dimensions of current, and $G_V$ will have dimensions of voltage. The value of $I_0$ is completely arbitrary and has no effect on the end result of this calculation. Once $G_I(x, y)$ and $G_V(x, y)$ are determined, we compute the nonlinear voltage and current by summing the contributions of the currents generated at each position along the transmission line.

$$\hat{V}(x) = -\frac{Y^{(2)}}{I_0}\int_0^l dy G_V(x,y)N(y) \quad (26)$$

$$\hat{I}(x) = -\frac{Y^{(2)}}{I_0}\int_0^l dy G_I(x,y)N(y) \quad (27)$$

We will solve for $G_I(x, y)$ and $G_V(x, y)$ following a very similar procedure to the one we used to solve for $\hat{I}_i(x)$, $\hat{V}_i(x)$ in Section II-B. In addition to the boundary conditions at the ends of the transmission line, the Green's functions satisfy additional boundary conditions at $x = y$. To accommodate these boundary conditions, we write the Green's function in a piecewise form

$$G_V(x,y) = g_V^L(x,y)\Theta(y-x) + g_V^R(x,y)\Theta(x-y) \quad (28)$$

$$G_I(x,y) = g_I^L(x,y)\Theta(y-x) + g_I^R(x,y)\Theta(x-y), \quad (29)$$

where $\Theta(x)$ is the unit step function, and the superscripts $R$ and $L$ stand for "left" and "right". The boundary conditions at $x = y$ are that the voltage is continuous, but the current has a discontinuous jump due to the point current source $I_0\delta(x-y)$.

$$g_I^R(x=y) - g_I^L(x=y) = I_0 \quad (30)$$

$$g_V^R(x=y) - g_V^L(x=y) = 0. \quad (31)$$

Hagerstrom, Aaron; Long, Christian; Orloff, Nathan; Booth, James; Marksz, Eric.
"Characterization of Transmission Lines with Nonlinear Dielectric Materials."
Paper presented at 90th ARFTG Microwave Measurement Conference, Boulder, CO, United States. November 28, 2017 - December 1, 2017.

Following the same approach we use to solve for $\hat{I}_i(x)$ and $\hat{V}_i(x)$ in section II-B, we will express the Green's function in terms of unknown coefficients.

$$g_V^L(x,y) = g_L^+(y)\exp(\gamma x) + g_L^-(y)\exp(-\gamma x) \quad (32)$$

$$g_V^R(x,y) = g_R^+(y)\exp(\gamma x) + g_R^-(y)\exp(-\gamma x) \quad (33)$$

$$g_I^L(x,y) = -\frac{g_L^+(y)}{Z}\exp(\gamma x) + \frac{g_L^-(y)}{Z}\exp(-\gamma x) \quad (34)$$

$$g_I^R(x,y) = -\frac{g_R^+(y)}{Z}\exp(\gamma x) + \frac{g_R^-(y)}{Z}\exp(-\gamma x) \quad (35)$$

The boundary conditions will lead to a matrix equation for the unknown coefficients.

$$\begin{bmatrix} \Gamma & 1 & 0 & 0 \\ 0 & 0 & e^{\gamma l} & \Gamma e^{-\gamma l} \\ -e^{\gamma y} & -e^{-\gamma y} & e^{\gamma y} & e^{-\gamma y} \\ -e^{\gamma y} & e^{-\gamma y} & e^{\gamma y} & -e^{-\gamma y} \end{bmatrix} \begin{bmatrix} g_L^+(y) \\ g_L^-(y) \\ g_R^+(y) \\ g_R^-(y) \end{bmatrix} = \begin{bmatrix} 0 \\ 0 \\ 0 \\ ZI_0 \end{bmatrix} \quad (36)$$

Equation (36) admits a closed form solution, which we found by standard techniques [10].

$$g_L^+(y) = \left(\frac{ZI_0}{2D}\right)\left[\Gamma e^{\gamma(y-l)} - e^{-\gamma(y-l)}\right] \quad (37)$$

$$g_L^-(y) = \left(\frac{ZI_0}{2D}\right)\left[-\Gamma^2 e^{\gamma(y-l)} + \Gamma e^{-\gamma(y-l)}\right] \quad (38)$$

$$g_R^+(y) = \left(\frac{ZI_0}{2D}\right)\left[\Gamma e^{\gamma(y-l)} - \Gamma^2 e^{-\gamma(y+l)}\right] \quad (39)$$

$$g_R^-(y) = \left(\frac{ZI_0}{2D}\right)\left[-e^{\gamma(y+l)} + \Gamma e^{-\gamma(y-l)}\right] \quad (40)$$

### D. Overview

In summary, here is a recipe to predict the 2nd-order mixing products generated a transmission line with a nonlinear distributed capacitance.

1) For each incident frequency $\omega_i$, we use Equation (20) to solve for the coefficients $\hat{V}_i^+$ and $\hat{V}_i^-$ from the measured $a$ waves at the edges of the transmission line.
2) From $\hat{V}_i(x)$, we compute the nonlinear driving term, $N(y)$, for each mixing frequency of interest.
3) We compute the voltage and current Greens functions, given by Equations (28-29), (32-35), and (37-40).
4) We then use Equations (26-27) to determine the spatial distribution of voltages and currents generated by nonlinear mixing.
5) Using boundary conditions given in Equations (16-17), we can compute the outgoing $b$ waves at the reference planes of the edge of the transmission line.

## III. Sample Preparation and Linear Measurements

Figure 2a shows the cross section of our nonlinear transmission lines, as designed. We lithographically fabricated transmission lines on a nonlinear BST film. The film was 1 μm thick and was deposited by pulsed laser deposition on a $LaAlO_3$ substrate. The transmission lines were gold coplanar waveguides, with 200 μm ground planes, a nominal 20 μm center conductor, 5 μm gaps, and 500 nm metalization thickness.

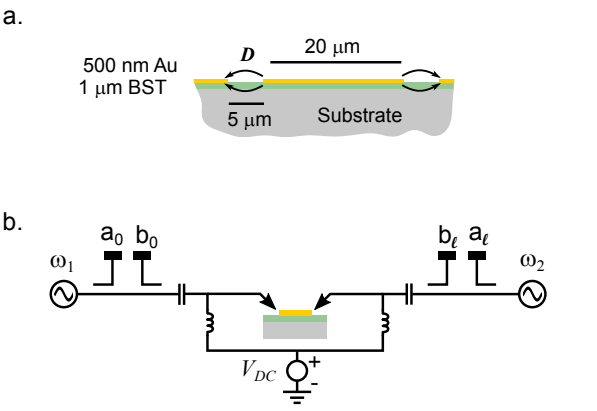


Fig. 2: Experimental configuration. a) Nonlinear transmission line cross section geometry with design dimensions. b) Measurement configuration. Both ends of the waveguide were excited simultaneously, and the $a$ and $b$ waves at $\omega_1$, $\omega_2$ and $\omega_1 + \omega_2$ were recorded.

To determine the linear circuit parameters necessary for the model (Figure 1b), we measured the scattering parameters of each of the transmission lines. These measurements were error-corrected by an on-wafer multiline TRL calibration [13] on a lossless, linear substrate. To get the distributed admittance $Y^{(1)}$, we performed a 2nd-tier multiline TRL calibration on the transmission lines fabricated on the BST chip to extract the propagation constant, $\gamma$. Finally, we computed the distributed resistance $R$ and inductance $L$ using a finite-element method [14]. From $\gamma$, $R$, and $L$, we were able to determine the distributed admittance.

## IV. Nonlinear Measurements

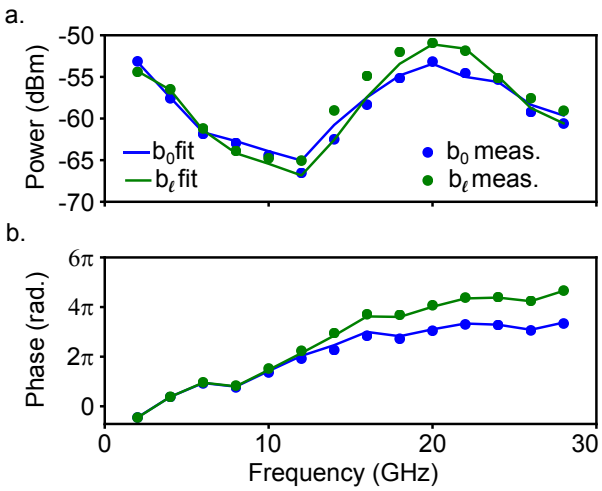


Fig. 3: Nonlinear measurements of the outgoing $b$ wave at $\omega_1 + \omega_2$, with $\omega_1/2\pi$ = 1 GHz. a) Power, de-embedded to on-wafer reference plane. b) Unwrapped phase at on-wafer reference plane.

Hagerstrom, Aaron; Long, Christian; Orloff, Nathan; Booth, James; Marksz, Eric.
"Characterization of Transmission Lines with Nonlinear Dielectric Materials."
Paper presented at 90th ARFTG Microwave Measurement Conference, Boulder, CO, United States. November 28, 2017 - December 1, 2017.

We performed "proof of concept" measurements with an NVNA (Figure 1.b). We found that our sample has no 2nd-order nonlinearity unless it is poled by an external electric field, so we applied a 10 V DC bias between the center conductor and ground planes of the CPW line. The transmission line, with a length of $l = 535$ μm, was excited by signals with a source power of 0 dBm. On the left port (port 0), we applied a tone with a fixed frequency of $\omega_1/2\pi$ = 1 GHz. On the right port (port $l$), we varied the frequency from $\omega_2/2\pi$ = 2 GHz to $\omega_2/2\pi$ = 28 GHz. The ports are denoted 0 and $l$, because the left and right ends of the transmission line are denoted by $x = 0$ and $x = l$, and because subscripts 1 and 2 refer to frequencies $\omega_1$ and $\omega_2$ throughout this paper.

We corrected these measurements using a two-tier calibration, as described in the manual for the NIST Uncertainty Framework software [15]. First, we performed a coaxial SOLT calibration, as well as phase and power calibrations to the coaxial reference plane. Then, we attached the coaxial cables to microwave probes and performed an on-wafer series resistor calibration. The two-tier calibration was necessary because on-wafer phase and power standards are not available. The on-wafer calibration allows us to roll the reference planes to an on-wafer reference plane (the edge of the series resistor).

Figure 3 shows the corrected $b$ wave, at the on-wafer reference plane, for the wave at $\omega_1+\omega_2$. We show both $b_0$ and $b_l$, the waves measured at the left side of the transmission line ($x = 0$) and the right side of the transmission line ($x = l$). $b_0$ and $b_l$ have similar, but non-identical frequency dependence; the amplitude and phase of these waves depends on frequency, because of distributed effects. There is no symmetry in this problem demanding that $b_0$ and $b_l$ be identical, and in a longer line, they may be very different. In this particular case, the phases are very similar below 10 GHz because the transmission line is relatively short and one of the waves is at 1 GHz. The nonlinear mixing products shown in this section are due to the nonlinearity of our BST sample, not the sources or the receivers in the NVNA. We verified this by performing identical measurements on transmission lines with an identical cross section on a linear material ($LaAlO_3$).

According to Equations (26) and (27), the $b$ nonlinear signal at $\omega_1 + \omega_2$ is proportional to $Y^{(2)}(\omega_1, \omega_2)$. So, we can compute $Y^{(2)}(\omega_1, \omega_2)$ in a straightforward way from these measurements. We take the measured $a$ waves at each port for all frequencies as known, and compute the $b$ waves as described in Section (II-D). Then, the nonlinear admittance can be computed as,

$$Y^{(2)}(\omega_1, \omega_2) = \frac{b_{obs}}{b_{NL}}, \tag{41}$$

where $b_{NL}$ is the nonlinear calculated wave with an assumed value of $Y^{(2)} = 1$, and $b_{obs}$ is the observed wave. In the calculations shown in Figure 3, the only fit parameter is $Y^{(2)}$. We determined the value of $Y^{(2)}$ by applying Equation (41) to the measured values of $b_0$ and $b_l$ to obtain two estimates of $Y^{(2)}$, and averaging these two estimates. In this data set, the magnitude of these two estimates agrees at all frequencies, but their phase only agrees below 10 GHz.

By repeating measurements of the $b$ waves on many different transmission lines of differing lengths, we can infer 2 independent measurements of $Y^{(2)}$ from each line corresponding to the 2 ends of the line. By performing measurements on several lines, we plan to both test the model and determine a better estimate of $Y^{(2)}$.

## V. Conclusion

These measurements demonstrate that we can measure the amplitude and phase of 2nd-order mixing products by NVNA. We have strong evidence for the validity of our analytic solution of the nonlinear wave equations, and are in the process of building confidence by performing more measurements. The mathematical formulation and proof-of-concept measurements presented here pave the way for on-wafer nonlinear dielectric characterization. As we described in Section (IV), we can infer the strength of the nonlinearity from these measurements. We expect that $Y^{(2)}$ and $\varepsilon^{(2)}$ are directly related, and that we will be able to quantify this relationship with element simulations.

## References


[1] E. G. Erker, A. S. Nagra, Y. Liu, P. Periaswamy, T. R. Taylor, J. Speck, and R. A. York, "Monolithic ka-band phase shifter using voltage tunable BaSrTiO3 parallel plate capacitors," *IEEE Microwave and Guided Wave Letters*, vol. 10, no. 1, pp. 10–12.

[2] X. Wang, J. Ren, and R. J. Hwu, "Millimeter-wave nonlinear transmission line tripler," vol. 3465. International Society for Optics and Photonics, pp. 98–104.

[3] Y. E. Wang, "Time-varying transmission lines (TVTL) - a new pathway to non-reciprocal and intelligent RF front-ends," in *2014 IEEE Radio and Wireless Symposium (RWS)*, pp. 148–150.

[4] A. K. Tagantsev, V. O. Sherman, K. F. Astafiev, J. Venkatesh, and N. Setter, "Ferroelectric materials for microwave tunable applications," *Journal of Electroceramics*, vol. 11, no. 1, pp. 5–66.

[5] J. C. Booth, I. Takeuchi, and K.-S. Chang, "Microwave-frequency loss and dispersion in ferroelectric $Ba_{0.3}Sr_{0.7}TiO_3$ thin films," *Applied Physics Letters*, vol. 87, no. 8, p. 082908.

[6] C.-H. Lee, N. D. Orloff, T. Birol, Y. Zhu, V. Goian, E. Rocas, R. Haislmaier, E. Vlahos, J. A. Mundy, L. F. Kourkoutis, Y. Nie, M. D. Biegalski, J. Zhang, M. Bernhagen, N. A. Benedek, Y. Kim, J. D. Brock, R. Uecker, X. X. Xi, V. Gopalan, D. Nuzhnyy, S. Kamba, D. A. Muller, I. Takeuchi, J. C. Booth, C. J. Fennie, and D. G. Schlom, "Exploiting dimensionality and defect mitigation to create tunable microwave dielectrics," *Nature; London*, vol. 502, no. 7472, pp. 532–6.

[7] A. E. Glazounov and A. K. Tagantsev, "Phenomenological model of dynamic nonlinear response of relaxor ferroelectrics," *Physical Review Letters*, vol. 85, no. 10, pp. 2192–2195.

[8] J. Mateu, C. Collado, N. Orloff, J. C. Booth, E. Rocas, A. Padilla, and J. M. O'Callaghan, "Third-order intermodulation distortion and harmonic generation in mismatched weakly nonlinear transmission lines," *IEEE Transactions on Microwave Theory and Techniques*, vol. 57, no. 1, pp. 10–18.

[9] J. Mateu, J. C. Booth, and S. A. Schima, "Frequency tuning and spurious signal generation at microwave frequencies in ferroelectric SrTiO3 thin-film transmission lines," *IEEE Transactions on Microwave Theory and Techniques*, vol. 55, no. 2, pp. 391–396.

[10] I. Stakgold and M. J. Holst, *Green's Functions and Boundary Value Problems*. John Wiley & Sons.

[11] M. Neshat, D. Saeedkia, and S. Safavi-Naeini, "Semi-analytical calculation of terahertz signal generated from photocurrent radiation in traveling-wave photonic mixers," *International Journal of Infrared and Millimeter Waves*, vol. 29, no. 9, pp. 809–822. [Online]. Available: https://link.springer.com/article/10.1007/s10762-008-9388-z

[12] D. M. Pozar, *Microwave Engineering*, 4th ed. Wiley.



Hagerstrom, Aaron; Long, Christian; Orloff, Nathan; Booth, James; Marksz, Eric.
"Characterization of Transmission Lines with Nonlinear Dielectric Materials."
Paper presented at 90th ARFTG Microwave Measurement Conference, Boulder, CO, United States. November 28, 2017 - December 1, 2017.

[13] R. B. Marks, "A multiline method of network analyzer calibration," *IEEE Transactions on Microwave Theory and Techniques*, vol. 39, no. 7, pp. 1205–1215.
[14] W. T. Weeks, L. L. H. Wu, M. F. McAllister, and A. Singh, "Resistive and inductive skin effect in rectangular conductors," *IBM Journal of Research and Development*, vol. 23, no. 6, pp. 652–660.
[15] D. Williams and A. Lewandowski, "NIST microwave uncertainty framework," *National Institute of Standards and Technology*, 2011.

Hagerstrom, Aaron; Long, Christian; Orloff, Nathan; Booth, James; Marksz, Eric.
"Characterization of Transmission Lines with Nonlinear Dielectric Materials."
Paper presented at 90th ARFTG Microwave Measurement Conference, Boulder, CO, United States. November 28, 2017 - December 1, 2017.

# Millimeter-wave Frequency FDTD Simulation for Error Vector Magnitude of Modulated Signals*


Joseph Elliott Diener
Colorado School of Mines
Golden, USA
jdiener@mines.edu

Jeanne Quimby
National Institute of Standards and Technology
Boulder, USA
jeanne.quimby@nist.gov

Kate A. Remley
National Institute of Standards and Technology
Boulder, USA
kate.remley@nist.gov

Atef Z. Elsherbeni
Colorado School of Mines
Golden, USA
aelsherb@mines.edu



***Abstract*— At millimeter-wave frequencies, a simulation of propagating complex modulated signals through an environmental channel can be computationally prohibitive using the finite difference time domain (FDTD) method. The "grid impulse response" method uses a delta-function as a source signal to solve for the transfer function of the finite difference time domain grid. Once the transfer function of the channel is known, any number of source signals of differing lengths, such as those involving M-ary quadrature amplitude modulation may be used to estimate the propagation of a complex modulated signal through the environmental channel. Numerical investigations show that the maximum error between the two approaches can be very small. Simple environmental channels are used to present the error vector magnitude at mmWave frequencies obtained from the grid impulse response method.**



***Keywords*— EVM, FDTD, QAM.**


## I. Introduction

Modern millimeter-wave communication systems have complex hardware and modulation schemes that can be modeled with finite difference time domain directly by propagating the source signal through a simulated channel. Use of the full FDTD approach can be a computationally-demanding task for dense FDTD grids propagating long-duration signals due to the gridding requirements based on the very small wavelengths found at millimeter-wave frequencies. Authors in [1-2] show that transfer functions derived from the system response to a delta-function source signal can be used to predict the response of a 1D FDTD grid for an arbitrary input. Perrin *et al*. use a similar technique to predict the grid response in 3D [3]. We extend this previous work to millimeter-wave frequencies and show numerically that a delta-function excitation of the grid can be used to obtain the transfer function of the FDTD grid. Once obtained, the transfer function can be used to solve for the signal received at any grid point when the source is excited by an arbitrary source signal. This approach is known as the grid impulse response (GIR) method. We will discuss the use of the GIR method to calculate the distortion of a modulated signal using error-vector-magnitude as the metric of distortion.

## II. The Transfer Function and Grid Impulse Response

We define the transfer function of the FDTD grid as:

$$T(\omega) = \frac{F(\,RX(t)\,)}{F(\,TX(t)\,)}\,, \tag{1}$$

where $F$ is the fast Fourier transform, $RX$ is the time-domain sampled signal at a point of interest in the FDTD grid, $TX$ is the source signal used to excite the FDTD grid, and $T(\omega)$ is the transfer function. Working with the time domain representation of the transfer function, the grid impulse response (GIR) is given by:

$$GIR(t) = F^{-1}(T\,(\omega)\,)\,. \tag{2}$$

Note that for a delta-function source signal incident on the FDTD grid, the GIR is directly obtained by sampling the grid, $GIR(t) = RX(t)$. Once the GIR is found, any signal of interest can be solved at the RX sampling point by convolution, and is given by:

$$RX_{calculated}(t) = GIR(t) * TX_{arbitrary}(t)\,, \tag{3}$$

where * indicates convolution and $RX_{calculated}$ is the predicted signal obtained from the arbitrary signal source $TX_{arbitrary}$. This formulation is most useful in solving for signals where the number of time steps needed to inject the signal into the grid is much larger than the number of time steps needed for the GIR to converge.

## III. Numerical Demonstration of Accuracy

We used an M-ary quadrature-amplitude modulation (M-QAM) signal to examine the accuracy of the GIR method. The FDTD code from [5] is used for all simulations, run in single precision. A source transmitting an M-QAM signal is placed in free-space and terminated in either convolutional perfectly-matched layer (CPML) [6] or perfect electrical conductor (PEC) boundaries. The signal is 16-QAM modulation, 10 GSym/s, with five symbol durations. The CPML is eight-cells thick. We compare a simulation using the full FDTD approach and another using the GIR method. The signals at a given point of interest in space as a function of time-step are recorded for both methods. The received signal from the full-length simulation $RX_{\text{full}}$ is compared with the predicted signal from the GIR method. The signals are compared with an error metric defined by:

$$Error = \left|RX_{full} - RX_{GIR}\right|. \tag{4}$$


* Work partially supported by US government not protected by US copyright.



Diener, Joseph; Quimby, Jeanne; Remley, Catherine; Elsherbeni, Atef.
"Millimeter-wave Frequency FDTD Simulation for Error Vector Magnitude of Modulated Signals."
Paper presented at 2018 International Applied Computational Electromagnetics Society (ACES) Symposium, Denver, CO, United States. March 24, 2018 - March 29, 2018.

$RX_{full}$ has its maximum amplitude normalized to 1 and $RX_{GIR}$ is normalized with the same normalization constant. The free-space propagation case is shown in the solid line in Fig. 1. At 500 time steps, the jump in the figure is due to the transmitted signal arriving at the receiver. The signal variation previous to this time step is due to numeric noise. The GIR determination uses 1816 time steps. Through time step 1816, the error is less than $10^{-6}$. At time step 1817, the error increases by ~10x, with a maximum error of approximately $10^{-3}$ from time step 1888 and beyond. Thus, for time steps less than or equal to the number of time steps used in the full FDTD simulation, the GIR method will capture the grid response with the error of a predicted signal $< 10^{-6}$. For time steps after this point, the error will reflect the degree to which the long-term GIR has been captured. When the GIR has begun to converge, the error for future time steps is relatively low ($\sim 10^{-3}$), and will be reduced further when the grid is sampled for more time steps. When the long-term GIR has not been captured, the error for future time steps will be large. This is shown in the dashed line in Fig. 1, where the convolutional perfectly matched layer (CPML) boundaries are replaced with PEC walls to simulate a metal enclosure shown by the box results. Through the time step of the GIR simulation, the response of the grid is captured well ($< 10^{-6}$ error). The maximum error very quickly approaches 0.5 for time steps after this point, corresponding to essentially no agreement between predicted and actual signals. This is due to the resonant nature of the box, and shows that the transfer function method can fail when used inappropriately.

## IV. Error Vector Magnitude Calculation

The GIR method is an excellent compromise between accuracy and computational expense for determining distortion in a modulated signal from a channel. By creating a modulated signal and convolving with the GIR, the effects of the channel will be seen on the received signal. This can show channel effects such as path loss, power delay profile, and the error vector magnitude (EVM) [4] introduced by the channel. Application of the technique to an EVM calculation is shown for two identical dipole antennas operating at 90 GHz as a TX/RX pair in a free-space channel and in a channel with an infinite ground plane below the antennas. The distance between the two antennas is swept through 0.12 m, as seen in Fig. 2. A 1000 symbol, duration 16-QAM signal is the excitation and the signal is post-processed to yield the EVM. The mean EVM is shown in Fig. 2. The ground-bounce case shows significantly increased distortion resulting from the reflected signal, with two distinct peaks appearing. These peaks are not present in the free-space case, and so are solely attributable to the reflected signal from the ground-plane.

## V. Conclusion

We have shown that the use of transfer functions in the full 3D FDTD grid can give long-term grid responses with error less than $< 10^{-6}$. An understanding of the error in such an approach has been introduced, showing clear cases where the GIR is not satisfactory. Through the use of the transfer function of the grid, simulations of the modulated signals can be solved rapidly, and channel effects on the EVM of the signal derived directly. Further investigation of the computational speedup is warranted.

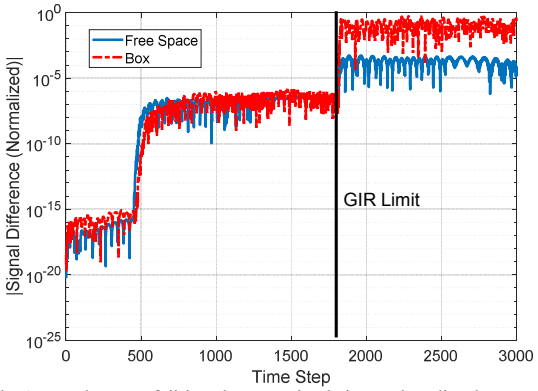


Fig. 1. Error between full-length FDTD simulation, and predicted response using the GIR method. Dashed line shows the PEC box case, while the solid line shows the free-space case. Truncated at 3000 timesteps for clarity.

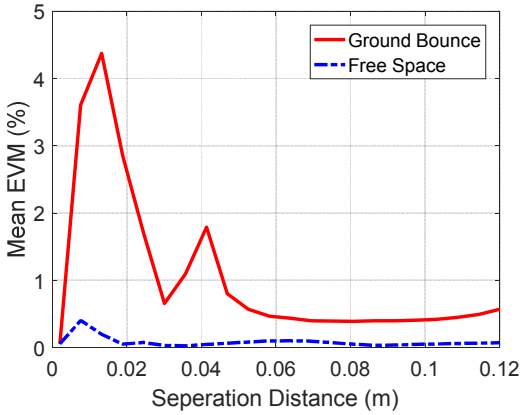


Fig. 2. EVM for a dipole-dipole case using 16-QAM signal, with results calculated by the GIR. Distinct peaks are seen from ground-bounce effects.

## References


[1] J. B. Schneider and C. L. Wagner, "FDTD dispersion revisited: Faster-than-light propagation," in *IEEE Microwave and Guided Wave Letters*, vol. 9, no. 2, pp. 54-56, Feb. 1999.

[2] J. P. Bérenger, "Propagation and aliasing of high frequencies in the FDTD grid," in *IEEE Transactions on Electromagnetic Compatibility*, vol. 58, no. 1, pp. 117-124, Feb. 2016.

[3] E. Perrin, C. Guiffaut, A. Reineix, and F. Tristant, "Using transfer function calculation and extrapolation to improve the efficiency of the finite-difference time-domain method at low frequencies," in *IEEE Transactions on Electromagnetic Compatibility*, vol. 52, no. 1, pp. 173-178, Feb. 2010.

[4] M. Mckinley, K. A. Remley, M. Mylinshi, and J. S. Kenney, "EVM Calculation for Broadband Modulated Signals," in ARFTG Microwave Measurement Conference, Orlando, FL, 2004.

[5] A. Z. Elsherbeni and V. Demir, *The Finite Difference Time Domain Method for Electromagentics with MATLAB Simulations,* second edition, ACES series on Computational Electromagnetics and Engineering, SciTech Publishing, an Imprint of IET, Edison, NJ, 2015.

[6] J. A. Roden and S. D. Gedney, "Convolutional PML (CPML): An efficient FDTD implementation of the CFS-PML for arbitrary media," *Microw. Opt. Technol. Lett*., vol. 27, pp. 334-339, 2000.



Diener, Joseph; Quimby, Jeanne; Remley, Catherine; Elsherbeni, Atef.
"Millimeter-wave Frequency FDTD Simulation for Error Vector Magnitude of Modulated Signals."
Paper presented at 2018 International Applied Computational Electromagnetics Society (ACES) Symposium, Denver, CO, United States. March 24, 2018 - March 29, 2018.

# Determining Carbon Fiber Composite Loading with Flip-Chip Measurements to 110 GHz

Nina B. Popovic[1,2*], Jasper Drisko[1], Aaron M. Hagerstrom[1], Joshua A. Orlicki[3], Jennifer M. Sietins[3], Daniel B. Knorr Jr[3], James C. Booth[1], Edward Garboczi[1], Christian J. Long[1], Nathan D. Orloff[1#]

[1]National Institute of Standards and Technology, Boulder, CO

[2]University of Colorado, Boulder, CO

[3]U.S. Army Research Laboratory, Aberdeen Proving Ground, MD

{[*]bastanp, [#]nathan.orloff} @colorado.edu, @nist.gov

**Abstract — Precise knowledge of electrical properties of materials are a necessary input to any circuit design. As applications at millimeter-wave frequencies increase, there is a need to develop new materials with low loss and multiple functionalities. Most material characterization techniques are destructive to the original sample. For example, most resonant cavity techniques require a sample to be diced into a sub-millimeter geometry. Alternatively, broadband on-wafer techniques require lithographically patterned devices on the material under test. Here, we demonstrate a technique that combines on-wafer calibration with a flip-chip transmission-line test fixture. This single-transmission-line fixture enables quantitative measurement of effective permittivity from 40 kHz to 110 GHz. The resulting materials characterization approach is non-destructive and directly applicable to measurements of dielectric, magnetic, and nonlinear properties. The broad applicability of the technique makes it well-suited for characterizing the next generation of materials, including tunable materials and complex structural composites.**

***Keywords*** **— millimeter waves, calibration, flip-chip, coplanar waveguide, dielectric spectroscopy, composites**

## I. Introduction

Both electrical and mechanical material properties are important for the design of electronic devices. In order to optimize these properties, multifunctional materials often require very specific micro- and nanostructures. For example, a multifunctional composite containing conducting fibers might provide both mechanical strength and electrical shielding. Understanding the mechanical and electrical properties and their relationships is paramount for identifying the possible applications for materials. The goal of this paper is to show a relationship between the measured electrical properties (distributed circuit parameters) and the physical properties (mass fraction) of a composite carbon fiber material. The data in this paper is the first step in understanding this relationship, however there are still many questions to answer and more measurements to be taken.

Unlike typical characterization techniques, the flip-chip technique discussed in this paper provides broadband, non-destructive, and quantitative measurements of distributed circuit parameters of a coplanar waveguide loaded with a material. The new method leverages a combination of broadband measurement techniques [1], [2] and low-frequency electrical property analysis to discern electrical characteristics [3]. As an example, we explore the range of dielectric properties and frequency dependence of a multi-functional material consisting of carbon-fibers embedded in a polymer matrix. As a structural material, carbon fiber serves as a mechanical reinforcement that finds applications ranging from sporting goods to aerospace and reducing the weight of automobiles. As an electrical material, it has been employed for both electrostatic discharge protection and suppression of electromagnetic interference [4].

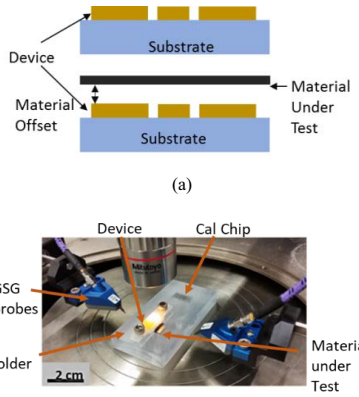


Fig. 1. The flip-chip transmission line for materials characterization from 40 kHz to 110 GHz. (a) A top view schematic of the coplanar waveguide device. (b) The cross-section of the two topologies needed to extract material properties. The chip is 500 µm thick fused silica with relative permittivity of 3.8, and the material offset is 100 µm.

The single-line flip-chip technique (Fig. 1), is inspired by on-wafer material characterization techniques designed for thin-film dielectric materials [2]. These techniques are based on the multiline thru-reflect-line (multiline TRL) calibration [5] in a coplanar waveguide topology. Broadly speaking, the previous work employs a two-tiered measurement procedure: first, a rigorous calibration sets the reference impedance and translates the measurement reference plane onto a test wafer; second, a set of transmission lines loaded by a material under test is

Basta, Nina; Drisko, Jasper; Hagerstrom, Aaron; Orlicki, Joshua; Sietins, Jennifer; Knorr, Jr., Daniel; Garboczi, Edward; Long, Christian; Orloff, Nathan.
"Determining Carbon Fiber Composite Loading with Flip-Chip Measurements to 110 GHz."
Paper presented at 48th European Microwave Conference, Madrid, Spain. September 23, 2018 - September 27, 2018.

characterized with multiline TRL and the properties of the material under test are extracted.

In this work, we follow a similar two-tiered approach, though in lieu of the more conventional multiline TRL technique in the second tier, we used a single coplanar waveguide device (Fig. 1a). We measure this single waveguide both with and without a material under test (Fig. 1b), and extract distributed circuit parameters.

The coplanar waveguide (CPW) device has electric (**E**) and magnetic (**H**) fields that penetrate above and below the metallization of the coplanar waveguide. These fields allow the waveguide to interrogate the electromagnetic properties of a material placed near the waveguide. To control the coupling between the fields and material under test, the measurements require a holder to elevate the sample a precisely-known distance above the waveguide (Fig. 1b).

From the single-line measurements, the distributed circuit parameters of the waveguide were extracted. While we expect that this single-line technique will not be as accurate as a multiline technique, it has two key advantages. First, the test fixture can be reused many times for different samples, and second, it does not require lithographic processing of each sample. This latter point is especially valuable for samples that are too rough or fragile for coplanar waveguides to be directly printed on the material's surface. These advantages open the door to fast, inexpensive, broadband material characterization.

In what follows, we first provide a description of the methodology behind the materials characterization technique. Next, we discuss the algorithm implemented to extract distributed circuit parameters of an unloaded and loaded transmission line. In Section IV, we analyze measured data and correlations between the electrical and physical parameters of the material.

## II. Description of Methodology

As an example of a multifunctional material, we chose to study a carbon fiber composite. Neat carbon fibers (Mitsubishi, DIALEAD K223HE[1,2]) were first ball milled, then combined with a polyetherimide polymer matrix (Sabic, ULTEM 1010) in a twin-screw extruder. The milled fibers up were up to 60 $\mu$m long, and had a nominal diameter of 5 $\mu$m. After mixing, the samples were injection molded into a rectangular blank, then diced to dimensions of approximately 10 mm × 10 mm × 2 mm. Here, we study samples with carbon fiber mass fractions of approximately 0.0 %, 8.4 %, and 27.3 % (Fig. 2), as defined by a precision scale.

The microstructure of the samples was characterized by X-ray computed tomography (CT) (Fig. 2b), which creates a 3-dimensional (3D) image of each sample. We qualitatively analyzed the 3D images, showing that the fibers were oriented in many different directions and appeared to be uniformly distributed throughout the polymer matrix. Based on these qualitative results, we treat the materials as an effective medium with an isotropic effective permittivity.

The surface roughness of the samples, as found with the X-ray CT analysis, is on the order of a few hundred nanometers and must be considered in the measurement setup. To minimize the effect of the surface roughness of the samples on electrical measurements, the material is separated from the surface of the coplanar waveguide with a sample holder (Fig. 3). The separation between the waveguide surface and the sample surface is chosen to be large compared to the sample's surface roughness, but small enough that the fields still interact with the sample. In this work, the gap width of the coplanar waveguide was 50 $\mu$m, and the sample was elevated 100 $\mu$m (Fig. 3b) above the device. Finite element simulations using ANSYS Q3D were used to determine the maximal distance between the coplanar waveguide and sample (Fig. 3c). Since the sample thickness (about 2 mm) is much larger than the gap width of the coplanar waveguide, it appears infinite and does not need to be simulated. It is clear from the simulation that a substantial amount of the incident wave propagates through the sample material. With the physical setup (Fig. 3), we can now take measurements to determine the electrical properties of the composite.

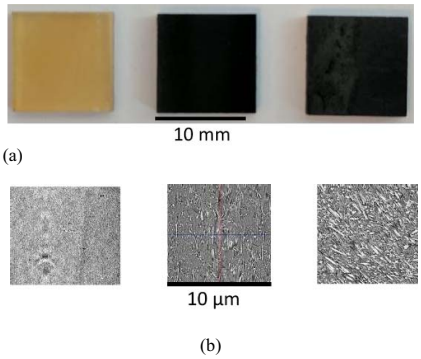


Fig. 2. Samples of milled carbon fiber in a polymer matrix with mass fractions of 0.0 %, 8.4 %, and 27.3 % as seen in (a) photograph and (b) X-ray CT.

To test the electrical properties of the composite, we measured the scattering-parameters (S-parameters) of coplanar waveguide devices with a vector network analyzer (VNA). The first-tier calibration was based on multiline TRL, as described elsewhere [2]. The first-tier calibration was used to solve for the error boxes associated with the VNA, cables, and probes. We also use it to solve for the characteristic impedance ($Z$) and propagation constant ($\gamma$) of the waveguide without loading by the material under test. Because these complex quantities are used for the second-tier calibration and they are related to the geometry of the CPW, the first- and second-tier CPWs must have the same geometry. The CPW has a nominal center conductor width of 20 $\mu$m, a gap width of 50 $\mu$m, a ground plane width of 200 $\mu$m, and a conductor thickness of 0.5 $\mu$m. We fabricated all devices on the same wafer using an in-house cleanroom and conventional i-line stepper lithography. The

[1] Mention of commercial products in this manuscript is for information purposes only; it does not imply recommendation or endorsement by NIST.



Basta, Nina; Drisko, Jasper; Hagerstrom, Aaron; Orlicki, Joshua; Sietins, Jennifer; Knorr, Jr., Daniel; Garboczi, Edward; Long, Christian; Orloff, Nathan.
"Determining Carbon Fiber Composite Loading with Flip-Chip Measurements to 110 GHz."
Paper presented at 48th European Microwave Conference, Madrid, Spain. September 23, 2018 - September 27, 2018.

CPW lines were made by electron-beam vapor deposition, depositing 0.5 $\mu$m thick gold with a 10 nm Ti adhesion layer on a fused silica substrate. For more details about the fabrication, see [6].

In the next section, we discuss how we measure the per-unit-length quantities of series resistance ($R$), series inductance ($L$), shunt conductance ($G$), and shunt capacitance ($C$).

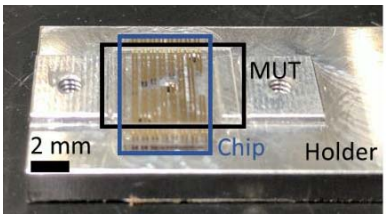


(a)

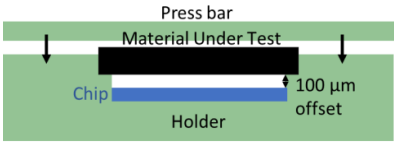


(b)

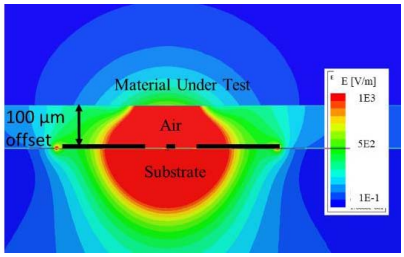


(c)

Fig. 3. (a) A photograph of the chip and a fused silica MUT on the holder (press bar not pictured). (b) A not-to-scale schematic of the cross-section of the holder, that elevates the sample 100 $\mu$m away from the surface of the chip. (c) A finite element simulation illustrating the change in **E**-field magnitude used to determine the offset. The black bars are a not-to-scale depiction of the coplanar waveguide.

## III. Extracting Distributed Circuit Parameters

To extract the distributed circuit parameters ($R$, $L$, $G$, and $C$) of the material-loaded line, we modeled the S-parameters using a T-matrix formalism. In this case, the model for a uniform, non-loaded transmission line in a 50 Ω system is

$$\boldsymbol{T} = Q_Z^{50}\begin{pmatrix} e^{-\gamma\ell} & 0 \\ 0 & e^{\gamma\ell} \end{pmatrix} Q_{50}^{Z}, \qquad (1)$$

and the model for a uniform, loaded transmission line in a 50 Ω system is given by:

$$T = Q_Z^{50}\begin{pmatrix} e^{-\gamma\ell} & 0 \\ 0 & e^{\gamma\ell} \end{pmatrix} Q_{Z_l}^{Z}\begin{pmatrix} e^{-\gamma_l l_l} & 0 \\ 0 & e^{\gamma_l l_l} \end{pmatrix} Q_{Z}^{Z_l}\begin{pmatrix} e^{-\gamma\ell} & 0 \\ 0 & e^{\gamma\ell} \end{pmatrix} Q_{50}^{Z}, \qquad (2)$$

where the impedance transformer $Q$ between any impedances $Z_n$ and $Z_m$ is given by

$$\boldsymbol{Q}_{Z_m}^{Z_n} = \frac{1}{2\sqrt{Z_n \cdot Z_m}}\begin{pmatrix} Z_m + Z_n & Z_m - Z_n \\ Z_m - Z_n & Z_m + Z_n \end{pmatrix}, \qquad (3)$$

where $\gamma$ is the complex propagation constant, $Z$ is the characteristic impedance, $\ell$ is the length of the line, and the $\ell$ subscript indicates parameters of the loaded transmission line. The standard definitions of $\gamma$ and $Z$ are used here:

$$\gamma \equiv \sqrt{(R + j\omega L)(G + j\omega C)}, \text{ and} \qquad (4)$$

$$Z \equiv \sqrt{\frac{(R+j\omega L)}{(G+j\omega C)}}. \qquad (5)$$

We note that expressions (1), (2), and (3) make several assumptions. Specifically, they assume that the system is linear, that there is only a single quasi-TEM mode of propagation in the coplanar waveguide, and that the interface between the unloaded segment of the waveguide and the material-loaded segment of the line can be modeled as an impedance transformer. These assumptions are discussed in the next section in the context of experimental data.

The distributed circuit parameters for each sample are extracted by a non-linear least-squares fitting algorithm that minimizes the error between the theoretical S-parameters expressions and the measured S-parameters [7], [8]. We tested our approach on three samples of milled carbon fiber in a polymer matrix (Fig. 2). These results are discussed in the following section.

## IV. Results

After extracting the distributed circuit parameters for the three samples shown in Fig. 2, we analyzed the data to identify how these parameters change in the presence of the material-under-test. Although not shown here, $R$ and $L$ were unaffected by our material-under-test. Therefore, we hold these parameters fixed as frequency-dependent values obtained after analyzing the CPW without the material-under-test. Holding $R$ and $L$ to these values allowed for a more robust extraction of the values of $C$ and $G$. We computed the difference between $C$ and $G$ with and without the material-under-test (Fig. 4), computing $\Delta C$ as a function of frequency.

At this point, we can do a short analysis of the validity of the single quasi-TEM mode of propagation assumption made earlier. We expect the single quasi-TEM approximation to be valid as long as the guided wavelength is small compared to the characteristic lengths of the waveguide [9]. This assumption breaks down at some frequency and is quantified as



Basta, Nina; Drisko, Jasper; Hagerstrom, Aaron; Orlicki, Joshua; Sietins, Jennifer; Knorr, Jr., Daniel; Garboczi, Edward; Long, Christian; Orloff, Nathan.
"Determining Carbon Fiber Composite Loading with Flip-Chip Measurements to 110 GHz."
Paper presented at 48th European Microwave Conference, Madrid, Spain. September 23, 2018 - September 27, 2018.

$$\frac{\lambda_0}{10\sqrt{\varepsilon_r}} = w + 2s, \tag{6}$$

where relative permittivity is 2.5, $w$ is the width of the center conductor, and $s$ is the gap width between center conductor and ground plane. From this analysis, we estimated that the assumption is not valid starting at $f = 158$ GHz, well above the measurements presented here.

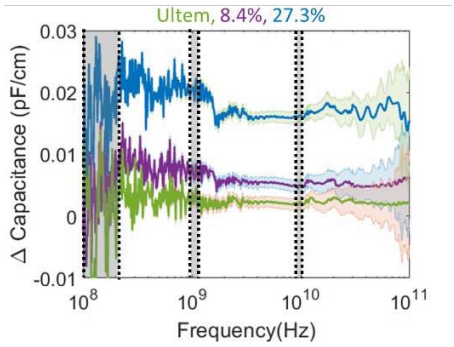


(a)

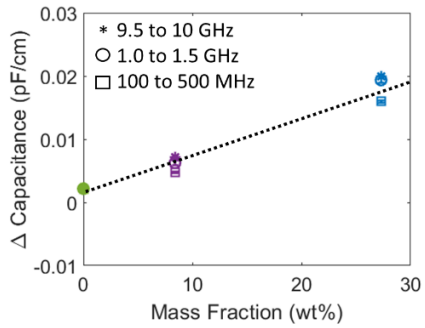


(b)

Fig. 4. Change in capacitance with uncertainty of three samples as a function of (a) frequency plotted from 100 MHz to 100 GHz and (b) sample mass fraction at frequency ranges of 100 MHz to 500 MHz, 1.0 GHz to 1.5 GHz, and 9.5 GHz to 10 GHz. The standard uncertainty for the frequency sweep is propagated through the analysis and added in quadrature for the normalization. The uncertainty for frequency slices is a single standard deviation in the mean. Where the error bars are not visible, they are smaller than the plot marker.

Inside the frequency range where a single quasi-TEM mode propagates, $\Delta C$ did not change significantly as a function of frequency (Fig. 4a). However, $\Delta C$ shows a systematic increase as a function of fiber mass fraction (Fig. 4b). This data means that as the mass fraction increased, the dielectric constant (real part of the permittivity) also changed. Interestingly, by taking the mean over frequency slices at 100 MHz to 500 MHz, 1.0 GHz to 1.5 GHz, and 9.5 GHz to 10 GHz, a roughly linear dependence of $\Delta C$ on mass fraction is determined. These points were chosen to highlight the extremes of the frequency spectrum; other points show a similar data point spread.

Future measurements and simulations are underway to help us understand how the change in capacitance should depend on the presence of the material-under-test. The relative change in capacitance related to the mass fraction is consistent with what was expected, as the capacitance change for the 8.4 % sample was roughly a third of the change for the 27 % sample.

## V. Conclusions

In this paper, we demonstrated a flip-chip approach for determining the effect on electrical properties based on changes in physical properties. Specifically, carbon fiber composite material loading of a coplanar waveguide from 100 MHz to 110 GHz. The distributed circuit parameters were correlated with the carbon fiber mass fraction. For future works, the change in extracted capacitance and conductance per-unit-length can be mapped to electrical properties (e.g., permittivity, permeability, conductivity) via finite element simulations (FEM) of the cross-sectional geometry. More generally, our approach demonstrates a quantitative nondestructive materials characterization that can be applied to material systems beyond those explored here.

## Acknowledgment

The authors acknowledge funding from the DARPA Tailorable Feedstock and Forming (TFF) project under inter agency agreement number 1607-647-16.

## References

[1] N. Orloff, J. Mateu, M. Murakami, I. Takeuchi, and J. C. Booth, "Broadband characterization of multilayer dielectric thin-films," in *2007 IEEE/MTT-S International Microwave Symposium*, 2007, pp. 1177–1180.

[2] C.-H. Lee *et al.*, "Exploiting dimensionality and defect mitigation to create tunable microwave dielectrics," *Nature*, vol. 502, no. 7472, pp. 532–536, Oct. 2013.

[3] J. M. Torrents, T. O. Mason, and E. J. Garboczi, "Impedance spectra of fiber-reinforced cement-based composites: a modeling approach," *Cem. Concr. Res.*, vol. 30, no. 4, pp. 585–592, Apr. 2000.

[4] D. D. L. Chung, "Electromagnetic interference shielding effectiveness of carbon materials," *Carbon*, vol. 39, no. 2, pp. 279–285, Feb. 2001.

[5] R. B. Marks, "A multiline method of network analyzer calibration," *IEEE Trans. Microw. Theory Tech.*, vol. 39, no. 7, pp. 1205–1215, Jul. 1991.

[6] C. A. E. Little, N. D. Orloff, I. E. Hanemann, C. J. Long, V. M. Bright, and J. C. Booth, "Modeling electrical double-layer effects for microfluidic impedance spectroscopy from 100 kHz to 110 GHz," *Lab. Chip*, vol. 17, no. 15, pp. 2674–2681, Jul. 2017.

[7] W. R. Eisenstadt and Y. Eo, "S-parameter-based IC interconnect transmission line characterization," *IEEE Trans. Compon. Hybrids Manuf. Technol.*, vol. 15, no. 4, pp. 483–490, Aug. 1992.

[8] F. Mirri *et al.*, "Lightweight, Flexible, High-Performance Carbon Nanotube Cables Made by Scalable Flow Coating," *ACS Appl. Mater. Interfaces*, vol. 8, no. 7, pp. 4903–4910, Feb. 2016.

[9] W. Heinrich, "Quasi-TEM description of MMIC coplanar lines including conductor-loss effects," *IEEE Trans. Microw. Theory Tech.*, vol. 41, no. 1, pp. 45–52, Jan. 1993.



Basta, Nina; Drisko, Jasper; Hagerstrom, Aaron; Orlicki, Joshua; Sietins, Jennifer; Knorr, Jr., Daniel; Garboczi, Edward; Long, Christian; Orloff, Nathan.
"Determining Carbon Fiber Composite Loading with Flip-Chip Measurements to 110 GHz."
Paper presented at 48th European Microwave Conference, Madrid, Spain. September 23, 2018 - September 27, 2018.

# Spatial Uniformity Study in a Loaded Reverberation Chamber at Millimeter-Wave Frequencies

Damir Senic, Kate A. Remley, Maria G. Becker, and Christopher L. Holloway
National Institute of Standards and Technology
Boulder, CO
damir.senic@nist.gov

***Abstract*—We performed a study of the spatial uniformity of the averaged fields in a reverberation chamber at millimeter-wave frequencies based on measurements of the power transfer function for six different reverberation chamber loading configurations. We show that chamber spatial uniformity is strongly influenced by loading. An unloaded chamber can be considered as a nearly uniform environment, while uniformity decreases with increased loading. The loading of a chamber is key for wireless tests involving modulated signals. Its purpose is to create a frequency-flat channel, which enables successful demodulation of the signal without distortion. Consequently, understanding this effect is important in quantifying measurement uncertainty in loaded conditions.**

***Keywords—measurements uncertainty; reverberation chamber; RF loading; spatial uniformity; wireless systems***

## I. Introduction

Reverberation chambers (RCs) have been traditionally used for various electromagnetic compatibility (EMC) measurements since the 1980s. Recently, they have become important to the wireless industry for over-the-air (OTA) tests of wireless devices such as smartphones, machine-to-machine (M2M) and internet-of-things (IoT) devices.

Reverberation chambers are electrically-large resonators where, when averaged over a mode-stirring sequence, fields ideally have a spatially-uniform distribution [1]. Spatial uniformity in RCs has been studied previously [2]-[11]. However, those studies did not investigate the decrease in uniformity that occurs when a chamber is loaded in order to flatten its frequency response.

Empirical study of real reverberation chamber spatial uniformity is particularly interesting to the wireless community, which employs RCs for OTA tests [3], [12]. The key difference between traditional EMC tests deploying continuous-wave signals and wireless tests of modulated signals is that wireless tests generally require a loaded chamber to mimic a realistic channel coherence bandwidth (CBW). RF loading creates a channel with fading characteristics [13] that act like a real channel for which the device is designed to operate in. Loading broadens and flattens the frequency response of the channel inside the chamber by increasing the CBW, which is necessary for demodulating modulated signals without distortion [4],[14]. However, heavy loading, if not properly accounted for in stirring sequence design, may have negative impacts on the chamber's behavior, as it decreases spatial uniformity and increases chamber anisotropy [15] due primarily to the unstirred multipath components. Common practice for wireless measurements involving RCs is to minimize unstirred energy by applying additional spatial stirring mechanisms (antenna platform stirring and antenna polarization stirring) in addition to paddle stirring, and by optimizing the antenna placement and orientation inside the chamber [4].

A real RC setup will exhibit some lack of spatial uniformity depending on the amount of loading. Field uniformity is an important figure of merit in standardized tests [12],[16]. A common way to characterize the chamber uniformity is to measure the electric field or received power at different locations using a field probe or an antenna. One method for performing field uniformity characterization of a reverberation chamber is described in the IEC 61000-4-21 standard [16]. The IEC test specifies electric-field measurements with an electric-field probe or power measurements with an antenna at eight different locations inside the chamber that form the edge of the chamber's working volume. Electric-field probes are suggested because they have small dimensions and, therefore, should not significantly perturb the fields inside the chamber. The small size of the field probe also means that undesirable field averaging typical of larger antennas, can be avoided. In [12], the chamber power transfer function is measured with a reference antenna that has "similar" radiation characteristics as the device under test (DUT). Measurements are conducted at nine spatially-independent locations, where independence is confirmed through cross correlation.

In the present work, we extend the work of [4],[17] by use of the method of [12] to study a chamber operating at millimeter-wave frequencies. The reverberation chamber environment is evaluated by measuring the chamber's power transfer function for different loading cases at nine locations inside the chamber (see Fig. 1). We compare the results to lower-frequency measurements performed inside a chamber operating at microwave frequencies. The results indicate that the extremely high-$Q$ of the millimeter-wave chamber provides a lower standard deviation in the chamber power transfer function between nine antenna locations for a given coherence bandwidth due to its rich modal characteristics. Consequently, since CBW increases with frequency, a millimeter-wave chamber is capable of achieving a broader CBW than a reverberation chamber operating at microwave frequencies, which should be very useful for future generation (5G) wireless OTA tests involving reverberation chambers.

* Work supported by U.S. government, not protected by U.S. copyright



Senic, Damir; Remley, Catherine; Becker, Maria; Holloway, Christopher.
"Spatial Uniformity Study in a Loaded Reverberation Chamber at Millimeter-Wave Frequencies."
Paper presented at 2018 IEEE Symposium on Electromagnetic Compatibility, Signal Integrity and Power Integrity (EMC, SI & PI), Long Beach, CA, United States. July 30, 2018 - August 3, 2018.

## II. Measurement Configuration and Chamber Characterization

We performed spatial uniformity measurements with a 50 GHz VNA in terms of the chamber power transfer function ($G_{\text{ref}}$) for the tabletop-sized reverberation chamber shown in Figs. 1 and 2. The chamber's power transfer function ($G_{\text{ref}}$) is defined as

$$G_{\text{ref}} = \frac{\left\langle \left| S_{21} \right|^2 \right\rangle}{\eta_{\text{TX}} \eta_{\text{RX}} \left(1 - \left| \left\langle S_{11} \right\rangle \right|^2\right)\left(1 - \left| \left\langle S_{22} \right\rangle \right|^2\right)}, \quad (1)$$

where the brackets denote the ensemble average over the mode-stirring sequence, $S_{21}$ is the forward transmission scattering parameter measured by a VNA, and the terms in the denominator represent the free-space radiation efficiencies ($\eta_{\text{TX}}$ and $\eta_{\text{RX}}$) and mismatch corrections for the two antennas. The radiation efficiency can be measured in either an anechoic chamber or in an unloaded reverberation chamber [5].

Our chamber is equipped with two mechanical stirrers. The larger one rotates about a horizontal ($H$) axis within a cylindrical volume of 0.6 m height and 0.2 m diameter, while the smaller one rotates about a vertical ($V$) axis within a cylindrical volume of 0.5 m height and 0.2 m diameter. The RC's inner dimensions are 1 m ($l$) × 0.65 m ($w$) × 0.55 m ($h$), which corresponds to an electrical size of approximately 150 λ × 100 λ × 80 λ, at 45 GHz. This is important to emphasize since the high operating frequency results in a large electrical size for the RC, despite its small physical size. All measurements are made in the stepped mode under steady state conditions.

The RC's bulkhead was equipped with two feedthroughs, one in waveguide that was connected through a coax-to-waveguide adapter to the VNA's port 2 and the other in a 2.4 mm coax that was connected to the VNA's port 1. The port 2 bulkhead was terminated with the receive WR22 Q-band waveguide horn antenna oriented toward the vertical stirrer (see Figs. 1 and 2). The signal from the 2.4 mm coaxial feedthrough was brought to an identical transmit waveguide horn antenna via a coaxial cable and coax-to-waveguide transition. The receive and transmit antennas were oriented away from each other in order to minimize the direct signal component between them. The transmit antenna was oriented toward the horizontal stirrer and positioned at nine different locations within the RC's working volume (see Figs. 1 and 2) in order to measure the distribution of received power inside the RC for different loading configurations. Key measurement parameters are summarized in Table I. A schematic representation of the measurement setup is given in Fig. 1.

To study the effect of chamber loading on spatial uniformity, measurements were repeated for six different loading configurations: an empty RC and the RC loaded with one, three, six, ten and fourteen pyramidally shaped RF absorber blocks, as shown in Fig. 2. The absorbers had dimensions of 15 cm ($l$) × 15 cm ($w$) × 7.5 cm ($h$). Absorber layout and orientation are shown in Figs. 1 and 2.

Chamber loading decreases the chamber $Q$ factor by increasing the loss inside the chamber and broadens the chamber's CBW by increasing correlations between frequencies [4],[18]. Loading also increases the correlations between stirrer positions which reduces the maximum number of independent paddle samples.

The CBW represents the average bandwidth over which signals measured at neighboring frequencies exhibit correlation above a specified threshold. The CBW can be determined from the autocorrelation function ($R$) of the frequency-domain transfer function $S_{21}$ [16],[18] given by

$$R\left(\Delta f_i, n_i\right) = \sum_{j=1}^{m} S_{21}\left(f_j, n_i\right) S_{21}^{*}\left(f_j + \Delta f_i, n_i\right), \quad (2)$$

where $S_{21}(f, n)$ corresponds to the measured complex $S_{21}$ at frequency step $f_j$ with $m$ frequency points measured within the bandwidth of interest, $\Delta f$ corresponds to one of several frequency offsets over the bandwidth of interest, the index $n_i$ is the mode-stirring sample (out of $N$), and the asterisk denotes complex conjugation.

The CBWs at 45 GHz (calculated for 1 GHz bandwidth) for the six loading configurations calculated for three different typical thresholds (1/$e$, 0.5, and 0.7) are shown in Fig. 3 and summarized in Table II. Different standards use different thresholds. Therefore, we present the results of our CBW study for three different thresholds.

TABLE I. Measurement Parameters

| Parameter | Value |
|---|---|
| Frequency range | 43 GHz – 47 GHz |
| Number of frequency points | 1601 |
| VNA IF bandwidth | 2 kHz |
| VNA output power level | -10 dBm |
| VNA dwell time | 100 μs |
| VNA sweep delay time | 10 μs |
| Paddle step size ($V$ × $H$) | 7.2° × 7.2° |
| Number of paddle positions-stepped ($V$ × $H$) | 50 × 50 = 2,500 |

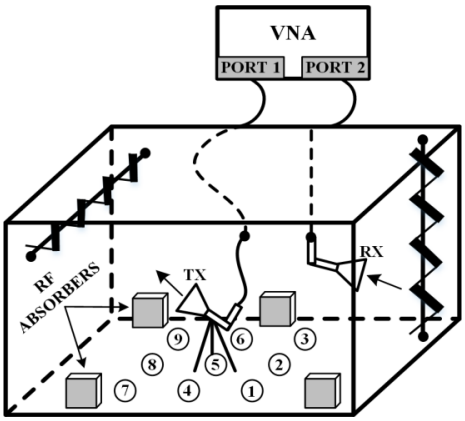


Fig. 1. Schematic of chamber setup for spatial uniformity measurements. Locations 1, 2, …, 9 reperesent the testing locations of the trasnmit antenna TX.



Senic, Damir; Remley, Catherine; Becker, Maria; Holloway, Christopher.
"Spatial Uniformity Study in a Loaded Reverberation Chamber at Millimeter-Wave Frequencies."
Paper presented at 2018 IEEE Symposium on Electromagnetic Compatibility, Signal Integrity and Power Integrity (EMC, SI & PI), Long Beach, CA, United States. July 30, 2018 - August 3, 2018.

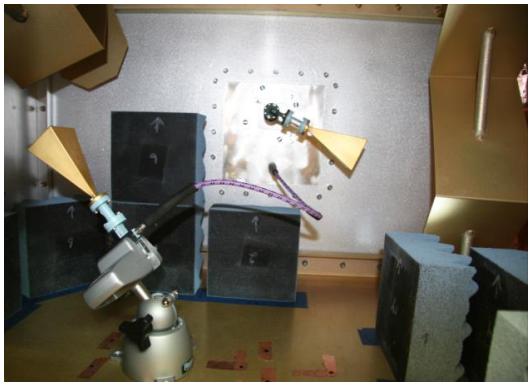

Fig. 2. Heavily loaded chamber setup showing RF absorber blocks and placement and orientation of transmit and receive antennas.

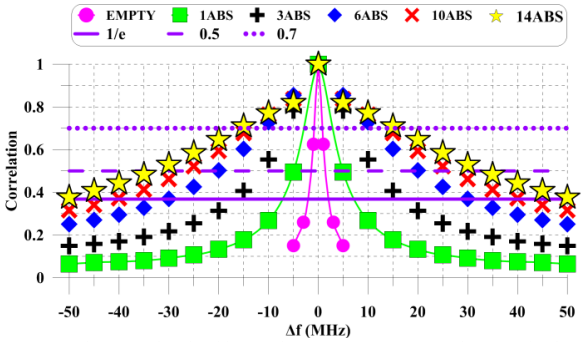


Fig. 3. Coherence bandwidth results at 45 GHz for the six loading configurations calculated for three different thresholds.

TABLE II. COHERENCE BANDWIDTH RESULTS FOR SIX LOADING CONFIGURATIONS AT 45 GHZ

| Loading | CBW (MHz) | | |
|---|---|---|---|
| | 1/*e* | 0.5 | 0.7 |
| Empty | 4 | 3 | 2 |
| 1 Absorber | 15 | 10 | 5 |
| 3 Absorbers | 35 | 24 | 14 |
| 6 Absorbers | 60 | 40 | 22 |
| 10 Absorber | 80 | 54 | 26 |
| 14 Absorbers | 100 | 65 | 30 |

## III. MEASUREMENTS OF SPATIAL UNIFORMITY

To study the RC's spatial uniformity as a function of loading, we used the method of [12],[16]. The chamber transfer function ($G_{ref}$) from (1) was calculated for six different chamber loading configurations and at nine transmit antenna locations. Placement of the RF absorbers inside the chamber can be seen in Fig. 2. The horn antenna efficiencies were previously measured with the method of [5]. The $G_{ref}$ results, averaged over the 4 GHz band (43 GHz – 47 GHz), are shown in Fig. 4 at each TX antenna location and for each chamber loading configuration.

$G_{ref}$ values averaged over nine antenna locations together with Rician $K$ factor values are given in Table III. The $K$ factor metric describes the unstirred energy present inside the RC which is defined as the ratio of unstirred to stirred power and can be estimated from $S$-parameters as

$$K = \frac{\left|\langle S_{21}\rangle\right|^2}{\left\langle\left|S_{21} - \langle S_{21}\rangle^2\right|\right\rangle}. \quad (3)$$

Generally, the unstirred energy is defined as the part of the total energy available inside the RC that reaches the receive antenna without prior interaction with paddles. The existence of the unstirred energy leads to the creation of "hot spots" which reduce spatial uniformity. In this case, additional stirring mechanisms, such as antenna platform stirring, need to be applied. The presence of RF absorbing material inside the RC reduces the total available stirred energy which is exhibited as poor stirring efficiency and a higher $K$ factor, as shown in Table III.

TABLE III. $G_{REF}$ AND $K$-FACTOR RESULTS AT 45 GHZ FOR SIX LOADING CONFIGURATIONS AVERGAED OVER NINE ANTENNA LOCATIONS AND A 4 GHZ BAND

| Loading | $G_{ref}$ (dB) | $K$ (dB) |
|---|---|---|
| Empty | -35.54 | -28.25 |
| 1 Absorber | -41.60 | -21.96 |
| 3 Absorbers | -45.30 | -19.58 |
| 6 Absorbers | -48.28 | -18.84 |
| 10 Absorber | -49.93 | -18.80 |
| 14 Absorbers | -51.03 | -18.25 |

Next, we studied the standard deviation in $G_{ref}$ between the nine antenna locations for different RC loading configurations given in Fig. 5 which illustrates the trend of decreased uniformity with increased loading. More loading creates stronger "hot spots" in the observed volume, thus causing larger deviations in the measured quantity with respect to the antenna location.

The unloaded chamber provides a nearly-uniform field distribution throughout the observed volume with a standard deviation of 0.02 dB between $G_{ref}$ measured at nine different locations. By adding loading inside the RC, the standard deviation in $G_{ref}$ increased from 0.06 dB, calculated for one RF absorber present inside the RC, to 0.27 dB for 14 RF absorbers. Based on the uncertainty analyses given in the next section, this illustrates the need to apply antenna location stirring for wireless tests in order to keep the uncertainty below 0.2 dB (~5%).

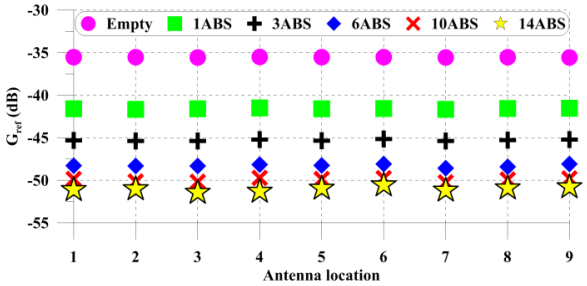


Fig. 4. $G_{ref}$ measured over 4 GHz band (43 GHz – 47 GHz) and averaged over nine TX antenna locations for six different loading configurations.



Senic, Damir; Remley, Catherine; Becker, Maria; Holloway, Christopher.
"Spatial Uniformity Study in a Loaded Reverberation Chamber at Millimeter-Wave Frequencies."
Paper presented at 2018 IEEE Symposium on Electromagnetic Compatibility, Signal Integrity and Power Integrity (EMC, SI & PI), Long Beach, CA, United States. July 30, 2018 - August 3, 2018.

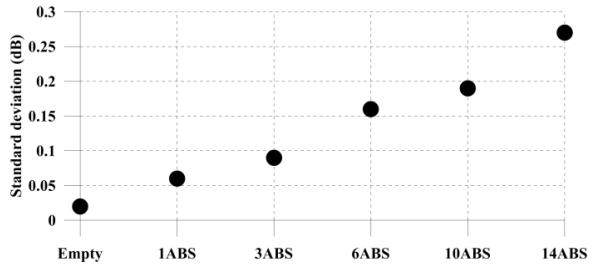


Fig. 5. Standard deviation in $G_{ref}$ between nine antenna locations for six different loading configurations.

Next, we compare these results to a chamber operating at microwave frequencies [15]. $G_{ref}$ measurements were performed at ten different locations inside a 1.9 m ($l$) × 1.4 m ($w$) × 2 m ($h$) reverberation chamber over the Personal Communications Service (PCS) band (1850 MHz – 1990 MHz) with a half-wavelength dipole receive antenna. As a transmit antenna, we used a broadband (650 MHz – 3.5 GHz) discone monopole. In order to study the effect of chamber loading on spatial uniformity, measurements were repeated for three different chamber loading configurations: unloaded, partially loaded, and heavily loaded. For the heavily-loaded case, we used five large absorbers with dimensions of 15 cm ($l$) × 6 cm ($w$) × 60 cm ($h$), and four small absorbers with dimensions of 15 cm ($l$) × 6 cm ($w$) × 15 cm ($h$). The partially-loaded chamber had three large absorbers.

A comparison of these chambers is presented in Table IV in terms of the chamber power transfer function ($G_{ref}$), standard deviation of $G_{ref}$ between different antenna locations, and CBW (1/$e$ threshold). For all loading configurations, we see a higher standard deviation in $G_{ref}$ for the reverberation chamber operating at microwave frequencies compared to the millimeter-wave chamber. The reason for this is the extremely high mode density of the millimeter-wave chamber where, even though the chamber is heavily loaded, it still preserves its rich modal characteristic where modes overlap at a much higher rate causing more modes to participate in reinforcing the randomness of the EM field, which results in better spatial uniformity. On the other hand, spatial uniformity of the undermoded chamber operating at microwave frequencies is greatly compromised by adding RF absorbers.

Table IV also shows that the CBW values are much lower for the chamber operating at microwave frequencies due to larger distance between adjacent modes. This indicates that more RF loading is required in order to achieve sufficient CBW at microwave frequencies. For example, both empty chambers exhibit similar CBWs: 2.86 MHz for the microwave chamber and 4 MHz for the millimeter-wave chamber. However, once when we start adding RF absorber to the chamber, the differences become significant: the heavily-loaded microwave chamber configuration has a CBW of 12.26 MHz, which is exceeded with only one absorber in the case of the millimeter-wave RC. Hence, the millimeter-wave chamber provides much broader CBWs (up to 100 MHz with a 1/$e$ threshold in our study) as compared to the traditional microwave RC. This indicates that the millimeter-wave chamber is a good candidate for the OTA tests of future 5G modulated signals whose bandwidth will be much broader than today's signals, which are only a few megahertz.

Note that these two chambers have very different $Q$ factors when not loaded. Therefore, more comprehensive study would involve a comparison based on the absorbers' absorption cross sections. Here, our main point is to show a potential RC application for millimeter-wave wireless communications tests.

TABLE IV. $G_{REF}$, STANDARD DEVIATION IN $G_{REF}$, AND COHERENCE BANDWIDTH FOR REVERBERATION CHAMBERS OPERATING AT MICROWAVE AND MILLIMETER-WAVE FREQUENCIES

| Frequency range | Loading | $G_{ref}$ (dB) | σ (dB) | CBW (MHz) |
|---|---|---|---|---|
| Microwave | Empty | -17.60 | 0.25 | 2.86 |
| | Partially loaded | -21.12 | 0.39 | 7.76 |
| | Heavily loaded | -24.53 | 0.97 | 12.26 |
| Millimeter-wave | Empty | -35.54 | 0.02 | 4 |
| | 1 Absorber | -41.60 | 0.06 | 15 |
| | 3 Absorbers | -45.30 | 0.09 | 35 |

## IV. UNCERTAINTY IN THE ESTIMATE OF $G_{REF}$

In tests involving loaded reverberation chambers, we generally distinguish between two key sources of uncertainty: (1) the uncertainty due to the finite number of mode-stirred measurement samples, within a given mode-stirring sequence, and (2) the uncertainty due to the lack of spatial uniformity of the averaged fields in the chamber, which originates between different antenna locations in the chamber.

In wireless tests, where chambers are often loaded, it is common that the uncertainty due to lack of spatial uniformity dominates, compared to the uncertainty arising from the finite number of mode-stirred samples in a mode-stirring sequence [17]. However, for low-loss (high-$Q$) unloaded RCs, this is not always the case [6], and the relative effects of these two contributions should be studied. Therefore, we need to find the uncertainties associated with the number of mode-stirred samples $N$ (2,500 in our setup) and the uniformity for $M$ (nine in our setup) measurement antenna locations.

In the previous section, we showed by calculating the standard deviation in $G_{ref}$ that loading deteriorates spatial uniformity. Hence, we expect that the uncertainty due to lack of spatial uniformity will dominate the overall uncertainty for a highly loaded chamber. To determine which RC-induced component of the uncertainty is dominant, a significance test may be performed [17].

The outcome of the significance test provides us with a metric for determining the correct expression for standard uncertainty in $G_{ref}$ measurements for a given chamber setup. The statistics for testing the significance of each uncertainty are based on an F distribution and given by [19]

$$\mathrm{F}\left(s_M^2, s_N^2\right) = \frac{s_M^2}{s_N^2}, \tag{4}$$

with $M - 1$ and $M(N - 1)$ degrees of freedom. The mean-squared deviation due to the mode-stirred samples is denoted by $s_N^2$, and the mean-squared deviation due to the lack of



Senic, Damir; Remley, Catherine; Becker, Maria; Holloway, Christopher.
"Spatial Uniformity Study in a Loaded Reverberation Chamber at Millimeter-Wave Frequencies."
Paper presented at 2018 IEEE Symposium on Electromagnetic Compatibility, Signal Integrity and Power Integrity (EMC, SI & PI), Long Beach, CA, United States. July 30, 2018 - August 3, 2018.

spatial uniformity is denoted by $s_M^2$. The expressions for calculating $s_N^2$ and $s_M^2$ can be found in [17].

The significance test can have two possible outcomes: (1) the uncertainty due to lack of spatial uniformity is not significant; *i.e.*,

$$\mathrm{F}\left(s_M^2, s_N^2\right) < \mathrm{F}_{\alpha, n_1, n_2}, \tag{5}$$

where α is the confidence level (*e.g.*, 95%), and $n_1 = M - 1$ and $n_2 = M(N-1)$ are degrees of freedom, or
(2) the uncertainty due to lack of spatial uniformity is significant; *i.e.*,

$$\mathrm{F}\left(s_M^2, s_N^2\right) > \mathrm{F}_{\alpha, n_1, n_2}. \tag{6}$$

In the first case, the uncertainty of the reference value is given as

$$u_{\mathrm{ref}} = \sqrt{\frac{\sum_{i=1}^{N}\sum_{j=1}^{M}\left[G_{\mathrm{ref}}\left(n_i, m_j\right) - \left\langle G_{\mathrm{ref}}\right\rangle_{N,M}\right]^2}{NM\left(NM-1\right)}}, \tag{7}$$

while in the second case, the uncertainty should be determined from

$$u_{\mathrm{ref}} = \sqrt{\frac{\sum_{j=1}^{M}\left[\left\langle G_{\mathrm{ref}}\left(m_j\right)\right\rangle_N - \left\langle G_{\mathrm{ref}}\right\rangle_{N,M}\right]^2}{M\left(M-1\right)}}. \tag{8}$$

The uncertainty results based on the significance test are presented in Table V, where the decibel representation of normalized uncertainty was calculated as

$$u_{\mathrm{ref}}^{\mathrm{dB}} = 10\log_{10}\left(\frac{G_{\mathrm{ref}} + u_{\mathrm{ref}}}{G_{\mathrm{ref}}}\right). \tag{9}$$

TABLE V. SIGNIFICANCE TEST RESULTS AND COMPARISON WITH F DISTRIBUTION CONFIDENCE LEVEL OF 95%

| **Loading** | **$F_{0.95,\,8,\,22491}$ = 1.94** | **$u_{\mathrm{ref}}$ (dB)** | **$u_{\mathrm{ref}}$ (%)** |
|---|---|---|---|
| Empty | 0.001 NOT SIGNIFICANT | 0.05 | 1.16 |
| 1 Absorber | 0.06 NOT SIGNIFICANT | 0.06 | 1.29 |
| 3 Absorbers | 1.49 NOT SIGNIFICANT | 0.13 | 2.93 |
| 6 Absorbers | 2.09 SIGNIFICANT | 0.19 | 4.45 |
| 10 Absorber | 2.88 SIGNIFICANT | 0.25 | 5.89 |
| 14 Absorbers | 3.57 SIGNIFICANT | 0.31 | 7.35 |

The significance test showed that the uncertainty due to lack of spatial uniformity is not significant for the empty millimeter-wave chamber or the chamber loaded with one or three RF absorbers. For these cases, we calculated the uncertainty in our estimate of $G_{\mathrm{ref}}$ from (7) as 1.16% for the empty RC, 1.29% for the RC loaded with one absorber, and 2.93% for the RC loaded with three absorbers. By adding more loading inside the RC, the uncertainty due to lack of spatial uniformity becomes dominant and we need to use (8) in order to calculate the uncertainty of the reference value. Calculated uncertainties were 4.45%, 5.89%, and 7.35% for six absorbers, ten absorbers, and fourteen absorbers, respectively. For the proposed F test, we used a 95% confidence level with $n_1 = 8$, and $n_2 = 2{,}2491$ degrees of freedom, which resulted in a value of 1.94. Other confidence levels with different F test values can be used as well. Please note that we did not study the impact of the absorber's geometry and position inside the RC on the $G_{\mathrm{ref}}$ uncertainty.

Please note that we report here only the uncertainty due to the finite number of mode-stirred measurement samples, within a given mode-stirring sequence, and the uncertainty due to the lack of spatial uniformity of the averaged fields in the chamber, which originates between different antenna locations in the chamber. The other sources of the uncertainty, such as cable movement, were not studied in this paper. The readers interested in more comprehensive uncertainty budget for similar test setup are referred to [5].

## V. CONCLUSION

In this paper, we presented an RC spatial uniformity study for six different loading configurations: an empty chamber and a chamber loaded with one, three, six, ten, and fourteen absorbers. In an ideal chamber, the fields are uniformly distributed throughout the observed volume when averaged over a stirring sequence. The empty chamber studied here provided a nearly-uniform field distribution similar to the ideal chamber. By adding RF loading inside the RC, the spatial uniformity deteriorated in such a way that the standard deviation in $G_{\mathrm{ref}}$ measurements increased from 0.06 dB for one absorber to 0.27 dB in the case of the chamber loaded with the maximum of fourteen absorbers. The former caused an increase of uncertainty in the estimate of $G_{\mathrm{ref}}$ from 1.16% to 7.31%. Hence, in order to create practical measurements involving heavier loading configurations, we generally need to apply antenna location stirring, otherwise measurements will be strongly location dependent.

Next, we made a comparison of spatial uniformity measurements between reverberation chambers operating at microwave and millimeter-wave frequencies. The results showed a significantly higher standard deviation in $G_{\mathrm{ref}}$ measured at different antenna locations for all loading configurations. Also, the chamber operating at millimeter-wave frequencies had a much broader CBW compared to that of the microwave chamber.

RF absorbers load the chamber and lower the number of excited modes. In the case of heavily-loaded chambers, modes can have different distributions which can be analytically studied. In this paper, we did not perform such a study which has much interest for the future. In future work, we will use the findings from chamber characterization presented here, in particular the CBW and uncertainty analyses, to perform true OTA measurements of modulated signals at millimeter-wave frequencies.



Senic, Damir; Remley, Catherine; Becker, Maria; Holloway, Christopher.
"Spatial Uniformity Study in a Loaded Reverberation Chamber at Millimeter-Wave Frequencies."
Paper presented at 2018 IEEE Symposium on Electromagnetic Compatibility, Signal Integrity and Power Integrity (EMC, SI & PI), Long Beach, CA, United States. July 30, 2018 - August 3, 2018.

## REFERENCES


[1] D. A. Hill, *Electromagnetic Fields in Cavities*, Piscataway: Wiley IEEE Press, 2009.

[2] C. L. Holloway, D. A. Hill, J. M. Ladbury, and T. M. Lammers, "Assessing loaded reverberation chambers: calculating threshold metrics," *IEEE International Symposium on Electromagnetic Compatibility* 2003, pp. 834–837.

[3] P.-S. Kildal, X. Chen, C. Orlenius, M. Franzen, and C. S. L. Patane, "Characterization of reverberation chambers for OTA measurements of wireles devices: Physical formulation of channel matrix and new uncertainty formula," *IEEE Trans. Antennas and Propag.*, vol. 60, no. 8, pp. 3875–3891, Aug. 2012.

[4] K. A. Remley, J. Dortmans, C. Weldon, R. D. Horansky, T. B. Meurs, C.-M. Wang, D. F. Williams, C. L. Holloway, and P. F. Wilson, "Configuring and verifying reverberation chambers for testing cellular wirelss devices," *IEEE Trans. Electromagn. Compat.*, vol. 58, no. 3, pp. 661–672, June 2016.

[5] D. Senic, D. F. Williams, K. A. Remley, C.-M. Wang, C. L. Holloway, Z. Yang, and K. F. Warnick, "Improved antenna efficiency measurement uncertainty in a reverberation chamber at millimeter-wave frequencies," *IEEE Trans. Antennas Propag*., vol. 65, no. 8, pp. 4209–4219, Aug. 2017.

[6] D. Senic, K. A. Remley, C.-M. Wang, D. F. Williams, C. L. Holloway, D. C. Ribeiro, and A. T. Kirk, "Estimating and reducing uncertainty in reverberation-chamber characterization at millimeter-wave frequencies," *IEEE Trans. Antennas and Propag.*, vol. 64, no. 7, pp. 3130–3140, Jul. 2016.

[7] K. Harima and Y. Yamanaka, "Evaluation of e-field uniformity for radiated immunity testing in a reverberation chamber," *IEEE International Symposium on Electromagnetic Compatibility* 2001, pp. 768–770.

[8] Y. J. Wang, W. J. Koh, Y. K. Tai, C. K. Lee, and K. Y. See, "Evaluating field uniformity of a mini-reverberation chamber with two mechanical stirrers," *IEEE International Symposium on Electromagnetic Compatibility* 2002, pp. 795–798.

[9] B. Zhang, W. Li, X. Li, Z. Yuan, J. He, and R. Zeng, "Field uniformity investigation of reverberation chamber at calibration stage," *IEEE International Symposium on Electromagnetic Compatibility (EMC Europe)* 2009, pp. 45–48.

[10] V. M. Primiani and F. Moglie, "Numerical determination of reverberation chamber field uniformity by a 3-D simulation," *IEEE International Symposium on Electromagnetic Compatibility (EMC Europe)* 2011, pp. 829–832.

[11] T. Hui, F. Chonghua, H. Mingliang, and T. Li, "Numerical simulation of field uniformity of reverberation chamber," *International Symposium on Antennas, Propagation and EM Theory (ISAPE)* 2016, pp. 481–484.

[12] CTIA Certification, "Test Plan for Wireless Large-Form-Factor Device Over-the-Air Performance" Oct. 2016.

[13] A. Goldsmith, *Wireless Communications*. Cambridge, U.K.: Cambridge Univ. Press, 2005.

[14] J. N. H. Dortmans, K. A. Remley, D. Senic, C.-M. Wang, C. L. Holloway, "Use of absorption cross section to predict coherence bandwidth and other characteristics of a reverberation chamber setup for wireless-system tests," *IEEE Trans. Electromagn. Compat.*, vol. 58, no. 5, pp. 1653–1661, Oct. 2016.

[15] D. Senic, D. Cavaliere, M. V. North, M. G. Becker, K. A. Remley, C.-M. Wang, and C. L. Holloway, "Isotropy study for Over-the-Air measurements in a loaded reverberation chamber," *IEEE International Symposium on Electromagnetic Compatibility and Signal/Power Integrity (EMCSI)* 2017, pp. 124–129.

[16] "IEC 61000-4-21: EMC, Part 4: Testing and Measurement Techniques; Section 21: Reverberation Chamber Test Methods," *Int. Electrotech. Comm*., Geneva, 2011.

[17] K. A. Remley, C.-M. Wang, D. F. Williams, J. Aan Den Toorn, and C. L. Holloway, "A significance test for reverberation-chamber measurement uncertainty in total radiated power of wireless devices", *IEEE Trans. Electromagn. Compat.*, vol. 58, no. 1, pp. 207–219, February 2016.

[18] X. Chen, P.-S. Kildal, C. Orlenius, and J. Carlsson, "Channel sounding of loaded reverberation chamber for over-the-air testing of wireless devices: Coherence bandwidth versus average mode bandwidth and delay spread," *IEEE Antennas Wireless Propag. Lett.*, vol. 8, pp. 678-681, Jun. 2009.

[19] Joint Committee for Guides in Metrology, "Evaluation of measurement data—Guide to the expression of uncertainty in measurement," International Bureau of Weights and Measures (BIPM): Sèvres, France, September 2008.




Senic, Damir; Remley, Catherine; Becker, Maria; Holloway, Christopher.
"Spatial Uniformity Study in a Loaded Reverberation Chamber at Millimeter-Wave Frequencies."
Paper presented at 2018 IEEE Symposium on Electromagnetic Compatibility, Signal Integrity and Power Integrity (EMC, SI & PI), Long Beach, CA, United States. July 30, 2018 - August 3, 2018.

# The New Large Antenna Positioning System for Over-The-Air Testing at the National Institute of Standards and Technology

Jeff R. Guerrieri, David Novotny, Josh Gordon, Alexandra Curtin, Michael Allman
National Institute of Standards and Technology, 325 Broadway, Boulder, CO 80305 USA, jguerrieri@nist.gov
Kim Hassett, Quong Ton, Scott Caslow
NSI-MI Technologies, 19730 Magellan Drive, Torrance, CA 90502

***Abstract* — This paper introduces the new Large Antenna Positioning System (LAPS) at the National Institute of Standards and Technology (NIST). For the last eight years NIST has been pioneering the use of robotics for antenna measurements. Starting with the development and integration of the Configurable Robotic Millimeter-Wave Antenna (CROMMA) facility. CROMMA was designed to be reconfigurable to different near-field antenna measurement geometries and perform antenna measurements from 100 to 500 GHz. Probe position repeatability of 25 µm was achieved using coordinate metrology feedback. However, the single-robotic-armed CROMMA was restricted to small antennas. To overcome this limitation, NIST developed the concept of a dual-robot system with one fixed and the other mounted on a large linear rail slide. Using characterization of the robotic arm joints and segments, the LAPS will have open loop probe position accuracies of 200 µm to facilitate antenna measurements up to 30 GHz.**

***Index Terms* — large antenna positioning system, robotic arm, antenna measurements, kinematics, 5G communications.**

## I. Introduction

The National Institute of Standards and Technology (NIST) pioneered the use of robotics for antenna measurements with its **C**onfigurable **RO**botic **M**illi**M**eter-wave **A**ntenna (CROMMA) facility, shown in Fig 1. [1]. The reconfigurability of CROMMA allows for extrapolation, planar, spherical, cylindrical, and mixed-geometry scanning. CROMMA consists of a robotic arm, hexapod, and rotary positioner, when operated closed loop with coordinate metrology feedback, provides probe position repeatability of 25 µm, which meets the λ/50 requirement for antenna measurements up to 200 GHz [2]. CROMMA has been validated through numerous tests at 118 and 183 GHz, for both spherical near-field and extrapolation gain measurements [3]. While CROMMA has been proven to be a valuable tool for high frequency antenna measurements, it is limited to use on electrically small antennas.

The multiple-input, multiple-output (MIMO) and multi-beam base station antennas of new 5G communications systems require testing of adaptive antennae at arbitrary angles, testing dynamic paths, looking at Doppler effects, and testing of devices with integrated antennas, where an RF test signal cannot be injected into the system. Most of these tests are performed on systems, such as base stations, that are too large for CROMMA. NIST developed the Large Antenna Positioning System (LAPS) to address these future testing requirements. The LAPS is a dual-robot system with one robot integrated with a linear slide, and is shown conceptually in Fig. 2.

**Fig. 1.** CROMMA facility at NIST.

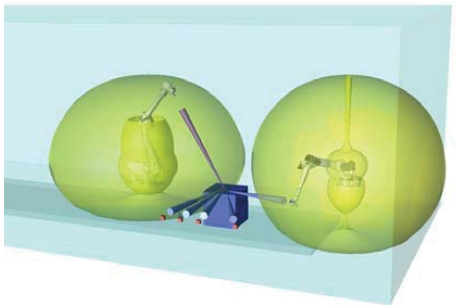

**Fig. 2.** LAPS conceptual design.



Guerrieri, Jeffrey; Novotny, David; Gordon, Joshua; Curtin, Alexandra; Allman, Michael; Hassett, Kim; Ton, Quang.
"The New Large Antenna Positioning System for Over-The-Air Testing at the National Institute of Standards and Technology."
Paper presented at 12th European Conference on Antennas and Propagation (EuCAP 2018), London, United Kingdom. April 9, 2018 - April 13, 2018.

## II. Antenna Measurement Facility

In order to accommodate space for the LAPS, NIST needed to decommission the existing multi-purpose antenna measurement facility. As a result, the LAPS also needs to replace the existing capabilities of planar, spherical and cylindrical near-field measurements and extrapolation gain needed for on-axis gain calibration services offered by NIST as a National Measurement Institute. NIST established the Antenna Measurement Facility (AMF), shown in Fig. 3 which is a Fully Shielded Anechoic Chamber (FASC) that will house the LAPS. The FASC dimensions are 17 m (L) X 7.6 m (W) X 7 m (H) and is lined with 0.5 m pyramidal absorber.

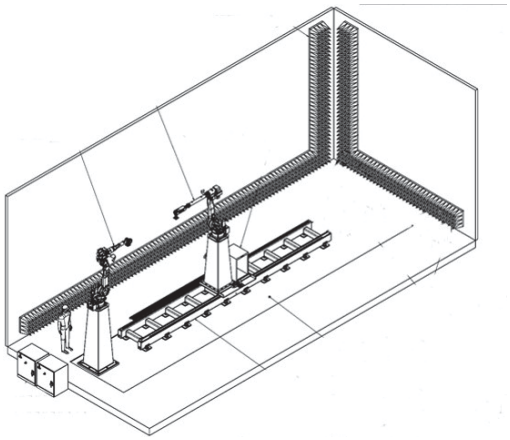

**Fig. 3.** Design drawing of the LAPS in the new AMF at NIST.

## III. LAPS Design

The LAPS was designed around two commercially available robots: one stationary robotic (SR) capable of a 2.5 m reach, and one moving robot (MR) with a 3.5 m reach that is mounted on a 7-m precision linear rail system. It is designed to have a large scan volume suitable for testing across common communications bands (500 MHz - 30 GHz) with specified absolute RMS accuracies of least 0.250 mm. This will allow for standard near–field testing, gain extrapolation, and physical separation needed to ensure reasonable field uniformity when illuminating small devices with moderate gain antennas. Multiple robots also allow for multiple bearings to a device, simultaneous emissions and immunity analysis, or interference testing.

The two robot controllers are linked together and share the same kinematic space. This allows the robots to position antennas, probes, and devices under test (DUT) either absolutely in space or relative to each other.

The two major tasks for characterizing a serial robotic system are extrinsic and intrinsic calibrations [4]. Extrinsic calibrations, shown in Fig. 4, typically remove most of the systematic measurement uncertainties, measure the robot relative to external references or where the robot frame is physically located, and define the location and orientations of base axes and antenna location or tool control points (TCP)s. This can reduce uncertainties to the millimeter level or less. However, effects from inaccuracies such as encoder/servo non-uniformity, axis warping, and motor eccentricities present practical limitations. These limitations can be addressed by characterization of each segment and axis of the robot and applying to the robot's kinematic model [5]. This approach will allow for open-loop antenna measurement without laser tracker feedback, which will provide fast dynamic movements and the ability of the system to rapidly respond to stimuli.

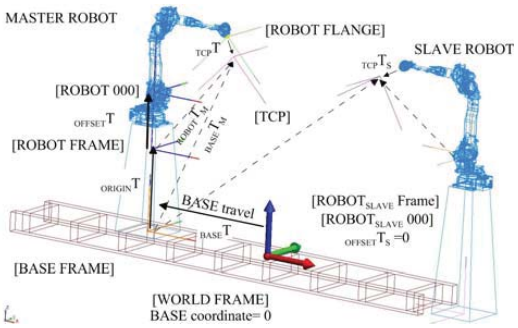


**Fig. 4.** Extrinsic frames and the 6D solid-line transforms between them, determined during calibration of a robot's kinematic model.

The LAPS is integrated with a Functional Safety Unit (FSU) that is aware of the unified coordinate space of the entire LAPS system. It is designed to prevent the collision of one robot with the other, itself, any attached antennas (or tooling), and collisions with the surrounding environment. The FSU also has redundant systems to protect operators. The robots can have large kinetic energy and control of that energy is integral to safe operation. The controllers are equipped with laser safety radars that stop autonomous motion when the working volume of the LAPS is encroached upon. When personnel are in the working envelope, during manual operation, alignment or mounting, enabling devices to allow robot movement must be positively activated prior to servo activation.

## IV. LAPS Initial Validation

Table 1 lists the basic physical design specifications for the LAPS. A selection of the initial validation tests results are presented in this section.

Guerrieri, Jeffrey; Novotny, David; Gordon, Joshua; Curtin, Alexandra; Allman, Michael; Hassett, Kim; Ton, Quang.
"The New Large Antenna Positioning System for Over-The-Air Testing at the National Institute of Standards and Technology."
Paper presented at 12th European Conference on Antennas and Propagation (EuCAP 2018), London, United Kingdom. April 9, 2018 - April 13, 2018.

**Table 1**. Basic physical design specifications of the LAPS

| **Moving Robot (MR) and Rail** | |
|---|---|
| Robot horizontal reach | 3.5 m |
| Robot vertical reach | 5 m |
| Robot path repeatability | 0.15 mm |
| Robot payload | 20 kg |
| Minimum planar scan plane size | 2.5 m x 3 m |
| Minimum spherical radius (with a 356 mm probe) | 1 m |
| Rail travel | 7 m |
| TCP wobble at scan plane center (deviation from best fit line) | RMS: 0.25 mm |
| TCP wobble at scan plane center (deviation from best fit line) | MAX: 0.5 mm |
| **Stationary Robot (SR)** | |
| Robot horizontal reach | 2.5 m |
| Robot vertical reach | 4 m |
| Robot path repeatability | 0.07 mm |
| Robot payload | 35 kg |
| Minimum planar scan plane size | 2 m x 2.5 m |
| Minimum spherical radius (with a 356 mm probe) | 1 m |

The TCP wobble specifications in Table 1, are a major component of positional uncertainty and is difficult to correct. It is affected by MR posture and loading, rail flatness, cart motion, the MR riser stiffness, and rail deflection under varying load conditions. The influence of the rail variations are magnified by the distance from the rail to the MR TCP.

Laser tracker targets were mounted to the MR pedestal and near the TCP of the MR in an extended pose, shown in Fig. 5. They were tracked as the MR was moved through a 2-m span of the rail at a constant rate of 23 mm/sec. The pedestal-mounted target deviation from the best fit line was 14 ± 7 µm, with a 61 µm maximum, and the TCP mounted target was 32 ± 20 µm deviation with a 182 µm maximum, as shown in Fig. 6. This result shows the basic mechanical capabilities of the system are adequate for λ/50 (200 µm) operation at 30 GHz.

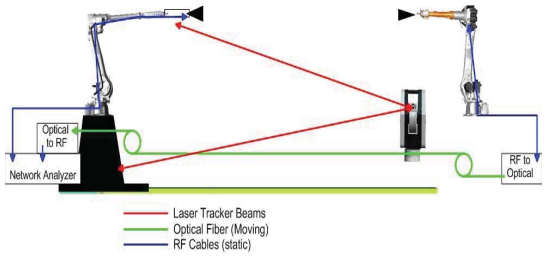


**Fig. 5.** Laser tracker and spherically mounted retroreflector (SMR) setup and RF measurement setup for initial validation tests.

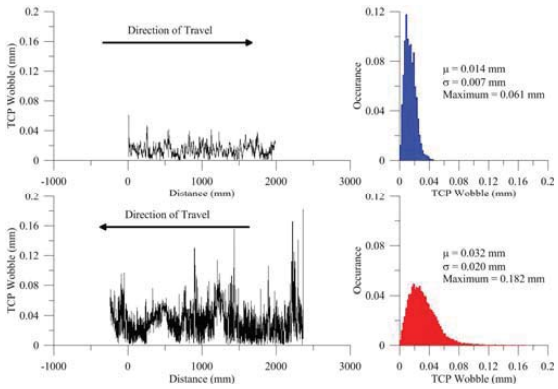


**Fig. 6.** Base wobble and distribution for the target on the MR base (top) and the TCP wobble and distribution for the target on the robot arm (bottom).

The system will be used for testing during motion, which requires coordination between the timing of the RF system and the motion of the LAPS. Standard gain horn antennas were mounted to each robot and aligned parallel to the axis of movement along the linear rails using the laser tracker. A vector network analyzer (VNA) based measurement system was setup to measure the insertion loss between the antennas at 9 GHz. By measuring more than 4 points per wavelength, $RF_i$, the RF separation is determined by taking the phase of the insertion measurement, unwrapping the phase vs. distance and then converting phase to distance [6]:

$$d_{phase} = \text{atan}\left(\frac{\text{Re}(RF_i)}{\text{Im}(RF_i)}\right)\frac{\lambda}{2\pi}360$$

The laser tracker was setup to measure the target mounted near the TCP. The MR was moved in 2.5 mm steps at a speed of 30 mm/sec along the rail, stopped, RF insertion data and laser tracker data were taken over a 1 sec time window, and then the motion restarted. The expectation was that the rapid-stop motion in different directions would highlight the vibrational modes of the system. The setup of the measurement is shown in Fig. 5.

The results of the RF insertion measurement, shown in the top half of Fig. 7, and the corresponding laser tracker measurements, shown in the bottom half, display good correlation as the separation gets larger. At close distances, the phase variations from linear distance increase noticeably at greater separations than the amplitude. The correlation of laser tracker and RF inferred distance show that the robot and cabling are not experiencing excessive movement during the position and velocity changes. These initial test results met the required specifications, and the LAPS was delivered and installed at NIST, as shown in Fig. 8.

Guerrieri, Jeffrey; Novotny, David; Gordon, Joshua; Curtin, Alexandra; Allman, Michael; Hassett, Kim; Ton, Quang.
"The New Large Antenna Positioning System for Over-The-Air Testing at the National Institute of Standards and Technology."
Paper presented at 12th European Conference on Antennas and Propagation (EuCAP 2018), London, United Kingdom. April 9, 2018 - April 13, 2018.

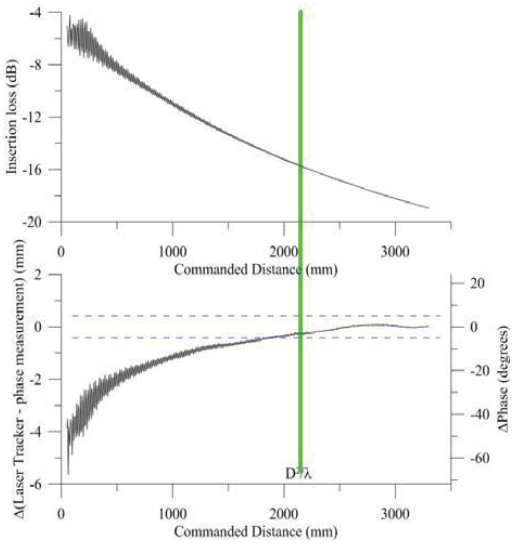


**Fig. 7.** RF insertion measurement (top), and laser tracker measurement (bottom) comparison results.

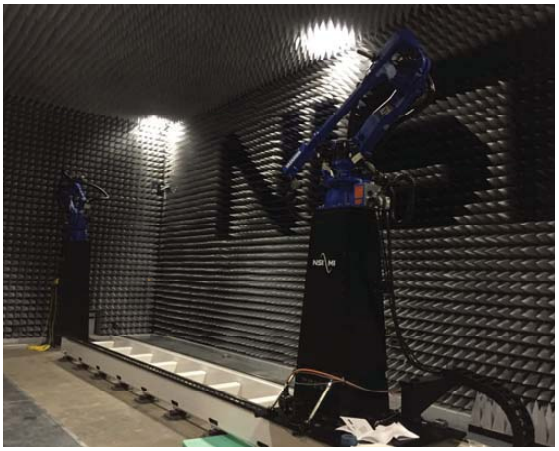

**Fig. 8**. The LAPS installed at NIST.

## V. LAPS Capabilities

The LAPS will perform the traditional near-field scanning geometries and hybrid geometries, which involve moving both robots and interrogating communications systems from multiple positions. Figures 9 and 10 demonstrate the spherical and planar scanning geometries of the MR, while Figures 11 and 12 show same geometries for the SR.

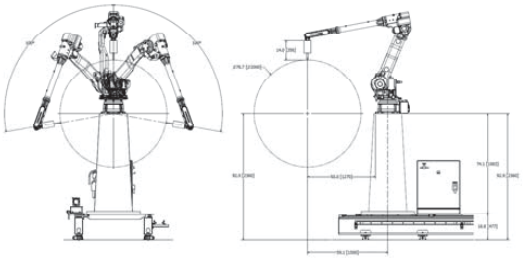

**Fig. 9**. MR typical spherical scanning geometry.

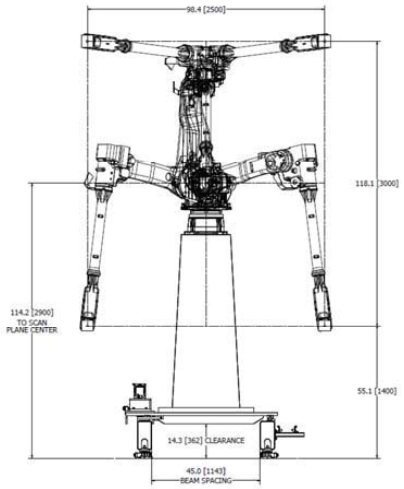


**Fig. 10.** MR typical planar scanning geometry.

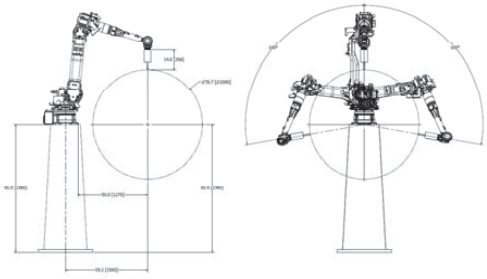

**Fig. 11.** SR typical spherical scanning geometry.

Guerrieri, Jeffrey; Novotny, David; Gordon, Joshua; Curtin, Alexandra; Allman, Michael; Hassett, Kim; Ton, Quang.
"The New Large Antenna Positioning System for Over-The-Air Testing at the National Institute of Standards and Technology."
Paper presented at 12th European Conference on Antennas and Propagation (EuCAP 2018), London, United Kingdom. April 9, 2018 - April 13, 2018.

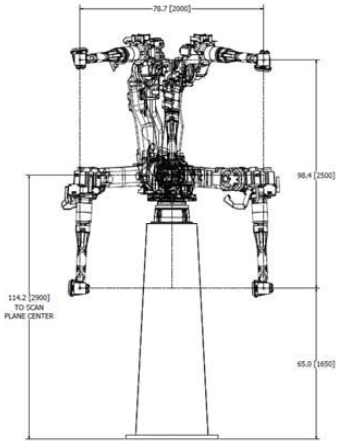


**Fig. 12.** SR typical planar scanning geometry.

Since the MR and linear rail are kinematically linked, coordinated motion between the two can be controlled to perform large planar near-field measurements, as illustrated in Fig. 13.

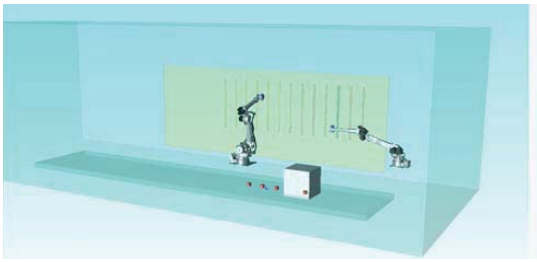

**Fig. 13.** The LAPS large planar scanning configuration.

The real advantage of the LAPS will be the ability to perform active over-the-air (OTA) interrogation of future communication systems. Fig. 14 illustrates a scenario for testing a beam-forming network by sampling the high signal-to-noise ratio (SNR) region while simultaneously and coherently measuring off-axis performance. By sampling the emissions coherently, in the near-field, pattern analysis can be made without the injection of an RF test signal into the system. This is a more realistic test, where, the system itself is used as the stimulus and response.

Figure 15 depicts two base station emulators interrogating a single DUT, performing a MIMO test. Utilizing the reach of the robots and the rail, a suitable uniform field could be generated to illuminate the DUT under conditions resembling the far field. This might also be used as a platform to develop OTA MIMO tests with rapidly varying spatial and Doppler conditions.

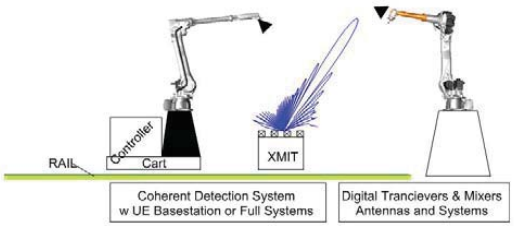


**Fig. 14.** A depiction of simultaneous measurements of a beam-forming system with the LAPS, SR (right) is measuring the main beam while the MR is probing off angle performance.

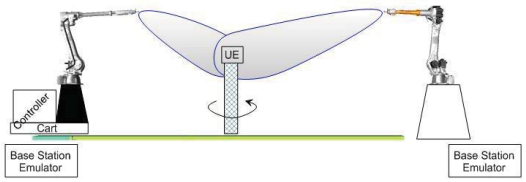


**Fig. 15.** A depiction of multiple interrogation of a beam-forming system with the LAPS, SR (right) and MR are illuminating the UE in a MIMO fashion from multiple orientations.

## VI. Conclusion

While the LAPS can perform standard antenna pattern and gain testing, the ultimate goal is to perform dynamic OTA system tests. Initial validation of the LAPS at the factory show that basic mechanical operation of the system is within the specified design tolerances for static and dynamic testing to at least 30 GHz. The LAPS has been installed at NIST and is going through final validation testing.

## References

[1] J.R. Guerrieri, J.A. Gordon, D.R. Novotny, M.H. Francis, R.C. Wittmann and M Butler, "Configurable Robotic Millimeter-Wave Antenna Facility", Proc. European Conf. on Antennas and Propagation, Lisbon, Portugal, 2015.

[2] J. A. Gordon, *et al*., "Millimeter-Wave Near-Field Measurements Using Coordinated Robotics," in IEEE Transactions on Antennas and Propagation, vol. 63, no. 12, pp. 5351-5362, Dec. 2015.doi: 10.1109/TAP.2015.2496110.

[3] J.R. Guerrieri, D.R. Novotny, J.A. Gordon, M.H. Francis and A.E. Curtin, "Validation of Robotics for Antenna Measurements", Proc. European Conf. on Antennas and Propagation, Paris, France, 2017.

[4] DX100 Instructions: FOR NORTH AMERICAN (ANSI/RIA) STANDARD, Part No. 155494-1CD, Rev. 2, Yaskawa Electric Corporation, pp 8-23,29.

[5] M.S. Allman, *et al*., "Serial Robotic Arm Joint Characterization Measurements for Antenna Metrology," in Proc. of the Antenna Measurement Techniques Assoc., Oct. 2017.

[6] J. Coder, D.R. Novotny, M Francis, J. Guerrieri, "On the Use of Phase Data When Conducting an Extrapolation Measurement," Proc. of the Antenna Measurement Techniques Assoc., Oct. 2013.

Guerrieri, Jeffrey; Novotny, David; Gordon, Joshua; Curtin, Alexandra; Allman, Michael; Hassett, Kim; Ton, Quang.
"The New Large Antenna Positioning System for Over-The-Air Testing at the National Institute of Standards and Technology."
Paper presented at 12th European Conference on Antennas and Propagation (EuCAP 2018), London, United Kingdom. April 9, 2018 - April 13, 2018.

# Problems with Stirred Immunity Measurements in a Reverberation Chamber

## Corrections to DO-160G Section 20.6

John Ladbury
U.S. Department of Commerce
National Institute of Standards and Technology
Communications Technology Laboratory, RF Technology Division
Boulder, Colorado 80305
Email: john.ladbury@nist.gov

***Abstract*—When DO-160G, Environmental Conditions and Test Procedures for Airborne Equipment [1], Section 20.6, was modified in 2010 to simplify electromagnetic susceptibility measurements in a reverberation chamber and switch from a stepped paddle (mode-stepped or mode-tuned) to a continuously moving paddle (mode-stirred), an error was introduced which overestimates the test level by approximately 1.4 to 3 dB, and possibly more (the error should increase with exposure frequency). We offer a possible explanation for the cause of the error, and suggest several possible ways to give a more accurate estimate of the exposure field.**

***Keywords— Airborne; field uniformity; immunity testing; mode-stirring; mode-tuning; reverberation chamber; susceptibility testing***

### I. Introduction

When RTCA (Radio Technical Commission for Aeronautics) published version G of DO-160, Environmental Conditions and Test Procedures for Airborne Equipment, in 2010 [1], there were a few apparently minor changes to section 20.6. That section describes a reverberation chamber test method that can be used for electromagnetic susceptibility testing as an alternative to anechoic chamber methods. The principal change between DO-160F [2] (Rev. F) and DO-160G (Rev. G) relates to how metal paddles are moved during the measurement. The rotating paddles change the electromagnetic boundary conditions and essentially randomize the fields in the chamber. In Rev. F, the paddles were stepped to a small number (on the order of 12) of fixed positions. A stepped measurement is also referred to as "mode tuned". The same number of paddle steps was required in both the chamber calibration and subsequent measurements, because the expected peak field generally increases with the number of paddle steps. In Rev. G, the paddles are moved continuously. This is also referred to as stirred or "mode stirred". The change was made because stirred measurements are perceived to be faster, simpler, more thorough, more accurate, and provide higher test levels. In this paper, we will not address the validity of these perceptions, or the relative merits of the two methods. Instead, we focus on the validity of the procedures and equations as given in Rev. G.



To make the change from stepping to stirring, a new method for estimating the test field was required. In Rev. F, the field is determined based on the *average* power received by an antenna in the chamber and a correction factor (which is a function of the number of paddle steps used in the calibration and measurement). However, there is a requirement that this method gives results consistent with measurements based on field as determined by a field probe.

In Rev. G, the field is determined based solely on measurement of the *peak* power received by an antenna in the chamber. Field uniformity evaluations are still performed with probes, but there is no requirement that a comparison be made between results using a probe and results using received power. However, in a companion user guide [3], there is a recommendation that the chamber performance be verified using data taken during the uniformity evaluation. The new stirred approach makes a significant assumption that the peak total field is directly related to the square root of the peak received power. This assumption is incorrect (a reasonably good assumption is that the peak linear or Cartesian field is directly related to the square root of the peak received power [4], but not the peak total field). This can result in undertesting by 1.4 to 3 dB, and possibly more. It is possible that such errors are considered to be within typical uncertainty bounds of immunity testing, but should be corrected to avoid a consistent bias resulting in undertesting of all systems.

In this paper, we discuss these results in greater detail. In Section II we give a summary of the electromagnetic and statistical theory of reverberation chambers and explain the error of the assumption above. Section III discusses possible remedies for these problems, followed by our conclusions.

### II. Background

The fields in a reverberation chamber are best described with respect to a three-axis field probe with three electrically small orthogonal dipoles. The individual dipoles measure a linear or Cartesian component of the electric field at a given point inside the chamber. These components are generally referred to as the x-, y-, and z-components of the electric field for an arbitrary Cartesian coordinate system inside the chamber. The *total* electric field is computed by taking the



Ladbury, John.
"Problems with Stirred Immunity Measurements in a Reverberation Chamber: Corrections to DO- 160G Section 20.6."
Paper presented at 2018 IEEE International Symposium on Electromagnetic Compatibility & 2018 IEEE Asia-Pacific Symposium on Electromagnetic Compatibility (EMC/APEMC) : 2018 Joint IEEE EMC & APEMC, Suntec City, Singapore. May 14, 2018 - May 17, 2018.

square root of the sum of the squared magnitudes (RSS) of the three individual linear components.

Assuming a fixed static paddle configuration, the fields should also be static (neglecting vibrations or thermal changes in the chamber or paddles). If the paddle position is changed by a very small amount (fractions of a degree to a few degrees, depending on frequency), the measured field will be essentially unchanged and can be estimated reasonably well from measurements at the previous position. If the paddle is moved sufficiently, the field can change significantly (tens of dB) and the new sample is effectively uncorrelated with the previous sample. Procedures for estimating the minimum rotational distance $\Delta\varphi_{min}$ required to generate uncorrelated samples are still being developed due to the complexity of the problem [5], but rough estimates are available. If the samples are approximately uncorrelated, it is assumed that they can be treated as if they are independent. Any step size greater than or equal to $\Delta\varphi_{min}$ is assumed to yield independent samples. The number of possible independent samples $M_{ind}$ that can be generated by a single paddle is $M_{ind} = 360°/\Delta\varphi_{min}$.

The linear field components are assumed to be the sum of many plane-waves, rays, or modes, each with "randomized" amplitudes, phases, path lengths, etc. which implies that a central limit argument can be used to describe the fields, with the real and imaginary components of $E_x$, $E_y$, and $E_z$ each independent and normally distributed with 0 mean and identical variances $\sigma^2$. From this, the squared magnitude of any rectangular component, which we will refer to generically as $E_{Rect}$, can be described as the sum of the squares of two iid (independent and identically distributed) zero-mean Gaussian random variables, so therefore has a $\chi_2^2$ or chi-squared distribution with two degrees of freedom, also known as an exponential distribution. Similarly, the squared magnitude of the total electric field $E_T$ can be described as the sum of the squares of six iid zero-mean Gaussian random variables so therefore has a $\chi_6^2$ or chi-squared distribution with six degrees of freedom. We can take the square root of the results, giving the magnitude of a rectangular component or total field as having a $\chi_2$ or $\chi_6$ (chi distribution with two or six degrees of freedom), respectively. These results are assumed to be independent of position within the working volume of the chamber or the orientation of the Cartesian coordinate system used for describing $E_x$, $E_y$, and $E_z$. Measurements have been consistent with these assumptions [4].

Hill has proposed a plane-wave-spectrum model for describing the fields inside a reverberation chamber [6] that requires fewer assumptions. Two important results are related to the power $P_{Rec}$ received by a perfectly matched lossless antenna. First, $P_{Rec}$ should have a $\chi_2^2$ distribution (the same as the squared magnitude of a rectangular component of the electric field), and second, a relationship between average squared magnitude of the total electric field $|E_{Total}|^2$ and the average power is

$$\langle P_{Rec} \rangle = \frac{1}{2}\frac{\langle |E_{Total}|^2 \rangle}{\eta_0}\frac{\lambda^2}{4\pi} = \frac{\langle |E_{Total}|^2 \rangle \lambda^2}{8\pi\eta_0}, \qquad (1)$$

where $\lambda$ is the wavelenth of the excitation frequency in free space, $\eta_0$ is the wave impedance of free space, and <·> represents the expected value or ensemble average over all paddle positions. Equation (1) can be rearranged to give $\langle |E_{Total}|^2 \rangle$as a function of $\langle P_{Rec} \rangle$,

$$\langle |E_{Total}|^2 \rangle = \frac{\eta_0 8\pi \langle P_{Rec} \rangle}{\lambda^2} \approx \frac{377 \cdot 8\pi \langle P_{Rec} \rangle}{\lambda^2}, \qquad (2)$$

where the approximation $\eta_0 \approx 377$ is used. Equation (2) is useful because measurements of received power are generally easier, faster, and more accurate, than measurements of electric field. However, for the susceptibility tests in DO-160, we need the maximum total electric field, not the average squared magnitude of the field. It is tempting to take the square root of both sides of (2) to get field instead of squared field, and to replace the average measured received power with the maximum measured received power to estimate the maximum fields, and it appears that this was done to derive the equation in section 20.6.2.b.iii of Rev. G. Unfortunately, both steps are incorrect.

As shown in [4], order of operations is important, and the square root of the average of a quantity is not the same as the average of the square root. Specifically, $\sqrt{\langle |E_{Total}|^2 \rangle} \neq \langle |E_{Total}| \rangle$. This error is relatively small, and taking $\sqrt{\langle |E_{Total}|^2 \rangle}$ overestimates $\langle |E_{Total}| \rangle$ by about 0.36 dB. A more significant error is introduced by assuming that, if an equation gives a valid relationship for the expected values of two random variables, then the same relationship holds for the extreme values of those random variables. This may be a reasonably good approximation *if both sides have the same statistical distribution*. In this case, however, the square root of received power has a $\chi_2$ distribution, and the total field has a $\chi_6$ distribution. The equation in Rev. G essentially assumes that the expected maximum total field is simply $\sqrt{3}$ times the expected maximum of a rectangular component of the field. Unfortunately, the relationship is not that simple. The expected maximums increase with the number of independent samples for each parameter, but the expected maximum of the total field increases more slowly than the expected maximum of a rectangular component. This means that the equation given in Rev. G overestimates the total field in all cases where $M_{ind} > 1$, and this overestimate increases with $M_{ind}$. To estimate the bias, we can take the mean values from Table 7 of [4] and compare it to $\sqrt{3}$ times mean values from Table 4 of [4]. The mean values from those tables, along with the resulting bias, are summarized in Table I for a few select values of $M_{ind}$. For larger values of $M_{ind}$, the bias will continue to increase, but by only a few tenths of a dB per order-of-magnitude increase in $M_{ind}$.

TABLE I. MEASUREMENT BIAS

| $M_{ind}$ | Normalized Expected Max Rect. Field | Normalized Expected Max Total Field | Bias (dB) |
|---|---|---|---|
| 10 | 2.370 | 3.472 | 1.5 |
| 100 | 3.199 | 4.253 | 2.3 |
| 1,000 | 3.857 | 4.869 | 2.7 |
| 10,000 | 4.415 | 5.394 | 3.0 |



Ladbury, John.
"Problems with Stirred Immunity Measurements in a Reverberation Chamber: Corrections to DO- 160G Section 20.6."
Paper presented at 2018 IEEE International Symposium on Electromagnetic Compatibility & 2018 IEEE Asia-Pacific Symposium on Electromagnetic Compatibility (EMC/APEMC) : 2018 Joint IEEE EMC & APEMC, Suntec City, Singapore. May 14, 2018 - May 17, 2018.

A better approach is to give a relationship between received power and a squared rectangular component of the field. Assuming an isotropic environment, the squared total field is simply the sum of the three rectangular components, $\langle|E_{Total}|^2\rangle = 3\langle|E_{Rect}|^2\rangle$, so

$$\langle|E_{Rect}|^2\rangle = \frac{\eta_0 8\pi\langle P_{Rec}\rangle}{3\lambda^2} = \frac{120\pi\cdot 8\pi\langle P_{Rec}\rangle}{3\lambda^2}, \quad (3)$$

where we use $\eta_0$ = 120$\pi$. Here, both sides have the same expected value, and also have the same distribution, so we can now say

$$|E_{RectMax}|^2 \cong \frac{120\pi\cdot 8\pi P_{RecMax}}{3\lambda^2}, \quad (4)$$

where we use ≅ to indicate that this relationship is somewhat loose. Measurements of $P_{RecMax}$ do not tell us the maximum field at the antenna or anywhere else in the chamber. It is more precise to say that measurements of $P_{RecMax}$ allow us to estimate $|E_{RectMax}|^2$. A better interpretation is that the terms on either side of the ≅ in (4) have essentially the same statistical distribution. Taking the square root of both sides of (4) and manipulating the result gives

$$|E_{RectMax}| \cong \frac{8\pi}{\lambda}\sqrt{5P_{RecMax}}. \quad (5)$$

In deriving (4) and (5), we avoided the order-of-operations problem where $\sqrt{\langle|E_{Rect}|^2\rangle} \neq \langle|E_{Rect}|\rangle$ by first switching from average to maximum, and then computing the square root, since $\sqrt{|E_{RectMax}|^2} = |E_{RectMax}|$.

The approximation given in (5) is not the best estimate of maximum field, since measurements of maximum received power can have relatively large uncertainties. A better approach is to estimate the maximum field based on the average received power and the number of independent measurements based on the equations and tables given in [4].

Equation (5) should be used with caution at lower frequencies (less than about 1 GHz), since the statistical link between received power and field can get distorted if chamber losses are very low [4]. For example, with 10,000 independent samples, maximum received power should be approximately 10 dB greater than the average received power, but if the losses in the chamber are much less than 10 dB, then the statistical model for received power is trumped by conservation of power and the power distribution will be compressed. For most stepped measurements with small numbers of samples, this problem will not be significant. For large numbers of samples, however, this can lead to a significant underestimate of the field

It is possible to generate an equation similar to (5) for the total field, but this requires simultaneous measurements of the power received from three different antennas and summed together (possibly using a calibrated power combiner). If we refer to the power received by a single antenna generically as $P_{Rec}$ and the summed power as $P_{Total}$, we have $\langle P_{Total}\rangle = 3\langle P_{Rec}\rangle$, so this gives us

$$\langle|E_{Total}|^2\rangle = \frac{\eta_0 8\pi\langle P_{Total}\rangle}{3\lambda^2} = \frac{120\pi\cdot 8\pi\langle P_{Total}\rangle}{3\lambda^2}, \quad (6)$$

which is the same equation as (3), but with $P_{Total}$ and $E_{Total}$, instead of $P_{Rec}$ and $E_{Rect}$. Since $P_{Total}$ and $E_{Total}$ have the same distribution, we can also write

$$|E_{TotalMax}| \cong \frac{8\pi}{\lambda}\sqrt{5P_{TotalMax}}. \quad (7)$$

This approach should be verified experimentally, but this is beyond the scope of this paper.

Equations (5) and (7) should be useable for stirred measurements as well as stepped measurements, with the caveats mentioned above for both increased uncertainty due to estimating field based on maximum power rather than average, and also the compression issue at lower frequencies. However, this should also be verified experimentally before it is used in practice.

## III. Remedies

Given the error described here, there are severable possible ways to address it, each with different degrees of expense, difficulty, and accuracy. None of the remedies are likely to be popular, since they all require more power for performing the tests. The simplest approach is to just ignore the issue and accept the error as being within typical uncertainty bounds of an immunity test. However, regulators are unlikely to accept this option, because it gives a consistent bias to the tests. An equally simple remedy is to decrease the claimed test level by a fixed correction factor. Since the bias tends to increase with frequency, a correction factor consistent with a large number of independent samples, such as 2.7 to 3 dB is recommended. Another possibility is to modify the standard so that the test level is defined in terms of $E_{Rect}$ rather than $E_{Total}$ since $E_{Rect}$ is much more closely related to the square root of the received power than $E_{Total}$. This has the significant advantage of making DO-160 consistent with the reverberation chamber test standard IEC 61000-4-21 [7], but will increase power requirements for the test even beyond the 2.7 to 3 dB suggested above. Finally, the power from three antennas could be combined to give $P_{Total}$ as described above. This has the advantage of leaving the standard mostly untouched except for some notation and an explanation on how to combine the signals and calibrate whatever power combining option is used. Of all of these options, the most accurate and defensible are the last two, switching the type of electric field used in the measurement from $E_{Total}$ to $E_{Rect}$ or using a calibrated power combiner to determine $P_{Total}$. However, whatever method is chosen, it should be verified experimentally before being accepted in the standard.

## IV. Conclusion

We have shown that RTCA DO-160G, section 20.6 has an error resulting in a consistent overestimate of the test field. The test field is generally overestimated by 1.4 to 3 dB. We also pointed out that measurements based on maximum received power can have larger uncertainties than measurements based on average received power, and that there are potential problems below 1 GHz due to power



Ladbury, John.
"Problems with Stirred Immunity Measurements in a Reverberation Chamber: Corrections to DO- 160G Section 20.6."
Paper presented at 2018 IEEE International Symposium on Electromagnetic Compatibility & 2018 IEEE Asia-Pacific Symposium on Electromagnetic Compatibility (EMC/APEMC) : 2018 Joint IEEE EMC & APEMC, Suntec City, Singapore. May 14, 2018 - May 17, 2018.

compression. We presented several different methods for addressing the error, from ignoring it to changing the measurement to give better results.

## V. References


[1] Environmental Conditions and Test Procedures for Airborne Equipment, RTCA/DO-160G, RTCA Inc. December 8, 2010.

[2] Environmental Conditions and Test Procedures for Airborne Equipment, RTCA/DO-160G, RTCA Inc. December 6, 2007.

[3] User Guide Supplement to DO-160G, RTCA Inc. December 16, 2014.

[4] Ladbury J M, Koepke G H, Camell D G, Evaluation of the NASA Langley research center mode-stirred chamber facility: Technical Note 1508, National Institute of Standards and Technology, Gaithersburg, Maryland USA, 1999

[5] Pfennig S, "A General Method for Determining the Independent Stirrer Positions in Reverberation Chambers: Adjusting the Correlation Threshold." IEEE Trans. Electromagn. Compat., vol. 58, no. 4, pp. 1252–1258, July, 2016.

[6] D. Hill, "Plane wave integral representation for fields in reverberation chambers", IEEE Trans. Electromagn. Compat., vol. 40, no. 3, pp. 209–217, Nov. 1998.

[7] IEC 61000-4-21, Electromagnetic compatibility (EMC): Testing and Measurement Techniques - Reverberation Chamber Test Methods, 2003.




Ladbury, John.
"Problems with Stirred Immunity Measurements in a Reverberation Chamber: Corrections to DO- 160G Section 20.6."
Paper presented at 2018 IEEE International Symposium on Electromagnetic Compatibility & 2018 IEEE Asia-Pacific Symposium on Electromagnetic Compatibility (EMC/APEMC) : 2018 Joint IEEE EMC & APEMC, Suntec City, Singapore. May 14, 2018 - May 17, 2018.

*Proc. of the 2018 International Symposium on Electromagnetic Compatibility (EMC Europe 2018), Amsterdam, The Netherlands, August 27–30, 2018.*

# Statistical Considerations for Total Isotropic Sensitivity of Wireless Devices Measured in Reverberation Chambers

Robert D. Horansky, Thomas B. Meurs, Matthew V. North, Chih-Ming Wang, Maria G. Becker, Kate A. Remley

National Institute of Standards and Technology
Boulder, CO, USA
horansky@nist.gov

***Abstract*— The vast array of wireless device form factors being developed for internet-of-things applications necessitates a flexible test environment for determining performance metrics such as total isotropic sensitivity. Reverberation chambers loaded with lossy absorbers at cellular frequencies are an ideal match for this need. However, the estimate of total isotropic sensitivity from measurements in the reverberation chamber depends on the amount of loading in the chamber and on the choice of statistical averaging used in the measurements. We present results showing the significance of these two variables.**

***Keywords—cellular devices; internet-of-things; over-the-air test; wireless systems; total isotropic sensitivity***

## I. INTRODUCTION

There will be more mobile-connected devices than people on the Earth by the year 2019 [1]. The largest number of these devices are supporting machine-to-machine (M2M) and internet-of-things (IoT) applications with no human interaction. Unlike smartphones, M2M and IoT devices take on a vast array of small and large form factors necessitating flexibility in a test environment. Cellular devices often have integrated antennas ruling out the use of conducted measurements so that over-the-air (OTA) techniques are needed. Some key metrics for network system performance of a device do not need angle-of-arrival information, such as total isotropic sensitivity (TIS) of the receiver, data throughput, and total radiated power (TRP). Reverberation chambers are a flexible solution for these averaged system-level metrics, giving users the ability to place a device-under-test (DUT) almost anywhere in the large working volume and providing relatively low cost of construction when compared to anechoic chambers [2-6].

The reverberation chamber is an electrically large, resonating cavity. The chamber utilizes various stirring mechanisms, traditionally asymmetric rotating paddles, that allow the boundary conditions to be altered sufficiently to mix many electrical modes. The mode mixing yields, on average, a uniform electric field distribution over a large volume of the chamber. The highly resonant, mixed environment is good for providing uniformity of the electric field, but it also has the effect of creating large fluctuations in the chamber transfer function as a function of frequency. In an unloaded chamber, the frequency selectivity of the channel is typically too high for a wireless device's receiver to correct with equalization and prevents a successful communication link. Therefore, the chamber is loaded with RF absorber to decrease the quality factor of the chamber and flatten the frequency response enough to allow communication between a base station simulator and the device under test [2]. Insufficient loading of the chamber, however, can have a large impact on metrics where the quality of the communication link is being measured, such as TIS [7].

The TIS of a wireless device is normally calculated based on two separate measurements. The first determines the power transfer function of the chamber configuration averaged over many boundary conditions, which is an estimate of the loss in the channel the DUT is experiencing. This measurement is typically done as a pre-characterization of the chamber to determine how much loading the chamber requires to flatten the frequency response sufficiently for the given communication link [7]. The second measurement, also averaged over boundary conditions, determines the proficiency with which the device can demodulate a received signal for a given transmitter power. This measurement is typically performed quickly on customer provided DUTs and combined with the previously measured pre-characterization parameters to yield the TIS of each device. The use of reverberation chambers for testing modulated-signal receiver performance is a relatively young field [3]. There are very few articles examining the dependence of the TIS measurement itself on chamber characteristics, e.g. [2, 8].

The measurements for channel response and receiver sensitivity can be performed at different times under similar but non-identical conditions so that each must be averaged separately. The choice of statistical averaging technique affects the value and uncertainty determined for TIS. Here, we examine the dependence of the TIS estimated for a large-form-factor wireless router and its uncertainty on the choice of averaging and as a function of chamber loading. We compare measurements made with two different chamber setups. The first is a typical configuration where the channel loss and the receiver sensitivity are measured with separate antennas, and the second setup automates the chamber characterization and DUT measurement to occur almost simultaneously. The automated setup allows the instantaneous channel experienced by the DUT at each boundary condition to be measured, facilitating comparison of averaging methods.




Horansky, Robert; Meurs, Thomas; Wang, Chih-Ming; Becker, Maria; Remley, Catherine.
"Statistical Considerations for Total Isotropic Sensitivity of Wireless Devices Measured in Reverberation Chambers."
Paper presented at 2018 International Symposium on Electromagnetic Compatibility (EMC), Amsterdam, Netherlands. August 27, 2018 - August 30, 2018.

We start, in Section II, by describing the measurements and calculations that go into the TIS metric in a reverberation chamber. Then, we describe the various measurement configurations in Section III. Section IV contains the results and analysis, while we conclude and describe future directions in Section V.

## II. Total Isotropic Sensitivity (TIS)

The TIS is a metric for determining the receiver sensitivity of a wireless device averaged over all angles-of-incidence. The measurement requires establishing a communication link with a device, sending a known sequence as a preamble, and determining the minimum power necessary at the device to maintain a bit-error-rate (BER) below a given threshold. This threshold is 1.2% for WCDMA in [7]. The TIS determines the power incident on the receiver antenna, so it can be compared to conducted measurements, if possible. Therefore, the TIS measurement requires a measurement of the power emitted by a base-station simulator, $P_{\mathrm{BSS}}$, and a measurement of the reverberation-chamber reference power transfer function, $G_{\mathrm{ch}}$, which is a comparable quantity to the range path loss in an anechoic chamber.

The $G_{\mathrm{ch}}$ is measured with a measurement antenna that remains in the chamber during the tests, and a reference antenna used for determining the chamber characteristics. It is measured at $N$ steps of a stirring sequence, which in our case is just the paddle of the chamber rotating in static, discrete steps. At each paddle location, $n$, $G_{\mathrm{ch}}$ is given by [2],

$$G_{\mathrm{ch}}(n)=\frac{\left\langle \left|S_{21}(n)\right|^2 \right\rangle_{\mathrm{F}}}{\left(1-\left|\left\langle \left\langle S_{22}\right\rangle_F\right\rangle_N\right|^2\right)\eta_{\mathrm{ref}}}, \tag{1}$$

where $S_{21}$ is the forward transmission scattering parameter measured by a vector network analyzer (VNA), $S_{22}$ is the reflection scattering parameter measured at the VNA port connected to the reference antenna, $\eta_{\mathrm{ref}}$ is the radiation efficiency of the reference antenna, and the brackets represent the ensemble average over the frequencies in the bandwidth of interest, $F$, and all the stirring positions, $N$. The efficiency and mismatch of the measurement antenna are not included in (1) since that antenna is used for both the $G_{\mathrm{ch}}$ and the $P_{\mathrm{BSS}}$. The chamber reference power transfer function, $G_{\mathrm{ref}}$, is related to (1) by including the measurement antenna terms in the denominator.

In addition to $G_{\mathrm{ch}}$, we measure $P_{\mathrm{BSS}}$ by using the measurement antenna used in (1), but connecting it to a base station simulator which will now measure the transmit and receive communication signals. At each step of the stirring sequence, a communication link is established at a given output power from the base station simulator. A pseudorandom bit sequence is used as the data and transmitted to the DUT. The DUT transmits the received sequence back to the communication tester, and the error rate in the returned sequence is calculated and reported. The output power is then lowered and the BER is measured again. The power output resulting in the threshold BER is recorded for each stirring-sequence step, $n$.

If the measurements for $G_{\mathrm{ch}}$ and $P_{\mathrm{BSS}}$ were taken in precisely the same configuration at each stirring sequence step, then the TIS power, $P_{\mathrm{TIS}}$, is the mean of the value at each step and is given by

$$P_{\mathrm{TIS}}=\frac{1}{N}\sum_{n=1}^{N}G_{\mathrm{ch}}(n)P_{\mathrm{BSS}}(n). \tag{2}$$

In the typical use of a reverberation chamber, $G_{\mathrm{ch}}$ will be characterized as a function of loading, with the absorber locations recorded, when the chamber is initially set up so that only a device measurement is necessary afterwards. Thus, $G_{\mathrm{ch}}$ and $P_{\mathrm{BSS}}$ are usually measured separately and must be averaged separately to calculate $P_{\mathrm{TIS}}$. Furthermore, $P_{\mathrm{TIS}}$ is an intrinsic quantity of the wireless device, so $G_{\mathrm{ch}}$ and $P_{\mathrm{BSS}}$ are dependent quantities. That is, at each stirrer step if one value goes up, the other should ideally compensate. Thus, we separate the dependence in (2) as,

$$\frac{P_{\mathrm{TIS}}}{P_{\mathrm{BSS}}(n)}=G_{\mathrm{ch}}(n), \tag{3}$$

so that if the chamber response and base station power are measured with different realizations of the stir sequence, represented by $N_1$ and $N_2$, we can calculate $P_{\mathrm{TIS}}$ by

$$\begin{aligned}\frac{1}{N_1}\sum_{n_1=1}^{N_1}\frac{P_{\mathrm{TIS}}}{P_{\mathrm{BSS}}(n_1)}&=\frac{1}{N_2}\sum_{n_2=1}^{N_2}G_{\mathrm{ch}}(n_2),\\ P_{\mathrm{TIS}}&=\frac{N_1}{\sum_{n_1=1}^{N_1}\frac{1}{P_{\mathrm{BSS}}(n_1)}}\frac{1}{N_2}\sum_{n_2=1}^{N_2}G_{\mathrm{ch}}(n_2).\end{aligned} \tag{4}$$

Typically, $N_1$ and $N_2$ are the same stirring sequence, but with slightly different measurement configurations, such as a different reference and DUT antenna. Eqn. (4) is calculating an arithmetic mean of $G_{\mathrm{ch}}$ and a harmonic mean of $P_{\mathrm{BSS}}$, and matches what is defined in the CTIA test plan for commercial test labs [7]. However, there is nothing unique about this choice of averaging and we could recast (2) as

$$\frac{P_{\mathrm{TIS}}}{G_{\mathrm{ch}}(n_2)}=P_{\mathrm{BSS}}(n_1), \tag{5}$$

leading to,

$$P_{\mathrm{TIS}}=\frac{N_2}{\sum_{n_2=1}^{N_2}\frac{1}{G_{\mathrm{ch}}(n_2)}}\frac{1}{N_1}\sum_{n_1=1}^{N_1}P_{\mathrm{BSS}}(n_1). \tag{6}$$

This calculation uses the harmonic mean of $G_{\mathrm{ch}}$ and the arithmetic mean of $P_{\mathrm{BSS}}$. Finally, using the median value of both $G_{\mathrm{ch}}$ and $P_{\mathrm{BSS}}$ is equally valid (since the median of the reciprocal values is equal to the median of the values), giving rise to

$$P_{\mathrm{TIS}}=\mathrm{med}\left(P_{\mathrm{BSS}}(n_1)\right)\mathrm{med}\left(G_{\mathrm{ch}}(n_2)\right). \tag{7}$$



Horansky, Robert; Meurs, Thomas; Wang, Chih-Ming; Becker, Maria; Remley, Catherine.
"Statistical Considerations for Total Isotropic Sensitivity of Wireless Devices Measured in Reverberation Chambers."
Paper presented at 2018 International Symposium on Electromagnetic Compatibility (EMC), Amsterdam, Netherlands. August 27, 2018 - August 30, 2018.

We will compare the ramifications of the choice of statistics for TIS calculations using (4), (6), and (7) in estimating the value as well as on uncertainty.

The uncertainty in TIS is derived from measuring $Q$ independent realizations of the stirring sequence, comprised of $N$ steps. Since these multiple realizations are, in practice, applied only to the $G_{ch}$ measurements, and since $G_{ch}$ and $P_{BSS}$ are correlated, the relative uncertainty found for $G_{ch}$ is typically applied to $P_{TIS}$ [7]. However, for the measurements here, both parameters have been measured with multiple realizations of the stirring sequence. We use a significance test to determine whether the uncertainty was dominated by lack of spatial uniformity between the $Q$ samples, or was comparable to the uncertainty contribution of the samples within the $N$ stirring sequence steps [9]. This can vary with loading, but for the setups that will be described here, the spatial uniformity was the dominant contribution to uncertainty. Therefore, the average value of TIS is given by

$$\left\langle P_{\mathrm{TIS}} \right\rangle_Q = \frac{1}{Q}\sum_{q=1}^{Q} P_{\mathrm{TIS}}(q), \tag{8}$$

and the uncertainty comes from the variance over $Q$ samples,

$$u_{P_{\mathrm{TIS}}} = \sqrt{\frac{1}{Q(Q-1)}\sum_{q=1}^{Q}\left(P_{\mathrm{TIS}}(q) - \left\langle P_{\mathrm{TIS}} \right\rangle_Q\right)^2}\,. \tag{9}$$

## III. Measurement Configuration

We used two configurations of antennas in the reverberation chamber to examine the effect of statistical averaging methods as a function of chamber loading. The first set of measurements used separate, but similar, antenna setups and placements for the measurements of $G_{ch}$ and $P_{BSS}$. From these measurements, we realized that there would be a lot of information about the statistical nature of the reverberation chamber if we measured the instantaneous channel experienced by the DUT at each set of boundary conditions. Thus, the second set of measurements were performed with a relay circuit setup with a common antenna for $G_{ch}$ and $P_{BSS}$ measurements.

Common to both configurations is the chamber itself which has interior dimensions of 4.6 m x 3.1 m x 2.8 m. There is a single vertical paddle with a height of 2.1 m which traces a cylinder with radius 0.5 m. Our stirring sequence consists 72 paddle angles with 5 degree steps, $N$ = 72. The angular coherence of the paddle was measured to be less than 5 degrees at the highest loading used here, meaning that we obtain independent measurements at each paddle orientation [10]. There was no antenna position stirring included in the stirring sequence to isolate the contribution of spatial uniformity in the chamber. The chamber was loaded with an increasing number of RF absorbers, each one measuring 0.60 x 0.60 x 0.09 m. The absorbers were added in a single stack, as is shown schematically in Fig. 1 and in the photographs in Fig. 2.

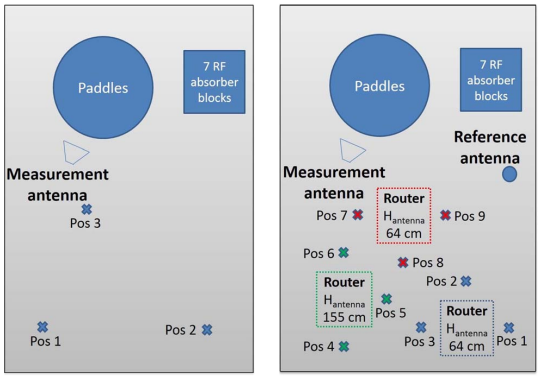


(a) $G_{ref}$ (b) $P_{BSS}$

Fig. 1: Top view of the antenna positions and heights used for the measurements in the reverberation chamber. In (a) the three discone antenna positions are denoted by Pos 1 - 3 and in (b) the nine omnidirectional DUT antenna positions are denoted by Pos 1 – 9.

We performed TIS measurements using a base station simulator for a communication link in the WCDMA Band 2, Channel 9662. This is centered at 1932.4 MHz with a 3.84 MHz bandwidth. The DUT was a cellular enabled wireless router measuring 0.47 x 0.44 x 0.09 m, classifying it as a large-form-factor device [7]. An external antenna was attached to the router with a 3 m coaxial cable.

In our initial setup, the chamber transfer function, $G_{ch}$, and the base station output power were measured separately using different antennas for $G_{ch}$ and $P_{BSS}$. For $G_{ch}$, the measurement antenna, which is used for both measurements, was connected to port 1 of a VNA, while the reference antenna was connected to port 2. The measurement antenna was a dual-ridge, broadband horn. The reference antenna was a discone monopole antenna. The efficiencies of the antennas were measured in the unloaded chamber [11]. We measured nine independent realizations of the stirring sequence by moving the reference antenna to three marked locations, as shown in Fig. 1(a), and at each location the reference antenna was positioned in three orthogonal polarizations. Furthermore, the independence of each stirring sequence was verified by a Pearson's correlation coefficient of less than 0.3 for all sequences [12]. We measured the chamber's power transfer function with the VNA from 1800 to 2200 MHz with 8001 points for 50 kHz steps, an IF bandwidth of 1 kHz, an output

(a) $G_{ref}$ (b) $P_{BSS}$

Fig 2: Photograph of set up shown in Fig. 1 for measuring (a) $G_{ch}$ and (b) $P_{BSS}$. The absorbers are shown in the back, right corner of the chamber. The measurement antenna is on the tripod on the left, the reference antenna is shown in the front of (a) and on the right in (b), and the router is shown in (b).



Horansky, Robert; Meurs, Thomas; Wang, Chih-Ming; Becker, Maria; Remley, Catherine.
"Statistical Considerations for Total Isotropic Sensitivity of Wireless Devices Measured in Reverberation Chambers."
Paper presented at 2018 International Symposium on Electromagnetic Compatibility (EMC), Amsterdam, Netherlands. August 27, 2018 - August 30, 2018.

power of -10 dBm, and a dwell time of 10 µs. However, for calculation of (1), only a 4 MHz bandwidth around 1932.4 MHz was used.

In the initial setup, for $P_{BSS,}$ the stirring sequence was still the 72 paddle rotations, but the nine realizations of the stirring sequence were achieved by moving the router to three spatially independent locations, then rotating the router and its external antenna, as shown in Fig. 1(b). The transmit/receive port of the base station simulator was connected to the measurement antenna and the reference antenna was terminated in a 50 ohm load outside the chamber. The base station simulator power started at -60 dBm, lowered in 2 dB steps, with the BER measured at each step. When the BER exceeded 1.2%, the output power of the simulator was increased in 2 dB steps back to 0% BER, then lowered again in 0.5 dB steps until the threshold was reached and the final power recorded. If no connection was established, or the value of TIS was 30 dB or higher than the minimum value found for the stirrer sequence, the result was ignored. Fig. 2(b) shows a photograph of the router in the measurement setup for $P_{BSS}$. The router was placed on blocks that were measured to be transparent to RF energy at the frequencies of interest in order to keep the DUT at least 0.08 m (half a wavelength) away from the metal floor.

The configuration described above was developed according to [7]. However, it assumes that the channel corresonding to the reference measurement is, on average, the same as the channel corresponding to the DUT measurement. To understand the effects of loading on the statistics that make up the TIS metric, we designed a second setup to measure the instantaneous channel at each paddle and antenna location as well as the receiver sensitivity without touching the configuration of the chamber. The second setup consisted of a relay circuit and switch so that we can use the DUT antenna as the reference antenna as well. Fig. 3 shows a schematic of the relay system used to automate the measurement of $G_{ch}$ and $P_{BSS}$ with no alteration of the channel between the measurements. The stirring sequence was identical to the previous setup with the 72 stepped paddle angles, but the nine realizations of the stirring sequence were accomplished by placing the antenna on a 1 m diameter turntable and using three angular increments. A translation stage provided automated height adjustment for three heights at each turntable position.

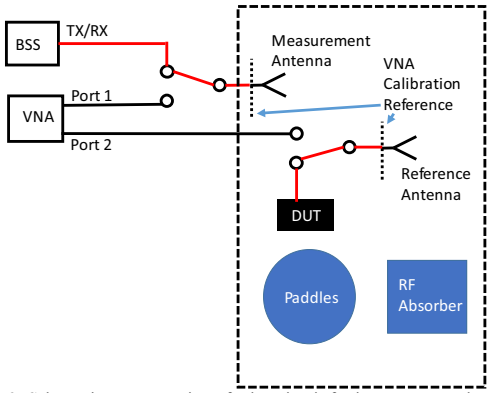


Fig 3: Schematic representation of relay circuit for instantaneous channel measurements. The dashed box represents the chamber walls. The circuit shown in red is not accounted by the calibration of the VNA measurement and that cable loss must be measured separately.

Fig. 4: Photograph of the automated setup for the reverberation chamber. The turntable has a translation stage for height adjustment and a platform with the router DUT attached by red straps.

At each location and each paddle step, the $G_{ch}(n)$ and $P_{BSS}(n)$ were measured with no change in the system except for a voltage on the relay. Chamber loss was measured with and without the relay activated to insure no effect from the presence of the relay in the chamber. A photograph of the automated setup is shown in Fig. 4.

## IV. Results

We first compare our results from separate measurements of chamber response and DUT sensitivity with those taken with the automated setup. Fig. 5 shows the separated setup TIS results in red, calculated from (4), with the arithmetic mean of the chamber response and the harmonic mean of sensitivity [7]. Based on previous experience and the measurement of the frequency coherence of the chamber, the flatness of the channel was found to be good enough at seven absorbers, with the absorbers stacked sequentially in the configuration shown in Fig. 4. Once the channel has a flat enough frequency response, the average value of TIS should not change with additional loss in the chamber. Yet, with seven absorbers in the chamber, the expected plateau in TIS is observed, but is not as significant as at higher absorber loading.

The uncertainties shown in Fig. 5 for the separate measurements scenario come from determining the uncertainties of the chamber response and base-station power similarly to (9), but with the respective variable, and taking the root sum square (RSS) of the coefficients of variance, given by[13],



Horansky, Robert; Meurs, Thomas; Wang, Chih-Ming; Becker, Maria; Remley, Catherine.
"Statistical Considerations for Total Isotropic Sensitivity of Wireless Devices Measured in Reverberation Chambers."
Paper presented at 2018 International Symposium on Electromagnetic Compatibility (EMC), Amsterdam, Netherlands. August 27, 2018 - August 30, 2018.

$$u_{P_{\mathrm{TIS}}} = \langle P_{\mathrm{TIS}} \rangle_Q \sqrt{\left( \frac{u_{P_{\mathrm{BSS}}}}{\langle P_{\mathrm{BSS}} \rangle_Q} \right)^2 + \left( \frac{u_{G_{ch}}}{\langle G_{ch} \rangle_Q} \right)^2}. \quad (10)$$

The error bars are then the standard uncertainty of $P_{\mathrm{TIS}}$ in dB units calculated as,

$$u\left(10\log_{10}\left(P_{\mathrm{TIS}}\right)\right) \approx 10\log_{10}\left( \frac{P_{\mathrm{TIS}} + u_{P_{\mathrm{TIS}}}}{P_{\mathrm{TIS}}} \right). \quad (11)$$

The uncertainties in Fig. 5 decrease with an increasing number of RF absorbers due to large uncertainty in the $P_{\mathrm{BSS}}$ term. This large uncertainty is not from lack of spatial uniformity, but rather from poorly established communication links with the DUT for channels that are highly frequency selective.

The results from the automated setup, also calculated from (4) are shown in black in Fig. 5 with excellent agreement in the overlap region of the two setups. The value of TIS does not change for seven absorbers and above indicating adequate flattening of the chamber frequency response in the communication channel, although for nine absorbers and above a distinct plateau in the mean is observed. Also, the results in the plateau region are in good agreement with anechoic chamber measurements on the same DUT which showed a $P_{\mathrm{TIS}}$ of 109.4 dBm. The uncertainties for the automated setup come from (9) and converted to dB with (11).

Our next analysis is to compare averaging methods for the final TIS result. In the automated setup we have access to the same instantaneous channels that the receiver measurements were performed. Thus, we can apply (2) and compare the results to those using (4), (6), and (7). Using (2), every value measured for TIS is given equivalent weighting. The harmonic mean used for (4) and (6) will tend to give more weight to lower values for $P_{\mathrm{BSS}}$ and $G_{\mathrm{ch}}$, respectively. Finally, the median taken in (7) will unweight extreme values.

Fig. 6 shows that the choice of averaging has a large effect

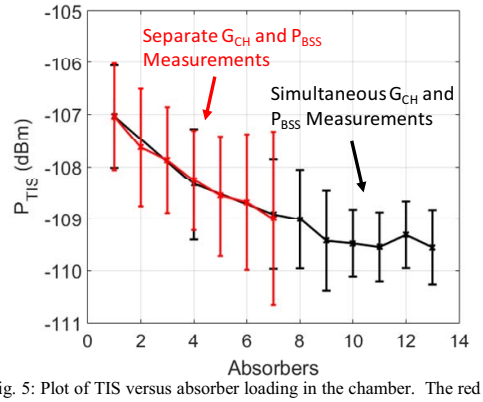


Fig. 5: Plot of TIS versus absorber loading in the chamber. The red curve is data taken with separate measurements for $G_{\mathrm{ch}}$ and $P_{\mathrm{BSS}}$. The black curve was taken six months later using the automated setup to study the instantaneous channel. The error bars come from the lack of spatial uniformity in $P_{\mathrm{TIS}}$ taken from (9) for the black curve and from the RSS of the coefficient of variation in $G_{\mathrm{ch}}$ and $P_{\mathrm{BSS}}$ for the red curve.

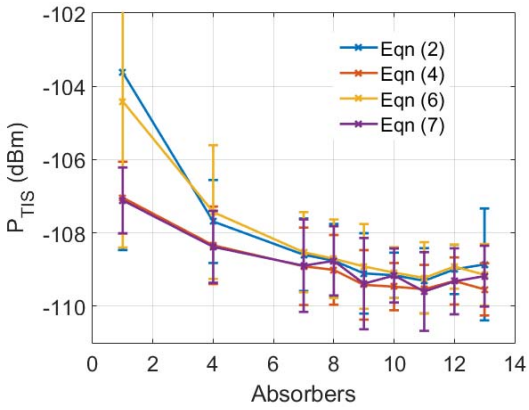


Fig. 6: Using the automated setup, plot of TIS versus absorber loading for the four averaging methods. The equation giving rise to each curve is shown in the legend. The uncertainties come from (9) .

on TIS when fewer than seven absorbers are used. However, in the plateau region with greater than eight absorbers, where the communication link is better, the averaging method is not as important. Also, in the plateau of TIS values, there is good agreement between all the methods within the uncertainty, as calculated by (9). The agreement in the plateau region leads us to conclude that the communication link is the largest contributor to uncertainty for lower absorber cases, which manifests itself as large values of $P_{\mathrm{BSS}}(n)$ when the communication link is dropped. The use of (4) and (7) tends to reduce the weight given to these higher values, leading to a more robust result. The robustness is seen in Fig. 7, which shows the relative uncertainty in $P_{\mathrm{TIS}}$ versus the absorber loading cases which are the error bars in Fig. 6. By using (4), as is the case in the CTIA test plan, the uncertainty in TIS is both minimized and more stable.

To verify the dominance of the uncertainty in $P_{\mathrm{BSS}}$, we take a closer look at the relative uncertainty in $G_{\mathrm{ch}}$. Fig. 8 shows the relative uncertainty of each of the averaging methods for $G_{\mathrm{ch}}$, calculated according to (10), but with $G_{\mathrm{ch}}$ replacing $P_{\mathrm{TIS}}$. The relative uncertainty varies only slightly at each absorber

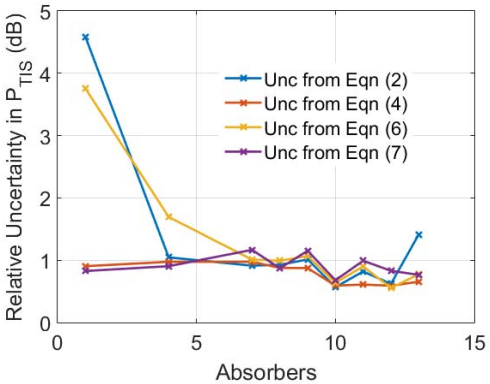


Fig. 7: The relative uncertainty due to lack of spatial uniformity in the full $P_{\mathrm{TIS}}$.



Horansky, Robert; Meurs, Thomas; Wang, Chih-Ming; Becker, Maria; Remley, Catherine.
"Statistical Considerations for Total Isotropic Sensitivity of Wireless Devices Measured in Reverberation Chambers."
Paper presented at 2018 International Symposium on Electromagnetic Compatibility (EMC), Amsterdam, Netherlands. August 27, 2018 - August 30, 2018.

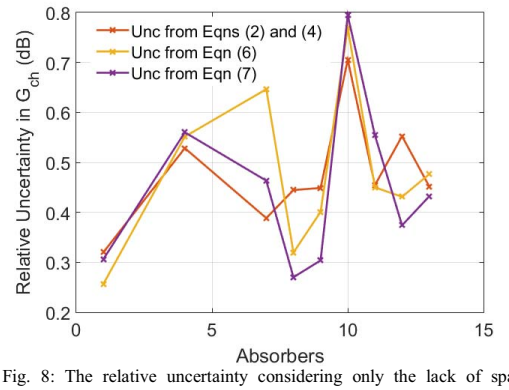


Fig. 8: The relative uncertainty considering only the lack of spatial uniformity in $G_{ch}$ with the various averaging methods.

loading, with a generally increasing trend. The increasing trend is due to lack of spatial uniformity with increased loading [2]. Both (2) and (4) utilize the arithmetic mean for $G_{ch}$ and are represented by the red curve. The agreement between all the curves in Fig. 7 shows that variation in $G_{ch}$ does not depend on outliers of the measurement, even for lower absorber loading. Averaging methods that take into account the weighting of the values do not alter the results. This leads us to conclude that the uncertainty in $P_{BSS}$ is dominated by outliers at lower absorber loading cases. Using a statistical method that reduces the weight of the high outliers in $P_{BSS}$ such as (4) and (7) yields more relevant results for TIS.

## V. Conclusion

The TIS of a wireless device is a universally utilized metric for determining its performance and requires measurement of both the link with the device as well as the channel of the measurement environment. In this paper, we presented results looking at TIS with different chamber setups and with increasing loading conditions.

With sufficient mode mixing and sampling of the chamber, the TIS of a wireless router was repeatable between two different measurement antenna setups. The first used a separate reference antenna for characterizing the chamber. The second method used a relay circuit to use the same antenna configuration for both characterizing the chamber and measuring the sensitivity of the DUT.

The relay setup allowed the instantaneous chamber characteristics at each stirrer sequence step to be known. This allowed a comparison of averaging methods. Averaging methods that reduced the weight of positive deviations in $P_{BSS}$ were more relevant to the TIS metric, since they weight channels with stable communication links. The loaded reverberation chamber achieved good agreement with anechoic chambers with relatively small uncertainties at loading conditions that allow stable communication links. Our automated relay system allowed analysis of the effect of the instantaneous channel in the reverberation chamber on the measurement results. We then compared mathematically motivated statistical averaging choices to find the most meaningful one for TIS. Finally, the relay circuit system allows study of even more statistical metrics in the reverberation chamber. Examining the effects of various metrics in the instantaneous channel on the TIS measurement will be discussed in a future article.

## Acknowledgment

We thank Edwin Mendivil at ETS-Lindgren for helpful discussion and verification of our BSS measurement procedure.

## References

[1] Cisco Visual Networking Index. (2014, Feb.) Global Mobile Data Traffic Forecast Update, 2014, San Jose, CA, USA. [Online]. Available: http://www.cisco.com/c/en/us/solutions/collateral/serviceprovider/visual-networking-index-vni/white_paper_c11-520862.htm

[2] K. A. Remley, J. Dortmans, C. Weldon, R. D. Horansky, T. B. Meurs, C.-M. Wang, D. F. Williams, C. L. Holloway, and P. F. Wilson, "Configuring and Verifying Reverberation Chambers for Testing Cellular Wireless Devices," *IEEE Trans. Electromagn. Compat.,* vol. 58, no. 3, June 2016.

[3] C. Orlenius, P. S. Kildal and G. Poilasne, "Measurements of total isotropic sensitivity and average fading sensitivity of CDMA phones in reverberation chamber," *2005 IEEE Antennas and Propagation Society International Symposium*, 2005, pp. 409-412 Vol. 1A.

[4] O. Delangre, P. De Doncker, F. Horlin, M. Lienard, and P. Degauque, "Reverberation chamber environment for testing communication systems: Applications to OFDM and SC-FDE," in *Proc. 68th IEEE Veh. Technol. Conf.*, Calgary, Canada, Sept. 2008, pp. 1–5.

[5] P.-S. Kildal, C. Orlenius, and J. Carlsson, "OTA testing in multipath of antennas and wireless devices with MIMO and OFDM," *Proc. IEEE*, vol. 100, no. 7, pp. 2145–2157, Jul. 2012.

[6] C. Lötbäck Patané, A. Skårbratt, R. Rehammar, and C. Orlenius, "On the use of reverberation chambers for assessment of MIMO OTA performance of wireless devices," in *Proc. 7th Eur. Conf. Antennas Propag.*, Gothenburg, Sweden, pp. 101–105, Apr. 2013.

[7] CTIA Certification, "Test Plan for Wireless Large-Form_Factor Device Over-the-Air Performance," Version Number: 1.1, July 2017.

[8] M. Andersson, C. Orlenius and P. S. Kildal, "Three Fast Ways of Measuring Receiver Sensitivity in a Reverberation Chamber," *2008 International Workshop on Antenna Technology: Small Antennas and Novel Metamaterials*, Chiba, 2008, pp. 51-54.

[9] K. A. Remley, C.-M. Wang, R. J. Pirkl, A. T. Kirk, J. Aan Den Toorn, D.F.Williams, C. L. Holloway, J. A. Jargon, and P. D. Hale, "A significance test for reverberation-chamber measurement uncertainty in total radiated power of wireless devices," *IEEE Trans. Electromagn. Compat.*, vol. 58, no. 1, pp. 207–219, Oct. 2015.

[10] R. J. Pirkl, K. A. Remley and C. S. L. Patane, "Reverberation Chamber Measurement Correlation," in *IEEE Transactions on Electromagnetic Compatibility*, vol. 54, no. 3, pp. 533-545, June 2012.

[11] C. L. Holloway, H. A. Shah, R. J. Pirkl, W. F. Young, D. A. Hill and J. Ladbury, "Reverberation Chamber Techniques for Determining the Radiation and Total Efficiency of Antennas," in *IEEE Transactions on Antennas and Propagation*, vol. 60, no. 4, pp. 1758-1770, April 2012

[12] D. F. Morrison, Multivariate Statistical Methods. New York: McGraw-Hill,1967.

[1] Joint Committee for Guides in Metrology, "Evaluation of Measurement Data-Guide to the Expression of Uncertainty in Measurement," BIPM, France, September, 2008.



Horansky, Robert; Meurs, Thomas; Wang, Chih-Ming; Becker, Maria; Remley, Catherine.
"Statistical Considerations for Total Isotropic Sensitivity of Wireless Devices Measured in Reverberation Chambers."
Paper presented at 2018 International Symposium on Electromagnetic Compatibility (EMC), Amsterdam, Netherlands. August 27, 2018 - August 30, 2018.

# A New Calibration Method for Achieving High Insertion-Loss Measurements with a Vector Network Analyzer*

Jeffrey A. Jargon and Dylan F. Williams

National Institute of Standards and Technology, 325 Broadway, M/S 672.03, Boulder, CO 80305 USA
Email: jeffrey.jargon@nist.gov, Tel: +1.303.497.4961

***Abstract* — We present a new calibration method for achieving high insertion-loss measurements with a vector network analyzer (VNA). The method requires a characterized attenuator and other additional hardware, including an amplifier, an isolator, two directional couplers, and two attenuators. With this setup, we measure wave-parameters rather than scattering-parameters. This technique enables us to shift the dynamic range of our measurements while decreasing uncertainties due to the noise floor of the VNA. With hardware available in our laboratory, we can measure values of insertion-loss up to 150 dB.**

***Index Terms* — attenuator, calibration, directional coupler, insertion loss, isolator, measurement, uncertainty, vector network analyzer.**

## I. Introduction

The need to accurately characterize high values of insertion loss is paramount to applications involving near- to mid-range antenna measurements. In free-field environments, insertion losses greater than 100 dB are often encountered, especially in non-line-of-sight applications or when separation distances between transmit and receive antennas are significant. Standard methods for measuring high values of insertion loss are inadequate, as the noise floor of the VNA limits the ability to accurately characterize such channels [1].

In a previous study [2], we presented a straightforward method for shifting the dynamic range of our VNA by measuring wave-parameters rather than scattering parameters (*S*-parameters), and utilizing only two additional pieces of hardware, namely an attenuator and an amplifier. This allowed us to increase the upper limit of insertion loss measurements from approximately 110 dB to 130 dB, while decreasing uncertainties due to the noise floor of the VNA.

In this paper, we further shift the upper limit of our VNA measurements to 150 dB by utilizing a new calibration method that requires a characterized attenuator and other additional hardware, and involves measuring wave-parameters. In the following sections, we describe our measurement setup, explain the new calibration method, and provide measured results with uncertainties.

## II. Measurement Setup

Figure 1 shows a simplified schematic diagram of a four-sampler VNA. The source is switched between Ports 1 and 2 so all four *S*-parameters can be calculated from the measured incident and reflected signals. This setup works well for moderate insertion losses, but as these values increase, the measurements become noisier due to the limited dynamic range of the VNA.

In our previous study [2], we developed a method that uses an amplifier between the source and the couplers on Port 1, and a compensating attenuator between the coupler and receiver on Port 1. This setup measures the incident power, while preventing damage to the receiver, as shown in Figure 2. Here, we were required to measure wave-parameters rather than *S*-parameters because the amplifier was placed in the system after the calibration, which changed the switch terms that correct for differences in the reflection coefficients of the terminating resistor switched between ports 1 and 2 [3]. Wave-parameters automatically compensate for this phenomena since incident and reflected signals are directly measured.

In this study, we further shift the upper limit of insertion-loss measurements by utilizing a new calibration method, along with additional hardware, shown in Figure 3. A 43 dB amplifier with a noise figure of 6.0 dB is placed external to the ports of the VNA so none of its internal components will be damaged. This requires two extra couplers for separating the incident and reflected signals, as well as two attenuators to protect the VNA's receivers on Port 1. Here, we had access to two 10 dB couplers, which required two 30 dB attenuators to protect the receivers. We also placed an isolator directly after the output of the amplifier to prevent any reflected signals from reaching it.

With this setup, both the calibration and device-under-test (DUT) measurements are performed with all the hardware in place. The new calibration is referred to as Short-Open-Load-Attenuator (SOLA). The attenuator is required to decrease the power incident on Port 2, and must be previously characterized with a separate calibration. In our case, we utilized a 40 dB attenuator calibrated with a Short-Open-Load-Thru (SOLT) technique. All measurements and calibrations in this study were performed with Type-N coaxial connectors on a frequency grid between 2.0-4.0 GHz (the bandwidth of our amplifier and isolator) with a spacing of 5 MHz (401 points), and an IF bandwidth of 20 Hz with no averaging. Furthermore, we measured wave-parameters rather than S-parameters since the switch terms could not be accurately measured at the lower powers originating from the source on Port 2, which are attenuated before reaching Port 1. In the following section, we describe the SOLA calibration in more detail.



Jargon, Jeffrey; Williams, Dylan.
"A New Calibration Method for Achieving High Insertion-Loss Measurements with a Vector Network Analyzer."
Paper presented at 91st ARFTG Microwave Measurement Symposium, Philadelphia, PA, United States. June 15, 2018 - June 15, 2018.

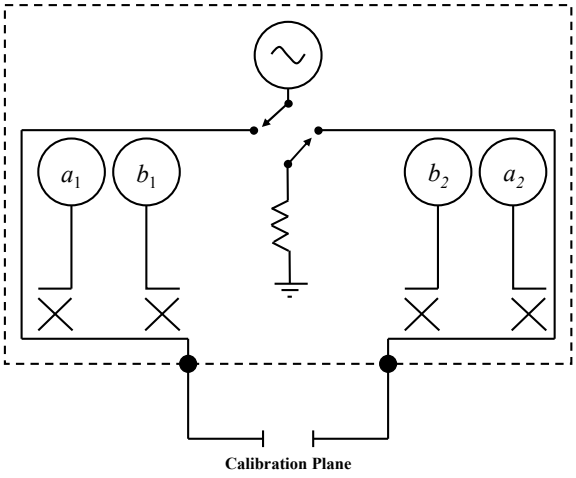


Fig. 1. Simplified schematic diagram of a four-sampler VNA.

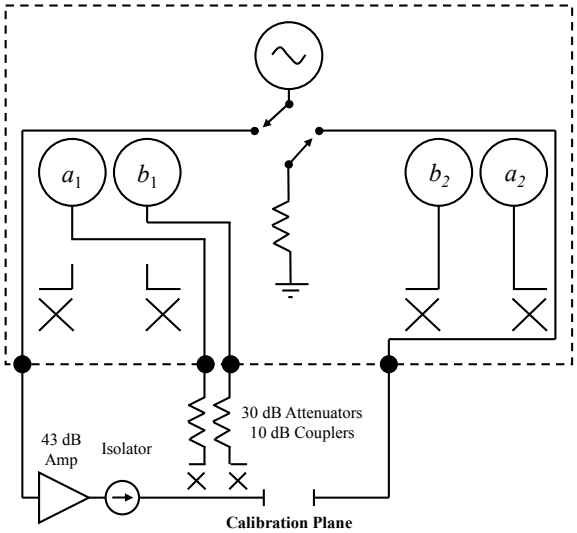


Fig. 3. Simplified schematic diagram of a four-sampler VNA with a 43 dB amplifier, isolator, two 10 dB couplers, and two 30 dB attenuators inserted for further improving high-insertion-loss measurements.

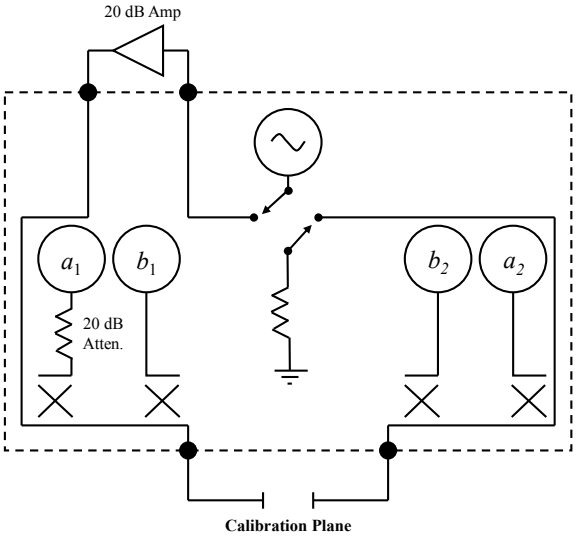


Fig. 2. Simplified schematic diagram of a four-sampler VNA with a 20 dB amplifier and 20 dB attenuator inserted for improving high-insertion-loss measurements.

## III. SOLA Calibration

SOLA and SOLT calibrations are similar. Both require three known standards to be connected to Ports 1 and 2, namely a short circuit, an open circuit, and a nominally-matched load. These standards need not be ideal assuming they are characterized and well-separated on the Smith Chart. Additionally, the SOLA calibration requires a characterized attenuator be placed between Ports 1 and 2 rather than a Thru.

Like SOLT, the SOLA calibration is realized with an eight-term error model in our software, the NIST Microwave Uncertainty Framework [4], [5]. The short, open, and load measurements, along with their respective definitions, allow us to determine the two reflection terms for each of the calibration error boxes. This leaves four transmission terms, of which only three are required since they can be arbitrarily normalized. Assuming the amplifier is placed on Port 1, as in Figure 3, the measured and defined values of the attenuator's forward transmission coefficients ($S_{21}$) allow us to solve for $S_{21}$ of the two error boxes. In our normalization scheme, $S_{12}$ of the Port 1 error box is set equal to $S_{21}$ of the Port 1 error box, and $S_{12}$ of the Port 2 error box is calculated to be consistent with the remainder of the Port 2 error box terms. Note that with any calibration utilizing an eight-term error model, either the measured *S*-parameters must be corrected for switch terms, or the *S*-parameters can be calculated directly from measured wave-parameters, in which case switch-term correction is not needed.

Jargon, Jeffrey; Williams, Dylan.
"A New Calibration Method for Achieving High Insertion-Loss Measurements with a Vector Network Analyzer."
Paper presented at 91st ARFTG Microwave Measurement Symposium, Philadelphia, PA, United States. June 15, 2018 - June 15, 2018.

TABLE I
COMPARING INSERTION-LOSS MEASUREMENTS OF TWO DIFFERENT CALIBRATIONS

| Attenuator Setting (dB) | $\|S_{21}\|$ Mean ± Std. Dev. (dB) | |
|---|---|---|
| | SOLT Calibration | SOLA Calibration |
| 40 | -40.51 ± 0.12 | -40.60 ± 0.12 |
| 50 | -50.54 ± 0.12 | -50.62 ± 0.12 |
| 60 | -60.47 ± 0.12 | -60.55 ± 0.13 |
| 70 | -70.49 ± 0.12 | -70.58 ± 0.13 |
| 80 | -80.42 ± 0.13 | -80.57 ± 0.13 |
| 90 | -90.40 ± 0.26 | -90.53 ± 0.13 |
| 100 | -100.40 ± 0.67 | -100.42 ± 0.14 |
| 110 | -110.32 ± 2.42 | -110.45 ± 0.15 |
| 120 | -118.83 ± 5.16 | -120.37 ± 0.21 |
| 130 | -121.12 ± 5.50 | -130.30 ± 0.57 |
| 140 | - | -140.08 ± 1.78 |
| 150 | - | -149.22 ± 4.19 |
| 160 | - | -153.65 ± 5.95 |

## IV. MEASUREMENT RESULTS

For comparison purposes, we performed both SOLT and SOLA calibrations, and measured a DUT consisting of a 40 dB fixed attenuator connected to a 120 dB step attenuator, which allowed us to vary the settings from 40 to 160 dB. Physical models of the SOLT calibration standards were developed and validated using a multiline Thru-Reflect-Line (TRL) calibration within the NIST Microwave Uncertainty Framework [4], [5]. The Short, Open, and Load standards of the SOLA calibration were the same as those of the SOLT calibration. The definition of the 40 dB attenuator utilized in the SOLA calibration was measurement-based rather than a physical model, and was previously determined with an SOLT calibration.

The SOLT calibration and corresponding DUT measurements were made with the standard VNA setup, as illustrated in Figure 1. Here, the output power of the VNA was set to 0 dBm, and we measured *S*-parameters.

The SOLA calibration and corresponding DUT measurements were performed with the high-insertion-loss setup, illustrated in Figure 3. Here, the output power of the VNA was set to –6 dBm, and we measured wave-parameters.

Table 1 lists the mean values and standard deviations of the magnitudes of $S_{21}$ calculated over the measured frequencies at attenuator settings of 40-160 dB using the two calibrations. Although both calibrations provided comparable mean values up to 110 dB, the standard deviations increased much more drastically with increased attenuator settings for the case where *S*-parameters were measured using the standard setup. For instance, at the attenuator's 110 dB setting, the SOLT measurements resulted in a standard deviation of ± 2.42 dB, while the SOLA measurements resulted in a much lower standard deviation of ± 0.15 dB.

At the 120 dB setting, the SOLT measurements were approaching the noise floor, while the SOLA measurements continued to deliver reasonable results up to 150 dB before reaching the noise floor.

Figures 4-6 illustrate the measurements of $|S_{21}|$ at the 90, 110, and 130 dB settings for the two calibrations. These graphs clearly show how much more noise is present in the SOLT measurements for the standard setup than the SOLA measurements for the modified setup.

Figure 7 plots the measurements and 95 % confidence intervals of $|S_{21}|$ for the variable attenuator at the 90 dB setting (a typical value we may encounter during non-line-of-sight, free-field measurements).

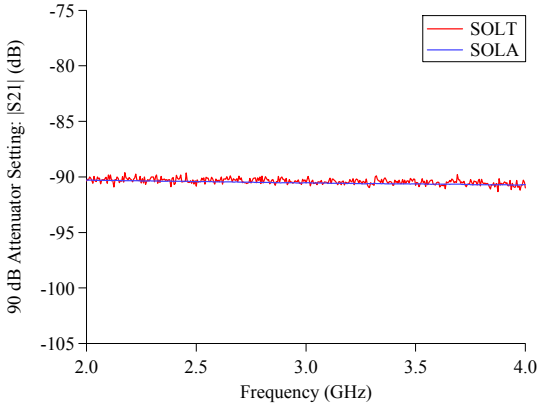


Fig. 4. Comparing measurements of $|S_{21}|$ at the 90 dB attenuator setting for two different calibrations.

Jargon, Jeffrey; Williams, Dylan.
"A New Calibration Method for Achieving High Insertion-Loss Measurements with a Vector Network Analyzer."
Paper presented at 91st ARFTG Microwave Measurement Symposium, Philadelphia, PA, United States. June 15, 2018 - June 15, 2018.

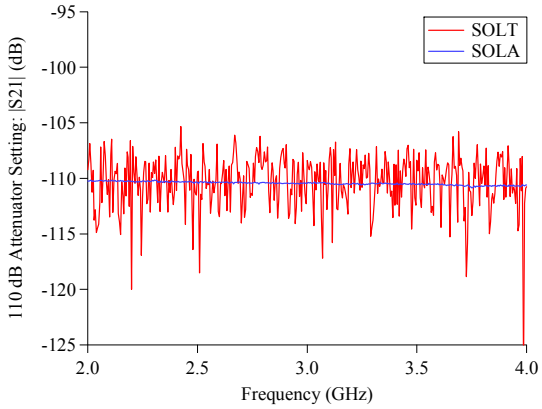


Fig. 5. Comparing measurements of $|S_{21}|$ at the 110 dB attenuator setting for two different calibrations.

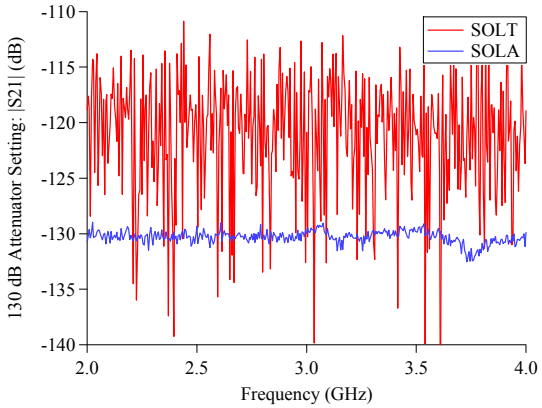


Fig. 6. Comparing measurements of $|S_{21}|$ at the 130 dB attenuator setting for two different calibrations.

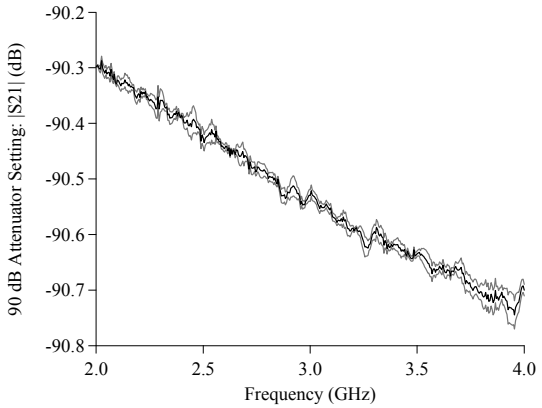


Fig 7. Nominal measurements (black curve) and 95 % confidence intervals (grey curves) of $|S_{21}|$ for the 90 dB setting as determined with the SOLA calibration.

## V. Conclusions

By measuring wave-parameters and utilizing a new SOLA calibration method in conjunction with a characterized attenuator and other additional hardware, we shifted the dynamic range of our VNA while decreasing uncertainties due to the noise floor. This modified setup decreased the standard deviations of $|S_{21}|$ by an order of magnitude for attenuator settings at and above 110 dB. Although we were limited to a maximum measured insertion loss of 150 dB with the equipment we had readily available in our laboratory, we should be able to measure even higher values with more powerful amplifiers and other hardware with higher power ratings. However, at some point leakage signals could potentially become problematic. This may be a topic of a future study.

## Acknowledgement

* This work was supported by the U.S. government, and is not subject to U.S. copyright.

The authors thank Paul Hale, Chihyun Cho, and Jeanne Quimby for their helpful comments.

## References

[1] "High Power Amplifier Measurements Using Nonlinear Vector Network Analyzer," Keysight Application Note, July 2014.

[2] J. A. Jargon and D. F. Williams, "A Method for Improving High-Insertion-Loss Measurements with a Vector Network Analyzer," 89th ARFTG Microwave Measurement Conference, Honolulu, HI, June 2017.

[3] R. B. Marks, "Formulations of the Basic Vector Network Analyzer Error Model Including Switch Terms," 50th ARFTG Microwave Measurement Conference, Portland, OR, Dec. 1997.

[4] D. F. Williams, NIST Microwave Uncertainty Framework, Beta Version, www.nist.gov/services-resources/software/wafer-calibration-software, 2017.

[5] J. A. Jargon, D. F. Williams, and P. D. Hale, "Developing Models for Type-N Coaxial VNA Calibration Kits within the NIST Microwave Uncertainty Framework," 87th ARFTG Microwave Measurement Conference, San Francisco, CA, May 2016.

# Measuring Ion-Pairing in Buffer Solutions with Microwave Microfluidics

Angela C. Stelson, Charles E. Little, Nathan D. Orloff, Christian J. Long, and James C. Booth

National Institute of Standards and Technology, Communications Technology Laboratory

James.booth@nist.gov

***Abstract*— Microwave microfluidics is an emergent technique for characterizing conductivity and permittivity of fluids and has wide-ranging applications in the materials science and biomedical fields. The electrical properties of fluids as a function of frequency can be leveraged to characterize interface effects such as electrical double layers (EDL), solvent-mediated ion interactions, and bound water molecules. However, extraction of quantitative electrical properties over a wide range of frequencies (100 kHz-67 GHz) is nontrivial, and calibrations are required. Here, we utilize a microfluidics device with incorporated coplanar waveguides to characterize buffer solutions *in situ* and non-destructively. With a two-step fitting procedure, we fit relaxations associated with the EDL, water molecules, and ion-pairing in solution. We compare the three-Debye relaxation (water loss, ion-pairing and EDL relaxations fit to a Cole-Cole/Debye (water loss Cole-Cole and EDL Debye relaxations) model which does not include the ion-pairing relaxation, and find improved goodness of fit. This technique is broadly applicable to ionic solutions, and provides critical information about solvated ions in biological systems.**

***Index Terms*— Permittivity measurement, Microfluidics, Transmission line measurements, Coplanar waveguides, Circuit testing**

## I. Introduction

Broadband dielectric measurements of fluids have been used detect the electrical properties of proteins, particles, and cells in solution.[1]–[3] Integration of microfluidics with on-chip microwave devices and calibration techniques enables quantitative measurements of nanoliter volumes of fluids for pharmaceutical, chemical and biotechnology applications. Advances in microwave metrology have enabled on-chip broadband dielectric measurements from DC to 110 GHz. Measuring a wide frequency range allows us to characterize charge-based phenomena in fluids including electrical double layers (EDL), ionic conductivity and molecular re-orientations.[4]

Here, we utilized coplanar waveguides (CPW) integrated into microfluidics devices to measure the broadband electrical properties of Tris-acetate-ethylenediaminetetraacetic acid buffer with magnesium (TAE-$Mg^{2+}$), which is commonly used in biological systems. Characterizing the electrical properties of ionic solutions is critical to advancing understanding of the interactions of biological systems with ions in solution. The frequency range (100 kHz-67 GHz) covered by our devices and calibration protocol captures both the low-frequency regime where EDL effects are strong, and the high-frequency regime where the solvent properties dominate. We extracted the electrical properties of bulk fluid, the EDL, and a weak signal that we associated with ion-pairing in the buffer [5]. We compared the goodness of fit for a function without an ion-pairing relaxation (Cole-Cole/Debye), and found that it improved the goodness of fit for the broadband fluid properties when the ion-pairing relaxation was included.

## II. Methods

### A. Device Fabrication

The device fabrication for the microwave microfluidics devices is described in detail in Ref. [4]. Briefly, all CPW structures were designed with 50 µm-wide center conductors, 5 µm-wide gaps and 200 µm-wide ground planes. In addition to CPWs of different lengths, devices including series resistors, series capacitors and short-circuited reflects were fabricated on the reference chip (bare device) to perform multiline-TRL [6] and series resistor calibrations [7]. We designed devices with two-layer microfluidic channels (test chip) consisting of ~50 µm of SU-8 photoresist, covered with an upper channel layer (~50 µm) of patterned polydimethylsiloxane (PDMS) (see Fig. 1B). The SU-8 microfluidic channels were ~80 µm wide, and exposed lengths of CPW to directly to fluid (0.5, 0.85, 1.55, and 3.314 mm). The CPW gap width and SU-8 height were chosen so that the electromagnetic fields interact with fluids and SU-8, not the PDMS layer. An acrylic press bar screwed into an aluminum chuck clamped the PDMS block to the chip (see assembled chip in holder in Fig. 1A).

### B. Microwave Measurements

We measured the CPWs with a vector network analyzer (VNA) on a microwave probe station (Fig. 1A-B). We measured the S-parameters at 640 frequency points from 100 kHz to 67 GHz on a logarithmic frequency scale, at an RF power of −20 dBm, and with an intermediate frequency (IF) bandwidth of 10 Hz. We performed our measurements on a temperature controlled stage programmed to 25 °C ± 2 °C. We performed a multiline thru- reflect-line (TRL) calibration to determine the propagation constant of the bare-CPW lines ($\gamma_0$), followed by the series-resistor calibration to compute the capacitance per unit length of the bare CPW section ($C_0$). For frequencies below 1 GHz, we use the series resistor calibration to determine $C_0$, and average the extracted circuit parameters across five line lengths. The propagation constant for the bare CPW lines is:

$$\gamma_0 = \sqrt{(R_0 + i\omega L_0)(G_0 + i\omega C_0)}, \qquad (1)$$

where ω is the angular frequency and $R_0$, $L_0$, $G_0$, and $C_0$ are the



Stelson, Angela; Little, Charles; Orloff, Nathan; Long, Christian; Booth, James.
"Measuring Ion-Pairing in Buffer Solutions with Microwave Microfluidics."
Paper presented at 2018 IEEE/MTT-S International Microwave Biomedical Conference, Philadelphia, PA, United States. June 14, 2018 - June 15, 2018.

distributed resistance, inductance, conductance, and capacitance per unit length of the bare-CPW lines, respectively. Here we assume that the CPW waveguide mode is TEM and that there are no magnetic materials present. Under these conditions, $R_0$ and $L_0$ are not sensitive to the dielectric properties of the surrounding materials. We derived the propagation constant of a non-magnetic loaded line:

$$\gamma_{tot} = \sqrt{(R_0 + i\omega L_0)(G_{tot} + i\omega C_{tot})}, \qquad (2)$$

where $G_{tot}$ and $C_{tot}$ are the distributed conductance and capacitance per unit length of the fluid-loaded CPW lines, respectively. Then we solved for the $G_{tot}$ and $C_{tot}$ by taking the square of the ratio (1) divided by (2) as,

$$G_{tot} + i\omega C_{tot} = \frac{\gamma_{tot}^2}{\gamma_0^2} \cdot i\omega C_o. \qquad (3)$$

For our measurement devices (Fig. 1A), the conductivity of quartz is negligible, thus $G_0$ is approximately zero. In practice, we obtain $G_{tot}$ and $C_{tot}$ two different ways. For high frequencies (1-67 GHz), we used the microfluidic-multiline TRL calibration on the microfluidic test chip to obtain $\gamma_{tot}$ and $\gamma_o$. For lower frequency measurements (less than 1 GHz), we de-embedded our raw measurements to the fluid-loaded portion of the line by accounting for the effect of cables, probes, and the CPW sections leading up to the fluid. Next, we performed a nonlinear least squares optimization to extract the propagation constant of the fluid-loaded and bare CPW test structures.

*C. Equivalent Circuit Model*

We developed a circuit model to describe total admittance $Y_{tot} = G_{tot} + i\omega C_{tot}$ of the TAE-$Mg^{2+}$ buffer (Fig. 1C):

$$\frac{1}{Y_{tot}} = \frac{2}{Y_{EDL}} + \frac{1}{Y_f}, \qquad (3)$$

where $Y_{EDL}$ and $Y_f$ are the admittances of the EDL and fluid, respectively. The fluid admittance, $Y_f$, is described as four parallel distributed circuit components (Fig. 1d):

$$Y_f = Y_{IP} + Y_w + G_\sigma + i\omega C_\infty \qquad (4a)$$

$$Y_f = i\omega \frac{C_{IP}}{1+(i\omega\tau_{IP})} + i\omega \frac{C_w}{1+(i\omega\tau_w)^{1-\alpha_w}} + G_\sigma + i\omega C_\infty \qquad (4b)$$

where $C_\infty$ is the capacitance of the suspension far above the relaxation of water, $C_w$ is the dipolar contribution of the water, $G_\sigma$ is the conductance due to ions, and $C_{IP}$ is the dipolar contribution of ions in the suspension. $G_{IP}$ and $G_w$ (Fig. 1D) represent the loss (imaginary part) of the Debye relaxations ($Y_w$ and $Y_{IP}$) and are related to $C_w$ and $C_{IP}$ *via* the Kramers-Kronig relations. The time constants $\tau_w$ and $\tau_{IP}$ correspond to the rotational relaxation times of the water and the ion-counterion pair, respectively. We describe the EDL as operating in series with the admittance of the fluid for fluids with dissolved ions (Fig 1C). The EDL can be modelled as a Cole-Cole relaxation[4], where $C_{EDL}$ is the capacitance associated with the EDL, $\alpha_{EDL}$ is a shape-broadening parameter and $\tau_{EDL}$ is the characteristic relaxation time associated with the formation of the EDL under electric field. The Cole-Cole relaxation is in parallel a constant phase element $Y_{CPE}$ (Fig. 1E). [4] By developing an equivalent circuit

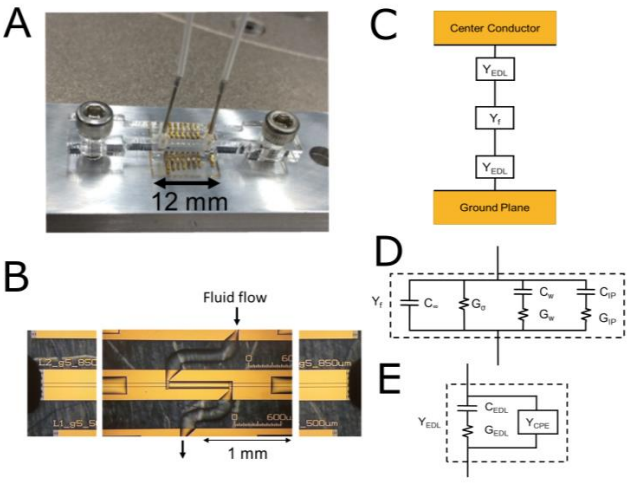


Fig. 1 Device design and measurement setup. (A) Image of microwave microfluidics device. (B) Composite microscope image of microfluidic channels with microwave probes landed. (C-E) Circuit model that describes the admittance of (C) the CPW, (D) fluid $Y_f$, and (E) the EDL $Y_{EDL}$.

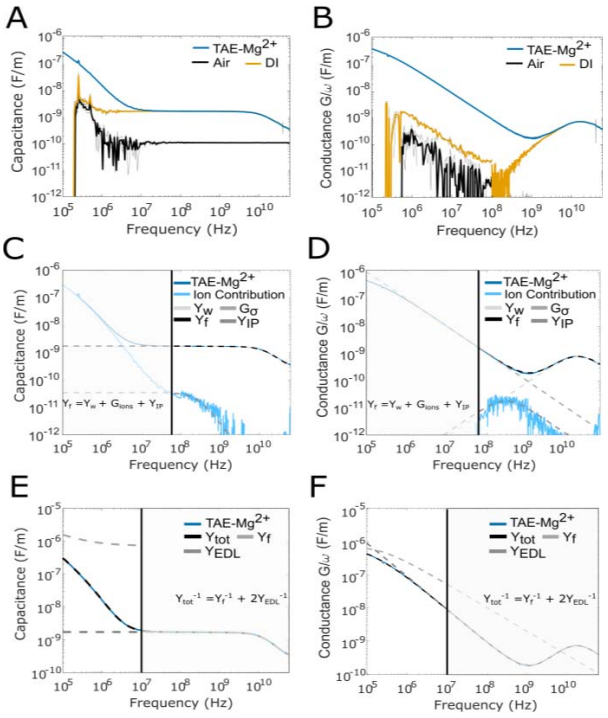


Fig. 2. (A) Broadband capacitance $C$ and (B) conductance $G$ per-unit-length of air, DI water and TAE-$Mg^{2+}$ buffer. (C, D) Fitting procedure of high-frequency response of TAE-$Mg^{2+}$ (dark blue solid line) with regions of fitting assigned for the water, ion and relaxations. Fit of (C) $C_f$ and (D) $G_f$ (black), fit of $C_w$ and $G_w$ (light gray), fit of $C_{ions}$ and $G_{ions}$ (medium gray), ion contribution (difference between data and $Y_w + G_\sigma$, light blue), and $G_\sigma$ (gray in (D)). (E, F) Fit of $C_{tot}$ and $G_{tot}$ (black), fit of $C_f$ and $G_f$ (gray) and fit of $C_{EDL}$ and $G_{EDL}$ (light gray). Shaded regions indicate regions of data not included in the fitting step.



Stelson, Angela; Little, Charles; Orloff, Nathan; Long, Christian; Booth, James.
"Measuring Ion-Pairing in Buffer Solutions with Microwave Microfluidics."
Paper presented at 2018 IEEE/MTT-S International Microwave Biomedical Conference, Philadelphia, PA, United States. June 14, 2018 - June 15, 2018.

model based on Debye-type relaxations, we can utilize broadband microwave measurements to extract physical parameters associated with these relaxations. Here we compare a three Debye model where $\alpha_w = 0$ with a Cole-Cole/Debye model, where $C_{IP} = 0$ .

## III. Results

### *D. Broadband Microwave Measurements: $C_{tot}$ and $G_{tot}$*

The calibrated distributed conductance and capacitance for measurements of air, de-ionized water (DI water), and TAE-$Mg^{2+}$ buffer is shown in Figs. 2a and 2b. To interpret the electromagnetic properties of the buffer over six decades of frequency, we assign regions of the frequency spectrum physical meaning for $C_{tot}$ and $G_{tot}$. Below 10 MHz, there is a peak in the conductance and a drop in the capacitance in the buffer, which we attribute to the relaxation of the EDL. The capacitance contribution from the EDL was significant compared to the fluid, approximately two to three orders of magnitude larger than the capacitance of the DI-loaded CPW. The bulk ionic conductivity $G_{tot}/\omega$ (region of constant slope from 10 MHz-1 GHz) increases in ionic solutions much like behavior of the TAE-$Mg^{2+}$ buffer. At approximately 20 GHz, the relaxation is due to the cooperative relaxation of water molecules.

### *E. Fitting Procedure for $Y_{tot}$*

To fit each relaxation with a Debye model, we performed a two-step fitting process. First, we modeled the high-frequency data (70 MHz- 67 GHz) to extract the water and ion relaxations, as well as the bulk fluid conductance $G_\sigma$. From this, we constructed the fluid capacitance and conductance (where $Y_f = G_f + i\omega C_f$), pictured in Figs. 2C-D (black dotted line). This model is the sum of the water Debye relaxation, the ion-pairing Debye relaxation and conductance associated with the ions. We propagated the fit parameters of $Y_f$ to lower frequencies (100 kHz-10 MHz) to fit the EDL region and extract $Y_{EDL}$ (fit pictured in Figs. 2e-f). The fit of the suspension $Y_{tot}$ agrees with the calibrated measured $C_{tot}$ and $G_{tot}$ from 100 kHz to 67 GHz. The relaxation of the EDL was also pictured (light gray dotted line). Because we propagated fit parameters from the high frequency regime to the EDL regime, the overall fit was sensitive to small relaxation peaks at intermediate frequencies, which perturbed the EDL fit.

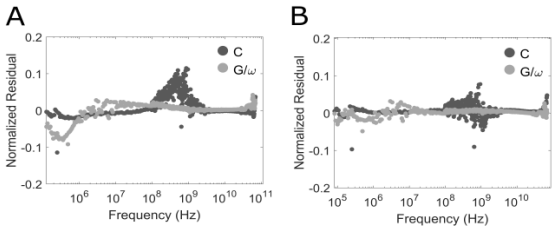


Fig. 3. Residuals of $Y_{tot}$ fit normalized by the fit for (A) Cole-Cole/Debye fit of water with no ion-pairing for the high-frequency fit and (B) Three Debye fit with water, ion-pairing and EDL relaxations).

### *F. Goodness of Fit*

Including the ion relaxation peak was necessary in TAE-$Mg^{2+}$ buffer measurements to produce Debye-type relaxations for the EDL and resulted in overall lower residuals across the high frequency regime. Fig. 3 compares residuals for a Cole-Cole/Debye (Fig. 3A) model versus the three-Debye model (Fig. 3B). Including the ion-pairing relaxation results in smaller residuals more centered around zero along the full frequency spectrum. Systematic errors are smaller for the fit in both the high-frequency and the EDL regimes with the three-Debye model.

## IV. Conclusion

In this report, we demonstrated broadband electrical measurements of TAE-$Mg^{2+}$ buffer. We extracted physical parameters associated with dipolar relaxations in the fluid, and compared two models to fit the data (Cole-Cole/Debye and three-Debye). The three-Debye model has a better fit over the entire data range, demonstrating the necessity of including the ion-pairing relaxation. These broadband measurements can inform more sensitive narrowband measurements, which may be more cost-effective and lead to real-time assessment of biological systems.


## Acknowledgment

This paper is an official contribution of NIST; not subject to copyright in the US. Usage of commercial products herein is for information only; it does not imply recommendation or endorsement by NIST.


## References


[1] J. Leroy *et al.*, "Microfluidic biosensors for microwave dielectric spectroscopy," *Sensors Actuators, A Phys.*, vol. 229, pp. 172–181, 2015.

[2] A. C. Sabuncu, J. Zhuang, J. F. Kolb, and A. Beskok, "Microfluidic impedance spectroscopy as a tool for quantitative biology and biotechnology," *Biomicrofluidics*, vol. 6, no. 3, 2012.

[3] K. Grenier *et al.*, "Recent advances in microwave-based dielectric spectroscopy at the cellular level for cancer investigations," *IEEE Trans. Microw. Theory Tech.*, vol. 61, no. 5, pp. 2023–2030, 2013.

[4] C. A. E. Little, N. D. Orloff, I. E. Hanemann, C. Long, V. M. Bright, and J. C. Booth, "Modeling Electrical Double-Layer Effects for Microfluidic Impedance Spectroscopy from 100 kHz to 110 GHz," *Lab Chip*, vol. 17, pp. 2674–2681, 2017.

[5] A. Solutions *et al.*, "Is There an Anionic Hofmeister Effect on Water Dynamics ? Dielectric Spectroscopy of," pp. 8675–8683, 2005.

[6] R. B. Marks, "A Multiline Method of Network Analyzer Calibration," *IEEE Trans. Microw. Theory Tech.*, vol. 39, no. 7, pp. 1205–1215, 1991.

[7] D. F. Williams and D. K. Walker, "Series-Resistor Calibration," in *50th ARFTG Conference Digest*, 1997, pp. 131–137.





Stelson, Angela; Little, Charles; Orloff, Nathan; Long, Christian; Booth, James.
"Measuring Ion-Pairing in Buffer Solutions with Microwave Microfluidics."
Paper presented at 2018 IEEE/MTT-S International Microwave Biomedical Conference, Philadelphia, PA, United States. June 14, 2018 - June 15, 2018.

# Importance of Preserving Correlations in Error-Vector-Magnitude Uncertainty

Benjamin F. Jamroz, Dylan F. Williams, Kate A. Remley, Robert D. Horansky
National Institute of Standards and Technology

***Abstract*—Correlations between measurement records, e.g. frequencies or time records, are an important consideration in the uncertainty analysis of high-frequency electronic systems. To study the importance of preserving correlations, we introduce a method to scramble the correlations of a correlated uncertainty analysis and develop a software tool to do this as part of the NIST Microwave Uncertainty Framework. We then compare the results of a correlated uncertainty analysis and the corresponding scrambled analysis in estimating the uncertainty in the Error-Vector-Magnitude of a modulated signal. This comparison shows that preserving these correlations is critical to accurately assessing system performance and uncertainty.**

***Index Terms*—measurement uncertainty, Monte Carlo methods, digital modulation, error-vector-magnitude.**

## I. Introduction

Uncertainty analysis is an essential element in designing and deploying microwave and millimeter-wave electronic systems. At high frequencies, as electronic components become less ideal, correlations between records of system response can become significant. These correlations can occur across frequencies, time points or, for modulated signals, symbols. Correlated uncertainty analyses can incorporate physical errors and accurately estimate the resulting effects on the system. This is apparent in frequency or time records as these data are transformed between the frequency and time domains where, for example, a frequency domain signal with an oscillatory correlated uncertainty profile may correspond to a pulse-like uncertainty profile in the time domain [1].

Error-Vector-Magnitude (EVM) is a common figure of merit for evaluating the accuracy of digitally modulated signals [2]. Recently, [3] a covariance-based correlated uncertainty analysis was performed for modulated signals from a precision source at 44 GHz using the NIST Microwave Uncertainty Framework (MUF) [4] to determine the uncertainty in EVM.

We develop a technique and software tool to allow us to test the effect of preserving correlated uncertainties and show, in a simple example, how scrambling these correlations, while preserving the variances but not the covariances, can substantially modify the results of uncertainty analyses.

## II. Correlated Uncertainties

Covariance-based uncertainty analyses as outlined in [1] and implemented in the MUF [4], are capable of propagating uncertainties through complex transformations while preserving correlations. These correlations can be attributed to systematic errors in underlying physical components or from a distribution of realized measurements. For example, if we measure the length of a line in a calibration standard the error in the measurement will induce a correlated uncertainty profile in all corrected measurements that use this standard. In addition to accurately estimating the overall uncertainty, these correlations constrain the realization of deviations from a nominal value. In order to test the importance of preserving correlations, we developed a method to scramble these correlations, modifying the covariances while preserving the variances.

### A. Sensitivity Analysis

A sensitivity analysis of a measurement can be defined as a collection of deviations from a nominal value, with each deviation attributed to a unique mechanism. Following the notation in [1], we can write the covariance matrix provided by a sensitivity analysis as $\Sigma_{\mathrm{SA}} = (\mathbf{J}_\sigma)(\mathbf{J}_\sigma)^T$, where $\mathbf{J}_\sigma$ is a $K \times N$ matrix where the $N$ columns are defined as sensitivity analysis vectors $\{\mathbf{S}_n\}_{n=1}^N$ of multivariate dimension $K$. Here the $n$th mechanism is perturbed by its standard uncertainty, transformations are applied (e.g., transforming between the time and frequency domains), and the resulting deviation from the nominal value of the measurement defines $\mathbf{S}_n = (S_{1,n}, S_{2,n}, \ldots, S_{K,n})^T$.

To change the covariances but preserve the variances of the sensitivity analysis, we "scramble" the correlations of the sensitivity analysis vectors by resampling these vectors at each multivariate component (i.e. permuting the columns of each row of $\mathbf{J}_\sigma$) and multiply by a randomly chosen $\pm 1$ to create a new collection of sensitivity analysis vectors $\{\mathbf{S}_n^{\mathrm{CB}}\}_{n=1}^N$. Thus at each multivariate index, $i = 1, \ldots, K$,

$$S_{i,n}^{\mathrm{CB}} = \gamma_{i,n} S_{i,\tilde{n}_{i,n}}, \tag{1}$$

where each $\tilde{n}_i = \{\tilde{n}_{i,n}\}_{n=1}^N$ is an index set drawn randomly without replacement from the original set of $n = 1, \ldots, N$ and $\gamma_{i,n}$ is randomly drawn from the set $\{-1, 1\}$. The $\gamma_{i,n}$ terms are added as the sensitivity analysis assumes symmetric distributions and produces identical results in either case.

### B. Monte Carlo Analysis

A Monte Carlo uncertainty analysis consists of a sample of Monte Carlo replicates $\{\mathbf{M}_q\}_{q=1}^Q$, where each $\mathbf{M}_q = (M_{1,q}, M_{2,q}, \ldots, M_{K,q})^T$ corresponds to a realization of all of the underlying error mechanisms propagated through the required transformations. An innate feature of this type of uncertainty analysis is that each of the Monte Carlo replicates has preserved the correlation with the underlying mechanisms through these transformations. The mean of the Monte Carlo sample $\overline{\mathbf{M}}$. represents a physically realistic estimate of the expected value of the measurement while the distribution



Jamroz, Benjamin; Williams, Dylan; Remley, Catherine; Horansky, Robert.
"Importance of Preserving Correlations in Error-Vector-Magnitude Uncertainty."
Paper presented at 91st ARFTG Microwave Measurement Symposium, Philadelphia, PA, United States. June 15, 2018 - June 15, 2018.

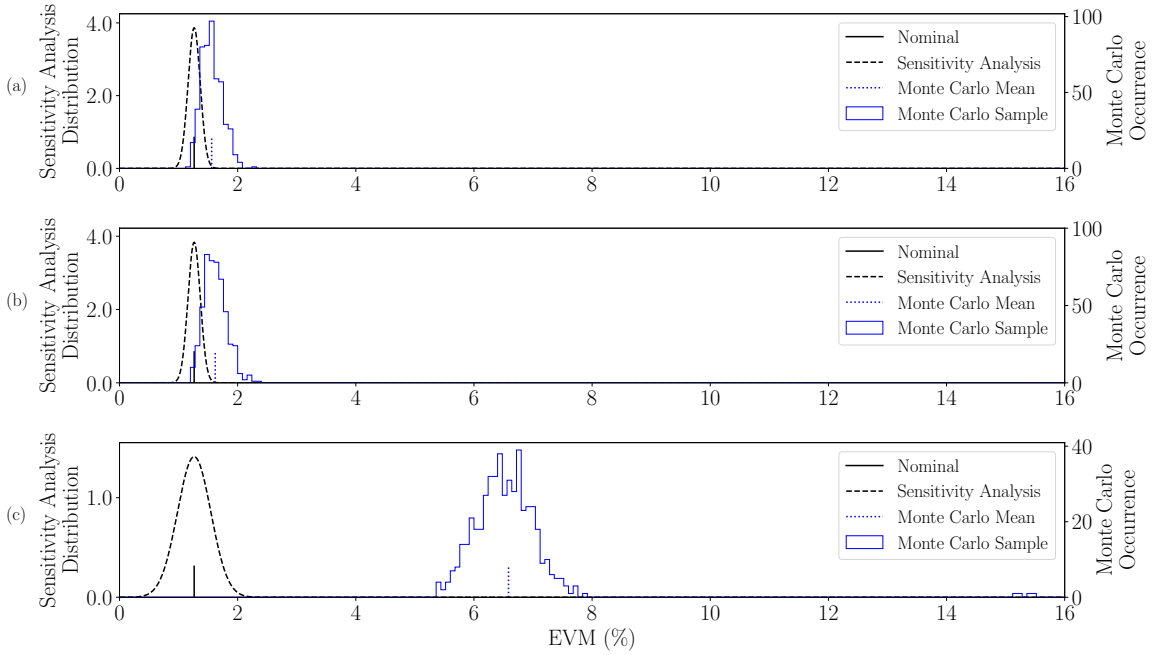


Fig. 1: EVM uncertainty analysis results (following [3]) using (a) a model for an ideal cable (b) the actual cable measurement with correlated uncertainties and (c) the actual cable with a scrambled uncertainty analysis. The mean of the Monte Carlo sample goes from 1.56% and 1.62% in the correlated analyses to 6.59% in the scrambled analysis. Statistics from these plots are shown in Table I.

of the sample about the mean defines a coverage interval corresponding to the likelihood that a value falls in this range. Additionally, the standard deviation of the distribution can be used as an estimate of the standard uncertainty [5].

To modify the covariances but preserve the variances, we obtain a new Monte Carlo sample $\{\mathbf{M}_q^{\text{CB}}\}_{q=1}^{Q}$ by resampling at each multivariate component, $i = 1, \ldots, K$,

$$M_{i,q}^{\text{CB}} = M_{i,\tilde{q}_{i,q}}, \tag{2}$$

where each $\tilde{q}_i = \{\tilde{q}_{i,q}\}_{q=1}^{Q}$ is drawn randomly without replacement from the original set of $q = 1, \ldots, Q$ as above.

### C. Conservation of Variance

Equations (1) and (2) show how to scramble correlations across a multivariate sensitivity analysis and Monte Carlo sample. We now show that these resampled distributions preserve variances as calculated from the original distribution.

For multivariate component $i$, the variance corresponding to the sensitivity analysis, i.e., the $i$th diagonal entry of the covariance matrix $\Sigma_{\text{SA}}$, can be written $\sum_{n=1}^{N} S_{i,n}^2$. The variance corresponding to the scrambled sensitivity analysis vectors can be shown to be identical to those of the original analysis as

$$\sum_{n=1}^{N} \left(S_{i,n}^{\text{CB}}\right)^2 = \sum_{n=1}^{N} \gamma_{i,n}^2 S_{i,\tilde{n}_{i,n}}^2 = \sum_{n=1}^{N} S_{i,n}^2.$$

This relationship also holds for the two Monte Carlo samples where we obtain the same variances in the distribution about the mean ($\overline{\mathbf{M}}_\cdot$).

Note that although the resampled distribution preserves variance, transforming the data (say from the frequency domain to the time domain) may lead to a change in the variance between the two distributions.

### D. MUF "Correlation Buster"

The above methodology for scrambling correlations has been introduced as a tool, the "Correlation Buster", in the NIST MUF to facilitate investigations into the importance of preserving correlations in uncertainty analyses. The MUF represents measurements with uncertainty as a collection of the nominal value, sensitivity analysis vectors, and Monte Carlo replicates. This collection can be used to define a new measurement with the same overall uncertainty but with significantly different correlations by resampling the sensitivity analysis vectors and Monte Carlos replicates, as in (1) and (2).

## III. Correlated Uncertainties in EVM

EVM is an important metric for characterizing the accuracy of a received modulated-signal waveform transmitted and received in a nonideal system [2]. EVM is calculated by comparing the relative difference between a received demodulated waveform and the symbols of the corresponding modulation scheme.

Jamroz, Benjamin; Williams, Dylan; Remley, Catherine; Horansky, Robert.
"Importance of Preserving Correlations in Error-Vector-Magnitude Uncertainty."
Paper presented at 91st ARFTG Microwave Measurement Symposium, Philadelphia, PA, United States. June 15, 2018 - June 15, 2018.

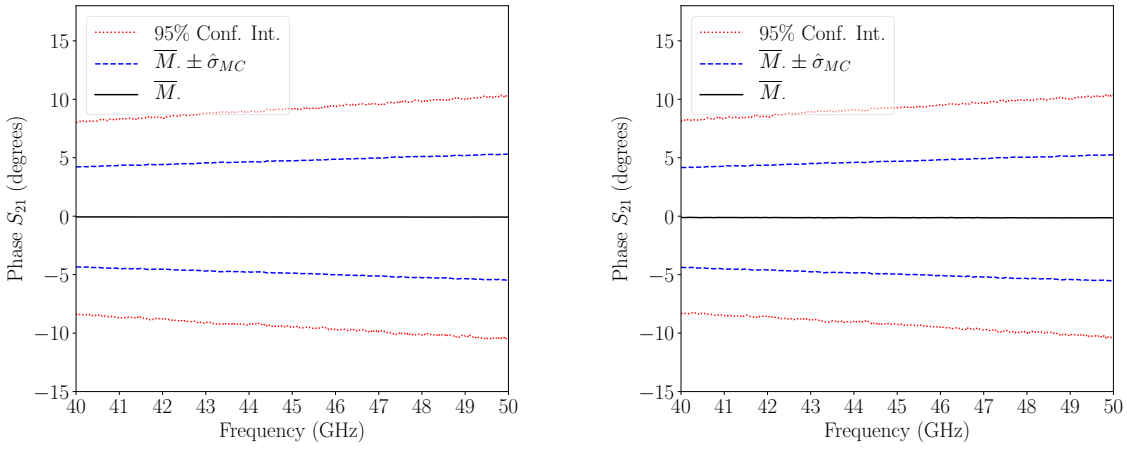


Fig. 2: Monte Carlo analysis of phase uncertainty corresponding to (a) the correlated MUF uncertainty analysis and (b) the scrambled uncertainty analysis using the Correlation Buster. The mean of the Monte Carlo sample $\overline{\mathbf{M}}.$, the range within the standard deviation of the sample $\hat{\sigma}_{\text{MC}}$, and the 95% confidence interval of the sample is shown. We see that the frequency-dependent uncertainties are nearly identical and the standard uncertainty in phase is approximately five degrees.

TABLE I: EVM statistics for the MUF analysis (MUF) and the scrambled analysis using the Correlation Buster (CB) using an ideal through (Ideal) or a cable measurement with uncertainty (Cable). We show the nominal value, the mean of the Monte Carlo sample $\overline{\mathbf{M}}.$, the standard uncertainty as calculated by the sensitivity analysis $\hat{\sigma}_{\text{SA}}$ and the standard deviation of the Monte Carlo sample $\hat{\sigma}_{\text{MC}}$.

| | Nominal | $\overline{\mathbf{M}}.$ | $\hat{\sigma}_{\text{SA}}$ | $\hat{\sigma}_{\text{MC}}$ |
|---|---|---|---|---|
| MUF - Ideal | 1.26 | 1.56 | .103 | .178 |
| MUF - Cable | 1.26 | 1.62 | .104 | .191 |
| CB - Cable | 1.26 | 6.59 | .283 | .910 |

One of the first components of any EVM algorithm is to time shift the received signal to determine the optimal sampling times. The time-shifted, demodulated, and sampled signal creates an I/Q trajectory on a constellation diagram. EVM is the normalized sum of the squared distance between ideal symbols and the received I/Q samples.

Several studies have investigated methods for estimating uncertainty in EVM measurements [6], [7] and the IEEE P1765 standards development working group is developing a recommended practice for estimating the uncertainty of EVM in modulated signals for wireless communications. Recently, [3] performed a covariance-based correlated uncertainty analysis using the MUF of a 1-GSymbol/sec, 64-state quadrature-amplitude-modulated (64-QAM) signal at 44 GHz including errors in the source and the receiver. The uncertainty analysis also included a characterization of the cable connecting the source and receiver under multiple bends.

In Figure 1(a) and (b) we reproduce the results of [3] modeling the cable with an ideal cable and with the actual cable including correlated uncertainties, respectively. We see the nominal EVM for both cases is $1.26\%$, while the mean of the Monte Carlo sample is $1.56\%$ for the ideal case and $1.62\%$ when including the cable and its uncertainties. Next, we applied the NIST Correlation Buster to scramble the correlations of the uncertainty analysis of (b) before converting to time domain, aligning the signals and calculating the EVM. The results of this scrambled analysis are shown in Fig. 1(c) and all of these results are tabulated in Table I. In the scrambled analysis we see a dramatic increase in EVM for the Monte Carlo sample which has a mean of 6.59%. Additionally, we see large increases in both the standard uncertainty, as calculated by the sensitivity analysis, and the standard deviation of the Monte Carlo sample.

## IV. Discussion

As shown in Fig. 1, scrambling the correlations has a significant effect on the EVM of the entire Monte Carlo sample. To analyze a potential cause for this, we look at the uncertainty of the scattering parameters of the cable due to bending. Figure 2(a), shows the Monte Carlo uncertainty analysis of the phase of the $S_{21}$ transmission coefficient of the cable averaged over ten different bending states as in [3] where we see a standard deviation of about five degrees. The uncertainty in phase of $S_{21}$ of this cable after running the Correlation Buster is shown in Fig. 2(b) where we see an almost identical uncertainty at each frequency. However, the underlying uncertainties have a different covariance structure.

Jamroz, Benjamin; Williams, Dylan; Remley, Catherine; Horansky, Robert.
"Importance of Preserving Correlations in Error-Vector-Magnitude Uncertainty."
Paper presented at 91st ARFTG Microwave Measurement Symposium, Philadelphia, PA, United States. June 15, 2018 - June 15, 2018.

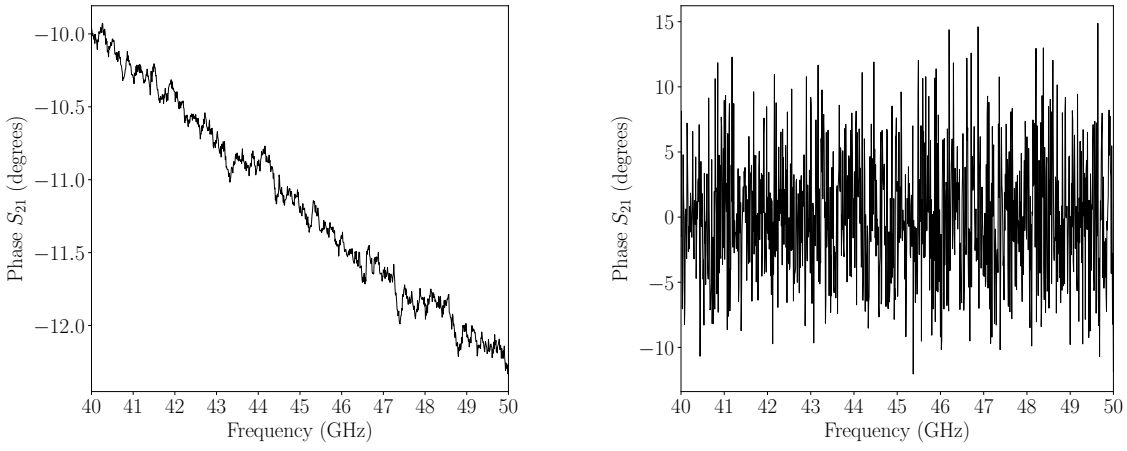


(a) (b)

Fig. 3: A typical Monte Carlo replicate for the transmission ($S_{21}$) of the cable for (a) the original MUF uncertainty analysis and (b) the MUF uncertainty analysis where the correlations have been scrambled using the Correlation Buster. We see that a linearly correlated trend in the original MUF analysis is resampled to provide a quasi-random phase variation by the Correlation Buster.

Although the total uncertainty is preserved, the cross-frequency correlations are modified by the Correlation Buster. We plot a representative Monte Carlo replicate from both the MUF correlated analysis and the scrambled analysis in Figs. 3(a) and (b) respectively. Here we see a linear trend as a function of frequency in the Monte Carlo replicate from the original analysis, while the replicate from the scrambled analysis has random phase errors. The linear frequency domain trend in Fig. 3(a) corresponds to a time offset in the time domain. The time shift of the signal in the EVM algorithm corrects for such a time offset. However, the distortion caused by the random phase errors in the scrambled analysis is not corrected.

This shows that the uncertainty analysis which preserves cross-frequency correlations can constrain the uncertainties so that the effect of time offsets can be corrected. Prescribing an *a priori* uncertainty bound without such constraints can introduce unphysical distortion and either underestimate (as is the case here) or overestimate the measured performance and uncertainty of a system.

## V. Conclusion

We have highlighted the importance of preserving correlations in the uncertainty analysis of microwave and millimeter-wave systems. We used the NIST MUF to reproduce the covariance-based correlated uncertainty analysis of a modulated signal as in [3]. We introduced a method which scrambles correlations while preserving overall uncertainty and introduced a tool in the MUF to create scrambled analyses.

We showed that the original correlated phase uncertainty in the transmission of a coaxial cable due to cable bending led to a time offset which is typically corrected by time shifting in an EVM algorithm. However, scrambling these correlations led to distortion of the signal which was not corrected and significantly increased EVM and the associated uncertainty.

This analysis presented a clear example of why tracking correlated uncertainties is important and how correlated uncertainty analysis can significantly impact measures of system performance and uncertainty.

## References

[1] A. Lewandowski, D. F. Williams, P. D. Hale, J. C. M. Wang, and A. Dienstfrey, "Covariance-based vector-network-analyzer uncertainty analysis for time- and frequency-domain measurements," *IEEE Transactions on Microwave Theory and Techniques*, vol. 58, no. 7, pp. 1877–1886, Jul. 2010.

[2] M. McKinley, K. A. Remley, M. T. Myslinski, J. Kenney, D. Schreurs, and B. Nauwelaers, "EVM calculations for broadband modulated signals," in *2004 64th ARFTG Microwave Measurement Conference (ARFTG)*. IEEE, Dec. 2004.

[3] K. A. Remley, D. F. Williams, P. D. Hale, C.-M. Wang, J. Jargon, and Y. Park, "Millimeter-wave modulated-signal and error-vector-magnitude measurement with uncertainty," *IEEE Transactions on Microwave Theory and Techniques*, vol. 63, no. 5, pp. 1710–1720, May 2015.

[4] D. F. Williams, "NIST Microwave Uncertainty Framework," https://www.nist.gov/services-resources/software/wafer-calibration-software, accessed: 2018-02-05.

[5] *Evaluation of measurement data - Supplement 1 to the Guide to the expression of uncertainty in measurement - Propagation of distributions using a Monte Carlo method*, ISO, Geneva Switzerland, 2008.

[6] D. A. Humphreys and J. Miall, "Traceable measurement of source and receiver EVM using a real-time oscilloscope," *IEEE Transactions on Instrumentation and Measurement*, vol. 62, no. 6, pp. 1413–1416, Jun. 2013.

[7] C. Cho, J.-G. Lee, J.-H. Kim, and D.-C. Kim, "Uncertainty analysis in EVM measurement using a Monte-Carlo simulation," in *29th Conference on Precision Electromagnetic Measurements (CPEM 2014)*. IEEE, Aug. 2014.

Jamroz, Benjamin; Williams, Dylan; Remley, Catherine; Horansky, Robert.
"Importance of Preserving Correlations in Error-Vector-Magnitude Uncertainty."
Paper presented at 91st ARFTG Microwave Measurement Symposium, Philadelphia, PA, United States. June 15, 2018 - June 15, 2018.

# Impact of Phase Calibration on EVM Measurement Quality

Diogo C. Ribeiro[a], Dylan F. Williams[b], Richard A. Chamberlin[b] and Nuno Borges Carvalho[a]
[a]Universidade de Aveiro - DETI, Instituto de Telecomunicações, Aveiro, Portugal
[b]NIST Communications Technology Laboratory, Boulder, CO 80305, USA

***Abstract*—In this paper, the calibrated measurement of wideband modulated signals by mixer-based large-signal network analyzers (LSNAs) will be evaluated, with a focus on the impact of the phase calibration in the error vector magnitude (EVM). The influence of the phase-reference standard on the $EVM_{RMS}$ will be addressed. The uncertainties of the $EVM_{RMS}$ results will also be analyzed.**

***Index Terms*—modulated signal measurements, uncertainties.**

## I. Introduction

Large-signal network analysis is becoming increasingly important to radio engineers. With the prospects of 5G communications migrating to even higher frequencies, a measurement apparatus capable of measuring wideband signals, together with mismatch correction, is important.

The LSNA is an instrument suitable for this task. One popular version is built upon a mixer-based network analyzer architecture. It is capable of measuring signals up to very high frequencies, well within the mm-Wave regions that are being considered for 5G communications.

This instrument's instantaneous bandwidth is limited, but at the expense of a longer measurement time, it is capable of measuring very wideband signals, frequency by frequency. An always present phase-reference, together with an additional phase calibration procedure, are used to obtain a phase-calibrated result. During the phase calibration procedure, a phase-reference standard needs to be measured, which usually is a pre-characterized comb-generator, [1].

When using an LSNA to measure a modulated signal and determine some of its signal quality metrics, such as EVM, a signal with a long period needs to be preferably used, as will be further discussed in section II. This requires increasing the period of the comb-generator, which causes the output power of each frequency tone from comb-generator to decrease, [2].

In this work, the dependence of the EVM on the phase calibration procedure is evaluated when using an LSNA to measure modulated signals. The EVM calculations were performed using an implementation of the definition in [3]. The uncertainty analysis was performed with the National Institute of Standards and Technology's (NIST) Microwave Uncertainty Framework (MUF). The uncertainty calculated for each signal measurement was propagated through the EVM calculation algorithm to provide final EVM results with uncertainties, following what was done in [4].

## II. The requirement for a long duration signal

When measuring the EVM of a modulated signal, the deviation of each measured symbol position in the constellation from its corresponding ideal position is assessed, [3]. For this metric to be calculated accurately and well determined statistically, a large number of values need to be measured at each constellation point.

This means that the greater the number of symbols at each constellation point, the more accurately the EVM will correspond to the device's behavior. This requires a signal that has a higher period, so that more symbols can be represented.

This necessity is accentuated when measuring high-order modulation signals. For example, to measure the EVM of a 64-quadrature amplitude modulation (QAM) modulation, a signal with 64 symbols may give only one symbol per constellation point. Thus, the number of symbols needed is proportional to the order of the modulation.

### A. Impact on the LSNA measurement

When using the LSNA to evaluate the EVM of modulated signals, two contrary conditions need to be considered: on the one hand, the number of symbols to evaluate needs to be as high as possible, so that the obtained EVM values are statistically meaningful; on the other hand, the maximum period duration of the signal is limited by the minimum frequency spacing that can be achieved.

The period of the signal is limited by the minimum frequency spacing achievable by the phase-calibrated measurement. As previously mentioned, when using a comb-generator as a phase-reference, its output power decreases with the frequency spacing, [2]. This means that the signal-to-noise ratio (SNR) of the comb-generator reading also decreases (if other conditions are maintained).

It is worth remembering that the low SNR affects two wave acquisitions: the wave from the calibration comb-generator and the wave from the reference comb-generator. The calibration comb-generator is only measured during the phase calibration stage, usually through the LSNA's internal coupler, which means an even lower power will be received; therefore, it will limit the measurement in terms of SNR. The reference comb-generator is used at all times, including during the phase calibration stage. This influence through different (and simultaneous) contributions means that the low output power per tone of the comb-generators may have a considerable impact in the final absolute phase results. Note that this does

Ribeiro, Diogo; Williams, Dylan; Chamberlin, Richard; Carvalho, Nuno.
"Impact of Phase Calibration on EVM Measurement Quality."
Paper presented at 91st ARFTG Microwave Measurement Symposium, Philadelphia, PA, United States. June 15, 2018 - June 15, 2018.

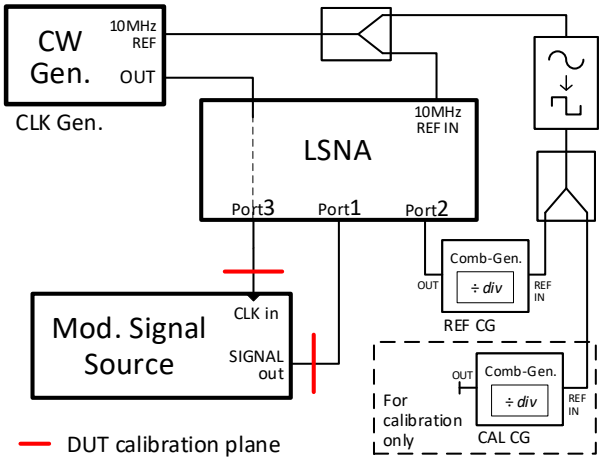


Fig. 1. Block diagram of the measurement setup used.

not result from a higher phase-noise at the output of the comb-generator, but from a lower measurement SNR.

## III. Measurement Setup

A block diagram of the measurement setup is shown in Fig. 1. The setup was configured around the LSNA (a Keysight N5245A[1]), with two Keysight U9391F[1] comb-generators.

### A. Measurement configuration

The clock (CLK) frequency used for the generation of all the signals was 2 GHz, and the carrier frequency was 630 MHz (within the 1st Nyquist zone of the modulated signal source). Signals with three different modulations were evaluated: 64-QAM, 16-QAM and QPSK, all with a baseband symbol rate of 480 MSymbols/s. Additional settings applied to all signals: a raised cosine baseband filter with a roll-off factor $\beta$ of 0.35; and the signal bandwidth was truncated to 712.5 MHz (approximately 10% more than $(1+\beta)\times$ symbol rate).

All the modulated signals were predistorted in order to generate the lowest EVM values, [4], based on a characterization of the modulated signal source, [5], realized with the same LSNA. The low EVM of the signals was confirmed by measuring them using an equivalent-time oscilloscope.

The duration of all signals was 800 nsec, which resulted in a total of 384 Symbols. Since the different modulation schemes have a different number of constellation points, a constant symbol duration for all different signals leads to a different number of symbols per constellation position, for each signal. The number of symbols per constellation position for each modulation scheme is as follows:

**QPSK** $\rightarrow$ 92 symbols per constellation point
**16-QAM** $\rightarrow$ 24 symbols per constellation point
**64-QAM** $\rightarrow$ 6 symbols per constellation point

[1]We use brand names only to describe the experiment accurately. National Institute of Standards and Technology (NIST) does not endorse commercial products. Other products may work as well or better.

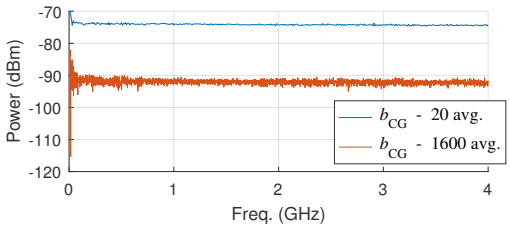


Fig. 2. Magnitude spectra of the calibrated incident and reflected waves from a single reading of the calibration comb-generator, with two different frequency spacing configurations: 10 MHz and 1.25 MHz. Measurements from 10 MHz to 4 GHz, in frequency steps equal to the comb-generator frequency spacing. The LSNA's IF BW for the 10 MHz reading was 100 Hz, while for the 1.25 MHz spacing, it was 30 Hz.

The symbols for each modulation scheme were generated randomly and independently, but with the following constraint: the number of symbols per constellation position needs to be the same, i.e. the symbols need to be well distributed throughout the constellation.

The frequency of the phase-reference was set to 1.25 MHz (10 MHz $\div$ 8), which corresponds to a reference period equal to the signal duration under measurement. Due to this low necessary reference frequency, the power of each tone at the output of the comb-generator is very low.

### B. Comb-generator power impact

Compared to a 10 MHz frequency spacing, the finer steps led to a power reduction, at the output of each comb-generator, of around 18 dB per tone, as can calculated from [2, eq. (1)].

Fig. 2 shows the calibrated wave $b_{CG}$ (in the outward direction from the comb-generator) when the frequency spacing on the comb-generator was set to 10 MHz and 1.25 MHz for a single acquisition (with no average). Note that $b_{CG}$ looks much noisier in the case of 1.25 MHz frequency spacing, than 10 MHz; besides having a lower power level, as expected. This is easily visible, even considering that the IF BW was reduced from 100 Hz to 30 Hz.

## IV. Results

To evaluate the impact of the comb-generator's low output power on the LSNA absolute calibration, different numbers of averages of the comb-generator readings were considered when performing the calibrations. Only the number of the comb-generator readings to average is swept, the raw signals we applied the calibration to were exactly the same (no averaging was done). In this evaluation the number of comb-generator readings we averaged was swept from 20 to 1600. Only 1600 consecutive comb-generator readings were performed, with the lower number of averages being subsets of these 1600 consecutive comb-generator readings.

Fig. 3 shows the nominal $EVM_{RMS}$ results for the different number of comb-generator averages (for all three modulations). As can be seen, in all cases, the $EVM_{RMS}$ decreases for higher number of comb-generator averages, showing the impact that the phase calibration step has on the final measured

Ribeiro, Diogo; Williams, Dylan; Chamberlin, Richard; Carvalho, Nuno.
"Impact of Phase Calibration on EVM Measurement Quality."
Paper presented at 91st ARFTG Microwave Measurement Symposium, Philadelphia, PA, United States. June 15, 2018 - June 15, 2018.

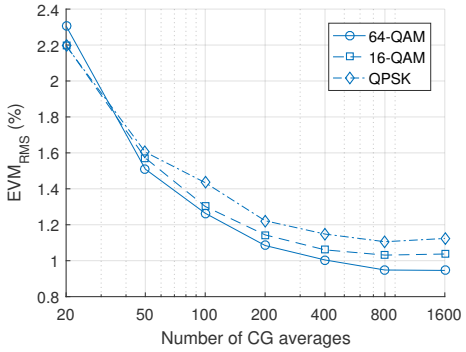


Fig. 3. Nominal $EVM_{RMS}$ values for the three modulations when calibrating the LSNA with the different number of comb-generator averages.

results. It can be seen that the nominal $EVM_{RMS}$ begins to stabilize for more than 800 comb-generator averages.

As a first conclusion, it is worth highlighting the very high number of averages (of comb-generator readings) that were required, so that the impact of the phase calibration on the final results could be reduced. This result illustrates well the attention that should be paid to the phase calibration stage when performing absolute signal measurements.

However, achieving this very high number of reading averages is very time consuming. Specifically, the 1600 readings of the calibration comb-generator took 3 days and 4 hours[2].

### A. *Uncertainty analysis*

The results of the uncertainty analysis presented in this manuscript are only for the 64-QAM modulated signal. Similar results were obtained for the other modulations. The EVM calculation algorithm was developed internally and the uncertainties were propagated from the calibrated signal measurement to the final $EVM_{RMS}$ values.

Before the calculation of the $EVM_{RMS}$ value, the uncertainties of the calibrated signals can also be evaluated. The cumulative standard deviation as a function of frequency (for a bandwidth of 600 MHz around the carrier) was also evaluated for magnitude and phase over the number of comb-generator averages. In Fig. 4 the cumulative magnitude result (summation of dBs) based on both the sensitivity analysis and the Monte-Carlo analysis is shown. In Fig. 5, the cumulative phase result is shown. Note that the cumulative magnitude result does not change with the increase of comb-generator averages, while the cumulative phase result decreases with the increase of comb-generator averages, in a similar way to what was observed for the EVM result in Figs. 6 and 7. Based on this, it was verified that only the phase uncertainty varies with the variation of the number of comb-generator averages.

Fig. 6 shows the obtained nominal $EVM_{RMS}$ as well as the obtained standard deviation from the sensitivity analysis along

[2]The comb-generator readings were performed by acquiring data from only the 3 required receivers. The detailed LSNA settings were: IF BW of 30 Hz, frequency span from 10 MHz to 4 GHz in 1.25 MHz steps, with the 'Stepped sweep' option turned ON for accurate frequency positioning and the 'IF BW reduction at low frequencies' option also turned ON.

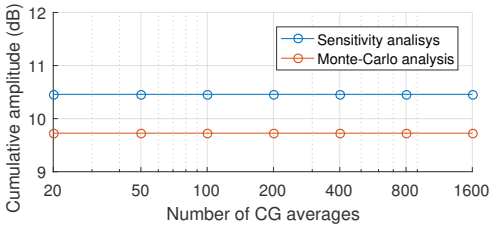


Fig. 4. Sum along frequency of standard uncertainty of reflected wave from sensitivity and from Monte-Carlo analysis

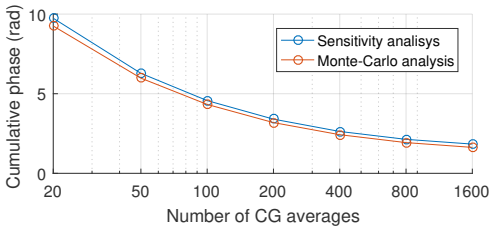


Fig. 5. Sum along frequency of standard uncertainty of reflected wave from sensitivity and from Monte-Carlo analysis

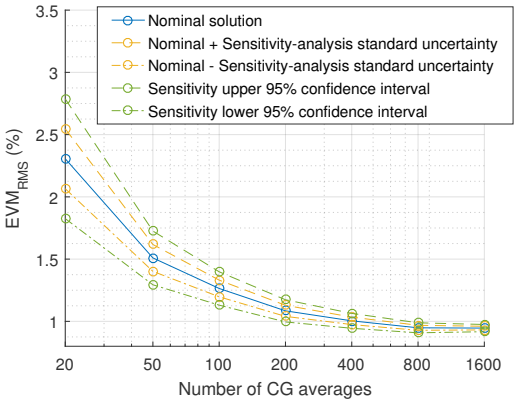


Fig. 6. Nominal $EVM_{RMS}$ value together with standard deviation from sensitivity analysis, for different number of comb-generator averages.

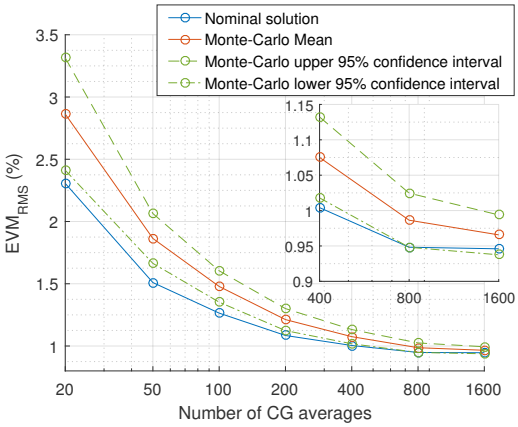


Fig. 7. Nominal $EVM_{RMS}$ value together with Monte-Carlo mean, higher and lower 95% confidence intervals, for different number of comb-generator averages.

Ribeiro, Diogo; Williams, Dylan; Chamberlin, Richard; Carvalho, Nuno.
"Impact of Phase Calibration on EVM Measurement Quality."
Paper presented at 91st ARFTG Microwave Measurement Symposium, Philadelphia, PA, United States. June 15, 2018 - June 15, 2018.

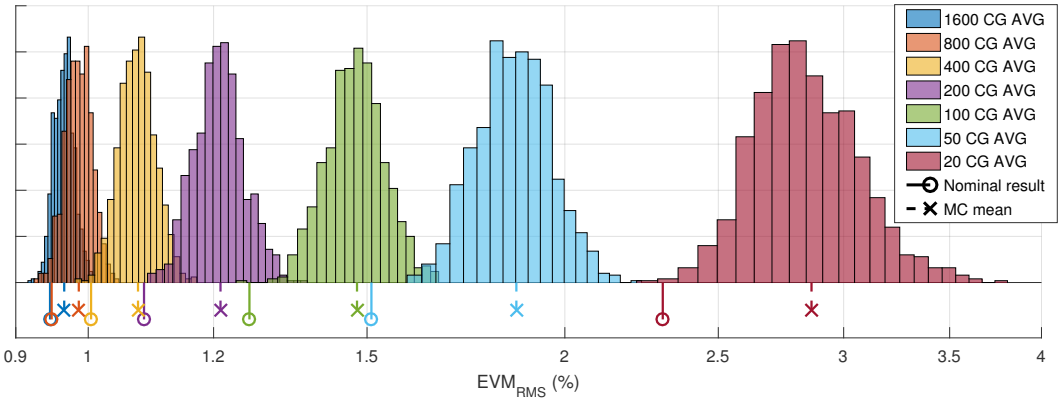


Fig. 8. Monte-Carlo histograms for each number of comb-generator averages used during the calibration stage. Histograms plotted on a logarithmic x-axis.

the number of considered comb-generator averages. Fig. 7 shows the same quantities, but for the results obtained from the Monte-Carlo analysis. The amplitude of the 95% confidence intervals agree for both analyses, however they are shifted to higher $\text{EVM}_{\text{RMS}}$ values, in Fig. 7, for the Monte-Carlo analysis.

From Fig. 7, it can clearly be seen that when using a low number of comb-generator averages, the nominal $\text{EVM}_{\text{RMS}}$ results are outside the 95% confidence intervals. Only with 1600 comb-generator averages was the nominal result within the confidence bounds. Similar results were obtained for the other evaluated modulated signals.

From the Monte-Carlo uncertainty analysis, it is also possible to get an histogram for each uncertainty analysis. These are shown in Fig. 8, on a logarithmic x-axis.

In Fig. 8, it can be seen that the nominal results are always at the lower extreme of each histogram. This is expected, as measurement errors are more likely to increase the measured $\text{EVM}_{\text{RMS}}$, not reduce it. Furthermore, each histogram gets narrower for a higher number of comb-generator averages, but the histograms are almost never contained within one another. They are consecutively shifted to lower $\text{EVM}_{\text{RMS}}$ values. Only, from 800 to 1600 comb-generator averages is possible to denote a partial overlap of the histograms.

These results show that increasing the number of averages in the phase calibration improves the EVM measured by the LSNA and decreases the uncertainty of the $\text{EVM}_{\text{RMS}}$ measurement, as expected. From this, we conclude that using a large number of averages to improve the phase calibration of the LSNA is important, as it allows us to decrease the phase uncertainty of the LSNA measurements and more accurately measure signals with low $\text{EVM}_{\text{RMS}}$ values. This is especially important when the LSNA is used to predistort a signal, as more averages allow the signal being predistorted to be generated more accurately.

Fig. 8 also illustrates the limitation that the uncertainty of the LSNA places on its ability to measure low values of EVM. For example, Fig. 8 indicates that our LSNA, when calibrated with 20 comb-generator averages may always measure an $\text{EVM}_{\text{RMS}}$ of about 2.5 % or higher. This is true, even if the actual actual $\text{EVM}_{\text{RMS}}$ of the signal is much lower, as it was in this case. This suggests that methods should be developed for estimating and subtracting the systematic bias that imperfect instruments with both noise and correlated systematic errors add to EVM measurements.

## V. Conclusion

In this work, the measurement of very wideband modulated signals was performed using a mixer-based LSNA. The influence of the comb-generator performance was evaluated for situations in which a low frequency spacing needs to be used. The low output power of the comb-generator, in the conditions of the tests we used, required the averaging of at least 800 comb-generator readings, in order to reduce its influence of the final calibrated $\text{EVM}_{\text{RMS}}$ results.

## Acknowledgment

The work of D. Ribeiro was supported by the PhD grant SFRH/BD/92746/2013, from F.C.T.; the author would also like to thank the ARFTG Roger Pollard Student Fellowship in Microwave Measurement.

## References

[1] W. Van Moer and L. Gomme, "NVNA versus LSNA: enemies or friends?" *IEEE Microw. Mag.*, vol. 11, no. 1, pp. 97–103, Feb 2010.

[2] D. C. Ribeiro, P. M. Cruz, and N. B. Carvalho, "Towards a denser frequency grid in phase measurements using mixer-based receivers," in *85th ARFTG Microwave Measurements Conf.*, May 2015, pp. 1–5.

[3] M. D. McKinley, K. A. Remley, M. Myslinski, J. S. Kenney, D. Schreurs, and B. Nauwelaers, "EVM Calculation for Broadband Modulated Signals," in *64th ARFTG Microwave Measurements Conf. Dig.*, Dec. 2004.

[4] K. A. Remley, D. F. Williams, P. D. Hale, C. M. Wang, J. Jargon, and Y. Park, "Millimeter-Wave Modulated-Signal and Error-Vector-Magnitude Measurement With Uncertainty," *IEEE Trans. Microw. Theory Techn.*, vol. 63, no. 5, pp. 1710–1720, May 2015.

[5] D. Ribeiro, A. Prata, P. Cruz, and N. Carvalho, "D-parameters: A Novel Framework for Characterization and Behavioral Modeling of Mixed-Signal Systems," *IEEE Trans. Microw. Theory Techn.*, vol. 63, no. 10, pp. 3277–3287, Oct 2015.

Ribeiro, Diogo; Williams, Dylan; Chamberlin, Richard; Carvalho, Nuno.
"Impact of Phase Calibration on EVM Measurement Quality."
Paper presented at 91st ARFTG Microwave Measurement Symposium, Philadelphia, PA, United States. June 15, 2018 - June 15, 2018.

# Traceable Characterization of Broadband Pulse Waveforms Suitable for Cryogenic Josephson Voltage Applications

Alirio S. Boaventura[1], Dylan F. Williams[1], Gustavo Avolio[2] and Paul D. Hale[1]

[1]National Institute of Standards and Technology, USA
[2]KU Leuven, Belgium

***Abstract* — We characterize broadband pulse waveforms using a large signal network analyzer (LSNA) and a sampling oscilloscope, both calibrated to the same reference plane and traceable to the NIST Electro-Optic Sampling System (EOS). The waveforms under test are passed through the LSNA test set and fed into the oscilloscope, allowing measurements to be carried out without disconnecting the measurement instruments, which reduces the measurement uncertainty. We calibrate the LSNA for operation with an external broadband pulse source and we correct the oscilloscope measurements for time-base distortion, impedance mismatch and the complex frequency response of the oscilloscope's sampler. We characterize several pulse waveforms and show good agreement between the LSNA and the oscilloscope measurements. The techniques presented will be applied in the characterization of cryogenic waveforms generated by NIST Josephson arbitrary waveform synthesizer (JAWS) systems.**

***Index Terms* — Pulse waveform characterization, LSNA, sampling oscilloscope, voltage standards, JAWS system.**

## I. Introduction

The NIST Quantum Voltage Project has traditionally developed and disseminated superconducting voltage standards for DC and audio metrology applications. These standards use 4 Kelvin cryogenically-cooled Josephson junctions (JJs) which generate quantum-accurate voltage pulses. The AC standard is called the Josephson Arbitrary Waveform Synthesizer (JAWS) [1]-[2]. To target wireless communications metrology, NIST is currently researching superconducting voltage standards at microwave frequencies.

To accurately characterize and de-embed cryogenic microwave waveforms generated by a superconducting source, a calibrated measurement instrument such as a large signal network analyzer (LSNA) will be required. As a first step toward traceable characterization of cryogenic microwave waveforms, in this work we compare broadband waveform measurements performed with an LSNA and a sampling oscilloscope at room temperature. This comparison increases the confidence in our measurement setup and sets the basis for future cryogenic waveform characterization.

Similar comparison studies exist [3]-[6]. Compared to those papers: 1) we fully calibrate both measurement instruments to the same reference plane; 2) we perform the measurements without disconnecting the measurement instruments, which reduces the measurement uncertainty; 3) we use the NIST Microwave Uncertainty Framework (MUF) to capture correlations in components of measurement uncertainty and transform them between frequency and time domains.

## II. The Measurement Setup

Fig. 1 shows the measurement setup used to characterize broadband pulse waveforms with an LSNA and a sampling oscilloscope both calibrated to the same reference plane and traceable to NIST electro-optic sampling system. During the measurement phase, the internal CW test signal of the LSNA was replaced with an external signal, generated either by an arbitrary waveform generator (AWG) or by a comb generator. This signal was passed through the LSNA test set and fed into the oscilloscope via the LSNA test port 3.

Synchronization is key in this setup, as all equipment including the LSNA (Keysight PNA-X N5245A)[1], AWG (Keysight M8195A), sampling oscilloscope (Keysight sampling head 86118A), and external phase references

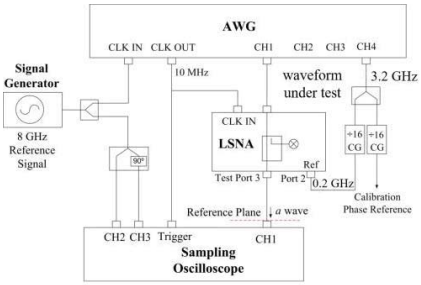


(a)

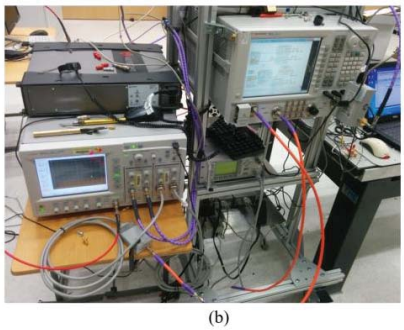

(b)

Fig. 1 a) Diagram of the measurement setup. b) Photograph of the measurement setup.

[1] Certain commercial equipment, instruments, or materials are identified in this paper to specify the experimental procedure adequately. Such identification is not intended to imply recommendation or endorsement by the National Institute of Standards and Technology, nor is it intended to imply that materials or equipment identified are necessarily the best available for the purpose.




Soares Boaventura, Alirio De Jesus; Williams, Dylan; Avolio, Gustavo; Hale, Paul.
"Traceable Characterization of Broadband Pulse Waveforms Suitable for Cryogenic Josephson Voltage Applications."
Paper presented at 2018 International Microwave Symposium, Philidelphia, PA, United States. June 10, 2018 - June 15, 2018.

(Keysight comb generators U9391F) must be locked to the same reference signal. An 8 GHz sine-wave signal generated by an external signal generator (Agilent 8365L) was used as the master reference signal to which all the other were locked.

In addition to generating the waveform of interest on channel 1, the AWG was used to synchronously trigger the sampling oscilloscope and to clock the LSNA with its 10 MHz output clock signal, and to drive the comb generators (CG) with a 3.2 GHz signal generated on channel 4. An in-phase and quadrature (IQ) version of the 8 GHz reference signal was measured by the oscilloscope simultaneously with the waveform of interest and was used in post-processing by the NIST Time-Base Correction (TBC) algorithm to correct for jitter and other time-base distortions in the oscilloscope time-base [7]. Note that increasing the frequency of the IQ signal improves discrimination between jitter and voltage amplitude noise in the TBC algorithm.

## III. Calibration And Measurement Correction

The full characterization of cryogenic microwave waveforms will require calibrated broadband measurements of the incident and reflected waves at the reference plane of the superconducting source using, for instance, an LSNA. As a first step, we compared room temperature measurements performed with an LSNA operated with an external broadband pulse source and a sampling oscilloscope. To compare the incident and reflected waves measured by the two instruments, they were calibrated to the same reference plane (Figs. 2-3). Note that the oscilloscope only measures the incident wave directly. The reflected wave can be calculated from the oscilloscope measurement of the incident wave and the oscilloscope reflection coefficient measured at the reference plane.

### *A. LSNA calibration*

Fig. 2 illustrates the two-step procedure followed for broadband calibration and measurements with the LSNA:

1. The LSNA was first operated in its default configuration where the internal CW sources were used for scattering-parameter, absolute amplitude, and absolute phase calibrations. This is sketched in Fig. 2a. For the scattering-parameter and amplitude calibrations, the CW sources were swept across the desired harmonic frequency grids (from 0.2 GHz to 50 GHz with a step of 0.2 GHz for the 0.2 GHz signals and from 1 GHz to 50 GHz with a step of 1 GHz for the 1 GHz signals). For the absolute phase calibration, the comb generators were driven with a 3.2 GHz signal (generated on the AWG channel 4), and their divide ratios were set to 16, defining a frequency resolution of 0.2 GHz;
2. During the measurement of the waveform of interest, the switching circuitry of port 3 was routed to the external pulse source connected to the LSNA back-panel (see Fig. 2b). Note that changing the source configuration does not affect the calibration performed in step 1, because the full wave calibration matrix is independent of the source [8].

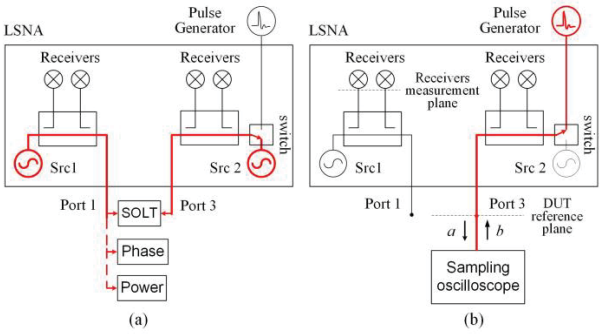


Fig. 2 a) Full wave calibration using the LSNA internal CW sources. b) Measurement with an external source.

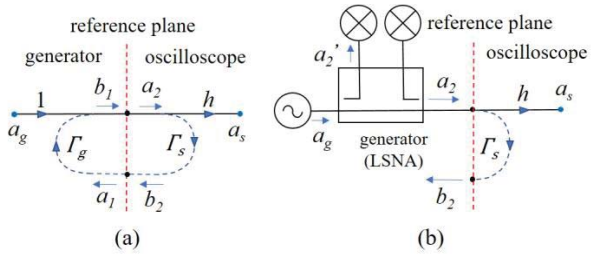


Fig. 3 a) Scope mismatch-corrected wave calibration. b) Calibration for the wave hitting the scope.

### *B. Sampling oscilloscope calibration*

First, we used the NIST TBC algorithm to correct the time-base of the oscilloscope by using the auxiliary IQ signal measured on channels 2 and 3 [7]. Since the time vector after correction is not evenly spaced, the new waveform was interpolated to a uniform time grid prior to further processing.

Afterward, we used the MUF to correct the TBC data for the complex frequency response of the oscilloscope's sampler, which has been pre-characterized using a photo-diode calibrated by the NIST electro-optic sampling system (EOS) [9]-[10]. Note that the post-processor available in the MUF for oscilloscope data calibration usually corrects for the mismatch-corrected wave, $a_g$, delivered by a generator to the oscilloscope Eqn. (1), given the oscilloscope's complex impulse response, $h$, the measured raw data, $a_s$, and the reflection coefficients of the generator and oscilloscope, $\Gamma_g$ and $\Gamma_s$ (see Fig. 3a).

$$a_g = \frac{a_s}{h}(1 - \Gamma_g \Gamma_s) \quad (1)$$

To reuse this MUF post-processor to correct instead for the incident wave at the reference plane of the oscilloscope, $a_2$, we set $\Gamma_g$ to zero so that $a_2 = a_g = a_s/h$ (Fig. 3b). A cable adaptor, not shown in Fig. 3 and not considered in Eqn. (1) for simplicity, was used to interconnect the oscilloscope head and the LSNA. To translate the oscilloscope data to the LSNA reference plane, the de-embedding of that cable was required.

Since the current impulse response characterization of the oscilloscope head has an arbitrary amplitude scaling, we further applied a correction scaling factor to the data given as the ratio of the magnitude of the LSNA fundamental component to the



Soares Boaventura, Alirio De Jesus; Williams, Dylan; Avolio, Gustavo; Hale, Paul.
"Traceable Characterization of Broadband Pulse Waveforms Suitable for Cryogenic Josephson Voltage Applications."
Paper presented at 2018 International Microwave Symposium, Philidelphia, PA, United States. June 10, 2018 - June 15, 2018.

magnitude of the oscilloscope's fundamental component, $\alpha = |a_{\mathrm{LSNA}}(\omega_0)|/|a_{\mathrm{Scope}}(\omega_0)|$. This scaling factor normalizes the amplitude of the oscilloscope data to the amplitude of LSNA's fundamental frequency component.

## IV. Measurement Results

### A. Measurement procedure

We characterized three waveforms: a 1 GHz square wave, a sinc-like waveform with a 1 GHz pulse repetition rate, and a broadband pulse signal with a 200 MHz pulse repetition rate. The first two signals were generated with a 25 GHz analog bandwidth AWG, and the third signal was generated by a broadband 50 GHz comb generator.

The comb waveform was used to exploit the 50 GHz measurement bandwidth of the LSNA. However, since this waveform has low average amplitude and the LSNA presents a large insertion loss from the back to front panel, the signal-to-noise ratio noticeably degraded, especially at higher frequencies, when the signal was passed through the LSNA test set. By using a calibrated Vector Network Analyzer (VNA), we measured the LSNA's back to front panel insertion loss at 50 GHz as being 22 dB for port 1 and 14 dB for port 3. Therefore, we chose to use port 3. To evaluate the impact of the LSNA test set on the comb waveform, we performed two different experiments. In the first experiment, we connected the comb generator directly to the oscilloscope. In the second experiment, we passed the comb signal through the LSNA test set and then we fed it into the oscilloscope via the LSNA test port 3. In both cases, we performed multiple oscilloscope measurements. The results are depicted in Fig. 4a and discussed in the next section.

The sinc-like test waveform intends to mimic the three-level sigma-delta modulated signal that is currently in use to bias the Josephson junction arrays of the NIST JAWS system [1]-[2]. For simplicity, we considered a periodic waveform with a single positive and negative pulse.

### B. Discussion

The upper and lower curves in Fig. 4a show respectively the repeated oscilloscope measurements with the comb generator signal directly connected to the oscilloscope and going through the LSNA test set. These results show a noticeable degradation of the noise standard deviation when the signal is passed through the LSNA test set. This is due to the large insertion loss of the LSNA back-to-front signal path. To improve the noise performance, we reduced the LSNA IF bandwidth to 3 Hz and we averaged 1000 oscilloscope measurements.

Fig. 4b depicts the repeated oscilloscope measurements of the comb signal in the time-domain. The waveforms were then corrected for systematic and random jitter errors, by use of the NIST time-base correction (TBC) algorithm [7], interpolated to a uniform time grid, and averaged (black line). Fig. 4c shows the standard deviation of the 1000 waveforms before and after applying TBC. The same procedure was applied for the other two AWG waveforms. As the later signals have higher signal-to-noise ratio, only 100 repeated measurements were used.

Figures 5 through 7 compare the incident waves of the three measured signals after amplitude scaling, phase normalization and phase detrending. Since the LSNA and oscilloscope measurements are performed at different arbitrary times, phase normalization and phase detrending are important for aligning the waveforms.

The spectrum difference (in amplitude and phase) increases with frequency due a degradation in the signal-to-noise ratio, but the difference is relatively small up to 30 GHz. The time-domain difference is also relatively small. Table I presents the peak time-domain difference and the spectrum difference at 30 GHz for the three waveforms.

Relatively large differences are seen above 30 GHz, but with no relevant impact on the reconstruction of the waveforms. Although the square wave presents energy at the even harmonics due to signal asymmetry, the spectrum difference at those harmonics can become large due to the low amplitude levels. As the square and sinc-like waveforms present low signal-to-noise ratio at higher frequencies, we fitted their phases only up to 30 GHz to guarantee proper phase-detrending (see Figs. 6-7).

Note the fundamental phase of the comb waveform at 180 degrees in Fig. 5b, corresponding to the inversion of the comb pulse with respect to the 10 MHz reference signal (see Fig. 5c).

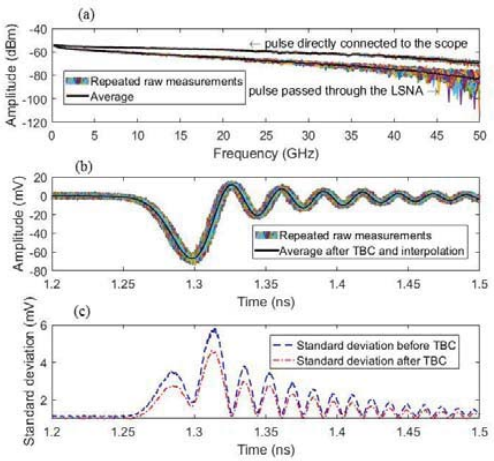


Fig. 4 a) Repeated scope measurements in the frequency domain with the comb generator directly connected to the scope and going through the LSNA test set. b) Time-domain of raw scope measurements and respective average after TBC correction. c) Standard deviation of the repeated scope measurements before and after TBC correction.

TABLE I Spectrum difference at 30 GHz and peak time-domain difference

| Waveform under test | Amplitude Diff. (dB) | Phase Diff. (degrees) | Time-domain Diff. (mV) |
|---|---|---|---|
| 200 MHz comb | 0.3 | 1.6 | 1.5 |
| 1 GHz square | 0.1 | 1.1 | 3.8 |
| 1 GHz sinc-like | 1.4 | 7.9 | 4.6 |



Soares Boaventura, Alirio De Jesus; Williams, Dylan; Avolio, Gustavo; Hale, Paul.
"Traceable Characterization of Broadband Pulse Waveforms Suitable for Cryogenic Josephson Voltage Applications."
Paper presented at 2018 International Microwave Symposium, Philidelphia, PA, United States. June 10, 2018 - June 15, 2018.

## V. Conclusion

We successfully compared pulse waveform measurements performed with a frequency-domain technique (LSNA) and a time-domain technique (scope). We calibrated the LSNA for operation with an external pulse source and we corrected the scope measurements to the same reference plane as the LSNA. The techniques presented will be combined with an on-wafer multiline Thru-Reflect-Line kit and a two-tier calibration approach, and applied to on-wafer cryogenic measurements.

## Acknowledgement

This research was supported by NIST's Innovations in Measurement Science program. Thanks to Rich Chamberlin, Jérôme Cheron, Konstanty Lukasik, Nathan Flowers-Jacobs, Jim Booth, Kate Remley and the NIST Superconductive Electronics Group. Gustavo Avolio is a post-doctoral researcher supported by FWO Flanders (Belgium).

## References

[1] Samuel P. Benz *et al*., "Low-distortion Waveform Synthesis with Josephson Junction Arrays", *Appl. Phys. Lett*., vol. 77, no. 7, 14 August 2000.

[2] N. E. Flowers-Jacobs, A. E. Fox, P. D. Dresselhaus, R. E. Schwall and S. P. Benz, "Two-Volt Josephson Arbitrary Waveform Synthesizer Using Wilkinson Dividers," in *IEEE Transactions on Applied Superconductivity*, vol. 26, no. 6, pp. 1-7, Sept. 2016.

[3] J. Scott *et al*., "Removal of cable and connector dispersion in time-domain waveform measurements on 40 Gb integrated circuits," *IEEE MTT-S International Microwave Symposium*, Seattle, WA, USA, 2002, pp. 1669-1672 vol.3.

[4] J. B. Scott *et al*., "Enhanced on-wafer time-domain waveform measurement through removal of interconnect dispersion and measurement instrument jitter," *IEEE Trans. Microwave Theory and Techniques*, vol. 50, no. 12, pp. 3022-3028, Dec 2002.

[5] D. Williams, P. Hale and K. A. Remley, "The Sampling Oscilloscope as a Microwave Instrument," in *IEEE Microwave Magazine*, vol. 8, no. 4, pp. 59-68, Aug. 2007.

[6] A. Aldoumani, P. J. Tasker, R. S. Saini, J. W. Bell, T. Williams and J. Lees, "Operation and calibration of VNA-based large signal RF I-V waveform measurements system without using a harmonic phase reference standard," 81st *ARFTG Microwave Measurement Conference*, Seattle, WA, 2013, pp. 1-4.

[7] P. D. Hale, C. M. Wang, D. F. Williams, K. A. Remley and J. D. Wepman, "Compensation of Random and Systematic Timing Errors in Sampling Oscilloscopes," in *IEEE Transactions on Instrumentation and Measurement*, vol. 55, no. 6, pp. 2146-2154, Dec. 2006.

[8] Valeria Teppati, Andrea Ferrero and Mohamed Sayed, "*Modern RF and Microwave Measurement Techniques*", Cambridge University Press, Cambridge UK, July 2013

[9] T.S. Clement, P. D. Hale, D. F. Williams, C. M. Wang, A. Dienstfrey, and D. A. Keenan, "Calibration of Sampling Oscilloscopes with High-Speed Photodiodes", *IEEE Trans. Microwave Theory and Techniques*, Aug. 6 A.D.

[10] D. F. Williams, T. S. Clement, P. D. Hale and A. Dienstfrey, "Terminology for high-speed sampling-oscilloscope calibration", *ARFTG Microwave Measurement Conference.*, vol. 68, pp. 9-14, 2006-Dec.

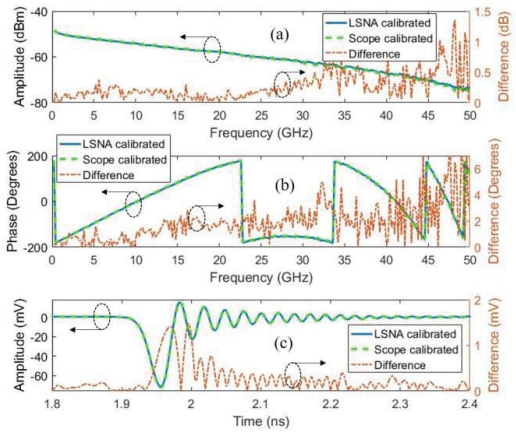


Fig. 5: 200 MHz comb pulse incident at the reference plane. a) Spectrum magnitude, b) Phase, c) Time-domain (zoom in)

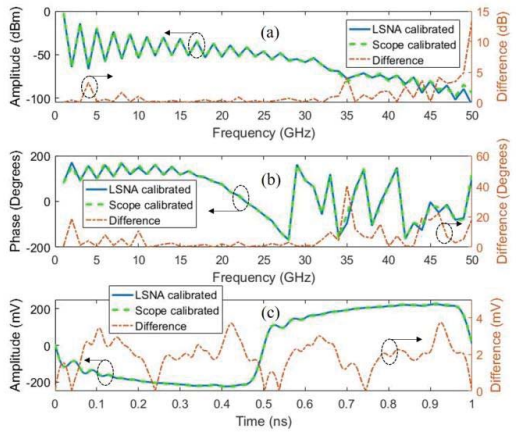


Fig. 6: 1 GHz square wave incident at the reference plane. a) Spectrum magnitude, b) Phase, c) Time-domain.

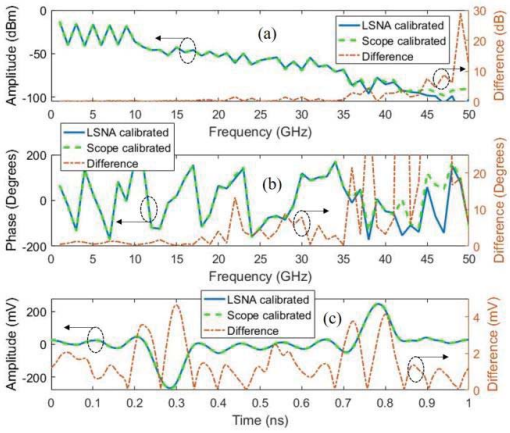


Fig. 7: 1 GHz sinc-like wave incident at the reference plane. a) Spectrum magnitude, b) Phase, c) Time-domain.



Soares Boaventura, Alirio De Jesus; Williams, Dylan; Avolio, Gustavo; Hale, Paul.
"Traceable Characterization of Broadband Pulse Waveforms Suitable for Cryogenic Josephson Voltage Applications."
Paper presented at 2018 International Microwave Symposium, Philidelphia, PA, United States. June 10, 2018 - June 15, 2018.

*Proc. of the 2018 International Symposium on Electromagnetic Compatibility (EMC Europe 2018), Amsterdam, The Netherlands, August 27–30, 2018.*

# Development and Applications of a Fiber-Coupled Atom-Based Electric Field Probe

Christopher L. Holloway, Matt T. Simons, Marc Kautz, Perry F. Wilson, and Joshua A. Gordon

National Institute of Standards and Technology (NIST)
325 Broadway, Boulder, CO 80305, USA
holloway@boulder.nist.gov

***Abstract*—We are developing a fundamentally new atom-based approach for electric (E) field measurements. This new approach will lead to a self-calibrated, SI traceable, E-field measurement, providing us with the capability to perform measurements on a fine spatial resolution in both the far- and near-fields. Here, we discuss the development and applications of the first moveable fiber-coupled version of this atom-based E-field measurement approach. We show results for various measurements including: far-field measurements of the E-fields, measurements of the E-field distribution along the surface of a circuit board, field measurements in apertures, measurements of the directivity pattern of a horn antenna, and measurements made in a GTEM cell.**

## I. Introduction

Significant progress has recently been made in the development of a novel Rydberg-atom spectroscopic approach for radio-frequency (RF) electric (E) field strength measurements [1]-[9]. This approach utilizes the phenomena of electromagnetically induced transparency (EIT) and Autler-Townes (AT) splitting [1]-[10], and leads to a direct International System of Units (SI) traceable, self-calibrated measurement.

While various international metrology organizations around the world are beginning to investigate this new approach as a possible new standard for E-field measurements and calibrations, all previous investigations and measurements have been confined to an optical table. This confinement is a result of the fact that this technique requires the two lasers (probe and coupling lasers) to overlap inside the vapor cell. In order to overcome these issues, we have developed the first fiber-coupled vapor cell (see Fig. 1) [11], where the two counter propagating lasers are carefully overlapped inside the vapor cell while it is moved off the optical table. Moving the probe off of the optical table allows measurements to be performed in free space and in other standard RF metrology environments. The new probe consists of a 10-mm cubic vapor cell (made with all dielectric material, i.e., glass) filled with cesium $^{133}$Cs and two optical fibers with lenses attached with UV curing epoxy at either end (see Fig. 1). We have performed various measurements in order to illustrate the new probe's capabilities. These experiments are described in this paper.

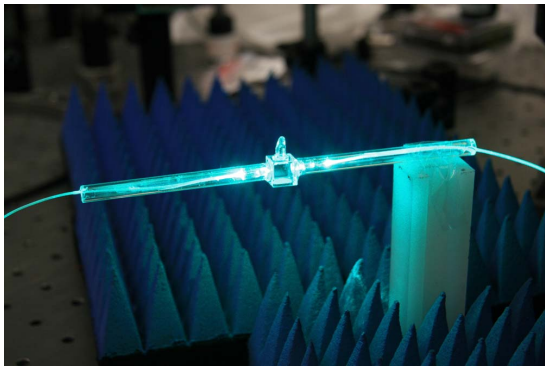

Fig. 1: Fiber-coupled atom-based E-field probe.

## II. Description of the Atom-Based Approach

The measurement approach uses a vapor of alkali atoms (placed in a glass cell, referred to as a "vapor- cell") as the active medium for the radio frequency (RF) E-field measurement. The basic concept is that by manipulating alkali atoms with both optical (laser) fields and RF fields, it is possible to cause a laser to transmit through the vapor cell where it would normally be absorbed by the atoms in the vapor cell. Rubidium ($^{85}$Rb) and cesium ($^{133}$Cs) are the two atomic species that are typically used in the approach. A typical measurement setup is shown in Fig. 2(a). This measurement approach can be represented by the four-level atomic system shown in Fig. 2(b), see [1]-[3] and [9] for details.

A "probe" laser is used to probe the response of the ground-state transition of the atoms and a second laser ("coupling" laser) is used to excite the atoms to a Rydberg state. In the presence of the coupling laser, a destructive quantum interference occurs and the atoms become transparent to the resonant probe laser. This is the concept of EIT, in which a transparency window is opened for the probe laser light, and the probe light transmission is increased. The coupling laser wavelength is chosen such that the atoms are in a sufficiently high state (a Rydberg state) so that a RF field coherently couples two Rydberg states (levels 3 and 4 in Fig. 2(b)). The RF field in the four-level atomic system causes constructive interference of excitation pathways within the EIT transmission window, resulting in a decreased




Holloway, Christopher; Simons, Matthew; Gordon, Joshua.
"Development and Applications of a Fiber-Coupled Atom-Based Electric Field Probe."
Paper presented at 2018 International Symposium on Electromagnetic Compatibility (EMC), Amsterdam, Netherlands. August 27, 2018 - August 30, 2018.

transmission of the probe laser and AT splitting of the EIT peak.

A typical power measurement from the detector when the laser is scanned across this wavelength is shown Fig. 3(a) (where $\Delta_p=\omega_p-\omega_o$, $\omega_o$ is the on-resonance angular frequency of the ground state transition and $\omega_p$ is the angular frequency of the probe laser). The bottom curve shows the measured probe laser spectrum with no coupling laser, the top curve is the spectrum with the coupling and no RF, and the middle curves is the spectrum with both the coupling laser and with RF on (note the wings of all three curves normally would lay on top of one another, but they are shifted here for ease of viewing). For the top curve, notice at $\Delta_p=0$, the power on the detector is larger than the Doppler background, i.e., the global inverted bell-shaped behavior.

The wavelength of the coupling laser is chosen judiciously such that the atoms are excited to a very high energy, where an RF source is at a resonant frequency that causes an atomic transition to a nearby state (i.e., an RF atomic transition). When the RF source is turned on, the EIT signal splits into two (this splitting is called Autler-Townes (AT) splitting), see the middle curve in Fig. 3(a). To increase the EIT signal-to-noise, we modulate the coupling-laser amplitude with a 50/50 duty-cycle 30 kHz square wave and detect any resulting modulation of the probe transmission with a lock-in amplifier. This removes the Doppler background and isolates the EIT signal. Fig. 3(b) shows a typical EIT signal from the lock-in amplifier for different values of RF field levels. The splitting of the EIT peak is indicated by $\Delta f_m$.

(a) Experimental setup.

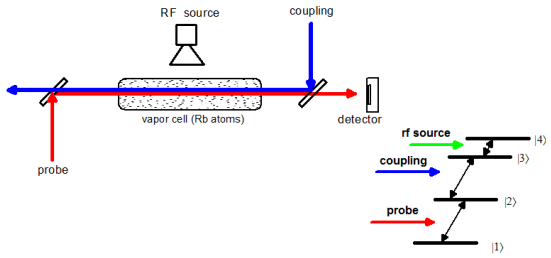


(b) Vapor-cell and four-level system.

Fig. 2: Measurement setup and four-level atomic system.

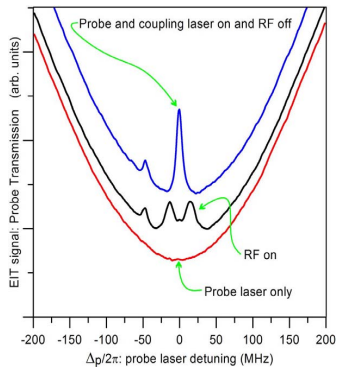


(a) EIT signal without lock-in.

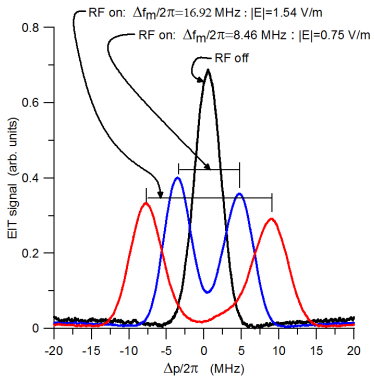


(b) EIT signal with lock-in.

Fig. 3: Typical measurement of the EIT signal.

This splitting ($\Delta f_m$) of the probe laser spectrum is easily measured and is directly proportional to the applied RF E-field amplitude. Once this $\Delta f_m$ is measured, the RF E-field strength is obtained from [1]-[3] and [9]:

$$|E| = 2\pi \frac{\hbar}{\wp} \frac{\lambda_p}{\lambda_c} \Delta f_m \quad , \tag{1}$$

where $\hbar$ is Planck's constant, $\wp$ is the atomic dipole moment of the RF atomic transition, and $\lambda_p$ and $\lambda_c$ are the wavelengths of the probe and coupling lasers, respectively. The ratio $\lambda_p/\lambda_c$ accounts for the Doppler mismatch of the probe and coupling lasers [10], assuming the probe and coupling lasers are counter-propagating in the cell. One can also scan the coupling laser and not the probe laser during the experiments. If the coupling laser is scanned, it is not required to correct for the Doppler mismatch, and $\lambda_p/\lambda_c$ ratio is not needed, see [9] for details. The measurement based on (1) is a direct SI-traceable measurement, in that it is directly related to Planck's constant. To estimate $|E|$, $\Delta f_m$ is obtained from a measurement, Planck's constant is known, and $\wp$ is



Holloway, Christopher; Simons, Matthew; Gordon, Joshua.
"Development and Applications of a Fiber-Coupled Atom-Based Electric Field Probe."
Paper presented at 2018 International Symposium on Electromagnetic Compatibility (EMC), Amsterdam, Netherlands. August 27, 2018 - August 30, 2018.

calculated from first principles (see [3] for discussion on determining $\wp$ ).

One of the advantages of this new approach is that it is very broadband. In fact, utilizing the experiment setup shown in Fig. 2(a), we can measure the E-field strength over a frequency range from hundreds of MHz to 1 THz. Fig. 4 shows measurements for six different frequencies ranging from 9.22 GHz to 182 GHz using two different atomic species ($^{85}$Rb and $^{133}$Cs). In this figure, we also compare the estimated E-field obtained for this atom-based approach to both far-field calculations and to numerical simulations. We see that the atom-based approach correlates very well with both (uncertainties are discussed below).

## III. Fiber-Coupled E-Field Probe

Most experiments using this atom-based approach have been confined to an optical table, see Fig. 2(a). For the technique to be useful, the probe needs to be moved off the table and constructed such that it can be moveable. Toward this goal, we have developed the first fiber-coupled vapor-cell E-field probe (see Fig. 1). We have used this probe in various experiments, which are discussed next.

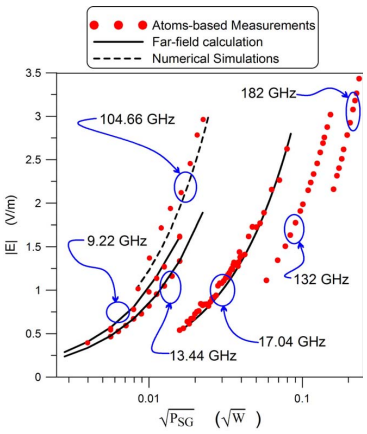


Fig. 4: A comparison of the measured E-field to results obtained from far-field calculations and from a full-wave numerical simulation.

### *A. Mapping the Fields In a GTEM Cell*

We used the fiber-probe to measure the E-field inside a gigahertz transverse electromagnetic (GTEM) cell. This allows us to access the field variability along the longitudinal axis as a function of frequency. The fiber probe was placed at the center of a GTEM cell and moved to different locations along the longitudinal axis, see Fig. 5. In these experiments, we measured the E-field at three different positions in the GTEM cell at three different frequencies. Fig. 6 shows the measured results for the total field. For reference, we also shown results for the calculated field inside the GTEM, see eq. (E.2) in [12]. From these experiments, we see that E-field varies as a function of frequency and position, due to impedance variations and higher-order modes. The high frequency variation with frequency is also shown in [13]. Notice that the variability becomes worst the furthest from the input of the GTEM feed, as expected.

Fig. 5: Fiber-probe inside a GTEM cell.

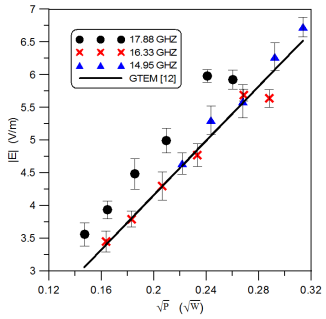


(a) 2.64-m from input.

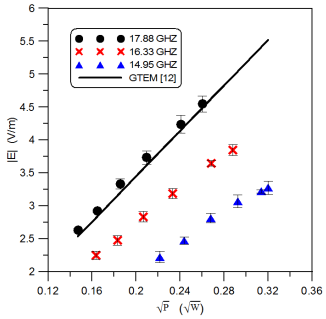


(b) 3.08-m from input.

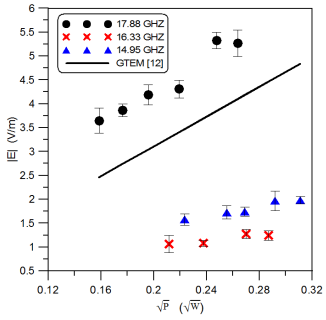


(c) 3.49-m from input.

Fig. 6: E-field mapping inside a GTEM cell.



Holloway, Christopher; Simons, Matthew; Gordon, Joshua.
"Development and Applications of a Fiber-Coupled Atom-Based Electric Field Probe."
Paper presented at 2018 International Symposium on Electromagnetic Compatibility (EMC), Amsterdam, Netherlands. August 27, 2018 - August 30, 2018.

### B. Imaging the Fields Above a CPW Line

In order to illustrate the near-field imaging capability of the fiber-coupled probe, we imaged the total E-field at various heights ($h$) across the surface of a co-planar waveguide (CPW) line, see Fig. 7. The CPW has a center strip of 3 mm, gaps of 2 mm, and a substrate ($\varepsilon = 3.5$) of thickness 1.52 mm. Fig. 8 shows the scans at six different heights for a frequency of 11.6 GHz. In order to show the repeatability of this probe we performed three sets of measurements for each height and the error-bars represent all these measurements. As a check, we show results obtained from HFSS (mentioning this full-wave simulator does not imply an endorsement, but serves to clarify the numerical program used) for $h$ = 6.64 mm. While the HFSS simulations have the same general behavior as the measured results, the differences are due to the fact the that the HFSS results are for an infinitely wide ground plane CPW. These results show the probe capability for near-field imaging and field-mapping across the surface of printed-circuit board structures, which will be used in the future to support calibrated on-wafer measurements of high-speed (high-frequency) integrated circuits. The fiber-coupled probe allows for much finer spatial resolution than is possible with current E-field probes. The spatial resolution is 70 µm, which is essentially the width of the laser beams [1].

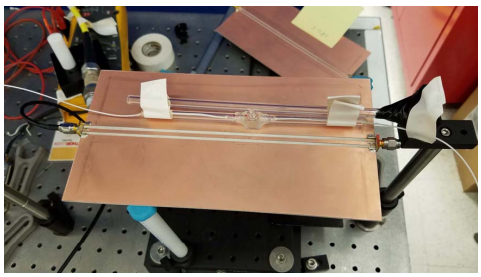

Fig. 7: Fiber-probe above a CPW line.

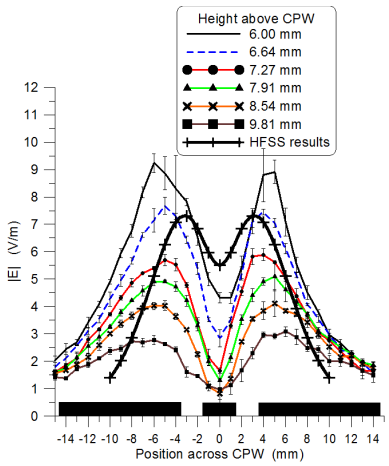


Fig. 8: Measured E-field above a CPW line.

### C. Antenna Pattern Measurements

We used the fiber-coupled probe to measure the antenna pattern of a Narda 640 standard gain horn antenna (mentioning this product does not imply an endorsement, but serves to clarify the antenna used). The experimental setup for these measurements is shown in Fig. 9. In these measurements, the fiber-coupled probe was placed 0.835 m from the horn antenna (in the quasi-far-field). During the experiments, we scanned the antenna from bore site to an angle of 60°. We scanned both the E-plane and H-plane of the horn antenna and the total E-field was measured. Fig. 10 shows the measured antenna patterns for both the E-plane and H-plane at 11.6 GHz. Also shown in this figure are results obtained in an anechoic chamber test range [14] at 9.4 GHz. Good correlation between the two types of measurements is seen. The deviations are because our measurements were performed in a laboratory with no RF absorber on the walls and the laboratory had several objects in the room, see Fig. 9. Thus, our results suffer from some background scattering.

### D. Imaging the Fields In an Aperture

As another mapping example, we performed measurements across an aperture located on the side of a small transverse electromagnetic (TEM) cell, see Fig. 11. The TEM cell size was 5.5 cm wide, 2.7 cm tall, with a circular aperture of radius 0.75 cm. The fiber-coupled probe was scanned across the aperture for a given input power to the TEM cell. We performed measurements of the total field at the aperture 6 mm from the aperture at 21.6 GHz and 29.5 GHz. These data are shown in Fig. 12. Since the TEM cell is highly multi-moded at these two frequencies and the aperture fields cannot readily be calculated, and measurements are the best approach to determine the near-fields. The fiber-probe allows for such a measurement.

## IV. Uncertainties

Understanding the uncertainties of this technique is an important step if this method is to be accepted as a standard calibration technique. The various aspects that contribute to the uncertainties of this technique are currently being investigated and are summarized in [1]-[6], [9], and [15]. While the uncertainty analysis is still being performed, initial results indicate the uncertainties have the possibility of being below 0.1 -to- 0.5 dB.

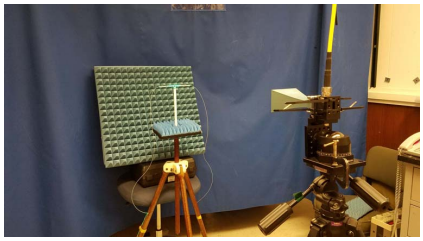

Fig. 9: Setup for the antenna pattern measurements.



Holloway, Christopher; Simons, Matthew; Gordon, Joshua.
"Development and Applications of a Fiber-Coupled Atom-Based Electric Field Probe."
Paper presented at 2018 International Symposium on Electromagnetic Compatibility (EMC), Amsterdam, Netherlands. August 27, 2018 - August 30, 2018.

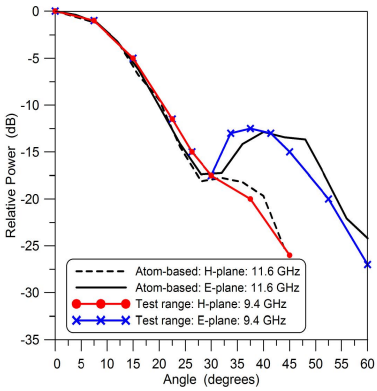


Fig. 10: Measured antenna pattern.

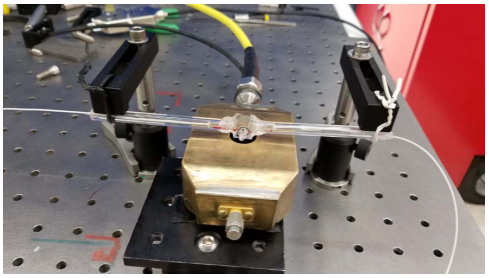

Fig. 11: Fiber-probe at aperture of small TEM cell.

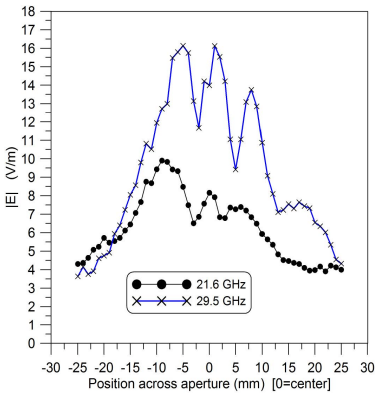


Fig. 12: Measured E-field across the aperture at a height of 6 mm for two different frequencies.

## V. Summary

In this paper, we discussed the development of a fundamentally new approach for a SI traceable E-field measurement. We have shown the evolution of this technique from being confined to an optics table to the first fiber-coupled atom-based E-field probe. We illustrate the utility of this probe by showing results for fields inside a GTEM, near-field imaging of printed circuit boards and apertures, and antenna pattern measurements. While there is still a lot of work to be done in order for this technique to accepted as a new E-field standard, these results in this paper are useful steps toward making this probe a practical device.

## References

[1] C.L. Holloway, M.T. Simons, J.A. Gordon, P.F. Wilson, C.M. Cooke, D.A. Anderson, and G. Raithel, "Atom-Based RF Electric Field Metrology: From Self-Calibrated Measurements to Sub-Wavelength and Near-Field Imaging", *IEEE Trans. on Electromagnetic Compat.,* vol. 59, no. 2, 717-728, 2017.

[2] J.A. Sedlacek, A. Schwettmann, H. Kubler, R. Low, T. Pfau and J.P. Shaffer, "Microwave electrometry with Rydberg atoms in a vapour cell using bright atomic resonances", *Nature Phys.,* vol. 8, 819, 2012.

[3] C.L. Holloway, J.A. Gordon, A. Schwarzkopf, D.A. Anderson, S.A. Miller, N. Thaicharoen, and G. Raithel, "Broadband Rydberg Atom-Based Electric-Field Probe for SI-Traceable, Self-Calibrated Measurements," *IEEE Trans. on Antenna and Propag.* vol. 62, no. 12, 6169-6182, 2014.

[4] H. Fan, S. Kumar, J. Sedlacek, H. Kubler, S. Karimkashi, and J.P. Shaffer, "Atom based RF electric field sensing," *J. of Phys. B: Atomic, Molecular and Optical Physics*, vol. 48, 202001, 2015.

[5] H. Fan, S. Kumar, J. Sheng, J.P. Shaffer, C.L. Holloway and J.A. Gordon, "Effect of Vapor Cell Geometry on Rydberg Atom-based Radio-frequency Electric Field Measurements", *Physical Review Applied*, vol. 4, 044015, November, 2015.

[6] C.L. Holloway, J.A. Gordon, M.T. Simons, H. Fan, S. Kumar, J.P. Shaffer, D.A. Anderson, A. Schwarzkopf, S. A. Miller, N. Thaicharoen, and G. Raithel, "Atom-based RF electric field measurements: an initial investigation of the measurement uncertainties," *Joint IEEE Intern. Symp. on EM and EMC Europe*, Dresden, Germany, pp. 467-472, Aug. 2015.

[7] D.A. Anderson, S.A. Miller, G. Raithel, J.A. Gordon, M.L. Butler, and C.L. Holloway, *Physical Review Applied*, vol. 5, 034003, 2016.

[8] D.A. Anderson, S.A. Miller, A. Schwarzkopf, C.L. Holloway, J.A. Gordon, N. Thaicharoen, and G. Raithelet, *Physical Review A*, vol. 90, 043419, 2014.

[9] C.L. Holloway, M.A. Simons, J.A. Gordon, A. Dienstfrey, D.A. Anderson, and G. Raithel, "Electric Field Metrology for SI Traceability: Systematic Measurement Uncertainties in Electromagnetically Induced Transparency in Atomic Vapor", *J. of Applied Physics*, vol. 121, 233106, 2017.

[10] A.K. Mohapatra, T.R. Jackson, and C.S. Adams, "Coherent optical detection of highly excited Rydberg states using electromagnetically induced transparency," *Phys. Rev. Lett.*, vol. 98, 113003, 2007.

[11] M.T. Simons, J.A. Gordon, and C.L. Holloway, "Fiber-coupled Vapor Cell for a Rydberg Atom-based RF Electric Field Sensor," submitted to *Applied Optics*, 2018.

[12] ICE 61000-4-20: Testing and measurement techniques Emission and immunity testing in transverse electromagnetic (TEM) waveguides.

[13] P.F. Wilson, "Higher-order mode fields distribution in asymmetric transverse electromagnetic cells, *Radio Science*, vol. 26, no. 2, 551-557, 1991.

[14] T.J. Duck, B. Firanski, F.D. Lind, and D. Sipler, "Aircraft-protection radar for use with atmospheric lidars", *Applied Optics*, vol. 44, no. 23, pp. 4937-4945, 2005.

[15] M.T. Simons, M. Kautz, J. Gordon, and C.L. Holloway, *"*Uncertainties in Rydberg Atom-based RF E-field Measurements*", EMC Europe 2018*, Amsterdam, NL, Aug. 27-30, 2018



Holloway, Christopher; Simons, Matthew; Gordon, Joshua.
"Development and Applications of a Fiber-Coupled Atom-Based Electric Field Probe."
Paper presented at 2018 International Symposium on Electromagnetic Compatibility (EMC), Amsterdam, Netherlands. August 27, 2018 - August 30, 2018.

# Optimal Dynamic Spectrum Access Scheme for Utilizing White Space in LTE Systems

Anirudha Sahoo, Timothy A. Hall, Charles Hagwood
National Institute of Standards and Technology
Email: {anirudha.sahoo, tim.hall, charles.hagwood}@nist.gov

***Abstract*—In this study, we design and implement an algorithm for optimal dynamic spectrum access (DSA) in a shared spectrum system where the primary user (PU) is a Long Term Evolution (LTE) system. The cumulative hazard function from survival analysis is used to predict the remaining idle time available in each channel for secondary user (SU) transmission subject to a probability of successful completion. Optimal allocation of physical resource blocks (PRBs) for the SU is shown to be a variation of the unbounded knapsack problem. We evaluate the algorithm performance using three data sets collected from real LTE systems. The algorithms achieve good white space utilization and have a measured probability of interference around the target threshold.**

## I. Introduction

Dynamic spectrum access (DSA) has been proposed as a means of making more efficient use of available spectrum. In a common DSA scenario, there are one or more primary users (PUs) operating in a given band with priority access. One or more secondary users (SUs) can opportunistically transmit during times that the PUs are idle. When the PUs want to use the band again, the SUs must stop transmitting. In general, the SUs know whether the band is occupied by the PUs at a given time, either by querying a central coordinator (i.e., scheduler) or by sensing the band. However, the SUs do not know future activity of the PUs. Hence, DSA can be thought of as a prediction scheme in which an SU scheduler has to predict, with a certain probability, that the SU can complete its transmission before a PU reappears.

LTE cellular systems provide various services using one or more frequency bands comprising multiple channels. LTE is slated to be the first technology to be deployed in the Citizens Broadband Radio Service (CBRS) band, which is based on the *shared spectrum* paradigm [1]. Although opportunistic DSA is not supported in the CBRS band at present, its semi-dynamic three tier priority-based spectrum sharing is a positive step towards that. The first tier (highest priority) is the federal incumbent, which operates infrequently and only in limited geographic areas. The second tier is licensed LTE; the third tier is unlicensed. Thus, it is appropriate to start thinking about DSA in a network where an LTE system acts as the PU and the SUs communicate by opportunistically accessing the spectrum.

Although an LTE eNodeB could in theory be tasked with scheduling the SUs along with its own PU UEs, we believe there are reasons why this is not desirable and, therefore, not likely. In general the SUs will not be subscribers to the PU service. Thus, it is better to deploy a separate and independent SU system whose operation is transparent to the primary LTE system, thereby requiring no changes to the LTE system. This approach also enables legacy LTE systems, i.e., those not implementing our scheme, to participate in the DSA system. The only interaction between PU and SU systems is at the operator level, where a Service Level Agreement (SLA) may be agreed upon that specifies various operational policies, e.g., an upper bound on the probability of interference.

Resources in LTE are allocated in chunks called physical resource blocks (PRBs). Each PRB is $0.5$ ms (one slot) long in time and $180$ kHz wide in frequency. In our scheme, therefore, DSA becomes a matter both of predicting spectrum occupancy by the PU and allocating PRBs for the SU transmission accordingly.

The contributions of this paper are as follows. We present a DSA algorithm that allocates PRBs to SUs in a system with a statistical guarantee on the probability of interference to the PU LTE system. We frame the allocation of PRBs across time and frequency as a variation of the unbounded knapsack problem. Our algorithm is simple and efficient, which makes it easier to implement in a real system. We show the effectiveness of our algorithm using LTE uplink datasets collected from real deployed LTE systems at the time scale used by LTE systems (1 ms).

## II. Related Work

Two state time-inhomogeneous Discrete-Time Markov Chain (DTMC) [2], semi-Markov DTMC models [3], Alternating Renewal Process [3], [4] and semi-Markov Continuous-Time Markov Chain (CTMC) based models [5], [6], [7] are some of the models proposed in the literature to represent spectrum occupancy.

There have been few models proposed for *predicting* spectrum occupancy, which is critical to allocating spectrum to the secondary users. The Partially-Observable Markov Decision Process (POMDP) model [8], prediction based on expected remaining OFF time [9] and the two state semi-Markov model [3] are some of the methods used for this purpose. In [10], the transmission duration of an SU is constrained based on the maximum bound on probability of interference to the PU. Residual idle time of an Alternating Renewal Process is used in [4] to indirectly predict reappearance of the PU. Pattern mining of spectrum occupancy data has been used to predict channel availability [11], [12]. In [13], [14], the authors used the cumulative hazard function from survival analysis to

Sahoo, Anirudha; Hall, Timothy; Hagwood, Robert.
"Optimal Dynamic Spectrum Access Scheme for Utilizing White Space in LTE Systems."
Paper presented at IEEE Wireless Communications and Networking Conference (WCNC), Marrakech, Morocco. April 15, 2019 - April 19, 2019.

design DSA algorithms that allocated resources (time duration) in a single dimension. In this work, we consider allocation of resources in two dimensions, namely time and frequency.

Long Term Evolution (LTE) systems employ packet schedulers that schedule users in the time domain and then allocate physical resource blocks (PRBs) among them according to criteria such as channel quality and service rate [15], but usually no distinction is made between different classes of User Equipments (UEs). Application-aware schedulers where the allocation of PRBs and power is based on UE real-time requirements, along with a guaranteed quality of experience (QoE) for all users, has been researched in [16]. However, these do not consider the requirement for an SU in a DSA system where the scheduler must account for predicting future PU activity.

## III. Allocation Algorithms

We begin this section with a more precise statement of the problem we are solving. Then we briefly explain how we use the cumulative hazard function from the field of *survival analysis* [17], [18] to limit the probability of interference caused by an SU transmission to the PU system. This is a key element of our DSA algorithm. We then present the optimization formulation for our problem, followed by the algorithm that optimally allocates PRBs for an SU.

### A. Problem Statement

We use an LTE system operating in a given band as the PU. The width of the band in *frequency* is ($N \times 180$) kHz, i.e., the width of $N$ PRBs. We refer to each 180 kHz range of frequency as comprising a channel to aid conceptual understanding. SUs may transmit on PRBs that are idle, but interference to the PUs should be limited. Hence in this DSA application, an SU requests $\mathcal{W}$ PRBs, and the goal is to devise an algorithm that allocates up to $\mathcal{W}$ PRBs, maintaining the probability of interference on each channel below a specified threshold. Hence, this is a two-dimensional resource allocation problem in which the number of allocated PRBs is maximized, subject to the constraint that the probability of interference on each channel is below a threshold.

### B. Use of Cumulative Hazard Function

A communication channel alternates between idle and busy states. Let $I_1, B_1, I_2, B_2, \ldots$ represent the successive idle and busy states of a channel. We assume these states are independent and the lengths of all the idle states have the same distribution, say $F(t)$. Our algorithm makes use of the hazard function associated with the distribution $F(t)$. The hazard function at time t, $h(t)$, measures how likely an idle period of unknown length $I$ will end in the next instance given that it has lasted for $t$ units of time and is given by

$$h(t) = \lim_{dt \to 0} \frac{Pr[t \leq I < t + dt \mid I \geq t]}{dt} = \frac{f(t)}{1 - F(t)} \quad (1)$$

where $f(t) = dF(t)/dt$. Given a specific channel to be shared, the algorithm allows a request to transmit for $\tau$ units of time only if the probability that the current idle period $I$ will last for additional duration $\tau$ given that it has been idle for duration $t$ (when the SU request arrived) is more than a set threshold $p$. That is, the SU request is granted if the following condition is satisfied.

$$Pr[I \geq t + \tau \mid I \geq t] > p \quad (2)$$

This threshold $p, 0 < p < 1$, is the probability of successful transmission by the SU. It can be shown that [13]

$$P[I \geq t + \tau \mid I \geq t] = \exp(-[H(t + \tau) - H(t)]) \quad (3)$$

where $H(t) = \int_0^t h(s)ds, t \geq 0$ is the cumulative hazard function. However, in practice, $H(t)$ needs to be estimated from the idle time data for which a large sample $I_1, I_2, \ldots, I_n$ of $n$ idle durations is collected. Let $I_{(1)} \leq I_{(2)} \cdots \leq I_{(n)}$ be the ordered $I_i, i = 1, \ldots, n$. Then it can be shown that a non-parametric estimate $H_n(t)$ of $H(t)$ is given by [13]

$$H_n(t) = \sum_{i:I_{(i)} \leq t} \frac{1}{n - i + 1} \quad (4)$$

From (2) and (3), using $H_n(t)$ in place of $H(t)$, it is easy to deduce that transmission is allowed by the SU if the following inequality is satisfied.

$$H_n(t + \tau) - H_n(t) < (-\ln p) \quad (5)$$

### C. Optimization Formulation

Let $x_i$ be the number of PRBs allocated on channel $i$, $w_i$ be the weight of the channel $i$ and $N$ be the number of channels. Let $H_n^i(\cdot)$ be the non-parametric estimate of the cumulative hazard funtion of channel $i$. Let $\theta_{th} = (-ln\, p)$, where $p$ is the set threshold for probability of successful transmission and $t_i$ be the amount of time that channel $i$ has been idle when the SU request for $\mathcal{W}$ number of PRBs arrives. Then the two dimensional resource allocation problem can be formulated as a variation of the well-known *unbounded knapsack problem* [19] given by

$$\textit{maximize} \sum_{i=1}^{N} w_i x_i, \quad \textit{subject to} \quad (6)$$

$$\sum_{i=1}^{N} x_i \leq \mathcal{W},\ x_i \in \{0, \mathbb{Z}^+\} \quad (7)$$

$$w_i \geq 0,\ i = 1, \ldots, N \quad (8)$$

$$\max_{1 \leq i \leq N} \theta_i \leq \theta_{th} \quad (9)$$

where $\theta_i = H_n^i(t_i + x_i) - H_n^i(t_i)$.

The above optimization formulation maximizes the total weighted value of the allocated PRBs subject to the constraints. Constraint (7) limits the allocation to a maximum of $\mathcal{W}$ PRBs requested by an SU, whereas constraint (9) makes sure that the probability of interference on any channel is below the specified threshold.

To keep our analysis simple, in this study, we have assumed that all channels have equal weight by setting $w_i = 1$, $1 \leq$

Sahoo, Anirudha; Hall, Timothy; Hagwood, Robert.
"Optimal Dynamic Spectrum Access Scheme for Utilizing White Space in LTE Systems."
Paper presented at IEEE Wireless Communications and Networking Conference (WCNC), Marrakech, Morocco. April 15, 2019 - April 19, 2019.

$i \leq N$. In general, the weights can be assigned based on (for example) channel quality or priority.

### D. Definition of Algorithm

The unbounded knapsack problem is known to be NP-Hard [19]. Hence, we use a *pseudo-polynomial* algorithm using *dynamic programming* to solve our two dimensional resource allocation problem [20]. Let $t_i$ be the length of the current idle period for channel $i$ and $H_n^i(\cdot)$ be the non-parametric estimate of cumulative hazard function of channel $i$. The algorithm for finding the optimal allocation of resource blocks is presented in Algorithm Fixed_PRB, which outputs $x_i$'s, the number of PRBs allocated to the SU in channel $i$. Essentially the algorithm uses the SU transmission constraint given in (5) across each channel and solves the optimization formulation presented in (6).

**Algorithm Fixed_PRB** : Request Grant of $\mathcal{W}$ PRBs

**input:**
$\mathcal{W}$ = number of PRBs requested
**parameters:**
$\mathbf{H} = \{H_n^1, H_n^2, \dots H_n^N\}$: non-parametric estimate of cumulative hazard function for channels 1 to $N$
$\mathbf{t} = \{t_1, t_2, \dots t_N\}$: length of current idle period for channels 1 to $N$ in terms of PRBs
$p$ - the probability of successful transmission threshold
**output:**
$\mathbf{x} = \{x_1, x_2, \dots x_N\}$: number of resource blocks allocated in channels 1 to $N$

$\theta_{th} := -\ln p$
$\theta := 0$
$\mathbf{x} := \mathbf{0}$
**while** $\sum_i x_i \leq \mathcal{W}$ **do**
  $\theta_{min} = \min_i \; H_n^i(t_i + x_i + 1) - H_n^i(t_i)$
  $i_{min} = \text{argmin}_i \; H_n^i(t_i + x_i + 1) - H_n^i(t_i)$
  **if** $\theta_{min} \leq \theta_{th}$ **then**
    $x_{i_{min}} = x_{i_{min}} + 1$
    $\theta = \theta_{min}$
  **else**
    break
  **end if**
**end while**
**return** $\mathbf{x}$

For some applications, an SU may want to request the maximum possible number of PRBs subject to the constraints. A minor modification to Algorithm Fixed_PRB can achieve that. The only change required is to remove the condition in the *while* loop and make it an infinite loop. The algorithm terminates when no more PRBs can be allocated on any of the $N$ channels, i.e., the *if* statement inside the while loop fails. We call this *Algorithm Max_PRB*.

### E. Example

Figure 1 illustrates a possible allocation using Algorithm Fixed_PRB with 5 channels. In the figure, the SU requests

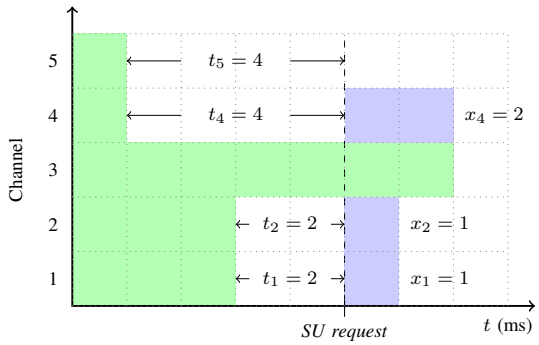


Fig. 1. Allocation of resource blocks for the SU. PU transmissions in green, SU transmissions in blue

$\mathcal{W} = 4$ PRB pairs at time shown. The idle time lengths of the channels are shown as $t_i,\ i = 1, 2, 4, 5$ (Channel 3 is busy at the time of request). The optimal allocation is shown as the set of $\{x_i : \sum_i x_i = \mathcal{W}\}$ that satisfies the interference constraint across all the channels.

## IV. Evaluation

### A. Spectrum Occupancy Data

We use three sets of collected data to model PU activity. The first set was collected using an indoor antenna on the National Institute of Standards and Technology (NIST) campus in Gaithersburg, MD. The second and third datasets were collected using outdoor antennas in the city of Philadelphia, PA. The locations were chosen to test our algorithms in indoor and outdoor settings in an urban environment. Data were collected in Band 17, a 10 MHz uplink (UL) LTE band centered at 709 MHz at all the three locations.

The NIST campus data collection system consisted of a 10.78 cm "rubber duck" antenna connected to an Ettus Universal Sofware Radio Peripheral (USRP) [1]. A 56 point power spectrum (in dB) for each 1 ms period (after aggregating I/Q samples every 80 ns) was computed and the middle 50 values used as power values of the 50 LTE channels. Since LTE allocates PRBs in pairs, our collected dataset consisted of an integer power value, in dB, for a pair of PRBs (1 ms in time). A noise power threshold was then applied to produce a binary occupancy sequence for each of the 50 channels. The noise power threshold was chosen 3 dB above the value that produced a probability of false alarm (PFA) below 1 %.

Data was collected for two different one hour periods:

- 3:00 PM to 4:00 PM local time, Monday, August 28, 2017 ($1^{st}$ day)
- 3:00 PM to 4:00 PM local time, Tuesday, August 29, 2017 ($2^{nd}$ day)

[1]The identification of any commercial product or trade name does not imply endorsement or recommendation by the National Institute of Standards and Technology, nor is it intended to imply that the materials or equipment identified are necessarily the best available for the purpose.

Sahoo, Anirudha; Hall, Timothy; Hagwood, Robert.
"Optimal Dynamic Spectrum Access Scheme for Utilizing White Space in LTE Systems."
Paper presented at IEEE Wireless Communications and Networking Conference (WCNC), Marrakech, Morocco. April 15, 2019 - April 19, 2019.

We chose these so that we could compare the same time period on two separate days.

The second and third datasets were collected at two locations in the metro Philadelphia area on the CityScape spectrum monitoring system [21] with additional processing of the I/Q samples to produce output files in the same format as the data collected at NIST. We converted the CityScape datasets into binary occupancy sequences using the noise threshold to which the CityScape USRPs were calibrated.

### B. Simulation

In our experiments, we used occupancy data of LTE uplink channels from channel 15 to 24 (total of 10 channels) as PU traffic. This ensures that the SU does not transmit over the control channels, *Physical Random Access Channel (PRACH)* and *Physical Uplink Control Channel (PUCCH)*. Idle and busy periods for each channels were built based on a sampling interval (1 ms) and noise threshold. Then a non-parametric estimation of the cumulative hazard function of each channel is computed. The threshold for probability of successful transmission is set to 0.9, which implies the threshold of probability of interference is 0.1.

We evaluate the performance of our algorithms in different configurations. The configurations are denoted with a concatenation of three text strings separated by underscores in the form *station_train_run*, where *station* $\in$ {*lab, upenn01, upenn02*} is the location where the data was collected, *train* $\in \{1^{st}, 2^{nd}\}$ represents the data used for *training* the algorithm, i.e., data used for building the cumulative hazard function and *run* $\in \{1^{st}, 2^{nd}\}$ denotes the data that represents the PU spectrum occupancy while *running* the algorithm. For lab station, values of $1^{st}$ and $2^{nd}$ represent one hour data from $1^{st}$ and $2^{nd}$ day respectively. For upenn01 and upenn02 station, $1^{st}$ and $2^{nd}$ represent the first and second half of the one hour data collected at those stations respectively. For example, in configuration *lab*_$1^{st}$_$2^{nd}$ an algorithm is trained using one hour data collected in NIST lab from the $1^{st}$ day and run using one hour data from the $2^{nd}$ day. An algorithm trained using the $1^{st}$ half-hour data collected at upenn01 station and run using the $2^{nd}$ half-hour data is denoted as configuration *upenn01*_$1^{st}$_$2^{nd}$.

The SU traffic is modeled as a Poisson arrival process. For Algorithm Fixed_PRB, an SU requests a fixed number of PRBs and the algorithm allocates up to that many PRBs while ensuring that the probability of interference is below the specified threshold. For Algorithm Max_PRB, an SU requests the maximum possible number of PRBs, and the algorithm allocates the maximum possible PRBs subject to the given interference probability constraint. The requests and allocations in our simulation are always in terms of 1 ms time lengths, but we use the term PRBs rather than "pair of PRBs" for simplicity.

### C. Metrics

Performance of the two algorithms was measured with the following metrics.

- White Space Utilization (WSU): Given the spectrum occupancy of a set of channels, the WSU by an SU is defined as the fraction of total idle PRBs used by the SU for its own transmission. In other words, it is the ratio of number of idle PRBs used by the SU for its own transmission to the total idle PRBs present in the spectrum occupancy of the set of channels.
- Probability of Interference (PoI): The PoI of the secondary user across a set of channels is defined as the probability that a transmission of the SU collides with that of the PU on those channels. Thus, it is the ratio of the number of times an SU transmission collides (or runs into a busy period) with a PU transmission across those set of channels to the total number of SU transmissions over a long observation period.
- Percentage Overlap of SU Transmission (POST): This is the number of PRBs used for SU transmissions that overlaps with PU transmissions across a set of channels expressed as a percentage of total PRBs used for SU transmissions across the same set of channels.

## V. Results

### A. Performance of Algorithm Max_PRB

Figures 2, 3 and 4 show the performance of Algorithm Max_PRB in terms of WSU as the average request inter-arrival duration increases for lab, upenn01 and upenn02 datasets respectively. As average request inter-arrival duration increases, the offered load to the algorithm decreases, leading to a decrease in WSU for all the datasets. However, for the lab dataset, WSU is much higher than for the upenn01 and upenn02 datasets. For the lab dataset, all ten channels are idle for about 95 % of the time (for $1^{st}$ day), whereas for upenn01, it varies between 89 % to 90 % and for upenn02, it varies between 57 % to 89 % (see Table I). Further, for the lab dataset, maximum idle duration across the ten channels (for $1^{st}$ day) vary between 35 345 ms to 51 532 ms. But the maximum idle durations in the upenn01 dataset lie between 136 ms and 191 ms. For upenn02 those numbers are 34 ms to 154 ms. Thus, the lab data has idle durations two orders of magnitude greater than those of upenn01, and upenn01 idle durations are significantly higher than those of upenn02. Also, the idle durations of the lab data were not continuous, causing long *flat* periods in the $H(\cdot)$ function, leading to allocations of more PRBs than in the upenn01 and upenn02 datasets. This also causes the slope of $H(\cdot)$ function of the lab data to be lower than that of upenn01 and upenn02 datasets. Since a lower slope of $H(\cdot)$ function leads to higher number of PRB allocation (see Eqn (5)), WSU for lab dataset is much higher compared to those of upenn01 and upen02. Comparing WSU between upenn01 and upenn02, we notice that the WSU of upenn01 is higher. This is attributed to the fact that fraction of idle time and the maximum idle duration of channels are much higher in upenn01 dataset than those of upenn02.

In Figure 2, we observe that the WSU for $lab\_1^{st}\_1^{st}$ is the highest and for $lab\_2^{nd}\_2^{nd}$ is the lowest. This is largely because there are larger idle durations on the $1^{st}$ day compared

Sahoo, Anirudha; Hall, Timothy; Hagwood, Robert.
"Optimal Dynamic Spectrum Access Scheme for Utilizing White Space in LTE Systems."
Paper presented at IEEE Wireless Communications and Networking Conference (WCNC), Marrakech, Morocco. April 15, 2019 - April 19, 2019.

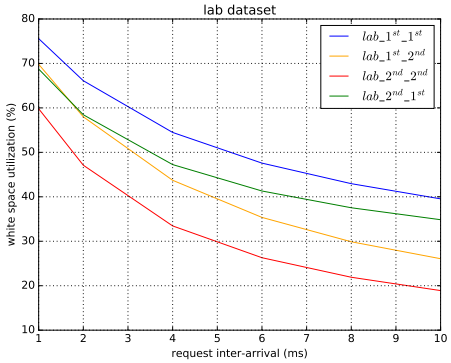


Fig. 2. WSU vs inter-arrival time for lab dataset running Algorithm Max_PRB

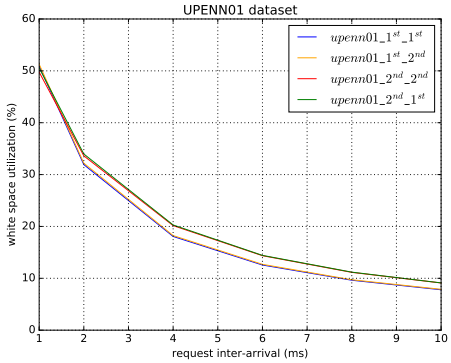


Fig. 3. WSU vs inter-arrival time for upenn01 dataset running Algorithm Max_PRB

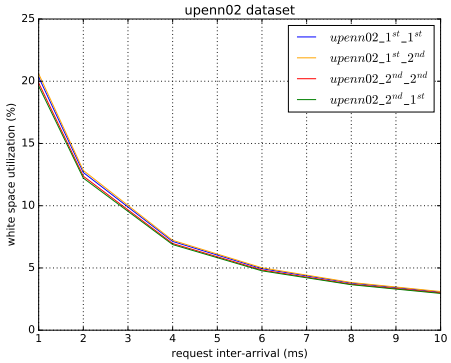


Fig. 4. WSU vs inter-arrival time for upenn02 dataset running Algorithm Max_PRB

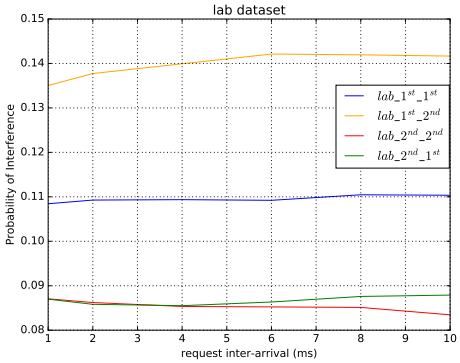


Fig. 5. Prob. of Interference vs inter-arrival time for lab dataset running Algorithm Max_PRB

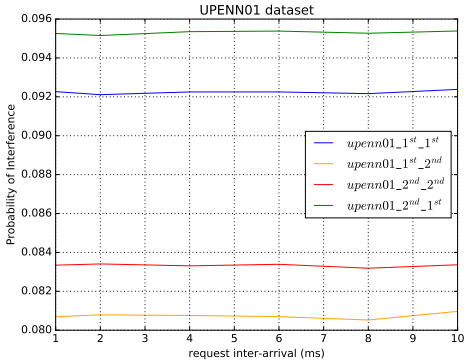


Fig. 6. Prob. of Interference vs inter-arrival time for upenn01 dataset running Algorithm Max_PRB

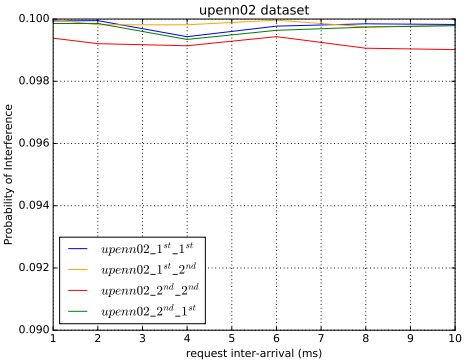


Fig. 7. Prob. of Interference vs inter-arrival time for upenn02 dataset running Algorithm Max_PRB

Sahoo, Anirudha; Hall, Timothy; Hagwood, Robert.
"Optimal Dynamic Spectrum Access Scheme for Utilizing White Space in LTE Systems."
Paper presented at IEEE Wireless Communications and Networking Conference (WCNC), Marrakech, Morocco. April 15, 2019 - April 19, 2019.

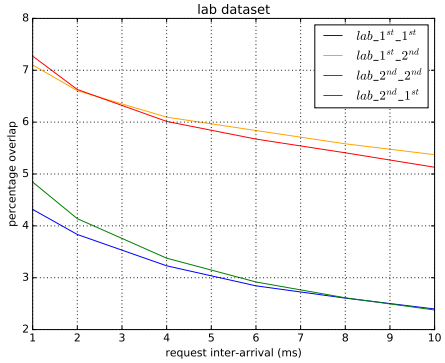


Fig. 8. Percentage overlap vs inter-arrival time for lab dataset running Algorithm Max_PRB

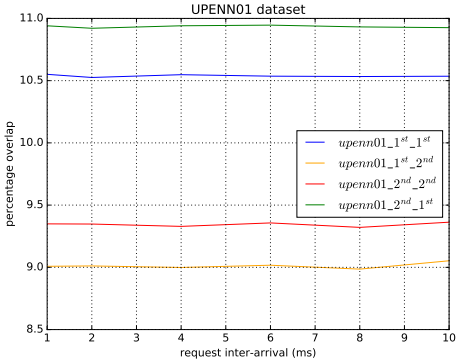


Fig. 9. Percentage overlap vs inter-arrival time for upenn01 dataset running Algorithm Max_PRB

to the $2^{nd}$ day. WSU of the other two configurations lies between these two.

For the upenn01 and upenn02 datasets, the relative performance of WSU among different configurations is close to each other. Note that configurations with $1^{st}$_$1^{st}$ and $2^{nd}$_$2^{nd}$ suffixes are not practical, since the algorithm is run on the same data as the training data. In practice, the algorithm will train (i.e., build the $H(\cdot)$ function) on the first half hour (or some fixed duration) data and then allocate PRBs to SU using the built $H(\cdot)$ function. So, $1^{st}$_$2^{nd}$ represents such a scenario. $2^{nd}$_$1^{st}$ represents a scenario where the PU traffic may be swapped between the two half hour periods (in case such traffic occurs in practice). Since the relative performances are close to each other, it shows that a system deploying Algorithm Max_PRB can perform as well as the theoretical system (e.g., $1^{st}$_$1^{st}$) when it trains on first half hour data and then runs on the next half hour.

Figures 5, 6 and 7 present the measured PoI as average SU request inter-arrival time increases for the three datasets. Measured PoI for the upenn01 and upenn02 datasets is always below the set threshold (0.1) for all configurations. For the lab dataset, the measured PoI is below the threshold for the $lab\_2^{nd}\_2^{nd}$ and $lab\_2^{nd}\_1^{st}$ configuration. However, for the other two configurations ( $lab\_1^{st}\_1^{st}$ and $lab\_1^{st}\_2^{nd}$) the measured PoI is slightly higher than the threshold. The first lab dataset has longer idle time durations and is idle for a higher fraction of time. So, when the algorithm is trained using this data, the PRB grants are more generous ($H(\cdot)$ function is more relaxed) and hence when the algorithm runs on the second dataset it encounters more interference. When the algorithm is trained and run on first dataset (configuration $1^{st}$_$1^{st}$), the PoI slightly exceeds the threshold mostly due to estimation error (of $H(\cdot)$ function). Measured PoI remains almost constant in all configurations of all datasets as the inter-arrival time between SU requests increases. Hence, the performance of the PU system remains almost the same regardless of the load on the SU system.

Figures 8, 9 and 10 show POST values for the lab, upenn01 and upenn02 datasets respectively. The percentage overlap is below 7.5 % for all configurations for the lab dataset. For upenn01 and upenn02 the maximum we see are 11 % and 13 %, respectively. The lab dataset has a higher fraction of idle duration, and some idle periods are very long, which leads to a lower POST value.

| chan num | lab ($1^{st}$ day) | | lab ($2^{nd}$ day) | | upenn01 | | upenn02 | |
|---|---|---|---|---|---|---|---|---|
| | % Idle duration | max Idle duration (ms) | % Idle duration | max Idle duration (ms) | % Idle duration | max Idle duration (ms) | % Idle duration | max Idle duration (ms) |
| 15 | 95.8 | 43431 | 92.3 | 28892 | 90.6 | 170 | 89.4 | 127 |
| 16 | 95.4 | 43471 | 92.1 | 28892 | 90.8 | 184 | 89.9 | 132 |
| 17 | 95.6 | 43432 | 92.4 | 28935 | 91.0 | 163 | 89.2 | 154 |
| 18 | 95.8 | 35345 | 92.7 | 28980 | 90.8 | 191 | 87.8 | 106 |
| 19 | 95.7 | 44151 | 92.8 | 28980 | 89.8 | 166 | 82.0 | 68 |
| 20 | 95.6 | 51532 | 92.8 | 28980 | 88.9 | 149 | 77.8 | 63 |
| 21 | 95.9 | 51532 | 92.9 | 28980 | 88.7 | 142 | 77.0 | 66 |
| 22 | 96.0 | 49255 | 93.1 | 19401 | 89.8 | 136 | 57.2 | 34 |
| 23 | 95.9 | 51529 | 93.1 | 31681 | 90.3 | 155 | 70.6 | 36 |
| 24 | 95.8 | 51529 | 93.2 | 30841 | 90.3 | 142 | 83.4 | 79 |

TABLE I
IDLE TIME DURATION INFORMATION FOR THE DATASETS

### B. Performance of Algorithm Fixed_PRB

Figures 11, 12 show how WSU varies when the number of requested PRBs increases for Algorithm fixed_PRB over the lab and upenn01 datasets, respectively, when the average SU request inter-arrival time is 1 ms. WSU increases as more PRBs are requested, since the algorithm exploits more white space before reaching a limiting value. The algorithm is limited by the available white space and the interference constraint. Hence, beyond a certain point, the algorithm cannot grant the requested number of PRBs and instead allocates the maximum possible within the constraints. In fact, the values at which WSU saturates match the WSU values of Algorithm Max_PRB corresponding to average request inter-arrival time of 1 ms.

Sahoo, Anirudha; Hall, Timothy; Hagwood, Robert.
"Optimal Dynamic Spectrum Access Scheme for Utilizing White Space in LTE Systems."
Paper presented at IEEE Wireless Communications and Networking Conference (WCNC), Marrakech, Morocco. April 15, 2019 - April 19, 2019.

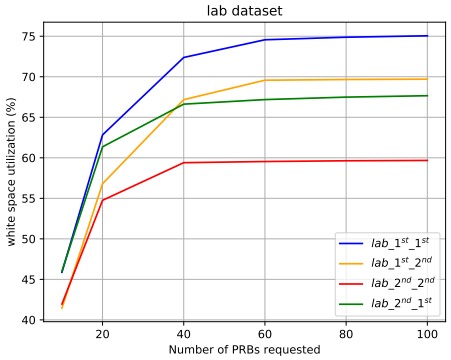


Fig. 11. WSU vs number of Requested PRBs for lab dataset running Algorithm Fixed_PRB

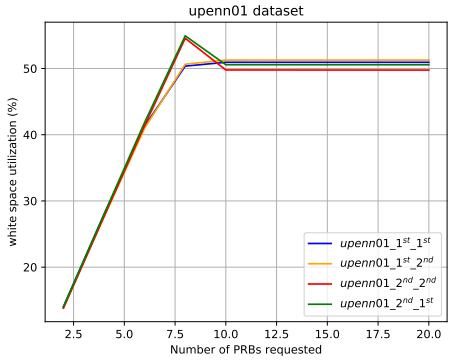


Fig. 12. WSU vs number of Requested PRBs for upenn01 dataset running Algorithm Fixed_PRB

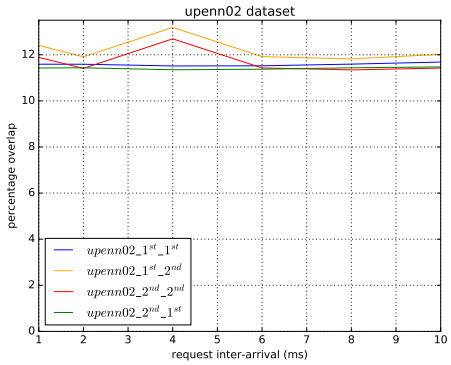


Fig. 10. Percentage overlap vs inter-arrival time for upenn02 dataset running Algorithm Max_PRB

Similar to Algorithm Max_PRB, the WSU values are close to each other for various configurations in the upenn01 dataset. For the lab dataset the WSU for $lab\_1^{st}\_1^{st}$ is the highest and for $lab\_2^{nd}\_2^{nd}$ is the lowest, and WSU for the other two configurations lies between these two. The reasons for these relative performances are the same as those given for Algorithm Max_PRB.

Figures 13, 14 show a measured PoI for the lab and upenn01 datasets that initially increases as the number of requested PRBs increases and then stays constant. These constant (saturated) PoI values match the corresponding values for Algorithm Max_PRB when the average request inter-arrival time is 1 ms. For all the datasets and all configurations, except for $lab\_1^{st}\_2^{nd}$, measured PoI is less than the set threshold. The anomaly in $lab\_1^{st}\_2^{nd}$ is due to the same reason given for Algorithm Max_PRB.

Performance of the algorithm in terms of POST as the requested number of PRBs increases is shown for the lab and upenn01 datasets in Figures 15, 16. Overall, the POST values are low. Similar to WSU and PoI, the saturated values match with those of Algorithm Max_PRB.

Due to space limitations, we have not provided the performance graphs of Algorithm Fixed_PRB over upenn02 dataset. But they are similar to those of upenn01 dataset.

## VI. Conclusion and Future Work

We presented an optimal DSA algorithm for allocation of PRBs to the SU. The algorithm is a form of the unbounded knapsack problem that maximizes the number of allocated PRBs such that the PoI across all the channels remains below a threshold using a non-parametric estimate of the cumulative hazard function. The algorithm was tested on real LTE datasets, one collected in our laboratory and two collected in center city Philadelphia. Our results show that the algorithm is able to make good use of the available white space while keeping the overall PoI around the desired threshold. Hence, our algorithm can be readily implemented in a practical LTE network.

In this study, we used equal weights for the channels. Our scheme should be studied when the channels have different weights due to different priority or channel quality. The SU scheduling model assumed ideal knowledge of the PU activity at the time of the SU request and the ability to schedule the SU transmission within one subframe. Further work should investigate imperfect sensing of the band and realistic scheduling overhead.

## Acknowledgment

The authors thank Prof. Sumit Roy and Mr. Kyeong Su Shin of the University of Washington for collecting and processing data for us from the Cityscape observatory in Philadelphia.

## References

[1] "Citizens broadband radio service," 2 C.F.R. § 96, 2016.
[2] M. Lopez-Benitez and F. Casadevall, "Discrete-time spectrum occupancy model based on Markov chain and duty cycle models," in *2011 IEEE International Symposium on Dynamic Spectrum Access Networks (DySPAN)*, May 2011, pp. 90–99.
[3] H. Kim, and K. Shin, "Efficient Discovery of Spectrum Opportunities with MAC-layer Sensing in Cognitive Radio Networks," *IEEE Transactions on Mobile Computing*, vol. 7, no. 5, pp. 533–545, May 2008.

Sahoo, Anirudha; Hall, Timothy; Hagwood, Robert.
"Optimal Dynamic Spectrum Access Scheme for Utilizing White Space in LTE Systems."
Paper presented at IEEE Wireless Communications and Networking Conference (WCNC), Marrakech, Morocco. April 15, 2019 - April 19, 2019.

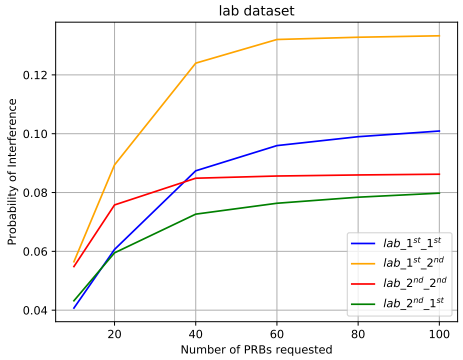


Fig. 13. Prob. of Interference vs number of Requested PRBs for lab dataset running Algorithm Fixed_PRB

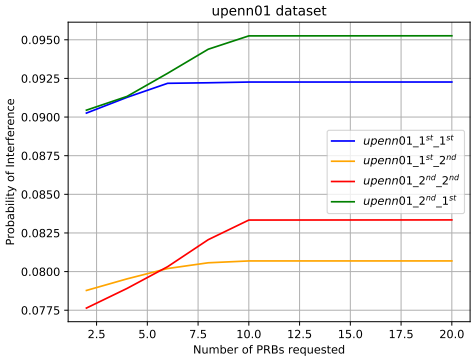


Fig. 14. Prob. of Interference vs number of Requested PRBs for upenn01 dataset running Algorithm Fixed_PRB

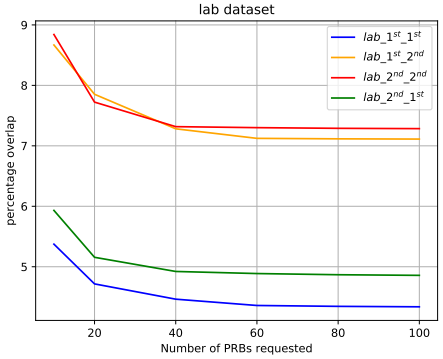


Fig. 15. Percentage overlap vs number of Requested PRBs for lab dataset running Algorithm Fixed_PRB

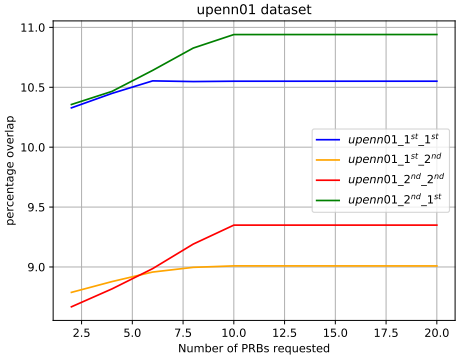


Fig. 16. Percentage overlap vs number of Requested PRBs for upenn01 dataset running Algorithm Fixed_PRB


[4] M. Sharma and A. Sahoo, "Stochastic Model Based Opportunistic Channel Access in Dynamic Spectrum Access networks," *IEEE Transactions on Mobile Computing*, vol. 13, no. 7, pp. 1625–1639, July 2014.

[5] S. Geirhofer, L. Tong, and B. M. Sadler, "Dynamic spectrum access in WLAN channels: Empirical model and its stochastic analysis," in *TAPAS '06 Proceedings of the First International Workshop on Technology and Policy for Accessing Spectrum*, August 2006.

[6] ——, "Dynamic spectrum access in the time domain: Modeling and exploiting white space," *IEEE Communications Magazine*, vol. 45, no. 5, pp. 66–72, May 2007.

[7] L. Stabellini, "Quantifying and modeling spectrum opportunities in a real wireless environment," in *2010 IEEE Wireless Communication and Networking Conference*, April 2010, pp. 1–6.

[8] Q. Zhao, L. Tong, A. Swami and Y. Chen, "Decentralized Cognitive MAC for Opportunistic Spectrum Access in Ad Hoc Networks: A POMDP Framework," *IEEE Journal on Selected Areas in Communications*, vol. 30, no. 2, pp. 589–600, April 2007.

[9] K. W. Sung, S. Kim and J. Zander, "Temporal Spectrum Sharing Based on Primary User Activity Prediction," *IEEE Transactions on Wireless Communications*, vol. 9, no. 12, pp. 3848–3855, December 2010.

[10] A. Plummer, M. Taghizadeh and S. Biswas, "Measurement based bandwidth scavenging in wireless networks," *IEEE Transactions on Mobile Computing*, vol. 11, no. 1, pp. 19–32, January 2012.

[11] S. Yin, D. Chen, Q.Zhang, M. Liu and S. Li, "Mining Spectrum Usage Data: A Large-Scale Spectrum Measurement Study," *IEEE Transactions on Mobile Computing*, vol. 11, no. 6, pp. 1033–1046, June 2012.

[12] P. Huang, C-J. Liu, X. Yang, L. Xiao and J. Chen, "Wireless Spectrum Occupancy Prediction Based on Partial Periodic Pattern Matching," *IEEE Transactions on Parallel and Distributed Systems*, vol. 25, no. 7, pp. 1925–1934, July 2014.

[13] T. A. Hall, A. Sahoo, C. Hagwood, and S. Streett, "Exploiting LTE white space using dynamic spectrum access algorithms based on survival analysis," in *2017 IEEE International Conference on Communications (ICC)*, May 2017, pp. 1–7.

[14] ——, "Dynamic spectrum access algorithms based on survival analysis," *IEEE Transactions on Cognitive Communications and Networking*, vol. 3, no. 4, pp. 740–751, Dec 2017.

[15] H. Safa and K. Tohme, "LTE uplink scheduling algorithms: Performance and challenges," in *2012 19th International Conference on Telecommunications (ICT)*, April 2012, pp. 1–6.

[16] T. Erpek, A. Abdelhadi, and T. C. Clancy, "Application-aware resource block and power allocation for LTE," in *2016 Annual IEEE Systems Conference (SysCon)*, April 2016, pp. 1–5.

[17] O. Aalen, O. Borgan, and H. Gjessing, *Survival and event history analysis: a process point of view*. Springer Science & Business Media, 2008.

[18] R. G. Miller Jr, *Survival analysis*. John Wiley & Sons, 2011, vol. 66.

[19] M. R. Garey and D. S. Johnson, *Computers and Intractability: A Guide to the Theory of NP-Completeness*. W. H. Freeman, 1979.

[20] T. H. Cormen, C. E. Leiserson, and R. L. Rivest, *Introduction to Algorithms*. McGraw-Hill Book Company, 1990.

[21] S. Roy, K. Shin, A. Ashok, M. McHenry, G. Vigil, S. Kannam, and D. Aragon, "Cityscape: A metro-area spectrum observatory," in *2017 26th International Conference on Computer Communication and Networks (ICCCN)*, July 2017, pp. 1–9.



Sahoo, Anirudha; Hall, Timothy; Hagwood, Robert.
"Optimal Dynamic Spectrum Access Scheme for Utilizing White Space in LTE Systems."
Paper presented at IEEE Wireless Communications and Networking Conference (WCNC), Marrakech, Morocco. April 15, 2019 - April 19, 2019.

# On-Wafer Transistor Characterization to 750 GHz –the approach, results, and pitfalls*

Dylan F. Williams, *Fellow*, *IEEE*, Jerome Cheron, Benjamin Jamroz, Richard Chamberlin

***Abstract*—We review approaches developed at the National Institute of Standards and Technology for on-wafer transistor characterization and model parameter extraction at sub-millimeter wavelengths and compare them to more common approaches developed for use at lower frequencies. We discuss important improvements in accuracy, approaches to estimating the uncertainty of the procedure, and recent research on further improving these methods.**

***Index Terms*—Vector-network-analyzer calibration, on-wafer measurements, scattering parameters, sub-millimeter-wave, transistor, uncertainty.**

## I. Introduction

The National Institute of Standards and Technology (NIST) has been a leader in the development of on-wafer measurement approaches. This work began in the early 1990s, and included the development of methods for extending the bandwidth of on-wafer thru-reflect-line (TRL) vector-network-analyzer (VNA) calibrations [1], measuring the characteristic impedance of the transmission lines used in the calibrations [2, 3], and resetting the reference impedance of the calibration to 50 Ω. This calibration strategy has become the de facto on-wafer calibration of reference to which all other on-wafer calibrations are compared. It has been successfully used in coplanar waveguide (CPW), microstrip, coaxial transmission lines, and rectangular waveguide.

However, excitation of higher-order modes in coplanar waveguide (CPW) makes it difficult to control calibrations at sub-millimeter wavelengths [4, 5]. Figure 1 illustrates this with an example of a measurement of the reverse transmission through a transistor. These measurements were calibrated with commercial impedance-standard substrate (ISS) placed on ceramic and metal chucks, and designed for use with 50 µm-pitch probes at sub-millimeter-wave frequencies. The curves labeled "ISS on ceramic" correspond to measurements performed with the ISS placed on a thick ceramic substrate. The curves labeled "ISS on metal" correspond to measurements calibrated when the ISS was placed directly on the metal chuck. The figure illustrates how difficult it is to accurately measure reverse transmission, which also impacts important figures of merit such as the maximum stable gain and unilateral gain of these transistors. We have only been able to do somewhat better with on-wafer CPW calibrations.

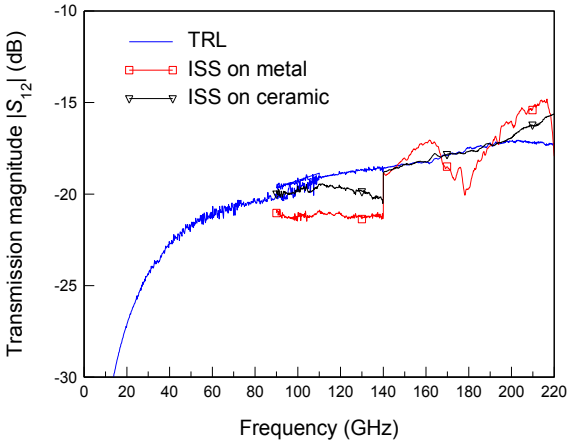


Fig. 1. Comparison of TRL measurements to measurements corrected with an impedance standard substrate (ISS) placed on a metal chuck and on a thick ceramic substrate. The measurements are banded over the frequency ranges 10 MHz – 110 GHz, 90-140 GHz, and 140-220 GHz, resulting in overlaps and discontinuities at the band edges. From [6].

In this paper we will show how on-wafer TRL calibration in microstrip lines fabricated on thin BCB layers can be used to make accurate measurements at submillimeter wavelengths. We will also touch on coupling corrections, uncertainty analyses, the importance of Monte-Carlo simulations, and how traceability can be established for transistor measurements at these frequencies.

## II. The TRL Approach

The same measurements calibrated with the TRL approach based on microstrip lines printed on the integrated circuit, as developed at the National Institute of Standards and Technology in [6], are shown in blue lines in Fig. 1. This is a true on-wafer calibration, as the calibration and transistor test structures use the same access lines. This ensures that electrical contact-pad and access-line parasitics are removed from the measurements as accurately as possible. This calibration

This work was supported by the Defense Advanced Research Projects Agency's Terahertz Electronics Program. The views, opinions, and/or findings contained in this article are those of the author and should not be interpreted as representing the official views or policies, either expressed or implied, of either the Defense Advanced Research Projects Agency or the Department of Defense.

D. F. Williams, Jerome Cheron, Benjamin Jamroz and Richard Chamberlin are with the National Institute of Standards and Technology, Boulder, CO 80305 USA (phone: 303-497-3138; e-mail: dylan.williams@ nist.gov).

*Work supported by US government, not subject to US copyright.



Williams, Dylan; Cheron, Jerome; Jamroz, Benjamin; Chamberlin, Richard.
"On-Wafer Transistor Characterization to 750 GHz: the approach, results, and pitfalls."
Paper presented at BiCMOS and Compound Semiconductor Integrated Circuits and Technology Symposium (BCICTS), San Diego, CA, United States. October 15, 2018 - October 17, 2018.

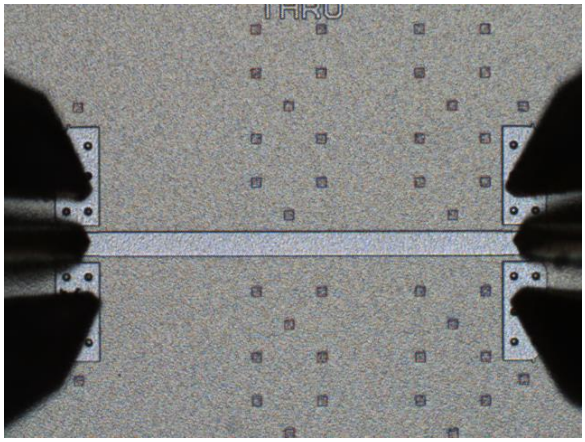


Fig. 2. The thru line used in our calibration kit. The small squares are dielectric fill patterns, and have a negligible impact on the electrical behavior of the microstrip transmission lines. From [6].

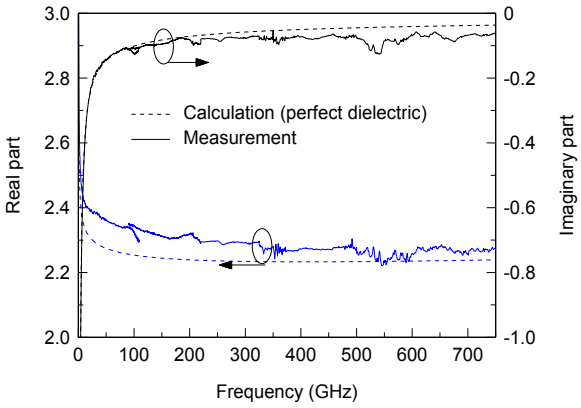


Fig. 3. Real and imaginary parts of the measured effective dielectric constant, as determined by our TRL calibration, compared to calculation. The measurements are banded over the frequency ranges 10 MHz – 110 GHz, 90-140 GHz, and 140-220 GHz, resulting in overlaps and discontinuities at the band edges. From [6].

exhibits none of the problems of the CPW calibrations.

The TRL calibration locates the measurement reference plane directly in small, single-mode microstrip lines shown in Fig. 2. These are placed adjacent to the transistor, minimizing extrinsic transistor parasitics. In this case, the transmission lines were low-loss 22 µm-wide microstrip lines printed on bisbenzocyclobutene-based (BCB) monomers approximately 8 µm thick, which raises the cutoff frequency of any higher-order modes to well over 1 THz.

The microstrip TRL calibration can be extended to very high frequencies. Fig. 3 compares measurements of the propagation constant of these microstrip lines to calculations performed with the microstrip transmission-line model of [7], and shows excellent agreement to 750 GHz, despite having to acquire these measurements over six different frequency bands,[1] and not always being able to reuse the same calibration kit in each band due to the inevitable damage to probe contacts caused by repeated alignment and testing.

## III. Uncertainty and Traceability

Since the introduction of on-wafer TRL calibrations, NIST has continued to work on understanding their uncertainties and developing traceability for these on-wafer measurements. However, because it is difficult to develop standard on-wafer calibration structures with specified metal conductivities, complex permittivities and geometries in different integrated-circuit technologies, the work has not focused on developing standard artifacts as has been done in coaxial transmission lines and rectangular waveguide. Instead, uncertainties and the traceability that follows from them are developed for each specific integrated-circuit technology.

Early work began with a straightforward analytic analysis [8]. This was followed with the automation of frequency-point-by-frequency-point uncertainties in the TRL calibration with the StatistiCAL[2] software package at NIST [9, 10]. This software package was used in [6], and leveraged ODRPACK [11] and its ability to estimate uncertainty from residuals in the measurements.

However, the level of automation was low, and the uncertainties developed with these early approaches were not in a form that could be propagated through more complex processes and analyses. For example, the measurement errors could not be easily propagated through Fourier Transforms used to support complex traceability chains and propagated through other complex analyses such as model parameter extraction.

## IV. The Microwave Uncertainty Framework

These limitations led to the development of the Microwave Uncertainty Framework [12] at NIST and VNATools [13] at the Swiss Federal Institute for Metrology (METAS). The Microwave Uncertainty Framework supports both conventional sensitivity analyses, which is useful for linear problems, and Monte-Carlo analysis, which is required for nonlinear problems. The Microwave Uncertainty Framework was developed specifically to support a broad range of measurement applications, including coaxial, rectangular waveguide, and on-wafer VNA calibrations, complex traceability chains including waveform, power, and oscilloscope calibrations, and system level measurements and applications, such as error-vector-magnitude determination, transistor model parameter extraction, and circuit simulations.

In the context of prior work, the Microwave Uncertainty Framework captures correlated uncertainties not available from

[1]The band edges occur at 90 GHz, 110 GHz, 140 GHz, 220 GHz, 325 GHz and 500 GHz.

[2]Registered trademark of the National Institute of Standards and Technology. NIST does not endorse commercial products. Trade names are included only to better define experiments. Other products may work as well or better.



Williams, Dylan; Cheron, Jerome; Jamroz, Benjamin; Chamberlin, Richard.
"On-Wafer Transistor Characterization to 750 GHz: the approach, results, and pitfalls."
Paper presented at BiCMOS and Compound Semiconductor Integrated Circuits and Technology Symposium (BCICTS), San Diego, CA, United States. October 15, 2018 - October 17, 2018.

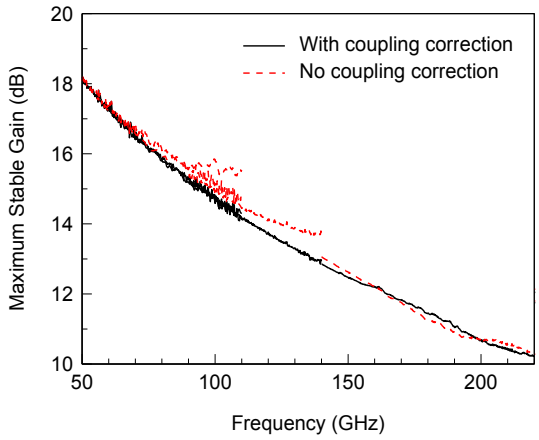


Fig. 4. The maximum-stable gain of a transistor corrected with standard TRL and with TRL augmented with coupling corrections. From [6].

StatisitiCAL. Correlated uncertainties are key to propagating uncertainty though Fourier Transforms, complex traceability chains, and other complex analyses, including the transistor-model-parameter-extraction process.

NIST has now applied the Microwave Uncertainty Framework to many of these problems [14-22], including transistor model parameter extraction and circuit design [23-25]. One of the key conclusions of our work is that correlated uncertainties are *not* enough to solve many of these problems accurately. Monte-Carlo approaches *must* be used in nonlinear problems such as transistor model parameter extraction and error-vector-magnitude calculations at millimeter-wave frequencies [23-25].

## V. Coupling

Despite the use of small single-mode microstrip transmission lines in our measurements, correcting for probe-to-probe coupling remains one of the key difficulties in performing accurate on-wafer measurements. Coupling behavior is complex, involves many tradeoffs, and can greatly impact the accuracy of on-wafer transistor measurements.

Nevertheless, probe-to-probe and other coupling in on-wafer measurement scenarios can be modeled and corrected for to first order [26, 27]. We illustrate this in Fig. 4 with a comparison of the maximum stable gain measured with TRL calibrations using different probes both before and after applying coupling corrections. Clearly, applying coupling corrections improves the consistency and accuracy of the measurements.

However, a key remaining problem is determining the uncertainty in coupling-corrected, on-wafer measurements. This is difficult because coupling models are not easy to develop, and assessing how much of the coupling is left uncorrected by the coupling-correction algorithm is challenging.

Current research at NIST is focusing on how to use measurement residuals to capture correlated uncertainty in coupling-corrected-transistor and other measurements where models of the corrections are suspect.

## VI. Conclusion

NIST algorithms allow for on-wafer calibrations traceable to dimensional and other measurements performed on the same integrated circuits on which the transistors are fabricated. These calibrations can now correct for most errors in the measurements, including probe-to-probe coupling, and then used to extract transistor models with measurement uncertainty and process variations [23, 24]. These models can then be used in conventional circuit simulators to estimate the expected range of circuit performance based on the uncertainty and process variations in the transistor models [25].

## VII. References

[1] R. B. Marks, "A multi-line method of network analyzer calibration," *IEEE Trans.Microw.Theory Techn.*, vol. 39, pp. 1205-1215, 1/1991 1991.

[2] D. F. Williams and R. B. Marks, "Transmission Line Capacitance Measurement," *IEEE Microwave and Guided Wave Letters*, vol. 1, pp. 243-245, 9/1991 1991.

[3] R. B. Marks and D. F. Williams, "Characteristic Impedance Determination using Propagation Constant Measurement," *IEEE Microw.and Guided Wave Letters*, vol. 1, pp. 141-143, 6/1991 1991.

[4] E. M. Godshalk, "Surface wave phenomenon in wafer probing environments," *Automatic RF Techniques Group Microwave Measurement Conference Digest*, vol. 40, pp. 10-19, 1992 1992.

[5] A. Rumiantsev, R. Doerner, and E. M. Godshalk, "The Influence of Calibration Substrate Boundary Conditions on CPW Characteristics and Calibration Accuracy at mm-Wave Frequencies," *Automatic RF Techniques Group Conference Digest*, vol. 72, pp. 168-173, 2008 2008.

[6] D. F. Williams, A. C. Young, and M. Urteaga, "A Prescription for Sub-Millimeter-Wave Transistor Characterization," *IEEE Trans.THz Sci.Technol.*, pp. 433-439, 7/1/2013 2013.

[7] H. M. Heiliger, M. Nagel, H. G. Roskos, H. Kurz, F. Schnieder, and W. Heinrich, "Thin-film microstrip lines for MM and sub-MM/wave on-chip interconnects," *IEEE MTT-S Int.Microwave Symp.*, vol. 2, pp. 421-424, 6/8/1997 1997.

[8] R. F. Kaiser and D. F. Williams, "Sources of Error in Coplanar-Waveguide TRL Calibrations," in *54th ARFTG Conference Digest*, 1999, pp. 1-6.

[9] D. F. Williams, C. M. Wang, and U. Arz, "An optimal vector-network-analyzer calibration algorithm," *IEEE Trans.Microw.Theory Techn.*, vol. 51, pp. 2391-2401, 12/2003 2003.

[10] D. F. Williams, C. M. Wang, and U. Arz, "An optimal multiline TRL calibration algorithm," *IEEE MTT-S Int.Microwave Symp.Dig.*, vol. 3, pp. 1819-1822, 6/2003 2003.

[11] P. T. Boggs, R. H. Byrd, J. E. Rogers, and R. B. Schnabel, "User's reference guide for ODRPACK



Williams, Dylan; Cheron, Jerome; Jamroz, Benjamin; Chamberlin, Richard.
"On-Wafer Transistor Characterization to 750 GHz: the approach, results, and pitfalls."
Paper presented at BiCMOS and Compound Semiconductor Integrated Circuits and Technology Symposium (BCICTS), San Diego, CA, United States. October 15, 2018 - October 17, 2018.

version 2.01 software for weighted orthogonal distance regression," Boulder, CO NISTIR 92-4834, 6/1992 1992.

[12] D. F. Williams and A. Lewandowski, "NIST Microwave Uncertainty Framework," ed: National Institute of Standards and Technology, http://www.nist.gov/ctl/rf-technology/related-software.cfm, 2011.

[13] *VNA Tools II*. Available: https://www.metas.ch/metas/en/home/fabe/hochfrequenz/vna-tools.html

[14] G. Avolio, A. Raffo, J. Jargon, P. D. Hale, D. M. M. Schreurs, and D. F. Williams, "Evaluation of Uncertainty in Temporal Waveforms of Microwave Transistors," *IEEE Trans.Microw.Theory Techn.*, vol. 63, pp. 2353-2363, 7/2015 2015.

[15] J. A. Jargon, U. Arz, and D. F. Williams, "Characterizing WR-8 waveguide-to-CPW probes using two methods implemented within the NIST Uncertainty Framework," in *80th ARFTG Microwave Measurement Conference*, 2012, pp. 1-5.

[16] J. A. Jargon, D. F. Williams, T. M. Wallis, D. X. LeGolvan, and P. D. Hale, "Establishing traceability of an electronic calibration unit using the NIST Microwave Uncertainty Framework," in *79th ARFTG Microwave Measurement Conference*, 2012, pp. 1-5.

[17] J. A. Jargon, D. F. Williams, P. D. Hale, and M. D. Janezic, "Characterizing a noninsertable directional device using the NIST uncertainty framework," in *83rd ARFTG Microwave Measurement Conference*, 2014, pp. 1-3.

[18] K. A. Remley, D. F. Williams, P. D. Hale, C. M. Wang, J. Jargon, and Y. Park, "Millimeter-Wave Modulated-Signal and Error-Vector-Magnitude Measurement With Uncertainty," *IEEE Transactions on Microwave Theory and Techniques*, vol. 63, pp. 1710-1720, 2015.

[19] J. A. Jargon, C. Cho, D. F. Williams, and P. D. Hale, "Physical models for 2.4 mm and 3.5 mm coaxial VNA calibration kits developed within the NIST microwave uncertainty framework," in *2015 85th Microwave Measurement Conference (ARFTG)*, 2015, pp. 1-7.

[20] J. A. Jargon, D. F. Williams, and P. D. Hale, "Developing models for Type-N coaxial VNA calibration kits within the NIST Microwave Uncertainty Framework," in *2016 87th ARFTG Microwave Measurement Conference (ARFTG)*, 2016, pp. 1-4.

[21] B. F. W. Jamroz, D.F.;Remley,K.A.;Horansky,R.D., "Importance of Preserving Correlations in Error-Vector-Magnitude Uncertainty," presented at the ARFTG Conference Digest, Philadelphia, PA, 2018.

[22] J. W. Jargon, D.F., "A New Calibration Method for Achieving High Insertion-Loss Measurements with a Vector Network Analyzer," presented at the ARFTG Microwave Measurements Conference, Philadelphia, PA, 2018.

[23] D. F. Williams, W. Zhao, R. Chamberlin, J. Cheron, and M. Urteaga, "Verification of a foundry-developed transistor model with measurement uncertainty," *ARFTG Microwave Measurement Conference Digest*, vol. 87, 5/27/2016 2016.

[24] D. F. Williams, R. Chamberlin, W. Zhao, J. Cheron, and M. Urteaga, "Transistor Model Verification Including Measurement Uncertainty," *IEEE Trans.Microw.Theory Techn.*, vol. 64, pp. 3927-3933, 11/2016 2016.

[25] D. F. Williams, R. A. Chamberlin, W. Zhao, J. Cheron, and M. E. Urteaga, "The Role of Measurement Uncertainty in Achieving First-Pass Design Success," in *2016 IEEE Compound Semiconductor Integrated Circuit Symposium (CSICS)*, 2016, pp. 1-4.

[26] F. J. Schmuckle, R. Doerner, G. N. Phung, W. Heinrich, D. F. Williams, and U. Arz, "Radiation, multimode propagation, and substrate modes in W-band CPW calibrations," *European Microwave Conf.*, vol. 41, pp. 297-300, 10/2011 2011.

[27] D. F. Williams, F. J. Schmuckle, R. Doerner, U. Arz, and W. Heinrich, "Crosstalk Corrections for Coplanar-Waveguide Scattering-Parameter Calibrations," *IEEE Transactions on Microwave Theory and Techniques*, vol. 62, pp. 1748-1761, 2014 2012.



Williams, Dylan; Cheron, Jerome; Jamroz, Benjamin; Chamberlin, Richard.
"On-Wafer Transistor Characterization to 750 GHz: the approach, results, and pitfalls."
Paper presented at BiCMOS and Compound Semiconductor Integrated Circuits and Technology Symposium (BCICTS), San Diego, CA, United States. October 15, 2018 - October 17, 2018.

# Probability of Coexistence of LTE-LAA and WLAN Systems Based on Delay Constraints*

Yao Ma, William Young†, Eric Anderson, and Jason Coder
Communications Technology Laboratory, National Institute of Standards and Technology
325 Broadway, Boulder, Colorado, USA

***Abstract*— To support efficient spectrum sharing and related standardization efforts in unlicensed spectrum, it is important to develop analytical tools to accurately quantify coexistence performance between long-term evolution license assisted access (LTE-LAA) and incumbent systems, such as wireless local area network (WLAN). Though joint throughput of spectrum sharing LTE-LAA and WLAN systems has been extensively studied, there lacks a systematic study on a high level metric – the probability of coexistence (PoC), which indicates whether coexistence is successful or not probabilistically. Another problem is that the majority of available results either ignored delay constraints, or studied only the mean (or variance) of delay, but have not considered the delay distribution and its impact on throughput. To address these problems, we define and analyze the original PoC metrics between LTE-LAA and WLAN systems based on two practical delay constraints. The first PoC is derived from the joint distribution probability of delays for successful transmissions; and the second PoC is defined upon the joint probability of delay-constrained throughput (DCT) of LAA and WLAN systems. To address the technical difficulties involved, we design a novel analytical framework to evaluate the moment generating function and cumulative distribution function (CDF) of the delay, and a new method to evaluate the DCT and its CDF. Consequently, the PoCs can be evaluated accurately with low complexity. The analytical results are verified by our Monte Carlo simulations, which demonstrate impacts of delay and throughput requirements on the PoCs, and illustrate design tradeoffs and insightful findings. These results provide theoretical and practical value for designing improved LTE-LAA and WLAN systems, and may be extended to other emerging spectrum sharing communication systems.**

Keywords: WLAN; LTE-LAA; Probability of Coexistence; Delay-Constrained Throughput; Delay Outage Probability

## I. Introduction

Accurately evaluating spectrum sharing performance between long-term evolution license assisted access (LTE-LAA) and IEEE 802.11 wireless local area network (WLAN) systems [1]–[5] is an important ongoing research topic. The listen before talk (LBT) scheme has been considered as a candidate in LAA to enable constructive coexistence [1], [2]. Category 3 and 4 LBT schemes are system-load based sensing schemes. Similar to WLAN, load-based LAA-LBT schemes may use carrier sense multiple access with collision avoidance (CSMA/CA) in the medium access control (MAC) layer, and their coexistence involves a complicated transmission backoff process.


†Dr. William Young participated in this work when he was affiliated with the NIST, USA. He is now with the MITRE Corporation.

Standardization efforts on spectrum sharing and coexistence are under way [1], [3], [6], [7]. In [6], coexistence is defined as "The ability of two or more spectrum-dependent devices or networks to operate without harmful interference." In [7], a likelihood of coexistence (LoC) is conceptually proposed. Yet, a detailed mathematical definition of this likelihood is not addressed in [7] but left open to future research based on system applications and environments. In [8], a logistic regression (LR) approach is developed to estimate the LoC between a WLAN system (as interference) and a Zigbee system (as device under test). This scheme uses a training dataset to track and learn the coexistence behaviors using measurements of several input and output parameters. Then, in the testing phase the LR algorithm estimates an LoC metric and the success or failure of each new transmission of the Zigbee system under WLAN interferences. This method relies on actual measurements and availability of training samples to track and predict coexistence performance.

In this paper, we seek to extend the prior art to the probabilistic coexistence research by introducing probability of coexistence (PoC) metrics, and develop methods to map system and MAC protocol parameters to PoCs, by considering two novel and practical successful transmission delay constraints. Here, we consider the LBT for the LAA system and the distributed coordination function (DCF) for the WLAN system. To distinguish from the LoC defined in [8] which is based on prediction of likelihood using logistic regression of measured data, in this paper we choose to use the term PoC for the probability analysis which is established by strict mathematical modeling of system and protocol parameters.

Both LTE-LAA and WLAN specifications have considered real-time audio and video services which are delay sensitive. We believe that two delay constraints are important for delay sensitive applications. The first constraint is related to the delay outage probability (DOP), defined as the probability that packets have not been successfully transmitted before a given delay threshold. The second constraint is based on the delay-constrained throughput (DCT), which is the packet throughput achieved before a given delay threshold. The DCT is more important than the average throughput in quantifying the coexistence performance, because it shows the impact of delay threshold on the throughput. Furthermore, a limiting case of the DCT (when the delay threshold becomes large) maps to static throughput studied in recent works [9]–[11]. Note that CSMA/CA channel access delay is a major consideration for

978-1-5386-5156-8/18/$31.00 ©2018 IEEE

Ma, Yao; Young, William; Anderson, Eric; Coder, Jason.
"Probability of Coexistence of LTE-LAA and WLAN Systems Based on Delay Constraints."
Paper presented at The 27th International Conference on Computer Communications and Networks (ICCCN 2018), Hangzhou, China. July 30, 2018 - August 2, 2018.

optimizing LAA based spectrum sharing schemes. However, to our knowledge, the DCT has not been clearly defined or analyzed for LAA-LBT and WLAN coexistence systems. The DCT defined here is different from those defined by Shannon information theory, which may involve fading channel distributions and signal to noise ratios (SNRs) of the channels.

To our knowledge, a majority of available methods use average throughput as a key performance metric without considering transmission delay constraints, such as [9]–[16], [18]. To study the impact of delay constraints on coexistence performance, current methods are insufficient. Some CSMA/CA MAC-layer performance analysis methods for WLAN systems were developed in [19], [20], and have been extended in [9]–[11] for coexistence analysis. The methods in [9]–[11] have not modeled transmission backoff wait time, a critical element for the delay analysis. [12] models the backoff counter hold time for the coexisting LAA and WLAN systems, but does not analyze the transmission delays. In [17], a joint optimization of LTE-LAA and WLAN systems is investigated, and the average packet transmission delay is evaluated. In [21], the authors model the backoff hold time, and provide an analysis on the mean and variance of transmission delay for a WLAN system. However, this method does not consider other important metrics, such as the cumulative distribution function (CDF) of delay and its impact on the throughput, a more difficult evaluation.

In this paper, we define new PoC metrics to quantify coexistence performance of LAA and WLAN systems, and design new analytical methods to assess transmission delay statistics to obtain PoCs. The contributions and novelties are highlighted as follows:

- We develop a novel transmission delay analysis for coexisting LAA and WLAN systems, and provide new formulas of DOP and DCT.
- We define and evaluate PoC metrics based on these delay criteria, which involve a joint CDF of delays and a joint CDF of DCTs.
- We implement computer programming and extensive Monte Carlo simulations, which demonstrate a good match between our analytical and simulation results. Numerical results illustrate some insightful findings.

These results fill a major gap in the coexistence analysis of LTE-LAA and WLAN systems with practical delay constraints. They provide new insight into understanding performance uncertainties caused by protocol and system parameters and their impact on the PoC metrics. The results allow us to achieve flexible performance tradeoffs between threshold values of delays and throughput, and between LAA and WLAN systems based on their different requirements.

The technical insight and methods provided by this work may be used for analysis and optimization of other spectrum sharing systems and technologies, such as coexisting WLAN and Bluetooth (or Zigbee) devices. Actually, when the moment generating function (MGF) of a link transmission delay in a different system is obtained, the link delay statistics (such as DOP and DCT) can be readily evaluated by using our technique. Here, the PoC is assessed in terms of delay and payload throughput in the MAC layer. With absorption of more information from application and physical layers, and depending on the particular devices or applications, additional PoC metrics may be defined and evaluated. For ease of reference, some symbols, expressions and their definitions are listed in Table I.

## II. System Model

Suppose that in several small cells the LTE-LAA and WLAN systems share the unlicensed spectrum in an industrial, scientific, and medical (ISM) radio band. There are $n_L$ LAA links coexisting with $n_W$ WLAN links. All LAA and WLAN links can hear each other, and at any time successful transmission happens when only one link transmits. Suppose that the LAA-LBT and WLAN systems use similar CSMA/CA MAC schemes, but with different parameters.

In this paper, the delay for a payload is defined as the duration from the time the packet becomes the head of the line (HoL) in the transmit queue until the instant that the payload transmission finishes successfully. The delay threshold is defined as the maximum delay duration allowed for a packet to finish its transmission. Otherwise, it is counted as a packet delay outage. In this model, the delay threshold is used to quantify performance of the MAC schemes, but it is not enforced to drop outdated packets. The LAA and WLAN systems considered still use their original MAC schemes (such as LBT and DCF) to schedule and transmit packets. If the delay thresholds are enforced to drop packets, the resulting MAC schemes will be different, and a new design may lead to better delay statistics. However, this extension and related optimization work are out of the scope of this paper, but would be considered in future work.

The DOP for a payload is defined as:

$$\text{DOP}_D(D_{\text{Th}}) = P\{D > D_{\text{Th}}\}, \tag{1}$$

where $D$ and $D_{\text{Th}}$ are the experienced delay and the delay threshold value (aka. permitted maximum delay), respectively.

We define a link's DCT as the total payload that is successfully transmitted by the delay threshold $D_{\text{Th}}$, divided by the average delay duration $\overline{D}_{\text{Th}}$. The DCT is given by

$$\text{DCT}(D_{\text{Th}}) = \frac{E[\text{payload successfully transmitted by } D_{\text{Th}}]}{\overline{D}_{\text{Th}}}, \tag{2}$$

where $\overline{D}_{\text{Th}}$ is the average duration including the effect of delay outage, and we can call it a modified delay threshold. It is given by

$$\overline{D}_{\text{Th}} = D_{\text{Th}} + T_{\text{DOP}}(D_{\text{Th}}). \tag{3}$$

In (3),

$$T_{\text{DOP}}(D_{\text{Th}}) = \int_{D_{\text{Th}}}^{\infty} x f_D(x) dx, \tag{4}$$

where $f_D(x)$ is the probability density function (PDF) of $D$. The PDF expression can be obtained by using numerical

Ma, Yao; Young, William; Anderson, Eric; Coder, Jason.
"Probability of Coexistence of LTE-LAA and WLAN Systems Based on Delay Constraints."
Paper presented at The 27th International Conference on Computer Communications and Networks (ICCCN 2018), Hangzhou, China. July 30, 2018 - August 2, 2018.

TABLE I: Definition of some symbols and expressions frequently used in this paper.

| Symbol or Expression | Definition |
|---|---|
| DCT | Delay constrained throughput |
| DOP | Delay outage probability |
| MGF | Moment generating function |
| $D_L$ (or $D_W$) | Transmission delay in an LAA (or WLAN) link. |
| $D_{L,\text{Th}}$ (or $D_{W,\text{Th}}$) | Delay threshold of an LAA (or WLAN) link. |
| $\text{DOP}_L(D_{L,\text{Th}})$ (or $\text{DOP}_W(D_{W,\text{Th}})$) | DOP with threshold $D_{L,\text{Th}}$ (or $D_{W,\text{Th}}$) in an LAA (or WLAN) link. |
| $G_{D_L}(s)$ (or $G_{D_W}(s)$) | MGF of delay $D_L$ (or $D_W$). |
| $P_{D_L}(D_{L,\text{Th}})$ (or $P_{D_W}(D_{W,Th})$ | CDF of delay $D_L$ (or $D_W$) with threshold value $D_{L,\text{Th}}$ (or $D_{W,Th}$). |
| $\text{PoC}_{\text{DOP}}(D_{L,\text{Th}}, D_{W,\text{Th}})$ | PoC based on LAA and WLAN joint DOPs with delay threshold pair $(D_{L,\text{Th}}, D_{W,\text{Th}})$. |
| $P_{L,\text{EX}}(n, D_{L,\text{Th}})$ (or $P_{W,\text{EX}}(n, D_{W,\text{Th}})$) | Probability that exactly $n$ payloads are transmitted by $D_{L,\text{Th}}$ (or $D_{W,\text{Th}}$) in an LAA (or WLAN) link. |
| $\text{PoC}_{\text{DCT}}(D_{L,\text{Th}}, D_{W,\text{Th}}, R_{L,\text{Th}}, R_{W,\text{Th}})$ | PoC based on joint DCTs with delay threshold pair $(D_{L,\text{Th}}, D_{W,\text{Th}})$ and throughput threshold pair $(R_{L,\text{Th}}, R_{W,\text{Th}})$. |
| $P_{t,L}$ (or $P_{t,W}$) | Conditional successful transmission probability of an LAA (or WLAN) link. |
| $R_L(D_{L,\text{Th}})$ (or $R_W(D_{W,\text{Th}})$) | DCT of an LAA (or WLAN) link based on delay threshold $D_{L,\text{Th}}$ or $(D_{W,\text{Th}})$. |
| $\tau_L$ (or $\tau_W$) | Channel access probability of an LAA (or WLAN) link. |

differentiation of the CDF of $D$, and the CDF is evaluated with the inverse Laplace transform (ILT) of the MGF of $D$, which is derived in detail in Section III. Eq. (3) has two parts: When the delay outage does not happen (with probability $1-\text{DOP}_D(D_{\text{Th}})$), the delay is given by $D_{\text{Th}}$; and when delay outage happens (aka, no packet was successfully transmitted) with probability $\text{DOP}_D(D_{\text{Th}})$, the involved additional delay is then given by $T_{\text{DOP}}(D_{\text{Th}})$. Note that $\overline{D}_{\text{Th}} \geq D_{\text{Th}}$ holds. Our DCT definition in (2) and (3) is original and non-trivial. It properly accounts for the effect of delay outage on the achieved throughput. Methods to analyze and evaluate $\text{DOP}_D(D_{\text{Th}})$ and $\text{DCT}(D_{\text{Th}})$ for LAA and WLAN links will be provided in Section III.

We use subscripts $L, W, i, S, C, p$ to denote LAA, WLAN, idle, successful transmission, collision, and payload, respectively. Suppose the LAA-LBT process has cutoff stage $M_L$, and stage $m$ has contention window (CW) size $Z_m$, for $m = 0, 1, \ldots, M_L$; and the WLAN has cutoff stage $M_W$, and stage $m$ has CW size $W_m$. We define $\delta_W$ as a backoff idle slot duration, which is identical for both WLAN and LAA systems. $T_{S,L}$ and $T_{C,L}$ are defined as durations for an LAA link's successful transmission and failed transmission, respectively; and $T_{S,W}$ and $T_{C,W}$ as durations of a WLAN link's successful and failed transmissions. Note that $T_{S,L}$ ($T_{S,W}$) and $T_{C,L}$ ($T_{C,W}$) include handshaking duration, and silence period after transmission, such as deferred extended clear channel assessment (DeCCA) duration [1], [11]. Here, the DeCCA duration is assumed to be equal to the WLAN DCF interframe space (DIFS) period. Both basic access and request-to-send and clear-to-send (RTS-CTS) access schemes can be modeled for both LAA and WLAN systems, by selecting proper values of $T_{S,L}$ ($T_{S,W}$) and $T_{C,L}$ ($T_{C,W}$).

## III. Delay Performance Analysis

The technical task flow of this work may be summarized as follows:

1) Define system and protocol parameters for LAA and WLAN systems.
2) Compute coexistence performance metrics, such as channel access probabilities, successful transmission probabilities, and average throughput.
3) Analyze delay statistics, such as the MGF and DOP.
4) Evaluate the first PoC based on the joint DOP metric.
5) Analyze the DCT and its distribution. Evaluate the second PoC based on the joint DCT metrics.

In this task list, each step is built on its previous step. Steps 1 and 2 have been implemented in several works [9]–[12], but Steps 3-5 are original in this paper. Analyzing the DCT in Step 5 is especially challenging, and a similar analytical technique could not be found in the available literature. Moreover, even a proper definition of the DCT is non-trivial, as shown by (2) and (3).

Define the conditional successful transmission probabilities (STPs) for an LAA link and a WLAN link as $P_{t,L}$ and $P_{t,W}$, respectively, when their backoff counters reduce to zero. Complementary, $P_{f,L} = 1 - P_{t,L}$ and $P_{f,W} = 1 - P_{t,W}$ are probabilities of collision (or failed transmission). Here, we assume that failed transmissions are only caused by packet collisions. It follows that

$$P_{t,L} = (1-\tau_L)^{n_L-1}(1-\tau_W)^{n_W}, \quad (5)$$

$$P_{t,W} = (1-\tau_L)^{n_L}(1-\tau_W)^{n_W-1}, \quad (6)$$

where $\tau_L$ and $\tau_W$ are the transmission (or channel access) probabilities of LAA and WLAN systems, respectively. Based

Ma, Yao; Young, William; Anderson, Eric; Coder, Jason.
"Probability of Coexistence of LTE-LAA and WLAN Systems Based on Delay Constraints."
Paper presented at The 27th International Conference on Computer Communications and Networks (ICCCN 2018), Hangzhou, China. July 30, 2018 - August 2, 2018.

on a result in [11], the transmission probability of an LAA link is given by

$$\tau_L = \frac{2(1-P_{f,L}^{M_L+1})}{(1-P_{f,L})\sum_{m=0}^{M_L} P_{f,L}^m (1+Z_m)}. \quad (7)$$

Assuming that WLAN nodes have a similar CSMA/CA backoff algorithm as the LAA nodes (but with different parameters), the transmission probability of a WLAN node is given by

$$\tau_W = \frac{2(1-P_{f,W}^{M_W+1})}{(1-P_{f,W})\sum_{m=0}^{M_W} P_{f,W}^m (1+W_m)}. \quad (8)$$

### A. MGF of the Delay

Define $D_{L,m}$ as the transmission delay of an LAA node at backoff stage $m$ ($m = 0, 1, \ldots, M_L$). It can be expressed as

$$D_{L,m} = \begin{cases} T_{L,m} + T_{S,L} & \text{with prob. } P_{t,L}, \\ T_{L,m} + T_{C,L} + D_{L,m+1} & \text{with prob. } P_{f,L}. \end{cases} \quad (9)$$

In (9), $T_{L,m}$ is the backoff hold time which includes the LBT sensing time and counter frozen duration. In the second line of (9), the term $D_{L,m+1}$ means that the backoff stage moves to $m+1$ due to a failed transmission. In the last stage, the delay is given by

$$D_{L,M_L} = \begin{cases} T_{L,M_L} + T_{S,L} & \text{with prob. } P_{t,L}, \\ T_{L,M_L} + T_{C,L} + D_{L,0} & \text{with prob. } P_{f,L}. \end{cases} \quad (10)$$

In the second line of (10), the term $D_{L,0}$ implies that the state moves to initial stage 0 due to a failed transmission and the packet is dropped. However, for fairness of evaluating performance metrics, the delay involved for the dropped packets is counted towards the total delay of the considered LAA link.

Based on (9) and (10), the successful transmission delay per payload in an LAA link is given by $D_{L,0}$. So we can use $D_L$ and $D_{L,0}$ interchangeably. For a WLAN link, the transmission delay is equal to $D_W$. We want to derive the statistics of $D_L$, including the MGF and CDF, to evaluate the DOP and DCT metrics. To evaluate (9) and (10), we need to analyze the $T_{L,m}$ and $P_{t,L}$.

To accurately model the interaction between LAA and WLAN systems, we use probabilities $\hat{P}$ and $P$ to denote events observed by a node when observing its own system (e.g., state of LAA system observed by an LAA node), and the other system (e.g., state of LAA system observed by a WLAN node), respectively. Let $\hat{P}_{i,L}$ (or $P_{i,L}$), $\hat{P}_{S,L}$ (or $P_{S,L}$), and $\hat{P}_{C,L}$ (or $P_{C,L}$) be probabilities of non-transmission (idle), successful transmission, and collision in the LAA system observed by an LAA node (or a WLAN node), respectively. It follows that $\hat{P}_{i,L} = (1-\tau_L)^{n_L-1}$ and $P_{i,L} = (1-\tau_L)^{n_L}$ because an LAA node is affected by activity of the other $n_L - 1$ LAA nodes, but a WLAN node is affected by $n_L$ LAA nodes. Also, we obtain $\hat{P}_{S,L} = (n_L-1)\tau_L(1-\tau_L)^{n_L-2}$, $P_{S,L} = n_L\tau_L(1-\tau_L)^{n_L-1}$, $\hat{P}_{C,L} = 1-(1-\tau_L)^{n_L-1} - (n_L-1)\tau_L(1-\tau_L)^{n_L-2}$, and $P_{C,L} = 1-(1-\tau_L)^{n_L} - n_L\tau_L(1-\tau_L)^{n_L-1}$.

Similarly, to model the activity of the WLAN system, we define $\hat{P}_{i,W}$ (or $P_{i,W}$), $\hat{P}_{S,W}$ (or $P_{S,W}$), and $\hat{P}_{C,W}$ (or $P_{C,W}$) be probabilities of non-transmission (idle), successful transmission, and collision in the WLAN system observed by a WLAN node (or an LAA node), respectively. It follows that $\hat{P}_{i,W} = (1-\tau_W)^{n_W-1}$, $P_{i,W} = (1-\tau_W)^{n_W}$, $\hat{P}_{S,W} = (n_W-1)\tau_W(1-\tau_W)^{n_W-2}$, $P_{S,W} = n_W\tau_W(1-\tau_W)^{n_W-1}$, $\hat{P}_{C,W} = 1-(1-\tau_W)^{n_W-1} - (n_W-1)\tau_W(1-\tau_W)^{n_W-2}$, and $P_{C,W} = 1-(1-\tau_W)^{n_W} - n_W\tau_W(1-\tau_W)^{n_W-1}$. Refer to Fig. 1, where the counter reduction (from value $z$ to $z-1$) at backoff stage $m$ in an LAA transmit node is depicted. We model the feedforward path for one backoff counter reduction as six mutually exclusive sub-events: all LAA and WLAN nodes are idle (with probability $\hat{P}_{i,L}P_{i,W}$ and duration $\delta_W$), successful transmission of an LAA node (with probability $\hat{P}_{S,L}P_{i,W}$ and duration $T_{S,L}$), collision of LAA nodes while WLAN system is idle (with probability $\hat{P}_{C,L}P_{i,W}$ and duration $T_{C,L}$), successful transmission of a WLAN node (with probability $P_{S,W}\hat{P}_{i,L}$ and duration $T_{S,W}$), collision of WLAN nodes while LAA system is idle (with probability $P_{C,W}\hat{P}_{i,L}$ and duration $T_{C,W}$), and LAA-WLAN inter-system transmission collision (with probability $(1-P_{i,W})(1-\hat{P}_{i,L})$ and duration $T_{C,M}$), where $T_{C,M} = \max(T_{C,L}, T_{C,W})$.

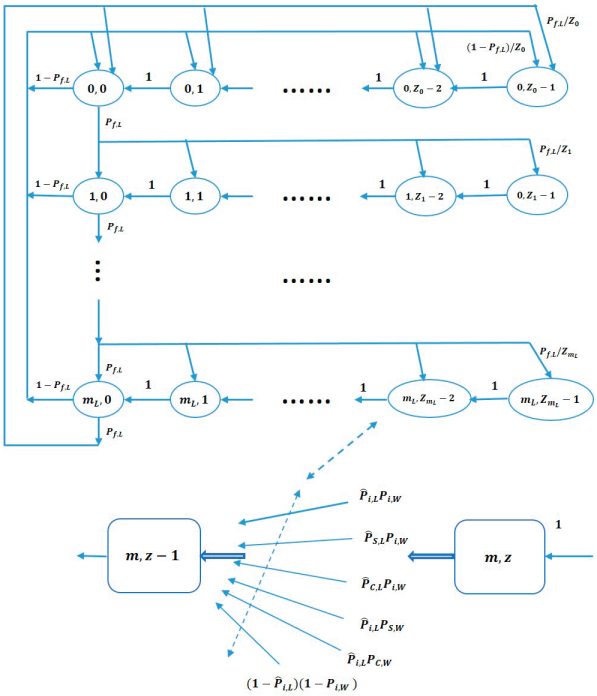


Fig. 1: Our proposed Markov model for the LTE-LAA LBT category 4 procedure (revised from [11]), where six probability paths in the backoff counter reduction process are highlighted.

Define $T_{\text{LCR}}$ and $T_{\text{WCR}}$ as the average hold time per counter reduction for an LAA node and a WLAN node, respectively. For an LAA node, its counter reduction must experience one

Ma, Yao; Young, William; Anderson, Eric; Coder, Jason.
"Probability of Coexistence of LTE-LAA and WLAN Systems Based on Delay Constraints."
Paper presented at The 27th International Conference on Computer Communications and Networks (ICCCN 2018), Hangzhou, China. July 30, 2018 - August 2, 2018.

of six mutually exclusive events, and $T_{\text{LCR}}$ is thus given by

$$\begin{aligned} T_{\text{LCR}} &= \hat{P}_{i,L}P_{i,W}\delta_L + \hat{P}_{S,L}P_{i,W}T_{S,L} + \hat{P}_{C,L}P_{i,W}T_{C,L} \\ &+ \hat{P}_{i,L}P_{S,W}T_{S,W} + \hat{P}_{i,L}P_{C,W}T_{C,W} \\ &+ (1-\hat{P}_{i,L})(1-P_{i,W})T_{C,M}. \end{aligned} \quad (11)$$

We can verify that the probability mass function (PMF) involved in (11) sums up to unity and is valid, as shown by

$$\begin{aligned} &\hat{P}_{i,L}P_{i,W} + \hat{P}_{S,L}P_{i,W} + \hat{P}_{C,L}P_{i,W} + P_{S,W}\hat{P}_{i,L} \\ &+P_{C,W}\hat{P}_{i,L} + (1-\hat{P}_{i,L})(1-P_{i,W}) = 1. \end{aligned} \quad (12)$$

The MGF of $T_{\text{LCR}}$ is defined as its Laplace transformation as $G_{T_{\text{LCR}}}(s) = E[\exp(sT_{\text{LCR}})]$. By modeling $T_{\text{LCR}}$ as a random variable with the six PMF-and-duration pairs shown in (11), we obtain

$$\begin{aligned} G_{T_{\text{LCR}}}(s) &= \hat{P}_{i,L}P_{i,W}\exp(s\delta_L) + \hat{P}_{S,L}P_{i,W}\exp(sT_{S,L}) \\ &+\hat{P}_{C,L}P_{i,W}\exp(sT_{C,L}) + \hat{P}_{i,L}P_{S,W}\exp(sT_{S,W}) \\ &+\hat{P}_{i,L}P_{C,W}\exp(sT_{C,W}) \\ &+(1-\hat{P}_{i,L})(1-P_{i,W})\exp(sT_{C,M}). \end{aligned} \quad (13)$$

Similarly, the MGF of $T_{\text{WCR}}$ is derived as

$$\begin{aligned} G_{T_{\text{WCR}}}(s) &= E[\exp(sT_{\text{WCR}})] \\ &= \hat{P}_{i,W}P_{i,L}\exp(s\delta_W) + \hat{P}_{S,W}P_{i,L}\exp(sT_{S,W}) \\ &+\hat{P}_{C,W}P_{i,L}\exp(sT_{C,W}) + \hat{P}_{i,W}P_{S,L}\exp(sT_{S,L}) \\ &+\hat{P}_{i,W}P_{C,L}\exp(sT_{C,L}) \\ &+(1-\hat{P}_{i,W})(1-P_{i,L})\exp(sT_{C,M}). \end{aligned} \quad (14)$$

At backoff stage $m$, the total wait time $T_{L,m}$ for an LAA link is a function of CW size $Z_m$ and per-counter reduction time $T_{\text{LCR}}$, and can be expressed as

$$T_{L,m} = \frac{1}{Z_m}\sum_{m=0}^{Z_m-1}(x_m + \delta_W), \quad (15)$$

where $x_m$ is the wait time if the backoff starts at the $m$th counter, and is the sum of $m$ independent and identically distributed (i.i.d.) waiting slots (each with duration $T_{\text{LCR}}$) and one additional $\delta_W$ duration. Thus, the MGF of $x_m$ is given by $G_{x_m}(s) = G^m_{T_{\text{LCR}}}(s)$. The MGF of $T_{L,m}$ is obtained as

$$\begin{aligned} G_{T_{L,m}}(s) &= \frac{1}{Z_m}\sum_{m=0}^{Z_m-1} G^m_{T_{\text{LCR}}}(s)e^{s\delta_W} \\ &= \frac{e^{s\delta_W}}{Z_m}\frac{1-G^{Z_m}_{T_{\text{LCR}}}(s)}{1-G_{T_{\text{LCR}}}(s)}. \end{aligned} \quad (16)$$

At stage $m$, total backoff wait time $T_{W,m}$ for a WLAN link is given by

$$G_{T_{W,m}}(s) = \frac{e^{s\delta_W}}{W_m}\frac{1-G^{W_m}_{T_{\text{WCR}}}(s)}{1-G_{T_{\text{WCR}}}(s)}. \quad (17)$$

Finally, by using the recursive relation shown in (9) and (10), the MGF of the delay $D_L$ is derived as

$$G_{D_L}(s) = \frac{\sum_{m=0}^{M_L}\left(\prod_{k=0}^{m}G_{T_{L,m}}(s)\right)e^{s(mT_{C,L}+T_{S,L})}(1-P_{t,L})^mP_{t,L}}{1-\left(\prod_{k=0}^{M_L}G_{T_{L,m}}(s)\right)e^{s((M_L+1)T_{C,L})}(1-P_{t,L})^{M_L+1}}. \quad (18)$$

When $M_L = 0$, (18) simplifies to

$$G_{D_L}(s) = \frac{\exp(sT_{S,L})P_{t,L}}{1-\exp(sT_{C,L})(1-P_{t,L})}. \quad (19)$$

The delay of successful transmission for a WLAN node is denoted by $D_W$. Similarly, its MGF is derived as

$$G_{D_W}(s) = \frac{\sum_{m=0}^{M_W}\left(\prod_{k=0}^{m}G_{T_{W,m}}(s)\right)e^{s(mT_{C,W}+T_{S,W})}(1-P_{t,W})^mP_{t,W}}{1-\left(\prod_{k=0}^{M_W}G_{T_{W,m}}(s)\right)e^{s(M_W+1)T_{C,W}}(1-P_{t,W})^{M_W+1}}. \quad (20)$$

### *B. CDF of Delay and the First PoC*

The DOP of $D_L$ is equal to its CDF for a given threshold $D_{L,\text{Th}}$, and can be obtained by using the ILT of the MGF $G_{D_L}(s)$, as shown by

$$P_{D_L}(D_{L,\text{Th}}) = \text{ILT}[\exp(sD_{L,\text{Th}})G_{D_L}(s)/s]. \quad (21)$$

An efficient ILT numerical formula for evaluating CDF of a variable from its MGF was developed in [22], and used for wireless communication outage probability computation in several works, such as [23], [24]. When a variable $D$ has MGF $G_D(s)$, its CDF $P_D(D_{\text{Th}})$ is given by

$$\begin{aligned} P_D(D_{\text{Th}}) &= P\{D < D_{\text{Th}}\} \\ &= 2^{-Q}e^{\frac{A}{2}}\sum_{q=0}^{Q}\binom{Q}{q}\sum_{n=0}^{N+q}(-1)^n\beta_n \\ &\times \Re\left(\frac{G_D\left(\frac{A+jn2\pi}{2D_{\text{Th}}}\right)}{A+jn2\pi}\right) + E_{A,N,Q}, \end{aligned} \quad (22)$$

where $\beta_n = \begin{cases} 1, & n=0 \\ 2, & n=1,\ldots,N+Q \end{cases}$, $A, N$, and $Q$ are parameters used to control the convergence, and $E_{A,N,Q}$ is an error term which diminishes as $N$ and $Q$ increase.

By replacing $D$ and $D_{\text{Th}}$ in (22) with $D_L$ and $D_{L,\text{Th}}$, we readily obtain the CDF $P_{D_L}(D_{L,\text{Th}})$. Define $D_W$ and $D_{W,\text{Th}}$ as the successful transmission delay and delay threshold for a WLAN link. The CDF of $D_W$ is given by

$$P_{D_W}(D_{W,\text{Th}}) = \text{ILT}[\exp(sD_{W,\text{Th}})G_{D_W}(s)/s], \quad (23)$$

which can be efficiently evaluated by using (22). The DOPs of LAA and WLAN systems are defined as the complementary CDF (CCDF) of $D_W$ and $D_L$, given by

$$\begin{aligned} \text{DOP}_L(D_{L,\text{Th}}) &= 1 - P_D(D_{L,\text{Th}}), \\ \text{DOP}_W(D_{W,\text{Th}}) &= 1 - P_{D_W}(D_{W,\text{Th}}). \end{aligned}$$

Ma, Yao; Young, William; Anderson, Eric; Coder, Jason.
"Probability of Coexistence of LTE-LAA and WLAN Systems Based on Delay Constraints."
Paper presented at The 27th International Conference on Computer Communications and Networks (ICCCN 2018), Hangzhou, China. July 30, 2018 - August 2, 2018.

Based on joint CDFs of both LAA and WLAN systems, we define the first PoC as

$$\text{PoC}_{\text{DOP}}(D_{L,\text{Th}}, D_{W,\text{Th}}) = P\{D_L \le D_{L,\text{Th}}, D_W \le D_{W,\text{Th}}\}.$$

Since the interactions between LAA and WLAN links are modeled in the backoff delay statistics, as shown by (18) and (20), it is reasonable to assume that DOPs of the LAA and WLAN links are conditionally independent. We obtain that

$$\begin{aligned}&\text{PoC}_{\text{DOP}}(D_{L,\text{Th}}, D_{W,\text{Th}})\\ &\quad\simeq P\{D_L \le D_{L,\text{Th}}\} \cdot P\{D_W \le D_{W,\text{Th}}\}\\ &\quad= \text{ILT}[\exp(sD_{L,\text{Th}})G_{D_L}(s)/s]\\ &\qquad\times\text{ILT}[\exp(sD_{W,\text{Th}})G_{D_W}(s)/s]. \end{aligned} \quad (24)$$

Eq. (24) is a new result which demonstrates how the joint DOPs of LAA and WLAN systems can be mapped to the PoC.

### C. Delay Constrained Throughput and the Second PoC

For a given delay threshold $D_{L,\text{Th}}$ of an LAA link, we denote its DCT as $R_L(D_{L,\text{Th}})$, which is defined as the successfully transmitted total payload with transmission delay no more than $D_{L,\text{Th}}$. Similarly, the DCT of a WLAN node is defined as $R_W(D_{W,\text{Th}})$. Define the sum DCTs of $n_L$ LAA links and $n_W$ WLAN links, respectively, as

$$\begin{aligned} R_{L,\text{All}}(D_{L,\text{Th}}) &= n_L R_L(D_{L,\text{Th}}),\\ R_{W,\text{All}}(D_{W,\text{Th}}) &= n_W R_W(D_{W,\text{Th}}). \end{aligned} \quad (25)$$

In general, we define the second PoC based on sum DCTs of all LAA and WLAN links as

$$\begin{aligned}&\text{PoC}_{\text{DCT}}(D_{L,\text{Th}}, D_{W,\text{Th}}, R_{L,\text{Th}}, R_{W,\text{Th}}),\\ &= P\{R_{L,\text{All}}(D_{L,\text{Th}}) > R_{L,\text{Th}}, R_{W,\text{All}}(D_{W,\text{Th}}) > R_{W,\text{Th}}\}, \end{aligned} \quad (26)$$

which indicates the joint probability that both LAA and WLAN systems can fulfill their required sum DCTs.

We propose to analytically evaluate $R_L(D_{L,\text{Th}})$ by

$$R_L(D_{L,\text{Th}}) = \sum_{n=1}^{N_{m,L}} nP_{L,\text{EX}}(n, D_{L,\text{Th}})T_{P,L}/\overline{D}_{L,\text{Th}}, \quad (27)$$

where $T_{P,L}$ is the payload duration of an LAA link, $P_{L,\text{EX}}(n, D_{L,\text{Th}})$ is a short-hand form for the probability that the LAA node has successfully transmitted exactly $n$ payloads with a total transmission delay of no more than $D_{L,\text{Th}}$, and $\overline{D}_{L,\text{Th}}$ is a modified delay threshold. Based on (3), we obtain

$$\overline{D}_{L,\text{Th}} = D_{L,\text{Th}} + \int_{D_{L,\text{Th}}}^{\infty} x f_{D_L}(x)dx, \quad (28)$$

where $f_{D_L}(x)$ is the PDF of $D_L$.

Here, the total transmission delay of $n$ payloads is defined as the duration from the instant that the first payload becomes the HoL in the transmit queue until the instant the transmission of the $n$th payload is successfully completed (without collision). The $N_{m,L}$ is the maximum number of payloads that can be transmitted before $D_{L,\text{Th}}$. The exact value of $N_{m,L}$ is not needed in computing (27), because if we use the value $\hat{N}_m$ in (27) with $\hat{N}_{m,L} > N_{m,L}$, then $P_{L,\text{EX}}(n, D_{L,\text{Th}}) = 0$, $(n = N_m + 1, \ldots, \hat{N}_m)$. A simple method to determine a realistic $\hat{N}_{m,L}$ is given by

$$\hat{N}_{m,L} = \lfloor D_{L,\text{Th}}/T_{S,L} \rfloor. \quad (29)$$

Mathematically, $P_{L,\text{EX}}(n, D_{L,\text{Th}})$ can be expressed as

$$\begin{aligned} P_{L,\text{EX}}(n, D_{L,\text{Th}}) &= \int_0^{D_{L,\text{Th}}} \cdots \int_0^{D_{L,\text{Th}}} F_L(\Delta t_1) \cdots F_L(\Delta t_n)\\ &\quad\times[1 - F_L(D_{L,\text{Th}} - \sum_{k=1}^{n} \Delta t_k)]d\Delta t_1 \cdots d\Delta t_n / D_{L,\text{Th}}^n\\ &\quad\text{subject to } \sum_{k=1}^{n} \Delta t_k \le D_{L,\text{Th}}, \end{aligned} \quad (30)$$

where $F_L(\Delta t_1), \cdots, F_L(\Delta t_n)$ refer to probabilities of the first $n$ successful transmissions, respectively, and $1 - F_L(D_{L,\text{Th}} - \sum_{k=1}^{n} \Delta t_k)$ refers to probability that the $(n+1)$th transmission is not finished before the threshold $D_{L,\text{Th}}$. However, (30) involves an $n$-dimensional integral and is very difficult to evaluate numerically.

To bypass this technical difficulty, we develop a novel approach to evaluate (30) accurately. We define $P_{\text{AL}}(n, D_{L,\text{Th}})$ as the probability that the LAA node has successfully transmitted *at least* $n$ payloads with a total transmission delay of no more than $D_{L,\text{Th}}$. Thus, we have $N_{m,L}$ equalities (for $n = 1, \ldots, N_{m,L}$), shown by

$$P_{\text{AL}}(n, D_{L,\text{Th}}) = \sum_{m=n}^{N_{m,L}} P_{L,\text{EX}}(m, D_{L,\text{Th}}). \quad (31)$$

From (31) we obtain

$$P_{L,\text{EX}}(N_{m,L}, D_{L,\text{Th}}) = P_{\text{AL}}(N_{m,L}, D_{L,\text{Th}}),$$

and

$$P_{L,\text{EX}}(n, D_{L,\text{Th}}) = P_{\text{AL}}(n, D_{L,\text{Th}}) - P_{\text{AL}}(n+1, D_{L,\text{Th}}), \quad (32)$$

for $n = 1, \ldots, N_{m,L} - 1$. When considering only one payload, we have

$$P_{\text{AL}}(1, D_{L,\text{Th}}) = \text{ILT}[e^{sD_{L,\text{Th}}} G_{D_L}(s)/s].$$

To analyze $P_{\text{AL}}(n, D_{L,\text{Th}})$ for $n > 1$, we realize that in this case $D_{L,\text{Th}}$ is the duration which allows at least $n$ successful transmissions. Then $D_{L,\text{Th}}$ is the sum of $n$ i.i.d. delay variables, and each of such a variable has the MGF $G_{D_L}(s)$. Thus, $G_{D_{L,\text{Th}}}(s) = G_{D_L}^n(s)$ holds. Consequently, we have (for $n = 1, \ldots, N_{m,L}$)

$$P_{\text{AL}}(n, D_{L,\text{Th}}) = \text{ILT}[e^{sD_{L,\text{Th}}} G_{D_L}^n(s)/s], \quad (33)$$

which can be evaluated efficiently by use of (22).

By substituting (32) and (33) into (27), we obtain the DCT

Ma, Yao; Young, William; Anderson, Eric; Coder, Jason.
"Probability of Coexistence of LTE-LAA and WLAN Systems Based on Delay Constraints."
Paper presented at The 27th International Conference on Computer Communications and Networks (ICCCN 2018), Hangzhou, China. July 30, 2018 - August 2, 2018.

for an LAA link as

$$R_L(D_{L,\text{Th}}) = \sum_{n=1}^{N_{m,L}} P_{\text{AL}}(n, D_{L,\text{Th}}) T_{P,L}/\overline{D}_{L,\text{Th}} = \sum_{n=1}^{N_{m,L}} \text{ILT}[e^{sD_{L,\text{Th}}} G^n_{D_L}(s)/s] \frac{T_{P,L}}{\overline{D}_{L,\text{Th}}}. \quad (34)$$

Similarly, for a given delay threshold $D_{W,\text{Th}}$, the DCT for a WLAN link is obtained as

$$R_W(D_{W,\text{Th}}) = \sum_{n=1}^{N_{m,W}} \text{ILT}[e^{sD_{W,\text{Th}}} G^n_{D_W}(s)/s] \frac{T_{P,W}}{\overline{D}_{W,\text{Th}}}, \quad (35)$$

where $N_{m,W} = \lfloor D_{W,\text{Th}}/T_{S,W} \rfloor$, $T_{P,W}$ is payload duration of a WLAN transmission, and

$$\overline{D}_{W,\text{Th}} = D_{W,\text{Th}} + \int_{D_{W,\text{Th}}}^{\infty} x f_{D_W}(x) dx, \quad (36)$$

with $f_{D_W}(x)$ being the PDF of $D_W$.

To our knowledge, (34) and (35) are new results on the DCT in spectrum sharing LAA and WLAN systems. After the DCTs of LAA and WLAN systems are obtained, we are also interested in their distributions. Here, we consider $R_L(D_{L,\text{Th}})$ and $R_W(D_{W,\text{Th}})$ as random variables, and study their CDFs. Consider an LAA link first. From (27), it is observed $\sum_{n=0}^{N_{m,L}} P_{L,\text{EX}}(n, D_{L,\text{Th}}) = 1$, where $P_{L,\text{EX}}(0, D_{L,\text{Th}})$ corresponds to the probability of zero DCT.

By using $\{P_{L,\text{EX}}(n, D_{L,\text{Th}})\}_{n=0,\ldots,N_{m,L}}$ as the PMF of the DCT $R_L(D_{L,\text{Th}})$, we derive its MGF as

$$G_{R_L(D_{L,\text{Th}})}(s) = \sum_{n=0}^{N_{m,L}} P_{L,\text{EX}}(n, D_{L,\text{Th}}) \exp(snT_{P,L}/\overline{D}_{L,\text{Th}}).$$

Similarly, the MGF of $R_W(D_{W,\text{Th}})$ is obtained as

$$G_{R_W(D_{W,\text{Th}})}(s) = \sum_{n=0}^{N_{m,W}} P_{W,\text{EX}}(n, D_{W,\text{Th}}) \exp\left(\frac{snT_{P,W}}{\overline{D}_{W,\text{Th}}}\right).$$

For the LAA sum DCT with threshold delay $D_{L,\text{Th}}$ and threshold throughput $R_{L,\text{Th}}$, we define the CDF of the sum DCT as $P\{n_L R_L(D_{L,\text{Th}}) < R_{L,\text{Th}}\}$, which can be evaluated as follows:

When $n_1 n_L T_{P,L}/\overline{D}_{L,\text{Th}} \le R_{L,\text{Th}} \le (n_1+1) n_L T_{P,L}/\overline{D}_{L,\text{Th}}$, aka., $n_1 = \lfloor R_{L,\text{Th}} \overline{D}_{L,\text{Th}}/(n_L T_{P,L}) \rfloor$, based on the PMF, we have

$$P\{R_{L,\text{All}}(D_{L,\text{Th}}) < R_{L,\text{Th}}\} = \sum_{n=0}^{n_1} P_{L,\text{EX}}(n, D_{L,\text{Th}}). \quad (37)$$

Similarly, the CDF of the sum DCT of $n_W$ WLAN links is derived as

$$P\{R_{W,\text{All}}(D_{W,\text{Th}}) < R_{W,\text{Th}}\} = \sum_{n=0}^{n_2} P_{W,\text{EX}}(n, D_{W,\text{Th}}), \quad (38)$$

where $n_2 = \lfloor R_{W,\text{Th}} \overline{D}_{W,\text{Th}}/(n_W T_{P,W}) \rfloor$, and $D_{W,\text{Th}}$ and $R_{W,\text{Th}}$ are the WLAN threshold values of delay and sum throughput, respectively.

To obtain the CDF of DCT of a single LAA link and a WLAN link, respectively, we just need to set $n_1 = \lfloor R_{L,\text{Th}} \overline{D}_{L,\text{Th}}/T_{P,L} \rfloor$, and $n_2 = \lfloor R_{W,\text{Th}} \overline{D}_{W,\text{Th}}/T_{P,W} \rfloor$ in (37) and (38), respectively.

Note that the CDFs in (37) and (38) are equivalent to outage probabilities (or CDFs) of the sum DCTs, because they give the probabilities that the achieved joint DCTs are less than the required DCT threshold values. Based on the CCDF of the sum DCTs, the second PoC defined in (26) can be evaluated as

$$\begin{aligned} &\text{PoC}_{\text{DCT}}(D_{L,\text{Th}}, D_{W,\text{Th}}, R_{L,\text{Th}}, R_{W,\text{Th}}) \\ &\simeq P\{R_{L,\text{All}}(D_{L,\text{Th}}) > R_{L,\text{Th}}\} \cdot P\{R_{W,\text{All}}(D_{W,\text{Th}}) > R_{W,\text{Th}}\} \\ &= [1 - \sum_{n=0}^{n_1} P_{L,\text{EX}}(n, D_{L,\text{Th}})] \cdot [1 - \sum_{n=0}^{n_2} P_{W,\text{EX}}(n, D_{W,\text{Th}})]. \end{aligned} \quad (39)$$

This is a function of delay threshold pairs $(D_{L,\text{Th}}, D_{W,\text{Th}})$, and throughput threshold pairs $(R_{L,\text{Th}}, R_{W,\text{Th}})$.

For comparison purposes, it is important to show the static sum throughput of LAA and WLAN systems (without delay constraints), and check if our derived DCTs converge to the static throughput when the delay thresholds become large. The average successful transmission probabilities for the LAA system and the WLAN system are given by

$$P_{S,L} = n_L \tau_L P_{t,L}, \quad (40)$$

$$P_{S,W} = n_W \tau_W P_{t,W}, \quad (41)$$

where $P_{t,L}$ and $P_{t,W}$ are given by (5) and (6). Using a procedure similar to that given in [11], the static sum throughput of LAA and WLAN systems can be computed as

$$R_{S,L} = P_{S,L} T_{P,L}/T_{\text{ave}}, \quad (42)$$

$$R_{S,W} = P_{S,W} T_{P,W}/T_{\text{ave}}. \quad (43)$$

Here, $T_{\text{ave}}$ is the average duration to enable a successful transmission in either LAA or WLAN system, given by

$$\begin{aligned} T_{\text{ave}} &= P_{i,L} P_{i,W} \delta_L + P_{S,L} P_{i,W} T_{S,L} + P_{C,L} P_{i,W} T_{C,L} \\ &+ P_{i,L} P_{S,W} T_{S,W} + P_{i,L} P_{C,W} T_{C,W} \\ &+ (1 - P_{i,L})(1 - P_{i,W}) T_{C,M}. \end{aligned} \quad (44)$$

Numerical comparisons of DCTs and static throughput of LAA and WLAN systems are provided in Section IV.

## IV. Numerical Results

In this section, we provide both analytical and simulation results on the delay-related PoC performance metrics of the spectrum sharing LAA-LBT and WLAN links. The parameters used for analysis and simulation are listed in Table II. We assume that the RTS/CTS type access is used for both LAA and WLAN systems. The DCT of a link shown here is the achieved time-efficiency, which is the time proportion of successful payload transmission of that link divided by the total simulation time. We assume $n_L = n_W = 3$. Here we set $n_L > 1$ due to assumption of multiple overlapped small cells. In our Monte Carlo computer simulation, we

Ma, Yao; Young, William; Anderson, Eric; Coder, Jason.
"Probability of Coexistence of LTE-LAA and WLAN Systems Based on Delay Constraints."
Paper presented at The 27th International Conference on Computer Communications and Networks (ICCCN 2018), Hangzhou, China. July 30, 2018 - August 2, 2018.

TABLE II: LTE-LAA and WLAN Parameters Used for Simulation

LTE-LAA parameters

| Parameter | Value |
|---|---|
| Payload per transmission | 1 ms |
| LBT defer period: $T_{\text{Defer}}$ (=$T_{\text{DIFS}}$) | 34 $\mu$s |
| LBT eCCA period: $T_{\text{eCCA}}$ (=$\delta_W$) | 9 $\mu$s |
| CW size $Z_0$ | 8 |
| Cutoff stage $m_L$ | 1 |

WLAN parameters

| Parameter | Value |
|---|---|
| Payload per transmission | 1 ms |
| Idle slot duration $\delta_W$ | 9 $\mu$s |
| CW size $W_0$ | 16 |
| Cutoff stage $m_W$ | 3 |

track the numbers of local events for each WLAN and LTE node: channel idle, counter freezing (due to channel being busy), successful transmission, and collision. We also track the experienced delays of all the successfully transmitted payloads in LAA and WLAN systems, and compare these with specified delay thresholds to obtain simulated DOP and DCT statistics of each link. The simulation results were obtained by running for $10^6$ time slots on each parameter setting.

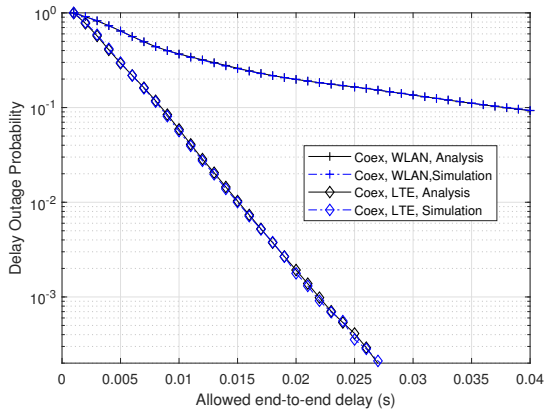


Fig. 2: Delay outage probabilities of LTE-LAA and WLAN systems vs. allowed transmission delays, when $n_L = n_W = 3$.

We provide the DOP and DCT results of LTE-LAA and WLAN systems in Figs. 2 and 3, respectively. The delay threshold vector for the x-axis is generated from $(1 \sim 40)$ ms and has step size of 1 ms. To compute the infinite range integrals in (4), (28), and (36), the integration upper-bound is chosen as 200 ms. This is sufficiently large as demonstrated by the achieved very low DOP. Figs. 2 and Fig. 3 show that as the delay threshold increases, both LAA and

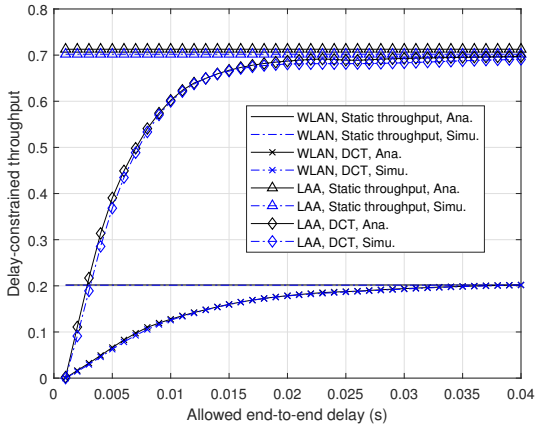


Fig. 3: Normalized sum DCTs (and static throughput) of LTE-LAA and WLAN systems vs. delay threshold.

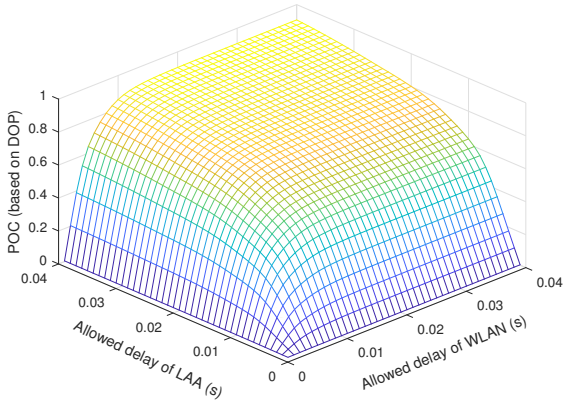


Fig. 4: DOP-based probability of coexistence of LTE-LAA and WLAN systems vs. delay threshold.

WLAN systems have decreased DOPs and increased DCTs, as expected. Furthermore, it is observed that all the analytical and simulation results match well with each other. Since we assume that the LAA system has smaller CW and cutoff stage than the WLAN system, as shown in Table II, Figs. 2 and Fig. 3 demonstrate that the LAA system has much lower DOP and higher DCT than those of the WLAN. In Fig. 3, the static throughput is defined as the throughput of LAA and WLAN systems without delay constraints, which can be computed by using (42) and (43). As the delay threshold increases, the DCTs of both LAA and WLAN systems smoothly converge to their static throughput, respectively. This result illustrates a design tradeoff of achieved DCT vs. delay threshold in comparison with throughput without delay constraint.

In Figs. 4 and 5, we present the PoCs of LAA and WLAN systems based on DOP and DCT criteria, respectively. Fig.

Ma, Yao; Young, William; Anderson, Eric; Coder, Jason.
"Probability of Coexistence of LTE-LAA and WLAN Systems Based on Delay Constraints."
Paper presented at The 27th International Conference on Computer Communications and Networks (ICCCN 2018), Hangzhou, China. July 30, 2018 - August 2, 2018.

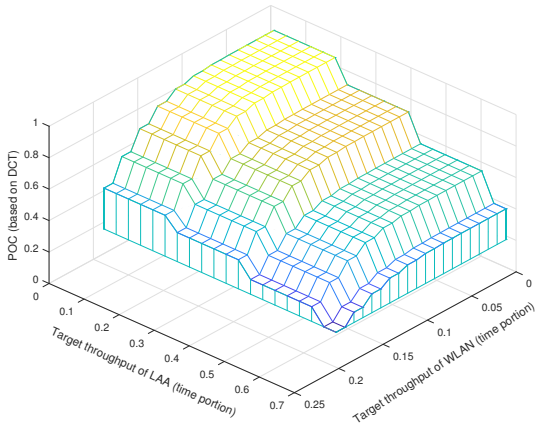


Fig. 5: DCT-based probability of coexistence of LTE-LAA and WLAN systems vs. target throughput when the delay threshold is 40 ms.

4 shows that as the permitted delays for LAA and WLAN system increase, the PoC increases monotonically towards unity. The target throughput of LAA (or WLAN) systems in Fig. 5 ranges from 0 to its maximum throughput in the coexistence scenario. We observe from Fig. 5 that as the target throughput values decrease, the PoC increases, and vice versa. This is a tradeoff between threshold throughput and PoC. Furthermore, to achieve the same (or very close) joint PoC metrics, there exist multiple pairs of target rates for LAA and WLAN systems. Therefore, there is another tradeoff between the two systems based on DCT thresholds and achieved PoC.

## V. Conclusion

In this paper, we have defined and evaluated original probability of coexistence metrics to quantify spectrum sharing performance of LAA and WLAN systems based on delay constraints. We have analyzed the delay-related performance metrics, including DOP and DCT which are practical and novel, but not well addressed due to technical difficulties in modeling and analyzing these metrics. We have implemented LTE-LAA and WLAN MAC scheme programming and extensive computer simulations, which have verified the accuracy of our analytical results. Numerical results show that there are a few tradeoffs between delay and throughput requirements, and between achieved performance of LTE-LAA and WLAN systems. These results fill a major technical gap on defining and analyzing meaningful PoCs to quantify success or failure of wireless coexistence performance, which incorporate effects of practical delay constraints. This method may be combined with the application layer and physical layer information to properly set threshold values of delay and throughput, and achieve diverse PoC targets, for LAA and other systems. In future work, we will implement hardware based experiments to validate the performance analysis.

## References


[1] 3GPP TSG RAN, "Study On Licensed-Assisted Access To Unlicensed Spectrum", *3GPP TR 36.889 V13.0.0*, Jun. 2015.

[2] Ericsson, "Discussion on LBT protocols," *3GPP Tech. Rep. R1-151996*, Apr. 2015.

[3] LTE-U Forum, "Coexistence study for LTE-U SDL", *LTE-U Technical Report*, V1.0, Feb. 2015.

[4] R. Zhang, M. Wang, L. X. Cai, Z. Zheng, and X. Shen, "LTE-unlicensed: the future of spectrum aggregation for cellular networks," *IEEE Wireless Commun.*, vol. 22, no. 3, pp. 150–159, Jun. 2015.

[5] A. Mukherjee et al., "Licensed-assisted access LTE: coexistence with IEEE 802.11 and the evolution toward 5G," *IEEE Commun. Mag.*, vol. 54, no. 6, pp. 50-57, Jun. 2016.

[6] "IEEE Standard Definitions and Concepts for Dynamic Spectrum Access: Terminology Relating to Emerging Wireless Networks, System Functionality, and Spectrum Management," in *IEEE Std 1900.1-2008*, pp.1-62, Oct. 2008.

[7] "American National Standard for Evaluation of Wireless Coexistence," in *ANSI C63.27-2017*, pp.1-77, May 2017.

[8] M. O. Al Kalaa, S. J. Seidman and H. H. Refai, "Estimating the likelihood of wireless coexistence using logistic regression: Emphasis on medical devices," in *IEEE Trans. Electromagn. Compat.*, vol. PP, no. 99, pp. 1-9.

[9] C. Chen, R. Ratasuk, and A. Ghosh, "Downlink performance analysis of LTE and WiFi coexistence in unlicensed bands with a simple listen-before-talk scheme," in *Proc. IEEE VTC*, Glasgow, May 2015, pp. 1–5.

[10] Y. Song, K. W. Sung, and Y. Han, "Coexistence of Wi-Fi and cellular with listen-before-talk in unlicensed spectrum," *IEEE Commun. Lett.*, vol. 20, no. 1, pp. 161–164, Jan. 2016.

[11] Y. Ma and D. G. Kuester, "MAC-Layer Coexistence Analysis of LTE and WLAN Systems Via Listen-Before-Talk," in *Proc. IEEE CCNC*, Las Vegas, Jan. 2017, pp. 534-541.

[12] Y. Ma, D. G. Kuester, J. Coder, and W. F. Young, "Coexistence analysis of LTE and WLAN systems with heterogenous backoff slot durations", in *Proc. IEEE ICC*, Paris, May 2017, pp. 1-7.

[13] Y. Ma, R. Jacobs, D. G. Kuester, J. Coder, and W. F. Young, "SDR-Based experiments for LTE-LAA based coexistence systems with improved design," in *Proc. IEEE GlobeCom*, Singapore, Dec. 2017, pp. 1–6.

[14] V. Valls, A. Garcia-Saavedra, X. Costa and D. J. Leith, "Maximizing LTE capacity in unlicensed bands (LTE-U/LAA) while fairly coexisting with 802.11 WLANs," *IEEE Commun. Lett.*, vol. 20, no. 6, pp. 1219–1222, Jun. 2016.

[15] S. Han, Y. C. Liang, Q. Chen and B. H. Soong, "Licensed-assisted access for LTE in unlicensed spectrum: A MAC protocol design," in *Proc. IEEE ICC*, Kuala Lumpur, Malaysia, May 2016, pp. 1–6.

[16] R. Yin, G. Yu, A. Maaref, and G. Y. Li, "A framework for co-channel interference and collision probability tradeoff in LTE licensed-assisted access networks," *IEEE Trans. Wireless Commun.*, vol. 15, no. 9, pp. 6078–6090, Sept. 2016.

[17] S. Han, Y. C. Liang, Q. Chen and B. H. Soong, "Licensed-Assisted Access for LTE in Unlicensed Spectrum: A MAC Protocol Design," *IEEE J. Sel. Areas Commun.*, vol. 34, no. 10, pp. 2550-2561, Oct. 2016.

[18] Z. Guan and T. Melodia, "CU-LTE: Spectrally-efficient and fair coexistence between LTE and Wi-Fi in unlicensed bands," in *Proc. IEEE INFOCOM*, San Francisco, CA, 2016, pp. 1-9.

[19] G. Bianchi, "Performance analysis of the IEEE 802.11 distributed coordination function," *IEEE J. Sel. Areas Commun.*, vol. 18, no. 3, pp. 535–547, Mar. 2000.

[20] I. Tinnirello, G. Bianchi, and X. Yang, "Refinements on IEEE 802.11 distributed coordination function modeling approaches," *IEEE Trans. Veh. Technol.*, vol.59, no.3, pp.1055–1067, Mar. 2010.

[21] L. Dai and X. Sun, "A unified analysis of IEEE 802.11 DCF networks: stability, throughput, and delay," *IEEE Trans. Mobile Computing*, vol. 12, no. 8, pp. 1558–1572, Aug. 2013.

[22] J. Abate and W. Whitt, "Numerical inversion of Laplace transforms of probability distribution," *ORSA J. Computing*, vol. 7, no. 1, pp. 36-43, Feb. 1995.

[23] Y.-C. Ko, M. S. Alouini, and M. K. Simon, "Outage probability of diversity systems over generalized fading channels," *IEEE Trans. Commun.*, vol. 48, no. 11, pp. 1783-1787, Nov 2000.

[24] Y. Ma and S. Pasupathy, "Efficient performance evaluation for generalized selection combining on generalized fading channels," *IEEE Trans. Wireless Commun.*, vol. 3, no. 1, pp. 29-34, Jan. 2004.



Ma, Yao; Young, William; Anderson, Eric; Coder, Jason.
"Probability of Coexistence of LTE-LAA and WLAN Systems Based on Delay Constraints."
Paper presented at The 27th International Conference on Computer Communications and Networks (ICCCN 2018), Hangzhou, China. July 30, 2018 - August 2, 2018.

# Analysis of Channel Access Priority Classes in LTE-LAA Spectrum Sharing System*

Yao Ma
Communications Technology Laboratory,
National Institute of Standards and Technology
325 Broadway, Boulder, Colorado, USA

*Abstract*— **To provide differentiated quality of service in long-term evolution (LTE) license assisted access (LAA) procedure, the 3GPP has defined several channel access priority classes (CAPCs). They use distinct arbitration inter-frame space (AIFS), contention window (CW) size, and payload duration. While evaluating the effects of CW size and payload duration is relatively straightforward, accurately modelling and analyzing the effect of AIFS has not been satisfactorily addressed. Available methods on analyzing different AIFSs are accurate for only limited parameter setups, or involve systematic approximations. Different from existing results, we develop a *non-homogeneous* per-slot Markov chain model to represent the state of each priority class during and after the AIFS, and analyze the channel access probability (CAP), successful transmission probability (STP), and average throughput of each class. Some novel features of our method include: 1) we model and solve the per-slot class-dependent link statistics (such as CAP and STP), which vary based on the slot location; and 2) we provide an in-depth analysis on the average throughput, and design a multi-class combinatorial procedure to evaluate average time spent per successful transmission on each delay cell. We program the LAA CAPC algorithms and implement extensive Monte Carlo simulations, which validate the accuracy of our analytical results even in very low throughput region for lower priority classes, and demonstrate the effects of AIFS and other parameters in an LAA system. These results provide solid progress for evaluating priority classes in the LTE-LAA system and other spectrum sharing systems, and can be extended to support system and parameter optimization.**

Keywords: Channel Access Priority Classes, CSMA/CA, LTE-LAA, QoS Differentiation, Spectrum Sharing, Throughput

## I. Introduction

To enable constructive coexistence between the long-term evolution (LTE) and incumbent systems, such as IEEE 802.11 wireless local area network (WLAN) in the unlicensed industrial, scientific, and medical (ISM) radio band, the 3rd Generation Partnership Project (3GPP) has specified a license assisted access (LAA) procedure [1]–[4]. To provide differentiated quality of service (QoS) for diverse applications (such as audio, video and background services), the recent 3GPP LAA specification [3] includes several channel access priority classes (CAPCs). These classes use carrier sense multiple access with collision avoidance (CSMA/CA), and have different channel access parameters, such as arbitrary inter-frame space (AIFS), contention window (CW) size, and transmit opportunity (TXOP) payload duration.



The AIFS for a CAPC is defined as the required silent duration after a channel busy event is over and before the backoff process is resumed. The AIFS is composed of a short IFS (SIFS) duration and several additional idle slots which are distinct for each CAPC [3]. The LTE-LAA specification [3] did not provide a name for this parameter, and we term it "AIFS" due to its conceptual equivalence (or high similarity) to a popular term used in the enhanced distributed channel access (EDCA) procedure of the IEEE 802.11 WLAN standard [5], [6]. A CAPC with higher priority uses a shorter AIFS, and the effect of adjusting AIFS is typically more significant than that achieved by adjusting the CW size. Besides 3GPP LAA channel access [3] and IEEE WLAN EDCA specifications [5], the European Telecommunications Standards Institute (ETSI) has recently introduced distinct AIFSs in different priority classes to provide differentiated QoS in its unlicensed spectrum access procedure [7].

Evaluating the effects of CW size and payload duration is relatively straightforward based on abundant available methods in LAA-based spectrum sharing systems [8]–[13]. In these works, the AIFS is not considered, or equivalently, assumed to be identical for all types of transmissions. In [14]–[17], several optimization schemes for LAA and WLAN coexistence systems are developed. Especially, [14], [16], [17] have considered use of a shorter idle channel wait timing than the WLAN counterpart to dominate the channel access, and provide fairness and/or throughput optimization.

To date, accurately modelling and analyzing the performance of CAPCs with different AIFSs is still a challenging task, and has yet to be rigorously addressed. In this paper, following the recent 3GPP LAA specification on the CAPCs [3], we provide a new performance analysis that is valid for a wide range of practical CSMA/CA parameters, including distinct AIFS numbers. The contributions and novelty of this paper are highlighted as follows:

- We develop a *non-homogeneous* Markov chain to model and compute the system channel access probability (SCAP) and other statistics at each delay cell after the channel busy event and SIFS.
- We analyze the CAP, STP, and average throughput of each CAPC link as functions of AIFS, and other CSMA/CA parameters. The result is accurate or a good approximation for the parameter ranges studied, including the important cases such as small CW sizes and non-trivial



Ma, Yao.
"Analysis of Channel Access Priority Classes in LTE-LAA Spectrum Sharing System."
Paper presented at The 27th International Conference on Computer Communications and Networks (ICCCN 2018), Hangzhou, China. July 30, 2018 - August 2, 2018.

differences in AIFS numbers, as considered by an LAA specification [3].
- We implement algorithm programming and extensive simulation to evaluate the coexistence performance of multiple CAPCs. Numerical results validate the accuracy of our analytical results, and demonstrate the effects of AIFS, CW, and payload of each priority class in an LAA downlink system.

This result is significant because it allows us to accurately evaluate the differentiated QoS and channel access performance of LAA priority classes for critical parameter ranges, and the evaluation involves only a low to moderate complexity. Our method can be easily extended to provide performance analysis and support parameter optimization in other spectrum sharing systems and specifications. Examples include priority classes for unlicensed spectrum access defined by ETSI, and coexisting LTE-LAA and IEEE 802.11 WLAN systems.

## II. Related Work

Analytical results addressing distinct AIFSs in the LAA or ETSI unlicensed access systems are rare to find, if available at all. Next, we briefly review a few state-of-the-art results in the analysis of the WLAN EDCA procedure [18]–[22]. The work discussed in [18]–[20] develop different AIFS zone models for performance analysis. Several major or minor approximations are involved in computing the channel access and successful transmission probabilities. In [18] a renewal process between transmissions is modelled, and the analysis assumes that the channel access probability (CAP) of each class is constant along the slots, which involves an approximation. A highly complicated multi-dimensional Markov chain model is developed in [19], and a simplified model is provided in [20] for the QoS control. In [19] the authors model the channel idle probability for each class to be constant within each AIFS zone. In [20] they assume that the throughput of each CAPC link is inversely proportional to its backoff wait time, and model the CAP for each link to be a constant along slot index. In [21] the authors seek to provide an analytical result that does not consider the per-slot differences after the SIFS. Instead, they use a model with a constant transmission probability per class. This result may be regarded as a good approximation under conditions that the CW sizes of all classes are large and differences between AIFSs are small.

In [22], based on an extension of the results in [23], the authors model the effect of different AIFSs by a power term of a successful transmission probability (STP), aka. $P_T^{\Delta_{\text{AIFS}}}$, where $P_T$ is the STP averaged over all links and all idle slots, and $\Delta_{\text{AIFS}}$ is the AIFS difference between classes of the highest priority and the considered class. This modelling method is simple and elegant, but it involves approximations: the STPs of different classes are approximated as a single STP term; furthermore, this STP is modelled as a constant along the $\Delta_{\text{AIFS}}$ slot duration. Thus, it only partially captures the effect of distinct AIFS, and involves approximations which can be observed from simulation results in [22], especially for low-priority classes.

TABLE I: Definitions of some symbols frequently used in this paper.

| Symbol | Definition |
|---|---|
| CAP | Channel access probability (per link) |
| CAPC | Channel access priority class |
| SCAP | System channel access probability |
| STP | Successful transmission probability |
| $\tau_{c,d_c}$ | CAP of class $c$ at delay index $d_c$ |
| $P_{\text{ex},S}$ | SCAP at delay cell index $S$ |
| $P_{c,d_c,T}$ | Conditional STP of class $c$ at delay index $d_c$ |
| $P_{\text{suc},c,S}$ | Unconditional STP of class $c$ at cell index $S$ |

In summary, the above-mentioned results provide various analytical techniques for evaluating the impact of distinct AIFS on the achieved differential QoS performance in WLAN EDCA systems. A common weakness of these methods is that the per-slot difference due to distinct AIFS is not adequately modelled. Consequently, the reliability of applying these methods for assessing performance of lower priority classes at small throughput region is unclear or questionable. Systematic approximations may rise by extending available methods to model and evaluate the different CAPCs. It remains a challenging technical problem to accurately model and evaluate effects of different parameter setups and achievable performance of distinct priority classes in the LTE-LAA, ETSI and other spectrum sharing scenarios.

For ease of reference, some symbols that are frequently used in this paper are listed in Table I.

## III. System Model

We assume that in a downlink LAA system, there are $C_{\max}$ active CAPC groups, with $n_C$ links for group $c$, with $c = 1, 2, 3, C_{\max}$ and $C_{\max} = 4$. Each link has a fully backlogged traffic. To provide differentiated QoS for different types of services, a recent 3GPP release [3] has defined four LAA channel access priority classes, as shown in Table II. Throughout this paper, we use terms "CAPC" and "class" interchangeably. Each class has a different defer period after a channel busy event (we term it AIFS in this paper), besides distinct CW size and TXOP duration. The AIFS duration of each link in class $c$ is given by

$$T_{c,\text{AIFS}} = T_{\text{SIFS}} + A_c T_{sl}, \tag{1}$$

where $T_{\text{SIFS}} = 16\mu s$, and $T_{sl}$ is a backoff idle slot duration with $T_{sl} = 9\ \mu s$, and $A_c$ is called the AIFS number of class $c$. Based on Table II, $A_c \in \{1, 1, 3, 7\}$ for classes 1-4. Let CAPC $c$ have 0 to $K_c$ backoff stages. From Table II, it is obvious that $K_1 = K_2 = 1$, $K_3 = 2$, $K_4 = 6$. Let $W_{c,k}$ be the CW size of class $c$ at stage $k$. Since the CW value listed in Table II is equal to $W_{c,k} - 1$, we have $W_{1,0} = 4, W_{1,1} = 8$ for class 1, $W_{2,0} = 8, W_{2,1} = 16$ for class 2, and $W_{3,0} = W_{4,0} = 16$, etc.

The channel access of all links follows a CSMA/CA procedure defined in Section 15.1.1 of [3]. We briefly summarize

Ma, Yao.
"Analysis of Channel Access Priority Classes in LTE-LAA Spectrum Sharing System."
Paper presented at The 27th International Conference on Computer Communications and Networks (ICCCN 2018), Hangzhou, China. July 30, 2018 - August 2, 2018.

TABLE II: List of channel access parameters of LTE-LAA downlink, adopted from Table 15.1.1-1 of [3].

| Class $c$ | AIFS number ($A_c$) | $CW_{\min}$ | $CW_{\max}$ | Occupancy Duration |
|---|---|---|---|---|
| 1 | 1 | 3 | 7 | 2 ms |
| 2 | 1 | 7 | 15 | 3 ms |
| 3 | 3 | 15 | 63 | 8 or 10 ms |
| 4 | 7 | 15 | 1023 | 8 or 10 ms |

the procedure below, but make some modifications to improve its clarity (without changing the procedure itself).

**LAA Channel Access Procedure**

Assume a random backoff counter value $W$ for a class $c$ link.

- 1) Initialize. If this link finishes a transmission successfully (or just joins the network), set backoff stage $k = 0$, and draw a counter value $W$ uniformly from $(0, W_{c,0}-1)$. Otherwise, if this link finishes a transmission that failed, increase the current stage $k_{\text{old}}$ by one to obtain $k_{\text{new}} = \min(k_{\text{old}} + 1, K_c)$. If $k_{\text{old}} = K_c$, then $k_{\text{new}} = K_c$. Draw a counter value $W$ uniformly from $(0, W_{c,k_{\text{new}}} - 1)$.
- 2) If $W = 0$, starts a transmission. Otherwise, go to 3).
- 3) If $W > 0$, do either of the following 2 steps based on the given conditions:
  3.1) If a channel busy event was just over, sense the channel for a duration $T_{c,\text{AIFS}}$; If the result is idle, reduce counter $W$ by one, and go to 2); otherwise, frozen counter due to channel busy, and continue with Step 3.1.
  3.2) If the channel continues to be idle for a $T_{sl}$ duration after a previous counter reduction, reduce counter $W$ by one, and go to step 2). Otherwise, frozen counter due to channel busy, and go to Step 3.1.

Based on Table II and the LAA channel access procedure, we depict the signal timing after a channel busy event (successful or failed transmission) in Fig. 1. Right after the SIFS, each slot $T_{sl}$ is called a delay cell, indexed from 0 to $S_{\max}$. With Table II, the $S_{\max}$ is determined by the maximum CW size of class 1, so that $S_{\max} = 7$ when a class 1 link is active and fully backlogged. When none of the class 1 links are active, but some class 2 links are active, we have $S_{\max} = 15$.

## IV. Performance Analysis

Technical flow of this section is described as follows: In the first step, we derive SCAP at each delay cell based on a novel non-homogeneous Markov chain model during and after the AIFS. The SCAP is equivalent to the reset and exit probability at each delay cell. In the second and third steps, we derive the CAP and the STP of a link of each class. The unknowns and equations in these steps are solved jointly to obtain the CAPs and STPs which are distinct among classes and along the delay cells. In the fourth and final step, we derive the average time spent per successful transmission at each delay cell. This involves a complicated multi-class combinatorial evaluation procedure. Then we obtain the average throughput of each class. Each step is built upon results from the previous steps.

### A. Non-Homogeneous Markov Model for Distinct AIFS

Based on Table II and Fig. 1, we provide a non-homogeneous Markov chain-based model of the LTE-LAA process, depicted in Fig. 2. In Figs. 1 and 2 we use the term "delay cell" for the idle slots after the SIFS instead of "counter" to distinguish it from the backoff counter. We use "delay cell" to model the global timing of all links during the AIFS period, but will use term "backoff counter" to model the individual Markov chain of each link in its channel access procedure.

We show Fig. 2 in order to support the evaluation of the statistics of each class in the spectrum sharing scenario. It is important to analyze the stationary probability of each delay cell $S_0, \ldots, S_{\max}$, as denoted by $P_{S_0}, \ldots, P_{S_{\max}}$. Based on Fig. 2, we also define $P_{S,S+1}$ as the feedforward transition probability from cells $S$ to $S+1$, and $P_{\text{ex},S}$ as the SCAP (or exit probability) from cell $S$ back to cell 0, respectively, for $S = 1, \ldots, S_{\max}$. Using a precise analysis, we have $P_{S-1,S} \neq P_{S,S+1}$, for any $S$. Furthermore, as $S$ increases, the effective CW sizes tend to decrease, causing increased transmission probability. This effect has not been explicitly modelled in available work on analyzing AIFS [18]–[22], but will be addressed in Subsection IV-B. Thus, the probability transition graph in Fig. 2 can be regarded as a new non-homogeneous Markov Model.

Define $\hat{A}_c$ as the difference between the AIFS numbers of class $c$ and class 1, which is $\hat{A}_c = A_c - A_1 = A_c - 1$. We have $\hat{A}_1 = \hat{A}_2 = 0$, $\hat{A}_3 = 2$, and $\hat{A}_4 = 6$. We define $d_c$ as the corresponding delay index (in units of idle slot $T_{sl}$) of the class $c$ with respect to that of class 1, given by

$$d_c = S - \hat{A}_c, \tag{2}$$

for $c = 1, 2, 3, 4$. For example, at cell index $S = 6$, $d_1 = d_2 = 6$, $d_3 = 4$, and $d_4 = 0$.

Define $\tau_c(S)$ as the CAP of class $c$ at cell $S$, then

$$\tau_c(S) = \begin{cases} 0 & S < \hat{A}_c \\ \tau_{c,d_c} & S \geq \hat{A}_c, \end{cases} \tag{3}$$

where $\tau_{c,d_c}$ is the CAP of class $c$ with delay index $d_c$. Define $P_{I,c}(d_c)$ as the class $c$ idle probability at its own delay index $d_c$. It follows that

$$P_{I,c}(d_c) = (1 - \tau_{c,d_c})^{n_c}. \tag{4}$$

From Fig. 2, we obtain (for $S = 0, 1, \ldots, S_{\max} - 1$)

$$\begin{aligned} P_{S,S+1} &= P_{I,1}(S - \hat{A}_1)P_{I,2}(S - \hat{A}_2) \\ &\quad \cdot P_{I,3}(S - \hat{A}_3)P_{I,4}(S - \hat{A}_4), \end{aligned} \tag{5}$$

$$P_S = P_{S_0} \prod_{s=0}^{S-1} P_{s,s+1}. \tag{6}$$

Furthermore, since $\sum_{d=0}^{S_{\max}} P_{S_d} = 1$, we obtain the stationary probability of cell 0 as

$$P_{S_0} = \left[1 + \sum_{n=1}^{S_{\max}} P_{0,1}P_{1,2}\cdots P_{n-1,n}\right]^{-1}.$$

Ma, Yao.
"Analysis of Channel Access Priority Classes in LTE-LAA Spectrum Sharing System."
Paper presented at The 27th International Conference on Computer Communications and Networks (ICCCN 2018), Hangzhou, China. July 30, 2018 - August 2, 2018.

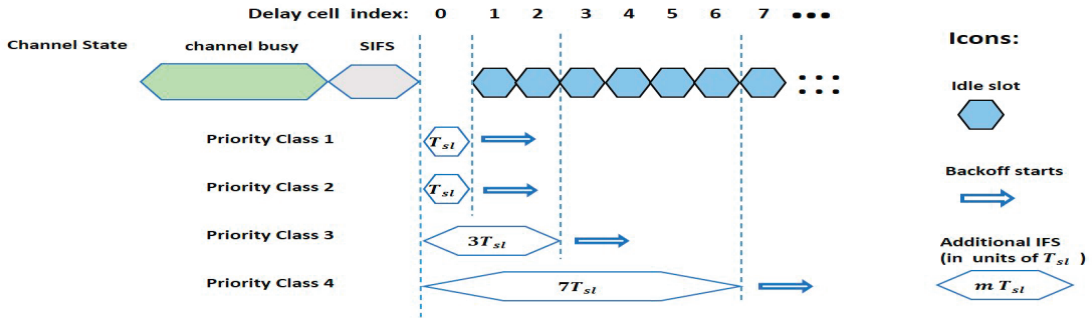


Fig. 1: Our proposed diagram of AIFS in 3GPP downlink LAA procedure for four channel access priority classes. The delay cell index refers to each idle slot after the SIFS but before a new transmission starts.

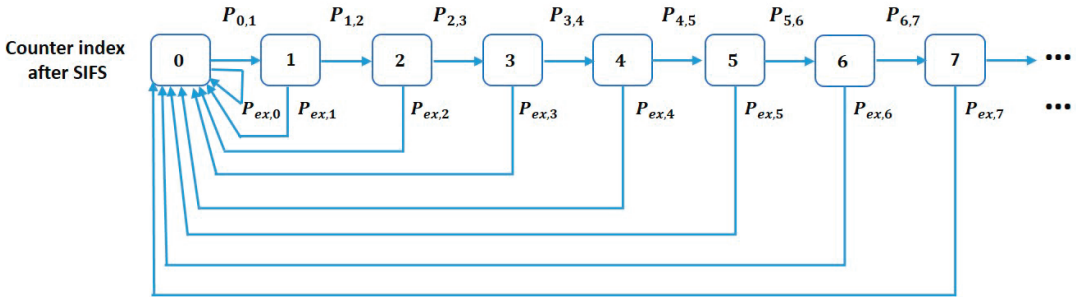


Fig. 2: Illustration of delay cells and the probability transition paths after the SIFS.

Probabilities of other delay cells $P_S$, $S = 1, \ldots, S_{\max}$ follow directly. To solve (5), we need to find the idle probability $P_{I,c}(d_c)$ for all $c$ and $d_c$, which is studied next.

The system idle probability at cell $S$ is obtained as

$$P_{I,S} = \prod_{c=1}^{C} (1 - \tau_c(S))^{n_c}, \tag{7}$$

where $\tau_c(S)$ is the CAP of class $c$ at cell $S$. Note that $\tau_c(S)$ can be zero based on the AIFS zones. The SCAP at cell $S$ is derived as

$$P_{\text{ex},S} = (1 - P_{I,S}) \prod_{s=0}^{S-1} P_{I,s}. \tag{8}$$

### B. Channel Access Probability and STP

In the literature, the CAP is typically modelled as constant in each AIFS zone, and changes only at zone boundary. Here, to be more accurate, we model CAP as variable along delay cell index $S$. As $S$ increases and $d_c \geq 0$, before a new transmission starts (aka, reset of cell to 0), the CAP shall increase with $d_c$. As $d_c$ increases, the backoff counter value of every class $c$ link decreases. To account for this effect, we model the effective CW size at each backoff stage of class $c$ as

$$\hat{W}_{c,k} = W_{c,k} - d_c. \tag{9}$$

For class $c$, the total probability of all the backoff counter states is unity. Therefore,

$$\sum_{k=0}^{K_c} \sum_{l=0}^{\hat{W}_{c,k}} b_{c,k,l} = 1, \tag{10}$$

where $b_{c,k,l}$ is the probability of backoff counter $l$ at stage $k$ for class $c$. Note that backoff counter index $l$ is different from the delay cell index $S$ after the SIFS, shown in Fig. 2. Using steps similar to those given in [24], we derive the CAP as

$$\tau_{c,d_c} = b_{c,0,0}/P_{c,d_c,T}, \tag{11}$$

where $P_{c,d_c,T}$ is the conditional STP of class $c$ at cell $d_c$, and

$$b_{c,0,0} = \Bigg[ \sum_{k=0}^{K_c-1} (1 - P_{c,d_c,T})^k (\hat{W}_{c,k} + 1)/2 + (\hat{W}_{c,K_c} + 1)(1 - P_{c,d_c,T})_c^K / (2P_{c,d_c,T}) \Bigg]^{-1}. \tag{12}$$

A major difference between (11) and the CAP given in [24] is that (11) is valid even when the CW size is not a power-of-two integer. Furthermore, our result models the effect of shrinking

Ma, Yao.
"Analysis of Channel Access Priority Classes in LTE-LAA Spectrum Sharing System."
Paper presented at The 27th International Conference on Computer Communications and Networks (ICCCN 2018), Hangzhou, China. July 30, 2018 - August 2, 2018.

CW size as the delay cell index increases. This method is consistent because when $d_c = W_{c,K_c}$ (for $c = 1$), we have $\hat{\tau}_{c,d_c} = 1$, which means that after the maximum possible counter reduction, the CAP must reach unity, as expected. To our knowledge, the majority of available methods have not explicitly modelled this effect.

After $\tau_{c,d_c}$ (for all $c$ and $d_c$) is derived, by using Fig. 2, we obtain the STP for a class $C$ link as

$$\begin{aligned} P_{C,d_C,T} &= (1-\tau_{C,d_C})^{n_C-1}\prod_{c=1}^{C-1}(1-\tau_{c,d_c})^{n_c} \\ &= \frac{\prod_{c=1}^{4}(1-\tau_{c,d_c})^{n_c}}{(1-\tau_{C,d_C})}. \end{aligned} \quad (13)$$

There are $4(S_{\max}+1)$ equalities based on (13) for all $c$ and $d_c$. We have the following parameters to be solved:

- CAPs $\{\tau_{c,d_c}\}$ (which are $4(S_{\max}+1)$ unknowns),
- STPs $\{P_{c,d_c,T}\}$ (which are $4(S_{\max}+1)$ unknowns).

Since (11) and (13) provide $8(S_{\max}+1)$ equations and involve $8(S_{\max}+1)$ unknowns, we can use an iterative search to uniquely solve for the unknowns.

### C. Throughput

Note that SCAP $P_{\text{ex},S}$ defined in (8) forms a probability set of mutually exclusive events, for $S = 0, 1, \ldots, S_{\max}$, and $\sum_{S=0}^{S_{\max}} P_{\text{ex},S} = 1$. By use of the SCAP set, the average sum throughput of class $c$ links is given by

$$R_c = \frac{n_c \sum_{S=0}^{S_{\max}} P_{\text{ex},S} P_{\text{suc},c,S} T_{p,c}}{\sum_{S=0}^{S_{\max}} P_{\text{ex},S} T_{\text{ave},S}}, \quad (14)$$

where $P_{\text{suc},c,S}$ is the unconditional successful transmission probability of a class $c$ link at cell $S$, $T_{p,c}$ is payload duration of class $c$, and $T_{\text{ave},S}$ is average time spent to enable a successful transmission at cell $S$. It follows that $P_{\text{suc},c,S} = \tau_{c,d_c} P_{I,S}$. Since $\sum_{S=0}^{S_{\max}} P_S = 1$ holds, we provide another formula for class $c$ sum throughput as:

$$R_c = \frac{n_c \sum_{S=0}^{S_{\max}} P_S P_{\text{suc},c,S} T_{p,c}}{\sum_{S=0}^{S_{\max}} P_S T_{\text{ave},S}}. \quad (15)$$

The $T_{\text{ave},S}$ is difficult to derive, since it involves interactions among $C = 4$ classes of links. We obtain

$$T_{\text{ave},S} = \begin{cases} T_{\text{TX},12}(S) & S \in (\hat{A}_2, \hat{A}_3 - 1) \\ T_{\text{TX},123}(S) & S \in (\hat{A}_3, \hat{A}_4 - 1) \\ T_{\text{TX},1234}(S) & S \in (\hat{A}_4, S_{\max}), \end{cases} \quad (16)$$

where $T_{\text{TX},12}(S)$ is the average channel busy duration to enable one successful transmission when classes 1 and 2 links can resume backoff (and hence possibly transmit) at cell $S$. Similarly, $T_{\text{TX},123}(S)$ and $T_{\text{TX},1234}(S)$ are the average channel busy durations caused by links in classes 1,2,3 and all 4 classes, respectively.

The link status in each class involves 3 types of events: idle channel, successful transmissions, and failed transmissions. The interactions among $C$ classes involve $3^C$ combinations of terms in order to calculate the average time per successful transmission. When $C = 4$, this is equal to $3^4 = 81$ terms which are too complex to present analytically. Next, we design an efficient method to evaluate such combinations for $C = 2, 3, 4$, respectively.

Define $T_{\text{act},C}(S)$ as the average channel busy duration when a class $c$ link (for $c = 1, 2, 3, 4$) is active at cell $S$. We derive it as

$$T_{\text{act},C}(S) = \frac{P_{\text{suc},C}(S) T_{\text{suc},C} + P_{F,C}(S) T_{F,C}}{1 - P_{I,C}(S)}, \quad (17)$$

where $P_{\text{suc},C}(S) = n_c \tau_{c,S} (1-\tau_{c,S})^{(n_c-1)}$ and $P_{F,C}(S) = 1 - P_{I,C}(S) - P_{\text{suc},C}(S)$ are the successful and failed transmission probabilities of class $c$ at cell $S$, respectively. Below, we suppress the index $S$ of $T_{\text{act},C}$ and $P_{I,C}$ when there is no confusion. We get:

$$\begin{aligned} T_{\text{TX},12} &= P_{I,1}(1-P_{I,2}) T_{\text{act},2} + P_{I,2}(1-P_{I,1}) T_{\text{act},1} \\ &\quad + (1-P_{I,2})(1-P_{I,1}) \max\{T_{F,1}, T_{F,2}\}, \end{aligned} \quad (18)$$

where the first term on the right hand side (RHS) is for an active transmission event of class 2 (when the class 1 system is idle), the second term is for active event of only class 1, and the third term is for the case that both classes 1 and 2 are active. Furthermore, we obtain

$$\begin{aligned} T_{\text{TX},123} &= \sum_{c_1=1}^{3} \prod_{\substack{c_2=1 \\ c_2 \neq C_1}}^{3} (1-P_{I,C_1}) P_{I,C_2} T_{\text{act},C_1} \\ &\quad + \sum_{c_1=1}^{3} \sum_{\substack{c_2=1 \\ c_2 \neq C_1}}^{3} \sum_{\substack{c_3 \neq C_1 \\ c_3 \neq C_2}} (1-P_{I,C_1})(1-P_{I,C_2}) \\ &\qquad \cdot P_{I,C_3} \max\{T_{F,C_1}, T_{F,C_2}\} \\ &\quad + (1-P_{I,1})(1-P_{I,2})(1-P_{I,3}) \max\{\{T_{F,C}\}_{c=1,2,3}\}, \end{aligned}$$

where the first term on the RHS is for the active transmission event of only one class, the second term represents the case of two active classes, and the third term is for the case that all three classes are active. Finally,

$$\begin{aligned} T_{\text{TX},1234} &= \sum_{c_1=1}^{4} (1-P_{I,C_1}) \left[ \prod_{\substack{c_2=1 \\ c_2 \neq C_1}}^{4} P_{I,C_2} \right] T_{\text{act},C_1} \\ &\quad + \sum_{c_1=1}^{4} \sum_{\substack{c_2=1 \\ c_2 \neq C_1}}^{4} \left[ \prod_{\substack{c_3 \neq C_1 \\ c_3 \neq C_2}} P_{I,C_3} \right] (1-P_{I,C_1}) \\ &\qquad \cdot (1-P_{I,C_2}) \max\{T_{F,C_1}, T_{F,C_2}\} \\ &\quad + \sum_{c_1=1}^{4} P_{I,C_1} \left[ \prod_{\substack{c_2=1 \\ c_2 \neq C_1}}^{4} (1-P_{I,C_2}) \right] \max\{\{T_{F,C_2}\}_{c_2 \neq C_1}\} \\ &\quad + \prod_{c_1=1}^{4} (1-P_{I,C_1}) \max\{\{T_{F,C_1}\}_{c_1=1,2,3,4}\}, \end{aligned}$$

where the first to the fourth terms on the RHS are for active transmission events of any one class only, of any two

classes only, of any three classes only, and of all four classes, respectively. By using (14)–(16), the sum throughput of each class can be accurately evaluated.

## V. Numerical Results

In this section, we provide both analytical and simulation results for an LAA downlink system with several priority classes. We implemented computer programming on the LAA algorithms, taking into account the diverse AIFSs, CW sizes, and payload durations. The simulation results were obtained by running for $10^6$ time slots on each parameter setting to obtain average statistics. Every analytical curve shown in this section is accompanied by a simulation curve and verified. Saturated traffic is assumed for all nodes. The spectrum sensing in the LTE-LAA system is assumed to be perfect (no hidden node problem, no false alarm or missed detection). To compare the achievable performance of different classes, time efficiency throughput is used, which is defined as the time portion of successful payload transmissions over the total simulation time. We consider two access schemes for the LAA system, a basic access scheme, and a request-to-send and clear-to-send (RTS/CTS) type of handshaking scheme. Note that downlink and uplink two-way unlicensed transmissions have been included in a recent LAA specification [3], which makes the RTS/CTS scheme more feasible to implement.

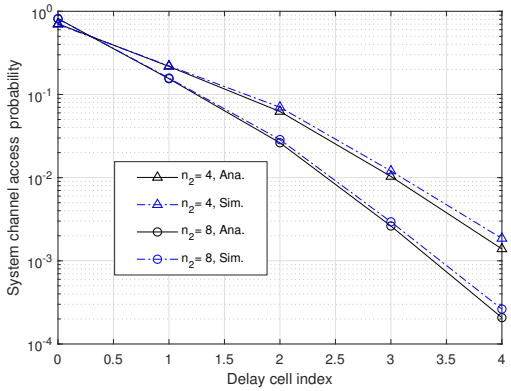


Fig. 3: System channel access probability vs. cell index of three access classes in an LTE-LAA system, when $A_1 = A_2 = 1$, $A_3 = 3$, $n_1 = 2$, $n_2 = 4$ or 8, $n_3 = 10$, $W_{1,0} = 4$, $W_{2,0} = 8$, $W_{3,0} = 16$, $K_1 = K_2 = 1$, $K_3 = 2$, $T_{P,1} = 2$ ms, $T_{P,2} = 3$ ms, and $T_{P,3} = 8$ ms, with RTS/CTS.

First, we study the QoS performance of the first three classes with parameters taken from Table II. We provide the SCAP (or cell exit probability) in Fig. 3 and the time efficiency throughput in Fig. 4. The result in Fig. 3 shows that as cell index $S$ increases, the SCAP drops sharply. This demonstrates that when the AIFS difference between classes 1 and 3 is only 2, a class 3 link only has a very small chance of transmission.

Fig. 4 shows that as $n_2$ increases, class 2 links have increased sum throughput, but the throughput of class 3 links decrease significantly. A class 4 link based on Table II is not shown here because its throughput is too low to be simulated reliably when higher priority classes have saturated traffic.

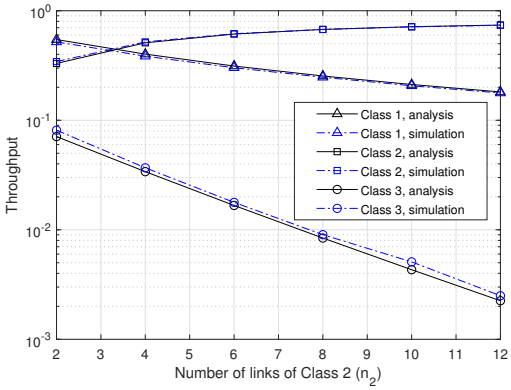


Fig. 4: Throughput of the first 3 classes in an LTE-LAA system, when $n_2$ increases from 2 to 12, and the other parameters are the same as those used for Fig. 3.

Next, to show the generality of our result, we consider a customized setup with 4 classes with different AIFS numbers $A_1 = 1$, $A_2 = 2$, $A_3 = 3$, and $A_4 = 4$. We provide the stationary cell probability $P_S$ in Fig. 5, which shows that as $S$ or $n_2$ increases, the $P_S$ may drop significantly. This shows that the CW size and cutoff stage setup of higher priority classes, in addition to the AIFS numbers, is critical to the achievable performance of lower priority classes.

Fig. 6 provides the sum throughput of the 4 classes. In computing the analytical throughput in Figs. 4 and 6, we used formulas from (14) and (15), respectively. As $n_2$ increases from 2 to 12, the sum throughput of class 3 and 4 links decreases significantly. Yet, class 4 links have a much lower sum throughput than other classes, about two orders of magnitude lower than that of class 3. Note that in the majority of available analytical results on distinct AIFSs, the throughput results of lower classes (with a higher AIFS number) were plotted in a linear scale, which causes the low-value detail to be ignored. Based on our new method, we can reliably evaluate the differentiated QoS performance for low-priority classes in practical parameter range. Thus, we show our results in the logarithm scale to highlight the impact of the AIFS on the throughput in even a very low value range (e.g. $10^{-5}$).

## VI. Conclusion

The use of diverse AIFSs to provide differentiated QoS have been included in the IEEE 802.11 WLAN, 3GPP LTE-LAA, and ETSI unlicensed spectrum access standards. The AIFS setup significantly impacts the channel access priority. In this paper, following a recent 3GPP LAA channel access specification, we have provided accurate modelling and performance analysis of the LTE-LAA priority classes. We have developed a flexible analytical approach to evaluate the transmission probability, collision probability, and time-efficiency throughput. We have implemented programming of LAA algorithms and

Ma, Yao.
"Analysis of Channel Access Priority Classes in LTE-LAA Spectrum Sharing System."
Paper presented at The 27th International Conference on Computer Communications and Networks (ICCCN 2018), Hangzhou, China. July 30, 2018 - August 2, 2018.

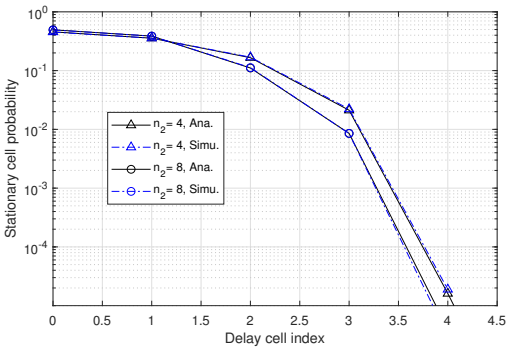


Fig. 5: Stationary cell probability vs. cell index of four access classes in an LTE-LAA system, when $A_1 = 1$, $A_2 = 2$, $A_3 = 3$, $A_4 = 4$, $n_1 = 2$, $n_3 = 10$, $n_4 = 40$, $W_{1,0} = W_{2,0} = W_{3,0} = W_{4,0} = 16$, $K_1 = K_2 = K_3 = K_4 = 0$, $T_{P,1} = 3$ ms, and $T_{P,2} = T_{P,3} = T_{P,4} = 8$ ms, with basic access.

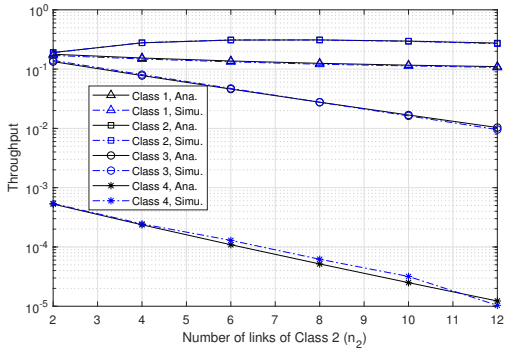


Fig. 6: Throughput of the four classes in an LTE-LAA system, when $n_2$ increases from 2 to 12, and the other parameters are the same as those used for Fig. 5.

extensive Monte Carlo simulations, which have verified the accuracy of our analytical results, even at very low throughput as found in lower priority classes. In future work, we will study the extension of this method to other systems, such as an ETSI unlicensed spectrum access system, and coexisting LTE-LAA and WLAN systems. Furthermore, measurement and testing procedure will be implemented to further validate the analytical and simulation results.

## REFERENCES


[1] R. Zhang, M. Wang, L. X. Cai, Z. Zheng, and X. Shen, "LTE-unlicensed: the future of spectrum aggregation for cellular networks," *IEEE Wireless Commun.*, vol. 22, no. 3, pp. 150–159, Jun. 2015.

[2] A. Mukherjee et al., "Licensed-assisted access LTE: coexistence with IEEE 802.11 and the evolution toward 5G," *IEEE Commun. Mag.*, vol. 54, no. 6, pp. 50-57, Jun. 2016.

[3] 3GPP TS RAN, "E-UTRA Physical Layer Procedures (Release 14)", 3GPP TS 36.213 V14.4.0, Sept. 2017.

[4] 3GPP TSG RAN, "Study on Licensed-Assisted Access to Unlicensed Spectrum", 3GPP TR 36.889 V13.0.0, Jun. 2015.

[5] IEEE WG802.11 Wireless LAN Working Group, "IEEE Std. 802.11e-2005 Part 11: Wireless LAN Medium Access Control (MAC) and Physical Layer (PHY) Specifications: Amendment 8: Medium Access Control (MAC) Quality of Service Enhancements," Sep. 2005.

[6] IEEE LAN/MAN Standards Committee, " IEEE Std 802.11-2012, Part 11: Wireless LAN Medium Access Control (MAC) and Physical Layer (PHY) Specifications," Feb. 2012.

[7] ETSI EN 301 893 V2.1.1 (2017-05), "5 GHz RLAN; Harmonised Standard Covering the Essential Eequirements of Article 3.2 of Directive 2014/53/EU," May 2017.

[8] C. Chen, R. Ratasuk, and A. Ghosh, "Downlink performance analysis of LTE and WiFi coexistence in unlicensed bands with a simple listen-before-talk scheme," in *Proc. IEEE VTC*, Glasgow, May 2015, pp. 1–5.

[9] Y. Song, K. W. Sung, and Y. Han, "Coexistence of Wi-Fi and cellular with listen-before-talk in unlicensed spectrum," *IEEE Commun. Lett.*, vol. 20, no. 1, pp. 161–164, Jan. 2016.

[10] A. K. Ajami and H. Artail, "Fairness in future licensed assisted access (LAA) LTE networks: What happens when operators have different channel access priorities?" in *Proc. IEEE ICC Workshops*, Paris, May 2017, pp. 67-72.

[11] Y. Ma and D. G. Kuester, "MAC-Layer Coexistence Analysis of LTE and WLAN Systems Via Listen-Before-Talk," in *Proc. IEEE CCNC*, Las Vegas, Jan. 2017, pp. 534-541.

[12] Y. Ma, D. G. Kuester, J. Coder, and W. F. Young, "Coexistence analysis of LTE and WLAN systems with heterogenous backoff slot durations", in *Proc. IEEE ICC*, Paris, May 2017, pp. 1-7.

[13] Y. Ma, R. Jacobs, D. G. Kuester, J. Coder, and W. F. Young, "SDR-Based experiments for LTE-LAA based coexistence systems with improved design," in *Proc. IEEE GlobeCom*, Singapore, Dec. 2017, pp. 1–6.

[14] V. Valls, A. Garcia-Saavedra, X. Costa and D. J. Leith, "Maximizing LTE capacity in unlicensed bands (LTE-U/LAA) while fairly coexisting with 802.11 WLANs," in *IEEE Commun. Lett.*, vol. 20, no. 6, pp. 1219–1222, Jun. 2016.

[15] R. Yin, G. Yu, A. Maaref, and G. Li, "A framework for co-channel interference and collision probability tradeoff in LTE licensed-assisted access networks," *IEEE Trans. Wireless Commun.*, vol. 15, no. 9, pp. 6078–6090, Sept. 2016.

[16] S. Han, Y. C. Liang, Q. Chen and B. H. Soong, "Licensed-assisted access for LTE in unlicensed spectrum: A MAC protocol design," in *Proc. IEEE ICC*, Kuala Lumpur, Malaysia, May 2016, pp. 1–6.

[17] S. Han, Y. C. Liang, Q. Chen and B. H. Soong, "Licensed-assisted access for LTE in unlicensed spectrum: A MAC protocol design," *IEEE J. Sel. Areas Commun.*, vol. 34, no. 10, pp. 2550–2561, Oct. 2016.

[18] Jie Hui and M. Devetsikiotis, "A unified model for the performance analysis of IEEE 802.11e EDCA," *IEEE Trans. Commun.*, vol. 53, no. 9, pp. 1498-1510, Sept. 2005.

[19] J. Y. Lee and H. S. Lee, "A performance analysis model for IEEE 802.11e EDCA under saturation condition," *IEEE Trans. Commun.*, vol. 57, no. 1, pp. 56-63, Jan. 2009.

[20] J. Y. Lee, H. S. Lee and J. S. Ma, "Model-based QoS parameter control for IEEE 802.11e EDCA," *IEEE Trans. Commun.*, vol. 57, no. 7, pp. 1914-1918, July 2009.

[21] I. Tinnirello and G. Bianchi, "Rethinking the IEEE 802.11e EDCA performance modeling methodology," *IEEE/ACM Trans. Netw.*, vol. 18, no. 2, pp. 540–553, April 2010.

[22] Y. Gao, X. Sun and L. Dai, "IEEE 802.11e Std EDCA networks: modeling, differentiation and optimization," *IEEE Trans. Wireless Commun.*, vol. 13, no. 7, pp. 3863–3879, July 2014.

[23] L. Dai and X. Sun, "A unified analysis of IEEE 802.11 DCF networks: stability, throughput, and delay," *IEEE Trans. Mobile Computing*, vol.12, no.8, pp.1558–1572, Aug. 2013.

[24] G. Bianchi, "Performance analysis of the IEEE 802.11 distributed coordination function," *IEEE J. Sel. Areas Commun.*, vol. 18, no. 3, pp. 535–547, Mar. 2000.



Ma, Yao.
"Analysis of Channel Access Priority Classes in LTE-LAA Spectrum Sharing System."
Paper presented at The 27th International Conference on Computer Communications and Networks (ICCCN 2018), Hangzhou, China. July 30, 2018 - August 2, 2018.

*Proc. of the 2018 International Symposium on Electromagnetic Compatibility (EMC Europe 2018), Amsterdam, The Netherlands, August 27–30, 2018.*

# Uncertainties in Rydberg Atom-based RF E-field Measurements

Matthew T. Simons, Marcus D. Kautz, Joshua A. Gordon, Christopher L. Holloway
National Institute of Standards and Technology, USA
matthew.simons@nist.gov

***Abstract*— A Rydberg atom-based electric-field measurement approach is being investigated by several groups around the world as a means to develop a new SI-traceable RF E-field standard. For this technique to be useful it is important to understand the uncertainties. In this paper, we examine and quantify the sources of uncertainty present with this Rydberg atom-based RF electric-field measurement technique.**

## I. Introduction

Currently, there are limitations to existing radio frequency (RF) electric field (E-field) metrology techniques. Standard RF E-field calibrations can be known to an uncertainty of at best 5 %. E-field probes must be calibrated in a 'known' field, however, a field can only really be 'known' by measuring it with a calibrated probe, creating a chicken-and-egg dilemma. Additionally, SI-traceability paths are very long and convoluted. Rydberg atom-based electromagnetically-induced transparency (EIT) is a fundamentally different approach to RF E-field metrology [1], [2], [4], [3], [5], [6], [7], [8]. This technique is based on interactions between RF fields and atomic transitions, directly linking the RF E-field measurement to fundamental units. Through this method, the uncertainties in RF E-field metrology can be reduced below present limits. For this approach to be accepted as a standard calibration method by national metrology institutes (NMIs), a comprehensive uncertainty analysis is necessary.

Electromagnetically-induced transparency is a phenomenon in which a medium that is normally absorptive becomes transparent when exposed to a particular electromagnetic field. For example, an alkali atom vapor such as rubidium (Rb) normally absorbs a 'probe laser' with a frequency tuned to the first excited state transition. When a second 'coupling' laser is tuned to a transition from the first excited state up to a high energy level Rydberg state, a destructive quantum interference occurs and the probe laser will be transmitted through the Rb vapor. The black line in Fig. 1 shows a typical EIT peak as a function of the probe laser frequency detuning from resonance.

Because the electron is far from the nucleus, Rydberg states are very sensitive to RF fields. If an RF field that is resonant with a transition to a nearby Rydberg state is applied, the EIT transmission peak splits into two peaks (blue and red lines in Fig. 1). This is known as Autler-Townes (AT) splitting. The frequency difference $\Delta f_0$ is directly related to the strength of the applied RF E-field $|E|$ by

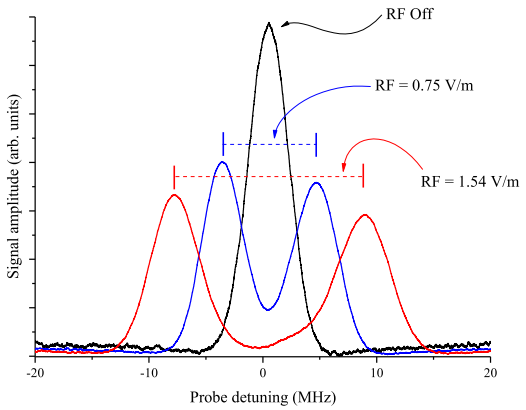


Fig. 1. EIT/AT splitting for three cases: EIT only with no RF field (black line), AT splitting with RF E-field = 0.75 V/m (blue line), AT splitting with RF E-field = 1.54 V/m (red line). The vertical axis is the transmitted probe laser intensity in arbitrary units, scaled for visibility.

$$|E| = \frac{2\pi\hbar}{\wp}\Delta f_0, \tag{1}$$

where $\hbar$ is Planck's constant and $\wp$ is the dipole moment of the transition. By calculating $\wp$ and measuring $\Delta f_0$, we directly get an SI-traceable measurement of the RF E-field strength. For example, in Fig. 1 we see that as the RF E-field is increased between the blue and red lines, the frequency separation between the peaks increases. Different frequencies can be measured by changing the frequency of the coupling laser to address different Rydberg states. Measurements can be done from $\sim 0.1$ GHz up to $\sim 1$ THz [1].

In this work we used several different glass cells evacuated and filled with a rubidium atom vapor ('vapor cells') to measure an RF field of 20.64 GHz with the Rydberg transition $47D_{5/2} \rightarrow 48P_{3/2}$. The EIT/AT signal was generated by a $\lambda_p = 780.24$ nm probe laser and a $\lambda_c = 480.270$ nm coupling laser overlapped inside the vapor cell (see Fig. 2). The laser beam diameters (full-width at half-maximum) were 270 $\mu$m, and 353 $\mu$m and the powers were 3.24 $\mu$W and 64 mW, respectively. The RF field was created by a signal generator

 

Simons, Matthew; Kautz, Marcus; Gordon, Joshua; Holloway, Christopher.
"Uncertainties in Rydberg Atom-based RF E-field Measurements."
Paper presented at 2018 International Symposium on Electromagnetic Compatibility (EMC), Amsterdam, Netherlands. August 27, 2018 - August 30, 2018.

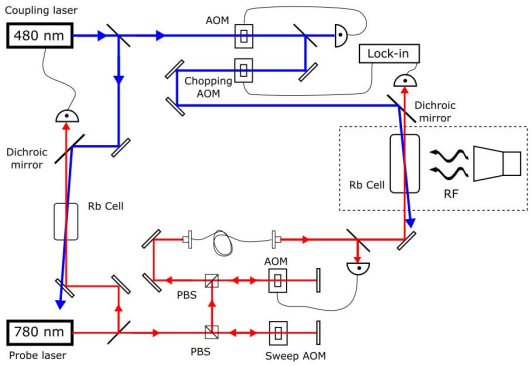


Fig. 2. Diagram of the Rydberg EIT experimental setup. The E-field measurement takes place in the area enclosed by the dashed lines. The second Rb vapor cell is used to lock the frequency of the coupling laser.

connected to a Narda 638 standard gain horn[1] placed at a distance 0.345 m from the lasers. We assessed the various sources of uncertainty through measurements of an RF field at different RF input powers and at different locations inside the vapor cell. Below we specify and quantify the uncertainties at each step in the measurement process.

## II. Sources Of Uncertainty

We group the sources of uncertainty in this system into two main types, which we refer to as the 'quantum-based' uncertainties and the 'measurement-based' uncertainties. Some of these sources were examined in [2]; here we explore additional sources of uncertainty. Quantum-based uncertainties include the determination of the dipole moment $\wp$ of the Rydberg transition and the validity of the linear relationship in Eq. 1. The quantity $\wp$ must be calculated for each Rydberg transition and can be determined to within 0.1 % [9]. The conditions for linearity between $|E|$ and $\Delta f_0$ are explored in [10]. For certain experimental conditions, the uncertainty in the deviation from linearity can be kept below 0.5 %. This is determined by comparing the Rabi frequencies (measures of the intensities) of the probe laser ($\Omega_p$), coupling laser ($\Omega_c$), and the RF field ($\Omega_{RF}$). The probe and coupling laser powers must be controlled such that $\Omega_{RF}$ is greater than the linewidth of the EIT peak, $\Gamma_{EIT}$, in Eq. 2. The EIT linewidth was measured to be $\Gamma_{EIT} = 2\pi \times 4.1$ MHz. The lowest RF field measured had a Rabi frequency of $\Omega_{RF} = 2\pi \times 8.6$ MHz, just over twice the EIT linewidth,

$$\Omega_{RF} > 2 \times \Gamma_{EIT}. \tag{2}$$

The measurement uncertainties are divided into three categories: (1) frequency scaling, (2) repeatability/peak measurement, and (3) vapor cell parameters. In the following sections we quantify the contributions of each of these to the overall measurement uncertainty budget for Rydberg atom-based RF E-field measurements.

[1]Certain commercial equipment, instruments, or materials are identified in this paper in order to specify the experimental procedure adequately. Such identification is not intended to imply recommendation or endorsement by the National Institute of Standards and Technology, nor is it intended to imply that the materials or equipment identified are necessarily the best available for the purpose.

## III. Frequency Scaling

In order to measure the frequency difference between the AT peaks, the frequency scale (the x-axis in Fig. 1) must be calibrated. The frequency difference between the AT split peaks $\Delta f_0$ is related to the measured splitting $\Delta f_m$ by $\Delta f_0 = D_\lambda \Delta f_m$. The factor $D_\lambda = \lambda_p/\lambda_c$ when the probe laser frequency is scanned and $D_\lambda = 1$ when the coupling laser frequency is scanned (see [10]). For the measurements discussed in this work, we scanned the probe laser using a voltage controlled oscillator (VCO)-driven acousto-optic modulator (AOM). The VCO was controlled with a 5 Hz, 2 V peak-to-peak triangle wave out of a high-voltage amplifier fed by a function generator. The VCO converted the input voltage to an RF signal at 10.37 MHz/V $\pm$0.05 MHz/V. We measured the peak-to-peak of the triangle wave with an oscilloscope, which for these measurements was $V_{pp} = 2.10$ V $\pm 0.14$ V. The frequency was measured to be 5 Hz to 10 ppm. Combined, this translates to an uncertainty of 6.8 % in the measured frequencies.

There are ways to improve the frequency scale calibration. The main limitation above is in the scope used to measure the voltage fed to the VCO. Using a better scope can significantly reduce the uncertainty, down to below 1.8 %. The best method is to use two known atomic lines to calibrate the scale. For instance, the hyperfine transition lines in Rb are known to 0.06 %. Since we are detuning the probe around the $|5S_{1/2}, F = 3\rangle$ to $|5P_{3/2}, F' = 4\rangle$ transition, we can use the frequency difference between this and the $|5S_{1/2}, F = 3\rangle$ to $|5P_{3/2}, F' = 3\rangle$ transition, which is 120.640$\pm$0.068 MHz [11]. Combining this with the scope timescale uncertainty results in an uncertainty in our frequency scale of 0.06 %. We have not yet implemented this into our system as our AOM scan is only over 40 MHz.

## IV. Repeatability

The AT splitting was determined by fitting the signal and finding the peak locations. The AT signal is most similar to a double Gaussian, but is actually a more complicated function. Figure 3 shows an example of peak fitting. The black dots are the raw data, the blue dashed line is a double Gaussian fit to the data, and the red solid line is a smoothing spline. In the inset, the double Gaussian fit is off from the actual peak by $\sim$ 0.5 MHz. For a splitting of 10 MHz, this is an error of 5 %. To better fit the data, it was smoothed with a smoothing spline, and the split was measured by finding the location of the maximum of each peak.

Four runs of data were collected as the RF power input to the horn antenna was varied. Each data run contained 10 data points at each of 17 different powers. These 10 points were then averaged and the standard deviation calculated. The averaged data are shown in Figure 4. To assess the uncertainty



Simons, Matthew; Kautz, Marcus; Gordon, Joshua; Holloway, Christopher.
"Uncertainties in Rydberg Atom-based RF E-field Measurements."
Paper presented at 2018 International Symposium on Electromagnetic Compatibility (EMC), Amsterdam, Netherlands. August 27, 2018 - August 30, 2018.

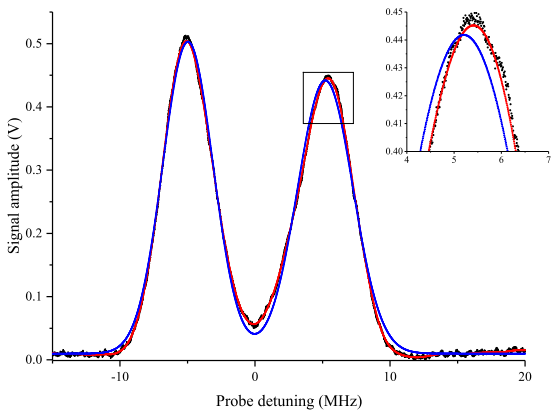


Fig. 3. Sample splitting measurement (black dots) with double Gaussian fit (blue dashed line) and smoothing spline (red solid line).

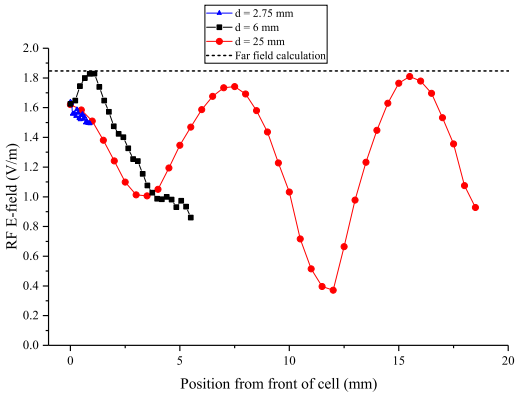


Fig. 5. Measured RF E-field vs. laser position inside cell for three different vapor cells.

from the peak fitting, we looked at the standard deviations of the averaged points. Between all four runs the average standard deviation was less than $0.5$ %. This compares to the statistical uncertainty in [2].

## V. Vapor Cell Parameters

While the atoms are measuring the absolute strength of the RF E-field that they observe, that E-field strength differs from the strength outside of the vapor cell due to the properties of the dielectric cell. There are two main factors that affect the apparent E-field strength: the dielectric constant of the glass and the shape/size of the vapor cell. These are manifested in two dominant effects. First, the E-field strength is reduced as the RF field enters the vapor cell, both from dielectric loss and reflection. The dielectric loss from the vapor cell material depends on the frequency of the E-field. Second, the dielectric vapor cell acts as a cavity, forming a standing wave in the

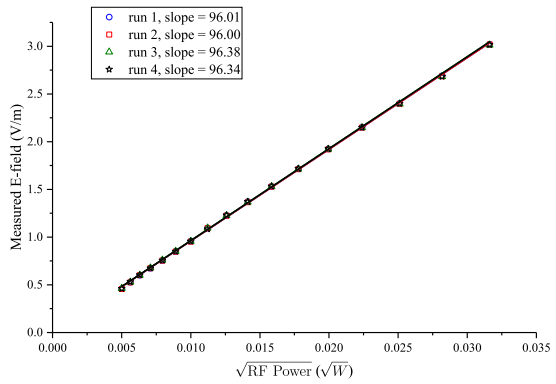


Fig. 4. Measured RF E-field vs. RF power input to horn for four separate runs.

E-field [12], [13]. Figure 5 shows the measured E-field strength as the lasers were scanned across three vapor cells (in the direction of the RF field propagation).

The three vapor cells used were all cylindrical glass cells, $75$ mm long (along direction of laser field propagation), and had inside diameters of $d = 2.75$ mm, $6$ mm, and $25$ mm. An RF field with frequency $20.64$ GHz and input-to-horn power of $-7.9$ dBm was applied with a Narda $638$ standard gain horn[1] (gain of $15.9$ dB) at a distance of $0.345$ mm from the overlapped lasers. A far-field calculation of the E-field based on the horn gain and distance is also shown in Fig. 5. If there is no knowledge about the location of the lasers inside the vapor cell, the uncertainty in the measured field can be very large. The standing wave scales with the ratio of RF wavelength to cell diameter ($\lambda_{RF}/d$), so if the diameter is sufficiently small compared to the wavelength the field variation can be made small. For instance, the $d = 25$ mm cell has a $\lambda_{RF}/d = 0.58$, and the field varies by more than $55$ % across the diameter of the cell. Using a cell with a $\lambda_{RF}/d = 7.2$ ($d = 2.75$ mm), the variation can be reduced to $\sim 5$ %. For a cell $\lambda_{RF}/d > 20$, the variation due to the standing wave is effectively eliminated. However, this is difficult to achieve for high frequencies (for $20.64$ GHz the cell would have to be less than $1$ mm).

Another way to account for this is to simulate the standing wave pattern to predict the correction factor. Figure 6 shows an example of HFSS simulations[1] compared to measured E-field data from different vapor cells [3]. As the size of the beam is less than $0.5$ mm, the variation of the field within this range at a standing wave peak is $0.5$ %. Using these simulations, and by measuring the location of the beam inside the vapor cell, the uncertainty associated with the field variation in the cell can be reduced to below $\sim 1$ %, even for a small $\lambda_{RF}/d$ ratio. If the beam is located at a standing wave peak, the uncertainty is on the order of $0.5$ %.



Simons, Matthew; Kautz, Marcus; Gordon, Joshua; Holloway, Christopher.
"Uncertainties in Rydberg Atom-based RF E-field Measurements."
Paper presented at 2018 International Symposium on Electromagnetic Compatibility (EMC), Amsterdam, Netherlands. August 27, 2018 - August 30, 2018.

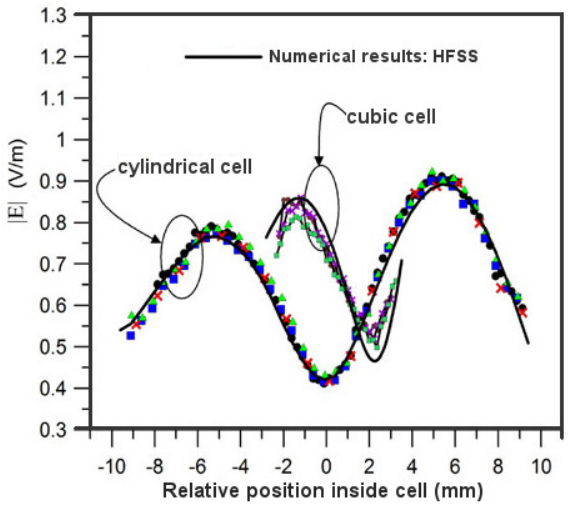


Fig. 6. Example of HFSS simulation comparison to cell position data, from [3]. Data are from multiple runs on both a cylindrical vapor cell and a cubic vapor cell.

## VI. Uncertainty Budget

For an estimate of the overall uncertainties, we collected the measurement uncertainties as determined above, including the frequency scale, peak finding, and vapor cell location. We also took into account the quantum-based uncertainties as determined in previous work, for the dipole moment calculation and the deviation from linearity. An initial uncertainty budget is presented in Table 1. These values assume ideal measurement conditions, such as the beam position within the vapor cell is known, the RF E-field Rabi frequencies are greater than the EIT linewidth, and the frequency scale is calibrated to an atomic transition.

Table 1. **Uncertainty Budget**

| Source | | Uncertainty |
|---|---|---|
| Frequency Scale | $\delta f_s$ | 0.06 % |
| Peak Finding | $\delta f_i$ | 0.5 % |
| Vapor Cell Location | $\delta E_v$ | 1.0 % |
| Deviation from Linearity | $\delta E_l$ | 0.5 % |
| Dipole Moment | $\delta\wp$ | 0.1 % |
| Total | $\delta\|E\|$ | $< 1.4$ % |

The uncertainty from the frequency scale ($\delta f_s$) is small enough that it does not significantly affect the combined uncertainty. The uncertainty in the measured frequency separation ($\delta f_m$) is then determined by combining the uncertainties from the measurement of each peak location ($\delta f_i$) in Eq. 3. The uncertainty in the measurement of the E-field ($\delta E_m$) is determined using Eq. 1, by adding the uncertainty from the dipole moment calculation, $\delta\wp$, in Eq. 4. Lastly, the E-field measurement uncertainty is combined with uncertainty from the vapor cell location ($\delta E_v$) and deviation from linearity $\delta E_l$), in Eq. 5. The resulting combined uncertainty is less than 1.4 %

$$\delta\Delta f_m = \sqrt{\delta f_1^2 + \delta f_2^2} = 0.71\ \%, \quad (3)$$

$$\delta E_m = |E_m| \times \sqrt{\left(\frac{\delta\Delta f_m}{\Delta f_m}\right)^2 + \left(\frac{\delta\wp}{\wp}\right)^2} = 0.73\ \%, \quad (4)$$

$$\delta|E| = \sqrt{\delta E_m^2 + \delta E_v^2 + \delta E_l^2} = 1.34\ \%. \quad (5)$$

## VII. Conclusions

The sources of uncertainty in Rydberg EIT-based RF E-field measurements must be understood for this technique to be useful as a calibration standard. The quantum-based uncertainties, from the dipole moment calculation and the deviation from linearity, have been previously determined [9], [10]. The measurement uncertainties in Rydberg EIT-based RF E-field measurements are from three main sources: the frequency scale, peak fitting, and the vapor cell parameters. The quantum based uncertainties can be limited by ensuring the experimental parameters are in the linear regime. The frequency scale and peak fitting uncertainties can likewise be controlled. The most difficult source to work with is the RF standing wave, and this uncertainty can be limited by measuring the vapor cell location and modeling the field distribution. Taking these steps, the uncertainties in this technique can be reduced to below those in present standard calibrations.

## Acknowledgment

The authors thank Amanda Koepke at NIST for assistance with statistical uncertainties.

## References

[1] C.L. Holloway, J.A. Gordon, A. Schwarzkopf, D.A. Anderson, S.A. Miller, N. Thaicharoen, and G. Raithel, "Broadband Rydberg Atom-Based Electric-Field Probe for SI-Traceable, Self-Calibrated Measurements", *IEEE Trans. on Antenna and Propag.*, **62**(12), 6169-6182, 2014.

[2] J. Sedlacek, A. Schwettmann, H. Kübler, R. Löw, T. Pfau, and J.P Shaffer, "Microwave electrometry with Rydberg atoms in a vapour cell using bright atomic resonances", *Nature Physics*, **8**, 819, 2012.

[3] C.L. Holloway, M.T. Simons, J.A. Gordon, P.F. Wilson, C.M. Cooke, D.A. Anderson, and G. Raithel, "Atom-Based RF Electric Field Metrology: From Self-Calibrated Measurements to Subwavelength and Near-Field Imaging", *IEEE Trans. on Electromagnetic Compat.,* **59**(2), 717-728, 2017.

[4] J.A. Sedlacek, A. Schwettmann, H. Kübler, and J.P. Shaffer, "Atom-Based Vector Microwave Electrometry Using Rubidium Rydberg Atoms in a Vapor Cell", *Phys. Rev. Lett.*, **111**, 063001, 2013.

[5] H. Fan, S. Kumar, J. Sedlacek, H. Kübler, S. Karimkashi and J.P Shaffer, "Atom based RF electric field sensing", *J. Phys. B: At. Mol. Opt. Phys.,* **48**, 202001, 2015.



Simons, Matthew; Kautz, Marcus; Gordon, Joshua; Holloway, Christopher.
"Uncertainties in Rydberg Atom-based RF E-field Measurements."
Paper presented at 2018 International Symposium on Electromagnetic Compatibility (EMC), Amsterdam, Netherlands. August 27, 2018 - August 30, 2018.

[6] M. Tanasittikosol, J.D. Pritchard, D. Maxwell, A. Gauguet, K.J. Weatherill, R.M. Potvliege and C.S. Adams, "Microwave dressing of Rydberg dark states", *J. Phys B*, **44**, 184020, 2011.

[7] C.G. Wade, N. Sibalic, N.R. de Melo, J.M. Kondo, C.S. Adams, and K.J. Weatherill, "Real-time near-field terahertz imaging with atomic optical fluorescence", *Nature Photonics,* **11**, 40-43, 2017.

[8] D.A. Anderson, S.A. Miller, G. Raithel, J.A. Gordon, M.L. Butler, and C.L. Holloway, "Optical Measurements of Strong Microwave Fields with Rydberg Atoms in a Vapor Cell", *Physical Review Applied*, **5**, 034003, 2016.

[9] M.T. Simons, J.A. Gordon,C.L. Holloway, "Simultaneous use of Cs and Rb Rydberg atoms for dipole moment assessment and RF electric field measurements via electromagnetically induced transparency", *Journal of Applied Physics*, **120**, 123103, 2016.

[10] C.L. Holloway, M.T. Simons, J.A. Gordon, A. Dienstfrey, D.A. Anderson, and G. Raithel, "Electric field metrology for SI traceability: Systematic measurement uncertainties in electromagnetically induced transparency in atomic vapor", *J. of Applied Physics*, **121**, 233106-1-9, 2017.

[11] D. A. Steck, *Rubidium 85 D Line Data, available online at http://steck.us/alkalidata*, revision 2.1.6, 20 September 2013.

[12] C.L. Holloway, J.A. Gordon, A. Schwarzkopf, D.A. Anderson, S.A. Miller, N. Thaicharoen, and G. Raithel, "Sub-wavelength imaging and field mapping via electromagnetically induced transparency and Autler-Townes splitting in Rydberg atoms", *Applied Physics Letters*, **104**, 244102, 2014.

[13] H. Fan, S. Kumar, J. Sheng, J.P. Shaffer, C.L. Holloway and J.A. Gordon, "Effect of Vapor-Cell Geometry on Rydberg-Atom-Based Measurements of Radio-Frequency Electric Fields", *Physical Review Applied*, **4**, 044015, Nov., 2015.



Simons, Matthew; Kautz, Marcus; Gordon, Joshua; Holloway, Christopher.
"Uncertainties in Rydberg Atom-based RF E-field Measurements."
Paper presented at 2018 International Symposium on Electromagnetic Compatibility (EMC), Amsterdam, Netherlands. August 27, 2018 - August 30, 2018.

# High-resolution antenna near-field imaging and sub-THz measurements with a small atomic vapor-cell sensing element

David A. Anderson*†, Eric Paradis†§, Georg Raithel†‡, Rachel E. Sapiro†, and Christopher L. Holloway¶
Rydberg Technologies, Ann Arbor, MI USA†
University of Michigan, Ann Arbor, MI USA‡
Eastern Michigan University, Ypsilanti, MI USA§
National Institute for Standards and Technology, Boulder, CO USA¶
*dave@rydbergtechnologies.com

***Abstract*—Atomic sensing and measurement of millimeter-wave (mmW) and THz electric fields using quantum-optical EIT spectroscopy of Rydberg states in atomic vapors has garnered significant interest in recent years towards the development of atomic electric-field standards and sensor technologies. Here we describe recent work employing small atomic vapor cell sensing elements for near-field imaging of the radiation pattern of a $K_u$-band horn antenna at 13.49 GHz. We image fields at a spatial resolution of $\lambda/10$ and measure over a 72 to 240 V/m field range using off-resonance AC-Stark shifts of a Rydberg resonance. The same atomic sensing element is used to measure sub-THz electric fields at 255 GHz, an increase in mmW-frequency by more than one order of magnitude. The sub-THz field is measured over a continuous $\pm$100 MHz frequency band using a near-resonant mmW atomic transition.**

***Index Terms*—Atomic sensors, quantum sensing, Rydberg, atom, millimeter-wave, mmW, terahertz, THz, microwave, electric field, metrology, antenna, antenna characterization.**

## I. Introduction

Sensing and measurement of millimeter-wave (mmW) and THz electric fields with atoms provide advantages over traditional antenna and solid-state detector technologies, including small sensor sizes, absolute measurement capability (SI-based measurement), higher accuracy and precision, as well as recalibration-free operation, affording greater long-term measurement stability and reliability. Atomic sensors for electric fields are based on quantum-optical spectroscopy of atomic Rydberg states in vapors contained in spectroscopic cells [1]. The approach has been developed as a practical means to exploit the sensitivity of Rydberg atoms [2] to electric fields over a wide frequency range, from the tens of MHz into the sub-THz regime [3]–[7], and has garnered significant interest at NIST and National Metrology Institutes worldwide for the establishment of new atomic standards for electric fields [8]–[10], as well as in industry for the development of quantum electric-field sensing, measurement, and imaging technologies [11], [12]. In the ongoing pursuit of Rydberg-based electric-field sensors and instrumentation for applications, the development and implementation of small atomic vapor-cell sensing elements suitable for high-spatial-resolution detection of mmW and sub-THz electric fields is desired. In this report we present recent work employing a small rubidium (Rb) vapor cell to image the electric-field radiation pattern of a $K_u$-band horn antenna. We demonstrate imaging at a $\sim \lambda/10$ spatial resolution for 13.4884 GHz fields over a dynamic range from 72 to 240 V/m. The Rydberg-based electric-field measurements are obtained by optical detection of field-induced AC-Stark shifts of an atomic Rydberg resonance. Measured field profiles are in good agreement with calculated distributions. We also demonstrate the use of the vapor-cell sensing element for measurements of 255 GHz electric fields over a $\pm$100 MHz continuous frequency band using near-resonant Autler-Townes splittings of a Rydberg resonance. This is among the highest mmW frequencies measured to date using the Rydberg-atom-based approach; the measurement also demonstrates that a single sensing element can serve a frequency range covering $> 4$ octaves. The presented work serves to pave the way towards practical Rydberg-based field-sensing elements, detectors, and probes that are small and capable of frequency coverage to 1 THz.

## II. mmW detection with atomic vapor-cell sensing elements

In our experiments, the sensing element comprises a glass cell filled with a Rb vapor. The active sensing region of the cell has a 3-mm inner dimension; an elongated reservoir with a sample of Rb metal is located several centimeters away. Two counter-propagating lasers at wavelengths of 780 nm and 480 nm are focused and counter-propagated through the active region of the vapor cell for EIT spectroscopy on field-sensitive Rydberg states. The 780 nm laser is frequency stabilized to the Rb $5S_{1/2}$ to $5P_{3/2}$ transition, whose absorption through the atomic medium is measured, as the 480 nm laser frequency is scanned linearly across a range of $5P_{3/2}$ to Rydberg-state transitions. The selection of states and the energy ranges scanned are adapted to the field-strength and frequency ranges of the mmW fields to be measured. When the 480 nm laser frequency is tuned into resonance with a transition into a mmW-field-perturbed Rydberg state, the laser mixes the 5P

Holloway, Christopher; Anderson, Dave; Raithel, Georg.
"High-resolution antenna near-field imaging and sub-THz measurements with a small atomic vapor-cell sensing element."
Paper presented at 2018 11th Global Symposium on Millimeter Waves (GSMM), Boulder, CO, United States. May 22, 2018 - May 24, 2018.

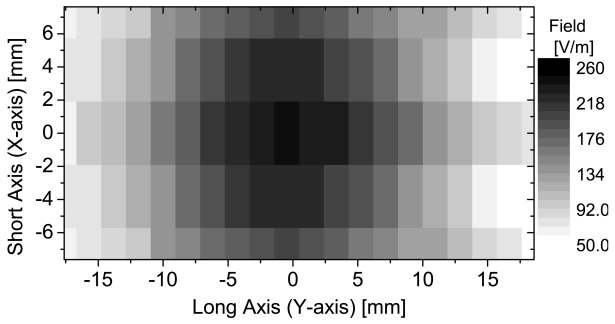


Fig. 1. Two-dimensional electric field distribution of a horn antenna measured with an atomic sensing element. The aperture size of the horn antenna is indicated by the white dashed line.

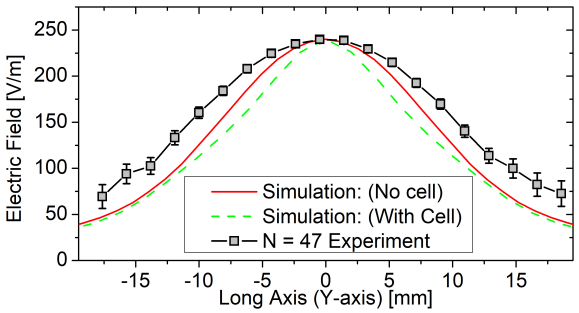


Fig. 2. One-dimensional electric field distribution along the long-axis of the horn at the short-axis zero for the measurement in Fig. 1 (gray), calculated distribution in free space (red), and calculated distribution with a dielectric glass cell (dashed green). The error bars in the measurement correspond to a 1 MHz experimental uncertainty of the atomic line shift.

and the Rydberg state. This leads to a destructive quantum interference of excitation pathways that, over a narrow frequency range at the center of the resonance, results in an increased transmission for the 780 nm light through the vapor cell. These transmission peaks serve to locate the energy levels of the mmW-field-perturbed Rydberg levels. The mmW-field-induced energy shifts of the Rydberg levels as well as the measured splitting patterns of the spectroscopic lines provide an excellent measure for the field strength of the mmW that causes the atomic perturbation.

## III. Near-field imaging of a horn antenna

We employ the sensing element to measure the near-field of a $K_u$-band 0.695 x 1 inch pyramidal horn antenna emitting 13.4884 GHz fields (near-field range = 58 mm). The horn is positioned at a distance z=7.5 mm from the sensing element and is translated in steps of $1.9 \pm 0.2$ mm across the long axis of the horn in the xy-plane.

Fig. 1 shows the two-dimensional spatial electric-field distribution. The image is composed of a field distribution measured over the top half of the plane and its mirror-image in the bottom half, symmetric across the short-axis zero. The electric field at each position of the horn is obtained from EIT detection of the mmW-induced AC-Stark shift of the $47S_{1/2}$ Rydberg state using the relation $E = (4\Delta/\alpha)^{0.5}$, where $\Delta$ is the measured peak shift of the atomic line, and $\alpha = 4.099 \times 10^{-3}$ MHz/(V/m)$^2$ is the Rb 47S AC polarizability at 13.5 GHz. This relation holds in fields low enough that the field does not induce transitions, and that higher-order, non-quadratic shifts of the Rydberg level are not significant. In Fig. 2 we plot the measured one-dimensional field profile across the long axis at the short-axis zero in Fig. 1 with calculated field distributions with and without a dielectric cell structure. We obtain overall good agreement between measured and calculated distributions. The slight increase in field measured at the wings of the distribution compared to the calculated distributions may be attributed to the imperfect modeling of detailed geometry and the material of the glass cell that holds the atomic vapor, and to the dielectric mount of the cell that is not accounted for in the present calculations. The detailed characterization of vapor-cell sensing elements on mmW fields for measurements with atomic sensors is a topic of on-going and future work.

## IV. Sub-THz electric-field measurements with millimeter vapor cells

A key advantage of atomic electric-field sensors is that a single small vapor-cell sensing element can be employed in measurements over a wide mmW frequency range. Here we perform measurements of electric fields at 255.2851 GHz using the same atomic vapor-cell sensing element. This is more than four octaves higher in frequency compared to the previous measurements. The measurements are performed in the far-field of a conical mmW horn emitting 255.2851 GHz sub-THz radiation field that is resonant with the $27S_{1/2}$ to $26P_{3/2}$ electric-dipole transition in Rb. The mmW frequency is varied around the atomic resonance for field measurements over a 200-MHz wide band.

Fig. 3 shows an experimental atomic spectral map where the 780nm laser transmission through the sensing element (gray-scale; dark = increased transmission) is plotted as a function of the relative 480 nm laser frequency (Y-axis) and the relative mmW frequency (X-axis). There, the laser frequency is relative to the mmW-field-free $27S_{1/2}$ Rydberg resonance, and the mmW frequency relative to the $27S_{1/2}$ to $26P_{3/2}$ transition frequency. The mmW power injected into the mmW transmission line is fixed at 0 dBm. The resonance condition is indicated by the arrow in the plot, at the center of the avoided crossing between two dressed atom-field states. As the sub-THz frequency is tuned away from the atomic resonance, the two Autler-Townes-split spectral lines, whose on-resonance splitting is directly proportional to the mmW electric field, separate further, with a splitting given by the effective Rabi frequency $\Delta f$. As the detuning of the sub-THz radiation is increased, the splitting of these off-resonant Autler-Townes lines is then given by $\Delta f^2 = (\Delta f_0)^2 + \delta^2$, where $\Delta f_0$ is the resonant Autler-Townes frequency splitting and $\delta$ is the

Holloway, Christopher; Anderson, Dave; Raithel, Georg.
"High-resolution antenna near-field imaging and sub-THz measurements with a small atomic vapor-cell sensing element."
Paper presented at 2018 11th Global Symposium on Millimeter Waves (GSMM), Boulder, CO, United States. May 22, 2018 - May 24, 2018.

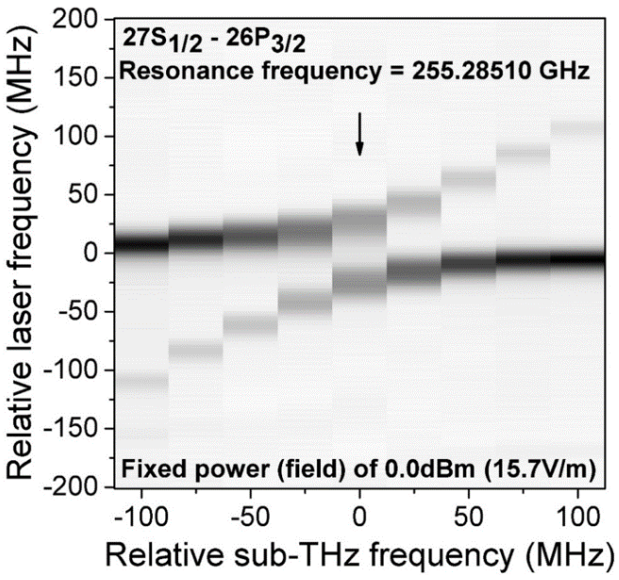


Fig. 3. Atom-based measurements of electric fields over a frequency range 255.185 GHz to 255.385 GHz.

detuning of the sub-THz field from the atomic resonance. In Fig. 3, the resonant splitting corresponds to a mmW field of 15.7 V/m, and $\delta$ is varied from -100 MHz to +100 MHz about the resonance frequency. The frequency range over which the measurement method is effective in measuring the field has a lower limit given by the range over which both Autler-Townes lines are visible, and an upper limit given by the range within which the dominant Autler-Townes component exhibits a detectable AC Stark shift. In the case of Fig. 3 the frequency range over which the measurement method is effective is at least 200 MHz.

## V. Conclusion

We report on near-field imaging of the radiation pattern of a horn antenna at 13.49 GHz using a small atomic vapor cell sensing element with a resolution of $\sim \lambda/10$ and covering a dynamic field range from 72 to 240 V/m using off-resonant AC-Stark shifts of a Rydberg resonance. The imaging results are in good agreement with calculations. The same atomic sensing element is used for sub-THz electric field measurements at 255 GHz, more than one order of magnitude higher in mmW-frequency. The sub-THz measurements are performed over a 200 MHz-wide frequency band centered on a resonant atomic transition.

## Acknowledgment

This work is supported by Rydberg Technologies, and by the Defense Advanced Research Projects Agency (DARPA) and the Army Contracting Command-Aberdeen Proving Ground (ACC-APG) under Contract No. W911NF-15-P-0032.

## References

[1] A. K. Mohapatra, T. R. Jackson, and C. S. Adams, "Coherent optical detection of highly excited rydberg states using electromagnetically induced transparency," *Phys. Rev. Lett.*, vol. 98, p. 113003, Mar 2007. [Online]. Available: http://link.aps.org/doi/10.1103/PhysRevLett.98.113003

[2] T.F.Gallagher, *Rydberg Atoms*, 1994.

[3] J. A. Sedlacek, A. Schwettmann, H. Kübler, R. Löw, T. Pfau, and J. P. Shaffer, "Microwave electrometry with rydberg atoms in a vapour cell using bright atomic resonances," *Nat. Phys.*, vol. 8, pp. 819–824, November 2012.

[4] C. Holloway, J. Gordon, S. Jefferts, A. Schwarzkopf, D. Anderson, S. Miller, N. Thaicharoen, and G. Raithel, "Broadband rydberg atom-based electric-field probe for si-traceable, self-calibrated measurements," *IEEE Transactions on Antennas and Propagation*, vol. 62, no. 12, pp. 6169–6182, Dec 2014.

[5] M. T. Simons, J. A. Gordon, C. L. Holloway, D. A. Anderson, S. A. Miller, and G. Raithel, "Using frequency detuning to improve the sensitivity of electric field measurements via electromagnetically induced transparency and autler-townes splitting in rydberg atoms," *Applied Physics Letters*, vol. 108, no. 17, p. 174101, 2016. [Online]. Available: https://doi.org/10.1063/1.4947231

[6] D. A. Anderson, S. A. Miller, G. Raithel, J. A. Gordon, M. L. Butler, and C. L. Holloway, "Optical measurements of strong microwave fields with rydberg atoms in a vapor cell," *Phys. Rev. Applied*, vol. 5, p. 034003, Mar 2016. [Online]. Available: http://link.aps.org/doi/10.1103/PhysRevApplied.5.034003

[7] S. A. Miller, D. A. Anderson, and G. Raithel, "Radio-frequency-modulated rydberg states in a vapor cell," *New Journal of Physics*, vol. 18, no. 5, p. 053017, 2016. [Online]. Available: http://stacks.iop.org/1367-2630/18/i=5/a=053017

[8] J. A. Gordon, C. L. Holloway, A. Schwarzkopf, D. A. Anderson, S. Miller, N. Thaicharoen, and G. Raithel, "Millimeter wave detection via autler-townes splitting in rubidium rydberg atomsa)," *Applied Physics Letters*, vol. 105, no. 2, pp. –, 2014. [Online]. Available: http://scitation.aip.org/content/aip/journal/apl/105/2/10.1063/1.4890094

[9] C. L. Holloway, J. A. Gordon, A. Schwarzkopf, D. A. Anderson, S. A. Miller, N. Thaicharoen, and G. Raithel, "Sub-wavelength imaging and field mapping via electromagnetically induced transparency and autler-townes splitting in rydberg atoms," *Applied Physics Letters*, vol. 104, no. 24, pp. –, 2014. [Online]. Available: http://scitation.aip.org/content/aip/journal/apl/104/24/10.1063/1.4883635

[10] C. L. Holloway, M. T. Simons, J. A. Gordon, P. F. Wilson, C. M. Cooke, D. A. Anderson, and G. Raithel, "Atom-based rf electric field metrology: From self-calibrated measurements to subwavelength and near-field imaging," *IEEE Transactions on Electromagnetic Compatibility*, vol. 59, no. 2, pp. 717–728, April 2017.

[11] D. A. Anderson and G. Raithel, "Continuous-frequency measurements of high-intensity microwave electric fields with atomic vapor cells," *Applied Physics Letters*, vol. 111, no. 5, p. 053504, 2017. [Online]. Available: http://dx.doi.org/10.1063/1.4996234

[12] (2015) Rydberg technologies. [Online]. Available: http://www.rydbergtechnologies.com

Holloway, Christopher; Anderson, Dave; Raithel, Georg.
"High-resolution antenna near-field imaging and sub-THz measurements with a small atomic vapor-cell sensing element."
Paper presented at 2018 11th Global Symposium on Millimeter Waves (GSMM), Boulder, CO, United States. May 22, 2018 - May 24, 2018.

IEEE MTT-S International Microwave Workshop Series on Advanced Materials and Processes for RF and THz Applications
(IMWS-AMP 2018), July 16-18, 2018, Ann Arbor, MI, USA

# Frequency- and electric field-dependent physical model of ferroelectric materials in the tens of GHz*

Aaron M. Hagerstrom*, Eric Marksz*†, Christian J. Long*, James C. Booth*, Ichiro Takeuchi†, Nathan D. Orloff*
*National Institute of Standards and Technology †University of Maryland

***Abstract*—Ferroelectric materials are attractive for tunable components because their permittivity can be controlled by an applied electric field. The permittivity of these materials also depends on frequency, and can have a strongly nonlinear electric field dependence. A quantitative understanding of these behaviors is relevant for integration of tunable materials into devices. In this paper, we provide a simple closed-form expression for this dependence, which to our knowledge has never appeared in the literature. This expression is based on thermodynamic principles, and we expect it to be both widely applicable and generalizable. We test this model with measurements of transmission lines lithographically patterned on a ferroelectric thin film, and find that the relaxation timescales become shorter at higher bias fields. We attribute this faster relaxation to the steepening of the free energy gradient when a bias field is applied.**

***Index Terms*—tunable microwave materials, tunable components, materials characterization, functional materials, device modeling**

## I. Introduction

Tunable dielectric materials are an attractive solution for frequency-agile microwave components because their permittivity can be tuned by an applied electric field. This field-dependent permittivity translates into a variable capacitance, which can be used to build voltage-tunable filters, phase shifters, and other components [1], [2]. In particular, reconfigurable phase shifters are a key enabling technology for phased array antennas, which will be employed in 5G [3] communications systems operating in the tens of GHz. To design tunable devices, we need to have a quantitative understanding of the tuning behavior of any materials involved. The alternative is costly iterations of trial and error design. Simple, closed-form models are convenient when available. An accurate and simple model of ferroelectric capacitors based on thermodynamic theory was provided by [4]. However, this model does not attempt to describe frequency dependence of the material, which is an important physical feature of nonlinear dielectrics. Ferroelectric materials often have relaxation processes that are active in the tens of GHz [5], [6].

In this paper, we present a thermodynamic model for the electric field and frequency dependence of ferroelectric materials based on very general physical considerations. We test this model by measuring coplanar waveguides (CPWs) lithographically patterned on a thin film of $Ba_{0.5}Sr_{0.5}TiO_3$ (BST). We find good agreement between our model and our measurements.



## II. Model

The tuning of ferroelectric materials with an electric field is often described in terms of a free energy $G$ with an anharmonic dependence on the polarization $P$ [4], [7]:

$$G = \frac{1}{2}\alpha P^2 + \frac{1}{4}\beta P^4 + ... \tag{1}$$

Here, $\alpha$ and $\beta$ are coefficients that describe the shape of the potential well. In equilibrium, the electric field is $E = \partial G/\partial P$.

A frequency-dependent model must describe how the material responds in time to an applied perturbation. In the Landau-Khalatnikov model, the material displays Debye-like relaxation with time constant $\tau$ [7]:

$$\tau\frac{dP}{dt} + P = \varepsilon_0\varepsilon_s\left[E(t) - \beta P^3\right], \tag{2}$$

where $\varepsilon_0$ is the permittivity of free space and $\varepsilon_s = \varepsilon_0/\alpha$.

Equation (2) does not accurately describe BST, because BST has a more complex time dependence. At microwave frequencies, BST shows dispersion over a wider range of frequencies. This dispersion can be described as a distribution of relaxation times, which are attributed to polar nano-regions (PNRs) [8]. According to [9], the distribution of relaxation times corresponds to a statistical distribution of sizes of PNRs. Acknowledging the non-Debye relaxation behavior of materials with PNRs, Glazounov and Tagantsev proposed a more general model which reduces to Equation (2) as a special case [7]:

$$P(t) = \varepsilon_0\varepsilon_s\int_{-\infty}^{\infty} dt'\; f(t-t')\left[E(t) - \beta P^3(t)\right]. \tag{3}$$

Equation (3) accommodates very general time-domain dynamics: $f(t-t')$ could potentially describe any linear, time-invariant behavior. These dynamics may also be expressed in the frequency domain via the Fourier transform $\hat{f}(\omega) = \int dt\; f(t)\exp(-j\omega t)$. For BST, the distribution of relaxation times has been phenomenologically parameterized by the Cole-Cole model, which we employ in this paper [5]:

$$\hat{f}(\omega) = \frac{1}{1 + (j\omega\tau)^a} \tag{4}$$

In Equation (4), $\tau$ and $a$ are empirical parameters. The special case $a = 1$ corresponds to Equation (2).

Marksz, Eric; Long, Christian; Booth, James; Takeicjo, Ichiro; Orloff, Nathan.
"Frequency- and electric field-dependent physical model of ferroelectric materials in the tens of GHz."
Paper presented at IEEE MTT-S International Microwave Workshop Series on Advanced Materials and Processes for RF and THz Applications, Ann Arbor, MI, United States. July 16, 2018 - July 18, 2018.

To derive a frequency- and electric field-dependent model, we Taylor-expand Equation (3) to first order about a large dc bias field. To do this, we write the electric field and polarization as $E(t) = E_{dc} + e\exp(j\omega t)$ and $P(t) = P_{dc} + p\exp(j\omega t)$. This linearization of Equation (3) yields:

$$P_{dc} = \varepsilon_0\varepsilon_s\left[E_{dc} - \beta P_{dc}^3\right], \tag{5}$$

$$p = \varepsilon_0\varepsilon_s\,\hat{f}(\omega)\left[e - 3\beta P_{dc}^2 p\right]. \tag{6}$$

The numerical value of $\beta$ can be hard to interpret intuitively. For this reason, we use the scaled parameter

$$E_{NL} = \sqrt{\frac{4\alpha^3}{3\beta}}. \tag{7}$$

The parameter $E_{NL}$ has units of electric field, and can be interpreted as the electric field that must be applied to tune the dc permittivity of the material by about 62% of its zero-bias value. In terms of this scaled parameter, Equation (5) can be solved in closed form [4]:

$$P_{dc} = (\varepsilon_s\varepsilon_0)E_{NL}T\left(\frac{E_{dc}}{E_{NL}}\right), \tag{8}$$

$$\text{where } T\left(\frac{E_{dc}}{E_{NL}}\right) = \sinh\left[\frac{1}{3}\sinh^{-1}\left(3\frac{E_{dc}}{E_{NL}}\right)\right]. \tag{9}$$

The function $T(\cdot)$ describes the tunability of the material. For small arguments, this function is approximately linear with a slope of 1, but it begins to saturate as $E_{dc} \sim E_{NL}$.

Equation (6) can be rearranged to describe the frequency- and electric field- dependent susceptibility, $\chi = p/\varepsilon_0 e$:

$$\chi(\omega, E_{dc}) = \varepsilon_\infty + \frac{\varepsilon_s\hat{f}(\omega)}{1 + 4T\left(\frac{E_{dc}-E_c}{E_{NL}}\right)^2\hat{f}(\omega)}. \tag{10}$$

For the remainder of this paper, we choose $\hat{f}(\omega)$ to be given by Equation (4) because this function fits our data well, but this is not essential to the theory. We have also added a parameter $E_c$, the coercive electric field, to reflect that our sample has a small amount of hysteresis at room temperature, and $\varepsilon_\infty$, to model non-tunable contributions to the polarization. Thus, the parameters in our model are $a$, $\tau$, $\varepsilon_s$, $\varepsilon_\infty$, $E_{NL}$, and $E_c$.

## III. Experiment

To test our model, we deposited a 1 μm-thick $Ba_{0.5}Sr_{0.5}TiO_3$ film by pulsed laser deposition on a $LaAlO_3$ substrate. In order to measure the permittivity, we lithographically patterned gold coplanar waveguides on the sample. The metalization thickness was 500 nm, and the ground planes had a width of 200 μm, the center conductor had a width of 20 μm, and the gap widths were 5 μm.

To characterize the permittivity, we performed on-chip scattering parameter measurements. We measured 6 CPWs whose lengths varied from 0.420 mm to 7.000 mm. Our network analyzer was calibrated to the probe tips by a multiline Thru-Reflect-Line calibration on a reference substrate with a known capacitance per unit length [10]. The dc bias voltage was applied between the center conductor and the ground planes by use of a bias tee. Electric field values are estimated from the bias voltage divided by the gap width.

We then determined the permittivity from the distributed circuit parameters of the CPWs: the inductance $L$, resistance $R$, capacitance $C$ and conductance $G$. We assume that the electromagnetic fields of the waveguide mode are confined to the transverse direction (TEM propagation). This assumption is common in the literature [5], but we hope to evaluate its accuracy in the future. If the mode is TEM, $R$ and $L$ do not depend on the permittivity of the sample, but $C$ and $G$ are proportional to the real and imaginary permittivity, respectively [11]. Thus $R$ and $L$ can be estimated through quasi-static finite element simulations. From the scattering parameters, we can estimate the propagation constant, $\gamma$, given by $\gamma = \sqrt{(R + j\omega L)(G + j\omega C)}$ [10]. Thus we can estimate $C$ and $G$ for our transmission lines, which can be used to determine the permittivity. The permittivity is related to $C$ and $G$ in a straightforward way:

$$C + \frac{G}{j\omega} = c_0 + c_1\varepsilon(\omega). \tag{11}$$

Equation (11), along with the values of $c_0$ and $c_1$ was derived analytically [12], but we determined the constants $c_0$ and $c_1$ from quasi-static finite element simulations.

## IV. Results

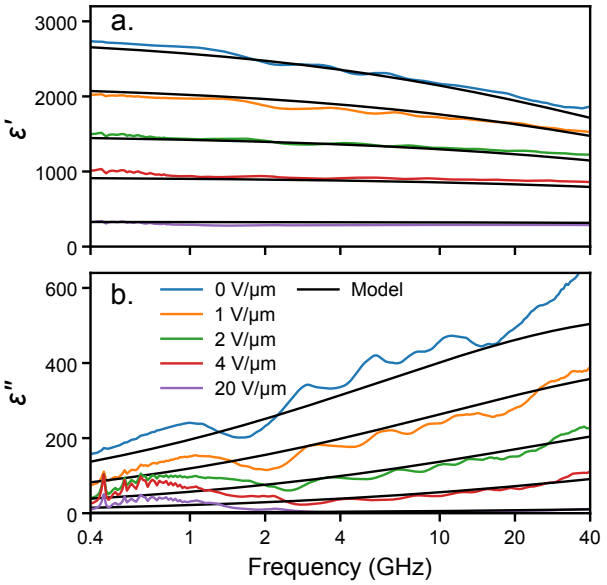


Fig. 1: Frequency dependence of the a) real and b) imaginary parts of the complex permittivity at different bias electric fields. We have used the notation $\varepsilon = 1 + \chi = \varepsilon' - j\varepsilon''$.

Fig. 1 shows the frequency dependence of the complex permittivity for several values of the bias electric field, and a fit of he model to the data. The fit parameters were: $E_{NL} = 3.04$ V/μm, $E_c = -0.06$ V/μm, $a = 0.46$, $\tau = 1.9$

Marksz, Eric; Long, Christian; Booth, James; Takeicjo, Ichiro; Orloff, Nathan.
"Frequency- and electric field-dependent physical model of ferroelectric materials in the tens of GHz."
Paper presented at IEEE MTT-S International Microwave Workshop Series on Advanced Materials and Processes for RF and THz Applications,
Ann Arbor, MI, United States. July 16, 2018 - July 18, 2018.

ps, $\varepsilon_s = 2760$, and $\varepsilon_\infty = 70$. Anticipating that our sample may exhibit hysteresis, we swept the field from 0 up to 20 V/μm, down to -20 V/μm, and up again. Here, we plot the 2nd increasing sweep. We note small variations in the frequency dependence, which we attribute to imperfections in our calibration. The loss, $\varepsilon''$, increases with frequency, and both the real and imaginary parts of the permittivity decrease with applied electric field.

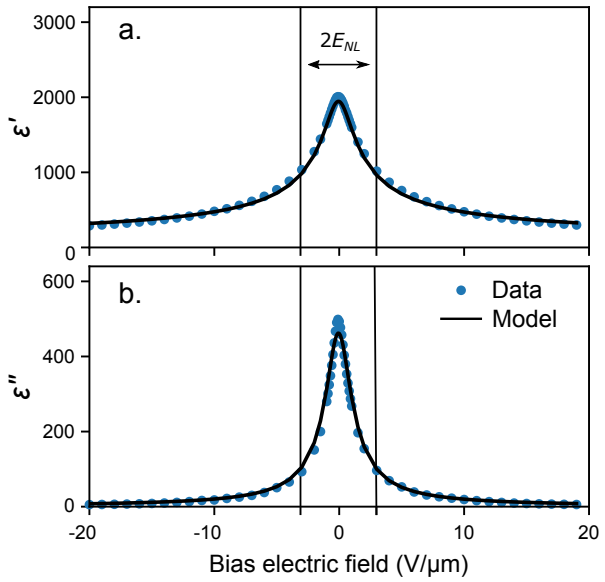


Fig. 2: Electric field dependence of the a) real part of the permittivity and b) imaginary part of the permittivity at 20 GHz. An interval of width $2E_{NL}$ centered on the peak value is indicated, showing that $E_{NL}$ is a characteristic scale for the tunability. Note that $\varepsilon''$ tunes more strongly (82 % at $E_{NL}$) than $\varepsilon'$ real part (49 %).

The imaginary part of the permittivity ($\varepsilon''$) tunes more strongly with bias electric field than $\varepsilon'$, as seen in Figure 2, which shows the tuning of the film with applied voltage at a frequency of 20 GHz. In our model, the function $\hat{f}(\omega)$ describes the distribution of PNR sizes, and does not depend on bias field. The change in loss is a direct consequence of the $P^3$ term in Equation (3). So, in our model, the loss decreases with DC bias because the gradient of the free energy with respect to $P$ is stronger when the sample is biased, so $P$ relaxes faster.

## V. Conclusion

We have introduced a physical model of the real and imaginary parts of the permittivity as a function of electric field and voltage. Because generalizations of Equations (1) are widely used in the ferroelectic literature, and Equation (3) is a straightforward generalization, we expect this model to be widely applicable. At the very least, the model works for BST in the paraelectric phase at microwave frequencies. We anticipate no difficulties with this model up to the THz regime, where phonon dispersion becomes important. The biggest approximation we have made is that the electric field in the CPW gaps is constant, which is not the case. Still, the model fits the experimental data well (root-mean-square error 140 permittivity units). In addition to the variations in the data that we attribute to imperfections in the calibration, there is some voltage-dependent deviation of the model from the data that we attribute electric field inhomogeneity.

In addition to fitting a complicated data set with a few parameters, our model offers some physical insight. In particular, the imaginary part of the permittivity tunes more strongly than the real part. We interpret this in terms of the gradient of the free energy with respect to $P$. Finally, we note that Equation (3) also predicts higher order nonlinear dynamical behavior, including frequency dependence for intermodulation products and harmonics. This characterization is underway [13].

## References

[1] A. K. Tagantsev, V. O. Sherman, K. F. Astafiev, J. Venkatesh, and N. Setter, "Ferroelectric materials for microwave tunable applications," vol. 11, no. 1, 2003.

[2] E. G. Erker, A. S. Nagra, Y. Liu, P. Periaswamy, T. R. Taylor, J. Speck, and R. A. York, "Monolithic ka-band phase shifter using voltage tunable BaSrTiO3 parallel plate capacitors," *IEEE Microwave and Guided Wave Letters*, vol. 10, no. 1, pp. 10–12, 2000.

[3] M. Sazegar, Y. Zheng, C. Kohler, H. Maune, M. Nikfalazar, J. R. Binder, and R. Jakoby, "Beam steering transmitarray using tunable frequency selective surface with integrated ferroelectric varactors," *IEEE Transactions on Antennas and Propagation*, vol. 60, no. 12, pp. 5690–5699, 2012.

[4] D. R. Chase, L.-Y. Chen, and R. A. York, "Modeling the capacitive nonlinearity in thin-film bst varactors," *IEEE transactions on microwave theory and techniques*, vol. 53, no. 10, pp. 3215–3220, 2005.

[5] J. C. Booth, I. Takeuchi, and K.-S. Chang, "Microwave-frequency loss and dispersion in ferroelectric $Ba_{0.3}Sr_{0.7}TiO_3$ thin films," *Applied Physics Letters*, vol. 87, no. 8, p. 082908, 2005.

[6] C.-H. Lee, N. D. Orloff, T. Birol, Y. Zhu, V. Goian, E. Rocas, R. Haislmaier, E. Vlahos, J. A. Mundy, L. F. Kourkoutis, Y. Nie, M. D. Biegalski, J. Zhang, M. Bernhagen, N. A. Benedek, Y. Kim, J. D. Brock, R. Uecker, X. X. Xi, V. Gopalan, D. Nuzhnyy, S. Kamba, D. A. Muller, I. Takeuchi, J. C. Booth, C. J. Fennie, and D. G. Schlom, "Exploiting dimensionality and defect mitigation to create tunable microwave dielectrics," *Nature; London*, vol. 502, no. 7472, pp. 532–6.

[7] A. E. Glazounov and A. K. Tagantsev, "Phenomenological model of dynamic nonlinear response of relaxor ferroelectrics," *Physical Review Letters*, vol. 85, no. 10, pp. 2192–2195, 2000.

[8] T. Teranishi, T. Hoshina, H. Takeda, and T. Tsurumi, "Polarization behavior in diffuse phase transition of $Ba_xSr_{1-x}TiO_3$ ceramics," *Journal of Applied Physics*, vol. 105, no. 5, p. 054111, 2009.

[9] Z. Lu and G. Calvarin, "Frequency dependence of the complex dielectric permittivity of ferroelectric relaxors," *Physical Review B*, vol. 51, no. 5, p. 2694, 1995.

[10] R. B. Marks, "A multiline method of network analyzer calibration," *IEEE Transactions on Microwave Theory and Techniques*, vol. 39, no. 7, pp. 1205–1215, 1991.

[11] R. B. Marks and D. F. Williams, "A general waveguide circuit theory," vol. 97, no. 5, pp. 533–562, 1992.

[12] E. Carlsson and S. Gevorgian, "Conformal mapping of the field and charge distributions in multilayered substrate CPWs," vol. 47, no. 8, pp. 1544–1552, 1999.

[13] A. M. Hagerstrom, E. Marksz, C. J. Long, J. C. Booth, and N. D. Orloff, "Characterization of transmission lines with nonlinear dielectric materials," in *90th ARFTG Microwave Measurement Symposium*. IEEE, 2017, pp. 1–6.

Marksz, Eric; Long, Christian; Booth, James; Takeicjo, Ichiro; Orloff, Nathan.
"Frequency- and electric field-dependent physical model of ferroelectric materials in the tens of GHz."
Paper presented at IEEE MTT-S International Microwave Workshop Series on Advanced Materials and Processes for RF and THz Applications, Ann Arbor, MI, United States. July 16, 2018 - July 18, 2018.

# Propagation of Compact-Modeling Measurement Uncertainty to 220 GHz Power-Amplifier Designs

Jerome Cheron[#1], Dylan F. Williams[#], Konstanty Łukasik[*%], Richard A. Chamberlin[#], Benjamin F. Jamroz[#], Erich N. Grossman[#], Wojciech Wiatr[%], Dominique Schreurs[*]

[#]*National Institute of Standards and Technology, Boulder, CO 80305, USA*
[1]jerome.cheron@nist.gov
[*]*ESAT-TELEMIC, KU Leuven, B-3000 Leuven, Belgium*
[%]*Institute of Electronic Systems, Warsaw University of Technology, 00-661 Warsaw, Poland*

***Abstract* — We study the impact of measurement uncertainties in a heterojunction bipolar transistor (HBT) model and their consequences on the electrical performance under large signal conditions at 9 GHz. Then we use the model with uncertainties to verify the ability of our model to accurately predict the electrical performance of power amplifier designs at 220 GHz. We compare the measured performance of the power amplifiers with simulations and estimated range of performance.**

**Index Terms — Semiconductor device modeling, Heterojunction bipolar transistors, Measurement uncertainty, Millimeter wave power amplifiers.**

## I. Introduction

Measurement uncertainties are not usually considered in the verification procedure of compact transistor models. This leaves open the possibility that observed differences between the actual and predicted behaviors of the transistor in the verification process are due to measurement errors, and not to the inability of the model to accurately predict transistor behavior.

The propagation of measurement errors through the model extraction process was investigated in [1-4] in several technologies. However, the impact of the propagation of measurement uncertainties through an entire circuit simulation has never been examined at millimeter-wave frequencies. Here, we investigate the propagation of measurement uncertainty through 220 GHz power-amplifier simulations and we compare with the measured performance.

## II. Model Extraction with Measurement Uncertainty

We extracted a model of a heterojunction bipolar transistor (HBT) with a single 6 $\mu$m emitter fabricated at Teledyne Scientific with a state-of-the-art 250-nm process [5]. A full description of the extraction process and a model verification under 1 GHz large signal operating conditions was presented by Williams *et al.* in [4]. We performed I-V curve and scattering (S-) parameter measurements up to 110 GHz under a wide range of bias points to extract this model. On-wafer thru–reflect–line (TRL) standards were designed and used for the calibration of our S-parameter measurements, which Williams *et al.* argued improve the accuracy of HBT and CMOS transistor measurements in [6].

We used the ICCAP[1] Keysight software to extract the HBT model parameters based on the model architecture developed in [7-8]. We first extracted an HBT model that did not consider measurement uncertainty. We will refer to this model as the "nominal" model. Then, we used the NIST Microwave Uncertainty Framework [9] to add uncertainties to our measurements and propagate them through the ICCAP model extraction procedure. We considered 415 error mechanisms in our calibration process. Most of those error mechanisms were related to the geometry of the lines and the characteristic of the substrate and the conductor. The contact probe placement error and the VNA drift were also considered by performing two calibrations. Then, we performed a 250-iteration Monte-Carlo analysis to estimate the impact of these error mechanisms during the calibration process. Each Monte Carlo iteration led to the extraction of one HBT model. Consequently, we extracted 250 HBT models through ICCAP, each of them having a unique assignment of measurement uncertainties.

Finally, we created a single model in the ADS[1] Keysight software, which integrated the nominal HBT model and the 250 models with uncertainties. The user can choose to run the nominal HBT model or all the models at the same time.

## III. Model Verification

The nominal model was verified in [4] using 1 GHz large-signal measurements under 50 ohms conditions. Here, we verified our HBT model with large-signal, multi-harmonic, load-pull measurements at 9 GHz. We used a conventional first-tier 2.4-mm short–open–load–thru (SOLT) calibration to perform the power and phase calibrations needed to fix the wave amplitudes and phases of the large-signal measurements. Then, we transferred these calibrations to the on-wafer reference plane by performing a second-tier TRL calibration.

We optimized the load at the fundamental and second harmonic frequency to obtain optimal electrical performance in terms of output power, gain and power-added efficiency

Work partially funded by U.S. government, not protected by U.S. copyright.

[1]We identify commercial products only to accurately describe the experiments and analysis we performed. NIST does not endorse commercial products. Other products may work as well or better.



Cheron, Jerome; Williams, Dylan; Lukasik, Konstanty; Chamberlin, Richard; Jamroz, Benjamin; Grossman, Erich; Wiatr, Wojciech; Schreurs, Dominique.
"Propagation of Compact-Modeling Measurement Uncertainty to 220 GHz Power-Amplifier Designs."
Paper presented at 2018 Asia-Pacific Microwave Conference (APMC), Kyoto, Japan. November 6, 2018 - November 9, 2018.

(PAE) when the transistor was saturated. The quiescent bias point was set to obtain a collector voltage $V_c$ = 1.5 V and collector current $I_c$ = 6 mA. Four harmonics were measured.

Fig. 1 illustrates a comparison between the 250 simulated HBT models with uncertainties and the measurements under the optimized load conditions ($ZL\_f_0$=0.64/5º and $ZL\_2f_0$=0.55/-175º). This simulation provided information regarding the expected range of performance. For example, we observed a very small spread in the range of the output power and the collector voltage waveform. However, under these specific conditions of DC bias points, loads and frequency, our HBT model with uncertainty showed a large expected range of PAE and current in the collector waveform in saturation.

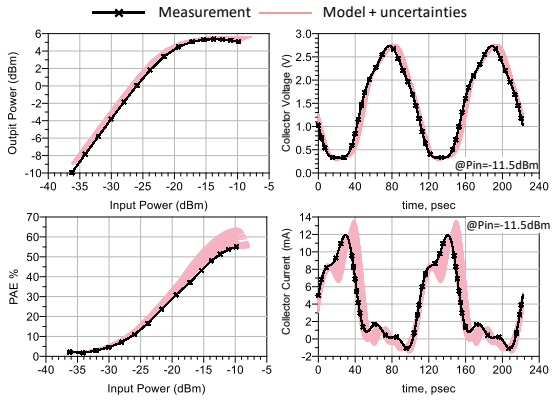


Fig. 1. Simulated HBT model with uncertainties versus load-pull measurements of a 6 µm HBT transistor. The load pull at the 9 GHz, fundamental and second harmonic loads were optimized.

Plotting the 95% confidence interval for the electrical performance of the transistor offers a convenient approach to investigate uncertainty in the model.

Fig. 2 illustrates the standard uncertainty related to the output power, PAE and the collector current and voltage waveforms at saturation. The standard uncertainty for the output power remains around 0.15 dBm in a linear operation, then drops when the transistor enters compression and increases up to 0.4 dBm at saturation. A standard uncertainty of 8% in PAE was simulated at saturation. We found significant variations in the DC collector current for the 250 Monte-Carlo models in saturation. This was largely responsible for the significant variation observed in the simulated PAE. We also observed that the simulated collector voltage and current waveforms at saturation presented a significant standard uncertainty at a time corresponding to the half period of the signal. This was due to uncertainties in the Kirk-effect model, and the contribution of the higher-order harmonics was mainly responsible for the uncertainties observed in the fall time of the collector current waveform. We also verified our model under different load conditions at 9 GHz and 16 GHz, and under small-signal conditions up to 110 GHz.

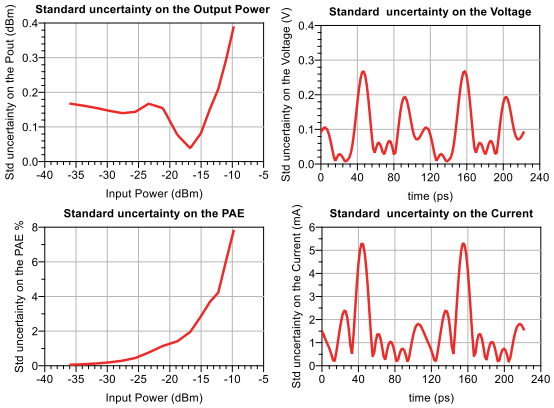


Fig. 2. 95% confidence interval for the output power (top left), collector voltage waveform at saturation (top right), PAE (bottom left) and collector current waveform at saturation (bottom right), resulting from a 9 GHz load-pull simulation of the HBT model with uncertainties included.

## IV. Propagation of Uncertainty to Power-Amplifier Design at 220 GHz

We performed circuit simulations of two 220 GHz power amplifiers with our HBT model. The circuit consisted of a one-stage power amplifier, made up of 8 HBT transistors in parallel, and a four-stage power amplifier, made up of 40 HBT transistors. Fig. 3 shows the two 220 GHz MMIC power amplifiers.

Cheron, *et al.* originally simulated and designed these two common-base power amplifiers using the model provided by the foundry and showed measured performance in [10]. All the passive circuits were simulated with ADS/Momentum[1] Keysight software.

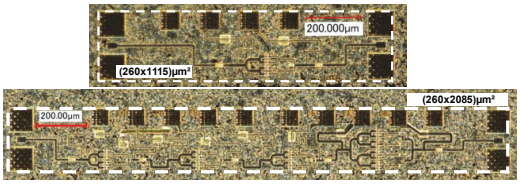


Fig. 3. Photograph of the 1-stage MMIC power amplifier (top) and the 4-stage MMIC power amplifier (bottom).

We compared the output power of the one-stage power amplifier, simulated using a model with uncertainties and using the measured data from [10]. In Fig. 4 we first observed a large expected range of output power from the model with uncertainties. We simulated up to 4.1 dBm of standard uncertainty in the output power at 208.5 GHz under linear operation, and 2.5 dBm at 222 GHz in saturation. In both



Cheron, Jerome; Williams, Dylan; Lukasik, Konstanty; Chamberlin, Richard; Jamroz, Benjamin; Grossman, Erich; Wiatr, Wojciech; Schreurs, Dominique.
"Propagation of Compact-Modeling Measurement Uncertainty to 220 GHz Power-Amplifier Designs."
Paper presented at 2018 Asia-Pacific Microwave Conference (APMC), Kyoto, Japan. November 6, 2018 - November 9, 2018.

cases, our simulated 95% confidence intervals overlapped the measurements. We observed that the simulation results from the nominal model and the average of the Monte-Carlo simulations better agreed with the measurements at saturation.

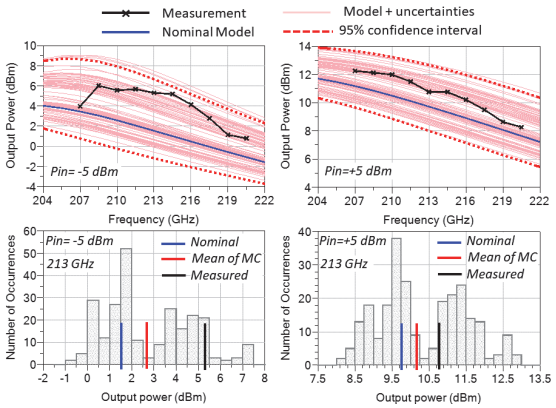


Fig. 4. 1-Stage PA: Simulations for a nominal model and a model with uncertainties versus measurements of the output power under linear operation (top left) and at saturation (top right). Histograms of Monte-Carlo simulations of the output power at 213 GHz under linear operation (bottom left) and in saturation (bottom right).

We compared the measured output power and power gain of the four-stage power amplifier with the simulated performance, using the nominal HBT model and the model with uncertainties, in Fig. 5. The two first stages of this power amplifier operate in a linear state when the last stage was saturated. The behavior of the simulated performance was similar to our observations of the one-stage power amplifier: (1) the simulated performance using the nominal HBT model is lower than the measured data; and, (2) we observed a large spread in the output power and power gain when we applied our model with uncertainties.

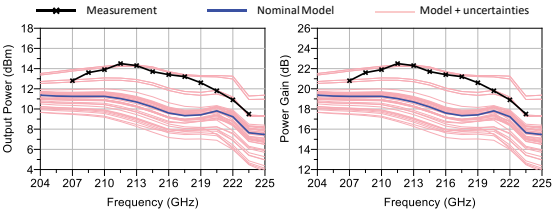


Fig. 5. 4-stage PA: Simulated performance using a nominal model and a model with uncertainties versus measurements.

We investigated the model parameters of the 250 HBT models we extracted. We determined that the models give a model parameter *TFC0* significantly higher than the nominal and provided a higher output power in this circuit simulation. The parameter *TFC0* is related to the definition of the low current transit time in the collector. The distribution of the *TFC0* model parameter illustrates that the ICCAP extraction procedure, using our set of measurements, failed to extract properly the model parameter *TFC0*, which is a critical parameter when the model is used at millimeter-wave frequencies.

## V. Conclusion

For the first time, we used an HBT model with uncertainties in power-amplifier circuit designs at 220 GHz to predict the circuit's expected range of performance. We illustrated how useful the propagation of correlated measurement uncertainties during the model extraction process and design is in providing estimates of the expected range of electrical performance of complex circuit designs at millimeter-wave frequencies.

## References


[1] F. Lenk and M. Rudolph, "Extraction of GaAs-HBT equivalaent circuit considering the impact of measurement errors," Innov. Microw. Light, Res. Rep. Ferdinand-Braun-Institut fur Hochstrfrequenztechnik, vol. 3, pp. 95–103, 2015.

[2] J. M. Miranda, C. Fager, H. Zirath, P. Sakalas, S. Munoz, and J. L. Sebastian, "Influence of the calibration kit on the estimation of parasitic effects in HEMT devices at microwave frequencies," IEEE Trans. Instrum. Meas., vol. 51, no. 4, pp. 650–655, Aug. 2002.

[3] G. Avolio, A. Raffo, J. Jargon, P. D. Hale, D. M. M.-P. Schreurs, and D. F. Williams, "Evaluation of uncertainty in temporal waveforms of microwave transistors," IEEE Trans. Microw. Theory Techn., vol. 63, no. 7, pp. 2353–2363, Jul. 2015.

[4] D. F. Williams, R. A. Chamberlin, W. Zhao, J. Cheron and M. E. Urteaga, "Transistor Model Verification Including Measurement Uncertainty," in IEEE Transactions on Microwave Theory and Techniques, vol. 64, no. 11, pp. 3927-3933, Nov. 2016.

[5] Z. Griffith, M. Urteaga, P. Rowell, R. Pierson and M. Field, "Multi-finger 250nm InP HBTs for 220GHz mm-wave power," Indium Phosphide and Related Materials (IPRM), 2012 International Conference on, Santa Barbara, CA, 2012, pp. 204-207.

[6] D. F. Williams et al., "Calibration-kit design for millimeter-wave silicon integrated circuits," in IEEE Transactions on Microwave Theory and Techniques, vol. 61, no. 7, pp. 2685-2694, July 2013.

[7] L.H. Camnitz, S. Kofol, T.S. Low, and S. R. Bahl, "An Accurate, Large Signal, High Frequency Model for GaAs HBTs," GaAs IC Symposium Technical Digest, pp. 303-306, 1996.

[8] M. Iwamoto et al., "Avanzo, "Large-signal HBT model with improved collector transit time formulation for GaAs and InP technologies," in IEEE MTT-S Int. Microw. Symp. Dig., vol. 2. Jun. 2003, pp. 635–638.

[9] D. F. Williams, B. F. Jamroz and A. Lewandowski. (2017). NIST Microwave Uncertainty Framework. Nat. Inst. of Standards and Technol. [Online]. Available: http://www.nist.gov/ctl/rf-technology/related-software.cfm.

[10] J. Cheron and E. Grossman, "High gain 220GHz power amplifier MMICs with minimal footprint," 2016 IEEE MTT-S International Microwave Symposium (IMS), San Francisco, CA, 2016, pp. 1-3.





Cheron, Jerome; Williams, Dylan; Lukasik, Konstanty; Chamberlin, Richard; Jamroz, Benjamin; Grossman, Erich; Wiatr, Wojciech; Schreurs, Dominique.
"Propagation of Compact-Modeling Measurement Uncertainty to 220 GHz Power-Amplifier Designs."
Paper presented at 2018 Asia-Pacific Microwave Conference (APMC), Kyoto, Japan. November 6, 2018 - November 9, 2018.

# 3.5 GHz Federal Incumbent Protection Algorithms

Michael R. Souryal and Thao T. Nguyen
Communications Technology Laboratory
National Institute of Standards and Technology
Gaithersburg, Maryland, U.S.
{souryal, thao.t.nguyen}@nist.gov

Nickolas J. LaSorte
Office of Spectrum Management
National Telecommunications and Information Administration
Washington, D.C.
nlasorte@ntia.doc.gov

***Abstract*—The current standardized algorithm for U.S. federal incumbent protection in the 3.5 GHz band is sub-optimum in that it moves more commercial transmissions out of the protected channel than necessary, in most cases. This paper proposes a more efficient algorithm that packs transmissions in the allowed interference budget jointly across incumbent receiver azimuths rather than independently, resulting in 18 % to 25 % fewer commercial transmissions affected.**

## I. Introduction

Regulatory rules for the Citizens Broadband Radio Service (CBRS) in the U.S. [1] permit commercial broadband users to operate in the radio frequency (RF) spectrum from 3550 MHz to 3700 MHz (3.5 GHz band) provided they do not compromise the operations of federal incumbents in and adjacent to this band. Industry standards for CBRS systems specify the mechanism for protecting federal incumbents from harmful interference [2]. This mechanism requires that Spectrum Access Systems (SASs)—centralized frequency coordinators that authorize access to the band by CBRS devices (CBSDs)—coordinate their authorizations using a common, standardized algorithm. Using agreed upon RF propagation and aggregate interference models, the algorithm identifies which authorized transmissions can continue in a protected channel and which must be suspended or possibly relocated to another channel. The list of transmissions that must be suspended or relocated to protect a given channel occupied by the incumbent is referred to as the "move list" for that channel.

This paper is a study of alternative move-list algorithms for federal incumbent protection. We show that in most cases the current standardized algorithm is sub-optimum in that it suspends more transmissions than necessary to meet the protection requirements. We propose an alternative move-list algorithm that achieves greater efficiency than the standard algorithm at the expense of additional computational complexity. The performance of each algorithm is evaluated with simulated CBSD deployments in the vicinity of federal protection areas.

Section II describes the standard and proposed move-list algorithms. Section III compares the results of each algorithm for three different protection areas. Section IV summarizes the results and draws conclusions.

## II. Move-List Algorithms

Given a set of transmissions that overlap in frequency with a protected channel, a move-list algorithm identifies which transmissions must be suspended (and possibly relocated to a different channel) to avoid excessive interference in a protected federal incumbent area. In the parlance of the CBRS specifications, an authorization to transmit is called a "grant." Hence, a move list is a list of grants that must be suspended when a federal incumbent protection area becomes active. Reasons for activation of a protection area on a given channel include detection of a federal incumbent signal within the protection area on that channel.

To obtain the move list, the algorithm computes the path loss from each transmitter to a point in the protected area and, using a stochastic model for the loss on each link, computes the distribution of the aggregate interference at that point. The algorithm then chooses a subset of the grants that must be suspended (relocated) such that the 95th percentile of the aggregate interference is below a threshold at any point in the protected area. Because the protection requirement is based on the 95th percentile of the aggregate interference, it is necessary that all SASs managing CBSDs in the vicinity of a protected area exchange grant information and execute the same move-list algorithm on the total grant population, hence the need for standardization of the move-list algorithm.

This section describes three move-list algorithms considered in the analysis below. The "standard" algorithm is that which is currently in force in CBRS industry standards; the "joint-azimuth" algorithm generates a smaller (i.e., more efficient) move list for a given deployment and protection threshold at the expense of additional computational complexity; and the third algorithm achieves much of the gain of the joint-azimuth algorithm but with the complexity of the standard algorithm.

### A. Standard Algorithm

For a given channel, point in the protection area, and protection threshold, the standard move-list algorithm [2] first sorts the grants by their median interference contribution to the protection point. It then identifies the minimal portion of the sorted list, starting with the strongest interferer, that must be removed from the channel so that the 95th percentile of the aggregate interference of the remaining grants does not exceed the protection threshold. The grants that must be removed to meet the protection threshold are placed on the move list.

Because the incumbent receiver antenna is directive in the azimuthal plane and its direction is variable, the algorithm must take into account every possible azimuth direction of

Souryal, Michael; Nguyen, Thao; LaSorte, Nickolas.
"3.5 GHz Federal Incumbent Protection Algorithms."
Paper presented at IEEE International Symposium on Dynamic Spectrum Access Networks (DySPAN), Seoul, Republic of Korea. October 22, 2018 - October 25, 2018.

the incumbent. For each possible direction, it must apply the azimuthal gains of the transmit and receive antennas accordingly, depending on the bearing of each transmitter relative to the protection point. The standard move-list algorithm accounts for the range of possible azimuths of the incumbent by determining the cutoff for every possible receiver azimuth separately, resulting in a component move list for each azimuth, and taking the union of those component move lists. This process is repeated for every protection point in the protection area, and the move list for the protection area is the union of the move lists of the points.

Pseudocode for the standard move-list algorithm is given in Algorithm 1. Line 5 finds the largest cutoff to the sorted list such that the 95th percentile of the aggregate interference does not exceed the protection threshold. The search for this cutoff can be performed with a binary search.

**Algorithm 1:** Standard move-list algorithm

**Input:** Protection channel $c$, protection threshold $t$, set of protection points $\mathcal{P}$, set of grants $\mathcal{G}$
**Output:** Move list for channel $c$, $\mathcal{M}_c \subseteq \mathcal{G}$

*// loop through every protection point*
1 **foreach** *point $p$ in set $\mathcal{P}$* **do**
  *// find the grants in the "neighborhood" of protection point $p$ and channel $c$*
2  $\mathcal{G}_{c,p} \leftarrow$ `Neighborhood` $(\mathcal{G}, c, p)$ ; // $\mathcal{G}_{c,p} \subseteq \mathcal{G}$
  *// sort grants by their median interference contribution, $P_i(c) + G_i(p) - L_i(p)$, smallest to largest, where $P_i(c)$ is the conducted power of the $i$th grant in channel $c$ in dB relative to 1 mW (dBm), $G_i(p)$ is the transmit antenna gain in the direction of point $p$ in dB relative to isotropic (dBi), and $L_i(p)$ is the median path loss from the transmitter to point $p$ (dB)*
3  $\mathbf{S} \leftarrow$ `Sort` $(\mathcal{G}_{c,p})$ ; // $\mathbf{S} = [G_1, G_2, \ldots, G_N]$
  *// loop through every receiver azimuth*
4  **for** $a \leftarrow \mathrm{minAzimuth}$ **to** $\mathrm{maxAzimuth}$ **do**
5  $n_{\max} \leftarrow$ largest $n$ s.t. `95thPrcntl` $(\{G_1, \ldots, G_n\}, a) \leq t$;
6  $\mathcal{M}_{c,p,a} = \{G_{n_{\max}+1}, \ldots, G_N\}$;
7  $\mathcal{M}_{c,p} = \bigcup_a \mathcal{M}_{c,p,a}$;
8 $\mathcal{M}_c = \bigcup_p \mathcal{M}_{c,p}$;

It is important to note that the median interference calculation used for sorting the grants (Line 3 in Algorithm 1) does not include the receive antenna gain. Hence, it is possible for the component move list of a given azimuth to include a grant that is higher on the sorted list in terms of median interference even though it is outside the main beam of the receive antenna, leading to sub-optimality of the standard algorithm. Advantages of the standard algorithm, on the other hand, are that the sort need only be done once per protection point and the calculation of the per-azimuth component move lists (the for-loop at Line 4) can be parallelized.

### B. Joint-Azimuth Algorithm

The joint-azimuth move-list algorithm departs from the standard algorithm in a key respect. Instead of treating each receiver azimuth independently of the others, it finds the receiver azimuth for which the aggregate interference is largest, that is, the worst-case azimuth. Then, starting with the highest contributor in terms of median interference contribution, it adds grants to the move list until the aggregate interference at that azimuth is no longer the highest; that is, until another azimuth is the worst case. It repeats this process until the aggregate interference at every azimuth is no greater than the protection threshold. Pseudocode for the joint-azimuth move-list algorithm is given in Algorithm 2.

**Algorithm 2:** Joint-azimuth move-list algorithm

**Input:** Protection channel $c$, protection threshold $t$, set of protection points $\mathcal{P}$, set of grants $\mathcal{G}$
**Output:** Move list for channel $c$, $\mathcal{M}_c \subseteq \mathcal{G}$

*// loop through every protection point*
1 **foreach** *point $p$ in set $\mathcal{P}$* **do**
  *// find the grants in the "neighborhood" of protection point $p$ and channel $c$*
2  $\mathcal{G}_{c,p} \leftarrow$ `Neighborhood` $(\mathcal{G}, c, p)$ ; // $\mathcal{G}_{c,p} \subseteq \mathcal{G}$
3  $\mathcal{M}_{c,p} \leftarrow \emptyset$;
4  **while** $\max_{a \in \mathrm{Azimuths}}$ `95thPrcntl` $(\mathcal{G}_{c,p} \setminus \mathcal{M}_{c,p}, a) > t$ **do**
5  $a_{\max} \leftarrow$ azimuth with highest aggregate interference;
6  $a_2$ azimuth with 2nd highest aggregate interference;
7  $I_2 \leftarrow$ `95thPrcntl` $(\mathcal{G}_{c,p} \setminus \mathcal{M}_{c,p}, a_2)$ ;
  *// sort grants by their median interference contribution, $P_i(c) + G_{tx,i}(p) - L_i(p) + G_{rx,i}(p, a_{\max})$, smallest to largest, where $P_i(c)$ is the conducted power of the $i$th grant in channel $c$ (dBm), $G_{tx,i}(p)$ is the transmit antenna gain in the direction of point $p$ (dBi), $L_i(p)$ is the median path loss from the transmitter to point $p$ (dB), and $G_{rx,i}(p, a_{\max})$ is the receive antenna gain in the direction of the transmitter*
8  $\mathbf{S} \leftarrow$ `Sort` $(\mathcal{G}_{c,p} \setminus \mathcal{M}_{c,p})$ ;
9  add grants to $\mathcal{M}_{c,p}$ starting with the largest in $\mathbf{S}$ until `95thPrcntl` $(\mathcal{G}_{c,p} \setminus \mathcal{M}_{c,p}, a_{\max}) \leq \max(I_2, t)$;
10 $\mathcal{M}_c = \bigcup_p \mathcal{M}_{c,p}$;

To compare the complexity of the standard and joint-azimuth algorithms, let $|\mathcal{A}|$ be the number of receiver azimuths, let $|\mathcal{G}|$ be the number of grants, and let $|\mathcal{M}|$ be the size of the move list. The complexity of each algorithm is dominated by the calculation of the 95th percentile of the aggregate interference. The standard algorithm performs this

Souryal, Michael; Nguyen, Thao; LaSorte, Nickolas.
"3.5 GHz Federal Incumbent Protection Algorithms."
Paper presented at IEEE International Symposium on Dynamic Spectrum Access Networks (DySPAN), Seoul, Republic of Korea. October 22, 2018 - October 25, 2018.

calculation approximately $|\mathcal{A}| \log |\mathcal{G}|$ times, assuming a binary search for Line 5 of Algorithm 1. The joint-azimuth algorithm, on the other hand, performs this calculation approximately $|\mathcal{A}||\mathcal{M}|$ times. Hence, the complexity of the joint-azimuth algorithm grows with $|\mathcal{M}|$ while that of the standard algorithm grows with $\log |\mathcal{G}|$. For large move lists, $|\mathcal{G}|$ and $|\mathcal{M}|$ are of the same order and can be in the thousands or tens of thousands. Furthermore, the standard algorithm can parallelize the processing of both the protection points and the azimuths, while the joint-azimuth algorithm can only parallelize the protection points.

The joint-azimuth algorithm constructs the move list by considering all possible receiver azimuths jointly rather than independently as in the standard algorithm. Further gains could be achieved by jointly considering all protection points as well as all azimuths, but the number of protection points can be in the thousands in practice.

### C. Modified Standard Algorithm

The modified standard algorithm is a minor variation of the standard algorithm. Instead of sorting grants by their *median* interference contribution at Line 3 of Algorithm 1, the modified standard algorithm sorts them by a higher percentile of their interference contribution. Otherwise, the two algorithms are identical, with no difference in computational complexity. We heuristically found that sorting the grants by the 99th percentile of their interference contribution yields the smallest move lists in the examples of the next section.

## III. Analysis

We executed the move-list algorithms described in Section II on simulated deployments of CBSDs along coastal areas of the U.S. The National Telecommunications and Information Administration (NTIA) has defined federal incumbent protection areas along the U.S. coasts [3]. The simulated deployments were conducted in the vicinity of three of these protection areas: along the northwest coast of the continental U.S. near La Push, Washington; along the Gulf coast near Pensacola, Florida; and along the East coast near Daytona Beach, Florida. These areas were chosen to yield small, medium, and large move lists, respectively.

Besides the CBSD deployment, additional inputs to the move-list algorithm, such as the protection threshold and the height and beamwidth of the incumbent receiver antenna, are specific to the area being protected and are given in keyhole markup language (KML) files [4].

The move-list calculations were performed using the reference implementations of the propagation model, antenna models, and the standard move list algorithm [5] and the reference geodata (terrain elevation and land classification) [6] employed in SAS certification testing.

### A. CBSD Deployment Model

We used a deployment model with the assumptions outlined below to distribute two categories of CBSDs. Category A CBSDs are lower power devices with a maximum effective isotropic radiated power (EIRP) of 30 dBm/10 MHz and are typically installed indoors. Category B CBSDs are higher power devices (47 dBm/10 MHz maximum EIRP) and are professionally installed outdoors [1].

TABLE I
Users Served by Each CBSD Category

| Area Type | Percent Users Served by | | Users per CBSD | |
|---|---|---|---|---|
| | Cat. A | Cat. B | Cat. A | Cat. B |
| **Urban** | 80 % | 20 % | 50 | 200 |
| **Suburban** | 60 % | 40 % | 20 | 200 |
| **Rural** | 40 % | 60 % | 3 | 500 |

TABLE II
CBSD Antenna Height and EIRP

| Area Type | Antenna Height (m) | | EIRP (dBm/10 MHz) | |
|---|---|---|---|---|
| | Cat. A | Cat. B | Cat. A | Cat. B |
| **Dense Urban** | 50 %: 3 to 15<br>25 %: 18 to 30<br>25 %: 33 to 60 | 6 to 30 | 26 | 40 to 47 |
| **Urban** | 50 %: 3<br>50 %: 6 to 18 | 6 to 30 | 26 | 40 to 47 |
| **Suburban** | 70 %: 3<br>30 %: 6 to 12 | 6 to 100 | 26 | 47 |
| **Rural** | 80 %: 3<br>20 %: 6 | 6 to 100 | 26 | 47 |

The model uses Geographic Information System (GIS) 2011 National Land Cover Database (NLCD) data [7] and 2010 U.S. Census population data [8] to distribute the CBSDs. CBSDs were deployed to each census tract based upon population and land coverage classification. CBSDs were placed as far as 250 km from the protection area boundary for Category A and as far as 600 km from the boundary for Category B.

First, the NLCD area classification codes were grouped and mapped to dense urban, urban, suburban, and rural regions and applied for each census tract. For the dense urban and urban regions, a daytime traveling factor expressed in terms of a percentage was included to account for the higher population densities that occur in cities during daytime [9].

Assuming a mature deployment, a market penetration factor of 20 % was assumed for this band. To account for distribution of users across ten available 10 MHz channels in the 3.5 GHz band, a scaling factor of 10 % was also included to determine the number of effective users potentially operating in each 10 MHz channel of interest.

The percentages of users served by Category A and Category B CBSDs vary depending on the classification regions and are noted in Table I. After calculating the number of users served by each category of CBSD, the numbers of Category A and Category B CBSDs were calculated based upon the effective number of users per CBSD, also shown in Table I.

The antenna height and EIRP of each CBSD was randomized with a uniform distribution based upon the land usage classification as shown in Table II. The antenna was assumed to be omnidirectional.

Souryal, Michael; Nguyen, Thao; LaSorte, Nickolas.
"3.5 GHz Federal Incumbent Protection Algorithms."
Paper presented at IEEE International Symposium on Dynamic Spectrum Access Networks (DySPAN), Seoul, Republic of Korea. October 22, 2018 - October 25, 2018.

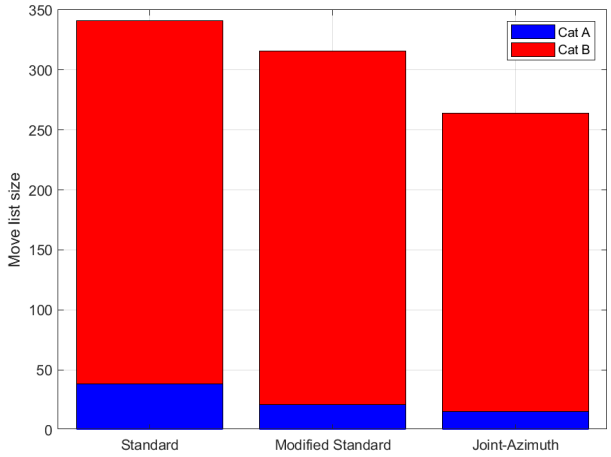


Fig. 1. Move list size, La Push, Washington, offshore protection area.

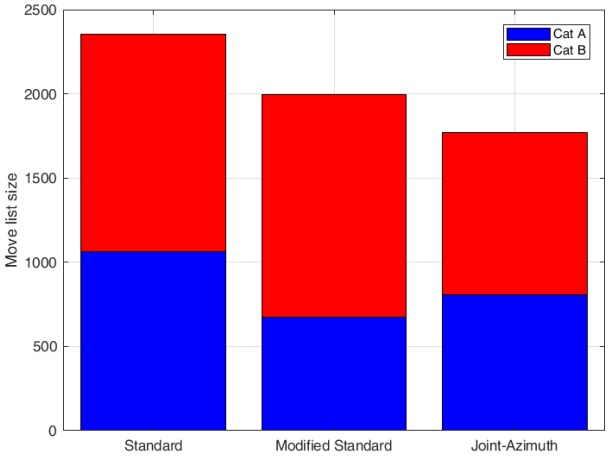


Fig. 2. Move list size, Pensacola, Florida, protection point.

### B. Protection Area Examples

*1) Small Move List:* As an example of a small move list, the algorithms were executed on the La Push coastal protection area. Each move list was calculated for a set of 50 protection points (35 points on the contour and 15 interior points). As shown in Fig. 1, the standard algorithm generates a move list of size 341 grants, 38 of which are from Category A CBSDs and the remainder are from Category B CBSDs. The joint-azimuth algorithm generates a total move list of size 264 grants, for a savings of 23 % over the standard algorithm, while the modified standard move list has 316 grants for a more modest savings of 7 %.

*2) Medium Move List:* The second example is for a protection area consisting of a single point, a training site in Pensacola, Florida. While the La Push protection area move lists are in the low hundreds, the move lists for Pensacola are in the low thousands. In this "medium" move list example, the efficiency gains of the joint-azimuth and modified standard move lists are somewhat greater than for the small move list. The joint-azimuth move list is 25 % smaller than the standard move list, while the modified standard move list is 15 % smaller than the standard move list (see Fig. 2), achieving more than half of the gain of the joint-azimuth list. However, the efficiency of the modified standard list is obtained solely in Category A grants, while the joint-azimuth list efficiencies are spread across Category A and Category B.

To illustrate how the algorithms utilize the available interference budget, we calculated the 95th percentile of the aggregate interference at the protection point after applying each move list. Fig. 3 plots the 95th percentile as a function of the incumbent receiver azimuth. The horizontal dash-dot line indicates the protection level for Pensacola of $-139$ dBm/10 MHz. While all three algorithms keep the interference below the protection level, it is clear from this plot that the joint-azimuth algorithm packs transmissions within the interference budget much more efficiently than the other algorithms at almost every azimuth.

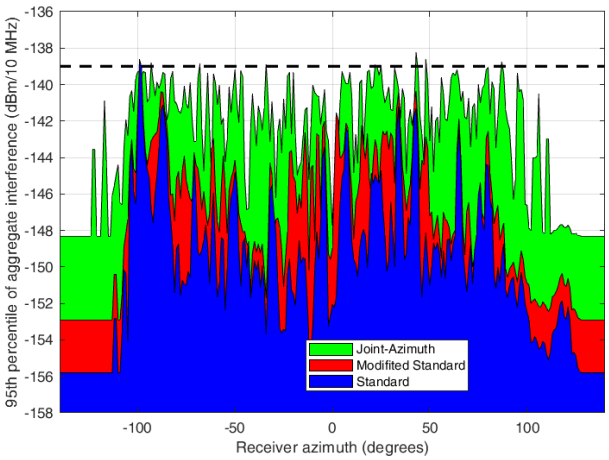


Fig. 3. Aggregate interference, Pensacola, Florida, protection point.

*3) Large Move List:* The move lists for the Daytona Beach protection area are 3 to 4 times larger than those of Pensacola (see Fig. 4) and were calculated for a set of 18 protection points along the contour of the protection area near the shore. The joint-azimuth move list is 18 % smaller than the standard move list, and the modified standard move list follows closely at 13 % smaller. Here again, the savings of the modified standard list are solely in Category A grants, while the joint-azimuth list has fewer grants in both categories.

Across all three examples, we observe that the performance of the modified standard algorithm relative to that of the joint-azimuth algorithm improves with increasing move list size. Furthermore, the aggregate interference results (Fig. 5) show once again that these algorithms use the interference budget more efficiently than the standard algorithm.

A geographic view of the difference between the standard

Souryal, Michael; Nguyen, Thao; LaSorte, Nickolas.
"3.5 GHz Federal Incumbent Protection Algorithms."
Paper presented at IEEE International Symposium on Dynamic Spectrum Access Networks (DySPAN), Seoul, Republic of Korea. October 22, 2018 - October 25, 2018.

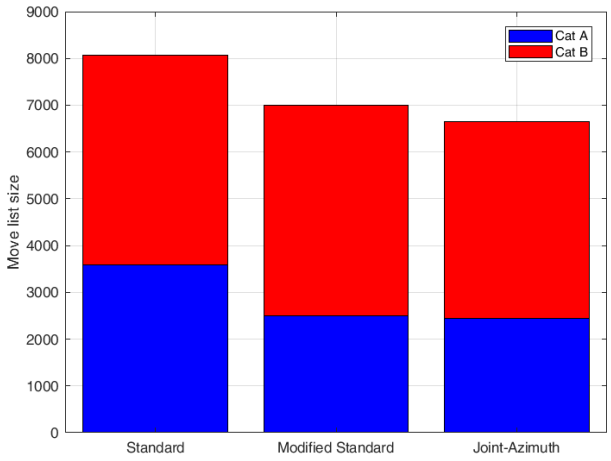


Fig. 4. Move list size, Daytona Beach, Florida, offshore protection area.

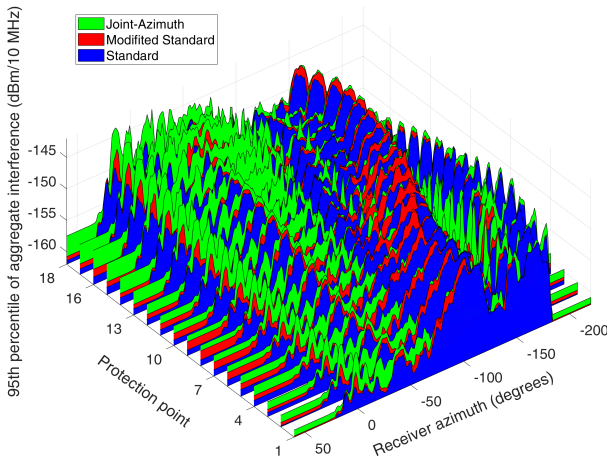


Fig. 5. Maximum aggregate interference, Daytona Beach, Florida, offshore protection area.

and joint-azimuth move lists is shown in Fig. 6.[1] Blue markers indicate CBSDs with grants on the standard move list but not on the joint-azimuth move list. Yellow markers are on the joint-azimuth move list but not on the standard move list (there is only one such CBSD). Markers with dots represent Category B CBSDs, while markers without dots are Category A. We observe that the excess Category A CBSDs on the standard move list are all within 90 km of the protection area, while the excess Category B CBSDs are 160 km to 375 km from the protection area.

[1]Certain commercial products are identified in this paper in order to specify the experimental results adequately. Such identification is not intended to imply recommendation or endorsement by the National Institute of Standards and Technology, nor is it intended to imply that the products identified are necessarily the best available for the purpose.

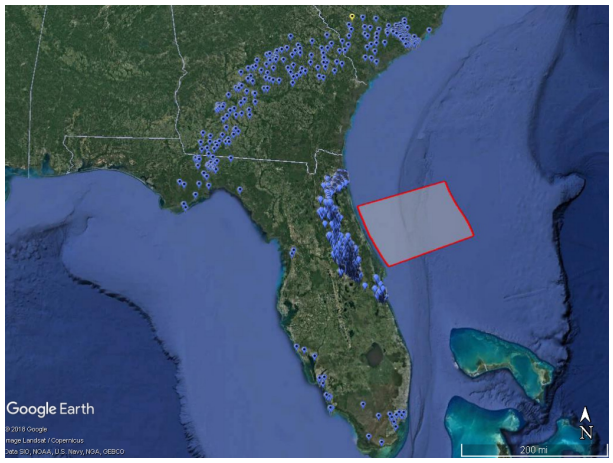


Fig. 6. Standard/joint-azimuth move list difference, Daytona Beach, Florida, offshore protection area. Blue marker: diff on standard move list; yellow marker: diff on joint-azimuth move list; blank marker: Category A; dot marker: Category B.

## IV. Conclusion

An analysis of alternative federal incumbent protection algorithms for the 3.5 GHz band finds that a more efficient selection of the CBRS transmissions to be moved from a protected channel results in 18 % to 25 % fewer transmissions being affected compared with the current standardized algorithm. The improved algorithm achieves these gains by considering all possible receiver azimuths jointly rather than independently, but at considerable additional computational cost. Alternatively, a simple change to the standard algorithm achieves much of these gains, mainly for Category A grants, and with no increase in computational complexity.

## References

[1] "Citizens broadband radio service," 2 C.F.R. § 96, 2016.
[2] "Requirements for commercial operation in the U.S. 3550–3700 MHz citizens broadband radio service band," Wireless Innovation Forum Document WINNF-TS-0112, Version V1.5.0, May 2018. [Online]. Available: https://workspace.winnforum.org/higherlogic/ws/public/document?document_id=6531
[3] Letter from Paige R. Atkins, Assoc. Admin., Office of Spectrum Mgt., NTIA, to Julius P. Knapp, Chief, Office of Eng. and Tech., FCC, May 2018. [Online]. Available: https://www.fcc.gov/ecfs/filing/1051705880764
[4] Dynamic Protection Area kml files, May 2018. [Online]. Available: https://github.com/Wireless-Innovation-Forum/Spectrum-Access-System/tree/master/data/ntia
[5] SAS Testing and Interoperability Repository. [Online]. Available: https://github.com/Wireless-Innovation-Forum/Spectrum-Access-System
[6] SAS Data Repository. [Online]. Available: https://github.com/Wireless-Innovation-Forum/SAS-Data
[7] 2011 National Land Cover Database, U.S. Geological Survey, 2011. [Online]. Available: http://viewer.nationalmap.gov/basic/
[8] 2010 National Census Tracts Gazetteer, U.S. Census Bureau, 2010. [Online]. Available: http://www.census.gov/geo/maps-data/data/gazetteer2010.html
[9] Commuter Adjusted Daytime Population: 2006-2010, U.S. Census Bureau. [Online]. Available: https://www.census.gov/data/tables/2010/demo/metro-micro/commuting-employment-2010.html

Souryal, Michael; Nguyen, Thao; LaSorte, Nickolas.
"3.5 GHz Federal Incumbent Protection Algorithms."
Paper presented at IEEE International Symposium on Dynamic Spectrum Access Networks (DySPAN), Seoul, Republic of Korea. October 22, 2018 - October 25, 2018.

# Practical Considerations When Using Commercial Robotic Arms for Antenna Metrology

David R. Novotny, Joshua A. Gordon
Communications Technology Laboratory, National Institute of Standards and Technology, Boulder, CO, USA

***Abstract* – The National Institute of Standards and Technology has been using commercial robotic arms to characterize antenna gain and radiation patterns. The transition from custom antenna hardware to commercial robotics has opened up new capabilities but has also highlighted some issues that need to be addressed to ensure full confidence when using these systems.**

***Index Terms* — Antennas, Calibration, Gain, Metrology, Near-Field, Pattern, Robotics.**

## 1. Introduction

The use of commercial robotics for measuring radio-frequency (RF) to milli-meter wave (mmWave) emissions and patterns is starting to leave research testbeds and entering main stream antenna testing [1]-[4]. There have been multiple groups measuring antenna performance, and characterizing the suitability and ease-of-use of coordinated-motion robotics for antenna measurements, see Fig.1 [3]-[8]. Antenna measurements up to 330 GHz have been reported, Fig. 2 [6], robot-mounted integrated sensor suites, which measure more than just antenna performance, have been demonstrated up to 18 GHz using a low-cost arm [7], and suitability for scanning geometries up to 500 GHz has been proposed when combined with external spatial metrology [3].

As more systems are being demonstrated, there is greater scrutiny being paid to performance, speed, safety, and general operability with other equipment. Individual design requirements show differences in optimized features, e.g., implementations that require a high degree of spatial knowledge to limit uncertainties in low signal-to-noise (SNR) parts of the pattern, may use spatial metrology to infer antenna positions at varying cost and complexity while systems that are optimized for throughput or lower frequency operation forgo these additional costs [8].

## 2. Design Considerations When Using Commercial Robotic Arms

Compared to traditional stacked-stage antenna measurement systems of approximately similar scan size, commercial serial-robotic arms on the surface can seem to have larger positioning errors which could limit their usability for antenna measurements, especially at mm-Wave frequencies [8]. Most commercial robotic arm systems are designed to operate in arbitrary poses over large volumes, moving large payloads at high speed in continuous operation and doing these tasks *repeatably*. In our case, accuracy is typically more important than speed, so we need to assess how to properly utilize robots for antenna measurements.



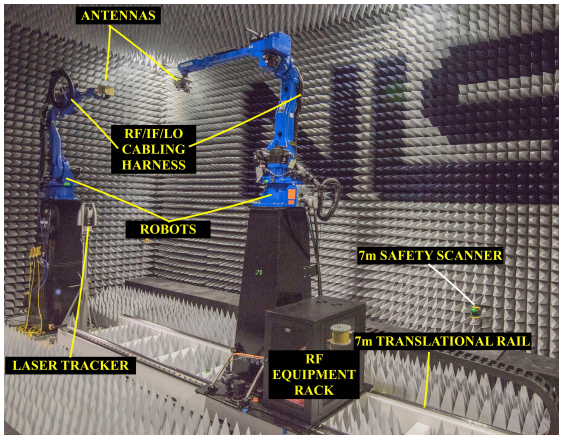


Fig. 1. The Dual-Arm Large Antenna-Positioning System at NIST.

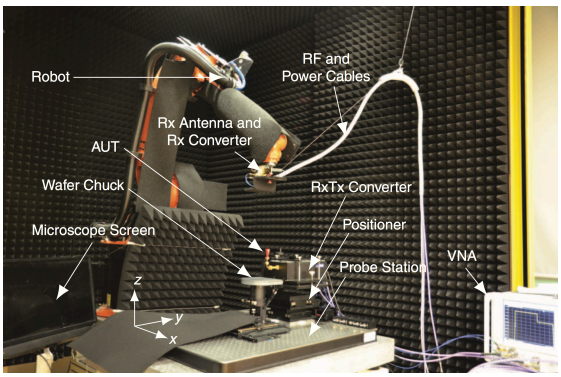


Fig. 2. A robotic arm antenna system with absorber treatment at ULM University [6] (Photo courtesy of ULM University, Germany).

Some of the factors that affect antenna performance results include: antenna and probe positioning *accuracy* and mechanical repeatability, signal repeatability, scan volume, and coordination with other pieces of equipment (for example, the robot, RF and spatial measurement equipment).

### (1) Accuracy and repeatability

Antenna ranges can use errors in probe position relative to the antenna under test (AUT) to assess gain and pattern uncertainty. A rule of thumb is that for a 20 dBi gain antenna, to achieve a noise level due to positioning errors of -50 dB, a position accuracy of $\lambda/50$ is required (where $\lambda$ is the operating

Novotny, David; Gordon, Joshua.
"Practical Considerations When Using Commercial Robotic Arms for Antenna Metrology."
Paper presented at 2018 International Symposium on Antennas and Propagation (ISAP), Busan, Republic of Korea. October 23, 2018 - October 26, 2018.

wavelength). Accuracy can be described as the average difference between a desired and actual probe to AUT position. Repeatability is the deviation of the accuracy over time. Robotic arms usually generate position using a variation of a serial Denavit-Hartenburg (DH) model [9]. The repeatability of a robot is determined by the quality of the motors and gearing. The accuracy is determined by the knowledge of the DH model. This model can be better determined by using spatial metrology tools to improve overall accuracy [10].

**(2) Spatial Metrology – Path vs DH Calibration**

Spatial metrology, determining AUT and probe location and orientation, can be costly in terms of budget, development, and measurement time. Laser trackers and laser radars can cost more than the 3 to 4 m reach robotic arm they are measuring, while photogrammetry systems can take longer to process and have limited spatial accuracy.

Using in-the-loop position metrology, basic path geometry can be corrected to the level of the robot or metrology resolution [3]. A less costly alternative can be to calibrate the DH model for a range of robot loads. This gives a calibration to the level of robot repeatability or motor backlash performance over a full volume rather than a specific path [11].

**(3) Robot to Process Synchronization**

In order to perform antenna measurements, synchronization between the robot and an RF measurement is required. The easiest, but slowest, method for doing this is to stop the robot at each point. Taking data as the robot moves or "on-the-fly" requires synchronization between all components, especially robot positioning and event triggering. Traditional near-field ranges can typically trigger more accurately in time than commerical robots. However if position is known, even if there is an error, accurate patterns can still be determined [12].

**(4) RF and mmWave Signal Stability**

As the operational frequency increases, the signal stability with movement tends to worsen [3],[6]. Using mixer-based systems to convert frequency, attenuation changes can be lessened. However, the phase variations can be augmented, as they scale with the multiplication order. Modern phased arrays can use 5 to 8 bit phase shifters, so to ensure proper testing of these systems, phase errors due to movement need to be kept to within $2^{-5}$ (11.25°) to $2^{-8}$ (1.5°)

The use of cable service loops to limit differential bending, Fig. 2, can be effective in limiting phase changes. Most industrial robotic arms have defined cable routing for control signals which are designed to provide a minimal stress to these cables to ensure longevity. By using this path for RF cabling, stress and phase change from the cables are minimized, Fig. 1.

## 3. Dynamic Measurements

New communication and phased array systems, especially systems that are expected use digital beamforming, will no longer have the ability to directly test the antenna [13]; furthermore, static tests will not suffice to exercise these systems. The ability to rapidly and arbitrarily move to a point and capture data is a task more suited for robots. Additionally, multiple robots can interrogate systems in concert or independently, providing additional over-the-air testing capabilities, see Fig. 1.

## 4. Conclusion

Multiple groups have shown the basic capability of robotic arms to perform antenna measurements at RF to mmWave frequencies. To achieve pattern and gain accuracies in a time frame commensurate with traditional near-field ranges, a robust analysis of system timing and position can greatly improve results. Furthermore, full six degree-of-freedom positioning capability can perform several scan geometries, dynamic measurements, and improve final pattern and gain results by actively correcting to the resolution of the robot.

## References


[1] N. Petrovic, T. Gunnarsson, N. Joachimowicz and M. Otterskog, "Robot controlled data acquisition system for microwave imaging," *2009 3rd European Conference on Antennas and Propagation*, Berlin, 2009, pp. 3356-3360.

[2] J. A. Gordon *et al*., "Millimeter-Wave Near-Field Measurements Using Coordinated Robotics," in *IEEE Transactions on Antennas and Propagation*, vol. 63, no. 12, pp. 5351-5362, Dec. 2015. doi: 10.1109/TAP.2015.2496110.

[3] D. Novotny, J. Gordon, J. Coder, M. Francis and J. Guerrieri, "Performance evaluation of a robotically controlled millimeter-wave near-field pattern range at the NIST," *2013 7th European Conference on Antennas and Propagation (EuCAP)*, Gothenburg, 2013, pp. 4086-4089.

[4] D. Novotny *et al*., "A multi-robot large antenna positioning system for over-the-air testing at the National Institute of Standards and Technology," *AMTA 2017 Proceedings*, Atlanta, GA, USA, 2017, pp. 399-404.

[5] J. A. Gordon *et al*., "An All-Metal, 3-D-Printed CubeSat Feed Horn: An assessment of performance conducted at 118.7503 GHz using a robotic antenna range.," in *IEEE Antennas and Propagation Magazine*, vol. 59, no. 2, pp. 96-102, April 2017. doi: 10.1109/MAP.2017.2655574

[6] L. Boehm, F. Boegelsack, M. Hitzler and C. Waldschmidt, "The Challenges of Measuring Integrated Antennas at Millimeter-Wave Frequencies [Measurements Corner]," in *IEEE Antennas and Propagation Magazine*, vol. 59, no. 4, pp. 84-92, Aug. 2017. doi: 10.1109/MAP.2017.2706652

[7] R. M. Lebrón, J. L. Salazar, C. Fulton, S. Duthoit, D. Schmidt and R. Palmer, "A novel near-field robotic scanner for surface, RF and thermal characterization of millimeter-wave active phased array antenna," *2016 IEEE International Symposium on Phased Array Systems and Technology (PAST)*, Waltham, MA, 2016, pp. 1-6. doi: 10.1109/ARRAY.2016.7832657

[8] J. Hatzis, P. Pelland and G. Hindman, "Implementation of a combination planar and spherical near-field antenna measurement system using an industrial 6-axis robot," *AMTA 2016 Proceedings*, Austin, TX, USA, 2016, pp. 1-6, doi: 10.1109/AMTAP.2016.7806306

[9] J. Denavit, R. Hartenberg,"A kinematic notation for lower-pair mechanisms based on matrices," *Trans ASME J. Appl. Mech.,* vol. 23, pp. 215–221, 1955.

[10] A. Nubiola and I. Bonev, "Absolute calibration of an ABB IRB 1600 robot using a laser tracker," *Robotics and Computer-Integrated Manufacturing*, vol. 29, issue 1, pp 236-245, 2013.

[11] M. Allman, D. Novotny, J. Gordon, A. Curtin and S. Sandwidth, "Serial-Robotic-Arm-Joint characterization measurements for antenna metrology," *AMTA 2017 Proceedings*, Atlanta, GA, USA, 2017, pp. 381-387.

[12] R. Wittmann, B. Alpert, M. Francis," Spherical near field antenna measurements using non-ideal measurement locations," *AMTA 2002 Proceedings*, Cleveland, OH, USA, pp 43-48, 2002.

[13] M. Fogelle, "Advances in Over-the-Air Performance Testing Methods for mmWave Devices and 5G Communications", *AMTA 2016 Proceedings*, Austin, TX, USA, pp. 272-279, 2016.



Novotny, David; Gordon, Joshua.
"Practical Considerations When Using Commercial Robotic Arms for Antenna Metrology."
Paper presented at 2018 International Symposium on Antennas and Propagation (ISAP), Busan, Republic of Korea. October 23, 2018 - October 26, 2018.

# DETECTION OF INCUMBENT RADAR IN THE 3.5 GHZ CBRS BAND

*Raied Caromi, Michael Souryal, and Wen-Bin Yang*

National Institute of Standards and Technology
Communications Technology Laboratory
Gaithersburg, Maryland, USA

## ABSTRACT

In the 3.5 GHz Citizens Broadband Radio Service (CBRS), 100 MHz of spectrum will be shared between commercial users and federal incumbents. Dynamic use of the band relies on a network of sensors dedicated to detecting the presence of federal incumbent signals and triggering protection mechanisms when necessary. This paper uses field-measured waveforms of incumbent signals in and adjacent to the band to evaluate the performance of matched-filter detectors for these sensors. We find that the proposed detectors exceed the requirements for performance in the presence of co-channel interference from commercial long term evolution (LTE) signals, meaning that more commercial devices can use the band in the proximity of sensors. Furthermore, the detectors are robust to out-of-band emissions into this band from adjacent-band radars, which prior studies have found can be significant.

***Index Terms***— 3.5 GHz, CBRS, detection, environmental sensing capability, radar

## 1. INTRODUCTION

The CBRS in the U.S. permits commercial broadband access to the radio frequency spectrum between 3550 MHz and 3700 MHz on a shared basis with incumbents in the band [1]. Among the incumbents is the U.S. military which operates radar systems in this band, including shipborne radar off the U.S. coasts. The CBRS rules permit dynamic access to the band in the proximity of military radar provided a sensor network detects the presence of incumbent radar and triggers interference mitigation measures when necessary. The scope of this study is on the achievable detection performance of this sensor network.

In order to operate in the CBRS ecosystem, sensors must be certified to meet specific re quirements. Among these requirements is the ability to detect the in-band incumbent radar signal at a minimum received power density of $-89\,\mathrm{dBm}$ (dB relative to $1\,\mathrm{mW})/\mathrm{MHz}$ [2], within 60 seconds of onset, and with a probability of detection of 99 % or better [3].[1] With this minimum required power density, the detection is clearly not thermal-noise-limited, as the detection threshold is 25 dB above the thermal noise floor. The challenge for detection is presented, rather, by co-channel interference.

[1] Government requirements do not specify a maximum probability of false alarm, although this figure o f m erit i s n aturally o f i nterest t o commercial users.

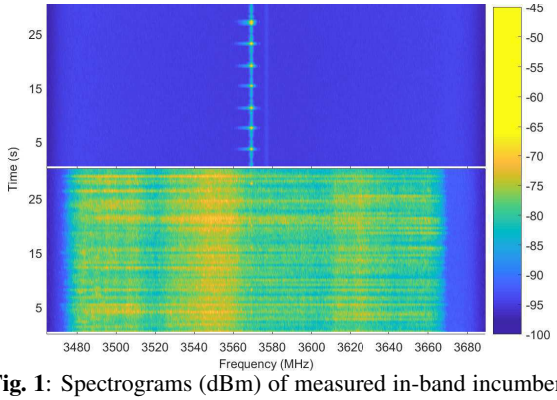


**Fig. 1**: Spectrograms (dBm) of measured in-band incumbent radar [5].

There are two primary sources of co-channel interference at the sensor's receiver. First, by design, the band is shared with commercial systems. Therefore, sensors must be able to detect the incumbent signal in channels occupied by commercial systems. These systems are expected to be fourth-generation LTE systems, at least initially. However, the emissions of commercial systems operating in the band can, in principle, be controlled by treating the sensors as protected entities in the CBRS system.

The second, more challenging, source of interference is the out-of-band emissions of systems operating in adjacent bands. These systems are also military radars, operate at frequencies below the CBRS band, and have been observed to generate significant emissions into the CBRS band [4, 5]. Fig. 1 shows the first 30 s of two spectrograms of the measured in-band SPN-43 radar present at 3570 MHz, one with and one without adjacent-band emissions.

This paper is a study of the performance of a class of detectors, namely matched-filter detectors, matched to the current in-band radar system and under realistic conditions of co-channel interference. This study leverages actual waveform recordings of both the in-band radar and the out-of-band emissions of adjacent-band radars collected in field measurements conducted at two U.S. coastal locations [4, 5]. We



Caromi, Raied; Souryal, Michael; Yang, Wen-Bin.
"Detection of Incumbent Radar In the 3.5 GHZ CBRS Band."
Paper presented at 6th IEEE Global Conference on Signal and Information Processing (GlobalSIP 2018), Anaheim, CA, United States.
November 26, 2018 - November 28, 2018.

present the achievable tradeoff between detection and false-alarm rates under different interference conditions for two variants of the matched filter (MF) detector, coherent and non-coherent. While this study is limited to detection of the current in-band radar, SPN-43, a similar analysis can be performed for future radars deployed in this band.

Detection by CBRS sensors differs from traditional radar detection primarily because the sensor aims to identify the presence of a radar signal rather than detecting and tracking a target. Additionally, unlike a typical radar receiver that has full access to the radar waveform, the sensor has only partial knowledge of radar waveform parameters. However, elements of classical radar detection can still be utilized. In particular, we use coherent and non-coherent MF detectors [6]. A comparable problem to the detection of incumbent radar in the $3.5\,\mathrm{GHz}$ band is the protection of radars in the $5\,\mathrm{GHz}$ band, namely, dynamic frequency selection (DFS) in wireless access systems. DFS systems must avoid, or vacate, a channel identified as being occupied by the radar. However, the detection requirement is more relaxed than in CBRS; for instance, the detection threshold for the lower-power wireless devices is $-62\,\mathrm{dBm}/18\,\mathrm{MHz}$ [7]. Furthermore, it is not clear that adjacent-band emissions are as much an issue as in CBRS.

## 2. SIGNAL MODEL

The $3.5\,\mathrm{GHz}$ CBRS band provides access to a total of $150\,\mathrm{MHz}$ bandwidth divided into 10 MHz channels. A sensor is required to detect the presence of in-band radar in any channel of the lower $100\,\mathrm{MHz}$ of the band, and multiple radar signals may be present in different channels. A capable sensor can simultaneously or sequentially acquire the signal from all channels in order to identify the possible presence of incumbent radar signals. Alternatively, a sensor may employ multiple detectors in parallel, for instance, one per channel.

Therefore, we simplify the signal model by assuming a single channel which may or may not be occupied by the incumbent in-band radar signal. In addition, we consider three types of noise: gaussian thermal noise, co-channel commercial LTE emissions, or adjacent-band radar emissions. The simplified model of the received baseband signal, then, is

$$x[n] = s[n] + v[n],$$

where $s$ is the in-band radar signal whose presence we are trying to detect, and $v$ is either complex white gaussian noise (CWGN), an LTE signal, or emissions from an adjacent-band radar.

## 3. INCUMBENT RADAR DETECTION

The statistical hypothesis testing for a single radar signal detection is

$$\begin{cases} H_0 : x[n] = v[n], \\ H_1 : x[n] = s[n] + v[n]. \end{cases}$$

If no interference is present, and $s[n]$ is known, the problem becomes the classical detection of a known complex deterministic signal in CWGN [8]. The optimal detector for this case is a MF (or equivalently, a replica correlator). A true MF detector requires perfect knowledge of the signal. We assume the pulse repetition interval and pulse duration are approximately known based on prior observation [4, 5]. Other parameters of the radar signal are simply unknown. For instance, neither the frequency nor the phase information is known a priori. Obviously, disregarding the phase information for the coherent detector will degrade the performance. However, the issue of not knowing the center frequency of the radar signal can be resolved by implementing a bank of MFs over the entire baseband. Prior observations [4, 5, 9] indicate that these radars typically operate on a $10\,\mathrm{MHz}$ grid.

Let $\hat{s}(t)$ be a template for the incumbent radar signal, defined as

$$\hat{s}(t) = \exp(j2\pi f_0 t)p(t),$$

where $f_0$ is the center frequency of the template in the baseband, and $p(t)$ is a train of rectangular pulses. If the number of pulses in $p(t)$ is equal to $L$, then

$$p(t) = \begin{cases} 1, & t \in [\ell T_{pr}, \ell T_{pr} + T_{pw}], \ell = 0, 1, \dots L-1 \\ 0, & \text{otherwise}, \end{cases}$$

where $T_{pw}$ is the pulse width, and $T_{pr}$ is the pulse repetition interval in seconds. Let $\hat{s}[n]$ be the sampled version of $\hat{s}(t)$. The impulse response of the MF is $h[n] = \hat{s}^*[-n]$. The output of the MF is given by the convolution $x[n] \circledast h[n]$. Alternatively, the same result can be obtained from the deterministic cross-correlation given by

$$r_{xs}[m] = \sum_{n=-\infty}^{\infty} x[n]\hat{s}^*[n+m], -\infty < m < \infty.$$

In practice we compute $r_{xs}[m]$ for the lag values $m = 0, \pm 1, \pm 2, \dots, \pm(N-1)$, where $N$ is the number of samples of $x[n]$. Let test statistic of the detector $\mathcal{T}\{r_{xs}[m]\}$ be a function of the output of the cross-correlator. The decision rule is given by

$$\mathcal{T}\{r_{xs}[m]\} \underset{H_0}{\overset{H_1}{\gtrless}} \gamma,$$

where $\gamma$ is the detection threshold for the MF. The probability of detection and the probability of false alarm are given by

$$P_D = P_r\left(\mathcal{T}\{r_{xs}[m]\} > \gamma \mid H_1\right),$$
$$P_{FA} = P_r\left(\mathcal{T}\{r_{xs}[m]\} > \gamma \mid H_0\right),$$

respectively. It is straightforward to calculate closed forms of these probabilities for a known signal in white gaussian noise (WGN) [6, 8]. However, we use empirical methods to estimate these probabilities since we do not have full knowledge of the signal, and the interference is not WGN.

## 4. PERFORMANCE ANALYSIS

We test two types of MF detectors. The first type is coherent MF. The input to the filter for this type is the complex



Caromi, Raied; Souryal, Michael; Yang, Wen-Bin.
"Detection of Incumbent Radar In the 3.5 GHZ CBRS Band."
Paper presented at 6th IEEE Global Conference on Signal and Information Processing (GlobalSIP 2018), Anaheim, CA, United States.
November 26, 2018 - November 28, 2018.

signal, and thus we label it complex correlator (CC). For the second type, non-coherent MF, the input to the MF is the signal stripped of its phase, i.e., $|x[n]|$. We label this filter as magnitude correlator (MC). The test statistic for CC is the maximum value of $|r_{xs}[m]|$ over all values of $m$. The MC, on the other hand, benefits from a different test statistic. Specifically, $\mathcal{T}\{r_{xs}[m]\}$ is the sum of the magnitudes of $L$ pulses from the output of the correlator. The sum is computed by aligning the pulses at the output of the filter.

Field-measured signals of shipborne radar are used in the simulation for both in-band and adjacent-band radar signals. These waveforms were originally $60\,\mathrm{s}$ in duration, sampled at $225\,\mathrm{MHz}$. We first decimate these waveform files to a $25\,\mathrm{MHz}$ sampling rate. For the in-band radar waveforms, we shift the signals so that they are centered at zero baseband frequency. A large set of waveform files with strong in-band and adjacent-band radar signals is selected for simulations. For each in-band radar waveform file, $(8$ to $15)$ segments are extracted for simulation. Each segment is $20\,\mathrm{ms}$ long, which is approximately the time it takes for the main beam of the radar antenna to illuminate the detector as the radar antenna rotates in the azimuth plane. The radar segments, in addition to the interference signals, are further filtered and downsampled to $2\,\mathrm{MHz}$ in order to reduce the computational time of the MF. A total of $16\,000$ different radar segments with SNR higher than $30\,\mathrm{dB}$ of the in-band radar signals are used for performance evaluation. Each evaluation consists of simulating both radar present and radar absent cases.

We choose a MF template of $10\,\mathrm{ms}$. Since the signal is $20\,\mathrm{ms}$ in duration, the template is padded with zeros for the difference in time length. Based on the analysis provided in [4, 5], we set $T_{pr} = 1\,\mathrm{ms}$ , and $T_{pw} = 1\,\mu\mathrm{s}$, i.e., $L = 10$. We define SNR as the peak power of the radar signal to the average noise power in $1\,\mathrm{MHz}$. However, since the $20\,\mathrm{ms}$ segments includes $20$ pulses of the radar signal, we use the average of the peak power of these pulses for the SNR and peak power settings. Although the original waveform captures include noise, its effect is ignored since the waveforms have high SNR values. However, the waveform captures include channel fading effect. The in-band radar signals are added to either WGN, LTE, or adjacent-band interference to generate realistic scenarios similar to what an actual sensor will observe. Radar signal power levels are adjusted to the desired SNR or desired radar peak power values.

### 4.1. Ideal signal detection in WGN

We first evaluate the detection performance when an actual radar signal extracted from field measurements is used as the template. The same template is then used as a signal after corrupting it with WGN and delaying it with a random time delay at each iteration of the simulation. Fig. 2 shows the achievable receiver operating characteristic (ROC) curves for this case. As expected, CC performs better than MC for this

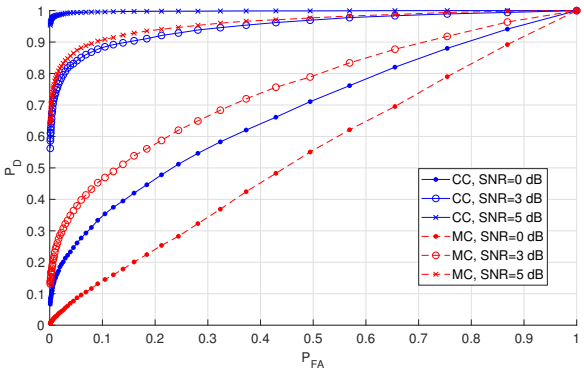


**Fig. 2**: Measured signal as template; signal with added WGN.

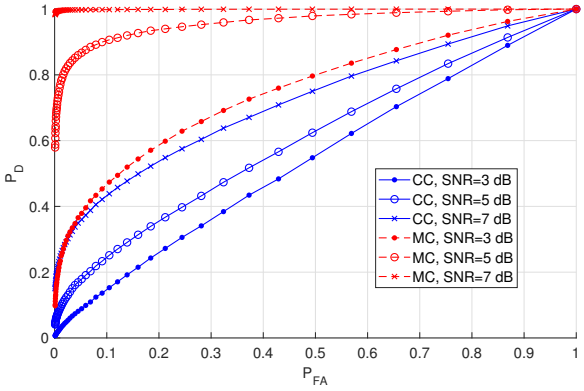


**Fig. 3**: Synthetic template; signal with added WGN.

case since the template contains the original phase information and the coherent detector performs to its fullest. In practice, a sensor will not have a priori access to the actual signal for use as the template. Therefore, this example demonstrates the best-case detection performance of a sensor.

### 4.2. Signal detection in WGN with synthetic template

For a realistic detection case, we use a synthetically generated pulse template. We use all $16\,000$ radar signal segments in the detection performance evaluation. The signals were corrupted with noise with a fixed power level, and the radar signal amplitudes were adjusted for specific SNR values. The threshold values were estimated from the cumulative distribution function (CDF) of the noise for a given set of $P_{FA}$ values. Fig. 3 shows the ROC curves for both CC and MC detectors. Clearly, MC performs better than CC due to unmatched phase between CC template and the radar signal. In addition, the difference between the performance of the perfectly matched filter, i.e., the CC detector in Fig. 2, and the MC detector in Fig. 3 is approximately $2\,\mathrm{dB}$ in SNR, which represents the loss from using the synthetic template instead of a perfectly matched detector.



Caromi, Raied; Souryal, Michael; Yang, Wen-Bin.
"Detection of Incumbent Radar In the 3.5 GHZ CBRS Band."
Paper presented at 6th IEEE Global Conference on Signal and Information Processing (GlobalSIP 2018), Anaheim, CA, United States.
November 26, 2018 - November 28, 2018.

**Table 1**: LTE TDD configurations

| TDD uplink/downlink configuration | 0 | 1 | 2 | 3 | 4 | 5 | 6 |
|---|---|---|---|---|---|---|---|
| Modulation and coding scheme index uplink/downlink[2] | 6/6 | 12/12 | 24/12 | 14/16 | 4/12 | 5/16 | 24/6 |
| Number of physical resource block uplink/downlink[3] | 50/15 | 50/50 | 25/50 | 50/50 | 15/50 | 6/50 | 50/6 |
| Downlink to uplink power ratio dB | 0 | 1 | 2 | 3 | 0 | 1 | 2 |

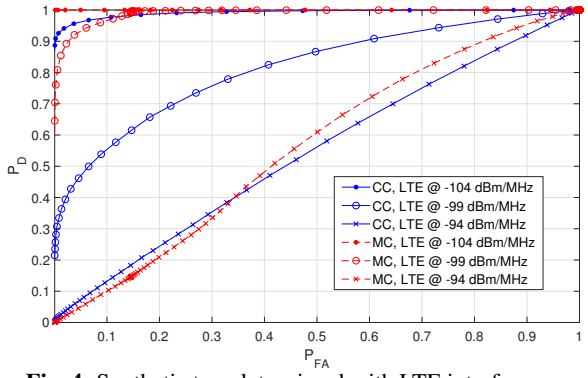


**Fig. 4**: Synthetic template; signal with LTE interference.

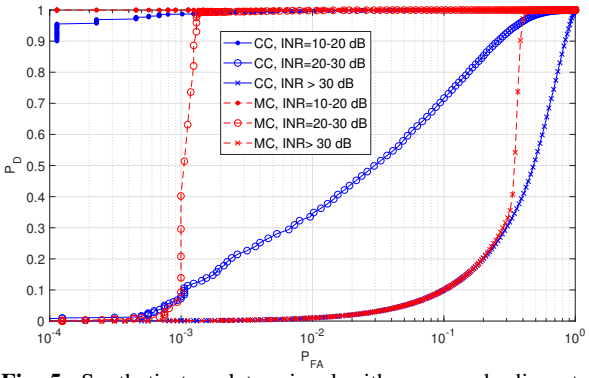


**Fig. 5**: Synthetic template; signal with measured adjacent-band radar emissions.

### 4.3. Detection in LTE interference

We subject the detectors to a single interfering LTE time division duplex (TDD) signal, representing a nearby dominant interferer. The LTE signals are set to be co-channel with the in-band radar signals. LTE TDD waveforms are generated with commercial software. At each iteration of the simulation, the LTE frame structure is randomly selected from the 7 TDD configurations in Table 1. Each configuration defines which subframes are utilized for downlink and for uplink. For each TDD configuration, we configure the LTE waveforms as shown in the table. The peak power of the radar signals is set at the required detection threshold of $-89\,\mathrm{dBm/MHz}$. Fig. 4 shows the ROC curves for multiple values of received LTE average power per $1\,\mathrm{MHz}$.

Note that sensors are required to tolerate only $-109\,\mathrm{dBm/MHz}$ of aggregate commercial emissions [2]. These results indicate, therefore, that the MC detector can tolerate $10\,\mathrm{dB}$ more commercial interference than required.

### 4.4. Detection in adjacent-band interference

For this case, measured adjacent-band signals are added to the in-band radar signals. The SNR for the in-band radar is set to $19\,\mathrm{dB}$. The generated waveforms are similar to the in-band radar with adjacent-band emissions shown in Fig. 1, but the power levels of the in-band and adjacent-band signals are set separately. We first extract strong adjacent-band bursts from the field-measured waveforms. We divide these emissions into three sets based on the peak interference to noise ratio (INR). The $>30\,\mathrm{dB}$ set has a median INR of $34\,\mathrm{dB}$ and a maximum INR of $72\,\mathrm{dB}$.

[2]Table 7.1.7.1-1 [10]
[3]Table 7.1.7.2.1-1 [10]

Fig. 5 shows ROC curves for multiple interference levels. We observe that, even with adjacent-band emissions at peak INR levels of $20\,\mathrm{dB}$ to $30\,\mathrm{dB}$, the MC detector can achieve near perfect detection with a false alarm probability of only $10^{-3}$. However, at higher interference levels, the false alarm rate increases to $40\,\%$.

## 5. CONCLUSION

We presented an analysis of federal incumbent detectors for the $3.5\,\mathrm{GHz}$ shared-spectrum CBRS band using field-measured signals of the in-band incumbent radar as well as of adjacent-band emissions into this band, which prior studies have shown to be significant. While coherent detection is shown to be superior with known signals in WGN as expected, a practical magnitude-correlator detector outperforms the coherent detector in the absence of phase information of the in-band radar. The magnitude detector performs well at a peak SNR of $5\,\mathrm{dB}$ in gaussian noise, but with interference from commercial CBRS (LTE) devices, a peak SIR of $10\,\mathrm{dB}$ is needed, suggesting that a single, dominant LTE signal is not well modeled by gaussian noise. Nevertheless, the detector's performance exceeds current requirements, meaning that more commercial devices can use the band in the proximity of sensors. Finally, the MC detector is quite robust to adjacent-band emissions having peak INR levels as high as $20\,\mathrm{dB}$ to $30\,\mathrm{dB}$.

In ongoing work, we are examining the effectiveness of machine-learning algorithms for detection of the incumbent radar in the presence of commercial LTE and adjacent-band emissions. While this study focused on detection of the current radar in the band, future work may address the detection of future radars entering this band.



Caromi, Raied; Souryal, Michael; Yang, Wen-Bin.
"Detection of Incumbent Radar In the 3.5 GHZ CBRS Band."
Paper presented at 6th IEEE Global Conference on Signal and Information Processing (GlobalSIP 2018), Anaheim, CA, United States.
November 26, 2018 - November 28, 2018.

## 6. REFERENCES


[1] "Citizens broadband radio service," 2 C.F.R. § 96, 2016.

[2] Frank H. Sanders, John E. Carroll, Geoffrey A. Sanders, Robert L. Sole, Jeffery S. Devereux, and Edward F. Drocella, "Procedures for laboratory testing of environmental sensing capability sensor devices," Technical Memorandum TM 18-527, National Telecommunications and Information Administration, Nov. 2017.

[3] "Requirements for commercial operation in the U.S. 3550–3700 MHz citizens broadband radio service band," Wireless Innovation Forum Document WINNF-TS-0112, Version V1.5.0, May 2018.

[4] Paul D. Hale, Jeffrey A. Jargon, Peter J. Jeavons, Michael R. Souryal, Adam J. Wunderlich, and Mark Lofquist, "3.5 GHz radar waveform capture at Point Loma: Final test report," Technical Note 1954, National Institute of Standards and Technology, May 2017.

[5] Paul D. Hale, Jeffrey A. Jargon, Peter J. Jeavons, Michael R. Souryal, Adam J. Wunderlich, and Mark Lofquist, "3.5 GHz radar waveform capture at Fort Story: Final test report," Technical Note 1967, National Institute of Standards and Technology, Aug. 2017.

[6] Mark A. Richards, *Fundamentals of Radar Signal Processing, Second Edition*, McGraw-Hill Education, 2014.

[7] "Dynamic frequency selection in wireless access systems including radio local area networks for the purpose of protecting the radiodetermination service in the 5 GHz band," Recommendation ITU-R M.1652-1, 2011.

[8] Steven M. Kay, *Fundamentals of Statistical Signal Processing: Detection theory*, Prentice Hall Signal Processing Series. Prentice-Hall PTR, 1998.

[9] Michael G. Cotton and Roger A. Dalke, "Spectrum occupancy measurements of the 3550-3650 megahertz maritime radar band near San Diego, California," Technical Report TR 14-500, National Telecommunications and Information Administration, Jan. 2014.

[10] "LTE-evolved universal terrestrial radio access (E-UTRA) physical layer procedures," 3GPP Std. TS 36.213, V10.3.0 Release 10, 2011.




Caromi, Raied; Souryal, Michael; Yang, Wen-Bin.
"Detection of Incumbent Radar In the 3.5 GHZ CBRS Band."
Paper presented at 6th IEEE Global Conference on Signal and Information Processing (GlobalSIP 2018), Anaheim, CA, United States.
November 26, 2018 - November 28, 2018.

*Proc. of the 2018 International Symposium on Electromagnetic Compatibility (EMC Europe 2018), Amsterdam, The Netherlands, August 27–30, 2018.*

# High-resolution near-field imaging and far-field antenna measurements with atomic sensors

David A. Anderson*†, Eric Paradis†§, Georg Raithel†‡, Rachel E. Sapiro†, Matthew T. Simons¶, and Christopher L. Holloway¶
Rydberg Technologies, Ann Arbor, MI USA†
University of Michigan, Ann Arbor, MI USA‡
Eastern Michigan University, Ypsilanti, MI USA§
National Institute for Standards and Technology, Boulder, CO USA¶
*dave@rydbergtechnologies.com

***Abstract*—Measurements of radio-frequency (RF) electric fields using atomic sensors based on quantum-optical spectroscopy of Rydberg states in vapors has garnered significant interest in recent years for the establishment of atomic standards for RF electric fields and towards the development of novel RF sensing instrumentation. Here we describe recent work employing atomic sensors for sub-wavelength near-field imaging of a $K_u$-band horn antenna. We demonstrate near-field imaging capability at a spatial resolution of $\lambda/10$ and measurements over a 72 to 240 V/m field range using off-resonance AC-Stark shifts of a Rydberg-atom resonance. A fiber-coupled atomic-sensor probe is also employed in far-field measurements of a WR-90 standard gain horn.**

***Index Terms*—Atomic sensors, quantum sensing, Rydberg, atom, radio-frequency, RF, microwave, electric field, metrology, antenna, antenna characterization, electromagnetic compatibility.**

## I. Introduction

Atom-based sensing and measurement instrumentation for radio-frequency (RF) electric fields provides advantages over traditional antenna and solid-state detector technologies. The advantageas include small sensor sizes, absolute measurement capability (SI-based measurement), higher accuracy and precision, as well as the prospect of re-calibration-free operation, affording greater long-term measurement stability and reliability. Atomic sensors for electric fields are based on quantum-optical spectroscopy of atomic Rydberg states in vapors contained in spectroscopic cells [1]. This field measurement approach exploits the sensitivity of Rydberg atoms [2] to electric fields over a wide frequency range (MHz into the sub-THz) [3]–[7], and has garnered significant interest at National Metrology Institutes worldwide for the establishment of new atomic standards for electric fields [8]–[10], as well as in industry for the development of quantum electric-field sensing, measurement, and imaging technologies [11], [12]. Towards the establishment of new atomic electric-field standards, as well as sensors and instrumentation for metrology and RF measurement applications, the development of compact atomic sensors and probes and their implementation in high-spatial-resolution RF field measurements is desired. In this report we present recent work employing an atomic sensing element to image the near-field electric-field distribution of a $K_u$-band horn antenna. We demonstrate imaging at a $\sim \lambda/10$ spatial resolution for 13.4884 GHz fields over a field range from $\sim$72 to 240 V/m. The electric-field readout is obtained by optical detection of field-induced AC-Stark shifts of atomic Rydberg resonances in the sensor. Measured field profiles are in good agreement with calculated distributions. We also demonstrate the use of a fiber-coupled atomic-sensor probe in antenna pattern measurements in the far-field of a WR-90 horn. The presented work serves to pave the way towards atomic sensors and probes for use in metrology and RF measurement applications.

## II. RF electric-field measurements with atomic sensors

In our near-field experiments, the atomic sensing element comprises a glass cell filled with a rubidium (Rb) vapor. The active sensing region of the cell has a 3-mm inner-dimension; an elongated reservoir with a sample of Rb metal is located several centimeters away. Two counter-propagating lasers at wavelengths of 780 nm and 480 nm are focused and counter-propagated through the active region of the vapor cell for electromagnetically induced transparency (EIT) spectroscopy on field-sensitive Rydberg states. The 780 nm laser is frequency stabilized to the Rb $5S_{1/2}$ to $5P_{3/2}$ transition, whose absorption through the atomic medium is measured, as the 480 nm laser frequency is scanned linearly across a range of $5P_{3/2}$ to Rydberg-state transitions. The range of states and energy ranges scanned is adapted to the field-strength and frequency ranges of the RF fields to be measured. When the 480 nm laser frequency is tuned into resonance with a transition into an RF-perturbed Rydberg state, the laser mixes the 5P and the Rydberg state. This leads to a destructive quantum interference of excitation pathways that, over a narrow frequency range at the center of the resonance, results in an increased transmission for the 780 nm light through the vapor cell. These transmission peaks serve to locate the energy levels of the RF-perturbed Rydberg levels. The RF-induced energy shifts of the Rydberg levels as well as the measured splitting patterns of the spectroscopic lines provide an excellent measure for the RF electric field strength.



Holloway, Christopher; Simons, Matthew; Anderson, Dave; Raithel, Georg.
"High-resolution near-field imaging and far-field antenna measurements with atomic sensors."
Paper presented at 2018 International Symposium on Electromagnetic Compatibility (EMC), Amsterdam, Netherlands. August 27, 2018 - August 30, 2018.

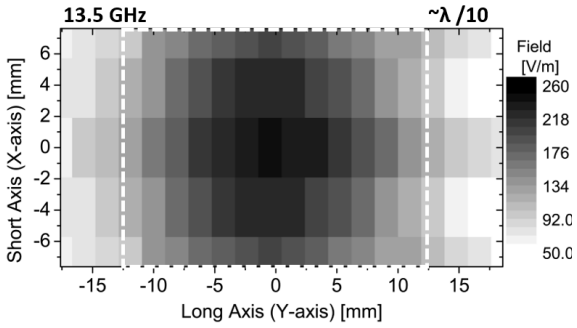


Fig. 1. Two-dimensional electric field distribution of a horn antenna, measured with an atomic sensing element on a plane of fixed distance from the horn aperture. The geometry of the horn aperture is indicated by the white dashed line.

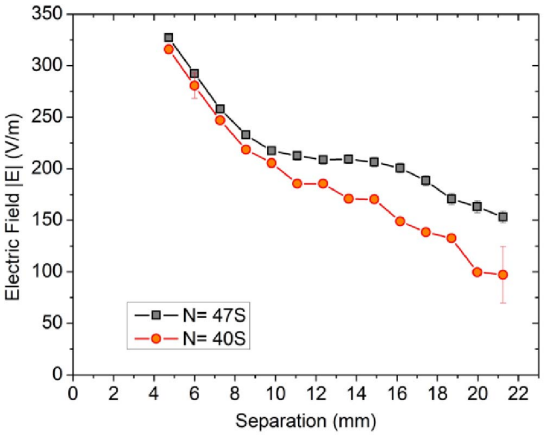


Fig. 2. Electric field versus distance along the bore-sight of the antenna measured with the atomic sensor.

## III. Near-field imaging of a horn antenna

We employ the atomic sensing element to measure the near-field of a $K_u$-band 0.695 x 1 inch pyramidal horn antenna emitting 13.4884 GHz fields (near-field range = 5.8 cm). The horn aperture is positioned at a distance z=7.5 mm from the sensing element and is translated in steps of $1.9 \pm 0.2$ mm across the long axis of the horn in the xy-plane.

Fig. 1 shows a two-dimensional spatial electric-field distribution. The image is composed of a field distribution measured over the top half of the plane and its mirror-image in the bottom half, symmetric across the short-axis zero. The electric field at each position of the horn is obtained from EIT detection of the RF-induced AC-Stark shift of the $47S_{1/2}$ Rydberg state using the relation $E = (4\Delta/\alpha)^{0.5}$, where $\Delta$ is the measured peak shift of the atomic line, and $\alpha = 4.099 \times 10^{-3}$ MHz/(V/m)$^2$ is the Rb 47S AC polarizability at 13.5 GHz. This relation holds in fields low enough that the field does not induce transitions, and that higher-order, non-quadratic shifts of the Rydberg level are not significant. The image shown in Fig. 1 is in good agreement with a calculated field distribution. A detailed analysis of experimental and calculated field distributions may provide insight into RF perturbations caused by the geometry and material of the vapor-cell sensing element, and is planned for upcoming work. This is a topic of particular importance in metrology applications of these atomic electric field sensors.

Fig. 2 shows measurements of the electric field as a function of distance along the bore-sight of the horn using the atomic sensor. Due to the $\sim n^7$-dependence of the atomic polarizability, the sensitivity of the atomic sensor to RF electric fields can be set by optically detecting states of different $n$ (and other quantum numbers). The measured profile along the bore-sight of the antenna was performed with the atomic sensor using both the $47S_{1/2}$ and $40S_{1/2}$ Rydberg states. The data in Fig. 2 for the $40S_{1/2}$ case shows a near-linear decrease in field strength as a function distance away from the horn, as one would expect. The data obtained with the more sensitive $47S_{1/2}$-state, on the other hand, exhibits a clear deviation from a linear drop-off. The measured deviation may be attributed to RF backscatter from nearby objects that could arise as the horn is translated away from the atomic sensor. In the data measured with the less sensitive $40S_{1/2}$-state this non-linear trend is seen less clearly (as one may expect from the lower sensitivity of that state). The deviations may also arise from standing-wave effects within the dielectric atomic sensing element itself, which has been seen in previous works. Simulations of this emitter and detector system are on-going to provide additional insight.

## IV. Far-field antenna pattern measurements

An atomic-sensor fiber-coupled probe is used to measure the antenna pattern of a Narda 640 standard gain horn antenna (mention of this product does not imply an endorsement, but serves to clarify the antenna used). The experimental setup for these measurements is shown in Fig. 3. Here, the probe was placed 0.835 m from the horn antenna in the quasi-far-field. The measurements are performed by scanning the antenna from bore-sight to an angle of $60^0$. The probe measures the RF E-field across both the E-plane and H-plane of the horn antenna using Autler-Townes splittings of a Rydberg resonance [3]. Fig. 4 shows the resultant measured antenna patterns for both the E-plane and H-plane at 11.6 GHz. For comparison and validation of the atom-based measurement method, we also show results obtained at a similar frequency (9.4 GHz) in an anechoic chamber test range [13]. The comparison measurements were performed with a traditional antenna-based microwave detector. We observe very good agreement between the atom-based and traditional (antenna-based) measurements. The observed deviations are attributed to the difference in frequency and to background scatter due to the atom-based measurements having been performed in a



Holloway, Christopher; Simons, Matthew; Anderson, Dave; Raithel, Georg.
"High-resolution near-field imaging and far-field antenna measurements with atomic sensors."
Paper presented at 2018 International Symposium on Electromagnetic Compatibility (EMC), Amsterdam, Netherlands. August 27, 2018 - August 30, 2018.

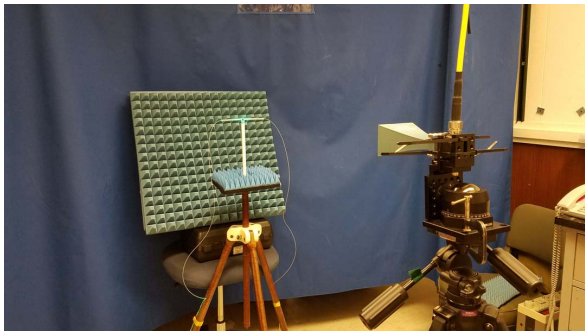

Fig. 3. Setup for horn antenna pattern measurements with a fiber-coupled atom-based microwave sensor.

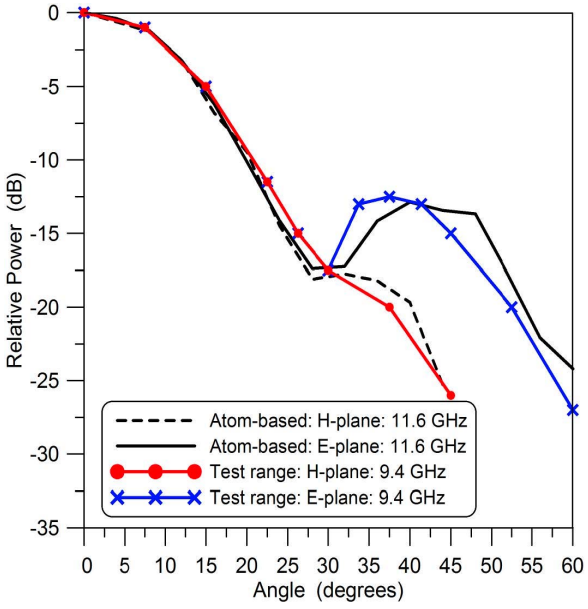


Fig. 4. Measured horn antenna pattern obtained with a fiber-coupled atom-based microwave sensor translated along a straight line from the horn (11.6-GHz data). For comparison and validation, we compare the atom-based data with data obtained on a traditional test range (9.4-GHZ data)

laboratory with no RF absorber on the walls and with several objects in the vicinity (see Fig. 3).

## V. Conclusion

We report on near-field imaging of a horn antenna using a small atomic vapor cell sensing element at a resolution of $\sim \lambda/10$ and covering a dynamic field range from $\sim$72 to 240 V/m using off-resonant AC-Stark shifts of a Rydberg resonance. The imaging results are in good agreement with calculations. We also demonstrate the implementation of a fiber-coupled atomic-sensor probe in far-field measurements of a WR-90 standard gain horn.

## Acknowledgment

This material was supported by Rydberg Technologies and is based upon work supported by the Defense Advanced Research Projects Agency (DARPA) and the Army Contracting Command-Aberdeen Proving Ground (ACC-APG) under Contract No. W911NF-15-P-0032.

## References

[1] A. K. Mohapatra, T. R. Jackson, and C. S. Adams, "Coherent optical detection of highly excited rydberg states using electromagnetically induced transparency," *Phys. Rev. Lett.*, vol. 98, p. 113003, Mar 2007. [Online]. Available: http://link.aps.org/doi/10.1103/PhysRevLett.98.113003

[2] T.F.Gallagher, *Rydberg Atoms*, 1994.

[3] J. A. Sedlacek, A. Schwettmann, H. Kübler, R. Löw, T. Pfau, and J. P. Shaffer, "Microwave electrometry with rydberg atoms in a vapour cell using bright atomic resonances," *Nat. Phys.*, vol. 8, pp. 819–824, November 2012.

[4] C. Holloway, J. Gordon, S. Jefferts, A. Schwarzkopf, D. Anderson, S. Miller, N. Thaicharoen, and G. Raithel, "Broadband rydberg atom-based electric-field probe for si-traceable, self-calibrated measurements," *IEEE Transactions on Antennas and Propagation*, vol. 62, no. 12, pp. 6169–6182, Dec 2014.

[5] M. T. Simons, J. A. Gordon, C. L. Holloway, D. A. Anderson, S. A. Miller, and G. Raithel, "Using frequency detuning to improve the sensitivity of electric field measurements via electromagnetically induced transparency and autler-townes splitting in rydberg atoms," *Applied Physics Letters*, vol. 108, no. 17, p. 174101, 2016. [Online]. Available: https://doi.org/10.1063/1.4947231

[6] D. A. Anderson, S. A. Miller, G. Raithel, J. A. Gordon, M. L. Butler, and C. L. Holloway, "Optical measurements of strong microwave fields with rydberg atoms in a vapor cell," *Phys. Rev. Applied*, vol. 5, p. 034003, Mar 2016. [Online]. Available: http://link.aps.org/doi/10.1103/PhysRevApplied.5.034003

[7] S. A. Miller, D. A. Anderson, and G. Raithel, "Radio-frequency-modulated rydberg states in a vapor cell," *New Journal of Physics*, vol. 18, no. 5, p. 053017, 2016. [Online]. Available: http://stacks.iop.org/1367-2630/18/i=5/a=053017

[8] J. A. Gordon, C. L. Holloway, A. Schwarzkopf, D. A. Anderson, S. Miller, N. Thaicharoen, and G. Raithel, "Millimeter wave detection via autler-townes splitting in rubidium rydberg atomsa)," *Applied Physics Letters*, vol. 105, no. 2, pp. –, 2014. [Online]. Available: http://scitation.aip.org/content/aip/journal/apl/105/2/10.1063/1.4890094

[9] C. L. Holloway, J. A. Gordon, A. Schwarzkopf, D. A. Anderson, S. A. Miller, N. Thaicharoen, and G. Raithel, "Sub-wavelength imaging and field mapping via electromagnetically induced transparency and autler-townes splitting in rydberg atoms," *Applied Physics Letters*, vol. 104, no. 24, pp. –, 2014. [Online]. Available: http://scitation.aip.org/content/aip/journal/apl/104/24/10.1063/1.4883635

[10] C. L. Holloway, M. T. Simons, J. A. Gordon, P. F. Wilson, C. M. Cooke, D. A. Anderson, and G. Raithel, "Atom-based rf electric field metrology: From self-calibrated measurements to subwavelength and near-field imaging," *IEEE Transactions on Electromagnetic Compatibility*, vol. 59, no. 2, pp. 717–728, April 2017.

[11] D. A. Anderson and G. Raithel, "Continuous-frequency measurements of high-intensity microwave electric fields with atomic vapor cells," *Applied Physics Letters*, vol. 111, no. 5, p. 053504, 2017. [Online]. Available: http://dx.doi.org/10.1063/1.4996234

[12] (2015) Rydberg technologies. [Online]. Available: http://www.rydbergtechnologies.com

[13] T. J. Duck, B. Firanski, F. D. Lind, and D. Sipler, "Aircraft-protection radar for use with atmospheric lidars," *Appl. Opt.*, vol. 44, no. 23, pp. 4937–4945, Aug 2005. [Online]. Available: http://ao.osa.org/abstract.cfm?URI=ao-44-23-4937



Holloway, Christopher; Simons, Matthew; Anderson, Dave; Raithel, Georg.
"High-resolution near-field imaging and far-field antenna measurements with atomic sensors."
Paper presented at 2018 International Symposium on Electromagnetic Compatibility (EMC), Amsterdam, Netherlands. August 27, 2018 - August 30, 2018.

# Antenna Radiation Pattern Measurements Using a Reverberation Chamber

Audrey K. Puls[12]
Dept. of Electrical, Computer, and Energy Engineering
University of Colorado – Boulder
Boulder, CO, USA
audrey.puls@colorado.edu

John M. Ladbury[3]
National Institute of Standards and Technology
Boulder, CO, USA
john.ladbury@nist.gov

William F. Young
University of Colorado – Denver
Denver, CO, USA
william.young@ucdenver.edu

***Abstract*— This paper investigates the use of a reverberation chamber for antenna radiation pattern measurements allowing for significant cost reduction compared to anechoic environments. Our method utilizes averaging of paddle measurements to replicate anechoic data. We discuss both a correlation experiment, to determine how many degrees the reverberation paddle must rotate to create an uncorrelated measurement based on a 0.5 correlation threshold, and a radiation pattern measurement. Two matched horn antennas are used and operated between 1 GHz and 18 GHz. Good agreement is found between our measurements taken in a reverberation chamber and those taken by the manufacturer of the antenna in an anechoic chamber. We find that the main lobe radiation pattern of our antenna can be estimated with more certainty than the back-lobe radiation using a reverberation chamber. The goal is to use this simple and cost-effective method to determine radiation patterns for embedded antennas with unknown patterns, such as those within wireless devices.**

***Keywords*— *Anechoic Chamber, Correlation, Directivity, Horn Antenna, Reverberation Chamber, Standard Deviation of the Mean, Vector Network Analyzer.***

## I. Introduction

Antenna radiation pattern measurements are typically performed in an anechoic chamber. These chambers are often expensive to install and inconvenient to rent from external facilities. Validating a lower cost method for these measurements is of general interest. Reverberation chambers are well understood [1] but have only recently been used for radiation pattern measurements [2][3] due to their significant cost reduction compared to anechoic environments. While [2] and [3] use plane wave decomposition, spherical wave decomposition, and Doppler effects to extract a radiation pattern, our approach lends simplicity to the problem by averaging scattering parameter data of uncorrelated paddle-positions. In this way, the variations in power, due to the position of the paddles, can be averaged out to mimic the isotropic environment typically found in an anechoic chamber. Our radiation pattern data will be shown and compared with manufacturer data taken in an anechoic chamber.

This method can potentially be used to measure radiation patterns of embedded antennas with unknown patterns, such as those within wireless devices.

The method discussed in this work utilizes an unloaded reverberation chamber, of dimensions 4.74 meters long by 4.13 meters wide by 5.18 meters tall, mode-stirring paddle, robotic arm, tripod, vector network analyzer, two horn antennas operating between 1 GHz and 18 GHz, and software to create an automated data collection system.

This paper is summarized as follows: Section II describes a paddle correlation experiment similar to that described in [4] and is performed to determine how many degrees the reverberation chamber paddle must rotate to create an uncorrelated measurement. This is important as it determines the minimum set of data, and hence shortest data collection time required to gather all necessary data. Section III uses the paddle step size correlation data from Section II to setup and determine the antenna radiation pattern measurements in a reverberation chamber. Section IV concludes this paper.

## II. Reverberation Chamber Paddle Correlation

This section describes the reverberation chamber paddle-angle correlation experiment which determines how many degrees the vertical reverberation chamber paddle must rotate to produce an uncorrelated measurement. The chamber also contains a horizontal paddle, which is kept fixed during the experiment. In this way, we replicate a single stirrer reverberation chamber which is most commonly used and most likely to be procured by other facilities who may wish to reproduce this work.

### *A. Setup and Procedure*

The setup for the paddle correlation experiment is shown in Fig. 1. The horizontal paddle is not shown as it is stationary for the duration of the test. The setup uses one horn antenna (our antenna under test (AUT)) attached to a robotic arm, which can rotate in the horizontal plane, and one horn

[1] This work was performed under the financial assistance award 70NANB18H006 from U.S. Department of Commerce, National Institute of Standards and Technology"

[2] Associate of the National Institute of Standards and Technology, Boulder, Colorado 80305, USA



Puls, Audrey.
"Antenna Radiation Pattern Measurements Using a Reverberation Chamber."
Paper presented at 40th Annual Meeting and Symposium of the Antenna Measurement Techniques Association (AMTA 2018), Williamsburg, VA, United States. November 4, 2018 - November 9, 2018.

antenna (our measurement antenna) attached to a stationary tripod. Both are connected to a vector network analyzer outside the chamber through bulkhead connections in the wall of the reverberation chamber. Note that the paddle is asymmetric about 180°. That is, if the paddle is rotated 1° clockwise, data will differ from that obtained when rotated 1° counterclockwise.

The antennas are cross-polarized and oriented with the main beams pointed away from each other in different height planes to minimize direct line-of-sight coupling and ensure coupling through reflections, thus aiding in creating a well-stirred environment.

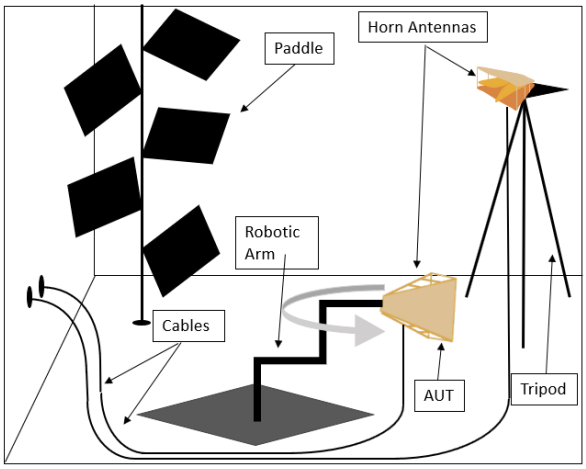


Fig. 1. Reverberation chamber paddle-angle correlation experiment setup. The antennas are cross polarized, in different height planes, and oriented away from each other to minimize direct line-of-sight coupling and ensure coupling through reflections in the chamber. Note that the arrow does not necessarily show the direction of rotation, but rather illustrates the axis of rotation and joint from which the robot pivots in the horizontal plane.

The procedure measures transmission S-parameter data ($S_{21}$) when the paddle is positioned at zero degrees. The data are taken in real and imaginary format. The paddle is then moved in 1° increments taking data each time, until one full rotation is complete (i.e., 1° steps in a 360° rotation). This 360° rotation and measurements are repeated 50 times.

### B. Post Processing and Results

The measured $S_{21}$ data were averaged over 50 trials, in which real and imaginary components were averaged separately, resulting in one complex average sample value per paddle position. A linear autocorrelation function, which utilizes the Fourier transform, is used with a 0.5 correlation threshold to determine how many degrees the paddle must rotate to produce an uncorrelated measurement. Note that a 0.5 correlation threshold is used to remain consistent with what was done in [4]. However, a 1/e threshold could also be used, which would produce an 8° rotation for an uncorrelated measurement. Results at 1 GHz and 18 GHz are shown in Fig. 2 via a solid and dotted line respectively. Mathematically, the autocorrelation function doubles the data, which can be seen in the spread about the 360° mark in Fig. 2. For this reason, Fig. 2 shows 720° on the x-axis, and the final rotation measurement required by the paddle to form an uncorrelated measurement is half the bandwidth at 360° which yields 6° at 1 GHz. These results determine paddle step size (6°) which will be used to collect antenna radiation pattern measurements discussed in Section III.

### C. Differences with Similar Work

While there are many similarities between this experiment and [4], there are also a few significant differences. The first is that our work uses a different chamber than in [4] so any values obtained in [4] will differ. In addition [4] used a loaded chamber, but we use an unloaded chamber. Also important is that [4] used two paddles (vertical and horizontal) while in our experiment only one vertical paddle is rotated. Lastly, the data shown in [4] utilized a circular autocorrelation, which results in 360 points on the x-axis of the Fig. 2 equivalent plot shown in [4]. This method allowed for the full bandwidth of the spike to be used to determine an uncorrelated measurement. Our method utilizes a linear autocorrelation which results in 720 points on the x-axis of Fig. 2. This method allows for the half bandwidth of the spike to be used to determine an uncorrelated measurement. Either method is valid and will produce similar results.

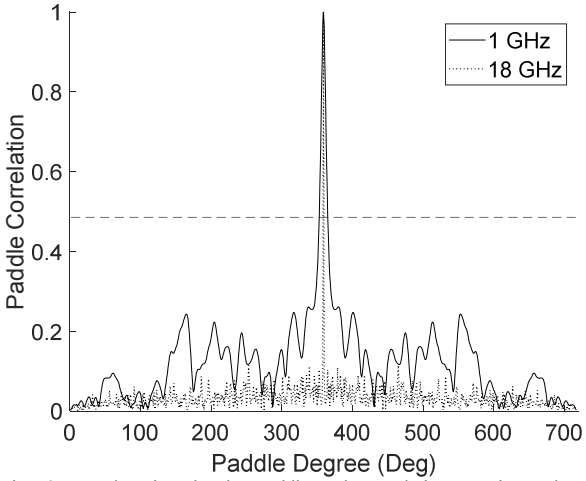


Fig. 2. Reverberation chamber paddle-angle correlation experiment data. Correlation results are indicated by half the bandwidth at 360° at the 0.5 correlation threshold mark. A 6° paddle rotation yields an uncorrelated measurement.

## III. Antenna Radiation Pattern Measurements

This section will discuss the setup, procedure, and results of the antenna radiation pattern measurements in the reverberation chamber.

### A. Setup and Procedure

The setup, shown in Fig. 3, aims to maximize transmission from one antenna to the other in order to collect the antenna radiation pattern. The idea is that the stirred energy will average to zero over the stirring sequence leaving only the line-of-sight, which corresponds to the antenna-to-

Puls, Audrey.
"Antenna Radiation Pattern Measurements Using a Reverberation Chamber."
Paper presented at 40th Annual Meeting and Symposium of the Antenna Measurement Techniques Association (AMTA 2018), Williamsburg, VA, United States. November 4, 2018 - November 9, 2018.

antenna coupling. For this reason, the antennas are co-polarized and directed at each other in the same height plane. Note also that the position of the tripod and attached antenna has changed from Fig. 1 to align the main lobe of the radiation pattern with the 0° mark, for easy comparison with manufacturer data, which will be shown later. Note that the antenna connected to the robot rotates in the horizontal plane.

The procedure starts by positioning the reverberation chamber paddles and both antennas at position zero (pointed towards each other) and collecting transmission data ($S_{21}$) in real and imaginary format. While both antennas are held constant, the vertical reverberation paddle is rotated in 6° increments until a full 360° rotation has been completed. This produces an uncorrelated measurement for frequencies between 1 GHz and 18 GHz using a 0.5 correlation threshold as found in the correlation study. Data are taken each time the paddle rotates 6°. The antenna attached to the robotic arm is then incremented by 1° and the process repeats until the antenna has made a full rotation.

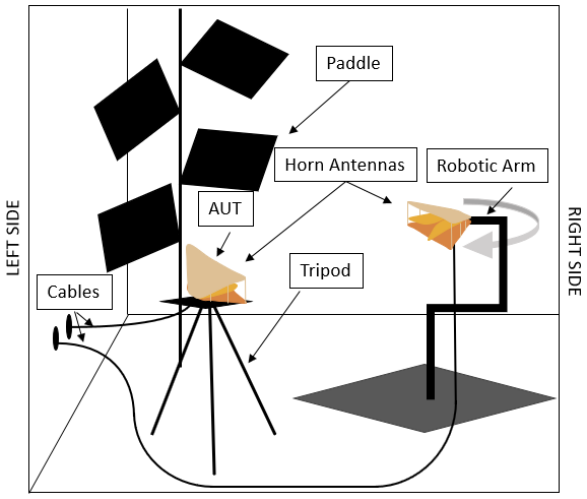


Fig. 3. Antenna pattern measurement setup in reverberation chamber. The antennas are co-polarized, pointed towards each other, and in the same height plane to maximize line-of-sight coupling. Note that the arrow does not necessarily show the direction of rotation, but rather illustrates the axis of rotation and joint from which the robot pivots in the horizontal plane.

Distances between the chamber and various components shown in Fig. 3 are given in Table I. Note that the antenna connected to the robot will rotate in the horizontal plane. Because of this, all measurements in Table I, that reference the antenna placed on the robot specify the position of the robot (towards the tripod antenna face or away from the tripod antenna face). The use of directional words (i.e., left and right) in Table I refer to the orientation specified in Fig. 3.

TABLE I. DISTANCES BETWEEN COMPONENTS IN FIG. 3 SETUP

| Measurement Start | Measurement End | Value |
|---|---|---|
| Base of Tripod Antenna | Left Wall | 75 cm |
| Tripod Antenna Face | Robot Antenna Face | 61 cm |
| Base of Robot Antenna Pointed Towards Tripod Antenna | Right Wall | 235 cm |
| Base of Robot Antenna Pointed 180° Away from Tripod Antenna | Right Wall | 175 cm |
| Robot's Point of Rotation | Face of Robot Antenna | 42 cm |
| Robot's Point of Rotation | Back Wall | 235 cm |
| Robot's Point of Rotation | Front Wall | 241 cm |
| Length of Chamber | N/A | 4.74 m |
| Width of Chamber | N/A | 4.13 m |
| Height of Chamber | N/A | 5.18 m |

### B. *Post Processing and Results*

Plots showing the real and imaginary $S_{21}$ components of the 60 paddle positions at 1, 3, 6, 12, and 18 GHz are shown in Fig. 4 when the antennas are pointed directly at each other. Note that the 60 paddle positions become more tightly grouped as the frequency increases, indicating lower uncertainties at higher frequencies. We will show that our radiation pattern data agree more closely with the radiation patterns measured by the manufacturer as the frequency increases.

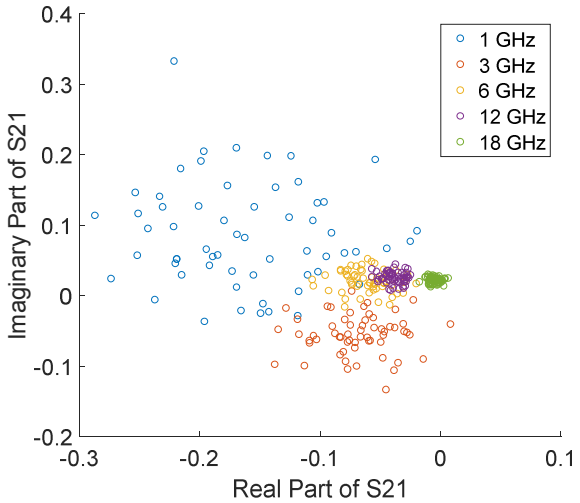


Fig. 4. 60 paddle positions at 1, 3, 6, 12, and 18 GHz when antennas are directly pointed at each other.

During post processing, all 60 paddle positions, taken each time the robotic arm antenna rotates 6°, are averaged (real and imaginary components are averaged separately). The magnitude of this complex value is taken and converted to dB. This value is what is plotted in Fig. 5 and Fig. 6. By averaging out the variations due to the paddle positions, the data mimics that which is typically taken in an anechoic

Puls, Audrey.
"Antenna Radiation Pattern Measurements Using a Reverberation Chamber."
Paper presented at 40th Annual Meeting and Symposium of the Antenna Measurement Techniques Association (AMTA 2018), Williamsburg, VA, United States. November 4, 2018 - November 9, 2018.

chamber. All data are frequency swept between 1 GHz and 18 GHz using 2001 equally-spaced points.

Radiation patterns in Fig. 5 and Fig. 6 show data from our measurements taken in a reverberation chamber compared with the manufacturer data taken in an anechoic chamber at 1, 3, 6, 12, and 18 GHz. No frequency averaging is performed on experimental data.

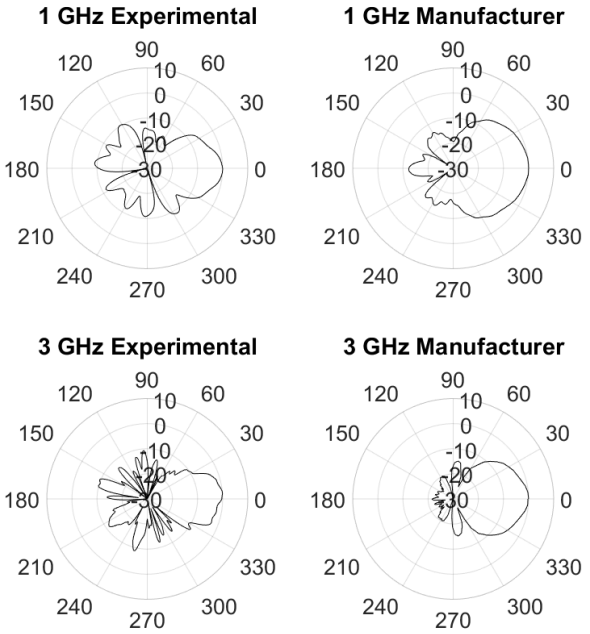


Fig. 5. Antenna-radiation pattern data from our experiment in the reverberation chamber (left) and from the manufacturer in an anechoic chamber (right) at 1 GHz and 3 GHz.

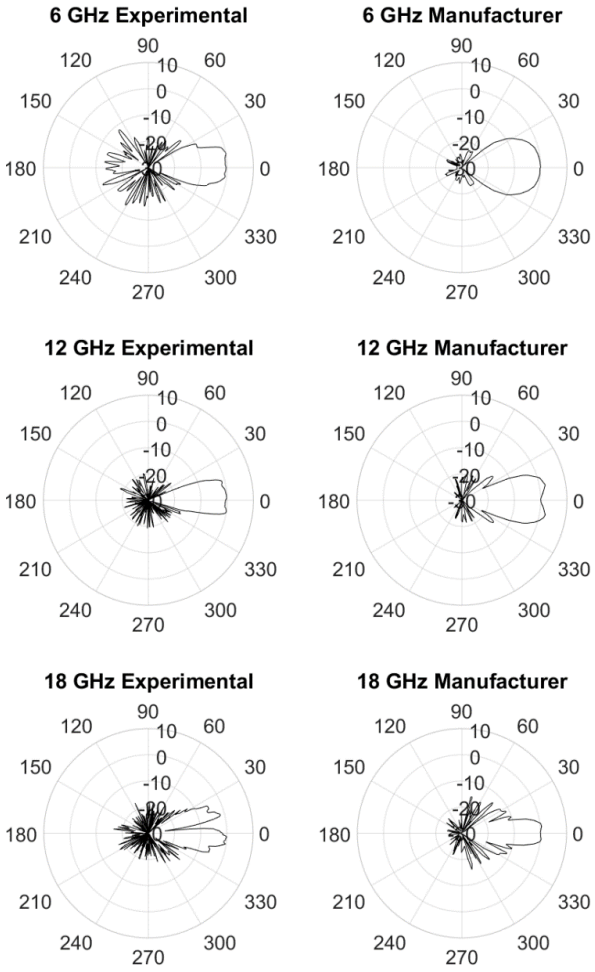


Fig. 6. Antenna-radiation pattern data from our experiment in the reverberation chamber (left) and from the manufacturer in an anechoic chamber (right) at 6 GHz, 12 GHz, and 18 GHz.

### *C. Estimate of Accuracy*

The standard deviation of the mean (σ) gives an estimate of the variability of our data, and is calculated according to (1), where < > indicates complex averaging over all 60 paddle positions.

$$\sigma = \frac{\sqrt{<|S_{21}-<S_{21}>|^2>}}{\sqrt{N}}, \sqrt{N} = 60 \quad (1)$$

If we divide $|<S_{21}>|$ by σ we can get an idea of the relative quality of the estimates at each frequency. This value would ideally be large, indicating σ is small relative to the measured $|<S_{21}>|$ value.

$|<S_{21}>|/\sigma$ ranges from 14 to 39 when the antennas are pointed at each other, and from 1 to 5 when one antenna is rotated 180 degrees away from the other for frequencies between 1 GHz and 18 GHz. The general trend of these values is to increase with frequency as the antennas align to

Puls, Audrey.
"Antenna Radiation Pattern Measurements Using a Reverberation Chamber."
Paper presented at 40th Annual Meeting and Symposium of the Antenna Measurement Techniques Association (AMTA 2018), Williamsburg, VA, United States. November 4, 2018 - November 9, 2018.

face each other. These data are plotted against frequency in Fig. 7.

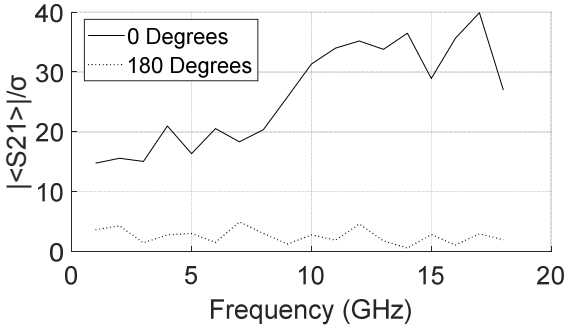


Fig. 7. $|<S_{21}>| / \sigma$ plotted against frequency when the faces of both antennas are pointed at each other (0° in legend, shown by solid line) and when the antenna connected to the robotic arm has rotated by 180° in the horizontal plane (180° in legend, shown by dotted line).

The estimate of quality decreases as the antenna connected to the robotic arm rotates further away from the face of the stationary antenna. This tells us that we are more confident in our ability to estimate the main lobe, and less confident in our sidelobe and back-lobe radiation estimate. This could explain why the experimental data of Fig. 5 and Fig. 6 show higher back-lobe radiation compared to manufacturer data.

Fig. 8 shows $|<S_{21}>|$ and σ versus frequency for antenna positions 0°, 5°, 20°, 90°, 180°, 270°, 340°, 355°, and 359°, where 0° indicates both antenna faces are pointed at each other, and 180° indicates the antenna on the robotic arm has been rotated by 180° in the horizontal plane. The ideal data would yield a σ that is significantly lower than $|<S_{21}>|$ in all cases. Fig. 8 shows that as the antenna connected to the robotic arm is rotated away from the face of the stationary antenna, σ and $|<S_{21}>|$ become closer together. This is a visual way of determining that our back-lobe radiation measurements are not as accurate as our main lobe measurements.

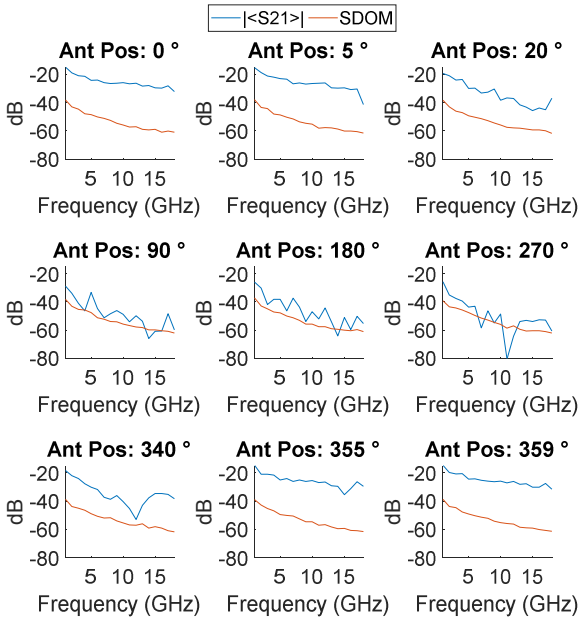


Fig. 8. S21 averaged over paddle positions and σ versus frequency for antenna positions 0°, 5°, 20°, 90°, 180°, 270°, 340°, 355°, and 359° where 0° indicates both antenna faces are pointed at each other, and 180° indicates one antenna has been rotated by 180° in the horizontal plane.

## IV. Conclusion

The process described in this paper results in good agreement between experimental and manufacturer data, with high certainty in estimating the main lobe beams. Our certainty decreases as the antenna attached to the robotic arm rotates further from the stationary antenna face. Our data show enough certainty to demonstrate the potential of our simplistic and cost-effective method of antenna radiation pattern measurements in a reverberation chamber. In the future, radiation pattern measurements for the same horn antenna with the same experimental setup will be performed in our facilities' anechoic chamber to eliminate any experimental differences between the manufacturer anechoic chamber data and our experimental reverberation chamber data.

## Acknowledgments

We acknowledge Jason Coder, Ryan Jacobs, Kate Remley, Robert Horansky, Robert Jones, and Michael Janezic for their help throughout this project.

## References

[1] D. A. Hill, "Electromagnetic Theory of Reverberation Chambers," in National Institute of Standards and Technology NIST Tech. Note 1506, Boulder, CO, USA, Dec. 1998.

[2] M. Á. García-Fernández, D. Carsenat, and C. Decroze, "Antenna Radiation Pattern Measurements in Reverberation Chamber Using Plane Wave Decomposition," IEEE Trans. Antennas Propag., vol. 61, no. 10, pp. 5000–5007, Oct. 2013.

[3] Q. Xu, Y. Huang, “3D Antenna Radiation Pattern Reconstruction in a Reverberation Chamber Using Spherical Wave Decomposition,” IEEE Trans. Antennas Propag., vol. 65, no. 4, pp. 1728-1739, Apr. 2017.

[4] Ryan J. Pirkl, Kate A. Remley, Christian S. Lötbäck Patané “Reverberation Chamber Measurement Correlation”, IEEE Trans. Electromagnetic Compatibility, vol. 54, no 3, pp. 533-545, June 2012.

Puls, Audrey.
”Antenna Radiation Pattern Measurements Using a Reverberation Chamber.”
Paper presented at 40th Annual Meeting and Symposium of the Antenna Measurement Techniques Association (AMTA 2018), Williamsburg, VA, United States. November 4, 2018 - November 9, 2018.

# Gradient-Based Solution of Maximum Likelihood Angle Estimation for Virtual Array Measurements

Peter Vouras, Alec Weiss, Maria Becker, Ben Jamroz, Jeanne Quimby, Dylan Williams, Kate Remley
*National Institute of Standards and Technology, Gaithersburg, MD*

***Abstract*—This paper derives a gradient-based implementation of maximum likelihood angle estimation for virtual planar arrays used to sound millimeter wave channels.**

## I. Introduction

Precise measurement and characterization of millimeter wave channels requires antennas capable of high angular resolution to resolve closely spaced multipath sources. To achieve angular resolution on the order of a few degrees these antennas must be electrically large which is impractical for phased array architectures at these frequencies. An alternative approach is to synthesize a virtual aperture in space by using an accurate mechanical positioner to move a receive antenna to points along a sampling grid. An advantage of creating virtual apertures is that the received signal is digitized at every spatial sample position which enables the use of sophisticated angle estimation algorithms such as maximum likelihood techniques. The main contribution of this paper is a new gradient based implementation of maximum likelihood angle estimation that was demonstrated on virtual array data collected at 28 GHz using a vector network analyzer.

## II. Overview of Maximum Likelihood Angle Estimation

Consider a virtual array that responds to a single polarization created using $N$ spatial samples taken with an omnidirectional antenna on a planar grid. Assume $Q$ narrowband sources in the far field of the receive antenna impinge on the array from the directions $(\theta_0,\phi_0),(\theta_1,\phi_1),\ldots,(\theta_{Q-1},\phi_{Q-1})$ in a spherical coordinate system. The complex envelope of the signal received at the $i$th virtual array element is

$$x_i(t)=\sum_{k=0}^{Q-1}s_k(t)e^{-j\omega_0\tau_i(\theta_k,\phi_k)}+n_i(t) \tag{1}$$

where $s_k(t)$ denotes the signal emanating from the $k$th source as observed at the first array element, $\omega_0$ is the center frequency of the sources, $\tau_i(\theta_k,\phi_k)$ is the incremental delay from the first array element to the $i$th array element for a plane wave impinging on the array from the direction $(\theta_k,\phi_k)$, and $n_i(t)$ is additive zero-mean white measurement noise at the $i$th element that is assumed to be independent across array elements. Since the sources are narrowband, the interelement delays of the $k$th signal, $\tau_i(\theta_k,\phi_k)$ for $i=0,\ldots,N-1$, correspond to incremental phase shifts as the plane wave traverses across the virtual aperture. Thus, (1) can be rewritten as

$$x_i(t)=\sum_{k=0}^{Q-1}s_k(t)e^{-j\frac{2\pi}{\lambda}(md_xu+nd_yv)}+n_i(t) \tag{2}$$

where for $N=N_xN_y$, $m=0,\ldots,N_x-1$ is the element index in the x-direction, $n=0,\ldots,N_y-1$ is the element index in the y-direction, $d_x$ is the spacing between elements in the x-direction, $d_y$ is the spacing between elements in the y-direction, and $u=\sin\theta\cos\phi$, $v=\sin\theta\sin\phi$.

The array output vector of signals received at each array element can be written as

$$\mathbf{x}(t)=\sum_{k=0}^{Q-1}\mathbf{a}(u_k,v_k)s_k(t)+\mathbf{n}(t) \tag{3}$$

where $\mathbf{x}(t)=[x_0(t),\ldots,x_{N-1}(t)]^T$, $\mathbf{n}(t)=[n_0(t),\ldots,n_{N-1}(t)]^T$ and $\mathbf{a}(u_k,v_k)$ is the $N\times 1$ steering vector of the array in the direction $(u_k,v_k)$ given by,

$$\mathbf{a}(u_k,v_k)= \tag{4}$$
$$\left[e^{-j\frac{2\pi}{\lambda}(md_xu_k+nd_yv_k)}\Big|\,0\leq m\leq N_x-1,0\leq n\leq N_y-1\right]^T.$$

Using matrix notation yields,

$$\mathbf{x}(t)=\mathbf{A}(\mathbf{u},\mathbf{v})\mathbf{s}(t)+\mathbf{n}(t) \tag{5}$$

where $\mathbf{A}(\mathbf{u},\mathbf{v})$ is the $N\times Q$ matrix of steering vectors

$$\mathbf{A}(\mathbf{u},\mathbf{v})=[\mathbf{a}(u_0,v_0),\ldots,\mathbf{a}(u_{Q-1},v_{Q-1})] \tag{6}$$

and $\mathbf{u}=[u_0,\ldots,u_{Q-1}]^T$, $\mathbf{v}=[v_0,\ldots,v_{Q-1}]^T$, and $\mathbf{s}(t)$ is the $Q\times 1$ vector of signals $\mathbf{s}(t)=[s_1(t)\quad s_2(t),\ldots,s_{Q-1}(t)]^T$. Assume the signals received at each array element are digitized over $M$ time instants $t_0,\ldots,t_{M-1}$. The sampled measurements can be expressed as

$$\mathbf{X}=\mathbf{A}(\mathbf{u},\mathbf{v})\mathbf{S}+\mathbf{N} \tag{7}$$

with

$$\begin{aligned}\mathbf{X}&=[\mathbf{x}(t_0),\ldots,\mathbf{x}(t_{M-1})]_{N\times M}\\ \mathbf{N}&=[\mathbf{n}(t_0),\ldots,\mathbf{n}(t_{M-1})]_{N\times M}\\ \mathbf{S}&=[\mathbf{s}(t_0),\ldots,\mathbf{s}(t_{M-1})]_{Q\times M}.\end{aligned} \tag{8}$$

The objective of the maximum likelihood (ML) angle estimator is to determine the incoming directions $(u_0,v_0),(u_1,v_1),\ldots,(u_{Q-1},v_{Q-1})$ of the $Q$ multipath sources from the $M$ array snapshots $\mathbf{x}(t_0),\ldots,\mathbf{x}(t_{M-1})$. The underlying assumptions necessary for deriving the ML

Vouras, Peter.
"Gradient-Based Solution of Maximum Likelihood Angle Estimation for Virtual Array Measurements."
Paper presented at 6th IEEE Global Conference on Signal and Information Processing (GlobalSIP 2018), Anaheim, CA, United States.
November 26, 2018 - November 28, 2018.

estimator are that the number of sources $Q$ is known or can be estimated and that $Q < N$, the steering vectors $\mathbf{a}(u_k, v_k)$ are linearly independent for $k = 0, \ldots, Q-1$, and $E[\mathbf{n}(t)\mathbf{n}(t)^H] = \sigma_n^2\mathbf{I}$. As described in [1], the computation of the ML angle estimator proceeds by determining the joint probability density function of the sampled data and subsequently the log-likelihood function that must then be maximized with respect to the unknown angles. The final result is that the ML estimates of the directions $(u_0, v_0), (u_1, v_1), \ldots, (u_{Q-1}, v_{Q-1})$ can be obtained by maximizing the function

$$\max_{\mathbf{u},\mathbf{v}} \quad J(\mathbf{u}, \mathbf{v}) = \text{tr}[\mathbf{P}_{\mathbf{A}(\mathbf{u},\mathbf{v})}\widehat{\mathbf{R}}] \tag{9}$$

where the sample covariance matrix is

$$\widehat{\mathbf{R}} = \frac{1}{M}\sum_{k=0}^{M-1} \mathbf{x}(t_k)\mathbf{x}(t_k)^H \tag{10}$$

and $\mathbf{P}_{\mathbf{A}(\mathbf{u},\mathbf{v})}$ is the projection matrix onto the range space of $\mathbf{A}(\mathbf{u}, \mathbf{v})$,

$$\begin{aligned}\mathbf{P}_{\mathbf{A}(\mathbf{u},\mathbf{v})} &= \mathbf{A}(\mathbf{u}, \mathbf{v})\left[\mathbf{A}(\mathbf{u}, \mathbf{v})^H\mathbf{A}(\mathbf{u}, \mathbf{v})\right]^{-1}\mathbf{A}(\mathbf{u}, \mathbf{v})^H \\ &= \mathbf{A}(\mathbf{u}, \mathbf{v})\mathbf{A}(\mathbf{u}, \mathbf{v})^\dagger,\end{aligned} \tag{11}$$

with † used to denote the pseudoinverse.

### A. Alternating Projections Algorithm

The alternating projections (AP) algorithm maximizes the MLE cost function $J(\mathbf{u}, \mathbf{v})$ with respect to one pair of parameters $(u_k, v_k)$ while holding the other parameters fixed. Since iterations of the AP algorithm perform a maximization at every step, the value of $J(\mathbf{u}, \mathbf{v})$ can never decrease, so the algorithm is guaranteed to converge to a local maximum. Depending on the initial conditions, the local maximum may or may not coincide with the global maximum. Since $J(\mathbf{u}, \mathbf{v})$ will in general have many local maxima, proper initialization is vital for the AP algorithm to converge to the global solution.

At the core of the AP algorithm is a projection matrix decomposition described as follows. Consider two arbitrary matrices $\mathbf{X}$ and $\mathbf{Y}$ with the same number of rows. The projection matrix $\mathbf{P}_{[\mathbf{X},\mathbf{Y}]}$ onto the column space of the augmented matrix $[\mathbf{X}, \mathbf{Y}]$ is equal to

$$\mathbf{P}_{[\mathbf{X},\mathbf{Y}]} = \mathbf{P}_{[\mathbf{X},\mathbf{Y}_\mathbf{X}]} \tag{12}$$

where the matrix

$$\mathbf{Y}_\mathbf{X} = \mathbf{P}_\mathbf{X}^\perp\mathbf{Y} = (\mathbf{I} - \mathbf{P}_\mathbf{X})\mathbf{Y}. \tag{13}$$

The symbol $\perp$ is used to denote the orthogonal complement of $\mathbf{P}_\mathbf{X}$. The columns of $\mathbf{Y}_\mathbf{X}$ span the subspace orthogonal to the projection of the range space of $\mathbf{Y}$ onto the range space of $\mathbf{X}$. Since the column space of $\mathbf{Y}_\mathbf{X}$ is orthogonal to the column space of $\mathbf{X}$ and their direct sum spans the column space of $[\mathbf{X}, \mathbf{Y}]$, it follows that

$$\mathbf{P}_{[\mathbf{X},\mathbf{Y}]} = \mathbf{P}_\mathbf{X} + \mathbf{P}_{\mathbf{Y}_\mathbf{X}}. \tag{14}$$

Applying (12) and (14) to $\mathbf{P}_{\mathbf{A}(\mathbf{u},\mathbf{v})}$ yields

$$\begin{aligned}\mathbf{P}_{\mathbf{A}(\mathbf{u},\mathbf{v})} &= \mathbf{P}_{[\mathbf{A}(\widehat{\mathbf{u}}_k,\widehat{\mathbf{v}}_k),\mathbf{a}(u_k,v_k)]} \\ &= \mathbf{P}_{\mathbf{A}(\widehat{\mathbf{u}}_k,\widehat{\mathbf{v}}_k)} + \mathbf{P}_{\mathbf{a}(u_k,v_k)_{\mathbf{A}(\widehat{\mathbf{u}}_k,\widehat{\mathbf{v}}_k)}}\end{aligned} \tag{15}$$

where the $(Q-1)\times 1$ vectors $\widehat{\mathbf{u}}_k$ and $\widehat{\mathbf{v}}_k$ are

$$\begin{aligned}\widehat{\mathbf{u}}_k &= [u_0, u_1, \ldots, u_{k-1}, u_{k+1}, \ldots, u_{Q-1}]^T \\ \widehat{\mathbf{v}}_k &= [v_0, v_1, \ldots, v_{k-1}, v_{k+1}, \ldots, v_{Q-1}]^T\end{aligned} \tag{16}$$

and the $N \times (Q-1)$ matrix $\mathbf{A}(\widehat{\mathbf{u}}_k, \widehat{\mathbf{v}}_k)$ is

$$\begin{aligned}&\mathbf{A}(\widehat{\mathbf{u}}_k, \widehat{\mathbf{v}}_k) = \\ &[\mathbf{a}(u_0, v_0), ..., \mathbf{a}(u_{k-1}, v_{k-1}), \mathbf{a}(u_{k+1}, v_{k+1}), ..., \mathbf{a}(u_{Q-1}, v_{Q-1})]\,.\end{aligned} \tag{17}$$

Rewriting the maximization problem in (9) to search along the $k$th spatial direction $(u_k, v_k)$ at the $(l+1)$st algorithm iteration while holding all other directions fixed yields

$$u_k^{(l+1)}, v_k^{(l+1)} = \arg\max_{u_k,v_k} \quad \text{tr}[\mathbf{P}_{[\mathbf{A}(\widehat{\mathbf{u}}_k^{(l)},\widehat{\mathbf{v}}_k^{(l)}),\mathbf{a}(u_k,v_k)]}\widehat{\mathbf{R}}]. \tag{18}$$

Equation (18) states that to obtain the angle estimates $u_k^{(l+1)}, v_k^{(l+1)}$ for the $k$th source at the $(l+1)$st algorithm iteration, the parameters $\widehat{\mathbf{u}}_k^{(l)}, \widehat{\mathbf{v}}_k^{(l)}$ are held fixed while the parameters $u_k, v_k$ are free to vary. Applying the matrix decomposition in (14) to (18) and ignoring the first term in the summation since it is constant yields the equivalent maximization problem

$$u_k^{(l+1)}, v_k^{(l+1)} = \arg\max_{u_k,v_k} \quad \text{tr}[\mathbf{P}_{\mathbf{a}(u_k,v_k)_{\mathbf{A}(\widehat{\mathbf{u}}_k^{(l)},\widehat{\mathbf{v}}_k^{(l)})}}\widehat{\mathbf{R}}]. \tag{19}$$

Using (13) and (11) the vector $\mathbf{a}(u_k, v_k)_{\mathbf{A}(\widehat{\mathbf{u}}_k^{(l)},\widehat{\mathbf{v}}_k^{(l)})}$ can be written as

$$\begin{aligned}&\mathbf{a}(u_k, v_k)_{\mathbf{A}(\widehat{\mathbf{u}}_k^{(l)},\widehat{\mathbf{v}}_k^{(l)})} = \left[\mathbf{I} - \mathbf{P}_{\mathbf{A}(\widehat{\mathbf{u}}_k^{(l)},\widehat{\mathbf{v}}_k^{(l)})}\right]\mathbf{a}(u_k, v_k) \\ &= \left[\mathbf{I} - \mathbf{A}(\widehat{\mathbf{u}}_k^{(l)}, \widehat{\mathbf{v}}_k^{(l)})\mathbf{A}(\widehat{\mathbf{u}}_k^{(l)}, \widehat{\mathbf{v}}_k^{(l)})^\dagger\right]\mathbf{a}(u_k, v_k).\end{aligned} \tag{20}$$

Equation (20) shows that the vector $\mathbf{a}(u_k, v_k)_{\mathbf{A}(\widehat{\mathbf{u}}_k^{(l)},\widehat{\mathbf{v}}_k^{(l)})}$ is orthogonal to the projection of $\mathbf{a}(u_k, v_k)$ onto the column space of $\mathbf{A}(\widehat{\mathbf{u}}_k^{(l)}, \widehat{\mathbf{v}}_k^{(l)})$. Also by (11)

$$\begin{aligned}&\mathbf{P}_{\mathbf{a}(u_k,v_k)_{\mathbf{A}(\widehat{\mathbf{u}}_k^{(l)},\widehat{\mathbf{v}}_k^{(l)})}} = \\ &= \frac{\left[\mathbf{a}(u_k, v_k)_{\mathbf{A}(\widehat{\mathbf{u}}_k^{(l)},\widehat{\mathbf{v}}_k^{(l)})}\right]\left[\mathbf{a}(u_k, v_k)_{\mathbf{A}(\widehat{\mathbf{u}}_k^{(l)},\widehat{\mathbf{v}}_k^{(l)})}\right]^H}{\left[\mathbf{a}(u_k, v_k)_{\mathbf{A}(\widehat{\mathbf{u}}_k^{(l)},\widehat{\mathbf{v}}_k^{(l)})}\right]^H\left[\mathbf{a}(u_k, v_k)_{\mathbf{A}(\widehat{\mathbf{u}}_k^{(l)},\widehat{\mathbf{v}}_k^{(l)})}\right]}.\end{aligned} \tag{21}$$

Define the unit norm vector

$$\mathbf{b}_k^{(l)} \equiv \mathbf{b}(u_k, v_k; \widehat{\mathbf{u}}_k^{(l)}, \widehat{\mathbf{v}}_k^{(l)}) = \frac{\mathbf{a}(u_k, v_k)_{\mathbf{A}(\widehat{\mathbf{u}}_k^{(l)},\widehat{\mathbf{v}}_k^{(l)})}}{\|\mathbf{a}(u_k, v_k)_{\mathbf{A}(\widehat{\mathbf{u}}_k^{(l)},\widehat{\mathbf{v}}_k^{(l)})}\|_2} \tag{22}$$

and substitute (21) into (20). By applying properties of the trace operator including $\text{tr}(\mathbf{AB}) = \text{tr}(\mathbf{BA})$, the optimization problem in (19) becomes

$$\begin{aligned}u_k^{(l+1)}, v_k^{(l+1)} &= \arg\max_{u_k,v_k} \quad {\mathbf{b}_k^{(l)}}^H\widehat{\mathbf{R}}\mathbf{b}_k^{(l)} \\ &\equiv \arg\max_{u_k,v_k} \quad J^l(u_k, v_k).\end{aligned} \tag{23}$$

Vouras, Peter.
"Gradient-Based Solution of Maximum Likelihood Angle Estimation for Virtual Array Measurements."
Paper presented at 6th IEEE Global Conference on Signal and Information Processing (GlobalSIP 2018), Anaheim, CA, United States.
November 26, 2018 - November 28, 2018.

The entire AP algorithm can now be summarized as follows,

Algorithm 1. MLE-AP Algorithm to Compute Angles of Arrival

**Require:** Initial or a priori angle estimates $u_0^{(0)},\ldots,u_{Q-1}^{(0)}$ and $v_0^{(0)},\ldots,v_{Q-1}^{(0)}$

1: Set algorithm iteration $l=1$

2: Until $\left|u_k^{(l+1)}-u_k^{(l)}\right|^2<\epsilon$ and $\left|v_k^{(l+1)}-v_k^{(l)}\right|^2<\epsilon$ for all $k=0,\ldots,Q-1$, compute the AOA estimates for the $k$th source by solving $u_k^{(l+1)},v_k^{(l+1)}=\arg\max_{u_k,v_k} \quad J^l(u_k,v_k)$

The two primary contributions of this paper described in the next sections are a successful approach to initialize the MLE-AP algorithm and a gradient-based method to maximize the cost function $J^l(u_k,v_k)$ at each iteration.

## III. Gradient-Based Implementation of MLE-AP Algorithm

### A. Derivation of Gradient Vector

In this section an analytical expression for the gradient vector of the $(l+1)$st cost function specified in (23) is derived. To start, rewrite the cost function as

$$J^l(u_k,v_k)= \tag{24}$$
$$\frac{\mathbf{a}(u_k,v_k)^H\left[\mathbf{I}-\mathbf{P}_{\mathbf{A}(\widehat{\mathbf{u}}_k^{(l)},\widehat{\mathbf{v}}_k^{(l)})}\right]^H\widehat{\mathbf{R}}\left[\mathbf{I}-\mathbf{P}_{\mathbf{A}(\widehat{\mathbf{u}}_k^{(l)},\widehat{\mathbf{v}}_k^{(l)})}\right]\mathbf{a}(u_k,v_k)}{\mathbf{a}(u_k,v_k)^H\left[\mathbf{I}-\mathbf{P}_{\mathbf{A}(\widehat{\mathbf{u}}_k^{(l)},\widehat{\mathbf{v}}_k^{(l)})}\right]\mathbf{a}(u_k,v_k)}$$
$$\equiv\frac{\mathbf{a}(u_k,v_k)^H\mathbf{B}\mathbf{a}(u_k,v_k)}{\mathbf{a}(u_k,v_k)^H\mathbf{Q}\mathbf{a}(u_k,v_k)}$$

by substituting (20) into (23) and noting that the idempotent and self-adjoint properties of orthogonal projection matrices imply that $\left[\mathbf{I}-\mathbf{P}_{\mathbf{A}(\widehat{\mathbf{u}}_k^{(l)},\widehat{\mathbf{v}}_k^{(l)})}\right]^H\left[\mathbf{I}-\mathbf{P}_{\mathbf{A}(\widehat{\mathbf{u}}_k^{(l)},\widehat{\mathbf{v}}_k^{(l)})}\right]=\left[\mathbf{I}-\mathbf{P}_{\mathbf{A}(\widehat{\mathbf{u}}_k^{(l)},\widehat{\mathbf{v}}_k^{(l)})}\right]$.

Note that the steering vector $\mathbf{a}(u_k,v_k)$ defined in (4) can be rewritten as the Kronecker product of two steering vectors,

$$\mathbf{a}(u_k,v_k)=\left[e^{-j\frac{2\pi}{\lambda}md_xu_k}\right]^T\otimes\left[e^{-j\frac{2\pi}{\lambda}nd_yv_k}\right]^T \tag{25}$$

with $0{\le}m{\le}N_x-1$ and $0{\le}n{\le}N_y-1$. Hereafter, to simplify notation, the subscript $k$ denoting the $k$th AOA source will be dropped from the coordinates $u,v$. Next consider a change in pointing direction corresponding to $(\delta_u,\delta_v)$. Then,

$$\mathbf{a}(u+\delta_u,v+\delta_v)= \tag{26}$$
$$\left[e^{-j\frac{2\pi}{\lambda}md_x(u+\delta_u)}\,\middle|\,0{\le}m{\le}N_x-1\right]^T\otimes$$
$$\left[e^{-j\frac{2\pi}{\lambda}nd_y(v+\delta_v)}\,\middle|\,0{\le}n{\le}N_y-1\right]^T.$$

Define the diagonal matrices,

$$\mathbf{\Delta}u=\delta_u\begin{bmatrix}0&0&0&0&0\\0&\frac{2\pi}{\lambda}d_x&0&0&0\\0&0&\frac{2\pi}{\lambda}2d_x&0&0\\\vdots&\vdots&\vdots&\ddots&\vdots\\0&0&0&0&\frac{2\pi}{\lambda}(N_x-1)d_x\end{bmatrix} \tag{27}$$
$$=\delta_u\mathbf{T}_x$$

and similarly $\mathbf{\Delta}v=\delta_v\mathbf{T}_y$ using $d_y$ instead of $d_x$. Then using the identity

$$\mathbf{\Delta}u\oplus\mathbf{\Delta}v=\mathbf{\Delta}u\otimes\mathbf{I}+\mathbf{I}\otimes\mathbf{\Delta}v \tag{28}$$

and the properties of the matrix exponential, the perturbed steering vector $\mathbf{a}(u+\delta_u,v+\delta v)$ can be written as

$$\mathbf{a}(u+\delta_u,v+\delta v)=e^{-j\mathbf{\Delta}u}\otimes e^{-j\mathbf{\Delta}v}\mathbf{a}(u,v) \tag{29}$$
$$=e^{-j(\mathbf{\Delta}u\oplus\mathbf{\Delta}v)}\mathbf{a}(u,v).$$

At this point it is useful to clarify the overarching strategy for computing the gradient vector of the cost function $J(u,v)$ in (24), where the superscript iteration index $l$ has been dropped for simplicity. A related approach is also described in [2]. The desired gradient vector of $J(u,v)$ to be computed is defined as $\nabla J=\left[{}^{\partial J}/_{\partial u}\quad {}^{\partial J}/_{\partial v}\right]^T$. In terms of numerator and denominator functions, $J(u,v)={}^{N(u,v)}/_{D(u,v)}$, so using the quotient rule for differentiation yields

$$\frac{\partial J}{\partial u}=\frac{\frac{\partial N}{\partial u}D(u,v)-\frac{\partial D}{\partial u}N(u,v)}{D(u,v)^2} \tag{30}$$
$$\frac{\partial J}{\partial v}=\frac{\frac{\partial N}{\partial v}D(u,v)-\frac{\partial D}{\partial v}N(u,v)}{D(u,v)^2}.$$

It is clear that to apply the quotient rule for computing $\nabla J$ it is also necessary to compute $\nabla N=\left[{}^{\partial N}/_{\partial u}\quad {}^{\partial N}/_{\partial v}\right]^T$ and $\nabla D=\left[{}^{\partial D}/_{\partial u}\quad {}^{\partial D}/_{\partial v}\right]^T$. A useful fact is that since the numerator function $N$ is continuously differentiable with respect to $u$ and $v$, the directional derivative $N'(\mathbf{p};\mathbf{d})$ of $N$ at the point $\mathbf{p}=[u\quad v]^T$ in the direction $\mathbf{d}=[\delta_u\quad \delta_v]^T$ is equal to [3]

$$N'(\mathbf{p};\mathbf{d})=\nabla N(\mathbf{p})^T\mathbf{d}. \tag{31}$$

In the case at hand, $\nabla N$ is unknown and the quantity to be determined, but the directional derivative $N'(\mathbf{p};\mathbf{d})$ can also be calculated as the derivative with respect to $t$ of the function $G_N(t)=N(\mathbf{p}+t\mathbf{d})$ evaluated at $t=0$,

$$N'(\mathbf{p};\mathbf{d})=\left.\frac{d}{dt}G_N(t)\right|_{t=0}=\left.\frac{d}{dt}N(\mathbf{p}+t\mathbf{d})\right|_{t=0}. \tag{32}$$

Thus $\nabla N$ can be recovered by using (32) to compute the directional derivative $N'(\mathbf{p};\mathbf{d})$ and then writing the result in a form compatible with (31) to recover the gradient vector. The same procedure also applies to the denominator function $D(u,v)$ using the derivative with respect to $t$ of the function $G_D(t)=D(\mathbf{p}+t\mathbf{d})$ evaluated at $t=0$.

Continuing along this tack and starting with $D(u,v)$ yields,

$$G_D(t)=D(u+t\delta_u,v+t\delta_v)= \tag{33}$$
$$=\mathbf{a}(u+t\delta_u,v+t\delta_v)^H\mathbf{Q}\mathbf{a}(u+t\delta_u,v+t\delta_v)$$
$$=\mathbf{a}(u,v)^He^{j(\mathbf{\Delta}u\oplus\mathbf{\Delta}v)t}\mathbf{Q}e^{-j(\mathbf{\Delta}u\oplus\mathbf{\Delta}v)t}\mathbf{a}(u,v)$$

Vouras, Peter.
"Gradient-Based Solution of Maximum Likelihood Angle Estimation for Virtual Array Measurements."
Paper presented at 6th IEEE Global Conference on Signal and Information Processing (GlobalSIP 2018), Anaheim, CA, United States.
November 26, 2018 - November 28, 2018.

and the desired directional derivative

$$
\begin{aligned}
D'(\mathbf{p};\mathbf{d}) &= j\mathbf{a}(u,v)^H \left[\boldsymbol{\Delta}u \oplus \boldsymbol{\Delta}v, \mathbf{Q}\right] \mathbf{a}(u,v) \qquad (34)\\
&= j\text{tr}\left(\left[\boldsymbol{\Delta}u \oplus \boldsymbol{\Delta}v, \mathbf{Q}\right] \mathbf{a}(u,v)\mathbf{a}(u,v)^H\right)\\
&= j\text{tr}\left(\left[\delta_v\mathbf{T}_y \oplus \delta_u\mathbf{T}_x, \mathbf{Q}\right] \mathbf{a}(u,v)\mathbf{a}(u,v)^H\right)\\
&= j\text{tr}\left(\left(\left[\delta_u\mathbf{T}_x \otimes \mathbf{I}, \mathbf{Q}\right] + \left[\mathbf{I} \otimes \delta_v\mathbf{T}_y, \mathbf{Q}\right]\right) \mathbf{a}(u,v)\mathbf{a}(u,v)^H\right)\\
&= j\left[\text{tr}\left(\left[\delta_u\mathbf{T}_x \otimes \mathbf{I}, \mathbf{Q}\right] \mathbf{a}(u,v)\mathbf{a}(u,v)^H\right)\right.\\
&\qquad \left.+\text{tr}\left(\left[\mathbf{I} \otimes \delta_v\mathbf{T}_y, \mathbf{Q}\right] \mathbf{a}(u,v)\mathbf{a}(u,v)^H\right)\right]\\
&= j\left[\delta_u\text{tr}\left(\left[\mathbf{T}_x \otimes \mathbf{I}, \mathbf{Q}\right] \mathbf{a}(u,v)\mathbf{a}(u,v)^H\right)\right.\\
&\qquad \left.+\delta_v\text{tr}\left(\left[\mathbf{I} \otimes \mathbf{T}_y, \mathbf{Q}\right] \mathbf{a}(u,v)\mathbf{a}(u,v)^H\right)\right]
\end{aligned}
$$

where the notation $[\mathbf{A},\mathbf{B}]$ denotes the Lie bracket, $[\mathbf{A},\mathbf{B}] = \mathbf{AB} - \mathbf{BA}$. Rewriting (34) in matrix form and comparing to (31) yields

$$
\begin{aligned}
&D'(\mathbf{p};\mathbf{d}) = \qquad (35)\\
&\begin{bmatrix} -\text{imag}\left(\text{tr}\left(\left[\mathbf{T}_x \otimes \mathbf{I}, \mathbf{Q}\right] \mathbf{a}(u,v)\mathbf{a}(u,v)^H\right)\right) \\ -\text{imag}\left(\text{tr}\left(\left[\mathbf{I} \otimes \mathbf{T}_y, \mathbf{Q}\right] \mathbf{a}(u,v)\mathbf{a}(u,v)^H\right)\right) \end{bmatrix}^T \begin{bmatrix} \delta_u \\ \delta_v \end{bmatrix}\\
&\equiv \nabla D(\mathbf{p})^T\mathbf{d}. \qquad (36)
\end{aligned}
$$

Repeating the same argument for the numerator function $N(u,v)$ results in

$$
\begin{aligned}
&N'(\mathbf{p};\mathbf{d}) = \qquad (37)\\
&\begin{bmatrix} -\text{imag}\left(\text{tr}\left(\left[\mathbf{T}_x \otimes \mathbf{I}, \mathbf{B}\right] \mathbf{a}(u,v)\mathbf{a}(u,v)^H\right)\right) \\ -\text{imag}\left(\text{tr}\left(\left[\mathbf{I} \otimes \mathbf{T}_y, \mathbf{B}\right] \mathbf{a}(u,v)\mathbf{a}(u,v)^H\right)\right) \end{bmatrix}^T \begin{bmatrix} \delta_u \\ \delta_v \end{bmatrix}\\
&\equiv \nabla N(\mathbf{p})^T\mathbf{d}. \qquad (38)
\end{aligned}
$$

Now the components of $\nabla N$ and $\nabla D$ are clearly available to substitute into (30) to compute $\nabla J$.

### B. Conjugate Gradient Algorithm

The conjugate gradient algorithm for maximizing the cost function in (23) for the $k$th AOA source at the $l$th iteration of the MLE-AP algorithm is,

Algorithm 2. Conjugate Gradient Algorithm

**Require:** Initial angle estimates $u_0$ and $v_0$. One approach for obtaining $u_0$ and $v_0$ is to compute (39) over all possible angles and choose the peaks in the output.

1: Set the initial search direction $\mathbf{d}_0 = \nabla J(u_0, v_0)$
2: Until $\|\nabla J(u_j, v_j)\|_2 \leq \epsilon$, where $j$ denotes the conjugate gradient iteration index, do the following:
3: Determine the step-size $\mu_j$
4: Set $\mathbf{p}_{j+1} = \mathbf{p}_j + \mu_j\mathbf{d}_j$ where $\mathbf{p}_j = [u_j \quad v_j]^T$
5: Set $\mathbf{g}_{j+1} = \nabla J(u_{j+1}, v_{j+1})$
6: Set $\mathbf{d}_{j+1} = \mathbf{g}_{j+1} + \alpha_j\mathbf{d}_j$
7: Set $\alpha_j = \frac{\mathbf{g}_{j+1}^T(\mathbf{g}_{j+1}-\mathbf{g}_j)}{\mathbf{g}_j^T\mathbf{g}_j}$
8: Set $j = j + 1$

The step-size $\mu_j$ for the $j$th conjugate gradient iteration can be set equal to a constant value small enough to ensure algorithm convergence or it can be chosen via a one-dimensional line search. The preferred approach is to use Armijo's rule. Given an initial stepsize, $0 < \rho < 1$, Armijo's rule chooses the final stepsize $\mu_j$ to be the first value in the sequence $1, \rho, \rho^2, \rho^3, \ldots$ that satisfies the condition $J(\mathbf{p}_j + \mu_j\mathbf{d}_j) \geq J(\mathbf{p}_j) + \mu_j\alpha\nabla J(\mathbf{p}_j)^T\mathbf{d}_j$, for a fixed scalar $0 < \alpha < 0.5$. In other words, $\mu_j = \rho^m$ for some integer $m$.

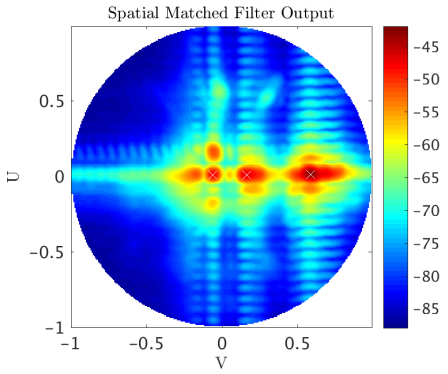


Fig. 1. Output of Spatial Matched Filter

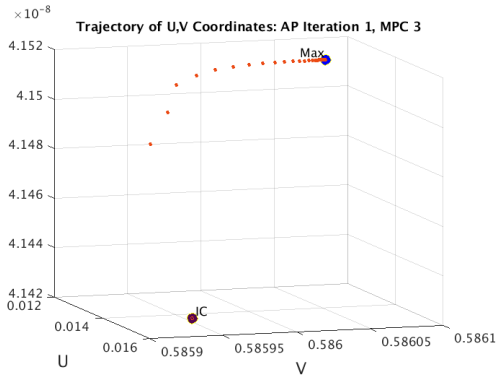


Fig. 2. Algorithm Convergence Trajectory: Multipath Cluster 3

## IV. Measured Results and Conclusions

Since the cost function $J(\mathbf{p})$ has multiple peaks it is necessary to properly initialize the conjugate gradient algorithm to ensure that it converges to the correct solution. A simple approach is to compute the output of a spatial matched filter $s$ for all $u, v$ directions in space as given by

$$s(u,v) = \mathbf{a}(u,v)^H\widehat{\mathbf{R}}\mathbf{a}(u,v) \qquad (39)$$

and then choose the largest peaks for initial angle estimates. Figure 1 illustrates the output of the spatial matched filter for virtual array data collected in a lab room. The white crosses correspond to the multipath peaks detected using a thresholding algorithm. These peaks are used to initialize the conjugate gradient MLE algorithm. Figure 2 illustrates the algorithm's path to convergence for the third multipath source. In all cases the algorithm converged within less than 40 iterations.

## References


[1] I. Ziskind and M. Wax, "Maximum Likelihood Localization of Multiple Sources by Alternating Projection," *IEEE Transactions on Acoustics,*



Vouras, Peter.
"Gradient-Based Solution of Maximum Likelihood Angle Estimation for Virtual Array Measurements."
Paper presented at 6th IEEE Global Conference on Signal and Information Processing (GlobalSIP 2018), Anaheim, CA, United States.
November 26, 2018 - November 28, 2018.

*Speech, and Signal Processing*, Vol. 36, No. 10, October 1988, pp. 1553-1560.

[2] S. T. Smith, "Optimum Phase-Only Adaptive Nulling," *IEEE Transactions on Acoustics, Speech, and Signal Processing*, Vol. 47, No. 7, July 1999, pp. 1835-1843.

[3] D. P. Bertsekas, *Nonlinear Programming*, 2nd ed., Athena Scientific, Belmont, MA, 1995.

Vouras, Peter.
"Gradient-Based Solution of Maximum Likelihood Angle Estimation for Virtual Array Measurements."
Paper presented at 6th IEEE Global Conference on Signal and Information Processing (GlobalSIP 2018), Anaheim, CA, United States.
November 26, 2018 - November 28, 2018.

# Systematic Study: Channel Sounding via Modal Expansion

Alex J. Yuffa, Benjamin F. Jamroz, Jacob D. Rezac, Dylan F. Williams
National Institute of Standards and Technology
Boulder, CO 80305, USA
alex.yuffa@nist.gov

***Abstract*—We present a preliminary study of a modal (partial wave) expansion of the field used to characterize a propagation channel. We assume that the measurements of the scalar, two-dimensional field from which the modal expansion coefficients are obtained, contain Gaussian phase noise with zero mean. Three spatial sampling patterns of the field are considered. We find that the accuracy of the reconstructed field is strongly influenced by the spatial sampling pattern.**

## I. Introduction

The use of robotics and optical tracking in RF measurements has created both new opportunities and challenges in the characterization of antennas and propagation channels. With these systems, it is possible to sample an RF field inside a volume while maintaining almost absolute control over the spatial positioning. For decades, antennas in the near field have been characterized via modal (partial wave) expansions, where the modal expansion coefficients are calculated from regularly spaced measurements on some canonical surface. Recently, these modal expansions have been used to characterize propagation channels [1]–[3] in order to accurately estimate the performance of advanced communications technology in complex environments.

A number of questions naturally arise when we use a modal expansion to characterize a propagation channel:

- How many modes should we keep in the expansion? What are the consequences of this on the condition number of the matrix that will need to be inverted to find the expansion coefficients?
- How should the RF field be spatially sampled? For example, should we sample the field on a canonical surface or is it better to sample the field throughout a volume? Should these samples be regularly or randomly spaced?
- How accurate should each measurement be in order to achieve an estimate of the expansion coefficients within a given tolerance?

The above questions are interdependent and, because of the large parameter space, answering them via computer simulations is a daunting task. Therefore, we present a systematic study of the above questions using the simplified model of scalar waves in two-dimensions.



In this work, we assume that each measurement contains zero-mean Gaussian phase noise. Phase error can be representative of component level distortions including thermal effects, cable bending [4], and timing errors. Additionally, the spatial positioning errors will primarily manifest themselves in the phase measurements because the amplitude varies very little over small distances relative to wavelength $\lambda$. Incorporating realistic phase errors into our analysis allows a more direct comparison to existing channel measurements.

To the best of our knowledge, no such systematic study has been previously reported in the literature. Throughout this paper, we use the Système International (SI) unit system and assume that all fields are harmonic in time with a suppressed $\exp(-\mathrm{i}\omega t)$ time factor, where $\omega$ is the angular frequency.

## II. Problem Formulation

Consider a disk region $\Omega$ of radius $R$ that is source-free. Then, the total field $U(r,\theta)$ in $\Omega$ can be written as

$$U(r,\theta) = \sum_{n=-\infty}^{\infty} A_n J_n(kr)\mathrm{e}^{\mathrm{i}n\theta}, \tag{1}$$

where $J_n$ is the integer order Bessel function of the first kind, $k$ is the free-space wavenumber, and $(r \geq 0, -\pi \leq \theta < \pi)$ are the polar coordinates centered on $\Omega$. In practical computations, the infinite sum in (1) must be truncated. One usually chooses to truncate the sum at $N \sim kR$ because $J_n(kr)$ decays rapidly when $n \geq kr$. In particular, we use the modified Wiscombe's criterion $N(\eta)$ [5], [6] to determine $N$; namely,

$$N(\eta) = \begin{cases} 2, & 0 < \eta < 0.02 \\ \lceil \eta + 4\eta^{1/3} + 1 \rceil, & 0.02 \leq \eta \leq 8 \\ \lceil \eta + 4.05\eta^{1/3} + 2 \rceil, & 8 < \eta < 4200 \\ \lceil \eta + 4\eta^{1/3} + 2 \rceil, & 4200 \leq \eta \end{cases}, \tag{2}$$

where $\lceil\ \rceil$ denotes the ceiling function. If all of the measurements are taken on the boundary of $\Omega$, then $N$ is given by (2) with $\eta = kR$. However, if the measurement is taken at the point $(r_m, \theta_m)$, where $r_m < R$, then we terminate the sum at $N(kr_m)$. In other words, the unknown coefficients $A_n$ are determined from a linear system

$$U(r_m,\theta_m) = \sum_{n=-N_m}^{N_m} A_n J_n(kr_m)\mathrm{e}^{\mathrm{i}n\theta_m}, \tag{3}$$

Yuffa, Alexey; Jamroz, Benjamin; Rezac, Jake; Williams, Dylan.
"A Systematic Study: Channel Sounding via Modal Expansion."
Paper presented at 2018 Antenna Measurement Techniques Association Symposium (AMTA), Williamsburg, VA, United States. November 4, 2018 - November 9, 2018.

where $N_m = N(kr_m)$, $U(r_m, \theta_m)$ is the measured (known) field at the point $(r_m, \theta_m)$, and $m = 1, \ldots, M$. We solve the linear system (3) in the least squares sense assuring that a formal solution exists. Of course, if the measured data are too noisy and/or the number of measurements $M$ is too small, then the least squares solution will produce a poor estimate of the field. In this case, we could consider a solution technique designed to operate well in the presence of noise, such as Tikhonov regularization. We note that terminating the sum in (3) based on the radial location of the measurement point instead of the boundary of $\Omega$ is important in order to maintain a reasonable condition number for the linear system. This is because the measurement at the radial distance $r_m$ contains very little information about the expansion coefficients $A_n$, where $n > kr_m$ (recall that $J_n(kr_m) \approx 0$ when $n > kr_m$).

## III. Results

We numerically study the method described in Sec. II by solving (3) in the least squares sense to obtain an approximation to the field $V(r, \theta)$. The field $V(r, \theta)$ is composed of 12 plane waves and is shown in Fig. 1. To avoid a possible source of confusion, we will refer to the field $V(r, \theta)$ as the "true" field in $\Omega$.

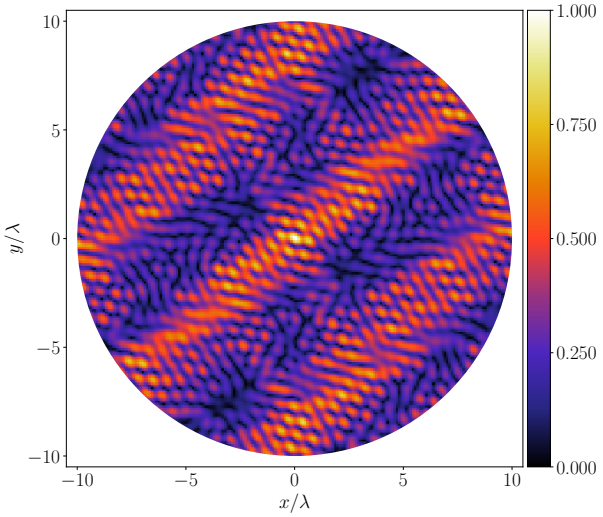


Fig. 1: (Color online) The amplitude (in arb. unit) of the true field $V(r, \theta) \in \Omega$ is shown as a function of $x = r\cos\theta$ and $y = r\sin\theta$.

Throughout the paper, we consider three spatial sampling patterns of the true field:

(i) a uniform Cartesian grid superimposed over $\Omega$,
(ii) a set of Cartesian points $(x_m, y_m)$ in $\Omega$ randomly drawn from a uniform distribution,
(iii) a set of points on the boundary of $\Omega$ separated by some angle $\triangle\theta$; i.e., $x_m = R\cos(m\triangle\theta)$ and $y_m = R\sin(m\triangle\theta)$.

We shall refer to these as uniform, random, and boundary sampling patterns, respectively.

The condition number of the matrix associated with (3) depends on the chosen spatial sampling pattern. The condition number for each of the spatial sampling patterns as a function of the sampling density is shown in Fig. 2. From the figure, we see that the three spatial sampling patterns have a similar condition number of $\sim 10^5$ if the field is estimated from a reasonable number of measurements. Thus, we conclude that the loss of precision caused by the numerical method used to solve the linear system is approximately the same for all three sampling patterns.

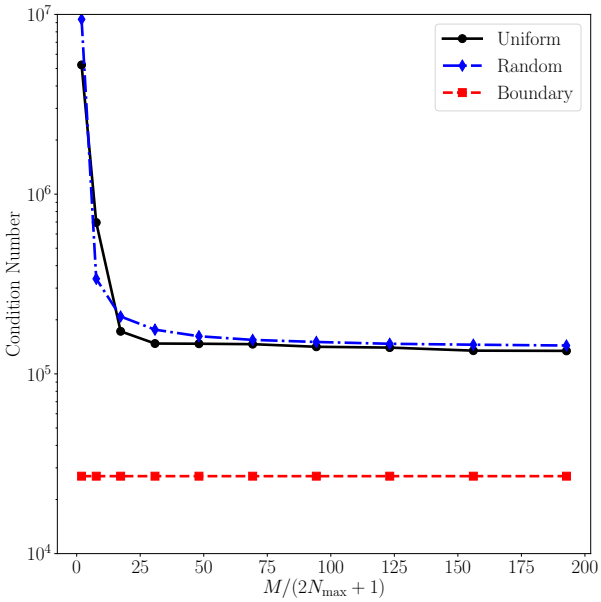


Fig. 2: (Color online) The condition number for uniform, random, and boundary sampling patterns is shown as a function of the sampling density.

We measure the accuracy of the reconstructed field $U(r, \theta)$ in terms of the number of significant digits it agrees with the true field $V(r, \theta)$. The number of the correct significant digits is approximated from the relative error via

$$\delta(r,\theta) = \begin{cases} -\log_{10}\frac{|U(r,\theta)-V(r,\theta)|}{|V(r,\theta)|} & \text{if} \quad |V(r,\theta)| > \epsilon \\ \text{undefined} & \text{if} \quad |V(r,\theta)| \le \epsilon \end{cases}, \quad (4)$$

where $\epsilon = 10^{-5/2}$ (50 dB). Figures 3–5 show the approximate number of the correct significant digits for each of the spatial sampling patterns when the measurement of the true field $V(r, \theta)$ contains $10^\circ$ zero-mean Gaussian phase noise. The expansion coefficients $A_n$ associated with Fig. 3 were calculated from $M = 1576$ measurement points; in the case of uniform sampling, this corresponds to sampling every $0.45\lambda$. From Fig. 3, we see that the uniform and random sampling methods yield approximately the same results at this sampling density. We also see that the boundary sampling method performs the worst, especially near the the boundary of $\Omega$. The expansion coefficients $A_n$ associated with Fig. 4 and Fig. 5

Yuffa, Alexey; Jamroz, Benjamin; Rezac, Jake; Williams, Dylan.
"A Systematic Study: Channel Sounding via Modal Expansion."
Paper presented at 2018 Antenna Measurement Techniques Association Symposium (AMTA), Williamsburg, VA, United States. November 4, 2018 - November 9, 2018.

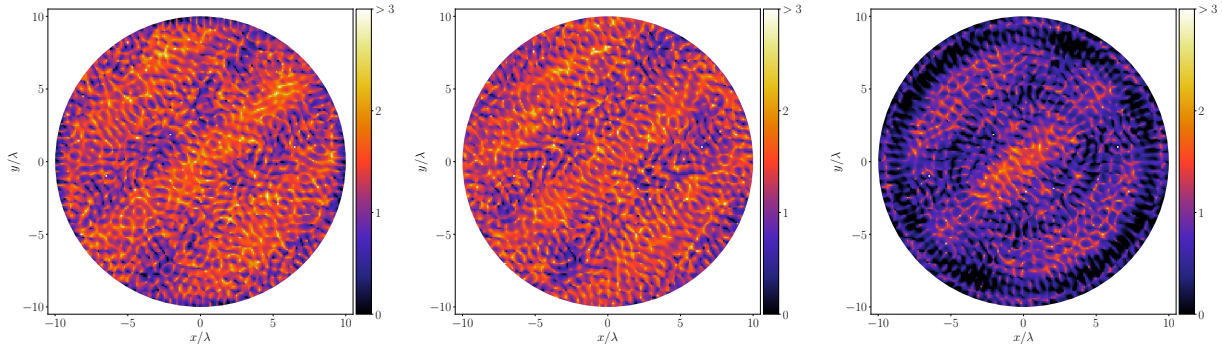


(a) Uniform sampling (b) Random sampling (c) Boundary sampling

Fig. 3: (Color online) The number of correct significant digits, $\delta$, of the reconstructed field $U$ is shown as a function of position. The expansion coefficients were calculated from $M = 1576$ measurements with $10^\circ$ zero-mean Gaussian phase noise. In the uniform sampling case, this corresponds to sampling every $0.45\lambda$.

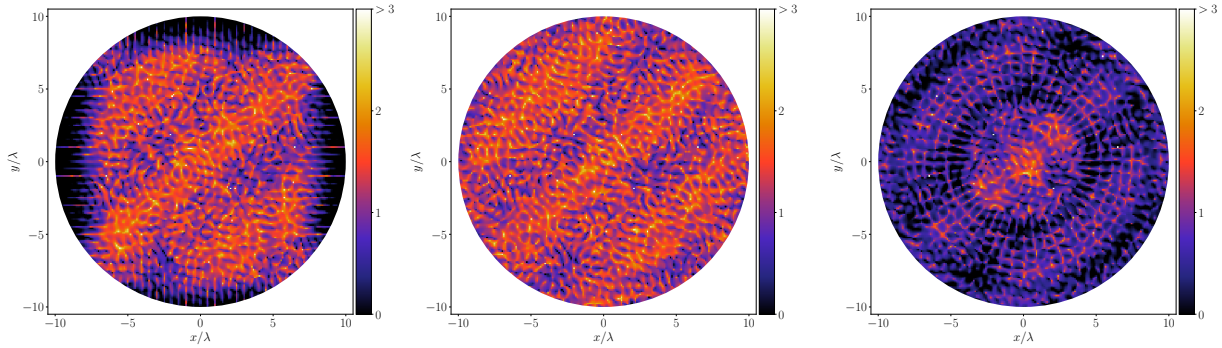


(a) Uniform sampling (b) Random sampling (c) Boundary sampling

Fig. 4: (Color online) The number of correct significant digits, $\delta$, of the reconstructed field $U$ is shown as a function of position. The expansion coefficients were calculated from $M = 1371$ measurements with $10^\circ$ zero-mean Gaussian phase noise. In the uniform sampling case, this corresponds to sampling every $0.48\lambda$.

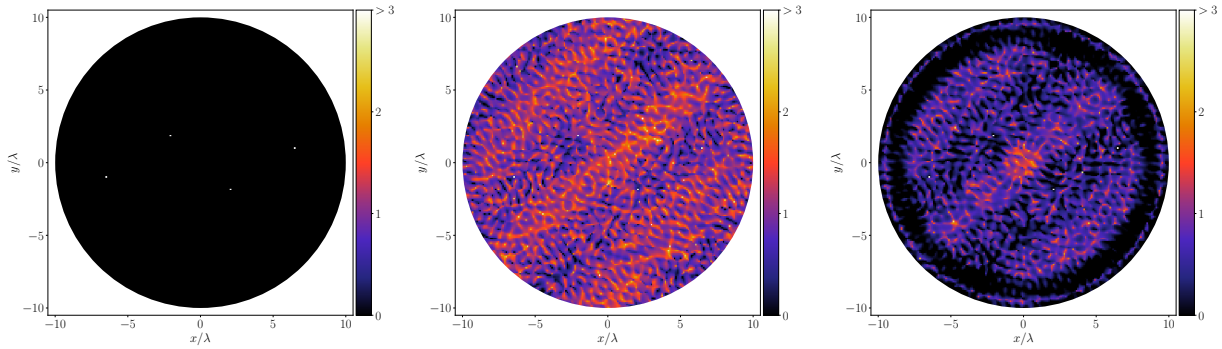


(a) Uniform sampling (b) Random sampling (c) Boundary sampling

Fig. 5: (Color online) The number of correct significant digits, $\delta$, of the reconstructed field $U$ is shown as a function of position. The expansion coefficients were calculated from $M = 1255$ measurements with $10^\circ$ zero-mean Gaussian phase noise. In the uniform sampling case, this corresponds to sampling every $\lambda/2$.

Yuffa, Alexey; Jamroz, Benjamin; Rezac, Jake; Williams, Dylan.
"A Systematic Study: Channel Sounding via Modal Expansion."
Paper presented at 2018 Antenna Measurement Techniques Association Symposium (AMTA), Williamsburg, VA, United States. November 4, 2018 - November 9, 2018.

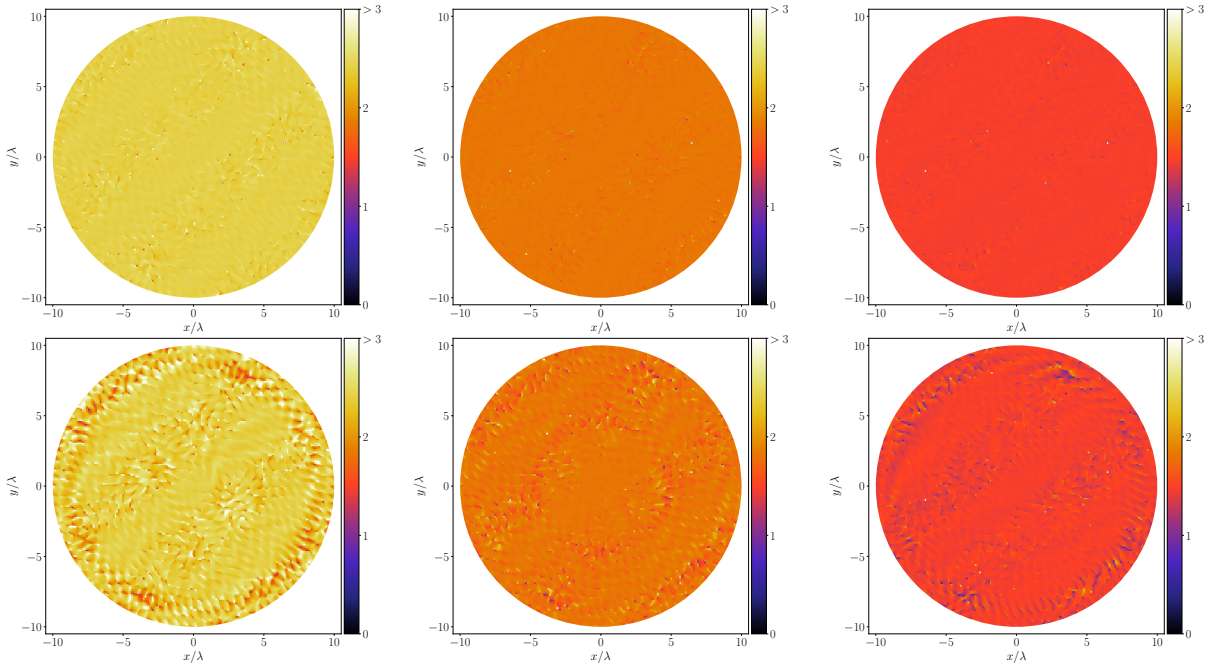


(a) 5° zero-mean Gaussian phase noise (b) 10° zero-mean Gaussian phase noise (c) 15° zero-mean Gaussian phase noise

Fig. 6: (Color online) The top (bottom) panel shows the expected number of correct significant digits, $\delta$, of the reconstructed field $U$ as a function of position for the random (boundary) sampling method at three phase noise levels: 5° (panel a), 10° (panel b), and 15° (panel c). The results shown are based on $10^4$ Monte Carlo simulations with $M = 1255$.

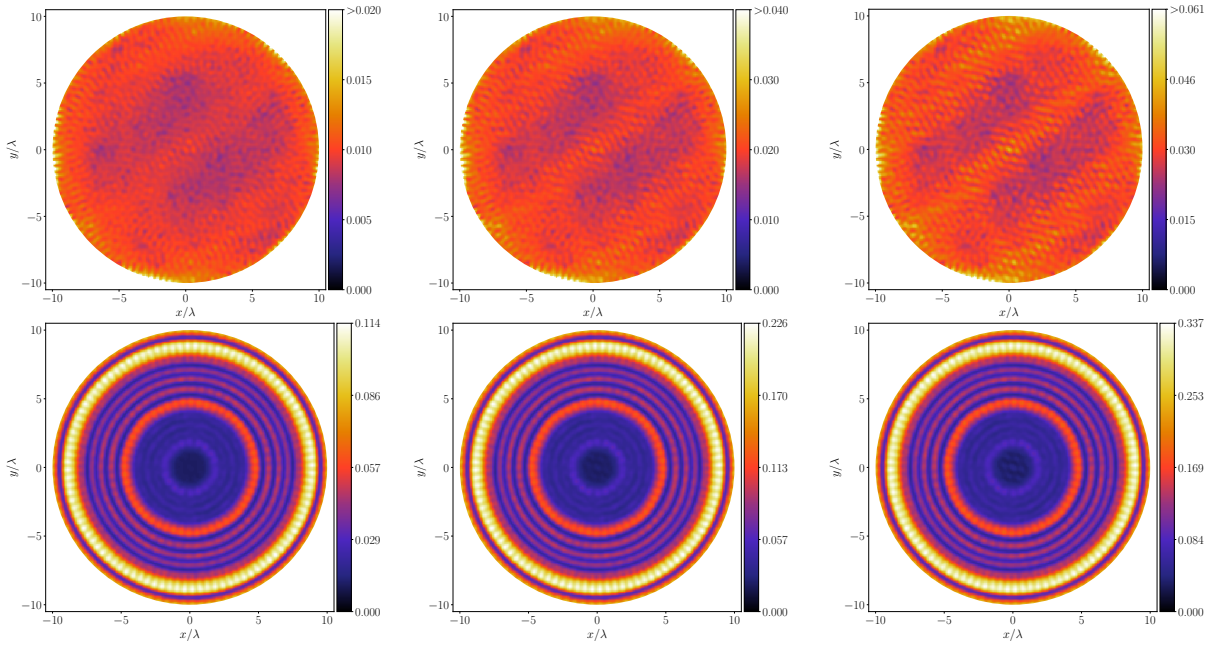


(a) 5° zero-mean Gaussian phase noise (b) 10° zero-mean Gaussian phase noise (c) 15° zero-mean Gaussian phase noise

Fig. 7: (Color online) The Monte Carlo sample standard deviation of the reconstructed field $U$ associated with the Fig. 6 is shown as a function of position.

Yuffa, Alexey; Jamroz, Benjamin; Rezac, Jake; Williams, Dylan.
"A Systematic Study: Channel Sounding via Modal Expansion."
Paper presented at 2018 Antenna Measurement Techniques Association Symposium (AMTA), Williamsburg, VA, United States. November 4, 2018 - November 9, 2018.

were calculated from $M = 1371$ and $M = 1255$ measurement points, respectively. In the case of uniform sampling, these sampling densities corresponds to sampling every $0.48\lambda$ and $\lambda/2$, respectively. From panel (a) in Figures 3–5, we see that the uniform sampling method is very sensitive to the sampling density and, generally speaking, it requires sampling more frequently than $\lambda/2$. In other words, the uniform sampling method deteriorates completely (zero-digit accuracy) when the sampling is at or below Nyquist sampling. However, from panels (b) and (c) in Figures 3–5, we see that the random and boundary sampling methods do not suffer from this highly sensitive dependence on the sampling density.

Figures 3–5 show the accuracy of the solution for one particular realization of random phase noise. However, these figures do not illustrate the expected (average) performance of each of the sampling methods. In Fig. 6, we show the expected (average) accuracy for the random and boundary spatial sampling methods (uniform sampling not shown because it yields zero-digit accuracy) computed from $10^4$ Monte Carlo simulations for three levels of zero-mean Gaussian phase noise: $5^\circ, 10^\circ$ and $15^\circ$. Here, we see that the random spatial sampling is the most accurate. For the phase noise below $10^\circ$, the random spatial sampling yields two- to three- digit accuracy and for $15^\circ$ phase noise it yields one- to two- digit accuracy. Notice that this accuracy is almost independent of the spatial position in $\Omega$. This is in contrast with the boundary sampling where the accuracy tends to decrease near the boundary of $\Omega$. Furthermore, the accuracy of the boundary sampling also appears to be correlated with the crests and troughs of the true field.

The Monte Carlo sample standard deviation values associated with the field in Fig. 6 are shown in Fig. 7. We see that the standard deviation of the field computed from the random sampling pattern is largely featureless and gradually increases with increasing phase noise. However, the standard deviation of the field computed from the boundary sampling pattern has a peculiar concentric ring structure. This ring structure suggests that the boundary sampling pattern is not robust with respect to the zero-mean Gaussian phase noise. Furthermore, the boundary sampling pattern yields noticeably higher standard deviation values, especially near the boundary of $\Omega$ (note scale of the colorbars in Fig. 7).

## IV. Conclusions

We have analyzed the feasibility of using a modal (partial wave) expansion of the field to characterize a two-dimensional propagation channel. We only considered scalar waves and measurements with zero-mean Gaussian phase noise. Under these limiting assumptions, our results suggest that the RF field should be randomly sampled in the region of interest, $\Omega$. If the field is sampled regularly in $\Omega$, then our results indicate that the field must be sampled more densely than $\lambda/2$ to yield an accuracy comparable to the random sampling method. Although the accuracy of the field computed from the random and boundary sampling methods are similar, their associated standard deviations are not. In particular, the boundary sample methods produces noticeably larger standard deviations in a concentric ring pattern, see bottom panel in Fig. 7.

The analysis above was done by solving the linear system (3) in the least squares sense and by using the Wiscombe criterion to choose $N_m$ for each measurement point. Thus, the work presented here also provides a benchmark for propagation channel characterization using modal expansions with a novel sampling-aware algorithm.

## References


[1] A. Bernland, M. Gustafsson, C. Gustafson, and F. Tufvesson, "Estimation of spherical wave coefficients from 3-D positioner channel measurements," *IEEE Antennas Wirel. Propag. Lett.*, vol. 11, pp. 608–611, 2012.

[2] J. Naganawa, K. Haneda, M. Kim, T. Aoyagi, and J. Takada, "Antenna de-embedding in FDTD-based radio propagation prediction by using spherical wave function," *IEEE Trans. Antennas Propag.*, vol. 63, no. 6, pp. 2545–2557, 2015.

[3] Y. Miao, K. Haneda, M. Kim, and J. Takada, "Antenna de-embedding of radio propagation channel with truncated modes in the spherical vector wave domain," *IEEE Trans. Antennas Propag.*, vol. 63, no. 9, pp. 4100–4110, 2015.

[4] K. A. Remley, D. F. Williams, P. D. Hale, C.-M. Wang, J. Jargon, and Y. Park, "Millimeter-wave modulated-signal and error-vector-magnitude measurement with uncertainty," *IEEE Transactions on Microwave Theory and Techniques*, vol. 63, no. 5, pp. 1710–1720, May 2015.

[5] W. J. Wiscombe, "Improved Mie scattering algorithms," *Appl. Opt.*, vol. 19, no. 9, pp. 1505–1509, May 1980.

[6] A. A. R. Neves and D. Pisignano, "Effect of finite terms on the truncation error of Mie series," *Opt. Lett.*, vol. 37, no. 12, p. 2418, Jun. 2012.



Yuffa, Alexey; Jamroz, Benjamin; Rezac, Jake; Williams, Dylan.
"A Systematic Study: Channel Sounding via Modal Expansion."
Paper presented at 2018 Antenna Measurement Techniques Association Symposium (AMTA), Williamsburg, VA, United States. November 4, 2018 - November 9, 2018.

# Rydberg Atom-based RF Power Measurements

Matt T. Simons, Marcus D. Kautz,
Abdulaziz H. Haddab, Joshua A. Gordon,
Christopher L. Holloway
National Institute of Standards and Technology
Boulder, CO 80305
matthew.simons@nist.gov

Thomas P. Crowley
Xantho Technologies, LLC
Madison, WI, 53705 USA

Abstract—The power transmitted through a waveguide was determined using in-situ atom-based electric-field measurements. The field distribution in the waveguide was measured using Rydberg atoms to find the maximum field, which was used to determine the power. For a proof-of-concept, the power of radio frequency fields at 17.86, 19.63, 26.53, and 33.03 GHz were measured in a WR42 waveguide. A section of waveguide was sealed and filled with cesium atoms. Directional couplers allowed RF power to be coupled through the atom-filled section, while two lasers were used to probe the atom vapor.

## I. Introduction

Accurately calibrated antennas, probes, and power meters are key to electromagnetic applications. In order to achieve high accuracy for next-generation technology, we are developing a calibration method for radio-frequency (RF) electric fields (E-fields) based on Rydberg states of alkali atoms that has a direct traceability path to the International System of Units. In this work, we extend this Rydberg atom-based approach to RF power measurements. This method has the potential to be a new international standard for RF E-field and power calibrations. The Rydberg atoms convert an RF amplitude measurement into an optical frequency measurement, which is directly proportional to the strength of the field through Planck's constant. This technique allows for self-calibrated, directly SI-traceable E-field measurements over a large range of frequencies, from 0.1 − 1000 GHz. The spatial resolution of these measurements can be much smaller than the RF wavelength. This allows us to measure the field distribution inside a waveguide and determine the maximum field.

To use Rydberg atoms for RF power measurements, we have assembled an atomic vapor cell integrated inside a WR42 waveguide. The RF E-field distribution inside the rectangular waveguide can be measured by probing the atomic vapor with two lasers, as described in the next section. If the RF field is propagating in the fundamental transverse electromagnetic mode ($TE_{10}$), the maximum E-field can be used to determine the power $P$ inside the waveguide (in W) [1]

$$P = E_0^2 \, \frac{ab}{4} \, \sqrt{\frac{\epsilon_0}{\mu_0}} \sqrt{1 - \left(\frac{c}{2af}\right)^2} \quad , \tag{1}$$

where $E_0$ is the field maximum (in V/m), $a$ and $b$ are the cross-sectional dimensions of the waveguide (in m), and $f$ is the frequency of the field (in Hz). The power determined using the atoms can be compared to the power output through the waveguide using a power meter. This system can provide a more direct traceability path, and potentially, lower uncertainties for RF power measurements and calibrations.

## II. Atom-based RF Measurements

Recently, electromagnetically-induced transparency (EIT) in Rydberg atoms has been studied as a method for measuring RF E-field amplitudes [2]-[10]. The process requires a probe laser to excite a vapor of alkali atoms from the ground state to an excited state, and a coupling laser to couple the excited state to a high energy level Rydberg state (more details in [3], [4]). In this work we use cesium ($^{133}$Cs) as our alkali atoms due to its relatively higher vapor pressure as compared with other alkali atoms, which results in a strong EIT signal. The transmission of the probe laser through the atoms is measured as the optical frequency of the probe laser is scanned through the ground-state-to-excited-state resonance. With the coupling laser off, the probe laser is absorbed by the atoms when it is on resonance. When the coupling laser is turned on, the probe laser is transmitted through the atom over a narrow frequency window, known as EIT. An RF field (when it has a frequency corresponding to a transition to a nearby Rydberg state) can further modify the EIT, splitting the EIT peak into two (this is known as Autler-Townes (AT) splitting).

Figure 1 shows a typical EIT spectrum with no RF present (the single peak). When an RF E-field is applied, the EIT peak splits in two (the two peaks labeled by RF = 0.75 V/m). The amplitude of the applied RF E-



Simons, Matthew; Kautz, Marcus; Haddab, Abdulaziz; Gordon, Joshua; Holloway, Christopher; Crowley, Thomas.
"Rydberg Atom-based RF Power Measurements."
Paper presented at 40th Annual Meeting and Symposium of the Antenna Measurement Techniques Association (AMTA 2018), Williamsburg, VA, United States. November 4, 2018 - November 9, 2018.

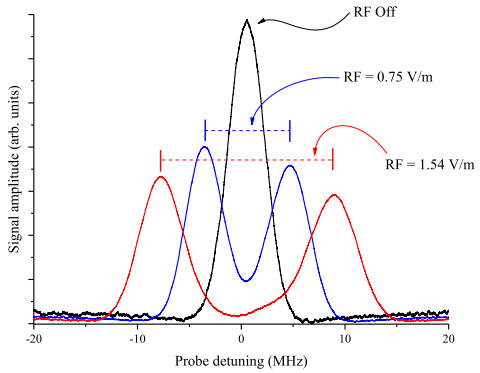


Fig. 1. Example of a typical EIT and AT splitting spectrum, showing a single EIT peak (no RF present), and AT peaks at two different RF field levels.

field $|E|$ is related to the separation in optical frequency between the two peaks $\Delta f_m$ by

$$|E| = 2\pi\frac{\hbar}{\wp}\Delta f_m \quad , \tag{2}$$

where $\hbar$ is Planck's constant and $\wp$ is the dipole moment of the Rydberg transition. The dipole moment can be calculated for a given Rydberg transition (for details see [3], [11], [12]). As the RF E-field increases, the AT splitting increases (shown by the red curve labeled by RF = 1.54 V/m in Fig. 1).

## III. Waveguide Vapor Cell

In order to obtain a power measurement from the E-field, a $^{133}$Cs atomic vapor is placed inside a waveguide to create a waveguide vapor cell. The waveguide vapor cell (Fig. 2) consists of a section of stainless steel WR42 rectangular waveguide with glass windows. The WR42 waveguide has cross-sectional dimensions of $a = 10.668$ mm and $b = 4.318$ mm. Two small holes in the sidewall allow the cell to be evacuated and filled with $^{133}$Cs atoms. A metal stem was attached to each of the holes in the sidewall, which were attached to glass tubes connected to a manifold that was used to supply the $^{133}$Cs. The glass tubes were pinched off to seal the cell. The glass windows allow two lasers to be counter-propagated through the cell to measure the E-field. Directional couplers were attached to either end of the waveguide cell to allow an RF field to be transmitted (Fig. 3) in the same direction as the lasers. The first directional coupler (on the left in the photo) was used to input the RF field, and the second (on the right) was used to monitor the power output. This setup allowed the lasers to travel unobstructed through the waveguide. Stub tuners were placed on either side of the vapor cell section to reduce reflections from the glass windows.

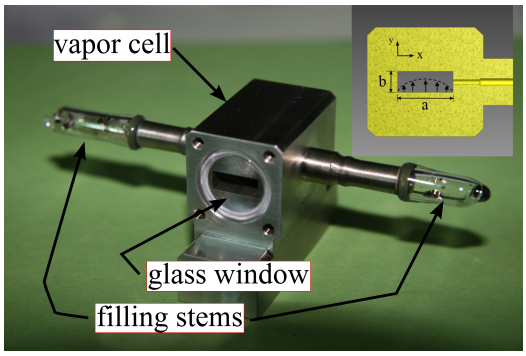


Fig. 2. Photo of the waveguide vapor cell section. The glass windows are attached using a vacuum epoxy, as are the glass tubes connected to the filling stems.

## IV. Waveguide Measurements

A probe laser beam (852 nm) was sent through the waveguide along the direction of propagation of the RF field, and the transmission was measured using a photodetector outside the other end of the waveguide (Fig. 3). The coupling laser (510 nm) was counter-propagated and overlapped with the probe laser inside the waveguide. The probe laser power was 3.2 $\mu$W, the coupling laser power was 17.3 mW, and both lasers were polarized along the short dimension of the waveguide ($b$). The E-field inside the waveguide is measured only where the two lasers overlap inside the vapor cell section. The full-width at half maximum diameter of the lasers was 0.3 mm. This allows for a measurement of the E-field distribution across the waveguide. The waveguide section was placed on a translation stage to move it relative to the lasers. Measurements of the E-field were taken at steps of 0.2 mm along the long dimension ($a$) of the waveguide. Measurements were done at several different frequencies (17.86, 19.63, and 26.53 GHz) spanning the range of single-mode operation of the WR42 waveguide, as well as at one frequency above the cut-off (33.03 GHz). Table I shows the atomic transitions used for these different frequencies.

TABLE I
$^{133}$Cs states, transition frequencies, and dipole moments used in the experiments. The dipole moments ($\wp$) are given in terms of the elementary charge $e$ and the Bohr radius $a_0$.

| $^{133}$Cs transition | RF frequency | $\lambda_c$ | $\wp/ea_0$ |
|---|---|---|---|
| $35D_{5/2} \rightarrow 36P_{3/2}$ | 17.86 GHz | 510.974 nm | 770.05 |
| $34D_{5/2} \rightarrow 35P_{3/2}$ | 19.63 GHz | 511.148 nm | 723.40 |
| $31D_{5/2} \rightarrow 32P_{3/2}$ | 26.53 GHz | 511.787 nm | 592.16 |
| $29D_{5/2} \rightarrow 30P_{3/2}$ | 33.03 GHz | 512.340 nm | 511.94 |

The E-field distribution of the $TE_{10}$ mode in a rectangular waveguide along the long side (from $x = 0$ to $x = a$) is given by

$$E = E_0 \sin\left(\frac{\pi}{a}x\right) \quad , \tag{3}$$

Simons, Matthew; Kautz, Marcus; Haddab, Abdulaziz; Gordon, Joshua; Holloway, Christopher; Crowley, Thomas.
"Rydberg Atom-based RF Power Measurements."
Paper presented at 40th Annual Meeting and Symposium of the Antenna Measurement Techniques Association (AMTA 2018), Williamsburg, VA, United States. November 4, 2018 - November 9, 2018.

where $E_0$ is the field maximum and $a$ is the length of the waveguide in the $\hat{x}$ direction. The field was input to the waveguide through the first directional coupler (10 dB coupler), and propagated through the first stub tuner, waveguide vapor cell, and second stub tuner. A portion of the field was split using the second directional coupler (10 dB coupler) and measured with a power meter.

The results of the atom-based E-field measurements versus position in the waveguide are shown in Figs. 4-7. The first three figures include fits of each cross-sectional scan to (3). In Fig. 4, a 19.63 GHz field is propagated through the waveguide at three different input powers ($-17.8$, $-20.8$, and $-23.8$ dBm). For each input power, we obtain a field distribution that follows (3), with errorbars that represent a 5% uncertainty. The uncertainty is mainly due to the effect of the glass windows (more detail on the uncertainties can be found in [6], [13]). The fit uses one free parameter $E_0$, which is the maximum field in the waveguide. For the three input powers, the maximum E-fields measured are $E_0 = 16.6, 11.8$, and $8.1$ V/m, which gives power levels of $P_{\text{atom}} = -22.3, -25.3$, and $-28.5 \pm 0.4$ dBm using (1). This is compared to the output power from the directional coupler measured using a power meter, which was (after subtracting the attenuation from the coupler, measured by an S-parameter measurement on a vector network analyzer) $P_{PM} = -22.3, -25.2$, and $-28.2$ dBm. The average difference between $P_{\text{atom}}$ and $P_{\text{PM}}$ is 0.2 dBm. We now have a measurement of RF power determined using a atom-based E-field measurement.

We repeated these measurements at frequencies near the low and high cutoffs, 17.86 and 26.53 GHz. For 17.86 GHz in Figure 5, we used input powers of $-16.8$, $-19.7$, and $-22.7$ dBm. The power levels determined by the maximum E-fields were $P_{\text{atom}} = -23.7$, $-26.6$, and $-29.5 \pm 0.4$ dBm, which compared to the powers determined using the power meter ($P_{\text{PM}} = -23.0$, $-25.4$, and $-29.0$ dBm) give an average difference of 0.8 dBm. For 26.53 GHz in Figure 6, we used input powers of $-16.9$, $-20.4$, and $-23.3$ dBm. The power levels determined by the maximum E-fields were $P_{\text{atom}} = -24.9$, $-28.2$, and $-30.8 \pm 0.4$ dBm, which, when compared to the powers determined using the power meter ($P_{\text{PM}} = -23.6$, $-27.1$, and $-29.9$ dBm) give an average difference of 1.1 dBm. For both cases, we are still

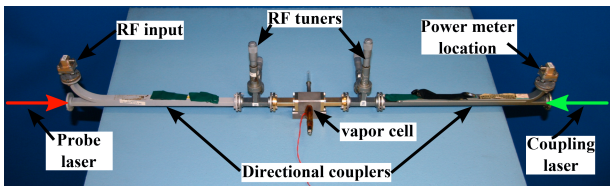


Fig. 3. Photo of the waveguide vapor cell connected to the directional couplers and stub tuners. The RF was input through one of the directional couplers and the power through the waveguide was measured with the other directional coupler.

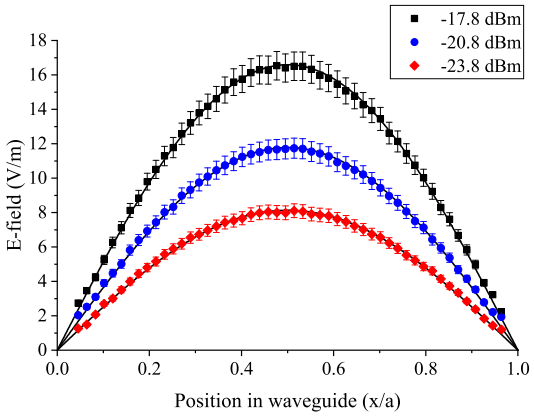


Fig. 4. E-field measurements at 19.63 GHz as function of position in the waveguide for three different input powers. The lines are fits to (3).

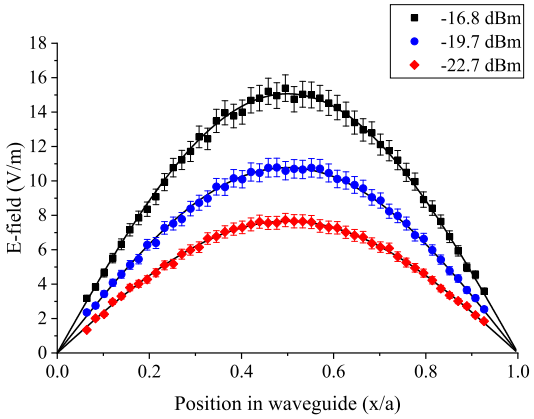


Fig. 5. E-field measurements at 17.86 GHz as function of position in the waveguide for three different input powers. The lines are fits to (3).

able to map the $TE_{10}$ mode and determine the maximum field and the power in the waveguide.

For each frequency, the stub tuners had to be adjusted to cancel the reflection of the RF field from the glass windows. Without this adjustment, the field inside the waveguide vapor cell was not the $TE_{10}$ mode. The signal from the atoms is very sensitive to this change, and a slight mis-adjustment of the stub tuner created a noisy signal.

We also took measurements of the field distribution in the waveguide for a frequency above the single-mode frequency (33.03 GHz), shown in Fig. 7. Here the field is no longer in the $TE_{10}$ mode, but is a combination of the $TE_{10}$ and $TE_{20}$ modes. We can see this structure in our E-field measurements, though it is difficult to fit this to

Simons, Matthew; Kautz, Marcus; Haddab, Abdulaziz; Gordon, Joshua; Holloway, Christopher; Crowley, Thomas.
"Rydberg Atom-based RF Power Measurements."
Paper presented at 40th Annual Meeting and Symposium of the Antenna Measurement Techniques Association (AMTA 2018), Williamsburg, VA, United States. November 4, 2018 - November 9, 2018.

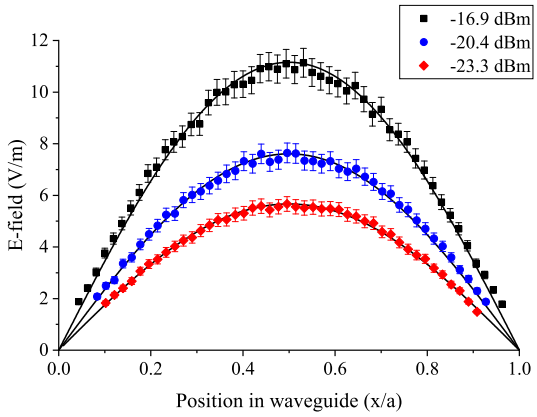


Fig. 6. E-field measurements at 26.53 GHz as function of position in the waveguide for three different input powers. The lines are fits to (3).

theory due to the imperfect cancellation of the reflections from the glass windows using the stub tuners at this dual mode.

## V. Conclusions

We demonstrated a method to determine RF power in a waveguide using Rydberg atom-based RF E-field measurements. This proof-of-concept demonstrates the potential for self-calibrated, SI-traceable, in-situ waveguide power measurements. The atom-based field measurements are directly SI-traceable through Planck's constant in (3), and are self-calibrated as they directly measure the amplitude of the field from atomic properties. As the power is determined by a field measurement, all of the power is available for use. This principle could be used to make a calibrated RF source. While more work must be done to reduce the uncertainties, this work is a step towards a quantum-based, SI-traceable RF power measurement technique.

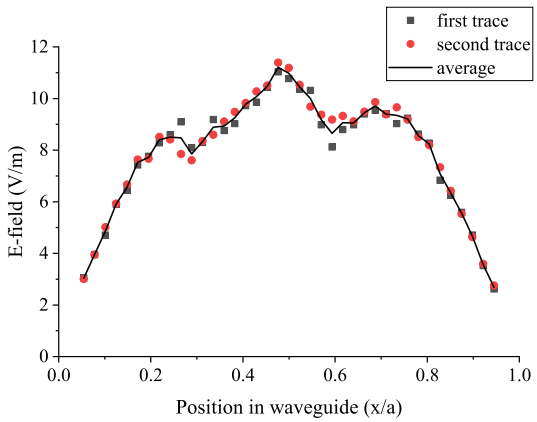


Fig. 7. E-field measurements at 33.03 GHz as function of position in the waveguide. Two different scans at the same input power are shown. The line is an average of the two runs.

## References

[1] C.T.A. Johnk, Engineering Electromagnetic Fields and Waves. John Wiley & Sons: N.Y., N.Y., 1975.

[2] C.L. Holloway, M.T. Simons, J.A. Gordon, P.F. Wilson, C.M. Cooke, D.A. Anderson, and G. Raithel, "Atom-Based RF Electric Field Metrology: From Self-Calibrated Measurements to Subwavelength and Near-Field Imaging", IEEE Trans. on Electromagnetic Compat., 59(2), 717-728, 2017.

[3] C.L. Holloway, J.A. Gordon, A. Schwarzkopf, D.A. Anderson, S.A. Miller, N. Thaicharoen, and G. Raithel, "Broadband Rydberg Atom-Based Electric-Field Probe for SI-Traceable, Self-Calibrated Measurements", IEEE Trans. on Antenna and Propag., 62(12), 6169-6182, 2014.

[4] J. Sedlacek, A. Schwettmann, H. Kübler, R. Löw, T. Pfau, and J.P Shaffer, "Microwave electrometry with Rydberg atoms in a vapour cell using bright atomic resonances", Nature Physics, 8, 819, 2012.

[5] C.L. Holloway, J.A. Gordon, A. Schwarzkopf, D.A. Anderson, S.A. Miller, N. Thaicharoen, and G. Raithel, "Sub-wavelength imaging and field mapping via electromagnetically induced transparency and Autler-Townes splitting in Rydberg atoms", Applied Physics Letters, 104, 244102, 2014.

[6] J.A. Sedlacek, A. Schwettmann, H. Kübler, and J.P. Shaffer, "Atom-Based Vector Microwave Electrometry Using Rubidium Rydberg Atoms in a Vapor Cell", Phys. Rev. Lett., 111, 063001, 2013.

[7] H. Fan, S. Kumar, J. Sedlacek, H. Kübler, S. Karimkashi and J.P Shaffer, "Atom based RF electric field sensing", J. Phys. B: At. Mol. Opt. Phys., 48, 202001, 2015.

[8] M. Tanasittikosol, J.D. Pritchard, D. Maxwell, A. Gauguet, K.J. Weatherill, R.M. Potvliege and C.S. Adams, "Microwave dressing of Rydberg dark states", J. Phys B, 44, 184020, 2011.

[9] C.G. Wade, N. Sibalic, N.R. de Melo, J.M. Kondo, C.S. Adams, and K.J. Weatherill, "Real-time near-field terahertz imaging with atomic optical fluorescence", Nature Photonics, 11, 40-43, 2017.

[10] D.A. Anderson, S.A. Miller, G. Raithel, J.A. Gordon, M.L. Butler, and C.L. Holloway, "Optical Measurements of Strong Microwave Fields with Rydberg Atoms in a Vapor Cell", Physical Review Applied, 5, 034003, 2016.

[11] T.F. Gallagher, Rydberg Atoms. Cambridge Univer. Press:Cambridge, 1994.

[12] M.T. Simons, J.A. Gordon, C.L. Holloway, "Simultaneous use of Cs and Rb Rydberg atoms for dipole moment assessment and RF electric field measurements via electromagnetically induced transparency", Journal of Applied Physics, 120, 123103, 2016.

[13] C.L. Holloway, M.T. Simons, J.A. Gordon, A. Dienstfrey, D.A. Anderson, and G. Raithel, "Electric field metrology for SI traceability: Systematic measurement uncertainties in electromagnetically induced transparency in atomic vapor", J. of Applied Physics, 121, 233106-1-9, 2017.

Simons, Matthew; Kautz, Marcus; Haddab, Abdulaziz; Gordon, Joshua; Holloway, Christopher; Crowley, Thomas.
"Rydberg Atom-based RF Power Measurements."
Paper presented at 40th Annual Meeting and Symposium of the Antenna Measurement Techniques Association (AMTA 2018), Williamsburg, VA, United States. November 4, 2018 - November 9, 2018.

# Precision Optical Antenna Alignment System for Tracking Antennas in 6-DOF

Joshua A. Gordon, David R. Novotny, Michael S. Allman
Communication Technology Laboratory
NIST
Boulder, CO, USA
josh.gordon@nist.gov



***Abstract*—We present on an all-optical spatial metrology system, the PiCMM, that aids in the alignment and tracking of antennas with accuracies on the order of 25 microns and 0.01 deg. This system speeds up millimeter-wave antenna alignment, does not require contact, and links spatial measurements to a laser tracker world coordinate frame. An automated Pixel Probe and dark-field imaging are used to directly measure the aperture geometry and its pose. These measurements are absolute in the world-frame of a laser tracker and associated coordinate metrology space of the antenna scanner. Thus, aperture geometries can be linked directly to any laser tracker target (i.e. 6DOF, 3DOF) and data such as that used to calibrate positioner kinematics. For example, the links and joints defining the Denavit-Hartenberg kinematic model of a robotic arm scanner. The new automated aspect of the system reduces alignment time to under an hour. The synergy with laser tracker targets allows for a high level of repeatability. Furthermore, antennas can be exchanged or realigned in the antenna scanner autonomously because antenna geometry and kinematic models reside in the same laser tracker coordinate metrology space.**

## I. Introduction

Aligning millimeter-wave antennas during near-field measurements can be challenging and time consuming. As frequencies climb, aligning and positioning antennas to within $\lambda/50$ or even $\lambda/100$ can be very challenging. Furthermore, tracking antenna position is useful for post processing correction of non-ideal motion [1] which inevitably exist to some degree in antenna scanning system kinematics. Here we present an all-optical, non-contact alignment system to aid and speed up the alignment of antennas in general, but that is particularly useful at higher millimeter-wave frequencies. Below we give a description of this system and show how it is used for antenna alignment.

## II. Alignment System Design

### A. PiCMM

For a thorough discussion of this system we refer the reader to [2],[3] here we present a terse discussion for the purpose of applying these concepts to precision antenna alignments. The system is comprised of three main parts: a Pixel Probe, a calibrated XYZ stage, and a laser tracker, and functions somewhat similar to a coordinate measuring machine (CMM) [4] but where the contact ball stylus of a traditional CMM is replaced by a (Pi)xel Probe. This system is therefore called the PiCMM.

The Pixel Probe is constructed from three specifically calibrated cameras [2] arranged in a tetrahedral configuration (see Figure 1) linked to either a six-degree-of freedom (6DOF) laser tracker target or constellation of point spherical mounted reflector (SMR) targets[5].

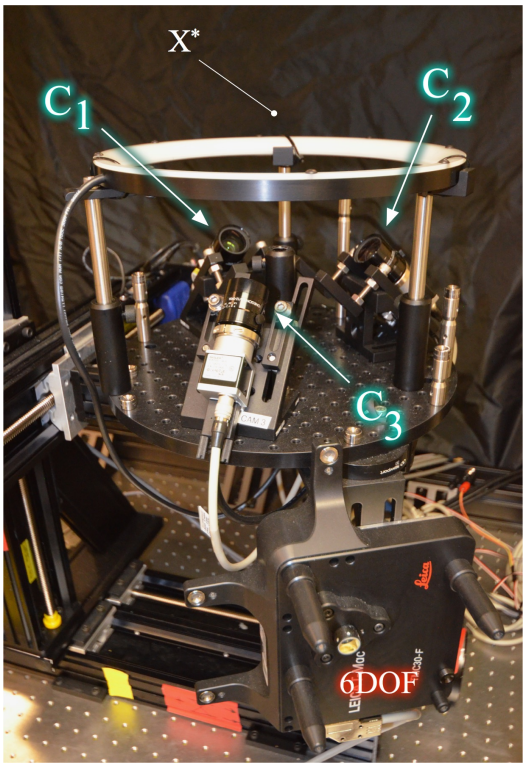


Fig. 1. Pixel Probe comprised of cameras $C_1$, $C_2$, $C_3$ and a 6DOF laser tracker. The location of the projected pixel point $\mathbf{X}^*$ is shown. A ring light is used for dark-field illumination of antenna apertures.

These cameras act to project a pixel to a single 3D coordinate in space represented by the vector $\mathbf{X}^* = [X^*, Y^*, Z^*]$

Gordon, Joshua; Novotny, David; Allman, Michael.
"Precision Optical Antenna Alignment System for Tracking Antennas in 6-DOF."
Paper presented at 40th Annual Meeting and Symposium of the Antenna Measurement Techniques Association (AMTA 2018), Williamsburg, VA, United States. November 4, 2018 - November 9, 2018.

which has a corresponding 2D pixel coordinate in each of the three cameras $C_1$, $C_2$, and $C_3$.

$$\mathbf{x}_{1*} = \begin{bmatrix} x_{1*} \\ y_{1*} \end{bmatrix} \quad \mathbf{x}_{2*} = \begin{bmatrix} x_{2*} \\ y_{2*} \end{bmatrix}, \quad \mathbf{x}_{3*} = \begin{bmatrix} x_{3*} \\ y_{3*} \end{bmatrix} \tag{1}$$

This projection from 3D measurement space to the 2D camera image is uniquely governed by the camera projection $[P_j]$ matrix [2],[6] for each camera via,

$$\mathbf{x}_{j*} = [P_j]\mathbf{X}^* \tag{2}$$

In the images captured by each camera $\mathbf{x}_{j*}$ is represented by a blue highlighted pixel see Figure 2. A ring light (see Figure 1) is used to establish dark-field illumination [7] which accentuates the antenna aperture edge. A dark-field image of a WR-08 wave guide flange as seen through camera $C_1$ is shown in Figure 2.

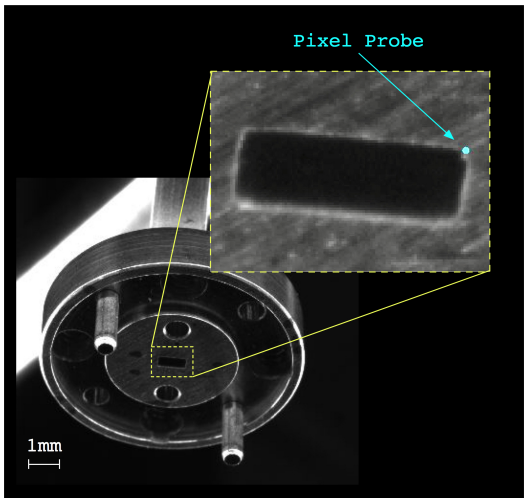


Fig. 2. A dark field image through camera $C_1$ of a WR-08 wave guide flange. The Pixel Probe shown as the blue dot is at the projected coordinate $[x_{1*}, y_{1*}]$. Blue dot size is exaggerated so it can be seen in the figure.

The function of the Pixel Probe is to link $\mathbf{X}^*$ to a laser tracker such that the location of $\mathbf{X}^*$ is known in the laser tracker's world frame. Anywhere the blue pixel appears at in the images of the cameras corresponds to a 3D coordinate measurable by the laser tracker. The point $\mathbf{X}^*$ thus acts as a small invisible stylus the size of the projected pixel, about 20 $\mu$m. The PiCMM is completed by mounting a Pixel Probe on a precision XYZ stage, see Figure 3.

A calibration process discussed in detail in [2] allows the XYZ stage to autonomously drive $\mathbf{X}^*$ to a target coordinate $\mathbf{X}_{target}$ specified by a user. In practice the user works within a graphical user interface (GUI) and specifies $\mathbf{X}_{target}$ through pointing and clicking with a mouse on a location in the images on the computer screen. This "invisible stylus" makes possible dimensional measurements of antenna apertures in the laser tracker world frame without contact and with a resolution of $< 25$ $\mu$m. It also overcomes one of the biggest

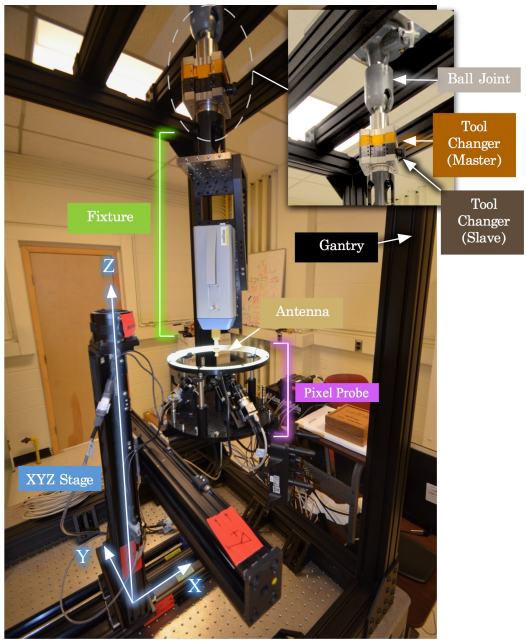


Fig. 3. The PiCMM system and gantry. Supported by the gantry, the fixture attached via the and ball joint and tool changer interface is mounted upside down allowing the antenna aperture to be measured.

challenges for a laser tracker, that is to measure a sharp edge directly. For at this spatial resolution the sharp edge of an antenna aperture appears blunt and becomes easily measurable in a laser trackers world frame. With this spatial resolution small mm-wave antennas that were previously difficult or not possible to measure and track with a laser tracker become straight-forward. Measurements of the antenna aperture are then used to construct a coordinate frame defining the antenna pose (position and orientation). We denote the pose of the antenna with coordinate frame $A_0$.

### *B. Gantry*

A gantry is used to hold antennas above the PiCMM while being scanned, shown in Figure 3. At the top of the gantry is a ball joint that is lockable via a manual hydraulic clamp (Figure 3) and that has the master side of a manual robot tool changer chuck at the end of it. The slave side of the tool changer is attached to the antenna (discussed below). Although the tool changer is designed to work with robotic arms such as in the NIST CROMMA [8] and LAPS [9] antenna ranges it can be adapted to any scanner. The tool changer provides a seamless way to exchange antennas between the PiCMM for alignment and the robots during measurement. When the antenna is attached to the gantry the ball joint is first disengaged so that the load of the antenna relaxes in alignment with gravity. This effectively relieves extra torque on the gantry that could result in stress and cause unwanted settling and deflection of the antenna pose while it is being measured



Gordon, Joshua; Novotny, David; Allman, Michael.
"Precision Optical Antenna Alignment System for Tracking Antennas in 6-DOF."
Paper presented at 40th Annual Meeting and Symposium of the Antenna Measurement Techniques Association (AMTA 2018), Williamsburg, VA, United States. November 4, 2018 - November 9, 2018.

by the PiCMM. Deflection even on the order of tens of microns can affect alignment at some millimeter-wave frequencies so effort has been made to mitigate sources of alignment error.

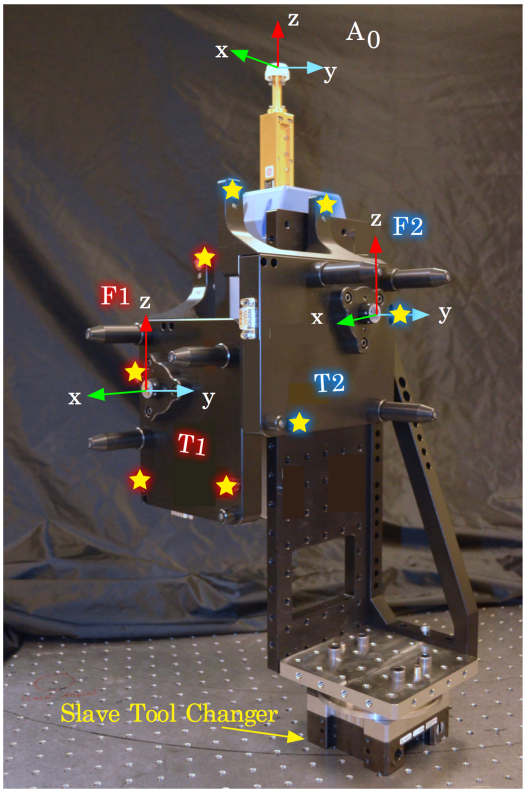


Fig. 4. Antenna fixture holds a frequency extender in fixed relation to 6DOF laser tracker targets T1 and T2. Corresponding coordinate frames F1 and F2 are shown. Stars define the locations of the four points making up CONST1 (red) and CONST2 (blue) each.

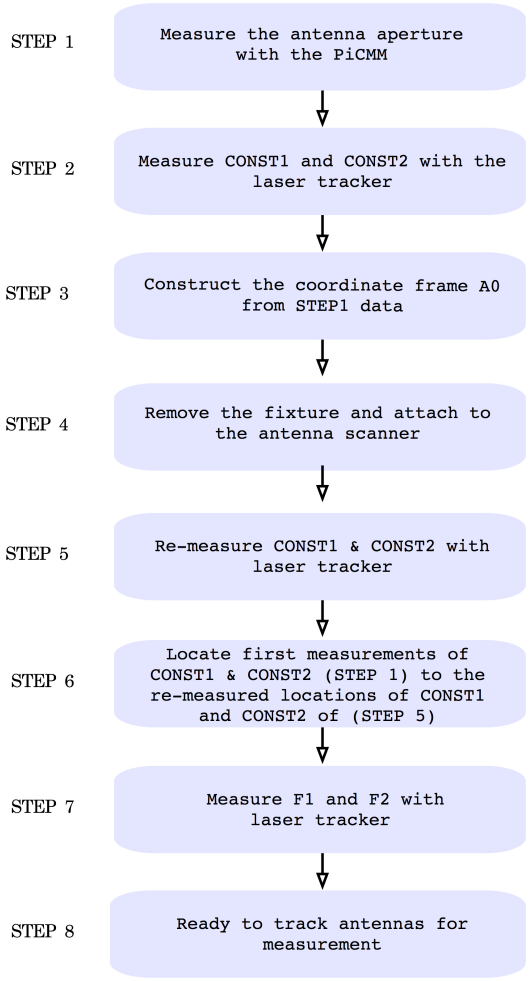


Fig. 5. Flow chart of the 8-step alignment process.

### C. Fixture

No matter the antenna scanner design there is some mounting structure required to physically mount and connect the antenna to the scanner. Here we have standardized the physical connection of the antenna to scanner with the tool changer as well as the way the antenna is mounted. Antennas are mounted in a fixture that acts to hold the antenna (along with any frequency extender) in a fixed pose relative to two 6DOF laser tracker targets T1 and T2 mounted nominally 90° from each other (one for each polarization orientation) see Figure 4. The fixture is constructed from optical grade mechanical components such that structural rigidity can be assumed between the the antenna and T1 and T2. When measured with the laser tracker targets T1 and T2 produce a local coordinate frame F1 and F2 respectively. They also have an auxiliary constellation of four additional kinematic magnetic nests that one can fix SMR targets to. When measured with the laser tracker the SMRs produce a constellation of four 3D points for each target that have a fixed relationship to frames F1 and F2. These constellations are denoted as CONST1 and CONST2, see Figure 4. The SMRs can be rotated so that they can be seen over a larger angle by the laser tracker and so they are useful for establishing the pose offset between T1 and T2. In the context of the 6-Axis robot arms of LAPS and CROMMA ranges, the fixture with antenna, frequency extender, and 6DOF targets comprises the robot end effector. This end effector is attached to the gantry via the tool changer. Next we discuss leveraging measurements with the PiCMM for antenna alignments.

## III. Alignment Process

In aligning the antennas, the goal is to measure the frame-to-frame transform between the frames produced by the two 6DOF targets (F1 and F2) and the antenna frame $A_0$. Once established, it is trivial to locate and track the actual antenna



Gordon, Joshua; Novotny, David; Allman, Michael.
"Precision Optical Antenna Alignment System for Tracking Antennas in 6-DOF."
Paper presented at 40th Annual Meeting and Symposium of the Antenna Measurement Techniques Association (AMTA 2018), Williamsburg, VA, United States. November 4, 2018 - November 9, 2018.

coordinate frame (to better than $\approx 30\ \mu$m) with a laser tracker for any pose the antenna is manipulated via the scanner.

Alignment is achieved by measuring the aperture geometry of the antenna with the PiCMM, constructing the antenna coordinate frame $A_0$, and linking it to CONST1, CONST2, F1 and F2. Commercial spatial metrology software supplied with the laser tracker was used to capture data and to construct the antenna frame $A_0$ as well as calculate frame-to-frame-transforms and distances between 3D points. The alignment process scales to any antenna and provides a consistent work flow.

After connecting and locking the fixture to the ball joint on the gantry via the tool changer interface, alignment can be summarized in eight easy steps shown in the flow chart in Figure 5. In the current configuration the typical time required to finish the process is 30 min or less.

## IV. Measurements

As an example a 15 dB WR-15 standard gain horn was measured. Figure 6 shows the point data taken of the aperture (insert) along with the constructed frame $A_0$. From these measurements the aperture dimensions were determined to be 10.780 mm $\times$ 7.448 mm which is consistent with the manufacture specified dimensions and tolerances of 10.693 mm ($\pm$0.127 mm) $\times$ 7.366 mm ($\pm$0.127 mm).

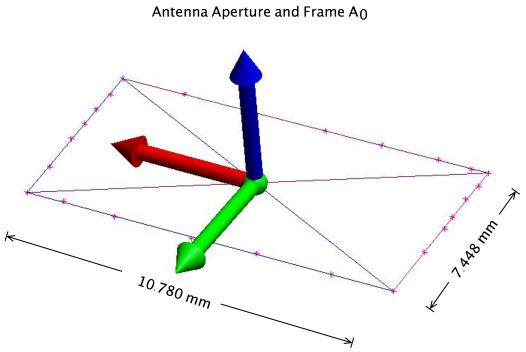


Fig. 6. Aperture measurement of the 15 dB WR-15 standard gain horn obtained with the PiCMM. Red X's mark the measurement locations on the aperture. Frame $A_0$ is defined such that it is centered and normal to the aperture and clocked perpendicular to the long side. Aperture dimensions measured with the PiCMM were 10.780 mm $\times$ 7.448 mm

The frame-to-frame transform ${}^{1}_{0}H$ between F1-to-$A_0$ and ${}^{2}_{0}H$ for F2-to-$A_0$ given in the form [10] of rotation and translation ${}^{A}_{B}H = [R|\mathbf{t}]$ are:

$$ {}^{1}_{0}H = \begin{bmatrix} -0.001 & -0.004 & -1.000 & -277.012 \\ 0.006 & 1.000 & -0.004 & -125.219 \\ 1.000 & -0.006 & -0.001 & 38.158 \\ 0.00 & 0.00 & 0.00 & 1.000 \end{bmatrix} \quad (3) $$

$$ {}^{2}_{0}H = \begin{bmatrix} -0.003 & 0.007 & 1.000 & 289.963 \\ 1.000 & -0.006 & 0.003 & -127.815 \\ 0.06 & 1.000 & -0.007 & 10.786 \\ 0.000 & 0.000 & 0.000 & 1.000 \end{bmatrix} \quad (4) $$

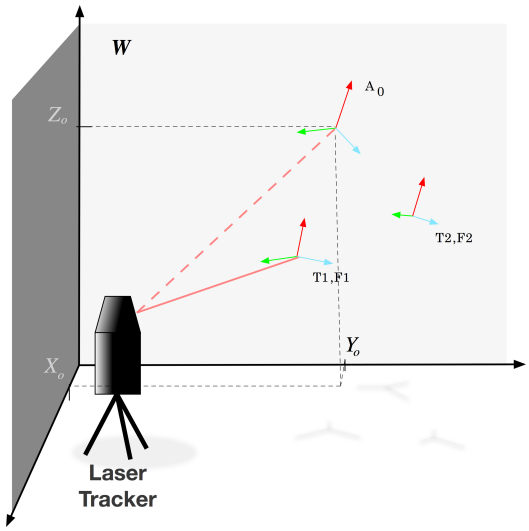


Fig. 7. After establishing the frame-to-frame transforms with the PiCMM, the antenna coordinate frame $A_0$ can be tracked in the world frame **W**. The Laser Tracker "sees" $A_0$ centered on coordinate $[X_o, Y_o, Z_o]$ (dotted red line) while it measures the 6DOF target T1 (solid red line).

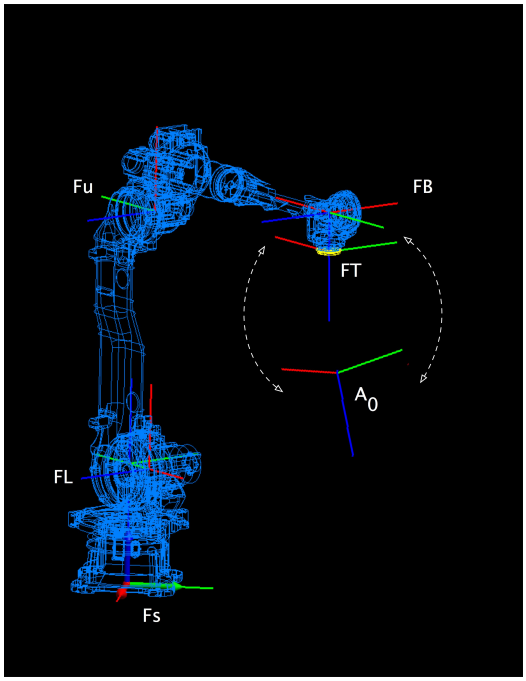


Fig. 8. D-H model seen by laser tracker for a 6-Axis robotic arm antenna scanner. Antenna end effector is located at frame $A_0$. The PiCMM is used to measure and define the antenna frame $A_0$ with respect to the last native robot D-H frame FT (dotted arrows). This completes the full D-H model for the 6-Axis robotic antenna scanner.

As can be seen, the largest terms for these transforms are contained in the last column that represents the translation



Gordon, Joshua; Novotny, David; Allman, Michael.
"Precision Optical Antenna Alignment System for Tracking Antennas in 6-DOF."
Paper presented at 40th Annual Meeting and Symposium of the Antenna Measurement Techniques Association (AMTA 2018), Williamsburg, VA, United States. November 4, 2018 - November 9, 2018.

vector **t**. This is consistent with the targets T1 and T2 being mounted with minimal rotation at nominally square orientations in the fixture relative to the antenna aperture. ${}^1_0H$ and ${}^2_0H$ for each target need only be input to the laser tracker and the antenna pose can be tracked in real-time and thus manipulated to achieve desired alignment to within the accuracy of the laser tracker (typically up to a few tens of microns). Antenna tracking with this method is depicted in Figure 7.

Completing the kinematic model of an antenna scanner can thus be achieved very accurately using the PiCMM. With respect to 6-Axis robot arm scanners the frame $A_0$ defines the end effector pose and completes and the D-H model. A complete kinematic model is paramount in achieving closed loop robot position correction for high frequency antenna scanning as in CROMMA [8] as well as proper robot calibration for open loop scanning as in LAPS [11]. The completed D-H model for the CROMMA robot is shown in Figure 8.

## V. Conclusion

We have discussed the use of a new spatial metrology tool the PiCMM for precision non-contact antenna alignment and tracking on the order of 25$\mu$m. This system is based on previous development of a Pixel Probe non-contact laser tracker probe. The PiCMM acts similar to a coordinate measuring machine, but where the Pixel Probe replaces the ball stylus. The PiCMM allows for non-contact coordinate measurements of antenna apertures with accuracy on the order of 25$\mu$m. Coordinate measurements of antenna apertures obtained with the PiCMM also exist in the world frame of a laser tracker. This achieves alignment and tracking of antennas in the laser tracker world frame. Furthermore, the PiCMM allows one to accurately include the antenna aperture in the kinematic chain of an antenna scanner which is paramount for high frequency millimeter-wave antenna metrology. The PiCMM and alignment workflow is presented. Coordinate metrology of a WR-15 standard gain horn using the PiCMM is given.

## References


[1] R. C. Wittmann, B. K. Alpert, and M. H. Francis, Near-field antenna measurements using nonideal measurement locations, IEEE Trans. Antennas Propag., vol. 46, no. 5, pp. 716722, May 1998.

[2] J. A. Gordon, S. Borenstein, Realizing A Non-Contact Coordinate Measuring Machine Using a Pixel Probe, Precision Engineering (submitted July 2018)

[3] Gordon, J A, Novotny D.R. A Single Pixel Touchless Laser Tracker Probe. J of the CMSC 2015;10;1221.

[4] Hocken JR, Pereira PH. Coordinate measuring machines and systems. 2nd Edition. CRC Press; 2016.

[5] Muralikrishnan B, Phillips S, Sawyer D. Laser trackers for large-scale dimensional metrology: a review. J Prec Eng 2016;44;13-28.

[6] Hartley R, Zisserman A. Multiple view geometry in computer vision. 2nd edition. Cambridge UK; 2003.

[7] Sanz JLC, Merkle F, Wong KY. Automated digital visual inspection with dark-field microscopy. J. Opt. Soc. Am. A, 1985;2;1857-1862.

[8] Millimeter-Wave Near-Field Measurements Using Coordinated Robotics, J. A. Gordon, D. R. Novotny, et. al. IEEE TRANSACTIONS ON ANTENNAS AND PROPAGATION, VOL. 63, NO. 12, DECEMBER 2015 5351

[9] The Multi-Robot Large Antenna Positioning System for Over- The-Air Testing at the National Institute of Standards and Technology, D. R. Novotny, J. A. Gordon, M. S. Allman, et. al. Proceedings of the Antenna Measurement Techniques Association Conference 2017.

[10] Introduction to Robotics Mechanics and Control, Third edition, J. J. Craig. (2009) Pearson.

[11] Serial Robotic Arm Joint Characterization Measurements for Antenna Metrology, M. S. Allma, D. R. Novotny, J. A. Gordon, et. al. Proceedings of the Antenna Measurement Techniques Association Conference 2017.




Gordon, Joshua; Novotny, David; Allman, Michael.
"Precision Optical Antenna Alignment System for Tracking Antennas in 6-DOF."
Paper presented at 40th Annual Meeting and Symposium of the Antenna Measurement Techniques Association (AMTA 2018), Williamsburg, VA, United States. November 4, 2018 - November 9, 2018.

# A Practical Approach to Placing Coastal Sensors for Spectrum Sharing in the 3.5 GHz Band

Thao T. Nguyen, Anirudha Sahoo, and Timothy A. Hall
National Institute of Standards and Technology
Gaithersburg, Maryland, U.S.A.
Email: {ttn1, ans9, tim.hall}@nist.gov

***Abstract*—Commercial-federal spectrum sharing in the 3.5 GHz band requires an Environmental Sensing Capability (ESC) system, consisting of sensors deployed along the coasts, to detect federal incumbent shipborne radar in order to protect it from harmful interference from commercial users. The coastal waters where the radar needs protection from interference are divided into a chain of contiguous polygons called Dynamic Protection Areas (DPAs). The sensor(s) associated with each DPA must cover that DPA completely but should minimize any excess coverage on land, in neighboring DPAs, and out at sea. Thus, placement of sensors and their operating parameters are determined by solving this coverage problem. We use existing tower sites as candidate locations for the sensors and the Irregular Terrain Model (ITM) in point-to-point mode to compute the path loss. We present an algorithm for computing the locations and operating parameters of the sensors such that the excess area, and thus the probability of false alarm, is minimized.**

## I. Introduction

The problem of spectrum scarcity has been addressed by spectrum-sharing technologies. Proposals have come from academia, such as Mitola et al. regarding spectrum sharing in 5G networks [1], from the private sector, e.g., Nokia's newsletter article on spectrum sharing [2], and also from government agencies. For example, in response to a 2010 Presidential Memorandum to free up 500 MHz of spectrum, the U.S. National Telecommunications and Information Administration (NTIA) has identified a number of bands in use by the Federal government as potentially suitable for commercial broadband service [3]. As part of this model, a new service called the Citizens Broadband Radio Service (CBRS) has been proposed to increase spectrum utilization and allow commercial access to the 3.5 GHz band currently used by Naval shipborne radar and other incumbents.

The 3550 MHz to 3700 MHz CBRS band in the U.S. has a three-tiered access model managed by a Spectrum Access System (SAS) with the assistance of an Environmental Sensing Capability (ESC). The first tier is called Incumbent Access (IA) and includes authorized Federal users. It is protected from harmful interference caused by users in any other tier. The second tier is called Priority Access (PA) and includes providers of residential, business, and mobile broadband services that use small cell technologies. It will operate with strict Quality of Service (QoS) guarantees and interference protection. The third tier is called General Authorized Access (GAA) and consists of general public access on an opportunistic non-interfering basis. PA (Tier 2) and GAA (Tier 3) devices are collectively referred to as CBRS devices (CBSDs).

Incumbent Navy shipborne radar will be protected through a contiguous chain of offshore polygonal regions called Dynamic Protection Areas (DPAs), defined along the coasts of the U.S. At any point in time, a DPA is either in an activated or a deactivated state on any channel in the band. A DPA is activated when the incumbent is detected inside its area by the ESC sensor(s) covering it, and it is deactivated otherwise. When a DPA is activated, the SAS will notify a sufficient number of CBSDs to vacate the channel so that the aggregate interference falls below a protection threshold of $-144$ dBm/10 MHz [4]. In the NTIA draft used in this paper, which was the latest publicly released version at the time of submission [5], there are 14 non-overlapping coastal DPAs covering the West coast and 26 non-overlapping DPAs covering the East and Gulf coasts of the contiguous United States (CONUS). Excepting those DPAs protecting U.S. Navy ports, all coastal DPAs begin at 10 km out from the shore and vary in shape and area from one another.

An ESC operator must deploy sensors along the coast in such a manner that each DPA is fully covered (or monitored), thus ensuring that the radar signal is detected when the radar is anywhere inside the DPA. The relevant factors in deployment are the number of sensors assigned to a DPA, the location, antenna height, antenna pattern, and detection threshold of each sensor. Full coverage of each DPA is necessary in order to prevent the incumbent from experiencing harmful interference anywhere inside the DPA. However, excess coverage, which can exist either out at sea (outside of any DPA) or in a neighbor DPA, is a problem. Detecting the presence of an incumbent outside of a DPA results in a higher probability of false alarm and unnecessary suspension of CBSD transmissions. This reduces spectrum utilization by commercial operators even though their continued operation would not result in harmful interference to the incumbent. This paper presents a method to determine location, orientation and operating parameters of the ESC sensors such that the DPAs are maximally covered while making sure that unnecessary suspension of CBSDs in the wake of a DPA activation is minimized.

This paper is structured as follows. Section II reviews related work in the literature. In Section III, we formulate the problem, present our approach and define our algorithm. In

Sahoo, Anirudha; Nguyen, Thao; Hall, Timothy.
"A Practical Approach to Place Coastal Sensors for Spectrum Sharing in the 3.5 GHz Band."
Paper presented at IEEE Wireless Communications and Networking Conference (WCNC), Marrakech, Morocco. April 15, 2019 - April 19, 2019.

Section IV, we describe the models and assumptions used in our analysis. Results are presented in Section V. Finally, Section VI summarizes our contributions and results and discusses future work.

## II. Related Work

The problem we are solving falls under the general category of sensor coverage problems. These have been extensively studied in many fields and applications, but generally address the question, "how well do the sensors monitor the physical space?" [6], which often reduces to "is every location of interest, whether defined as a continuous area [7]–[9] or a set of points [10], [11], covered by one or more sensors?" Much of the literature considers omnidirectional sensors, with the coverage area of an individual sensor being a circle, assuming propagation loss is the same in all directions. ESC sensors, however, will be deployed along the coast and must cover an area out at sea. Thus, sensors equipped with directional antennae pointing at computed azimuth angles are more suitable to our application, resulting in a coverage problem similar to that in [12], Sec. 6.2.

An abstract, piecewise linear representation of the coastline and the area to be covered was used in [13] to find the optimal non-uniform (i.e., not equidistant) placement of sensor nodes. They solve for the minimum number of sensors using a sequential convex programming algorithm for both redundant and non-redundant coverage. Similarly, a simple technique for uniform placement of ESC sensors is proposed in [14], assuming a linear coastline with a parallel line in the water representing radar detection distance. In our work here, we use an actual map of the coastline and a DPA database, and we use a greedy algorithm to solve our optimization problem. Maps of the U.S. coastlines and realistic CBSD deployments are used in [15] and [16] to compute aggregate interference from CBSDs to the radar receiver and to estimate an interference contour at sea. The result was in turn used to determine non-uniform sensor locations and their detection thresholds. We formulated sensor placement as a *set cover* problem and solved using a greedy approach for both redundant and non-redundant coverage. However, we assumed omni-directional antennae and covered discrete points along the interference contour. In this paper, we use directional antennae and attempt to cover the entire area within a given DPA.

All of the work discussed above ([13]–[16]) was published before DPAs were introduced. Thus, instead of covering a set of DPAs, they covered either a large coastal area (e.g., entire East or West coast of the U.S.) [13], [14] or specific points along the boundary of an area to be protected from harmful interference [15], [16]. Since those approaches deal with a single large area, rather than a set of smaller connecting areas like DPAs, they are not concerned with excess coverage into any neighboring coverage areas or any false alarms that result from this. Therefore, a direct performance comparison of those schemes with ours is not possible.

Our previous work [17] considered the problem of excess area and used an earlier set of DPAs defined by the NTIA. We formulated the problem as a generalized coverage problem where an ESC sensor covers a geometric shape called a required coverage area (RCA). We considered circle coverage (i.e., an omnidirectional antenna) as well as coverage by a set of antenna patterns and used the Irregular Terrain Model (ITM) in area mode [18] as our propagation model. In this paper, we use the ITM point-to-point mode. We also use the locations of existing towers along the coastal U.S. as candidate ESC sites, rather than a set of equidistant points along the shoreline.

## III. Methodology

### A. Problem Formulation

As mentioned earlier, to protect a DPA, one or more ESC sensors need to be deployed along the coast such that the sensor(s) can detect radar signal at any point inside the DPA. The deployment has to consider location, antenna pattern and azimuth of the ESC sensors to achieve maximum or full coverage of the DPA. Since the DPA polygon and the ESC coverage area cannot match exactly, the sensors will detect some excess area outside of the DPA. This excess area represents unnecessary activation of the DPA and thus results in unnecessary suspension of transmission for some CBSDs.

The goal is to deploy ESC sensors such that it maximizes the detection coverage area inside the DPA while minimizing the excess area covered by the ESC sensor. Since protecting radar from harmful interference is more important than extraneous detection from the excess area, the first objective of maximizing the coverage area of the DPA has higher precedence than minimizing the excess area. Therefore, our problem can be treated as a two-stage optimization as follows. In the first stage, for a given DPA $dpa$, a set of locations $loc$, antenna patterns $pattern$ and azimuths $az$, find a set of one or more sensor placement tuples $(loc, pattern, az)$ that provide maximum coverage of the DPA. Then, in the second stage, choose the tuple that has the minimum excess area among all the set of tuples found in the first stage.

Therefore, our problem can be formulated as follows. For a DPA, given a set of locations, beamwidths, azimuths and detection thresholds, find a set of one or more sensor placement tuples that maximizes coverage of the DPA and has the minimum excess area among all the set of tuples that give the same maximum coverage. Since we do not want any location to have multiple sensors, no two tuples should have the same location.

### B. Approach

We use the ITM point-to-point mode, which is currently adopted as a reference model by the CBRS industry standard [19], to compute propagation loss in our study. The ITM model is essentially an implementation of the Longley-Rice model that predicts long term median propagation loss over irregular terrain in the frequency range 20 MHz to 20 GHz [18]. To apply the ITM point-to-point model, we discretize areas into a set of grid points. We first find the set of sensor placement tuples that maximizes the number of points detected by the sensor. The well-known *set cover* problem, which is

Sahoo, Anirudha; Nguyen, Thao; Hall, Timothy.
"A Practical Approach to Place Coastal Sensors for Spectrum Sharing in the 3.5 GHz Band."
Paper presented at IEEE Wireless Communications and Networking Conference (WCNC), Marrakech, Morocco. April 15, 2019 - April 19, 2019.

NP-complete [20], can be reduced to this problem. We take the brute force approach to solve this part. Since standards [4] require that a DPA be fully monitored, we assume that the required number of the points covered by the ESC sensors is all the points inside the DPA. We begin with one location at a time and identify the tuple(s) which cover all DPA points. If at least one tuple can detect all the points, then we stop. Otherwise, we take all possible combinations of two locations at a time. For each such combination, we gather the tuple pairs that detect all the DPA points. If at least one such pair exists, then we stop, otherwise we take all possible combinations of three locations at a time and repeat the same process. For our application this brute force approach is computationally not that expensive, since for a DPA, there will be only a few candidate locations, which are the existing tower locations. Moreover, the complexity of this algorithm may not be a major concern since it will be run offline prior to ESC deployment.

At the end of the above process, we will have a set of tuples that provides $100\ \%$ coverage of the DPA. Of those tuples, we choose the one that has the minimum excess area. Note that this final choice could be a set of one or more tuples depending on how many locations are chosen to provide full coverage of the DPA.

### C. Algorithm

We design Algorithm 1 based on the above approach to solve the ESC sensor placement problem. The main inputs to the algorithm are radar parameters, ITM parameters, a set of DPA polygons of a U.S. coast, tower locations to be considered for sensor placement, a set of antenna patterns, and a minimum detection threshold.

Fig. 1 is used to explain the working of our algorithm. The algorithm first creates a polygon called *dpa_union_polygon* by taking the union of all the DPA polygons in each coast. This polygon is shown in violet red in Fig. 1. To bring excess area into the geometry, the dpa_union_polygon is dilated by a width of *dilation_width*. The dilated polygon, called *dilated_dpa_union*, is the annular polygon around the dpa_union_polygon. The annular area between the outer edge of dpa_union_polygon and dilated_dpa_union, which is in the sea, is called *excess_sea_polygon* and is shown in shaded green in Fig. 1. Likewise, the annular area between the inner edge of dpa_union_polygon and dilated_dpa_union that is mostly on land is called *excess_land_polygon*, shown in shaded yellow. Using a certain grid size, the polygonal areas dpa_union_polygon, excess_sea_polygon and excess_land_polygon are discretized to generate 3 sets of points *all_protected_points*, *excess_sea_points* and *excess_land_points*, respectively.

For a given DPA, a set of candidate locations along the coast is selected (Line 9). Using the ITM point-to-point propagation loss model over water, the maximum detection radius is computed based on radar parameters, sensor location, sensor height and the sensor's minimum detection threshold (Line 10). For a given candidate sensor location, the maximum detection

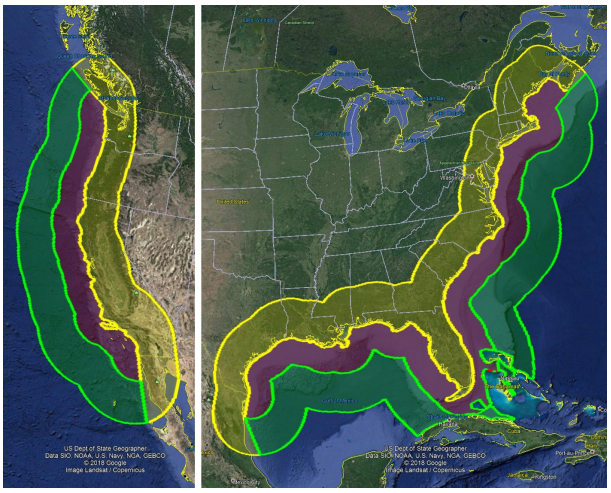

Fig. 1. Land (in shaded yellow), union DPAs (in shaded violet red), and sea (in shaded green) regions.

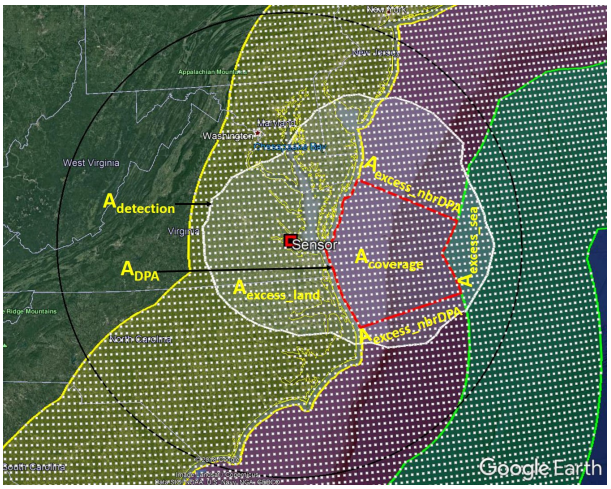


Fig. 2. Illustration of detection and excess areas.

circle is drawn using the maximum detection radius as shown in Fig. 2. All points inside the circle, called $points\_of\_interest$ will be used to estimate the detection coverage of the sensor $A_{detection}$ at that location.

Let $A_{DPA}$ be the total area of the DPA covering all points inside and on the DPA polygon. We define the area that is inside both the DPA and the detection coverage area as $A_{coverage} = A_{DPA} \cap A_{detection}$. The area that is outside the DPA but inside its detection coverage area is defined as $A_{excess} = \overline{A_{DPA}} \cap A_{detection}$. We further divide the excess area $A_{excess}$ of a DPA into three components: a) excess area overlapping with its neighboring DPAs ($A_{excess\_nbrDPA}$), b) excess area extending out to sea ($A_{excess\_sea}$), and c) excess area covering the sea and land region along the shoreline ($A_{excess\_land}$). These areas are illustrated in Fig. 2.

For a given antenna pattern and a given azimuth, the Received Signal Strength (RSS) from each point, which belongs to the

Sahoo, Anirudha; Nguyen, Thao; Hall, Timothy.
"A Practical Approach to Place Coastal Sensors for Spectrum Sharing in the 3.5 GHz Band."
Paper presented at IEEE Wireless Communications and Networking Conference (WCNC), Marrakech, Morocco. April 15, 2019 - April 19, 2019.

set $points\_of\_interest$, to the sensor location is computed (Line 18). Out of those points, the ones which can be detected are identified and the corresponding areas are computed (Lines 21 to 29).

We denote the weights associated with excess areas in neighboring DPAs, sea, and land as $w_{excess\_nbrDPA}, w_{excess\_sea}, w_{excess\_land}$, respectively. Thus, the total weighted excess area can be computed as follows.

$$A_{excess} = w_{excess\_nbrDPA} * A_{excess\_nbrDPA} + w_{excess\_sea} * A_{excess\_sea} + w_{excess\_land} * A_{excess\_land} \quad (1)$$

After all the results are computed, the set of tuples of $(loc, pattern, az)$ for which the maximum DPA coverage is achieved are identified (Line 32). Among those tuples the one with minimum weighted excess area is chosen as the final solution (Line 33).

To keep the description of our algorithm simple, we have not shown the part of the algorithm that tests different combinations of multiple sensor locations for DPA coverage. For our dataset, it so happens that all the DPAs can be provided 100 % coverage by just one sensor per DPA. If this is not the case for some other datasets, the algorithm presented here should have an outer loop to take different combinations of multiple sensor locations to find the final solution.

## IV. Model

In this section, we present the models and assumptions used in our analysis. Table I lists all important technical parameters of the radar, ESC sensor, and ITM propagation model.

The operational parameters of the radar can be found in [22], [23], while the technical parameters of an ESC sensor are available in [16], [24]. We utilize the antenna pattern specified in CBRS standards [4] for the ESC sensor antenna pattern. Thus, using the method outlined in [25], the mathematical model for computing ESC antenna gain is as follows:

$$G_{ESC}(\theta) = G_{ESC\_peak} - \min\left[12\left(\frac{\theta}{\theta_{3dB}}\right)^2, \quad A_H\right] \quad (2)$$

where $G_{ESC}(\theta)$ is the sensor antenna gain (dBi) at the off-axis angle $\theta$, $-180^\circ \leq \theta \leq 180^\circ$, $G_{ESC\_peak}$ is the ESC peak antenna gain (dBi), $\theta_{3dB}$ is the 3-dB beamwidth of the antenna (degree), and $A_H = 20$ dB is the maximum attenuation. We use the ITM point-to-point mode to compute the propagation loss between the radar and the ESC sensor [18], [26]. In addition to those parameters listed in Table I, the ITM point-to-point mode requires terrain profile as inputs to the model. We leverage the CBRS standard reference implementations of the antenna pattern and propagation model [19] as well as the terrain elevation data used for SAS testing [27].

Given the locations of a shipborne radar and an ESC sensor, the received signal strength at the ESC antenna output (Line 18 in Algorithm 1) can be computed as follows:

$$RSS = P_{radar} + G_{peak\_radar} - L_{i\_radar} - PL + G_{ESC}(\theta) - L_{i\_ESC} \quad (3)$$

TABLE I
Technical Parameters.

| **Shipborne Radar-1 Parameter** | **Value** |
|---|---|
| Transmitted Power to Ant. (dBm) | 90 |
| Peak Antenna Gain (dBi) | 32 |
| Transmit/Receive Bandwidth (MHz) | 1 |
| Center Frequency (MHz) | 3650 |
| Antenna Height (m) | 50 |
| Insertion/Cable Losses (dB) | 2 |
| **ESC Sensor Parameter** | **Value** |
| Antenna Directivity/Patterns | 3GPP |
| 3-dB Beamwidth (degree)/ Peak Ant. Gain (dBi) | (90,15), (60,16), (45,17), (30,18) |
| Receive Bandwidth (MHz) | 1 |
| Center Frequency (MHz) | 3650 |
| Min. Detection Theshold (dBm/MHz) | -89 |
| Antenna Height (m) | import from database [21] subject to min=10 and max=100 |
| Insertion/Cable Losses (dB) | 2 |
| **ITM Point-to-Point Parameter** | **Value** |
| Polarization | 1 (Vertical) |
| Dielectric constant | 81 (Sea Water) |
| Conductivity | 5 (Sea Water) |
| Surface Refractivity (N-units) | 350 (Maritime, Over Sea) |
| Radio Climate | 7 (Maritime, Over Sea) |
| Mode of Variability | 3 (Broadcast) |
| Terrain Irregularity (m) | 0 (Flat/Smooth Water) |
| Transmitter Siting Criteria | 2 (Very Careful) |
| Receiver Siting Criteria | 0 (Random) |
| Confidence/Reliability Var. (%) | 50/50 |
| **Miscellaneous** | **Value** |
| Grid Spacing (km) | 10 |

where $P_{radar}$ is the transmit power of the radar (dBm), $G_{peak\_radar}$ is the peak antenna gain of the radar (dBi), $L_{i\_radar}$ is the radar transmitter insertion loss (dB), $PL$ is the median path loss between the radar transmitter and ESC receiver (dB), $G_{ESC}(\theta)$ is the ESC antenna gain in the direction of the radar (dBi), $L_{i\_ESC}$ is the ESC receiver insertion loss (dB). Note that given the azimuth of the sensor, angle $\theta$ is the angle that radar transmitter subtends relative to the boresight of the ESC sensor antenna. The ESC sensor can detect the radar if the received signal strength at the ESC sensor is above its detection threshold.

## V. Experiment and Results

We ran our algorithm on the set of DPAs published in [5]. We used the tower locations and tower heights published by American Tower [21] as candidate sensor locations and antenna heights, respectively. The results presented in this section were obtained by setting all three weights, $w_{excess\_nbrDPA}, w_{excess\_sea}, w_{excess\_land}$, to 1.

### A. ESC Detection Coverage

We implemented the algorithm described in Section III to determine sensor locations and estimate their detection

Sahoo, Anirudha; Nguyen, Thao; Hall, Timothy.
"A Practical Approach to Place Coastal Sensors for Spectrum Sharing in the 3.5 GHz Band."
Paper presented at IEEE Wireless Communications and Networking Conference (WCNC), Marrakech, Morocco. April 15, 2019 - April 19, 2019.

**Algorithm 1:** Calculate sensor locations, antenna parameters, and performance metrics for all DPAs in a given U.S. coast

**Input**: $radar\_pars$: radar parameters including transmit power, bandwidth, main beam attenna gain, height, and insertion loss.
$itm\_p2p\_pars$: ITM point to point propagation parameters.
$tower\_locs$: a set of tower locations used as candidate locations for ESC sensors.
$min\_det\_threshold$: minimum detection threshold of ESC sensors.
$ant\_patterns$: a set of sensor antenna patterns, each having a tuple of (beam_width, peak_gain).
$az\_step$: step size of change in azimuth.
$dpa\_polygons$: a set of polygons, each representing a coastal DPA.
$dilation\_width$: width used to dilate the combined DPA polygon to cover land and sea areas.
$grid\_size$: grid size.
$w\_excess\_sea, w\_excess\_land, w\_excess\_nbrDPA$: weighting factors applied to excess areas over sea, land, and neighboring DPAs, respectively.

**Output**: Results for each DPA including sensor location ($C\_out$), antenna pattern ($pattern\_out$), azimuth ($az\_out$), probability of detection coverage ($P\_coverage$), probability of false alarms from neighboring DPAs ($P\_fa\_nbrDPA$) and out in the sea ($P\_fa\_sea$).

$dpa\_union\_polygon \leftarrow \bigcup(dpa \in dpa\_polygons)$; /* union of consecutive DPA polygons along the coast */
$dilated\_dpa\_union \leftarrow$ DilatePolygon($dpa\_union\_polygon, dilation\_width$); /* dilate DPA union polygon */
$grid\_points \leftarrow$ GenerateGrid($dilated\_dpa\_union, grid\_size$); /* generate points within dilated polygon */
$(excess\_land\_polygon, excess\_sea\_polygon) \leftarrow$ FormLandSeaPolygon($dpa\_union\_polygon, dpa\_union\_polygon$); /* form excess land/sea polygons, adjacent to DPA union polygon, over land/sea areas */
$(all\_protected\_points, excess\_land\_points, excess\_sea\_points) \leftarrow$ GetPoint($grid\_points, dpa\_union\_polygon, excess\_land\_polygon, excess\_sea\_polygon$); /* get all protected/land/sea points inside DPA union/land/polygon, respectively */
**foreach** $dpa \in dpa\_polygons$ **do**
  $A\_dpa \leftarrow$ ComputeArea($dpa$); /* compute area of DPA */
  $dpa\_points \leftarrow$ GetDPAPrtnPoint($dpa, all\_protected\_points$); /* get protected points on and within DPA polygon */
  $cand\_sensor\_locs \leftarrow$ GetCandSensorLoc($dpa, tower\_locs$); /* get tower locations along the inner edge of DPA */
  $max\_det\_radius \leftarrow$ EstMaxDetRadius($cand\_sensor\_locs, min\_det\_threshold, radar\_pars$); /* estimate maximum sensor detection radius */
  **foreach** $C \in cand\_sensor\_locs$ **do**
    $points\_of\_interest \leftarrow$ GetPointInsideCircle($C, max\_det\_radius, grid\_points, dpa$); /* get grid points (including those on DPA polygon) inside the circle centered at $C$ and radius of $max\_det\_radius$ */
    $azimuths \leftarrow$ CalcAzimuths($C, dpa, az\_step$); /* compute antenna azimuths, with $az\_step$ step size, between 2 inner edge corners of DPA polygon */
    **foreach** $pattern \in ant\_patterns$ **do**
      **foreach** $az \in azimuths$ **do**
        $detected\_points = \emptyset$;
        **foreach** $point \in points\_of\_interest$ **do**
          $RSS \leftarrow$ CalcRSS($points\_of\_interest, radar\_pars, itm\_p2p\_pars, C, pattern, az$); /* calculate received signal strength from radar location $point$ to sensor location $C$ */
          **if** $RSS \geq min\_det\_threshold$ **then**
            $detected\_points$ += $point$;
        $detected\_dpa\_points \leftarrow \{\forall p : p \in detected\_points \wedge p \in dpa\_points\}$;
        $detected\_excess\_sea \leftarrow \{\forall p : p \in detected\_points \wedge p \in excess\_sea\_points\}$;
        $detected\_excess\_land \leftarrow \{\forall p : p \in detected\_points \wedge p \in excess\_land\_points\}$;
        $detected\_excess\_nbrDPA \leftarrow \{\forall p : p \in detected\_points \wedge p \in all\_protected\_points \wedge p \notin dpa\_points\}$;
        $A\_detection[C][pattern][az] \leftarrow$ ComputeArea($detected\_points$);
        $A\_coverage[C][pattern][az] \leftarrow$ ComputeArea($detected\_dpa\_points$);
        $A\_excess\_sea[C][pattern][az] \leftarrow$ ComputeArea($detected\_excess\_sea$);
        $A\_excess\_land[C][pattern][az] \leftarrow$ ComputeArea($detected\_excess\_land$);
        $A\_excess\_nbrDPA[C][pattern][az] \leftarrow$ ComputeArea($detected\_excess\_nbrDPA$);
        $A\_weighted\_excess[C][pattern][az] \leftarrow A\_excess\_sea[C][pattern][az] \times w\_excess\_sea +$
        $A\_excess\_nbrDPA[C][pattern][az] \times w\_excess\_nbrDPA +$
        $A\_excess\_land[C][pattern][az] \times w\_excess\_land$;
  $max\_A\_coverage \leftarrow \max_{\forall(C,pattern,az)}(A\_coverage[C][pattern][az])$;
  $max\_coverage\_indices \leftarrow \{(C, pattern, az) : A\_weighted\_excess[C][pattern][az] = max\_A\_coverage\}$;
  $(C\_out, pattern\_out, az\_out) = \min_{\forall(C,pattern,az)\in\{max\_coverage\_indices\}}(A\_weighted\_excess[C][pattern][az])$;
  $P\_coverage \leftarrow max\_A\_coverage/A\_dpa$;
  $P\_fa\_nbrDPA \leftarrow A\_excess\_nbrDPA[C\_out][pattern\_out][az\_out]/A\_detection$;
  $P\_fa\_sea \leftarrow A\_excess\_sea[C\_out][pattern\_out][az\_out]/A\_detection$;

coverages for all coastal DPAs on the West coast as well as on the East and Gulf coasts. Fig. 3 shows the DPA polygons in red contours, the resulting sensor locations in red squares and their detection coverages in white shaded areas.

Upon examination of the results, we found that only a single sensor equipped with a single antenna is needed to fully cover each DPA. The West coast requires 14 sensors, whereas the East and Gulf coasts require 26 sensors located near the shoreline. Most of these sensors employ a maximum antenna height of 100 m; only a few sensors have antenna height ranging from 50 m to 95 m. Selecting higher antenna height provides a larger detection coverage of the DPA. Antenna patterns with small beamwidths and high peak gains are preferred

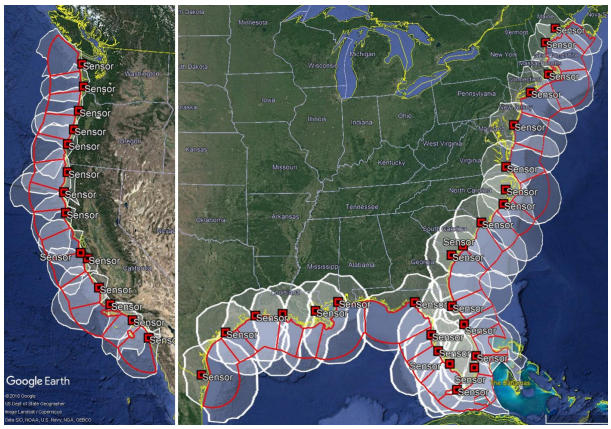


Fig. 3. Sensor locations and detection coverages for all coastal DPAs. DPA polygons are in red contours, resulting sensor locations in red squares and their detection coverages in white shaded areas.

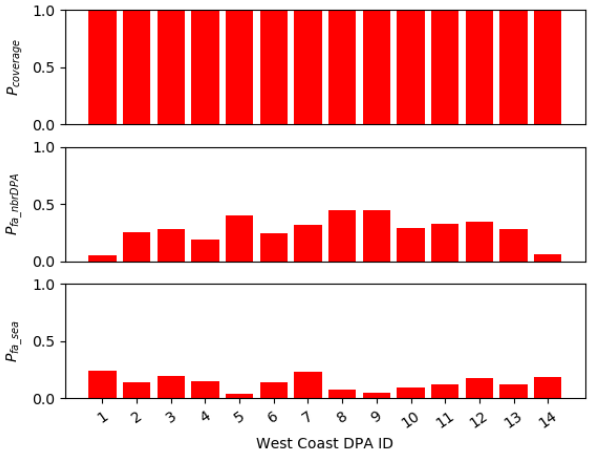


Fig. 4. Performance results of West coast.

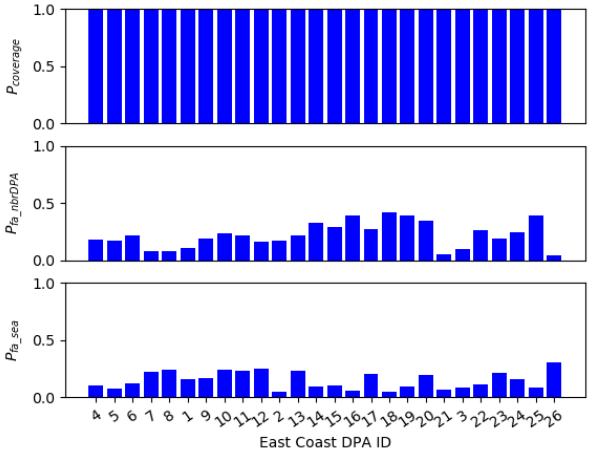


Fig. 5. Performance results of East and Gulf coasts.

to minimize the excess area outside the DPA. Our results show that only 9 locations used antenna patterns of $(90°, 15$ dBi) and $(60°, 16$ dBi) to cover large DPAs, whereas the remaining locations used antenna patterns $(30°, 18$ dBi) and $(45°, 17$ dBi).

Comparing with the results presented in [17], it is observed that our scheme uses fewer sensors and antenna patterns. However, it is worth noting that the DPA dataset used in [17] is an older version and slightly different. Besides, the sensor sensitivity in [17] was varied while it is fixed at the minimum detection threshold at $-89$ dBm/MHz in this study. We found no meaningful benefit in the form of lower excess coverage from raising the detection coverage above this minimum threshold at any location.

### B. Performance Results

We analyze our detection coverage results for each DPA in terms of two performance metrics, i.e., *probability of coverage* and *probability of false alarm*. Figs. 4 and 5 show performance results of our algorithm when applied to the DPAs along the West coast and the combined East and Gulf coasts, respectively.

*1) Probability of Detection Coverage:* We define probability of DPA detection coverage as $P_{coverage} = A_{coverage}/A_{DPA}$, conditioned on the median pathloss value, to represent the probability of a shipborne radar being detected when it is inside the DPA. To ensure the DPA is fully monitored by the ESC sensor(s), $P_{coverage}$ needs to be close to one. The top subplots in Figs. 4 and 5 present $P_{coverage}$ computed for each DPA. In all cases, $P_{coverage} = 1$, which meets the objective of detecting the shipborne radar anywhere within DPA contours.

*2) Probability of False Alarm:* We consider two types of false alarms as follows.

*a) False Alarm from Neighboring DPAs:* This false alarm is raised when a DPA is activated because its associated ESC sensor(s) detects signal from a shipborne radar present in its neighboring DPA. This is clearly an undesired event since the radar in the neighboring DPA should only be detected by the ESC sensor(s) in that neighboring DPA. The probability of this false alarm is defined as $P_{fa\_nbrDPA} = A_{excess\_nbrDPA}/A_{detection}$.

The middle subplots in Figs. 4 and 5 show $P_{fa\_nbrDPA}$ for each DPA, and it is within the range of (0.05 to 0.45). DPAs that are small narrow polygons are prone to have larger values of $P_{fa\_nbrDPA}$.

*b) False Alarm Out at Sea:* This is the false alarm due to the excess coverage area further out at sea and is defined as $P_{fa\_sea} = A_{excess\_sea}/A_{detection}$. This metric captures the likelihood that an ESC sensor activates its associated DPA even though the radar is further out at sea and outside of the DPA. $P_{fa\_sea}$ should be as low as possible to avoid unnecessary shutdown of CBSDs.

The bottom subplots in Figs. 4 and 5 depict $P_{fa\_sea}$ for each DPA. For both coasts, DPAs have $P_{fa\_sea}$ values in the range of (0.04 to 0.3). Because of the geometric shapes of the DPAs, sensor deployment, and antenna patterns, there is always a trade-off between $P_{fa\_nbrDPA}$ and $P_{fa\_sea}$.

Sahoo, Anirudha; Nguyen, Thao; Hall, Timothy.
"A Practical Approach to Place Coastal Sensors for Spectrum Sharing in the 3.5 GHz Band."
Paper presented at IEEE Wireless Communications and Networking Conference (WCNC), Marrakech, Morocco. April 15, 2019 - April 19, 2019.

Comparing with the results presented in [17] for comparable DPAs, we found that this algorithm along with the selected parameters provide better performance for all $P_{coverage}$, $P_{fa\_nbrDPA}$, and $P_{fa\_sea}$.

To further decrease excess area to land and neighboring DPAs, we applied weighting factors $w_{excess\_land} = 10$, $w_{excess\_nbrDPA} = 5$, $w_{excess\_sea} = 1$ to the total excess area. However, we found that the improvement is insignificant, indicating the selection of sensor locations and operation parameters provide a near-optimal solution.

## VI. Conclusion and Future Work

This paper presents an approach to determine locations and operational parameters of ESC sensors to detect the presence of federal incumbent shipborne radar operating in the 3.5 GHz band. We formulate the problem as a coverage problem where one or more ESC sensors fully covers the DPA while minimizing the excess areas both out at sea and in its neighboring DPAs. We design and implement an algorithm that achieves this objective. We apply our algorithm to DPAs along the coasts of the contiguous United States as defined by NTIA at the time of this submission [5] and present the performance results for each DPA.

We used the ITM point-to-point mode [18] to compute the path loss between the radar and the sensor. In addition, we used existing tower locations along the coast as candidate sites for the sensors. Future work should consider a higher reliability value for the ITM model to compute the path loss and deploy more than one sensor for each DPA if there is an outage area within the DPA. Other propagation models applicable to the CBRS band, e.g., ITU-R P.2001 [28] and extended Hata [23], should also be examined.

## References


[1] J. Mitola, J. Guerci, J. Reed, Y. D. Yao, Y. Chen, T. C. Clancy, J. Dwyer, H. Li, H. Man, R. McGwier, and Y. Guo, "Accelerating 5G QoE via public-private spectrum sharing," *IEEE Communications Magazine*, vol. 52, no. 5, pp. 77–85, May 2014.

[2] Nokia, "Bridging the spectrum gap with 5G," http://networks.nokia.com/news-events/insight-newsletter/articles/bridging-the-spectrum-gap-with-5g, 2013, [Online; accessed 07-July-2016].

[3] National Telecommunications and Information Administration (NTIA), "An assessment of the near-term viability of accommodating wireless broadband systems in the 1675-1710 MHz, 1755-1780 MHz, 3500-3650 MHz, and 4200-4220 MHz, 4380-4400 MHz band," National Telecommunications and Information Administration (NTIA), Fast Track Report, Oct. 2010.

[4] "Requirements for Commercial Operation in the U.S. 3550–3700 MHz Citizens Broadband Radio Service Band," Wireless Innovation Forum Document WINNF-TS-0112, Version V5.0, Mar. 2018. [Online]. Available: https://workspace.winnforum.org/higherlogic/ws/public/document?document_id=4743&wg_abbrev=SSC

[5] "DPA kml file (e-dpas.kml)," [Accessed 17-Sep-2018]. [Online]. Available: https://www.ntia.doc.gov/fcc-filing/2015/ntia-letter-fcc-commercial-operations-3550-3650-mhz-band

[6] M. Cardei and J. Wu, "Energy-efficient coverage problems in wireless ad-hoc sensor networks," *Computer communications*, vol. 29, no. 4, pp. 413–420, 2006.

[7] J. Carle and D. Simplot-Ryl, "Energy-efficient area monitoring for sensor networks," *Computer*, vol. 37, no. 2, pp. 40–46, 2004.

[8] S. Slijepcevic and M. Potkonjak, "Power efficient organization of wireless sensor networks," in *Communications, 2001. ICC 2001. IEEE International Conference on*, vol. 2. IEEE, 2001, pp. 472–476.

[9] D. Tian and N. D. Georganas, "A coverage-preserving node scheduling scheme for large wireless sensor networks," in *Proceedings of the 1st ACM international workshop on Wireless sensor networks and applications*. ACM, 2002, pp. 32–41.

[10] M. Cardei and D.-Z. Du, "Improving wireless sensor network lifetime through power aware organization," *Wireless Networks*, vol. 11, no. 3, pp. 333–340, 2005.

[11] K. Kar and S. Banerjee, "Node placement for connected coverage in sensor networks," in *WiOpt'03: Modeling and Optimization in Mobile, Ad Hoc and Wireless Networks*, 2003, pp. 2–pages.

[12] M. A. Guvensan and A. G. Yavuz, "On coverage issues in directional sensor networks: A survey," *Ad Hoc Networks*, vol. 9, no. 7, pp. 1238 – 1255, 2011. [Online]. Available: http://www.sciencedirect.com/science/article/pii/S1570870511000461

[13] S. Joshi and K. B. S. Manosha and M. Jokinen and T. Hänninen and Pekka Pirinen and H. Posti and M. Latva-aho, "ESC sensor nodes placement and location from moving incumbent protection in CBRS," *Proceedings of WInnComm 2016*, Mar. 2016.

[14] "Application of Google Inc. for Certification to Provide Spectrum Access System and Environmental Sensing Capability Services," GN Docket No. 15-319, Appendix B: Environmental Sensing Capability (ESC) Siting Considerations, 2016. [Online]. Available: https://ecfsapi.fcc.gov/file/60001851224.pdf

[15] T. T. Nguyen, A. Sahoo, M. Souryal and T. A. Hall, "3.5 GHz Environmental Sensing Capability Sensitivity Requirements and Deployment," in *IEEE DySPAN '17*, March 2017, pp. 1–10.

[16] T. T. Nguyen and M. R. Souryal and A. Sahoo and T. A. Hall, "3.5 GHz Environmental Sensing Capability Detection Thresholds and Deployment," *IEEE Transactions on Cognitive Communications and Networking*, vol. 3, no. 3, pp. 437–449, Sept 2017.

[17] A. Sahoo, M. Ranganathan, T. T. Nguyen and T. A. Hall, "Sensor Placement and Detection Coverage for Spectrum Sharing in the 3.5 GHz Band," in *to appear in IEEE PIMRC '18*, Sep 2018.

[18] "Irregular Terrain Model (ITM) (Longley-Rice) (20 MHz–20 GHz)." [Online]. Available: https://www.its.bldrdoc.gov/resources/radio-propagation-software/itm/itm.aspx

[19] "Reference models for SAS testing." [Online]. Available: https://github.com/Wireless-Innovation-Forum/Spectrum-Access-System/tree/master/src/harness/reference_models

[20] M. R. Garey and D. S. Johnson, *Computers and Intractability: A Guide to the Theory of NP-Completeness*. W. H. Freeman, 1979.

[21] "American Tower." [Online]. Available: http://www.americantower.com/corporateus/articles/find-sites.htm

[22] F. H. Sanders, E. F. Drocella, and R. L. Sole, "Using On-Shore Detected Radar Signal Power for Interference Protection of Off-Shore Radar Receivers," National Telecommunications and Information Administration, Technical Report TR 16-521, Mar. 2016. [Online]. Available: http://www.its.bldrdoc.gov/publications/2828.aspx

[23] E. Drocella, J. Richards, R. Sole, F. Najmy, A. Lundy, and P. McKenna, "3.5 GHz Exclusion Zone Analyses and Methodology," National Telecommunications and Information Administration, Technical Report TR 15-517, Mar. 2016. [Online]. Available: http://www.its.bldrdoc.gov/publications/2805.aspx

[24] "3.5 GHz Radar Waveform Capture at Point Loma," National Institute of Standards and Technology (NIST), Technical Note NIST.TN.1954, May 2017. [Online]. Available: http://nvlpubs.nist.gov/nistpubs/TechnicalNotes/NIST.TN.1954.pdf

[25] "Technical Specification Group Radio Access Network; Feasibility study for enhanced uplink for UTRA FDD," Technical Report 3GPP-TR25.896, Mar. 2004. [Online]. Available: http://www.qtc.jp/3GPP/Specs/25896-600.pdf

[26] G. Hufford, A. Longley, W. Kissick, U. S. N. Telecommunications, and I. Administration, *A Guide to the Use of the ITS Irregular Terrain Model in the Area Prediction Mode*, ser. NTIA report. U.S. Department of Commerce, National Telecommunications and Information Administration, 1982. [Online]. Available: https://www.ntia.doc.gov/files/ntia/publications/ntia_82-100_20121129145031_555510.pdf

[27] "SAS data repository." [Online]. Available: https://github.com/Wireless-Innovation-Forum/SAS-Data

[28] "ITU-R P.2001 : A general purpose wide-range terrestrial propagation model in the frequency range 30 MHz to 50 GHz." [Online]. Available: https://www.itu.int/rec/R-REC-P.2001-2-201507-I/en



Sahoo, Anirudha; Nguyen, Thao; Hall, Timothy.
"A Practical Approach to Place Coastal Sensors for Spectrum Sharing in the 3.5 GHz Band."
Paper presented at IEEE Wireless Communications and Networking Conference (WCNC), Marrakech, Morocco. April 15, 2019 - April 19, 2019.

# Some Advantages of Using Bi-directional S-Parameters in Near-Field Measurements[1]

David R. Novotny, Alex J. Yuffa, Ronald C. Wittmann, Michael H. Francis, Joshua A. Gordon
Communications Technology Laboratory
National Institute of Standard and Technology
Boulder, Colorado, United States of America
david.novotny@nist.gov

***Abstract*—The unknown-thru calibration technique is being used to achieve a system level calibration at millimeter wave frequencies (>50 GHz) on the robotic ranges at NIST. This two-port calibration requires the use of a full bi-directional measurement, instead of a traditional single-direction antenna measurement. We explored the value of the additional data acquired. We find that we can use this information to verify antenna/scan alignment, image the scattering from the positioner/facility, and perform a first order correction to the transmission data for uncertainties due to LO cable flexure.**

## I. Introduction

It has been shown that vector network analyzers (VNA) can be used to great effect in antenna measurements [1,2]. However, in most production antenna scanning applications, measurement speed and costs are usually overarching concerns. Bi-directional calibrations and scans with a network analyzer take longer than conventional measurement receivers because at least twice the number of measurements and four times the data are required in comparison to the single-direction case. These measurements must be taken at different times to isolate the forward and reverse scattering parameters. Such measurements take more time and require more resources, system drift can increase with longer operational times and space-time coordination between the forward and reverse measurements can complicate processing.

Despite the many operational drawbacks, a fully calibrated bi-directional system can reveal information on antenna-to-antenna interaction (is the scan too close), real-time drift checks for cable bending or other environmental changes. The redundant measurements can also provide a consistency check. When using broad frequency sweeps, we can use software position correction to compensate for the moving probe results. Then we might use more tools, like time domain gating, to examine and remove extra reflections, back image to the antenna-under-test (AUT) to assess scan alignment and see changes in horn reflections.

We hope to show that the extra effort and resources associated with this measurement might lead to some advantages in situations where lower uncertainty measurements are desired.

## II. CROMMA and the Unkown Thru

The Configurable Robotic Millimeter Antenna (CROMMA) facility, Figure. 1, is based on two robotic structures [3]: the probe positioner is a six degree of freedom (DoF) serial robotic arm with 15 μm resolution. The antenna under test (AUT) positioner is a parallel hexapod positioner with 0.2 μm resolution. These motion stages are guided by a laser tracker with ~10 μm accuracy. This resolution is acceptable for positioning antennas, but it is larger than the 3 μm machining tolerances specified in the UG-385/U connector specification. Further exacerbating the situation, the RF hardware is mechanically linked to several large and heavy (~ 10 kg) laser tracker targets, so precise connections for calibration and normalization, are difficult.

Since we cannot perform a robotic-guided mechanical connection between the robotic arm and the hexapod mounted equipment, we use the unknown-thru calibration to characterize and remove the systematic effects of the VNA from the desired transmission between the antennas. The unknown-thru requires a full reflection calibration on each port, which establishes the port-to-samplers' loss and phase relation for each port [4,5]. A reciprocal thru and a frequency spacing that avoids aliasing in the electrical length of the unknown-thru is needed to establish the relative phase relations between the samplers.

Assuming reciprocity between the ports and through the antennas, *i.e.* $S_{21}=S_{12}$, this allows us to calibrate each port and perform a "thru" given a minimal loss (< 30 dB) between the probe and AUT. The robots are sufficiently accurate that the "unknown-thru" reference point can be repeated to less than 30 μm, better than λ/80 for these tests, and be used as a drift check and re-calibration point during the measurements.

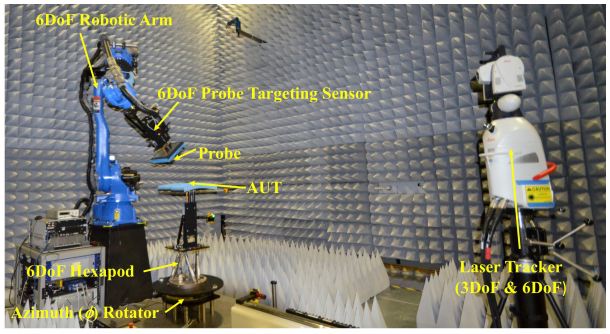

Figure 1. The CROMMA facility installed at NIST.

[1] US Government Work – NOT SUBJECT TO US COPYRIGHT

Yuffa, Alexey; Wittmann, Ronald; Francis, Michael; Gordon, Joshua; Novotny, David.
"Some Advantages of Using Bi-directional S-Parameters in Near-Field Measurements."
Paper presented at 40th Annual Meeting and Symposium of the Antenna Measurement Techniques Association (AMTA 2018), Williamsburg, VA, United States. November 4, 2018 - November 9, 2018.

### A. Antennas

We characterized a WR-08 system feed horn operating across a frequency range of 112–125 GHz [6,7]. To characterize the radiation from the AUT, we performed a three-antenna gain extrapolation with the AUT (a WR-08 feed horn), the probe (a μ=±1 antenna), and a 15 dBi pyramidal horn. The on-axis gains were determined via the extrapolation method [8]. Then the far-field (FF) pattern measurements were performed on the probe, using the pyramidal horn. Finally, spherical near-field (SNF) scans of AUT were performed using the probe.

### B. Idealized S-parameters

One issue with using remote mixing and fully bi-directional measurements is that there are multiple ways to introduce errors. In Figure 2, we see a block diagram of the VNA setup. Changes in the local oscillator (LO) cable, $C_{LO1}$, affects primarily waves $a_1$ and $b_1$, while changes in $C_{LO2}$ affects waves $a_2$ and $b_2$. If harmonic mixers are used, changes in the LO signals at the mixers may not linearly transfer through the mixers.

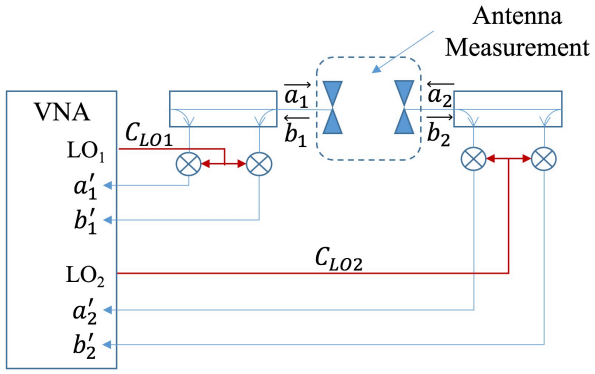


Figure 2. Simplified signal block diagram for a bi-directional frequency-converting two-port VNA measurement. The source is not shown as changes in the source signal are minimized by the ratioed nature of the S-parameter measurement.

If Figure 2 is idealized by perfect couplers, ideal and balanced mixers and matched interfaces, we can assume that the received wave parameters $a_1', b_1'$ are just frequency offset versions of $a_1, b_1$ with a shift due to the $C_{LO1}$ cable of $C_1 e^{j\varphi_{LO1}}$. This allows us to simplify the S-parameter calibration equations:

$$S'_{11} \approx \frac{b_1'}{a_1'} \approx \frac{b_1 C_1 e^{j\varphi_{LO1}}}{a_1 C_1 e^{j\varphi_{LO1}}} \qquad S'_{21} \approx \frac{b_2'}{a_1'} \approx \frac{b_2 C_2 e^{j\varphi_{LO2}}}{a_1 C_1 e^{j\varphi_{LO1}}}$$
$$S'_{12} \approx \frac{b_1'}{a_2'} \approx \frac{b_1 C_1 e^{j\varphi_{LO1}}}{a_2 C_2 e^{j\varphi_{LO2}}} \qquad S'_{22} \approx \frac{b_2'}{a_2'} \approx \frac{b_2 C_1 e^{j\varphi_{LO2}}}{a_2 C_1 e^{j\varphi_{LO2}}} \qquad (1).$$

(1) shows that cable stress on the LO cables will directly affect $S_{21}$ and $S_{12}$ but has little effect on $S_{11}$ or $S_{22}$. To first order, $S_{21}$ and $S_{12}$ will change reciprocally, so taking the geometric mean, $(S'_{21}S'_{12})^{1/2} \approx \sqrt{b_1 b_2 / a_1 a_2} \approx b_2/a_1 = S_{21}$, should give a better estimate of the actual transmission. In the ideal case, $S'_{21}$ and $S'_{12}$ have opposite LO induced phase shifts, but practically there are non-linear amplitude shifts as well. As we can't directly measure the LO cable changes [9], we are forced to minimize phase and amplitude variations in the LO cabling [3].

### C. Setup and Calibration

We align the antennas for a given antenna test and note the encoder counts for the robot, hexapod and rotator. Our alignments, once calculated and checked with the laser tracker, are mechanically repeatable to λ/50 [3]. This allows us to depend on the long-term stability of the alignments and calibrate the mmWave equipment as needed. Figure 3 shows a conceptualization of the VNA system. The LO which generates the phase and amplitude reference at mmWave, needs to be properly routed to minimize stress on the cabling [3].

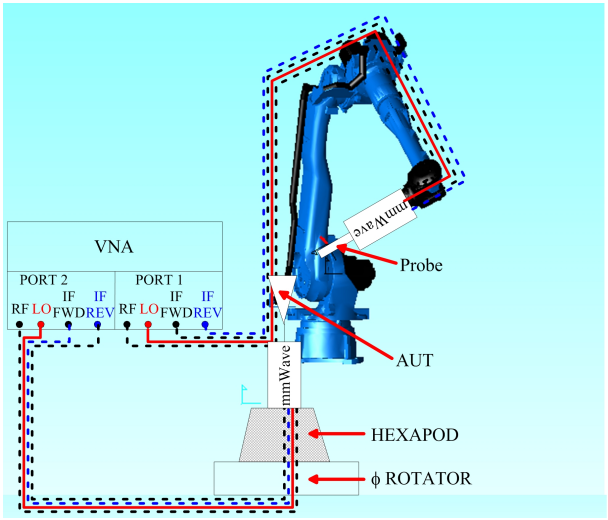


Figure 3. The RF setup of CROMMA. The LO cables (solid lines) from the VNA to the mmWave converters are the major contributors to drift due to bending and temperature.

We chose a nominally aligned position along the on-axis extrapolation path ($d \cong 75$ mm) as the unknown-thru point, Figure 4, and noted encoder counts and path to the unknown-thru point so it can be repeated with minimal robotic backlash and maximum repeatability. The calibration was then performed from 103.2503 to 133.2503 GHz in 100 MHz steps at an intermediate-frequency bandwidth (IFBW) of 100 Hz, which

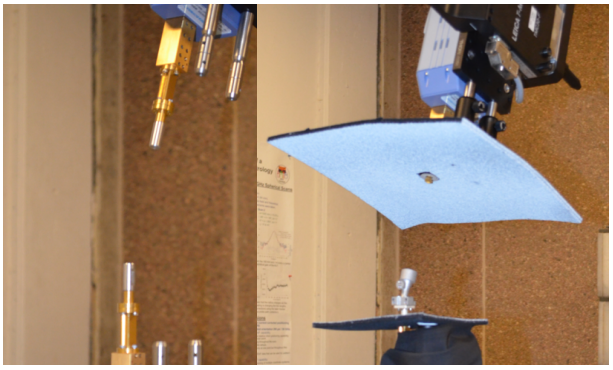

Figure 4. Calibration of the VNA on CROMMA during the AUT tests. The left shows characterization of the ports using the calibration kit standards. The right shows the "unknown-thru" at the 17 ° main beam offset and a separation of 75 mm.

Yuffa, Alexey; Wittmann, Ronald; Francis, Michael; Gordon, Joshua; Novotny, David.
"Some Advantages of Using Bi-directional S-Parameters in Near-Field Measurements."
Paper presented at 40th Annual Meeting and Symposium of the Antenna Measurement Techniques Association (AMTA 2018), Williamsburg, VA, United States. November 4, 2018 - November 9, 2018.

yielded approximately 100 dB of flange-to-flange dynamic range. While this setup resulted in an unaliased distance of $c/\Delta f$ = 3 m, much longer than the scan distance or the anticipated unknown-thru length, it provided improved estimation of the insertion phase and delay of the unknown-thru.

## III. Measurements and Results

After the broadband calibration, pattern and gain measurements were taken at the desired frequencies of 112.7503, 118.7503 and 124.7503 GHz [7].

### A. Bi-directional Gain-Extrapolation

The three-antenna extrapolation method [8] can return more than the far-field gain and polarization of the antennas. Using the unknown-thru, we can also infer the free-space reflection coefficients of each antenna and attempt to assess the effects of multiple reflections [8,10]. Figure 5 shows the transmission loss between the antennas and the difference between the forward, $S_{21}$, and reverse, $S_{12}$, measurement. This difference should be ideally near zero dB, not exactly zero as the unknown-thru calibration requires measurements be taken at different times, and the probe was constantly moving. Figure 6 shows the insertion phase (and inferred distance from phase) versus separation [3]. As the phase measures relative distance, the zero error was set at 75 mm, where the unknown-thru was measured.

Figure 6 shows a 0.018 mm shift between the forward and reverse measurements. At close distances (<50 mm), the phase is taking the expected deviation from flat as the antennas are electrically very close. At far distances (>350 mm), we see deviations probably due to excessive cable flexure. In the central region, we expect to see an approximate 0.016 mm difference as the robot is moving at a 1mm/s velocity and at 100 Hz IFBW, the measurement time is approximately 2*0.8/IFBW=16 ms for the bi-directional measurement.

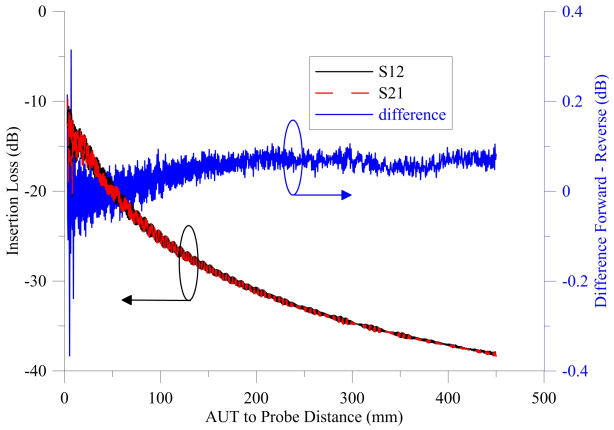


Figure 5. The on-axis co-polarized insertion loss between the AUT and the probe. Since the unknown-thru calibration requires a bi-directional measurement, we see the effect of movement and LO cable flexure on the measured transmission.

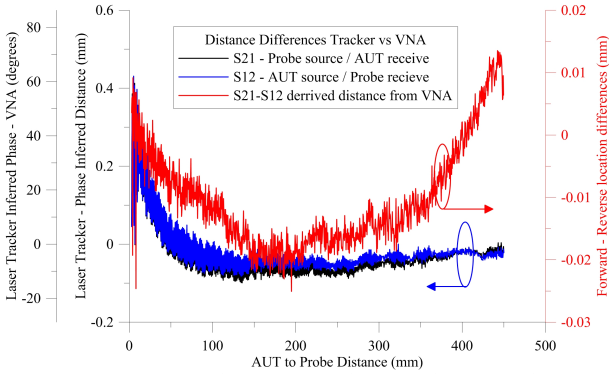


Figure 6. Comparing the insertion phase (and inferred distance) from the VNA to the direct distance by the laser tracker, as well, as the VNA inferred differences in distance using $S_{21}$ and $S_{12}$.

Continuing the examinations of the extrapolation data, Figure 7 shows the reflections at both ports as distance increases. It is common to correct the extrapolated pair gain and the measured pattern in near-field scanning by the free space reflection coefficient. Measuring the actual reflections show that even at $2D^2/\lambda$, the reflections have not fully settled to a stable, much less the far-field state. So, correcting the results to just the FF, or free-space, reflection value may not remove all the near-field reflection induced errors in the final gain result [8,12].

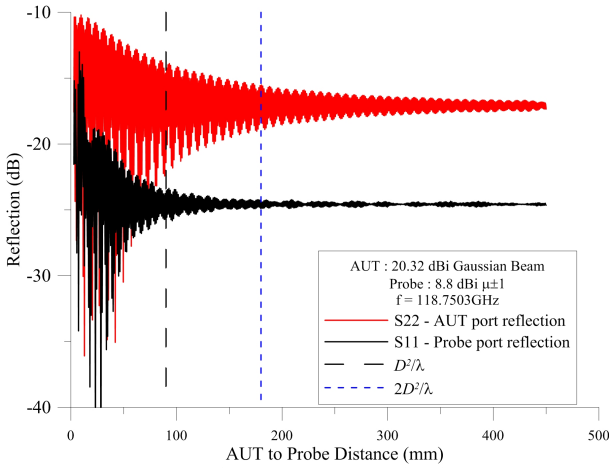


Figure 7. Examining the reflections seen by the AUT (top) and probe (bottom) as distance increases.

### B. Bi-directional Pattern Measurements

The SNF scan distance of 125 mm was chosen, because during the extrapolation scans, the change in measured reflection variations seen by the probe were less than ±0.1 dB, see Fig. 7. Other measurement parameters are listed in Table I. If the reflections seen by the AUT were fully considered, the choice of scan distance may have been larger.

Yuffa, Alexey; Wittmann, Ronald; Francis, Michael; Gordon, Joshua; Novotny, David.
"Some Advantages of Using Bi-directional S-Parameters in Near-Field Measurements."
Paper presented at 40th Annual Meeting and Symposium of the Antenna Measurement Techniques Association (AMTA 2018), Williamsburg, VA, United States. November 4, 2018 - November 9, 2018.

TABLE I. PATTERN MEASUREMNT PARAMETERS.

| Parameter | Description |
|---|---|
| Frequency | 112.7503, 118.7503, 124.7503 GHz |
| Scan Type | Spherical |
| Coverage | Double coverage – upper hemipshere |
| $\theta$ range | $-90° \le \theta \le 90°$ |
| $\phi$ range | $0° \le \phi \le 360°$ |
| Angular increment | $\Delta\phi = \Delta\theta = 1°$ |
| Radius | 125 mm |
| IFBW | 200 Hz |
| Measurment time | *8 ms ≈ 2*(0.8/IFBW)* Bi-directional |
| Modal Analysis | $2ka_{AUT} \approx 100$ modes<br>$\Delta\phi, \Delta\theta \approx 360$ modes, asssures oversampling |
| Robot velocity | 10 mm/sec |

### C. *Examining the transmission data and pattern.*

Similar to the extrapolation data, $S_{21}$ should equal $S_{12}$, however, the robot is moving. To keep our positional uncertainties low, we do not want to move the probe more than λ/50 during the primary, forward, $S_{21}$ measurement. At 10 mm/sec, the 4 ms single direction measurement transits 40 μm or λ/62.5. This means using the laser tracker data for the reverse measurement, we can expect a systematic ~λ/30 offset. We processed the forward measurement, Figure 8, and calculated the pattern and compared it to the simulated pattern, Figure 9.

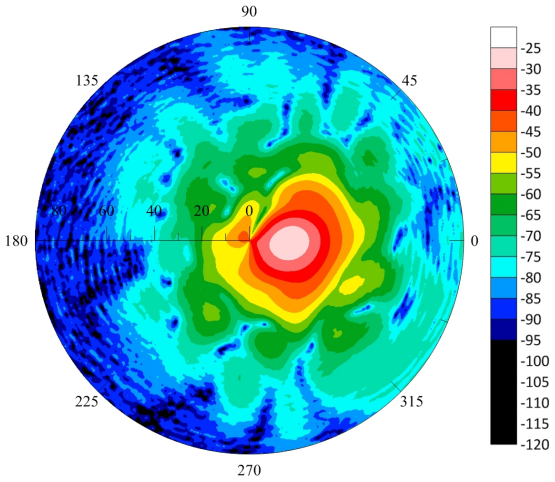


Figure 8. The on-axis co-polarized forward near-field insertion loss between the AUT and the probe.

We see both the raw near-field (NF) and far-field (FF) data, show that there is an asymmetry in the pattern. We believe that the alignment is acceptable as the FF peak lies on the $\phi$=0° axis. We expected that there may be some asymmetry along $\theta$ because the 17° waveguide bend/transition may cause a non-uniform phase illumination of the aperture.

### D. *Examining the reflection data*

Figure 10(a) shows the raw reflection data seen at the AUT and probe measurement ports. The raw $S_{11}$ and $S_{22}$ include the FF reflection of the individual antennas, as well as, the unwanted AUT-to-probe interaction and other reflections seen by the probe and AUT. We extrapolated the complex reflection data,

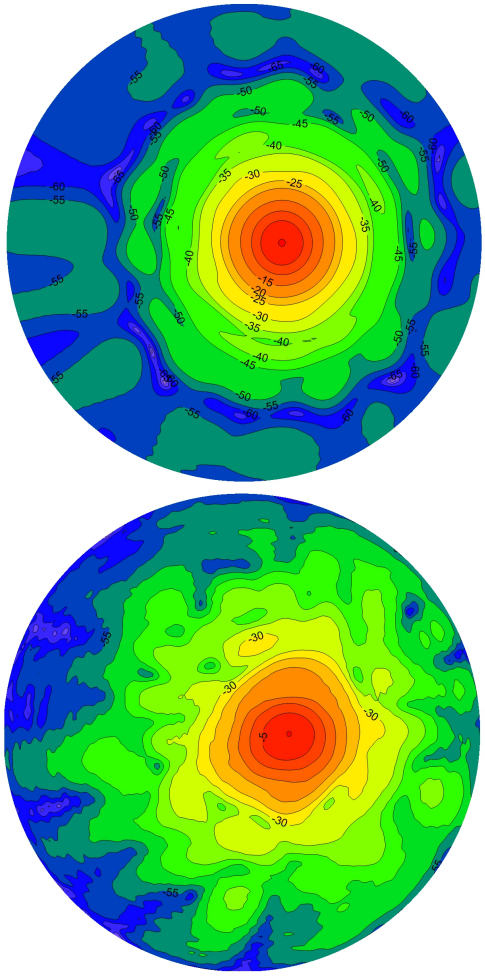

Figure 9. Simulated (top) and measured (bottom) Far-Field patterns for a WR-08 corrugated antenna.

Figure 7, to infinity to determine the free space reflection coefficient of each antenna. These values were subtracted from the reflection scan data, Figure 10(b). *While there is rather limited mathematical basis for using reflection data in the near-field to far-field (NF2FF) forward transform*, we wanted to see the results of processing the reflection data through the forward NF2FF transform, Figs. 10(c)-(d). We then examined the resultant "patterns" for qualitative analysis purposes.

The raw subtracted SNF data, Figure 10(b), show the direct horn-to-horn interaction centered at $\phi$=0°, $\theta$=17°. It also highlights alignment accuracy between the AUT and the probe. Reflections from the robot, the room, the AUT flange and mounting structure can also be seen. The FF "pattern" data, 10(c)-(d), seem to suggest that these interactions may be removed by using a limited transmission equation which includes multiple reflections [13]. We should examine the possibility that there is sufficient data to do this from the bi-directional measurement.

Yuffa, Alexey; Wittmann, Ronald; Francis, Michael; Gordon, Joshua; Novotny, David.
"Some Advantages of Using Bi-directional S-Parameters in Near-Field Measurements."
Paper presented at 40th Annual Meeting and Symposium of the Antenna Measurement Techniques Association (AMTA 2018), Williamsburg, VA, United States. November 4, 2018 - November 9, 2018.

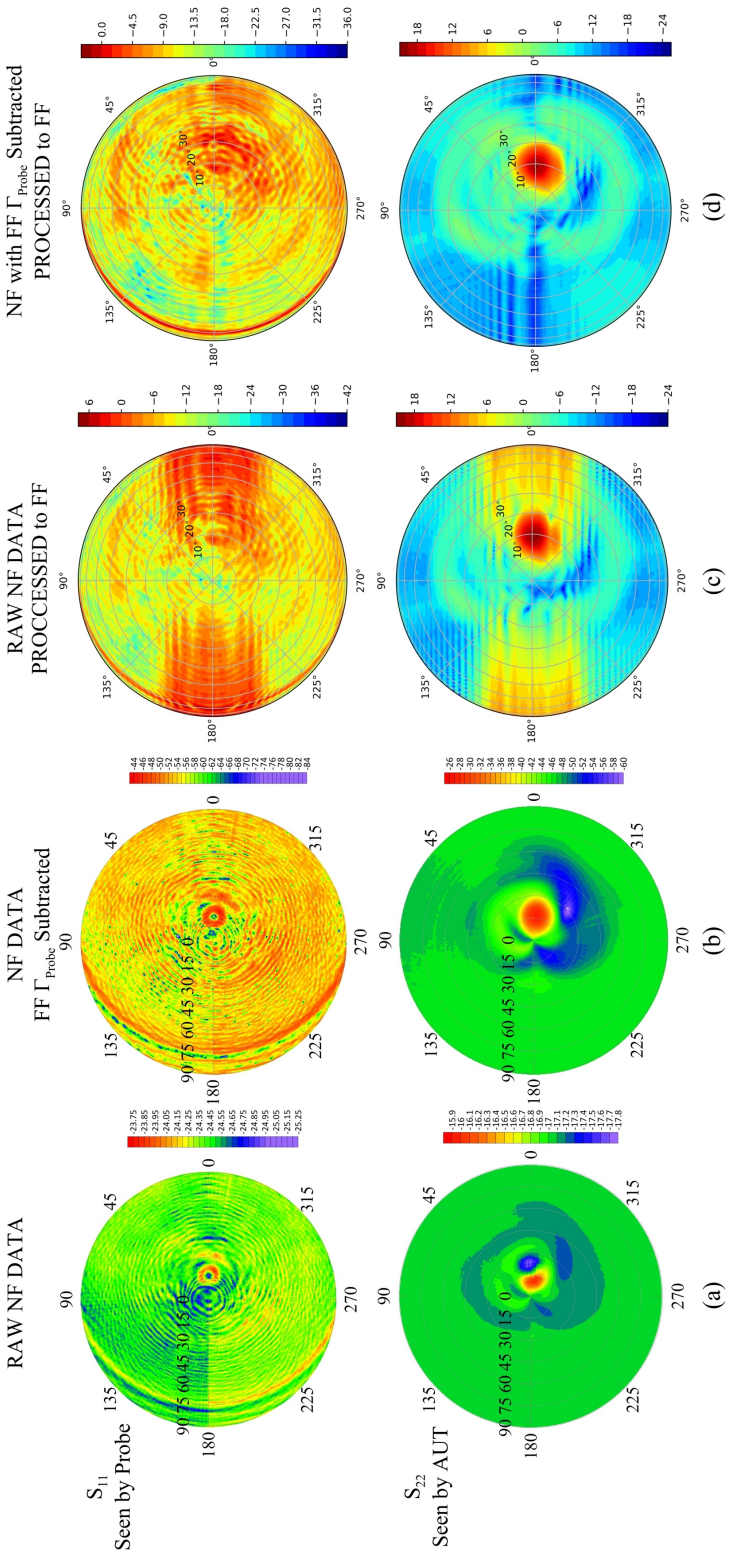


Figure 10. The reflection data as seen by the probe port (1, top) and AUT port (2, bottom) are shown in their raw form (a) and with the far-field (FF) antenna mismatch for each port subtracted (b). The AUT-to-probe interactions centered at $\phi$=0°, $\theta$=17° is more obvious as seen by the AUT versus the probe. The reflection data was then processed using the NF2FF transform as if it were transmission data. The raw reflection data transformed into the FF, (c), and the data with the antenna mismatch subtracted transformed to the FF, (d) are shown. We used the transmission measurement distance of 125mm for processing the reflection data through the NF2FF transform.

Yuffa, Alexey; Wittmann, Ronald; Francis, Michael; Gordon, Joshua; Novotny, David.
"Some Advantages of Using Bi-directional S-Parameters in Near-Field Measurements."
Paper presented at 40th Annual Meeting and Symposium of the Antenna Measurement Techniques Association (AMTA 2018), Williamsburg, VA, United States. November 4, 2018 - November 9, 2018.

To attempt this change in the transmission equation, the subtracted SNF reflection data needs to be spatially or modally gated and the energy needs to be properly accounted for in the transmission parameter. This is an exercise for future analysis.

### *E. Forward versus Revese transmission data*

We compare $S_{21}$ and $S_{12}$ in Figure 11. The difference in the forward and reverse measurements are generally less than ±0.5 dB when the signal is within 20 dB of the peak at $\phi$=0°, $\theta$=17°. If we can assume that to first order (1) holds and that the LO induced signal error is reciprocal in $S_{21}$ and $S_{12}$, this can lead us to believe that the uncertainty in $S_{21}$, versus uncertainty the final measured result, due to cable flexure can be limited to approximately half of the difference in Figure 11 [9]. Furthermore, using the geometric mean of the forward and reverse measurements in the NF2FF transform, may result in a lower uncertainty level compared to a single-direction measurement.

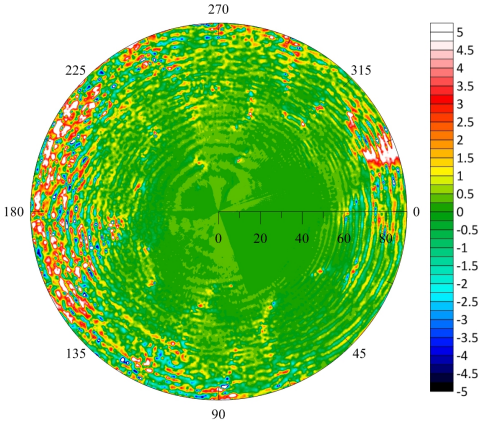


Figure 11. Difference (in dB) between $S_{21}$ and $S_{12}$. Levels are less than ±0.5 dB in the region within 20 dB of the peak.

## IV. Discussions and Conclusion

We performed extrapolation and SNF measurements from 112 to 125 GHz, in the WR-08 waveguide band. The inability to make a direct connection between the AUT and probe ports lead us to use the unknown-thru calibration technique to remove the systematic effects in the VNA and WR-08 extender heads. While at first glance, the disadvantages of the increased complexity over the single source/receiver setups used in many systems and the increased measurement time were troublesome, we found that insight from the additional data could be advantageous.

Especially when using harmonic mixers, LO cable changes during movement can affect measurement results. The most important insight we garnered is that, to first order, the bi-directional two-port measurement can be used to characterize and minimize the effect of LO cable changes by combining the forward and reverse measurements.

This extrapolation data show that the horn-to-horn interaction may be significant and could affect the extrapolation and NF pattern data, even though the SNF measurement radius was greater than $D^2/\lambda$ at approximately 50λ.

The reflections taken during the SNF measurement can be used to assess the level of AUT-to-probe interactions and may show setup and facility imperfections. Finally, the possibility exists that there is enough information in the reflection data to reduce the AUT-to-probe interaction in the final SNF pattern data and improve the uncertainty of the SNF measurement pattern and gain results.


## Acknowledgement

We would like to thank Professor Albin J. Gasiewski and the PolarCube team at the University of Colorado Space Grant Consortium for providing the feed horn, support on the systems and designs for PolarCube, and many helpful discussions.


## References


[1] E. B. Larsen, R. L. Ehret, D. G. Camell and G. H. Koepke, "Calibration of antenna factor at a ground screen field site using an automatic network analyzer," *National Symposium on Electromagnetic Compatibility*, Denver, CO, USA, 1989, pp. 19–24. doi: 10.1109/NSEMC.1989.37143.

[2] M. E. Bialkowski and G. S. Woods, "Application of a six-port network to a near-field antenna measurement system," in *Electronics Letters*, vol. 21, no. 23, pp. 1066–1068, 7 November 1985. doi: 10.1049/el:19850756.

[3] D. Novotny, J. Gordon, J. Guerrieri, " Antenna Alignment and Positional Validation of a mmWave Antenna System Using 6D Coordinate Metrology." *Proceedings of the 36th AMTA*, Tuscon, AZ, USA, 2014, pp. 247–252.

[4] K. Wong, "The "unknown thru" calibration advantage," *ARFTG 63rd Conference, Spring 2004*, Fort Worth, TX, USA, 2004, pp. 73–81. doi: 10.1109/ARFTG.2004.1387858.

[5] A. Ferrero, U. Pisani and F. Sanpietro, "Save The Thru in the A.N.A. Calibration," *40th ARFTG Conference Digest*, Orlando, FL, USA, 1992, pp. 128–135. doi: 10.1109/ARFTG.1992.327007.

[6] J. A. Gordon, D. R. Novotny, M. H. Francis, R. C. Wittmann, M. L. Butler, A. E. Curtin, J. R. Guerrieri, L. Periasamy, and A. J. Gasiewski, "An All-Metal, 3-D-Printed CubeSat Feed Horn: An assessment of performance conducted at 118.7503 GHz using a robotic antenna range.," in IEEE Antennas and Propagation Magazine, vol. 59, no. 2, pp. 96–102, April 2017. doi: 10.1109/MAP.2017.2655574.

[7] R. C. Wittmann, M. H. Francis, D. R. Novotny, J. A. Gordon, M. S. Allman, "Near-Field Spherical Scanning Measurement of a 3DPrinted Horn at WR-8 Frequencies," *AMTA 2018 Proceedings*, WIlliamsburg, VA, USA, 2018.

[8] A. Newell, R. Baird and P. Wacker, "Accurate measurement of antenna gain and polarization at reduced distances by an extrapolation technique," in *IEEE Transactions on Antennas and Propagation*, vol. 21, no. 4, pp. 418–431, July 1973. doi: 10.1109/TAP.1973.1140519.

[9] D. Hess, "Principle of the three-cable method for compensation of cable varitiaon," *AMTA 1992 Proceedings*, Columbus, OH, USA, 1992, pp. 10-26–10-31.

[10] D. Kerns, Plane-Wave Scattering-Matrix Theory of Antennas and Antenna-Antenna Interactions, NBS Monograph 162, Washington, DC: US GPO, 1981, pp.27–34.

[11] J. Hansen, Spherical Near-Field Antenna Measurements, London, England: Peter Peregrinus Ltd, 1988, pp. 217–219.

[12] D. Hess, "An apparent discrepancy between impedance mismatch factors for near-field and far-field measurments," *AMTA 2005 Proceedings*, Newport, RI, USA, 2005, pp. 116–121.

[13] Ref [11], pp. 82–87.



Yuffa, Alexey; Wittmann, Ronald; Francis, Michael; Gordon, Joshua; Novotny, David.
"Some Advantages of Using Bi-directional S-Parameters in Near-Field Measurements."
Paper presented at 40th Annual Meeting and Symposium of the Antenna Measurement Techniques Association (AMTA 2018), Williamsburg, VA, United States. November 4, 2018 - November 9, 2018.

# Using LZMA Compression for Spectrum Sensing with SDR Samples

André R. Rosete
*Interdisciplinary Telecom. Program*
*University of Colorado Boulder*
Boulder, Colorado, USA
andre.rosete@colorado.edu

Kenneth R. Baker
*Interdisciplinary Telecom. Program*
*University of Colorado Boulder*
Boulder, Colorado, USA
kbaker@colorado.edu

Yao Ma
*Communications Technology Laboratory*
*National Institute of Standards and Technology*
Boulder, Colorado, USA
yao.ma@nist.gov

***Abstract*—Successful spectrum management requires reliable methods for determining whether communication signals are present in a spectrum portion of interest. The widely-used energy detection (ED), or radiometry method is only useful in determining whether a portion of radio-frequency (RF) spectrum contains energy, but not whether this energy carries structured signals such as communications. In this paper we introduce the Lempel-Ziv Markov-chain Sum Algorithm (LZMSA), a spectrum sensing algorithm (SSA) that can detect the presence of a structured signal by leveraging the Liv-Zempel-Markov chain algorithm (LZMA). LZMA is a lossless, general-purpose data compression algorithm that is widely available on many computing platforms. The new algorithm is shown to have good performance at distinguishing between samples containing communication signals, and samples of noise, collected with a software-defined radio (SDR). This algorithm does not require any information about the signal beforehand. The algorithm is tested with computer-generated as well as SDR-captured samples of LTE signals.**

***Index Terms*—spectrum sensing algorithm, compression, SDR, ROC, AUC**

## I. Introduction

COMPRESSION algorithms remove redundancies in data sets to encode data using fewer bits. Communication signals, unlike noise, contain regularly reoccurring features; a reflection of the fact that they are protocols designed to convey information. While Shannon [1] has shown that the optimal channel coding theorem is a randomly-encoded signal, actual attempts at communication are pseudo-random at best because the random sequence needs to be able to be regenerated by the receiver to demodulate the signal. Since the compressibility of a sequence serves as a test of its randomness [2], we can expect that communication signal samples will be more compressible than Gaussian noise samples, as the latter are random values. The Lempel-Ziv-Markov chain Algorithm (LZMA) is a lossless, general-purpose data compression algorithm designed to achieve high compression ratios with low compute time. [3] We have found that, all else held constant, SDR-collected, LZMA-compressed files containing in-phase and quadrature (IQ) samples signals with higher signal-to-noise ratios (SNRs) show better compression ratios than files containing IQ samples of lower-SNR channels, or of channels known to contain only noise. Because a significant difference exists in the size of compressed sample sets of noise and compressed sample sets of communication signals, the compressibility of a spectrum sample set presents itself as a possible test statistic for spectrum sensing. Throughout this paper, we consider noise specifically as white Gaussian noise.

In this paper we explore the utility of this phenomenon in detecting the presence of communications signals from a sampled waveform at various SNRs. Section II sets the mathematical notation for our analysis and explains our evaluation metric. Section III summarizes LZMA's operation. Section IV introduces the new Lempel-Ziv Markov-chain Sum Algorithm (LZMSA). Section V explains how the sample sets for testing the algorithm were generated, and describes the testing procedure and results. Section VI presents discussion of the results.

## II. Spectrum Sensing

In a general sense, spectrum sensing is the task of quantifying how the spectrum is occupied. This can be considered from the general occupancy, structure, or protocol point of view. The choice depends on the objectives of the spectrum sensing task. Often, spectrum sensing is used to refer to on/off detection - whether there is any kind of occupant in a channel beyond some threshold, usually set at some estimate of the noise floor. However, it may prove necessary to probe whether a present waveform has structure, which would indicate the presence of a spectrum occupier other than noise, or to take it further, identify which protocol the structured waveform follows.

This work utilized the RMACC Summit supercomputer, which is supported by the National Science Foundation (awards ACI-1532235 and ACI-1532236), the University of Colorado Boulder, and Colorado State University. The Summit supercomputer is a joint effort of the University of Colorado Boulder and Colorado State University.

Certain commercial equipment, instruments, or software are identified in this paper in order to adequately specify the experimentation procedure. Such identification is not intended to imply recommendation or endorsement by the National Institute of Standards and Technology, nor is it intended to imply that the software or equipment identified are necessarily the best available for the purpose.

This work was performed under the financial assistance award 70NANB18H006 from the National Institute of Standards and Technology, U.S. Department of Commerce.



Rosete, Andre; Baker, Kenneth; Ma, Yao.
"Using LZMA Compression for Spectrum Sensing with SDR Samples."
Paper presented at 2018 9th IEEE Annual Ubiquitous Computing, Electronics & Mobile Communication Conference (UEMCON), New York City, NY, United States. November 8, 2018 - November 10, 2018.

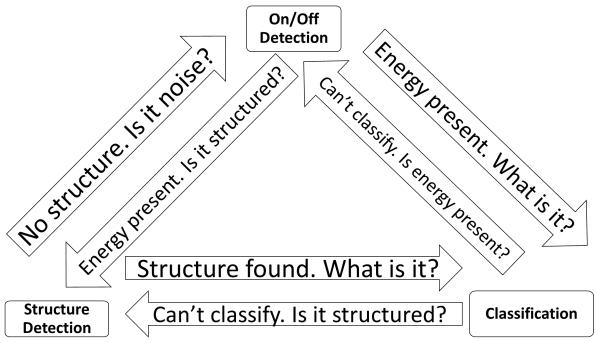


Figure 1. Spectrum Sensing Tasks.

Fig. 1 shows the flow of the spectrum sensing task, which revolves around three stages, on/off detection, structure detection, and classification. On/off detection is simply estimating whether energy is present on a threshold. Classification is identifying what kind of signal protocol is present, e.g. LTE, Wi-Fi, FM, etc. In this manuscript we focus on structure detection. Structure detection is the task of determining whether a channel $x(t)$ contains a structured signal $s(t)$ in addition to noise $n(t)$. The null hypothesis $H_0$ is that only noise is present in the channel, and the detection hypothesis $H_1$ is that a structured signal, such as a communications signal, is present in the channel in addition to noise. We use the definition:

$$\hat{H}_0, \quad \text{if } x(t) = n(t) \qquad t \in [0, T] \tag{1}$$

$$\hat{H}_1, \quad \text{if } x(t) = n(t) + s(t) \qquad t \in [0, T] \tag{2}$$

where $t$ is a time in a continuous period of time of duration $T$.

A spectrum sensing algorithm (SSA) is usually implemented on digital systems which sample and quantize the signal into values that are discrete in both time and magnitude. The resulting $N_s$ samples are denoted:

$$\boldsymbol{x}[n] = [x_0[n], x_1[n], \ldots, x_{N_s-1}[n]]^T \tag{3}$$

where each $n$ is an integer, a discrete point in time on which each sample of the channel was taken, relative to the start of the sampling. An SSA takes $\boldsymbol{x}[n]$ as an input and returns a test statistic $\gamma$, which is a score meant to estimate the probability that $x(t)$ contains some $s(t)$. However, $\gamma$ is not a measure of probability, and has different meanings depending on the SSA. For example, in ED, $\gamma$ is the total energy contained in the sample set, while in covariance-based methods $\gamma$ is a function of the relationship between covariance measurements across the sample set. Let us define $x[n]$ as the set of channel samples, $p_{fa}$ the desired probability of false alarm (false positive rate), and $L$ as the window size for covariance-based SSAs. In all cases, the decision on whether a channel contains a signal is made by comparing the test statistic with a chosen threshold $\gamma_0$. The choice of $\gamma_0$ is made to reach some desired $p_{fa}$ based on the constant false alarm rate criterion [4].

$$\text{decision} = \begin{cases} H_0, & \text{if } \gamma \leq \gamma_0 \\ H_1, & \text{if } \gamma > \gamma_0 \end{cases} \tag{4}$$

Since we wish to compare various types of detection methods, we are interested in the performance of the SSAs independent of the choice of threshold.

One such threshold-independent evaluation method is the area under the Receiver Operating Characteristic (ROC) curve, or Area Under the Curve (AUC) [5]. The ROC curve is a plot of the true positive rate (TPR) versus the false positive rate (FPR) of an SSA.

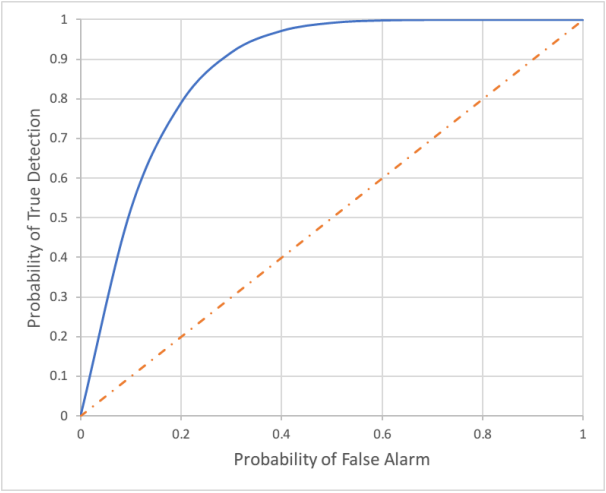


Figure 2. Receiver Operating Characteristic Example.

Fig. 2 shows a ROC curve (solid blue line) and an ignorance line (dashed orange line). Any portion of an SSA's ROC curve under the ignorance line means that the SSA is worse than random guessing at that point in the curve. AUC is the area between the ROC curve and the x-axis.

The area under the ROC curve (AUC) is a value between 0 and 1 that summarizes the statistical strength of a classifier. AUC at or below 0.5 means that the statistical strength of the classifier is no better than guessing and is therefore not useful. AUC at 1 means that the classifier always makes the correct decision and never makes an incorrect decision. AUC at 0 means that the classifier always makes an incorrect decision [4]. The benefit of AUC is that it enables a performance evaluation of spectrum-sensing algorithms by summarizing the ROC curve with a single number, which permits one to visualize performance as a function of a number of parameters, such as the number of samples or SNR, both important constraints in spectrum sensing implementations.

ED [6] is a popular SSA, with applications from the Federal Communication Commission's (FCC) spectrum regulation, where interference thresholds are measured in microvolts per meter [7], to Wi-Fi coexistence [8]. It works by calculating

Rosete, Andre; Baker, Kenneth; Ma, Yao.
"Using LZMA Compression for Spectrum Sensing with SDR Samples."
Paper presented at 2018 9th IEEE Annual Ubiquitous Computing, Electronics & Mobile Communication Conference (UEMCON), New York City, NY, United States. November 8, 2018 - November 10, 2018.

how much energy is contained in the received samples $x[n]$, working on the assumption that any electromagnetic emission contains energy. This can be a disadvantage when specifically looking for communications signals, since ED will detect non-communications emissions as well. However, ED may be particularly useful in detecting natural interferers or to get a quick overview of which channels may warrant further scrutiny with more structure-aware SSAs. ED is not a communications detector, as it will detect natural noise, based on its energy content, just as much as a communications signal at the same power.

One example of an SSA meant to look for structure in a signal, included here for comparison, is the Covariance Absolute Value (CAV) algorithm described in [9] in Eqs. 26-30. This SSA seeks to measure the self-covariance of a set of samples within a window of $l$ samples, with the assumption that samples of a structured signal tend to be more co-variant than samples of noise. Like LZMSA, this algorithm does not require any information about the signal beforehand.

## III. Lempel-Ziv-Markov Chain Algorithm

In order to understand how the LZMA algorithm might be useful detecting signals within noise, it is instructive to understand the basics of how this compression algorithm operates. LZMA is a chain of three compression algorithms: 1) a delta encoder, 2) the compression algorithm known as "LZ77", and 3) a range encoder [10].

Initially, the input data is processed by the delta encoder as follows [11]:

$$\delta(v_1, v_2) = (v_1 \setminus v_2) \cup (v_2 \setminus v_1) \tag{5}$$

where $v_1$ represents the first sequence in the sliding window, and $v_2$ represents the second sequence in the sliding window, $\setminus$ is the set minus operator, and $\cup$ is the set union operator. For example, the data set [3, 4, 6, 9, 3] would be stored as [3, 1, 2, 3, -6]; each data point in the set is stored as the difference from the previous data point in the set, with the exception of the first value, which is kept as-is; it is the difference from zero.

The resulting sequence is input to the LZ77 compression algorithm [12]. This resulting sequence is then input to a range encoder [13].

The purpose of this chain operation is that the delta encoder prepares the data in such a way that it may be more compressible by the sliding window algorithm in LZ77. The output is then passed on to a range encoder, which is able to further remove some redundancies not caught by the LZ77 algorithm.

The goal of LZMA is to compress data as much as possible with a reasonably low processing time [3]. Furthermore, a fast field-programmable gate array (FPGA) implementation of LZMA has been demonstrated [10].

## IV. LZMSA Detection

We propose a new signal detection algorithm based on LZMA. The algorithm begins by compressing the set of samples $\boldsymbol{x}[n]$ with the LZMA compression algorithm.

$$\boldsymbol{x}[n] \xrightarrow{\text{LZMA}} \boldsymbol{y}[m] \tag{6}$$

Let $\boldsymbol{y}[m]$ be the LZMA output for $\boldsymbol{x}[n]$. $\boldsymbol{y}[m]$ is a data object containing $M$ bytes.

$$\boldsymbol{y}[m] = [y_0[m], y_1[m], \ldots, y_{M-1}[m]]^T \tag{7}$$

The LZMSA decision statistic is produced as follows:

$$\gamma_{LZMA} = \underline{1}^T \boldsymbol{y}[m] = \sum_{k=0}^{M-1} y_k[m] \tag{8}$$

where $\underline{1} = [1, \ldots, 1]^T$.

One possible explanation for why this method may work is that information-carrying signals tend to be more compressible by LZMA than samples representing only random noise. By the nature of random numbers, it is a reasonable expectation that a sequence of random numbers cannot be significantly compressed [2]. This is due to the fact that truly random numbers, such as those in Gaussian noise, already represent a sequence composed almost entirely of Shannon information, which would represent maximum entropy. The Kolmogorov complexity [14] of such a random sequence, that is, the shortest possible descriptor that could fully generate such a sequence, cannot be shorter than the sequence itself.

## V. Test Sample Sets Generation and Testing

Two data sets were generated: A) A digital chain set generated with MATLAB™ R2017b running on the Rocky Mountain Advanced Computer Consortium (RMACC) Summit supercomputer. B) A set generated with a vector signal transceiver (VST), transmitted over a coaxial copper cable, and captured with a SDR. In both cases, the target SNRs for the sample sets were -12 dB through 12 dB in increments of 3 dB.

### *A. Computer-Generated Signal Set*

Digital chain samples were generated in MATLAB™ , forming a fully computer-generated (CG) set, free of potential hardware artifacts. These samples were of Long-Term Evolution (LTE) Test Model 3.3, with a bandwidth of 20 MHz. The samples were summed with generated Gaussian noise to reach the target SNRs.

### *B. SDR Set*

LTE Test Model 3.3 signals were generated with a National Instruments™ PXIe-5645R Vector Signal Transceiver. The signals were captured using an Ettus Research™ B200mini Software-Defined Radio (SDR) controlled by a PC running GNU Radio on Ubuntu Linux. All signals were generated and captured at a center frequency of 5.8 GHz, which is a relevant spectrum portion due to the fact it is shared between Band 255 LTE and U-NII-3-band Wi-Fi. The SDR captured 20 MHz of bandwidth at 20 million samples per second, which is the Shannon rate considering that each IQ sample consists

Rosete, Andre; Baker, Kenneth; Ma, Yao.
"Using LZMA Compression for Spectrum Sensing with SDR Samples."
Paper presented at 2018 9th IEEE Annual Ubiquitous Computing, Electronics & Mobile Communication Conference (UEMCON), New York City, NY, United States. November 8, 2018 - November 10, 2018.

of both an in-phase and a quadrature component. Signals were generated at different power levels to reach the target SNRs with respect to the hardware noise. Both the LTE and noise samples collected in this manner were found to be non-zero mean. Furthermore, the noise samples were found to show IQ correlation even though noise samples should be expected to be independent.

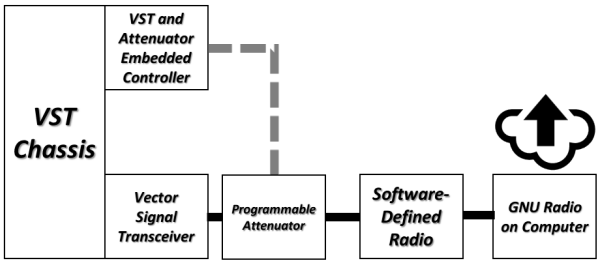


Figure 3. VST-SDR Generation and Capture.

Computations were carried out using a Python™ program to compare the detection performance of LZMSA versus the CAV algorithm on the Gaussian and LTE sample sets. Simulations were run for each SNR set, with $N_s$ from 10 to 5000 samples per decision in steps of 100 samples. 1000 Monte Carlo trials per SNR and number of samples were performed to calculate the AUC. The covariance window was set at 10 samples for the CAV algorithm. All tests were run on the RMACC Summit supercomputer. The simulations consist of Monte Carlo trials where, for each number of samples $N_s$ and and each SNR, the algorithm under test is fed a randomly selected consecutive set of $N_s$ samples from the available signal samples file, repeating the process for the noise-only samples file. Test statistics are produced for both detection hypotheses, $H_1$ and $H_0$. These test statistics are processed through an algorithm [15] which produces the AUC measure for the particular scenario, indicating how much the test statistics tend to be different between $H_1$ and $H_0$ cases.

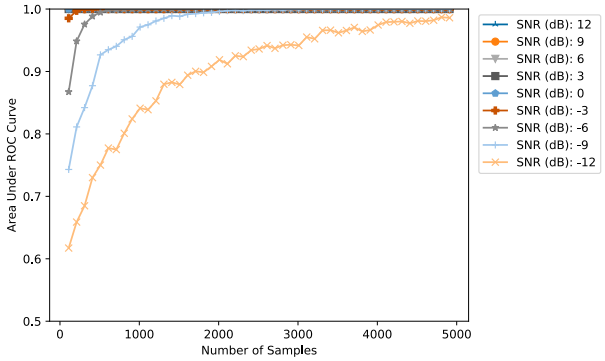


Figure 4. Energy Detection on a Gaussian Emitter.

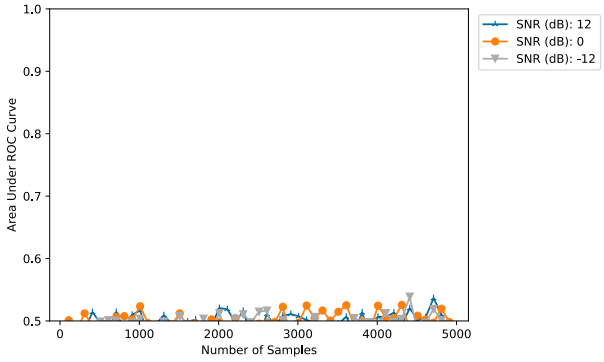


Figure 5. Covariance Absolute Value Detection on a Gaussian Emitter.

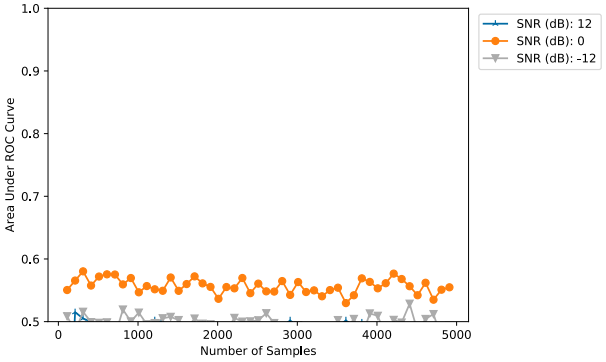


Figure 6. LZMSA Detection on a Gaussian Emitter.

In Figs. 4, 5, and 6, a Gaussian emitter was added to the background noise and compared to when only background noise was present. Fig. 4 shows that ED can yield high AUCs, even when SNR is low or when the number of samples is under 1000. AUC is strongly dependent on SNR and number of samples. The generally high AUC means that ED differentiates well between a Gaussian emitter, known to lack communications, and the background Gaussian noise. This shows that ED cannot differentiate communications from a Gaussian emitter. A communications detector should have AUC close to 0.5 in this case, as both the emitter and the background channel are lacking in communications content, and are thus indistinguishable to such a detector. Figs. 5 and 6 show that CAV and LZMSA both are incapable of differentiating between a Gaussian emitter and background Gaussian noise, regardless of the SNR or number of samples. This is due to the fact that both the emitter and the background noise lack features that would be found in communications signals, such as sample covariance or redundancy.

Fig. 7 shows CAV consistently outperforms LZMSA when CG samples are used, with CAV's AUC increasing with number of samples, when SNR is 12 dB or 0 dB. However, when SNR is reduced to -12 dB, both algorithms have an AUC around 0.5 regardless of the number of samples used.

Rosete, Andre; Baker, Kenneth; Ma, Yao.
"Using LZMA Compression for Spectrum Sensing with SDR Samples."
Paper presented at 2018 9th IEEE Annual Ubiquitous Computing, Electronics & Mobile Communication Conference (UEMCON), New York City, NY, United States. November 8, 2018 - November 10, 2018.

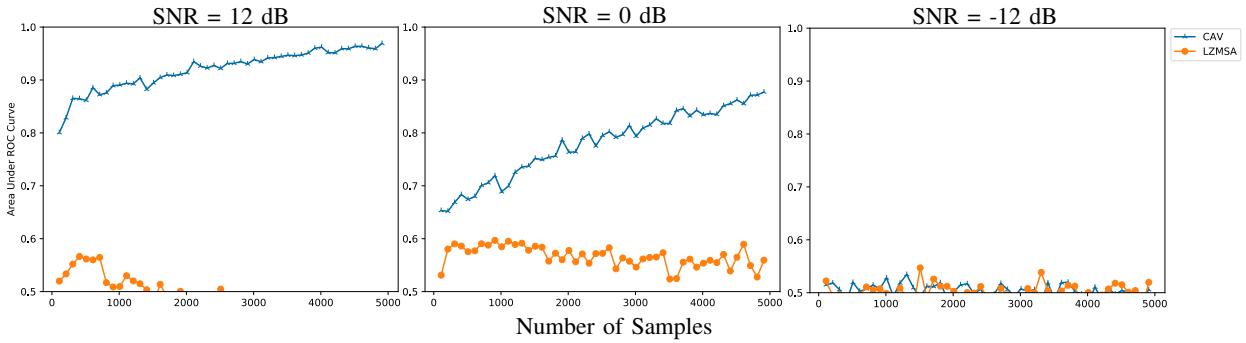


Figure 7. CAV vs. LZMSA on CG LTE Signal.

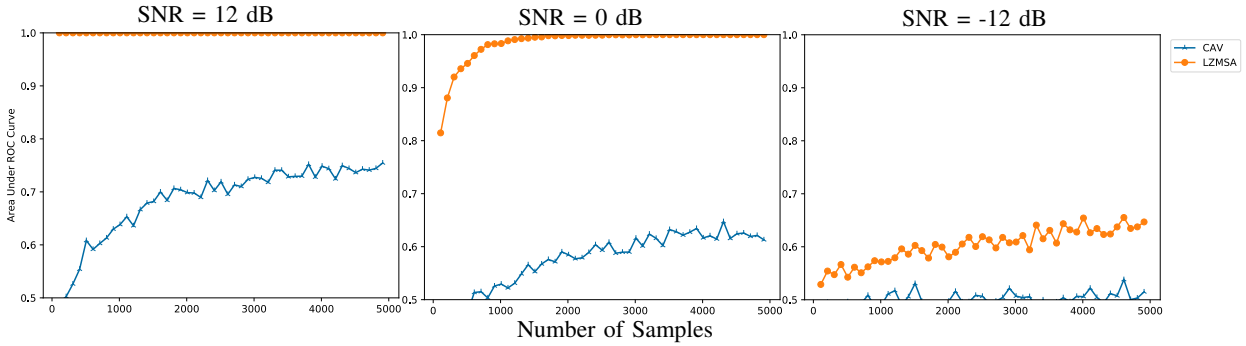


Figure 8. CAV vs. LZMSA on VST-SDR LTE Signal.

Fig. 8 shows LZMSA consistently outperforming CAV on all three SNRs when SDR-collected samples are used, with AUC increasing as more samples are used. Even with an SNR of 12 dB, CAV shows consistently low performance; at 5000 samples, its AUC is around 0.75, while LZMSA's AUC is 1 even at 10 samples. At 0 dB and 2000 samples, CAV's AUC is under 0.6, while LZMSA's is 1. Not only is the situation reversed from where the CG LTE samples were used, but LZMSA actually shows higher AUC across the board for VST-SDR samples than CAV does for the CG LTE samples.

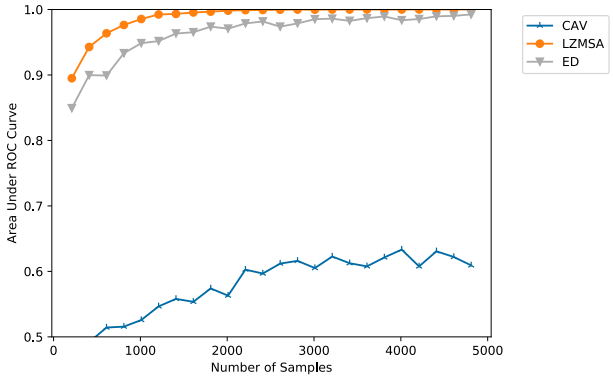


Figure 9. ED vs. LZMSA on VST-SDR LTE Signal. SNR = 0 dB.

Fig. 9 shows that there are some cases where LZMSA even performs better than ED for classical on/off detection. LZMSA shows a higher AUC than ED, with a greater gap in AUC evident when using fewer samples. Both outperform CAV significantly in this case, with CAV's AUC barely rising above 0.6 when $N_s$ is above 3000. AUC shows little positive relation to the number of samples used.

The SDR-collected samples of both LTE and noise were found to be non-zero mean and IQ-correlated, which may offer insight into the wide performance discrepancies found between the CG and VST-SDR scenarios. It could be that the IQ correlation present in the VST-SDR noise samples made it difficult for the CAV algorithm to differentiate between LTE and noise, since the mechanism through which this algorithm differentiates a structured signal from noise is the difference in sample correlation, with the assumption that noise samples are independent and uncorrelated. If correlation is introduced to the noise samples, they cannot be well differentiated from a correlated waveform like LTE on this basis. However, it is unclear why these effects enable LZMSA to work so well with the VST-SDR samples as opposed to the CG samples.

## VI. Conclusion

In this manuscript we tested three spectrum sensing algorithms, ED, CAV, and LZMSA, in a scenario where both the emitted signal and the background noise are Gaussian. We

Rosete, Andre; Baker, Kenneth; Ma, Yao.
"Using LZMA Compression for Spectrum Sensing with SDR Samples."
Paper presented at 2018 9th IEEE Annual Ubiquitous Computing, Electronics & Mobile Communication Conference (UEMCON), New York City, NY, United States. November 8, 2018 - November 10, 2018.

showed ED to not be a communications detector because its high AUC indicated differentiation between a Gaussian emitter and the background Gaussian noise. We then showed CAV and LZMSA to not be sensitive to this Gaussian emitter. The next scenarios were comprised of CG and SDR-implemented LTE Test Model 3.3 signals where we compared the performance of CAV and LZMSA. While CAV is shown to differentiate CG LTE samples from the background noise fairly well, this result doesn't apply to the VST-SDR LTE samples, where performance is poor. Conversely, while LZMSA shows poor performance on CG LTE samples, we show that it can perform well on SDR-collected LTE samples. The causes for the discrepancy in the performance of these two algorithms between the CG and SDR-collected scenarios warrant further research into the interactions between spectrum sensing algorithms and effects introduced by SDRs on waveforms during their digitization process. Further research must also be carried out to find out how the SDR's hardware effects enable LZMSA to differentiate an LTE input from a noise input. It is of note, that LZMSA shows promise as a viable SSA that could perform well in some scenarios. Notably, it works well in conjunction with SDR collected-samples, even outperforming ED at on/off detection of an LTE signal. In our future work we will address the differentiation in performance of the algorithms between CG and SDR-collected samples. Furthermore, we will be studying the efficiency of these algorithms in the context of a spectrum monitoring application utilizing SDRs, with additional scenarios such as detection of a variety of signals in noisy conditions.

## ACKNOWLEDGMENTS

We would like to thank Dr. Adam Wunderlich for his advice on ROC and AUC theory, and to W. Max Lees for providing the fast ROC and AUC implementations in Python™.

## REFERENCES

[1] C. E. Shannon, "Communication in the presence of noise", *Proceedings of the IRE*, vol. 37, no. 1, pp. 10–21, 1949.

[2] A. Rukhin, J. Soto, J. Nechvatal, M. Smid, E. Barker, S. Leigh, M. Levenson, M. Vangel, D. Banks, A. Heckert, J. Dray, and S. Vo, "A statistical test suite for random and pseudorandom number generators for cryptographic applications", Booz Allen & Hamilton, NIST Special Publication 800-22, May 15, 2001.

[3] I. Pavlov, *7z Format*, 2018. [Online]. Available: https://www.7-zip.org/7z.html.

[4] H. L. Van Trees, *Detection, estimation, and modulation theory, part I: detection, estimation, and linear modulation theory*. John Wiley & Sons, 2004.

[5] J. A. Hanley and B. J. McNeil, "The meaning and use of the area under a receiver operating characteristic (ROC) curve.", *Radiology*, vol. 143, no. 1, pp. 29–36, Apr. 1, 1982.

[6] H. Urkowitz, "Energy detection of unknown deterministic signals", *Proceedings of the IEEE*, vol. 55, no. 4, pp. 523–531, Apr. 1967.

[7] "47 CFR § 15.209 Radiated emission limits; general requirements.", in *United States Code of Federal Regulations*.

[8] IEEE, *802.11-1997: IEEE standard for wireless LAN medium access control (MAC) and physical layer (PHY) specifications.* 1997.

[9] Y. Zeng and Y. C. Liang, "Covariance Based Signal Detections for Cognitive Radio", in *2007 2nd IEEE International Symposium on New Frontiers in Dynamic Spectrum Access Networks*, Apr. 2007, pp. 202–207.

[10] E. J. Leavline and D. A. A. Gnana Singh, *Hardware Implementation of LZMA Data Compression Algorithm*, Mar. 2013.

[11] R. Conradi and B. Westfechtel, "Version models for software configuration management", *ACM Computing Surveys (CSUR)*, vol. 30, no. 2, pp. 232–282, 1998.

[12] J. Ziv and A. Lempel, "A universal algorithm for sequential data compression", *IEEE Transactions on Information Theory*, vol. 23, no. 3, pp. 337–343, May 1977.

[13] G. Martin, "Range encoding : An algorithm for removing redundancy from a digitised message", *Video and Data Recording Conference, Southampton, 1979*, pp. 24–27, 1979.

[14] A. N. Kolmogorov, "On Tables of Random Numbers", *Sankhyā: The Indian Journal of Statistics, Series A (1961-2002)*, vol. 25, no. 4, pp. 369–376, 1963.

[15] X. Sun and W. Xu, "Fast Implementation of DeLong's Algorithm for Comparing the Areas Under Correlated Receiver Operating Characteristic Curves", *IEEE Signal Processing Letters*, vol. 21, no. 11, pp. 1389–1393, Nov. 2014.

Rosete, Andre; Baker, Kenneth; Ma, Yao.
"Using LZMA Compression for Spectrum Sensing with SDR Samples."
Paper presented at 2018 9th IEEE Annual Ubiquitous Computing, Electronics & Mobile Communication Conference (UEMCON), New York City, NY, United States. November 8, 2018 - November 10, 2018.

## ABSTRACT

This paper presents an approach and apparatus for laboratory evaluation of environmental sensing capability (ESC) sensors for the $3.5\,\mathrm{GHz}$ band. These sensors are designed to detect federal incumbent signals in the band so that the incumbent can be dynamically protected from harmful interference. The proposed approach is unique in that it utilizes waveforms captured in the field to reproduce in a controlled laboratory environment what the sensor would experience in the field, and with repeatability unattainable in live field testing. Test signals comprise the incumbent signal to be detected, co-channel commercial signals, and the out-of-band emissions of adjacent-band incumbents, including channel propagation effects that can affect sensor performance. We describe an implementation of this approach in software-controlled instrumentation for automated testing of large numbers of test waveforms capable of producing statistically significant performance metrics such as rates of detection and false alarm in a time efficient manner. The material described in this paper is based on research conducted at the National Institute of Standards and Technology and is not related to any certification testing of ESC sensors.


## 1 INTRODUCTION

The Citizens Broadband Radio Service (CBRS) in the United States permits commercial broadband access to the radiofrequency spectrum between $3550\,\mathrm{MHz}$ and $3700\,\mathrm{MHz}$ ($3.5\,\mathrm{GHz}$ band) on a shared basis with existing incumbents in the band [1]. Among the incumbents is the U.S. military which operates radar systems in this band, including shipborne radar off the U.S. coasts. The CBRS rules permit dynamic access to the band in the proximity of military radar provided a sensor network detects the presence of incumbent radar and triggers interference mitigation measures when necessary. The scope of this paper is the quantitative evaluation of the detection performance of these sensors.

In order to operate in the CBRS ecosystem, sensors must meet specific requirements. Among these requirements is the ability to detect the in-band incumbent radar signal at a minimum received power density of $-89\,\mathrm{dBm}$ ($\mathrm{dB}$ relative to $1\,\mathrm{mW}$)/$\mathrm{MHz}$ [2], within $60\,\mathrm{s}$ of onset, and with a probability of detection of $99\,\%$ or better [3].[1] With this minimum required power density, the detection is clearly not thermal-noise-limited, as the detection threshold is $25\,\mathrm{dB}$ above the thermal noise floor. The challenge for detection is presented, rather, by co-channel interference.

There are two primary sources of co-channel interference at the sensor's receiver. First, by design, the band is shared with commercial systems. Therefore, sensors must be able to detect the incumbent signal in channels occupied by commercial systems. These systems are expected to be fourth-generation time-division-duplex (TDD) long term evolution (LTE) systems, at least initially. However, the emissions of commercial systems operating in the band can, in principle, be controlled by treating the sensors as protected entities in the CBRS system.

The second, more challenging, source of interference is the out-of-band emissions of systems operating in adjacent bands. These systems are also military radars, operate at frequencies below the CBRS band, and have been observed to generate significant emissions into the CBRS band [4, 5].

This paper presents a testing approach and apparatus that utilizes field-measured waveforms of emissions in the $3.5\,\mathrm{GHz}$ band to verify that a sensor meets the requirements for federal incumbent detection. It leverages an extensive library of high-resolution digital recordings of emissions collected by the National Advanced Spectrum Communications and Test Network (NASCTN) [4, 5] to reproduce in a controlled laboratory environment what a sensor would "see" in the field from offshore radars currently operating in the band as well as the out-of-band emissions from adjacent-band radars that can potentially interfere with the in-band signals of interest.

There are several advantages of using field-measured waveforms for laboratory testing. First, because they were recorded by instruments mounted in locations similar to where sensors will eventually be deployed, they represent the channel propagation and other effects that signals received by the sensors will experience, such as tropospheric scatter and time-varying multipath fading, which can distort the transmitted radar signal. Second, these waveforms can be scaled and combined with other signals expected to be present in the band, such as commercial LTE signals, to produce a wide range of scenarios including multiple co-incident radar signals and a multitude of different frequency and amplitude offsets between these signals. Third, the waveforms can be generated by calibrated instrumentation with a degree of repeatability unattainable in live field testing. Finally, the framework is extensible to include additional signals not currently operating but anticipated to operate in the band.

[1] Government requirements do not specify a maximum probability of false alarm, although this figure of merit is of interest to commercial users.


Caromi, Raied; Mink, John; Wedderburn, Cosburn; Souryal, Michael; El Ouni, Naceur.
"3.5 GHz ESC Sensor Test Apparatus Using Field-Measured Waveforms."
Paper presented at WInnComm 2018, Melbourne, FL, United States. November 14, 2018 - November 15, 2018.

The remainder of the paper is organized as follows. Section 2 reviews the current testing approach and contrasts it with the proposed approach. After providing an overview of the test system in Section 3, we describe the major sub-systems including pre-testing waveform generation (Section 4) and the test harness itself (Section 5) which automates signal generation and sensor notification logging. The paper concludes in Section 6 with several examples of practical test scenarios generated by the test harness.

## 2 BACKGROUND AND MOTIVATION

### 2.1 Prior Work

Procedures and waveforms for certification testing of the first commercial environmental sensing capability (ESC) systems are documented in [2]. These procedures are intended to evaluate the ability of an ESC sensor to meet established detection requirements in a laboratory environment, prior to field testing and deployment. The test plan describes five categories of radar pulse waveforms that represent current and future radars in the CBRS band. Each category specifies a pulse modulation type and a range of values for several parameters of the pulse, including pulse duration, pulse repetition rate, and chirp width (if applicable). Tests will expose the sensor to bursts of pulses of each category, with parameter values selected randomly from the given ranges, and will record positive detections. A signal generator will inject the radio frequency (RF) radar pulse waveforms into the sensor under test. The test signals will be conducted if the sensor supports a direct RF cable connection, or radiated otherwise.

In deployment, ESC sensors will be required to detect federal incumbent signals in the presence of background noise from commercial CBRS devices (CBSDs), such as LTE small cells, operating in the band. The laboratory test procedures outlined in [2] specify that Gaussian noise will be added to the radar pulse waveforms to represent the background signal. The test plan mentions that consideration will be given to the out-of-band emissions from adjacent-band radars into the CBRS band, but it does not provide procedures for quantitatively assessing a sensor's ability to detect in-band radar in the presence of these emissions. Furthermore, the test plan omits consideration of channel propagation effects, such as multipath fading, which can distort the transmitted radar pulse waveforms.

### 2.2 Field-Measured Waveforms

This paper builds on the work in [2] and proposes procedures for evaluating ESC sensors using pre-recorded waveforms measured in the field. We propose to use such field-measured waveforms, in conjunction with simulated waveforms of commercial devices that will enter the band as well as signal processing that models channel effects, to create test waveforms that are more reflective of the signals these sensors will receive in real-world deployments.

Field measurements of the incumbent radar currently operating in the CBRS band were conducted at two U.S. coastal locations over a period of two months at each location [4, 5]. The outcome of these measurement campaigns is an extensive library of radar pulse waveforms in the form of in-phase and quadrature (I/Q) samples spanning an instantaneous acquisition bandwidth of $200\,\mathrm{MHz}$. Each acquisition is continuously sampled at $225\,\mathrm{MSa}\,(\text{megasample})/\mathrm{s}$ for a duration of $60\,\mathrm{s}$.

The measurements were collected at coastal locations and with antenna heights similar to what a deployed ESC sensor may use. The recorded waveforms, therefore, include the channel propagation effects the received signals would likely experience in practice. In addition to the in-band radar, the measurements include recordings of the out-of-band emissions (OOBE) of adjacent-band radars, both coincident with and in the absence of the in-band radar. The test procedures described below make use of these out-of-band emissions to form the background signal received by the sensor under test.

## 3 SYSTEM OVERVIEW

The proposed ESC testing system utilizes field-measured signals of both incumbent radar and OOBE of adjacent-band radars. In addition, generated LTE signals with fading channel effects (or measured LTE signals) can be added. In contrast, the current ESC testing procedure adds white gaussian noise (WGN) as interference based on the assumption that the aggregate LTE signals from CBSDs can be represented by WGN [2]. However, certain operating scenarios may result in an interference signal that includes one dominant LTE signal. Unlike WGN, an LTE signal has structure; the shape of its power spectrum is not flat and is subject to the LTE signal configuration. Additionally, channel fading will further affect the LTE signal. Therefore, we consider the scenario in which one LTE signal is dominant in addition to the WGN case.

The test allows for one or more incumbent radar signals with different combinations of interference signals. Since the original field-measured waveforms are $60\,\mathrm{s}$ long, we choose $90\,\mathrm{s}$ for the generated test files. This configuration provides the possibility for starting the radar signal at a random time in the test with some constraints. Specifically, we limit the incumbent radar signal start time to values between $4\,\mathrm{s}$ and $30\,\mathrm{s}$. The start time randomization is important for measuring the latency between the actual radar signal appearance and its reported detection time. Additionally, if the sensor reports a detection before the radar signal appears, the test harness can log a false alarm. Furthermore, waveforms with no incumbent radar signals and similar interference power levels can be generated to test for the probability of false alarm. These waveforms are generated with the $3.5\,\mathrm{GHz}$ waveform generator software tool [6] as shown in Fig. 1. The waveform generator also logs the waveform generation parameters including instantaneous measurements of the signal to interference ratio (SIR). The parameters can be used for fine tuning

Caromi, Raied; Mink, John; Wedderburn, Cosburn; Souryal, Michael; El Ouni, Naceur.
"3.5 GHz ESC Sensor Test Apparatus Using Field-Measured Waveforms."
Paper presented at WInnComm 2018, Melbourne, FL, United States. November 14, 2018 - November 15, 2018.

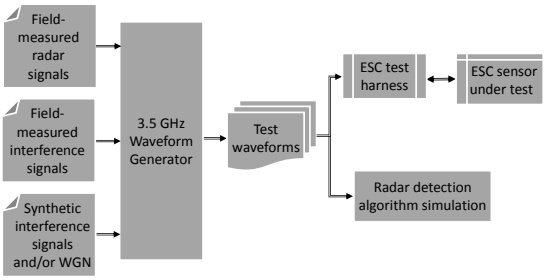


Figure 1: ESC testing system overview

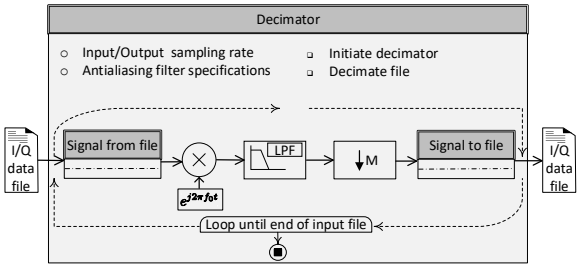


Figure 2: Radar source waveform decimation with a low-pass filter (LPF)

the selection of waveform files for a specific test. They are also used in post-processing to calculate performance metrics.

The selected waveforms are fed to the ESC test harness which consists of a control logic unit, an RF playback device, and RF recording device. The control logic unit is responsible for organizing the flow of the test and logging the test results. It first sends the appropriate file and some additional playback parameters to the RF playback device. Then, it monitors when the playback of each file finishes, listens to a response from the ESC sensor under test, logs the test metadata, and sends the next file to the RF playback device. The test finishes when all the files in a list of selected files are played. Alternatively, the waveforms can be used for development of ESC detection algorithms without RF playback. Throughout this paper, we use a sampling rate of $25\,\mathrm{MHz}$ for all the generated waveforms with effective bandwidth of $20\,\mathrm{MHz}$. This configuration enables us to include up to two $10\,\mathrm{MHz}$ LTE signals with no overlap in the frequency domain.

## 4 WAVEFORM GENERATION

A waveform generator software tool handles the process of generating the RF playback waveforms [6, 7]. The waveform generator utilizes the field-measured waveforms to generate multiple testing scenarios in which one or more radars operate in the presence of interference such as LTE signals and adjacent-band radar emissions. The waveform generator consists of a signal input/output framework, signal processing procedures, and a graphical user interface (GUI). The signal input/output framework handles the process of reading and writing the signals from/to signal files. All signals are saved as 16-bit integer interleaved in-phase/quadrature (I/Q) data files with appropriate scaling. The reading, writing, and signal processing procedures are performed in terms of segments of samples. The framework also handles the tracking of signal timing and multi-task process execution.

### 4.1 Signal Preprocessing and Measurement Preparations

Certain tasks are performed prior to the waveform generation process. Specifically, the field-measured waveforms are decimated from $225\,\mathrm{MHz}$ to $25\,\mathrm{MHz}$ sampling rate and an anti-aliasing low-pass filter is applied to the waveform. The waveforms are shifted with an appropriate frequency for each waveform to center the radar signal at zero Hz baseband. The decimation process is preformed in parallel to reduce the run time when processing multiple files. Fig. 2 demonstrates the decimation process with its attributes and tasks for one waveform. In addition, the instantaneous signal to interference ratio (SIR) calculation performed during the generation process requires estimation of radar peak amplitudes and their times for every rotation of the radar antenna. The peak estimation is performed on the all selected waveforms before the generation process.

In addition to the adjacent-band interference (ABI) signals, we generate waveforms that incorporate LTE interference signals. Specifically, TDD LTE signals are simulated and upsampled to the final waveform sampling rate in advance. These signals represent the case when one LTE signal per CBRS channel is dominant at the ESC receiver. Furthermore, captured LTE TDD signals with more realistic out-of-band characteristics can be used instead of computer-generated LTE signals.

### 4.2 Waveform Generator

Fig. 3 shows the generation process of one waveform with all the required attributes and tasks. The attributes define the characteristics of the waveform, while the tasks control the generation process. A single waveform consists of one or more radar and interference signals. For radar signals, the output waveforms from Fig. 2 are used as inputs to the waveform of Fig. 3. Each signal in the waveform has attributes such as status, center frequency in the baseband, start time, and channel effect for LTE signals. The gain for each signal is estimated from either the desired power signal power level, or the desired SIR. A higher level object in the framework controls the process of generating multiple waveforms. Specifically, the waveform generator object randomizes certain parameters for each waveform such signal start time, frequency, and SIR. Furthermore, it automates and parallelizes the generation process of these waveforms.

In addition, we develop a GUI to visualize the resulting waveforms and simplify the selection of waveform parameters. The

Caromi, Raied; Mink, John; Wedderburn, Cosburn; Souryal, Michael; El Ouni, Naceur.
"3.5 GHz ESC Sensor Test Apparatus Using Field-Measured Waveforms."
Paper presented at WInnComm 2018, Melbourne, FL, United States. November 14, 2018 - November 15, 2018.

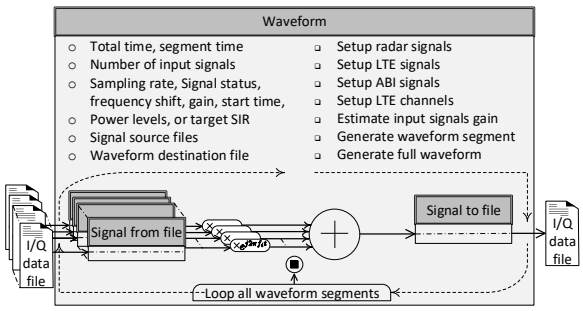


Figure 3: Test waveform generation

GUI utilizes the waveform generation framework to perform the generation process. The GUI allows up to two radar signals, two LTE signals and one ABI signal. The waveform parameters can be changed interactively in the preview mode to visualize the waveforms as shown in Fig. 4. In addition, the waveform generation panel simplifies the selection and randomization of the parameters [6]. The generated waveforms are $90\,\mathrm{s}$ long and sampled at $25\,\mathrm{MHz}$.

## 5 ESC TEST HARNESS

### 5.1 Harness Overview

The test harness consists of two independent parts that run in realtime and a post processing portion that runs after the test is complete; a controller that manages the entire set of files (stored on a redundant array of independent disks, or RAID), and a player that plays a single waveform file at a time as issued by the controller. For auditing purposes the test harness also includes a recorder which digitally samples and records to a file the waveform being played as it is seen by the ESC sensor. A block diagram of the test harness is shown in Fig. 5.

The ESC test harness was implemented using a National Instruments (NI) PXIe chassis containing an NI vector signal transceiver (VST) to play the signals at RF, an NI vector signal analyzer (VSA) to record the signal being played, and an NI PC to act as the controller.[2] Also included in the setup is an RF splitter allowing the signal from the VST to go to both the ESC sensor as the unit under test and to the VSA/recorder. Additional hardware, such as a spectrum analyzer, can be used for realtime viewing of the waveform. This hardware can be seen in Fig. 6.

The ESC sensor connects to the test harness by an RF cable used to receive the signals sent by the test harness, and a network cable used by the ESC sensor to transmit detection messages to the test harness over HTTP.

[2]Certain commercial equipment, instruments, or materials are identified in this paper in order to specify the experimental procedure adequately. Such identification is not intended to imply recommendation or endorsement by the National Institute of Standards and Technology, nor is it intended to imply that the materials or equipment identified are necessarily the best available for the purpose.

### 5.2 Controller

The controller presents a web interface with a login page that prompts for credentials. After logging in, the user then inputs specific parameters for a manual test of a single waveform file or the filepath of a JavaScript Object Notation (JSON) file for an automated test of a batch of waveform files. In case of the latter, the controller takes this list of waveform files from the JSON file, issues them one at a time to the player, and waits for a response indicating completion of playback from the player. The controller also creates a new timestamped log file for the duration of the test batch. During playback, the controller is also listening for any messages from the ESC sensor; all such messages are timestamped and logged. The log file is used later in post-processing to generate performance metrics, as described in Section 5.5.

The test harness uses a single clock for reference, as supplied by the controller, to avoid the risk of clock drift when comparing events from the separate components of the test harness: controller, player, or the ESC sensor. The controller time-stamps the start of a waveform just prior to issuing it to the player, and time-stamps notifications it receives from the ESC sensor under test.

A possible timing hazard may arise from an ESC sensor that aggregates reporting data, for example every $60\,\mathrm{s}$. The risk of this hazard is mitigated by ensuring that each test waveform exceeds $60\,\mathrm{s}$. Furthermore, a delay can be inserted between consecutive test waveforms to reduce the likelihood that the response to one test waveform appears during playback of the next waveform.

### 5.3 RF Player Functionality and Operation

The RF player is the portion of the test harness that plays a single waveform file at a time over an RF cable, using the VST, to the ESC sensor. This is done by wrapping the player in a state machine to handle the metadata. The list of states is shown in Fig. 5.

The instruction to play a waveform file is received as a JSON message over a HTTP socket from the controller. This message tells the player both what file to play (by full filepath) and the metadata for how to play that file (i.e., baseband gain, RF gain, center frequency).

Once the player receives the JSON message from the controller, the player parses the message into its individual elements, conditionally converts the file to NI's technical data management solution (TDMS) format, and then generates the RF waveform to the ESC sensor under test. The player sends a message to the controller over HTTP to indicate that the file has finished playing. The player then proceeds to wait for the next message from the controller indicating which file to play next. This flow, implemented in NI LabVIEW software, is shown in Fig. 7.

If an error is experienced at any stage, the player proceeds to an error handling stage and reports back to the controller rather

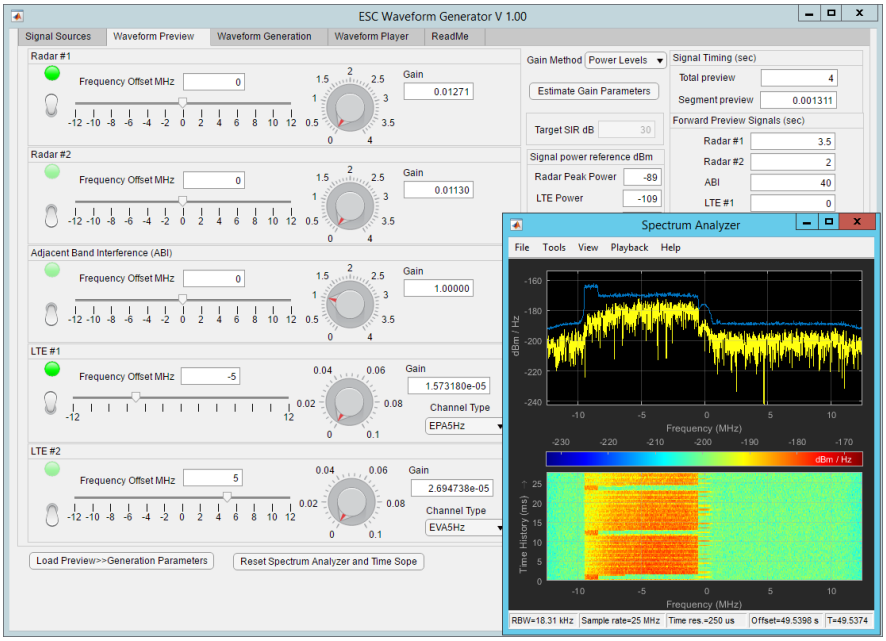


Figure 4: Preview panel of the waveform generator GUI

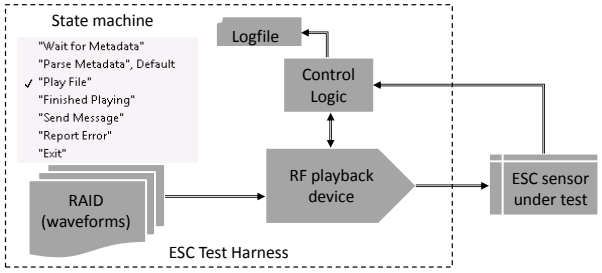


Figure 5: Block diagram and list of states for waveform player

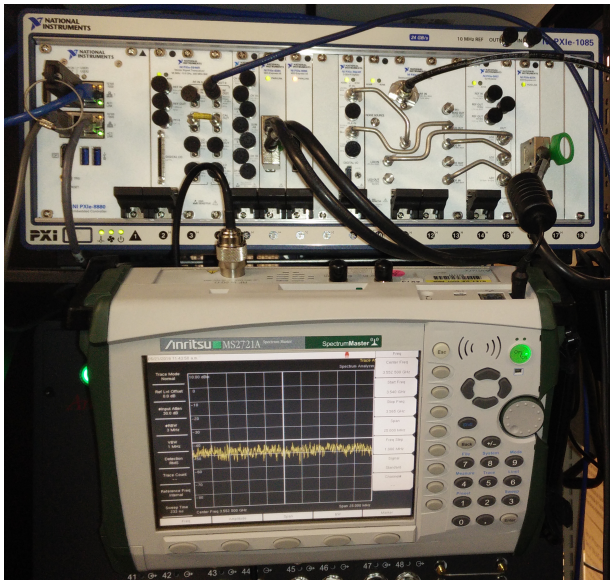


Figure 6: Photo of the hardware comprising the ESC test harness

than playing the file. This error handling is not shown in Fig. 7.

Fig. 8 expands the RF playback device block of Fig. 5 in more detail. The figure illustrates the hardware and software components associated with the RF playback subsystem, including the VST (NI 5646) and VSA (NI 5668). LabVIEW code implements NI RF Signal Generator (niRFSG) drivers which configure the VST as an arbitrary waveform generator (AWG) and a TDMS file reader, enabling the application to function as a waveform file player. The VST RF drivers configure parameters within the VST RF chain to enable signal generation at a specific center frequency, I/Q sampling rate, and RF output power.

The LabVIEW code also configures the first-in, first-out (FIFO) memory of the VST to be used as a buffer by the internal Virtex6 field programmable gate array (FPGA). Considering that the size of each waveform file is approximately 9 GB, which is significantly larger than the 1 GB on-board host VST dynamic

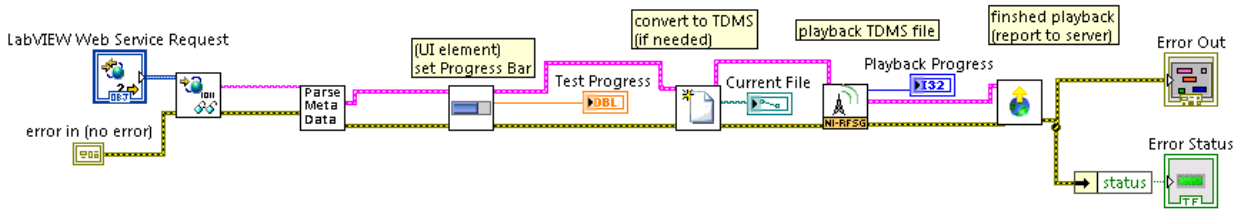


Figure 7: Block diagram of the RF player portion of the ESC test harness

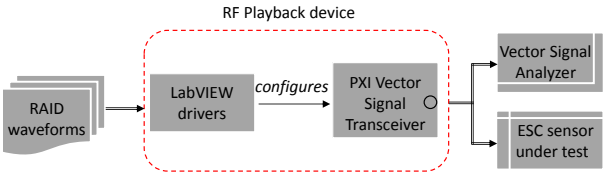


Figure 8: RF playback and record subsystem

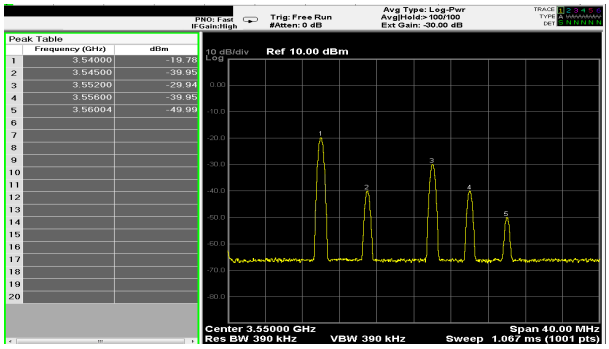


Figure 9: Multiple tones used to derive power correction

random-access memory, it is necessary to process each waveform file in chunks. The configuration of the FPGA involves specifying the capacity, or depth, in elements of the FIFO. A direct memory access channel is formed between the FIFO buffer on the host VST and FPGA target enabling chunks of data to be transferred between the two nodes. As a result, the configuration allows for continuous data streaming of the TDMS waveform file for RF playback.

### 5.4 RF Power Correction

In order to generate the waveforms at desired power levels, the playback subsystem must be calibrated to compensate for cable loss and to correct for any other offsets in the RF chain. To calculate the correction, the cable losses were measured and added into the RF budget along with a correction factor derived from a custom test waveform file. The file contains five predefined tones with varying amplitudes at five different frequencies. An illustration of the tones is shown in Fig. 9. The correction factor which reproduced the tones at their expected amplitudes was then applied to the VST for playback of all waveform files.

### 5.5 Post-Processing of Detection Results

After the entire test is complete, the controller has generated a single timestamped log file. This logfile contains the start and end time of every portion of the test as reported by the player, as well as any messages received by the ESC sensor. All log entries are timestamped by the controller as they are written.

From the log file and the known characteristics, or ground truth, of each test waveform file (i.e., presence/absence of in-band radar, and its center frequency if present), a post-processing script can identify true detections, missed detections, false detections, and late detections. A true detection occurs when the waveform contains an in-band radar signal, and the ESC sensor under test correctly identifies the channel(s) on which it transmits. False detections occur when the ESC sensor reports a federal incumbent signal on a channel which contains no in-band radar signal. Late detections are a subset of correct detections where the radar was detected on the correct channel but not within 60 s of the time it first exceeded the detection threshold of $-89\,\mathrm{dBm/MHz}$.

## 6 SAMPLE TEST SCENARIOS

To illustrate use of the test harness, we generated playback files with combinations of in-band radar and interference signals using the waveform generator tool described in Section 4. The generated waveforms were played consecutively using the ESC test harness described in Section 5. The waveforms were played with a 25 MHz sampling rate and 20 MHz bandwidth at 3.6 GHz and captured into a single I/Q file with the recorder as demonstrated in Fig. 10. For demonstration purposes, the waveform files were played at higher power levels than an actual test since the VSA in the absence of a preamplifier has a noise floor of $-150\,\mathrm{dBm/Hz}$. In an actual test, a preamplifier would be required to record these signals with a lower noise floor.

Six 90 s waveforms were played consecutively and recorded by the ESC test harness. From the recorded I/Q samples, a $6 \times 90\mathrm{s}$ spectrogram was generated with a max-hold of 0.2 s

Caromi, Raied; Mink, John; Wedderburn, Cosburn; Souryal, Michael; El Ouni, Naceur.
"3.5 GHz ESC Sensor Test Apparatus Using Field-Measured Waveforms."
Paper presented at WInnComm 2018, Melbourne, FL, United States. November 14, 2018 - November 15, 2018.

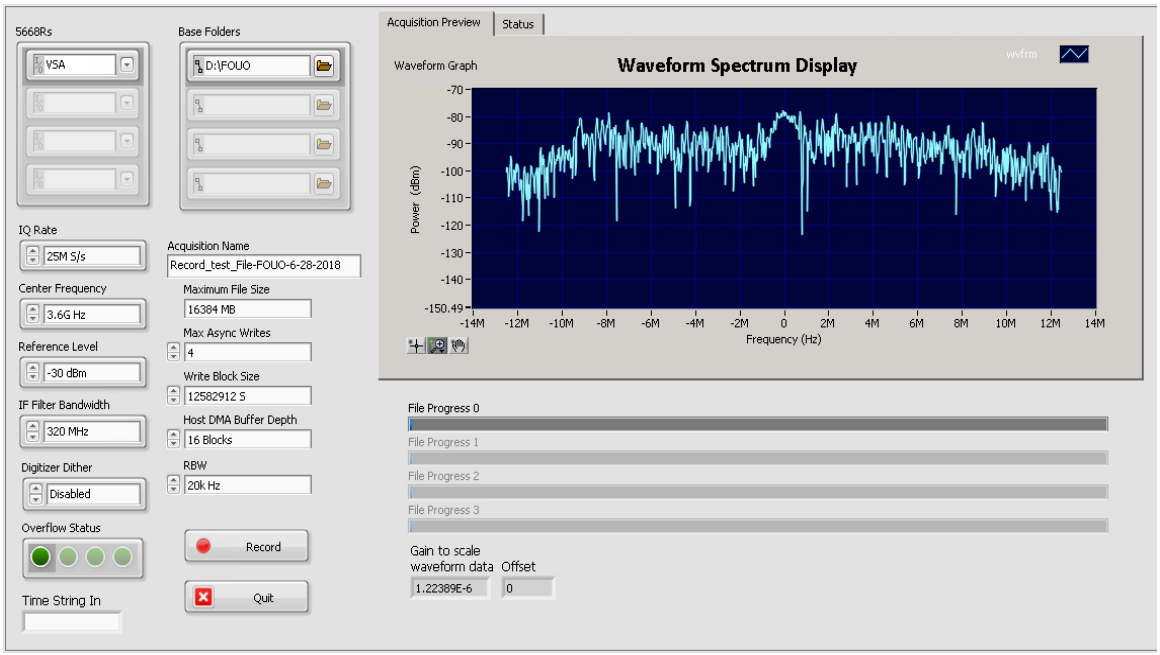


Figure 10: RF recorder

per spectral line. The remainder of this section briefly describes each 90 s portion of this test and presents a detection example of the incumbent radar signal over the entire recorded file.

### 6.1 In-band Radar

The first example shows a single in-band radar signal at a center frequency of 3.6 GHz. The radar signal starts after a delay of approximately 10 s and first rises above the detection threshold at approximately 13.4 s from the beginning of the waveform, as shown in Fig. 11. This case demonstrates a simple scenario where only one radar signal is present and no interference signal exists in the band.

### 6.2 Two Faded LTE Signals

The second portion of the test, shown in Fig. 12, demonstrates the presence of LTE signals when the in-band radar is absent. Two 10 MHz TDD LTE signals are assumed to be the dominant signals in their respective channels. The two LTE signals differ in terms of their TDD configurations and their up-link to down-link power ratios. In addition, time-varying multipath channel fading is applied to both signals.

### 6.3 In-band Radar with Co-Channel LTE

The next segment of the playback test shows an in-band radar signal co-channel with a fading LTE signal. As shown in Fig. 13, both the radar and the LTE signals are centered at 3.6 GHz. The radar signal in this waveform is relatively strong as shown in the time-domain plot of Fig. 14. The time-domain plot clearly shows the main-beam emission of the radar antenna as it sweeps past the receive antenna, as well as emissions from side lobes or strong reflections. Furthermore, the LTE signal envelope varies because of the channel fading.

### 6.4 In-Band Radar Between Two Faded LTE Signals

Fig. 15 shows a typical configuration with two LTE signals in adjacent channels and an in-band radar signal in the guard-band between the two channels. The radar signal is easily observable in this waveform since each LTE signal has a 9 MHz occupied bandwidth and is placed at $\pm 5$ MHz from the radar center frequency.

### 6.5 Adjacent-Band Emissions

The segment of the test starting at 366 s and shown in Fig. 16 demonstrates interference from adjacent-band radar emissions. The in-band radar signal is absent and a robust ESC detector is expected to report no detection of in-band radar during this 90 s period. The adjacent-band emissions end approximately 60 s from the start of this segment since the original field-measured waveforms were 60 s in duration.

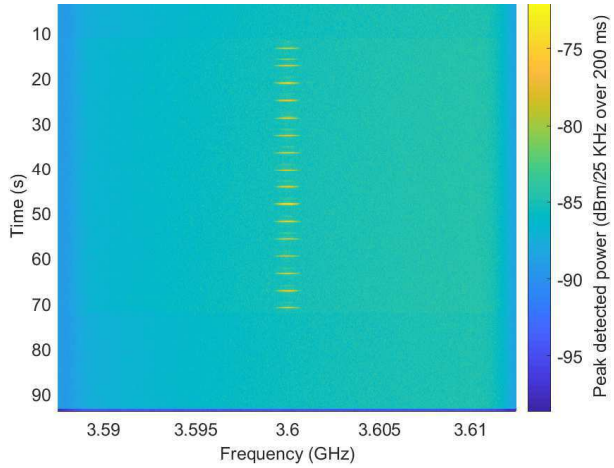


Figure 11: Spectrogram of in-band radar signal

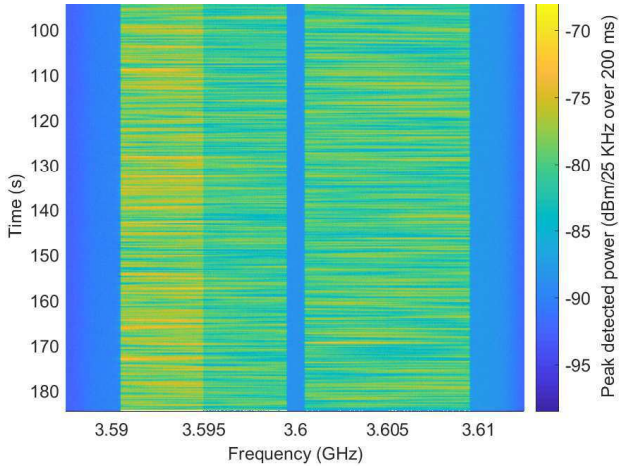


Figure 12: Spectrogram of two LTE signals with fading

### 6.6 Two In-Band Radars with Adjacent-Band Emissions

Finally, a more challenging scenario is shown in the last segment. As shown in Fig.17, two in-band radar signals are placed at center frequencies of 3.60 GHz and 3.61 GHz, respectively. In addition, the waveform contains adjacent-band interference. The two in-band radar signals start 28 s and 30 s into the generated waveform, respectively. The ESC detector is expected to detect both in-band radar signals during this portion of the test. Fig. 18 shows a time-domain plot of a 0.2 s slice of this segment during which the main beam of one of the in-band radars sweeps past the receiver; the stronger peaks are adjacent-band emissions.

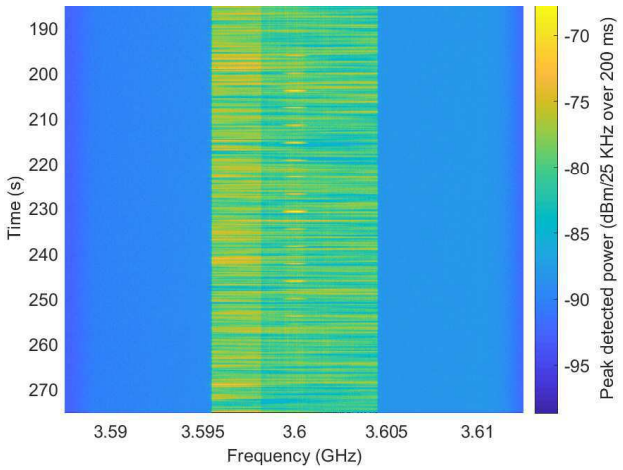


Figure 13: Spectrogram of in-band radar signal with co-channel LTE

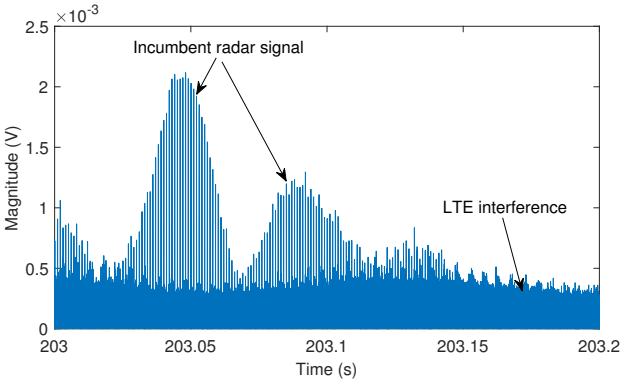


Figure 14: Time-domain plot of a 0.2 s portion of the in-band radar signal with co-channel LTE (at the 203 s mark of the test)

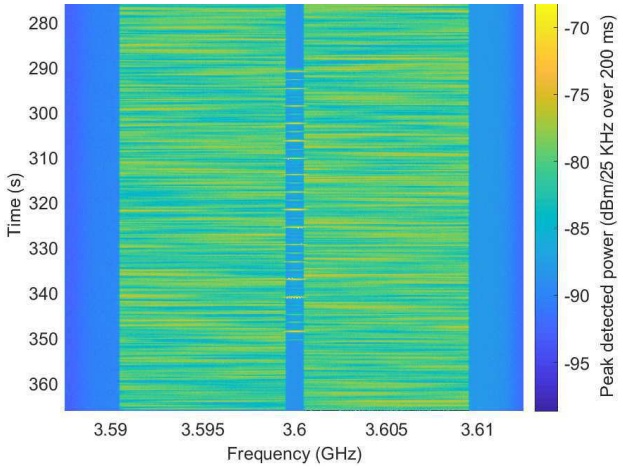


Figure 15: Spectrogram of in-band radar signal between two fading LTE signals

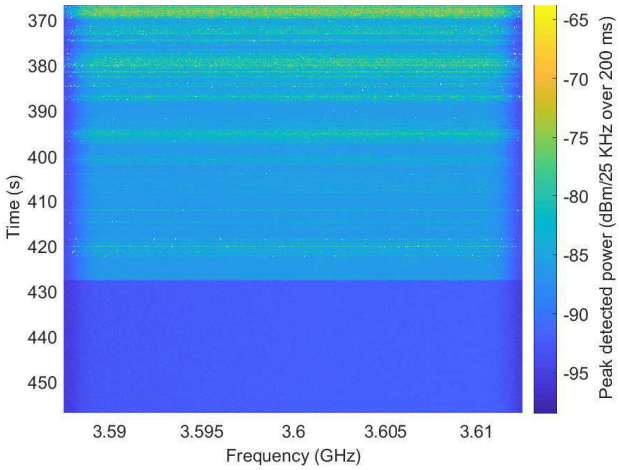


Figure 16: Spectrogram of adjacent-band interference

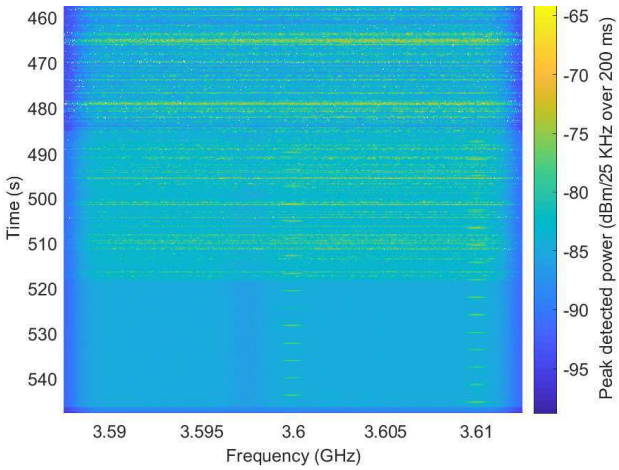


Figure 17: Spectrogram of two in-band radar signals with adjacent-band interference

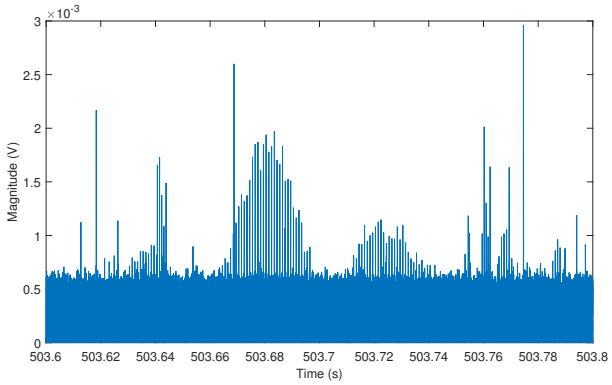


Figure 18: Time-domain plot of a 0.2 s portion of the two in-band radar signals with adjacent-band interference (at the 503.6 s mark of the test)

### 6.7 Detection Example

In addition to off-line verification of the test signal, the recorded file from the ESC test harness can be used to evaluate a detection algorithm by simulation. To demonstrate, we fed the recorded sequence of waveforms to a matched-filter detector matched to the currently deployed in-band radar signal and centered at 3.6 GHz. The matched filter uses a 10 ms synthetically generated pulse burst with a pulse repetition time of 1 ms and a pulse width of 1 µs, similar to the one presented in [8]. Fig. 19 shows the output of the detector versus test time. The peak values at the output of the detector are proportional to the received signal amplitude, and most correspond to sweeps of the main beam of the radar antenna. The detector output accurately reflects the presence of the in-band radar signal at 3.6 GHz as the test time advances. A threshold can be applied at the output of the detector to decide whether an in-band radar signal is present or absent at this frequency. The threshold value shown in Fig. 19 is for demonstration only.

## 7 SUMMARY

This paper presented a framework and apparatus for quantitatively assessing the performance of a 3.5 GHz ESC sensor using test signals comprised of field-measured and synthetically generated waveforms. Test signals are generated prior to the test for a variety of commercial-federal signal scenarios in which the relative amplitudes and frequency offsets of all signal components can be varied. A test harness automates the test process by generating a script of RF test signals and logging sensor detections. It can also record the test signals as they are seen by the sensor under test for auditing purposes. Following the test, test scripts and test logs can be processed to generate sensor performance metrics such as detection and false alarm rates.

The paper concludes with a series of example scenarios generated by the test apparatus to illustrate its flexibility and expected uses. Further work can incorporate the signals of federal incumbent systems yet to be deployed in the band and which the sensors are expected to detect.

## REFERENCES

[1] "Citizens broadband radio service," 2 C.F.R. § 96, 2016.

[2] F. H. Sanders, J. E. Carroll, G. A. Sanders, R. L. Sole, J. S. Devereux, and E. F. Drocella, "Procedures for laboratory testing of environmental sensing capability sensor devices," National Telecommunications and Information Administration, Technical Memorandum TM 18-527, Nov. 2017. [Online]. Available: http://www.its.bldrdoc.gov/publications/3184.aspx

[3] "Requirements for commercial operation in the U.S. 3550–3700 MHz citizens broadband radio service band," Wireless Innovation Forum Document WINNF-TS-0112, Version V1.5.0, May 2018. [Online]. Available: https://workspace.winnforum.org/higherlogic/ws/public/document?document_id=6531

Caromi, Raied; Mink, John; Wedderburn, Cosburn; Souryal, Michael; El Ouni, Naceur.
"3.5 GHz ESC Sensor Test Apparatus Using Field-Measured Waveforms."
Paper presented at WInnComm 2018, Melbourne, FL, United States. November 14, 2018 - November 15, 2018.

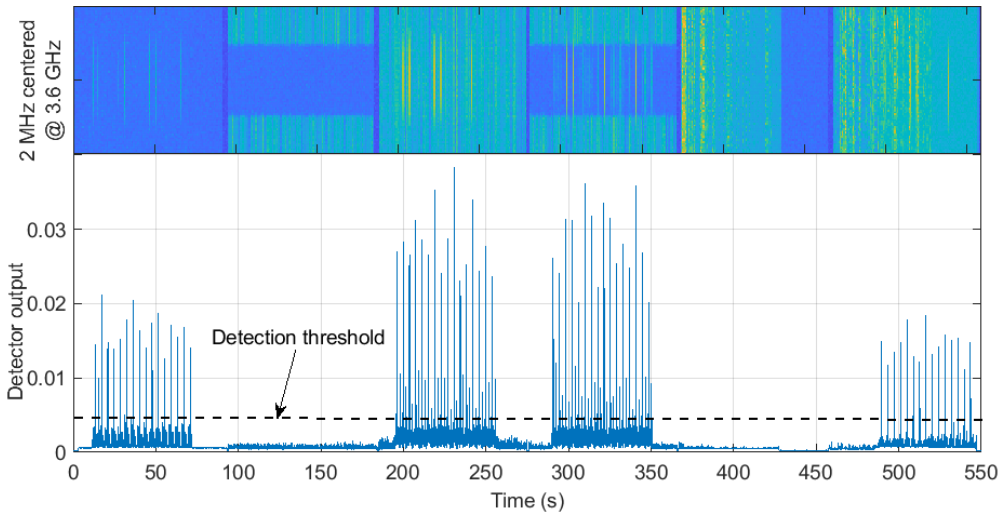


Figure 19: Response of in-band radar matched filter to the recorded test waveform


[4] P. D. Hale, J. A. Jargon, P. J. Jeavons, M. R. Souryal, A. J. Wunderlich, and M. Lofquist, "3.5 GHz radar waveform capture at Point Loma: Final test report," National Institute of Standards and Technology, Technical Note 1954, May 2017. [Online]. Available: https://www.nist.gov/publications/35-ghz-radar-waveform-capture-point-loma

[5] P. D. Hale, J. A. Jargon, P. J. Jeavons, M. R. Souryal, A. J. Wunderlich, and M. Lofquist, "3.5 GHz radar waveform capture at Fort Story: Final test report," National Institute of Standards and Technology, Technical Note 1967, Aug. 2017. [Online]. Available: https://www.nist.gov/publications/35-ghz-radar-waveform-capture-fort-story-final-test-report

[6] R. Caromi, J. Mink, and M. Souryal, "3.5 GHz waveform generation for testing and development of ESC detectors," WInnComm, San Diego, Nov. 2017.

[7] R. Caromi, J. Mink, and M. Souryal, "3.5 GHz waveform generation for testing and development of ESC detectors," https://github.com/usnistgov/ESCWaveformGenerator, 2017.

[8] R. Caromi, M. Souryal, and W. Yang, "Detection of incumbent radar in the 3.5 GHz CBRS band," in *Proc. IEEE GlobalSIP*, Nov. 2018.

# Detection of Incumbent Radar in the 3.5 GHz CBRS Band Using Support Vector Machines

Raied Caromi and Michael Souryal
*Communications Technology Laboratory*
*National Institute of Standards and Technology*
Gaithersburg, Maryland, U.S.
raied.caromi@nist.gov, souryal@nist.gov

***Abstract*—In the 3.5 GHz Citizens Broadband Radio Service (CBRS), 100 MHz of spectrum will be dynamically shared between commercial users and federal incumbents. Dynamic use of the band relies on a network of sensors dedicated to detecting the presence of federal incumbent signals and triggering protection mechanisms when necessary. This paper uses field-measured waveforms of incumbent signals in and adjacent to the band to evaluate the performance of support vector machine (SVM) classifiers for these sensors. We find that a peak analysis classifier and a higher-order statistics classifier perform comparably when the signal is in white Gaussian noise or commercial long term evolution (LTE) emissions, but with out-of-band emissions of adjacent-band systems the peak analysis classifier is far superior This result also highlights the importance of including adjacent-band emissions in any performance evaluation of 3.5 GHz sensors.**

***Index Terms*—3.5 GHz, CBRS, radar detection, machine learning, sensor**

## I. Introduction

The Citizens Broadband Radio Service (CBRS) in the U.S. permits commercial broadband access to the radio frequency spectrum between 3550 MHz and 3700 MHz on a shared basis with incumbents in the band [1]. Among the incumbents is the U.S. military which operates radar systems in this band, including shipborne radar off the U.S. coasts. The CBRS rules permit dynamic access to the band in the proximity of military radar provided a sensor network detects the presence of the incumbent radar and triggers interference mitigation measures when necessary. The scope of this study is on the achievable detection performance of this sensor network.

In order to operate in the CBRS ecosystem, sensors must be able to detect the in-band incumbent radar signal at a minimum received power density of $-89$ dBm (dB relative to 1 mW)/MHz [2], within 60 seconds of onset, and with a probability of detection of 99 % or better [3][1]. With this minimum required power density, the detection is clearly not thermal-noise-limited, as the detection threshold is 25 dB above the thermal noise floor. The challenge for detection is presented, rather, by co-channel interference.

There are two primary sources of co-channel interference at the sensor's receiver. First, by design, the band is shared with commercial systems. Therefore, sensors must be able to detect the incumbent signal in channels occupied by commercial systems. These systems are expected to be LTE systems, at least initially. However, the emissions of commercial systems operating in the band can, in principle, be controlled by treating the sensors as protected entities in the CBRS ecosystem.

The second, more challenging, source of interference is the out-of-band emissions of systems operating in adjacent bands. These systems are also military radars, operate at frequencies below the CBRS band, and have been observed to generate significant emissions into the CBRS band [4], [5]. Detection by CBRS sensors differs from traditional radar detection primarily because the sensor aims to identify the presence of a radar signal rather than detecting and tracking a target. Additionally, unlike a typical radar receiver that has full access to the radar waveform, the sensor has only partial knowledge of radar waveform parameters. However, elements of classical radar detection can still be utilized. In prior related work, we evaluated coherent and non-coherent matched-filter detectors for this band [6]. Machine learning techniques have been used for cognitive radio and proposed for physical layer applications [7], [8]. Higher-order statistics and cumulant features were utilized for detection and classification in [9]–[11]. In addition, SVM and deep learning techniques were used for signal classification in [12]–[15].

This paper is a study of the performance of SVM classifiers trained to detect the current radar signal in the 3.5 GHz band. The analysis uses sets of training and evaluation waveforms derived from field measurements. Classifiers are trained on higher-order statistics of the signal amplitude as well as on temporal features of the peaks of the signal amplitude. The waveforms used for training and evaluation of the classifiers include field recordings of both the in-band radar and the out-of-band emissions of adjacent-band radars collected at two U.S. coastal locations [4], [5]. The field recordings were supplemented with computer-generated LTE signals and Gaussian noise. We present the achievable tradeoff between detection and false-alarm rates under different interference conditions for two SVM classifiers. While this study is limited to detection of the current in-band radar, SPN-43, a similar analysis can be performed for future radars deployed in this band.

[1]Government requirements do not specify a maximum probability of false alarm, although this figure of merit is naturally of interest to commercial users.

Caromi, Raied; Souryal, Michael.
"Detection of Incumbent Radar in the 3.5 GHz CBRS Band Using Support Vector Machines."
Paper presented at Sensor Signal Processing for Defence (SSPD), Brighton, United Kingdom. May 9, 2019 - May 10, 2019.

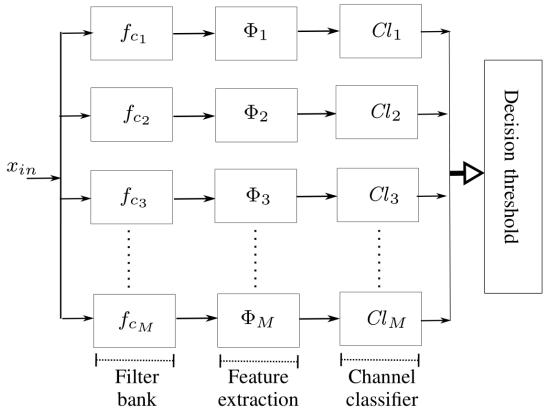


Fig. 1: Classification system overview

## II. System Model

A sensor is responsible for detecting incumbent radar signals and identifying which 10 MHz channel each signal occupies within the lower 100 MHz of the band. One alternative is for a capable sensor to sample the entire 100 MHz and employ $M$ filters to cover the entire bandwidth, each filter being centered at an appropriate frequency, $f_{c_i}$. The output of each filter is fed to a radar signal detector. The simplest form of a detector is a binary classifier indicating presence or absence of an incumbent radar signal. Fig. 1 demonstrates this configuration. In addition to filtering, the signal can be downsampled to an appropriate sampling rate, $F_s$, to reduce computations. After filtering, a set of features, $\Phi_i$, is extracted from the signal for use by a trained classifier $Cl_i$ to decide whether the radar signal is present or absent in the channel.

For simplicity, we will assume that the classification branches are identical and thus we will drop the branch subscript $i$ for the remainder. As in [6], the simplified signal model is given by

$$x[n] = s[n] + v[n],$$

where $s$ is the in-band radar signal whose presence we are trying to detect, and $v$ is either complex white Gaussian noise (CWGN), an LTE signal sharing the band, or adjacent-band interference (ABI) from radar emissions outside the band. The SVM classifier requires training before its use for detection. The model is trained on signal data that include scenarios similar to what a sensor will observe in field operation. The statistical hypothesis testing for the radar signal detection is

$$\begin{cases} H_0 : x[n] = v[n], \\ H_1 : x[n] = s[n] + v[n]. \end{cases}$$

Two probabilities are of interest for evaluating detection performance, the probability of false alarm, $P_{FA} = Pr(\hat{H}_1|H_0)$, and the probability of detection, $P_D = Pr(\hat{H}_1|H_1)$.

## III. SVM binary signal classification

We model the detection problem of the incumbent radar signals as a binary classification problem. In supervised learning, the classifier requires the ground truth for the presence of the radar signal. Therefore, we generate training signal data with an appropriate response variable for the state of the incumbent radar signal. For both training and testing, all signals pass through a two-step normalization process. First, we subtract the mean of the signal from itself. This step reduces the direct current (DC) components in the signal. Second, we normalize the signal by its root mean square (RMS). RMS normalization removes the dependency of the extracted features on the magnitude of the signal.

### A. Feature extraction

For signal classification, the features are signal attributes that emphasize some phenomena of interest in the signal. Particularly, we are interested in signal features that are useful for detecting pulsed radar signals. Two examples of such signals with different types of background interference are shown in Fig. 2. In one case (Fig. 2a), the interference is an LTE signal and the pulsed radar signal is relatively easy to distinguish. In the other case (Fig. 2b), the interference also appears pulsed and detection is more challenging. We consider

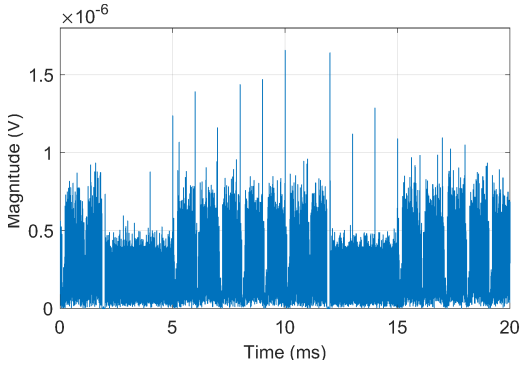


(a) Incumbent radar plus LTE.

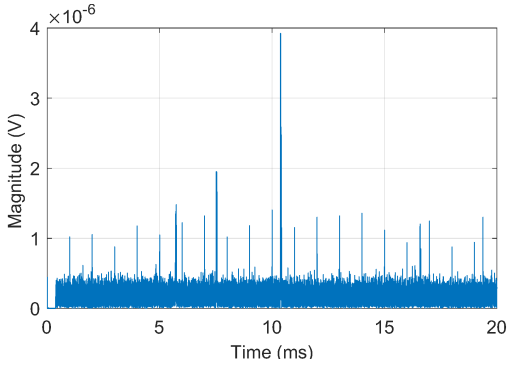


(b) Incumbent radar plus ABI.

Fig. 2: Time domain radar signals plus interference.

Caromi, Raied; Souryal, Michael.
"Detection of Incumbent Radar in the 3.5 GHz CBRS Band Using Support Vector Machines."
Paper presented at Sensor Signal Processing for Defence (SSPD), Brighton, United Kingdom. May 9, 2019 - May 10, 2019.

two classification models, each with a distinct set of features extracted from the time-domain signals. One set is comprised of higher-order statistics of the signal amplitude and the other of temporal features of the peaks of the signal amplitude. We use state-of-the-art SVM classifiers with the kernel method for both models due to its efficiency for solving classification problems that include non-linear features.

*1) Higher-order statistics classifier (HSC):* We consider the third and fourth moments of the magnitude of the signal in terms of its skewness and kurtosis, respectively. Skewness is a measure of the lack of symmetry of a distribution, and kurtosis is a measure of whether the distribution is heavy-tailed or light-tailed relative to a normal distribution [16]. Skewness and kurtosis provide a measure of the deviation of the signal distribution from normality towards burstiness. The distribution of the amplitude when a strong radar signal is present is heavy-tailed and highly skewed to the right. On the downside, skewness and kurtosis may not be able to distinguish between the intended radar signal and similar, pulsed interference signals. In order to improve detection performance amid non-uniform bursts in the interference, we partition the signal into $P$ contiguous partitions. Each signal partition, $x_p$, has a number of samples, $N_p = \frac{N}{P}$, where $N$ is the number of samples of the signal. We choose $N$ and $P$ to produce an integer number of partitions, $N_p$. The kurtosis, $\kappa_p$, and skewness, $\varsigma_p$, of each partition are computed as follows,

$$\kappa_p = \frac{\frac{1}{N_p}\sum_{i=1}^{N_p}(|x_p[i]| - \overline{(|x_p|)})^4}{\sigma_p^4},$$
$$\varsigma_p = \frac{\frac{1}{N_p}\sum_{i=1}^{N_p}(|x_p[i]| - \overline{(|x_p|)})^3}{\sigma_p^3},$$

where $\overline{(\cdot)}$ denotes the mean, and $\sigma_p$ is the standard deviation of $|x_p|$. The features for this model are computed as the mean of the kurtosis and skewness over all signal partitions. Specifically,

$$\Phi_{\kappa\varsigma} = \{\frac{1}{P}\sum_{p=1}^{P}\kappa_p,\ \ \frac{1}{P}\sum_{p=1}^{P}\varsigma_p\}.$$

*2) Peak analysis classifier (PAC):* The peak analysis method relies on finding the peaks of the time domain signal with certain constraints. A threshold $\gamma$ is first applied to the signal. The threshold rule ensures only peaks of a sufficient amplitude are considered for the peak search. Then, we use the second derivative test to find all the local maxima in the signal. The local maxima are further filtered by minimum separation time. This step ensures that only one sufficient peak is selected per time interval of $T_m$. In the last step, we limit the number of peaks by selecting the largest $L$ peaks. We use the resulting set of peak amplitudes, $\{\alpha_\ell\}$, and their corresponding times, $\{\tau_\ell\}$, to extract the desired features for the peak analysis classifier. The differences between the times of the peaks indicate the level of uniformity of the peak separation. Specifically, the more uniform the time separation is, the higher likelihood that an in-band SPN-43 radar signal is present. Hence, we define $\{\Delta\tau_\ell := \tau_{\ell+1} - \tau_\ell, \ell = 1, 2, 3, \ldots, L-1\}$ as the set of time differences between the peaks. In addition to the statistics of the set $\{\Delta\tau_\ell\}$, we use the average of the peak amplitudes as one of the features. The set of features for peak analysis is defined as

$$\Phi_{\alpha\tau} = \{\overline{(\{\Delta\tau_\ell\})},\ \ \mathrm{var}(\{\Delta\tau_\ell\}),\ \ \max(\{\Delta\tau_\ell\}),\ \overline{(\{\alpha_\ell\})}\},$$

where $\mathrm{var}(\cdot)$ is the variance, and $\max(\cdot)$ is the maximum.

### B. Classification model

The SVM classifier constructs an optimal separating hyperplane between two linearly separable classes. Since the classes in our model are not linearly separable, we use the kernel method which expands the features into higher dimensional feature space. Specifically, we use the Gaussian kernel function. Furthermore, we tune the model hyperparameters using Bayesian optimization [17], [18][2]. In particular, the hyperparameters are box-constraint and kernel-scale. The box-constraint is the regularization parameter for the soft margin of the SVM. As a result, it provides a tradeoff between misclassification and over-fitting. On the other hand, the kernel-scale regulates the influence of individual support vectors on the decision boundary. Furthermore, Platt scaling with a sigmoid function is used to map the SVM scores into class posterior probabilities [18], [19]. The probability output enables us to compute detection performance against a range of threshold values.

## IV. Performance Analysis

Field-measured signals of shipborne radar mixed with three types of interference are used to train and test the classifier. The radar and interference signals are generated separately, processed similarly to [6], and later added together in simulation. All the radar and interference signals consist of $20\,\mathrm{ms}$ segments, each with $F_s = 2$ MHz. The radar signals contain 20 pulses. The interference is either WGN, a single time-division duplex (TDD) LTE signal, or ABI. Radar peak power and interference peak and average power are computed in a $1\,\mathrm{MHz}$ bandwidth. In addition, the signal-to-noise ratio (SNR) is defined as the peak power of the radar signal to the average noise power in $1\,\mathrm{MHz}$. Field-measured radar and ABI signals are divided into two separate groups, one for training and another for evaluating detection performance. The WGN and LTE signals are generated randomly during training and testing. The TDD LTE signal configurations are selected randomly from columns of Table 1 in [6].

### A. SVM classifier training

We generated $35\,200$ training waveforms. Half of the set contains a radar signal plus interference and the other half contains interference only. The training set includes

[2]Certain commercial equipment, instruments, or materials are identified in this paper to foster understanding. Such identification does not imply recommendation or endorsement by the National Institute of Standards and Technology, nor does it imply that the materials or equipment identified are necessarily the best available for the purpose.

Caromi, Raied; Souryal, Michael.
"Detection of Incumbent Radar in the 3.5 GHz CBRS Band Using Support Vector Machines."
Paper presented at Sensor Signal Processing for Defence (SSPD), Brighton, United Kingdom. May 9, 2019 - May 10, 2019.

12 800 waveforms with WGN, another 12 800 waveforms with LTE interference, and 9600 waveforms with ABI. The signal state is stored in the response variable as 0 when the incumbent radar signal is absent, and as 1 when the incumbent radar signal is present. We set different levels of interference power for each scenario. For WGN, the SNR was set at $(11, 13, 15, 17)$ dB. For LTE, the peak radar signal power was fixed at $-89\,\mathrm{dBm/MHz}$, the required detection threshold, while the LTE power was set at $(-100, -103, -106, -109)$ dBm/MHz.[3] The training waveforms with ABI were equally selected from three groups based on their peak interference to noise ratio (INR). In particular, the groups are selected based on three ranges of INR, $(10 < \mathrm{INR} < 20, 20 < \mathrm{INR} < 30, \mathrm{INR} > 30)$ dB. The SNR for the waveforms with ABI was fixed at 19 dB, which corresponds to the SNR when the peak radar signal power is at the required detection threshold and the detector has a thermal noise figure of 6 dB.

The training data was used to extract $\Phi_{\kappa\varsigma}$ features for HSC, and $\Phi_{\alpha\tau}$ features for PAC. For the PAC model, $T_m = 0.5$ ms, $L = 20$, and $\gamma$ was set to 3 dB above the average power of the signal. The features and the response variable were fed to the SVM training algorithm. The SVM model was initially tested with 10-fold cross-validation with equal probability of the class. The confusion matrices for both classifiers are shown in Fig. 3. The percentages of correctly and incorrectly classified observations are shown in the diagonal and off-diagonal cells of the confusion matrix, respectfully. In addition, the far right column and last row give the percentages of correct and incorrect classifications of each class. For example, Fig. 3(b) shows that the PAC model correctly predicts class 0 84.7% of the time. Finally, the lower right cell of each matrix shows overall accuracy. Clearly, the PAC model has higher accuracy and mis-detection rates than the HSC model.

While the confusion matrix of the cross-validation is useful for understanding overall performance and tuning the model hyperparameters, a better measure of detection performance is the receiver operating characteristic (ROC). The following ROC curves were generated with waveform data that was not used for training.

### B. Detection performance

We used the trained SVM models for HSC and PAC to evaluate ROC curves. Given the input, the trained model generates the probability of the class which is compared to a threshold to decide the presence or absence of the radar signal. We use a range of threshold values to evaluate detections and false alarms and average them over all simulation points to compute $P_D$ versus $P_{FA}$ curves.

*1) Signal detection in WGN:* Fig. 4 shows the ROC curves for HSC and PAC for the WGN scenario. Both classifiers require SNR of roughly 12 dB to achieve low $P_{FA}$ at $P_D = 0.99$. While HSC performs better for the lower SNR values, PAC converges faster to a low $P_{FA}$ at higher SNR. In comparison to the matched filter detector with a similar scenario [6], both HSC and PAC classifiers require about 7 dB higher SNR to achieve the same detection performance. However, considering that current detection requirements [2] equate to an SNR of about 19 dB, both HSC and PAC perform acceptably in Gaussian noise.

[3]Current CBRS requirements stipulate that commercial interference at a sensor not exceed $-109$ dBm/MHz [3], but this analysis also considers higher levels of interference.

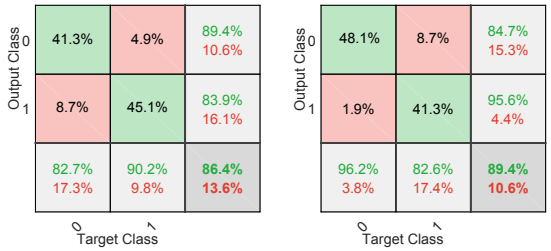


(a) HSC (b) PAC

Fig. 3: Confusion matrix of classifiers' cross validation.

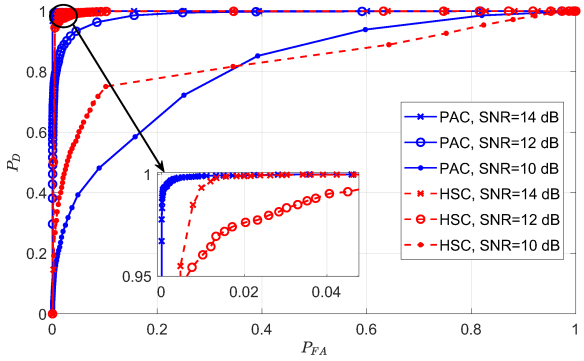


Fig. 4: Radar signal with added WGN.

*2) Detection in LTE interference:* The performance of HSC and PAC in the presence of LTE interference is shown in Fig. 5. The performance of both classifiers degrades slightly from the WGN case due to relatively large variations of the LTE signal in time. Nevertheless, the performance of both detectors is still within the acceptable range since the sensors are required to tolerate $-109\,\mathrm{dBm/MHz}$ of aggregate commercial emissions [3].

*3) Detection in adjacent-band interference:* Finally, Fig. 6 shows the performance in ABI. The PAC classifier performs well for this case and not very far behind the matched filter detector for the same scenario [6]. Evidently, the HSC yields poor performance and is unreliable for this type of interference. This is not surprising since the HSC cannot distinguish between the burst of pulses of incumbent radar and ABI. This example demonstrates that a specific detector may perform well within official requirements [2] for detecting the federal incumbent radar but may perform poorly in certain realistic interference scenarios such as radar emissions from

Caromi, Raied; Souryal, Michael.
"Detection of Incumbent Radar in the 3.5 GHz CBRS Band Using Support Vector Machines."
Paper presented at Sensor Signal Processing for Defence (SSPD), Brighton, United Kingdom. May 9, 2019 - May 10, 2019.

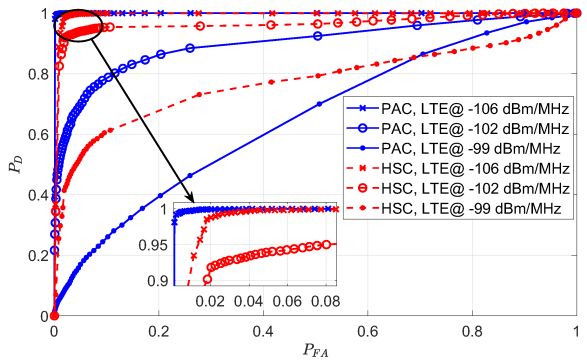


Fig. 5: Radar signal with LTE interference.

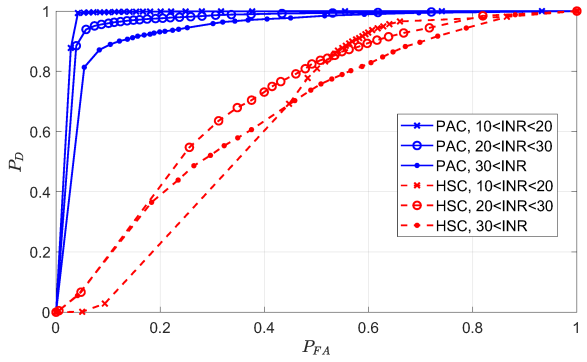


Fig. 6: Radar signal with adjacent-band radar emissions.

adjacent bands.

## V. Conclusion

We presented two feature-based SVM classifiers for detecting federal incumbent radar in the 3.5 GHz shared-spectrum CBRS band. We evaluated their performance using field-measured signals of the in-band incumbent radar in WGN, and in the presence of interference from dominant LTE signals or adjacent-band emissions. Although both classifiers require higher SNR values to achieve the same detection rate as the matched-filter detector, their performance is within the acceptable range of current detection requirements. In addition, the proposed SVM classifiers may provide a practical advantage since they are less computationally expensive to generalize than a matched filter for the same in-band radar signal with a partially known set of parameters. For instance, a matched-filter detector requires correlation with multiple templates if the radar pulse repetition rate is not known, while the SVM classifiers only need to be trained once with multiple templates. However, the features of the classifier should be chosen carefully since a specific detector may meet official requirements but may perform poorly in certain realistic interference scenarios such as radar emissions from adjacent bands.

## References


[1] "Citizens broadband radio service," 2 C.F.R. § 96, 2016.

[2] Frank H. Sanders, John E. Carroll, Geoffrey A. Sanders, Robert L. Sole, Jeffery S. Devereux, and Edward F. Drocella, "Procedures for laboratory testing of environmental sensing capability sensor devices," Technical Memorandum TM 18-527, National Telecommunications and Information Administration, Nov. 2017.

[3] "Requirements for commercial operation in the U.S. 3550–3700 MHz citizens broadband radio service band," Wireless Innovation Forum Document WINNF-TS-0112, Version V1.5.0, May 2018.

[4] Paul D. Hale, Jeffrey A. Jargon, Peter J. Jeavons, Michael R. Souryal, Adam J. Wunderlich, and Mark Lofquist, "3.5 GHz radar waveform capture at Point Loma: Final test report," Technical Note 1954, National Institute of Standards and Technology, May 2017.

[5] Paul D. Hale, Jeffrey A. Jargon, Peter J. Jeavons, Michael R. Souryal, Adam J. Wunderlich, and Mark Lofquist, "3.5 GHz radar waveform capture at Fort Story: Final test report," Technical Note 1967, National Institute of Standards and Technology, Aug. 2017.

[6] Raied Caromi, Michael Souryal, and Wen-Bin Yang, "Detection of incumbent radar in the 3.5 GHz CBRS band," in *Proc. IEEE GlobalSIP*, Nov. 2018.

[7] M. Bkassiny, Y. Li, and S. K. Jayaweera, "A survey on machine-learning techniques in cognitive radios," *IEEE Communications Surveys Tutorials*, vol. 15, no. 3, pp. 1136–1159, 2013.

[8] T. O'Shea and J. Hoydis, "An introduction to deep learning for the physical layer," *IEEE Transactions on Cognitive Communications and Networking*, vol. 3, no. 4, pp. 563–575, Dec 2017.

[9] A. Schmidt, C. Rügheimer, F. Particke, T. Mahr, H. Appel, and H. Klle, "Kurtosis based approach for detection of targets in noise," in *2016 17th International Radar Symposium (IRS)*, May 2016, pp. 1–3.

[10] Tian-Tsong Ng, Shih-Fu Chang, and Qibin Sun, "Blind detection of photomontage using higher order statistics," in *2004 IEEE International Symposium on Circuits and Systems*, May 2004, vol. 5.

[11] C. M. Spooner, "Classification of co-channel communication signals using cyclic cumulants," in *Conference Record of The Twenty-Ninth Asilomar Conference on Signals, Systems and Computers*, Oct. 1995, vol. 1, pp. 531–536 vol.1.

[12] M. Petrova, P. Mähönen, and A. Osuna, "Multi-class classification of analog and digital signals in cognitive radios using support vector machines," in *2010 7th International Symposium on Wireless Communication Systems*, Sep. 2010, pp. 986–990.

[13] M. M. Ramn, T. Atwood, S. Barbin, and C. G. Christodoulou, "Signal classification with an svm-fft approach for feature extraction in cognitive radio," in *2009 SBMO/IEEE MTT-S International Microwave and Optoelectronics Conference (IMOC)*, Nov 2009, pp. 286–289.

[14] T. J. O'Shea, T. Roy, and T. C. Clancy, "Over-the-air deep learning based radio signal classification," *IEEE Journal of Selected Topics in Signal Processing*, vol. 12, no. 1, pp. 168–179, Feb 2018.

[15] S. Rajendran, W. Meert, D. Giustiniano, V. Lenders, and S. Pollin, "Deep learning models for wireless signal classification with distributed low-cost spectrum sensors," *IEEE Transactions on Cognitive Communications and Networking*, vol. 4, no. 3, pp. 433–445, Sep. 2018.

[16] "NIST/SEMATECH e-Handbook of Statistical Methods," http://www.itl.nist.gov/div898/handbook, April 2012.

[17] Trevor Hastie, Robert Tibshirani, and Jerome Friedman, *The Elements of Statistical Learning*, Springer New York, second edition, 2009.

[18] *Statistics and Machine Learning Toolbox*, The MathWorks, Inc., Natick, Massachusetts, Release 2018a, https://www.mathworks.com/help/pdf_doc/stats/stats.pdf.

[19] John C. Platt, "Probabilities for SV machines," in *Advances in Large Margin Classifiers*, Alexander J. Smola et al., Eds., chapter 5, pp. 61–74. MIT Press, Cambridge, Massachusetts, 2000.



Caromi, Raied; Souryal, Michael.
"Detection of Incumbent Radar in the 3.5 GHz CBRS Band Using Support Vector Machines."
Paper presented at Sensor Signal Processing for Defence (SSPD), Brighton, United Kingdom. May 9, 2019 - May 10, 2019.

# Three-Port Vector-Network-Analyzer Calibrations using the NIST Microwave Uncertainty Framework

Jeffrey A. Jargon, Dylan F. Williams, and Aric Sanders

National Institute of Standards and Technology, 325 Broadway, M/S 672.03, Boulder, CO 80305 USA
Email: jeffrey.jargon@nist.gov, Tel: +1.303.497.4961

***Abstract* — We have implemented methods for calibrating three-port vector network analyzers (VNAs) and propagating correlated uncertainties using the NIST Microwave Uncertainty Framework. We describe our calibration procedures, which utilize measured wave-parameters rather than scattering parameters to account for switch-term corrections, and present results for a three-port power splitter. We compare our calibrated measurements with those performed using the firmware of a commercial VNA, and show the results agree to within our confidence intervals at most frequencies.**

***Index Terms* — calibration, coaxial, power splitter, physical models, three-port, uncertainty, vector network analyzer.**

## I. Introduction

Numerous commercial vector network analyzers (VNAs) are available for measuring scattering-parameters (*S*-parameters) of multiport devices such as circulators, coupled transmission lines, directional couplers, power dividers, and power splitters, to name just a few.

In this paper, we focus on three-port *S*-parameter measurements, utilizing the NIST Microwave Uncertainty Framework (MUF) [1] to perform calibrations and propagate correlated uncertainties. The MUF utilizes parallel sensitivity and Monte-Carlo analyses, and allows us to capture and propagate the significant *S*-parameter measurement uncertainties and statistical correlations between them [2]. By identifying and modeling the physical error mechanisms in the calibration standards, we can determine the statistical correlations between both the *S*-parameter uncertainties at a single frequency and uncertainties at different frequencies. These uncertainties can then be propagated to measurements of the devices under test (DUTs).

In the following sections, we describe how our three-port calibration methods are implemented in the MUF and compare our calibrated measurements of a resistive power splitter to those using a calibration performed with the firmware of a commercial VNA.

## II. Three-Port Calibrations

Figure 1 illustrates a model of the systematic errors to be calibrated in a three-port VNA. The DUT is embedded within the error boxes X, Y, and Z, which represent impedance mismatches, losses in the test cables and connectors, and frequency response errors in the sources and receivers. For linear networks, the VNA supplies measurements of uncalibrated *S*-parameters at ports 1, 2, and 3. In the MUF, the error boxes, X, Y, and Z, are arranged into "s6p" files, with the following port nomenclature: ports 1, 2, and 3 correspond to the physical ports of the VNA, and ports 4, 5, and 6 correspond to the ports between the error boxes and the DUT. There are numerous ways to solve for the error boxes [3-4], but in the current version of the MUF software, they can be determined either with two separate short-open-load-thru (SOLT) calibrations or three one-port SOL calibrations in conjunction with two reciprocal connections, commonly referred to as SOLR. Both calibrations assume no crosstalk, so 24 of the 36 error terms are zero.

The SOLR calibration [5-6] is akin to the SOLT calibration [7] in that it is relatively easy to perform, is inherently broadband, and makes use of three characterized standards (open, short, and load) connected to each port of the VNA. The SOLR calibration is an attractive alternative to the SOLT when a zero-length thru is unavailable or difficult to implement, such as when measuring non-insertable or multiport devices. Here, the thru need not be characterized. The only knowledge required is the standard must be reciprocal.

The SOLT and SOLR calibrations are realized with eight-term error models in the MUF. Furthermore, in the case of multiport measurements, the software makes use of measured wave-parameters ($a_i$ and $b_i$), and then converts them to *S*-parameters prior to calibration to avoid measuring and correcting for the switch-terms of each port [8]. The short, open, and load measurements, along with their respective definitions, allow us to determine the two reflection terms for each of the error boxes. This leaves the transmission terms.

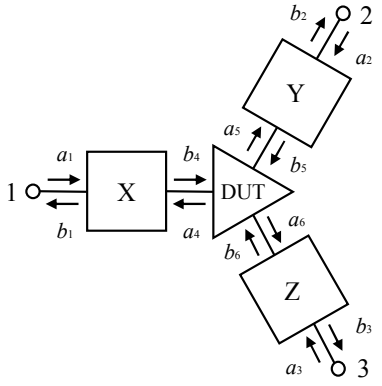


Fig. 1. Model of systematic errors in a three-port VNA.



Jargon, Jeffrey; Williams, Dylan; Sanders, Aric.
"Three-Port Vector-Network-Analyzer Calibrations using the NIST Microwave Uncertainty Framework."
Paper presented at 92nd ARFTG Microwave Measurement Conference, Orlando, FL, United States. January 19, 2019 - January 22, 2019.

The SOL-family of calibrations determines the product of the transmission-terms ($S_{ij}\cdot S_{ji}$) of each one-port error box [7]. In the MUF, the two individual terms are arbitrarily set equal by taking the square root of the product. Then, a sequential method is used to adjust the ratios of the Y and Z error boxes' transmission-terms by setting complex constants $\alpha$ and $\beta$ so the calibration is consistent with measurements of the reciprocal or thru standard, as illustrated in Figure 2. Error box X contains two identical transmission-terms ($S_{41}$=$S_{14}$). After error box Y is determined, its transmission-terms, which are initially identical ($S_{52}$=$S_{25}$), are adjusted to be consistent with error box X by multiplying and dividing the terms by $\alpha$ so the product of the two ($\alpha S_{52}\cdot\alpha^{-1}S_{25}$) remains unchanged. Likewise, after error box Z is determined, its transmission terms, which are initially identical ($S_{63}$=$S_{36}$), are adjusted to be consistent with error box X by multiplying and dividing the terms by $\beta$ so the product of the two ($\beta S_{63}\cdot\beta^{-1}S_{36}$) remains unchanged.

For the SOLT case, the definition of the thru is constrained to be ideal, while for the SOLR case, the thru is merely assumed to be reciprocal. In the case of large-signal calibrations, the transmission terms are adjusted again to account for amplitude and phase corrections.

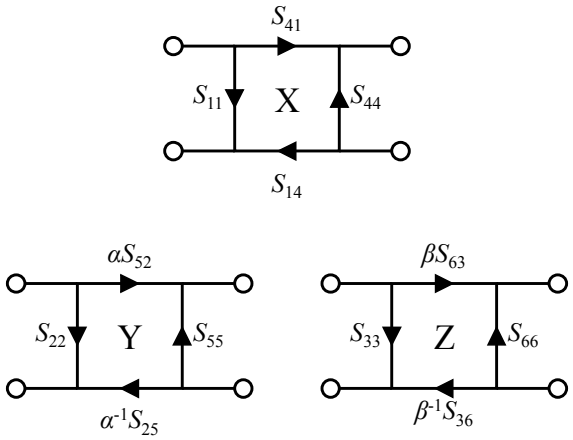


Fig. 2. Model of consistent error boxes in a three-port VNA.

## III. Three-Port Measurements

We measured a resistive power splitter, shown in Figure 3. Such a device has *S*-parameters with the following nominal values: $S_{31} = S_{21} = 0.50$ (-6 dB); $S_{23} = S_{32} = 0.25$ (-12 dB); $S_{22} = S_{33} = 0.25$ (-12 dB); and $S_{11} = 0$. Our power splitter was equipped with 3.5 mm connectors, a female on port 1 and males on ports 2 and 3, as shown in Figure 4. For the SOLT case, we performed an insertable calibration between port 1 (male) and port 2 (female), and another insertable calibration between port 1 (male) and port 3 (female). For the SOLR case, we performed one-port SOL calibrations on ports 1, 2, and 3, and connected our insertable, reciprocal thru between ports 1 and 2, and 1 and 3. Thus, both types of calibrations made use of identical connections. Our calibration standards were modeled with closed-form expressions for coaxial lines of finite metal conductivity [9, 10].

All measurements were performed with 3.5 mm coaxial connectors between 0.2 – 18.0 GHz, and an IF bandwidth of 20 Hz with no averaging. We measured wave-parameters of each device, and then converted them to uniquely-defined *S*-parameters, rather than measuring the switch-terms separately and then correcting the measured *S*-parameters.

The MUF contains a program called the 'VNA Uncertainty Calculator' for performing both covariance-based and Monte-Carlo uncertainty analyses using general connector models and common calibration engines. Figures 5 and 6 illustrate the menus for our three-port SOLT and SOLR calibrations, respectively. The first column of each menu contains the filenames of the standard definitions; the second column refers to the standard types; the third column contains the measurement filenames; and columns 4 and 5 refer to the ports of the VNA to which the devices were connected. For example, in row 1 of Figure 5, the open standards were simultaneously connected to ports 1 and 3.

In addition to performing the SOLT and SOLR calibrations with the MUF, we also performed a calibration using the firmware of our commercial VNA with the same calibration kit. We compared the calibrated measurements of the power splitter using the three methods. Figures 7-10 plot the magnitudes of $S_{31}$, $S_{23}$, $S_{33}$, and $S_{11}$, respectively, along with the 95% confidence intervals of our SOLT and SOLR calibrations. Figure 11 plots the differences in phase of $S_{31}$. The nominal values and associated uncertainties agree almost perfectly for the two calibrations processed by the MUF; in part since they were performed using identical measurements and calibration standard definitions. The small variations can be attributed to differences in the calibration algorithms. The variations between the two MUF calibrations and the VNA's firmware calibration are more noticeable but lie within the confidence intervals of the MUF calibrations at most frequencies. Here, some of discrepancies may be attributed to repeatability of the connections, different calibration algorithms, and different definitions of the calibration standards. In our case, we developed physical models for the standards, while the VNA firmware utilized polynomial models.

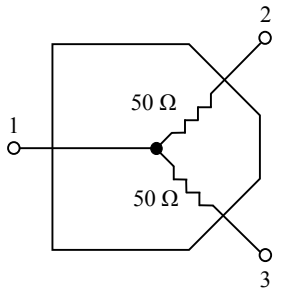


Fig. 3. Simplified schematic of a three-port power splitter.

Jargon, Jeffrey; Williams, Dylan; Sanders, Aric.
"Three-Port Vector-Network-Analyzer Calibrations using the NIST Microwave Uncertainty Framework."
Paper presented at 92nd ARFTG Microwave Measurement Conference, Orlando, FL, United States. January 19, 2019 - January 22, 2019.

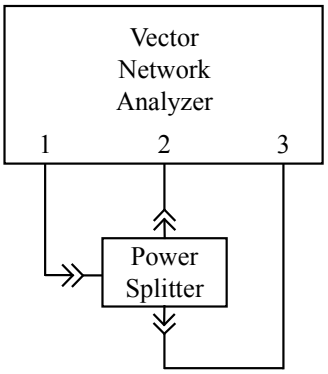


Fig. 4. Simplified schematic of a three-port measurement setup.

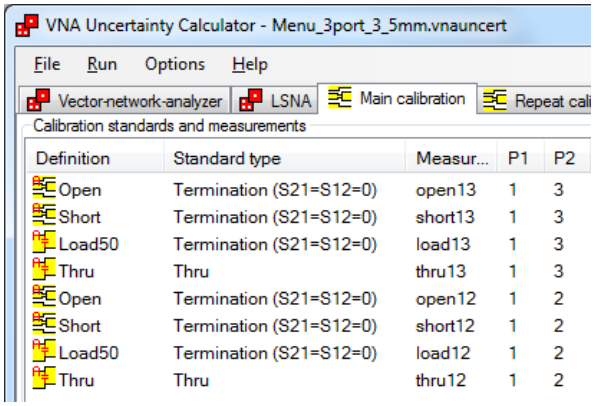


| Definition | Standard type | Measur... | P1 | P2 |
|---|---|---|---|---|
| Open | Termination (S21=S12=0) | open13 | 1 | 3 |
| Short | Termination (S21=S12=0) | short13 | 1 | 3 |
| Load50 | Termination (S21=S12=0) | load13 | 1 | 3 |
| Thru | Thru | thru13 | 1 | 3 |
| Open | Termination (S21=S12=0) | open12 | 1 | 2 |
| Short | Termination (S21=S12=0) | short12 | 1 | 2 |
| Load50 | Termination (S21=S12=0) | load12 | 1 | 2 |
| Thru | Thru | thru12 | 1 | 2 |

Fig. 5. Calibration menu for the three-port SOLT calibration utilized by the NIST Microwave Uncertainty Framework.

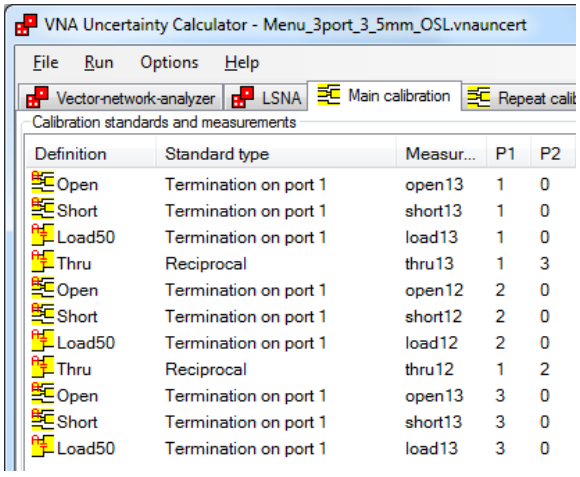


| Definition | Standard type | Measur... | P1 | P2 |
|---|---|---|---|---|
| Open | Termination on port 1 | open13 | 1 | 0 |
| Short | Termination on port 1 | short13 | 1 | 0 |
| Load50 | Termination on port 1 | load13 | 1 | 0 |
| Thru | Reciprocal | thru13 | 1 | 3 |
| Open | Termination on port 1 | open12 | 2 | 0 |
| Short | Termination on port 1 | short12 | 2 | 0 |
| Load50 | Termination on port 1 | load12 | 2 | 0 |
| Thru | Reciprocal | thru12 | 1 | 2 |
| Open | Termination on port 1 | open13 | 3 | 0 |
| Short | Termination on port 1 | short13 | 3 | 0 |
| Load50 | Termination on port 1 | load13 | 3 | 0 |

Fig. 6. Calibration menu for the three-port SOLR calibration utilized by the NIST Microwave Uncertainty Framework.

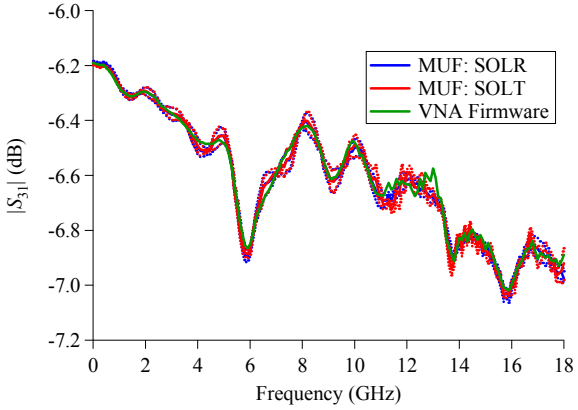


Fig. 7. Comparing magnitudes and 95% confidence intervals (dotted lines) of the power splitter's $S_{31}$ measurements.

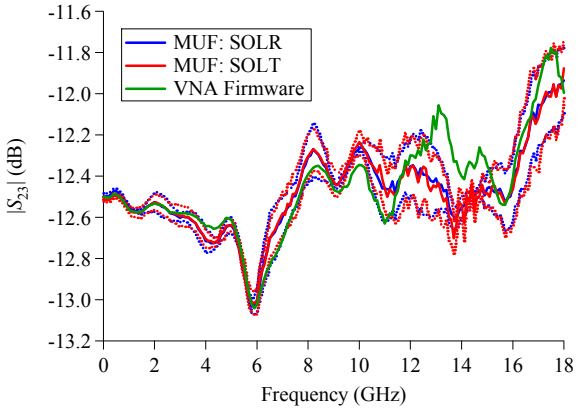


Fig. 8. Comparing magnitudes and 95% confidence intervals (dotted lines) of the power splitter's $S_{23}$ measurements.

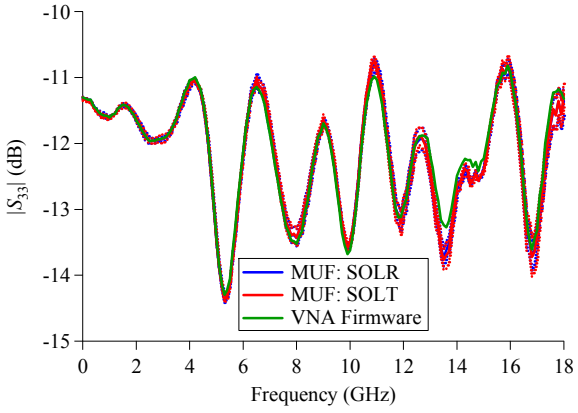


Fig. 9. Comparing magnitudes and 95% confidence intervals (dotted lines) of the power splitter's $S_{33}$ measurements.

Jargon, Jeffrey; Williams, Dylan; Sanders, Aric.
"Three-Port Vector-Network-Analyzer Calibrations using the NIST Microwave Uncertainty Framework."
Paper presented at 92nd ARFTG Microwave Measurement Conference, Orlando, FL, United States. January 19, 2019 - January 22, 2019.

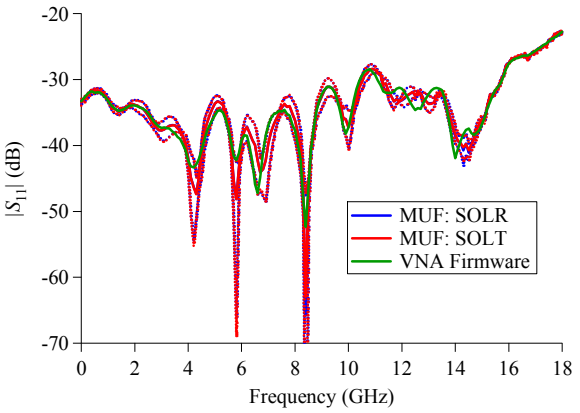


Fig. 10. Comparing magnitudes and 95% confidence intervals (dotted lines) of the power splitter's $S_{11}$ measurements.

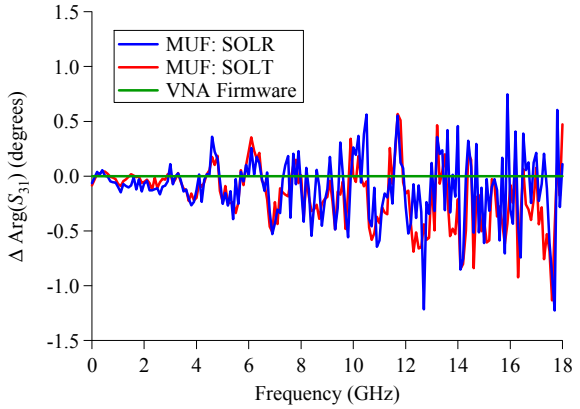


Fig. 11. Comparing differences in phase (MUF – VNA firmware) of the power splitter's $S_{31}$ measurements.

## IV. Conclusions

We have developed the capability for characterizing three-port DUTs and propagating correlated uncertainties using the MUF. Our calibration procedures, which utilize measured wave-parameters, provide results that compare well with those performed by the firmware of a commercial VNA.


## Acknowledgement

The authors thank Paul Hale, Mitch Wallis, and Richard Chamberlin for their helpful comments.


## References


[1] D. F. Williams, NIST Microwave Uncertainty Framework, Beta Version, www.nist.gov/services-resources/software/wafer-calibration-software, 2017.

[2] A. Lewandowski, D. F. Williams, P. D. Hale, C. M. Wang, and A. Dienstfrey, "Covariance-Matrix-Based Vector-Network-Analyzer Uncertainty Analysis for Time- and Frequency-Domain Measurements," IEEE Trans. Microwave Theory Tech., vol. 58, no. 7, pp. 1877-1886, July 2010.

[3] A. Ferrero, V. Teppati, M. Garelli, and A. Neri, "A Novel Calibration Algorithm for a Special Class of Multiport Vector Network Analyzers," *IEEE Trans. Microwave Theory Tech*., vol. 56, no. 3, pp. 693–699, Mar. 2008.

[4] A. Ferrero, M. Garelli, B. Grossman, S. Choon, and V. Teppati, "Uncertainty in Multiport S-parameter Measurements," *77th ARFTG Microwave Measurement Conference*, Baltimore, MD, Jun. 2011.

[5] A. Ferrero and U. Pisani, "Two-Port Network Analyzer Calibration Using an Unknown Thru," *IEEE Microwave and Guided Wave Letters*, vol. 2, no. 12, pp. 505-507, Dec. 1992.

[6] S. Basu and L. Hayden, "An SOLR Calibration for Accurate Measurement of Orthogonal On-Wafer DUTS," *IEEE MTT-S International Microwave Symposium*, Denver, CO, Jun. 1997.

[7] D. K. Rytting, "Network Analyzer Error Models and Calibration Methods," 52nd ARFTG Conference, Short Course on Computer-Aided RF and Microwave Testing and Design, Dec. 1998.

[8] J. A. Jargon, D. F. Williams, and A. Sanders, "The Relationship Between Switch-Term-Corrected Scattering-Parameters and Wave-Parameters Measured with a Two-Port Vector Network Analyzer," *IEEE Microwave and Wireless Components Letters*, vol. 28, no. 10, pp. 951-953, Oct. 2018.

[9] A. Lewandowski, "Multi-Frequency Approach to Vector-Network Analyzer Scattering-Parameter Measurements," Ph.D. Thesis, Warsaw University of Technology, 2010.

[10] J. A. Jargon, C. H. Cho, D. F. Williams, and P. D. Hale, "Physical Models for 2.4 mm and 3.5 mm Coaxial VNA Calibration Kits Developed within the NIST Microwave Uncertainty Framework," *85th ARFTG Microwave Measurement Conference*, Phoenix, AZ, May 2015.



Jargon, Jeffrey; Williams, Dylan; Sanders, Aric.
"Three-Port Vector-Network-Analyzer Calibrations using the NIST Microwave Uncertainty Framework."
Paper presented at 92nd ARFTG Microwave Measurement Conference, Orlando, FL, United States. January 19, 2019 - January 22, 2019.

# Analytical Modeling of White Space Utilization for a Dynamic Spectrum Access System

Charles Hagwood, Anirudha Sahoo, Timothy A. Hall
National Institute of Standards and Technology
Email: {charles.hagwood, anirudha.sahoo, tim.hall}@nist.gov

***Abstract*—Dynamic Spectrum Access (DSA) promises to be a shared spectrum technology that can alleviate the artificial spectrum crunch created by the static allocation of spectrum. There have been many studies on DSA systems in the literature. However, most of them are analyzed using simulation studies rather than analytical modeling. Analytical models are useful in evaluating performance of such systems quickly and easily. In this paper, we present an analytical model of an opportunistic DSA system. Using an alternating renewal process to represent primary user traffic of the DSA system and applying theory from survival analysis and stochastic process, we derive an expression to compute the white space utilization (WSU) of a DSA system for a general distribution of idle durations of primary traffic. Taking the exponential distribution as an example, we validate our analytical model by comparing its results to results obtained from two simulation experiments. One experiment uses idle durations generated from pseudorandom variates and the other uses data collected from a real Long-Term Evolution (LTE) system whose idle duration distribution is approximately exponential. Our analytical WSU results match closely with those from the first experiment and match reasonably well with those obtained from the second experiment.**

## I. Introduction

Most of the spectrum in the sub 6 GHz frequency has been allocated to incumbents. However, the utilization of spectrum in some of these bands is low. Thus, the static allocation of spectrum has led to inefficient use and artificial shortage of spectrum in the sub 6 GHz band. Dynamic Spectrum Access (DSA) promises to be a shared spectrum paradigm that can make the spectrum usage more efficient and alleviate the artificial shortage. In a DSA system, there are two types of users. The incumbent is the Primary User (PU) of the system and has the higher priority. Secondary Users (SUs) have lower priority and access the channel opportunistically when it is not being used by the PUs. However, the SUs have to vacate the channel as soon as a PU starts to use the channel. There are quite a few methods proposed in the literature to provide access to the channel by an SU [1], [2], [3], [4]. One such method was proposed in [5]. In this scheme, given an SU request for transmission for a duration $\tau$ that arrives after an idle period of duration $t$ has elapsed, the DSA system accepts the request if the probability that the idle period will last for another $\tau$ units of time is above a predetermined threshold. It uses the theory of *survival analysis* to make the decision whether to accept or reject an SU request. One of the important performance metrics of a DSA system is the proportion of idle duration that is utilized by the SUs commonly referred to as *White Space Utilization* (WSU). In the study presented in [5] we used simulation experiments to calculate WSU of the DSA system based on Long-Term Evolution (LTE) as the PU system.

### A. Motivation

Many previous works, including ours [5], have reported performance of their respective DSA system through simulation studies. While those studies have been helpful in understanding different DSA systems and their performance, they lack analytical modeling. In the absence of analytical models, if a DSA service provider wants to evaluate the performance of its system in a given PU system without installing it, then it has to resort to simulation. A DSA service provider, for example, may want to estimate the WSU achievable when operating in a PU system. This information may be useful to the service provider for making various business decisions. If an analytical model is available, then a DSA service provider can quickly and easily get the DSA system performance numbers (e.g., WSU). If a provider has to compare performance of its DSA systems across multiple PU system locations, then obviously using an analytical model can save cost.

Hence, in this work we present an analytical model for the opportunistic DSA scheme proposed in [5], which is based on survival analysis. Our analytical model uses an alternating renewal process to model the PU traffic and uses theory and methods from survival analysis and stochastic processes to come up with WSU for the SUs. So, this can be a very useful tool for the DSA service providers to compare the WSU of SUs operating in different PU systems and pick the best PU system in which to deploy the DSA system. For a given PU system, if there are different traffic patterns at different times of the day, then our analytical model can be used to find out what time of the day gives the best performance in terms of WSU and hence the SU traffic can be accordingly controlled.

## II. Related Work

A definition of channel occupancy and methods for measuring it have been studied in [6]. Spectrum occupancy models have been studied in the literature for quite some time. Spectrum occupancy has been modeled using a two state Discrete-Time Markov Chain (DTMC) in [7]. Time-inhomogeneous DTMC models have been used [7] in place of stationary DTMC models to overcome some of the limitation of stationary DTMC. In [8], the authors used a semi-Markov

Hagwood, Robert; Sahoo, Anirudha; Hall, Timothy.
"Analytical Modeling of White Space Utilization for a Dynamic Spectrum Access System."
Paper presented at IEEE Wireless Communications and Networking Conference, Marrakech, Morocco. April 15, 2019 - April 19, 2019.

model to represent spectrum occupancy and model idle and busy periods using a general distribution. Some works in the literature have represented spectrum occupancy as an Alternating Renewal Process [8], [4], since it has only two states. Spectrum idle and busy periods have also been modeled using Continuous-Time Markov Chain (CTMC). The studies reported in [9], [10], [11] used semi-Markov CTMC to account for non-exponential distribution of ON and OFF periods of spectrum. A Two-dimensional Markov chain has been used to model adjacent channel occupancy in [12], [13].

A prediction scheme for SU spectrum access based on the expected remaining idle time of spectrum is proposed in [2]. Zhao et al. have proposed a Partially-Observable Markov Decision Process (POMDP) based model for SU spectrum access in [1]. In [8], the authors use a two-state semi-Markov process to model PU channel occupancy and try to maximize spectrum opportunities by sensing period adaptation and minimize the delay in finding an available channel. The authors in [3] have proposed a spectrum access scheme for SUs which limits the maximum bound on probability of interference to the primary user (PU). A SU spectrum access scheme based on the residual idle time distribution of PU traffic which is modeled as an Alternating Renewal Process is presented in [4]. In [5], [14], authors proposed a DSA scheme based on survival analysis. The scheme uses a non-parametric estimate of cumulative hazard function to predict remaining idle time. An SU is then given access to the spectrum based on this prediction, subject to the constraint that the probability of the SU successfully finishing the transmission is above a preset threshold. Opportunistic channel access schemes based on the Restless Multiarm Bandit model have been proposed in [15], [16]. Pattern mining of spectrum occupancy data has also been used to provide spectrum opportunity to SUs [17], [18].

## III. Analytical Model

### A. PU Traffic Process

We assume that there are two categories of users accessing a single communications channel. A user may be either a primary user (PU) or a secondary user (SU). PUs are the incumbent of the channel and have higher priority. The SUs have lower priority and access the channel opportunistically when it is not being used by the PUs. Consider a period of time, $[0, T]$, over which the channel is observed for PU traffic. The channel starts out in an idle state and alternates between idle and busy periods. We record all the successive lengths of idle and busy periods as $\mathbf{I} = (I_1, I_2, \ldots, I_n)$ and $\mathbf{B} = (B_1, B_2, \ldots, B_n)$, respectively. It is assumed that the random vectors $(I_j, B_j), j = 1, 2, \ldots$ are independent with the same joint distribution, having marginal distribution functions $F(x)$ and $G(x)$, respectively and with means $\mu_{\text{idle}}$ and $\mu_{\text{busy}}$.

This PU traffic model generates an alternating renewal process [19]. Let random variables $Y_j = I_j + B_j$ represent interarrival times between renewals (consecutive idle and busy periods). Let $S_n = Y_1 + Y_2 + \cdots + Y_n$ denote the length of time for $n$ renewals to occur. Note that each renewal ends in a busy period. Let $F_Y(t) = F * G(t)$ be the convolution distribution of $Y_j$. The number of renewals in the time interval $(0, t]$ is given by

$$M_t = \max\{n : S_n \leq t\} \quad t \geq 0 \tag{1}$$

The process $M_t, t \geq 0$ is called an renewal process. The current life of the renewal system at time $t$, $\gamma_t = t - S_{M_t}$, is the elapsed time since the last busy period. Except in the case of a few distributions, e.g., the exponential, no closed form expression for the distribution $C_t(s)$ of $\gamma_t$ exists. In the limit, (see [20]) as $t \to \infty$

$$P[\gamma_t > s] \to \frac{1}{\mu_{\text{idle}} + \mu_{\text{busy}}} \int_s^\infty \bar{F}_Y(y) dy \tag{2}$$

where $\bar{F}_Y(s) = 1 - F_Y(s)$. This asymptotic distribution is often used to approximate $\bar{C}_t(s)$. For the special case of exponential $I_j$ and $B_j$, the current life has distribution function [20]

$$C_t(s) = \begin{cases} 1 - e^{-(\mu_{\text{idle}} + \mu_{\text{busy}})s} & 0 \leq s \leq t \\ 1 & s > t \end{cases}$$

### B. SU Channel Access Scheme

Using the above PU traffic model, an SU channel access scheme was presented in [5] that is based on *survival analysis*. When an SU requests $\tau$ units of time to transmit during an idle period and the channel has been observed idle for $s \geq 0$ units of time, then the decision to allow the SU to transmit is based on the hazard function of $F(s)$. By definition, the hazard function $h(s)$, measures how likely an idle period of unknown length $I$ will end in the next instance, given it has lasted for $s$ units of time and is given by

$$h(s) = \lim_{ds \to 0} \frac{Pr[s \leq I < s + ds \mid I \geq s]}{ds} = \frac{f(s)}{1 - F(s)} \tag{3}$$

where $f(s) = dF(s)/ds$. The SU is allowed to transmit if the probability that the current idle period $I$ will last for additional duration $\tau$ given that it has been idle for duration $s$ (when the SU request arrived) is more than a given threshold $p$. Thus, the SU is allowed to transmit if the following condition is satisfied.

$$Pr[I \geq s + \tau \mid I \geq s] > p \tag{4}$$

This threshold $p, 0 < p < 1$, is the probability of successful transmission by the SU. It is shown in [5] that

$$P[I \geq s + \tau \mid I \geq s] = \exp(-[H(s + \tau) - H(s)]) \tag{5}$$

where $H(s) = \int_0^s h(t)dt, s \geq 0$ is the cumulative hazard function. Using (4) and (5), it can easily be deduced that an SU is allowed to transmit if the change in the cumulative hazard function over the time period $[s, s + \tau]$, $H(s + \tau) - H(s)$, is below a certain value $\theta = (-\ln p)$, i.e., $H(s + \tau) - H(s) < \theta$. Thus, an SU request at time $t$ is evaluated using the following criteria,

$$\text{Request is } \begin{cases} \text{Denied} & \text{if channel is busy} \\ \text{Granted} & \text{if channel is idle and } H(\gamma_t + \tau) - H(\gamma_t) < \theta \\ \text{Denied} & \text{if channel is idle and } H(\gamma_t + \tau) - H(\gamma_t) \geq \theta \end{cases} \tag{6}$$

Hagwood, Robert; Sahoo, Anirudha; Hall, Timothy.
"Analytical Modeling of White Space Utilization for a Dynamic Spectrum Access System."
Paper presented at IEEE Wireless Communications and Networking Conference, Marrakech, Morocco. April 15, 2019 - April 19, 2019.

In practice, the cumulative hazard function $H(\cdot)$ is estimated from an observed sample of idle time lengths $I_j, j = 1, \ldots, n$. The cumulative hazard function is estimated by

$$H_n(s) = \sum_{j:I_{(j)} \le s} \frac{1}{n - j + 1} \tag{7}$$

where $I_{(1)} \le I_{(2)} \le \cdots \le I_{(n)}$ are the ordered $I_j, j = 1, \ldots, n$. Since $H_n(s) \to H(s)$, for large $n$, this estimate of cumulative hazard function $H_n(s)$ is then used in (6) to decide if an SU request should be granted or denied.

From an SU's perspective, the utilization of available idle time, commonly called white space utilization, is an important metric. For the scheme proposed in [5] the proportion of the white space utilized in the time interval $[0, T]$ by a sequence of SU requests that arrive according to a Poisson process, $N(t), t \ge 0$ with intensity $\lambda$ is determined. An SU requests $\tau$ units of channel time to transmit. It is assumed that transmission times requested by SUs vary sufficiently such that $\tau$ can be reasonably assumed to be a random variable with distribution function $K(x)$, i.e.,

$$K(x) = P[\tau \le x] \tag{8}$$

Furthermore, they are assumed to be independent of one another and independent of the alternating renewal process. In this study, we assume that the probability of arrival of SU requests during an ongoing SU transmission is negligible. In the next subsection we derive a closed form approximation for the proportion of the white space utilized by the SUs.

### C. White Space Utilization

Let the random variable $R_T$ denote the total amount of time the channel is idle (i.e., no PUs are transmitting) in the interval $[0, T]$ and the random variable $W_T$ denote the total amount of time in $R_T$ when SUs are transmitting. Then the fraction of white space utilized is given by

$$\rho_{ws} = \frac{W_T}{R_T}. \tag{9}$$

To estimate $R_T$, we use a well-known result from the theory of alternating renewal processes [19],

$$\lim_{T \to \infty} \frac{R_T}{T} = \frac{\mu_{\text{idle}}}{\mu_{\text{idle}} + \mu_{\text{busy}}} = q \tag{10}$$

where $q$, $0 \le q \le 1$, represents the mean proportion of time the system is idle. Thus, the total white space in $[0, T]$ can be approximated by

$$R_T \approx Tq. \tag{11}$$

In addition to $R_T$, an approximation for $W_T$ is needed. The fraction of white space utilized is then approximated by

$$\hat{\rho}_{ws} = E[W_T]/Tq \tag{12}$$

where $E[\cdot]$ denotes the expectation operator. Next, we need a closed form expression for $E[W_T]$ using the SU channel access scheme presented above.

We use the theory of "thinning" or decomposition of the Poisson SU request arrival process, $N(t)$ having rate $\lambda$ [21], [22] . When a SU request arrives, the channel is either idle or busy. It is idle with asymptotic probability $q$, see (10), and busy with asymptotic probability $(1 - q)$. The first thinning occurs here. Requests made when the system is idle form a Poisson process, $N_1(t)$, with rate $\lambda_1 = \lambda q$.

For the second thinning we need the probability that a request is granted for an SU to transmit when the system is idle at time $t$. Since $H_n(t) \to H(t)$, for large $n$, the following approximation is used.

$$\begin{aligned} P_t(\theta) &= P[H(\gamma_t + \tau) - H(\gamma_t) < \theta] \\ &= \int_0^\infty P[H(s + \tau) - H(s) < \theta \mid \gamma_t = s] dP[\gamma_t \le s] \\ &= \int_0^\infty P[H(s + \tau) - H(s) < \theta] dP[\gamma_t \le s] \\ &= \int_0^\infty L_H(s) c_t(s) ds \end{aligned} \tag{13}$$

where $c_t(s)$ denotes the density function of $\gamma_t$ and

$$L_H(s) = P[H(s + \tau) - H(s) < \theta] \tag{14}$$

So, an SU request that arrives during an idle period is granted with probability $P_t(\theta)$ or equivalently rejected with probability $(1 - P_t(\theta))$. Thus thinning of $N_1(t)$ occurs here. The sequence of times the SUs are allowed to transmit when the channel is idle forms a nonhomogeneous Poisson process, $N_2(t)$ with rate $\lambda_2(t) = \lambda_1 P_t(\theta) = \lambda q P_t(\theta)$ and probability of m arrivals in $[0, t]$:

$$P[N_2(t) = m] = \frac{e^{-\int_0^t \lambda_2(s) ds} (\int_0^t \lambda_2(s) ds)^m}{m!} \quad m = 0, 1, \ldots \tag{15}$$

$m = 0$ means no request is made and the requested transmission time is defined to be zero when this happens.

Let us say there are exactly $m$ transmission requests granted to the SUs in duration $[0, T], m = 0, 1, 2, \ldots$, i.e., $N_2(T) = m$, occurring at $0 < t_1 < t_2 < \ldots < t_m \le T$ for $m \ge 1$ (see Figure 1). Then the amount of white space utilized is $(\tau_1 + \cdots + \tau_m)$ if $(t_m + \tau_m) \le T$ and is $(\tau_1 + \cdots + \tau_{m-1} + (T - t_m))$ if $(t_{m-1} + \tau_{m-1}) < t_m < T < (t_m + \tau_m)$, where $\tau_k, k = 1, \ldots, m$ are requested transmission durations.

The average amount of white space utilized is

$$\begin{aligned} E[W_T] &= \sum_{m=0}^{\infty} E[W_T \mid N_2(T) = m] P[N_2(T) = m] \\ &= \sum_{m=1}^{\infty} E[(\sum_{i=1}^{m-1} \tau_i) + J_m \mid N_2(T) = m] P[N_2(T) = m] \\ &= \sum_{m=1}^{\infty} \Big[ (m-1) E[\tau] P[N_2(T) = m] + \\ &\qquad E[J_m \mid N_2(T) = m] P[N_2(T) = m] \Big] \end{aligned} \tag{16}$$

where

$$J_m = \begin{cases} \tau_m & \text{if } t_m + \tau_m < T \\ T - t_m & \text{otherwise} \end{cases} \tag{17}$$

Hagwood, Robert; Sahoo, Anirudha; Hall, Timothy.
"Analytical Modeling of White Space Utilization for a Dynamic Spectrum Access System."
Paper presented at IEEE Wireless Communications and Networking Conference, Marrakech, Morocco. April 15, 2019 - April 19, 2019.

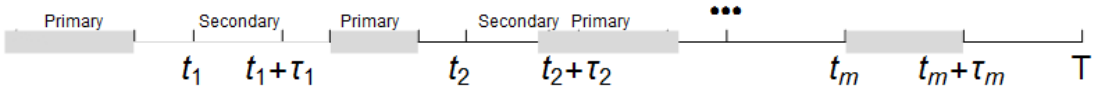


Fig. 1. Schematic of exactly $m$ successful transmissions by SUs. The shaded regions represent PU transmissions. $t_i, i = 1, \ldots, m$ denote all the request times distributed according to the nonhomogeneous Poisson process $N_2(t)$

Now

$$\begin{aligned} &E[J_m \mid N_2(T) = m] \\ &= E[J_m I[t_m + \tau_m < T] \mid N_2(T) = m] + \\ &\quad E[J_m I[t_m + \tau_m \geq T] \mid N_2(T) = m] \\ &= E[\tau_m I[t_m + \tau_m < T] \mid N_2(T) = m] + \\ &\quad E[(T - t_m) I[t_m + \tau_m \geq T] \mid N_2(T) = m] \end{aligned} \tag{18}$$

To complete this computation, we need the following result about nonhomogeneous Poisson processes [19].

*Theorem: If $\{N_2(t), t \geq 0\}$ is a nonhomogeneous Poisson process with intensity function $\lambda_2(t)$, then given $N_2(T) = m, T \geq 0$, its $m$ arrival times, $t_1, t_2, \ldots, t_m$ have the same distribution as the order statistics from a sample of $m$ independent and identically distributed random variables having distribution function, $F_2(x)$ given by*

$$F_2(x) = \begin{cases} \frac{\Lambda_2(x)}{\Lambda_2(T)} & x \leq T \\ 1 & x > T \end{cases} \tag{19}$$

*where $\Lambda_2(x) = \int_0^x \lambda_2(s)ds, 0 \leq x \leq T$. Thus, given $N_2(T) = m$, $t_m$ is distributed as $\max\{t_1^*, t_2^*, \ldots, t_m^*\}$ where the $t_i^*$ are the order statistics from a sample with distribution function $F_2(x)$ and furthermore*

$$P[t_m \leq x] = P[\max\{t_1^*, t_2^*, \ldots, t_m^*\} \leq x] = P[t_m^* \leq x] = F_2^m(x), \quad 0 \leq x \leq T \tag{20}$$

This is analogous to a well known result for homogeneous Poisson processes which says given, $N(t) = m$, the $m$ occurrence times are distributed as the order statistics from a uniform $(0, t]$ distribution [19].

Using the Theorem, the two terms in (18) can be evaluated by conditioning on $\tau_m$ as follows.

$$\begin{aligned} &E[\tau_m I[t_m + \tau_m < T] \mid N_2(T) = m] = \\ &\qquad E[\tau_m I[t_m^* < (T - \tau_m)]] = \\ &\qquad \int_0^\infty \tau F_2^m(T - \tau) dK(\tau) \end{aligned} \tag{21}$$

and,

$$\begin{aligned} &E[(T - t_m) I[t_m + \tau_m \geq T \mid N_2(T) = m] = \\ &\qquad E[(T - t_m^*) I[t_m^* + \tau_m \geq T]] = \\ &\qquad \int_{\tau=0}^\infty E[(T - t_m^*) I[t_m^* + \tau \geq T]] dK(\tau) = \\ &\int_{\tau=0}^\infty \int_{t=0}^\infty (T - t) I[t \geq (T - \tau)] dF_2^m(t) dK(\tau) = \\ &\qquad \int_{\tau=0}^\infty \int_{t=(T-\tau)}^T (T - t) dF_2^m(t) dK(\tau) \end{aligned} \tag{22}$$

where $F_2(t)$ is given by (19).

Using (21) and (22) in (16) we have

$$\begin{aligned} E[W_T] &= E[\tau] \sum_{m=1}^\infty (m-1) P[N_2(T) = m] + \\ &\quad \sum_{m=1}^\infty \int_0^\infty \tau F_2^m(T - \tau) dK(\tau) P[N_2(T) = m] + \\ &\quad \sum_{m=1}^\infty \int_0^\infty \Big[ \int_{T-\tau}^T (T - t) dF_2^m(t) \Big] dK(\tau) P[N_2(T) = m] \\ &= E_1 + E_2 + E_3 \end{aligned} \tag{23}$$

where $E_1$, $E_2$ and $E_3$ are the three terms in (23) respectively.

We know that for the nonhomogeneous Poisson process $N_2(T)$,

$$P[N_2(T) = m] = e^{-\Lambda_2(T)} \frac{(\Lambda_2(T))^m}{m!} \quad m = 0, 1, \ldots \tag{24}$$

So,

$$\begin{aligned} E_1 &= E[\tau] \Big[ \sum_{m=1}^\infty (m-1) e^{-\Lambda_2(T)} \frac{(\Lambda_2(T))^m}{m!} \Big] \\ &= E[\tau] e^{-\Lambda_2(T)} \Big[ \sum_{m=1}^\infty (m-1) \frac{(\Lambda_2(T))^m}{m!} \Big] \\ &= E[\tau] e^{-\Lambda_2(T)} \Big[ \sum_{m=1}^\infty m \frac{(\Lambda_2(T))^m}{m!} - \sum_{m=1}^\infty \frac{(\Lambda_2(T))^m}{m!} \Big] \\ &= E[\tau] (\Lambda_2(T) - 1 + e^{-\Lambda_2(T)}) \end{aligned} \tag{25}$$

Note that we have used the power series definition of exponential function in the derivation of (25). Using (15) and (19)

Hagwood, Robert; Sahoo, Anirudha; Hall, Timothy.
"Analytical Modeling of White Space Utilization for a Dynamic Spectrum Access System."
Paper presented at IEEE Wireless Communications and Networking Conference, Marrakech, Morocco. April 15, 2019 - April 19, 2019.

in the expression for $E_2$, we have

$$\begin{aligned}E_2 &= \int_0^\infty \tau\Big[\sum_{m=1}^{\infty} F_2^m(T-\tau)e^{-\Lambda_2(T)}\frac{(\Lambda_2(T))^m}{m!}\Big]dK(\tau)\\ &= e^{-\Lambda_2(T)}\int_0^\infty \tau(e^{F_2(T-\tau)\Lambda_2(T)}-1)dK(\tau)\\ &= e^{-\Lambda_2(T)}\int_0^\infty \tau(e^{\Lambda_2(T-\tau)}-1)dK(\tau) \qquad (26)\end{aligned}$$

To compute $E_3$, note that $dF_2^m(t)/dt = mf_2(t)F_2^{m-1}(t)$ and $f_2(t)\Lambda_2(T) = \lambda_2(t)$.

$$\begin{aligned}E_3 &= \int_0^\infty \Big[\int_{T-\tau}^{T}(T-t)\sum_{m=1}^{\infty} mf_2(t)F_2^{m-1}(t)\\ &\qquad e^{-\Lambda_2(T)}\frac{(\Lambda_2(T))^m}{m!}dt\Big]dK(\tau)\\ &= e^{-\Lambda_2(T)}\int_0^\infty \Big[\int_{T-\tau}^{T}(T-t)f_2(t)\Big(\sum_{m=1}^{\infty} mF_2(t)^{m-1}\\ &\qquad \frac{(\Lambda_2(T))^m}{m!}\Big)dt\Big]dK(\tau)\\ &= e^{-\Lambda_2(T)}\int_0^\infty \Big[\int_{T-\tau}^{T}(T-t)f_2(t)\Lambda_2(T)e^{F_2(t)\Lambda_2(T)}\\ &\qquad dt\Big]dK(\tau)\\ &= e^{-\Lambda_2(T)}\int_0^\infty \Big[\int_{T-\tau}^{T}(T-t)\lambda_2(t)e^{\Lambda_2(t)}dt\Big]dK(\tau)\\ &= e^{-\Lambda_2(T)}\Big[\int_0^\infty\Big(\int_{T-\tau}^{T}T\lambda_2(t)e^{\Lambda_2(t)}dt\Big)dK(\tau)-\\ &\qquad \int_0^\infty\Big(\int_{T-\tau}^{T}t\lambda_2(t)e^{\Lambda_2(t)}dt\Big)dK(\tau)\Big] \qquad (27)\end{aligned}$$

By a change of variables in the first integral and an integration by parts in the second, we get

$$\begin{aligned}E_3 &= e^{-\Lambda_2(T)}\Big[\int_0^\infty\Big(T(e^{\Lambda_2(T)}-e^{\Lambda_2(T-\tau)})-\\ &\Big(Te^{\Lambda_2(T)}-(T-\tau)e^{\Lambda_2(T-\tau)}+\int_{T-\tau}^{T}e^{\Lambda_2(t)}dt\Big)\Big)dK(\tau)\Big]\\ &= e^{-\Lambda_2(T)}\Big[\int_0^\infty\Big(-\tau e^{\Lambda_2(T-\tau)}-\int_{T-\tau}^{T}e^{\Lambda_2(t)}dt\Big)dK(\tau)\Big]\\ &= \int_0^\infty\Big[-\tau e^{\Lambda_2(T-\tau)-\Lambda_2(T)}-\\ &\qquad \int_{T-\tau}^{T}e^{\Lambda_2(t)-\Lambda_2(T)}dt\Big]dK(\tau) \qquad (28)\end{aligned}$$

Thus, from (23)

$$\begin{aligned}E[W_T] &= E[\tau](\Lambda_2(T)-1+e^{\Lambda_2(T)})+\\ &\quad e^{-\Lambda_2(T)}\int_0^\infty\tau(e^{\Lambda_2(T-\tau)}-1)dK(\tau)\\ &\quad +\int_0^\infty\Big[-\tau e^{\Lambda_2(T-\tau)-\Lambda_2(T)}-\\ &\qquad \int_{T-\tau}^{T}e^{\Lambda_2(t)-\Lambda_2(T)}dt\Big]dK(\tau) \qquad (29)\end{aligned}$$

In this study, we take the simple case of SUs sending requests to transmit for a constant duration, i.e., $\tau$ is a constant. Then the expression for $E[W_T]$ reduces to

$$\begin{aligned}E[W_T] &= \tau(\Lambda_2(T)-1+e^{-\Lambda_2(T)})+\tau e^{-\Lambda_2(T)}(e^{\Lambda_2(T-\tau)}-1)\\ &\quad -\tau e^{\Lambda_2(T-\tau)-\Lambda_2(T)}-\int_{T-\tau}^{T}e^{\Lambda_2(t)-\Lambda_2(T)}dt\\ &= \tau(\Lambda_2(T)-1)-\int_{T-\tau}^{T}e^{\Lambda_2(t)-\Lambda_2(T)}dt \qquad (30)\end{aligned}$$

### *D. Exponential Idle Times Distribution*

In this section we take the exponential distribution as an example distribution for idle times (of PU traffic) to illustrate our analytical model. We then compare simulation based results with the results from our analytical model to validate the correctness of our model.

In this case we assume $I_j \sim Exp(\alpha)$ and $B_j \sim Exp(\beta)$ where $\mu_{idle} = 1/\alpha$ and $\mu_{busy} = 1/\beta$ and the SU requests arrive as per a Poisson process with parameter, $\lambda$. Then,

$$q = \frac{1/\alpha}{1/\alpha + 1/\beta} \qquad (31)$$

and $R_T \approx Tq$ (see (11)). In the exponential case, the hazard function of the idle time distribution $F(x)$ is a constant, viz, $h(t) = \alpha$ and thus $H(t+\tau) - H(t) = \tau\alpha$. The criteria for granting a SU request becomes

$$\text{Request is } \begin{cases}\text{Denied} & \text{if channel is busy}\\ \text{Granted} & \text{if channel is idle and } \tau\alpha < \theta\\ \text{Denied} & \text{if channel is idle and } \tau\alpha \geq \theta\end{cases} \qquad (32)$$

$\alpha$ can be estimated as $1/\bar{I}_n$, where $\bar{I}_n = (I_1+I_2+\cdots+I_n)/n$ is the sample means estimate of $\mu_{idle}$ and $n$ denotes the sample size of observed values. Hence, the SU request grant criteria becomes

$$\text{Request is } \begin{cases}\text{Denied} & \text{if channel is busy}\\ \text{Granted} & \text{if channel is idle and } \frac{\tau}{\theta} < \bar{I}_n\\ \text{Denied} & \text{if channel is idle and } \frac{\tau}{\theta} \geq \bar{I}_n\end{cases} \qquad (33)$$

In this case

$$P_t(\theta) = p(\theta) = P[I_1 + \cdots + I_n > n\frac{\tau}{\theta}] \qquad (34)$$

When the $I_j$'s are exponential, $I_1 + \cdots + I_n$ has a gamma distribution [19, pp. 35] and

$$p(\theta) = \sum_{j=0}^{n-1} e^{-\alpha n\tau/\theta}(\alpha n\tau/\theta)^j/j! \qquad (35)$$

In this case, $N_2(t)$ is a homogeneous Poisson process, with parameter $\lambda_2 = q\lambda p(\theta)$ and $\Lambda_2(t) = \lambda_2 t$. Using these values in (30) we have

$$E[W_T] = \tau\lambda_2 T - \tau - \frac{1}{\lambda_2}(1-e^{-\lambda_2\tau}) \qquad (36)$$

Hagwood, Robert; Sahoo, Anirudha; Hall, Timothy.
"Analytical Modeling of White Space Utilization for a Dynamic Spectrum Access System."
Paper presented at IEEE Wireless Communications and Networking Conference, Marrakech, Morocco. April 15, 2019 - April 19, 2019.

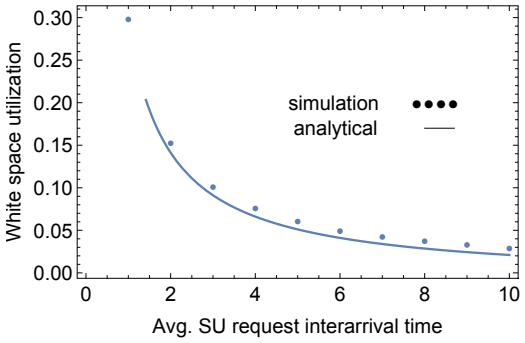


Fig. 2. Comparison of WSU computed using analytical model and simulation

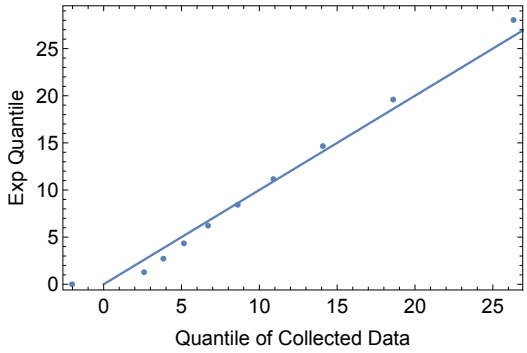


Fig. 3. Q-Q plot of the collected channel 15 data

Hence, using (12) an approximation of white space utilization is obtained as

$$\hat{\rho}_{ws} = \frac{\tau\lambda_2 T - \tau - \frac{1}{\lambda_2}(1 - e^{-\lambda_2\tau})}{Tq} = \frac{\tau}{q}\lambda_2 - \frac{1}{Tq}(\tau + \frac{1}{\lambda_2}(1 - e^{-\lambda_2\tau})) \quad (37)$$

## IV. Experiments and Results

To validate our analytical formulation we ran two types of experiments as follows. In the first set of experiments we simulate an alternating renewal process which represents PU traffic. The idle and busy durations of the PU traffic were generated using pseudorandom exponential variates whose means were 10 and 5 units respectively, i.e., $\mu_{idle} = 10$ and $\mu_{busy} = 5$. Then a sequence of SU request arrival times are generated with pseudorandom exponential interarrival times. The requested transmission duration ($\tau$) was set to 0.3 units and the probability of successful transmission ($p$) was set to 0.9. The simulation was run for a duration $T = 10\,000$ units. An SU request is granted or denied based on the criteria outlined in (32). If a request is granted, then $\tau$ units are added to the white space utilized. Figure 2 plots approximation of WSU as per our analytical model ($\rho_{ws}$) and the simulated WSU as a function of the mean interarrival times of SU requests. The results for the analytical model match very closely with those from the simulation.

In the second set of experiments, we used the I/Q samples collected at a location in the metro Philadelphia area on the CityScape spectrum monitoring system [23] on September 9th, 2017 at around 17:55 hours for a duration of 30 minutes. After carrying out additional processing of the collected I/Q samples and applying the noise threshold to which the CityScape Software Defined Radios (SDRs) were calibrated, the dataset was converted into binary occupancy sequences. We chose channels 15 and 16 for our simulation. Some important statistics of collected data for those two channels are listed in Table I. The first step to run our simulation was to estimate the cumulative hazard of the given channel using (7) over the collected idle time duration data of the channel. We then simulated arrival of SU requests to transmit for 1 ms ($\tau = 1$ ms) as per a Poisson process. The request is granted or denied as per (6) using $p = 0.9$. Each successful SU transmission is counted towards total white space usage of the SU. Then the WSU of the channel is computed as the ratio of total white space usage of the SU to total idle duration of the channel. The histograms of idle duration of channels 15 and 16 are shown in Figure 4 and Figure 5 respectively. The two histograms look approximately exponentially distributed, so we used a *quantile-quantile* (Q-Q) plot using the data from channel 15 to verify this visual observation. For the Q-Q plot of channel 15 shown in Figure 3, a kernel density estimate was used to smooth the idle duration data. Then, the $k^{th}, k = 1, 2, \ldots, 10$, deciles (10-quantiles) of the kernel density were calculated and plotted against the same deciles for the exponential distribution with parameter $\lambda_{data}$. The mean of the kernel density is $1/\lambda_{data}$. If the idle time data are generated from this exponential distribution, then these pairs of quantiles should follow the $45^\circ$ line. The plot in Fig 3 indicates that the distribution of the data is close to an exponential. Using the mean idle time of the channels as the parameter for exponential distribution, we then use (37) to calculate analytical WSU. Figure 6 and Figure 7 compare the WSU obtained by simulation and by the analytical method for channels 15 and 16 respectively. For both the channels the difference between the analytical and simulation results is insignificant for an SU request inter-arrival time of 5 ms or more. During simulation, some SU requests fall into the current SU transmission interval, in which case that request is ignored and one or more exponential inter-arrival times are generated until an SU request arrives after the current SU transmission ends. As the request inter-arrival time become smaller, more SU requests fall within an SU transmission duration. Since this phenomenon is not accounted for in the analytical model, the model allows SU requests that arrive during an ongoing SU transmission to be admitted. Thus, the WSU of the analytical model is higher than the WSU of simulation when the SU request inter-arrival time is small. Since idle lengths of the collected data only approximate an exponential distribution, this also contributes to the discrepancy between analytical and simulation WSU.

Hagwood, Robert; Sahoo, Anirudha; Hall, Timothy.
"Analytical Modeling of White Space Utilization for a Dynamic Spectrum Access System."
Paper presented at IEEE Wireless Communications and Networking Conference, Marrakech, Morocco. April 15, 2019 - April 19, 2019.

| channel number | mean idle duration ($\mu_{idle}$) (ms) | mean busy duration ($\mu_{busy}$) (ms) | total idle duration (ms) | observed duration (T) (ms) |
|---|---|---|---|---|
| 15 | 11.175 | 1.1527 | 1 631 690 | 180 000 |
| 16 | 11.341 | 1.1454 | 1 634 880 | 180 000 |

TABLE I
STATISTICS OF COLLECTED DATA

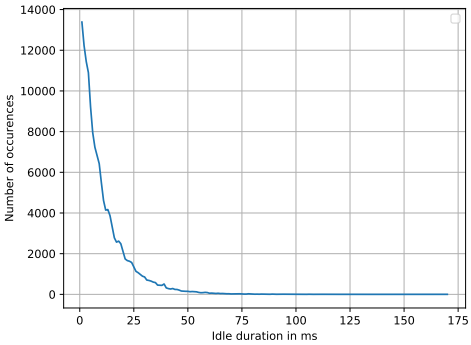


Fig. 4. Idle Duration Histogram of Channel 15 of Collected Data

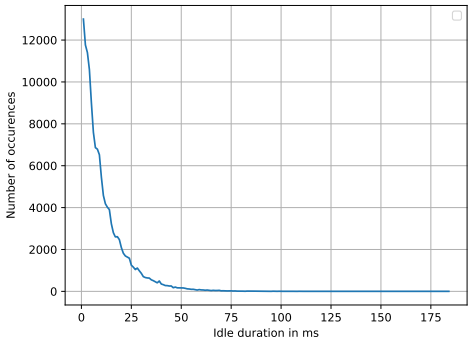


Fig. 5. Idle Duration Histogram of Channel 16 of Collected Data

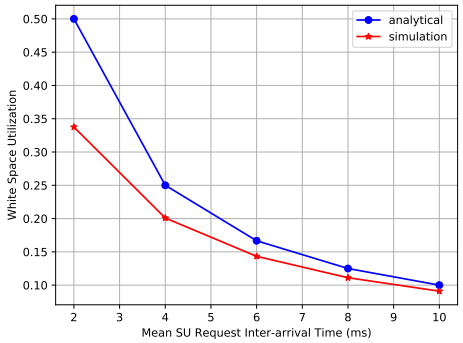


Fig. 6. WSU vs Mean SU Request Inter-arrival time for Channel 15 ($\tau = 1$ ms)

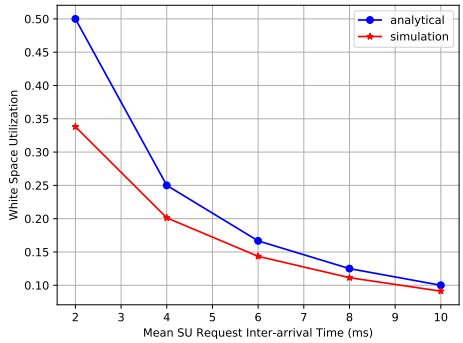


Fig. 7. WSU vs Mean SU Request Inter-arrival time for Channel 16 ($\tau = 1$ ms)

## V. DISCUSSION

We presented an analytical model for the opportunistic DSA scheme proposed in [5] that is based on survival analysis. The PU traffic was modeled as an alternating renewal process. Applying theory and methods from survival analysis and stochastic process, we derived an expression to compute the WSU of the DSA system for any general distribution of idle duration of PU traffic. We used an exponential distribution of idle duration as an example to validate our model. The WSU computed using our analytical model was compared against the WSU obtained from two simulation experiments. In one simulation experiment the idle durations were generated from pseudorandom variates whereas in the other the idle durations were taken from data collected from a real LTE system whose idle durations are approximately exponentially distributed. Our analytical results closely match the results from the first experiment and match reasonably well with those obtained from the second experiment.

In this work, we have modeled PU Idle and Busy periods as stationary distributions. In practice, it may not be the case. One way to address this issue is to assume that PU traffic distributions do not change appreciably during a certain period of a day and therefore have different PU traffic distibutions at different time of the day. Based on the time of the day corresponding PU traffic distributions can be used in our analytical model to compute WSU.

In our analytical formulation we assumed that the probability of arrival of SU requests during an ongoing SU transmission

Hagwood, Robert; Sahoo, Anirudha; Hall, Timothy.
"Analytical Modeling of White Space Utilization for a Dynamic Spectrum Access System."
Paper presented at IEEE Wireless Communications and Networking Conference, Marrakech, Morocco. April 15, 2019 - April 19, 2019.

is negligible. While this assumption is valid for high SU request inter-arrival times, it does not hold for low inter-arrival times. Hence, we would like to update our model to remove this assumption so that it rejects SU requests arriving during an ongoing SU transmission. We plan to derive analytical expression to compute the WSU for a few other distributions of idle durations. The Generalized Pareto Distribution (GPD) has been used to model the idle and busy durations of a channel [24], [25]. We will take up GPD as the next example distrubtion. Apart from WSU, the Probability of Interference (PoI) is also an important performance metric for DSA systems. Hence we plan to develop an analytical model of PoI for the DSA system. Also, we will validate the model using SU distributions other than the exponential, potentially including mixture distributions.

## ACKNOWLEDGMENT

The authors would like to thank Prof. Sumit Roy and Mr. Kyeong Su Shin of the University of Washington for collecting and processing data for us from the Cityscape observatory in Philadelphia.

## REFERENCES

[1] Q. Zhao, L. Tong, A. Swami and Y. Chen, "Decentralized Cognitive MAC for Opportunistic Spectrum Access in Ad Hoc Networks: A POMDP Framework," *IEEE Journal on Selected Areas in Communications*, vol. 30, no. 2, pp. 589–600, April 2007.

[2] K. W. Sung, S. Kim and J. Zander, "Temporal Spectrum Sharing Based on Primary User Activity Prediction," *IEEE Transactions on Wireless Communications*, vol. 9, no. 12, pp. 3848–3855, December 2010.

[3] A. Plummer, M. Taghizadeh and S. Biswas, "Measurement based bandwidth scavenging in wireless networks," *IEEE Transactions on Mobile Computing*, vol. 11, no. 1, pp. 19–32, January 2012.

[4] M. Sharma and A. Sahoo, "Stochastic Model Based Opportunistic Channel Access in Dynamic Spectrum Access networks," *IEEE Transactions on Mobile Computing*, vol. 13, no. 7, pp. 1625–1639, July 2014.

[5] T. A. Hall, A. Sahoo, C. Hagwood, and S. Streett, "Dynamic spectrum access algorithms based on survival analysis," *IEEE transactions on cognitive communications and networking*, vol. 3, no. 4, pp. 740–751, 2017.

[6] A. Spaulding and G. Hagn, "On the definition and estimation of spectrum occupancy," *IEEE Transactions on Electromagnetic Compatibility*, vol. EMC-19, no. 3, pp. 269–280, August 1977.

[7] M. Lopez-Benitez and F. Casadevall, "Discrete-time spectrum occupancy model based on Markov chain and duty cycle models," in *2011 IEEE International Symposium on Dynamic Spectrum Access Networks (DySPAN)*, May 2011, pp. 90–99.

[8] H. Kim, and K. Shin, "Efficient Discovery of Spectrum Opportunities with MAC-layer Sensing in Cognitive Radio Networks," *IEEE Transactions on Mobile Computing*, vol. 7, no. 5, pp. 533–545, May 2008.

[9] S. Geirhofer, L. Tong, and B. M. Sadler, "Dynamic spectrum access in WLAN channels: Empirical model and its stochastic analysis," in *TAPAS '06 Proceedings of the First International Workshop on Technology and Policy for Accessing Spectrum*, August 2006.

[10] ——, "Dynamic spectrum access in the time domain: Modeling and exploiting white space," *IEEE Communications Magazine*, vol. 45, no. 5, pp. 66–72, May 2007.

[11] L. Stabellini, "Quantifying and modeling spectrum opportunities in a real wireless environment," in *2010 IEEE Wireless Communication and Networking Conference*, April 2010, pp. 1–6.

[12] A. Gibson and L. Arnett, "Statistical modelling of spectrum occupancy," *Electronics Letters*, vol. 29, no. 25, pp. 2175–2176, 1993.

[13] ——, "Measurements and statistical modelling of spectrum occupancy," in *HF Radio Systems and Techniques, 1994., Sixth International Conference on*, July 1994, pp. 150–154.

[14] T. A. Hall, A. Sahoo, C. Hagwood, and S. Streett, "Exploiting LTE white space using dynamic spectrum access algorithms based on survival analysis," in *2017 IEEE International Conference on Communications (ICC)*, May 2017, pp. 1–7.

[15] C. Tekin and M. Liu, "Online learning of rested and restless bandits," *IEEE Transactions on Information Theory*, vol. 58, no. 8, pp. 5588–5611, August 2012.

[16] Y. Gai and B. Krishnamachari, "Decentralized online learning algorithms for opportunistic spectrum access," in *2011 IEEE Global Telecommunications Conference - GLOBECOM 2011*, December 2011, pp. 1–6.

[17] S. Yin, D. Chen, Q.Zhang, M. Liu and S. Li, "Mining Spectrum Usage Data: A Large-Scale Spectrum Measurement Study," *IEEE Transactions on Mobile Computing*, vol. 11, no. 6, pp. 1033–1046, June 2012.

[18] P. Huang, C-J. Liu, X. Yang, L. Xiao and J. Chen, "Wireless Spectrum Occupancy Prediction Based on Partial Periodic Pattern Matching," *IEEE Transactions on Parallel and Distributed Systems*, vol. 25, no. 7, pp. 1925–1934, July 2014.

[19] S. M. Ross, "Stochastic processes. john wiley& sons," *New York*, 1983.

[20] S. Karlin, *A first course in stochastic processes*. Academic press, 2014.

[21] S. I. Resnick, *Adventures in stochastic processes*. Springer Science & Business Media, 2013.

[22] E. Cinlar, *Introduction to stochastic processes*. Courier Corporation, 2013.

[23] S. Roy, K. Shin, A. Ashok, M. McHenry, G. Vigil, S. Kannam, and D. Aragon, "Cityscape: A metro-area spectrum observatory," in *2017 26th International Conference on Computer Communication and Networks (ICCCN)*, July 2017, pp. 1–9.

[24] V. Raj, I. Dias, T. Tholeti, and S. Kalyani, "Spectrum access in cognitive radio using a two-stage reinforcement learning approach," *IEEE Journal of Selected Topics in Signal Processing*, vol. 12, no. 1, pp. 20–34, 2018.

[25] M. López-Benítez and F. Casadevall, "Time-dimension models of spectrum usage for the analysis, design, and simulation of cognitive radio networks," *IEEE transactions on vehicular technology*, vol. 62, no. 5, pp. 2091–2104, 2013.

Hagwood, Robert; Sahoo, Anirudha; Hall, Timothy.
"Analytical Modeling of White Space Utilization for a Dynamic Spectrum Access System."
Paper presented at IEEE Wireless Communications and Networking Conference, Marrakech, Morocco. April 15, 2019 - April 19, 2019.

# Interlaboratory Millimeter-Wave Channel Sounder Verification

J. Quimby[1], D. G. Michelson[2], M. Bennai[3], K. A. Remley[1], J. Kast[1], A. Weiss[1]
[1] National Institute of Standards and Technology (NIST), Boulder, USA, jeanne.quimby@nist.gov*
[2] University of British Columbia, Vancouver, Canada, davem@ece.ubc.ca
[3] Communications Research Centre (CRC), Ottawa, Canada, mustapha.bennai@canada.ca

***Abstract*—The channel sounder verification program within the National Institute of Standards and Technology-coordinated 5G mmWave Channel Model Alliance aims to place channel sounders on a sound metrological foundation by using well-established laboratory verification methods coupled with modern waveform metrology tools. To provide comparison-to-reference verification of channel sounder hardware measurements, we begin by measuring deterministic conducted channels, established using a channel sounder verification artifact and temperature control unit. This artifact produces multiple stable and repeatable environments to compare the channel sounders' hardware performance to a reference measurement provided by a vector network analyzer. The reference vector network analyzer measurements have an uncertainty analysis including systematic and random components to verify the channel sounder performance. Due to its portable nature, this artifact has potential use in a robin-robin testing between laboratories. General insights and common problems are provided using measurements of the verification box from a one channel sounder in the Alliance.**

***Index Terms*—5G technology, channel sounder, conducted measurements, measurement verification, millimeter-wave wireless communications, propagation channel, wireless system.**

## I. Introduction

The quest for increased capacity and throughput by the wireless communications industry has pushed spectrum usage into millimeter-wave (mmWave) frequencies. In-depth understanding of mmWave channel characteristics is imperative for the design and standardization of mmWave communication systems. MmWave applications such as Internet of Things (IoT) in manufacturing and cellular [1-3] facilities can generate numerous communication channels with scattering and multipath components (MPCs). Designing communications systems to handle potential distortion may involve techniques such as error correction, equalization, and/or new modulation [4] schemes. Understanding the characteristics of mmWave channel is often provided through measurements via a channel sounder.

Successful characterization of a channel depends upon the trustworthiness of the channel sounder's measurements. Obtaining trustworthy measurements requires verification of the channel sounder's hardware and data post-processing performance, combined with accurate measurement best-practices. At mmWave frequencies, verification is vitally important because channel sounder hardware becomes less ideal and non-linear, so calibration and quantification of the hardware-measurement-induced error often becomes critical. As an example, sampling circuits in a channel sounder may introduce distortion when operating at the state-of-the-art sampling speeds. Signal distortion in the measurement may come from every step from signal generation and transmission to signal reception and demodulation. Verification of the channel sounder's hardware and post-processing requires separating measurement errors from the channel variations. Quantification of the signal distortion may be determined using a comparison-to-reference channel sounder verification methodology [5].

The participants of the 5G mmWave Channel Model Alliance [6], formed in July 2015, have different channel sounder architectures, each with unique hardware and data post-processing. While there are multiple verification approaches to determine the performance of the hardware, they provide different levels of channel sounder verification, based upon the needs of the researchers [6].

One straight-forward type of channel sounder verification is known as "in-situ" verification. It leverages propagation environments with "known" or predictable propagation conditions during measurement campaigns [7,8] for easy comparison to simulated models such as a two-ray bounce or free-space propagation. Another type of channel sounder verification uses controlled environments such as anechoic chambers, reverberation chambers, or conducted measurements [9] with comparison to simulated models. The comparison-to-reference method presented here does not rely on a simulation of the RF environment. Rather, it extends the controlled measurement approach by using a temperature-controlled channel sounder verification box [10] (as seen in Fig. 1) with known propagation channel characteristics measured by a reference measurement system.

The value of this approach lies in a direct measurement-to-measurement comparison of a stable and controlled channel. There are no assumptions required about the environment modeling ambiguities such as erroneous dielectric descriptions, misalignment of the antenna position and rotation, and/or improper handling of the boundary conditions in a full-wave simulation. However, this approach does require a channel sounder with a removable antenna to connect to the channel sounder verification box.

The NIST verification box provides multiple repeatable and stable conducted channels with known time delays and

Quimby, Jeanne; Michelson, David; Bennai, Mustapha; Remley, Catherine; Kast, Joshua; Weiss, Alec.
"Interlaboratory Millimeter-Wave Channel Sounder Verification."
Paper presented at 13th European Conference on Antennas and Propagation (EuCAP), Krakow, Poland. March 31, 2019 - April 5, 2019.


Fig. 1: The temperature-controlled NIST channel sounder verification box. The box dimensions are approximately 210 x 240 x 300 $cm^3$.

MPC magnitudes with a frequency range from 10 GHz to 62.5 GHz. Using these conducted channels, we can construct Power Delay Profiles (PDPs) of different channel configurations. The PDP is the magnitude squared of the complex impulse response. The verification box is capable of multiple channel configurations including a direct path with a single pulse, single multipath, and double multipath (DM) configurations. Examples of the direct path and double multipath configurations are shown in Fig. 2. The verification box serves as a portable system for round-robin testing across laboratories.

## II. Comparison-To-Reference Channel Sounder Verification Methodology

The approach starts with the characterization of the box's channels by a vector network analyzer (VNA) [11, 12]. A requirement for the VNA is a comprehensive error analysis such as the NIST Microwave Uncertainty Framework [13]. During the comparison, if the channel sounder does not have an error analysis associated with its measurements, the comparison provides some confidence toward the trustworthiness of the channel sounder's measurements. If the channel sounder does have an error analysis, overlapping errors bars in the PDPs would indicate agreement between the systems. The channel sounders in this paper demonstrate the adaptability of the verification box to verify hardware and post-processing performance.

Key to enabling the comparison, the channel sounder and NIST reference VNA measurement parameters such as frequency range and frequency spacing are set to identical values. Connector type and use of adapters is particularly important. This is because the VNA is calibrated at the reference plane seen in Fig. 3 (see the green and yellow boxes) to ensure that systematic and random errors such as VNA system drift are captured during the calibration. This allows errors in measurements of the verification box to be

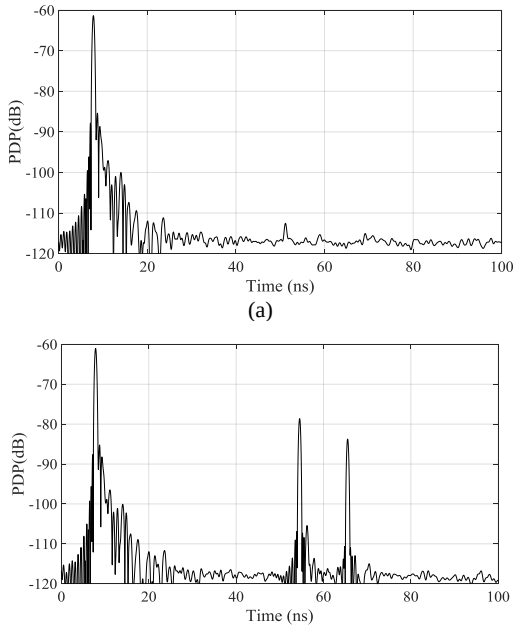


Fig. 2: (a) Power delay profile measured by a vector network analyzer of a direct path configuration. (b) Power delay profile measured by a vector network analyzer of a double multipath configuration of the channel sounder verification box.

Quimby, Jeanne; Michelson, David; Bennai, Mustapha; Remley, Catherine; Kast, Joshua; Weiss, Alec.
"Interlaboratory Millimeter-Wave Channel Sounder Verification."
Paper presented at 13th European Conference on Antennas and Propagation (EuCAP), Krakow, Poland. March 31, 2019 - April 5, 2019.

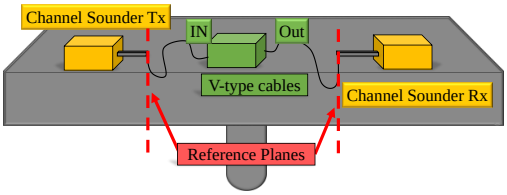


Fig. 3: Channel sounder verification box reference planes.

propagated into the channel metrics during the VNA post-processing.

Prior to use, the box is warmed up for approximately 1 hour prior to connecting to the channel sounder. The channel sounder measures the verification box at the same reference plane as the VNA. A channel sounder from the Alliance and a NIST reference VNA comparison of the PDP, delay window and RMS delay spread [14] are shown later in a Table III.

### A. *Reference Vector Network Analzyer Description*

The reference VNA is vital for the comparison-to-reference channel sounder verification. The VNA measures the complex scattering-parameter (S-parameter) response of the artifact. The VNA S-parameter measurements are post-processed using the same parameters as the channel sounder to emulate the system response of the artifact including filter type, center frequency, bandwidth, slope and phase dispersion. During the post-processing of the VNA data, we propagate random and systematic uncertainties to channel metrics of interest. The VNA's parameters are provided in Table I for channel sounder verification shown here.

Table I: Reference vector network analyzer measurement parameters.

| **Vector Network Analyzer Settings for comparison with the Communications Research Centre Canada channel sounder** | | |
|---|---|---|
| Center Frequency (GHz) | 26 | 38 |
| Bandwidth (MHz) | 1250 | 1000 |
| IF Bandwidth (Hz) | 10 | 10 |
| Number of points | 1601 | 1601 |
| Output power (dBm) | -5 | -5 |

### B. *VNA-Based Channel Sounder*

As an example of the comparison-to-reference technique, we used a VNA-based channel sounder as shown in Fig. 4. This channel sounder records complex scattering parameters such as S21 data across seven frequency bands. The VNA is connected to custom-developed TX and RX units via coaxial cables for a maximum link distance of 50 m. To prevent excessive signal attenuation over the long cables, frequency up- and down-converters are used for the higher bands (26, 38 and 61 GHz). A common 10-MHz reference signal generated at the VNA is distributed to the TX and RX units via separate coaxial cables. This serves to phase-lock the frequency converters. In order to suppress out-of-band interference, separate bandpass filters (BPFs) and low-noise amplifiers (LNAs) are used.

The measured transmission gains are compensated for the complex frequency response of the measurement system

Fig. 4: VNA-based multiband channel sounder.

itself, determined from back-to-back measurements [15] that bypass the antennas with a precisely characterized cable. This provides the complex channel transfer functions (including antenna gains, estimated separately) for each band. The system can be configured with different transmit power levels and IF bandwidths, and to perform coherent averaging over multiple channel transfer functions, for example, when measuring at locations with very high propagation loss. The block diagram of the channel sounding system is shown in Fig. 5.

Dual-polarized horn antennas, mounted on top of tripods and mechanically steered by pan-tilt units (PTUs), shown in Fig. 5 are controlled by software run on the host computer. These provide directional fully customized scanning capabilities to the system in terms of angle, frequency and polarization, and displays the corresponding channel estimates in the frequency and time domains. Table II shows the frequency bands available to this channel sounder. It also provides the gains, half power beam widths (HPBWs) and cross-polarization discriminations (XPDs) of the horn antennas as they were measured in the configuration shown in the photograph. The XPDs listed are the minimum off-axis values determined over the 6-dB beam widths and averaged over both ports.

## III. Results

Comparison of the channel sounder's measurements of the verification box against the NIST reference VNA has led to insightful information about the channel sounder. The

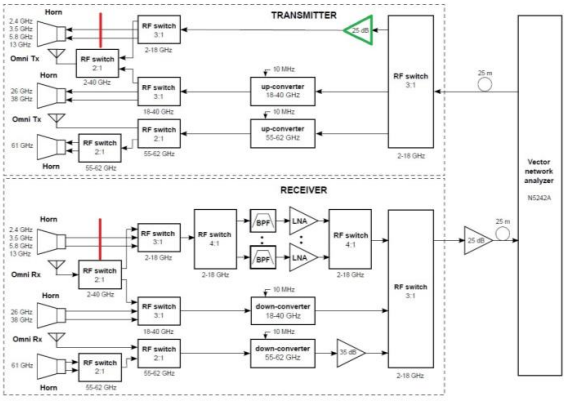


Fig. 5: Block diagram of the VNA-based channel sounder. Red lines indicate channel sounder reference planes. Green triangle indicates power amplifier.

Table II: Properties of the channel sounder.

| Parameter | Value | | | | | | | | |
|---|---|---|---|---|---|---|---|---|---|
| Center frequency (GHz) | Band | 2.4 | 3.5 | 5.8 | 13 | 26 | 38 | 61 |
| | Start | 2.4 | 3.4 | 5.725 | 12.75 | 25.25 | 37.50 | 61 |
| | End | 2.5 | 3.475 | 5.875 | 13.25 | 26.50 | 38.50 | 61.5 |
| Bandwidth (MHz) | | 100 | 75 | 150 | 500 | 1250 | 1000 | 500 |
| Gain (dBi) | Horn | 8.7 | 10.6 | 12.8 | 18.4 | 16.7 | 18.8 | 19.4 |
| | Omni Tx | 3.6 | 3.9 | 0.7 | 4.8 | 5.6 | 4.5 | 6.6 |
| | Omni Rx | 4.0 | 4.0 | 1.6 | 4.0 | 5.8 | 5.6 | 3.5 |
| HPBW (degrees) | E-Plane | 58 | 38 | 36 | 17 | 22 | 17 | 20 |
| | H-plane | 68 | 53 | 33 | 15 | 20 | 14 | 20 |

representative results provided here relate to common problems encountered across many channel sounder architectures, post-processing techniques, and measurement set-up parameters. During the post-processing of the data, a Blackman filter and maximum scaling was applied to the NIST data.

### A. *Power Amplifier Input Setting*

A power amplifier is commonly used in a channel sounder to increase the transmitted power and extend the physical range between transmitter and receiver. Determining the appropriate input power setting without affecting the channel measurement is a challenge facing many researchers. For example, if the power setting is too high, the power amplifier may create a false artifact. As an example of this is shown by the arrow in the PDP in Fig. 6(a). When the channel sounder input power was set to a high-power setting, the false artifact power was -86 dB near 11 ns but at a low-power setting, the false artifact power was -92 dB. This is a 6 dB difference in the power while the channel sounder was operating at a center frequency of 38 GHz. Next, the channel sounder center frequency was changed from 38 GHz to 26 GHz. Near 11 ns in Fig. 6(b), the artifact shown by the arrow is independent of the input power into the power amplifier. This difference in behavior is due to the channel sounder frequency of operation. It is important to note that the power amplifier was operated within its operational specifications.

### B. *Channel Sounder Dynamic Range*

The verification box direct path configuration compares the power level of the NIST reference VNA to the channel sounder versus time for a known channel without any MPCs. As seen in Fig. 7, the channel sounder dynamic range between the main peak and the power level at 457 ns is approximately 57 dB while the NIST reference power level is 80 dB ± 5 dB. This is a difference of 22 dB. This particular box configuration of the verification box provides an independent view of the actual channel sounder. It also enables researchers to assess if the system's dynamic range meets their needs for their measurement campaigns.

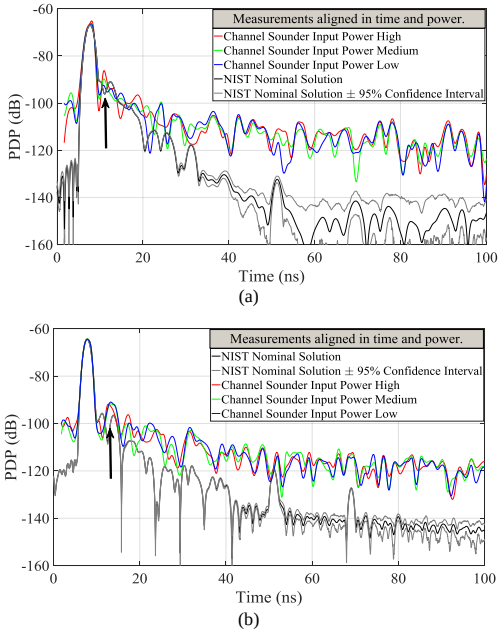


Fig. 6: (a) Channel sounder measurements at a center frequency of 38 GHz, (b) Channel sounder measurements at a center frequency of 26 GHz. Channel sounder data aligned to NIST nominal solution in time and power. The same power amplifier was used for both figures.

### C. *Power Delay Profile Metrics*

A channel sounder user's ability to distinguish actual multipath components from false artifacts due to reflections from non-ideal hardware is very important. The channel sounder verification box double multipath configuration provides a known channel with MPCs at 51 and 68 ns, as seen in Fig. 8 (the box can be configured to an alternative double multipath configuration with MPCs at 55 and 65 ns). The channel sounder PDP results above -100 dB falls within the error bars of the NIST reference VNA results.

A comparison of the arrival time of the main peak delay window, RMS delay spread, and number of MPCs is shown in Table III for this configuration of the box. The multipath threshold was set to -30 dB and the percent of energy in the delay of 90% for calculation of the channel metrics. Note that

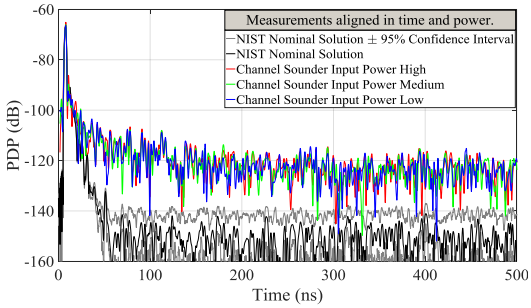


Fig. 7: Power delay profile comparison out to 500 ns. Channel sounder data aligned to NIST nominal solution in time and power.

Quimby, Jeanne; Michelson, David; Bennai, Mustapha; Remley, Catherine; Kast, Joshua; Weiss, Alec.
"Interlaboratory Millimeter-Wave Channel Sounder Verification."
Paper presented at 13th European Conference on Antennas and Propagation (EuCAP), Krakow, Poland. March 31, 2019 - April 5, 2019.

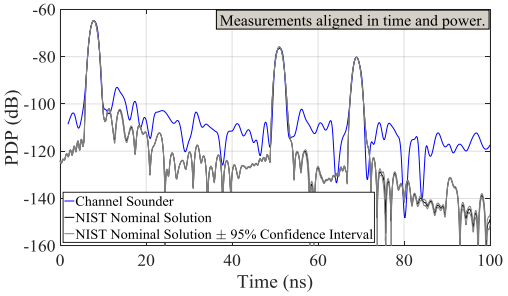


Fig. 8: Comparison of a double multipath configuration with time alignment. Channel sounder data aligned to NIST nominal solution in time and power.

Table III: Comparison of channel metrics [14].

| | **Arrival Time (ns)** | **Delay Window (ns)** | **RMS Delay Spread (ns)** | **Number of MPCs** |
|---|---|---|---|---|
| NIST Reference VNA | 7.81 | 44.25 ± 0.001 | 14.1 ± 0.01 | 3 |
| Channel Sounder | 6.4 | 44.2 | 20.5 | 3 |

the channel sounder results were time-aligned to the NIST nominal solution in Fig. 8 but the initial time of arrival is provided in the table.

### *D. PDP Post-Processing*

In the channel sounder, the received signal must be post-processed to recover the PDP of the channel. Even small errors in, or incorrect configuration of, the post-processing software can result in spurious responses, distortion and reduced dynamic range [16]. For VNA-based channel sounders, the choice and correct implementation of the windowing function and IFFT routines are critical. For correlation-based channel sounders, the choice and correct implementation of the correlation routine are critical. The verification box provides a convenient method for identifying deficiencies in the post-processing software that would otherwise be very difficult to detect.

## IV. CONCLUSIONS

We illustrated a comparison-to-reference channel sounder verification technique by use of a known and stable channel artifact. We illustrated a comparison between a channel sounder and a NIST reference VNA, which provided insightful understanding of the channel sounder hardware, post-processing and important channel metrics. The calculation of the reference channel metrics with uncertainties such as PDP and RMS delay spread helps to establish the accuracy of the channel sounder's performance.

## REFERENCES


[1] M. Cheffena, "Industrial wireless communications over the millimeter wave spectrum: opportunities and challenges," *IEEE Commun. Mag.*, vol. 54, no. 9, pp. 66-72, September 2016.
doi: 10.1109/MCOM.2016.7565190

[2] The Institute of Electrical and Electronics Engineers (IEEE) Future Directions 5G Initiative, Online: https://5g.ieee.org/, accessed Oct. 30, 2017.

[3] 3GPP, "Technical specification group radio access network; Study on channel model for frequencies from 0.5 to 100 GHz (Release 14)," 3rd Generation Partnership Project (3GPP), TR 38.901 V14.2.0, Sept. 2017. Online: http://www.3gpp.org/DynaReport/38901.htm, accessed Oct. 30, 2017.

[4] Christopher Cox, *An Introduction to LTE: LTE, LTE-Advanced, SAE, and 4G Mobile Communicatins*. John Wiley & Sons, 2012.

[5] K.A. Remley, Ed., Contributors: A. Zajic, R. Thomä, S. Salous, J. T. Quimby, T. Rappaport, G. MacCartney, A. Sayeed, A. Molisch, D. Michelson, J. Senic, R. Sun, P. Papazian, R. Krueger, C. Gentile, J.-K. Choi, R. Müller, J. Lee, M.-D. Kim, J.-J. Park, H. K. Chung, R. He, Y. de Jong, M. Bennai, and P. Bouchard, "Verification Techniques for mmWave Channel Sounders, Activities of the 5G mmWave Channel Model Alliance" (in process).

[6] 5G mmWave Channel Model Alliance Wiki Website, https://sites.google.com/a/corneralliance.com/5g-mmwave-channel-model-alliance-wiki/home

[7] A. Karstensen, W. Fan, I. Carton, and G. F. Pedersen, "Comparison of ray tracing simulation and channel measurements at mmwave bands for indoor scenarios," in *Proc. EuCAP 2016* (Davos), 2016, pp. 1-5.

[8] C. Cheng, S. Kim and A. Zajić, "Comparison of path loss models for indoor 30 GHz, 140 GHz, and 300 GHz channels," in *Proc. EUCAP 2017* (Paris), 2017, pp. 716-720.

[9] J. Quimby, K. A. Remley, J. A. Jargon, R. Leonhardt, P. D. Hale, S. Streett, A. Koepke, R. Johnk, C. Hammerschmidt, P. McKenna, I. Stange, N. DeMinco, J. E. Diener, R. C. Smith, C. Hoyt, and S. Springer, "Channel Sounder Measurement Comparison: Conducted Test" – CAC Tech Note 1 (in process).

[10] J. Dortmans, J. T. Quimby, K. A. Remley, D. Williams, J. Senic, R. Sun, and P. Papazian, "Design of a portable verification artifact for millimeter-wave-frequency channel sounder," *IEEE Trans. Antennas Propag.* (submitted Mar. 2018).

[11] D. F. Williams, J C. M. Wang, and U Arz, "An optimal vector-network-analyzer calibration algorithm," *IEEE Trans. Microw. Theory Tech.*, vol. 51, no. 12, pp. 2391–2401, Dec. 2003.

[12] A. Koepke and J. A. Jargon, "Quantifying Variance Components for Repeated Scattering-Parameter Measurements," in *Proc. 90th ARFTG Microwave Measurement Conference*, Boulder, CO, Nov. 2017.

[13] https://www.nist.gov/services-resources/software/wafer-calibration-software

[14] ITU Radiocommunication Sector (ITU-R) Rec. P.1407-5, 2013.

[15] P. B. Papazian, J.K. Choi, J. Senic, P. Jeavons, C. Gentile, N Golmie, R. Sun, D. Novotny, K. A. Remley, "Calibration of millimeter-wave channel sounders for super-resolution multipath component extraction," *2016 10th European Conference on Antennas and Propagation (EuCAP)*, Davos, 2016, pp. 1-5.

[16] N. Stanchev, A. J. Corbett, and D. G. Michelson, "Suppression of self-noise in stepping correlator channel sounders," in *Proc. IEEE AP-S/URSI Symp.* (Spokane), 2011.




Quimby, Jeanne; Michelson, David; Bennai, Mustapha; Remley, Catherine; Kast, Joshua; Weiss, Alec.
"Interlaboratory Millimeter-Wave Channel Sounder Verification."
Paper presented at 13th European Conference on Antennas and Propagation (EuCAP), Krakow, Poland. March 31, 2019 - April 5, 2019.

# Large-Signal Network Analysis for Over-the-Air Test of Up-Converting and Down-Converting Phased Arrays

Alec J. Weiss[#^1], Dylan F. Williams[#2], Jeanne Quimby[#3], Rod Leonhardt[#4], Thomas Choi[$5], Zihang Cheng[$6], Kate A. Remley[#7], Andreas Molisch[$8], Benjamin Jamroz[#9], Jake Rezac[#10], Peter Vouras[#11], Charlie Zhang[*12]
[#]National Institute of Standards and Technology, Boulder, CO USA
[^]Colorado School of Mines, Golden, CO USA
[$]University of Southern California, Los Angeles, CA USA
[*]Samsung Electronics, Richardson, TX USA
[1]alec.weiss@nist.gov, [2]dylan.williams@nist.gov, [3]jeanne.quimby@nist.gov, [4]leonhardt@nist.gov, [5]choit@usc.edu, [6]zihangch@usc.edu, [7]kate.remley@nist.gov, [8]molisch@usc.edu, [9]ben.jamroz@nist.gov, [10]jacob.rezac@nist.gov, [11]peter.vouras@nist.gov, [12]jianzhong.z@samsung.com

***Abstract*— We explore large-signal network analysis for the over-the-air test of up-converting and down-converting phased arrays. The approach first uses a vector network analyzer to characterize a three-dimensional test environment at RF. The vector network analyzer is then power- and phase-calibrated for the characterization of up-converting and down-converting phased arrays with an IF input or output. We illustrate the approach with measurements of a down-converting phased array.**

***Keywords*— down-converter, large-signal network analysis, over-the-air test, phased array, phase calibration, spatial channel, up-converter, vector network analyzer, wireless system.**

## I. Introduction

We present a practical approach for calibrating an over-the-air (OTA) test system with a vector network analyzer and then applying it to the characterization of up-converting and down-converting phased arrays. We accomplish this by use of a vector network analyzer (VNA) configured to operate as a large-signal network analyzer (LSNA) capable of performing calibrated amplitude and phase measurements across different frequency bands. This approach allows the VNA to first calibrate a static free-field channel in the OTA test system at RF frequencies, and then to characterize the response of the phased array at its connectorized IF port when it is inserted in that same channel. The approach is equally applicable to the characterization of up-converting IF-RF and down-converting RF-IF phased arrays without accessible RF ports between the phased-array elements and the converters.

We demonstrate the approach on a National Institute of Standards and Technology (NIST) OTA Test System, known as the Synthetic Aperture Measurement with Uncertainty and Angle of Incidence (SAMURAI) system, to characterize an experimental 28 GHz Samsung [1] up-converting and down-converting phased array [1]. This system consists of an LSNA, cables, antennas and a scanning positioner for the receive antenna. The SAMURAI system is focused on using synthetic aperture measurements at millimeter-wave frequencies to determine angle of arrival and other aspects of the channel for OTA test.

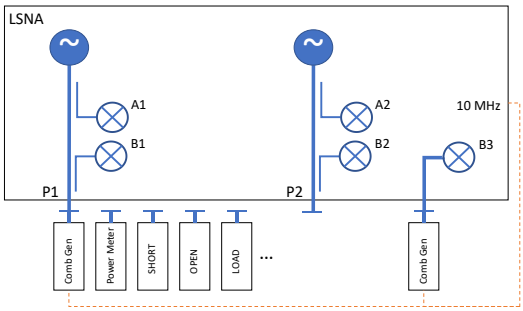


Figure 1. Simplified sketch of an LSNA and its calibration.

## II. LSNA Calibration

Large-signal network analyzers are vector network analyzers configured both to determine conventional scattering parameters from the ratios of the forward and backward waves at their measurement ports and also to measure the amplitudes and "cross-frequency" phases of those forward and backward waves at their measurement ports. This greatly increases the utility of the VNA [2]. LSNAs now find application not only in the characterization of nonlinear transistors, amplifiers and other devices [3, 4], but in modulated-signal characterization [5], mixer characterization [6-9], and the characterization of distortion in devices excited by modulated signals [10-12].

Figure 1 shows a simplified sketch of a typical two-port LSNA and illustrates its calibration sequence. The LSNA is first calibrated with conventional VNA scattering-parameter calibration artifacts (short, open, load, thru, etc.) at its two ports. Then, the power meter is used to measure the power on port 1 with the LSNA's port 1 source turned on. The readings on the A1 and B1 receivers are compared to the power-meter reading

[1] The National Institute of Standards and Technology does not endorse commercial products. We use brand names only to better describe the experiments. Other products may work as well or better.

Weiss, Alec; Williams, Dylan; Quimby, Jeanne; Leonhardt, Rodney; Choi, Thomas; Chen, Zihang; Remley, Catherine; Molisch, Andreas; Jamroz, Benjamin; Rezac, Jake; Vouras, Peter.
"Large-Signal Network Analysis for Over-the-Air Test of Up-Converting and Down-Converting Phased Arrays."
Paper presented at 2019 International Microwave Symposium, Boston, MA, United States. June 2, 2019 - June 7, 2019.

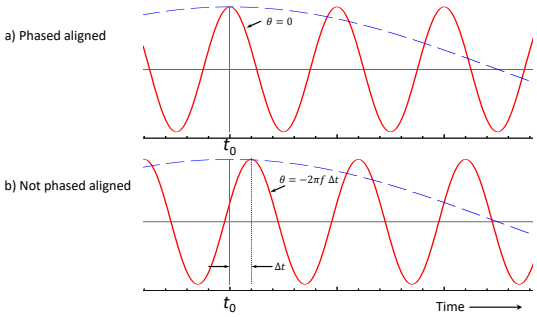


Figure 2. LSNA phase relationships between the lowest IF frequency (blue dashed line) and a higher frequency (red solid line) signals.

to establish the relationships between the forward and backward wave amplitudes at the ports of the LSNA and perform the LSNA's power calibration [2].

Finally, the LSNA's cross-frequency phase calibration is performed to establish the phase relationships across different frequency bands measured by the LSNA. In essence, the LSNA is calibrated to measure the phases of the forward and backward waves at different frequencies with respect to a single fixed time zero. In our case, this aspect of the calibration required the use of two comb generators, each triggered with the 10 MHz reference of the LSNA. These comb generators create a comb of phase-stable tones at multiples of 10 MHz.

The first of these comb generators is connected to the LSNA's receiver B3 and is left on during the entire calibration and measurement sequence. This comb generator provides a stable but unknown set of tones to which the LSNA references all its measurements. That is, the LSNA is configured to perform raw measurements on each of its receivers simultaneously, and then set a uniform time reference by dividing these raw complex receiver measurements acquired on A1, B1, A2, and B2 by $b_3/|b_3|$, where $b_3$ is the measurement performed on B3 at the same frequency. This operation is performed before any other processing of the data is performed.

To complete the cross-frequency phase calibration, the source connected to port 1 is switched off, and a calibrated comb generator that creates tones with already characterized electrical phases is connected to port 1 of the LSNA, as illustrated in Fig. 1. The measurements on A1 and B1, after normalization by $b_3/|b_3|$, are compared to the known response of the comb generator to perform the phase calibration. The phase relationships between the tones generated by this comb generator were characterized by a sampling oscilloscope that was calibrated with an electrooptic sampling system [13, 14].

In the final step of the phase calibration, the time zero $t_0$ for the LSNA measurements is set to the time at which the phase of the incoming wave on port 1 from the comb generator at the lowest frequency in the calibration (the lowest-frequency IF component in this case) is set equal to zero, as illustrated by the dashed blue line in Fig. 2. The solid red line in Fig. 2 illustrates how the phases of a second forward or backward wave at a different frequency are then related to the phase of the first wave after calibration. If the peak voltage of the second wave aligns perfectly in time with the peak voltage of the first wave

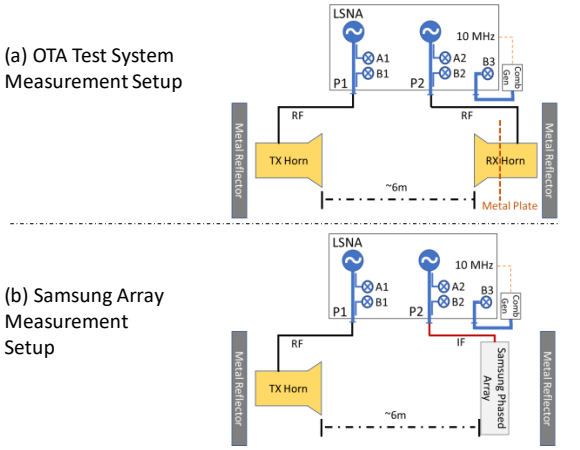


Figure 3. The measurement configuration. Optional metal plate added for measurements in Figure 5.

at the lowest frequency in the calibration, as illustrated in Fig. 2(a), the phase θ of the second wave is zero. However, if the peak of the second wave was offset by $\Delta t$, as shown in Fig. 2(b), the phase of the second wave would be $\theta = -2\pi f\ \Delta t$.

For our application, the phase calibration was performed over all the RF and IF frequencies that were used in the experiment, establishing their phases with respect to a single point in time and forming the basis for determining the RF-IF frequency response of the phased array.

## III. NIST OTA Test System

Figure 3 shows the NIST OTA Test System. The LSNA performs all the electrical measurements in the system. After calibration, the LSNA is first used as a conventional VNA, where the output frequency is assumed to equal the input frequency, to characterize the RF environment in the NIST OTA Test System. Here, we don't require the cross-frequency phases. However, to simplify the overall calibration approach, the RF scattering parameters are determined from the magnitudes and phases of the forward and backward waves at the ports of the LSNA, as shown in Fig. 3(a). The calibrated horn on the right can be scanned to perform synthetic-aperture and other measurements that characterize angle and time of arrival, and other characteristics of the three-dimensional RF environment (sometimes called the "spatial channel") between the horns.

After the RF environment has been characterized, the horn and positioning system on the right are replaced by the phased array, as illustrated in Fig. 3(b), and the amplitude and phase calibrations of the LSNA come into play. When characterizing a down-converting phased array, the LSNA measures the IF response of the array in the configuration shown in Fig. 3(b) relative to the RF free-field excitation characterized by the LSNA in the configuration shown in Fig. 3(a). Since the LSNA is capable of measuring both the amplitudes and phases of the array's IF output signals compared to the amplitudes and phases of the array's RF input signals, it can construct the RF-to-IF power-delay-profiles (PDPs) measured by the down-converting

Weiss, Alec; Williams, Dylan; Quimby, Jeanne; Leonhardt, Rodney; Choi, Thomas; Chen, Zihang; Remley, Catherine; Molisch, Andreas; Jamroz, Benjamin; Rezac, Jake; Vouras, Peter.
"Large-Signal Network Analysis for Over-the-Air Test of Up-Converting and Down-Converting Phased Arrays."
Paper presented at 2019 International Microwave Symposium, Boston, MA, United States. June 2, 2019 - June 7, 2019.

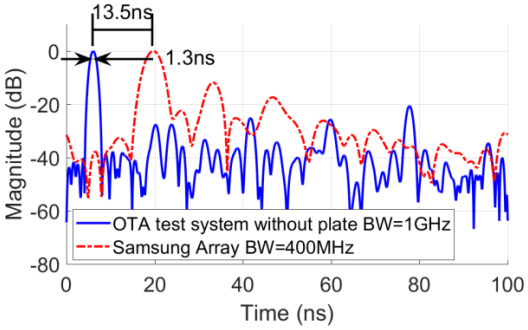


Figure 4. Comparison of the measured OTA boresight RF-RF (solid) and Samsung RF-IF (dashed) PDPs.

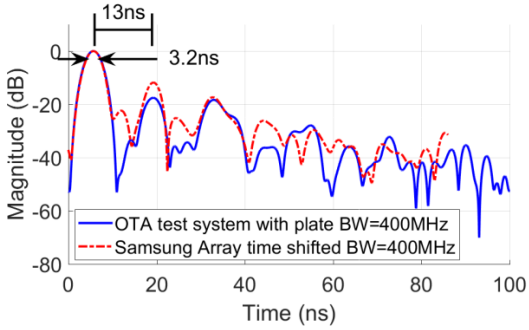


Figure 5. Comparison of the measured boresight OTA RF-RF and Samsung RF-IF PDPs after reducing the OTA-test-system bandwidth to 400 MHz, adding an optional metal plate behind the OTA horn (this boosts the first multipath component 13 ns after the first line-of-sight pulse), and shifting the arrival time of the first line-of-sight impulse measured by the Samsung array to 6 ns.

phased array and the frequency and impulse responses of the down-converting phased array as described in [8].

Characterizing the frequency and impulse responses of an up-converting phased array is performed in the same way, except that the IF-RF up-converting performance of the phased array is tested.

## IV. Samsung Phased-Array Measurement Demonstration

We calibrated the LSNA and performed a series of tests to explore its use within the NIST OTA Test System. We used a 28 GHz experimental up-converting and down-converting Samsung phased array with a 400 MHz bandwidth for the demonstration [1]. We tested the array in its down-converting mode of operation in the reflective environment between the two metal reflectors sketched in Fig. 3.

For these experiments, we first used the LSNA to characterize the three-dimensional RF channel with a pair of Sage-Millimeter[2] 26.5-40 GHz, 23 dBi, WR 28 horns over a 1 GHz frequency range spanning 27.65 GHz to 28.65 GHz. This horn was selected because it has a beamwidth similar to that of the Samsung array. Then we replaced the RX horn, which has a small form factor, with the much larger Samsung array and measured its RF-to-IF characteristics over the 400 MHz frequency range spanning 27.65 GHz to 28.05 GHz in the same highly reflective environment. For these measurements, the Samsung array was physically positioned to point directly at the horn and its beam was electronically steered to boresight.

Figure 4 compares the RF-RF PDP measured by the NIST OTA Test System with the full 1 GHz bandwidth, which includes the response of the WR-28 RX horn and the RF-IF PDP measured by the Samsung array over its smaller 400 MHz bandwidth. For this comparison, both peaks of the PDP were normalized to 0 dB (amplitude comparisons were not meaningful due to unknown gain and loss in the IF amplifiers and other electronics integrated into the Samsung array).

While the levels of the multipath components measured by the NIST OTA Test System in this reflective environment were much higher than we see in quieter environments, the 1 GHz bandwidth, 1.3-ns wide, 3-dB response of the test system to the first line-of-sight component is significantly sharper than that of the 400 MHz bandwidth, 3.2 ns wide, 3 dB response of the Samsung array. This is expected due to the different bandwidths of the systems. The 6-ns arrival time of the first line-of-sight component measured by the NIST OTA Test System was also very close to what we expected, based on the roughly two-meter distance between the two horns. However, the arrival time of the first line-of-sight component measured by the Samsung array was delayed by an additional 13.5 ns due to the internal electronics in the array. This example illustrates the ability of the LSNA to track the phases (and timing) during both the RF-RF system characterization and the ensuing RF-IF array measurement.

In Fig. 5, we were able to improve the comparison and explain most of the discrepancy between the two measurements. This was done by reducing the bandwidth of the RF-RF NIST OTA Test System measurements to 400 MHz and adding a metal plate of the same size as the Samsung array's metal housing behind the horn, which increased the amplitude of the first multipath component. We also shifted the arrival time of the first line-of-sight component measured by the Samsung array to better compare measurements.

## V. Impact of LSNA Uncertainty

While the overall uncertainty of the NIST OTA Test System is still being evaluated, we were able to estimate the impact of measurement errors due to the scattering-parameter and phase calibration, the LSNA's repeatability and drift, as determined from 10 repeat measurements, and cable bending, as determined from repeated measurements of the cables during

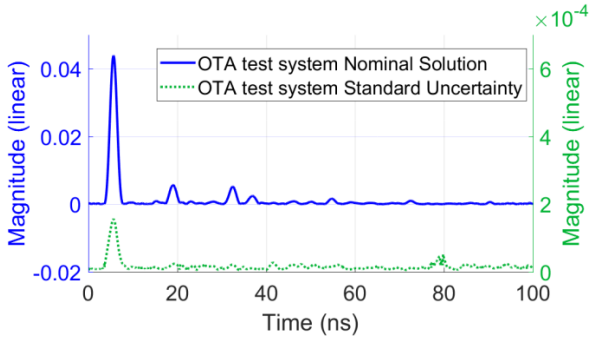


Weiss, Alec; Williams, Dylan; Quimby, Jeanne; Leonhardt, Rodney; Choi, Thomas; Chen, Zihang; Remley, Catherine; Molisch, Andreas; Jamroz, Benjamin; Rezac, Jake; Vouras, Peter.
"Large-Signal Network Analysis for Over-the-Air Test of Up-Converting and Down-Converting Phased Arrays."
Paper presented at 2019 International Microwave Symposium, Boston, MA, United States. June 2, 2019 - June 7, 2019.

Figure 6. OTA test system PDP and its uncertainties.simulated measurements.

Figure 6 compares the uncertainty attributable to the LSNA measurements due to these factors. We used the NIST Microwave Uncertainty Framework [15] to capture the correlations in these frequency-domain uncertainties and propagate them through the Fourier transform to the time domain for comparison [16, 17]. The figure illustrates how the correlated uncertainty analysis performed by the Microwave Uncertainty Framework is able to temporally line up the uncertainty in the direct line-of-sight component with the arrival of the component itself. This is not possible in conventional frequency-point-by-frequency-point uncertainty analyses [18, 19].

The figure also shows that the error in the measurements attributable to the LSNA is quite low. Thus, we expect error in the NIST OTA Test System to be dominated by other sources, including characterization of the antenna responses, positioning errors, and interactions of the positioning equipment, cables and horns. These are the subject of future work.

## VI. Conclusion

We demonstrated the use of a VNA configured to operate as an LSNA for calibrated measurements as an OTA test system. We showed that the LSNA allows the system to be used both to perform RF-RF characterization tasks and RF-IF measurements that characterize the performance of up-converting and down-converting arrays in the test environment. These tests allow for the characterization of phased arrays without a connectorized RF port, including their hardware latency compared to that of the standard horn.

While we only showed measurements of the array in its down-converting mode of operation in a highly reflective environment, testing in a less-reflective environment would have provided a simpler and less-demanding RF environment for the array and de-emphasized the impact of the large array form factor on its frequency response.

In addition, the LSNA's RF-IF characterization can be used with the full synthetic-aperture capability of the NIST OTA Test System. Using fully characterized horn antennas together with the synthetic-aperture techniques of the NIST OTA Test System will allow us to precisely determine times and angles of arrival in the three-dimensional, spatial-channel test environment and develop a better understanding of the actual performance of up-converting and down-converting arrays.

## Acknowledgment

We thank Prof. Atef Elserbeni, Dobelman Distinguished Professor of Electrical Engineering at the Colorado School of Mines, for support of Alec Weiss and many helpful discussions.

## References

[1] C. U. Bas *et al.*, "A Real-Time Millimeter-Wave Phased Array MIMO Channel Sounder," in *2017 IEEE 86th Vehicular Technology Conference (VTC-Fall)*, 2017, pp. 1-6.

[2] J. Verspecht, "Large-Signal Network Analysis," *IEEE Microwave Magazine*, vol. 6, no. 4, pp. 82-92, 2005.

[3] J. Verspecht, "Calibration of a Measurement System for High Frequency Nonlinear Devices," *Ph.D.Thesis, Free University of Brussels*, 1995.

[4] F. D. Groote, J. Teyssier, T. Gasseling, O. Jardel, and J. Verspecht, "Introduction to measurements for power transistor characterization," *IEEE Microwave Magazine*, vol. 9, no. 3, pp. 70-85, 2008.

[5] N. B. Carvalho, K. A. Remley, D. Schreurs, and K. G. Card, "Multisine signals for wireless system test and design [Application Notes]," *IEEE Microwave Magazine*, vol. 9, no. 3, pp. 122-138, 2008.

[6] J. Dunsmore, "Novel method for vector mixer characterization and mixer test system vector error correction," *IEEE MTT-S Int.Microwave Symp.Dig.*, vol. 3, pp. 1833-1836, 2002.

[7] J. Dunsmore, S. Hubert, and D. F. Williams, "Vector mixer characterization for high-side LO cases," *IEEE MTT-S Int.Microwave Symp.Dig.*, vol. 3, pp. 1743-1746, 2004.

[8] D. F. Williams, F. Ndagijimana, K. A. Remley, J. Dunsmore, and S. Hubert, "Scattering-parameter models and representations for microwave mixers," *IEEE Trans.Microw.Theory Techn.*, vol. 53, no. 1, pp. 314-321, 2005.

[9] J. Dunsmore, "System for characterizing mixer or converter response," USA Patent US8744370B2, 2011.

[10] J. Verspecht, F. Verbeyst, and M. Vanden Bossche, "Network Analysis Beyond S-parameters: Characterizing and Modeling Component Behaviour under Modulated Large-Signal Operating Conditions," *ARFTG Conference Digest*, vol. 56, pp. 1-4, 2009.

[11] J. Verspecht, D. F. Williams, D. Schreurs, K. A. Remley, and M. D. McKinley, "Linearization of large-signal scattering functions," *IEEE Transactions on Microwave Theory and Techniques*, vol. 53, no. 4, pp. 1369-1376, 2005.

[12] K. A. Remley, D. F. Williams, D. M. M. Schreurs, and J. Wood, "Simplifying and interpreting two-tone measurements," *IEEE Transactions on Microwave Theory and Techniques*, vol. 52, no. 11, pp. 2576-2584, 2004.

[13] T. S. Clement, P. D. Hale, D. F. Williams, C. M. Wang, A. Dienstfrey, and D. A. Keenan, "Calibration of Sampling Oscilloscopes with High-Speed Photodiodes," *IEEE Trans.Microw.Theory Techn.*, vol. 54, no. 8, pp. 3173-3181, 2006.

[14] H. C. Reader, D. F. Williams, P. D. Hale, and T. S. Clement, "Comb-Generator Characterization," *IEEE Transactions on Microwave Theory and Techniques*, vol. 56, no. 2, pp. 515-521, 2008.

[15] D. F. Williams and A. Lewandowski, "NIST Microwave Uncertainty Framework," ed: National Institute of Standards and Technology, http://www.nist.gov/ctl/rf-technology/related-software.cfm, 2011.

[16] K. A. Remley, D. F. Williams, P. D. Hale, C. M. Wang, J. Jargon, and Y. Park, "Millimeter-Wave Modulated-Signal and Error-Vector-Magnitude Measurement With Uncertainty," *IEEE Transactions on Microwave Theory and Techniques*, vol. 63, no. 5, pp. 1710-1720, 2015.

[17] G. Avolio, A. Raffo, J. Jargon, P. D. Hale, D. M. M. Schreurs, and D. F. Williams, "Evaluation of Uncertainty in Temporal Waveforms of Microwave Transistors," *IEEE Trans.Microw.Theory Techn.*, vol. 63, no. 7, pp. 2353-2363, 2015.

[18] D. F. Williams, P. D. Hale, T. S. Clement, and J. M. Morgan, "Calibrated 200 GHz Waveform Measurement," *IEEE Trans.Microw.Theory Techn.*, vol. 53, no. 4, pp. 1384-1389, 2005.

[19] B. F. W. Jamroz, D.F.;Remley,K.A.;Horansky,R.D., "Importance of Preserving Correlations in Error-Vector-Magnitude Uncertainty," presented at the ARFTG Microwave Measurement Conference, Philadelphia, PA, 6/15/2018.

# Large-Signal-Network-Analyzer Phase Calibration on an Arbitrary Grid

Aric Sanders[1], Dylan F. Williams[2], Joshua M. Kast[3], Kate A. Remley[1], Robert D. Horansky[1]
[1]Department of Physics, University of Colorado, Boulder, CO USA
[2]National Institute of Standards and Technology, Boulder, CO USA
[3]Department of Electrical Engineering, Colorado School of Mines, Golden, CO USA
aric.sanders@nist.gov, dylan.williams@nist.gov

***Abstract*— We have developed a method for improving the synchronization of large-signal network analyzers and transferring "cross-frequency" phase calibrations from a calibrated sampling oscilloscope to the large-signal network analyzer on an arbitrary frequency grid. The approach can be applied to the measurement of modulated signals and other waveforms on arbitrary and fine frequency grids. This translates into the ability to measure complex and arbitrarily long signals traceably with high dynamic range.**

***Keywords*—phase calibration, oscilloscope, arbitrary waveform generator, large-signal network analyzer, wireless system.**

## I. Introduction

We present a practical and accurate way of calibrating the "cross-frequency" phases of large-signal network analyzer (LSNA) measurements on arbitrary, irregularly-spaced, and fine frequency grids. The method overcomes spacing and placement limitations of the calibration frequency grids inherent in the current approach to LSNA calibration, which uses comb generators to calibrate the cross-frequency phases of large-signal network analyzer measurements. The method is based on commercially available instrumentation.

Large-signal network analyzers add power and cross-frequency phase calibrations to the conventional vector-network-analyzer (VNA) scattering-parameter calibration. These additional calibration steps allow the LSNA to measure not only scattering parameters, but the amplitude and phase of each of the forward and backward waves at the ports of the LSNA [1]. LSNAs find applications in nonlinear device characterization [1-3], modulated-signal characterization [4] and the characterization of devices excited by modulated signals [5].

While LSNAs are available in both sampler-based and mixer-based architectures [6], the mixer-based architectures are more common and typically offer higher dynamic range. Mixer-based architectures usually make use of comb generators to provide a constant set of constant-phase reference tones for the LSNA as well as to calibrate the cross-frequency phase of the LSNA [1, 2]. However, this limits the LSNA to measurements on uniform commensurate frequency grids. As the frequency spacing is reduced, the total power available in the grid is also reduced, limiting the upper frequency limit of the LSNA.

There has been considerable work on creating finer LSNA frequency grids with varying degrees of success. Recently, Verbeyst, et al. [7] and Vanden Bossche, et al. [8] used lower-frequency pseudo-random bit sequences (PRBS) to trigger the comb, moving energy from the harmonics of the fundamental to a fine grid around the fundamental and a few harmonics of that fundamental. Verspecht, et al. [9] used a similar approach to generate finely-spaced tones with a chirped input. While this allows for finer frequency grids, these approaches do not have complete flexibility in the choice of the grid and are still limited in the total number and bandwidth of frequency points over which the LSNA can be calibrated and perform measurements.

Hale, et al. [10] added a band-pass filter and amplifier after the comb generator to boost the power available to the LSNA over the bandwidth of the filter and amplifier. This is useful for band-limited signals but cannot be applied to perform measurements on arbitrary frequency grids.

Zhang, et al. [11, 12] proposed a multistep calibration process that stitches multisine signals together in postprocessing to perform broadband calibrations at fine tone spacings. However, we have found that stitched multistep calibration processes degrade calibration accuracy, particularly when they contain many stitched frequency bands.

Here, we circumvent these limitations by 1) using an arbitrary waveform generator (AWG) to synchronize the measurement apparatus using a method similar to that used in [13, 14] and 2) direct calibration of the LSNA with a calibrated oscilloscope following the approach of [15]. This offers a practical and accurate way of transferring oscilloscope cross-frequency phase calibrations to large-signal network analyzers on arbitrary (including arbitrarily fine) frequency grids.

Our approach has the following advantages:

- The method is applicable to any frequency grid that can be generated by the AWG.
- The phase lock of the measurement apparatus can be implemented at high frequencies (10 GHz in our case), lowering phase noise.
- The AWG can provide power at only the frequencies of interest, greatly increasing the signal-to-noise ratio compared to standard comb-based approaches and lifting restrictions on the upper frequency limit and tone spacing.
- The measurement apparatus can be operated at the highest frequency that can measured by a calibrated oscilloscope, currently about 110 GHz.
- The LSNA can be calibrated with single-tone signals on an arbitrary frequency grid for slightly more than a cycle, making them fast and easy to measure on the sampling oscilloscope.

Sanders, Aric; Williams, Dylan; Kast, Joshua; Remley, Catherine; Horansky, Robert.
"Large-Signal-Network-Analyzer Phase Calibration on an Arbitrary Grid."
Paper presented at 2019 International Microwave Symposium, Boston, MA, United States. June 2, 2019 - June 7, 2019.

- The sampling oscilloscope can be calibrated directly with a calibrated photodiode [16-18], eliminating comb generators from the traceability path.
- In theory, the measurement apparatus could be directly calibrated and operated on wafer to the highest frequency at which electro-optic sampling can be used to provide the phase calibration in place of the oscilloscope, currently about 1 THz.

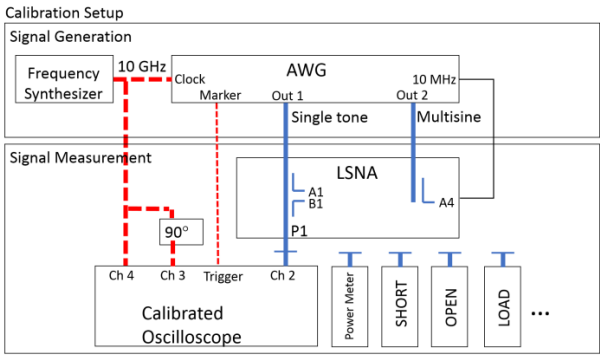


Fig. 1. The measurement apparatus during calibration. Once calibrated, the oscilloscope, power meter and scattering-parameter calibration standards can be removed and the LSNA used to perform measurements on P1.

## II. Measurement Apparatus

Figure 1 shows the measurement apparatus during calibration. During calibration, the AWG provides sinusoids to the LSNA at Out 1. These are used to perform the standard frequency-point-by-frequency-point LSNA scattering-parameter and power calibrations on port 1 (P1) of the LSNA. These sinusoids from the AWG Out 1 are also used to provide a sinusoid at each frequency that can be measured by both the oscilloscope and the LSNA, a process in which the oscilloscope need only measure one cycle of the sinusoid. A comparison of the phases of the sinusoid measured by the LSNA and the oscilloscope is used to transfer the oscilloscope's cross-frequency phase calibration to the LSNA.

The AWG in Fig. 1 provides synchronization for the measurement apparatus in a similar manner to [13, 14]. It generates a 10 MHz or other lock signal for the VNA and the oscilloscope trigger signal. The frequency synthesizer also creates the precision 10 GHz IQ reference signals for correcting for time-base-distortion for the oscilloscope using the methods of [19-21] and the clock signal for the AWG.[1]

After calibration with the oscilloscope, power meter, and scattering-parameter calibration standards (shown as an open, short and load in the figure), these calibration standards can be disconnected and the LSNA used to measure modulated forward-wave and backward-wave signals on port 1 of the LSNA (labeled P1 in Fig. 1). These signals on P1 can be

[1] The frequency synthesizer could be eliminated by using an AWG with more channels to create these 10 GHz IQ reference signals.

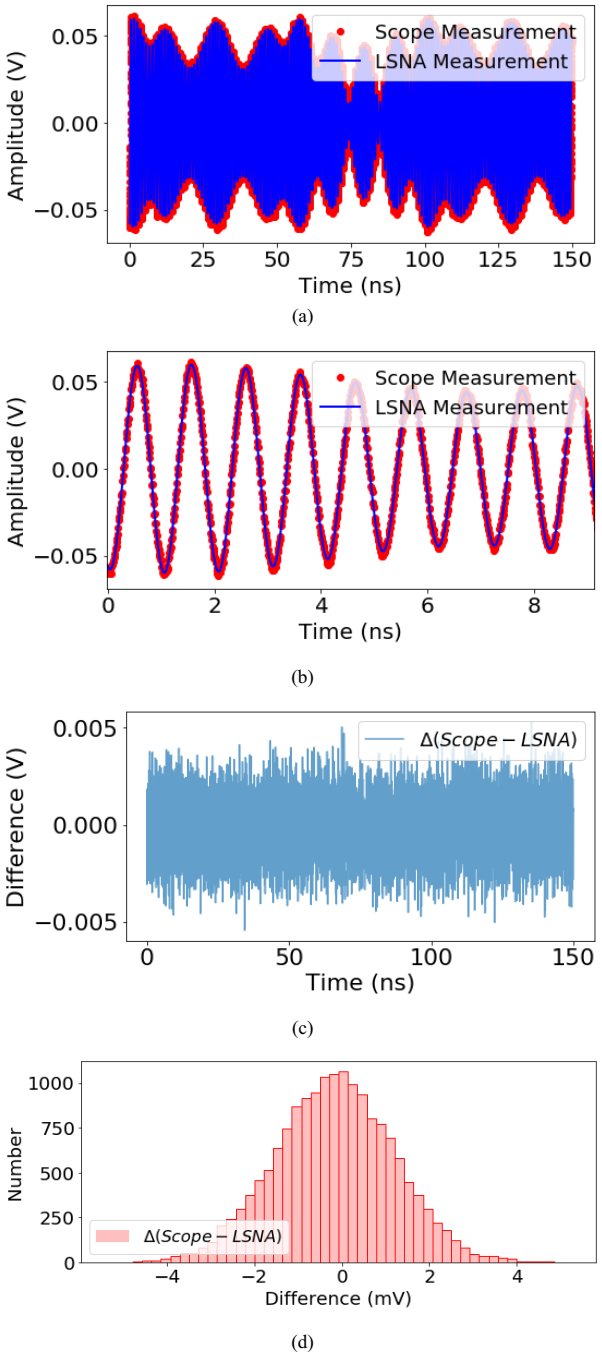


Fig. 2. Time-domain comparison of the 11-tone 10 MHz multisine measured by the LSNA and oscilloscope. (a) Signal envelope. (b) Closeup of the signal. The time-base correction algorithm moves points off of a regular grid. (c) The difference of the scope and LSNA measurements. (d) Histogram of the difference of the scope and LSNA measurements, with a mean of 0.2 mV and standard deviation of 1.4 mV.



Sanders, Aric; Williams, Dylan; Kast, Joshua; Remley, Catherine; Horansky, Robert.
"Large-Signal-Network-Analyzer Phase Calibration on an Arbitrary Grid."
Paper presented at 2019 International Microwave Symposium, Boston, MA, United States. June 2, 2019 - June 7, 2019.

generated by the AWG on Out 1 or externally by other instruments or devices that are locked to the frequency synthesizer or AWG.

During both calibration and measurement, the AWG provides a multisine reference signal on Out 2 for the LSNA with tones at each of the frequencies of interest. This signal serves as a phase reference for the LSNA as it makes measurements. The purpose of this phase reference is to provide the LSNA with a set of unknown but stable tones to use as a reference for other signals it measures. In postprocessing each phase measured by the LSNA on P1 is referred to the fixed phase of the tone at the same frequency generated on the AWG's Out 2, minimizing the need accuracy in the LSNA's 10 MHz reference. To minimize distortion in the LSNA, we used a Schroeder multisine [22] to keep the peak-to-average power ratio low.

## III. Measurement Results

We first illustrate the technique on a multisine measurement where the tone spacing corresponds to the standard minimum spacing of commercially available comb generators, 10 MHz. This allows easy comparison to the sampling oscilloscope calibrated measurements. Then, we illustrate the method on a 25 kHz grid, which requires an exceedingly long sampling oscilloscope measurement (40 µs total time) and showcases the strength of our method.

We first calibrated the oscilloscope with a photodiode calibrated on the National Institute of Standards and Technology's electro-optic sampling (EOS) system [16-18]. We then used the procedure described in the previous section to calibrate the LSNA with scattering-parameter artifacts, a power meter, and the EOS-calibrated oscilloscope, from which we transferred the phase calibration to the LSNA. Finally, we used the apparatus to measure several multisines centered at 1 GHz.

### A. 10 MHz Multisine Measurement Example

After completing the calibrations, we generated an 11-tone Schroeder multisine on Out 1 of the AWG and measured that multisine with both the LSNA and the calibrated oscilloscope. Figure 2 compares the direct measurement of the signal with the oscilloscope after time-base and mismatch corrections to the measurement performed by the LSNA after transformation to the time domain. Figure 2 (a) shows that the two instruments measure nearly the same 100 ns long envelope. Figure 2 (b) shows a closeup view of the actual signals measured by the two instruments. The two signals overlap to such a great extent that it is almost impossible to tell the difference in the plot.

Figure 2 (c) shows that the difference of the two measurements is small and has no discernible structure. The histogram in Fig 2 (d) shows the difference to be approximately Gaussian with a mean of 0.2 mV and a standard deviation of 1.4 mV, much smaller than the roughly 100 mV peak-to-peak amplitude of the signal, identical to the residual distribution of a multisine fit of the oscilloscope and close to the 1.3 mV rms noise specification of the manufacturer.

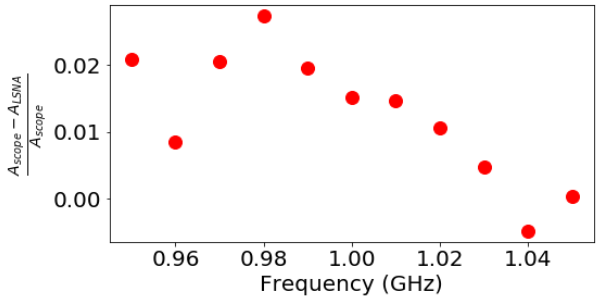


(a)

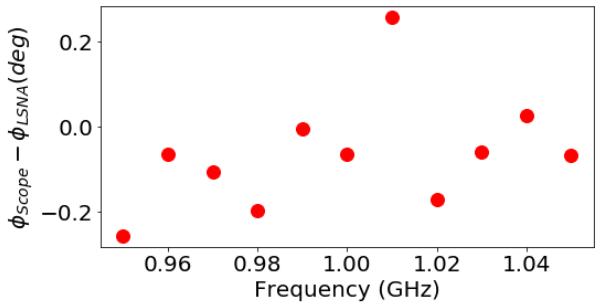


(b)

Fig. 3. Frequency-domain comparison of the 11-tone 10 MHz multisine measured by the LSNA and oscilloscope. (a) Fractional difference in the voltage measurements. (b) Phase difference of the two measurements.

We also examined the results in the frequency domain to better assess the consistency of the LSNA and oscilloscope power-meter calibrations and the accuracy of the transfer of the oscilloscope's cross-frequency phase calibration to the LSNA. Figure 3 (a) shows that the fractional difference of the forward-wave voltage measurements made by the oscilloscope ($A_{\mathrm{Scope}}$) and the LSNA ($A_{\mathrm{LSNA}}$) are within about 2 % of each other.

Figure 3 (b) shows that the differences in phase measured by the LSNA and oscilloscope differ by less than a quarter of a degree, despite that fact that the phase at each frequency point in the calibration was calibrated separately. These phase differences correspond to a drift of less than 1 ps in the synchronization of the measurement apparatus.

### B. 25 kHz Multisine Measurement Example

We also created an 11-tone Schroeder multisine on the AWG with a 25 kHz tone spacing. Figure 4 (a) compares the envelope of the signal we uploaded to the AWG and measured with the LSNA. The time offset is due to the various hardware between the AWG's converters and the LSNA's calibration reference plane at P1. This 25 kHz narrow tone spacing resulted in a signal with a 40 µs repetition rate, too long to measure accurately with our sampling oscilloscope. However, because of the way that the measurement apparatus is synchronized by the AWG, we were able to measure portions of the signal with our oscilloscope and compare those to the temporal signal reconstructed by the LSNA, as shown in Fig. 4 (b). Here again,



Sanders, Aric; Williams, Dylan; Kast, Joshua; Remley, Catherine; Horansky, Robert.
"Large-Signal-Network-Analyzer Phase Calibration on an Arbitrary Grid."
Paper presented at 2019 International Microwave Symposium, Boston, MA, United States. June 2, 2019 - June 7, 2019.

the comparison is excellent, even at the narrow tone spacing of this multisine.

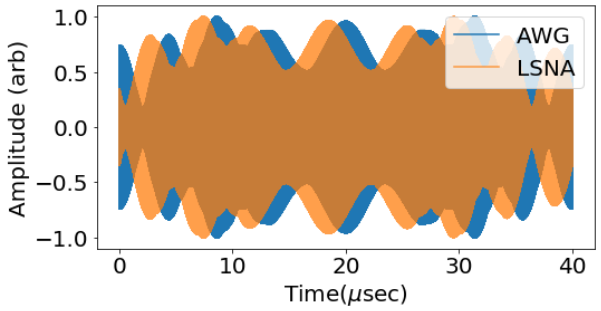


(a)

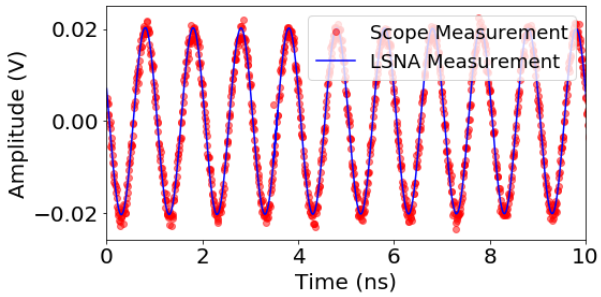


(b)

Fig. 4. Time-domain comparison of an 11-tone 25 kHz multisine. (a) Temporal envelope uploaded to AWG and measured by LSNA, offset caused by path delay. (b) Time-domain comparison of LSNA and oscilloscope measurements. The time-base correction algorithm reassigns time points based on the 10 GHz signal from the frequency synthesizer.

## IV. Conclusion

We described a fast, accurate and practical way of calibrating the cross-frequency phases of LSNAs on any frequency grid that can be generated with an AWG and measuring any repetitive communications signal that we can create with the instrument. We used an AWG to synchronize the measurements and then transferred the cross-frequency phase calibration of the oscilloscope to the LSNA.

We verified the approach with two 11-tone multisines having 10 MHz and 25 kHz tone spacings, demonstrating that we could transfer the phase calibration of the oscilloscope to the LSNA over a wide range of tone spacing to within accuracy of a fraction of a degree.

## References


[1] J. Verspecht, "Large-Signal Network Analysis," *IEEE Microwave Magazine,* vol. 6, no. 4, pp. 82-92, 2005.

[2] J. Verspecht, "Calibration of a Measurement System for High Frequency Nonlinear Devices," *Ph.D.Thesis, Free University of Brussels,* 1995.

[3] J. Verspecht, D. F. Williams, D. Schreurs, K. A. Remley, and M. D. McKinley, "Linearization of large-signal scattering functions," *IEEE Transactions on Microwave Theory and Techniques,* vol. 53, no. 4, pp. 1369-1376, 2005.

[4] N. B. Carvalho, K. A. Remley, D. Schreurs, and K. G. Card, "Multisine signals for wireless system test and design [Application Notes]," *IEEE Microwave Magazine,* vol. 9, no. 3, pp. 122-138, 2008.

[5] J. Verspecht, F. Verbeyst, and M. Vanden Bossche, "Network Analysis Beyond S-parameters: Characterizing and Modeling Component Behaviour under Modulated Large-Signal Operating Conditions," *ARFTG Conference Digest,* vol. 56, pp. 1-4, 2009.

[6] W. V. Moer and L. Gomme, "NVNA versus LSNA: enemies or friends?," *IEEE Microwave Magazine,* vol. 11, no. 1, pp. 97-103, 2010.

[7] F. Verbeyst, M. V. Bossche, and G. Pailloncy, "Next-generation comb generators for accurate modulated measurements," in *81st ARFTG Microwave Measurement Conference*, 2013, pp. 1-4.

[8] M. V. Bossche, F. Verbeyst, and A. Samant, "Traceable phase calibration of a wide-bandwidth microwave Vector Signal Analyzer," in *2015 IEEE MTT-S International Microwave Symposium*, 2015, pp. 1-4.

[9] J. Verspecht, "Generation and measurement of a millimeter-wave phase dispersion reference signal based on a comb generator," in *2016 IEEE MTT-S International Microwave Symposium (IMS)*, 2016, pp. 1-4.

[10] P. D. Hale, K. A. Remley, D. F. Williams, J. A. Jargon, and C. M. J. Wang, "A compact millimeter-wave comb generator for calibrating broadband vector receivers," in *2015 85th Microwave Measurement Conference (ARFTG)*, 2015, pp. 1-4.

[11] Y. Zhang, Z. He, H. Li, and M. Nie, "Dense Spectral Grid NVNA Phase Measurements Using Vector Signal Generators," *IEEE Transactions on Instrumentation and Measurement,* vol. 63, no. 12, pp. 2983-2992, 2014.

[12] Y. Zhang *et al.*, "Characterization for Multiharmonic Intermodulation Nonlinearity of RF Power Amplifiers Using a Calibrated Nonlinear Vector Network Analyzer," *IEEE Transactions on Microwave Theory and Techniques,* vol. 64, no. 9, pp. 2912-2923, 2016.

[13] K. A. Remley, P. D. Hale, D. F. Williams, and C. M. Wang, "A precision millimeter-wave modulated-signal source," in *Microwave Symposium Digest (IMS), 2013 IEEE MTT-S International*, 2013, pp. 1-3.

[14] A. S. Boaventura, D. F. Williams, G. Avolio, and P. D. Hale, "Traceable Characterization of Broadband Pulse wavefroms Suitable for Cryogenic Josephson Voltage Applications," in *2018 IEEE/MTT-S International Microwave Symposium - IMS*, 2018, pp. 1176-1179.

[15] A. Aldoumani, P. J. Tasker, R. S. Saini, J. W. Bell, T. Williams, and J. Lees, "Operation and calibration of VNA-based large signal RF I-V waveform measurements system without using a harmonic phase reference standard," in *81st ARFTG Microwave Measurement Conference*, 2013, pp. 1-4.

[16] T. S. Clement, P. D. Hale, D. F. Williams, C. M. Wang, A. Dienstfrey, and D. A. Keenan, "Calibration of Sampling Oscilloscopes with High-Speed Photodiodes," *IEEE Trans.Microw.Theory Techn.,* vol. 54, no. 8, pp. 3173-3181, 2006.

[17] P. D. Hale *et al.*, "Traceable waveform calibration with a covariance-based uncertainty analysis," *IEEE Trans.Instrum.Meas.,* vol. 58, pp. 3554-3568, 2009.

[18] P. D. Hale *et al.*, "Traceability of high-speed electrical waveforms at NIST, NPL, and PTB," in *2012 Conference on Precision electromagnetic Measurements*, 2012, pp. 522-523.

[19] C. M. Wang, P. D. Hale, and K. J. Coakley, "Least-squares estimation of time-base distortion of sampling oscilloscopes," *IEEE Trans.Instrum.Meas.,* vol. 48, no. 6, pp. 1324-1332, 1999.

[20] C. M. J. Wang, P. D. Hale, J. A. Jargon, D. F. Williams, and K. A. Remley, "Sequential Estimation of Timebase Corrections for an Arbitrarily Long Waveform," *IEEE Transactions on Instrumentation and Measurement,* vol. 61, no. 10, pp. 2689-2694, 2012.

[21] H. C. Reader, D. F. Williams, P. D. Hale, and T. S. Clement, "Comb-Generator Characterization," *IEEE Transactions on Microwave Theory and Techniques,* vol. 56, no. 2, pp. 515-521, 2008.

[22] M. Schroeder, "Synthesis of low-peak-factor signals and binary sequences with low autocorrelation (Corresp.)," *IEEE Transactions on Information Theory,* vol. 16, no. 1, pp. 85-89, 1970.




Sanders, Aric; Williams, Dylan; Kast, Joshua; Remley, Catherine; Horansky, Robert.
"Large-Signal-Network-Analyzer Phase Calibration on an Arbitrary Grid."
Paper presented at 2019 International Microwave Symposium, Boston, MA, United States. June 2, 2019 - June 7, 2019.

# Investigating the Effects of IF Bandwidth and Averaging on Calibrated Scattering-Parameter Measurements

Jeffrey A. Jargon, Amanda A. Koepke, and Paul D. Hale

National Institute of Standards and Technology, 325 Broadway, M/S 672.03, Boulder, CO 80305 USA
Email: jeffrey.jargon@nist.gov, Tel: +1.303.497.4961

***Abstract* — We investigate the effects of IF (intermediate-frequency) bandwidth and averaging on calibrated scattering-parameter measurements made with a vector network analyzer. We begin by examining the sweep times and noise-floor levels for various combinations of the two settings. Then, we study how these settings influence calibrated measurements and compare the results to uncertainties due to systematic and random effects for devices with varying insertion-loss values.**

***Index Terms* — averaging, bandwidth, calibration, intermediate frequency, measurements, scattering parameters, vector network analyzer.**

## I. Introduction

The dynamic range of a vector network analyzer (VNA) is an important specification. This is especially true when measuring devices with high insertion loss, such as high-valued attenuators and filters, which may have both low-insertion loss in the passband and high-insertion loss in the stopband [1]. There are two ways to extend the dynamic range of a VNA: (1) by increasing the averaging, and (2) by decreasing the bandwidth of the IF filter [2-3].

Most commercial VNAs perform averaging by taking exponentially-weighted moving averages of the complex data from each sweep. Increasing the averaging by a factor of ten lowers the noise floor by 10 dB, but also increases the sweep time by approximately a factor of ten. The IF bandwidth (BW) reduces the noise floor by filtering noise outside the bandwidth of the digital IF filter. Decreasing the IF bandwidth by a factor of ten lowers the noise floor by 10 dB, but also increases the sweep time by almost tenfold. According to reference [2], reducing IF bandwidth has a slightly smaller effect on sweep time than increasing averaging a corresponding amount.

In this paper, we begin by examining the sweep times and noise-floor levels of our commercial VNA for various combinations of averaging and IF bandwidth. Next, we study how these settings influence calibrated measurements for devices with varying insertion-loss values and compare these results to uncertainties due to systematic and random effects.

## II. Sweep Times and Noise Floor

Prior to performing any calibrations, we investigated the sweep times and noise-floor levels of our VNA for various combinations of averages between 1 and 1,000, and IF bandwidths ranging from 1 Hz to 10,000 Hz. To achieve this, we measured a 150-dB attenuator with our VNA at frequencies between 50 MHz and 18 GHz (360 points). From experience, we know the noise-floor level is higher than -150 dBm, so we measured the transmission parameter $S_{21}$ of the attenuator with a VNA output power of 0 dBm.

Table 1 lists the sweep times in seconds for various combinations of averaging and IF bandwidth settings. We did not measure the blank entries, which required sweep times of over an hour. From the tabulated results, we see for a given number of averages, decreasing the IF bandwidth by a factor of ten increases the sweep time by about ten times. Likewise, for a given IF bandwidth, increasing the averages by a factor of ten increases the sweep time approximately tenfold.

Table 2 lists the means of the magnitudes of $S_{21}$ taken over all measured frequencies for various combinations of averaging and IF bandwidth. These means effectively provide us with the noise-floor level of our VNA. From the tabulated results, for a given number of averages, decreasing the IF bandwidth by a factor of ten decreases the noise floor by about 10 dB until a lower limit is reached. Likewise, for a given IF bandwidth, increasing the number of averages by a factor of ten decreases the noise floor by about 10 dB until the lower limit is reached. The lowest value we measured was -131 dB, corresponding to a noise-floor level of -131 dBm.

From Table 2, we find we can reach the lowest noise-floor level with the following combinations (IF BW = 1 Hz and Avg. = 1; IF BW = 10 Hz and Avg. = 10; IF BW = 100 Hz and Avg. = 100; or IF BW = 1,000 Hz and Avg. = 1,000). Each of these combinations requires a sweep time of over ten minutes. If the user does not need the entire dynamic range for their application, other combinations may be chosen that offer much faster sweep times (i.e., IF BW = 10 Hz and Avg. = 1 provides a noise-floor level of -125 dBm with a sweep time of 67 sec.)

Table 1. Sweep time of a vector network analyzer as a function of IF bandwidth and number of averages.

| **Sweep Time (sec.)** | | | | |
|---|---|---|---|---|
| IF BW | Number of Averages | | | |
| (Hz) | 1 | 10 | 100 | 1,000 |
| 1 | 637 | - | - | - |
| 10 | 67 | 687 | - | - |
| 100 | 7 | 74 | 728 | - |
| 1,000 | 1 | 10 | 104 | 1036 |
| 10,000 | <1 | 4 | 40 | 387 |



Jargon, Jeffrey; Koepke, Amanda; Hale, Paul.
"Investigating the Effects of IF Bandwidth and Averaging on Calibrated Scattering-Parameter Measurements."
Paper presented at 93rd ARFTG Microwave Measurement Conference, Boston, MA, United States. June 7, 2019 - June 7, 2019.

Table 2. Mean of a 150-dB attenuator's $|S_{21}|$ values as a function of IF bandwidth and number of averages.

| **mean{\|S21\|} (dB)** | | | | |
|---|---|---|---|---|
| IF BW | Number of Averages | | | |
| (Hz) | 1 | 10 | 100 | 1,000 |
| 1 | -130 | - | - | - |
| 10 | -125 | -130 | - | - |
| 100 | -116 | -125 | -130 | - |
| 1,000 | -106 | -115 | -124 | -131 |
| 10,000 | -96.3 | -106 | -116 | -125 |

## III. Calibrated Measurements

Next, we examined how IF bandwidth influences calibrated measurements for devices with varying insertion-loss values and compared these effects to systematic and random uncertainties.

We performed short-open-load-thru (SOLT) calibrations and measured four devices, an airline, a 20-dB attenuator, a 40-dB attenuator, and a 110-dB attenuator. Measurements were made on a frequency grid from 50 MHz to 18 GHz in steps of 50 MHz at a VNA output power of 0 dBm with 3.5 mm coaxial connectors. The offline calibrations and associated uncertainty analyses were performed using the NIST Microwave Uncertainty Framework (MUF) [4-6].

The calibration standards and devices were each measured using Avg. = 1 and IF bandwidths of 10 Hz, 100 Hz, 1,000 Hz, and 10,000 Hz. In this experiment, we kept the number of averages constant, while varying the IF bandwidth. We could have also kept the IF bandwidth constant, and varied the number of averages, but since the two methods have the same effect, we chose the former since reducing IF bandwidth is a more common practice. To avoid variations due to repeated connections, each calibration standard and device was measured at all the IF-bandwidth settings without disconnections. From a previous study, we know that variability due to repeated measurements without disconnections is very low [7]. For example, we connected our short standard to the VNA and measured it at each of the various IF-bandwidth settings prior to disconnecting it and connecting the open standard. After all the standards and devices were measured and the data saved, we performed four offline calibrations at the respective IF-bandwidth settings. Thus, we could isolate the effects of IF bandwidth from connector repeatability.

Figures 1 and 2 illustrate measurements of $|S_{21}|$ for the 40-dB and 110-dB attenuators, respectively, at the various IF-bandwidth settings. For the 40-dB attenuator, the measurements were noticeably noisier at the higher IF-bandwidth settings but followed the same curve as a function of frequency. In contrast, measurements of the 110-dB attenuator were not just noisier at the higher-bandwidth settings, but the noise-floor levels at the 1,000 Hz and 10,000 Hz settings were too high to accurately measure the device.

To quantify the effect of varying the IF bandwidth, including noise and amplitude offset, we considered one setting as a baseline (IF BW = 10 Hz and Avg. = 1), and compared measurements taken with the other settings to the baseline using the mean (over the frequencies) of the absolute values of the differences of the two $S_{21}$ magnitudes. For example, to compare the baseline $S_{21}$ magnitude (IF BW = 10 Hz and Avg. = 1) to the setting of IF BW = 100 Hz and Avg. = 1, we calculated

$$\text{mean}\{\text{abs}[|S_{21}|_{\text{IFBW=100Hz}} - |S_{21}|_{\text{IFBW=10Hz}}]\}.$$

These differences, reported in Table 3, increase as the IF BW increases for all the measured devices.

To put the differences between IF bandwidth settings in context, we quantified the uncertainties due to systematic and random effects using the baseline setting (IF BW = 10 Hz and Avg. = 1). To determine the uncertainties due to random effects, we repeated the calibration five times with disconnects between every device and standard measurement. Figures 3 and 4 illustrate repeated measurements of $|S_{21}|$ for the 40-dB and 110-dB attenuators, respectively.

From these repeated measurements, we used the half-width of a prediction interval to describe the spread of the measurement results at a given frequency and a reasonable range for a new observation [8]. The half-width for a two-sided 95% prediction interval (referred to as "95% HW Random") is

$$t_{.975,n-1}s\left(1+\frac{1}{n}\right)^{1/2},$$

where $n$ = 5, $t_{.975,4}$ = 2.776, and $s$ is the sample standard deviation of the five $S_{21}$ magnitudes at that frequency. This half-width tells us how far we expect a new measurement taken with this baseline setting to be from the mean of these five measurements. We report the mean value (over the frequencies) of this half-width as "mean{95% HW Random}" for each measured device in Table 3.

In Table 3, we also report the mean values (over the frequencies) for the half-widths reported by the MUF for the uncertainties due to systematic effects for one of the calibrations as "mean{95% HW Systematic}." The random and systematic half-widths give us a sense of scale when comparing against the differences calculated from the various IF-bandwidth settings. This is not a statistical test for significant differences, but rather a general guideline for the range of differences we expect to see due to random and systematic effects. Here we assumed that the uncertainty about the baseline measurement used to calculate the differences was the same as the uncertainty for the distribution we observed for the five repeat calibrations under the baseline setting. This provides us with an idea of how unlikely these differences are, given the distribution of baseline measurements and the uncertainty due to systematic effects. Figures 5 and 6 illustrate 95% uncertainty bounds of $|S_{21}|$ for the 40-dB and 110-dB attenuators, respectively.

Jargon, Jeffrey; Koepke, Amanda; Hale, Paul.
"Investigating the Effects of IF Bandwidth and Averaging on Calibrated Scattering-Parameter Measurements."
Paper presented at 93rd ARFTG Microwave Measurement Conference, Boston, MA, United States. June 7, 2019 - June 7, 2019.

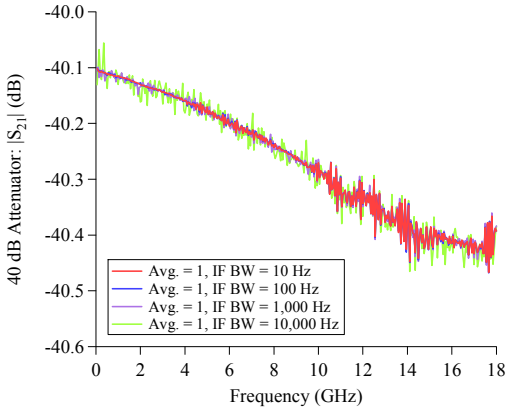


Fig. 1. Measurements of $|S_{21}|$ for the 40-dB attenuator at various IF bandwidth settings.

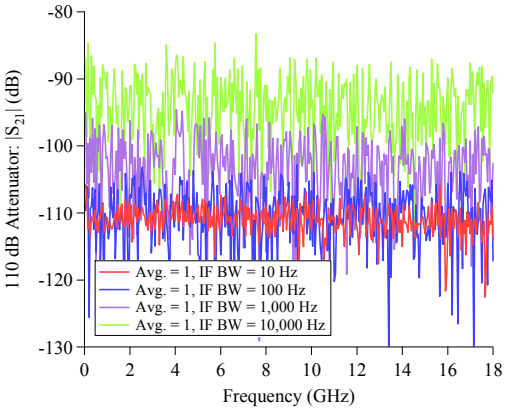


Fig. 2. Measurements of $|S_{21}|$ for the 110-dB attenuator at various IF bandwidth settings.

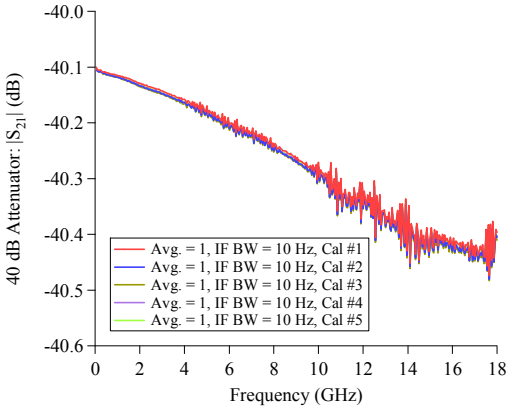


Fig 3. Five repeated measurements of $|S_{21}|$ for the 40-dB attenuator at an IF bandwidth of 10 Hz.

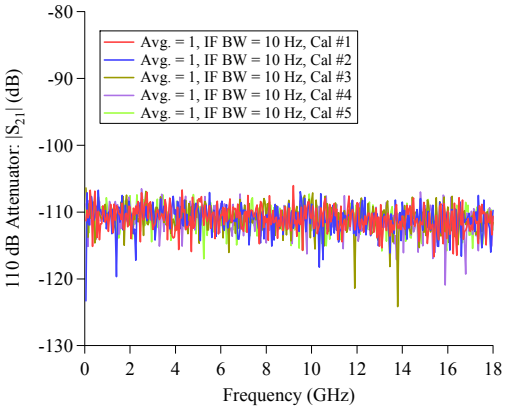


Fig 4. Five repeated measurements of $|S_{21}|$ for the 110-dB attenuator at an IF bandwidth of 10 Hz.

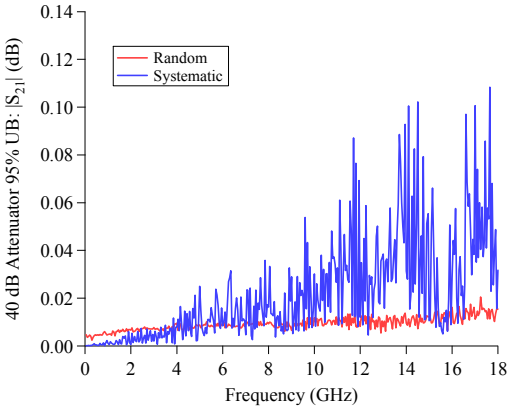


Fig. 5. The 95% interval half-widths for uncertainties of the 40-dB attenuator at an IF bandwidth of 10 Hz.

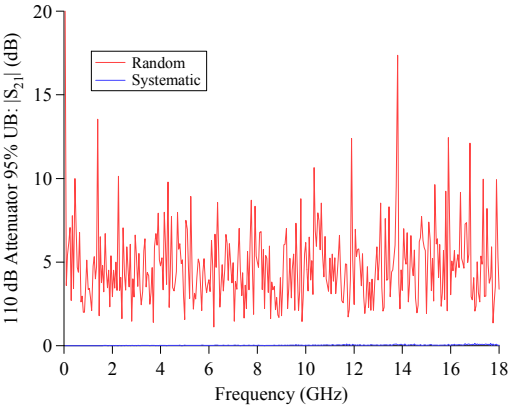


Fig. 6. The 95% interval half-widths for uncertainties of the 110-dB attenuator at an IF bandwidth of 10 Hz.

Jargon, Jeffrey; Koepke, Amanda; Hale, Paul.
"Investigating the Effects of IF Bandwidth and Averaging on Calibrated Scattering-Parameter Measurements."
Paper presented at 93rd ARFTG Microwave Measurement Conference, Boston, MA, United States. June 7, 2019 - June 7, 2019.

Table 3. Comparison of baseline setting (IF BW = 10 Hz) to other IF BW settings, and 95% interval half-widths for the airline and attenuators.

| **Airline** | |
|---|---|
| mean{abs[$\|S_{21}\|_{IFBW=100Hz}$ - $\|S_{21}\|_{IFBW=10Hz}$]} | 0.0006 dB |
| mean{abs[$\|S_{21}\|_{IFBW=1,000Hz}$ - $\|S_{21}\|_{IFBW=10Hz}$]} | 0.0010 dB |
| mean{abs[$\|S_{21}\|_{IFBW=10,000Hz}$ - $\|S_{21}\|_{IFBW=10Hz}$]} | 0.0024 dB |
| mean{95% HW Random} | 0.0189 dB |
| mean{95% HW Systematic} | 0.0218 dB |
| **20 dB Attenuator** | |
| mean{abs[$\|S_{21}\|_{IFBW=100Hz}$ - $\|S_{21}\|_{IFBW=10Hz}$]} | 0.0003 dB |
| mean{abs[$\|S_{21}\|_{IFBW=1,000Hz}$ - $\|S_{21}\|_{IFBW=10Hz}$]} | 0.0006 dB |
| mean{abs[$\|S_{21}\|_{IFBW=10,000Hz}$ - $\|S_{21}\|_{IFBW=10Hz}$]} | 0.0039 dB |
| mean{95% HW Random} | 0.0067 dB |
| mean{95% HW Systematic} | 0.0210 dB |
| **40 dB Attenuator** | |
| mean{abs[$\|S_{21}\|_{IFBW=100Hz}$ - $\|S_{21}\|_{IFBW=10Hz}$]} | 0.0013 dB |
| mean{abs[$\|S_{21}\|_{IFBW=1,000Hz}$ - $\|S_{21}\|_{IFBW=10Hz}$]} | 0.0040 dB |
| mean{abs[$\|S_{21}\|_{IFBW=10,000Hz}$ - $\|S_{21}\|_{IFBW=10Hz}$]} | 0.0116 dB |
| mean{95% HW Random} | 0.0093 dB |
| mean{95% HW Systematic} | 0.0218 dB |
| **110 dB Attenuator** | |
| mean{abs[$\|S_{21}\|_{IFBW=100Hz}$ - $\|S_{21}\|_{IFBW=10Hz}$]} | 3.920 dB |
| mean{abs[$\|S_{21}\|_{IFBW=1,000Hz}$ - $\|S_{21}\|_{IFBW=10Hz}$]} | 8.253 dB |
| mean{abs[$\|S_{21}\|_{IFBW=10,000Hz}$ - $\|S_{21}\|_{IFBW=10Hz}$]} | 16.37 dB |
| mean{95% HW Random} | 4.781 dB |
| mean{95% HW Systematic} | 0.024 dB |

Examining Table 3 in more detail, we made several observations: (1) the mean{95% HW Random} is higher for the airline than for the 20-dB and 40-dB attenuators, which may be attributed to the airline being more difficult to connect due to its "floating" center conductor; (2) the mean{95% HW Random} for the 110-dB attenuator is much higher than for the other devices since its measurement is approaching the noise-floor level of the VNA; (3) the mean{95% HW Systematic} for the four devices have similar values since they all share the same calibration standards and associated uncertainties; (4) all the means of the differences due to varying IF bandwidth settings are less than mean{95% HW Random} for the airline and 20-dB attenuator, and just slightly larger for the 40-dB attenuator at the highest IF bandwidth setting; (5) the means of the differences due to varying IF bandwidth settings are on the same order or greater than the mean{95% HW Random} for the 110-dB attenuator due to increased noise and amplitude offsets.

## IV. Conclusions

We investigated the effects of averaging and IF bandwidth on calibrated scattering-parameter measurements made with a VNA. We began by examining the sweep times and noise-floor levels for various combinations of the two settings. We verified that decreasing the IF bandwidth by a factor of ten decreases the noise floor by about 10 dB until a lower limit is reached and increasing the averaging by a factor of ten decreases the noise floor by about 10 dB until the lower limit is reached. Next, we studied how these settings influence calibrated measurements and compared the results to uncertainties due to systematic and random effects for devices with varying insertion-loss values. We found that at lower attenuation levels, the mean difference (over frequency) we see between measurements made with different IF bandwidth settings and the baseline are similar in magnitude to the mean difference (over frequency) we expect to see between a new measurement under the baseline setting and the mean of the replicate baseline measurements (quantified by mean{95% HW Random}). Thus, the user may employ higher IF bandwidths or less averaging for faster sweep times without a significant penalty in terms of uncertainty. However, as the attenuation levels approach the VNA's noise-floor level, it becomes more important to choose a lower IF bandwidth setting or make use of more averaging.


## Acknowledgement

The authors thank Jolene Splett, Jerome Cheron, Ari Feldman, and Dylan Williams for their helpful comments.


## References


[1] Y. S. Lee, "Testing Dynamic Accuracy of Vector Network Analyzers Using the 40 GHz Step Attenuator," *65th ARFTG Microwave Measurement Conference*, Long Beach, CA, Jun. 2005.

[2] "Understanding and Improving Network Analyzer Dynamic Range," Keysight Application Note, 2018.

[3] M. Hiebel, "Fundamentals of Vector Network Analysis," Rohde & Schwarz, 2008.

[4] D. F. Williams, NIST Microwave Uncertainty Framework, Beta Version, www.nist.gov/services-resources/software/wafer-calibration-software, 2017.

[5] A. Lewandowski, D. F. Williams, P. D. Hale, C. M. Wang, and A. Dienstfrey, "Covariance-Matrix-Based Vector-Network-Analyzer Uncertainty Analysis for Time- and Frequency-Domain Measurements," IEEE Trans. Microwave Theory Tech., vol. 58, no. 7, pp. 1877-1886, July 2010.

[6] J. A. Jargon, C. H. Cho, D. F. Williams, and P. D. Hale, "Physical Models for 2.4 mm and 3.5 mm Coaxial VNA Calibration Kits Developed within the NIST Microwave Uncertainty Framework," *85th ARFTG Microwave Measurement Conference*, Phoenix, AZ, May 2015.

[7] A. Koepke and J. A. Jargon, "Quantifying Variance Components for Repeated Scattering-Parameter Measurements," *90th ARFTG Microwave Measurement Conference*, Boulder, CO, Nov. 2018.

[8] G. J. Hahn and W. Q. Meeker, "Statistical Intervals: A Guide for Practitioners," vol. 92, John Wiley & Sons, 201

# An Approach for Characterizing the Frequency Response of Sampling-Oscilloscopes Using a Large-Signal Network Analyzer

Alirio S. Boaventura[#^1], Dylan F. Williams[#2], Paul D. Hale[#], Gustavo Avolio[$3]
[#]Communications Technology Laboratory, National Institute of Standards and Technology, USA
[^]Department of Physics, University of Colorado Boulder, USA
[$]Anteverta-mw, The Netherlands
[1]aliriodejesus.soaresboaventura@nist.gov, [2]dylan.williams@nist.gov, [3]gustavo@anteverta-mw.com

***Abstract*—We propose an approach for characterizing the complex frequency response of sampling oscilloscopes using a calibrated large-signal network analyzer (LSNA) and a broadband pulse source. First, we perform a full wave-parameter calibration of the LSNA using its internal continuous wave (CW) sources. Then, we replace the internal CW sources with an external broadband pulse source and measure it with the calibrated LSNA and oscilloscope connected to the LSNA test port. The complex frequency response of the oscilloscope's sampler is derived in the frequency domain as the ratio of the oscilloscope signal spectrum to the calibrated LSNA signal spectrum. We achieve less than 0.7 dB amplitude and 5 degrees phase difference up to 45 GHz between the proposed LSNA calibration and previous NIST electro-optic sampling (EOS) characterization of the same sampler.**

***Keywords*—Sampling-oscilloscope characterization, large-signal network analysis, standard transfer.**

## I. Introduction

There has been a growing interest in the use of sampling oscilloscopes for microwave applications [1]-[3], due to their flexibility, low cost and increasing bandwidths. However, at microwave frequencies, oscilloscopes must be corrected for imperfections such as jitter, time-base distortion, impedance mismatch and frequency response [1].

The frequency response is typically characterized using an electro-optic sampling (EOS)-characterized high-speed pulse source [4]-[6]. This source is measured by the oscilloscope and the frequency response is derived by deconvolving the known reference signal from the measured signal. The deconvolution is usually performed in the frequency domain by dividing the measured signal spectrum by the reference signal spectrum, yielding the scope response.

In [7], we compared waveform measurements made simultaneously with an LSNA and a sampling oscilloscope, both calibrated to the same reference plane. In the present paper, we leverage the concepts presented in [7] and propose an approach for extracting the complex frequency response of a sampling oscilloscope using a calibrated LSNA to calibrate a broadband pulse at the reference plane of the oscilloscope.

The key points of our approach include: 1) the reference pulse source does not need to be pre-characterized, 2) the measurements are performed without disconnecting the measurement instruments, 3) oscilloscope match measurement is not required, 4) as a consequence of 2 and 3, the impact of drift and measurement uncertainty is reduced, 5) This approach provides a convenient way of traceably transferring NIST EOS absolute phase and calorimetric power to sampling oscilloscopes using a calibrated LSNA.

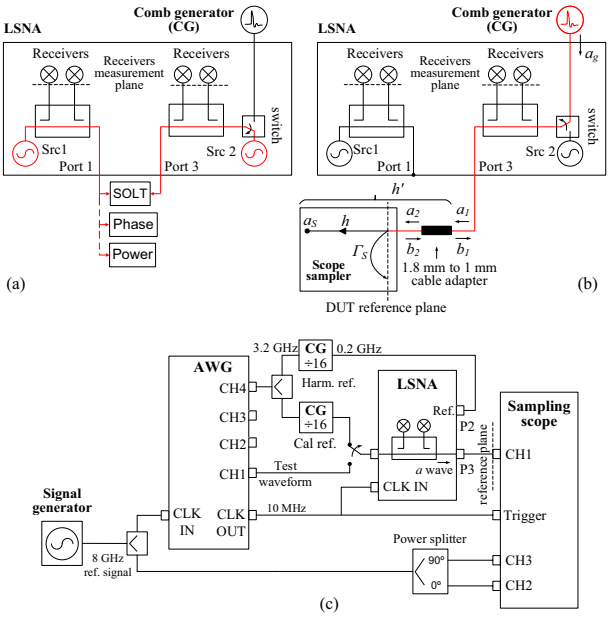


Fig. 1 a) LSNA calibration setup. b) Setup used during the scope characterization. c) Illustration of the measurement synchronization scheme.

## II. Measurement Setup

The measurement setup is shown in Fig. 1. First, the LSNA was calibrated using its internal continuous wave (CW) sources (Fig. 1a). Afterward, the LSNA source on port 3 was replaced with an external comb generator during the scope characterization experiment (Fig. 1b) and with an arbitrary waveform generator (AWG) during the validation measurements (Fig. 1c). In both cases, the external signal was passed through the LSNA test set and fed into the oscilloscope through the LSNA test port 3.

Passing the signal of interest through the LSNA test set allows us to perform the LSNA and oscilloscope measurements without disconnecting the instruments, which reduces drift and measurement uncertainty related to cable movement and connector repeatability.

Soares Boaventura, Alirio De Jesus; Williams, Dylan; Hale, Paul; Gustavo, Avolio.
"An Approach for Characterizing the Frequency Response of Sampling-Oscilloscopes Using a Large- Signal Network Analyzer."
Paper presented at International Microwave Symposium Digest, 2019, Boston, MA, United States. June 2, 2019 - June 7, 2019.

Synchronization is key in this experiment, as all equipment including the LSNA (Keysight PNA-X N5245A[1]), sampling oscilloscope (Keysight sampling head 86118A), phase references (Keysight comb generators U9391F) and AWG (Keysight M8195A) must be locked to the same reference signal (see Fig. 1c). An 8 GHz sine-wave signal generated by an external signal generator was used as the master reference signal to which all the others were locked.

In addition to generating validation test signals on channel 1, the AWG synchronously triggers the sampling oscilloscope and clocks the LSNA through its 10 MHz output clock and drives the comb generators with a 3.2 GHz signal generated on channel 4.

An in-phase and quadrature (IQ) signal derived from the 8 GHz reference was measured by the oscilloscope simultaneously with the waveform of interest. This signal was used in the NIST Time-Base Correction (TBC) algorithm to correct for jitter and other time-base distortions in the oscilloscope-measured signal [8].

## III. Complex Frequency Response Characterization

### A. LSNA calibration and measurements

The two-step procedure used to perform calibrated LSNA measurements with an external source is illustrated in Fig. 1:

1. First, we operated the LSNA in the default configuration using its internal CW sources, and performed short-open-load (SOLT), absolute amplitude and absolute phase calibrations (Fig. 1a).
2. Then, with the sampling oscilloscope connected to the LSNA front test port 3, we routed that port to the LSNA back-panel connector, where a 50 GHz bandwidth comb generator was connected during the oscilloscope characterization, and a 65 GSample/s, 20 GHz bandwidth AWG was connected during the validation measurements (see Fig. 1b and 1c). Note that changing the source configuration does not affect the calibration performed in step 1, as the full-wave calibration is independent of the source [9].

We measured 0.2 GHz and 1 GHz harmonic signals. For the 0.2 GHz signals, we used a 0.2 GHz to 50 GHz measurement grid with a step of 0.2 GHz, and for the 1 GHz signals, we used a 1 GHz to 50 GHz measurement grid with a step of 1 GHz. For both measurements, we drove the comb generators with a 3.2 GHz signal generated on the AWG channel 4 and we set their divide ratios to 16, defining a frequency resolution of 0.2 GHz.

### B. Deriving the oscilloscope complex frequency response

First, we applied the NIST TBC algorithm [8] to the oscilloscope raw data to correct for time-base distortion, using the IQ signal measured on channels 2 and 3, and we interpolated the corrected waveform to a uniform time grid.

After calibrating the LSNA data (referenced to the input of the cable adapter, Fig. 1b[2]), we derived the complex frequency response of the oscilloscope plus cable adapter cascade, $h'$. This was done in the frequency domain by dividing the Fourier transform of the TBC-corrected oscilloscope signal, $a_s$, by the calibrated LSNA signal, $a_{1\mathrm{LSNA}}$ (1).

Afterward, we used (2) to de-embed the cable adapter and find the oscilloscope frequency response, $h$. De-embedding the cable adapter was necessary to compare our results to the previous NIST characterization [5], which is referenced to the input of the oscilloscope sampling head (without the cable adaptor).

In addition, we defined a scaling factor, $\alpha$, to amplitude-normalize the NIST characterization, $h_{\mathrm{NIST}}$, to the amplitude of the LSNA fundamental component measured here (3).

$$h'(\omega) = \frac{a_s(\omega)}{a_{1\mathrm{LSNA}}(\omega)} \tag{1}$$

$$h(\omega) = h'(\omega)\frac{1-\Gamma_S(\omega)S_{22}(\omega)}{S_{21}(\omega)}$$

$$= h'(\omega)\left(S_{21}(\omega) + S_{22}(\omega)\frac{b_1(\omega) - a_1(\omega)S_{11}(\omega)}{a_1(\omega)S_{12}(\omega)}\right)^{-1} \tag{2}$$

$$\alpha = \frac{|h(\omega_0)|}{|h_{\mathrm{NIST}}(\omega_0)|} \tag{3}$$

where $a_{1\mathrm{LSNA}}$ is the LSNA calibrated measurement, $a_s$ is the oscilloscope data (after TBC-correction), $S_{21}$ and $S_{22}$ are measured scattering parameters of the cable adapter and $\Gamma_S$ is the measured reflection coefficient of the oscilloscope sampling head. Since LSNA-calibrated measurements of $a_1$ and $b_1$ are available, using the right side of (2) to de-embed the cable adapter avoids the uncertainty in a separate measurement of $\Gamma_S$.

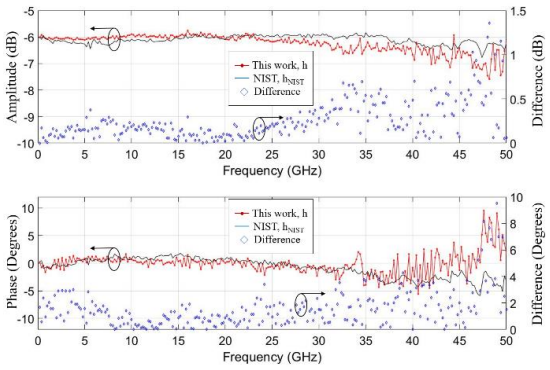


Fig. 2 Frequency response of Keysight sampling head 86118A obtained in this work and previously obtained by NIST.

[1] We specify brand names only to better explain the experiments. NIST does not endorse commercial products. Other products may perform as well or better.

[2] A 1.85 mm to 1 mm cable adapter was required to interconnect the 2.4 mm LSNA to a 1 mm connector attached to the oscilloscope sampling head.



Soares Boaventura, Alirio De Jesus; Williams, Dylan; Hale, Paul; Gustavo, Avolio.
"An Approach for Characterizing the Frequency Response of Sampling-Oscilloscopes Using a Large- Signal Network Analyzer."
Paper presented at International Microwave Symposium Digest, 2019, Boston, MA, United States. June 2, 2019 - June 7, 2019.

## IV. Measurement Results

### A. Extracting the oscilloscope complex frequency response

The comb generator used in our experiment has low amplitude compared to the dynamic range of the measurement instruments. Furthermore, the LSNA that we used presents a large back-to-front panel insertion loss. As such, the signal-to-noise ratio (SNR) of the comb waveform measurement is degraded when the signal is passed through the LSNA test set, especially at higher frequencies.

This was evaluated in [7], where it was also found that this LSNA presents lower insertion loss at port 3 (14 dB at 50 GHz) compared to port 1 (22 dB at 50 GHz). For that reason, we used port 3 in this experiment.

To further improve the measurement quality: 1) we reduced the LSNA IF bandwidth to 3 Hz and averaged 10 measurements of the calibration phase reference and 28 measurements of the test comb generator. 2) we corrected the time-base of the oscilloscope for jitter and time-base distortion and we averaged 1000 oscilloscope measurements.

Fig. 2 shows the frequency response of the Keysight sampling head 86118A obtained in this work and previously obtained by NIST, up to 50 GHz. The NIST frequency response was normalized to the LSNA fundamental amplitude using the scaling factor $\alpha$. We achieved less than 0.7 dB amplitude difference and less than 5 degrees phase difference up to 45 GHz.

### B. Validating the proposed approach

To validate our procedure, we replaced the comb generator used during the oscilloscope characterization with an AWG, which was used to generate several test signals, including a 200 MHz square wave, a 1 GHz square wave and a 1 GHz pulse repetition rate sinc-like waveform. We measured these signals with the LSNA, we calibrated them and translated them to the reference plane of the sampling oscilloscope.

Without disconnecting the instruments, we measured the same signals with the sampling oscilloscope and we corrected for jitter and time-base distortion. Afterward, we corrected for the frequency response of the oscilloscope obtained in this work, $h$, and previously obtained by NIST, $h_{\mathrm{NIST}}$. Finally, we time-aligned all the waveforms by phase-normalizing them to their fundamental components. The results, presented in Fig. 3, display excellent agreement.

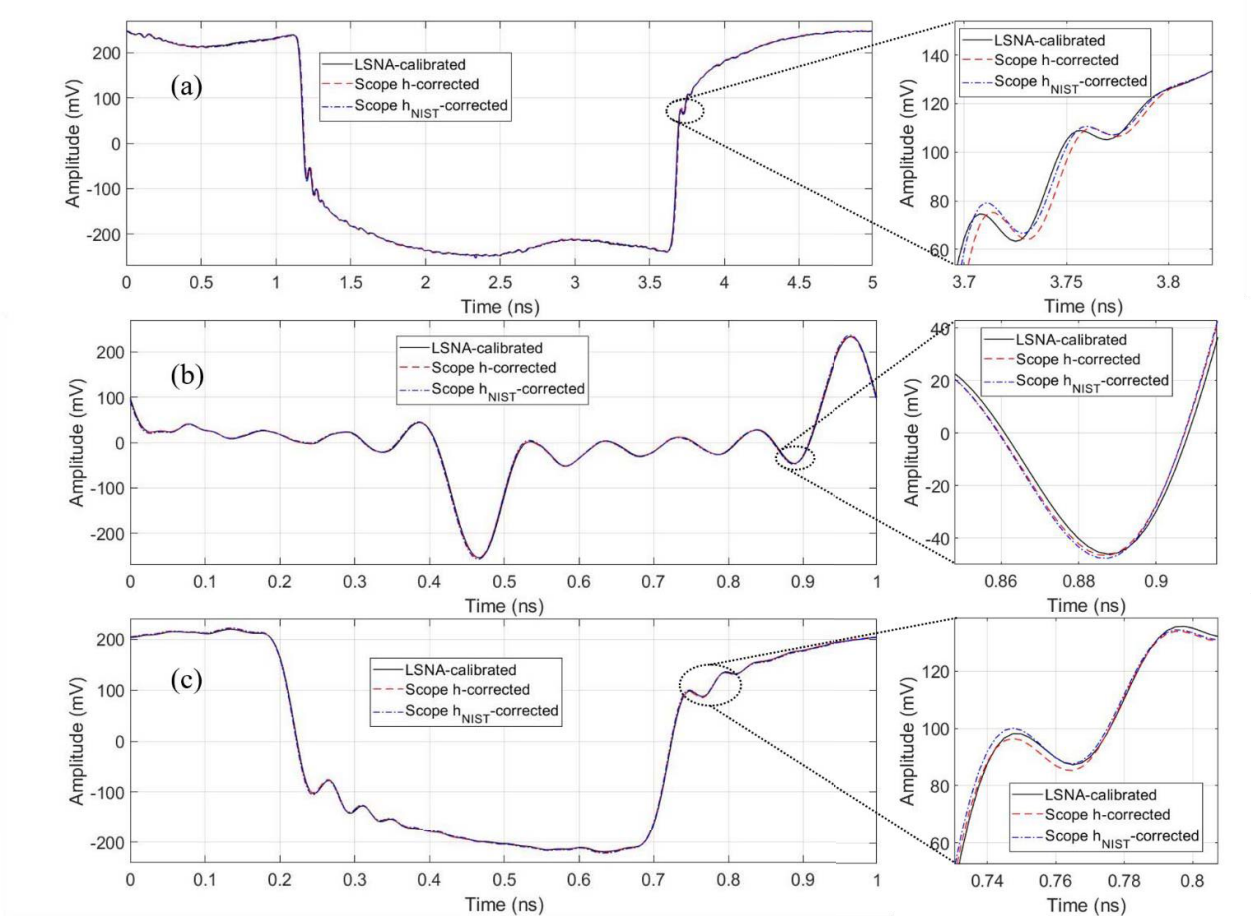


Fig. 3 Reconstructed incident wave at the oscilloscope input, calibrated with the LSNA and corrected for the oscilloscope frequency response obtained in this work and previously obtained by NIST. a) 200 MHz square wave, b) 1 GHz sinc-like waveform, c) 1 GHz square wave.



Soares Boaventura, Alirio De Jesus; Williams, Dylan; Hale, Paul; Gustavo, Avolio.
"An Approach for Characterizing the Frequency Response of Sampling-Oscilloscopes Using a Large- Signal Network Analyzer."
Paper presented at International Microwave Symposium Digest, 2019, Boston, MA, United States. June 2, 2019 - June 7, 2019.

## V. Conclusion

We proposed a new approach for characterizing the complex frequency response of sampling oscilloscopes that enables traceable standards transfer through a calibrated LSNA. We showed good agreement between our results and previous NIST results, typically less than 0.7 dB amplitude and 5 degrees phase difference up to 45 GHz.

As an alternative to the use of an external broadband source to characterize the oscilloscope, the internal LSNA CW source could be swept across the bandwidth of interest. However, using an external broadband source significantly reduces the oscilloscope measurement time, as the signal is acquired in the time-domain in a single take. Furthermore, cross-frequency phase-coherence is desired in some applications [10].

Improvements to our setup and procedure may include the use of external couplers to improve the SNR of the LSNA measurements and the use of a two-tier calibration approach that includes the cable adapter.

## References


[1] D. Williams et al., "The Sampling Oscilloscope as a Microwave Instrument," *IEEE Microwave Mag.*, vol. 8, no. 4, pp. 59-68, Aug. 2007.

[2] K. A. Remley *et al*., "Millimeter-Wave Modulated-Signal and Error-Vector-Magnitude Measurement With Uncertainty," in *IEEE Transactions on Microwave Theory and Techniques*, vol. 63, no. 5, pp. 1710-1720, May 2015.

[3] D. F. Williams *et al*., "Sampling-oscilloscope measurement of a microwave mixer with single-digit phase accuracy," in *IEEE Transactions on Microwave Theory and Techniques*, vol. 54, no. 3, pp. 1210-1217, March 2006.

[4] D. Henderson et al., "Recent developments in the calibration of fast sampling oscilloscopes," *IEE Proc*., vol. 139, no. 5, pp. 254–260, Sept. 1992.

[5] T. S. Clement, et al., "Calibration of sampling oscilloscopes with high-speed photodiodes," *IEEE Transactions on Microwave Theory and Techniques*, vol. 54, no. 8, pp. 3173-3181, Aug. 2006.

[6] Fuser H. et al. "Optoelectronic time-domain characterization of a 100 GHz sampling oscilloscope", Meas. Science and Tech., 2012. 23 1–10.

[7] Alirio Boaventura et al., "Traceable Characterization of Broadband Pulse Waveforms using a Large Signal Network Analyzer and a Sampling Oscilloscope", IMS 2018, Pennsylvania, June 2018.

[8] P. D. Hale et al., "Compensation of Random and Systematic Timing Errors in Sampling Oscilloscopes," *IEEE Trans. on Inst. and Meas.*, vol. 55, no. 6, 2146-2154, Dec. 2006.

[9] Valeria Teppati, Andrea Ferrero and Mohamed Sayed, "Modern RF and Microwave Measurement Techniques", Cambridge University Press, Cambridge UK, July 2013.

[10] D. Kim et al. "Traceable calibration for a digital real-time oscilloscope with time interleaving architecture", Meas. Science and Tech., 29 015003, 2018.




Soares Boaventura, Alirio De Jesus; Williams, Dylan; Hale, Paul; Gustavo, Avolio.
"An Approach for Characterizing the Frequency Response of Sampling-Oscilloscopes Using a Large- Signal Network Analyzer."
Paper presented at International Microwave Symposium Digest, 2019, Boston, MA, United States. June 2, 2019 - June 7, 2019.

# Accurate Monte Carlo Uncertainty Analysis for Multiple Measurements of Microwave Systems

Benjamin F. Jamroz[#1], Dylan F. Williams[#2], Jacob D. Rezac[#3], Michael Frey[$4], Amanda A. Koepke[$5]
[#]Communications Technology Lab, National Institute of Standards and Technology, USA
[$]Information Technology Lab, National Institute of Standards and Technology, USA
[1]benjamin.jamroz@nist.gov, [2]dylan.williams@nist.gov, [3]jacob.rezac@nist.gov, [4]michael.frey@nist.gov, [5]amanda.koepke@nist.gov

***Abstract* — Uncertainty analysis of microwave electronic measurements enables the quantification of device performance and aides in the development of robust technology. The Monte Carlo method is commonly used to attain accurate uncertainty analyses for complicated nonlinear systems. Combining multiple similar measurements, each with a Monte Carlo uncertainty analysis, allows one to incorporate the uncertainty given by their spread. In this paper, we compare two Monte Carlo sampling methods, illustrate that one method reduces the bias of averaged quantities, show how this impacts computed uncertainties, and highlight microwave applications for which this corrected method can be applied.**

***Keywords* — Measurement uncertainty, Monte Carlo methods, Microwave technology.**

## I. Introduction

Uncertainty analysis quantifies the precision of measurements and facilitates accurate characterization of systems; Here we focus on applications to microwave engineering. The Monte Carlo method is a key component of uncertainty analysis [1] and is primarily used to propagate uncertainties through nonlinear transformations. It has been used by several national metrology institutes [2], [3] to accurately determine uncertainty in high-frequency electronic measurements and systems. At the Communications Technology Lab at the National Institute of Standards and Technology (NIST) we perform Monte Carlo analyses for many of our measurements including VNA calibrations [4], electro-optic sampling [5], as well as derived communication metrics including error vector magnitude (EVM) [6].

Repeating equivalent measurements gives insight into variability, noise, etc., allowing a more complete characterization of the measurement setup and environment. Incorporating the spread of these measurements in uncertainty analyses often increases the estimate of uncertainty in the measurement. This can account for differing or changing environments (including temperature or humidity fluctuations), lack of precise control in the measurement (including connection repeatability [7], cable bending [6], probe placement or other spatial positioning), reproducibility using different components [8] or other unknown random processes (*e.g.* unknown radio-frequency interference in the laboratory). Thus it is often of interest to combine multiple measurements, each with their own errors, to determine the mean measurement response and its associated variability.

For Monte Carlo uncertainty analyses, this requires combining multiple Monte Carlo samples, one for each measurement, to calculate an estimate of the mean response and its variance as represented by a further Monte Carlo sample. Frey *et al.* [9] analyzed two Monte Carlo sampling methods applied to this situation, determined that one of the variants is typically more accurate, and recommended its use in the NIST Microwave Uncertainty Framework (MUF), a software tool for representing, propagating, and reporting uncertainty in microwave measurement systems.

In this paper we illustrate the trade-offs of these Monte Carlo sampling techniques, verify their implementation in the MUF, and discuss the relevance to microwave systems. We begin with a review of covariance-based uncertainty analysis and the Monte Carlo method.

## II. Uncertainty Analysis

Covariance-based uncertainty analysis [10] preserves correlations across records (*e.g.* time records or frequency data) through transformations. This allows the accurate propagation of uncertainties in measurements through to derived data, including corrected device responses, modulated signals, or system-level metrics. Linear transfomations, such as the Fourier transform, can use sensitivity analysis [11] to propagate these uncertainties. However, sensitivity analysis assumes that the transformation is linear and reduces to a local approximation for nonlinear transformations.

### A. The Monte Carlo Method

The typical method for propagating uncertainties through nonlinear transformations is the Monte Carlo method. This method tracks the statistical biases introduced by nonlinearities, which are not captured by a sensitivity analysis. These biases can include differences of the center (mean), spread (variance) and shape of the probability distribution of the transformed data.

Here we represent a quantity with known uncertainty as a random variable $S$ which is characterized by a nominal value, $s_{\text{nom}}$, and a probability distribution. The Monte Carlo method draws random realizations of $S$ from the probability distribution, attaining a sample of size $Q$ as $\{s_q\}_{q=1}^{Q}$.

Repeated measurements of a quantity can give an estimate of its uncertainty. Taking multiple, $J$, measurements of a



Jamroz, Benjamin; Williams, Dylan; Rezac, Jake; Frey, Michael; Koepke, Amanda.
"Accurate Monte Carlo Uncertainty Analysis for Multiple Measurements of Microwave Systems."
Paper presented at 2019 International Microwave Symposium, Boston, MA, United States. June 2, 2019 - June 7, 2019.

random variable $X$ gives a sample $\{x_j\}_{j=1}^{J}$ of its distribution. These data can be propagated through transformations to obtain uncertainty in derived measurements. One relevant transformation for high-frequency measurements takes a form similar to

$$Y = F(X, S) \tag{1}$$

which maps the random variables $X$ and $S$ into another random variable $Y$. Equations of the form Eq. (1) can represent a correction or calibration of measured data $X$ using a standard $S$ which is only known up to some uncertainty. The Monte Carlo method maps the nominal values

$$y_{j,\text{nom}} = F(x_j, s_{\text{nom}}) \tag{2}$$

and Monte Carlo samples

$$y_{j,q} = F(x_j, s_q) \tag{3}$$

for $j = 1, \ldots, J$ and $q = 1, \ldots, Q$ through this transformation. Thus, for each $j$ we have a complete Monte Carlo uncertainty analysis of $y_j$: a nominal value $y_{j,\text{nom}}$ and a Monte Carlo sample $\{y_{j,q}\}_{q=1}^{Q}$. The $y_j$ incorporate the uncertainty due to the uncertainty in $S$, however the spread of the $x_j$ has not been included in these individual quantities.

In order to calculate the mean and the uncertainty of the mean of the $y_j$, we need to combine the $y_j$ to capture the uncertainty due to the spread of the $x_j$. That is, we want to combine the multiple Monte Carlo samples to produce a new Monte Carlo sample which estimates the mean of these data and the uncertainty in the mean. However, as the random variable $S$ is shared across all of the $J$ measurements the values $s_q$ are perfectly correlated across all of the $y_{j,q}$. In combining these data, care must be taken to preserve this correlation.

### B. The Microwave Uncertainty Framework

The NIST MUF is a tool that performs covariance-based and Monte Carlo uncertainty analyses for high-frequency electronic measurements. It supports many operations used in microwave and millimeter wave applications including calibrations, de-embedding, transformations between the time and frequency domains, and the evaluation of system metrics such as EVM. The MUF propagates uncertainties in parameters through such operations obtaining uncertainty in derived quantities. The specified uncertainty in the parameters is typically given by an *a priori* model of the uncertainty in these values. Examples for which a model can be provided include uncertainties in the length of a transmission line or in the alignment of a waveguide. However, there are some uncertainty mechanisms which are difficult or impossible to model. Often these uncertainties are characterized using multiple measurements. Therefore, the process of estimating uncertainties from multiple measurements is an essential issue for users of the MUF and is an important feature that should be handled accurately.

## III. Monte Carlo Sampling Methods

Frey *et al.* [9] presented two procedures for combining multiple Monte Carlo samples to estimate the uncertainty of the mean of multiple measurements with uncertainty while preserving these correlations. The first method corresponds to the original MUF formulation, denoted here as "Original", which estimates the variance of the multiple measurements using their nominal values, the $y_{j,\text{nom}}$. This intuitive approach uses the spread of measurements as transformed using the nominal value of any quantities with uncertainty (the $s_{\text{nom}}$ values) as in Eq. (2). The other method, denoted here as the "Alternative" method, estimates this variance using the averages of the $J$ Monte Carlo samples,

$$\bar{y}_{j,\cdot} = \frac{1}{Q} \sum_{q=1}^{Q} y_{j,q}.$$

In [9] it was shown that both methods produce Monte Carlo samples with unbiased means but biased variances. Monte Carlo samples with an unbiased mean will have an average value that, when averaged over many equivalent experiments, will converge to the true value. The biased variance of the Monte Carlo sample implies that the expected value of the variance of Monte Carlo samples will not approach the true variance. That is, these Monte Carlo samples will not yield the correct value of uncertainty even when averaged over many equivalent experiments. The bias of the Original method was shown to be $\Psi/J$ while the bias of the Alternative method is $\Phi/(JQ)$ where both $\Psi$ and $\Phi$ depend upon the function $F$ as well as the distributions of $X$ and $S$ (for more details please see [9]). Although there are trade-offs between these approaches, an analysis of these biases, the variability of the underlying statistic, and the order of the parameters $J$ and $Q$ in [9] yielded a recommendation to use the Alternative method to combine the Monte Carlo samples.

## IV. Examples

We apply these two methods to two examples where we can analytically calculate the variance and corresponding bias terms. Using these closed-form expressions, we analyze the performance of each Monte Carlo sampling method. Each of these examples, like the examples in [9], amount to taking $J$ independent samples of $X$, $Q$ samples of the systematic error $S$ that are shared across all $J$ samples, and propagating these samples through a nonlinear function, as in Eq. (3).

These examples each take $X_j \sim N(\mu, \sigma_x^2)$ and $S_q \sim N(0, \sigma_s^2)$ and only differ in the nonlinear functions. The first example is a quadratic

$$F(X_j, S_q) = (X_j + S_q)^2 \tag{4}$$

while the second example is a cubic

$$F(X_j, S_q) = (X_j + S_q)^3. \tag{5}$$

These simple polynomial examples allow us to calculate the true mean and variance of the data and also derive closed-form expressions for the the biases ($\psi/J$ and $\phi/(JQ)$ as in [9]) for

Jamroz, Benjamin; Williams, Dylan; Rezac, Jake; Frey, Michael; Koepke, Amanda.
"Accurate Monte Carlo Uncertainty Analysis for Multiple Measurements of Microwave Systems."
Paper presented at 2019 International Microwave Symposium, Boston, MA, United States. June 2, 2019 - June 7, 2019.

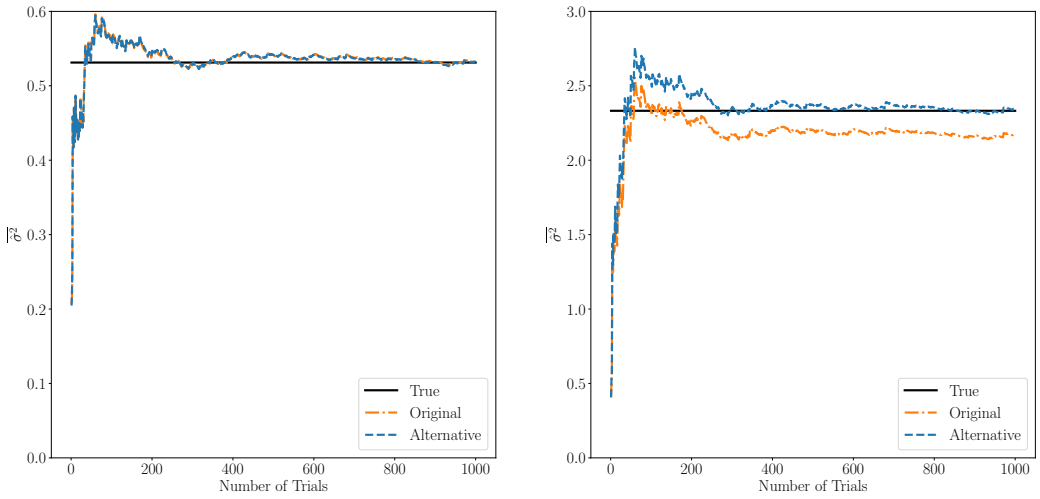


(a) Quadratic Example

(b) Cubic Example

Fig. 1. The sample variance cumulatively averaged over trials for each of the sampling methods applied to the quadratic, Eq. (4), and cubic, Eq. (5), examples. The Original and Alternative methods produced little or no bias for the quadratic example (a). The Original method had a pronounced bias for the cubic example (b), while the Alternative method showed little bias.

Table 1. Analytically calculated values of the mean, variance and the biases of each method for the quadratic and cubic examples.

| | Mean | Variance | Original Bias | Alternative Bias |
|---|---|---|---|---|
| Quadratic | 0.7500 | 0.5313 | 0.0000 | $6.250 \times 10^{-4}$ |
| Cubic | 0.8750 | 2.332 | -0.1446 | $6.016 \times 10^{-3}$ |

each method. We use these analytic expressions to examine the effect of these biases for the examples and use these relations to verify the numerical implementation in the MUF.

### A. *Analytic Results*

For each example, Eqs. (4) and (5), we choose $\mu = 0.5, \sigma_x = 0.5, \sigma_s = 0.5$, $J = 4$, and $Q = 100$[‡], evaluate the closed-form expressions for these parameters, and tabulate the analytically computed values of the true mean and variance as well as the biases of the variance estimates for each sampling method in Table 1. Here we see that the Original method produces no bias of the variance in the quadratic example but a significant bias in cubic example while the Alternative method produces relative biases of $\approx .1\%$ for both cases.

### B. *Microwave Uncertainty Framework Numerical Results*

We now turn to numerical experiments to verify the implementation in the MUF. Using the parameters above (for each example and sampling method) we run 1,000 independent trials and compute the sample mean and variance of the resulting Monte Carlo samples of each trial. Figure 1 shows the value of the sample variance of the Monte Carlo samples produced by the Original and Alternative methods cumulatively averaged over trials — we see that this statistic begins to converge around 400 trials. Both methods approach the true variance for the quadratic case in Fig. 1a, while the variance of the Original method is clearly biased for the cubic example in Fig. 1b.

[‡]We chose $Q = 100$ for computational convenience and this was sufficient for illustration purposes for these simple polynomial examples. In general, we recommend using 10,000 Monte Carlo samples or more.

Table 2. The averaged mean and variance along with the variance of these quantities as computed from 1,000 simulated Monte Carlo trials.

| | | Mean | Var. | Var. of Mean | Var. of Var. |
|---|---|---|---|---|---|
| Quadratic | Original | 0.7515 | 0.5331 | 0.3193 | 0.3892 |
| | Alternative | 0.7518 | 0.5324 | 0.3194 | 0.3902 |
| Cubic | Original | 0.8755 | 2.170 | 0.6646 | 2.296 |
| | Alternative | 0.8745 | 2.342 | 0.6661 | 2.508 |

Histograms of the sample variance, along with the true and averaged values, are shown in Fig. 2. Here we see the center of this statistic (mean of the variance) as well as the spread (variance of the variance) and we tabulate these values in Table 2 along with the corresponding values of the mean.

## V. Discussion

Table 2 shows that both methods produce Monte Carlo samples whose mean on average had little deviation from the analytic value. For the quadratic example, the Original method produced Monte Carlo samples whose average variance produced a value close to the analytically calculated value verifying that there is no significant bias in this case. Similarly, the Alternative scheme produced an average variance very close to the predicted value in agreement with the calculated bias shown in Table 1. However, in the cubic case the averaged variance produced by the Original method differed from the true value by $-0.1620$ which is very close to the analytically calculated bias $-0.1446$ (from Table 1). The Alternative method differed by $0.010$ a bias an order of magnitude smaller than the Original method.

Jamroz, Benjamin; Williams, Dylan; Rezac, Jake; Frey, Michael; Koepke, Amanda.
"Accurate Monte Carlo Uncertainty Analysis for Multiple Measurements of Microwave Systems."
Paper presented at 2019 International Microwave Symposium, Boston, MA, United States. June 2, 2019 - June 7, 2019.

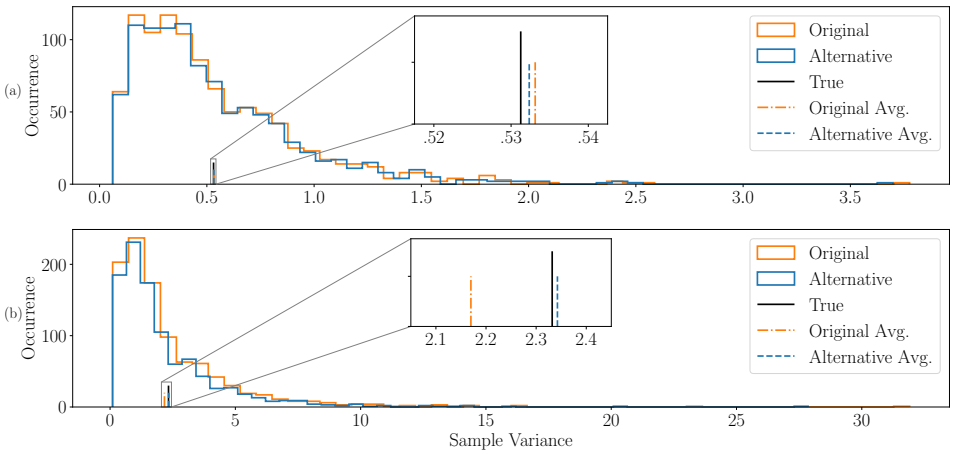


Fig. 2. Histograms of the sample variance using 1,000 trials for both sampling methods. The inset images show small or no significant biases for the quadratic example (a) but a significant bias for the Original method in the cubic example (b).

These results support the intuition for choosing the Alternative sampling method over the Original. Although the Original method is unbiased for some specific examples, such as the quadratic example above, it can produce significant bias in relevant transformations. The Alternative method is biased for both of our examples but, as this bias decreases with Monte Carlo sample size $Q$, this bias can be quite small even for the limited Monte Carlo sample size used here. Using the Monte Carlo averaged values to calculate the variance, as in the Alternative method, can yield more accurate uncertainty analyses when applying nonlinear transformations. As many microwave systems employ such nonlinear calculations (EVM, bit error rate), this more accurate method will improve the uncertainty analysis of such systems.

This numerical study also verified that the MUF implementation of the Original and Alternative methods agree with the analytically calculated results derived from [9].

## VI. Conclusion

We applied the two Monte Carlo sampling methods outlined in [9] to two polynomial examples. These simple examples allowed us to derive closed-form expressions for the true variance and the bias of each method, examine the effect of bias in these methods, and verify the implementations in the MUF. The Original method, which estimates the variance of multiple measurements using the corresponding nominal values, can produce significant bias in the estimate of variance. The Alternative method, which estimates the variance of multiple measurements using the averages of the Monte Carlo samples, produces small biases for these examples, even for the small Monte Carlo sample size considered here. As the Alternative sampling method produces more accurate results for these examples and the numerical simulations verified this implementation in the MUF, the MUF will use the Alternative sampling method moving forward, providing more accurate uncertainty analyses for microwave measurement systems.

## References

[1] *Evaluation of measurement data - Supplement 1 to the Guide to the expression of uncertainty in measurement - Propagation of distributions using a Monte Carlo method*, ISO, Geneva Switzerland, 2008.

[2] M. J. Salter and N. M. Ridler, "Measuring the capacitance coefficients of coaxial open-circuits with traceability to national standards," *Microwave Journal*, vol. 49, no. 10, pp. 138–154, 2006.

[3] H. Füser, S. Eichstädt, K. Baaske, C. Elster, K. Kuhlmann, R. Judaschke, K. Pierz, and M. Bieler, "Optoelectronic time-domain characterization of a 100 GHz sampling oscilloscope," *Measurement Science and Technology*, vol. 23, no. 2, p. 025201, 2012. [Online]. Available: http://stacks.iop.org/0957-0233/23/i=2/a=025201

[4] J. A. Jargon, C. Cho, D. F. Williams, and P. D. Hale, "Physical models for 2.4 mm and 3.5 mm coaxial VNA calibration kits developed within the NIST microwave uncertainty framework," in *2015 85th Microwave Measurement Conference (ARFTG)*. IEEE, May 2015.

[5] D. F. Williams, A. Lewandowski, T. S. Clement, J. C. M. Wang, P. D. Hale, J. M. Morgan, D. A. Keenan, and A. Dienstfrey, "Covariance-based uncertainty analysis of the NIST electrooptic sampling system," *IEEE Transactions on Microwave Theory and Techniques*, vol. 54, no. 1, pp. 481–491, Jan 2006.

[6] K. A. Remley, D. F. Williams, P. D. Hale, C.-M. Wang, J. Jargon, and Y. Park, "Millimeter-wave modulated-signal and error-vector-magnitude measurement with uncertainty," *IEEE Transactions on Microwave Theory and Techniques*, vol. 63, no. 5, pp. 1710–1720, May 2015.

[7] A. Koepke and J. A. Jargon, "Quantifying variance components for repeated scattering-parameter measurements," in *2017 90th ARFTG Microwave Measurement Symposium (ARFTG)*, Nov 2017, pp. 1–6.

[8] P. D. Hale, A. Dienstfrey, J. C. M. Wang, D. F. Williams, A. Lewandowski, D. A. Keenan, and T. S. Clement, "Traceable waveform calibration with a covariance-based uncertainty analysis," *IEEE Transactions on Instrumentation and Measurement*, vol. 58, no. 10, pp. 3554–3568, Oct 2009.

[9] M. Frey, B. F. Jamroz, A. Koepke, J. D. Rezac, and D. Williams, "Monte Carlo Sampling Bias in the Microwave Uncertainty Framework," *arXiv e-prints*, p. arXiv:1902.05979, Feb 2019.

[10] A. Lewandowski, D. F. Williams, P. D. Hale, J. C. M. Wang, and A. Dienstfrey, "Covariance-based vector-network-analyzer uncertainty analysis for time- and frequency-domain measurements," *IEEE Transactions on Microwave Theory and Techniques*, vol. 58, no. 7, pp. 1877–1886, Jul. 2010.

[11] *Evaluation of measurement data - Guide to the expression of uncertainty in measurement*, ISO, Geneva, Switzerland, 1993.

Jamroz, Benjamin; Williams, Dylan; Rezac, Jake; Frey, Michael; Koepke, Amanda.
"Accurate Monte Carlo Uncertainty Analysis for Multiple Measurements of Microwave Systems."
Paper presented at 2019 International Microwave Symposium, Boston, MA, United States. June 2, 2019 - June 7, 2019.

# Machine Learning in a Quality-Managed RF Measurement Workflow*

Aric W. Sanders[1,5], John M. Bass[2], Arpita Bhutani[3], MaryAnn S. Ho[4], James C. Booth[5]

[1]University of Colorado, Department of Physics, Boulder, CO, [2]Rose-Hulman Institute of Technology, Terre Haute, Indiana, [3]Peak to Peak Charter School, Lafayette, Colorado, [4]Fairview High School, Boulder, Colorado, [5]National Institute of Standards and Technology, Boulder, Colorado

***Abstract* — Advances in artificial intelligence, or more specifically machine-learning, have made it possible for computers to recognize patterns as well as or better than, humans. The process of quality management in radio-frequency measurements is an arduous one that requires a skilled human to interpret complex data sets and frequently leads to long diagnostic routines when a measurement fails a quality check, or an operator makes a mistake. We demonstrate the application of machine-learning classifiers to improve a common task in a quality managed measurement workflow. Specifically, we demonstrate that a machine-learning classifier can predict the device attached to a measurement apparatus and additionally predict if one of the connections has been improperly torqued, furthermore predicting which connection is loosened.**

***Index Terms* — Artificial intelligence, machine-learning, quality management, rf metrology, verification standards.**

## I. Introduction

Recent progress in the quality and ease of implementing machine learning in computer science has made the technology ubiquitous in our daily lives. From cell phones to smart speakers, this technology makes it possible for computers to recognize patterns as well as or better than, humans in some cases. Simultaneously, the complexity of radio-frequency measurements in communications and elsewhere has increased in complexity as measurements are extended to higher frequencies, larger number of ports, and non-linear devices. The process of insuring quality measurements in these complex situations largely falls upon well trained humans that make judgments based on quality management protocols established over many years or decades [1]. While these quality protocols have proven to be reliable for measurements with few process variables, they are costly in terms of time and labor when a system or device fails, normally signaling a non-compliance event that must either be rectified by re-measurement or become the subject of an extensive review. This process could be revolutionized through the implementation of the disruptive technologies in machine learning. In the future, artificial intelligence agents could be trained to recognize common faults in complex systems, informing humans of the most likely cause of a non-conformance event and even suggesting the best course of action. However, before this future is realized, the most promising technologies must be tested and proven to be capable of the performing tasks that humans currently do.

Here we demonstrate a methodology to train machine-learning classifiers to perform the task of identifying a connected device under test (DUT) and to determine whether that device has been properly torqued at each of several points in an adapter chain. We test eight popular machine-learning classifiers, first training them to recognize the raw, uncorrected scattering parameters of a system of adapters and calibration devices. We further extend this training to a set of states or labels where specific adapter connections have been intentionally loosened to an uncontrolled torque. Next, we assess the trained machine-learning classifiers against two training accuracy data sets and one test accuracy to determine their accuracy in determining the DUT, the state of the connections to that DUT and the precise location of loosened connection.

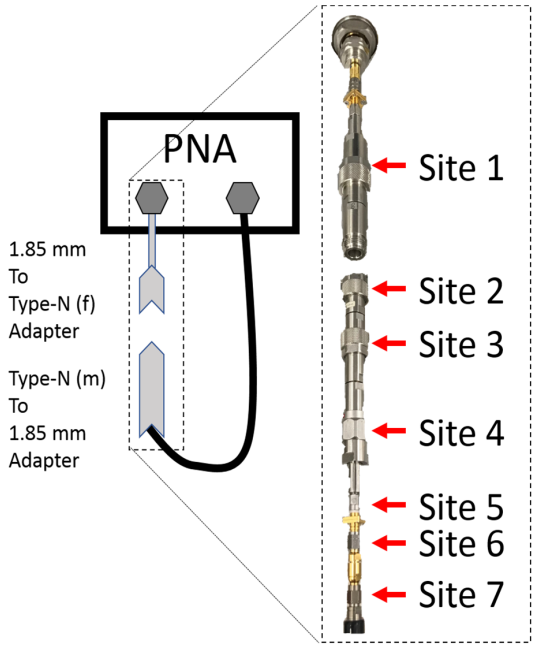


Fig. 1. Experimental setup for training measurements with connection sites labelled. The precision network analyzer (PNA) is adpated from its 1.85 mm port connector to the device under test's type-N connector.

Sanders, Aric; Bass, John; Bhutani, Arpita; Ho, Mary; Booth, James.
"Machine Learning in a Quality-Managed RF Measurement Workflow."
Paper presented at 93rd ARFTG Microwave Measurement Conference, Boston, MA, United States. June 7, 2019 - June 7, 2019.

## II. Experimental Setup

In order to establish the statistics of different DUTs in properly and improperly torqued connecter states, a standard type-N Short–Open–Load-Thru (SOLT) insertable calibration kit (Agilent** 85054B) was measured on an Agilent E8631A precision network analyzer (PNA). The measurements were of standard two port scattering parameters, carried out using an intermediate frequency of 10 Hz, a nominal power of 10 µW (-20 dBm), with no averaging. The frequency of the measurements spanned from 100 MHz to 18 GHz in frequency increments of 895 MHz for a total of 201 points. Fig. 1 shows the standard setup that consists of a cable and adapters that step from the 1.85 mm connector of the PNA ports to the type-N connecter of the calibration devices. Seven sites separated from the instrument ports were chosen to sequentially loosen, measure, and then torque to specification (1.4 Nm for type N, 0.9 Nm for all other connectors) and measure again. The inset in Fig. 1 shows an exploded view of the insertable test ports with each site labelled. Data in both the properly torqued and loosened conditions was taken without a correction applied.

## III. Classifier Training

In order to train the classifiers of interest, a large amount of data representing the patterns of interest should be used. The amount of data to accurately predict the state of the measurement is typically unrealistic to acquire on a laboratory time scale, hence we increase the amount of data used in training by determining the statistics of each device and state of connections and then use these statistics to randomly generate more robust training data. We do this by first acquiring a pre-training set that has at least three repeated measurements of each DUT (S, O, L, and T) and connector state for a total of 32 states or labels. Each repeated measurement is a single acquisition in a connect / disconnect cycle, where the site of interest is loosened by approximately 30 – 50 degrees from the properly torqued state and data is collected, after which the experiment is returned to the properly torqued state. After each loosen cycle, data for the DUT in the properly torqued state is recorded. This leads to three measurements of the loosened state and between 10-25 measurements of the properly torqued state for each DUT, for a total of 173 measurements of the 32 labels or states.

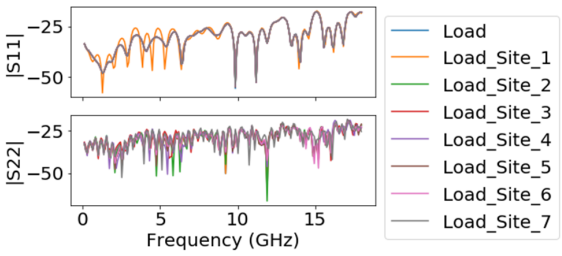


Fig. 2. Measurement of the amplitudes of the reflection coefficients in dB for 8 states of the load device.

In Fig. 2, the magnitude of the reflection coefficients in logarithmic units for 8 of the pre-train data measurements for a broadband load are shown. It is interesting to note that the measurements show only small differences for the loosened cases. The mean and standard deviations of these measurements are then calculated for each real and imaginary component of the scattering parameter at each frequency. A set of 1000 training sets for each state is then generated by choosing a random number from a Gaussian distribution with the same mean and standard deviation as the pre-training data. A small value, 1.0 $*10^{-9}$ was added to the standard deviation of the Gaussian to insure no points would have zero variation. The training set is then vectorized or flattened to a 1-d array containing the real and imaginary parts of each scattering parameter so that each training set is 1608 points.

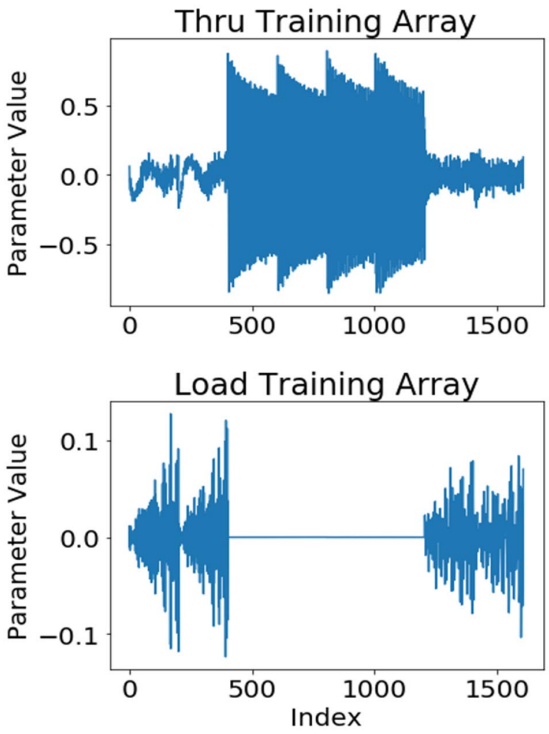


Fig. 3. A typical vectorized training set for the thru and load standards. Each training set has the real and imaginary components for each of four scattering parameters.

Fig. 3. shows a typical vectorized training set for the torqued thru and load. It should be noted that because the training of a classifier is a probabilistic process, classifiers of the same type will have slightly different prediction results for the same pre-train data. The classifiers and the training process

Sanders, Aric; Bass, John; Bhutani, Arpita; Ho, Mary; Booth, James.
"Machine Learning in a Quality-Managed RF Measurement Workflow."
Paper presented at 93rd ARFTG Microwave Measurement Conference, Boston, MA, United States. June 7, 2019 - June 7, 2019.

TABLE I
CLASSIFIER RESULTS

| | | Classification Method | | | | | | | |
|---|---|---|---|---|---|---|---|---|---|
| | **Metric** | **Quadratic Discriminant** | **Bernoulli Naïve Bayes** | **Decision Tree** | **Random Forest** | **Ridge** | **Stochastic Gradient Descent** | **Passive Aggressive** | **Perceptron** |
| Training Accuracy (Training Data) | State Accuracy | 100.0% | 100.0% | 100.0% | 100.0% | 100.0% | 78.1% | 93.8% | 96.9% |
| | Device Accuracy | 100.0% | 100.0% | 100.0% | 100.0% | 100.0% | 100.0% | 100.0% | 96.9% |
| | Connection Accuracy | 100.0% | 100.0% | 100.0% | 100.0% | 100.0% | 96.9% | 100.0% | 96.9% |
| Training Accuracy (Pre-train Measurements) | State Accuracy | 64.7% | 100.0% | 99.4% | 100.0% | 99.4% | 86.7% | 95.4% | 83.8% |
| | Device Accuracy | 100.0% | 100.0% | 100.0% | 100.0% | 100.0% | 95.4% | 99.4% | 96.1% |
| | Connection Accuracy | 67.1% | 100.0% | 99.4% | 100.0% | 99.4% | 90.2% | 98.8% | 84.4% |
| Test Accuracy (Test Measurement Data) | State Accuracy | 25.5% | 96.1% | 82.4% | 74.5% | 86.3% | 86.3% | 86.3% | 76.5% |
| | Device Accuracy | 100.0% | 100.0% | 100.0% | 100.0% | 94.1% | 100.0% | 100.0% | 100.0% |
| | Connection Accuracy | 64.7% | 100.0% | 100.0% | 100.0% | 94.1% | 100.0% | 100.0% | 100.0% |

were implemented in the Python programing language using the scikit-learn [2] and numpy [3] packages.

## IV. ACCURACY ASSESSMENT OF CLASSIFIERS

Eight classification methods were tested, a quadratic discriminant analysis, Bernoulli naïve Bayes, decision tree, random forest, ridge, stochastic gradient descent, passive aggressive, and a perceptron all of which are covered in detail elsewhere [4]-[5]. Each of the eight classification methods were used to train a classifier and to predict the particular states or labels of three different test data sets. Fig. 4. shows the role of each data set in the process of training and testing. The classification labels consisted of the DUT name and the site of a loosened connection, for instance short and short_site_1. Theses labels or states were sub-divided into two other categories after classification, device type and the presence of any loosened connection. The first data set is a copy of the data set used to train the classifiers (32000 sets) and represents a benchmark test, or training accuracy, that determines if the classifier is suited to this type of task. The second training accuracy set are the measurements of the devices used to determine the statistics of the states, or the pre-train data (173 sets). These measurements only determine the mean and standard deviation of the training data set and are never used in training unaltered. This training accuracy assessment is meant to determine the ability of the classifier to discern the different states. Finally, a set of new measurements taken at a different time are used to assess the accuracy of this method for data completely independent of the training process (53 sets), which we denote as test measurement data. The results of the tests are subdivided into three categories, the total accuracy of predicting the state (DUT and any loosened location), the accuracy of predicting the DUT attached, and the accuracy of predicting if the DUT is in a properly torqued state without regard to the location of the loosened connection.

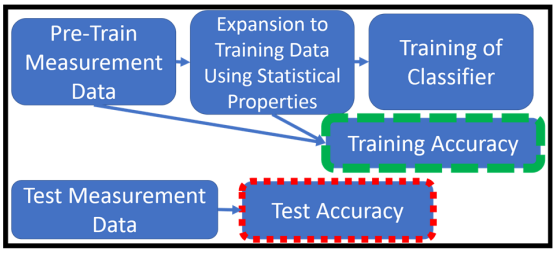


Fig. 4. Process of training and testing of the classification techniques. The training data is derived from the pre-training measurements and used to create a trained classifier. The training accuracy of the classifier is assessed by comparing the labels predicted for pre-training measurements and the training data sets. The testing of the classification technique is done with a separate set of test measurements.

**Certain commercial equipment, instruments, or software are identified in this paper to foster understanding. Such identification does not imply recommendation or endorsement by the National Institute of Standards and Technology, nor does it imply that the materials or equipment identified are necessarily the best available for the purpose.

Sanders, Aric; Bass, John; Bhutani, Arpita; Ho, Mary; Booth, James.
"Machine Learning in a Quality-Managed RF Measurement Workflow."
Paper presented at 93rd ARFTG Microwave Measurement Conference, Boston, MA, United States. June 7, 2019 - June 7, 2019.

## V. Results and Discussion

Table I. summarizes the results of the training and test accuracy assessments. The first training accuracy set, or what the trained classifier predicts when operating on the training data set, reveals that quadratic discriminant analysis, Bernoulli naïve Bayes, decision tree, random forest, and ridge classifiers can with 100% accuracy recover the 32 states in the training data. The training accuracy statistics are calculated for all of the 32,000 training sets. This is quite promising for the prospect of using these types of classifiers and statistically similar data sets to distinguish small variations in experimental data and link them to experimental states. The other three classifiers did well overall, but sometimes devices and states that had similar characteristics, such as terminations that have no transmission, are misclassified. For instance, the perceptron classifier misclassifies several short training set as being from a load.

When applied to the measurements used to determine the statistics for the training set, or the pre-train data, we observe that five of the classifiers have training accuracy exceeding 95% in the prediction of the specific state of the 173 experimental measurements and all classifiers are capable of determining the device type with greater than 95% accuracy. This indicates the process of determining the statistics of the measurements and statistically extending the training data does not cause significant degradation in the classifier's ability to recognize the DUT, and for select classifiers there is a strong ability to determine loosened connection location based on the limited statistics of three measurements. However, this training accuracy assessment only represents how well a statistically interrelated data set is labeled by the trained classifiers; to test the prediction capability, we must use a separate set of measurements not linked to training.

The test set of 53 measurements of randomly sampled devices and loosened connections assesses the potential not only for classification of the devices and connection errors based on known experimental conditions, but also the ability to do this for future experiments. Six classifiers predicted the device connected and that there was some connection error with perfect fidelity. The Bernoulli naïve Bayes was capable of locating the connection error 96.1 % of the time, and in the event it misclassified the location of the loosened condition, it classified it as a neighboring connection. In fact, of all the tested data sets the Bernoulli naïve Bayes only misclassified two of the thru measurements loosened at site 3 as being loosened at site 2. Although these tests confirm that a machine-learning classifier has the potential to locate and inform the user of known errors, more research into the long-term stability of this type of classification is needed before being implemented into a lab quality management process.

## VI. Conclusion

We have tested the ability of eight machine-learning classification techniques to determine if a loosened connection is present, what device is attached to a measurement setup, and the location of any loosened connection. Six trained classifiers were capable of accurately predicting the presence any loosened connection 100% of the time, determining the connected device 100% of the time and the determining the exact location of a loosened connection > 74% in 53 randomly sampled measurements. The best performing classifier in this set of tests was the Bernoulli naïve Bayes, which only misclassified two measurements as being from a neighboring loosened connection.

In addition to determining the test accuracy of these machine learning classification techniques, we report on two training accuracy assessments for our training protocol. The pre-training data that consisted a total of 173 measurements of 32 states, or four DUTs with eight connector configurations, were used to create a statistically similar training set of 32,000 labeled patterns. Once the machine-learning classifiers were trained with these statistically similar data, four had training accuracy identifying the presence of any loosened connection > 99% of the time, identifying the connected device 100% of the time and the location of the loosened connection > 99% of the time when used in a training accuracy assessment of the original 143 measurements. This demonstrates that the process of creating synthetic training sets does not prevent proper classification of the original measurement data.

In summary, we find that the quality management process in radio frequency measurements can be extended using techniques in machine learning to identify devices, if all connections are torqued properly, and even suggest the most likely position of any loosened connections.


## Acknowledgement

The authors wish to thank Michael Schwartz of Cal Labs Solutions for insight and conversations regarding artificial intelligence in calibrations. In addition, we acknowledge the summer high-school internship program (SHIP) at NIST for support of John Bass, Arpita Bhutani and MaryAnn Ho.


## References


[1] ISO/IEC 17025:2005, "General requirements for the competence of testing and calibration laboratories", International Organization for Standardization, 2nd Ed. 2005

[2] Pedregosa et al., "Scikit-learn: Machine-learning in Python" , JMLR 12, pp. 2825-2830, 2011.

[3] Travis E. Oliphant. *A guide to NumPy*, USA: Trelgol Publishing, (2006).

[4] T. Hastie, R. Tibshirani, J. Friedman, *The Elements of Statistical Learning*, Springer Publishing, 2008

[5] S.Shlaev-Shwartz and S. Ben-David, *Understanding Machine-learning Theory and Algorithms,* Cambridge University Press, 2014



Sanders, Aric; Bass, John; Bhutani, Arpita; Ho, Mary; Booth, James.
"Machine Learning in a Quality-Managed RF Measurement Workflow."
Paper presented at 93rd ARFTG Microwave Measurement Conference, Boston, MA, United States. June 7, 2019 - June 7, 2019.

# Analysis of Generalized CCA Errors and Mitigation in LTE-LAA Spectrum Sharing System

Yao Ma and Jason Coder
Communications Technology Laboratory,
National Institute of Standards and Technology
325 Broadway, Boulder, Colorado, USA

***Abstract*— Carrier sense multiple access with collision avoidance (CSMA/CA) procedures have been specified for medium access control (MAC) in several incumbent and emerging wireless systems, such as wireless local area network (WLAN) and long-term evolution (LTE) with license assisted access (LAA). Clear channel assessment (CCA) errors in carrier sensing can cause significantly degraded network performance. Analyzing the impact of CCA errors in the MAC backoff and transmission process is a challenging task, and very few works have explicitly addressed this. Existing analytical work is only valid for special cases such as independent CCA errors, and the result lacks generality for extension to coexistence systems. In this paper, we try to fill this technical gap by modelling generalized CCA sensing errors which can be either fully correlated or independent due to the fading channel. We develop a new Markov model using matrix-vector representation which captures generalized CCA error events, and analyze the impact of CCA errors on the key performance indicators (KPIs), such as the throughput of both LTE-LAA and WLAN systems. To mitigate the effects of mis-detection and collisions which can cause the network throughput to drop to nearly zero, we propose a soft-collision method to reduce the performance loss. Finally, we program the LTE-LAA and WLAN CCA algorithms and implement extensive computer simulations. Comparisons between analytical and simulation results show consistent matching, and illustrate loss caused by sensing errors and improvement brought by the soft-collision method. This result provides a powerful analytical tool on CSMA/CA MAC-layer performance evaluation with imperfect sensing, applicable to both single and coexistence systems, and has practical value for countermeasure designs against sensing errors.**

## I. Introduction

In spectrum sharing systems, such as long-term evolution license assisted access (LTE-LAA) [1]–[5] and the IEEE 802.11 wireless local area network (WLAN) systems [6], [7], reliable spectrum sensing of channel busy/idle states is needed to properly implement carrier sense multiple access with collision avoidance (CSMA/CA) schemes. In CSMA/CA, the clear channel assessment (CCA) result is subject to false alarm and mis-detection events, which can cause either unwanted transmission delay or collisions, and significantly reduce the network throughput. Accurate evaluation of the impact of CCA errors and design of effective countermeasures are critical to improve network performance, and enable constructive coexistence.

The effects of sensing errors on wireless spectrum access systems have been studied in a few works, such as [8]–[11]. The authors of [8] have evaluated the effects of sensing errors on the performance of opportunistic spectrum access, assuming a constrained partially observable Markov decision process (POMDP). An IEEE 802.11-based cognitive radio scheme is proposed and analyzed in [9], and the impact of sensing errors of primary user activity on secondary transmissions is studied. In [10], the authors propose a throughput-optimal CSMA scheme to mitigate the impact of imperfect sensing, especially the mis-detection event. They use a retransmission probability instead of modelling backoff countdown process. The effect of CCA errors in the CSMA/CA backoff process is not explicitly modelled or studied in [8]–[10].

In [11], the authors model and analyze the effect of CCA errors on the medium access control (MAC) backoff countdown and transmission processes for a CSMA/CA network. However, this method has restrictions and major approximations. First, it assumes the special case of independent CCA errors among counter reduction (CR) steps, which may hold when the channel fading is very fast (aka, channel changes independently among backoff slot durations). This assumption is not valid for a slow fading (or blockwise fading) channel where the mis-detection events in multiple sensing slots on a transmission packet are highly correlated. Second, similar to available works [12], [13] of Markov chain-based CSMA/CA modelling, it uses a scalar-variable probability transition method to analyze system states, and cannot model generalized CCA errors. Third, some analytical steps in [11] involve approximations which are tight only for certain ranges of parameters.

In WLAN and LAA small-cell networks where the channel fading is not very fast, the CCA sensing output among backoff slots can be highly correlated, and therefore so are the CCA errors. We define generalized CCA errors to encompass both correlated and independent CCA errors in CSMA/CA backoff process. A flexible and precise modeling and analysis approach which can handle generalized CCA errors is still missing in the literature.

Recently, some analytical or optimization approaches for the LTE-LAA and WLAN coexistence systems have been developed assuming perfect spectrum sensing, see e.g., [14]–[18]. In these works, CCA errors were not modelled or analyzed. Evaluating impact of CCA errors on coexistence systems is a nontrivial task, and has not been well explored. Thus, we identify the following challenging open problems:

1) Analyzing effect of generalized CCA errors on CSMA/CA network performance (explicitly counting for



Ma, Yao; Coder, Jason.
"Analysis of Generalized CCA Errors and Mitigation in LTE-LAA Spectrum Sharing System."
Paper presented at IEEE Global Communications Conference (GLOBECOM 2019) , Waikoloa, HI, United States. December 9, 2019 - December 13, 2019.

the backoff process).
2) Evaluating impact of generalized CCA errors on unlicensed spectrum sharing systems, such as coexisting LTE-LAA and WLAN.

In this paper, we model and address these challenging problems in a unified framework. The novel contributions are highlighted as follows:

- New model of backoff process assuming generalized CCA errors. Instead of the majority of available works which represent the CSMA/CA backoff in a scalar process, we develop a matrix-vector Markov tool to model generalized CCA errors, and compute the backoff counter stationary probability vector. To do this, we enumerate all the channel access and CCA sensing events, and provide in-depth and accurate performance analysis.
- We provide the result for two spectrum sharing CSMA/CA networks, aka. coexisting LAA and WLAN networks, and derive key performance indicators (KPIs), including the channel access probability (CAP), successful transmission probability (STP), and throughput.
- Direct retransmission of collided packets in LAA and WLAN is equivalent to a hard-collision model because the packets experiencing collisions are lost. To mitigate the performance loss, we also propose a soft-collision scheme. We program the MAC algorithms and implement extensive simulations, which validate our analytical results, and demonstrate the performance improvement of the soft-collision method.

This new technique fills a major gap in modelling and analysis of generalized CCA errors in CSMA/CA systems, with applications such as LTE-LAA and WLAN coexistence. The technical insight and method provided by this work may be used for analysis and optimization of other coexisting systems, and mitigate the impact of significant sensing errors.

## II. System Model

Consider two spectrum sharing systems on an industrial, scientific, and medical (ISM) radio band, where there is an LTE-LAA system with $n_L$ links and a WLAN system with $n_W$ links. They share a single wide-band channel, and use CSMA/CA type of MAC channel access procedures specified in [1], [2], [6]. Suppose that with perfect CCA, every link can hear the channel access activity of any other links. With imperfect CCA, there are two types of sensing errors, false alarm on an idle slot and mis-detection of an ongoing transmission.

In this section, we use subscripts $L, W, I, S, C, P$ to denote LAA, WLAN, idle, successful transmission, collision, and payload, respectively. We define the false alarm and mis-detection probabilities of the LAA (and WLAN) system as $P_{\text{Fa},L}$ and $P_{m,L}$ (and $P_{\text{Fa},W}$ and $P_{m,W}$), respectively. For the LAA (and WLAN) system, we define $\delta_L$, $T_{P,L}$, $T_{S,L}$ and $T_{C,L}$ (and $\delta_W$, $T_{P,W}$, $T_{S,W}$ and $T_{C,W}$) as the durations of the idle slot, payload, successful transmission, and collided transmission, respectively.

Assume that the background white noise power is negligible compared to the interference power. Based on a popular Jake's fading spectrum [19] for a time-selective Rayleigh fading channel, we obtain the channel power correlation between slots of $n$-slot separation as

$$\rho(n) \simeq |J_0(2\pi f_d n \delta_L)|^2 \tag{1}$$

where $J_0$ is the Bessel function of zeroth-order, $f_d$ is maximum Doppler frequency shift, $\delta_L = 9\mu s$ is an idle slot duration. Based on pedestrian moving speed of 2 m/s at carrier frequency 5.2 GHz, we obtain $f_d \leq 34.67$ Hz, and $\rho(1) \simeq 1$, which means that adjacent CCA results are fully correlated. For two CCA results that are seperated by 1 ms, we have $n \simeq 111$, and $\rho(111) \simeq 0.977$, which is close to full correlation. Therefore, in LAA small cells and WLAN, during sensing of a transmission packet, the involved CCA errors are typically highly correlated. To our knowledge, this case has not been adequately analyzed in the literature. We will address this difficult and practical case, and our result can be applied to independent CCA errors as well (aka, fast fading channel).

Direct retransmission of collided packets can suffer substantially from CCA errors. Hybrid automatic repeat request (H-ARQ) has been discussed for adoption in 3GPP LTE-LAA [2] and new-radio (NR)-LAA [20] channel access procedures. With H-ARQ, receiver can combine several corrupted copies of the original packet and maintain partial throughput at a lower rate. By considering H-ARQ, we propose a CCA soft-collision (CCA-SC) scheme.

***The CCA-SC scheme:***

1) Initialize counter and starts backoff based on CSMA/CA. When the counter reduces to zero, transmit one packet.
2) If transmission is successful, receiver sends back ACK. The next packet is scheduled. Go to step 1).
3) If transmission fails:
   - Increase backoff stage, and another encoded copy of the failed packet is scheduled for retransmission. The receiver combines the corrupted copies to recover the original packet, and send ACK/NACK to the transmitter. Go to step 1).
   - Retransmission is stopped when either the packet is recovered correctly or the maximum retransmission count is exceeded.

For ease of reference, some symbols, expressions and their definitions are listed in Table I.

## III. Performance Analysis

### A. Throughput Under CCA Errors and Hard-Collision

We use $H_0$ and $H_1$ to denote that the channel are truly idle and busy, respectively. We define $\tau_{L,H_0}$ and $\tau_{L,H_1}$ (and $\tau_{W,H_0}$ and $\tau_{W,H_1}$) as channel access probabilities of an LAA (and WLAN) link under $H_0$ and $H_1$ states. Let $Z_0$ and $W_0$ be the initial contention window (CW) sizes of LAA and WLAN systems, respectively. For LAA (and WLAN) system, we define $P_{I,L,H_0}$, $P_{I,L,H_1}$, $P_{S,L,H_0}$, and $P_{C,L}$ (and $P_{I,W,H_0}$, $P_{I,W,H_1}$, $P_{S,W,H_0}$, and $P_{C,W}$) as the CCA-determined system idle probability under true $H_0$ or $H_1$ system state, successful transmission probability under $H_0$, and probability of collision, respectively. Here, $P_{I,L,H_1}$ is the probability that mis-detection in the LAA nodes on the current LAA or WLAN

Ma, Yao; Coder, Jason.
"Analysis of Generalized CCA Errors and Mitigation in LTE-LAA Spectrum Sharing System."
Paper presented at IEEE Global Communications Conference (GLOBECOM 2019) , Waikoloa, HI, United States. December 9, 2019 - December 13, 2019.

TABLE I: Definition of common symbols and expressions frequently used in this paper.

| Symbol or Expression | Definition |
|---|---|
| $S_L^{\text{HC}}$ (or $S_L^{\text{SC}}$) | Throughput of LAA link with hard collision (or soft collision). |
| $P_{I,L,H_0}$ (or $P_{I,L,H_1}$) | Idle probability of LAA system under true $H_0$ (or $H_1$) case. |
| $P_{S,L,H_0}$ (or $P_{S,W,H_0}$) | Successful transmission probability of LAA (or WLAN), valid under $H_0$ only. |
| $P_{C,L}$ (or $P_{C,W}$) | Collision probability of LAA (or WLAN) system. |
| $P_{\text{Fa},L}$ and $P_{m,L}$ (or $P_{\text{Fa},W}$ and $P_{m,W}$) | False alarm and mis-detection probabilities of LAA (or WLAN) |
| $\tau_{L,H_0}$ (or $\tau_{L,H_1}$) | Channel access probability (CAP) of an LAA link under true $H_0$ (or $H_1$) case. |
| $\mathbf{P}_L^{\text{P-CCA}}$ (or $\mathbf{P}_L^{\text{E-CCA}}$) | Backoff state probability transition matrix with perfect CCA (or erroneous CCA). |

transmission event has not caused improper transmissions, and so does not contribute to a collision immediately. Based on hard-collision retransmission model of LAA and WLAN, the sum of MAC throughput of $n_L$ LAA nodes and $n_W$ WLAN nodes are, respectively, given by

$$S_L^{\text{HC}} = P_{S,L}P_{I,W}T_{P,L}/T_{\text{ave},L}, \quad (2)$$
$$S_W^{\text{HC}} = P_{S,W}P_{I,L}T_{P,W}/T_{\text{ave},W}, \quad (3)$$

where $T_{\text{ave},L}$ and $T_{\text{ave},W}$ are the average total durations to support one successful transmission in LAA and WLAN systems, respectively. $P_{S,L}$ refers to the STP in the LAA system. This occurs when only one LAA node starts transmission in an idle slot (with probability $P_{S,L,H_0}$), and then the rest of $n_L - 1$ LAA links, even with possible mis-detection of this transmission, have not caused a collision (with probability $\hat{P}_{I,L,H_1}$). Here, we use $P$ (or $\hat{P}$) to denote probabilities of this system observed by another system (or by its own system). $P_{I,W}$ in (2) is the probability that none of the $n_W$ WLAN links is active during the observation of the LAA transmission. Thus, $P_{S,L}P_{I,W}$ in (2) gives the overall STP of the LAA links. In detail, we obtain:

$$P_{S,L} = P_{S,L,H_0}\hat{P}_{I,L,H_1} \quad (4)$$
$$P_{S,W} = P_{S,W,H_0}\hat{P}_{I,W,H_1}, \quad (5)$$
$$P_{I,L} = P_{I,L,H_0}P_{I,L,H_1}, \quad (6)$$
$$P_{I,W} = P_{I,W,H_0}P_{I,W,H_1}, \quad (7)$$

where $P_{S,L,H_0} = n_L\tau_{L,H_0}(1-\tau_{L,H_0})^{n_L-1}$, and $P_{S,W,H_0} = n_W\tau_{W,H_0}(1-\tau_{W,H_0})^{n_W-1}$. Thus, we obtain for the LAA system that $P_{I,L,H_0} = (1-\tau_{L,H_0})^{n_L}$, $P_{I,L,H_1} = (1-\tau_{L,H_1})^{n_L}$, $\hat{P}_{I,L,H_0} = (1-\tau_{L,H_0})^{n_L-1}$, and $\hat{P}_{I,L,H_1} = (1-\tau_{L,H_1})^{n_L-1}$. Similarly, we have for the WLAN system that $P_{I,W,H_0} = (1-\tau_{W,H_0})^{n_W}$, $P_{I,W,H_1} = (1-\tau_{W,H_1})^{n_W}$, $\hat{P}_{I,W,H_0} = (1-\tau_{W,H_0})^{n_W-1}$, and $\hat{P}_{I,W,H_1} = (1-\tau_{W,H_1})^{n_W-1}$.

The collision probability among the LAA links is

$$P_{C,L} = 1 - P_{I,L,H_0} - P_{S,L} = P_{C,L,H_0} + \hat{P}_{C,L,H_1}, \quad (8)$$

where $P_{C,L,H_0} = 1 - P_{I,L,H_0} - P_{S,L,H_0}$ is the probability of collisions which are not related with mis-detection events, and $\hat{P}_{C,L,H_1} = P_{S,L,H_0}(1-\hat{P}_{I,L,H_1})$ refers to the probability that an initial transmission starts without collision, but then collision happens due to mis-detection(s).

To evaluate the throughput of LAA and WLAN systems under CCA errors, we still need to obtain $\tau_{L,H_0}$ and $\tau_{L,H_1}$, and $T_{\text{ave},L}$ for LAA, and $\tau_{W,H_0}$, $\tau_{W,H_1}$, and $T_{\text{ave},W}$ for WLAN, respectively.

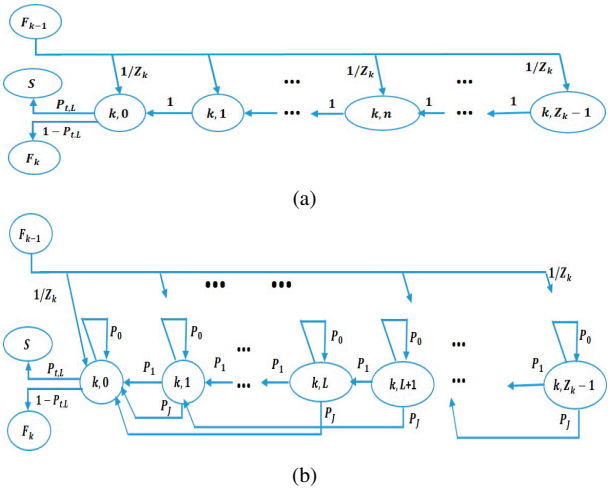


Fig. 1: Proposed Markov model of a CSMA/CA backoff process in one stage (a) without CCA errors (b) with CCA errors.

### B. Modeling and Analysis of the Backoff Process

We develop a new probability analysis method involving probability transition matrix in the Markov chain to model the LAA and WLAN CW countdown process, when both systems have CCA errors. We show the backoff-and-transmission Markov transition model in Fig. 1(a) and (b), for the cases of perfect sensing and with CCA errors, respectively. $F_{k-1}$ (and $F_k$) refers to state of failed transmission at backoff stage $k-1$ (and $k$), $S$ refers to state of successful transmission, and $P_{t,L}$ is the conditional STP once a transmission starts. In Fig. 1(b), $P_0$ and $P_1$ are the probabilities that the counter value does not change, and reduces by one, respectively, during observation of one discrete event. Here, $P_0 > 0$ is caused by false alarm. The $P_J$ in Fig. 1(b) refers to a CR up to $J$-step, caused by mis-detection of an ongoing transmission when the CCA errors are highly correlated. This means that an CCA error event can spread up to $J$ CCA slot durations.

Consider a Category-3 LAA listen before talk (LBT) process [2], [3], which has a single backoff stage with CW range

Ma, Yao; Coder, Jason.
"Analysis of Generalized CCA Errors and Mitigation in LTE-LAA Spectrum Sharing System."
Paper presented at IEEE Global Communications Conference (GLOBECOM 2019) , Waikoloa, HI, United States. December 9, 2019 - December 13, 2019.

$(0, Z_0-1)$. The result can be extended to a multi-stage backoff scheme. Let the backoff counter stationary probability vector be $\mathbf{b}_L = [b_0, b_1, \ldots, b_{Z_0-1}]^T$, where $b_k$ is the probability that the backoff process stays at counter $k$. Define $\mathbf{P}_L$ as the $Z_0 \times Z_0$ Markov probability transition matrix for $\mathbf{b}_L$. When the backoff process of an LTE-LAA node achieves a steady state, via the limiting distribution property of stationary Markov chain [21], we obtain

$$\mathbf{b}_L = \mathbf{P}_L \mathbf{b}_L. \tag{9}$$

So, $\mathbf{b}_L$ can be solved as the null vector of matrix $\mathbf{I}_{Z_0} - \mathbf{P}_L$, subject to $\sum_{k=0}^{Z_0-1} b_k = 1$, where $\mathbf{I}_Z$ is an $Z \times Z$ identity matrix.

By mapping the backoff probability transition in matrix form, we derive the probability transition matrix with perfect CCA (P-CCA):

$$\mathbf{P}_L^{\text{P-CCA}} = \begin{bmatrix} 1/Z_0 & 1 & 0 & \ldots & 0 \\ 1/Z_0 & 0 & 1 & \ddots & \vdots \\ \vdots & \vdots & \ddots & \ddots & 0 \\ \vdots & \vdots & \vdots & 0 & 1 \\ 1/Z_0 & \vdots & \vdots & 0 & 0 \end{bmatrix}. \tag{10}$$

By solving (9) and (10), it follows that $b_0 = 2/(1+Z_0)$, which matches with the result in [7], [12], [16] for a given backoff stage. Also, all elements in $\mathbf{b}_L$ can be solved uniquely.

**Stand-alone LAA System with CCA Errors**
We list the probability and duration pairs at counter $k$ in Table II, where we define events $C_I$ = {Idle channel}, $C_S$= {Successful transmission}, $C_C$ = {Immediate collision}, and $C_{SC}$ = {No collision initially, but collision happens later due to mis-detection}, and denote their probabilities as $P_{C_I}$, $P_{C_S}$, $P_{C_C}$, and $P_{C_{SC}}$, respectively. We can verify that $P_{C_I} + P_{C_S} + P_{C_C} + P_{C_{SC}} = 1$, as expected.

Define $L_{S,L} = \text{round}(T_{S,L}/\delta)$ and $L_{C,L} = \text{round}(T_{C,L}/\delta)$, where round$(x)$ rounds $x$ to its nearest integer. We denote the CR steps (or called lengths) caused by $C_S$ and $C_{SC}$ (normalized by $\delta$) events in mis-detection as $J_1$ and $J_2$, respectively. We obtain $J_1 = L_{S,L}$ and $J_2 = L_{S,L} + L_{C,L}$, respectively, which are the normalized length of successful or failed transmission durations. When an LAA packet with length $L_{S,L}$ experiences a mis-detection in an LAA sensing node, this causes a CR of up to $\hat{J}_1 = \min(Z_0-1, L_{S,L})$ in the backoff process of this node. We denote this by the probability $P_{J_1}$. Also, $\hat{J}_2 = \min(Z_0 - 1, L_{S,L} + L_{C,L})$. Based on Table II, we obtain:

$$\begin{aligned} P_0 &= \hat{P}_{I,L,H_0} P_{\text{Fa},L}, && (11)\\ P_1 &= \hat{P}_{I,L,H_0}(1 - P_{\text{Fa},L}) + \hat{P}_{S,L,H_0}(1 - P_{m,L}) \\ &\quad + P_{C,L,H_0}, && (12)\\ P_{J_1} &= \hat{P}_{S,L,H_0} \hat{P}_{I,L,H_1} P_{m,L} && (13)\\ P_{J_2} &= \hat{P}_{S,L,H_0}(1 - \hat{P}_{I,L,H_1}) P_{m,L}, && (14) \end{aligned}$$

where $P_{J_k}$ (for $k = 1, 2$) is the probability that the counter value reduces by $\hat{J}_k$, due to mis-detection of an ongoing transmission. The effect of $P_0, P_1$ and $P_{J_k}$ is shown in Fig. 1(b). For conciseness, we show only one jump transition path due to $P_{J_k}$ $(k = 1, 2)$ in Fig. 1. (b).

**Coexisting LAA and WLAN Systems with CCA Errors**
Refer to Table III. For convenience, we assume that $T_{C,L} = T_{C,W} = T_C$. We use $C_I$ and $C_C$ to denote idle channel event and collision event that has a fixed duration $T_C$, respectively. We use $C_{S,L}$ (or $C_{S,W}$) to denote successful transmission of an LAA (or WLAN) link, and $C_{SC,L}$ (or $C_{SC,W}$) to denote initial LAA (or WLAN) link transmission which fails later due to collisions caused by mis-detection. Let $P_{C_1}, \ldots, P_{C_4}$ denote the probabilities of the 4 channel busy events for $C_{S,L}, C_{SC,L}, C_{S,W}, C_{SC,W}$, respectively. We obtain:

$$\begin{aligned} P_{C_1} &= \hat{P}_{S,L} P_{I,W}, && (15)\\ P_{C_2} &= \hat{P}_{S,L,H_0} P_{I,W,H_0} - \hat{P}_{S,L} P_{I,W}, && (16)\\ P_{C_3} &= \hat{P}_{I,L} P_{S,W}, && (17)\\ P_{C_4} &= \hat{P}_{I,L,H_0} P_{S,W,H_0} - \hat{P}_{I,L} P_{S,W}. && (18) \end{aligned}$$

We verify that $P_{C_I} + P_{C_C} + P_{C_1} + P_{C_2} + P_{C_3} + P_{C_4} = 1$, which shows that Table III provides a complete probability set.
We construct the counter state probability transition matrix with erroneous-CCA as

$$\mathbf{P}_L^{\text{E-CCA}} = \mathbf{P}_{L,0} + \sum_{k=1}^{4} \mathbf{P}_{L,J_k}, \tag{19}$$

where $\mathbf{P}_{L,0}$ is a transition matrix caused by regular backoff and false alarm events, and is given by

$$\mathbf{P}_{L,0} = \begin{bmatrix} 1/Z_0 & P_1 & 0 & \ldots & 0 \\ 1/Z_0 & P_0 & P_1 & \ddots & \vdots \\ \vdots & \vdots & \vdots & \ddots & 0 \\ \vdots & \vdots & \vdots & P_0 & P_1 \\ 1/Z_0 & \vdots & \vdots & 0 & P_0. \end{bmatrix} \tag{20}$$

where $P_0$ and $P_1$ refer to probabilities of no CR and 1-step CR, respectively. They are derived as

$$\begin{aligned} P_0 &= \hat{P}_{I,L,H_0} P_{I,W,H_0} P_{\text{Fa},L}, && (21)\\ P_1 &= \hat{P}_{I,L,H_0} P_{I,W,H_0}(1 - P_{\text{Fa},L}) \\ &\quad + [\hat{P}_{S,L,H_0} P_{I,W,H_0} + \hat{P}_{I,L,H_0} P_{S,W,H_0}](1 - P_{m,L}) \\ &\quad + \hat{P}_{C,L,H_0} P_{I,W,H_0} + \hat{P}_{I,L,H_0} P_{C,W,H_0} \\ &\quad + (1 - \hat{P}_{I,L,H_0})(1 - P_{I,W,H_0}). && (22) \end{aligned}$$

When there are no CCA errors, we have $P_1 = 1$ and $P_0 = 0$, and (20) is simplified to (10), as expected. The impact of mis-detection is studied next.

Based on Table III, we derive the $T_{\text{ave},L}$ as

$$\begin{aligned} T_{\text{ave},L} &= P_{C_I}\delta_L + P_{C_C} T_C + P_{C_1} T_{S,L} + P_{C_2}(T_{S,L} + T_C) \\ &\quad + P_{C_3} T_{S,W} + P_{C_4}(T_{S,W} + T_C) && (23) \end{aligned}$$

where the hat sign on $\hat{P}_{I,L,H_0}$, $\hat{P}_{C,L,H_0}$ and $\hat{P}_{S,L,H_0}$ involved in $P_{C_I}, P_{C_C}, P_{C_1}, P_{C_2}, P_{C_3}$, and $P_{C_4}$ should be removed. The formula for $T_{\text{ave},W}$ can be obtained by following a similar procedure.

In (19), $\mathbf{P}_{L,J_k}$ is a matrix that models mis-detection related

Ma, Yao; Coder, Jason.
"Analysis of Generalized CCA Errors and Mitigation in LTE-LAA Spectrum Sharing System."
Paper presented at IEEE Global Communications Conference (GLOBECOM 2019) , Waikoloa, HI, United States. December 9, 2019 - December 13, 2019.

TABLE II: Backoff probability and duration pairs at LAA node (Stand-alone LAA system).

| Event | Event Probability | Sensing Probability & CR step (case 1) | Sensing Probability & CR step (case 2) |
|---|---|---|---|
| $C_I$ | $\hat{P}_{I,L,H_0}$ | $P_{\text{Fa},L}$ and 0 | $1-P_{\text{Fa},L}$ and 1 |
| $C_C$ | $\hat{P}_{C,L,H_0}$ | NA and 1 | |
| $C_S$ | $\hat{P}_{S,L}$ | $P_{m,L}$ and $\hat{J}_1$ | $1-P_{m,L}$ and 1 |
| $C_{SC}$ | $\hat{P}_{S,L,H_0}-\hat{P}_{S,L}$ | $P_{m,L}$ and $\hat{J}_2$ | $1-P_{m,L}$ and 1. |

TABLE III: Backoff probability and duration pairs at LAA node (Coexisting LAA and WLAN systems).

| Event | Event Probability | Sensing Probability and CR step (case 1) | Sensing Probability and CR step (case 2) |
|---|---|---|---|
| $C_I$ | $P_{C_I}=\hat{P}_{I,L,H_0}P_{I,W,H_0}$ | $P_{\text{Fa},L}$ and 0 | $1-P_{\text{Fa},L}$ and 1 |
| $C_C$ | $P_{C_C}=\hat{P}_{C,L,H_0}P_{I,W,H_0}+\hat{P}_{I,L,H_0}P_{C,W,H_0}$ + $(1-\hat{P}_{I,L,H_0})(1-P_{I,W,H_0})$ | NA and 1 | |
| $C_{S,L}$ | $P_{C_1}=\hat{P}_{S,L}P_{I,W}$ | $P_{m,L}$ and $\hat{J}_1$ | $1-P_{m,L}$ and 1 |
| $C_{SC,L}$ | $P_{C_2}=\hat{P}_{S,L,H_0}P_{I,W,H_0}(1-\hat{P}_{I,L,H_1}P_{I,W,H_1})$ | $P_{m,L}$ and $\hat{J}_2$ | $1-P_{m,L}$ and 1. |
| $C_{S,W}$ | $P_{C_3}=\hat{P}_{I,L}P_{S,W}$ | $P_{m,L}$ and $\hat{J}_3$ | $1-P_{m,L}$ and 1 |
| $C_{SC,W}$ | $P_{C_4}=P_{S,W,H_0}\hat{P}_{I,L,H_0}(1-\hat{P}_{I,L,H_1}P_{I,W,H_1})$ | $P_{m,L}$ and $\hat{J}_4$ | $1-P_{m,L}$ and 1. |

event $P_{C_k}$ (for $k=1,\ldots,4$), and is given by

$$\mathbf{P}_{L,J_k}=\begin{bmatrix} 0 & \mathbf{P}_{J_k} & 0 & \ldots & 0 \\ 0 & 0 & \mathbf{P}_{J_k} & \ddots & 0 \\ \vdots & \vdots & \vdots & \ddots & 0 \\ 0 & 0 & 0 & 0 & \mathbf{P}_{J_k} \end{bmatrix} \tag{24}$$

where $\mathbf{P}_{J_k}=[P_{J_k}(1),\ldots,P_{J_k}(\hat{J}_k)]$, and $P_{J_k}(n)$ ($n=1,\ldots,\hat{J}_k$) is the transition probability for a $n$-step CR. Here, $\hat{J}_k$ (for $k=1,2,3,4$) are the CR sizes due to the 4 mis-detection events. We obtain $\hat{J}_1=\min(Z_0-1,L_{S,L})$, $\hat{J}_2=\min(Z_0-1,L_{S,L}+L_{C,L})$, $\hat{J}_3=\min(Z_0-1,L_{S,W})$ and $\hat{J}_4=\min(Z_0-1,L_{S,W}+L_{C,W})$, where $L_{S,W}=\text{round}(T_{S,W}/\delta)$ and $L_{C,W}=\text{round}(T_{C,W}/\delta)$.

The $\mathbf{P}_{L,0}$ completely models the effect of false alarm, and $\mathbf{P}_{L,J_k}$ (for $k=1,2,3,4$) additionally models the effect of mis-detection. Next, we derive $P_{J_k}(n)$ for correlated and independent CCA errors, respectively.

**Correlated CCA Errors**

In a slow fading channel, the mis-detection of the first slot of the packet is highly correlated with the detection of the remaining part of the packet. We assume the detection results in multiple slots to be fully correlated, and obtain:

$$P_{J_k}(n)=\begin{cases} 0, & \text{when } n\in(1,\ldots,\hat{J}_k-1) \\ P_{C_k}P_{m,L}, & \text{when } n=\hat{J}_k. \end{cases} \tag{25}$$

Here, $P_{J_k}(1)=\cdots=P_{J_k}(\hat{J}_k-1)=0$ because if the mis-detection occurs, it will spread until the last slot of the transmission. Furthermore, we can evaluate the case of partially-correlated CCA errors by developing a semi-analytical approach, which will be addressed in our future work.

**Independent CCA Errors**

In a fast fading channel, if the channel gain or power varies significantly between adjacent CCA slots, the CCA errors may be approximated as being uncorrelated among slots. We obtain an approximate solution to the transition probability of $n$-step CR of event $J_k$ as

$$P_{J_k}(n)\simeq\binom{\hat{J}_k}{n}P_{C_k}P_{m,L}^n(1-P_{m,L})^{\hat{J}_k-n}. \tag{26}$$

Here, $\binom{\hat{J}_k}{n}$ denotes the binomial coefficient that mis-detection of $n$ slots happens in a $\hat{J}_k$-slot duration. Based on knowledge of busy slot durations of transmissions, a better sensing decision strategy may be developed. For example, if a sensing node makes an $H_1$ decision, the node can use a larger time window than idle slot duration $\delta$ to do sensing for the rest of channel busy period, and achieve a more reliable detection performance.

### C. Transmission Probabilities

***Channel Access Probabilities (CAP)***

By using the new state transition probability analysis, we derive the CAP $\tau_{L,H_0}$ as

$$\tau_{L,H_0}=b_{L,1}P_1+b_{L,0}/Z_0, \tag{27}$$

where $b_{L,1}P_1$ refers to transition from counter 1 to 0 without mis-detection, and $b_{L,0}/Z_0$ is the probability of counter reset after either a successful or failed transmission. Also, we have

$$\tau_{L,H_1}=\sum_{k=1}^{4}\sum_{n=1}^{\hat{J}_k}P_{J,k}(n)b_{L,n}, \tag{28}$$

where $P_{J,k}(n)b_{L,n}$ is the probability that the counter of this LAA link reduces from $n$ to zero after mis-detection of event $J_K$. The CAPs $\tau_{W,H_0}$ and $\tau_{W,H_1}$ in the WLAN system can be obtained using a similar procedure, omitted here for brevity.

***Successful Transmission Probabilities***

In deriving (2) through (7), it is assumed that $\tau_{L,H_0}$ and $\tau_{L,H_1}$ are independent, so are $\tau_{W,H_0}$ and $\tau_{W,H_1}$. A slightly

Ma, Yao; Coder, Jason.
"Analysis of Generalized CCA Errors and Mitigation in LTE-LAA Spectrum Sharing System."
Paper presented at IEEE Global Communications Conference (GLOBECOM 2019) , Waikoloa, HI, United States. December 9, 2019 - December 13, 2019.

more accurate result can be obtained if we drop this independence assumption. Then we obtain improved formulas to replace (4)–(7), shown below,

$$P_{S,L} = n_L \tau_{L,H_0}(1-\tau_{L,H_0}-\tau_{L,H_1})^{n_L-1} \quad (29)$$

$$P_{S,W} = n_W \tau_{W,H_0}(1-\tau_{W,H_0}-\tau_{W,H_1})^{n_W-1}, \quad (30)$$

$$P_{I,L} = (1-\tau_{L,H_0}-\tau_{L,H_1})^{n_L}, \quad (31)$$

$$P_{I,W} = (1-\tau_{W,H_0}-\tau_{W,H_1})^{n_W}. \quad (32)$$

We derive the conditional STPs (conditioned upon that a transmission starts) of LAA and WLAN systems as

$$P_{t,L} = (1-\tau_{L,H_0}-\tau_{L,H_1})^{n_L-1}(1-\tau_{W,H_0}-\tau_{W,H_1})^{n_W}$$

$$P_{t,W} = (1-\tau_{L,H_0}-\tau_{L,H_1})^{n_L}(1-\tau_{W,H_0}-\tau_{W,H_1})^{n_W-1}.$$

Based on (2), (3), (4)–(7), and (23), the throughput and other KPIs of LAA and WLAN links with CCA errors and hard-collisions can be evaluated.

### D. Throughput Under CCA Errors and Soft-Collision

In the soft-collision case, we assume that H-ARQ is used for the miss-detection caused collided packets, and reduces the collision loss. With CCA-SC, the recovered payload for the LAA system is

$$\alpha_L(P_{S,L,H_0}P_{I,W,H_0} - P_{S,L}P_{I,W})T_{P,L} \quad (33)$$

where $\alpha_L$ $(0 \le \alpha_L < 1)$ is the packet recovery ratio due to soft combining of collided packets, and $(P_{S,L,H_0}P_{I,W,H_0} - P_{S,L}P_{I,W})$ refers to the probability that an original LAA transmission is corrupted by other LAA or WLAN links, but is later partially recovered.

We provide the soft-collision throughput for the LAA and WLAN systems as

$$S_L^{\text{SC}} = \frac{1}{T_{\text{ave},L}} T_{P,L}[P_{S,L}P_{I,W} + (P_{S,L,H_0}P_{I,W,H_0} - P_{S,L}P_{I,W})\alpha_L], \quad (34)$$

$$S_W^{\text{SC}} = \frac{1}{T_{\text{ave},W}} T_{P,W}[P_{S,W}P_{I,L} + (P_{S,W,H_0}P_{I,L,H_0} - P_{S,W}P_{I,L})\alpha_W]. \quad (35)$$

where $\alpha_W$ $(0 \le \alpha_W < 1)$ is the packet recovery ratio of the WLAN system. Based on (34), (35), (4)–(7), and (23), the KPIs of the coexisting LAA and WLAN links with CCA sensing errors and soft-collisions can be readily evaluated.

A discussion about result in [11] is in order. The work [11] provided solid progress on the effect of CCA errors on a single CSMA/CA system. Yet, besides the restrictive assumption of independent CCA errors, some analytical steps in [11] involved major approximations. For example, in (11) of [11] the throughput was set to be equal to the successful transmission probability, which lacked theoretical justification. The key throughput result in (13) of [11] included effects of mis-detection and false alarm probabilities, but it could not be shown to be consistent to the result of perfect CCA even when the mis-detection and false alarm probabilities are set to zero therein. Nevertheless, results in [11] may be regarded as useful approximations for certain range of parameters.

## IV. Numerical and Simulation Results

In this section, we provide both analytical and simulation results to show the impact of sensing errors on the coexistence KPI performance of LTE-LAA and WLAN links.

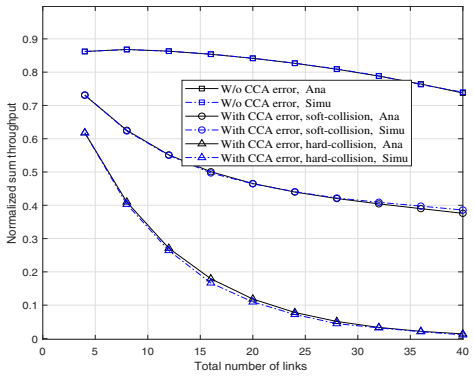


Fig. 2: Normalized sum throughput of the LTE-LAA and WLAN systems, when $P_{m,L} = P_{m,W} = 0.1$, $P_{\text{Fa},L} = P_{\text{Fa},W} = 0.1$, $W_0 = Z_0 = 32$, and $n_L + n_W$ changes from 4 to 40, with RTS/CTS scheme.

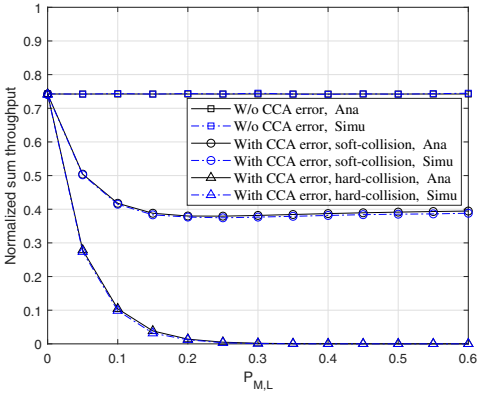


Fig. 3: Normalized sum throughput of the LTE-LAA and WLAN systems vs. $P_{m,L}$, when $n_L = n_W = 10$, $P_{\text{Fa},L} = P_{\text{Fa},W} = 0$, and $W_0 = Z_0 = 16$.

Both LTE-LAA and WLAN systems can use request-to-send/clear to send (RTS/CTS) type of handshaking schemes. Some CSMA/CA parameters and equations to compute $T_{S,L}$ (and $T_{C,L}$) from $T_{P,L}$, and to compute $T_{S,W}$ (and $T_{C,W}$) from $T_{P,W}$ are provided in [16], [17]. We set $\delta_L = \delta_W = \delta = 9$ $\mu s$ following the default values [1], [6].

We assume a blockwise slow fading channel. This is realistic for the small cell or indoor fading channels which experience small Doppler spread. In computer simulation, we track all the backoff, transmission, and sensing error events, as described in Table III. Besides the case of perfect CCA, under CCA errors both hard-collision (CCA-HC) and soft collisions (CCA-SC) schemes are simulated (where we assume $\alpha_L = \alpha_W = 0.5$). On each parameter setting we ran the

Ma, Yao; Coder, Jason.
"Analysis of Generalized CCA Errors and Mitigation in LTE-LAA Spectrum Sharing System."
Paper presented at IEEE Global Communications Conference (GLOBECOM 2019) , Waikoloa, HI, United States. December 9, 2019 - December 13, 2019.

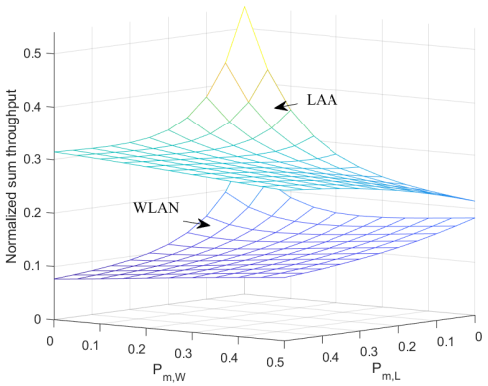


Fig. 4: Normalized sum throughput of the LTE-LAA and WLAN systems vs. $P_{m,L}$ and $P_{m,W}$ (from 0 to 0.5), respectively, when $n_L = n_W = 10$, $P_{\text{Fa},L} = P_{\text{Fa},W} = 0$, $W_0 = 32$, and $Z_0 = 16$.

algorithms for $10^5$ time slots to obtain the average statistics on the throughput and transmission probabilities. We provide the time efficiency MAC throughput which is the time proportion of successful payload transmission of the system divided by the total observation duration. The normalized payload durations of LAA and WLAN are $L_{P,L} = L_{P,W} = 100$.

Fig. 2 shows the sum throughput of LAA and WLAN systems of 3 cases (without CCA errors, CCA-SC and CCA-HC) as $n_L + n_W$ increases. Fig. 3 provides the sum throughput vs. $P_{m,L}$, and the result shows that the throughput of the CCA-HC scheme decreases fast to zero when $P_{m,L} \simeq 0.2$, while the throughput of the CCA-SC scheme is partially maintained and robust against mis-detection. All results in Figs. 2 and 3 verify close matches among analytical and simulation results, and show that the proposed CCA-SC scheme is much more robust than the CCA-HC against CCA errors.

Finally, we provide analytical throughput of LAA and WLAN CCA-SC schemes vs. $P_{m,L}$ and $P_{m,W}$ in Fig. 4, which shows several observations: 1. The $P_{m,L}$ and $P_{m,W}$ affect the LAA and WLAN systems differently; 2. The LAA system has a higher throughput than the WLAN due to the CSMA parameter setting that $Z_0 = W_0/2$. This result suggests that we can use adaptive CSMA parameters (such as CW size and backoff stage) to achieve different throughput allocation even under CCA errors.

## V. Conclusion

In this paper, we have modeled and evaluated the MAC layer performance of CSMA/CA coexisting systems (LTE-LAA and WLAN) assuming generalized CCA sensing errors. This technique applies to both slow fading (correlated CCA errors) and fast fading channels (independent CCA errors). To our knowledge, this is the first result that explicitly models generalized CCA errors on CSMA/CA backoff process, and provides accurate analysis of KPIs with applications to spectrum sharing systems. We have programmed LTE-LAA and WLAN MAC schemes under CCA errors and implemented extensive computer simulations, which have verified the accuracy of our analysis results. Simulation results have showed that sensing errors can significantly degrade the throughput, and the soft-collision method can reduce the performance loss substantially. These results have provided significant progress on the modeling, analysis, and mitigation of the impact of CCA errors on the CSMA/CA MAC layer, with application to coexistence systems. In the future work, we will implement hardware experiments, such as that reported in [18], to further validate our results.

## References


[1] 3GPP TS RAN, "E-UTRA Physical layer procedures (Release 14)", 3GPP TS 36.213 V14.4.0, Sept. 2017.

[2] 3GPP TSG RAN, "Study On Licensed-Assisted Access To Unlicensed Spectrum", 3GPP TR 36.889 V13.0.0, Jun. 2015.

[3] Ericsson, "Discussion on LBT protocols," 3GPP Tech. Rep. R1-151996, Apr. 2015.

[4] R. Zhang, M. Wang, L. X. Cai, Z. Zheng, and X. Shen, "LTE-unlicensed: the future of spectrum aggregation for cellular networks," *IEEE Wireless Commun.*, vol. 22, no. 3, pp. 150–159, Jun. 2015.

[5] A. Mukherjee et al., "Licensed-assisted access LTE: coexistence with IEEE 802.11 and the evolution toward 5G," *IEEE Commun. Mag.*, vol. 54, no. 6, pp. 50-57, Jun. 2016.

[6] IEEE LAN/MAN Standards Committee, IEEE Std 802.11-2012, Part 11: Wireless LAN Medium Access Control (MAC) and Physical Layer (PHY) Specifications, Feb. 2012.

[7] L. Dai and X. Sun, "A unified analysis of IEEE 802.11 DCF networks: stability, throughput, and delay," *IEEE Trans. Mobile Comput.*, vol.12, no.8, pp.1558–1572, Aug. 2013.

[8] Y. Chen, Q. Zhao and A. Swami, "Joint design and separation principle for opportunistic spectrum access in the presence of sensing errors," *IEEE Trans. Inf. Theory*, vol. 54, no. 5, pp. 2053–2071, May 2008.

[9] A. T. Hoang, D. T. C. Wong, and Y.-C. Liang, "Design and analysis for an 802.11-based cognitive radio network," in *Proc. IEEE Wireless Commun. Netw. Conf. (WCNC)*, Apr. 2009, pp. 1–6.

[10] T. H. Kim, J. Ni, R. Srikant and N. H. Vaidya, "Throughput-optimal CSMA with imperfect carrier sensing," in *IEEE/ACM Trans. Netw.*, vol. 21, no. 5, pp. 1636–1650, Oct. 2013.

[11] J. W. Chong, D. K. Sung and Y. Sung, "Cross-layer performance analysis for CSMA/CA protocols: impact of imperfect sensing," *IEEE Trans. Veh. Technol.*, vol. 59, no. 3, pp. 1100-1108, March 2010.

[12] G. Bianchi, "Performance analysis of the IEEE 802.11 distributed coordination function," *IEEE J. Sel. Areas Commun.*, vol. 18, no. 3, pp. 535–547, Mar. 2000.

[13] I. Tinnirello, G. Bianchi, and X. Yang, "Refinements on IEEE 802.11 distributed coordination function modeling approaches," *IEEE Trans. Veh. Technol.*, vol.59, no.3, pp.1055–1067, Mar. 2010.

[14] R. Yin, G. Yu, A. Maaref, and G. Li, "A framework for co-channel interference and collision probability tradeoff in LTE licensed-assisted access networks," *IEEE Trans. Wireless Commun.*, vol. 15, no. 9, pp. 6078–6090, Sept. 2016.

[15] S. Han, Y. C. Liang, Q. Chen and B. H. Soong, "Licensed-assisted access for LTE in unlicensed spectrum: A MAC protocol design," *IEEE J. Sel. Areas Commun.*, vol. 34, no. 10, pp. 2550–2561, Oct. 2016.

[16] Y. Ma and D. G. Kuester, "MAC-layer coexistence analysis of LTE and WLAN systems via listen-before-talk," in *Proc. IEEE CCNC*, Las Vegas, NV, 2017, pp. 534-541.

[17] Y. Ma, D. G. Kuester, J. Coder and W. Young, "Slot jamming effect and mitigation between LTE-LAA and WLAN systems with heterogenous slot durations," *IEEE Trans. Commun.*, vol. 67, no. 6, pp. 4407-4422, June 2019.

[18] Y. Ma, R. Jacobs, D. G. Kuester, J. Coder, and W. F. Young, "SDR-Based experiments for LTE-LAA based coexistence systems with improved design," in *Proc. IEEE GlobeCom*, Singapore, Dec. 2017.

[19] W. C. Jakes, Jr., *Microwave Mobile Communications,* New York: Wiley, 1974.

[20] 3GPP TSG RAN, "Study on NR-based access to unlicensed spectrum", 3GPP TR 38.889 V16.0.0, Dec. 2018.

[21] A. Papoulis and S. U. Pillai, *Probability, Random Variables, and Stochastic Processes,* 4th ed. New York: McGraw-Hill, 2002.



Ma, Yao; Coder, Jason.
"Analysis of Generalized CCA Errors and Mitigation in LTE-LAA Spectrum Sharing System."
Paper presented at IEEE Global Communications Conference (GLOBECOM 2019) , Waikoloa, HI, United States. December 9, 2019 - December 13, 2019.

# Enhancing LAA Co-existence Using MIMO Under Imperfect Sensing

Susanna Mosleh[†§], Yao Ma[‡], Jason B. Coder[‡], Erik Perrins[*], and Lingjia Liu[**]

[†]*Associate, Communications Technology Laboratory, National Institute of Standards and Technology, Boulder, Colorado, USA*
[§]*Department of Physics, University of Colorado, Boulder, Colorado, USA*
[‡]*Communications Technology Laboratory, National Institute of Standards and Technology, Boulder, Colorado, USA*
[*]*Department of Electrical Engineering and Computer Science, the University of Kansas, Lawrence, Kansas, USA*
[**]*Bradley Department of Electrical and Computer Engineering, Virginia Tech, Blacksburg, Virginia, USA*

***Abstract*—To meet the ever growing wireless network demands, in terms of subscribers and data throughput, operating long term evolution (LTE) in unlicensed bands, such as license assisted access (LAA), is introduced as a promising solution. However, the LAA network must co-exist with incumbent IEEE 802.11 systems. In this paper, we use MIMO operation to boost LAA-WLAN coexistence. We take the impact of imperfect sensing into account and analyze key performance indicators (KPIs), such as throughput, probabilities of successful transmissions, and collisions. Moreover, we characterize the optimal LAA contention window size to maximize the LAA sum rate while assuring Wi-Fi throughput above a predetermined threshold. Numerical results show the efficiency of the introduced algorithm and that if the parameters are appropriately selected, the throughput of both systems increases.**

***Index Terms*—Beamforming, coexistence, contention window, imperfect sensing, LTE-LAA, MAC layer, PHY layer, WLAN.**

## I. Introduction

The big data era is being shaped with the ongoing growth of commercial data services, with mobile wireless networks constituting a major source of data. Wireless communication is becoming tightly integrated in our daily lives; especially with the global spread of laptops, tablets, smartphones, video streaming, and online social networking applications. This globalization has paved the way to dramatically increase wireless network dimensions in terms of subscribers and amount of data traffic. Cisco Systems forecasts that the number of mobile-connected devices per capita will reach 3.6 by 2022 and global mobile data traffic will increase sevenfold between 2017 and 2022 [1]. Licensed spectrum bands are high-priced and the theoretical potential of the physical layer is almost achieved. However, there are still some licensed bands that are under utilized. As a consequence, sharing the under utilized licensed spectrum among networks and using the unlicensed spectrum bands are inescapable.

Formerly, the unlicensed bands were dominated by Wi-Fi traffic, and occasionally used by commercial cellular carriers for offloading data that would otherwise have been sent via long term evolution (LTE) in licensed spectrum. Lately, mobile network operators have paid close attention to operate LTE in unlicensed bands, such as license-assisted access (LAA), in addition to data offloading. However, this coexistence may have an enormous influence on Wi-Fi operation and create a number of challenges for both Wi-Fi and LTE networks to constructively share the spectrum. Having a good comprehension of these challenges demands a deep dive into the operations of both networks in the MAC and physical layers.

In this paper we boost LAA-Wi-Fi coexistence by employing multiple-input multiple-output (MIMO) operation and reducing the interference between LAA and Wi-Fi networks. We take the impact of imperfect sensing (the networks' cross-technology probability of detection and false alarm) into account and obtain the LAA and Wi-Fi throughput as a function of the sensing errors. Moreover, by maximizing the LAA sum rate while assuring Wi-Fi throughput above a predetermined threshold, we find the optimum LAA contention window size.

The remainder of this paper is organized as follows. Section II describes the system model and assumptions required for our analysis. Section III presents the problem formulation and analysis. Section IV explains the impact of the sensing threshold and imperfect spectrum sensing in a coexistence scenario. Numerical results are shown in Section V. Finally, in Section VI, a summary of the results and some concluding remarks are presented.

*Notation*: Throughout this paper, normal letters are used for scalars. Boldface capital and lower case letters denote matrices and vectors, respectively. The Hermitian of a complex vector $\mathbf{a}$ is denoted by $\mathbf{a}^H$. $\mathcal{CN}(0,\sigma^2)$ represents a circularly symmetric complex Gaussian random variable and $\mathbb{E}[\cdot]$ denotes the expectation operator. See Table I for major notations and symbols used in this paper.

## II. System Model and Assumptions

We consider a downlink multi-cell coexistence scenario where $n_L \in \mathcal{L} \triangleq \{n_\ell | \ell = 1, 2, \ldots, L\}$ LTE-LAA eNodeBs and $n_W \in \mathcal{W} \triangleq \{n_w | w = 1, 2, \ldots, W\}$ Wi-Fi access points (APs) share the same unlicensed band $k \in \mathcal{K} \triangleq \{1, 2, \ldots, K\}$ in an industrial, scientific, and medical (ISM) radio band[1].



[1]Note that the focus of this study is the operation of cellular base stations in an unlicensed band. However, these base stations may have permission to utilize a licensed band as well.

Mosleh, Somayeh; Ma, Yao; Coder, Jason; Perrins, Erik; Liu, Lingjia.
"Enhancing LAA Co-existence Using MIMO Under Imperfect Sensing."
Paper presented at 2019 IEEE Global Communications Conference: Workshop on Advancements in Spectrum Sharing, Waikoloa, HI, United States. December 13, 2019 - December 13, 2019.

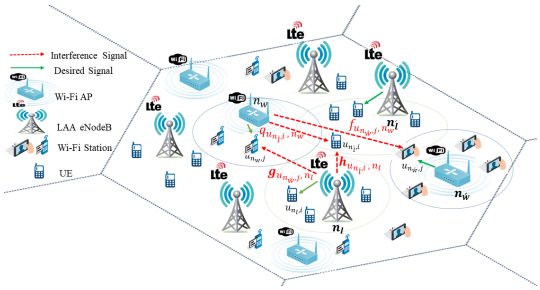


Fig. 1: Multi-cell system model in a coexistence scenario

We assume a coexistence scenario in which both Wi-Fi and LAA are in the saturated traffic condition. We also assume that LAA uses orthogonal frequency-division multiple access (OFDMA). Hence, we equally divide the unlicensed band $k$ into $N_k$ sub-channels, i.e., $\mathcal{N}_k = \{1, 2, \ldots, N_k\}$, where each sub-channel has a bandwidth of $B_k$. Moreover, we assume that each unlicensed sub-channel can be shared between the UEs and Wi-Fi stations in a time-sharing fashion.

### A. Network Topology

We also assume that the eNodeBs and APs are randomly distributed over each cell, while Wi-Fi clients (LTE user equipment (UEs)) are distributed around each AP (eNodeB) independently and uniformly, as depicted in Figure 1. The eNodeB $n_\ell$ is equipped with $N_t$ transmit antennas and simultaneously serves a set of $|\mathcal{U}_{n_\ell}|$ single antenna UEs on the unlicensed band, where $\mathcal{U}_{n_\ell} = \{u_{n_\ell,1}, u_{n_\ell,2}, \ldots, u_{n_\ell,|\mathcal{U}_{n_\ell}|}\}$. Since multiple eNodeBs and UEs are operating on the same unlicensed band as Wi-Fi devices, this coexistence may have an enormous influence on the Wi-Fi operation, and vice versa. Hence, multiple transmit antennas at each eNodeB can provide beamforming and interference-nulling opportunities for the associated UEs and the Wi-Fi nodes, respectively. We assume that the eNodeB $n_\ell$ transmits with power $p_{n_\ell}$ and the user association is based on the received power (*i.e.,* each UE will be assigned to the eNodeB that provides it with the highest power).

The $n_w$-th AP is equipped with a single antenna and serves a set of $|\mathcal{U}_{n_w}|$ single antenna Wi-Fi stations, one station at a time, where $\mathcal{U}_{n_w} = \{u_{n_w,1}, u_{n_w,2}, \ldots, u_{n_w,|\mathcal{U}_{n_w}|}\}$. Similar to the LAA network, each Wi-Fi station will be associated with the Wi-Fi AP that delivers the largest received power to it. We also assume that the Wi-Fi AP $n_w$ transmits with power $p_{n_w}$.

### B. Channel Model

The channel (propagation) coefficients between the $n_\ell$ eNodeB and the $u_{n_{\ell'},i}$ UE form the channel matrix $\mathbf{h}_{u_{n_{\ell'},i},n_\ell} = \sqrt{\beta_{u_{n_{\ell'},i},n_\ell}}\tilde{\mathbf{h}}_{u_{n_{\ell'},i},n_\ell} \in \mathbb{C}^{N_t}$ where $\beta_{u_{n_{\ell'},i},n_\ell}$ is a large-scale fading coefficient that depends upon the shadowing and distance between the corresponding UE and eNodeB. The large-scale fading coefficient is denoted by $\beta_{u_{n_{\ell'},i},n_\ell} = \psi_{u_{n_{\ell'},i},n_\ell} d^{-\alpha}_{u_{n_{\ell'},i},n_\ell}$, where $d_{u_{n_{\ell'},i},n_\ell}$ is the distance between the $u_{n_{\ell'},i}$ UE and the $n_\ell$ eNodeB, $\alpha$ is the path-loss exponent, and $\psi_{u_{n_{\ell'},i},n_\ell}$ is a log-normal random variable (*i.e.*, the quantity $10\log_{10}(\psi_{u_{n_{\ell'},i},n_\ell})$ is distributed as zero-mean Gaussian with a standard deviation of $\sigma_{\text{shadowing}}$). The small-scale fading coefficients (*i.e.*, elements of $\tilde{\mathbf{h}}_{u_{n_{\ell'},i},n_\ell}$) are modeled as i.i.d. complex Gaussian variables with zero-mean and unit-variance. We further assume a block fading model, where small-scale channels are constant over a few time slots with respect to channel estimation and channel state information (CSI) feedback procedures. Similarly, we assume that large-scale fading coefficients $\beta_{u_{n_{\ell'},i},n_\ell}$ stay constant during large-scale coherence blocks. The small-scale and large-scale fading coefficients in different coherence blocks are assumed to be independent.

Similarly, the channel matrix $\mathbf{g}_{u_{n_{w'},j},n_\ell} = \sqrt{\beta_{u_{n_{w'},j},n_\ell}}\tilde{\mathbf{g}}_{u_{n_{w'},j},n_\ell} \in \mathbb{C}^{N_t}$ denotes the channel coefficient between the $n_\ell$ eNodeB and the Wi-Fi station $u_{n_{w'},j}$. Moreover, the channel coefficient between Wi-Fi AP $n_w$ and UE $u_{n_{\ell'},i}$ and Wi-Fi station $u_{n_{w'},j}$ form the channel metrics $q_{u_{n_{\ell'},i},n_w} = \sqrt{\beta_{u_{n_{\ell'},i},n_w}}\tilde{q}_{u_{n_{\ell'},i},n_w} \in \mathbb{C}$ and $f_{u_{n_{w'},j},n_w} = \sqrt{\beta_{u_{n_{w'},j},n_w}}\tilde{f}_{u_{n_{w'},j},n_w} \in \mathbb{C}$, respectively.

TABLE I: Nomenclatures and Notations Used

| Notation | Description |
|---|---|
| $n_\ell$ | The $\ell$-th eNodeB |
| $n_w$ | The $w$-th AP |
| $u_{n_\ell,i}$ | The $i$-th UE associated to the $n_\ell$-th eNodeB |
| $u_{n_w,j}$ | The $j$-th Wi-Fi client associated to the $n_w$-th AP |
| $\beta_{u_{n_{\ell'},i},n_\ell}$ | Large-scale fading coefficient between $u_{n_{\ell'},i}$ and $n_\ell$ |
| $d_{u_{n_{\ell'},i},n_\ell}$ | The distance between $u_{n_{\ell'},i}$ and $n_\ell$ |
| $\mathbf{h}_{u_{n_{\ell'},i},n_\ell}$ | The channel coefficient between $u_{n_{\ell'},i}$ and $n_\ell$ |
| $\mathbf{g}_{u_{n_{w'},j},n_\ell}$ | The channel coefficient between $u_{n_{w'},j}$ and $n_\ell$ |
| $q_{u_{n_{\ell'},i},n_w}$ | The channel coefficient between $u_{n_{\ell'},i}$ and $n_w$ |
| $f_{u_{n_{w'},j},n_w}$ | The channel coefficient between $u_{n_{w'},j}$ and $n_w$ |
| $\mathbf{x}^{(m,k)}_{n_\ell}$ | Precoded symbol vector from $n_\ell$ to its associated UEs |
| $\tilde{p}^{(m,k)}_{u_{n_\ell,i},n_\ell}$ | Transmit power allocated to $u_{n_\ell,i}$ from $n_\ell$ at $(m,k)$ |
| $\mathbf{v}^{(m,k)}_{u_{n_\ell,i},n_\ell}$ | Beamformer $n_\ell$ uses to transmit to the $u_{n_\ell,i}$ at $(m,k)$ |
| $s^{(m,k)}_{u_{n_\ell,i},n_\ell}$ | Transmitted signal from $n_\ell$ to the $u_{n_\ell,i}$ at $(m,k)$ |
| $\tilde{s}^{(k)}_{u_{n_w,j},n_w}$ | Transmitted signal from $n_w$ to the $u_{n_w,j}$ at the sub-channel $k$ |
| $y^{(m,k)}_{u_{n_\ell,i},n_\ell}$ | Received signal at the $u_{n_\ell,i}$ at $(m,k)$ |
| $W^{(k)}_{\min,i}$ | Min. CW size of the $i$-th transmitter on the $k$-th channel |
| $m^{(k)}_i$ | Max. back-off stage of the $i$-th transmitter |
| $p^{(k)}_{tr}$ | The prob. of occupation on the $k$-th unlicensed channel |
| $p^{(k)}_{tr,i}$ | The prob. of transmitting a packet by the $i$-th transmitter |
| $p^{(k)}_{c,i}$ | The prob. of collision experienced by the $i$-th transmitter |
| $p^{(k)}_{s,i}$ | The prob. of successful transmission of the $i$-th transmitter |
| $p^{(k)}_{s,\mathcal{W}}$ | The prob. of successful transmission of Wi-Fi network |
| $p^{(k)}_{s,\mathcal{L}}(\gamma_{k,n_\ell})$ | The prob. of successful transmission of LAA network |
| $p^{(k)}_{c,\mathcal{W}}$ | The prob. of collision among Wi-Fi transmissions |
| $p^{(k)}_{c,\mathcal{L}}$ | The prob. of collision among LAA transmissions |
| $p^{(k)}_{c,\mathcal{W},\mathcal{L}}$ | The prob. of collision between LAA and Wi-Fi transmissions |
| $p^{(k)}_{tr,\mathcal{L}}$ | The prob. of transmission of LAA network |
| $p^{(k)}_{tr,\mathcal{W}}$ | The prob. of transmission of Wi-Fi network |
| $\lambda_{u_{n_\ell,i}}$ | The priority of user $u_{n_\ell,i}$ in the LAA network |
| $\lambda_{u_{n_w,j}}$ | The priority of user $u_{n_w,j}$ in the Wi-Fi network |

Mosleh, Somayeh; Ma, Yao; Coder, Jason; Perrins, Erik; Liu, Lingjia.
"Enhancing LAA Co-existence Using MIMO Under Imperfect Sensing."
Paper presented at 2019 IEEE Global Communications Conference: Workshop on Advancements in Spectrum Sharing, Waikoloa, HI, United States. December 13, 2019 - December 13, 2019.

### C. Received Signals

Prior to transmitting on the sub-channel $m \in \mathcal{N}_k$ of the unlicensed channel $k$, the $n_\ell$ eNodeB linearly precodes its symbol vector

$$\mathbf{x}_{n_\ell}^{(k,m)} = \sum_{u_{n_\ell,i} \in \mathcal{U}_{n_\ell}} \sqrt{\tilde{p}_{u_{n_\ell,i},n_\ell}^{(k,m)}} \mathbf{v}_{u_{n_\ell,i},n_\ell}^{(k,m)} s_{u_{n_\ell,i},n_\ell}^{(k,m)}$$

where $\tilde{p}_{u_{n_\ell,i},n_\ell}^{(k,m)}$ stands for the transmit power allocated to user $u_{n_\ell,i}$ from the $n_\ell$ eNodeB on the sub-channel $m$ of the unlicensed band $k$, and $\mathbf{v}_{u_{n_\ell,i},n_\ell}^{(k,m)}$ denotes the unit-norm beamformer that eNodeB $n_\ell$ uses to transmit the signal $s_{u_{n_\ell,i},n_\ell}^{(k,m)}$ to receiver $u_{n_\ell,i}$ on the $m$-th sub-channel of the unlicensed band channel $k$ [2], [3]. Each eNodeB $n_\ell$ on the unlicensed channel $k$ is under a transmit power constraint of $P_{n_\ell}^{k,\max}$ due to the regulations on the unlicensed channels [4]. Under our assumptions, the received signal at the UE $u_{n_\ell,i}$ on the $(k,m)$ unlicensed band can be written as

$$\begin{aligned} y_{u_{n_\ell,i}}^{(k,m)} = & \underbrace{\sqrt{\tilde{p}_{u_{n_\ell,i},n_\ell}^{(k,m)}} \mathbf{h}_{u_{n_\ell,i},n_\ell}^{(k,m)H} \mathbf{v}_{u_{n_\ell,i},n_\ell}^{(k,m)} s_{u_{n_\ell,i},n_\ell}^{(k,m)}}_{\text{Desired signal}} \\ & + \underbrace{\sum_{\substack{\acute{i}=1 \\ \acute{i}\neq i}}^{|\mathcal{U}_{n_\ell}|} \sqrt{\tilde{p}_{u_{n_\ell,\acute{i}},n_\ell}^{(k,m)}} \mathbf{h}_{u_{n_\ell,i},n_\ell}^{(k,m)H} \mathbf{v}_{u_{n_\ell,\acute{i}},n_\ell}^{(k,m)} s_{u_{n_\ell,\acute{i}},n_\ell}^{(k,m)}}_{\text{Intra-cell interference from the serving eNodeB}} \\ & + \underbrace{\sum_{\substack{\acute{\ell}=1 \\ \acute{\ell}\neq \ell}}^{L} \sum_{\acute{i}=1}^{|\mathcal{U}_{n_{\acute{\ell}}}|} \sqrt{\tilde{p}_{u_{n_{\acute{\ell}},\acute{i}},n_{\acute{\ell}}}^{(k,m)}} \mathbf{h}_{u_{n_\ell,i},n_{\acute{\ell}}}^{(k,m)H} \mathbf{v}_{u_{n_{\acute{\ell}},\acute{i}},n_{\acute{\ell}}}^{(k,m)} s_{u_{n_{\acute{\ell}},\acute{i}},n_{\acute{\ell}}}^{(k,m)}}_{\text{Inter-cell interference from other eNodeBs}} \\ & + \underbrace{\sum_{w=1}^{W} \sqrt{p_{n_w}^{(k)}} q_{u_{n_\ell,i},n_w}^{(k)} \tilde{s}_{u_{n_w,j},n_w}^{(k)}}_{\text{Interference from Wi-Fi APs}} + \underbrace{\epsilon_{u_{n_\ell,i}}^{(k,m)}}_{\text{Noise}}, \end{aligned} \tag{1}$$

where $\tilde{s}_{u_{n_w,j},n_w}^{(k)}$ is the transmitted signal from the AP $n_w$ to the Wi-Fi station $u_{n_w,j}$ on the channel $k$, and $\epsilon_{u_{n_\ell,i}}^{(k,m)} \sim \mathcal{CN}(0, \sigma_{u_{n_\ell,i}}^{(k,m)^2})$.

Recall that the signal-to-interference-plus-noise ratio (SINR) is defined as the ratio of the received signal power at the desired user to the interference plus noise power. The SINR for serving user $u_{n_\ell,i}$ on the $(k,m)$ unlicensed band can be expressed as (2). Assuming each sub-channel $m$ can be shared between the UEs associated with $n_\ell$ eNodeB in a time sharing fashion, the transmission rate for the UE $u_{n_\ell,i}$ on the $(k,m)$ unlicensed band can be expressed as

$$R_{u_{n_\ell,i}}^{(k,m)} = \gamma_{k,n_\ell} c_{u_{n_\ell,i}}^{(k,m)} B_{k,m} \log_2(1 + \chi_{u_{n_\ell,i}}^{(k,m)} \cdot \text{SINR}_{u_{n_\ell,i}}^{(k,m)}),$$

where $\gamma_{k,n_\ell}$ represents the fraction of time when the $n_\ell$-th eNodeB is active on the unlicensed channels $k$, $0 \leq c_{u_{n_\ell,i}}^{(k,m)} \leq 1$ denotes the time sharing component of the UE $u_{n_\ell,i}$ on the $(k,m)$ unlicensed band that fulfills $0 \leq \sum_{n_\ell \in \mathcal{N}_L} \sum_{u_{n_\ell,i} \in \mathcal{U}_{n_\ell}} c_{u_{n_\ell,i}}^{(k,m)} \leq 1$, and $\chi_{u_{n_\ell,i}}^{(k,m)}$ is the channel access indicator which is 1 if the eNodeB $n_\ell$ serves the UE $u_{n_\ell,i}$ on the $(k,m)$, and is 0 otherwise.

It is worth noting that the LAA transmission on the unlicensed channel $k$ will happen if $(i)$ there is no Wi-Fi transmission in the network and the LAA eNodeB's channel observations do not generate any false alarms or $(ii)$ the Wi-Fi transmission is occurring but the LAA network does not become aware of that. While the latter happens with probability $(1 - P_{d,\mathcal{L}}^{(k)}) p_{tr,\mathcal{W}}^{(k)}$, the probability of the former is $(1 - P_{fa,\mathcal{L}}^{(k)})(1 - p_{tr,\mathcal{W}}^{(k)})$, where $P_{d,\mathcal{L}}^{(k)}$, $P_{fa,\mathcal{L}}^{(k)}$, and $p_{tr,\mathcal{W}}^{(k)}$ denotes the LAA's cross-technology probability of detection, probability of false alarm, and Wi-Fi's transmission probability on the unlicensed channel $k$ (which will be discussed in Section IV), respectively. Hence, the achievable data rate of the UE $u_{n_\ell,i}$ can be expressed as

$$\begin{aligned} R_{u_{n_\ell,i}} = \sum_{k \in \mathcal{K}} \sum_{m \in \mathcal{N}_k} \big( & (1 - p_{tr,\mathcal{W}}^{(k)})(1 - P_{fa,\mathcal{L}}^{(k)}(\eta_\mathcal{L})) R_{u_{n_\ell,i}}^{(k,m)^{\mathcal{H}_0}} \\ & + p_{tr,\mathcal{W}}^{(k)}(1 - P_{d,\mathcal{L}}^{(k)}(\eta_\mathcal{L})) \cdot R_{u_{n_\ell,i}}^{(k,m)^{\mathcal{H}_1}} \big) \end{aligned}$$

where $\eta_\mathcal{L}$ indicates the LAA's carrier sense threshold level (function of SINR), $R_{u_{n_\ell,i}}^{(k,m)^{\mathcal{H}_1}}$ and $R_{u_{n_\ell,i}}^{(k,m)^{\mathcal{H}_0}}$ denote the achievable data rate of the UE $u_{n_\ell,i}$ on the $(k,m)$ unlicensed band when there is and is not Wi-Fi transmission, respectively.

Similarly, the received signal at the Wi-Fi station $u_{n_w,j}$ on the $k$-th unlicensed band can be written as

$$\begin{aligned} y_{u_{n_w,j}}^{(k)} = & \underbrace{\sqrt{p_{n_w}^{(k)}} f_{u_{n_w,j},n_w}^{(k)} \tilde{s}_{u_{n_w,j},n_w}^{(k)}}_{\text{Desired signal}} + \underbrace{\epsilon_{u_{n_w,j}}^{(k)}}_{\text{Noise}} \\ & + \underbrace{\sum_{\substack{\acute{w}=1 \\ \acute{w}\neq w}}^{W} \sqrt{p_{n_{\acute{w}}}^{(k)}} f_{u_{n_w,j},n_{\acute{w}}}^{(k)} \tilde{s}_{u_{n_{\acute{w}},\acute{j}},n_{\acute{w}}}^{(k)}}_{\text{Interference from other Wi-Fi APs}} \\ & + \underbrace{\sum_{m=1}^{N_k} \sum_{\ell=1}^{L} \sum_{i=1}^{|\mathcal{U}_{n_\ell}|} \sqrt{\tilde{p}_{u_{n_\ell,i},n_\ell}^{(k,m)}} \mathbf{g}_{u_{n_w,j},n_\ell}^{(k,m)H} \mathbf{v}_{u_{n_\ell,i},n_\ell}^{(k,m)} s_{u_{n_\ell,i},n_\ell}^{(k,m)}}_{\text{Interference from LTE-LAA eNodeBs}}, \end{aligned} \tag{4}$$

where $\epsilon_{u_{n_w,j}}^{(k)} \sim \mathcal{CN}(0, \sigma_{u_{n_w,j}}^{(k)^2})$. Accordingly, the SINR for serving the Wi-Fi station $u_{n_w,j}$ on the $k$-th unlicensed band can be given by (3) and the transmission rate for the Wi-Fi station $u_{n_w,j}$, on the $k$-th unlicensed band can be expressed in general form as

$$R_{u_{n_w,j}}^{(k)} = \tilde{\gamma}_{k,n_w} B_k \log_2(1 + \chi_{u_{n_w,j}}^{(k)} \text{SINR}_{u_{n_w,j}}^{(k)}),$$

where $0 \leq \tilde{\gamma}_{k,n_w} \leq 1$ represents the time fraction that the Wi-Fi AP $n_w$ occupied the unlicensed channel $k$, $B_k$ denotes the bandwidth of the $k$-th unlicensed band, and $\chi_{u_{n_w,j}}^{(k)} = 1$ if the Wi-Fi AP $n_w$ serves the Wi-Fi station $u_{n_w,j}$ on the unlicensed channel $k$, and is 0 otherwise. Following the same notation, the achievable data rate of the Wi-Fi station $u_{n_w,j}$ can be written as

$$\begin{aligned} R_{u_{n_w,j}} = \sum_{k \in \mathcal{K}} \big( & (1 - p_{tr,\mathcal{L}}^{(k)})(1 - P_{fa,\mathcal{W}}^{(k)}(\eta_\mathcal{W})) R_{u_{n_w,j}}^{(k)^{\mathcal{H}_0}} \\ & + p_{tr,\mathcal{L}}^{(k)}(1 - P_{d,\mathcal{W}}^{(k)}(\eta_\mathcal{W})) R_{u_{n_w,j}}^{(k)^{\mathcal{H}_1}} \big), \end{aligned}$$

Mosleh, Somayeh; Ma, Yao; Coder, Jason; Perrins, Erik; Liu, Lingjia.
"Enhancing LAA Co-existence Using MIMO Under Imperfect Sensing."
Paper presented at 2019 IEEE Global Communications Conference: Workshop on Advancements in Spectrum Sharing, Waikoloa, HI, United States. December 13, 2019 - December 13, 2019.

$$\text{SINR}_{u_{n_\ell,i}}^{(k,m)} = \frac{\tilde{p}_{u_{n_\ell,i},n_\ell}^{(k,m)} |\mathbf{h}_{u_{n_\ell,i},n_\ell}^{(k,m)^H} \mathbf{v}_{u_{n_\ell,i},n_\ell}^{(k,m)}|^2}{\sum\limits_{\substack{i=1 \\ i\neq i}}^{|\mathcal{U}_{n_\ell}|} \tilde{p}_{u_{n_\ell,i},n_\ell}^{(k,m)} |\mathbf{h}_{u_{n_\ell,i},n_\ell}^{(k,m)^H} \mathbf{v}_{u_{n_\ell,i},n_\ell}^{(k,m)}|^2 + \sum\limits_{\substack{\ell=1 \\ \ell\neq\ell}}^{L} \sum\limits_{i=1}^{|\mathcal{U}_{n_\ell}|} \tilde{p}_{u_{n_\ell,i},n_\ell}^{(k,m)} |\mathbf{h}_{u_{n_\ell,i},n_\ell}^{(k,m)^H} \mathbf{v}_{u_{n_\ell,i},n_\ell}^{(k,m)}|^2 + \sum\limits_{w=1}^{W} p_{n_w}^{(k)} |q_{u_{n_\ell,i},n_w}^{(k)}|^2 + \sigma_{u_{n_\ell,i}}^{(k,m)^2}}. \quad (2)$$

$$\text{SINR}_{u_{n_w,j}}^{(k)^{\mathcal{H}_1}} = \frac{p_{n_w}^{(k)} |f_{u_{n_w,j},n_w}^{(k)}|^2}{\sum\limits_{\substack{\acute{w}=1 \\ \acute{w}\neq w}}^{W} p_{n_{\acute{w}}}^{(k)} |f_{u_{n_w,j},n_{\acute{w}}}^{(k)}|^2 + \sum\limits_{m=1}^{N_k} \sum\limits_{\ell=1}^{L} \sum\limits_{i=1}^{|\mathcal{U}_{n_\ell}|} \tilde{p}_{u_{n_\ell,i},n_\ell}^{(k,m)} |\mathbf{g}_{u_{n_w,j},n_\ell}^{(k,m)^H} \mathbf{v}_{u_{n_\ell,i},n_\ell}^{(k,m)}|^2 + \sigma_{u_{n_w,j}}^{(k)^2}}. \quad (3)$$

where $R_{u_{n_w,j}}^{(k)\ \mathcal{H}_1}$ and $R_{u_{n_w,j}}^{(k)\ \mathcal{H}_0}$ denote the achievable data rate of the Wi-Fi station $u_{n_w,j}$ on the $k$-th unlicensed band when there is and is not LAA transmission, respectively.

Considering this system model, in the next section, we will propose an efficient spectrum sharing method between Wi-Fi and LAA networks on the unlicensed bands. In this scheme, each LAA eNodeB adjusts its contention window size on an unlicensed band in such a way that guarantees the Wi-Fi's network throughput while maximizing its achievable rate.

## III. Problem Formulation and Analysis

In this section, the problem of interest is to maximize the LTE-LAA network throughput on an unlicensed band while Wi-Fi network performance is assured above a predetermined threshold, taking into account the contribution of both MAC-layer parameters (like contention window size) and PHY-layer characteristics (such as carrier sense threshold, transmit power, beamforming). To be specific, the problem of maximizing the weighted sum rate of the LTE-LAA network with respect to the fraction of time that LAA is active is formulated subject to the Wi-Fi throughput constraint as follows

$$\max_{\boldsymbol{\gamma}} \quad \sum_{\ell=1}^{L} \sum_{i=1}^{|\mathcal{U}_{n_\ell}|} \lambda_{u_{n_\ell,i}} R_{u_{n_\ell,i}} \quad (5a)$$

$$\text{s.t.} \quad \sum_{w=1}^{W} \sum_{j=1}^{|\mathcal{U}_{n_w}|} \lambda_{u_{n_w,j}} R_{u_{n_w,j}} \geq \hat{r}_w, \quad (5b)$$

$$0 \leq \gamma_{k,n_\ell} \leq 1, \quad (5c)$$

where $\hat{r}_w$ denotes the required data rate by the Wi-Fi network, $\lambda_{u_{n_\ell,i}}$ ( $\lambda_{u_{n_w,j}}$) indicates the priority of user $u_{n\ell,i}$ ($u_{n_w,j}$) in the LAA (Wi-Fi) network, and (5b) guarantees the Wi-Fi network's throughput in the aforementioned coexistence scenario.

**Proposition 1.** *The problem of maximizing the weighted sum rate of the LAA network with respect to $\boldsymbol{\gamma}$ is convex.*

*Proof.* The second derivative of the twice differentiable function $R_{u_{n_\ell,i}}^{(k,m)}$ with respect to $\gamma_{k,n_\ell}$ is negative and its Hessian is symmetric negative definite. Hence, the objective function is concave in the vector of eNodeBs' occupying unlicensed channel factor. Moreover, the constraint set is composed of linear constraints. These render the optimization problem (5) convex. Hence, the optimization problem (5) can be efficiently solved using numerical iterative algorithms [5]. ■

**Remark 1.** *Depending on the time occupation of the unlicensed band $k$ by the eNodeB $n_\ell$, i.e. $\gamma_{k,n_\ell}$ ,the eNodeB $n_\ell$ is able to adaptively alter its minimum backoff contention window size $\text{CW}_{\min,n_\ell}^{(k)}$ at the beginning of each LTE frame on the $k$-th unlicensed channel. The reason is, in a coexistence scenario, the $n_L$ eNodeBs compete with the $n_W$ APs to access the unlicensed band. This rivalry is based on the Wi-Fi time slot duration. As the LTE frame duration exceeds the length of Wi-Fi time slot, the probability of a successful transmission by the eNodeB $n_\ell \in \mathcal{L}$ can be interpreted as the time fraction in which the eNodeB $n_\ell$ occupies the $k$-th unlicensed channel, i.e. $0 \leq \gamma_{k,n_\ell} = p_{s,n_\ell}^{(k)} \leq 1$ [6].*

In the next section, we will calculate the impact of imperfect sensing in Wi-Fi's and LAA's transmission and collision probabilities.

## IV. Imperfect Spectrum sensing and Impact of sensing threshold

### A. MAC Layer Schemes

Wi-Fi systems count on a contention-based medium access with a random back off process, a.k.a. Carrier Sense Multiple Access with Collision Avoidance (CSMA/CA) [7], [8]. LTE uses a listen before talk (LBT) channel access mechanism to maintain fair coexistence with the Wi-Fi. Among different LAA-LBT schemes, in this paper, we consider the Category 4 (Cat 4 LBT). Since it is based on the same Wi-Fi CSMA/CA scheme, it is well-suited in a coexistence scenario, as recommended by [9].

According to the analytical model based on Markov chain in [10], the probability of transmitting a packet by a transmitter $i \in \mathcal{I} = \{n_w, n_\ell\}$ in a following idle time slot on the unlicensed channel $k$ can be expressed by

$$p_{\text{tr},i}^{(k)} = \frac{2(1-2p_{c,i}^{(k)})}{(1-2p_{c,i}^{(k)})(1+\text{CW}_{\min,i}^{(k)}) + p_{c,i}^{(k)} \text{CW}_{\min,i}^{(k)} A}, \quad (6)$$

where $p_{c,i}^{(k)}$ is the probability of collision experienced by the $i$-th transmitting node on the $k$-th unlicensed channel, $A = (1-(2p_{c,i}^{(k)})^{m_i^{(k)}})$, and $\text{CW}_{\min,i}^{(k)}$ and $m_i^{(k)}$ are the minimum

Mosleh, Somayeh; Ma, Yao; Coder, Jason; Perrins, Erik; Liu, Lingjia.
"Enhancing LAA Co-existence Using MIMO Under Imperfect Sensing."
Paper presented at 2019 IEEE Global Communications Conference: Workshop on Advancements in Spectrum Sharing, Waikoloa, HI, United States. December 13, 2019 - December 13, 2019.

contention window size and the maximum back-off stage of the transmitting node $i$ on the unlicensed band $k$, respectively.

Therefore, in a coexistence scenario, the probability of occupation of the $k$-th unlicensed channel either by Wi-Fi or LAA can be expressed as

$$p_{\text{tr}}^{(k)} = 1 - \prod_{w=1}^{W}(1 - p_{\text{tr},n_w}^{(k)}) \prod_{\ell=1}^{L}(1 - p_{\text{tr},n_\ell}^{(k)}), \tag{7}$$

and the collision probability of the transmitting node $i \in \{n_w, n_\ell\}$ on a shared unlicensed band $k$ can be indicated as

$$p_{c,i}^{(k)} = 1 - \prod_{\acute{i}\neq i}(1 - p_{\text{tr},\acute{i}}^{(k)}) \prod_{\mathcal{I}/i}(1 - p_{\text{tr},-i}^{(k)}), \tag{8}$$

where $\acute{i} \in \mathcal{W}(\mathcal{L})$, if $i = n_w(n_\ell)$ and $p_{\text{tr},-i}^{(k)} \triangleq \left(p_{\text{tr},j}^{(k)}\right)_{j\neq i}$. The probability of a successful transmission for the transmitting node $i$ on the unlicensed band $k$ can be calculated as

$$p_{s,i}^{(k)} = p_{\text{tr},i}^{(k)} \prod_{\acute{i}\neq i}(1 - p_{\text{tr},\acute{i}}^{(k)}) \prod_{\mathcal{I}/i}(1 - p_{\text{tr},-i}^{(k)}). \tag{9}$$

Accordingly, the successful transmission probability of the whole Wi-Fi and LAA networks on the $k$-th unlicensed channel can be given as $p_{s,\mathcal{W}}^{(k)} = \sum_w p_{s,n_w}^{(k)}$ and $p_{s,\mathcal{L}}^{(k)} = \sum_\ell p_{s,n_\ell}^{(k)}$, respectively. Moreover, the collision probability can be divided into three probabilities, i.e., the collision probability among the Wi-Fi transmissions which is given by

$$p_{c,\mathcal{W}}^{(k)} = (1 - p_{tr,\mathcal{L}}^{(k)})\left[p_{tr,\mathcal{W}}^{(k)} - p_{s,\mathcal{W}_0}^{(k)}\right], \tag{10}$$

the collision probability among the LAA transmissions, i.e.,

$$p_{c,\mathcal{L}}^{(k)} = (1 - p_{tr,\mathcal{W}}^{(k)})\left[p_{tr,\mathcal{L}}^{(k)} - p_{s,\mathcal{L}_0}^{(k)}\right], \tag{11}$$

and the collision probability between the Wi-Fi and the LAA transmission that can be calculated as

$$p_{c,\mathcal{W},\mathcal{L}}^{(k)} = p_{tr,\mathcal{L}}^{(k)} \cdot p_{tr,\mathcal{W}}^{(k)}, \tag{12}$$

where, $p_{tr,\mathcal{L}}^{(k)} = 1 - \prod_{\ell=1}^{L}(1 - p_{\text{tr},n_\ell}^{(k)})$ denotes the LAA's probability of transmission on the $k$-th unlicensed channel and implies that at least one of the $n_L$ eNodeBs transmits a packet, and $p_{tr,\mathcal{W}}^{(k)} = 1 - \prod_{w=1}^{W}(1 - p_{\text{tr},n_w}^{(k)})$ represents the Wi-Fi's transmission probability on the unlicensed channel $k$. The probability of a successful transmission for the LAA eNodeB $n_\ell$ (Wi-Fi AP $n_w$) in an LAA-only (a Wi-Fi only) network is indicated and given by $p_{s,\mathcal{L}_0}^{(k)} = \sum_\ell p_{\text{tr},n_\ell}^{(k)} \prod_{\acute{\ell}\neq\ell}(1 - p_{\text{tr},n_\ell}^{(k)})$ ($p_{s,\mathcal{W}_0}^{(k)} = \sum_w p_{\text{tr},n_w}^{(k)} \prod_{\acute{w}\neq w}(1 - p_{\text{tr},n_{\acute{w}}}^{(k)})$). Therefore, the average duration to support one successful transmission in the unlicensed channel $k$ can be calculated by following the procedures incorporated by $T_{\text{ave}}$ in [11, Eq. (19)]:

$$\begin{aligned} T_{\text{avg}}^{(k)} = {} & (1 - p_{tr}^{(k)})\mathbb{E}\{T_{\text{idle}}^{(k)}\} + p_{s,\mathcal{W}}^{(k)}\mathbb{E}\{T_{s,\mathcal{W}}^{(k)}\} + p_{s,\mathcal{L}}^{(k)}\mathbb{E}\{T_{s,\mathcal{L}}^{(k)}\} \\ & + p_{c,\mathcal{W}}^{(k)}\mathbb{E}\{T_{c,\mathcal{W}}^{(k)}\} + p_{c,\mathcal{L}}^{(k)}\mathbb{E}\{T_{c,\mathcal{L}}^{(k)}\} + p_{c,\mathcal{W},\mathcal{L}}^{(k)}\mathbb{E}\{T_{c,\mathcal{W},\mathcal{L}}^{(k)}\}, \end{aligned}$$

where $T_{s,\mathcal{L}}^{(k)}$, $T_{s,\mathcal{W}}^{(k)}$, $T_{c,\mathcal{W}}^{(k)}$, $T_{c,\mathcal{L}}^{(k)}$, and $T_{c,\mathcal{W},\mathcal{L}}^{(k)}$ indicate the time that the $k$-th channel is being occupied by: an LAA successful transmission, a Wi-Fi successful transmission, a collision among the Wi-Fi transmissions, a collision among the LAA transmissions, and a collision between the Wi-Fi and the LAA transmissions, respectively.

### *B. Impact of sensing threshold*

In a coexistence scenario, the main problem of interest of each transmitting node is to figure out whether or not the unlicensed band is equipped with other active transmitters. Therefore, the detection problem can be formulated based on the following hypothesis tests

$$\begin{cases} \mathcal{H}_0: & \text{Channel is idle} \\ \mathcal{H}_1: & \text{Channel is busy.} \end{cases} \tag{13}$$

In the sensing mechanism, the probabilities of interest include the probability of detection ($P_d = P(T(y) > \eta|\mathcal{H}_1)$) and the probability of false alarm ($P_{fa} = P(T(y) > \eta|\mathcal{H}_0)$), where $y$ is the received signal, $T(y)$ denotes the test statistic of the energy detector, and $\eta$ states the carrier sense threshold level that may vary among different technologies.

In order to maximize both networks' spectral efficiency, selecting the carrier sense threshold level of both systems plays an important role. In a coexistence scenario, the threshold in each system is not only based on the cross-technology false alarm, but also is based on the cross-technology probability of miss-detection since miss-detection leads to the supplementary collisions on the unlicensed band.

**Proposition 2.** *Taking the impact of the sensing thresholds into account, the collision and the successful transmission probabilities of the Wi-Fi AP $n_w$ (LAA eNodeB $n_\ell$) on the shared unlicensed band $k$ can be respectively given as*

$$\begin{aligned} p_{c,n_w}^{(k)} &= p_{c,n_w,\mathcal{W}_0}^{(k)} + p_{tr,\mathcal{L}}^{(k)}(1 - P_{d,\mathcal{W}}(\eta_{\mathcal{W}}))(1 - p_{c,n_w,\mathcal{W}_0}^{(k)}), \\ &= 1 - \left(1 - p_{tr,\mathcal{L}}^{(k)}P_{md,\mathcal{W}}(\eta_{\mathcal{W}})\right) \prod_{\acute{w}\neq w}(1 - p_{tr,n_{\acute{w}}}^{(k)}) \\ p_{c,n_\ell}^{(k)} &= p_{c,n_\ell,\mathcal{L}_0}^{(k)} + p_{tr,\mathcal{W}}^{(k)}(1 - P_{d,\mathcal{L}}(\eta_{\mathcal{L}}))(1 - p_{c,n_\ell,\mathcal{L}_0}^{(k)}) \\ &= 1 - \left(1 - p_{tr,\mathcal{W}}^{(k)}P_{md,\mathcal{L}}(\eta_{\mathcal{L}})\right) \prod_{\acute{\ell}\neq\ell}(1 - p_{tr,n_{\acute{\ell}}}^{(k)}) \\ p_{s,n_w}^{(k)} &= \left(1 - p_{tr,\mathcal{L}}^{(k)}P_{d,\mathcal{W}}(\eta_{\mathcal{W}})\right)p_{tr,n_w}^{(k)} \prod_{\acute{w}\neq w}(1 - p_{tr,n_{\acute{w}}}^{(k)}), \\ p_{s,n_\ell}^{(k)} &= \left(1 - p_{tr,\mathcal{W}}^{(k)}P_{d,\mathcal{L}}(\eta_{\mathcal{L}})\right)p_{tr,n_\ell}^{(k)} \prod_{\acute{\ell}\neq\ell}(1 - p_{tr,n_{\acute{\ell}}}^{(k)}) \end{aligned}$$

*where $p_{c,n_w,\mathcal{W}_0}^{(k)}$ ($p_{c,n_\ell,\mathcal{L}_0}^{(k)}$) states the collision probability of the Wi-Fi AP $n_w$ (LTE-LAA eNodeB $n_\ell$) in a Wi-Fi (LTE-LAA) only network, and $\eta_{\mathcal{W}}$ ($\eta_{\mathcal{L}}$) indicates the Wi-Fi (LAA) carrier sensing threshold level. This modification is due to the fact that the inaccuracy in detecting the Wi-Fi APs by the LAA eNodeBs ensues the supplementary collisions on the unlicensed band, and vice versa.*

*Proof.* In order to capture the effect of miss-detection probability (in sensing the LAA users) on the performance of the Wi-Fi network, we show that the collision probability consists of the sensing threshold level, by rewriting (8) as follows

$$\begin{aligned} p_{c,n_w}^{(k)} &= p_{tr,\mathcal{L}}^{(k)} \prod_{\acute{w}\neq w}(1 - p_{\text{tr},n_{\acute{w}}}^{(k)}) + 1 - \prod_{\acute{w}\neq w}(1 - p_{\text{tr},n_{\acute{w}}}^{(k)}) \\ &= p_{tr,\mathcal{L}}^{(k)}(1 - p_{c,n_w,\mathcal{W}_0}^{(k)}) + p_{c,n_w,\mathcal{W}_0}^{(k)} \end{aligned}$$

Mosleh, Somayeh; Ma, Yao; Coder, Jason; Perrins, Erik; Liu, Lingjia.
"Enhancing LAA Co-existence Using MIMO Under Imperfect Sensing."
Paper presented at 2019 IEEE Global Communications Conference: Workshop on Advancements in Spectrum Sharing, Waikoloa, HI, United States. December 13, 2019 - December 13, 2019.

since the inaccuracy in detecting the LAA eNodeBs by the Wi-Fi APs ensues the supplementary collisions on the unlicensed band, we multiply $p_{tr,\mathcal{L}}^{(k)}$ with the probability of cross-technology miss-detection $P_{md,\mathcal{W}} = 1 - P_{d,\mathcal{W}}$ to capture the impact of the sensing threshold in calculating $p_{c,n_w}^{(k)}$. Following the same approach, the other probabilities can be calculated. ■

**Proposition 3.** *Taking the impact of imperfect sensing on the MAC layer performance into account, the collision probability discerned by the Wi-Fi AP $n_w$ (caused by the LAA transmission) in the $k$-th unlicensed band is a function of cross-technology probability of detection, Wi-Fi's transmission probability, and LAA's transmission probability, and can be revised as follows*

$$p_{c,n_w}^{(k)} = (1 - P_{d,\mathcal{L}}^{(k)}) Pr\{\phi_k = 1 | \psi_k = 0, \theta_k = 1\} + P_{d,\mathcal{L}}^{(k)} Pr\{\phi_k = 1 | \psi_k = 1, \theta_k = 1\}$$

*where $\phi_k$, $\psi_k$, and $\theta_k$ denote the channel access decision (0: no access and 1: access), the sensing outcome (0: idle and 1: busy), and the channel status (0: idle and 1: busy) of the $k$-th unlicensed band.*

*Proof.* The collision probability discerned by the Wi-Fi AP $n_w$ in the $k$-th unlicensed band can be determined as

$$\begin{aligned} p_{c,n_w}^{(k)} &= \Pr\{\phi_k = 1 | \theta_k = 1\} \\ &= \Pr\{\psi_k = 0 | \theta_k = 1\} \Pr\{\phi_k = 1 | \psi_k = 0, \theta_k = 1\} \\ &\quad + \Pr\{\psi_k = 1 | \theta_k = 1\} \Pr\{\phi_k = 1 | \psi_k = 1, \theta_k = 1\}, \end{aligned}$$

where $\Pr\{\phi_k = 1 | \psi_k = 0, \theta_k = 1\} = \left(p_{tr,\mathcal{L}}/(1 - P_{d,\mathcal{L}}) \cdot p_{tr,\mathcal{W}}\right) \cdot \Pr\{\psi_k = 0, \theta_k = 1 | \phi_k = 1\}$. ■

## V. Simulation Evaluations

In this preliminary numerical evaluation, we evaluate the performance of the proposed scheme in a coexistence scenario. The setup of parameters is given in Table II, as in [6] and [11].

Fig. 2 shows the normalized throughput of both LAA and Wi-Fi networks for the different numbers of APs and eNodeBs. As the number of transmitters in each network gets bigger, the overall throughput of that network increases. However, there is a tradeoff between increasing the number of transmitters in one network and maintaining the desired throughput of the other network. Specifically, the throughput of LAA will decrease if the number of APs increases in the network. The Wi-Fi throughput follows the same trend.

The normalized throughput of LAA versus the minimum contention window size of LAA and Wi-Fi are demonstrated in Figures 3 and 4. It is observed that the larger the contention window size of the Wi-Fi, the better throughput can be obtained at the LAA network. However, by increasing the contention window size of the LAA, the LAA throughput increases until some point and then starts decreasing. It can be interpreted as follows: as CW increases the channel is less crowded and the chances of collision are low, however, setting

TABLE II: PHY/MAC Layer Parameters

| Parameter | value |
|---|---|
| LAA's packet payload duration | 2 ms |
| Wi-Fi's packet payload duration | 1 ms |
| Mac header | 272 bits |
| PHY header | 128 bits |
| ACK | 112 bits + PHY header |
| SIFS | 16 $\mu$s |
| DIFS | 34 $\mu$s |
| Slot time | 9 $\mu$s |
| eNodeB transmit power | 30 dBm |
| AP transmit power | 24 dBm |
| Noise figure | 9 dB |
| Thermal noise | -174dBm/Hz |
| Path loss model | COST-231 Hata model [12] |
| Shadowing standard deviation | 8 dB |

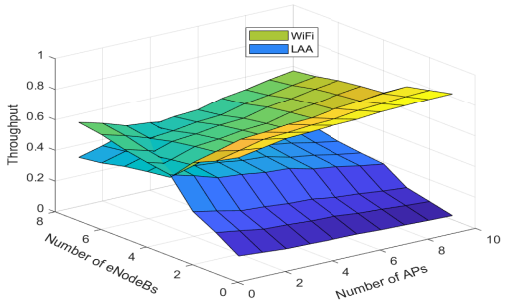


Fig. 2: Normalized Throughput of both LAA and Wi-Fi networks.

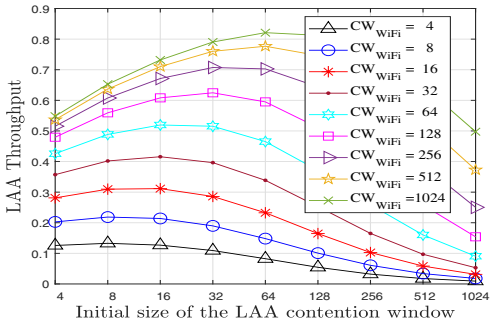


Fig. 3: LAA throughput versus $\text{CW}_{LAA}$.

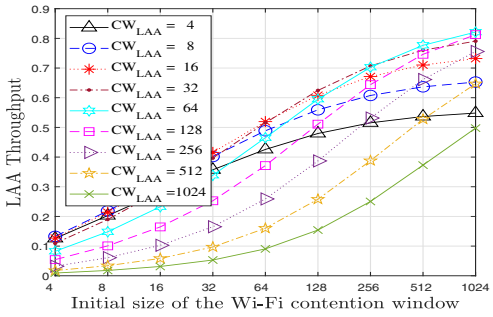


Fig. 4: LAA throughput versus $\text{CW}_{Wi-Fi}$.

Mosleh, Somayeh; Ma, Yao; Coder, Jason; Perrins, Erik; Liu, Lingjia.
"Enhancing LAA Co-existence Using MIMO Under Imperfect Sensing."
Paper presented at 2019 IEEE Global Communications Conference: Workshop on Advancements in Spectrum Sharing, Waikoloa, HI, United States. December 13, 2019 - December 13, 2019.

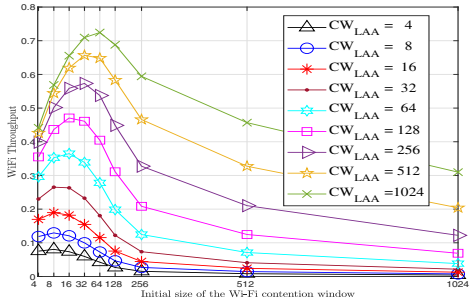


Fig. 5: Wi-Fi throughput versus $\text{CW}_{Wi-Fi}$.

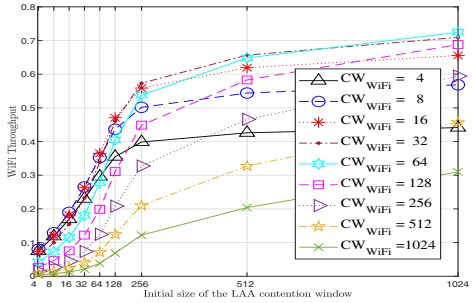


Fig. 6: Wi-Fi throughput versus $\text{CW}_{LAA}$.

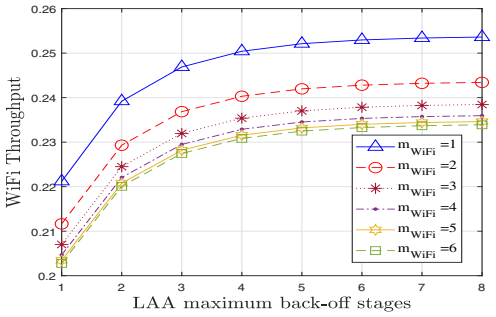


Fig. 7: Wi-Fi throughput versus $m_{LAA}$.

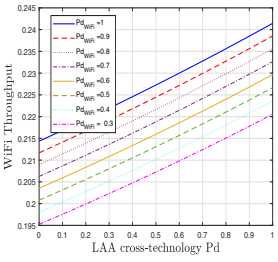


Fig. 8: Wi-Fi throughput versus $P_{d,\mathcal{L}}$.

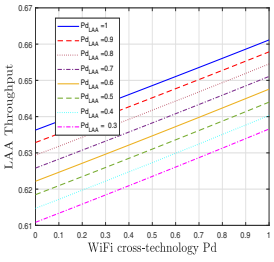


Fig. 9: LAA throughput versus $P_{d,\mathcal{W}}$.

up the CW to a large value minimizes the channel access probability and reduces the network throughput. Figures 5 and 6 plot the Wi-Fi throughput versus the Wi-Fi and the LAA minimum contention window size and follows the same trend as the LAA throughput.

The effect of the LAA maximum backoff stage on the Wi-Fi throughput is investigated in Figure 7. As shown, the larger the LAA maximum backoff stage, the larger Wi-Fi throughput can be achieved.

Figures 8 and 9 demonstrate the impact of the cross-technology probability of detection on the network throughput. The results can be interpreted as follows: the probability of detection (miss-detection) plays a critical role in computing the network throughput. When $P_d$ approaches zero, the performance decreases. However, increasing $P_d$ significantly increases both networks' throughput.

## VI. Conclusion

In this paper, we studied the MAC-layer performance of the LAA and Wi-Fi networks by considering the contribution of both MAC and PHY layers characteristics. By taking the impact of imperfect sensing into account, we analyzed each network's KPIs, such as throughput, and probabilities of succcessful transmissions and collisions. By maximizing the LAA throughput while assuring Wi-Fi throughput above a predetermined threshold, the optimum LAA contention size was found. Numerical results demonstrate that efficiently selecting the MAC-layer and PHY-layer parameters greatly influences the network throughput of both systems.

## References


[1] "Cisco visual networking index: Global Mobile Data Traffic Forecast Update, 2017-2022 White Paper," *Cisco Systems*, Feb. 2019.

[2] S. Mosleh, J. D. Ashdown, J. D. Matyjas, M. J. Medley, J. Zhang, and L. Liu, "Interference alignment for downlink multi-cell LTE-Advanced systems with limited feedback", *IEEE Trans. Wireless Commun.*, vol. 15, no. 12, pp. 8107-8121, Dec. 2016.

[3] S. Mosleh, L. Liu, Y. Li, and J. Zhang, "Interference alignment and leakage-based iterative coordinated beam-forming for multi-user MIMO in LTE-Advanced", *IEEE GC Wkshps*, Dec. 2015.

[4] FCC White Paper, "The mobile broadband spectrum challenge: international comparisons", *Wireless Telecommunications Bureau Office of Engineering and Technology*, Washington, DC, Feb. 2013.

[5] S. Boyd and L. Vandenberghe, "Convex optimization", Cambridge, U.K. Cambridge Univ. Press, 2004

[6] R. Yin, G. Yu, A. Maaref, and G. Y. Li, "A framework for co-channel interference and collision probability tradeoff in LTE licensed-assisted access networks", *IEEE Trans. Wireless Commun.*, vol. 15, no. 9, pp. 6078-6090, Sep. 2016.

[7] A. Babaei, J. Andreoli-Fang, Y. Pang, and B. Hamzeh, "On the impact of LTE-U on Wi-Fi performance," *Int. J. of Wireless Inf. Netw.*, vol. 22, issue 4, pp. 336–344, Dec. 2015.

[8] E. Perahia and R. Stacey, "Next generation wireless LANs: 802.11n and 802.11ac," Cambridge, U.K. Cambridge Univ. Press, June 2013.

[9] "Study on Licensed-Assisted Access to Unlicensed Spectrum (Release 13)", *3GPP TR 36.889 V13.0.0*, June 2015.

[10] G. Bianchi, "Performance analysis of the IEEE 802.11 distributed coordination function," *IEEE J. Sel. Areas Commun.*, vol. 18, no. 3, pp. 535-547, Mar. 2000.

[11] Y. Ma and D. G. Kuester, "MAC-layer coexistence analysis of LTE and WLAN systems via listen-before-talk," *IEEE Ann. Consum. Commun. & Netw. Conf.*, pp. 534-541, Jan. 2017.

[12] COST Telecom Secretariat, "Digital mobile radio toward future generation system: COST 231 final report," *Brussels: European COST Action 231*, 1999.



Mosleh, Somayeh; Ma, Yao; Coder, Jason; Perrins, Erik; Liu, Lingjia.
"Enhancing LAA Co-existence Using MIMO Under Imperfect Sensing."
Paper presented at 2019 IEEE Global Communications Conference: Workshop on Advancements in Spectrum Sharing, Waikoloa, HI, United States. December 13, 2019 - December 13, 2019.